

**UNIVERSITY/NETL STUDENT PARTNERSHIP PROGRAM
(DE-FC26-98FT40143)**

3rd Year Technical Report

September 1, 2000 – August 31, 2001

Submitted to:

National Energy Technology Laboratory

Submitted by:

**Gerald D. Holder
School of Engineering
University of Pittsburgh
Pittsburgh, PA 15261**

Volume I of VI

TABLE OF CONTENTS

	<u>Page</u>
Table of Contents.....	i
Executive Summary.....	1
University/NETL Student Partnership Program 4th Annual Meeting Agenda	3
Reports	
I. “Novel Amine Enriched Sorbents for CO ₂ Capture” Robert Stevens, Jr. (S) and Steven Chuang (F), University of Akron with Yee Soong (M), NETL.	
II. “Computation of Solids Transport Using Hypoplasticity Theory” Yong Cao (S), Carnegie Mellon University, and Jayathi Murthy (F), Purdue University with Thomas O’Brien (M), NETL.	
III. “Modeling and Simulation of Granular Flows” Dhanunjay Boyalakuntla (S), Carnegie Mellon University, and Jayathi Murthy (F), Purdue University with Thomas O’Brien (M), NETL.	
IV. “Microstructure and the Thermophysical Properties of Ash Deposits” Soon Kweon (S) and Allen Robinson (F), Carnegie Mellon University with Everett Ramer (M), NETL.	
V. “Density Functional Theory Study of Iodine Chemisorption on Chiral Metal Surfaces” Preeti Kamakoti (S) and David Sholl (F), Carnegie Mellon University with Brad Bockrath (M), NETL	
VI. “Oxidative Desulfurization of Fuels Through TAML [®] Activators and Hydrogen Peroxide” Yelda Hangun (S) and Terrance Collins (F), Carnegie Mellon University with Mark McDonald(M), NETL.	
VII. “Hydrate Formation and Dissociation in Porous Media – An Experimental Study” Timothy White (S) and Goodarz Ahmadi (F), Clarkson University with Duane Smith (M), NETL.	
VIII. “Computational Modeling of Carbon Dioxide Sequestration” Ali Reza Mazaheri (S) and Goodarz Ahmadi (F), Clarkson University with Duane Smith (M), NETL.	

- IX. “Experimental Study of Immiscible Two-Phase Flows In a Two-Dimensional Flow Cell”
Chuang Ji (S) and Goodarz Ahmadi (F), Clarkson University with
Duane Smith (M) and T. Robert McLendon, NETL.
- X. “Application of Computational Fluid Mechanics to Design of Industrial Filter Vessels”
Chaosheng Liu (S) and Goodarz Ahmadi (F), Clarkson University with
Duane Smith (M), NETL.
- XI. “Distribution of Porosity in an Artificially-Induced Tensile Fracture and Its Relationship
to the Surrounding Matrix”
Claudia Parada (S), Abraham Grader (F), The Pennsylvania State University with
Duane Smith (M), NETL.
- XII. “A Real-time State Estimation of the Standpipe of a Circulating Fluidized Bed using an
Extended Kalman Filter”
Hoowang Shim (S) and Parviz Famouri (F), West Virginia University with
Edward Boyle (M), NETL.
- XIII. “Experimental Investigation of Oscillatory Heat Release Mechanisms and Stability
Margin Analysis in Lean-Premixed Combustion”
Don Ferguson (S) and Mridul Gautam (F), West Virginia University with
George Richards (M), NETL.
- XIV. “Particle-Wall Shear Stress Measurements within the Standpipe of a Circulating
Fluidized Bed”
Angela Sarra (S) and Aubrey L. Miller (F), West Virginia University with
Lawrence Shadle (M), NETL.
- XV. “Application Evaluation of a Prototype Backscatter Imaging LDV system (BILS)”
Preetanshu Pandey (S) and Richard Turton (F), West Virginia University with
Lawrence Shadle (M), NETL.
- XVI. “Transient Modeling of a Gas Turbine in a Hybrid System Including a Fuel Cell”
Emre Tatli (S), Daniel DeFede and Ismail Celik (F), West Virginia University with
Randy Gemmen (M), NETL.
- XVII. “Synthesis of Methane Gas Hydrate in Porous Sediments and Its Dissociation by
Depressurizing”
Feng Song (S), Sridhar Narasimhan (S), and H.O. Kono (F), West Virginia University
with
Duane Smith (M), NETL.
- XVIII. “Mapping Acid Mine Drainage with Remotely Sensed Data”
Jennifer Shogren (S) and Thomas Wilson (F), West Virginia University with
Terry Ackman (M), NETL.

- XXIX. “Modeling and Control of Circulating Fluidized Bed using Neural Networks”
Amol Patankar (S), Praveen Koduru (S) and Asad Davari (F),
West Virginia University Institute of Technology with
Lawrence Shadle (M) and Larry Lawson (M), NETL.
- XX. “Formation of Carbon Dioxide Hydrates from Single-Phase Aqueous Solutions”
Lakshmi Mokka (S) and Gerald Holder (F), University of Pittsburgh with
Robert Warzinski (M), NETL.
- XXI. “A Geophysical Investigation and Stream Grouting Trial at Streamflow Loss Zones in
Headwater Reach of Nanticoke Creek, Luzerne County, Pennsylvania”
Robert Dilmore (S), Ronald Neufeld (F), and Kathi Beratan (F), University of Pittsburgh
with Terry Ackman (M), NETL.
- XXII. “Passive Treatment of Coal Mine Drainage and Characterization of Iron-Rich Precipitates
Associated with Coal Mine Drainage”
Candace Kairies (S) and Rosemary Capo (F), University of Pittsburgh with
George Watzlaf (M), NETL.
- XXIII. “Preliminary Results on the Kinetic Study of the Homogeneous Non-Catalytic High-
Temperature, High- Pressure Water Gas Shift Reaction”
Filipe Bustamante (S) and Robert Enick (F), University of Pittsburgh with
Kurt Rothenberger (M), NETL.
- XXIV. “Phase Transitions of Adsorbed Fluids Computed for Multiple Histogram Reweighting”
Wei Shi (S) and Karl Johnson (F), University of Pittsburgh with
Brad Bockrath (M), NETL.
- XXV. “Strontium Isotopic Tracers as Indicators of AMD Provenance and Abatement
Efficiency”
Barbara Homison (S) and Brian Stewart (F), University of Pittsburgh with
Ann Kim (M), NETL.
- XXVI. “Chemistry of Coal Seam Sequestration of Carbon Dioxide”
Ekrem Ozdemir (S) and Badie Morsi (F), University of Pittsburgh with
Karl Schroeder (M), NETL.
- XXVII. “CFD Simulation of Slurry Bubble Column”
Jonghwun Jung (S) and Dimitri Gidaspow (F), Illinois Institute of Technology with
Isaac Gamwo(M), NETL.

Executive Summary

The University/National Energy Technology Laboratory (NETL) Student Partnership Program provides graduate student support for research for least 20 hours per week at an NETL facility under the joint supervision of NETL and university faculty. Twenty-nine projects were funded in the program's 3rd year with several universities receiving multiple awards, and three new universities, University of Akron, Pennsylvania State University, and University of Texas – Austin, joining the program. A summer student from Illinois Institute of Technology was also supported summer through the University of Pittsburgh.

Participating universities for the 3rd year of this program were, University of Akron, Carnegie Mellon University, Clarkson University, Pennsylvania State University, West Virginia University, West Virginia University Institute of Technology, University of Texas–Austin, and the University of Pittsburgh, with the latter serving as the Lead University for administration of the program. Each project received \$30,000 for graduate student support, except the West Virginia University Institute of Technology, which split one award with West Virginia University, and the University of Texas, which received a partial award for summer support of a student.

The 4th Annual Meeting and lunch were held at NETL-Pittsburgh on November 1, 2001 with faculty, students and NETL personnel in attendance. Each university faculty, student, or NETL mentor presented an overview of his or her research topics. Larry Headley, Associate Director of the Office of Science and Technology at NETL also presented NETL's and the OTC's perspective for the program. New participants for the 4th year of the program also presented an overview of their proposed projects. The meeting agenda is attached.

The 3rd Year awards – and their university faculty (F), students (S) and NETL mentor (M) – were:

University of Akron

Steven Chuang (F), Robert Stevens, Jr. (S) and Yee Soong (M)

Carnegie Mellon University

Jayathi Murthy (F), Yong Cao (S) and Thomas O'Brien (M)

Jayathi Murthy (F), Dhanunjay Boyalakuntla (S) and Thomas O'Brien (M)

Allen Robinson (F), Soon Kweon (S) and Everett Ramer (M)

Terry Collins (F), Yelda Hangun (S) and Mark McDonald (M)

David Sholl (F), Preeti Kamakoti (S) and Brad Bockrath (M)

Clarkson University

Goodarz Ahmadi (F), Timothy White (S) and Duane Smith (M)

Goodarz Ahmadi (F), Ali Reza Mazaheri (S) and Duane Smith (M)

Goodarz Ahmadi (F), Chuang Ji (S) and Duane Smith (M)

Goodarz Ahmadi (F), Chaosheng Liu (S) and Isaac Gamwo (M)

Pennsylvania State University

Abraham Grader (F), Claudia Parada (S) and Duane Smith (M)

West Virginia University

Parviz Famouri (F), Hoowang Shim (S), Edward Boyle (M) and
Lawrence Shadle (M)

Mridul Gautam (F), Don Ferguson (S), and George Richards (M)

H.O. Kono (F), Feng Song (S), and Duane Smith (M)

Richard Turton (F), Vijay Iyer (S), Matthew Honaker (S) and Dave Berry (M)

Aubrey Miller (F), Richard Turton (F), Angela Sarra (S), Preetanshu Pandey (S)
and Lawrence Shadle (M)

Ismail Celik (F), Daniel DeFede (S), Emre Tatli (S) and Randy Gemmen (M)

Thomas Wilson (F), Jennifer Shogren (S), and Terry Ackman (M)

John Zondlo (F), James Bowers (S) and Brad Bockrath (M)

West Virginia University Institute of Technology

Asad Davari (F), Sridar Macha (S), Rammohan Sankar (S),
Edward Boyle (M) and Lawrence Shadle (M)

University of Pittsburgh

Gerald Holder (F), Lakshmi Mokka (S), and Robert Warzinski (M)

Kathi Beratan (F), Robert Dilmore (S) and Terry Ackman (M)

Rosemary Capo (F), Candace Kairies (S) and George Watzlaf (M)

Ronald Neufeld (F), Robert Cimmaroli (S) and Ann Kim (M)

Badie Morsi (F), Ekrem Ozdemir (S) and Karl Schroeder (M)

Karl Johnson (F), Wei Shi (S), and Brad Bockrath (M)

Robert Enick (F), Felipe Bustamante (S), and Kurt Rothenberger (M)

Brian Stewart (F), Barabara Homison (S), and Ann Kim (M)

Gerald Holder (F), Dimitri Gidaspow (F – Illinois Institute of Technology),
Jonghwun Jung (S), and Isaac Gamwo (M).

University of Texas – Austin

Gary Pope (F), Vikas Vikas (S), and Duane Smith (M)

Attached are the 3rd year technical reports submitted by each participant. A report was not submitted by Mridul Gautam at West Virginia University.

Session I (continued)

- 12:45** “Evaluation of Combustion Instabilities in Lean-Premixed Combustion”
WVU: Mridul Gautam(F), Don Ferguson(S)
NETL: George Richards(M)
- 1:00** “Neural Network Control of Circulating Fluidized Bed” – new project
WVUITech: Asad Davari(F), Amol Patanka(S)
NETL: Lawrence Shadle(M)
- 1:10** “Modeling of Circulating Fluidized Bed with Neural Networks” – new project
WVUITech: Asad Davari(F), Proveen Koduru(S)
NETL: Lawrence Shadle(M)
- 1:20** “Developing Constitutive Relations for Mixtures Using the Multiple Natural Configurations Theory”
– new project
Texas A&M: K.R. Rajagopal(F), Mohan Anand(S), and Parag Ravindran(S)
NETL: Mehrdad Massoudi(M)
- 1:30** “Micromechanics of Granular Materials” – new project
Tulane: M.M. Mehrabadi(F), Huaning Zhu(S)
NETL: Mehrdad Massoudi(M)
- 1:40** “CFD Simulation of Slurry Bubble Column” – new project
IIT: Dimitri Gidaspow(F), Jonghwun Jung(S)
NETL: Isaac Gamwo(M)
- 1:50** **Break**
- 2:00** “Carbon Fibers Derived from Coal” – new project
WVU: John Zondlo(F), James Bowers(S)
NETL: Brad Bockrath(M)
- 2:10** “Gas-Water Shift Reaction – Membrane Reactor”
Pitt: Robert Enick(F), Felipe Bustamante(S)
NETL: Kurt Rothenberger(M)
- 2:25** “First Principles Studies of CuPd Alloys as Hydrogen-Selective Membranes”
CMU: David Sholl(F), Preeti Kamokoti(S)
NETL: Brad Bockrath(M)
- 2:45** “A Simulation of Ash Deposit Structure and Thermal Property in Utility Boilers”
CMU: Allen Robinson(F), Soon Kweon(S)
NETL: *Everett Ramer(M)*
- 3:00pm** **Closing Remarks** – Gerald Holder, Pitt

GROUP PHOTO

Presenter, (F) faculty, (S) student, and (M) mentor.

Session II

- 10:00am** **Welcome/Opening Remarks** – Gerald Holder, Dean of Engineering, University of Pittsburgh
– Michael Nowak, National Energy Technology Laboratory (NETL)
- 10:10** **NETL Perspective** – Larry Headley, Associate Director, Office of Science and Technology, NETL
- 10:30** "Experimental and Computational Studies of Fluid Flow Phenomena in Carbon Dioxide Sequestration in Brine and Oil Fields"
Clarkson: Goodarz Ahmadi(F), Chuang Ji(S)
NETL: Duane Smith(M), Robert McLendon(M)
- 10:45** "Computational Modeling Carbon Dioxide Sequestration"
Clarkson: Goodarz Ahmadi(F), Alireza Mazaheri(S)
NETL: Duane Smith(M)
- 11:00** "Hydrate Formation and Dissociation in a Porous Media – An Experimental Study"
Clarkson: Goodarz Ahmadi(F), Timothy White(S)
NETL: Duane Smith(M)
- 11:15** "Production of Natural Gas Associated with Hydrates: Formation and Dissociation of Methane Gas Hydrate (MGH) and Some Preliminary Experimental Work on Propane Gas Hydrate (PGH)"
WVU: H.O. Kono(F), Feng Song(S)
NETL: Duane Smith(M), Robert McLendon (M)
- 11:30** "Fracture-Flow Matrix"
PSU: Abraham Grader, Claudia Parada(S)
NETL: Duane Smith(M)
- 11:40** "Properties of Natural Gas Hydrates" – new project
Pitt: Gerald Holder(F), Eilis Rosenbaum(S)
NETL: Robert Warzinski(M)
- 11:50** "A Comprehensive Equation of State" – new project
WVU: Joseph Wilder(F), Justin Korona(S)
NETL: Duane Smith(M)
- 12:00** **Break/Lunch (provided)**
- 12:30** "Mapping Acid Mine Drainage with Remotely Sensed Data"
WVU: Thomas Wilson(F), Jennifer Shogren(S)
NETL: Terry Ackman(M)

Presenter, (F) faculty, (S) student, and (M) mentor.

Session II (continued)

- 12:45** "Passive Treatment of Mine Drainage and Characterization of Iron-Rich Coal Mine Drainage Precipitates"
Pitt: Rosemary Capo(F), Candace Kairies(S)
NETL: George Watzlaf(M)
- 1:00** "The Use of Strontium Isotope Ratios to Determine the Source of Mine Drainage"
Pitt: Brian Stewart(F), Barbara Hamel(S)
NETL: Ann Kim(M)
- 1:15** "Biological Flue Gas Treatment" – new project
Pitt: Ronald Neufeld(F), Robert Dilmore(S)
NETL: Richard Hammack(M)
- 1:25** "Compositional Modeling of Multi-Component Gas Transport in Coal Seams" – new project
PSU: Turgay Ertekin(F), Olefumi Odusote(S)
NETL: Mara Dean(M)
- 1:35** "X-Ray Tomography of Carbon Dioxide Sequestration in Coal" – new project
PSU: Jonathan Mathews (F), TBD(S)
NETL: Karl Schroeder(M)
- 1:45** **Break**
- 1:55** "Chemistry of Coal Seam Sequestration of Carbon Dioxide"
Pitt: Badie Morsi(F), Ekrem Ozdemir(S)
NETL: Karl Schroeder(M)
- 2:10** "Oceanic CO₂ Sequestration Research"
Pitt: Gerald Holder(F), Lakshmi Mokka(S), Yi Zhang(S)
NETL: Robert Warzinski(M)
- 2:25** "Novel Amine Enriched Sorbents for CO₂ Capture"
Akron: Steven Chuang(F), Robert Stevens, Jr.(S)
NETL: Yee Soong(M)
- 2:45** "Hydrogen Storage on Novel Carbonaceous Sorbents"
Pitt: Karl Johnson(F), Wei Shi(S)
NETL: Brad Bockrath(M)
- 3:00pm** **Closing Remarks** – Gerald Holder, Pitt

GROUP PHOTO

Presenter, (F) faculty, (S) student, and (M) mentor.

I. “Novel Amine Enriched Sorbents for CO₂ Capture”

**Robert Stevens, Jr. (S) and Steven Chuang (F), University of Akron
with
Yee Soong (M), NETL**

Amine Enriched Solid Sorbents for Carbon Dioxide Capture

University Partnership Program Report (2001)

Robert Stevens, Jr., Rajesh Khatri, Chen-Chang Chang, and Steven Chuang
Department of Chemical Engineering, University of Akron, Akron, OH 44325-3906

Yee Soong and McMahan Gray
U.S. Department of Energy, National Energy Technology Laboratory, Pittsburgh, PA 15236

Table of Contents

List of Tables	1
List of Figures	1
Introduction	2
Experimental	3
Apparatus	3
Calibration	4
Adsorption	4
Desorption/Regeneration	5
Results and Discussion	5
Total Capture	7
Conclusions	10
References	16

List of Tables

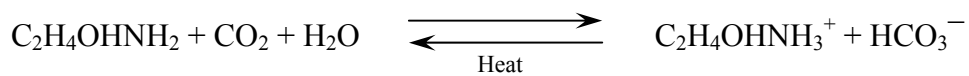
Table 1. CO ₂ capture capacities of recent sorbents operated under an air-containing atmosphere tested via the adsorption/desorption scheme	7
Table 2. Total CO ₂ capture amounts and the respective breakdown of chemisorbed and physisorbed species	10

List of Figures

Figure 1. Experimental Apparatus	11
Figure 2. DRIFTS analysis of CO ₂ adsorption over commercial sample SA9T	12
Figure 3. DRIFTS analysis of the CO ₂ temperature programmed desorption (regeneration) of commercial sample SA9T	13
Figure 4. MS analysis of the CO ₂ temperature programmed desorption (regeneration) of commercial sorbent SA9T	14
Figure 5. MS analysis during the adsorption of CO ₂ onto commercial sample SA9T using	15

Introduction

CO₂ is a green house gas and has been identified as one of the primary contributors to global warming. There has been much research in new methods to utilize and/or capture CO₂ in order to decrease its concentration in the atmosphere. Industrial flue gases alone contributed to 25% of the global CO₂ emission in the 1980's; this correlates to 14% of the estimated global warming. Current technologies used for CO₂ capture of these industrial flue gases are often based on aqueous amine solutions. These processes generally contain monoethanolamine (MEA), diethanolamine (DEA), or methyldiethanolamine (MDEA) as the amine source to capture CO₂. This wet chemical stripping of CO₂ involves reversible reactions which may be regenerated through the application of heat:



These process are generally very energy intensive and the adsorption of CO₂ is effected by the availability of the gas/liquid interaction surface. The capacity of these sorbents are normally low and therefore require a large volume of liquid to capture a small amount of CO₂. Other problems that plague this technology include degradation of the sorbent due to oxidation and corrosion to the process equipment.

Forming a CO₂ sorbent from a solid material has advantages. The mass transfer limitation of the process is greatly reduced due to the large gas/solid interface available. This may lead to a much greater capacity than in the related liquid system. There has been much research recently in the design of solid, amine-based, CO₂ sorbents.¹⁻⁴ The objective of our

research is to develop a novel amine enriched sorbent for the capture of CO₂ from industrial flue gas streams.

Experimental

Apparatus

All CO₂ sorbent samples were provided by the National Engineering and Technology Laboratory (NETL) for analysis. Their chemical preparation, as well as their composition will not be discussed for confidential reasons. Prior to their analysis, each sample was loaded into the experimental system and was “activated” in situ by purging the sample with He for 2 h at room temperature to remove any contaminants from its surface.

Figure 1 displays the experimental system. It consists of three sections: (i) a gas metering section, (ii) a reactor section, and (iii) an effluent gas analysis section. The gas metering section consists of Brooks 5850 mass flow controllers (not shown) and a water saturator, which delivers controlled gas flows to the reactor system. The reactor system consists of an in situ diffuse reflectance infrared Fourier transform spectroscopy (DRIFTS) reactor (Spectra-Tech, Inc.), which is situated inside of an IR bench (Nicolet Magna 560). The effluent section is analyzed via a quadrupole mass spectrometer (Pfeiffer QMS 200). This arrangement allows one to study the dynamics of the sorbent surface, its adsorbates, and the effluent composition during the course of the reaction study.

For each experiment, approximately 300 mg of sorbent was used. 20 mg was placed into the DRIFTS reactor and the remaining 280 mg were loaded into a tubular reactor connected downstream of the DRIFTS – increasing the total capture. All spectra were collected at a resolution of 4 cm⁻¹ and were a result of 32 coadded scans. Throughout all experiments, total gas flow rates were maintained at 30 cm³/min. Species monitored via the Pfeiffer QMS 200 mass

spectrometer (MS) system were CO₂, CO, O₂, ammonia, and H₂O corresponding to m/e values of 44, 28, 32, 17, and 18, respectively.

The 4-port valve allows for a rapid switch between the sweeping stream (Stream A) and the adsorption stream (Stream B) to the sorbent system. Water was introduced to the system through use of a saturator; the inlet flow stream (He/Air or CO₂/Air/He) was redirected into the saturator through a pair of inter-connected 3-way valves. The saturator was maintained at room temperature, yielding a water vapor pressure of 22.5 mmHg.

Calibration

In order to quantitatively measure the capture capacity of the sorbents, it is first necessary to calibrate the mass spectrometer (MS). This is accomplished by pulsing known volumes of CO₂ into flowing He directly to the MS via a six-port valve equipped with a 1-cm³ pulse loop (omitted from Figure 1 for clarity) prior to each experiment (1 cm³ = 40.9 μmol). Several pulses are conducted; an average area is recorded. The calibration factor is then calculated in units of μmol/area; thereby permitting us to calculate the amount of CO₂ desorbed from the sorbent's surface in the following stages of the experiment.

Adsorption

Following the purge of the sorbent surface, the sorbent system is heated to 30 °C in preparation of the CO₂ adsorption. The surface is then “conditioned” with moisture for 15 – 20 minutes via redirecting the He/air flow into the water saturator. Adsorption is initiated via a rapid switch of Streams A & B (See Figure 1) through use of the 4-port valve. Both IR (DRIFTS) and MS data are concurrently collected continuously during this procedure. The surface of the sorbent is exposed to the adsorption stream for approximately 20 minutes to fully

saturate it. After the surface is saturated, the adsorption stream is replaced once again by the sweeping stream to purge the extraneous, gaseous CO₂ from the sorbent system.

Desorption/Regeneration

Following the gaseous CO₂ purge, water flow was halted by redirecting the sweeping stream (Stream A) through the saturator bypass. Both the DRIFTS and the tubular reactor are heated simultaneously from 30 °C to 120 °C at a rate of 10 °C/min. As in the CO₂ adsorption step, this procedure is monitored with both IR and MS throughout the experiment.

Results and Discussion

The adsorption of CO₂ onto an amine surface can be classified as an acid-base interaction; the amine serves as the base whereas the CO₂ is the acid. In order for a sorbent to be effective, its basicity should be moderate. If its basicity is too weak, no CO₂ will be captured. On the other hand, if the basicity is too high, much CO₂ will be captured; however, it cannot be desorbed – complicating regeneration. The ability of a sorbent to be regenerated is as important as its ability to capture CO₂.

Since our initial investigation last year, we have decided to use air in the flow streams to mimic the condition that would be used in a realistic application of the sorbent. It was necessary to still include He as a major component of the flow stream due to the adverse effect that O₂ can have on the filament of the mass spectrometer. It was initially believed that air may oxidize the sorbent and render it less effective – in actuality, some samples were somewhat degraded in their performance whereas others were somewhat enhanced when comparing the results of a sample under a He environment versus that of air/He. Only the results of the sorbents tested under the

air-containing atmosphere will be presented here. The results of those samples tested under He only are omitted for simplicity.

We have chosen a commercial sample, SA9T, as a basis to compare the performance of the samples that we studied.⁵ The goal of this research is to match or better the performance of this commercial sample.

Figure 2 illustrates the DRIFTS analysis of CO₂ adsorption over the SA9T commercial sample. Times indicated are relative to the time of the step switch from He/air to CO₂/He/air. Initially, a vibration is present at approximately 1650 cm⁻¹, which is due to H₂O (HOH bending vibration). As the sorbent is exposed to CO₂, three bands emerge concurrently and grow with time: 1562, 1413, and 1311 cm⁻¹. The vibrations at 1562 cm⁻¹ and 1413 cm⁻¹ suggest the presence of carboxylate CO₂⁻ on the surface^{6,7}; the presence of the three bands together may also be attributed concurrent presence of both monodentate carbonate and bidentate carbonate with overlapping contributions.

The DRIFTS analysis of the regeneration/desorption of the SA9T sample is shown in Figure 3. Upon heating, H₂O is evolved, as indicated by the growth of the broad region between 3000 – 3700 cm⁻¹ as well as the vibration at 1650 cm⁻¹. Increasing the temperature from 70 °C to 90 °C caused most of the adsorbed CO₂ species to desorb. The surface is returned back to its original condition after holding for several minutes at 120 °C as suggested by the last spectrum; its flat profile indicates that the CO₂ species were removed as well as all traces of H₂O are no longer present. The mass spectral analysis of the sorbent regeneration by temperature programmed desorption is shown in Figure 4, displaying the output of the CO₂ signal (m/e = 44) versus temperature. As the sample is heated from 30 °C to 120 °C, a large peak desorption peak is formed. The CO₂ signal returned back to the baseline intensity shortly after reaching 120 °C,

indicating that the desorption was complete. The capture capacity of the sorbent was calculated by integrating the area under this curve and along with the calibration factor obtained prior to the experiment. As indicated on the figure itself, the capture of this commercial sorbent was calculated to be 376.7 $\mu\text{mol/g}$ sorbent.

Table 1 summarizes the CO₂ capture capacities from the results of recent samples as analyzed by the procedure described above. The capture amounts have been normalized on a per gram of sorbent basis for ease of comparison. It is clearly shown that the commercial sample is the best-performing among this set. Aside from the commercial sample, the DRIFTS analysis did not provide any insight into the mode of capture; all of the sorbent materials tested showed no adsorbate during the experimentation. This is probably due to the smaller capture capacity of the sorbent materials; the concentration of CO₂ on the surface of these sorbents may be below the detection limit of our IR bench.

Table 1. CO₂ capture capacities of recent sorbents operated under an air-containing atmosphere tested via the adsorption/desorption scheme.

Sample	Capture capacity ($\mu\text{mol/g}$)
SA9T (commercial)	441
124A	127.4
124B	115.2
124C	19.2
MG-001-114C	10.3
122B	12.8
123A	9.7
123B	31.7
123C	7.6

Total Capture

The capture capacities summarized above are related to the CO₂ strongly bound to the surface of the sorbent. This is due the He/air purge to remove gaseous CO₂ that is conducted

immediately following the adsorption. Only the strongly bound surface species remain; these species are termed “chemisorbed”. We postulated that there was a significant amount of CO₂ that was bound more weakly to the sorbent and was purged along with the gaseous CO₂. These species were not be accounted for in our technique – and may be significant. In actual applications of the sorbent systems, the apparatus generally consists of two adsorption beds.^{8,9} While capture is taking place in one sorbent bed, the other is being regenerated. The inlet stream is cycled between the two beds thus maximizing the overall capture of the sorbent beds. In this case, there is never a time whereby the sorbent must retain CO₂ while CO₂ is not in the inlet stream; thus no weakly bound species are removed from the surface.

We have recently developed a new methodology that permits us to quantify the weakly bound species; for convenience, we termed these weakly bound species as “physisorbed” species. The total capture of a sorbent then is the sum of the “physisorbed” and the “chemisorbed” amounts. The procedure itself is very similar to the adsorption procedure as described in the experimental section. The differences are as follows: (a) the sorbent bed is pretreated with moisture with the He/air carrier gas, (b) flow is redirected around the sorbent bed via the “sorbent system bypass” (see Fig 1), (c) the He/air stream (Stream A) is replaced with the CO₂/air/He (Stream B), and (d) flow is redirected once again to the sorbent system. Figure 5 illustrates the MS analysis of this procedure. Initially, while the adsorption stream is flowing through the sorbent system bypass line, no capture takes place and the CO₂ signal on the MS is a constant, positive value. When the flow is redirected to the sorbent bed, capture begins and the signal drops rapidly. After some time, the sorbent becomes saturated and the CO₂ concentration exiting the sorbent system increases once again. The negative area shown in Figure 5 thus represents “total capture” of the sorbent. The amount may be calculated from this area and the

same calibration factor. The experiment from this point onward continues as previously; the sorbent system is regenerated via a temperature programmed desorption – in which the “chemisorbed” species are calculated. We may then calculate the “physisorbed” species from the difference of the total capture amount and the chemisorbed amount.

Table 2 presents a summary of this new technique on some newer samples. The commercial sample, SA9T, was still the best performer in the sense of the chemisorbed amount. However, when comparing the total capture or the physisorbed amount, our samples did not look as inferior. It was indeed promising that one sample, 125E, showed a higher total capture than the commercial sample.

Table 2 also displays the capture amount of regenerated SA9T and 125E. In both cases, the capture amounts decreased significantly from that of the fresh samples. This phenomena is not well understood at this stage. This could be due to: (1) not all of the CO₂ is removed during the regeneration step, or (2) the sorbent itself is degraded during the regeneration stage. If this is due to CO₂ not being completely removed, then we would not expect to see a further decrease in capture capacity after a second regeneration; a further decline is realized with sample 125E, suggesting that CO₂ removal is not the problem. Thus, this phenomena is probably due to degradation of the sorbent material. While we are using a temperature-swing regeneration technique, actual application of these sorbent materials are generally based on a pressure-swing regeneration. That is, when desorption of the CO₂ is desired, the sorbent bed is evacuated. This technique would probably have a less detrimental impact on the sorbent material; regenerated sorbent may behave more similarly to that of the fresh sorbent.

Table 2. Total CO₂ capture amounts and the respective breakdown of chemisorbed and physisorbed species

Sample	Total Capture ($\mu\text{mol/g}$)	Physisorbed amt. ($\mu\text{mol/g}$)	Chemisorbed amt. ($\mu\text{mol/g}$)
SA9T	1012	571	441
SA9T (Regen)	871	494	377
124	925.7	898.0	27.7
124A	455.1	349.5	105.6
124B	272.2	250.8	21.3
124C	442.9	439.1	3.8
125E	1262.6	1230.0	32.6
125E (Regen #1)	1021.7	1018.6	3.1
125E (Regen #2)	534.3	533.2	1.1
125F	408.6	386.2	22.4
125G	462.1	419.2	42.9
127	426.9	419.9	7.1
127A	277.6	275.8	1.8
127B	372.3	370.1	2.2
127C	417.7	415.6	2.1
127D	365.1	364.2	0.9

Conclusions

Of all the sorbents that we tested, sample 125E appears to be the most promising; it may be able to compete with the commercial sample SA9T. Regeneration appears to be a problem for both 125E and the commercial sample; their capture capacities are significantly reduced in subsequent analyses. One difference that separates the two samples is that the strongly bound (chemisorbed) species are almost reduced to nothing after only one regeneration in the case of sample 125E. Investigation of these regeneration problems is currently underway. Other methods for regeneration may be required.

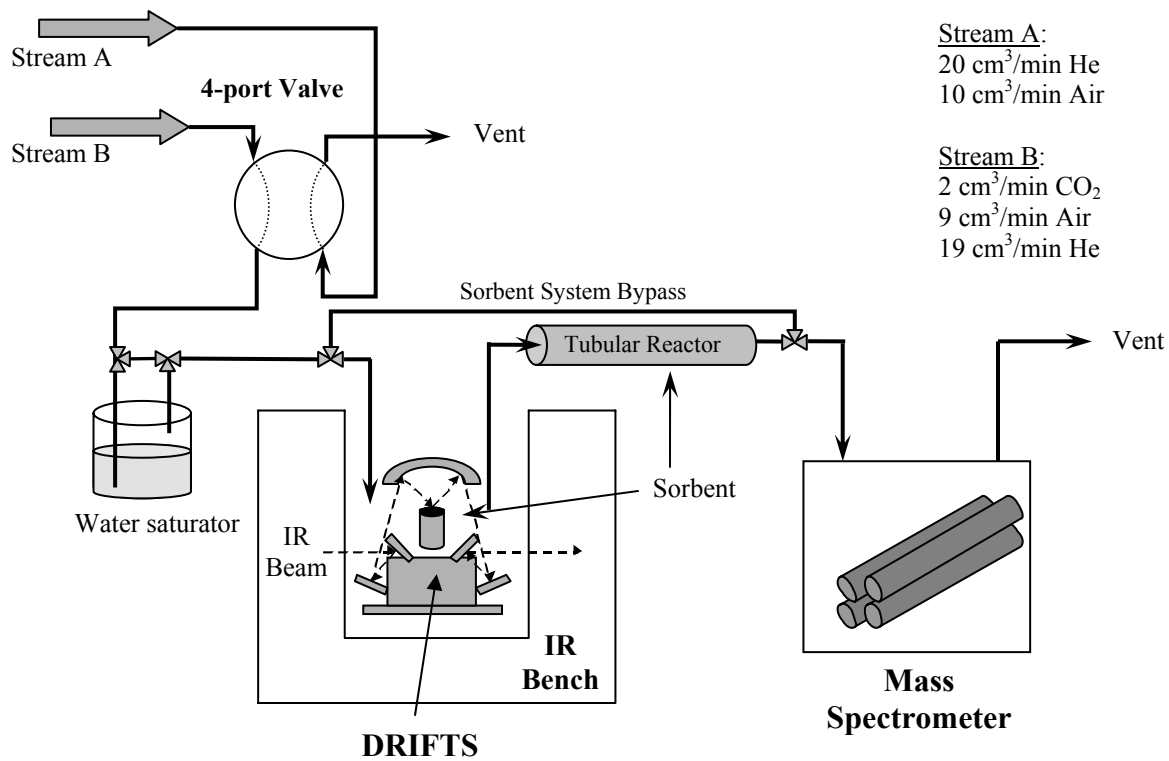


Figure 1. Experimental Apparatus

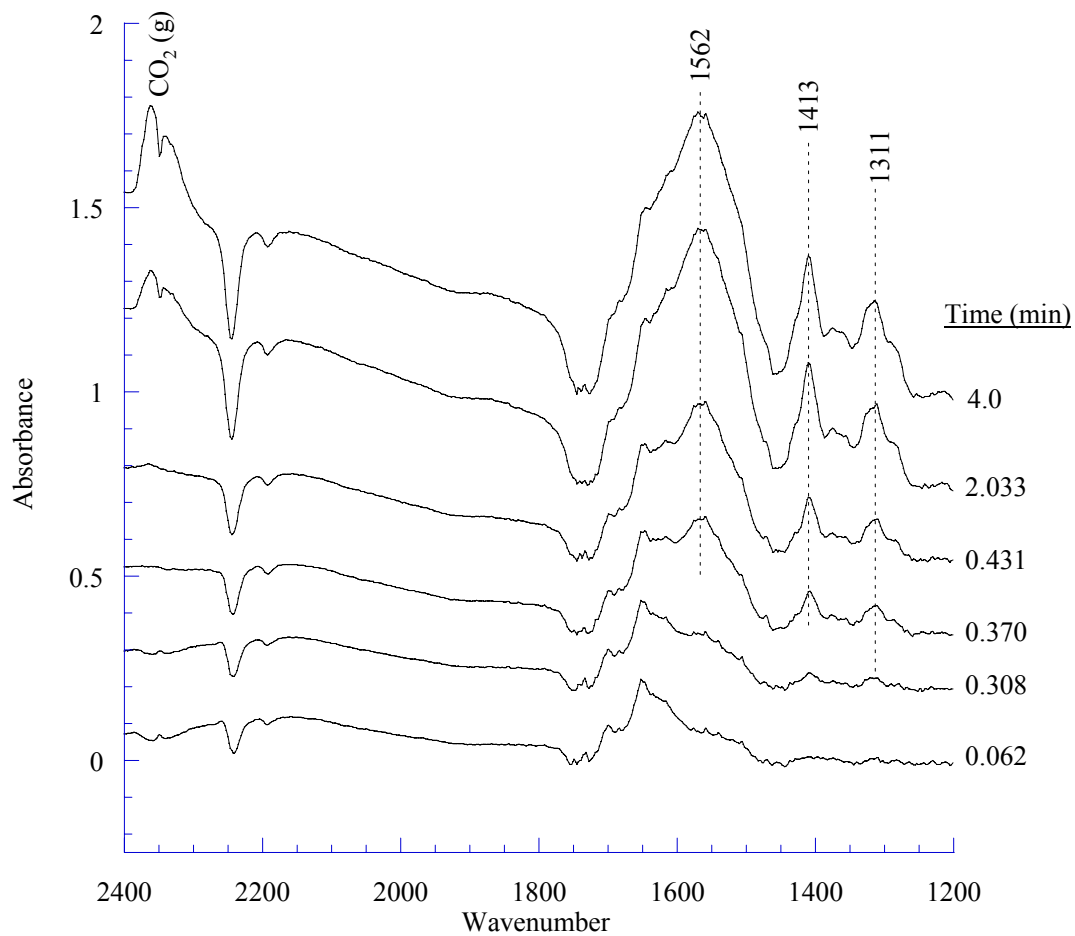


Figure 2. DRIFTS analysis of CO₂ adsorption over commercial sample SA9T

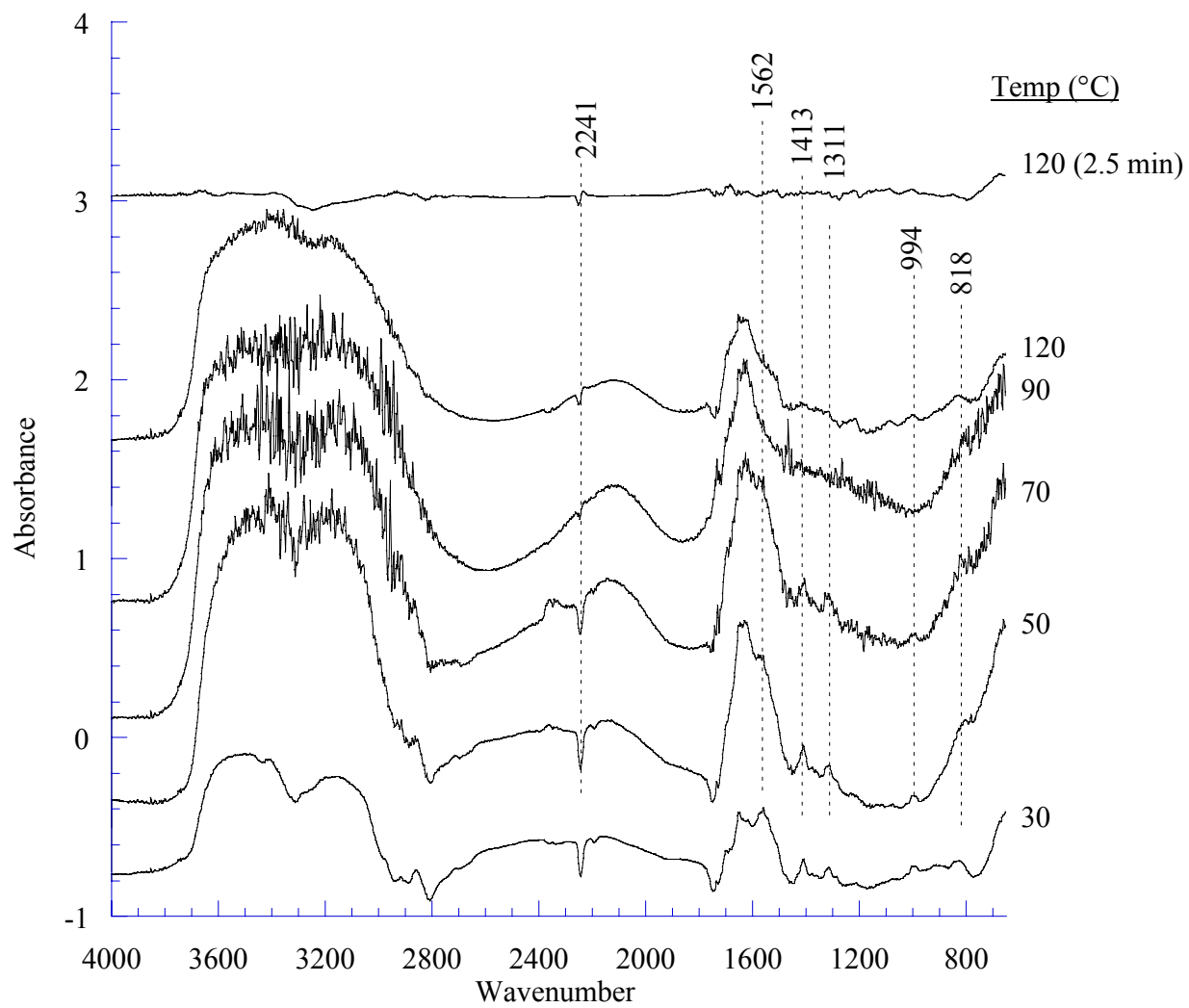


Figure 3. DRIFTS analysis of the CO₂ temperature programmed desorption (regeneration) of commercial sample SA9T

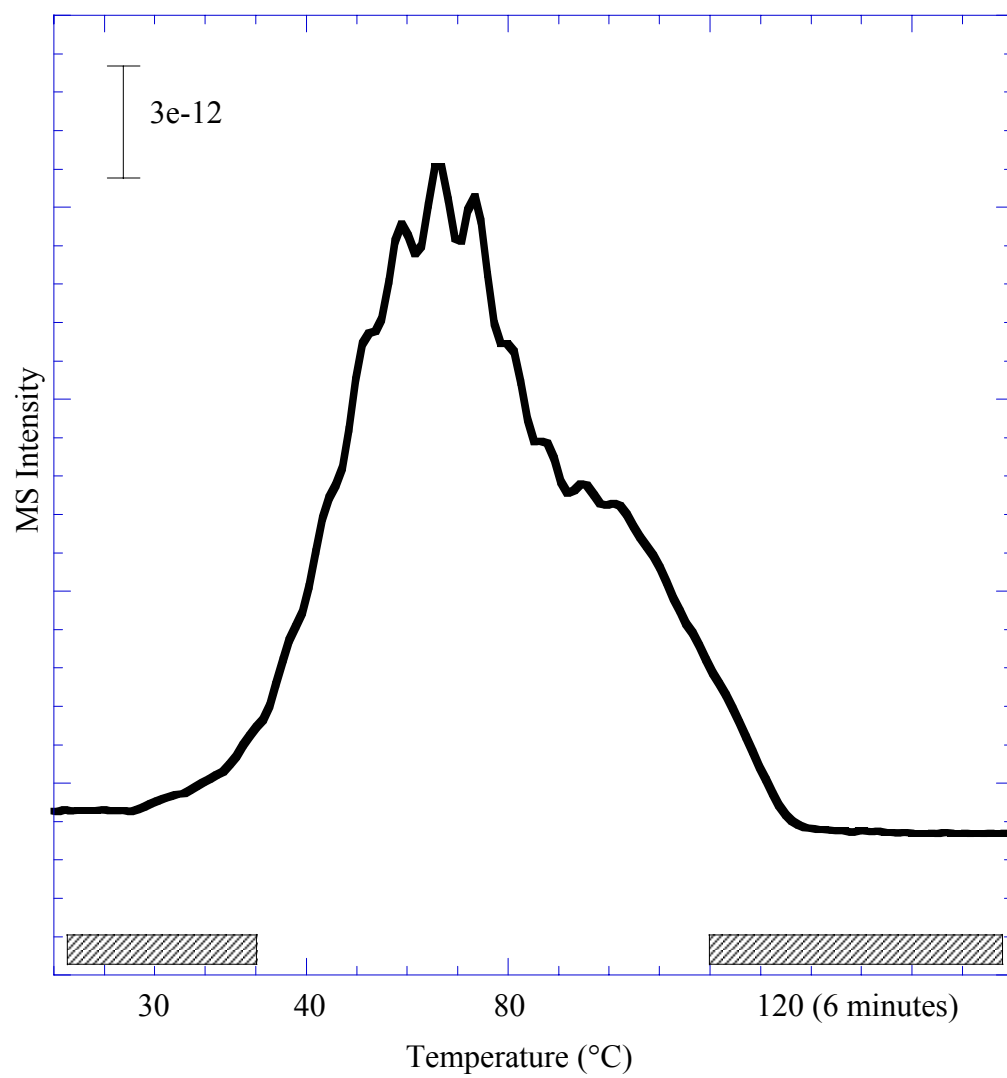


Figure 4. MS analysis of the CO₂ temperature programmed desorption (regeneration) of commercial sorbent SA9T

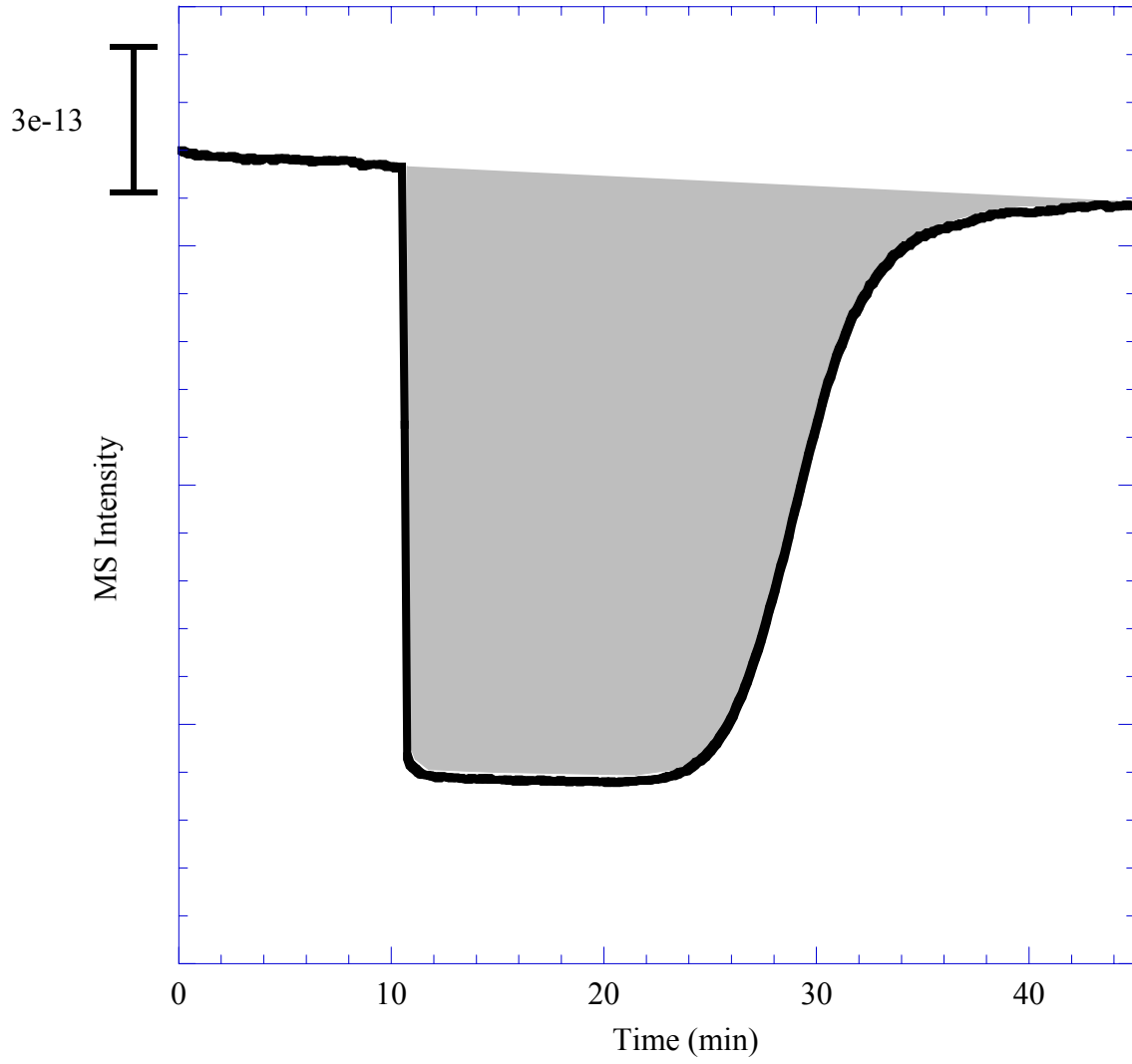


Figure 5. MS analysis during the adsorption of CO₂ onto commercial sample SA9T using

References

- ¹ Zinnen, H. A., Oroskar, A R., Chang, C-H, US Patent 4,810,266, 1989
- ² Birbara, P. J., Nalette, T. A., US Patent 5,492,683, 1996
- ³ Birbara, P. J., Filburn, T. P., Nalette, T. A., US Patent 5,876,488, 1999
- ⁴ Leal, O., Bolivar, C., Ovalles, C., Garcia, J. J., Espidel, Y., *Inorganica Chemical Acta*, **240** (1995) 183
- ⁵ Filburn, T., Nalette, T., Graf, J., “The Design and Testing of a Fully Redundant Regenerative CO₂ Removal System (RCRS) for the Shuttle Orbiter”, International Conference On Environmental Systems, July 2001, Orlando, FL, USA
- ⁶ Davydov, A. A., “Infrared Spectroscopy of Adsorbed Species on the Surface of Transition Metal Oxides”, John Wiley & Sons, Chichester, 1990
- ⁷ Little, L. H., “Infrared Spectra of Adsorbed Species”, Academic Press, New York, 1966
- ⁸ Satyapal, S., Filburn, T., Trela, J, Strange, J., *Energy & Fuels*, **15** (2001) 250
- ⁹ Colling, Jr., A., Nalette, T., Cusick, R., Reysa, R., ”Development Status of Regenerable Solid Amine CO₂ Control Systems”, 15th Intersociety Conference on Environmental Systems, July 1985, San Francisco, CA, USA

II. “Computation of Solids Transport Using Hypoplasticity Theory”

**Yong Cao (S), Carnegie Mellon University, and Jayathi Murthy (F), Purdue University
with
Thomas O’Brien (M), NETL**

Annual Report
Student/NETL Partnership Program
Computation of Solids Transport Using Hypoplasticity Theory

Yong Cao
Graduate Student
Carnegie Mellon University
Pittsburgh, PA 15221

Jayathi Y. Murthy
Professor
School of Mechanical Engineering
Purdue University
West Lafayette, IN 47907-1288

NETL Sponsor: Dr. Thomas O'Brien

December 2001

Abstract

The objective of the project is to investigate the use of hypoplasticity theory in soil mechanics to model the dense granular regime in gas-solid flows and to combine this theory with kinetic theory for granular flows in the dilute regime. The solid phase in the gas-solid flow is modeled as a dense hypoplastic medium using the theory of Wu and Bauer (1993). The theory requires the solution of three stress transport equations in two dimensions, one each for the normal stresses, and one for the shear stress; these transport equations incorporate history effects and a dependence of the stress state on the solids volume fraction. The numerical development is done in the MFIX code. A co-located stress storage scheme is developed with both the normal and shear stresses being stored at cell centroids. An added dissipation scheme is developed for the shear stress to mitigate checkerboarding. A volume fraction correction equation is derived by combining the discrete normal stress equations with the momentum equations, and enforcing solids mass conservation. A segregated iterative scheme is used to solve for momentum and mass conservation of the granular phase, as well as the three stress transport equations. An example problem is solved addressing the filling of a square cavity. Successful simulations are obtained for volume fractions up to the critical packing limit, but beyond this limit, convergence difficulties are encountered. Causes and possible cures for the numerical behavior are discussed.

Table of Contents

	Page
Abstract.....	2
List of Figures.....	4
1. Introduction.....	5
2. Executive Summary.....	5
3. Numerical Method.....	5
4. Results and Discussion.....	7
5. Conclusions.....	8
6. Nomenclature.....	9
7. References.....	9

List of Figures

- Figure 1: Arrangement of velocities, volume fraction and stresses
- Figure 2: Shear stress interpolation
- Figure 3: Filling of a square box
- Figure 4: Void fraction contours at (a) $t=0.05$ seconds, (b) $t=0.1$ seconds, (c) $t=0.15$ seconds
- Figure 5: Velocity vectors at (a) $t=0.05$ seconds, (b) $t=0.1$ seconds, (c) $t=0.15$ seconds
- Figure 6: Contours of σ_{11} (a) $t=0.05$ seconds, (b) $t=0.1$ seconds, (c) $t=0.15$ seconds
- Figure 7: Contours of σ_{22} (a) $t=0.05$ seconds, (b) $t=0.1$ seconds, (c) $t=0.15$ seconds

1. Introduction

Gas-solid flows occur in a vast variety of industrial applications including pneumatic transport of coal, fluidized beds, separation and/or mixing of pharmaceutical powders and many more. A number of different approaches have been taken to model this class of flows. In terms of broad classification, we may take either a discrete approach, treating each of the elements (particles) as a separate body, and tracking its motion, or treat the granular medium as a continuum. A variety of continuum models have been published in the literature (Lun et al (1984), Ding and Gidaspow(1990) for example). During the 1980's, a kinetic theory approach was developed (Lun et al (1984) for example) to address the rapid granular regime. This theory, though widely used, does not address the dense regime in granular flow. On the other hand, many flows of industrial interest span the range of volume fractions from dilute to dense. There exist a variety of constitutive models from the soil mechanics literature (Wu and Bauer, 1993; Wu et al, 1996) with which it may be possible to model the dense granular regime. Bauer and colleagues have developed a variety of models based on hypoplasticity theory which exhibit some important features of dense granular flows such as barotropy and pyknotropy. Another attractive feature of their formulation is that model constants can be determined through simple experiments, and values for these constants have been provided for some sands (Wu and Bauer,1993). Thus, this class of models provides a good starting point for the modeling of dense granular regimes in gas-solid flows.

2. Executive Summary

The objective of the project is to incorporate a hypoplastic model for the dense granular regime in a continuum description of gas-solid flows and to explore its performance for different classes of industrial flows. We focus in particular on the hypoplastic model of Wu and Bauer(1993); the model incorporates the primary features necessary, and a numerical methodology that addresses it would be applicable to other models of the same type. During the last year, a numerical implementation of the model has been completed in the MFIX code. We have retained the basic framework for the computation of gas and solid flow in MFIX, but have added to it additional stress transport equations from Wu and Bauer (1993). We have also modified the solution procedure for computing the volume fraction of solid. To solve the stress transport equations successfully, it was necessary to develop an added dissipation scheme for the shear stress. The implementation is now complete and a few simple tests for pure granular flows have been done to establish correctness. Our formulation performs reasonably well in general; reasonable time-steps (comparable to the existing kinetic theory implementation in MFIX) can be used for the most part. However, convergence difficulties are encountered when the maximum packing limit is reached. Explorations of model and algorithm behavior in this limit are still underway and results from these investigations will be reported in due course.

3. Numerical Method

In this section, we present the hypoplastic model of Wu and Bauer(1993) and describe the numerical method we have developed and implemented in MFIX.

3.1 Governing Equations

The equations governing gas/solid flow are the continuity and momentum equations for the two phases, and the constitutive equations for stress:

Continuity Equations:

$$\begin{aligned}\frac{\partial}{\partial t}(\mathbf{e}_g \mathbf{r}_g) + \nabla \cdot (\mathbf{e}_g \mathbf{r}_g \vec{v}_g) &= 0 \\ \frac{\partial}{\partial t}(\mathbf{e}_s \mathbf{r}_s) + \nabla \cdot (\mathbf{e}_s \mathbf{r}_s \vec{v}_s) &= 0\end{aligned}\quad (1)$$

Momentum Equations:

$$\begin{aligned}\frac{\partial}{\partial t}(\mathbf{e}_g \mathbf{r}_g \vec{v}_g) + \nabla \cdot (\mathbf{e}_g \mathbf{r}_g \vec{v}_g \vec{v}_g) &= -\mathbf{e}_g \nabla P_g + \nabla \cdot \boldsymbol{\tau}_g + F_g (\vec{v}_s - \vec{v}_g) - \mathbf{e}_g \mathbf{r}_g \vec{g} \\ \frac{\partial}{\partial t}(\mathbf{e}_s \mathbf{r}_s \vec{v}_s) + \nabla \cdot (\mathbf{e}_s \mathbf{r}_s \vec{v}_s \vec{v}_s) &= -\mathbf{e}_s \nabla P_g + \nabla \cdot \boldsymbol{\tau}_s - F_g (\vec{v}_s - \vec{v}_g) - \mathbf{e}_s \mathbf{r}_s \vec{g}\end{aligned}\quad (2)$$

Solid Stress Equations:

$$\begin{aligned}\overset{\circ}{\mathbf{T}}_s &= C_1 (\text{tr} \mathbf{T}_s) \mathbf{D}_s + C_2 \frac{\text{tr}(\mathbf{T}_s \mathbf{D}_s) \mathbf{D}_s}{\text{tr} \mathbf{T}_s} + (C_3 \frac{\mathbf{T}_s^2}{\text{tr} \mathbf{T}_s} + C_4 \frac{\mathbf{T}_s^{*2}}{\text{tr} \mathbf{T}_s}) \|\mathbf{D}_s\| I_e \\ \overset{\circ}{\mathbf{T}}_s &= \dot{\mathbf{T}}_s - \mathbf{W}_s \mathbf{T}_s + \mathbf{T}_s \mathbf{W}_s \\ I_e &= (1-a) \frac{e - e_{\min}}{e_{\text{crt}} - e_{\min}} + a \\ e &= \frac{1 - e_s}{e_s}\end{aligned}\quad (3)$$

3.2 Basic Numerical Scheme

We retain the basic framework of MFIX for the development of the numerical scheme (Syamlal (1994)). A segregated finite volume method is adopted. The domain is divided into rectangular control volumes and the governing equations are integrated over the control volume, leading to a balance of incoming and outgoing fluxes and the accumulation inside the control volume. A variety of differencing schemes are available in MFIX to write these fluxes in terms of the discrete cell-centered values of the dependent variables; these are adopted unchanged. MFIX employs a staggered grid for storing pressures and velocities; the gas-phase pressure is stored at cell centroids and the solid and gas-phase velocities are stored at the cell faces. The volume fraction of solid is stored at the cell centroid. Discretization yields a set of nominally linear algebraic equations corresponding to each governing equation; these are solved sequentially and iteratively.

3.3 Stress Storage and Discretization

In 2D, we must solve for three stresses – the two normal stresses, and the shear stress. All three components are stored at cell centroids, as shown in Fig. 1. For the normal stresses, this choice is akin to storing the pressure at the cell centroid in a typical staggered mesh scheme. The normal stresses appear on the faces on the momentum control volumes, and can be incorporated naturally into the force balance without any need for interpolation. For shear stress however, a cell-centered storage is not ideal; interpolation of shear stress from the cell centroid to the corners of the main control volume is required. Other choices are possible: one option is to store the shear stress at the control volume corners. However, this could be problematic at corners where there are stress singularities; also, the added geometric complexity is daunting. As a result, we choose to store all stresses at cell centroids.

3.4 Added Dissipation Scheme for Shear Stress

Since the shear stress is stored at the cell centroid, interpolation is required to find the shear stress at the correct location. This is shown in Fig. 2. We see that for the staggered control volume for u_p , the shear stress is required on the ‘nw’ and ‘sw’ faces, but is available at cell centroids P and W. Direct linear interpolation to ‘nw’ and ‘sw’ from the cell centroid values leads to checkerboarding in the net shear stress term added to the u -momentum balance because the stresses at W and P are eliminated in the process. We have observed this checkerboarding in preliminary calculations. To eliminate this checkerboarding, we have developed an added dissipation scheme. The discrete equation for the shear stress τ_p at point P in Fig. 2 can be written as:

$$\mathbf{t}_p = \left(\frac{\sum_{nb} A_{nb} \cdot \mathbf{t}_{nb} + S}{A_p} \right)_p - \left(\Gamma \frac{u_{sn} - u_{ss}}{\mathbf{d}y} \right)_p \quad (4)$$

The added dissipation scheme writes the shear stress at point ‘nw’ as:

$$\mathbf{t}_{nw} = \left\langle \frac{\sum_{nb} A_{nb} \cdot \mathbf{t}_{nb} + S}{A_p} \right\rangle_{nw} - \langle \Gamma \rangle \frac{u_{sN} - u_{sP}}{\mathbf{d}y_n} \quad (5)$$

The interpolation scheme interpolates the quantities in $\langle \rangle$ linearly from the cell centroids but replaces the velocity term with a direct difference of the velocities bounding τ_{nw} . This direct dependence does not allow the u -velocity to pick up a checkerboarded pattern.

3.5 Solids Volume Fraction Correction Equation

MFIX solves for the volume fraction correction, rather than the volume fraction itself directly. In order to formulate the equation, it is necessary to write relationships between the volume fraction and the velocity. This is typically done using the kinetic theory by relating the solids pressure to the volume fraction. Since the solid pressure appears in the solids momentum equation, a relationship between ϵ_s and \dot{u}_s and \dot{v}_s can be derived. For the hypoplastic equations, there is no solids pressure equation. Instead, we derive a

relationship between ϵ_s and the normal stresses using the discrete form of the stress transport equation; recall that ϵ appears in the I_e term in Equation (3). A relationship $\epsilon_s' = f(\sigma_{11}')$ is derived for use in the u_s -momentum equation; a relationship $\epsilon_s' = f(\sigma_{22}')$ is derived for use in the v_s -momentum equation. The dependence of these velocities on the shear stress is not included in the derivation of the corrections. Finally, the discrete u_s - and v_s - momentum equations are used to derive the relations $u_s' = f(\epsilon_s')$, $v_s' = f(\epsilon_s')$. These are substituted into the solids volume conservation equation to derive a correction equation for the solids volume fraction.

3.6 Overall Iterative Algorithm for Solids Transport

The overall algorithm for the solids transport may be written as:

1. Initialize the solids velocity, volume fraction and stress fields.
2. Take a forward time step. Within the time step:
 - a. Discretize the solids momentum equations using current stress fields and solve.
 - b. Discretize and solve the stress equations.
 - c. Find the coefficients for the ϵ_s' equation using the procedure described above.
 - d. Solve the ϵ_s' equation.
 - e. Correct the solids volume fraction, solids velocity and the stresses.
 - f. Compute residuals and check for convergence. If converged, go to next time step. Else, go to step (a).
3. If maximum time is reached, stop. Else go to step 2.

4. Results and Discussion

We consider the filling of a box of size 0.2m x 0.2m with Karlsruhe sand, the properties of which have been given by Wu and Bauer (1993). The situation is shown schematically in Fig. 3. Sand enters the box through the top boundary with a velocity of 2m/s with a void fraction of 0.8 ($\epsilon_s=0.2$); the stresses are assumed to be negligibly small. The initial value of σ_{22} is taken to be $\epsilon_s \rho_s g y$ in the box. The other stress values are assumed zero, and the initial solids volume fraction in the box is also 0.2. On the boundaries, the shear stress is assumed zero; the values of the other stresses do not matter since they are not used. The tangential velocity gradient on the wall is assumed zero; all normal velocities are set to zero. The objective is to simulate the filling process, and to examine the variation of the solids normal stresses with height.

The properties of Karlsruhe sand are taken from Wu and Bauer(1993). The model constants are taken to be $C_1=-33.5$, $C_2=-341.4$, $C_3=-339.7$, $C_4=446.5$. The dependence on the void fraction is expressed in terms of the constants e_{min} , e_{crit} and a in Eq.(3), which are taken to be 0.53, 0.84 and 0.8 respectively. The minimum void fraction corresponding to e_{min} is $\epsilon_g=0.3464$. An estimate of the time to fill the box to the maximum packing limit is approximately 0.33 seconds. We use a 10x10 uniform mesh for the calculation, with a time step of 10^{-4} seconds.

Figs. 4(a-c) show the fields of void fraction at $t= 0.05, 0.1$ and 0.15 seconds. The velocity field is shown at the same time instants in Figs. 5(a-c). The normal stress σ_{11} at the three time instants is shown in Figs. 6(a-c) and the normal stress σ_{22} is shown in Figs. 7(a-c). The shear stress is zero everywhere in this flow. We see from Fig.4 that the void fraction increases on average from its initial value of 0.8 to values as low as 0.40 at the bottom of the box at $t=0.15$ seconds. At early times, we see that the compression front travels at a finite speed through the bed, so that bands of low void fraction are seen about half way through the bed at $t=0.015$ seconds. Plots of the solids velocity show the filling process; as the sand accumulates in the box, the solid velocity falls to zero. The plots of the normal stresses show a buildup of compressive stresses at the bottom of the box. Beyond $t=0.18$ seconds or so, locations at the bottom of the box reach the maximum packing limit. Our algorithm fails in this limit, and calculations cannot proceed beyond this point. The failure appears to be related to the change in the nature of the governing equations once the maximum packing limit is reached. In this limit, the medium becomes essentially incompressible, and void fraction becomes constant. Small changes in void fraction engender large changes in stress, rather like relationship between pressure and density in the incompressible limit, when the speed of sound becomes infinitely large. We are examining alternatives to the volume fraction correction equation to address this limit. For void fractions above the packing limit, however, the algorithm appears to behave quite robustly.

5. Closure

The hypoplasticity model of Wu and Bauer (1993) has been used to model the dense granular limit for gas solid flows. The model has been implemented in MFIx. A co-located algorithm for solids stresses is developed whereby normal and shear stresses are stored at cell centroids. An added-dissipation scheme for the shear stress is developed to prevent stress-velocity checkerboarding. The solids volume fraction correction equation is modified to account for the relationship between stress, void fraction and velocity. The resulting discrete equations are solved sequentially and iteratively. The algorithm is applied to the filling of a two-dimensional box. The algorithm is found to work reasonably well as long as void fractions are greater than the packing limit. Efforts for the next year will concentrate on modifying the algorithm to better address the packing limit and on completing the coupling with the gas phase.

6. Nomenclature

D	deformation tensor
P	pressure
T	stress tensor
t	time
u,v	velocity components in (x,y) directions
x,y	coordinate directions
\vec{v}	velocity vector
ε	volume fraction
ρ	density
σ_{11}, σ_{22}	normal stresses
τ	shear stress

Γ coefficient multiplying velocity gradient in stress equation

Subscripts and Superscripts

s solid

g gas

7. References

Ding, J. and Gidaspow, D. (1990): A bubbling fluidization model using kinetic theory of granular flow. *AICHE Journal*, 36(4),523-538.

Lun, C.K.K., Savage, S.B., Jeffrey, J.B., and Chepuruiy, N (1984): Kinetic theories for granular flow: Inelastic particles in Couette flow and slightly inelastic particles in a general flow field. *Journal of Fluid Mechanics*,140, 223-256.

Syamlal, M. (1994). *MFIX documentation: User Manual*, DOE/METC-95/1013 (DE95000031), US Department of Energy, Morgantown Energy Technology Center, Morgantown, W. Va.

Wu, W. and Bauer, E. (1993): A hypoplastic model for barotropy and pyknotropy of granular soils. *Proc. Int. Workshop on Modern Approaches to Plasticity*, Elsevier, 225-245.

Wu, W., Bauer, E., Kolymbas, D. (1996): Hypoplastic constitutive model with critical state for granular materials. *Mechanics of Materials* 23, 45-69.

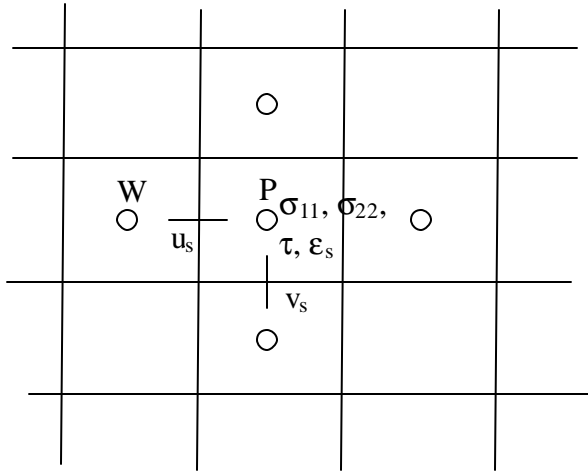


Figure 1: Arrangement of velocities, volume fraction and stresses

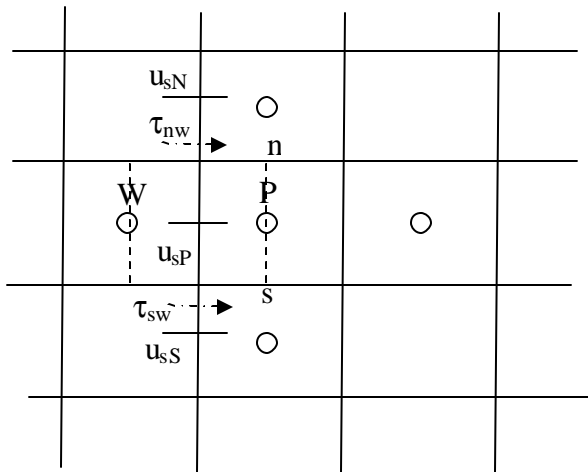


Figure 2: Shear stress interpolation

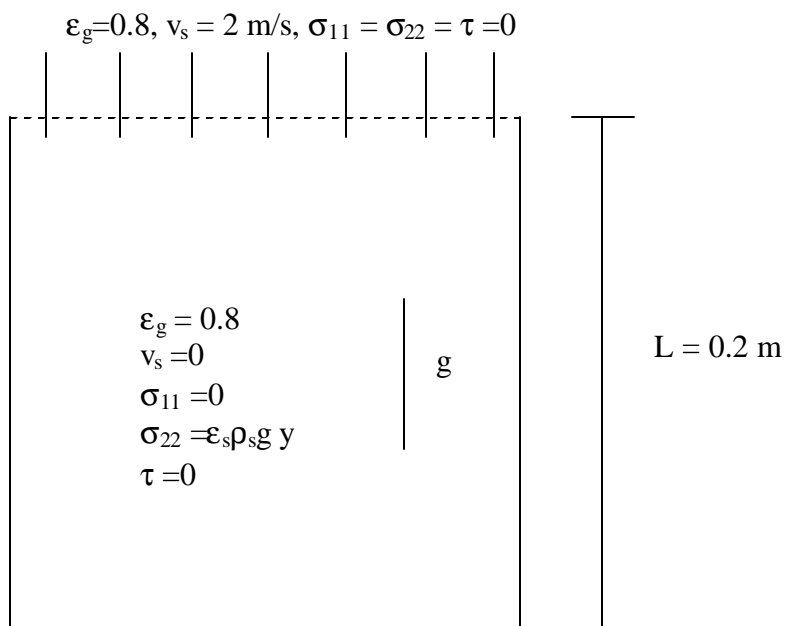


Figure 3: Filling of a square box

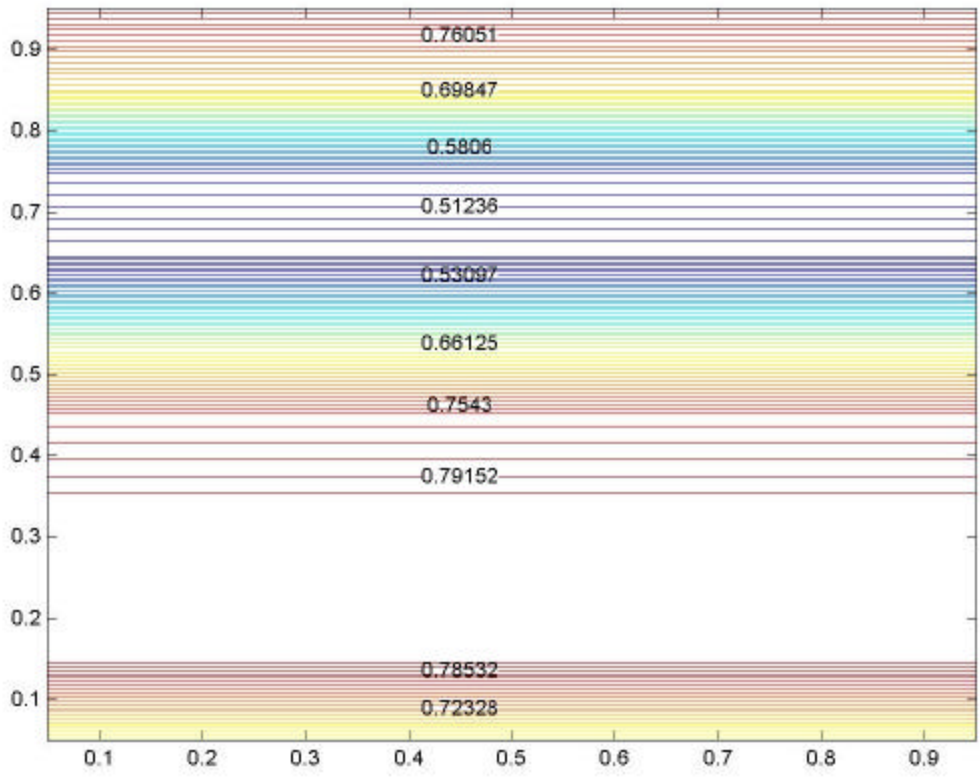


Figure 4 (a) : Void fraction at t=0.05 seconds

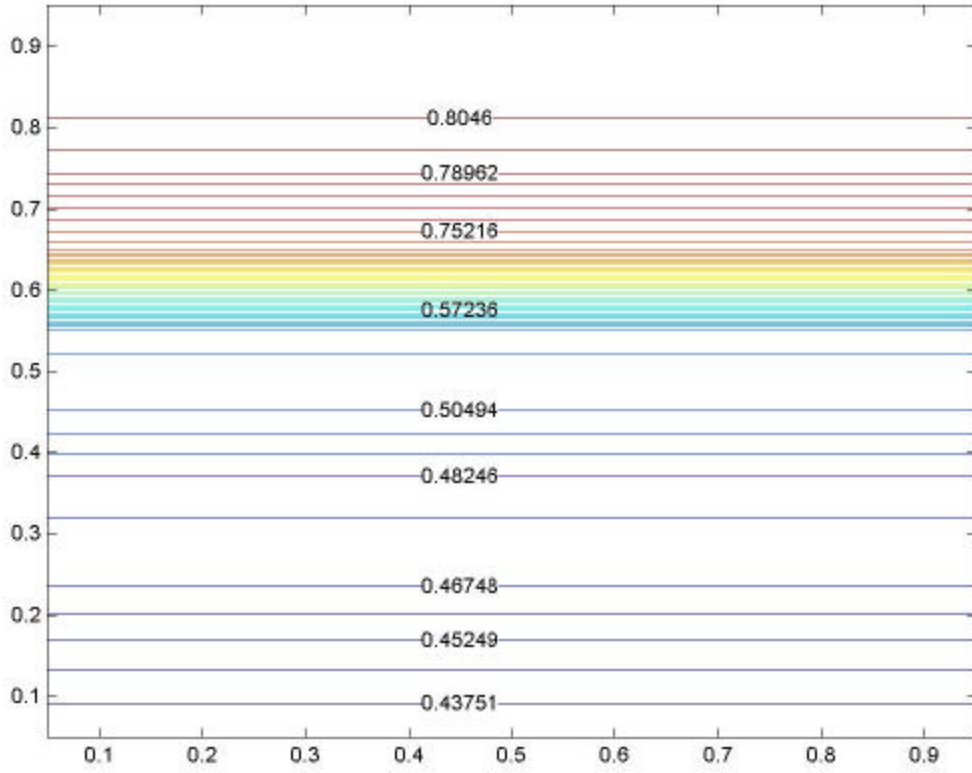


Figure 4(b): Void fraction at $t=0.1$ seconds

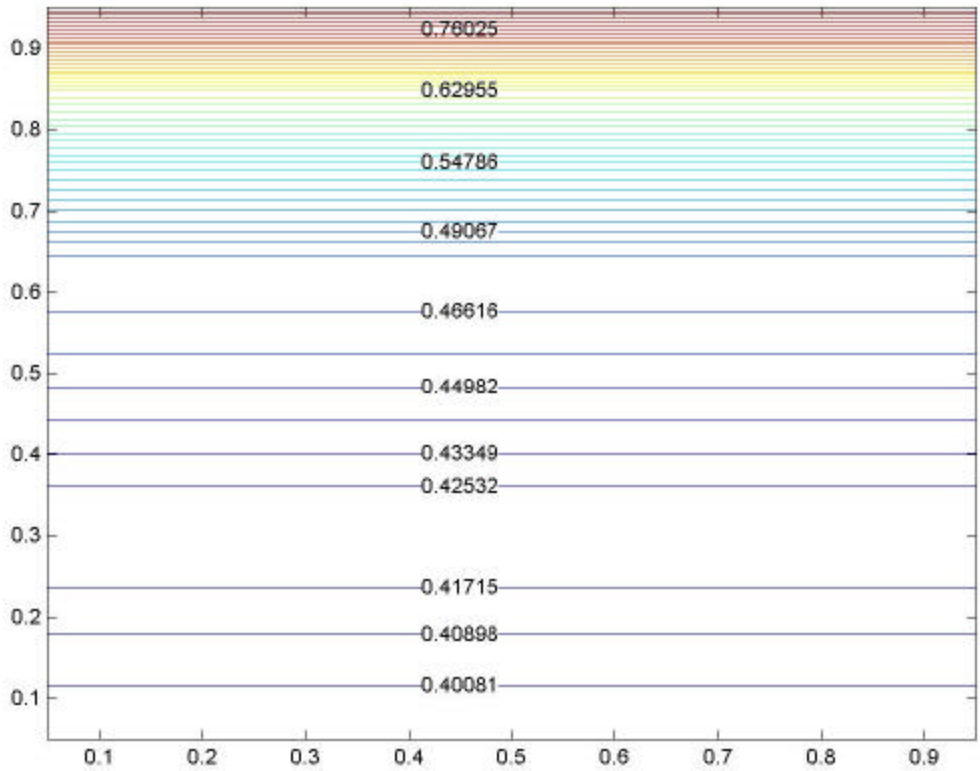


Figure 4(c): Void fraction at t=0.15 seconds

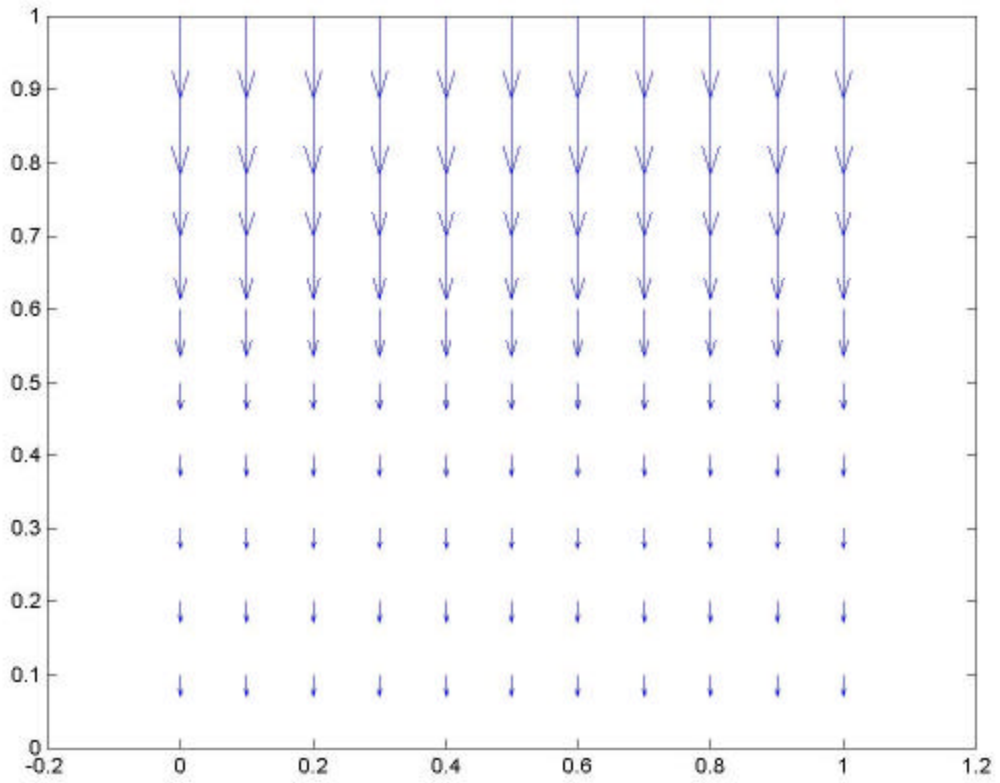


Figure 5(a): Solid velocity vectors at $t=0.05$ seconds

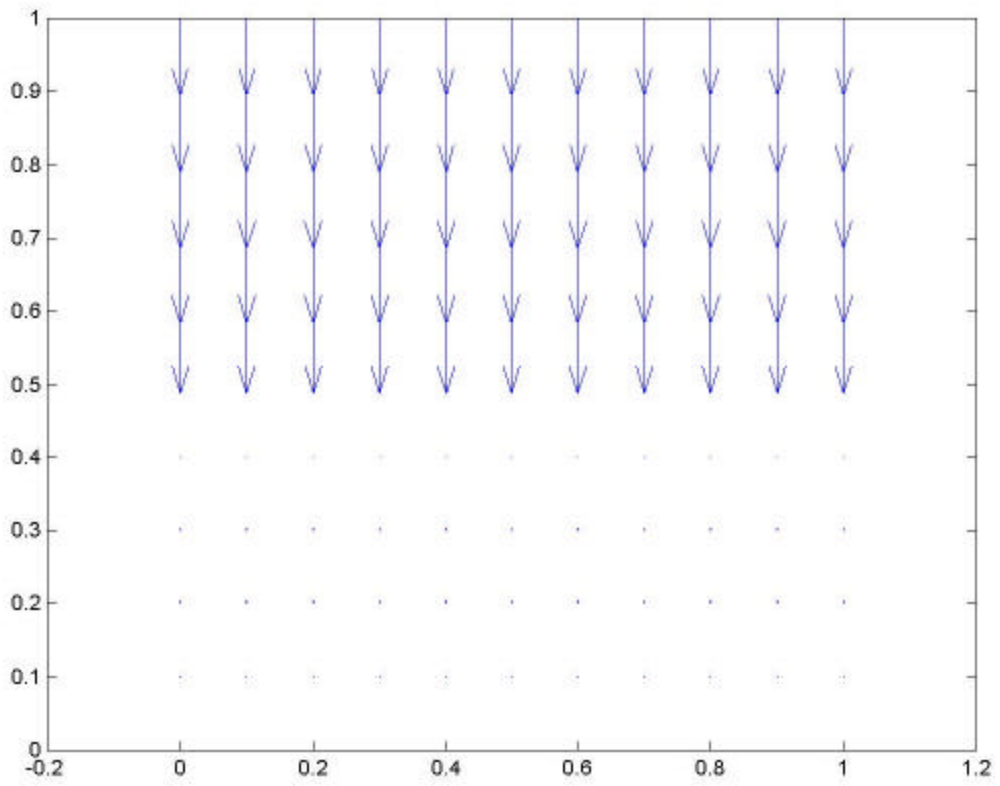


Figure 5(b): Solid velocity vectors at $t=0.1$ seconds

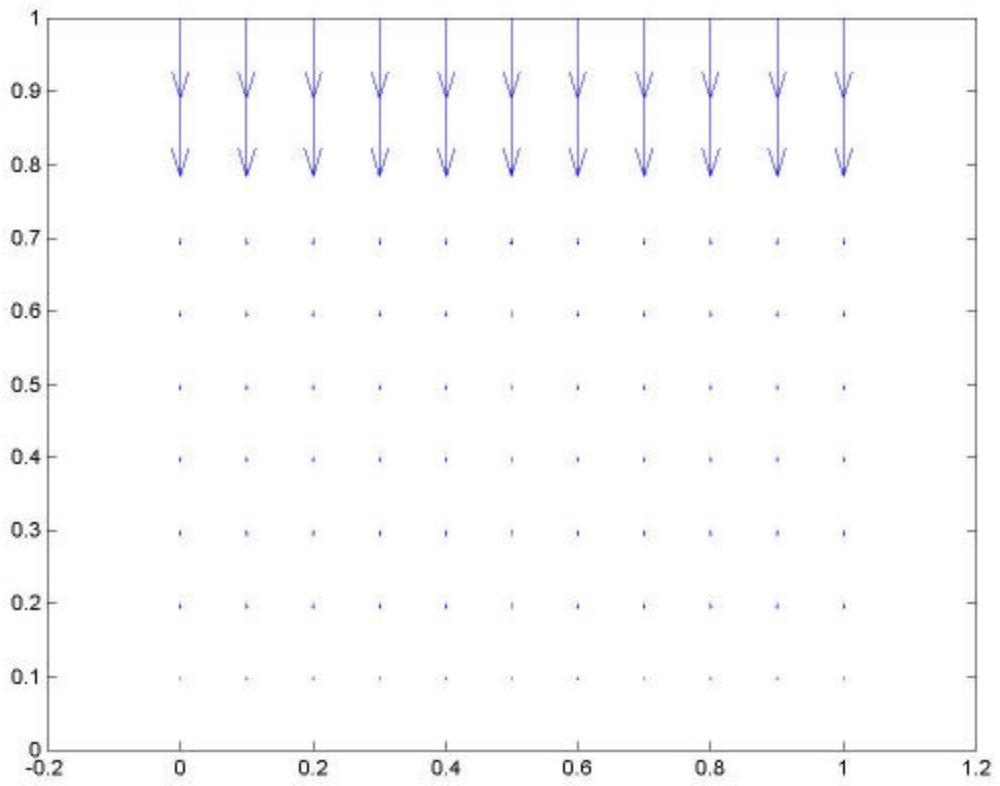


Figure 5(c): Solid velocity vectors at $t=0.15$ seconds

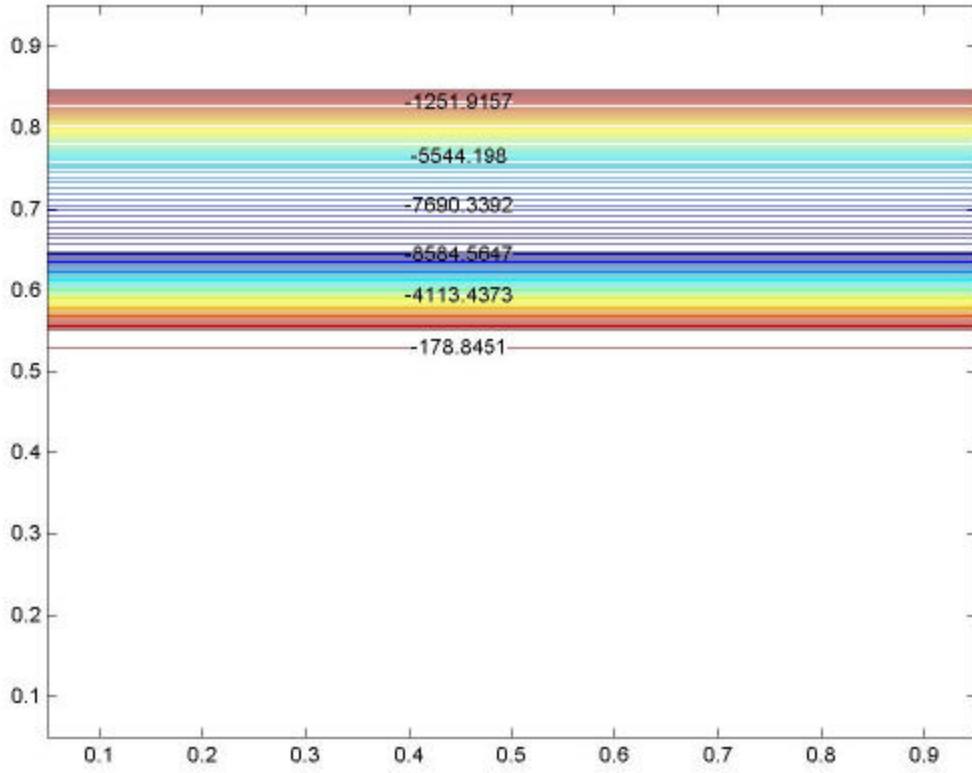


Figure 6(a): Contours of σ_{11} at $t=0.05$ seconds

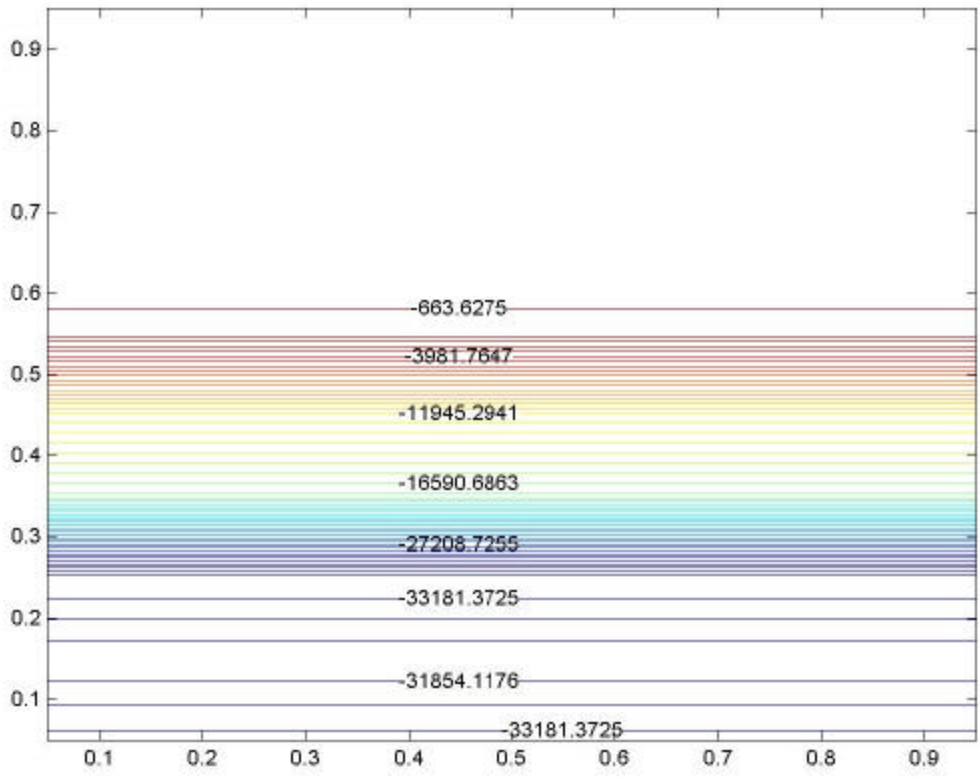


Figure 6(b): Contours of σ_{11} at $t=0.1$ seconds

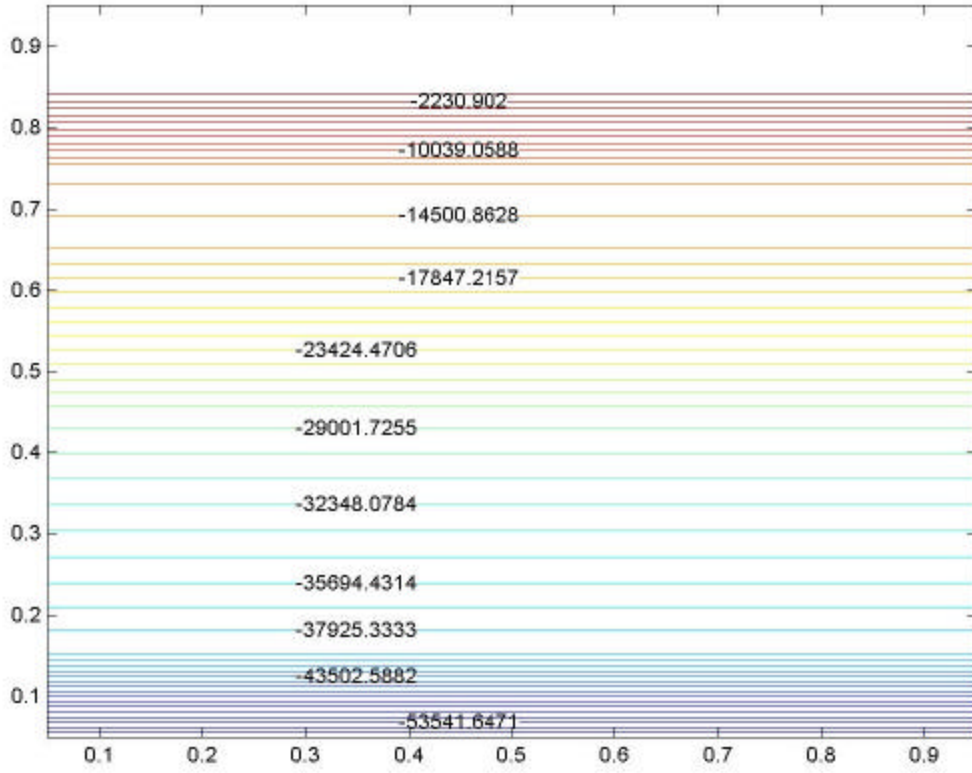


Figure 6(c): Contours of σ_{11} at $t=0.15$ seconds

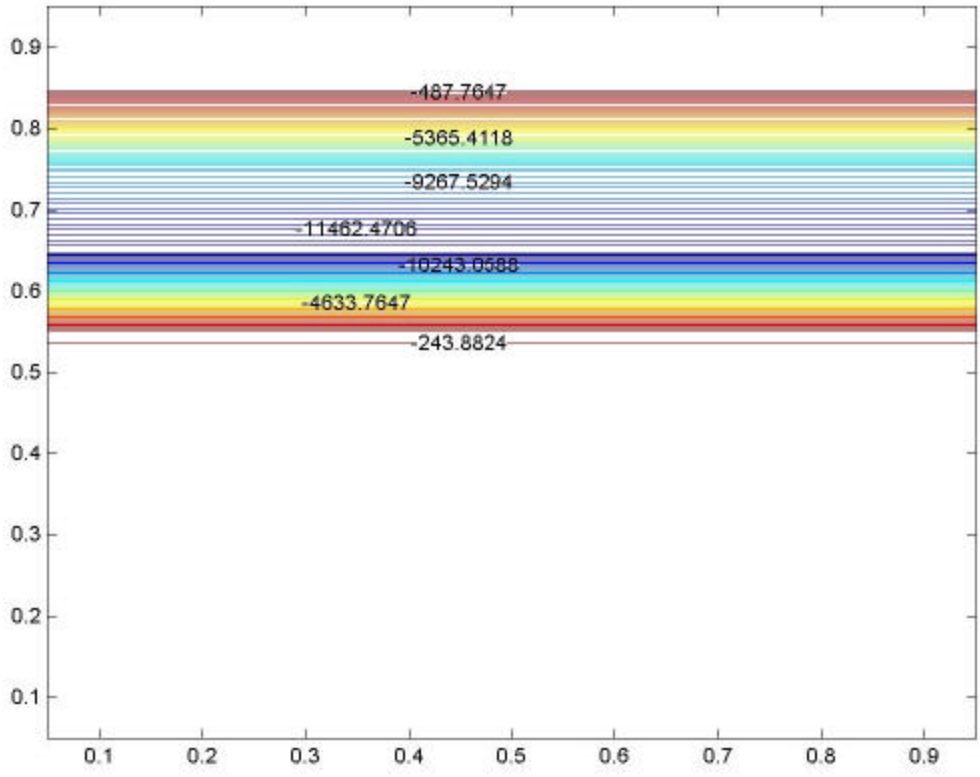


Figure 7(a): Contours of σ_{22} at $t=0.05$ seconds

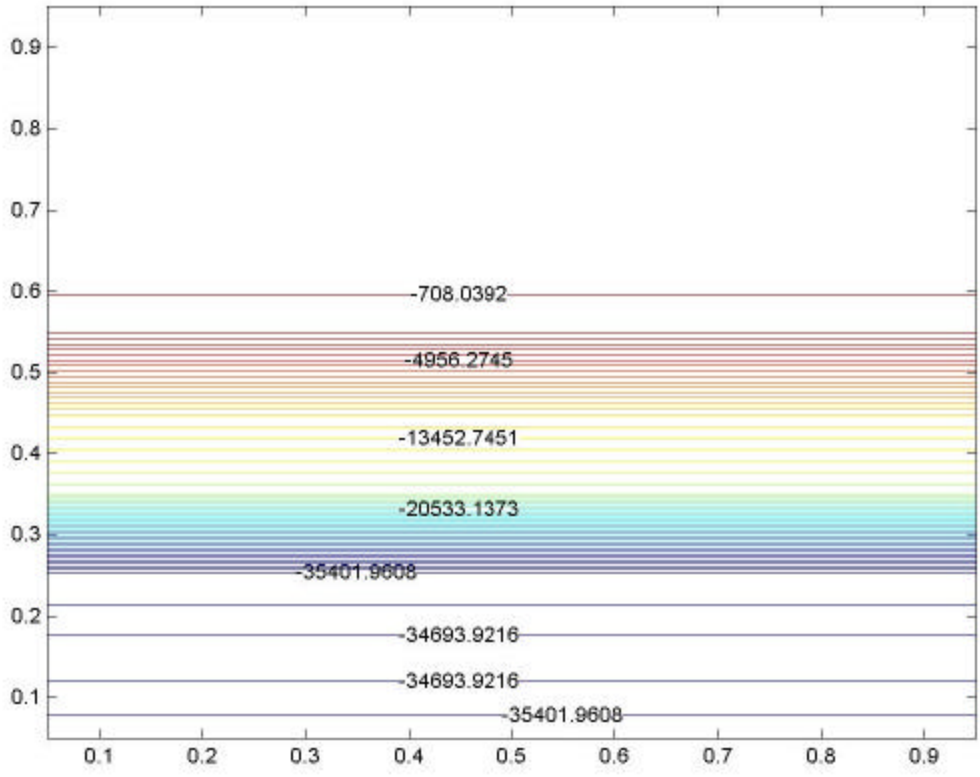


Figure 7(b): Contours of σ_{22} at $t=0.15$ seconds

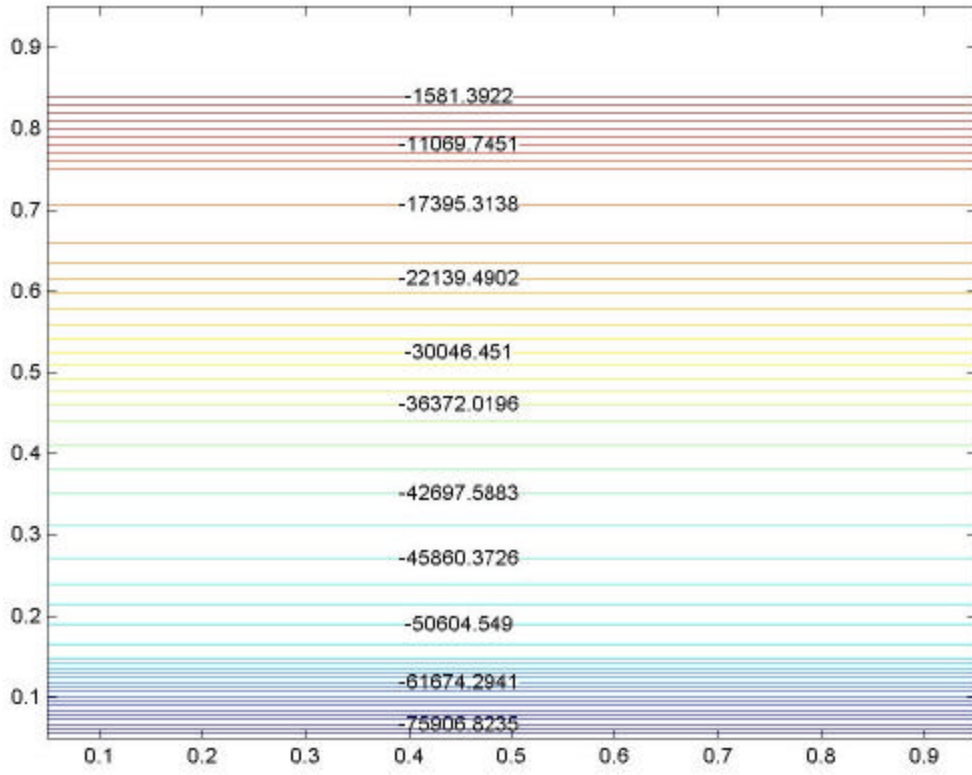


Figure 7(c): Contours of σ_{22} at $t=0.15$ seconds

III. “Modeling and Simulation of Granular Flows”

**Dhanunjay Boyalakuntla (S), Carnegie Mellon University,
and Jayathi Murthy (F), Purdue University**

with

Thomas O’Brien (M), NETL

Annual Report
Student/NETL Partnership Program
Modeling and Simulation of Granular Flows

Dhanunjay S. Boyalakuntla
Graduate Student
Carnegie Mellon University
Pittsburgh, PA 15221

Jayathi Y. Murthy
Professor, School of Mechanical Engineering
Purdue University
West Lafayette, IN 47907-1288

NETL Sponsor: Dr. Thomas O'Brien

December 2001

Abstract

The objective of the proposed work is to develop a solver for gas-solid flows based on discrete element simulations of the solid phase. The solid phase is modeled as a set of spherical particles interacting with each other through a soft-sphere model which includes a spring-mass-damper mechanism. The motions of individual particles are tracked using an explicit time stepping scheme. Wall interactions are modeled using both soft-sphere (finite time) and hard-sphere (instantaneous) interactions. Efficient search algorithms are implemented which scale either as $O(N)$ or as $O(N \log(N))$. The implementation is done in the MFIX code. Demonstration calculations are done to test the implementation for vibrating beds and different regimes of flow are traced. The present implementation is done in serial. Proposed work for the next year includes coupling with the fluid flow in MFIX and parallelization of the code.

Table of Contents

Abstract.....	2
List of Figures.....	4
1. Introduction.....	5
2. Executive Summary.....	5
3. Numerical Method.....	5
4. Results and Discussion.....	7
5. Conclusions.....	8
6. Nomenclature.....	9
7. References.....	9

List of Figures

Figure 1: Comparison of neighbor search techniques

Figure 2: Schematic of vibrating bed

Figure 3: Bed vibration at different time instants

1. Introduction

During the last decade there has been a great deal of effort devoted to developing simulation capabilities for gas-solid flows. The effort has been in two different directions: (i) a continuum approach whereby the gas and solid phases are both represented as continua (Lun et al (1984); Ding and Gidaspow(1990)), or (ii) a continuum approach is retained for the gas phase, but the solid phase is represented as a collection of discrete elements, and the motion of these elements is computed from first principles, using an interaction model to represent collisions. Cundall and Strack (1979) and Walton (1992) were among the first to develop a model for particle-particle interaction using a spring-mass-damper model. Tsuji and co-workers (1993) computed the first coupled gas/solid flows using discrete element simulations (DES). Nearly all published simulations in the literature are relatively small scale in scope, with 10^4 - 10^5 particles at the most. Typical simulations require several days to several weeks to complete, and must frequently be done using particle sizes much larger than realistic in order to achieve realistic void fractions. In order for DES to be used in industrial gas/solid flows, large-scale parallel computation of coupled DES and gas-phase flows is necessary. The objective of this project is to first implement DES in the MFI code, and couple it to the fluid flow solver in MFI using a serial implementation. During the second phase of the project, a parallel implementation for both distributed and shared memory architectures will be pursued. This report describes progress made during the last year on the first phase of the project and discusses the plans for the next year of work.

2. Executive Summary

During the last year, a DES capability has been implemented in the MFI solver. The implementation is for both 2D and 3D. Three different nearest-neighbor search algorithms have been implemented, tested and benchmarked for performance. The first is a simple N^2 search. The second is a non-binary search published by Munjiza et al (1998). The third employs a quadtree/octree data structure for storing particle locations. We have shown that the fastest of these searches is the non-binary search, which scales as $O(N)$; however, it is limited to particles of similar size. A DES implementation based on the model of Cundall and Strack (1979) has been implemented and tested, with wall collision being modeled with both a soft-sphere and a hard-sphere approach. The model is used to compute pure granular flows in vibrating beds. For the next year, we plan to couple the DES implementation to the fluid flow solver in MFI and pursue parallelization.

3. Numerical Method

3.1 Governing Equations

The equations governing the motion of a discrete particle in the discrete element simulation are written using the model of Cundall and Strack (1979). From Newton's law of motion, the particle velocity in the absolute frame is given by:

$$\dot{\vec{v}}_s = \frac{\vec{F}}{m} + \vec{g} \quad (1)$$

where the force vector is composed of contact and drag forces:

$$\vec{F} = \vec{f}_C + \vec{f}_D \quad (2)$$

The contact force is composed of the contributions of all particles with which the present particle has contact. It can be broken up into normal and tangential contact forces:

$$\vec{f}_{Ci} = \sum_j (\vec{f}_{Cnij} + \vec{f}_{Ctij}) \quad (3)$$

The normal contact force is modeled using a spring and damper; the damping term is based on the normal component of the relative velocity of the particle, and the normal direction is the direction connecting the particle centers.

$$\vec{f}_{Cni} = -k\vec{d}_{nij} - h\vec{v}_{nij} \quad (4)$$

The tangential component is written in a similar way, but incorporates a slip (slider) when the tangential force exceeds the frictional resistance:

$$\vec{f}_{Cti} = -k\vec{d}_{tij} - h\vec{v}_{tij}$$

$$\left| \vec{f}_{Ctij} \right| > \mathbf{m}_f \left| \vec{f}_{Cnij} \right| \quad \vec{f}_{Ctij} = -\mathbf{m}_f \left| \vec{f}_{Cnij} \right| \vec{t}_{ij} \quad (5)$$

In the above definitions, the normal and tangential velocity vectors are defined as:

$$\vec{v}_n = (\vec{v}_r \cdot \vec{n})\vec{n} \quad \vec{v}_t = \vec{v}_r - \vec{v}_n + r(\vec{\omega}_i + \vec{\omega}_j) \times \vec{n}$$

$$\vec{t}_{ij} = \frac{\vec{v}_{tij}}{|\vec{v}_{tij}|} \quad (6)$$

In addition, the Cundall and Strack model also solves the angular velocity of the particle using:

$$\dot{\vec{\omega}} = \frac{\vec{T}_C}{I} \quad \vec{T}_{Ci} = \sum_j (r\vec{n}_{ij} \times \vec{f}_{Ctij}) \quad (7)$$

3.2 Boundary Treatment

Two different boundary treatments were implemented and tested. The first is a soft-sphere treatment resulting in a finite time of contact. Here, the bounding wall is assumed to be sphere of infinite radius with given k and η ; a wall motion may be prescribed. The interaction between the particle and the boundary is then determined by equations (1-7). In the hard-sphere treatment, the particle is assumed to hit the wall and bounce back instantaneously. The velocity component normal to the wall changes sign, and the both the normal and tangential components are attenuated by a single coefficient of restitution.

3.3 Solution Algorithm

An explicit time-stepping scheme is adopted for the time integration. The time step is limited by the stiffness, and is estimated as

$$\Delta t = 2p\sqrt{m/k} \quad (8)$$

The time-stepping algorithm may be summed up by the following steps:

1. Initialize all particle positions, linear and angular velocities. Initialize wall positions.
2. Find particle neighbors using one of the three search algorithms. Find particle overlaps.
3. Take a time step Δt .
 - For $N=1, N_{\text{particles}}$
 - (i) Find contact and body forces due to inter-particle collision
 - (ii) Find contact forces due to wall interaction
 - (iii) Find new particle velocities and positions
4. If maximum time is reached, stop. Else go to (2).

4. Results and Discussion

4.1 Search Algorithms

Here we present results from the benchmarking of the three neighbor search algorithms we tested in the course of the development. These are the simple $O(N^2)$ search algorithm, a non-binary search (NBS) algorithm, and one in which a quadtree/octree-based search is employed. Fig. 1 shows a comparison of the three search methods for a range of particle numbers. We see that the NBS and the quadtree/octree searches far outperform the simple-minded N^2 search, with the NBS performing approximately as $O(N)$ and the tree searches approximately as $O(N \log(N))$. The NBS algorithm is limited to particles of similar size, whereas the tree-searches are applicable to arbitrary-sized particles. Both options are offered in MFIX and may be used as appropriate.

4.2 Demonstration Calculation

The DES implementation was used to compute flow in a vibrating granular bed. Wassgren (1997) computed pure granular flow in vibrating beds for a variety of operating parameters and made some comparisons with experiments. The basic configuration we simulated is similar to that of Wassgren but not identical. It is shown in Fig. 2. A rectangular box contains 3000 particles of diameter $d=0.975$ mm and density 2500 kg/m³. The initial depth of the bed is $h/d=14$, and the width is $w/d=200$. The normal spring stiffness and damping coefficients are $k=3602$ N/m and $\eta=0.02092$ N/(m/s). The lateral boundaries are assumed to be walls, with equivalent stiffness and damping coefficients of $k=7204$ N/m and $\eta=0.04184$ N/(m/s). The top wall is much higher than the bed free surface, and does not enter the calculation. The bottom wall vibrates sinusoidally as:

$$y = A \sin \omega t \quad (9)$$

A soft-sphere wall contact model was used in the calculation. The computations presented here employ a wall vibration frequency of 25 cycles/second, and a dimensionless acceleration parameter $\gamma = A\omega^2/g = 2.0$. A fixed time-step $\Delta t = 4.337 \times 10^{-6}$ is used for the computation. With this time step, one cycle of wall motion is completed in approximately 10^4 time steps. Typically 25-50 cycles are required before a periodic condition is reached. Each cycle requires approximately 15 minutes of computational time on a single process Dell personal computer operating at 1.5 GHz.

Fig. 3 show different time instants in one cycle of bed motion. The presence of surface waves is clearly visible. An analysis of the frequency content of the wave motion establishes that the frequency of the surface waves is $f/4$, i.e., four cycles of the wall motion correspond to one complete cycle of the bed motion. A similar determination was made by Wassgren (1997) for a similar set of parameters, albeit with periodic conditions on the lateral walls.

5. Conclusions

An implementation of discrete element simulation (DES) has been done in the MFIX code. The model of Cundall and Strack (1979) has been implemented for interparticle collision, with efficient neighbor search algorithms which scale nearly linearly with particle number. Sample calculations have been done in vibrating beds, corresponding to cases published in the literature, and a match with published bed frequencies has been found. For the next two months, more extensive comparisons will be made for vibrating beds, choosing from the experimental and numerical results of Wassgren (1997). Once we have established that all is satisfactory, we will couple the DES module to the fluid flow computation in MFIX. The second phase of the project will be the porting of the code to the parallel version of MFIX and the parallelization of the DES module.

6. Nomenclature

A	amplitude of bed vibration
\vec{F}	force on particle
\vec{f}_c	net contact force on particle
\vec{g}	acceleration due to gravity
k	spring constant
\vec{T}_c	torque due to contact force
t	time
\vec{v}_s	solid velocity in laboratory frame
η	damping constant
ω	frequency of bed vibration
μ_f	friction coefficient
\vec{d}	overlap vector

7. References

- Cundall, P.A. and Strack, O.D.L., "A Discrete Numerical Model for Granular Assemblies," Vol. 29, No. 1, pp. 47-65, 1979.
- Ding, J. and Gidaspow, D., "A Bubbling Fluidization Model Using Kinetic Theory of Granular Flow," AICHE Journal, Vol. 36, No. 4, pp. 523-538, 1990.
- Lohner, R., "Some Useful Data Structures for the Generation of Unstructured Grids", Communications in Applied Numerical Methods, Vol. 4, 123-135, 1998.
- Lun, C.K.K., Savage, S.B., Jeffrey, J.B., and Chepur, N., "Kinetic Theories for Granular Flow: Inelastic Particles in Couette Flow and Slightly Inelastic Particles in a General Flow Field," Journal of Fluid Mechanics, Vol. 140, pp. 223-256, 1984.
- Munjiza, A. and Andrews, K. R. F., "NBS Contact Detection Algorithm for Bodies of Similar Size", International Journal for Numerical Methods in Engineering, Vol. 43, 131-149, 1998.
- Tsuji, Y., Kawaguchi, T. and Tanaka, T., "Discrete Particle Simulation of Two-Dimensional fluidized Bed", Powder Technology, Vol. 77, No.1, pp. 79-87, 1993.
- Walton, O.R., "Numerical Simulation of Inclined Chute Flows of Monodisperse Inelastic Frictional Spheres, " Advances in Micromechanics of Granular Materials, H.H. Shen et al, Editors, Elsevier Science Publishers, B.V., 1992.
- Wassgren, C., Vibration of Granular Materials, Ph.D Thesis, California Institute of Technology, 1997.

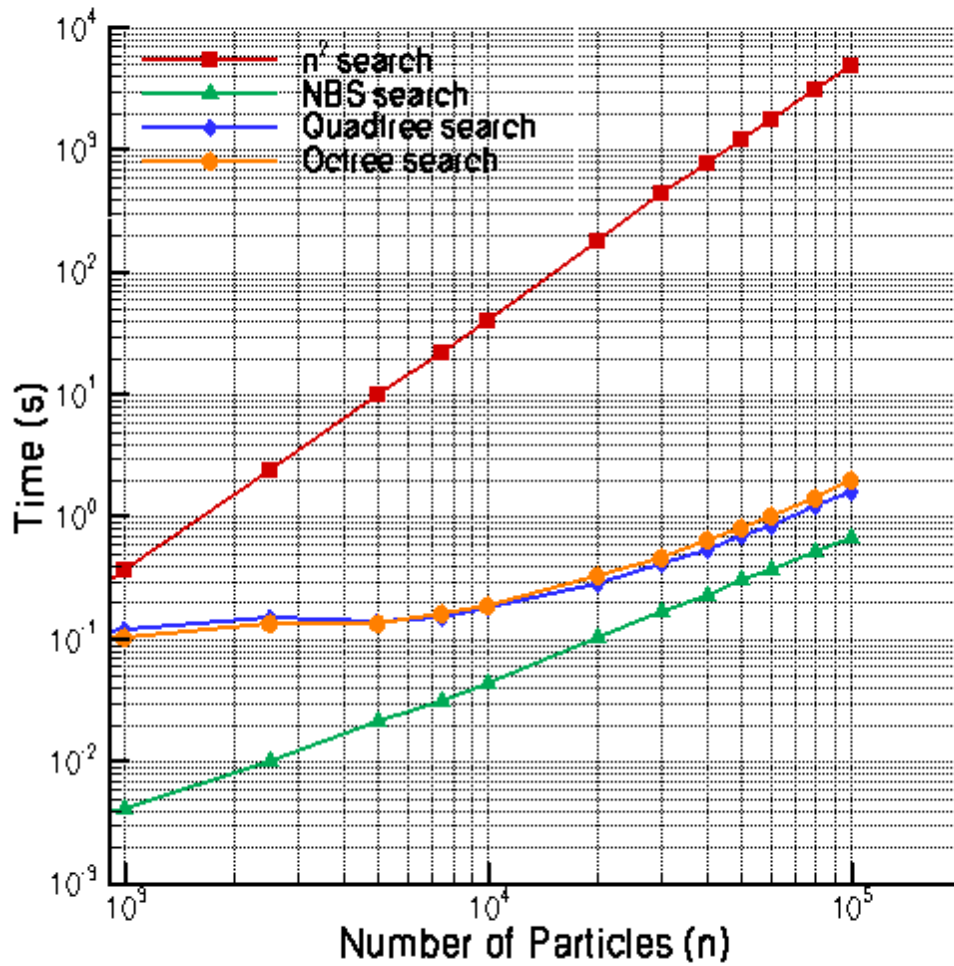


Figure 1: Comparison of neighbor search techniques

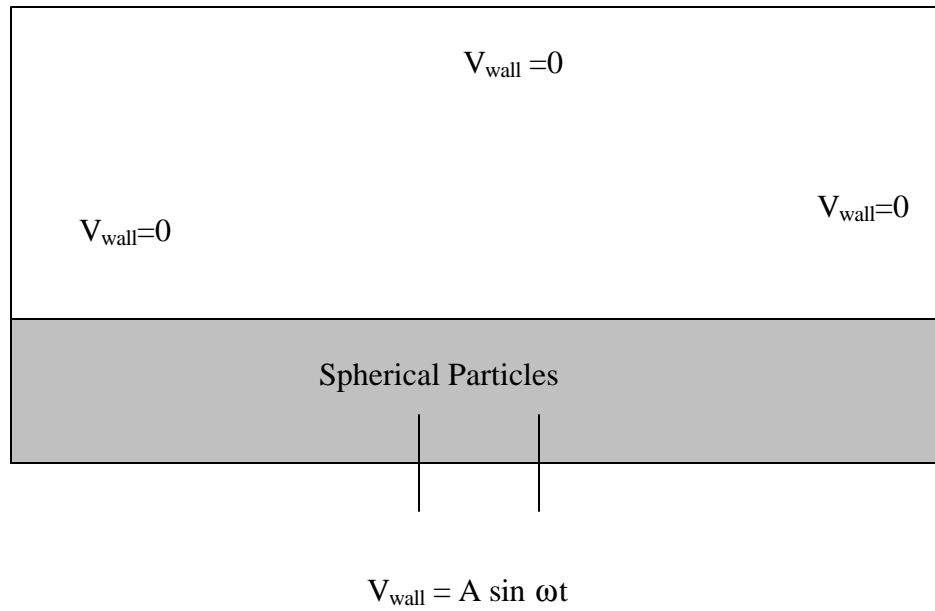


Figure 2: Schematic of vibrating bed

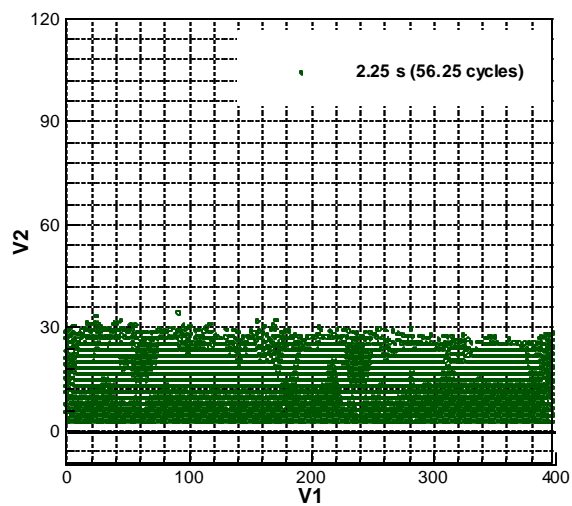
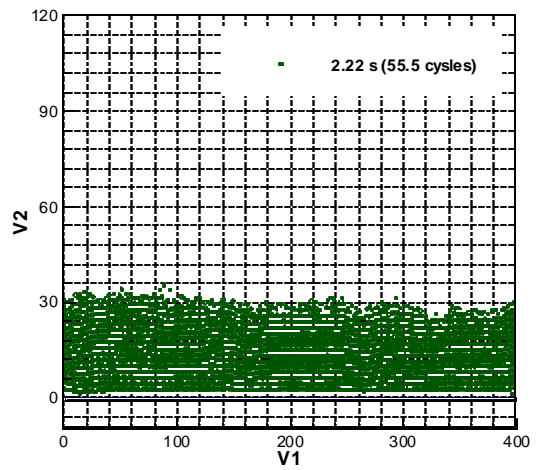
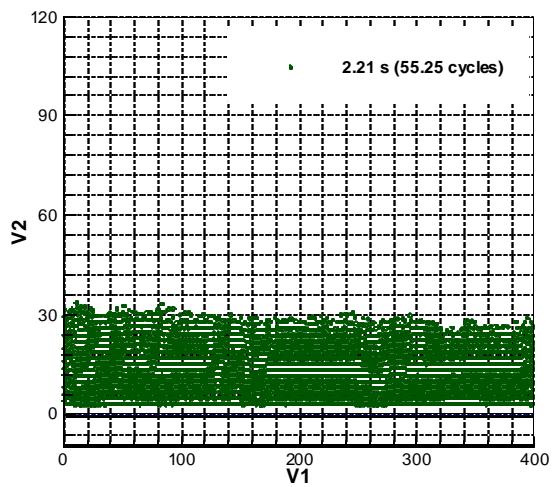
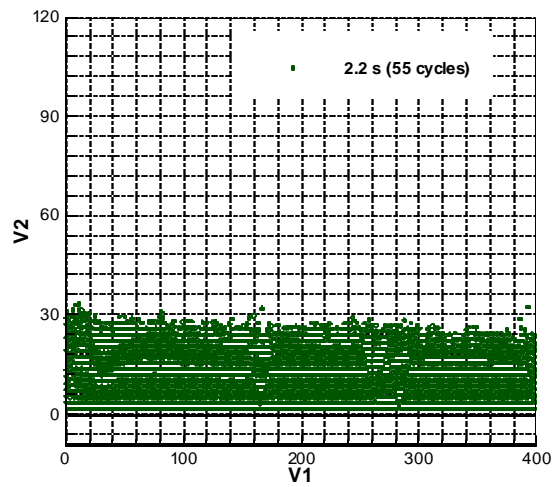
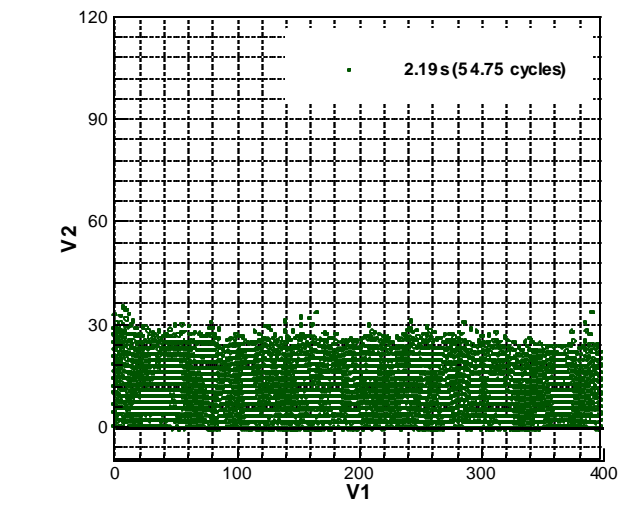


Figure 3: Particle positions for one cycle of wall motion

IV. “Microstructure and the Thermophysical Properties of Ash Deposits”

**Soon Kweon (S) and Allen Robinson (F), Carnegie Mellon University
with
Everett Ramer (M), NETL**

University/NETL Partnership Program

Annual Progress Report

PROJECT TITLE: Microstructure and the Thermophysical Properties of Ash Deposits

PIs: Allen L. Robinson (Carnegie Mellon University)
Everett Ramer (National Energy Technology Laboratory)

STUDENT: Soon Kweon (Carnegie Mellon University)

INSTITUTION: Carnegie Mellon University
Dept. of Mechanical Engineering, Scaife Hall
Pittsburgh, PA 15213
(412) 268 – 3657; (412) 268 – 3348 (fax)
e-mail: alr@andrew.cmu.edu

PERIOD: 10/1/00 – 9/30/01

DATE: December, 2001

Abstract

Ash deposits reduce heat transfer rates to furnace walls, superheat tubes, and other heat transfer surfaces in coal-fired power plants. Thermal conductivity and emissivity are the two deposit properties that influence strongly this heat transfer. These properties are thought to depend mainly on the microstructure of the deposit. In our previous work, the microstructure of two sample ash deposits was characterized using image analysis techniques to determine structural parameters such as particle volume density, particle specific surface area, contiguity, particle aspect ratio, particle number density, density-density correlation functions, and particle size distribution. This report describes the use of a ballistic deposition model to simulate deposit structure under conditions similar to those of the measurements. Model inputs include fly ash size distribution, particle viscosity, and particle sintering. Values for these parameters are chosen to match boiler operations and coal quality. The microstructure of the simulated deposits and the sampled deposits are quantitatively compared using the structural parameters defined above. Both sampled and simulated deposits are coincident in terms of the structural parameters. Analysis is performed to examine the sensitivity of the simulated deposit microstructure to the rolling probability, a critical model input.

Table of Contents

Abstract	2
Table of Contents	3
Introduction	4
Methods	4
Deposition model	4
Particle size distribution	5
Particle rolling and sticking probability	6
Sintering	7
Model-Measurement comparison	7
Results and Discussion	11
Conclusions	13
References	13

Introduction

Coal fired power plants generate more than 50% of the electricity in the United States. Key to the successful operation of coal-fired power plants is the management of the ash that is produced by burning the coal. Uncontrolled or unexpected deposits of this ash on the heat transfer surfaces in and around the boiler interfere with its operation, cause unplanned shutdowns, and reduced output and efficiency. Advanced power systems under development that use coal, such as those proposed in the DOE Vision 21 program, will not be immune to ash management issues. In fact, the operators of these plants will have to address problems such as high-temperature ash deposition and the cleaning of high-temperature heat exchangers that are beyond current experience, and which will be more challenging.

Ash deposits form from fly ash, inorganic vapors, and some gas species that deposit or react through a variety of mechanisms. Ash deposit can obstruct or even block the flow through the boiler or the convective pass. Ash deposits also reduce heat transfer rates to furnace walls, superheater tubes, and other heat transfer surfaces. The thermal conductivity and emissivity are the critical properties that control heat transfer rates through the deposit.

The specific objective of this project is to develop a method of predicting the heat transport properties of the ash deposits that form on heat exchanger tubes. These deposits are granular materials formed by the inertial impaction of fly ash particles entrained in the combustion gases. Their heat transfer properties are determined primarily by the deposit structure, most notably its porosity and the extent of contact between the particles that compose the deposit. The hypothesis is that these structural factors are directly related to the stickiness, or softness, of the impacting particles; which, for a given ash chemistry, is determined by the particle temperature.

In this report we use a ballistic deposition model to simulate deposit microstructure. Critical input parameters for the model are particle size distribution, particle rolling frequency, and particle swelling. These parameters are determined using semi-empirical models that depend on boiler operations and coal quality. Predictions of the model are quantitatively compared to measurements of deposit microstructure. Parametric simulations are performed to evaluate the sensitivity of the predicted microstructure parameters to model inputs.

Methods

Deposition model

A simple ballistic deposition model is used to simulate deposit microstructure. The model was originally developed to simulate random packing of hard spheres [1; 2; 3]. The model drops solid spheres from random coordinate positions over a pile of spheres deposited in advance. The sphere impacting on the pile of spheres rolls over the pile until it finds a stable three-point contact position. Tassopoulos and Rosner[4] applied a version of this basic model to the problem of ash deposits.

In this work we use a modified version of the model used by Tassopoulos and Rosner[4]. The model is modified to allow the use of polydisperse particles and to allow specification of the rolling on an individual particle basis. The main features of the model include[4]:

1. Three dimensional off-lattice simulations. Particles are started at random positions above the existing deposit and are assumed to travel in straight lines normal to the target. The target is a flat surface.

2. The particles are hard spheres with a polydisperse size distribution.

3. Already deposited particles cannot be displaced by subsequent particle arrivals.

4. A particle that hits the target surface (heat transfer surface) sticks immediately. If the particle hits another particle, as is likely after the initial layer of the deposit has built up, then it rolls in the direction of steepest descent. The rolling motion is continued until contact is established with another particle, in which case it continues to move towards the target while maintaining contact with both fixed particles. Each new contact between the rolling particle and another fixed particle is considered as a new “rolling event.” If a particle while rolling reaches a position where it hangs below the contacted particle it drops vertically until it hits another particle or the target surface. Rolling is continued until a specified number of rolling events are completed, the particle reaches a position of local minimum potential energy, or the original target surface is reached.

5. At rest, point contacts exist between particles and their adjacent neighbors. To increase the contact area between particles, the size of the particles is increased – this process is referred to as swelling.

The deposition model requires three inputs: 1) the particle size distribution, 2) the particle rolling frequency, and 3) the particle swelling. The goal of this project is to determine values for these parameters based on boiler operations and coal quality. For example, the particle size distribution is determined from predictions of the fly ash size distribution and the probability that the fly ash particle will strike and stick to the heat transfer tube. The rolling frequency depends on the ability of the deposit and particle to deform to adsorb the kinetic energy of the particle. If this energy is not adsorbed in the collision, the particle will bounce or roll. The particle swelling is determined by deposit sintering, which increases the connectivity of particles within the deposit. This approach will result in an independent model to the determination of deposit microstructure.

Particle size distribution

The particle size distribution is estimated by combining predictions of the fly ash size distribution with estimates of the particle capture efficiency. The fly ash size distribution is estimated using a full coalescence model. The full coalescence model assumes that all of the inorganic constituents in each coal particle combine to form a single fly ash particle.

Particle capture efficiency is the probability that a fly ash particle will strike the deposit or the deposition surface. This probability is determined by the physical processes such as inertial impaction, thermophoresis, and condensation that control deposit formation. For this study, the model only accounts for the effects of inertial impaction onto a cylindrical tube in cross flow. Inertial impaction is responsible for the deposition of the majority of the deposit mass in commercial boilers. The probability that a particle will strike a tube due to inertial impaction depends almost exclusively upon the geometry of the tube target, particle size and density, and gas flow properties. This process is most important for the particles larger than 10 μm . The impaction rates are highest at the stagnation point of the cylinder, decreasing rapidly with

angular position along the tube surface. The particle capture efficiency is defined as the ratio of the number of particles impacting on the tube surface to the number of particles traveling to the tube surface in the free stream. The probability that a particle will strike a cylindrical tube in cross flow is [10]

$$\eta(\text{St}_{\text{eff}}) \cong \left[1 + 1.25(\text{St}_{\text{eff}} - 0.125)^{-1} - 1.4 \times 10^{-2}(\text{St}_{\text{eff}} - 0.125)^{-2} + 0.508 \times 10^{-4}(\text{St}_{\text{eff}} - 0.125)^{-3} \right]^{-1} \quad (1)$$

where St_{eff} is the particle Stokes number. The Stokes number is defined for a cylinder in cross flow as

$$\text{St}_{\text{eff}} = \frac{\rho_p d_p^2 \overline{U_p}}{9 \mu_g d_c} \quad (2)$$

where ρ_p is particle density, d_p particle diameter, and $\overline{U_p}$ mean velocity of particles. μ_g is the gas viscosity, and d_c tube diameter [7; 8].

Particle rolling and sticking probability

All of the particles that strike the deposition surface or the deposit contribute to the deposit mass – these particles are not re-entrained in the flow past the surface. The final location of the particles depends on particle rolling, which depends on the ability of the particle and the deposit to absorb the impact energy. If this energy is not absorbed by the initial contact then the particle will roll and collide with another part of the deposit. We predict that the particle rolling probability based on the particle viscosity, which is a measure of the ability of the particle to deform to absorb the energy of the collision. The model does not account for the deformation of the deposit. The particle viscosity depends on the particle chemical composition and the particle temperature.

The particle temperature is calculated assuming that the particle is in uniform temperature and accounting for the heat transfer between the particle and surrounding gases by convection and radiation,

$$m_p \frac{d C_p T}{dt} = A_p h_m (T_g - T_p) + \varepsilon \cdot \sigma A_p (T_{\text{rad}}^4 - T_p^4) \quad (3)$$

where h_m is the convective heat transfer coefficient for a sphere, T_p is the particle temperature impacting on the deposit, T_g is the gas temperature around the traveling particle, T_{rad} is the radiant temperature around the traveling particle, σ is the Stefan-Boltzman constant, ε is the emissivity of the particles, A_p is the particle surface area, m_p is the particle mass, and C_p is the particle heat capacity. The heat capacity is a function of the particle chemical composition and the particle temperature.

The particle viscosity is estimated using PSI model [13],

$$\log \left(\frac{\mathbf{m}}{T_p} \right) = A + \frac{10^3 B}{T_p} \quad (4)$$

where \mathbf{m} is the particle viscosity in poise, T_p is the particle temperature in degree Kelvin. A and B are constants which depend on composition. The relationship is

$$-\ln A = 0.2693 \cdot B + 11.6725 \quad (5)$$

where A has units of [Poise K⁻¹] and B has units of [K].

Particle sticking probability is determined from the particle viscosity -- as a first approximation, particle viscosity has been found to provide a reasonable measure of the particle properties that affect sticking behavior [13]. Previous work suggests sticking probability was assumed to be inversely proportional to viscosity [13; 15; 16]

$$P_{sticking}(T_p) = \frac{\mathbf{m}_{ref}}{\mathbf{m}} \quad \mu > \mu_{ref} \quad (6a)$$

$$P_{sticking}(T_p) = 1 \quad \mu \leq \mu_{ref} \quad (6b)$$

where \mathbf{m}_{ref} is the reference viscosity when the ash particles were assumed to become perfectly sticky at a viscosity of 950 poise in 1550 [K] of particle temperature[19].

Particle rolling probability is defined as

$$P_{rolling}(T_p) = 1 - P_{sticking}(T_p) \quad \mathbf{m} > \mathbf{m}_{ref} \quad (7a)$$

$$P_{rolling}(T_p) = 1 - P_{sticking}(T_p) \quad \mathbf{m} \leq \mathbf{m}_{ref} \quad (7b)$$

The particle rolling probability does not account for the possibility of particle shedding or erosion after the initial impaction on the pile of the ash particles. The particle rolling is assumed to be independent of the particle size.

Sintering

The development of deposit strength is due primarily to viscous flow sintering of deposit particles [17; 19; 20; 21]. Viscous flow sintering between particles within a slagging deposit is largely determined by surface tension and viscous forces. Surface tension forces cause adjacent particles to sinter together by increasing the width of the neck between particles and decreasing the distance between the center of the particles, while viscous flow makes this movement possible. Neck growth continues until the two particles are no longer distinguishable. The model simulates the effects of sintering by swelling the particle size. For this report, the degree of swelling was assumed based on the measurements of particle contact area. The ultimate goal is to estimate particle swelling using a viscous sintering model.

Model-Measurement comparison

Predictions of the deposition model are compared to previously reported measurements of deposit microstructure. The ash deposit samples examined by this project were generated in the Multi-Fuel Combustor (MFC) at Sandia National Laboratories. The MFC is a pilot-scale (~ 30 kW), 4.2-m-high, down-fired, turbulent flow combustor that simulates gas temperature, gas composition, and residence times experienced by particles in entrained flow combustion systems such as pulverized-coal-fired boilers. The combustor has electrically heated walls that can be maintained at a specified temperature. The MFC fires commercial grind pulverized coal.

The coal used in this study was Antelope coal, a Powder River Basin sub-bituminous coal. The deposits are collected on an air-cooled tube placed across the flow at the furnace exit. The surface temperature of this tube was maintained at 500°C to simulate a typical tube surface temperature of a heat transfer surface in the convective pass of a commercial boiler. Two sets of deposits were collected -- in one case the furnace walls were maintained at a temperature of 1300°C, and in the other case they were maintained at 900°C. The higher temperature experiment simulates conditions at the boiler exit, whereas the lower temperature case corresponds to conditions later in the convective pass. One effect of changing the furnace wall temperature is to change the temperature of the particles impacting the deposition probe. Particle temperatures are estimated to be 830 °C and 1200 °C for the 900 °C and 1300 °C cases, respectively. This temperature difference, in turn, affects particle viscosity and rolling probability. Measurements of the microstructure of these deposits were presented in the annual progress report for this project for the year ending in October 2000.

Values for the deposition model inputs, particle size distribution, rolling frequency, and particle swelling were selected to match the conditions of the experiments. The fly ash size distribution used for the simulation is a lognormal distribution fit to predictions made by Richard and Harb[5]. We have assumed an average particle density of 2.0 g/cm³, and a mean particle velocity of 5 m/s. The diameter of the deposition probe is 17 mm.

The chemical composition of the particles is based on the measured bulk elemental composition of the fly ash, which is shown in Table 1. Figure 1 shows the probability of particle rolling as a function of particle temperature for the Antelope fly ash.

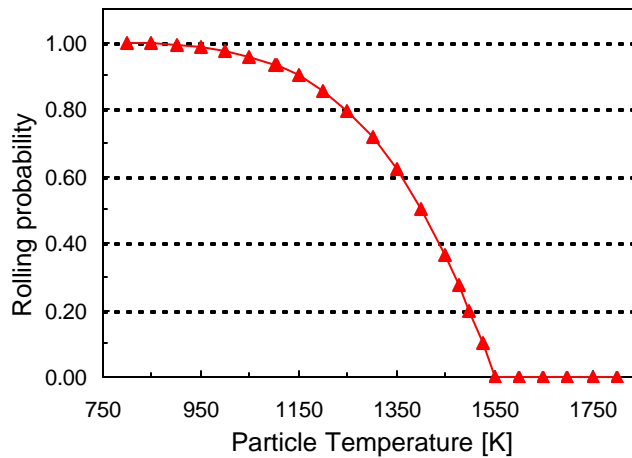


Figure 1 Particle rolling probability with particle temperature

Table 1 Fly ash elemental oxide compositions of Antelope coal [5]

Wt % of Ash	Antelope 900°C	Antelope 1300°C
SiO ₂	29.6	25.1
Al ₂ O ₃	17.1	15.4
Fe ₂ O ₃	10.2	10.7
TiO ₂	0.9	0.9
CaO	31.3	36.5
MgO	6.1	6.8
Na ₂ O	2.5	2.3
K ₂ O	0.9	0.6
P ₂ O ₅	1.4	1.8
P ₂ O ₅	4.6	3.5
SO ₃	2.3	1.8
% Carbon in Ash		

We have not yet implemented a deposit sintering algorithm in the model to predict particle swelling. For these simulations, particle swelling was determined based on measurements of particle contact area shown Figure 3. The 900 °C deposit does not show any particle sintering so that the degree of swelling is given as 0%, the 1300 °C deposit show a significant linear increase of particle sintering so that the degree of swelling is adopted from the fit of the linear increase of contiguity from the collection surface to the outer deposit layer ranged from 16% to 25 %.

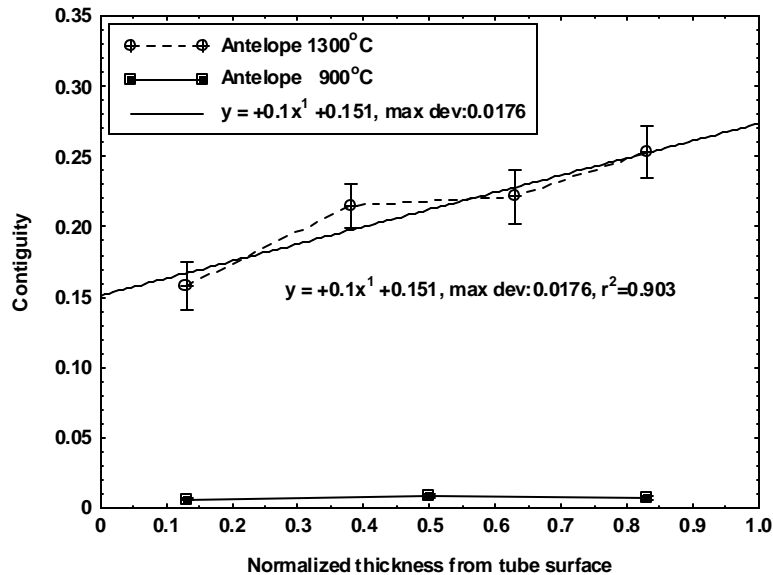


Figure 3. The degree of particle swelling from Contiguity

Table 2 summarizes the model inputs for the simulations. Two sets of simulations were conducted for each case. The first set labeled “PSI model” in Table 2 uses the PSI models to calculate the rolling probability. The second set labeled “enforced” assigned a rolling probability to obtain the best agreement between the model and the measurements of the various structural parameters.

Table 2. The input parameters for the deposition model

Input parameters	Antelope 900°C		Antelope 1300°C	
	PSI model	Enforced	PSI model	Enforced
Particle size distribution [micron]				
Average [μ m]	6.5	6.5	6.5	6.5
Std. Dev.	2.3	2.3	2.3	2.3
Number of rolling	1	1	1	1
% of particle rolling once	93 %	85 %	28 %	20 %
% of swelling	0 %	0 %	16 ~ 25 %	16 ~ 25 %

The microstructure of the simulated deposits was determined by cross-sectioning the simulated deposit parallel to the direction of the deposition. A cross section of a typical simulated deposit is shown in Figure 2. The light regions indicate the particles; the dark regions indicate void space between particles. Image analysis procedures were then performed to determine the following structural parameters: size distribution, particle volume fraction, particle number density [$\#/mm^3$], specific surface area [$1/\mu$ m], contiguity, mean chord length [μ m], mean path length [μ m], density-density correlation.

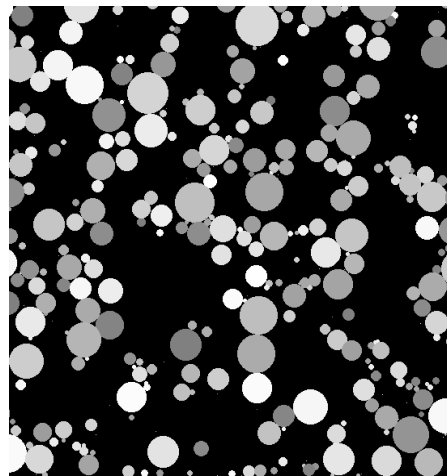


Figure 2. Cross-section of simulated deposit.

Results and Discussion

Figures 4 and 5 compare cross-sections of the PSI model, the enforced and the measured deposit microstructure for the 900 °C and 1300 °C cases, respectively. Qualitatively there appears to be reasonable agreement between the actual deposit microstructure and the results from both the PSI model and the simulations in which the value of the particle rolling probability was determined to obtain the best-model measurement comparison. Quantitative comparisons between the simulations and the measurements are summarized in Tables 3 and 4. Again, both model simulations agree reasonably well with the measurements. There is slightly better agreement with the “enforced” case compared to the “PSI model” case.

Table 3. Model measurement comparison of deposit collected at 900 °C furnace wall temperature.

Structure parameter	Measured	PSI model	Enforced model
Volume fraction	0.22 - 0.34	0.36	0.31
Specific surface area [micron]	0.050 - 0.070	0.057	0.052
Number density [#/mm ³]	17000 - 24000	24800	22900
Mean cord length [micron]	11.0 – 28.7	25.2	23.9
Mean path length [micron]	38.4 – 60.5	45.0	51.9

Table 4. Model measurement comparison of deposit collected at 1300 °C furnace wall temperature.

Structure parameter	Measured	PSI model	Enforced model
Volume fraction	0.18 - 0.30	0.30	0.25
Specific surface area [micron]	0.028 - 0.037	0.043	0.032
Number density [#/mm ³]	6660 – 11300	10900	6800
Mean cord length [micron]	18.5 – 41.1	27.7	31.4
Mean path length [micron]	77.3 – 110.5	64.9	92.3

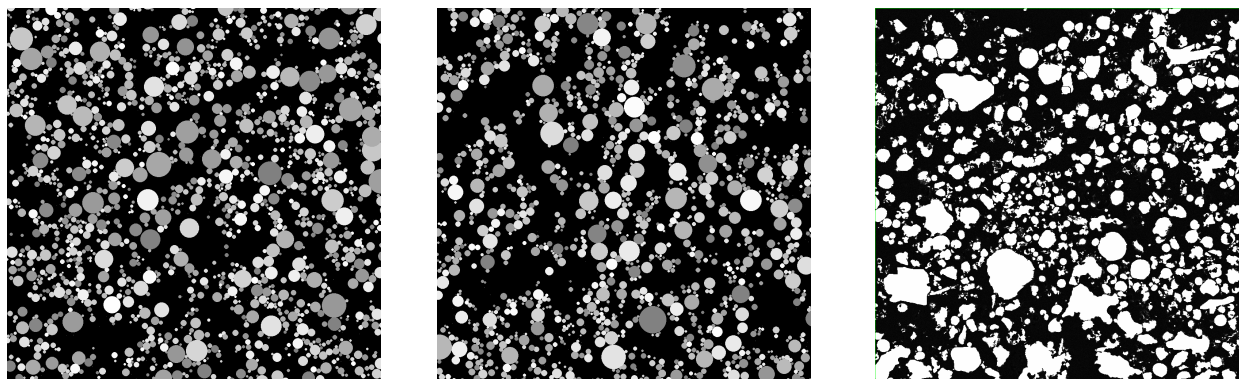


Fig. 4 Comparison of the cross-section of PSI model (left), enforced (middle), and actual deposit (right) collected at 900°C furnace wall temperature.

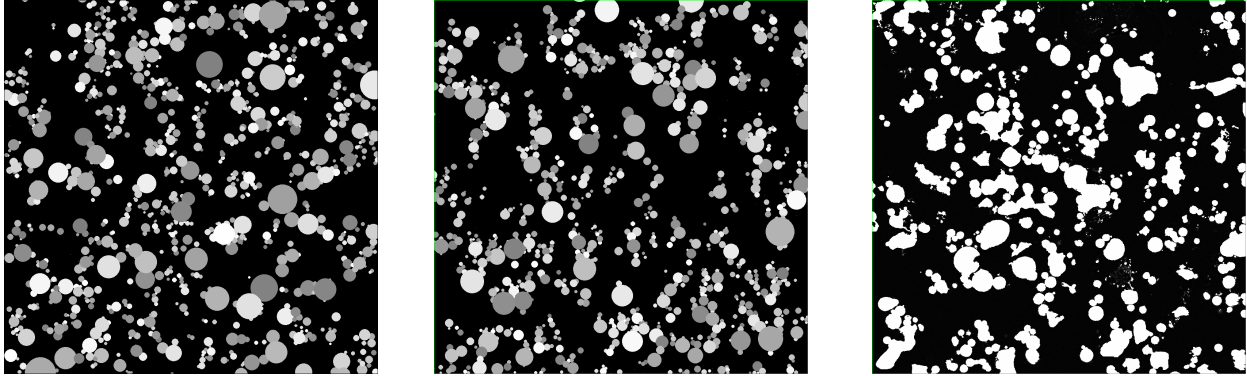


Fig. 5 Comparison of the cross-section of PSI model (left), enforced (middle), and actual deposit (right) collected at 1300°C furnace wall temperature.

It is important to note that values of the input parameters (particle size distribution, rolling frequency, and particle swelling) for these simulations were determined using a combination of independent models that account for boiler operations and coal quality and by forcing the simulations to match the measurements. The ultimate objective of this project is to derive these parameters independently based on boiler operation and coal quality.

The size distribution of the particles was predicted using a fly ash model and assuming particle impaction of inertial impaction. The comparability of the size distribution of the particles in the actual deposit and the simulated deposit suggests that this approach yields reasonable predictions for the deposit particle size distribution.

The values for the particle rolling frequency were determined two ways: using the predicted particle temperature and the PSI model, and by selecting a value to obtain the optimum model measurement agreement. The PSI model indicates that 93% of the particles in the 900 °C case and 28% of the particles in the 1300 °C case will roll once. Slightly adjusting these values (enforced case) so that 85% of the particles in the 900 °C case and 28% of the particles in the 1300 °C case roll once improves the model measurement comparison. However, considering the number of assumptions, the PSI model appears to provide reasonable predictions of the deposit microstructure. A possible explanation for the PSI model under predicting the amount of rolling is that the model does not account for particle shedding and erosion.

Results from parametric simulations are shown in Figures 6 to illustrate the variation of the various deposit solid fraction to the rolling probability. The results indicate how sensitive the solid fraction is to particle rolling. We are currently working at refining the algorithm that determines particle rolling from the coal quality and boiler operations.

Particle sintering within the deposit was evaluated based on experimental measurements of contiguity. Contiguity is a measure of the connectedness of the particles within the deposit. In case of 900°C, particle sintering is not considered in generating the simulated deposit because the contiguity showing the particle sintering is not significant in the measured real deposit. The 1300°C deposit has the consideration of the linear increase in contiguity across the deposit as shown in Fig.3.

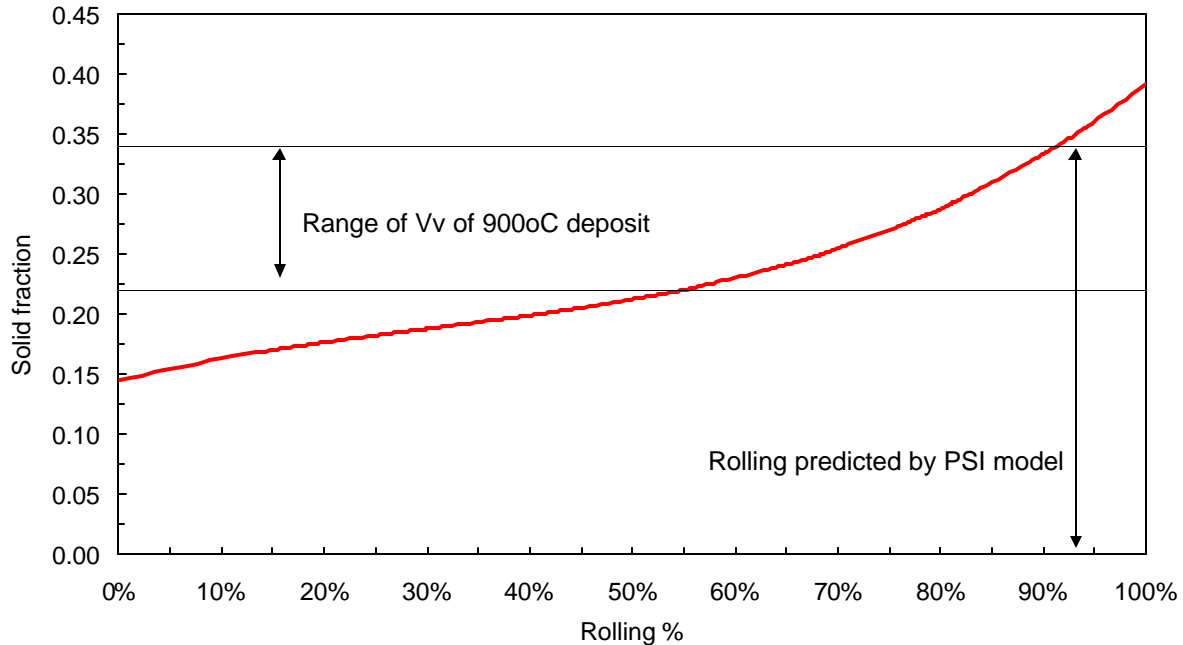


Fig.6 Variation in deposit volume fraction as a function of percentage of particle rolling for the 900 °C case (top). Sensitivity of deposit volume fraction as a function of percentage of particle rolling (bottom). Percentage of particle rolling is the percentage of particles that roll once after the initial contact with the deposit.

Conclusions

A ballistic deposition model was used to simulate deposit structure under conditions similar to those of the measurements. Model inputs include fly ash size distribution, particle viscosity, and particle sintering. Values for these parameters are chosen to match boiler operations and coal quality. The microstructure of the simulated deposits and the sampled deposits are quantitatively compared using the structural parameters defined above. Both sampled and simulated deposits are coincident in terms of the structural parameters. The particle rolling probability is a strongly influences the microstructure of the simulated deposits.

References

- [1] Visscher, W.M. and Bolsterli, M., *Nature*, 239, 1972, PP.504.
- [2] Tory, E.M., Church, B.H., Tam, M.K, and Ratner, M, *Canadian Journal of Chemical Engineering*, 51, 1973, PP.484.
- [3] Matheson, A.J., *Journal of Physics, C*, 7, 1974, PP.2569.
- [4] Tassopoulos, M. and Rosner, D.E., *Chemical Engineering Science*, Vol.46, PP.001-023, 1991.
- [5] Richards, G.H., “Investigation of Mechanisms for the Formation of Fly Ash and Ash Deposits for Two Powder River Basin Coals.” Ph.D. dissertation, Brigham Young University, 1994.

- [6] Smith, J.E. and Jordan, M.L., Mathematical and Graphical Interpretation of the Log-normal Law for Particle Size Distribution Analysis, *Journal of Colloid Science*, 19, 1964, PP. 549.
- [7] Baxter, L.L., Ash Deposition during Biomass and Coal Combustion: A Mechanistic Approach, *Biomass and Bioenergy*, Vol.4, No2, PP.85-102, 1993.
- [8] Wilke, C.R., A viscosity equation for gas mixtures, *Journal of Chemistry Physics*, Vol.18, No.4, PP.517-519, 1950.
- [9] Israel, R. and Rosner, D.E., Use of a Generalized Stokes Number to Determine the Aerodynamic Capture Efficiency of Non-Stokesian Particles from a Compressible Gas Flow, *Aerosol Science and Technology*, 2:PP.45-51, 1983.
- [10] Baxter, L.L., Ash Deposit Formation and Deposit Properties, Sandia Report SAND2000-8253, August 2000.
- [11] Boow, J. *Fuel*, 1969, 48, PP.171.
- [12] Boow, J. *Fuel*, 1972, 51, PP.170.
- [13] Senior, C.L. and Srinivasachar, S., Viscosity of Ash Particles in Combustion Systems for Prediction of Particle Sticking, *Energy & Fuels*, 1995, 9, PP.277-283.
- [14] Richards G.H., Slater, P.N. and Harb, J.N., Simulation of Ash Deposit Growth in a Pulverized Coal-Fired Pilot Scale Reactor, *Energy & Fuels*, 1993, 7, PP.774-781.
- [15] Wang, H. and Harb, J.N., Modeling of Ash Deposition in Large-Scale Combustion Facilities Burning Purverized Coal, *Progress on Energy and Combustion Science*, Vol.23, PP.267-282, 1997.
- [16] G.J. Cheng, A.B. Yu, and P.Zulli, Evaluation of effective thermal conductivity form the structure of a packed bed, *Chemical Engineering Science* 54, pp.4199-4209, 1999.
- [17] Raask, *Mineral Impurities in Coal Combustion*, 1985.
- [18] Lee, F.C.C. and Lockwood, F.C. Modeling Ash Deposition in Pulverized Coal-Fired Applications, *Progress in Energy and Combustion Science*, 1999.
- [19] Walsh, P.M., Sayre, A.N., Loehden, D.O., Monroe, L.S., Beer, J.M., and Sarofim, A.F., Deposition of Bituminous Coal Ash on an Isolated Heat Exchanger Tube: Effects of Coal Properties on Deposit Growth.
- [20] Nowok, J.W., Benson, S.A., Jones, M.L., and Kalmanovitch, D.P., Sintering Behavior and Strength Development in Various Coal Ashes, *Fuel*, 1990, Vol.69, August.
- [21] Wang, Huafeng, Modeling of Ash Formation and Deposition in PC Fired Utility Boilers, Ph.D. dissertation, Brigham Young University, December 1998.

**V. “Density Functional Theory Study of Iodine Chemisorption
on Chiral Metal Surfaces”**

**Preeti Kamakoti (S) and David Sholl (F), Carnegie Mellon University
with
Brad Bockrath (M), NETL**

**Density Functional Theory Study of Iodine Chemisorption
on Chiral Metal Surfaces.**

Preeti Kamakoti

Advisor: David S. Sholl

Department of Chemical Engineering
Carnegie Mellon University
Pittsburgh, PA 15213

4 December 2001

Abstract:

Many biologically active molecules are chiral, and often one enantiomer has a radically different biological effect than the other. The chirality of pharmaceuticals has led to strong demand for enantio-pure drugs. Certain high Miller index planes of single crystal metal surfaces are chiral, and have been theoretically and experimentally shown to exhibit enantiospecific adsorption properties. All work done to date on these materials has been on bare, chiral metal surfaces. This work investigates the possibility of further modifying the chiral environment by irreversibly adsorbing functional groups on the chiral metal surface. We report a Density Functional Theory (DFT) study of iodine chemisorption on Cu(111), Cu(100) and chiral Cu(531). DFT has been used to determine preferred binding sites and examine desorption pathways. Our calculations show that I prefers to adsorb on sites that maximizes its coordination with the Cu surface. This corresponds to the threefold, hollow and kink site on Cu(111), Cu(100) and Cu(531) respectively. In the case of Cu(111) and Cu(100), I desorbs from the surface as an atomic species. We attempt to resolve discrepancies with certain experimental observations of halide desorption. Overall, our results are in excellent quantitative agreement with experimental values. Results for Cl and Br on Cu(111) and Cu(100) show same qualitative trends as those for I. The adsorption energies increase in the order of halogen electronegativities from $I < Br < Cl$. A coverage dependent study of adsorption energy to understand formation of specific long-range adlayer structures on Cu(111) and Cu(100) is currently in progress. This work can be extended to other chiral surface/functional group combinations. This project served as a means of introduction to DFT and its ability to model many chemical processes at the atomic scale. We will apply this knowledge to examine another long-term project involving hydrogen separation using Pd/Cu alloy membranes.

Table of Contents:

- 1) Introduction
- 2) Executive Summary
- 3) Computational Methods
- 4) Results and Discussion
- 5) Conclusions and Future work
- 6) References

Introduction:

Phenomena associated with chiral molecules have held a deep fascination for scientists since Pasteur's initial discovery of enantiomeric crystals in the 1850's [1]. Biological systems are highly stereoselective. As a result, while one enantiomer may be biologically active, the other may be useless at best, or cause negative effects at worst. Thalidomide is a tragic example of the latter situation: *R*-thalidomide is a mild sedative, while *S*-thalidomide resulted in horrific birth defects [1]. The chirality of many pharmaceuticals has led to an enormous market for single enantiomer drugs. This is reflected in the growth in worldwide sales of enantio-pure drugs from \$US35 billion in 1994 to \$US115 billion in 1999 [1].

One way to develop a physical process that differentiates between molecular enantiomers is to have them interact with a solid surface that is itself chiral on molecular length scales. High-symmetry single-crystal surfaces of simple metals can be terminated to yield faces that are enantiomorphic. Enantiospecific effects on certain high Miller index metal surfaces have been observed experimentally by Attard *et al.* [2] and Gellman *et al.* [3]. All work to date on naturally chiral metal surfaces has involved molecular adsorption on bare surfaces that have not been altered using adsorbents [1-3]. It is interesting to consider whether it is possible to functionalize these surfaces by pre-adsorbing atoms or functional groups, then allowing the modified chiral surface to interact with chiral molecules. As a first step towards this goal, the aim of this study is to gain atomic scale insight into the adsorption process and energetics of halogen atoms on chiral copper surfaces. This work was done in conjunction with experimental studies of iodine on copper surfaces by Horvath & Gellman (Chem. Eng., CMU).

A theoretical study of chemisorption requires the ability to describe the energies and geometries of a variety of atoms and molecules interacting with complex surfaces. It is therefore important to use a method that quantitatively describes chemical bonds and has the ability to treat a broad range of atomic species. Density Functional Theory (DFT) is a first principles theory of electronic ground-state structure based on the electronic density distribution. DFT can be used for the understanding and calculation of ground state electron density and total energy of any system consisting of nuclei and electrons. In principle, it can be applied to all atoms in the periodic table, and can be used for systems involving metallic, covalent and ionic bonds. DFT consistently predicts quantities such as interatomic equilibrium distances in solids, molecules and surfaces to within 0.02 Å of experiment and vibrational frequencies to within 10 - 50 cm⁻¹ [4].

DFT can be used to model systems of the order of 100 atoms, though the computation time required increases rapidly with the number of atoms in the system.

Executive Summary:

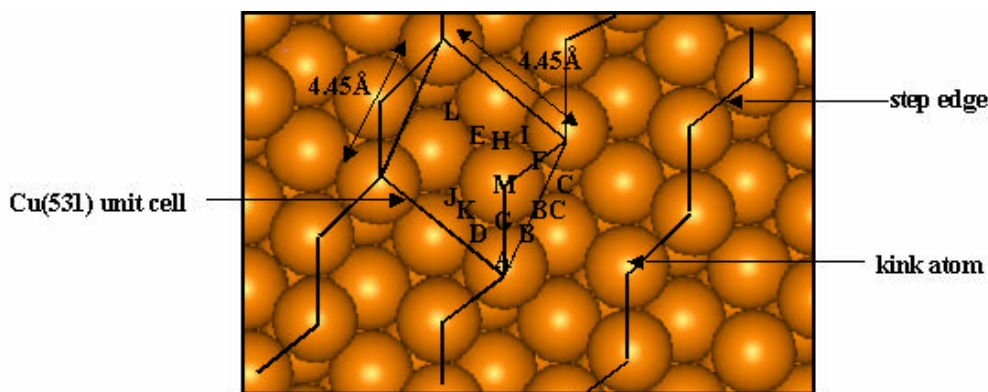
We studied the dissociative chemisorption of molecular iodine on Cu(111), Cu(100) and the chiral Cu(531) surface using plane wave Density Functional Theory. Iodine was found to adsorb on sites that maximize its coordination with the surfaces. In the case of the atomically flat surfaces, I desorbed as atomic species. Our results were found to be in excellent agreement with those from experiments. Analogous calculations done for other halogens showed that the adsorption energy increased in the order $I < Br < Cl$. The knowledge of DFT and its potential to be gained from this project will be used to examine another long-term project involving hydrogen separation using Pd/Cu alloy membranes.

Computational Methods:

Methods:

DFT was used to study the adsorption of iodine on three Cu surfaces: Cu(111), Cu(100) and Cu(531). Cu(531) is a chiral surface [2], and exhibits complex surface characteristics due to kinked steps on the surface (see Fig. 1).

Fig. 1: Schematic of Cu(531) surface with step edges, unit cell and adsorption sites.



The (531) surface has the smallest unit cell of any chiral fcc surface and, as we will see below, is well suited to adsorption of I. The adsorption of I on Cu(531) has not yet been examined experimentally, but I adsorption on Cu(100) and Cu(111) has been studied in numerous experiments [5-9]. For this reason, DFT was first used to examine I adsorption on these two surfaces. The results of these calculations allow direct comparison with experimental data and also provide valuable insight into the behavior of I on more complex surfaces such as Cu(531).

Calculation Details:

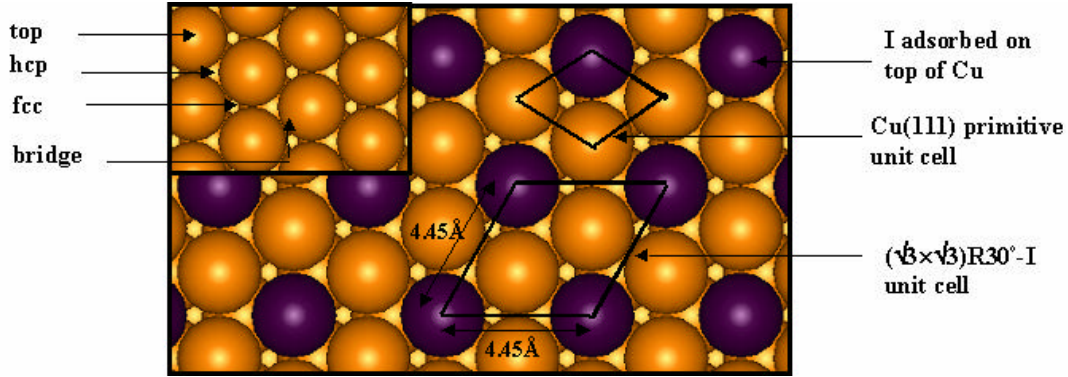
The DFT calculations were done using VASP (Vienna *ab initio* simulation package) [10]. This package applies DFT to a set of atoms repeated periodically in three dimensions to form a material of infinite extent [11]. This study employed the Local Density Approximation (LDA) and the Generalized Gradient Approximation (GGA) [12] for the exchange potential. A plane wave expansion with a cutoff of 233.729 eV was used in all calculations. Total energy calculations were done using the residual minimization method for electronic relaxation, accelerated using Methfessel Paxon Fermi-level smearing with a width of 0.2 eV. The atomic positions were relaxed using the Quasi-Newton algorithm until the forces on all unconstrained atoms were less than 0.03 eV/Å. A Monkhorst-Pack mesh with a 5×5×1 k-grid was used for Cu(111) and Cu(100), and 6×6×1 grid for Cu(531) calculations. The lattice parameter and bulk modulus calculated using DFT for bulk copper were 3.64 (3.53) Å and 152 (195) GPa using GGA (LDA). Experimental values [13] for these parameters are 3.61 Å and 142 GPa. Clearly, GGA gives good agreement with experiment whereas LDA tended to overbind the system resulting in low lattice constant and high bulk modulus. Unless otherwise stated, all results in the remainder of the paper used GGA. A supercell containing 4 layers of Cu and vacuum spacing equivalent to 4 or 5 lattice units were used in most calculations. Atoms in the top two surface layers and the iodine adlayer were allowed to relax in all directions during geometry optimizations.

Results and Discussion:

Iodine on Cu(111):

The adsorption of I on Cu(111) has been experimentally investigated since the end of the 1970's [9]. Iodine and other halogens undergo dissociative chemisorption on metal surfaces to give adsorbed atoms. Low energy electron diffraction (LEED) [5] and scanning tunneling microscope (STM) [9] studies have indicated the formation of a ($\sqrt{3} \times \sqrt{3}$)R30°-I adlayer at a coverage of 0.33 monolayer (ML), when the surface is saturated by exposure to gaseous I₂. This adlayer is schematically shown in Fig. 2. A surface extended x-ray absorption fine structure (SEXAFS) study [5] determined the threefold hollow to be the favorable site and estimated a Cu-I bond length of 2.66 ± 0.02 Å.

Fig. 2: Schematic of Cu(111) surface with I adlayer, inset with adsorption sites



We have performed DFT calculations to determine the energetically favorable binding site for adsorption at the $(\sqrt{3} \times \sqrt{3})R30^\circ$ adlayer of I on Cu(111). As shown in Fig. 2, Cu(111) exhibits four high-symmetry binding sites: fcc, hcp, bridge and top. The threefold fcc and hcp hollow sites differ in their relationship with the second layer. The hcp site has a Cu atom directly below it in the second layer, while the fcc hollow has a Cu atom below it in the third layer. Adsorption energies were calculated for the dissociation of molecular iodine and are reported per I atom. DFT results for adsorption energies and predicted bond-lengths are presented in Table 1. The fcc and hcp sites were found to be energetically preferred over the low coordination bridge and top sites, in agreement with the surface coordination determined experimentally [5]. The bond-length at the most favored site was 2.68 Å, in quantitative agreement with the experimental SEXAFS result [5]. This bond-length is significantly different than that in gaseous CuI, where Cu and I are separated by 2.38 Å. There is almost no energy difference between adsorption in the fcc and hcp sites.

Table 1: Adsorption sites for I/Cu(111)

Site	Coordination	Energy (kcal/mol)	CuI Bond Length (Å)	Site	Coordination	Energy (kcal/mol)	CuI Bond Length (Å)
Fcc	3	33.20	2.68	Bridge	2	32.28	2.60
Hcp	3	33.20	2.68	Top	1	26.24	2.49

The energies corresponding to desorption of atomic I, I₂ and CuI from ordered $(\sqrt{3} \times \sqrt{3})R30^\circ$ adlayers were studied. A study by Bent *et al.* [8] has reported desorption of CuI and Cu sublimation. This and a subsequent TPD study [7] reported peak desorption temperatures of 900 - 950 K. This corresponds to an energy barrier of ~57 - 60 kcal/mol. Our preliminary DFT analysis suggests that atomic iodine would be the predominant desorption product on a perfect, atomically flat surface covered by a $(\sqrt{3} \times \sqrt{3})R30^\circ$ adlayer. DFT predicts

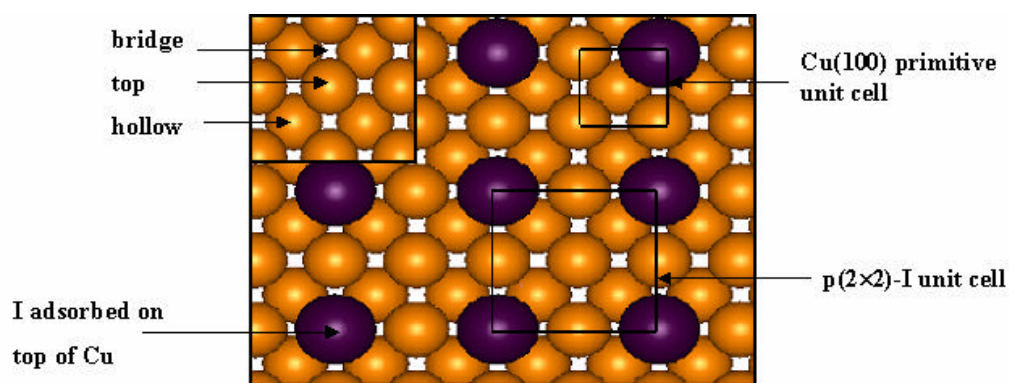
desorption energies of 58.8 kcal/mol for atomic I, 66.4 kcal/mol for I₂ and 88.4 kcal/mol for CuI desorption. In the absence of any additional barriers, the energy computed using DFT corresponds to the energy barrier for desorption observed experimentally.

DFT was also used to study Cu sublimation and analyze origins of halide desorption observed experimentally. The sublimation energy for a Cu atom on surface increased with coordination and ranged from 46.0 kcal/mol (3-fold coordination) to 101.1 kcal/mol (12-fold coordination). The source of subliming Cu atoms could be surface defects, atomic step edges and other sites of low coordination. Furthermore, at a given coordination, the desorption energy for CuI is lower than that for a Cu atom. Thus, it is possible that CuI desorbs from surface defects at similar temperatures to those where atomic I desorbs from the defect-free regions of the surface. A review by Dowben [14] states that it is difficult to make decisive conclusions of desorption products from thermal desorption studies due to variability in experimental conditions and reported results. It also points out that some observations of halide desorption may be attributable to surface defects and sample preparation methods.

Iodine on Cu(100):

A SEXAFS study [5] for I on Cu(100) was performed on a p(2×2) adlayer corresponding to 0.25 ML (see Fig. 3). This appears to be the only study reporting an adlayer structure for this system, although it is not known if it corresponds to saturation coverage. Cu(100) contains three high-symmetry binding sites: hollow, bridge and top.

Fig. 3: Schematic of Cu(100) surface with I adlayer, inset with adsorption sites



DFT calculations were performed similar to those for Cu(111). A summary of results can be seen in Table 2. The 4-fold hollow site was found to be the most energetically favorable binding site. The Cu-I bond-length corresponding to adsorption in the hollow site was obtained as 2.75 Å, in good agreement with experimental estimate of 2.69 ± 0.02 Å. As with Cu(111), the

desorption product at this coverage was predicted to be atomic I. The desorption energy for this process was found as 64.2 kcal/mol, ~5.4 kcal/mol higher than the corresponding case for Cu(111).

Table 2 Adsorption sites for I/Cu(100)

Site	Coordination	Energy (kcal/mol)	CuI Bond Length (Å)
Hollow	4	38.56	2.75
Bridge	3	34.27	2.59
Top	1	27.97	3.52

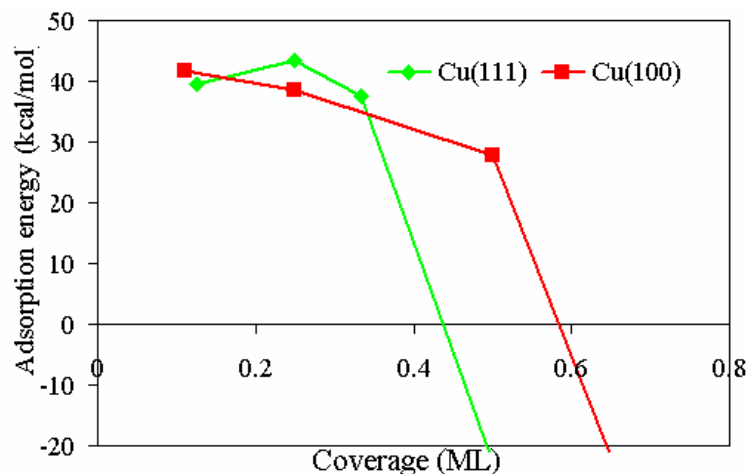
Other halogen/Cu systems:

The chemisorption of chlorine and bromine on Cu surfaces have been subject to numerous experimental studies [15-17]. Cl and Br form a $(\sqrt{3}\times\sqrt{3})R30^\circ$ structure on Cu(111) at a coverage of 0.33 ML, and a $(\sqrt{2}\times\sqrt{2})R45^\circ$ structure on Cu(100) corresponding to 0.5 ML coverage. We used DFT to study Cl and Br adsorption on Cu(111) and Cu(100). The fcc site on Cu(111) and hollow site on Cu(100) were found to be the most favorable for both halogens. The preferred desorption product was found to be the atomic species. These results were in excellent agreement with experiments and prior theoretical DFT studies [13,15-17].

Coverage-Dependent Studies:

The adsorption of I was studied on Cu(111) and Cu(100) as a function of varying coverages. The adsorption energy at the lowest coverage provides an estimate of the adsorption energy in the dilute coverage limit. This information could also hold insight into why specific adlayer structures are observed. The variation of adsorption energy as a function of coverage on Cu(111) and Cu(100) is shown in Fig. 4. No prior coverage-dependent structure determination studies are available for these systems. One question raised by Fig. 4 is why a (2×2) adlayer structure has not been reported for I/Cu(111). Further investigation of this question is currently in progress.

Fig. 4: Coverage dependent adsorption energies for Cu(111) and Cu(100)



Iodine on Cu(531):

A schematic of the Cu(531) surface and its corresponding unit cell is shown in Fig. 1. The lengths of the unit cell vectors are identical to those of the $(\sqrt{3}\times\sqrt{3})R30^\circ$ -I phase on Cu(111). This also corresponds to the distance between neighboring I atoms adsorbed on this surface, assuming the adsorption of one I atom per unit cell. Coverage-dependent studies on flat surfaces suggest that further adsorption in a particular unit cell would most likely be hindered by strong repulsive effects from neighboring I atoms. Based on this observation, it is reasonable to expect the formation of an ordered I overlayer on the Cu(531) surface, an assumption made for calculations in this section. Using the results from the flat surfaces as a guide, thirteen potential sites were identified for I adsorption (see Fig. 1). These include sites of two-fold or greater coordination on the terrace and along step edges, and one atop site. This is illustrated in Fig. 1. Adsorption energies for these sites are given in Table 3. During structural relaxation, the I adatoms moved a significant amount from their initial positions in some cases. The adsorption site BC below the kink was found to be the most energetically favored. This is also the site providing the most coordination for the I atom. We found that the energies for adsorption on terrace sites below the (111) step were consistently higher than similar sites below the (100) step.

Table 3: Adsorption sites for I/Cu(531)

Site	Energy (kcal/mol)	Site	Energy (kcal/mol)
A	26.91	H	37.98
B	40.19	I	37.89
C	40.17	J	39.87
D	39.78	K	39.85
E	38.14	L	36.41
F	36.23	M	16.37
G	37.36	BC	40.31

A common trend observed in all systems is the tendency of I to maximize its coordination and occupy the highest-available coordination site. Analysis on the low Miller index surfaces showed that adsorption energies increased in the order of increasing halogen electronegativities: $I < Br < Cl$. Theoretical studies by Power *et al.* [1] of physisorption of small chiral hydrocarbons on chiral platinum surfaces have shown that molecules prefer to adsorb at the kink. This also corresponds to the most preferred binding site for I on Cu(531). Josh Horvath (Chem. Eng., CMU) is currently performing experiments to study the adsorption of chiral molecules on I modified Cu(643) surfaces. His preliminary results suggest that I inhibits adsorption of the chiral molecule in its most firmly bound state. As the next step, one could study a system of chiral molecules interacting with an I modified Cu(531) surface. DFT can also tackle more complex problems such as coadsorption, diffusion and deduction of reaction mechanisms. This can be extended to examine various chiral surface/functional group combinations. Combined with experiments, this would generate a wealth of information about the behavior of different functional groups on various surfaces, and their impact on enantiospecific processes. Most importantly, it allows one to address the following issues: Can chemically modified chiral surfaces enhance the adsorption properties of enantiomers? Is it possible to apply these principles to chiral catalysis and preferentially synthesize the desired enantiomer? What specific functional group/surface combinations would be more effective for chiral separation/synthesis?

Conclusions and Future Work:

This work has been used as a means of introduction to DFT and gain familiarity with its immense capacity to model chemical processes in a variety of systems. The knowledge gained will be applied to a long-term project involving hydrogen separation using palladium/copper alloy membranes. Pd catalyzes the dissociation of molecular H_2 , followed by a high rate of diffusion through the metal. Presence of even trace amounts of sulfur in the feed during

hydrogen separation can lead to significant degradation of Pd membrane properties. Preliminary experimental work by Way & McCormick [18] showed that Pd/Cu alloy membranes have a potential for higher resistance to S poisoning, with excellent hydrogen permeance and H₂ selectivity. We would like to use DFT to study alloy characteristics and atomic-level processes such as poisoning, H adsorption and diffusion. This research will be done in close collaboration with Way's experimental group at the Colorado School of Mines and research staff in the Ultra-Clean Fuels Focus Area at NETL.

References

- 1) Sholl, D. S.; Asthagiri, A.; Power, T. D. *J. Phys. Chem.* **2001**, *105*, 4771.
- 2) Attard, G.; et al. *J. Phys. Chem. B* **1999**, *103*, 1381.
- 3) Horvath, J. D.; Gellman, A. J.; Buelow, M. T. *J. Mol. Catal. A.* **2001**, *167*, 3.
- 4) Kohn, W.; Becke, A. D.; Parr, R. G. *J. Phys. Chem.* **1996**, *100*, 12974.
- 5) Citrin, P.H.; Eisenberger, P.; Hewitt, R.C. *Phys. Rev. Lett.* **1980**, *45*, 1948.
- 6) DiCenzio, S. B.; Wertheim, G. K.; Buchanan, D. N. E. *Appl. Phys. Lett.* **1982**, *40*, 888.
- 7) McFadden, C. F.; Gellman, A. J. *Surf. Sci.* **1997**, *391*, 287.
- 8) Bent, B. E.; Lin, J. L.; Teplyakov, A.V. *J. Phys. Chem.* **1997**, *100*, 10721.
- 9) Eltsov, K. N.; et al. *Surf. Sci.* **2001**, *488*, L541.
- 10) Kresse, G.; Furthmüller, J. *Comp. Mater. Sci.* **1996**, *6*, 15.
- 11) Payne, M. C.; et al. *Rev. Mod. Phys.* **1992**, *64*, 1045.
- 12) Perdew, J. P.; Chevary, S.H.; Fiolhas, C. et al. *Phys. Rev. B.* **1992**, *46*, 6671.
- 13) Doll, K.; Harrison, N. M. *Chem. Phys. Lett.* **2000**, *317*, 282.
- 14) Dowben, P. A. *CRC Crit. Revs. in Solid State and Materials Science.* **1987**, *13*, 191.
- 15) Goddard, P. J.; Lambert, R. M. *Surf. Sci.* **1977**, *67*, 180.
- 16) Zheng, G.; Nakakura, C. Y.; Atman, E. I. *Surf. Sci.* **1998**, *401*, 173.
- 17) Walter, W. K.; Manolopoulos, D. E.; Jones, R. G. *Surf. Sci.* **1996**, *348*, 115.
- 18) Way, D. J., McCormick, R. L. *Private Communication.*

**VI. “Oxidative Desulfurization of Fuels Through TAML^o Activators
and Hydrogen Peroxide”**

**Yelda Hangun (S) and Terrance Collins (F), Carnegie Mellon University
with
Mark McDonald(M), NETL**

**Oxidative Desulfurization of Fuels Through
TAML^o Activators and Hydrogen Peroxide**

Abstract

U.S. EPA has mandated reduction of the maximum sulfur content in diesel to 15 ppm by 2006. The conventional method for reducing sulfur is catalytic hydrodesulfurization(HDS) under severe conditions. In order to reduce sulfur concentration in fuels, desulfurization of 4-Methyldibenzothiophene(4-MDBT) and 4,6-Dimethyldibenzothiophene(4,6-DMDBT) is required. Desulfurization of 4-MDBT and 4,6-DMDBT is very difficult by HDS due to their steric-hindrance even under deep desulfurization conditions. Therefore, a new method to reduce sulfur content is needed today. We have developed a series of iron (III) complexes called TAML[®] (for Tetra Amido Macrocyclic Ligand) activators that enhance the oxidizing ability of hydrogen peroxide at low catalyst. TAML/H₂O₂ oxidation of alkyl sulfides, thiophenes and benzothiophenes results into the corresponding sulfones. The processes are characterized by quantitative yields at 60° C and atmospheric pressure within 3-6 minutes. GC-AED and GC-MS studies indicated that the oxidative desulfurization of thiophene compounds by TAML/H₂O₂ to yield corresponding sulfones with sulfur content of less than 1.0 ppm.

Table of Contents

Abstract	1
List of Graphical Materials	2
Introduction	3
Experimental Section	6
Results and Discussion	8
Conclusion	11
References	12

List of Graphical Materials

Figure.....	Caption.....	Page
1.....	Structure of TAML [®] activators.....	6
2.....	Oxidation of DBT at 60 °C.....	8

Table.....	Caption.....	Page
1.....	Dibenzothiophene derivatives investigated and the characterization techniques applied to reactants and products.....	11
2.....	Reaction times of DBT derivatives at 40°C.....	12

Introduction

The removal of sulfur from petroleum is necessary for both industrial and environmental reasons. Sulfur in petroleum products poisons catalytic converters, corrodes parts of internal combustion engines and refineries because of the formation of oxyacids of sulfur,¹ and air pollution due to exhaust from diesel engines is a major concern to the public.²⁻⁴ The U. S. Environmental Protection Agency (EPA) has mandated reduction of sulfur content of diesel fuel and gasoline. The requirement will decrease the sulfur content of diesel fuel and gasoline to 15 ppm by 2006 and to 30 ppm by 2004, respectively.^{5,6}

The conventional method for reducing sulfur is catalytic hydrodesulfurization (HDS). In the HDS method, hydrogen and the organic sulfur compound react together at high temperature and high partial pressure of hydrogen.⁷ The effectiveness of the HDS process depends on the type of sulfur compound. The complete removal of sulfur present in petroleum as sulfides, disulfides and mercaptans is relatively easy and an inexpensive process. However, benzothiophenes and dibenzothiophenes (DBTs) are difficult to remove by this process.⁸ Particularly, the sterically hindered ones, 4-Methyldibenzothiophene and 4,6-dimethyldibenzothiophene are the most resistant to the current HDS process and they retard the rate of HDS.⁹ Most of the sulfur contamination in petroleum can be traced to the dibenzothiophene derivatives. In order to remove these compounds by HDS, it would require more hydrogen capacity and the maintenance of high temperatures and pressures for longer time periods. This would increase operating costs and enhance the likelihood that saturation of olefins and aromatics will occur resulting in a lower-grade fuel and additional processing steps.¹⁰ Thus, it is likely that

HDS processing has reached a stage where increasing temperature and pressure are just not enough to remove the residual sulfur without affecting the octane number. This process also produces increased volumes of hydrogen sulfide. Although HDS processes have dominated desulfurization of petroleum in the past, their cost and the requirements of strict fuel specifications combine to motivate the development of innovative process technologies.

An oxidative desulfurization (ODS) approach to sulfur removal serves as an alternative to the HDS process. An ODS process has the significant advantage over HDS in that the sulfur compounds that are the most difficult to reduce by HDS are the most reactive for ODS. In effect, the ODS process has the reverse order of reactivity as compared to the HDS process. This effect arises because the reactivity of sulfur compounds for oxidation is augmented with an increase of electron density on the sulfur atom. The electron donating properties of methyl groups on the aromatic rings positively influences DBT derivatives and the one with the most electron rich sulfur atom will react fastest.⁹ Of significant importance is that this increased electron density at sulfur upon methyl incorporation overshadows their steric effects. The oxidation of thiophenes to sulfones increases their polarity, and molecular weight.¹¹ The enhanced polarity makes it easier to remove them by adsorption on a solid material such as silica, alumina, clay or activated carbon.¹² It also facilitates their separation by extraction,¹³ distillation¹¹ or alkali treatment.¹⁴

Several peroxy organic acids (formic, acetic, propionic etc.) and Caro's acid (peroxysulfuric acid) have been used for selective oxidation of organic-sulfur compounds.^{11,13,15-18} The other oxidative processes involve nitrogen dioxide,² transition

metal-based catalysts in conjunction with hydroperoxide as oxidant, and photo-^{19,20} or ultrasound-induced²¹ oxidation. The catalysts reported include mixed molybdenum/tungsten oxides^{4,14}, tungstophosphoric acid (TPA)¹² and methyl trioxorhenium.²² However, reaction selectivity, safety and cost are the important concerns for the selection of oxidant, catalyst and operating conditions for ODS processing. The peroxyacids are generated *in situ* at operating conditions of 200-250° F near atmospheric pressure. The catalytic systems reported are toxic and expensive. While these are significant technologies, there are still issues relating to ultimate fuel quality and economy of the process that need to be determined. Thus there is a need for a new technology that can perform the oxidation reaction under mild conditions and one that can selectively oxidize the sulfur compounds.

We have developed a series of iron (III) complexes called TAML[®] (for Tetra Amido Macrocyclic Ligand) activators that enhance the oxidizing ability of hydrogen peroxide at low catalyst concentration and mild reaction conditions.²³ These peroxide activators are finding uses in many different areas including the pulp and paper industry, the textile and laundry industries, mineralization of organohalogenes, and others. Their versatility as oxidants lead to their use in the current study where it was found that they are capable of rapidly oxidizing the dibenzothiophene derivatives that are of concern to the petroleum industry. The general structure of TAML[®] activators is shown in Figure 1. The R and X groups are used to control activator reactivity, selectivity and lifetime. The activator used for this study has R = H and X = F and is referred to as FeF₂B. The FeF₂B form of the activator is particularly active in neutral pH water. Fe-TAML[®] activators, which have been developed over twenty years to be long-lived activators of hydrogen

peroxide, can be used under different reaction conditions including variable pH, temperature and solvent composition.²⁴ They are non-toxic and are most effective at very low concentrations (1 – 5 μ M; 0.5 – 2 ppm). Here we report a practical system using Fe-TAML[®] and H₂O₂ as catalyst and oxidant, respectively. We show that micromolar concentrations of FeF₂B activate H₂O₂ to convert greater than 99% of millimolar solutions (>7000:1 substrate: catalyst concentrations) of dibenzothiophene derivatives to the corresponding sulfones under mild conditions. The choice of dibenzothiophene derivatives was based on their relative abundance in petroleum.

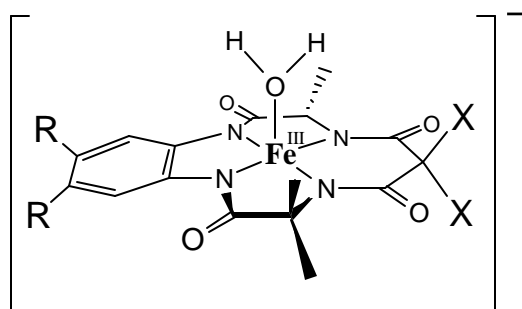


Figure 1: Structure of TAML activators

Experimental Section

General Materials and Methods.

Dibenzothiophene, 4-Methyldibenzothiophene and 4,6-Dimethyldibenzothiophene, 2-Methyl dibenzothiophene, 1,2-Benzophenylenesulfide, Benzothiophene, 3-Methylbenzothiophene, tert-butanol and hydrogen peroxide were purchased from Aldrich and Acros and used without further purification. Deuterated solvents for NMR spectroscopy were supplied from Cambridge Isotope labs. All aqueous solutions were made with doubly distilled water. H₂O₂ (30%) was diluted with water as

necessary. UV-visible spectra were obtained on a Hewlett Packard 8453 Diode Array Spectrophotometer. The kinetic oxidation reactions were maintained at 40 °C. Quartz cuvettes of 1 cm optical path were used. Infrared spectra were obtained on a Mattson Galaxy 5000 FT-IR spectrophotometer. ¹H NMR spectra were measured at 300 MHz on a IBM NR/300 spectrometer. Gas Chromatography-Mass Spectroscopy (GC-MS) data were recorded on a Agilent 6890 Series Gas Chromatography and 5973 Network Mass Selective detector spectrometer. Gas Chromatography-Atomic Emission Detector (GC-AED) data were measured on an Agilent 6890 GC and 2350A AED. Midwest Microlabs of Indiana performed elemental analyses of the dibenzothiophenes and corresponding sulfones.

General Procedure for Bulk Oxidation of Dibenzothiophenes.

A procedure is given for dibenzothiophene. Dibenzothiophene (20 mg, 0.11 mmol) was dissolved in tert-butanol (2 mL, 54.3 mM) and the resulting solution added to 8 mL of a 50% pH 7 KH₂PO₄ buffer: 50% tert-butanol solution with stirring (10.9 mM final concentration). Then, FeF₂B (3 μL, 1.5 μM final concentration) and H₂O₂ (50 μL, 30 vol% solution, 44 mM final concentration) were added. The mixture was stirred for 20 min at 60 °C. Upon cooling, a white solid precipitated from solution. The solid was recovered by filtration, washed, dried and fully characterized as dibenzothiophene sulfone.

General Procedure for the Kinetics of Oxidation of Dibenzothiophene.

In a typical case, dibenzothiophene (1.8 mg) was dissolved in tert-butanol (1 mL, 9.8 mM) and then added to 3 mL of a pH 7 KH_2PO_4 buffer solution (25 μL , 83 μM final concentration). The FeF_2B activator (7.35 μL , of 0.1 mM solution, final concentration 0.25 μM) was added and then the reaction was initiated by the addition of H_2O_2 (3.4 μL , 1 mM final concentration). The reaction was maintained at 40 °C and was determined to be complete when there were no further changes in absorbance.

Results and Discussion

A wide range of benzothiophenes and dibenzothiophenes are rapidly oxidized by hydrogen peroxide at atmospheric pressure in the presence of the Fe-TAML[®] activator FeF_2B , Figure 1, in water/tert-butanol to give the corresponding sulfone. Figure 2 shows the oxidation of DBT by UV-vis spectrophotometer.

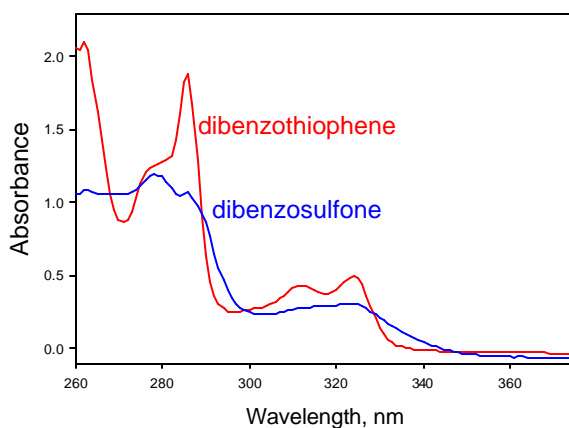


Figure 2. Oxidation of DBT at 60 °C

Table 1 lists the DBT derivatives that we have examined thus far. The ones that are of prime interest for an ODS process, dibenzothiophene, 4-methyldibenzothiophene, and 4,6-dimethyldibenzothiophene, have been the ones most extensively investigated. The products of these reactions were fully characterized by the techniques indicated in the table. The reaction product is the corresponding sulfone with 99% isolated yield. These conversions, which generally require less than one hour, are accomplished with molar ratios of substrate to catalyst of approximately 7000:1 and a reaction temperature of 60 °C. Since the sulfones are, like the starting DBTs, very insoluble in water rich mixtures, they precipitate from solution upon cooling to near room temperature.

The data presented in Table 2, which are preliminary kinetic measurements, reflect reactions carried out at 40 °C. These conditions are chosen to facilitate the ongoing kinetic studies and the ability to obtain high quality data. The data correspond to the reaction times to achieve greater than 95% conversion of the DBT derivative to the sulfone as determined by UV/visible spectroscopy. The differences between the starting DBT derivative and its corresponding sulfone are significant enough that this is readily determined. The overall efficiency of the oxidation process, the reaction rates, and the reaction pathways are still under investigation. It is worthwhile to note that increasing the temperature to 60 °C and raising the FeF₂B concentration to 1.5 μM (0.25 μM for kinetic studies), results in the oxidation of 4,6-Dimethyldibenzothiophene (approx. 80 μM, 17 ppm) in less than 1 minute as determined by UV/vis measurements. Thus the oxidation of the thiophenes is extremely rapid with this catalyst system.

The oxidation reaction with Fe-TAML[®]/H₂O₂ is flexible with respect to the type of the medium in which it is performed. For example, the kinetic studies described above

were carried out in essentially pure water with only enough tert-butanol to solubilize the dibenzothiophene derivatives (the KH_2PO_4 buffer (see **Experimental** section) can be eliminated from the reaction mixture but was used to maintain constant ionic strength). When bulk reactions are performed to produce sufficient product for full characterization, the reaction medium was 50% water/50% tert-butanol; the higher concentrations of tert-butanol are required for solubility of the starting dibenzothiophene derivatives. The concentration of tert-butanol could be raised to 70% without negatively impacting the oxidation process. These observations indicate that the Fe-TAML[®]/H₂O₂ system is amenable to variations in operating conditions and determining the breadth of reaction conditions under which this oxidation can take place is part of the ongoing investigation.

Each table should have a number and heading, formatted as follows above the table:

Table 1. Dibenzothiophene derivatives investigated and the characterization techniques applied to reactants and products

Compound	Benzothiophenes	Benzothiophene sulfones
DBT	UV-vis, NMR, IR, GC-MS, GC-AED, elemental analysis	UV-vis, NMR, IR, GC-MS, GC-AED, elemental analysis
4-MethylDBT	UV-vis, NMR, GC-MS, GC-AED, elemental analysis	UV-vis, NMR, GC-MS, GC-AED, elemental analysis
4,6-dimethylDBT	UV-vis, NMR, GC-MS, elemental analysis	UV-vis, GC-MS, NMR, GC-AED, elemental analysis
2-MethylDBT	UV-vis	UV-vis
1,2-BenzoPS	UV-vis	UV-vis
BT	UV-vis	UV-vis
3-MethylBT	UV-vis	UV-vis

DBT : Dibenzothiophene
 1,2-BenzoPS : 1,2-Benzophenylenesulfide
 BT : Benzothiophene

Table 2. Reaction times of DBT derivatives at 40°C^a

Compounds^b	Reaction Time (sec)
	>95% conversion
Dibenzothiophene	200
4-Methyldibenzothiophene	1500
2-Methyldibenzothiophene	800
4,6-dimethyldibenzothiophene	150
1,2-Benzophenylenesulfide	>8000

^aFeF₂B concentration 0.25 μM

^bCompound concentrations approximately 80 μM

Conclusions

A new method to reduce sulfur content in petroleum is needed to meet future regulations. The results presented here indicate that the Fe-TAML activators of H₂O₂ are capable of rapidly oxidizing the dibenzothiophene derivatives present in fuels under mild reaction conditions. The results further indicate that an ODS process with Fe-TAML activators is a promising technology for decreasing sulfur content in fuels especially since these are non-corrosive.

Acknowledgement. We would like to acknowledge NETL Student Partnership Program for supporting this research.

References

- (1) Parkinson, G. *Chem. Eng.* **2000**, 45-48.
- (2) Tam, P. S.; Kittrell, J. R.; Eldridge, J. W. *Ind. Eng. Chem. Res.* **1990**, 29, 321-324.
- (3) Koch, T. A.; Krause, K. R.; Manzer, L. E.; Mehdizadeh, M.; Odom, J. M.; Sengupta, S. K. *New J. Chem.* **1996**, 20, 163-173.
- (4) Collins, F. M.; Lucy, A. R.; Sharp, C. *J. Mol. Catal.* **1997**, 117, 397-403.
- (5) USEPA, <http://www.epa.gov/sbrefa/documents/pnl13f.pdf>.
- (6) Parkinson, G. *Chem. Eng.* **2001**, 37-41.
- (7) Altar, A.; Corcoran, W. H. *Ind. Eng. Chem. Prod. Res. Dev.* **1978**, 17, 102-109.
- (8) Yu, K.; Li, H.; Watson, E. J.; Virkaitis, K. L.; Carpenter, G. B.; Sweigart, D. A. *Organometallics* **2001**, 20, 3550-3559.
- (9) Otsuki, S.; Nonaka, T.; Takashima, N.; Qian, W.; Ishihara, A.; Imai, T.; Kabe, T. *Energy & Fuels* **2000**, 14, 1232-1239.
- (10) Higgins, B. W. *Chem. Innov.* **2001**, 39-40.
- (11) Dolbear, G. E.; Skov, E. R. *Prepr. Pap.- Am. Chem. Soc., Div. Fuel. Chem.* **2000**, 375-378.
- (12) Yazu, K.; Yamamoto, Y.; Furuya, T.; Miki, K.; Ukegawa, K. *Energy & Fuels* **2001**.
- (13) Bonde, S. E.; Gore, W.; E., D. G. *Prepr. Pap.- Am. Chem. Soc., Div. Fuel. Chem.* **1999**, 199-201.
- (14) LaCount, R. B.; Friedman, S. *J. Org. Chem.* **1977**, 42, 2751-2754.

- (15) Paybarah, A.; Bone, R. L.; Corcoran, W. H. *Ind. Eng. Chem. Res.* **1982**, *21*, 426-431.
- (16) Gore, W. *U.S. Patent 6,274,785* **2001**.
- (17) Bonde, S. E.; Dolbear, G. E. *Prepr. Pap.- Am. Chem. Soc., Div. Fuel. Chem.* **2001**, 69-73.
- (18) Gore, W.; Bonde, S. E.; Dolbear, G. E.; Skov, E. R. *Prepr. Pap.- Am. Chem. Soc., Div. Fuel. Chem.* **2000**, 364-366.
- (19) Shiraishi, Y.; Hara, H.; Hirai, T.; Komasaawa, I. *Ind. Eng. Chem. Res.* **1999**, *38*, 1589-1595.
- (20) Shiraishi, Y.; Hirai, T.; Komasaawa, I. *Solvent Extraction Research and Development* **1999**, *6*, 137-143.
- (21) Government & Business *Chem. Eng.* **2001**, 15.
- (22) Brown, K. N.; Espenson, J. H. *Inorg. Chem.* **1996**, *35*, 7211-7216.
- (23) Horwitz, C. P.; Fooksman, D. R.; Vuocolo, L. D.; Gordon-Wylie, S. W.; Cox, N. J.; Collins, T. J. *J. Am. Chem. Soc.* **1998**, *120*, 4867-4868.
- (24) Collins, T. J. *Acc. Chem. Res.* **1994**, *27*, 279-285.

**VII. “Hydrate Formation and Dissociation in Porous Media –
An Experimental Study”**

**Timothy White (S) and Goodarz Ahmadi (F), Clarkson University
with
Duane Smith (M), NETL**

HYDRATE FORMATION AND DISSOCIATION IN POROUS MEDIA – AN EXPERIMENTAL STUDY

By Timothy K. White¹, Goodarz Ahmadi¹, Duane H. Smith²

1 Department of Mechanical and Aeronautical Engineering
Clarkson University, Potsdam, NY 13699-5725

2 Federal Energy Technology Center
Department of Energy, Morgantown, WV 26507-0880

Abstract

An experimental setup for measuring the spatial variation of pressure and temperature during formation and dissociation of hydrate in a vessel is developed. The main chamber is made of aluminum that accommodates several pressure and temperature sensors. The objective is to provide insight into the pressure and temperature distributions within the sample during the hydrate formation and dissociation processes. Particular attention will be given to a detailed understanding of hydrate dissociation by depressurization.

Introduction

The use of fossil fuels as the main source of energy has been on a steady rise since the industrial revolution. Among fossil fuels, the consumption of natural gas has been rising sharply over the last few decades. If this increasing consumption rate continues, it has been estimated that by year 2050, the supply of natural gas will be depleted. According to Makogon (1997) the reservoirs of natural gas hydrate found on the earth's crust is estimated to be larger than the other fossil fuel reserves (oil and natural gas) combined. As a result, there is a considerable amount of interest in developing this important source of energy. This project is concerned with the experimental investigation of propane hydrate formation and natural gas production from hydrate by depressurization. A hydrate is a lattice of ice that encages molecules of natural gas. If this gas could be economically extracted, hydrates could become a viable source of energy for the 21st century.

Hydrates were first thought of as nothing more than a nuisance. They would form in natural gas pipes such as the Alaskan pipe line and cause blockages that would interrupt the delivery process. Recent studies have shown promise in decomposing natural hydrate deposits and recovering the gas to be used as fuel. Certain conditions are required for the formation of natural gas hydrate. More specifically, pressures of the order of 5 to 20 MPa and temperatures near freezing are required to for the formation of hydrates. There are two main geological settings in which hydrates can occur naturally.

The first is on land where permafrost is dominant and the second is beneath the ocean floor at water depths of more than 500 meters.

Makogon (1997) and Sloan (1998) provided extensive reviews of hydrate formation and decomposition processes. Verigin et al. (1980) and Holder and Anglert (1982) reported theoretical and numerical modeling of hydrate decomposition process. Makogon used the analogy to Stefan's problem for melting to describe the decomposition process of hydrates. More recently, Ahmadi et al. (1999) and Ji et al. (2001) described the variation of pressure and temperature profiles in a hydrate reservoir, which included the effects of heat transfer.

Experimental studies of hydrate formation and decomposition were reported by Yousif and Sloan (1991), Cherskii, et. al. (1970), Kamath (1983), Sloan (1990), Holder et al. (1982), Ullerich, Selim and Sloan (1987), and Lysen (1993) among others. As a result of these studies, a significant amount of information on the nature of hydrate formation, as well as decomposition has become available (Makogon, 1997; Sloan, 1998). Most of the available experimental data of the hydrate decomposition are limited to the bulk production measurements while the details of the time evolution of pressure and temperature profiles have not been studied.

Objectives

The present project is concerned with a comprehensive experimental study of hydrate formation and decomposition process. The main objectives of the project are:

1. To provide insight into the process of propane hydrate formation in a porous media.
2. To provide a fundamental understanding of hydrate dissociation process in porous media by depressurization.
3. To provide descriptive experimental data for natural gas production from hydrate by depressurization.
4. To provide detailed information about the time evolution of pressure and temperature profiles during hydrate formation and dissociation processes.
5. To provide experimental data that can be used for verification of the theoretical model for hydrate dissociation by depressurization, as well as model improvement.

Experimental Apparatus

To create a hydrate sample, a sealed enclosure is required to contain the media and propane gas, while maintaining a required pressure. An aluminum block was machined to facilitate the insertion and extraction of a porous media, as well as the injection of propane gas. The top and bottom of the vessel are Plexiglas reinforced with an aluminum ring to provide the required strength. The Plexiglas was utilized so a visual observation of the formation and decomposition processes could be made. The vessel has 12 ports on either side to facilitate mounting of the pressure and temperature sensors. Any combination of the 6 pressure sensors and 6 temperature sensors can be utilized. A circulation bath, combined with a chiller, contains the vessel and cool the surrounding fluid to the required temperature. To measure the amount of gas entering and exiting the vessel, a mass flow sensor is developed. To collect the data, a data acquisition (DAQ) system is used. This consists of two digital to analog (D/A) cards, two connector blocks and all the sensors and mass flow meter. A sample is taken every second and stored in a file to be analyzed later. Figure 1 shows a schematic diagram of the pressure vessel and Figure 2 shows a picture of the fabricated vessel.

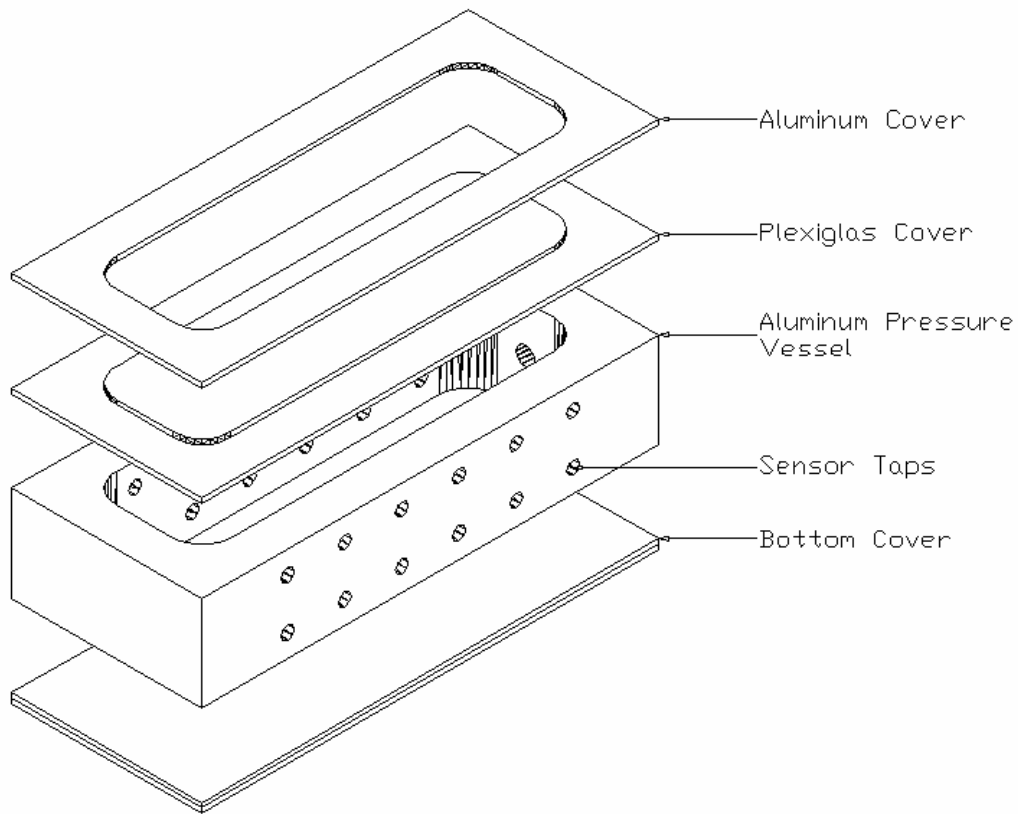


Figure 1: Schematic diagram of the hydrate pressure vessel.

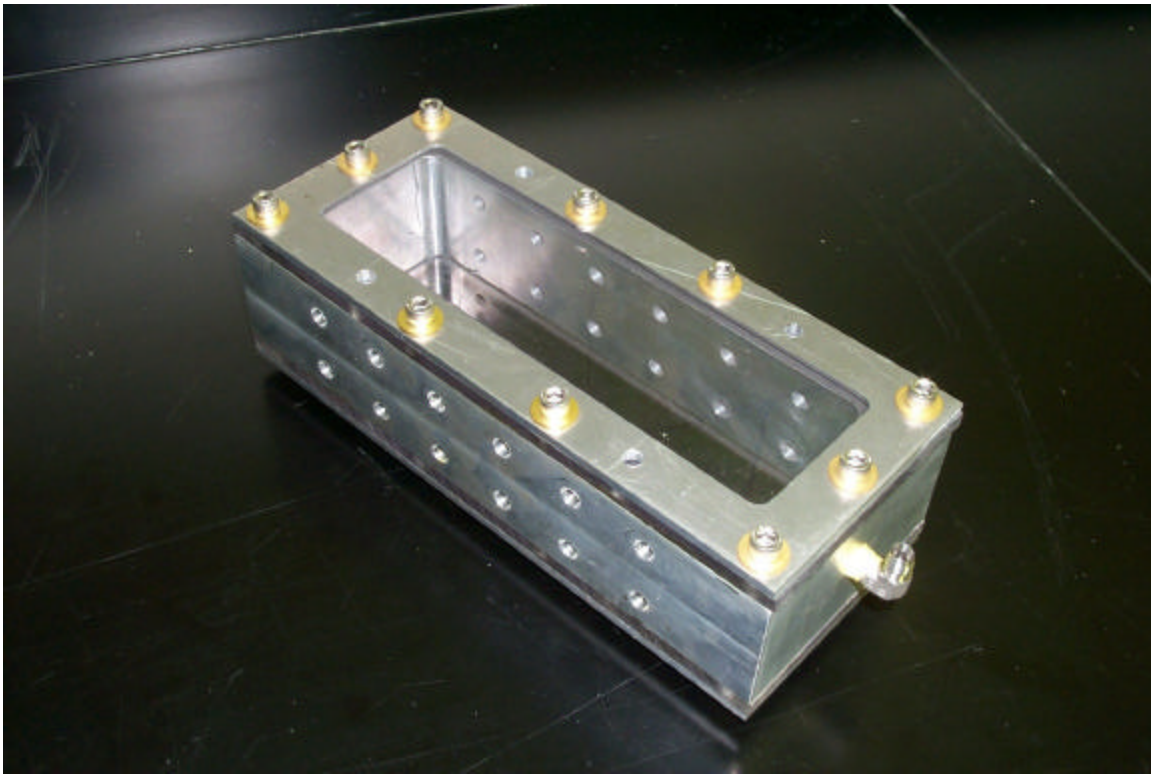


Figure 2: Fabricated hydrate pressure vessel.

Experimental Procedure

To prepare the apparatus for the experiment, a series of steps are taken to ensure that the results are consistent and valid. In the first experiment, ice is used as the media, the entire system (pressure vessel and sensors) are cooled to a predetermined temperature. For a propane hydrate, a temperature of -10°C ensures that the vessel is close to the quadruple point and reduces the amount of time required to cool the media. Once the vessel is cooled to the desired temperature, ice is crushed with a blender and ground into a powder, resembling snow. The snow is packed into the vessel through its removable top. The top is then replaced and the bolts tightened to the proper specification to ensure there will be no gas leaks. The vessel is then placed into the cooling bath and the gas lines are connected. Once the temperature has stabilized, the propane gas is allowed to enter the vessel. The gas pressure is increased and maintained with a pressure regulator. Once a pressure of 40 psi is reached, the inlet valve is closed to isolate the gas inlet line from the vessel. Over time, the pressure gradually decreases as the propane hydrate forms. After some time, the pressure needs to be increased above the quadruple point so that hydrate production can resume. This process is repeated until the pressure decrease over time is negligible. This constant cycling ensures that hydrate is being formed in the pressure vessel. During this entire time period, which is approximately 24 hours, the DAQ system records six pressure and temperature signals every second and records the data in a file.

The depressurization and decomposition experiment are then performed. This is accomplished by allowing the propane gas to exit through the mass flow sensor and exhaust into a fume hood. The decomposition by depressurization appears to take on the order of one hour, but the variations in decomposition time will be measured when the mass flow meter is functioning. The amount of propane entering the system will also be measured to make sure that it is equal to the amount leaving the system during dissociation.

Results

Hydrate Formation

Sample preliminary results are presented in this section. Figure 3 shows the pressure time history during the hydrate formation. It is seen after each sharp pressure increase due to opening of the valve, there is an exponential decay of gas pressure resulting from hydrate formation. The amount of time that separates the peaks, as well as the slope of the exponential decay curve, continue to decrease with time. This is due to the ever-decreasing amount of media available to react with the newly introduced propane gas. The long span in the middle of the curve is a night period that the experiment was running. The decaying slope becomes very shallow when compared to the beginning slopes. After 24 hours, the slopes are almost zero. As there is no further drop in pressure, it is conjectured that the process of hydrate formation is complete.

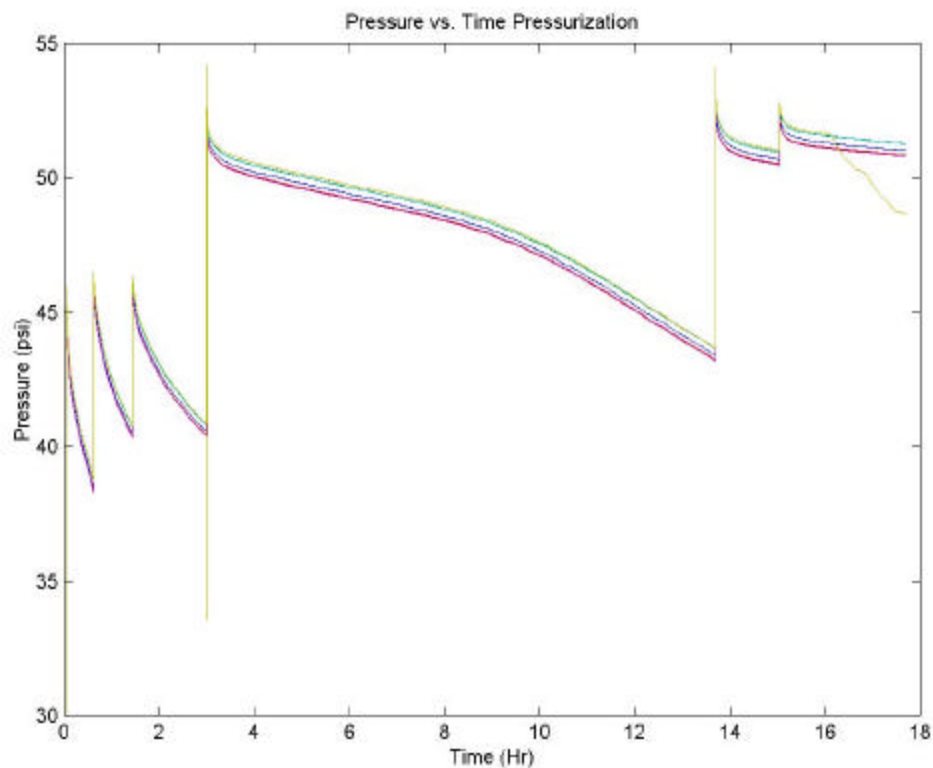


Figure 3: Pressure versus time during hydrate formation.

Figure 4 shows the time variation of temperature in the pressure vessel during the formation phase over the same time period. There are sharp peaks in the profile where the temperature increases and then returns to normal. The timing of these peaks corresponds to the pressure increases. It is conjectured that the increase in temperature is a result of the pressure increase.

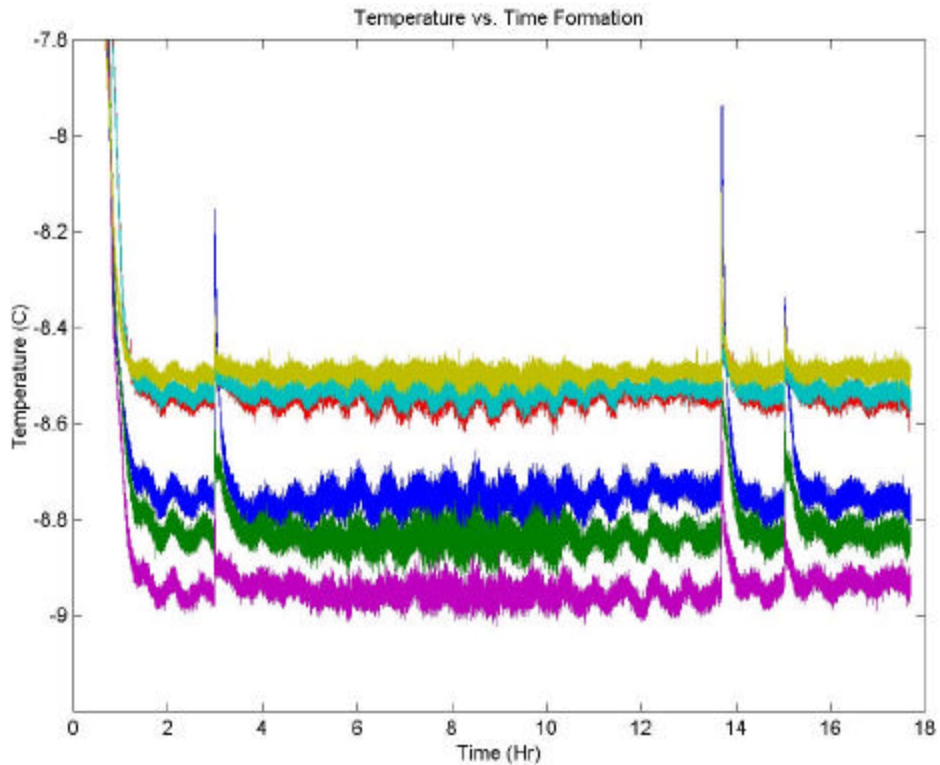


Figure 4: Temperature versus time during hydrate formation

Hydrate Dissociation

For the dissociation process to begin the outlet pressure valve is opened and the propane gas is allowed to escape. Figure 5 displays the pressure variation for the six pressure transducers while the pressure vessel is depressurized. The pressure starts at a value of 40 psi and is lowered to atmospheric (zero gauge). This allows the hydrate to dissociate into water and propane gas.

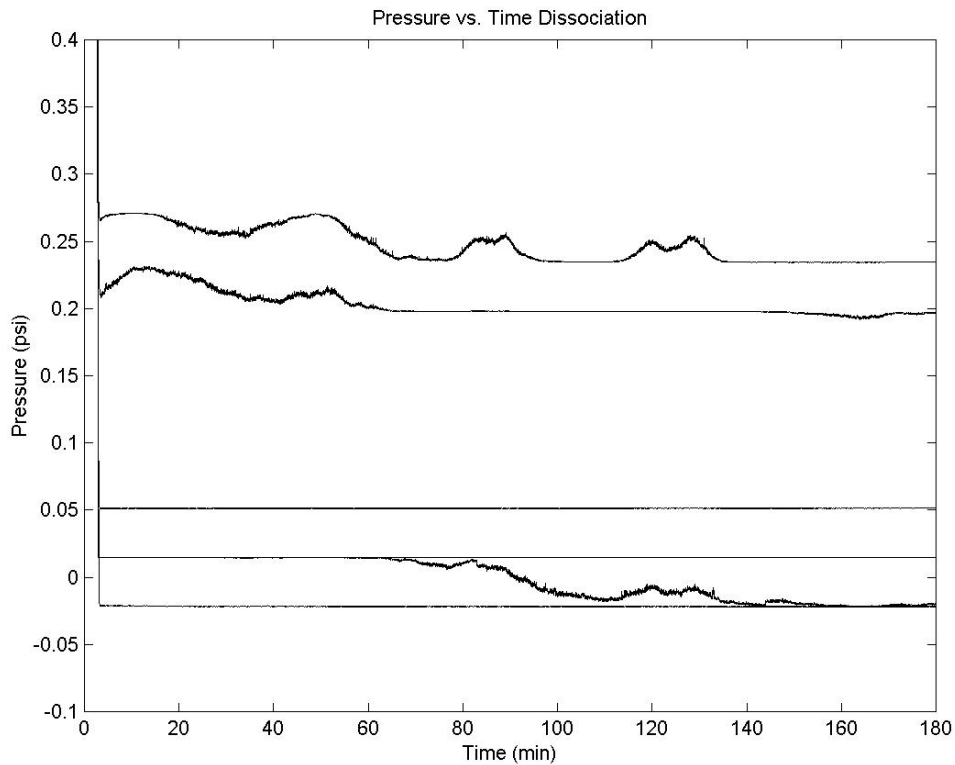


Figure 5: Time variation of pressure during hydrate dissociation.

Figure 6 shows the time variation of temperature during hydrate dissociation. The drop in temperature represents the same time period that the pressure is decreased. It is noticed that the decrease in pressure leads to a decrease in the temperature. Hydrate dissociation is an endothermic reaction and therefore absorbs heat. As a result, when the hydrate dissociates, the temperature is decreased. The temperature then begins to rise as the system approaches the bath temperature. The temperature values before the depressurization occurred are slightly higher than after.

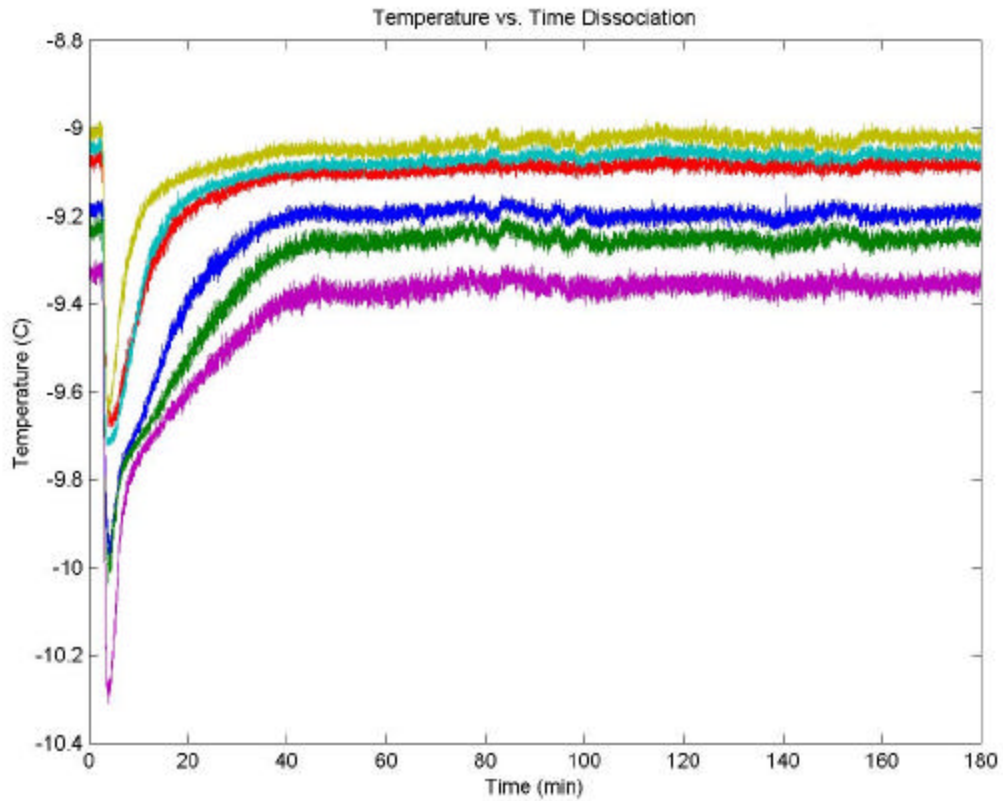


Figure 6: Time variation of temperature during hydrate dissociation.

Figure 7 shows an enlarged section of the temperature curve during the initial stages of hydrate dissociation. This figure clearly shows the rapid decrease in temperature that is experienced when the outlet valve is opened and the pressure decreased to atmospheric. The cooling process lasts for approximately 60 seconds, after which the temperature starts to increase toward the bath temperature.

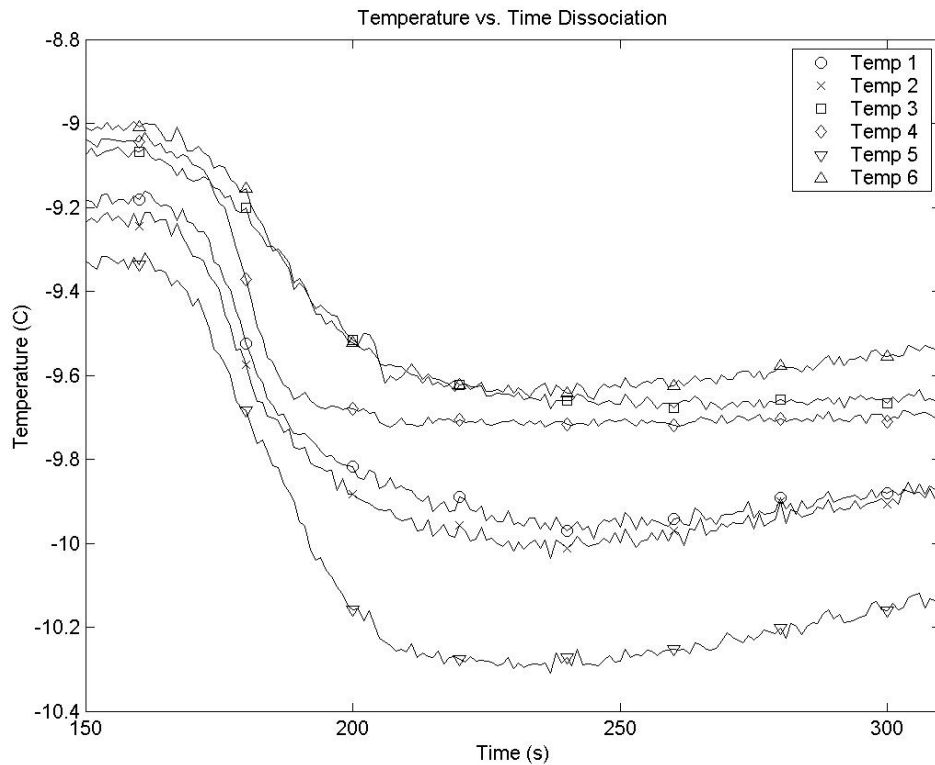


Figure 7: Time variation of temperature during hydrate dissociation

Discussion and Future Work

There are some items that need to be addressed in the future. First, the experiment is to be run with a properly functioning mass flow sensor. Once this problem is resolved, the comparison of mass balance for the propane gas entering and exiting the system can be made and the total hydrate production will be evaluated. Secondly, we plan to investigate propane hydrate formation and dissociation for different mixtures. Uniform mixtures of ice and sand or silica gel will be used in these experiments.

References

1. Ahmadi, G., Ji, C., Smith, D.H., (1999) "A Simple Model for Natural Gas Production from Hydrate Decomposition", Clarkson University, New York.
2. Cheresihii, N.V. and Pondarev, E.A., (1970) "Thermal Method for Producing Natural Gas Hydrate Deposits", Dokl. Akad. Nauk SSSR.
3. Holder, G.D. and Angert, P.F., (1982) "Simulation of Gas Production from a Reservoir Containing Both Gas Hydrates and Free Natural Gas", Proceedings of 57th Society of Petroleum Engineers Technology Conference, New Orleans, Sept 26-29, SPE11105.
4. Kamath, V., (1983) "Study of Heat Transfer Characteristics During Dissociation of Gas Hydrates in Porous Media", Ph.D. Thesis, University of Pittsburgh, Pittsburgh, PA.
5. Lysne, D., (1993) "Hydrate Plug Dissociation by Pressure Reduction, International Conference on Natural Gas Hydrates", Sloan, E.D., Happel, J., and Hnatow, M.A., Acad. NY Acad. Sci., Vol. 715, pp. 714-717.
6. Makogon, Y.F., (1997) "Hydrates of Hydrocarbons", Penn Well, Tulsa, OK.
7. Makogon, Y.F. and Sloan, E.D., Jr., (1994) "Phase Equilibrium for Methane Hydrate form 190 to 262K", J. Chem. Eng. Data. Vol. 39, p. 351.
8. Sloan, E.D., Jr., (1998) "Clathrate Hydrates of Natural Gases", Marcel Dekker, New York.
9. Ullerich, J.W., Salim, M.S., and Sloan, E.D., (1987) "Theory and Measurements of hydrate Dissociation", AIChE J.
10. Yousif, M.H., Sloan, E.D., (1991) "Experimental Investigation of Hydrate Formation and dissociation in Consolidated Porous Material", SPE Reservoir Engineering, November 1991.

VIII. “Computational Modeling of Carbon Dioxide Sequestration”

**Ali Reza Mazaheri (S) and Goodarz Ahmadi (F), Clarkson University
with
Duane Smith (M), NETL**

COMPUTATIONAL MODELING OF CARBON DIOXIDE SEQUESTRATION

Ali Reza Mazaheri¹, Goodarz Ahmadi¹ and Duane H. Smith²

¹ Department of Mechanical and Aeronautical Engineering

Clarkson University

Potsdam, NY 13699-5725

² National Energy Technology Laboratory

U.S. Department of Energy

Morgantown, WV 26510

INTRODUCTION

Carbon Dioxide released during fossil fuel consumption is a major source of greenhouse gases. In order to manage the future climatic changes, the CO₂ must be removed from the flue gas and be permanently stored. Reducing CO₂ emission in order to control the overall levels of carbon dioxide in the atmosphere has become an international priority.

Carbon dioxide sequestration in brine and depleted oil reservoirs and oil recovery enhancement by CO₂ injection has renewed the interest in gas-liquid flows in porous media. Several methods for CO₂ sequestration in the ocean floor and in geological formations have been proposed. The sequestration in geological formations including depleted oil and gas reservoirs and deep brine fields have been studied. Hattenbach et al. (1999) and Holloway et al (1996) reported studies of the use of CO₂ for oil recovery. Models for flow and heat transfer in porous

media using volume-averaging techniques are described by Sattery (1972) and Kaviany (1995). Hasanizadeh and Gray (1993) proposed a new theory of two-phase flows through porous media. Their model included the effects of the presence of interfaces and of common lines.

OBJECTIVES

The general objective of this project is to develop a theoretical foundation and a computational tool for modeling the CO₂ sequestration processes in underground reservoirs. The specific objectives are:

- To develop a continuum model for multiphase flows through porous media.
- To develop a physical model for predicting the relative permeability in practical application.
- To analyze process of CO₂ sequestration in depleted oil reservoirs.
- To provide a detailed understanding of the enhanced oil recovery through CO₂ injection.
- To predict the CO₂ sequestration and oil recovery enhancement for several realistic reservoir scenarios.

PRELIMINARY RESULTS

In the course of last year progress was made in various aspect of the project. These are summarized in this section.

1. BRAVO DOME RESERVOIR

The gas leakage conditions in the Bravo dome CO₂ reservoir is studied and preliminary results are obtained. The Bravo dome field contains one of the largest accumulations CO₂ in North America. The filed is located about 200 miles from

enhanced oil recovery projects in West Texas, to which the CO₂ is transported by pipeline. The principle reservoir in the Bravo dome field is the Tubb sandstone at depth of 1900-2950 feet. The Tubb is 0-400 feet thick and consists of fine-to medium-grained thin bedded, orange-to-red shale and rare dolomite.

The Bravo dome field encompasses about 800,000 acres. Estimates of recoverable proven reserves range from 5.3-9.8 TCF. The percentage of the CO₂ gas in the field is about 98.6-99.8%. Pressure gradients range from 0.13 psi/feet in the northeastern part of the field to 0.40 psi/feet in the western part of the field.

A two-dimensional model of the Bravo dome field is studied. A computational model is developed using the FLUENT code. It is assumed that the lower region of the reservoir is at a pressure of 2×10^6 Pa. Figure 1 shows a sample result of this simulation study.

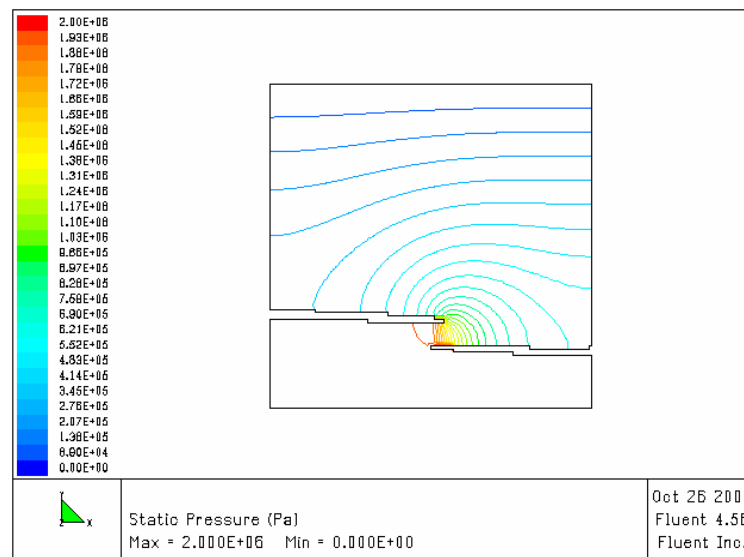


Figure 1. Sample Pressure field in the Bravo dome reservoir.

2. TOUGH2

The TOUGH2 code, which was developed at Lawrence Berkeley Laboratory, is a multi-purpose reservoir simulator and can handle multiphase flows. Since the version of the code we have does not have a CO₂-oil equation of state, we have

initiated a simulation study of to model CO₂ sequestration in an underground water saturated reservoir. We also plan to study the case that water is being injected into a depleted oil reservoir system. Figure 2 shows a schematic geometry of the preliminary model being studied. The computational model contains more than 100,000 blocks. The mesh consists of 49 horizontal by 49 vertical blocks of 50m×50m×50m. We also specified 50 blocks in the third direction to make a 3-D mesh.

We plan to complete these simulations in the coming year. Comparing the results of these two simulations may be useful for a better understanding of the oil recovery enhancement process.

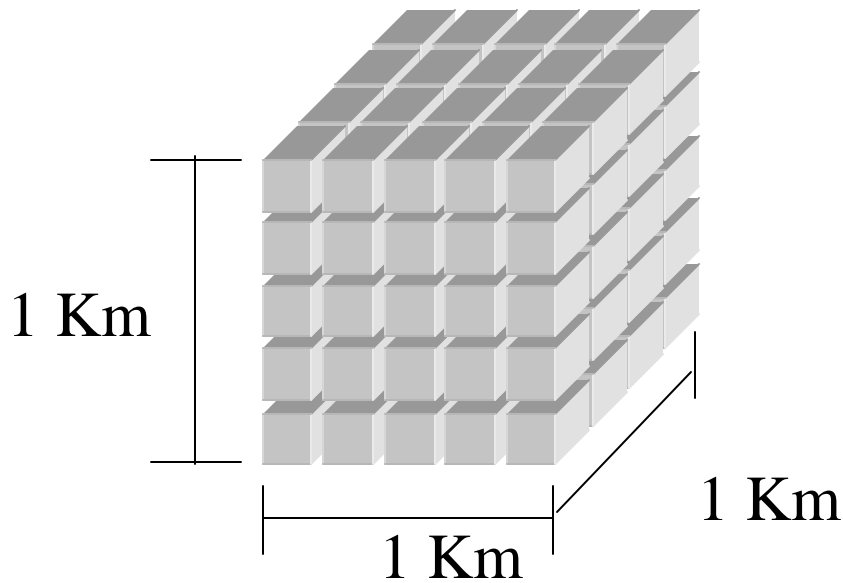


Figure 2. A schematic geometry of CO₂ and water injection models.

3. **MODLING MULTIPHASE FLOW THROUGH POROUS MEDIA**

Formulation of a continuum model for a multiphase flows through a poro-elastic media is being studied. The preliminary results show that that the new model leads to the extended Darcy's law.

Consider a dispersed mixture of m distinct fluid phases in a deformable porous media. In the absence of chemical reaction and interfacial mass transfer, starting from the global conservation laws for each phase and using an spatial averaging method, the local forms of the laws for different constituents were developed by Whitaker (1986), Ahmadi (1987), Hassanizadeh and Gray (1993), and Kaviany (1995), among others. Accordingly, the differential forms of the equations of conservation of mass for each of phases becomes,

$$\frac{\partial \rho^s}{\partial t} + \frac{\partial}{\partial x_j} (\rho^s \tilde{v}_j^s) = 0 \quad (1)$$

$$\frac{\partial \rho^f}{\partial t} + \frac{\partial}{\partial x_j} (\rho^f \tilde{v}_j^f) = 0 \quad (2)$$

Here ρ is the mass density, and \tilde{v}_i is the volume averaged mean velocity vector. The superscripts f refers to the f^{th} fluid phase and superscript s identifies the solid (porous) media. When the particulate and fluid phases are incompressible, it follows that

$$\rho^s = \rho_0^s v^s, \quad \rho^f = \rho_0^f v^f \quad (3)$$

where v is the mean volume fraction.

The local forms of balance of linear momentum for each phase are given as,

$$\rho^f \frac{d\tilde{v}_i^f}{dt} = \rho^f f_i^f + \frac{\partial t_{ji}^f}{\partial x_j} + \bar{P}_i^f \quad (4)$$

$$\rho^s \frac{d\tilde{v}_i^s}{dt} = \rho^s f_i^s + \frac{\partial t_{ji}^s}{\partial x_j} + \bar{P}_i^s \quad (5)$$

where f_i is the body force per unit mass, t_{ij} is the average stress tensor, and \bar{P}_i is the interaction momentum supply.

Equations governing the balance of equilibrated force are given by

$$\rho^f k^f \left\{ \frac{d\dot{v}^f}{dt} + (\dot{v}^f)^2 \right\} = \frac{\partial h_i^f}{\partial x_i} + \rho^f \ell^f + g^f \quad (6)$$

$$\rho^s k^s \left\{ \frac{d\dot{v}^s}{dt} + (\dot{v}^s)^2 \right\} = \frac{\partial h_i^s}{\partial x_i} + \rho^s \ell^s + g^s \quad (7)$$

where k is the equilibrated inertia, h_i is the equilibrated stress vector, ℓ is the equilibrated force per unit mass and g is the interaction equilibrated force supply (internal equilibrated force).

The equation of conservation of equilibrated inertia are also given as,

$$\frac{dk^f}{dt} - 2\dot{v}^f k^f = 0 \quad (8)$$

$$\frac{dk^s}{dt} - 2\dot{v}^s k^s = 0 \quad (9)$$

Equations governing the balance of equilibrated force and conservation of equilibrated inertia are the traces of the general stress-moment and micro-inertia equations developed by Twiss and Eringen (1971) and Ahmadi (1988).

The equation of conservation of energy for porous media and the fluid phase are given as

$$\rho^s \frac{de^s}{dt} = q_{j,j}^s + t_{ji}^s \tilde{v}_{j,i}^s + h_j^s \dot{v}_{j,j}^s - g^s \dot{v}^s - \bar{P}_j^s \tilde{v}_j^s + r^s + e^{s+} \quad (10)$$

$$\rho^f \frac{de^f}{dt} = q_{j,j}^f + t_{ji}^f \tilde{v}_{j,i}^f + h_j^f \dot{v}_{j,j}^f - g^f \dot{v}^f - \bar{P}_j^f \tilde{v}_j^f + r^f + e^{f+} \quad (11)$$

where e is mean internal energy per unit mass, q_j is the mean heat flux vector pointing outward of an enclosed volume, r is the internal heat source per unit volume and e^+ is the interaction energy supply.

In the limiting case, when porous solid is rigid the phasic momentum balance reduces to

$$\rho^f \dot{\tilde{v}}^f = -\nabla \bar{P}^f + 2\alpha_0^f (v^f)^2 \nabla^2 \tilde{v}^f - K^f \tilde{v}^f - 2\alpha_0^f \nabla v^f \quad (12)$$

where α_0^f is positive constant, and $f=1,2,..$ refers to the f^{th} fluid phase. For steady motion and small spatial variation of the phasic fluid velocity as obtained from Equation (12) simplifies to

$$\tilde{\mathbf{v}}^f = -\frac{1}{\mathbf{K}^f} (\nabla \bar{\mathbf{P}}^f + 2\alpha_0^f \nabla \mathbf{v}^f) \quad (13)$$

where $\frac{1}{\mathbf{K}^f}$ is the phase permeability of the f^{th} phase. Equation (13) shows that the gradient of the f^{th} phase volume fraction affects the phasic velocity. Equation (13) is a generalized Darcy's equation.

PLAN OF STUDY

In the coming year we plan to perform a number of studies. These are:

- We plan to complete the formulation of the continuum model for multiphase flows in porous media. The original Darcy's law can not properly account for the hysteresis effects of capillary pressure. We plan to make use of the new continuum theory to develop a generalized Darcy's law for multiphase flows through porous media.
- We plan to make use of the TOUGH2 code for studying CO₂ sequestration in underground brine reservoirs and oil recovery enhancement. We plan to incorporate the newly developed extended Darcy's law in the TOUGH2 code and compare the findings with those obtained with use of standard Darcy's law.
- We plan to further study the Bravo dome field using both the FLUENT model and TOUGH2 code.

REFERENCES

Ahmadi, G., (1987), "*On the Mechanics of Incompressible Multiphase Suspensions*", Adv. Wat. Res., **10**, 21.

Hassanizadeh, M., and Gray, W. G. (1993) *“Thermodynamic Basis of Capillary Pressure in Porous Media”*, Water Resources Research, **29**, 3389.

Hattenbach, R.P., Wilson, M., Brown, K. (1999) *“Capture Of Carbon Dioxide From Coal Combustion And Its Utilisation For Enhanced Oil Recovery,”* in "Greenhouse Gas Control Technologies", Elsevier Science, New York.

Holloway, S., Heederik, J.P., van der Meer, L.G.H., Czernichowski-Lauriol, I., Harrison, R., Lindeberg, E., Summerfield, I.R., Rochelle, C., Schwarzkopf, T., Kaarstad, O., Berger, B. (1996) *“The Underground Disposal Of Carbon Dioxide,”* British Geological Survey, Keyworth, Nottingham, U.K.

Kaviany, M. (1995) *“Principles of Heat Transfer in Porous Media,”* Springer-Verlag, New York.

Lawrence Berkeley Lab., (1999) *“TOUGH2,”* Berkeley, CA.

Slattery, J.C. (1972) *“Momentum, Energy, and Mass Transfer in Continua”* McGraw-Hill, New York.

Twiss, R.J., and Eringen, A.C. (1971), *“Theory of Mixtures for Micromorphic Materials-I, Balance Laws”*, Int. J. Engng. Sci., **9**, 1019.

Whitaker, S., (1986), *“Flow In Porous Media II, The Governing Equations for Immiscible Two-Phase Flow”*, Transport in Porous Media, **1**, 105.

**IX. “Experimental Study of Immiscible Two-Phase Flows In a Two -
Dimensional Flow Cell”**

**Chuang Ji (S) and Goodarz Ahmadi (F), Clarkson University
with
Duane Smith (M) and T. Robert McIendon, NETL**

EXPERIMENTAL STUDY OF IMMISCIBLE TWO-PHASE FLOWS IN A TWO-DIMENSIONAL FLOW CELL

Chuang Ji¹, Goodarz Ahmadi¹, Duane H. Smith² and T. Robert McIlendon²

1 Department of Mechanical and Aeronautical Engineering

Clarkson University

Potsdam, NY 13699-5725

2 National Energy Technology Laboratory

U.S. Department of Energy

Morgantown, WV 26508

ABSTRACT

In this project, an experimental method was developed to investigate the viscous fingering phenomena occurring during carbon dioxide sequestration underground. In the experiment, the displacement of two immiscible fluids in a lattice-like flow cell was studied with different injection flow rates of displacing fluid. The flow patterns during the displacement were analyzed, the residual saturations of the displaced fluid were measured, and the relative permeabilities of the fluids were computed. The results showed that the characteristics of the flow patterns were consistent with that of the fractals, and the residual saturation of the displaced fluid was a function of capillary number and viscosity ratio of the two fluids.

INTRODUCTION

The process of underground sequestration of CO₂ in brine-field formation involves multiple-phase liquid-gas flows through water saturated rock pores (Ferrer, et al., 1999). The fluid characteristics, flow patterns, and variations of rock pore physical properties with the fluid flow play important roles in the sequestration process. Smith, et al. (2000) developed an experimental method for providing a fundamental understanding of the CO₂ flows through the porous media that was saturated with brine. In this experiment, a flow cell, which was made of etching channels with random width in a flat glass plate, was used to simulate the porous media underground. Figure 1 shows the geometry of the flow cell and the magnified channels. It is seen that a lattice-like network is formed in the flow cell by etched channels, which width was uniformly ranged from 300 to 600 microns.

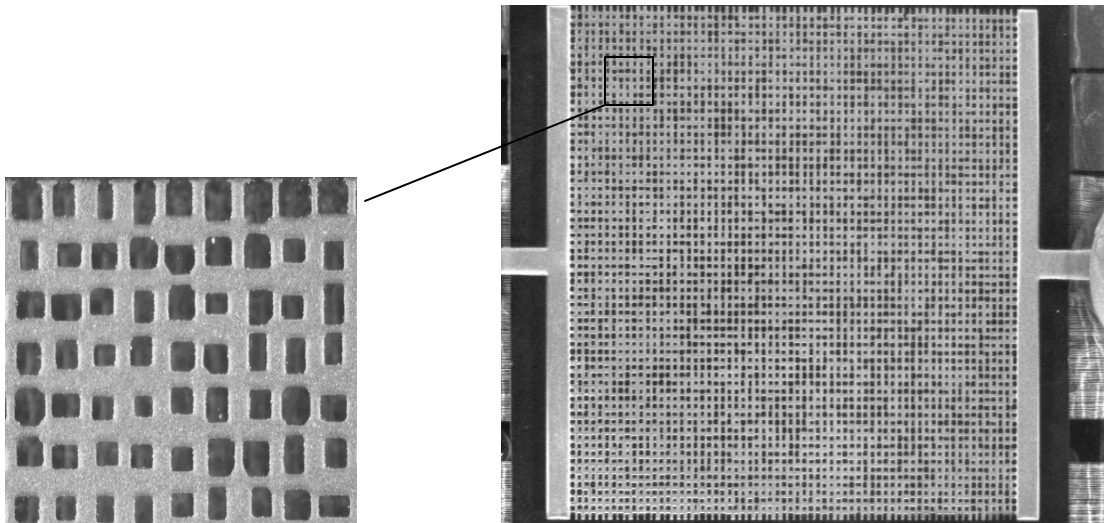


Figure 1. The geometry of the flow cell and the magnified channels.

At the beginning of the experiment, the flow cell was fully saturated with water, which was used as the wetting fluid (brine). Then air, the simulation of non-wetting fluid (CO₂), was injected into the flow cell by a syringe pump with a constant flow rate to displace the wetting fluid. The whole process was monitored and videotaped until the displacement reached a stable state. The pressure drop across the flow cell, and mass of displaced fluid were measured. The diagram of experimental setup is shown in Figure 2.

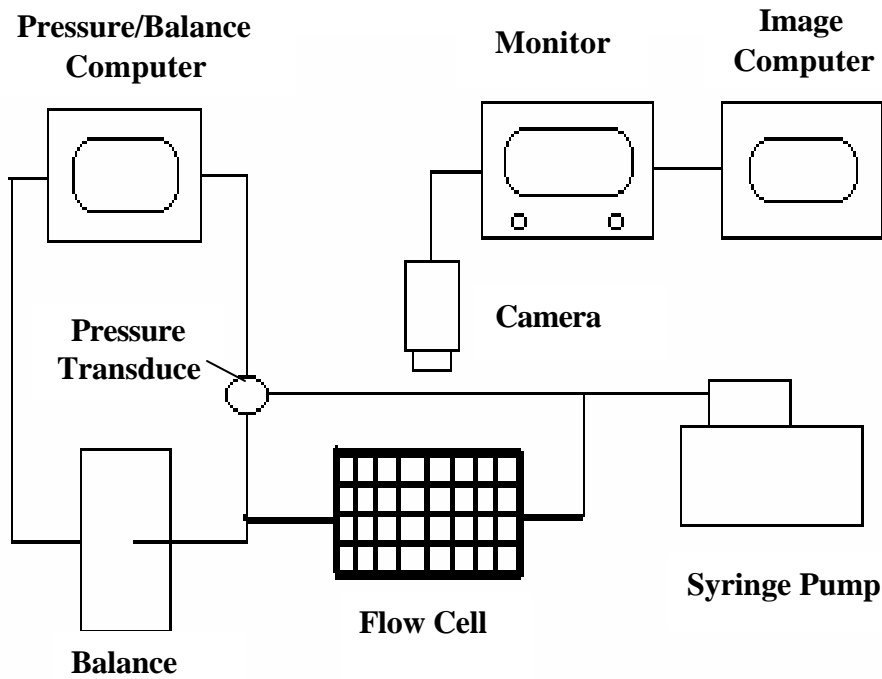


Figure 2. Experimental Setup

RESULTS

This section presents the results of the measured stable gas saturation under various conditions. In addition, the flow patterns during the displacement are analyzed, and the relative permeabilities of gas and water are also evaluated.

In the experiment, the time needed to reach the stable displacement state and the stable gas saturation in the flow cell are important to know. Figure 3 presents time variations of the gas saturation when gas displaces water at different flow rates. It is seen that the stable gas saturation increases with the gas injection flow rate, while the time used to reach the stable state is shortened. This may indicate that in a real CO₂ sequestration process, a higher CO₂ injection flow rate leads to a higher efficiency and a larger storage volume of CO₂ underground.

Figure 4 shows the stable gas saturation with capillary number for the displacement of water. Here the viscosity ratio of gas and water is $C = 1.79 \times 10^{-2}$, the

capillary number is defined as

$$C_a = \frac{\mu V}{\sigma \cos \theta} \quad (1)$$

where μ is the viscosity of the injected fluid, σ is the surface tension, θ is the contact angle. V is the inlet velocity of the injected fluid, which is given as

$$V = \frac{Q}{A_i} \quad (2)$$

where Q is the flow rate of the injected fluid, A_i is the cross section area of the channels at the flow cell inlet. From Figure 4, it is seen that as the capillary number increases from 10^{-8} to 10^{-3} , which corresponds to the variation of gas injection flow rate from 5 $\mu\text{l}/\text{min}$ to 100 ml/min, the stable gas saturation first decreases slightly to a minimum value, then goes up linearly with the capillary number. The transition of the flow pattern from capillary fingering to viscous fingering may account for the decrease in the stable gas saturation at a very small capillary number, which needs to be proven with more experimental data. A linear increase in the stable gas saturation at a large capillary number indicates that the stable gas saturation is proportional to the gas injection flow rate in a certain range.

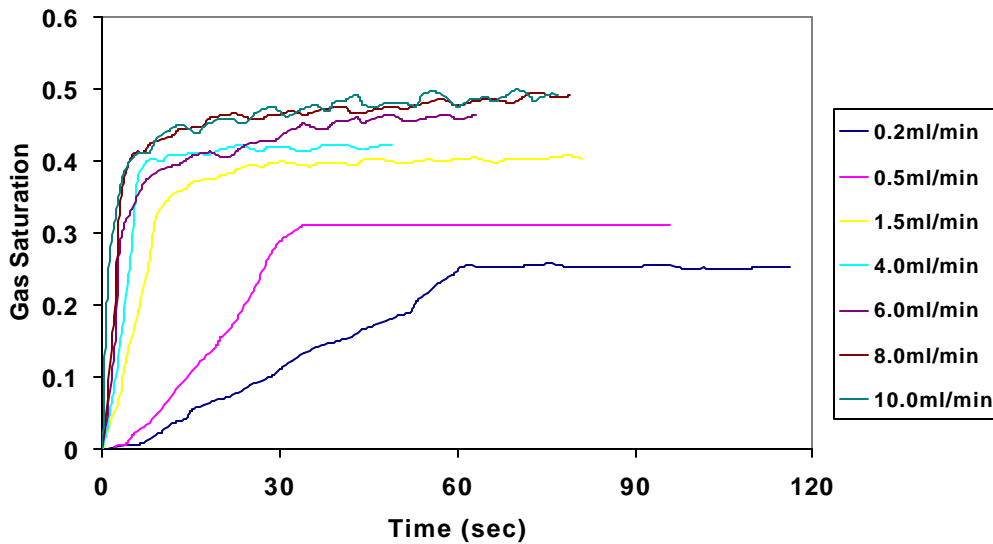


Figure 3. Time variations of gas saturation with different gas injection flow rates when the water is displaced by gas.

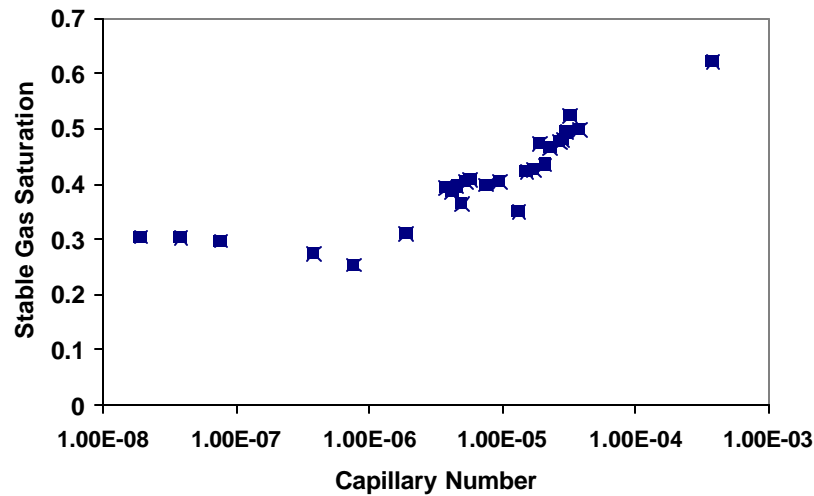
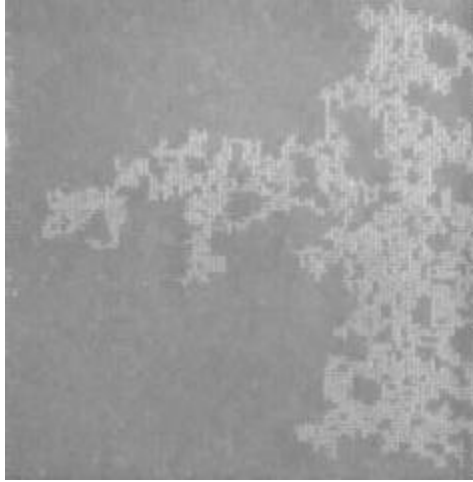


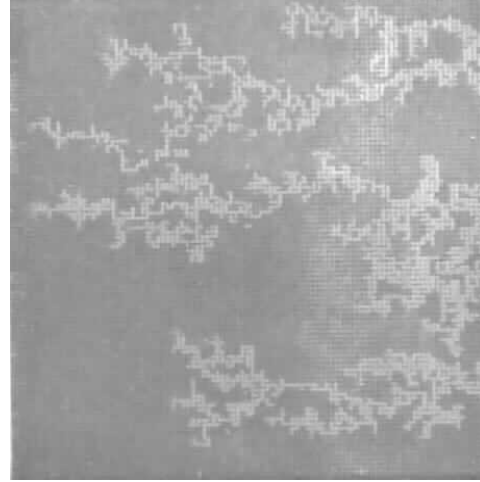
Figure 4. Stable gas saturation with different capillary numbers when water is displaced by gas.

In addition to the study of stable gas saturation, the flow pattern during the displacement is another important factor to be concerned. According to Leonard (1986), there are totally three kinds of flow pattern occurring during the displacement of two immiscible fluids: stable displacement, viscous fingering and capillary fingering. In our experiment, two kinds of flow pattern are observed due to the limitations of gas injection flow rate and viscosity ratio of gas and water: capillary fingering, which is dominated by capillarity, occurring at a very low capillary number, and viscous fingering, which is driven by the viscosity of the gas, occurring as the capillary number increases.

Figure 5 shows the typical capillary fingering and viscous fingering recorded in the experiment. The capillary fingering shown in Figure 5 (a) occurs when the capillary number is 7.36×10^{-7} . It is seen that as the gas penetrates into the flow cell, it forms fingers which consist of loops trapping the displaced water. The size of the water clusters varies from the width of the channel to the order of the flow cell size. In Figure 5 (b), a viscous fingering is shown as the capillary number is 3.25×10^{-5} . In this figure, the gas fingers grow like trees without any loops.



(a) Capillary Fingering



(b) Viscous Fingering

Figure 5. Flow patterns observed during the displacement with different capillary numbers.

CONCLUSION

In this study, an experimental study of displacement of two immiscible fluids in a flow cell is conducted. The stable gas saturation is measured, the flow patterns during the displacement are analyzed, and the relative permeabilities of the fluids are computed. It is found that as the capillary number increases, stable saturation of the displacing fluid first decreases when the capillary number is small, then increases with the capillary number.

REFERENCE

1. Ferer, M., Bromhal, G.S., and Smith, D. H., (2000) "Pore-Level Modeling: Injection of Carbon Dioxide into a Brine-Saturated Reservoir," Seventeenth Annual International Pittsburgh Coal Conference, Pittsburgh, PA, September 11-14, 2000.
2. Ogunsola, O.M., Ramer, E.R. and Smith, D.H. (2000) "Immiscible Fluid Flow In Two-Dimensional Microcell," Seventeenth Annual International Pittsburgh Coal Conference, Pittsburgh, PA, September 11-14, 2000.

**X. “Application of Computational Fluid Mechanics to Design
of Industrial Filter Vessels”**

**Chaosheng Liu (S) and Goodarz Ahmadi (F), Clarkson University
with
Duane Smith (M), NETL**

APPLICATION OF COMPUTATIONAL FLUID MECHANICS TO DESIGN OF INDUSTRIAL FILTER VESSELS

Chaosheng Liu¹, Goodarz Ahmadi¹ and Isaac K. Gamwo²

¹ Department of Mechanical and Aeronautical Engineering,
Clarkson University, Potsdam, NY 13699-5725, USA

² U.S. Department of Energy
National Energy Technology Laboratory
P.O. Box 10940, Pittsburgh, PA 15236-0940

ABSTRACT: Gas flow in an industrial hot-gas filter vessel is studied. The filter vessel contains a large number of candle filters, which are arranged in two tiers. The filters are modeled by six upper and seven lower cylindrical effective filters. An unstructured grid generated by GAMBIT is used in the simulations. The Reynolds stress model of FLUENT code is used for evaluating the gas mean velocity and root mean square fluctuation velocities in the vessel. For future study of particle transport and deposition in the filter vessel, a particle code for unstructured grid is developed and tested by simulating particle transport and deposition in pipe flow. The particle equation of motion used includes drag, gravitational and lift forces. The turbulent instantaneous fluctuation velocity is simulated by a filtered Gaussian white-noise model provided by the FLUENT code. The particle transport and deposition patterns are evaluated and the effect of particle size is studied.

I. INTRODUCTION

Developing advanced clean coal technology for electric power generation with high efficiency and low pollutants has seen considerable interest in the recent years. As a result, the advanced pressurized fluidized bed combustion (PFBC) and integrated gasification combined cycles (IGCC) are developed and are being tested as part of the Clean Coal Technology Program of the US Department of Energy. These highly efficient advanced coal energy systems require effective removal of ash and un-reacted and reacted sulfur sorbent from the hot gases.

Thambimuthu (1993), Clif and Seville (1993) provided extensive reviews of gas cleaning at high temperatures. Recent developments on hot-gas cleaning with the use of ceramic candle filters were described by Dittler et al. (1999). Smith and Ahmadi (1998) discuss the progress and issues concerning the hot-gas filtration in connection with PFBC and IGCC systems. While the candle filters generally have a very high cleaning efficiency of the order of 99%, there are still a number of unresolved issues with buildup of dust cake on the filters, occasional filter-ash bridging and filter failure and breakage.

For improving the reliability of hot-gas filtration systems in commercial applications, a fundamental understanding of the ash transport and deposition processes in the filter

vessels is needed. A computational modeling of filter vessel was reported by Ahmadi and Smith (1998a,b), and Zhang and Ahmadi (2001).

In this study, hot-gas flow in the recently operating Siemens-Westinghouse Particulate Control Device (PCD) at the demonstration-scale PSDF in Wilsonville, Alabama, is studied. A refined grid and the Reynolds stress turbulence model of the FLUENT™ code is used for evaluating the gas mean velocity and the root mean-square fluctuation velocity in the filter vessel.

A particle code for unstructured grid is developed for future study of particle transport and deposition in the filter vessel. The particle code is tested by simulating particle transport and deposition in pipe flow. The particle equation of motion including the drag, the lift and the gravitational forces are used in the simulation. The deposition patterns of silicon particles of different sizes are evaluated and compared with the simulation results of the FLUENT™ code.

II. WILSONVILLE HOT-GAS FILTER VESSEL

The Siemens-Westinghouse tangential flow hot-gas filter vessel (PCD) is currently being tested at the Southern Research Company Facility (PSDF) at Wilsonville near Birmingham, Alabama. The PCD vessel at PSDF is 1.6 m (63 in) in diameter and 8.27 m (325.7 in) long. The vessel accommodates 91 candle filters arranged in two clusters. The upper and lower tiers have, respectively, 36 and 55 candle filters. The ceramic candle filters are about 6cm (2.36 in) in outer diameter and 1.5m (4.92 ft) long. A special feature of PCD at Wilsonville is that the hot-gas enters the vessel tangentially into the vessel. There is a large cylindrical shroud in the vessel and the inlet hot-gas flows in the gap between the vessel refractory and the shroud. Figure 1 shows a schematic of the Siemens-Westinghouse Particle Control Device (PCD).

The average gas mass flow rate into the filter vessel is 2.95 kg/s (23,500 lb/hr), with the PCD operating at a pressure of 1344 kPa (195 psia), and a temperature 1033 K (760 °C). Under these operating conditions, the corresponding inlet flow velocity is 9.8 m/s, the air density is 4.53 kg/m³ and the air viscosity is 3.7×10^{-5} kg/ms.

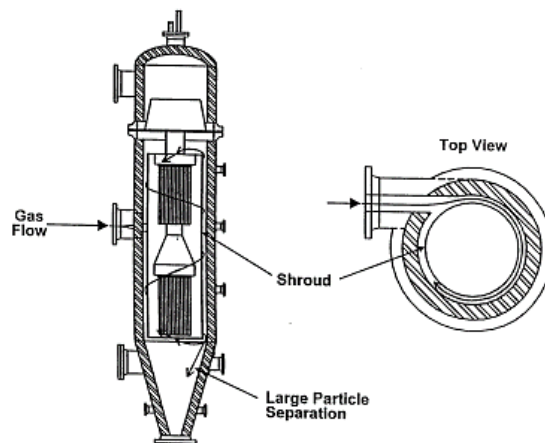


Figure 1. Schematic of the Siemens-Westinghouse Particle Control Device (PCD) at PSDF.

EQUIVALENT FILTER

To keep the computational effort manageable, the group of 36 candle filters in the upper tier is modeled by six equivalent filters and the 55 lower filters are replaced by seven equivalent candle filters. The lengths of the equivalent filters are all identical to that of the actual candle filters. All equivalent candle filters, except for the one at the center of the lower cluster, have an outer diameter of 11 inch and inner diameter of 9.4 inch. The one at center of the lower tier has an outer diameter of 16 inch and an inner diameter of 13.6 inch.

The permeability of the effective candle filters is adjusted so that they have the same pressure drop as the actual candle filters. Assuming that the candle filters have a permeability of $10^{-12} m^2$, the effective permeability of the upper and lower 11 inch equivalent filters is $2.033 \times 10^{-12} m^2$ and of the 16 inch equivalent candle filter at the center of the lower tier is $3.05 \times 10^{-12} m^2$.

GAS FLOW SIMULATION

The gas flow in the PCD at PSDF at Wilsonville, Alabama are described in this section. The simulation makes use of the Reynolds stress transport model of FLUENT™ version 5 (FLUENT User's Guide 1998 Vol. 2) for evaluating the turbulent gas flow condition in the filter vessel.

Computational Grid

Due the rather complex geometry of the PCD an unstructured grid of 1,371,162 cells generated by GAMBIT code is used in the simulations. To allow a more accurate analysis of ash transport and deposition in the spacing between the shroud and vessel wall, the grid is further refined in these regions. Figure 2 shows the surface grid of the equivalent filters and at the mid-section of the vessel. In the computational model, the origin of the coordinate system is set in the center of the top of the vessel. The z-axis is in the vertical direction pointing downward (along the gravitational direction) and the x-axis is along the inlet flow direction.

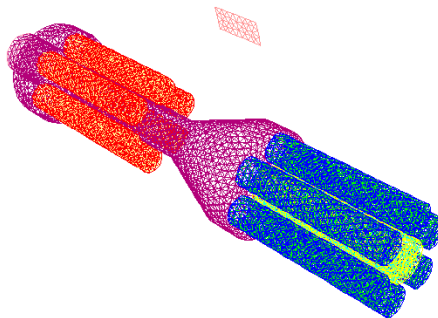


Figure 2. Grid schematic of the modeled filter vessel.

Gas Flow

Figure 3 shows the velocity vector plot in a plane at the mid-section of the vessel. This figure shows that about half of the inlet gas moves upward in the shroud and the other half moves downward. Thus, the hot-gas enters the body of the vessel both from the top and the bottom of the shroud. The flow velocity is downward and somewhat larger in the region between the upper filter and the shroud. Near the top of the vessel, the upward gas flow in the shroud turns sharply downward to enter the main body of the vessel. Also the downward gas flow near the outlet of the shroud at the bottom turns upward to enter the main body of the vessel.

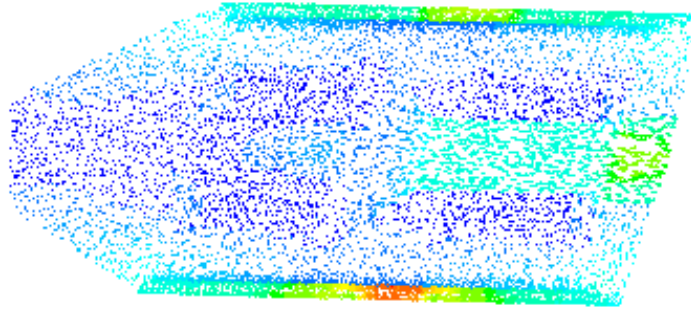


Figure 3. Velocity vector plot at the vessel mid-section.

Figure 4 shows the contour plots for variations of the static pressure in a plane at the mid-section of the PCD vessel. This figure shows that the pressure remains almost constant inside the shroud and in the main body of the vessel. It is also shown that the main pressure drop occurs across the filter wall, and the pressure decreases inside the filter cavity. The air pressure inside the filter cavity and connecting pipes is roughly constant with a slight decrease toward the vessel outlet. It is also clearly seen the sharp pressure drop across the filter wall. It should be noted that in the body of the filter vessel the pressure is high and roughly uniform and reduces significantly as the gas passes through ceramic filter wall and enters the candle filter cavity.



Figure 4. Contour plot for variations of the static pressure at the vessel mid-section.

III. PARTICLE TRANSPORT AND DEPOSITION IN PIPE FLOW

An unstructured grid of 148,698 cells generated by GAMBIT code for a 0.2 m wide, 0.8 m long pipe is used in the simulations. A temperature of 300 K, $\mu = 1.789 \times 10^{-5} \text{ N} \cdot \text{s}/\text{m}^2$ and $\rho = 1.225 \text{ kg}/\text{m}^3$ for air are used. The mean velocity in the pipe is assumed to be $u = 1.0 \text{ m}/\text{s}$. Figure 5 shows the grid of the pipe. In the computational model, the origin of the coordinate system is set in the center of the inlet of the pipe. The y-axis is in the vertical direction pointing upward (opposite to the gravitational direction) and the z-axis is along the inlet flow direction.

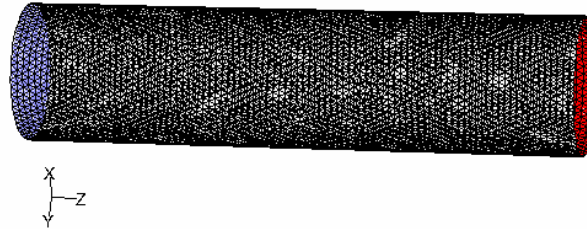


Figure 5. Grid schematic of the modeled pipe.

Air Flow

Figure 6 shows the mean velocity magnitude contours in plot in a plane along the inlet flow direction. It is observed the air velocity is quite low near the wall.

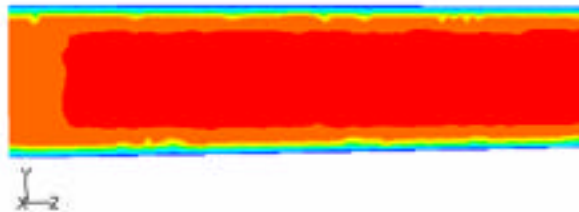


Figure 6. Mean velocity magnitude contours in the pipe

Figure 7 shows the contour plots for variations of the static pressure in a plane along the inlet flow direction. This figure shows that the pressure decreases along with the inlet flow direction.



Figure 7. Contour plot for variations of the static pressure in the pipe.

Particle Deposition And Transportation

In this work, particle deposition rates are evaluated by releasing 1000 particles in a ring area at the pipe inlet as shown in Figure 8.

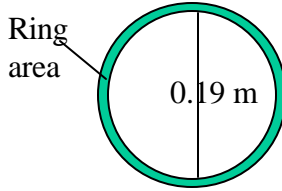


Figure 8. The inlet plane of the pipe

For 0.1 μm , 1 μm and 10 μm particles, table 1 shows the simulation results of particle deposition rates from FLUENT code and particle code. Noticeable high deposition rates are observed for 10 μm particles. It is also observed that FLUENT code and the particle code have similar simulation results and deposition rates from particle code simulation are lower than those from FLUENT code simulation.

Particle diameter	FLUENT code simulation results		Particle code simulation results	
	Number of escaped particles	Number of deposited particles	Number of escaped particles	Number of deposited particles
0.1 μm	864	136	881	119
1 μm	872	128	895	105
10 μm	754	246	789	211

Table 1. Deposition rates on the wall for different sized particles

Figures 9 and 10 show sample trajectories of 1 μm and 10 μm particles, respectively. For each case, 50 particles are released at the center of the pipe inlet plane. It is observed that the trajectories of 1 and 10 μm particles are comparable.

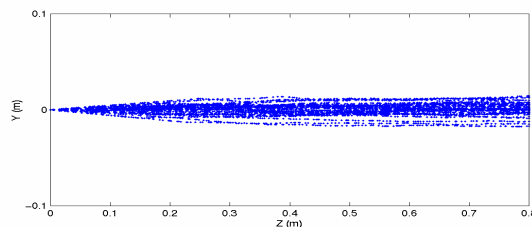


Figure 9. Trajectories of 1 μm particles released at the center of the inlet.

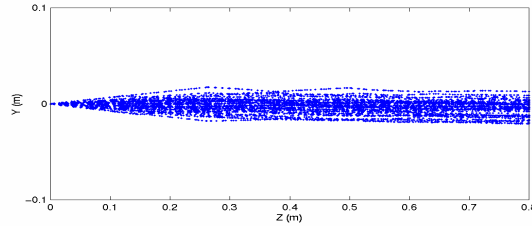


Figure 10. Trajectories of 10 μm particles released at the center of the inlet.

CONCLUSION

In this work, the FLUENT code is used to simulate the mean turbulent flow field in the hot-gas filter vessel at Wilsonville is studied. A computer code for analyzing particle transport and deposition in unstructured grid is developed. A preliminary test is performed and particle transport and deposition in a pipe flow is simulated. On the basis on the presented results, the following conclusions are drawn:

- The computational model could provide information about the gas flow in the filter vessel.
- The sample results shows that gas velocity magnitude inside the shroud of the vessel is generally high, while it is relatively low inside the vessel.
- The main pressure drop occurs across the filter due to a significant pressure drop across the filter wall.
- The computational model for particle transport analysis using unstructured grid appears to give reasonable results.

FUTURE WORK

For the next year we plan to further develop the computational model for particle transport and deposition analysis. Comparison with experimental data will be performed to verify its accuracy. The model will then be applied to ash deposition in the filter vessel.

We also plan to study the effect of thermal variation in the vessel. In particular the variation of temperature field in vessel during the normal operation and with ash bridging will be studied.

REFERENCE

Ahmadi, G., and Smith, D. H., (1998a). “*Particle transport and deposition in a hot-gas cleanup pilot plant*”, *Aerosol Sci. Technol.* **29**, 183-205.

Ahmadi, G., and Smith, D. H., (1998b). “*Gas flow and particle deposition in the hot-gas filter vessel at the Tidd 70 MWE PFBC demonstration power plant*”, *Aerosol Sci. Technol.* **29**, 206-223.

Clift, R. and Seville, J. P. K., (1993). “*Gas cleaning at high temperatures*”, Blackie Academic & Professional, New York.

Dittler, A., Hemmer, G. and Kasper, G., (1999). "High Temperature Gas Cleaning," Vol II, G. Braun ems GmbH, Karlsruhe.

Thambimuthu, K.V., (1993). "*Gas cleaning for advanced coal-based power generation*", EACR/53, IEA Coal Research, London.

Zhang, H., and Ahmadi, G., (2001). Particle Transport and Deposition in the Hot-Gas Filter Vessel at Wilsonville, *Powder Technology*, **116**: 53-68.

**UNIVERSITY/NETL STUDENT PARTNERSHIP PROGRAM
(DE-FC26-98FT40143)**

3rd Year Technical Report

September 1, 2000 – August 31, 2001

Submitted to:

National Energy Technology Laboratory

Submitted by:

**Gerald D. Holder
School of Engineering
University of Pittsburgh
Pittsburgh, PA 15261**

Volume II of VI

XI. “Distribution of Porosity in an Artificially-Induced Tensile Fracture and Its Relationship to the Surrounding Matrix”

**Claudia Parada (S), Abraham Grader (F), The Pennsylvania State University
with
Duane Smith (M), NETL**

The Pennsylvania State University

The Graduate School

The Department of Energy & Geo-Environment Engineering

**DISTRIBUTION OF POROSITY IN AN ARTIFICIALLY – INDUCED TENSILE
FRACTURE AND ITS RELATIONSHIP TO THE SURROUNDING MATRIX**

A Thesis in

Petroleum and Natural Gas Engineering

by

Claudia Helena Parada

© 2001 Claudia Helena Parada

Submitted in Partial Fulfillment
of the Requirements
for the Degree of

Master of Science

December 2001

We approve the thesis of Claudia Helena Parada.

Date of Signature



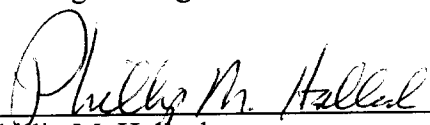
Abraham S. Grader
Professor of Petroleum and Natural Gas
Engineering
Thesis Advisor

Dec. 4, 2001



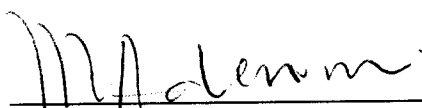
Turgay Ertekin
Professor of Petroleum and Natural Gas
Engineering

December 4, 2001



Phillip M. Halleck
Associate Professor of Petroleum and
Natural Gas Engineering

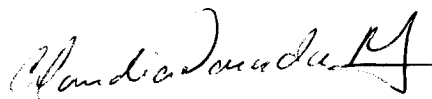
4 Dec, 2001



Michael Adewumi
Professor of Petroleum and Natural Gas
Engineering
In charge of Graduate Program in Petroleum
and Natural Gas Engineering

Dec 5, 2001

I grant The Pennsylvania State University the nonexclusive right to use this work for the University's own purposes and to make single copies of the work available to the public on a not-for-profit basis if copies are not otherwise available.

A handwritten signature in cursive script, appearing to read "Claudia Helena Parada".

Claudia Helena Parada

ABSTRACT

The relationship between the distribution of the fracture aperture, expressed as porosity distribution, in an artificially induced fracture and the structure of the adjacent matrix in a Berea sandstone was verified using computed tomography analysis. Detailed examination of the high-resolution images indicated that large fracture apertures were aligned with high-porosity layers.

In order to characterize and study the morphology of the core and the induced fracture, the rock sample was scanned in two different X-ray scanners; a medical scanner, the HD250, and a high-resolution industrial scanner, the OMNI-X. Due to the difference in spatial resolution, the images acquired by the OMNI-X were stacked in groups of 21 to obtain images of same thickness as those acquired by the HD250. The medical scanner provided a good observation of the morphology of the matrix sample while the industrial scanner was a better tool for analyzing the detailed structure of the fracture. The superiority of the high-resolution images acquired by OMNI-X over the corresponding low-resolution medical scanner was confirmed.

The porosity distribution of the sample was determined by analyzing low- and high-resolution images acquired before and after saturating it with tagged water. The average porosity of the core was determined by material balance. Various CT and porosity profiles were generated by digital manipulation of the acquired data. The contrast between the spatial resolutions of the equipment was reflected in the profiles,

providing additional evidence that high fracture apertures are aligned with high porosity layers.

TABLE OF CONTENTS

LIST OF FIGURES.....	vii
LIST OF TABLES	xv
ACKNOWLEDGMENTS.....	xvi
Chapter 1 INTRODUCTION	1
Chapter 2 OBJECTIVE AND APPROACH.....	3
Chapter 3 EXPERIMENTAL SYSTEM, MATERIALS, AND PROCEDURES	4
3.1 Experimental System	4
3.1.1 Medical-Based X-Ray CT Scanner, HD250.....	5
3.1.2 The Industrial-Based X-Ray CT Scanner, OMNI-X	7
3.1.3 The Core Holder	8
3.1.4 Fluid Saturation System.....	11
3.2 Materials.....	12
3.2.1 Rock Sample	12
3.2.2 Fluids	13
3.3 Procedures	13
3.3.1 Creating The Induced Fracture	13
3.3.2 Rock Preparation.....	15
3.3.3 Scanning Procedures to Compare the Scanners.....	16
3.3.4 Scanning Procedures to Determine Porosity Distribution	17
Chapter 4 THE ACQUIRED DATA.....	20
4.1 CT Data of the Dry and Fractured Berea Core Sample	20
4.1.1 CT Data from the HD250 Medical Scanner	20
4.1.2 CT Data from the OMNI-X Industrial Scanner	24
4.2 CT Data of the Dry and Saturated Sample for Porosity Determination.....	28
4.2.1 Dry and Wet CT Data from the HD250 Medical Scanner.....	29

4.2.2 Dry and Wet CT Data from the OMNI-X Industrial Scanner	38
4.3 Average Porosity Through Material Balance.....	41
Chapter 5 DISCUSSION OF RESULTS	42
5.1 Characterization of the Fractured Berea Core Sample with X-Ray Computed Tomography (CT).	44
5.2 Computed Tomography Analysis and Porosity Distribution.....	65
5.2.1 Medical Scanner HD250.....	67
5.2.1.1 CT Profile Analysis	71
5.2.1.2 Porosity Distribution.....	84
5.2.2 Industrial Scanner OMNI-X.	95
5.2.2.1 CT Profile Analysis	98
5.2.2.2 Porosity Distribution.....	107
5.3 Comparison of Profiles Generated with the Data Acquired by both Scanners.....	111
5.4 Fracture Aperture	117
Chapter 6 SUMMARY AND CONCLUSIONS	122
BIBLIOGRAPHY	124
Appendix A Scanning Sequences Acquired by HD250.....	126
Appendix B Scanning Sequences Acquired by the OMNI-X High Resolution Scanner.....	133

LIST OF FIGURES

Figure 3–1:	X-ray CT scanner HD250.....	6
Figure 3–2:	High-resolution x-ray CT scanner, OMNI-X.	8
Figure 3–3:	Core holder.	9
Figure 3–4:	A schematic drawing of the core holder.	10
Figure 3–5:	Schematic of the saturation system.....	11
Figure 3–6:	Stress element and preferred plane of fracture.	14
Figure 3–7:	Sandstone sample prior to fracturing using a modified Brazilian test.....	14
Figure 3–8:	Load versus time during the fracturing process of the sample.	15
Figure 4–1:	CT image of the dry Berea core without the core holder. Scanner: HD250.....	21
Figure 4–2:	CT image of the dry Berea core without core holder at different CT number range. Scanner: HD250.	22
Figure 4–3:	Plate of CT images of the dry fractured Berea core. Scanner: HD250.....	23
Figure 4–4:	CT image of the dry Berea core. Scanner: OMNI-X. Resolution: 256x256 pixels.....	25
Figure 4–5:	CT image of the dry Berea core. Scanner: OMNI-X. Resolution: 512x512 pixels.....	26
Figure 4–6:	CT image of the dry Berea core. Scanner: OMNI-X. Resolution: 1024x1024 pixels.....	27
Figure 4–7:	Original image of the dry fractured Berea scanned in the aluminum core holder by the HD250 scanner.	30

Figure 4–8:	Cut image of the dry fractured Berea scanned in the aluminum core holder by the HD250. CT number range: 1250 – 1550.	31
Figure 4–9:	Image of the fractured Berea saturated with tagged water, scanned in the aluminum core holder, by the HD250 scanner.	32
Figure 4–10:	Image of the saturated fractured Berea core with tagged water scanned in the aluminum core holder by the HD250 medical scanner.	33
Figure 4–11:	Schematic of the positions scanned by the HD250 during the fluid displacement.....	34
Figure 4–12:	Plate of images during the tagged water displacement and the corresponding PVI at the first position (bottom-tip of the fracture) scanned by the HD250 scanner.....	35
Figure 4–13:	Plate of images during the tagged water displacement and the corresponding PVI at the second position (middle of the core) scanned by the HD250 scanner.....	36
Figure 4–14:	Plate of images during the tagged water displacement and the corresponding PVI at the third position (top-tip of the fracture) scanned by the HD250 scanner.....	37
Figure 4–15:	Image of the dry Berea core reconstructed at 512x512 scanned by the OMNI-X scanner.	39
Figure 4–16:	Image of the saturated Berea core (tagged water) reconstructed at 512x512 scanned by the OMNI-X scanner.....	40
Figure 5–1:	Vertical cross-section and horizontal section along the core.....	43
Figure 5–2:	Plate of 19 images close to one tip of the fracture acquired with the medical scanner HD250. Slice thickness: 2mm. Slice spacing: 2mm. Total sweep length: 38 mm.	45
Figure 5–3:	Image acquired by the HD250 scanner. 200x200 pixels.	46
Figure 5–4:	Longitudinal sections through the rock sample. Scanner: HD250.....	47
Figure 5–5:	Plate of 19 dry images close to one tip of the fracture acquired with the industrial scanner OMNI-X reconstructed at 256x256 pixels. Thickness: 95 μ m with a spacing of 1.995 mm. Length covered by these images: 37.9 mm.....	48

Figure 5–6:	Single image of the core sample acquired by the OMNI-X close to the tip of the fracture. Matrix size: 256x256.	49
Figure 5–7:	Single image of the core sample acquired by the OMNI-X close to the tip of the fracture. Matrix size: 512x512.	50
Figure 5–8:	Single image of the core sample acquired by the OMNI-X close to the tip of the fracture. Matrix size: 1024x1024.	51
Figure 5–9:	Expanded region showing the details of the fracture.....	52
Figure 5–10:	A quarter image of the fractured Berea at different levels of reconstruction.	53
Figure 5–11:	Comparison of an image scanned by the HD250 and OMNI-X scanners at the same location.....	54
Figure 5–12:	Relationship between image thicknesses from the two scanners. ...	55
Figure 5–13:	Horizontal sections through images acquired by both scanners. Total length: 38 mm.....	56
Figure 5–14:	Average of images reconstructed at 256x256 pixels compare with a single slice. Total sweep length 38 mm. OMNI-X scanner.	57
Figure 5–15:	Average of images reconstructed at 512x512 pixels compare with a single slice. Total sweep length 38 mm. OMNI-X scanner.	58
Figure 5–16:	Average of images reconstructed at 1024x1024 pixels compare with a single slice. Total sweep length 38 mm. OMNI-X scanner.	59
Figure 5–17:	Single and averaged OMNI-X images at different levels of reconstructions.....	61
Figure 5–18:	A quarter average image of the fractured Berea core at different levels of reconstruction by the OMNI-X scanner.....	62
Figure 5–19:	Comparison between OMNI-X average images 512x512 and HD250 single images at the same location.....	63
Figure 5–20:	Comparison of an image scanned by the HD250 and OMNI-X average images. Thickness of the displayed images: 2 mm.	64

Figure 5–21:	Comparison of the section scanned by both scanners.	66
Figure 5–22:	Enlargement of the horizontal section of 30 mm scanned by both scanners.	66
Figure 5–23:	Plate of 15 dry images scanned by the HD250 scanner.....	68
Figure 5–24:	Plate of 15 NaI-tagged water images scanned by the HD250 scanner.	70
Figure 5–25:	Plate of 15 distilled water images scanned by the HD250 scanner.	71
Figure 5–26:	Average CT numbers profiled along the fracture in the dry image # 96 acquired by the HD250 scanner.....	73
Figure 5–27:	CT number profile along the middle of the fracture in the dry image # 96 acquired by the HD250 scanner.	73
Figure 5–28:	CT profiles through the matrix 6 pixels above and below the fractured region in the dry image # 96 acquired by the HD250 scanner.	74
Figure 5–29:	Comparison between profiles in the matrix and profiles in the fractured region of the dry image # 96 acquired in the HD250 scanner.	75
Figure 5–30:	Average CT profiles through the fractured region for the following conditions: dry, NaI-tagged water, and distilled water. Scanner: HD250.....	76
Figure 5–31:	CT profiles through the center of the fractured region of the image #96 for the following conditions: dry, NaI-tagged, water, and distilled water. Scanner: HD250.	77
Figure 5–32:	CT profiles through the matrix six pixels above the edges of the fractured region of the image #96 for the following conditions: dry, NaI-tagged, and distilled water. Scanner: HD250.....	78
Figure 5–33:	CT profiles through the matrix six pixels below the edges of the fractured region of image #96 for the following conditions: dry, NaI-tagged, and distilled water. Scanner: HD250.	78
Figure 5–34:	Comparison between profiles in the matrix and the fracture of the NaI-tagged water image #96. Scanner: HD250.	79

Figure 5–35:	Comparison between profiles in the matrix and the fracture of the distilled water image #96. Scanner: HD250.	80
Figure 5–36:	Comparison between profiles in the matrix and profiles in the fractured region of the dry image # 100. Scanner: HD250.....	81
Figure 5–37:	Comparison between profiles in the matrix and profiles in the fractured region of the NaI-tagged water image # 100. Scanner: HD250.....	81
Figure 5–38:	Comparison between profiles in the matrix and profiles in the fractured region of the distilled water image #100. Scanner: HD250.....	82
Figure 5–39:	Comparison between profiles in the matrix and profiles in the fractured region of the dry image # 105. Scanner: HD250.....	83
Figure 5–40:	Comparison between profiles in the matrix and profiles in the fractured region of the NaI-tagged water image # 105. Scanner: HD250.....	83
Figure 5–41:	Comparison between profiles in the matrix and profiles in the fractured region of the distilled water image # 105. Scanner: HD250.....	84
Figure 5–42:	Plate of 15 porosity images calculated with the NaI-tagged water images acquired by the HD250 medical scanner.....	86
Figure 5–43:	Plate of 15 porosity images calculated with the distilled water images acquired by the HD250 medical scanner.....	87
Figure 5–44:	Comparison between porosity in the fractured region and the matrix calculated using NaI-tagged water images. Porosity image #96. Scanner: HD250.....	88
Figure 5–45:	Comparison between porosity in the fractured region and the matrix calculated using distilled water images. Porosity image #96. Scanner: HD250.....	88
Figure 5–46:	Comparison between porosity profiles for image #96. Scanner: HD250.....	90
Figure 5–47:	Comparison between porosity in the fractured region and the matrix calculated using NaI-tagged water images. Porosity image #100. Scanner: HD250.....	91

Figure 5–48:	Comparison between porosity in the fractured region and the matrix calculated using distilled water images. Porosity image #100. Scanner: HD250.....	91
Figure 5–49:	Comparison between average porosity profiles in the fracture for image #100. Scanner: HD250.....	92
Figure 5–50:	Comparison between porosity in the fractured region and the matrix calculated using NaI-tagged water images. Porosity image #105. Scanner: HD250.....	93
Figure 5–51:	Comparison between porosity in the fractured region and the matrix calculated using distilled water images. Porosity image #105. Scanner: HD250.....	94
Figure 5–52:	Comparison between porosity profiles in the fractured region for image #105. Scanner: HD250.....	94
Figure 5–53:	Plate of 15 averaged dry images scanned by the OMNI-X scanner.....	96
Figure 5–54:	Plate of 15 averaged NaI-tagged water images scanned by the OMNI-X scanner.....	97
Figure 5–55:	Average CT numbers profiled along the fracture in the first averaged dry image. OMNI-X scanner.....	99
Figure 5–56:	CT number profile along the middle of the fracture in the first averaged dry image. OMNI-X scanner.....	99
Figure 5–57:	CT profiles through the matrix four pixels above and below the fractured region in the first averaged dry image. Scanner: OMNI-X.....	100
Figure 5–58:	Comparison between profiles in the matrix and profiles in the fractured region in the first dry averaged image. Scanner: OMNI-X.....	101
Figure 5–59:	Average CT profile through the fractured region for first dry and wet averaged images. Scanner: OMNI-X.....	102
Figure 5–60:	Profiles four pixels above the fracture for the first dry and wet averaged images. Scanner: OMNI-X.....	102
Figure 5–61:	Profiles four pixels below the fracture for the first dry and wet averaged images. Scanner: OMNI-X.....	103

Figure 5–62:	Comparison between profiles in the matrix and profiles in the fractured region of the first NaI-tagged averaged image. Scanner: OMNI-X.	104
Figure 5–63:	Comparison between profiles in the matrix and profiles in the fractured region in the fifth dry averaged image. Scanner: OMNI-X.	105
Figure 5–64:	Comparison between profiles in the matrix and profiles in the fractured region of the fifth NaI-tagged averaged image. Scanner: OMNI-X.	105
Figure 5–65:	Comparison between profiles in the matrix and profiles in the fractured region in the tenth dry averaged image. Scanner: OMNI-X.	106
Figure 5–66:	Comparison between profiles in the matrix and profiles in the fractured region of the tenth NaI-tagged averaged image. Scanner OMNI-X.....	106
Figure 5–67:	Plate of 15 porosity images calculated with the averaged images from the Scanner: OMNI-X.	108
Figure 5–68:	Comparison between porosity profiles in the matrix and profiles in the fractured region in the first averaged porosity image. Scanner: OMNI-X.	109
Figure 5–69:	Comparison between porosity profiles in the matrix and profiles in the fractured region of the averaged porosity image #5. Scanner: OMNI-X.	110
Figure 5–70:	Comparison between porosity profiles in the matrix and profiles in the fractured region in the averaged porosity image #10. Scanner: OMNI-X.	110
Figure 5–71:	Profiles through the fractured region generated with the data acquired by both scanners. HD250 dry image #96 and averaged OMNI-X dry image #1.	112
Figure 5–72:	Profiles above the fractured region generated with the data acquired by both scanners. HD250 dry image #96 and averaged OMNI-X dry image #1.	112
Figure 5–73:	Porosity distribution in the fractured region generated with the data acquired by both scanners. HD250 image #96 and averaged OMNI-X image #1.....	114

Figure 5–74:	Profiles through the fractured region generated with the data acquired by both scanners. HD250 dry image #100 and averaged OMNI-X dry image #5.....	115
Figure 5–75:	Porosity distribution in the fractured region generated with the data acquired by both scanners. HD250 image #100 and averaged OMNI-X image #5.	115
Figure 5–76	Profiles through the fractured region generated with the data acquired by both scanners. HD250 dry image #105 and averaged OMNI-X dry image #10.....	116
Figure 5–77:	Porosity distribution in the fractured region generated with the data acquired by both scanners. HD250 image #105 and averaged OMNI-X image #10.	116
Figure 5–78:	Averaged imaged of 21 images acquired by the OMNI-X scanner reconstructed at 1024x1024.....	118
Figure 5–79:	Single OMNI-X imaged reconstructed at 1024x1024.	119
Figure 5–80:	Expanded sections of 200x200 pixels of an averaged and a single image acquired by the OMNI-X and reconstructed at 1024x1024.	120
Figure 5–81:	Plate of 20 single expanded images acquired by the OMNI-X scanner reconstructed at 1024x1024.....	121

LIST OF TABLES

Table A-1:	Dry Scanning Sequence by the CT X-Ray Scanner HD250.....	127
Table A-2:	Wet Tagged Water Scanning Sequence by the CT X-Ray Scanner HD250.....	129
Table A-3:	Wet Plain Water Scanning Sequence by the CT X-Ray Scanner HD250.....	131
Table B-1:	Dry Scanning Sequence of 38 mm Length at One Tip of The Fracture	134
Table B-2:	Wet Tagged Water Scanning Sequence of 38 mm Length at One Tip of The Fraction.....	136

ACKNOWLEDGMENTS

I would like to express my sincerest gratitude to my thesis advisor, Dr. Abraham S. Grader, whose guidance, assistance and encouragement created the background for this work.

Also, I wish to express my appreciation to Dr. Turgay Ertekin, Dr. Phillip Halleck and Dr. Ozgen Karacan for their valuable advice, help and suggestions throughout the development of this work. Thanks are extended to my fellow graduate students Mr. Gaoming Li and Mr. Abdullah Alajmi, for their insightful contributions and invaluable assistance during the course of this research. I also extend my gratitude to my mentor from The Department of Energy, Dr. Duane Smith, for his participation in this project.

The financial support for this research was provided by The Department of Energy of the United States and the University/NETL Student Partnership program of the University of Pittsburgh, by the department of Energy and Geo-Environmental Engineering as well as The Energy Institute of The Pennsylvania State University, and by the Fundación Gran Mariscal de Ayacucho in Venezuela.

Above all, my sincerest and deepest gratitude remain with my parents, Cristina Minakowski and Silvestre Parada, for being my greatest source of inspiration and encouragement. I am especially indebted to my sister, Rosa Cristina, whose patience, understanding and sacrifices made this dream come true. Lastly, special gratitude is extended to my aunt, Ursula Minakowski, for her continuous and endless moral support.

Chapter 1

INTRODUCTION

Fractures in reservoirs have a great impact on fluid flow patterns and on transport mechanisms. Natural and artificially induced fractures are channels through which fluids can flow in the direction of production wells or away from injection wells. Both types of fractures may have positive or negative effects on the efficiency of recovery process. In single-phase hydrocarbon production, the fractures provide access to the matrix and reduce the magnitude of the pressure drop between the well and the reservoir, thus, enhancing productivity. In cases where two-phase displacements are dominant, the presence of a fracture network may cause fluid bypassing, early breakthroughs, reductions of sweep efficiencies, and overall decreases in productivities.

Fractures may also be non-conductive and form barriers to fluid flow. In other cases when the main flow directions are perpendicular to the orientation of the fractures, they can be used to enhance the efficiency of displacement operations. However, efficiency becomes poor if the flow is parallel to the orientation of the fractures. The understanding of displacement processes in the presence of fractures will improve recoveries from oil and gas reservoirs.

There are many papers in the literature documenting single-phase transport in an individual fracture and few papers dealing with multiphase flow. These papers examine the effects of confining stress, temperature, and fluid composition on transport properties.

One of these two-phase flow experiments was presented by Grader et al. (2000). In this paper, the relationship between the distribution of fracture width and the porosity structure of the adjacent rock was observed in two stages. In the first stage, oil was injected into a water saturated Berea sample with an artificial fracture. Injection was stopped before the entire fracture was flooded. Then, the sample was scanned showing oil fingers in the fracture. The oil moved ahead in the fracture where adjacent layers had high porosity. In the second stage, a single position at the end of the fracture was continuously scanned during oil injection. The oil first appeared in this fixed position in the fracture at locations adjacent to high porosity layers.

The present work verifies the relationship between the distribution of the fracture aperture in an artificially induced fracture and the porosity structure in the adjacent layers. A fracture was induced in a layered Berea rock sample from a sandstone quarry in Northern Ohio using a modified Brazilian Test. X-ray computed tomography (CT) was used to determine porosity distribution, non-destructively, using NaI-tagged water as the fluid phase.

Two x-ray imaging systems that provide different spatial resolutions were used in the experiments. A comparison between the different spatial resolutions of the images is done in order to characterize the structure of the rock sample and the induced fracture, and to develop a new technique for acquiring and comparing images obtained by high- and low-resolution scanners.

Chapter 2

OBJECTIVE AND APPROACH

The main objective of this research is to determine whether or not there is a relationship between the distribution of the fracture aperture in an artificially induced fracture and the porosity structure in the adjacent rock.

The second objective is to develop a technique for acquiring and comparing images obtained by high- and low-resolution scanners.

The approach of this research was as follows:

1. Characterize the morphology of the induced fracture in the rock sample and the distribution of layers of diverse rock densities in a porous medium using computed tomography (CT).
2. Compare different spatial resolutions provided by different CT scanners as a method of characterization of porous media.
3. The determination of whether or not there is a relationship between the internal structure of the induced fracture and the surrounding matrix by combination of CT analysis and saturation processes.
4. Generation of porosity profiles through the induced fracture and the matrix by digital manipulation of the acquired CT data.

Chapter 3

EXPERIMENTAL SYSTEM, MATERIALS, AND PROCEDURES

3.1 Experimental System

The experimental system includes two CT units, medical and industrial, and a fluid flow apparatus. The fluid flow system is moved between the two scanners.

Computed Tomography (CT) is a non-destructive imaging technique that uses X-rays and mathematical algorithms to view a cross-sectional slice of an object by the reconstruction of a matrix of X-ray attenuation coefficients. A computer system receives signals from the detector and reconstructs the image. The first X-ray CT imaging technique was developed by Dr. Hounsfield in Great Britain in 1972. It was primarily used for medical purposes.

First generation CT scanners use a single pencil-beam source and a single detector moving together in a translate-rotate mode. Second generation scanners use multiple detectors and a single source in a translate-rotate mode, resulting in improved image quality. Third generation CT scanners use a rotational fan beam geometry with the source and detectors rotating together around the object. Fourth generation scanners use a fan-beam geometry with the source rotating within a fixed ring of detectors to gain higher resolution and to improve image quality.

With the improvements in data collection and resolution, the use of CT scanners has become common in disciplines other than medical radiology. One particular

discipline is petroleum engineering where it is now used to characterize porous media, and to study fluid flow processes and rock mechanics. Particular applications include the characterization of rock samples, determination of porosity and bulk density, and quantification and visualization of fluid displacement processes with special focus on saturation determination, viscous fingering, and gravity segregation.

The use of CT as a core analysis tool was discussed by Bergosh et al. (1985), Honarpour et al. (1985), Honarpour et al. (1986), Hunt et al. (1988), Narayanan and Deans (1988), Gilliland and Coles (1989), Sprunt (1989), Raynaud et al. (1989), Fabre et al (1989), Jasti et al (1990), Kantzas (1990), Moss et al (1992), Peters and Afzl (1993), Johns et al (1993) and Grader et al. (2000). The particular applications include the determination of fractures and heterogeneities, bulk density and porosity measurements, the visualization of mud invasion, lithologic characterization, and the evaluation of damage in unconsolidated cores.

3.1.1 Medical-Based X-Ray CT Scanner, HD250

The HD250 scanner is a high-throughput fourth generation CT system. Manufactured by Picker/Marconi/Phillips, this scanner consists of three major components: gantry, CT control unit, and couch. Figure 3-1 shows a photograph of the medical-based scanner.

An electro luminescent touch panel (ELTP) is used at the CT control unit. This ELTP allows the operator to select scanning protocols by touching areas on the menu screens. The gantry houses the X-ray tube, detector, and data collection. The couch is

easily maneuvered for scanning positioning. Table-top movement can be initiated by release tape switches on the sides of the table top or by a foot switch located between the gantry and the couch pedestal. A medical light is also used for correct positioning of the sample.

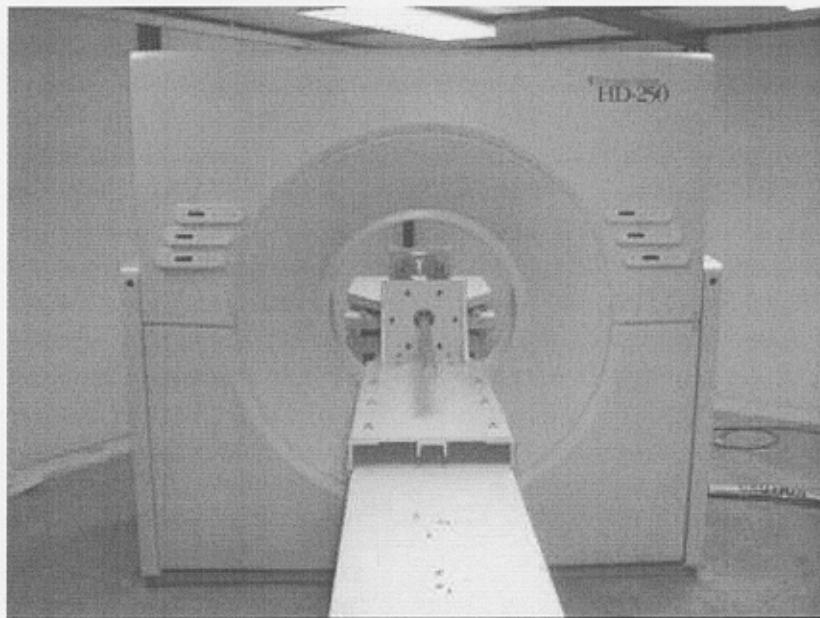


Figure 3-1: X-ray CT scanner HD250.

The HD250 medical unit produces images that have 512 x 512 pixels. The typical resolution that is used is 0.5x0.5x2.0 mm. The in-plane resolution can be enhanced partly by reconstruction of a sub-region. But most of the gain in resolution is mathematical. Thus it is safe to point out that the typical pixel resolution is 0.5x0.5 mm. The scanner can collect images with thickness of 2, 5, and 10 mm. Most operations are done at scan thickness of 2 mm. The scanner can acquire scans over periods of 1, 2, and 4 seconds.

Four-second scans were used to reduce noise effects. The scanner can collect images using up to 130 kV and up to 125 mA. At this high-energy output the tube heats up and after a few scans it requires between 8 and 18 seconds of cooling time. At lower energy settings of 120 kV and 105 mA the scanner can scan continuously at a rate of 3-5 scans a minute.

3.1.2 The Industrial-Based X-Ray CT Scanner, OMNI-X

The OMNI-X is a high-resolution industrial scanner. The system is mounted on a rigid optical grade structure that can be rotated at any angle between the vertical and the horizontal positions (0 to 90 degrees). The axial positioning table can also move between x-ray source and the detector to change the magnification of the object on the image intensifier. The system has two x-ray sources that can be used one at a time. The large focal spot source can generate 320 kV at a maximum current setting of 5 mA. The microfocus x-ray source can generate 220 kV at a maximum current setting of 1 mA. The x-ray sources produce cone-shaped beams that allows the collection of volumetric data. Figure 3–2 shows a photograph of the industrial-based scanner OMNI-X.

The system produces 256x256, 512x512, and 1024x1024 pixels per image and enables a maximum resolution of 5-10 microns with the micro-focus x-ray tube. The system is also capable of collecting data at various numbers of views during scanning, allowing the user to match image quality with research needs.

For the present study, core samples were scanned with 145 KV and 1000-microA using the microfocus x-ray source. The in-plane pixel resolution was 45x45 microns and

the slice thickness was 91 microns per single slice. Three hundred scans were acquired in single scan mode which covered about 3.0 cm volume of the samples. The x-y resolution was 82 microns and the z resolution was 91 microns.

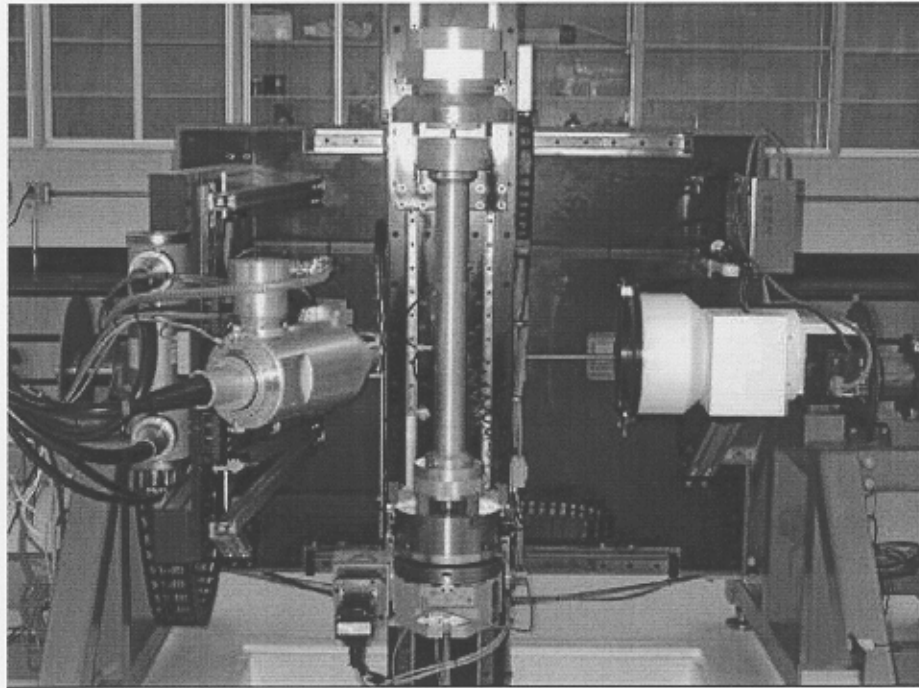


Figure 3-2: High-resolution x-ray CT scanner, OMNI-X.

3.1.3 The Core Holder

The core holder used in these experiments is an aluminum tube threaded at both ends. It has a 2 ½ inch inner diameter with ¼ inch wall thickness. Two stainless steel plugs fit at each end. The inlet plug has seven connections: three inlets, three outlets, and

one differential pressure port. The outlet plug has two connections: one outlet, and one differential pressure port. The core is placed in a rubber jacket that transmits the radial confining pressure. Both end plugs are provided with sealing o-rings to prevent the loss of fluids from the core. These end plugs are held in place by two aluminum end-caps that are threaded at the interior. Figure 3-3 shows a picture of the different pieces of the core holder. Figure 3-4 shows a schematic drawing of the core holder.

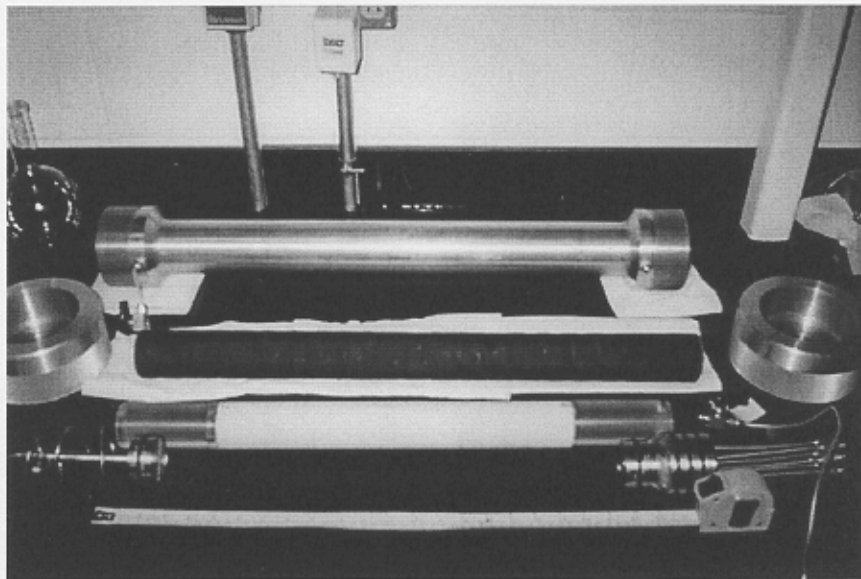


Figure 3-3: Core holder.

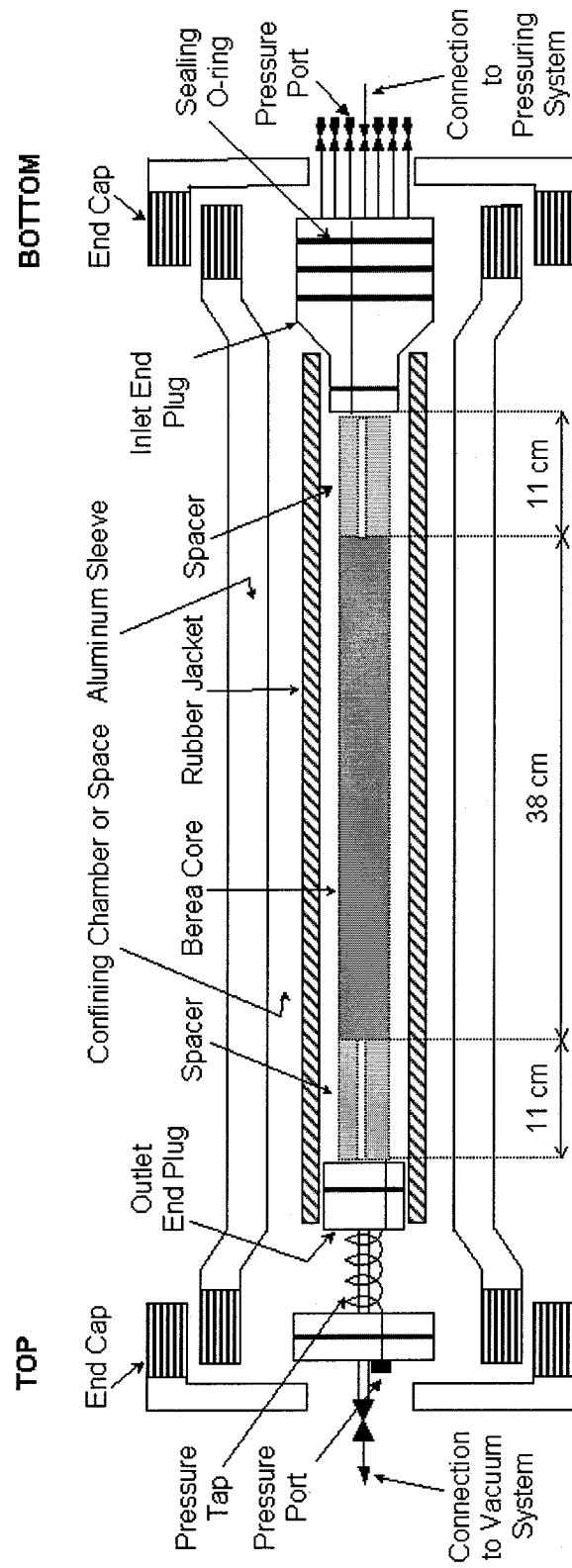


Figure 3-4: A schematic drawing of the core holder.

3.1.4 Fluid Saturation System

A schematic of the saturation system used in the experiments is shown in Figure 3-5. It consists of a vacuum system (3) connected to the inner section of the core holder, where the core sample is placed (1), a pressure system (4) connected to the confining space of the core holder, and a burette filled with tagged water (2) that provides and measures the amount of water required to entirely saturate the core. The burette is connected to the core at the inlet end plug of the core.

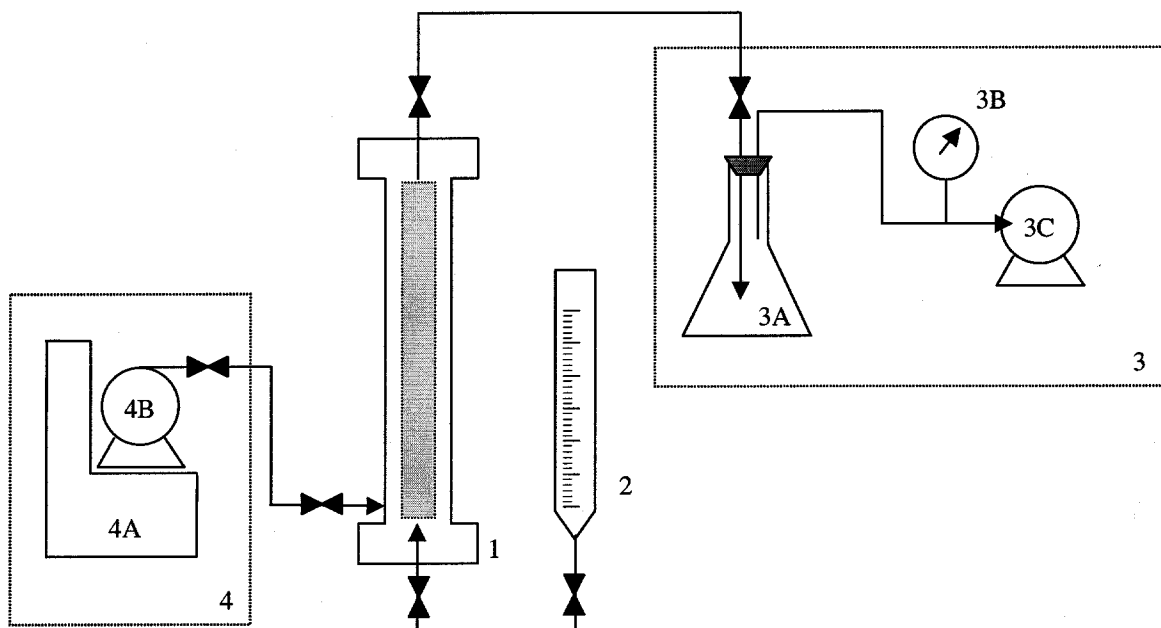


Figure 3-5: Schematic of the saturation system.

The vacuum system was connected to the outlet end plug of the core holder. This system was used to evacuate the air from the core prior to initial water saturation. The

system consists of a 2000 ml vacuum trap (3A), a vacuum gauge (3B), and a vacuum pump (3C). The vacuum pump is a Leybold Trivac “A” dual stage rotary vane pump model D4B. The gauge used is a Leybold gauge model TM 20. A vacuum level of approximately 200 microns of mercury was reached prior to introduction of water.

The pressure system was used to maintain confining pressure and seal the rubberized jacket which held the core. The pressure system consisted of a positive displacement pump, Syringe LC-5000 (4B), mounted on a tank of 500 ml of capacity (4A). The pump can operate by setting either constant flow rate or constant flow pressure. The maximum operation conditions are 400 ml/hr flow rate or 1000 Psig.

3.2 Materials

This section describes the rock and fluids used in the experiments.

3.2.1 Rock Sample

A layered Berea sandstone sample that originated from a sandstone quarry in Northern Ohio was used in the experiments. The core had a length of 380 mm and a diameter of 50.8 mm. Berea is a calcite-cemented natural sand stone with about 5% clay content, and typical porosities of 18-22%. The sample was cored parallel to the bedding planes. The induced fracture was perpendicular to the bedding.

3.2.2 Fluids

Distilled water was used in the experiments. The water was tagged with 8% by weight sodium iodide, thus increasing its x-ray attenuation. Plain water was used to clean the core. This allowed us to monitor and to analyze the displacement process since plain water has a lower CT signature than the tagged water.

3.3 Procedures

3.3.1 Creating The Induced Fracture

Differences between the principal stresses are required in order to generate a fracture. If fluid pressure were applied locally within rocks under this condition, and the pressure increased until rupture or parting of the rock results, the plane along which fracture parting is first possible to break is the one perpendicular to the least principal stress. That plane is also the one along which parting is most likely to occur as shown in Figure 3–6.

The core sample was fractured by a Brazilian-like test. In order to obtain a longitudinal planer fracture, the cylindrical sample was compressed between two parallel plates with a diameter of 150 mm, thereby inducing a tensile state of stress in the center of the cylinder. Figure 3–7 shows the rock sample on the lower plate of the mechanical press just before it was fractured.

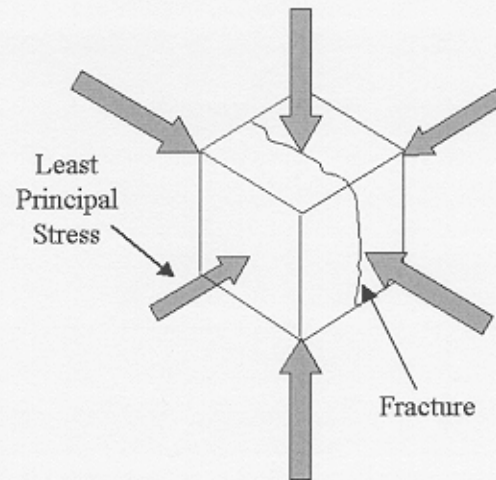


Figure 3-6: Stress element and preferred plane of fracture.

As the compression of the core is increased, a vertical fracture formed in the longitudinal direction of the core. The fracture length was about 180 mm. The fracture was internal and did not reach either end of the core. Figure 3-8 shows the load on the sample as a function of time. The core fractured when the load was 10,750 lbs.

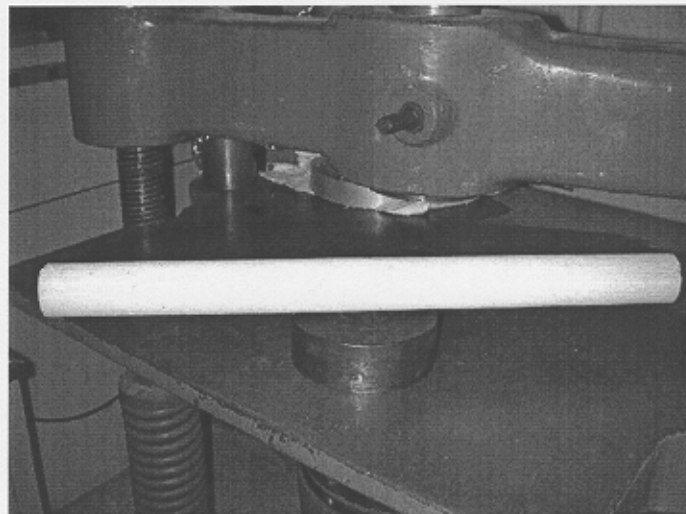


Figure 3-7: Sandstone sample prior to fracturing using a modified Brazilian test.

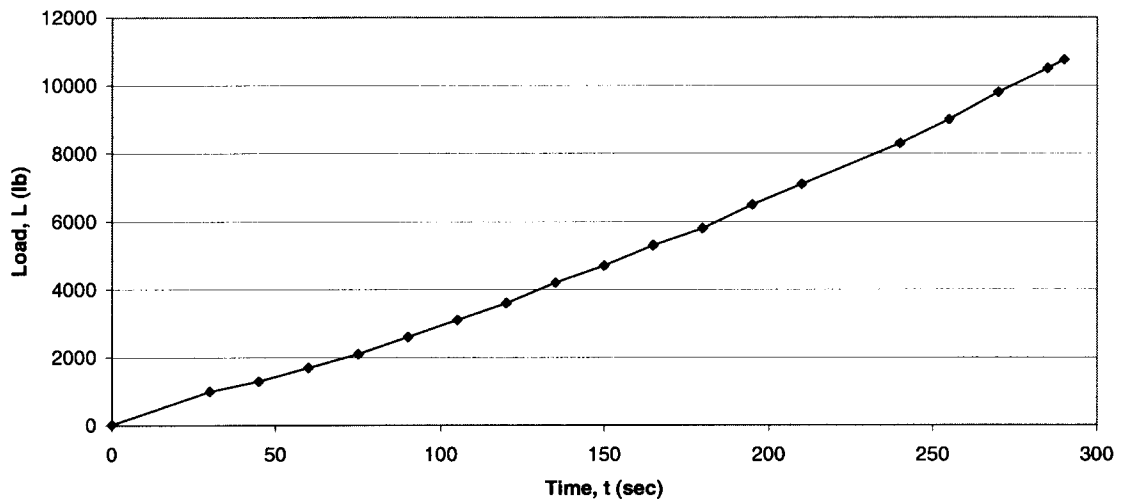


Figure 3–8: Load versus time during the fracturing process of the sample.

This process is a modification of the Brazilian test. In classical rock mechanics, this test is used with a thin disc loaded by uniform pressure applied radially over a short strip of the circumference at opposing sides. The underlying hypothesis of the Brazilian test is that the fracture starts from the center of the disc assuming that the material is homogeneous, isotropic and linearly elastic. The core sample was initially 60 cm (2 feet) long. After inducing the fracture, the core length was reduced to 38 cm by cutting 11 cm at each end.

3.3.2 Rock Preparation

The core was dried at 60° C for 24 hours. The core was cooled down and placed into the rubber jacket. Since the core was shorter than the jacket, two plastic spacers were placed at each end of the core to fill up the empty spaces and center the core inside the

jacket (Figure 3–4). The spacers were perforated in the middle to allow fluid to flow. The inlet end plug was placed at the bottom and the outlet end plug at the top of the rubber jacket. This jacket was fastened to the end plugs with steel wire in order to seal the core from the confining space, allowing the vacuum stage and the confining pressure conditions in the outer annulus of the core holder.

The assembled rubber jacket containing the core was placed into the core holder aluminum sleeve and the inlet end cap was screwed into place. Then, the pressure tap was connected to the outlet end plug and the retaining ring was placed over the traveling shaft of the outlet plug. The confining space was filled with plain water and the retaining ring was pushed into position. The outlet end cap was finally installed at the top of the aluminum sleeve.

The vacuum system was connected to the outlet end plug and the aluminum sleeve was connected to a pressure system. These two systems remained connected to the core holder for 19 hours before starting the experiment in order to reach 100 psig of confining pressure and to ensure all possible moisture in the core was evaporated.

3.3.3 Scanning Procedures to Compare the Scanners

After cutting, the core was scanned by both scanners without the core holder in order to characterize the fracture, study the structure and compare the resolution obtained by the two scanners. Two series of scans were taken:

- A dry scanning sequence of the entire core without core holder by the X-ray CT scanner HD250, to characterize the core. A total of 192 scans were acquired with 2 mm spacing. Scan thickness was 2 mm and the energy level was 130 kV and 125 mA.
- A dry scanning sequence of a section of the core (38 mm) without core holder by the high resolution X-ray CT scanner OMNI-X, in order to compare the resolution between the two scanners. 400 scans were acquired using 95 μ m spacing. Scan thickness was 95 μ m and the energy level was 145 kV and 1 mA.

3.3.4 Scanning Procedures to Determine Porosity Distribution

Porosity is defined as the fraction of the bulk volume of a material or formation that is not occupied by solids. Porosity provides a measure of the storage capacity of a reservoir and is defined as:

$$\phi = \frac{V_{voids}}{V_{bulk_volume}} \quad (3.1)$$

where V represents volume.

The porosity of a core sample was determined experimentally by saturating the sample with a fluid and measuring the volume of this fluid. Then, the porosity, ϕ , of a cylindrical core is:

$$\phi = \frac{V_{Injected_Fluid}}{V_{Core}} = \frac{V_{Injected_Fluid}}{\pi * r^2 * l} \quad (3.2)$$

where $V_{Injected_Fluid}$ is the volume necessary to saturate the core in cubic cm, and r and l are the radius and the length of the core in cm, respectively.

After assembling the core in the core holder, different sequences of CT scans were taken in order to determine porosity distribution. The vacuum and confining pressure system were disconnected when the core was scanned with the high-resolution scanner OMNI-X to allow the core holder to rotate. Two sets of scans were obtained before saturating the core:

- A dry scanning sequence of the entire core by the X-ray CT scanner HD250, providing the fracture topology. A total of 191 scans were acquired using 2mm spacing. Scan thickness was 2 mm and the energy level was 130 kV and 125 mA.
- A dry scanning sequence of a section of the core (3 mm) by the high resolution X-ray CT scanner OMNI-X. A number of 330 scans were acquired using 91 μ m spacing. Scan thickness was 91 μ m and the energy level was 145 kV and 1 mA.

The core was then saturated with tagged water with sodium iodine under vacuum and confining pressure, without moving the core from the OMNI-X. The saturation system was connected at the inlet end plug and the vacuum system to the outlet end plug. When the tagged water reached the top of the core holder, the vacuum system was shut down and disconnected. The saturation system remained connected for 12 hrs to ensure

100% of saturation. Confining pressure was maintained during this period of time. Then, two sets of scans were taken:

- A wet scanning sequence of the same section of the core by the high-resolution X-ray CT scanner OMNI-X. A total of 330 scans were acquired using 91 μ m spacing. Scan thickness was 91 μ m and the energy level was 145 kV and 1 mA.
- A tagged water saturation scanning sequence of the entire core by the X-ray CT scanner HD250, to establish a base line for porosity computations. A number of 191 scans were acquired using 2mm spacing. Scan thickness was 2 mm and the energy level was 130 kV and 125 mA.

Plain water was then flooded into the core to remove the tagged water and clean the core. The core was scanned by the medical scanner during the flooding process at three different positions along the core: at both extremes and the middle of the fracture. This set of scans was collected in order to observe fluid distribution at various levels of pore volumes of plain water injected. A total of 175 scans of 2mm thickness were obtained. The energy level was 130 kV and 125 mA.

Chapter 4

THE ACQUIRED DATA

4.1 CT Data of the Dry and Fractured Berea Core Sample

The Berea core was entirely scanned after fracturing in order to characterize the topology of the induced fracture. For this experiment, the core was not placed in the aluminum core holder. The sample was scanned with the two different CT scanners.

4.1.1 CT Data from the HD250 Medical Scanner

The entire core was scanned with 2 mm thick scans at 2 mm spacing (100% coverage). One sequence of 192 scans was taken through the 38 cm core length, with a tube energy of 130kV and a current of 125 mA, using water calibration. Figure 4–1 shows a typical CT image of the dry Berea core without the aluminum core holder. Since the images taken by this scanner are bigger than the actual core diameter, Figure 4–1 also displays the plastic tube used to hold the core while scanning. The plastic tube is divided into two parts. The dark lines that appear as extensions of the fracture are the edges of the two parts of the plastic tube. The artificial fracture is clearly visible as the horizontal black feature in the center. However, it is not possible to distinguish the layers of different density due to the CT number scale. A wide range was set to show the rock sample and the plastic holder.

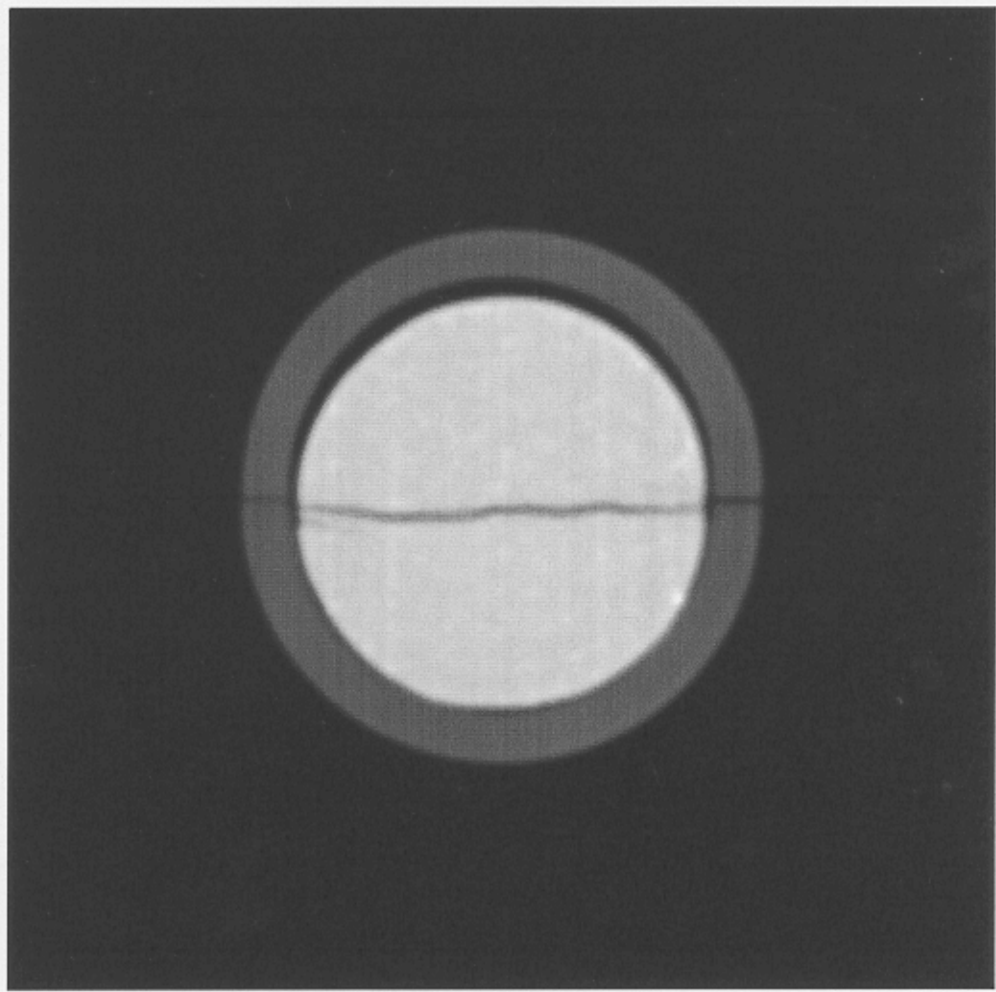


Figure 4-1: CT image of the dry Berea core without the core holder. Scanner: HD250.

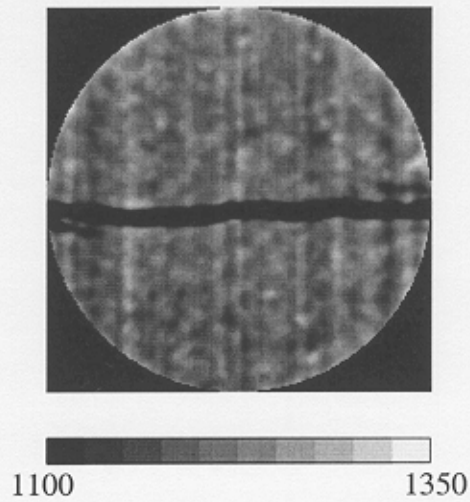


Figure 4-2: CT image of the dry Berea core without core holder at different CT number range. Scanner: HD250.

By setting a small CT number range so that only the fracture and the rock sample are displayed, the layers of the core become more visible as shown in Figure 4-2. Then, the image clearly shows layers of low density (dark regions) and high density (bright regions). Figure 4-3 displays a plate of the images showing the fractured region.

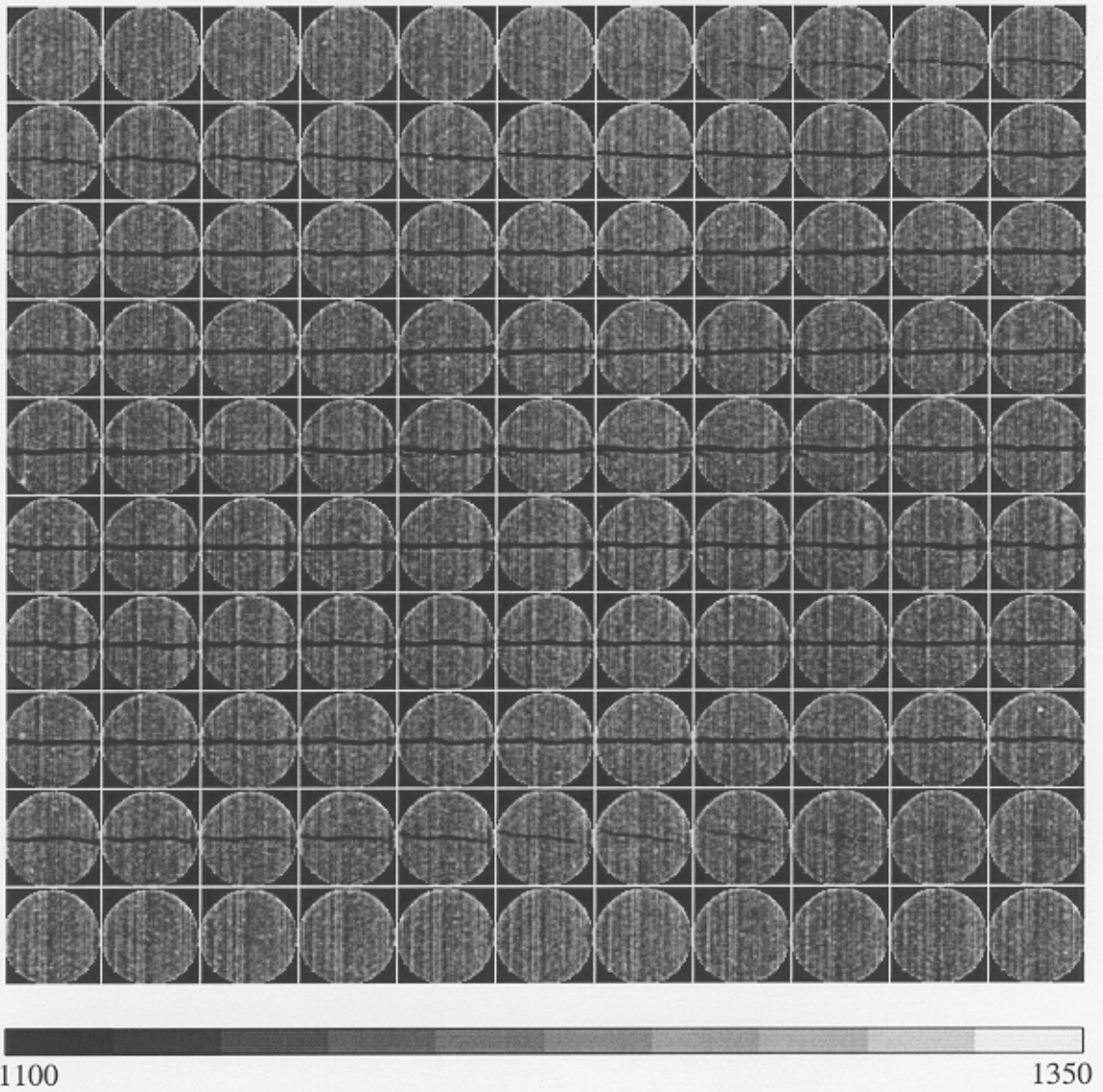


Figure 4-3: Plate of CT images of the dry fractured Berea core. Scanner: HD250.

4.1.2 CT Data from the OMNI-X Industrial Scanner

A small section at one tip of the fractured region of the core was scanned by the high-resolution CT X-ray scanner OMNI-X. Four hundred images were acquired in single-scan mode through 3.8 cm length every 95 μ m, with a tube voltage and current of 145 kV and 1 mA, respectively. The images were reconstructed at three different matrix sizes: 256x256, 512x512, and 1024x1024 pixels per image.

Figure 4-4 shows a typical CT image of the dry Berea core reconstructed at 256x256 pixels, Figure 4-5 shows the same image reconstructed at 512x512 pixels and Figure 4-6 also shows the same image reconstructed at 1024x1024. The images shown in Figure 4-4, Figure 4-5, and Figure 4-6 are pixilated. Thus, in Figure 4-4 the actual square pixels are observed. However, in the other two images, as they are shown in the figures, the pixels are small and cannot be detected.

The plastic core holder is not displayed in this sequence of scans since this equipment was calibrated to obtain images with the diameter of the rock sample. The CT number scale used to display these images allow the observation of the fracture, which is the dark horizontal feature in the center of the image, and spots of different shades, which are incrustations of diverse densities. The CT numbers in the industrial system are not Hounsfield units. They are integers scaled between 0 and 4095 (12 bits) and are arbitrary.

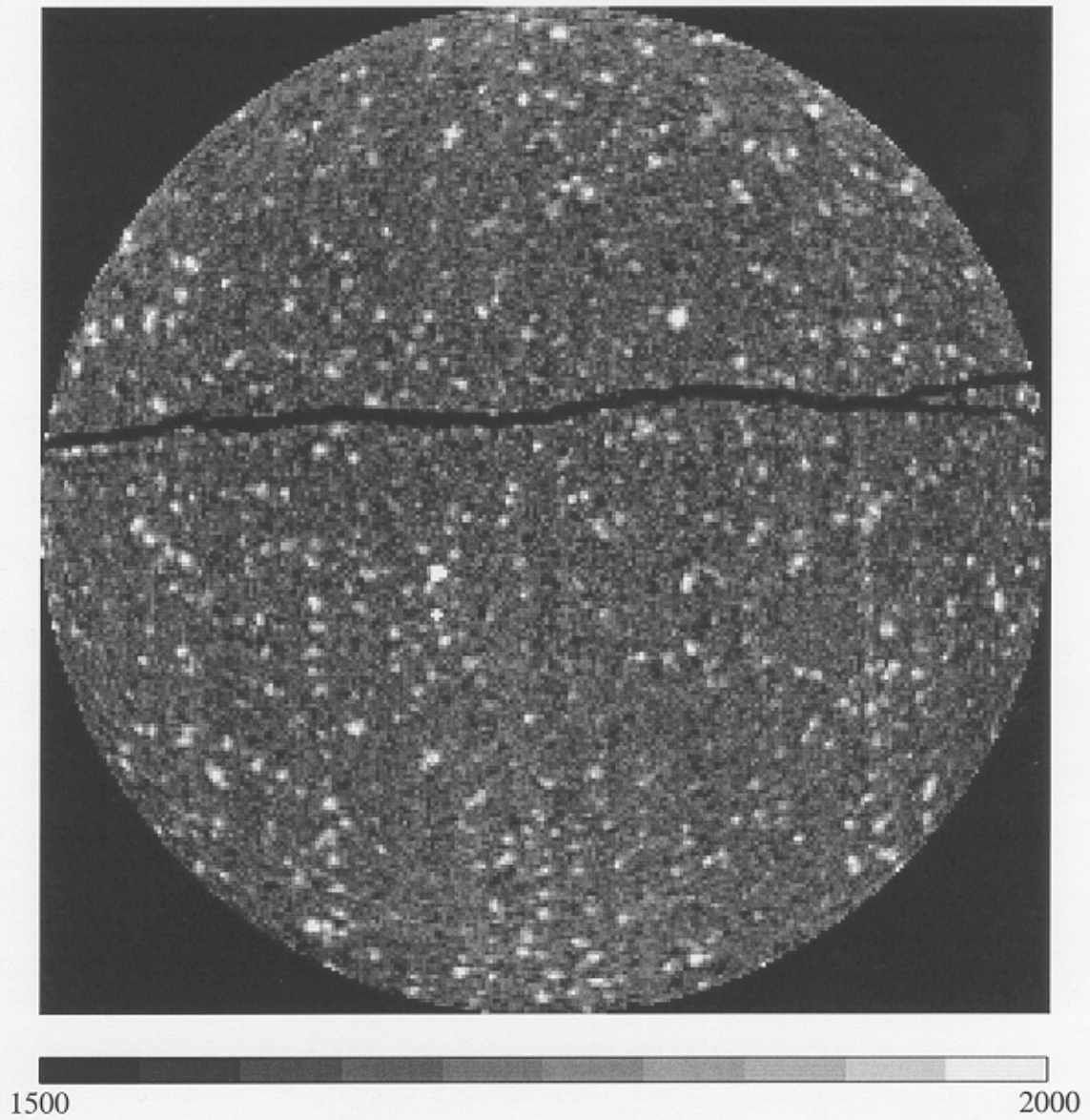


Figure 4-4: CT image of the dry Berea core. Scanner: OMNI-X. Resolution: 256x256 pixels.

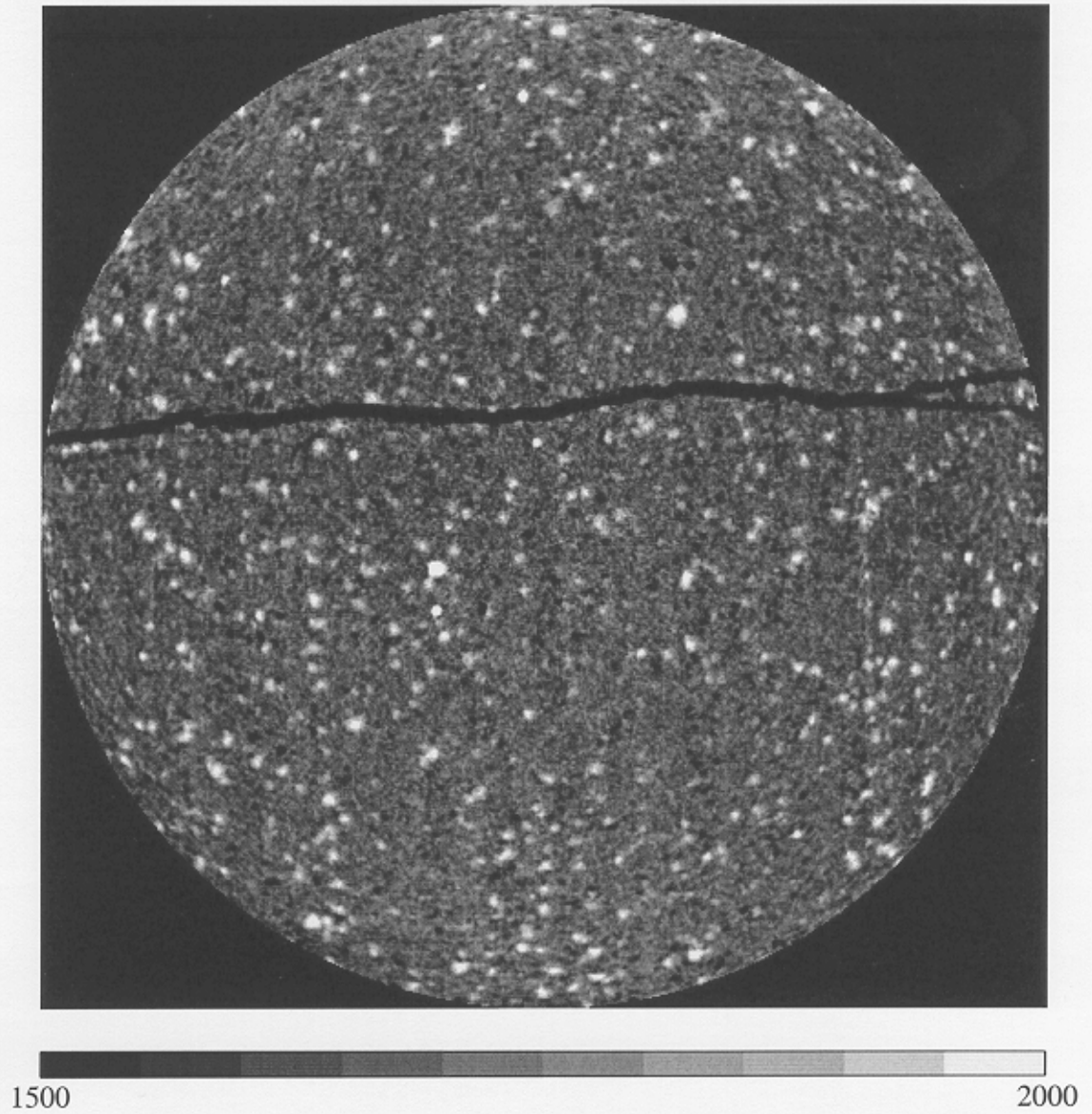


Figure 4-5: CT image of the dry Berea core. Scanner: OMNI-X. Resolution: 512x512 pixels.

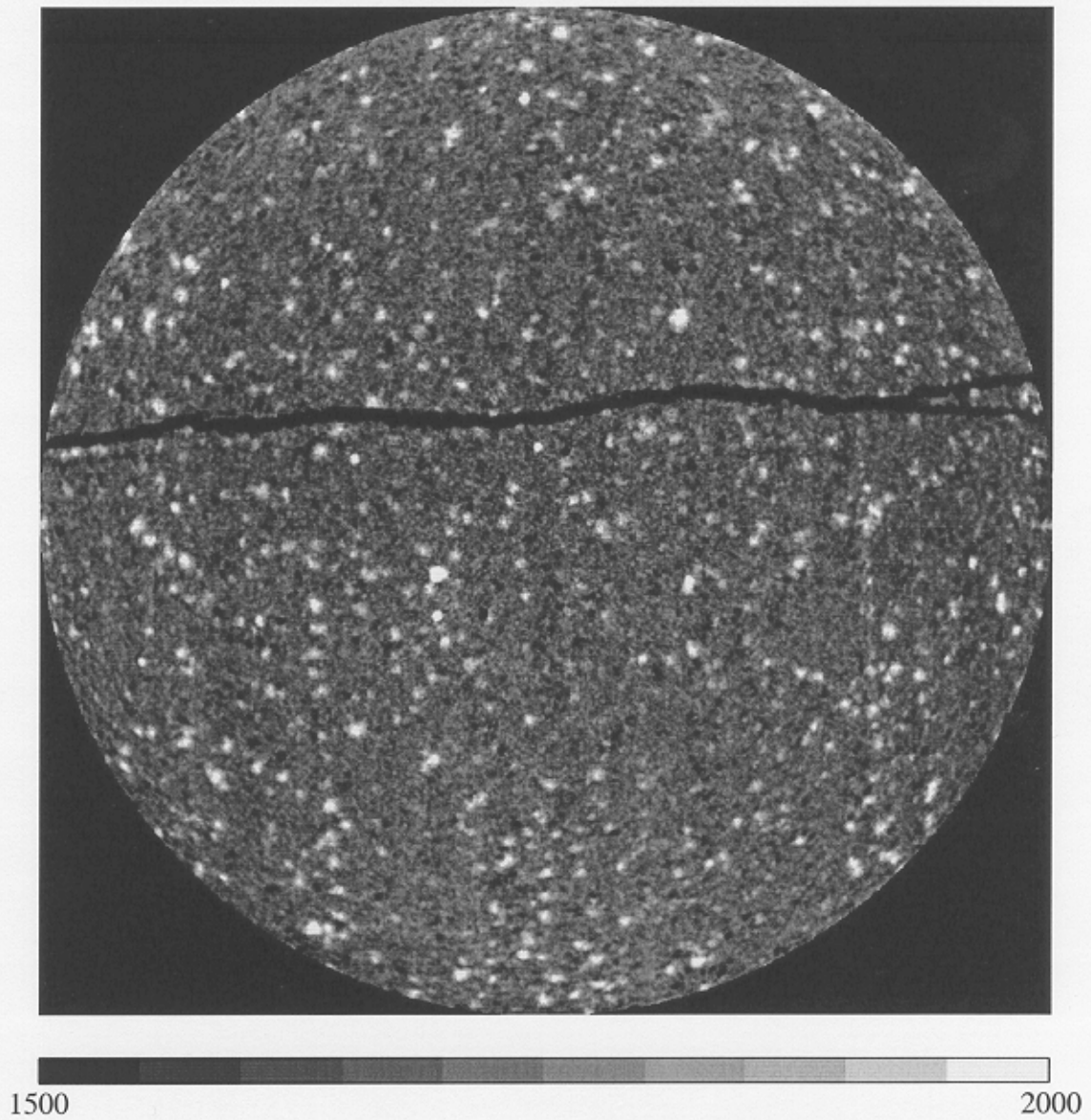


Figure 4-6: CT image of the dry Berea core. Scanner: OMNI-X. Resolution: 1024x1024 pixels.

4.2 CT Data of the Dry and Saturated Sample for Porosity Determination.

In order to determine the porosity distribution in the induced fracture and its relationship with the porosity structure of adjacent layers, the core sample was scanned dry and wet with tagged water after assembling it into the aluminum core holder. The core was put under vacuum and 100 Psig of confining pressure for 19 hours before obtaining the scanning sequences. The scanning stages were:

- The core in the core holder was placed in the medical CT scanner HD250. A pilot, a single direction view or radiograph, of the entire core was acquired to determine the first and last image to be scanned. The position of the first scan was marked on the aluminum sleeve with the help of the medical light. Then, the entire core was scanned.
- The core in the core holder was placed in the high-resolution Scanner, the OMNI-X. A small portion of the fractured region of the core was scanned.
- The saturation process was carried on with the core placed in the OMNI-X in order to obtain a wet sequence of scans in the same position as the dry one.
- After saturating with tagged water, the same portion that was scanned dry was again scanned in the OMNI-X.
- The core holder was then removed from the OMNI-X and placed back in the HD250 medical scanner in the same position as the sequence of dry scans. One sequence of wet scans along the entire core was acquired.
- The core was cleaned by injection of plain water. During this process the core was scanned at three different positions: at the both tips of the fracture and at the

center of the fracture. The scans were taken at various values of pore volumes (PV) of plain water injected.

- The core was entirely scanned after injecting 8.8 PV of distilled water.

4.2.1 Dry and Wet CT Data from the HD250 Medical Scanner

The core was completely scanned dry and wet in order to establish a base line for porosity calculations. Images were scanned every 2 mm with a tube energy of 130kV and current of 125 mA, acquiring a total of 191 scans. The scanner was calibrated using Teflon.

Figure 4–7 shows a typical image of the dry Berea sandstone placed in the core holder acquired by the HD250. The bright ring bordering the rock is the aluminum core holder. Between the sample and the core holder there is the rubber jacket, but this cannot be clearly identified due to the low-attenuation of its material and the selected viewing range. The induced fracture is observed as the horizontal long and dark feature in the center. A wide CT number range was set to display this image allowing the observation of the aluminum core holder, the rubber jacket and the rock sample. However, the heterogeneities of the rock sample are not observed at this display range.

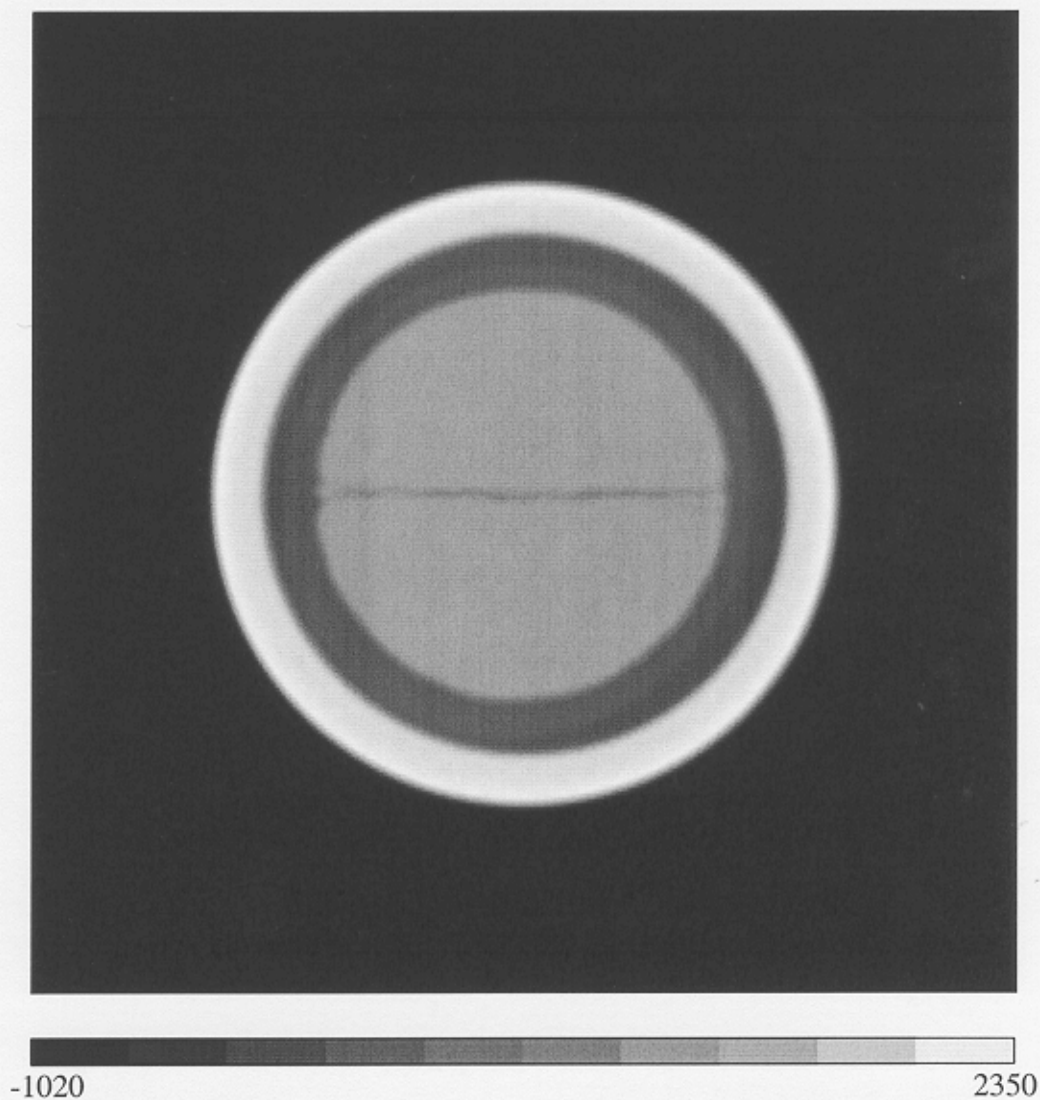


Figure 4-7: Original image of the dry fractured Berea scanned in the aluminum core holder by the HD250 scanner.

Figure 4-8 shows the same image as in Figure 4-7 with the CT number scale set to display the fracture and the layers of the core. The dark color indicates zones of low density (high porosity) while the bright regions represent zones of high density (low porosity). The image was processed by cutting all the data external to the core, reducing

the size of the image matrix to the dimension of the core, and finally, setting a low arbitrary value to the external portion of the image beyond the radius of the core.

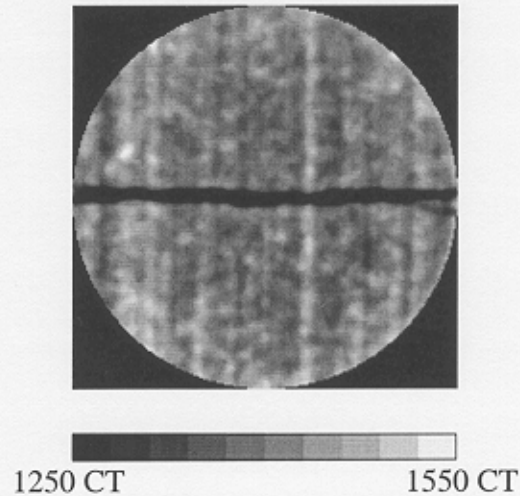


Figure 4–8: Cut image of the dry fractured Berea scanned in the aluminum core holder by the HD250. CT number range: 1250 – 1550.

Figure 4–9 shows a typical image of the wet core (tagged water) placed in the core holder taken by the HD250 medical scanner. The high attenuation of the NaI water, in addition to the wide range of CT number used to display this image, does not allow the clear identification of either the fracture or the layers.

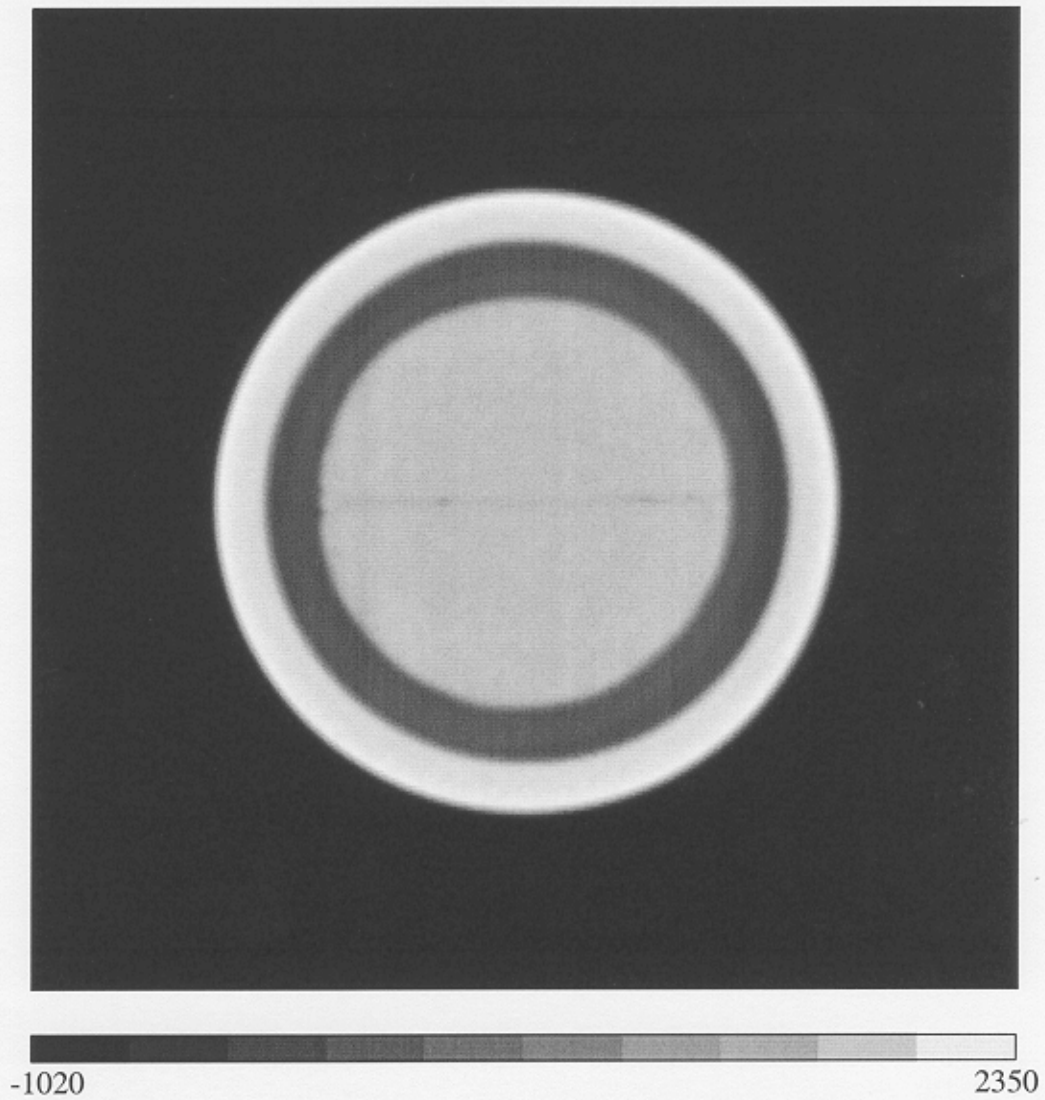


Figure 4-9: Image of the fractured Berea saturated with tagged water, scanned in the aluminum core holder, by the HD250 scanner.

By resetting the CT number scale the fracture and layers become more visible, as it is shown in Figure 4-10.

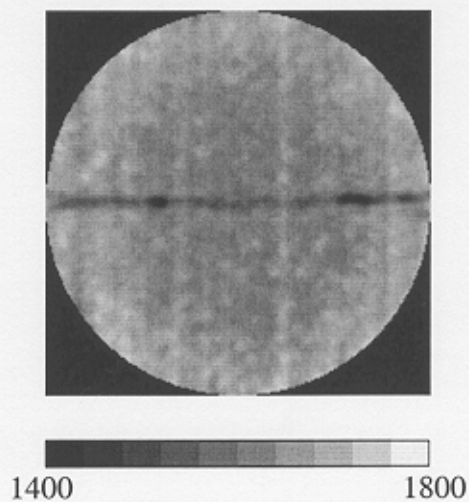


Figure 4–10: Image of the saturated fractured Berea core with tagged water scanned in the aluminum core holder by the HD250 medical scanner.

After saturating the core with tagged water, the core was cleaned by injecting plain water. During this procedure the sample was scanned to visualize the fluid displacement process. The scanning process was done at three different locations in the core as indicated in Figure 4–11.

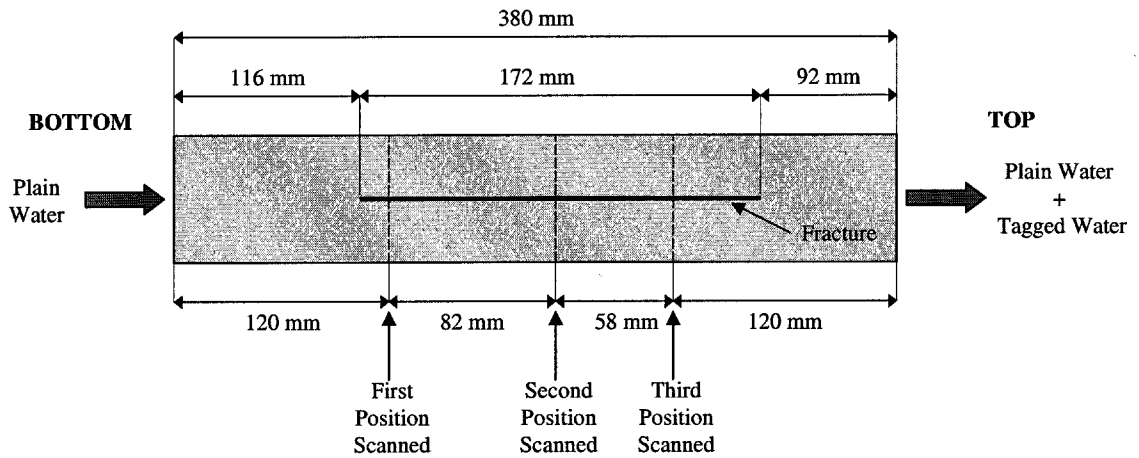


Figure 4–11: Schematic of the positions scanned by the HD250 during the fluid displacement.

Figure 4–12 shows a plate of images at different PVI during the flooding experiment at the bottom tip of the fracture (first position) scanned by the HD250 scanner. The low CT number spectrum corresponds to the plain water (blue colors), which is displacing the tagged water, represented by the high CT number spectrum (red colors). Figure 4–13 displays a plate of images at the middle of the fracture (second scanned position) and Figure 4–14 displays a plate of images at the top tip of the fracture (third scanned position).

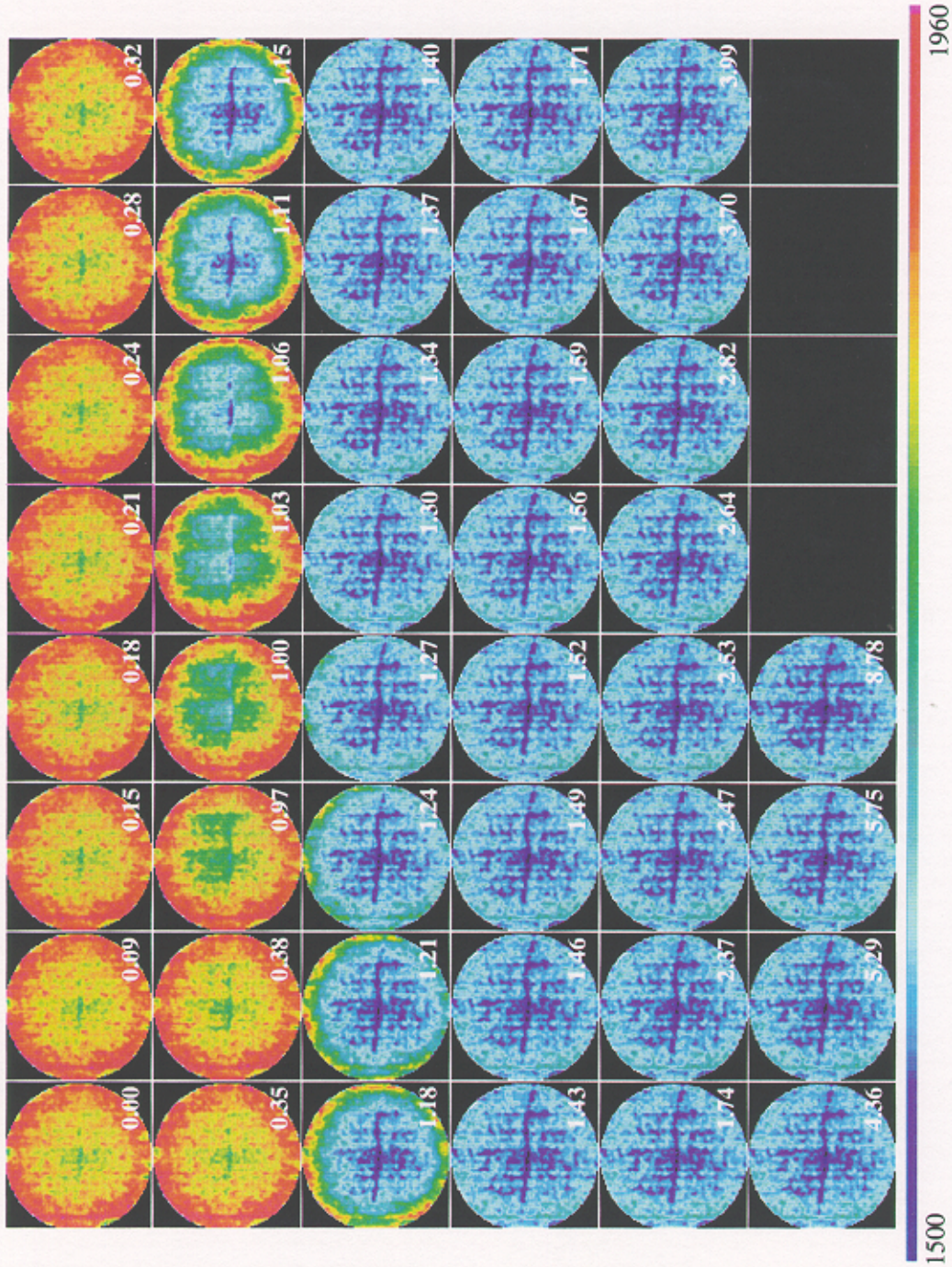
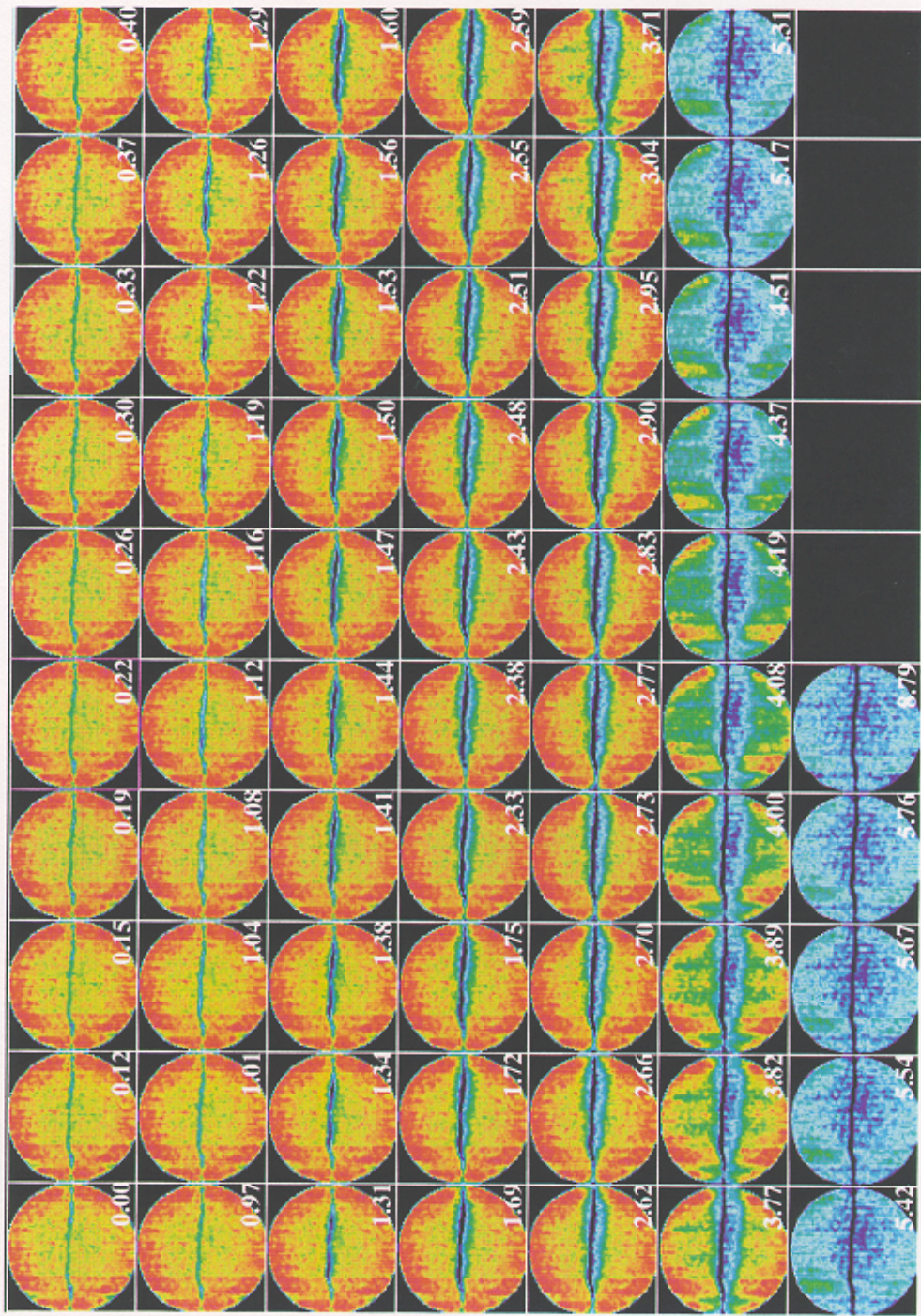


Figure 4-12: Plate of images during the tagged water displacement and the corresponding PVI at the first position (bottom-tip of the fracture) scanned by the HD250 scanner



1500 1960

Figure 4-13: Plate of images during the tagged water displacement and the corresponding PVI at the second position (middle of the core) scanned by the HD250 scanner.

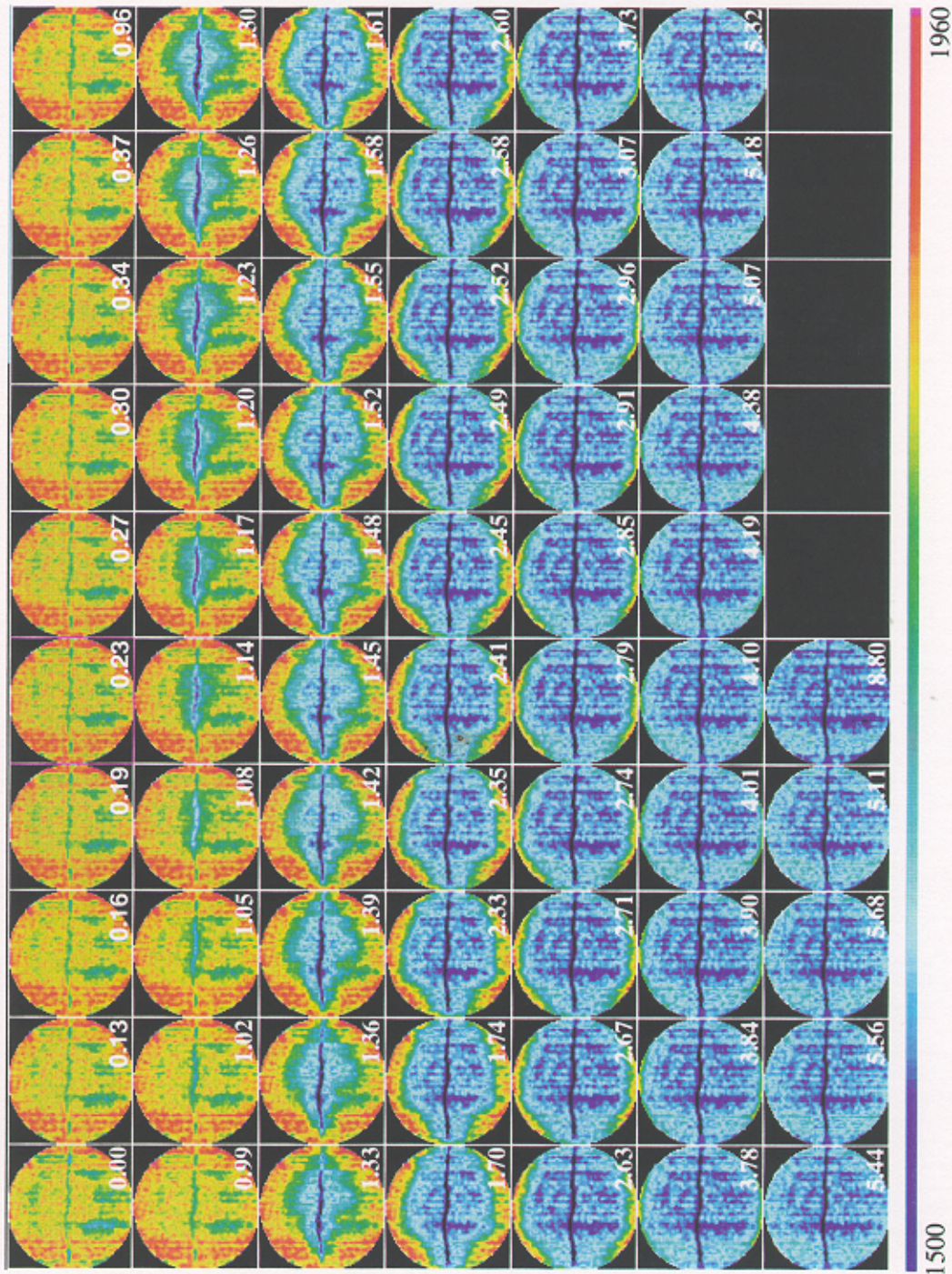


Figure 4-14: Plate of images during the tagged water displacement and the corresponding PVI at the third position (top-tip of the fracture) scanned by the HD250 scanner.

4.2.2 Dry and Wet CT Data from the OMNI-X Industrial Scanner

The core was scanned dry and wet every 91 μm with 91 μm spacing along a small section of 30 mm at the middle of the fracture, with a tube energy and current of 145 and kV 1 mA, respectively. Figure 4–15 shows an image of the dry core scanned by the OMNI-X, reconstructed at 512x512. All images scanned during this experiment were reconstructed at 512x512 pixels. The fracture is denoted by the dark linear feature in the middle of the sample. The dark spots represent zones of low density, or high porosity, and the bright spots correspond to zones of high density, or low porosity.

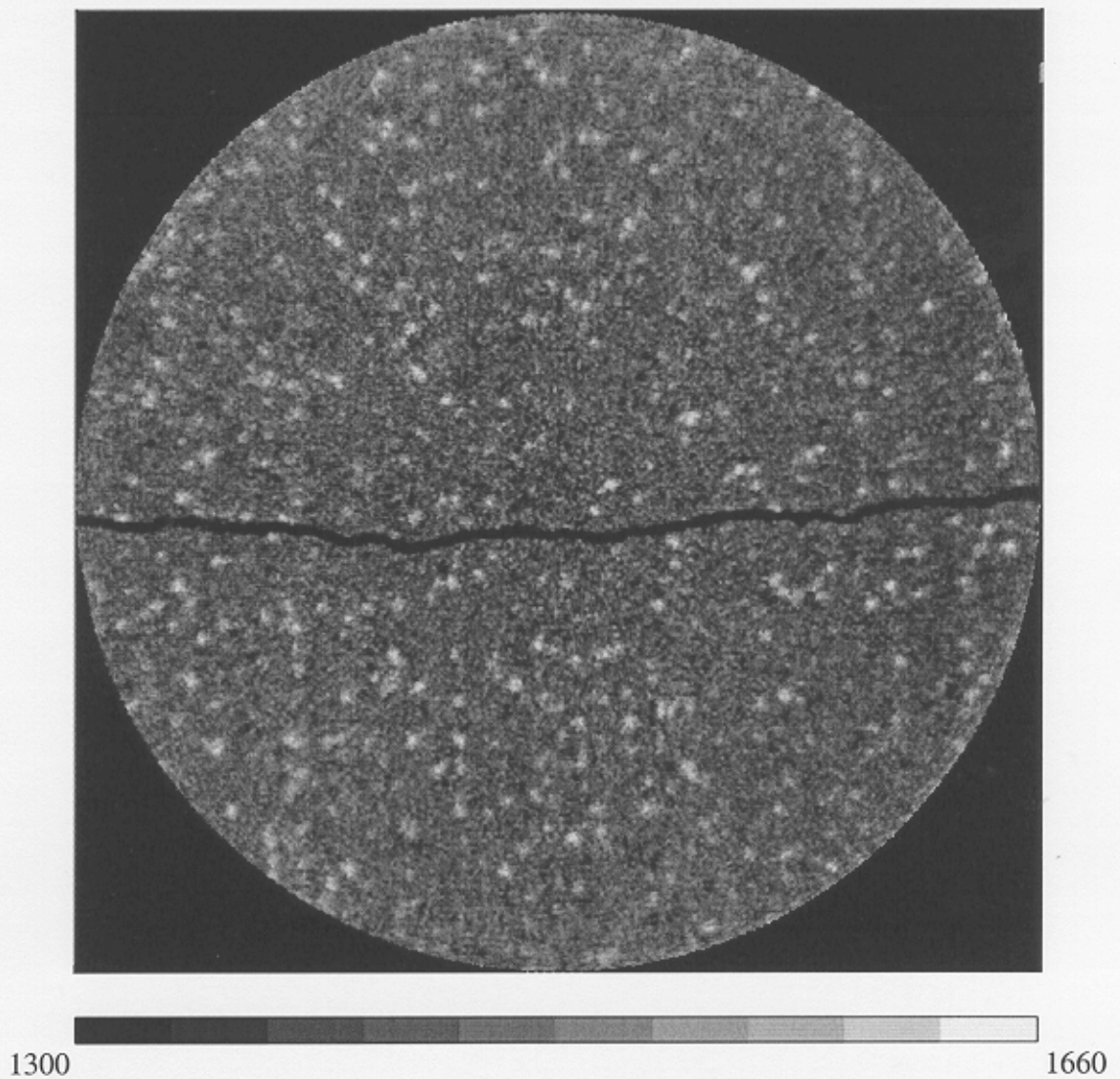


Figure 4–15: Image of the dry Berea core reconstructed at 512x512 scanned by the OMNI-X scanner.

After saturating the core with tagged water, the same portion of the core that was scanned dry was rescanned. Figure 4–16 displays an image of the wet core reconstructed as a matrix of 512x512 pixels. Again, all images obtained in this rotation were reconstructed at 512x512 pixels. This time, the fracture is barely observed due to the high

attenuation of the tagged water. However, the high attenuation of the tagged water enhances the detectability of the fracture by image subtraction.

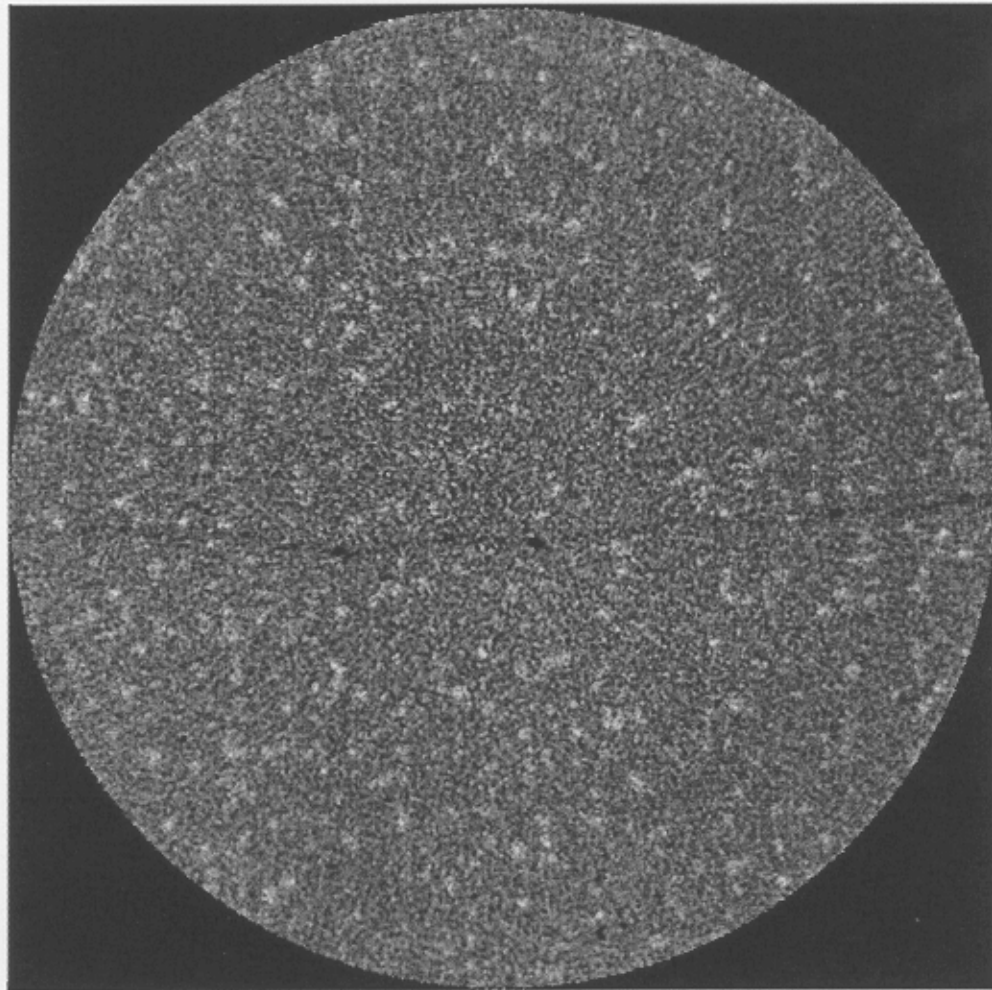


Figure 4-16: Image of the saturated Berea core (tagged water) reconstructed at 512x512 scanned by the OMNI-X scanner.

4.3 Average Porosity Through Material Balance

The average porosity of the rock sample was calculated by material balance. The amount of tagged water necessary to saturate 100% the core sample was measured experimentally. The total volume of water that was used to flood the sample was 141.4 ml. By subtracting the dead volume of the system, 16.94 ml, the void volume of the rock sample was 142.46 ml, leading to an average porosity of 15.8%.

Chapter 5

DISCUSSION OF RESULTS

Several sequences of CT scans were obtained in order to characterize the morphology of the core after inducing an artificial fracture, and to determine if there is a relationship between the porosity distribution in the fracture and the porosity structure in the adjacent layers in the matrix.

The scans acquired by the high resolution CT scanner, the OMNI-X, were analyzed in three different reconstruction settings: 256x256, 512x512, and 1024x1024 pixels per image. The high-resolution scanner was adjusted so that the rock sample data occupy the entire image and there was no need for cutting the exterior region of each image.

The images scanned by the medical CT scanner, the HD250, have an original matrix size of 512x512 pixels. However, the core diameter is represented by a circle with a radius of 100 pixels internal to this matrix. Therefore, the images were reduced to 200x200 pixels to include only the rock sample. The first step of the cutting process was to determine the center of the circle that represents the sample. Then, all the CT number values outside a radius of 100 pixels from this center point were assigned an arbitrary value of -1000, cutting out the core holder and the rubber jacket, as well as the points very close to the interface between the sample and the rubber that may be affected by beam hardening or material discontinuities. Each image was then saved as a 200x200

matrix which reduces computer storage and facilitates the manipulation of the data. The vertical cross section shown in Figure 5-1 is a single image that was reduced in size to include only the core.

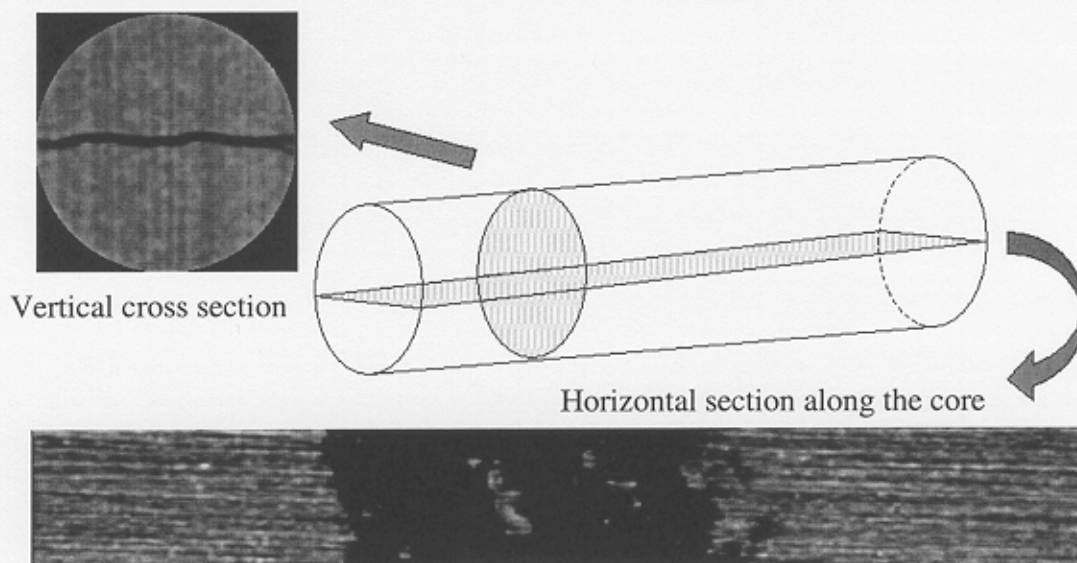


Figure 5-1: Vertical cross-section and horizontal section along the core.

The stack of two-dimensional scans forms a three-dimensional representation of the rock sample. The three-dimensional volume can be dissected at any angle to produce cross-sectional views of the internal structure of the rock. A longitudinal horizontal view through the center of the sample is shown in Figure 5-1, showing the layers. The dark region in the center is the fracture intersected by the horizontal cross-sectional plane.

To perform data analyses of the images taken by both scanners, several computer programs were developed in PV-WAVE, preserving the spatial resolution provided by

the scanners. Furthermore, the software package VolxelCalc made by Kehlco was used in processing some of the CT data.

5.1 Characterization of the Fractured Berea Core Sample with X-Ray Computed Tomography (CT).

The Berea core was scanned dry by both scanners after fracturing in order to characterize the fracture and compare the results of the two scanners. One sequence of 192 images with a slice thickness of 2 mm and spacing of 2 mm was acquired by the HD250, sweeping the entire length of the core (380 mm).

Figure 5–2 shows a plate of 19 images taken by the HD250. These images sweep a length of 38 mm close to one tip of the fracture. The dark spectrum represents low density regions while the high density regions are represented by the bright spectrum. Here, the fracture appears as the horizontal dark feature at the centers of the images. The width of this dark feature in the center of the sample does not represent the actual fracture width. The fracture width detectable by Computed Tomography depends on the resolution of the scanner and the contrast between the matrix and the fracture fill. These images clearly show layers of high (bright) and low (dark) density.

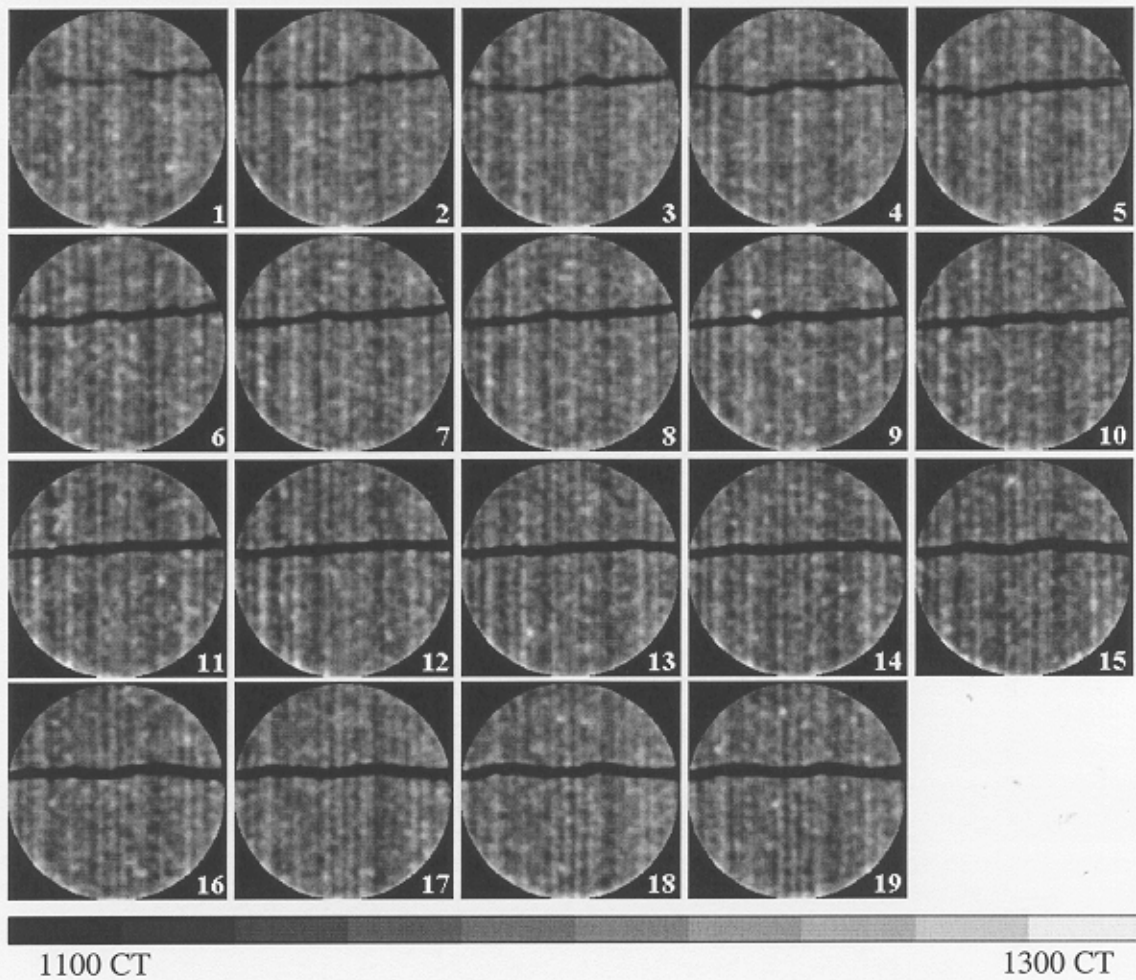


Figure 5-2: Plate of 19 images close to one tip of the fracture acquired with the medical scanner HD250. Slice thickness: 2mm. Slice spacing: 2mm. Total sweep length: 38 mm.

Figure 5-3 displays an enlargement of a single image at the center of the fractured zone. Due to the resolution of the HD250, the matrix shows smooth layers of different rock densities, and just a few incrustations or heterogeneities. The fracture appears to be open at the edge and continuous, and it is well differentiated from the matrix.

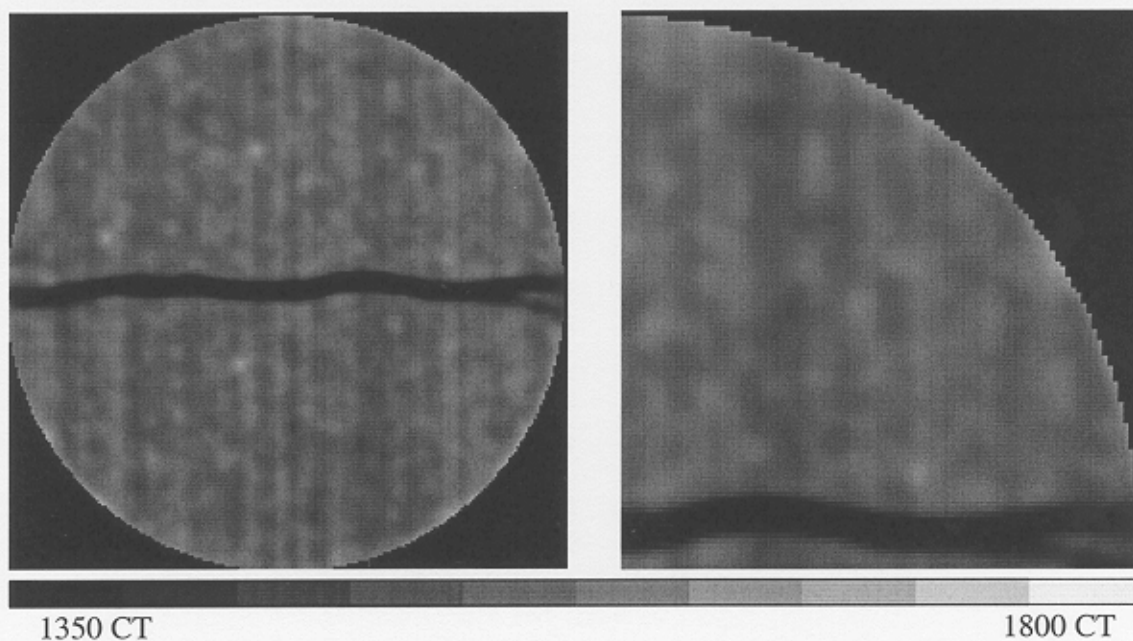


Figure 5-3: Image acquired by the HD250 scanner. 200x200 pixels.

At this section of the core the induced fracture is fairly horizontal and perpendicular to the layers, and it is also open at its edges. However, it cannot be established if the fracture is horizontal through the core just by looking at a single image. The $\frac{1}{4}$ image shown at the right side of Figure 6-3 is pixilated (every pixel is shown as a square). Each pixel represents a rock volume of $0.25 \times 0.25 \times 2.0$ mm. The large density contrast between the fracture and the matrix creates the appearance of a large artificial fracture width that is resolved with the high-resolution scanner.

Figure 5-4 presents four longitudinal reconstructions, three horizontal (A-C) and one vertical (D). The horizontal sections show the layers as well as portions of the

fracture (the dark regions). The vertical section is perpendicular to the fracture plane and highlights the extent of the fracture

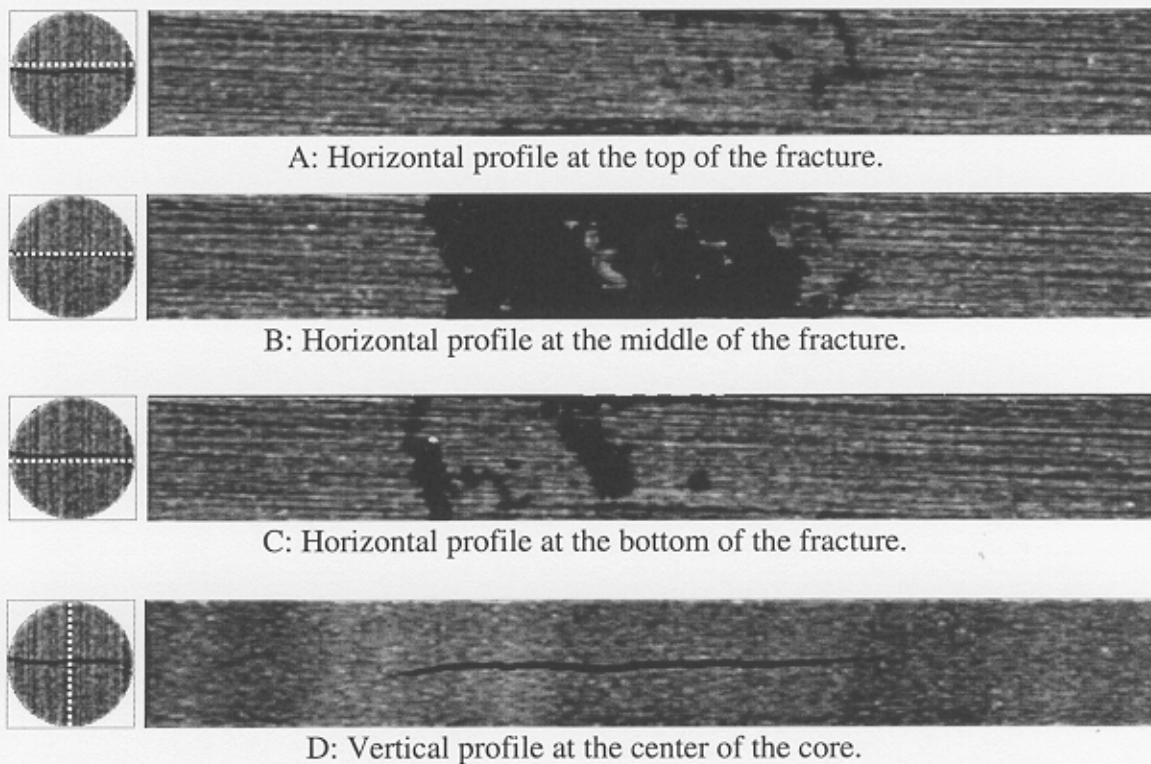


Figure 5-4: Longitudinal sections through the rock sample. Scanner: HD250.

Four hundred images, with a thickness of 95 μm , were acquired in single-scan mode covering 38 mm of the core at one tip of the artificial fracture. These images were reconstructed by the OMNI-X at 256x256, 512x512, and 1024x1024 pixels per each slice. Figure 5-5 displays 19 consecutive images reconstructed at a resolution of 256x256. Since the diameter of the sample is about 50 mm, a matrix of 256x256 yields a pixel resolution of about 200 microns. A resolution of 1024x1024, the maximum

resolution available using the OMNI-X scanner, yields a pixel resolution of about 50 microns in this specific case.

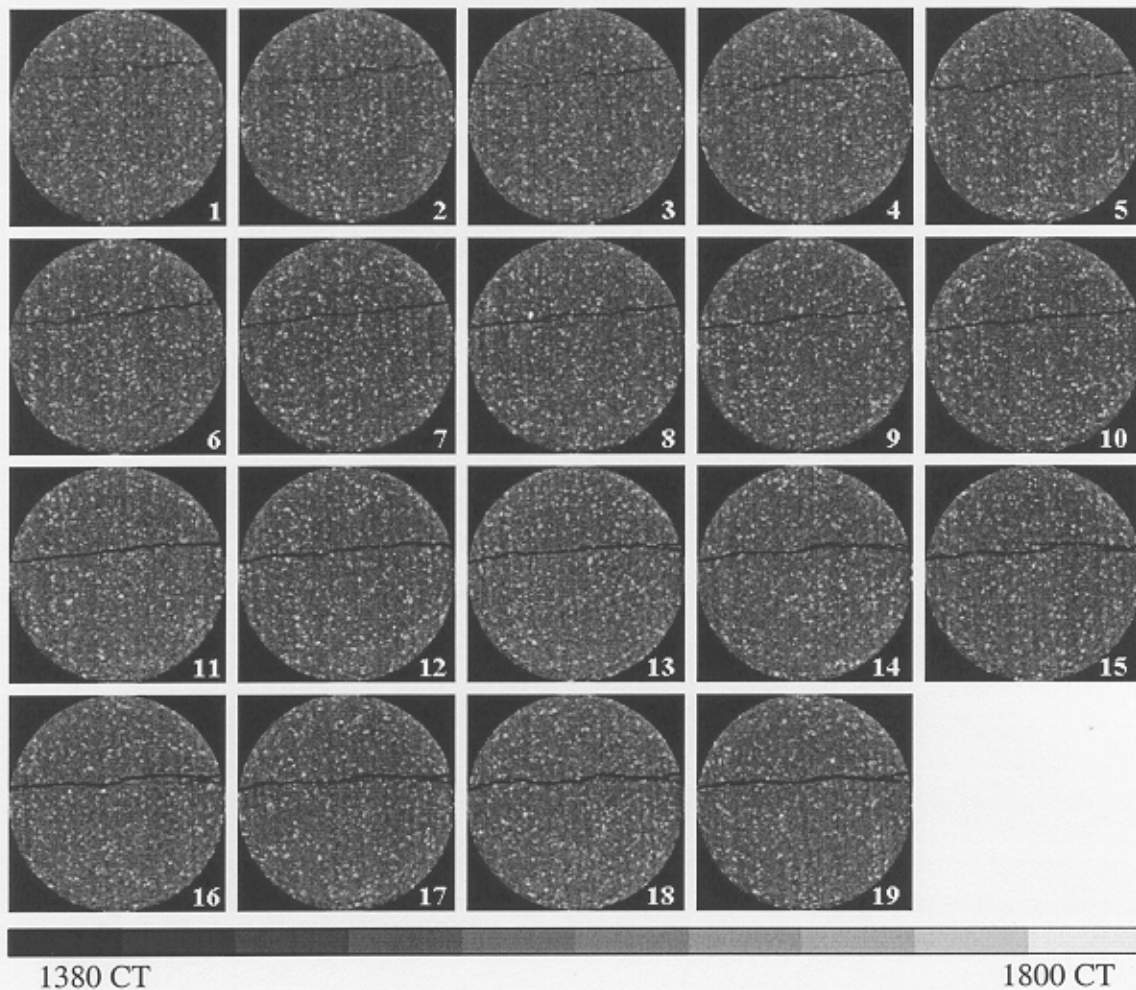


Figure 5-5: Plate of 19 dry images close to one tip of the fracture acquired with the industrial scanner OMNI-X reconstructed at 256x256 pixels. Thickness: 95 μm with a spacing of 1.995 mm. Length covered by these images: 37.9 mm.

The fracture becomes more visible away from the tip. The vertical layers are also visible but not as distinct as in the scans acquired by the medical scanner.

Figure 5-6 shows an image acquired at one of the ends of the fractured region by the OMNI-X scanner reconstructed at 256x256 pixels. The fracture is not continuous at this position. Figure 5-7 displays the same image reconstructed at 512x512 and Figure 5-8 at 1024x1024 pixels per image. Each pixel in the 256x256 image is represented by a 4x4 group of pixels in the 1024x1024 image.

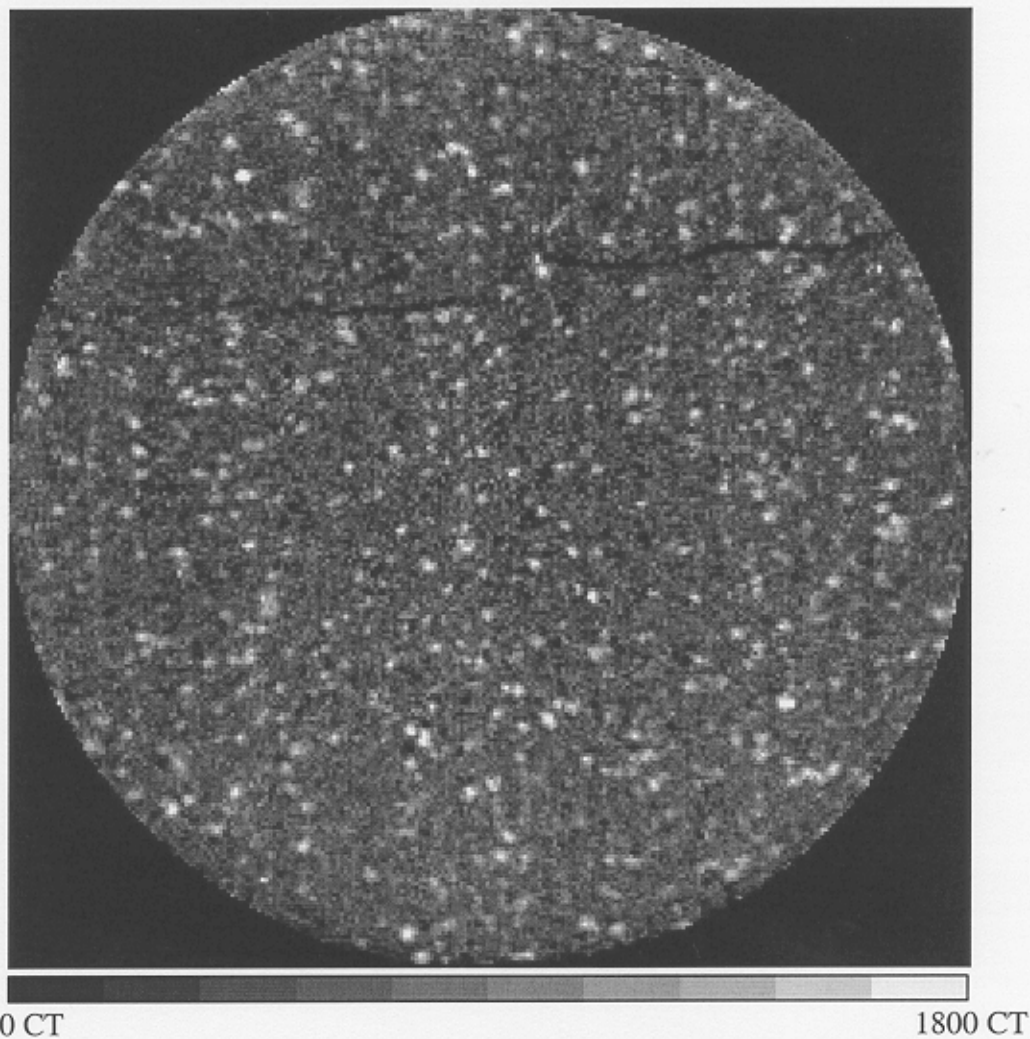


Figure 5-6: Single image of the core sample acquired by the OMNI-X close to the tip of the fracture. Matrix size: 256x256.

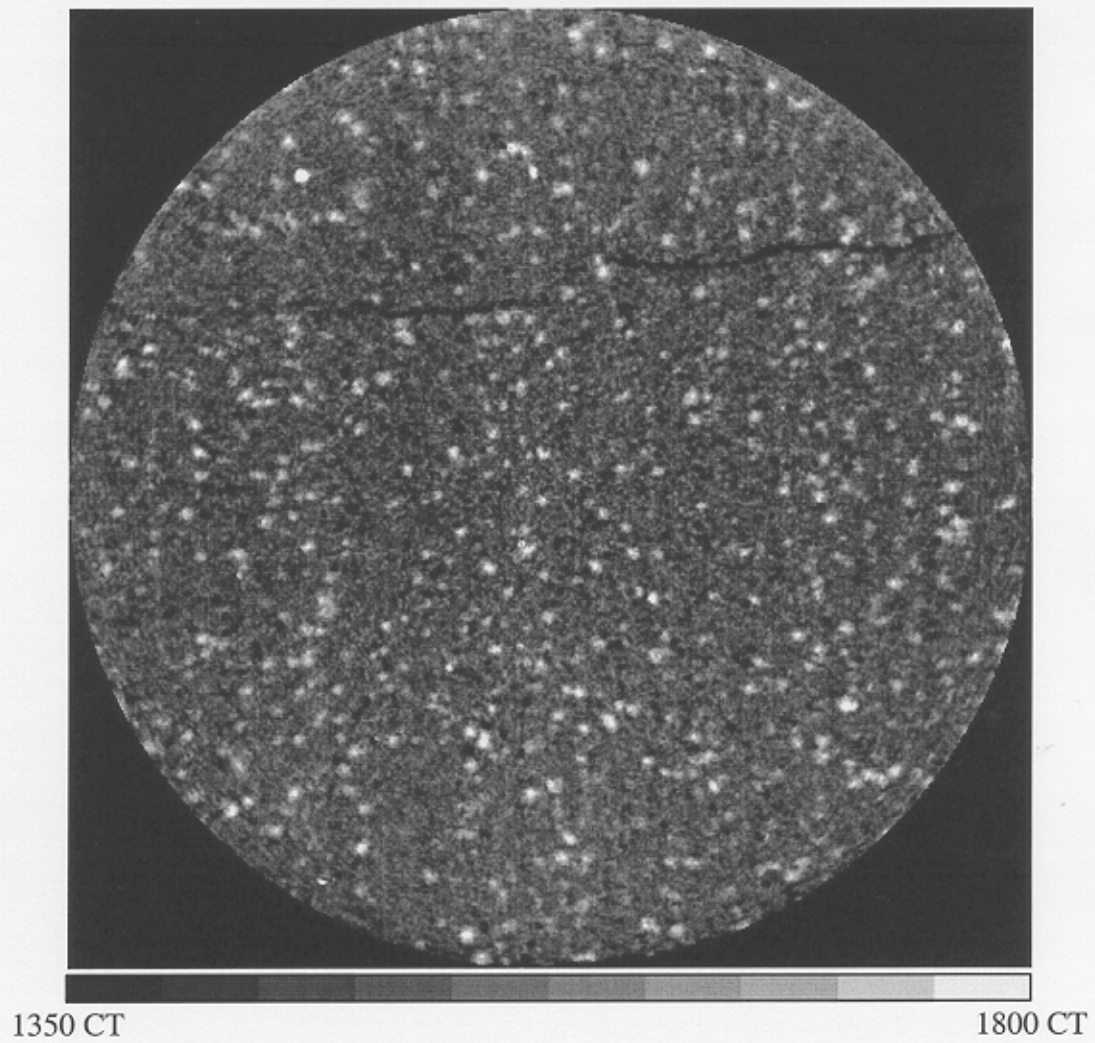


Figure 5-7: Single image of the core sample acquired by the OMNI-X close to the tip of the fracture. Matrix size: 512x512.

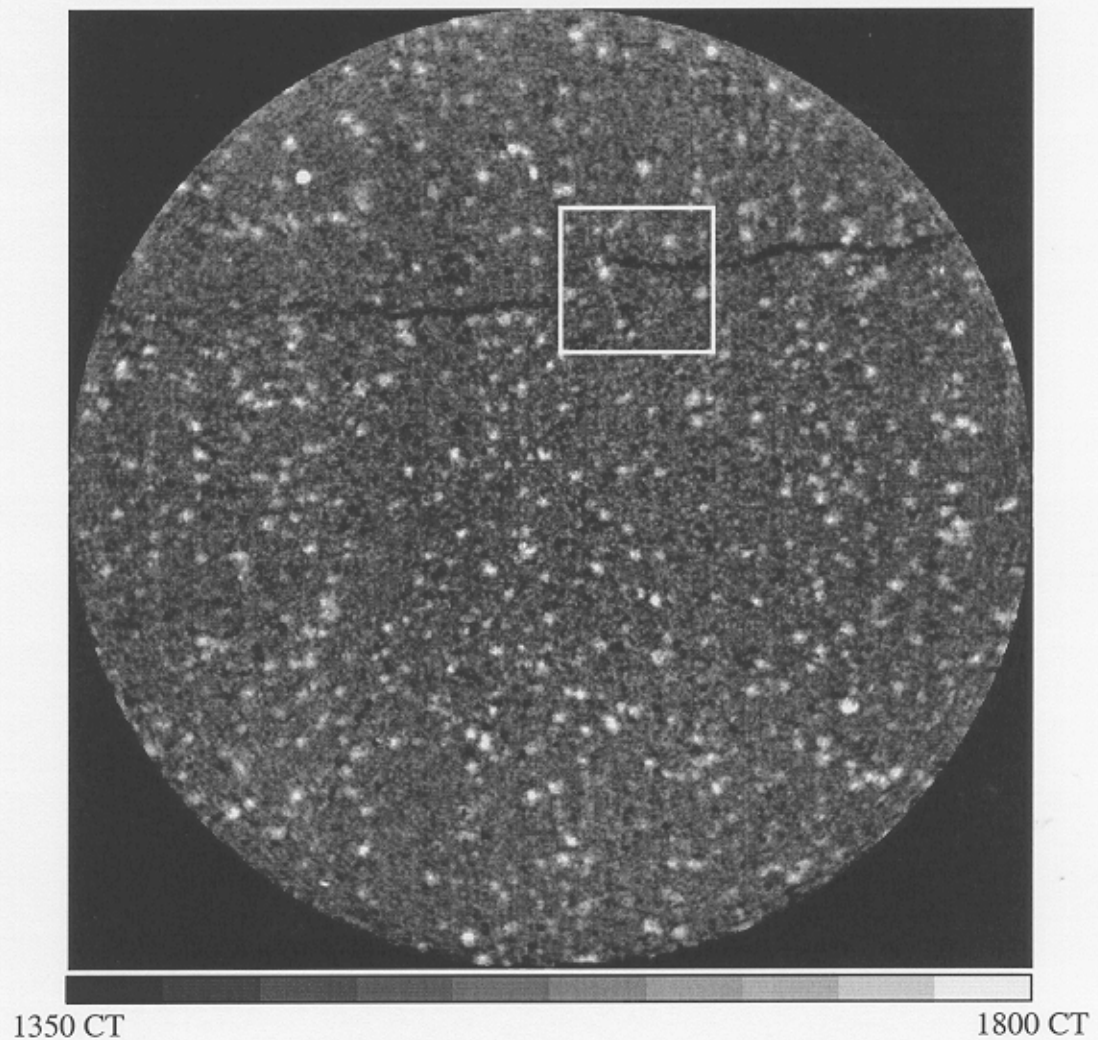


Figure 5–8: Single image of the core sample acquired by the OMNI-X close to the tip of the fracture. Matrix size: 1024x1024.

The highlighted region on Figure 5–8 is expanded in Figure 5–9, pixilated and smoothed. At this resolution, there is little difference between the smoothed and pixilated images. The rough nature of the fracture is visible in the expanded images. The bright spots in the figures are most likely iron-rich inclusions or quartz crystals.

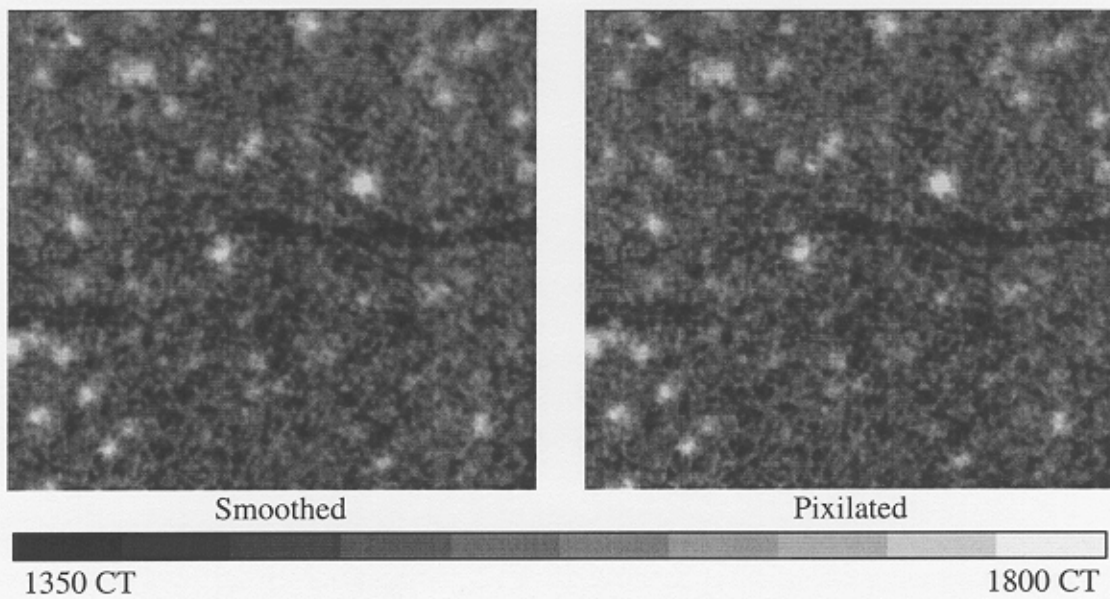
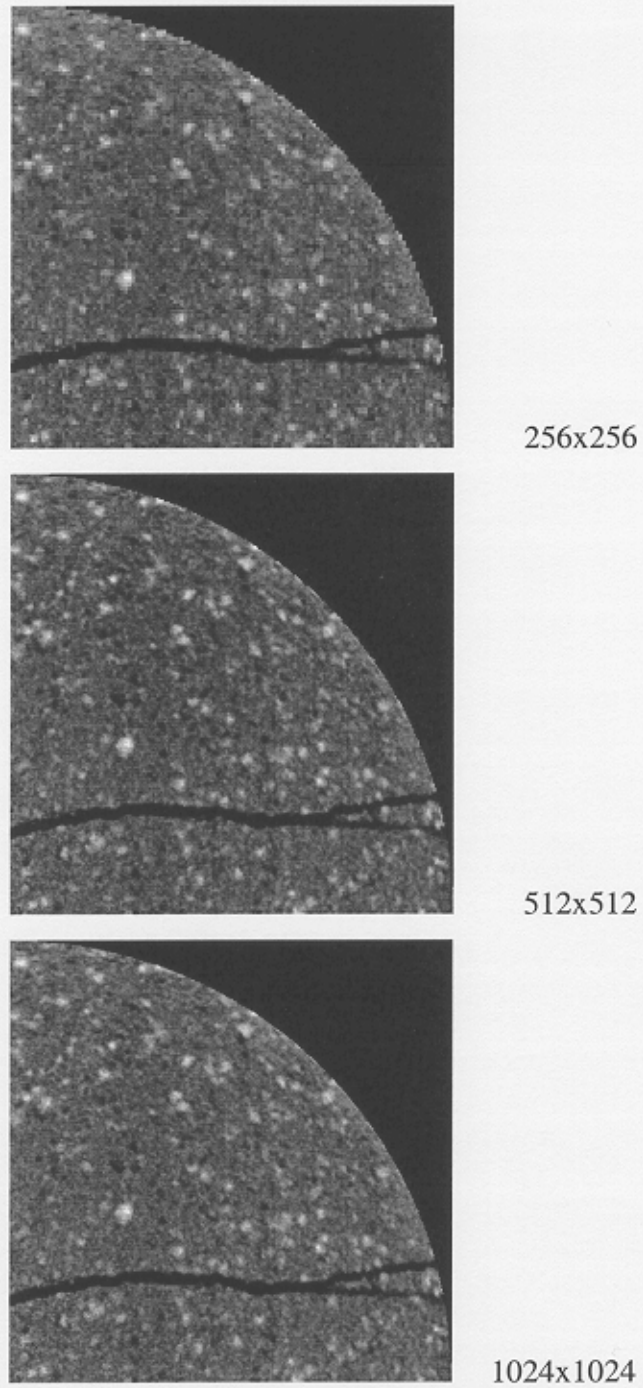


Figure 5-9: Expanded region showing the details of the fracture.

To increase the distinction among the different levels of reconstructions, only a quarter of one image is displayed in Figure 5-10, reconstructed at 256x256, 512x512, and 1024x1024 pixels. The iron inclusions are clearly exposed on the image reconstructed at 1024x1024.



1350 CT

1800 CT

Figure 5-10: A quarter image of the fractured Berea at different levels of reconstruction.

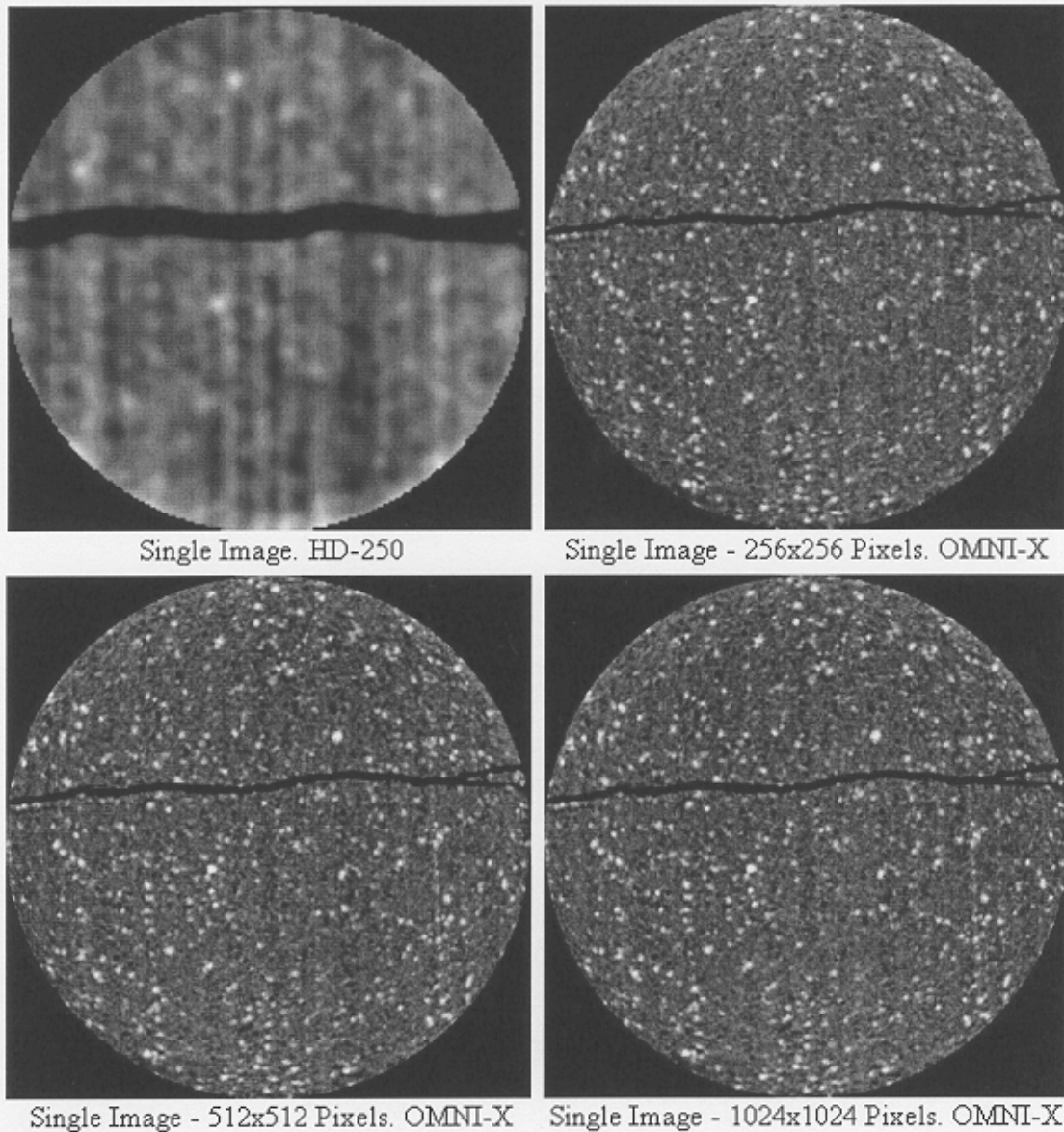


Figure 5-11: Comparison of an image scanned by the HD250 and OMNI-X scanners at the same location.

Figure 5-11 displays an image scanned by HD250 and different reconstructions of an image scanned by OMNI-X at the same position. The resolution of the medical scanner makes the fracture width appear wider than it actually is and the layers of the

Berea core are more visible in comparison to the OMNI-X image. Figure 5–12 shows a longitudinal section of the core derived from the HD250 images, spanning 380 mm. The small section below was derived from the 400 slices taken by the OMNI-X scanner.

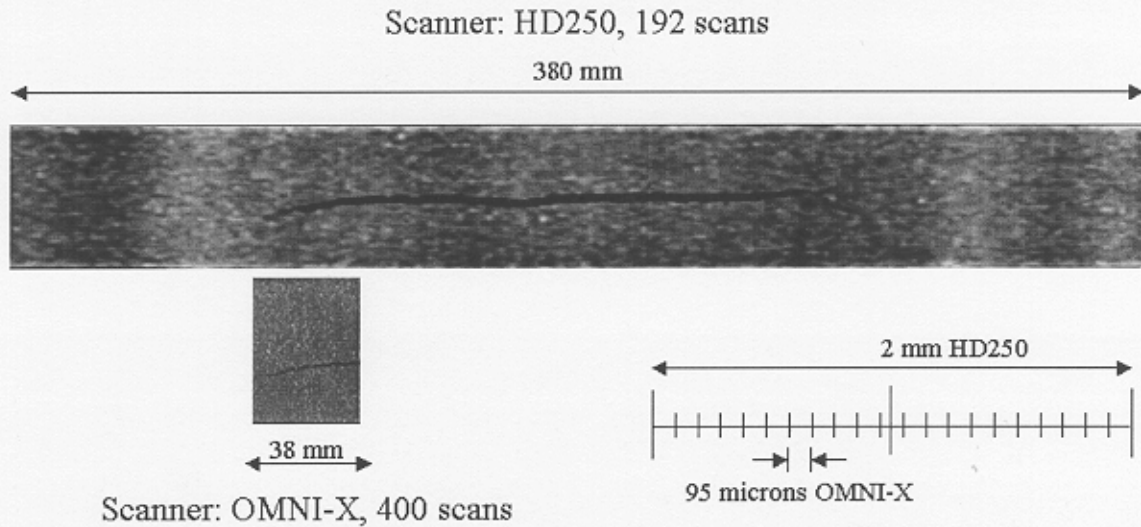
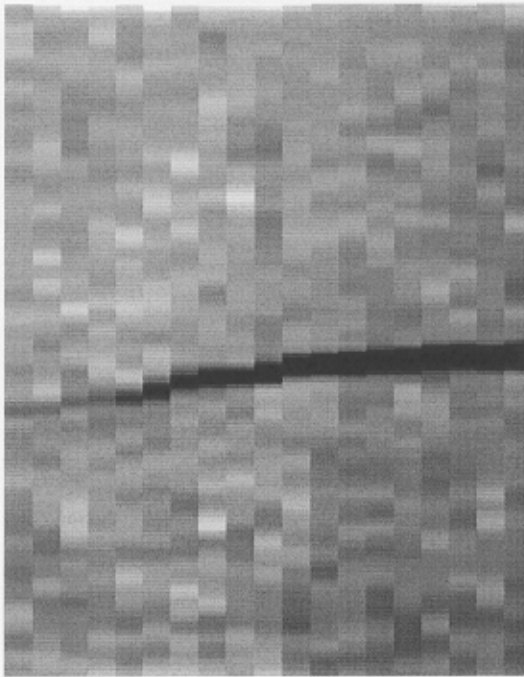
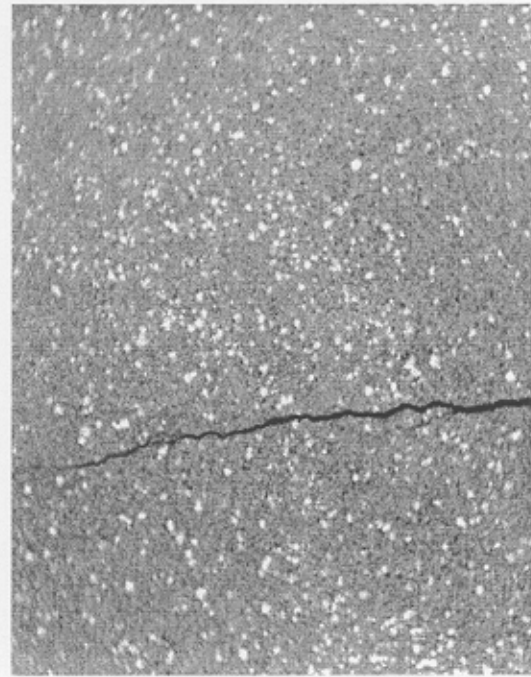


Figure 5–12: Relationship between image thicknesses from the two scanners.

Figure 5–13 displays an expanded view of the vertical section scanned by both scanners. The section corresponding to the HD250 was generated using only the 19 images that match the same location scanned by the OMNI-X. The images sweep 38 mm of the core. The high resolution of the industrial scanner shows the heterogeneities of the core while the horizontal section obtained by the medical scanner is diffused and the heterogeneities are blurred. The horizontal section acquired by the OMNI-X images also shows a thinner fracture than the one in the vertical cross section of the HD250.



Scanner: HD250, 19 images



Scanner: OMNI-X, 400 Images

Figure 5–13: Horizontal sections through images acquired by both scanners. Total length: 38 mm.

The thickness of each image taken by HD250 is 2 mm while the thickness of the images taken by OMNI-X is 0.095 mm, as it is shown in Figure 5–12. Due to this difference in thickness, a better comparison should be made between images with the same thickness. The OMNI-X images were stacked in groups of 21 in order to obtain averaged images with a thickness of 2 mm, resulting in a total of 19 averaged images.

Figure 5–14, Figure 5–15, and Figure 5–16 compare the 19 averaged images derived from the 256x256, 512x512, and 1024x1024 OMNI-X data with single OMNI-X images at the same reconstruction and location in the sample, respectively.

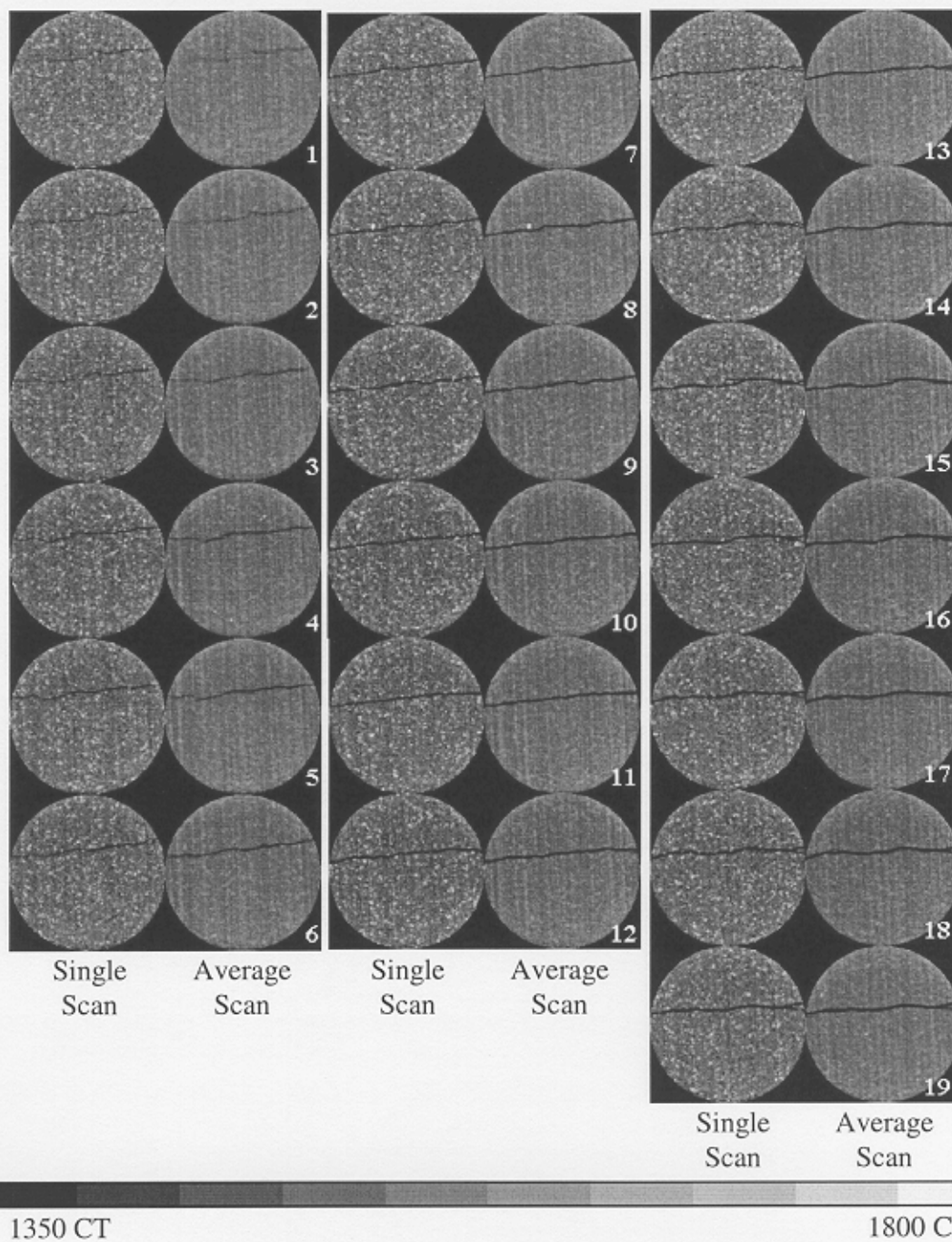


Figure 5-14: Average of images reconstructed at 256x256 pixels compare with a single slice. Total sweep length 38 mm. OMNI-X scanner.

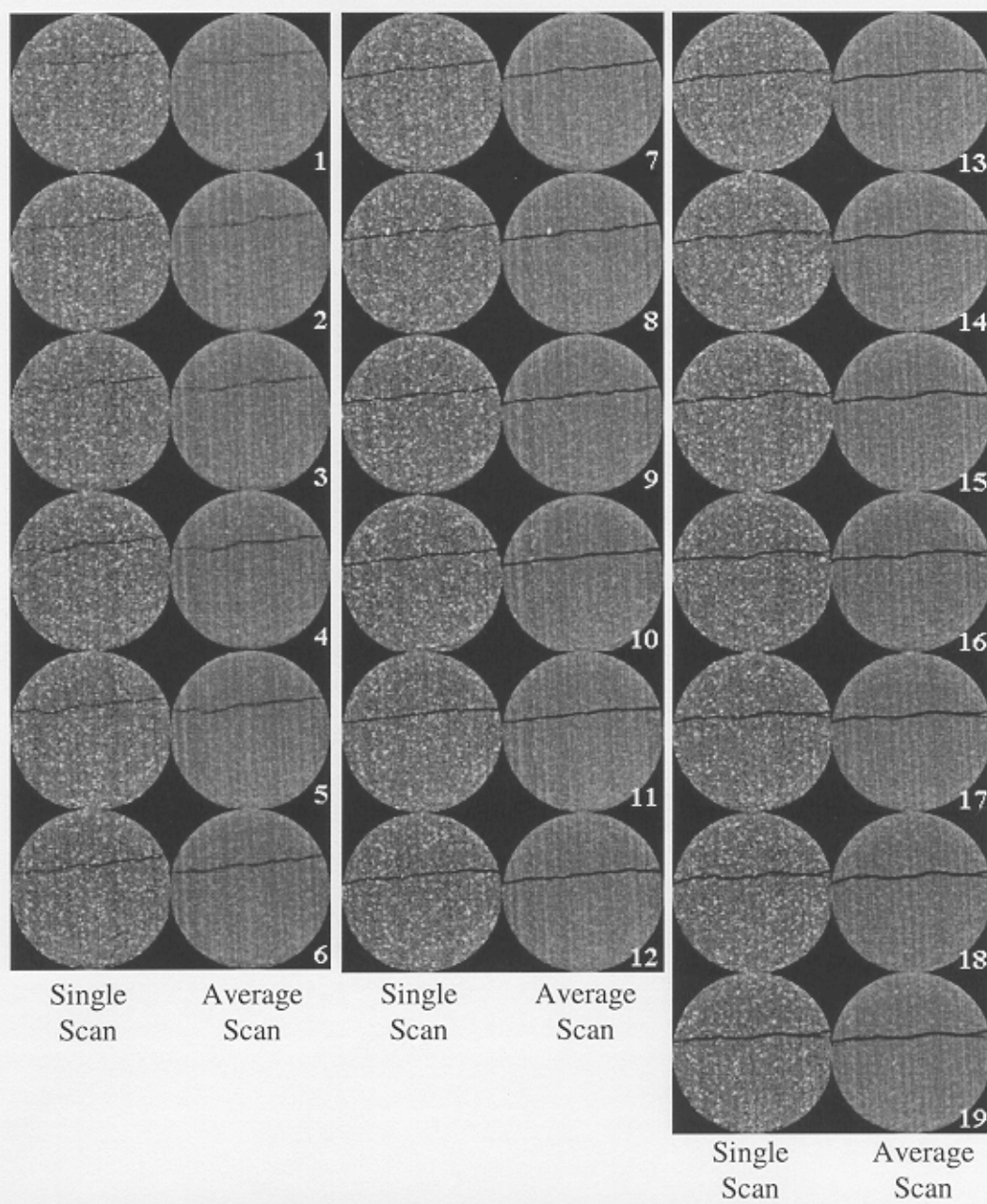


Figure 5-15: Average of images reconstructed at 512x512 pixels compare with a single slice. Total sweep length 38 mm. OMNI-X scanner.

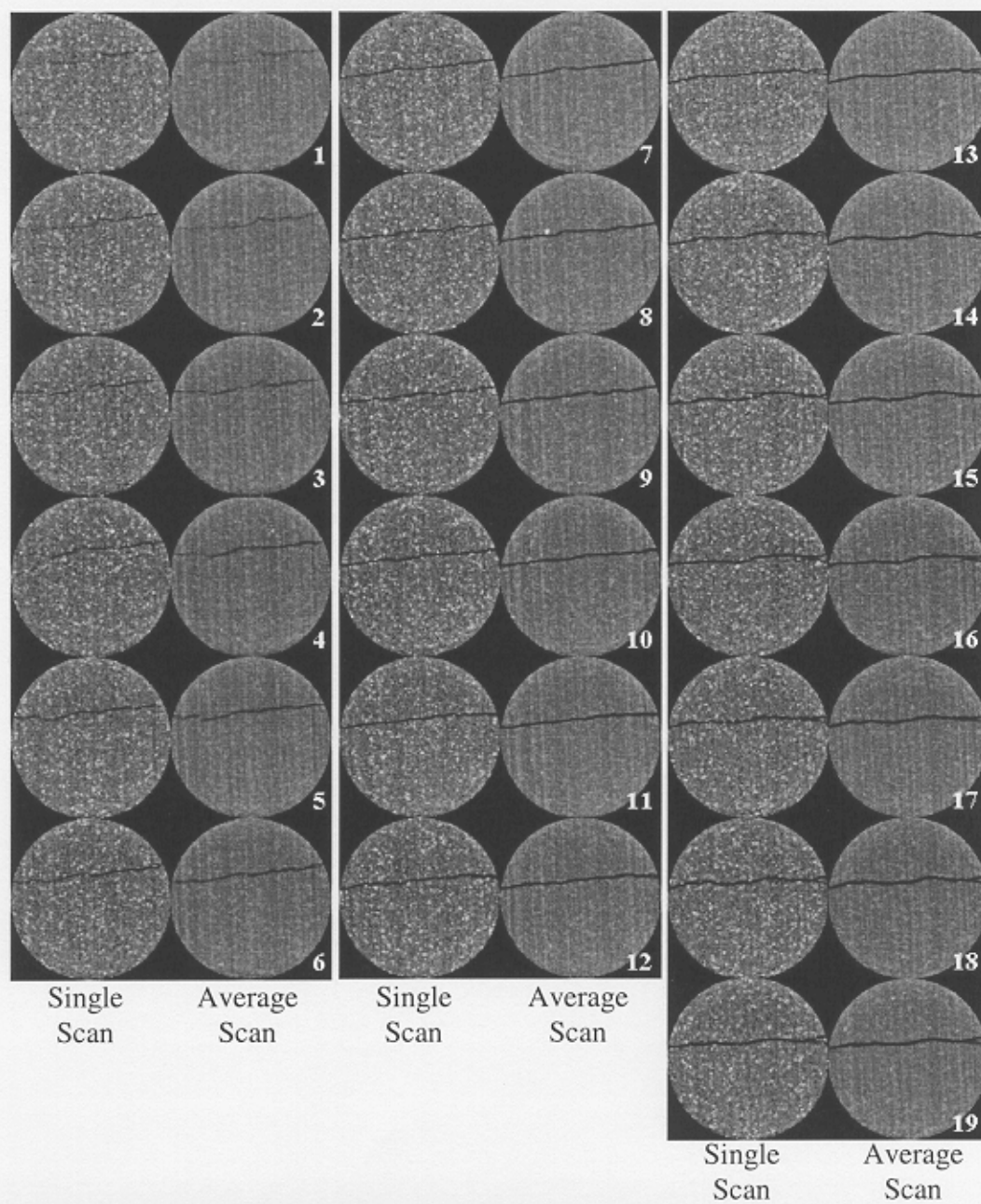
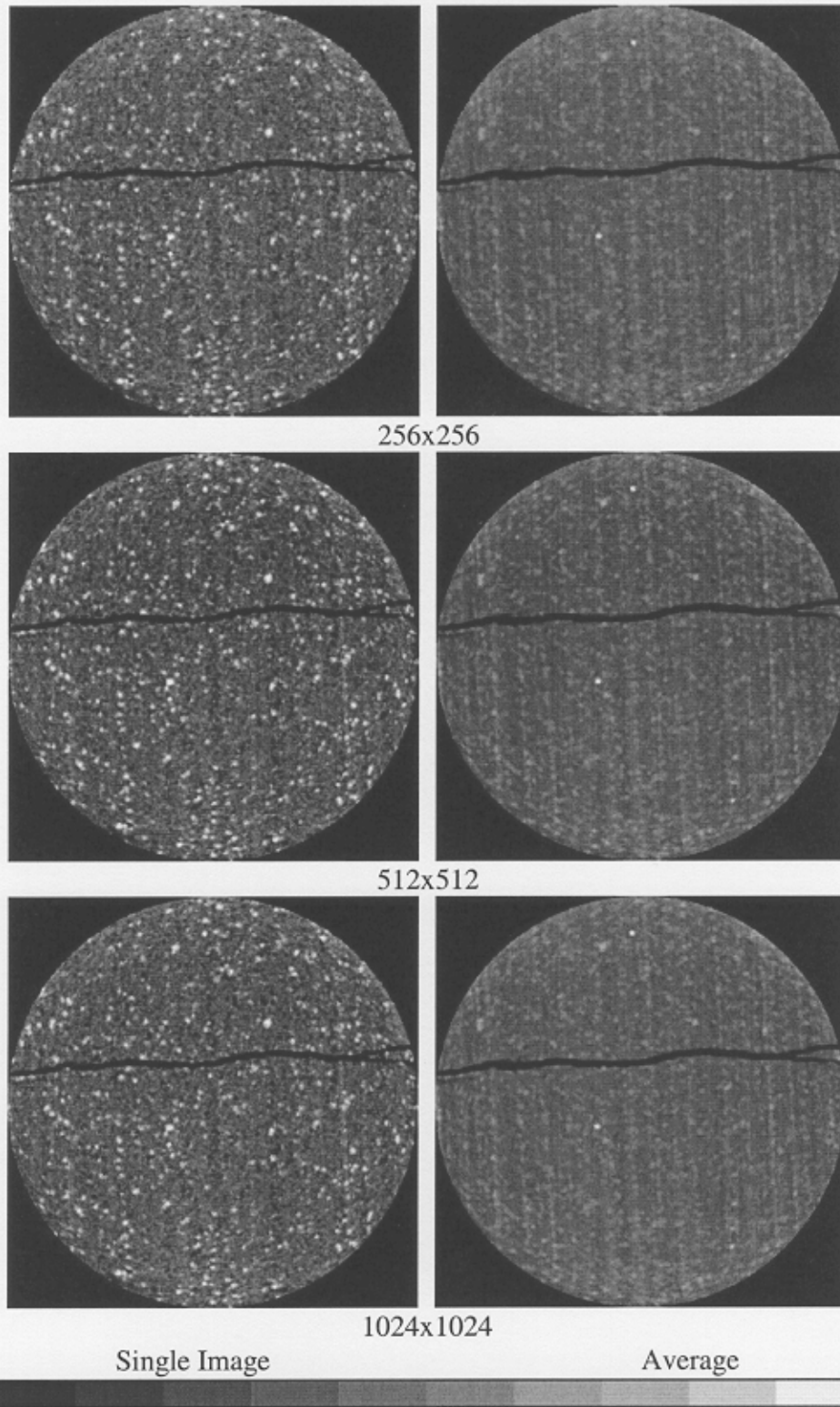


Figure 5-16: Average of images reconstructed at 1024x1024 pixels compare with a single slice. Total sweep length 38 mm. OMNI-X scanner.

Figure 5–17 compares one average to a single image for different reconstructions acquired by the OMNI-X. The layers of the Berea core are not well observed in the single images due to the high resolution of the OMNI-X scanner. The layers are well defined in the averaged images as they represent a thicker volume of rock. The fracture width appears to be the same in both single and average images, but the fracture borders are more defined in the single images.

Figure 5–18 shows quarters of averaged images at different reconstructions levels. Notice that the resolution of the single images used to create these averages directly affects the resolution of the final average. The fracture is fuzzy in the average obtained using single images reconstructed at 256x256 pixels, and the layers of the core are not as clear as in the average obtained from the 1024x1024 reconstruction.

The 19 averages were matched with those HD250 single images taken at the same position. Figure 5–19 displays the 19 averages of 512x512 pixel images and the corresponding 19 HD250 images. Figure 5–20 Displays an enlargement of one single image obtained by HD250 and the corresponding average image matched at the same position at different levels of reconstruction. The averages show a smaller fracture width and the layers are clearly exposed. Because of the high resolution of the industrial scanner, very small incrustations in the core, which are not observed in the HD250 image, are distinguished.



1350 CT 1800 CT
Figure 5-17: Single and averaged OMNI-X images at different levels of reconstructions.

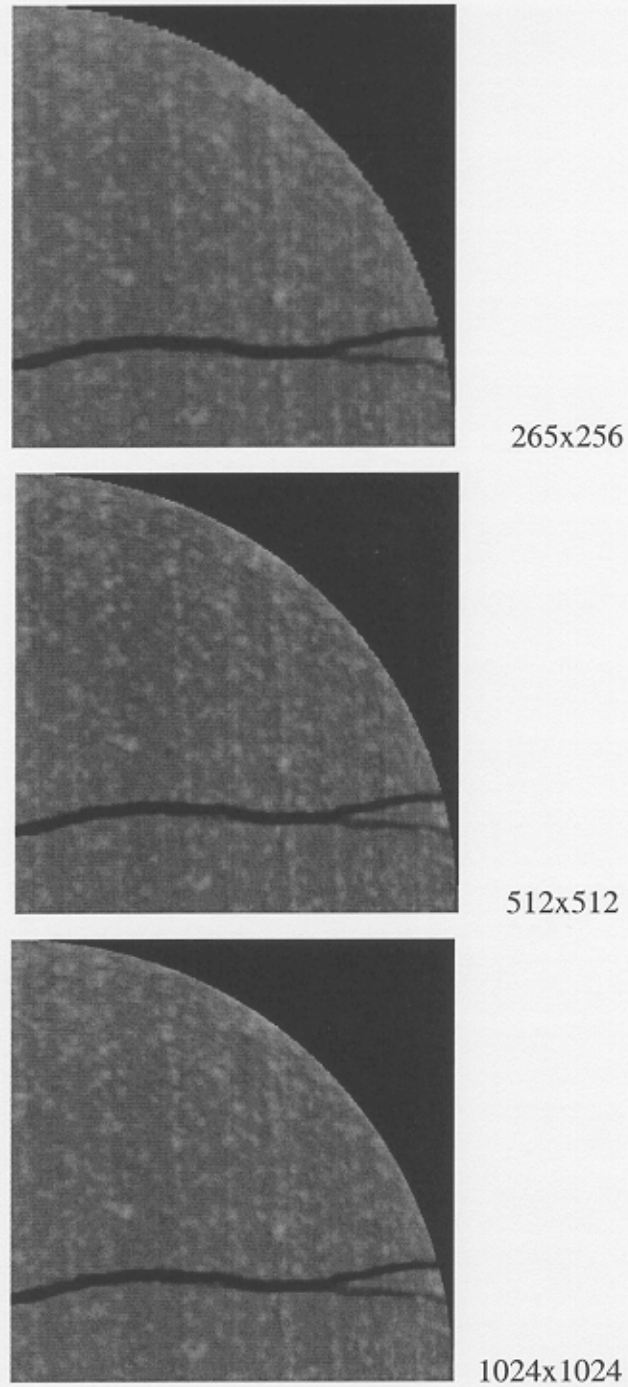


Figure 5-18: A quarter average image of the fractured Berea core at different levels of reconstruction by the OMNI-X scanner.

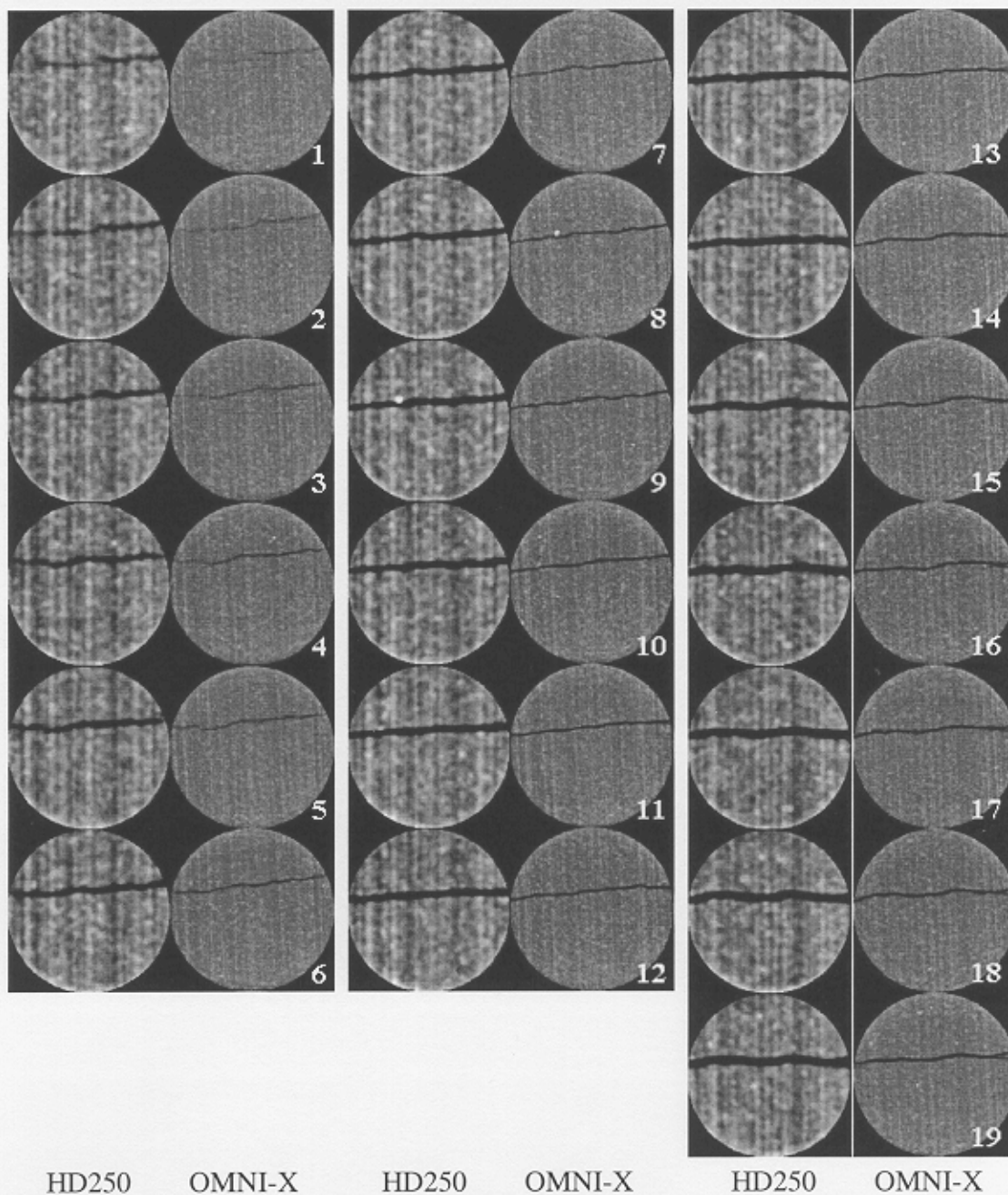


Figure 5-19: Comparison between OMNI-X average images 512x512 and HD250 single images at the same location.

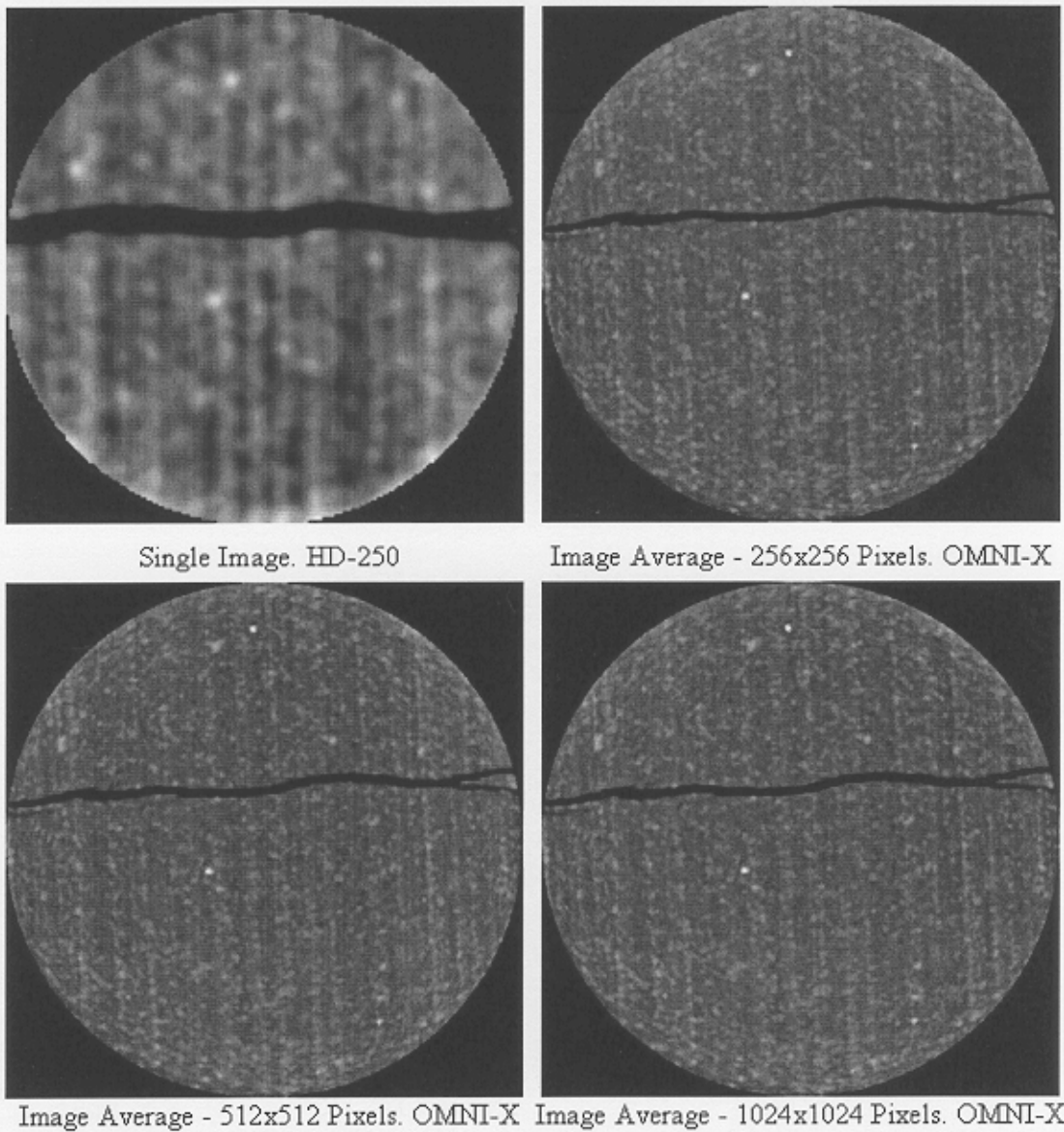


Figure 5-20: Comparison of an image scanned by the HD250 and OMNI-X average images. Thickness of the displayed images: 2 mm.

5.2 Computed Tomography Analysis and Porosity Distribution

The porosity distribution of the Berea core was obtained by using the scanning sequences taken by both scanners and the average material balance porosity of the rock. The average porosity of the fractured sample was measured experimentally by saturating the core with tagged water. The average porosity was 15.8%.

The subtraction of the dry scans from the NaI water scans leads to the net CT values of the tagged water in the rock sample. The average porosity divided by the average CT value of the net water images provides the basis for computing the porosity distribution. The entire core, 380 mm, was scanned dry and wet by the medical scanner HD250, obtaining images 2 mm thick. Similarly, 30 mm of core were scanned by the industrial scanner OMNI-X, obtaining images 91 μm thick. Figure 5–21 shows the horizontal sections of the core that were scanned by the two scanners. These images were stacked in groups of 22 to obtain images 2 mm thick, resulting in 15 averages.

Figure 5–22 shows an enlargement of the horizontal section scanned by both scanners. The section obtained with the HD250 data was generated using only the 15 images that match the 15 averaged images of the OMNI-X. The high resolution of the OMNI-X images shows the small iron inclusions in the core while these are diffused in the HD250 section. The fracture width also appears to be smaller in the OMNI-X section.

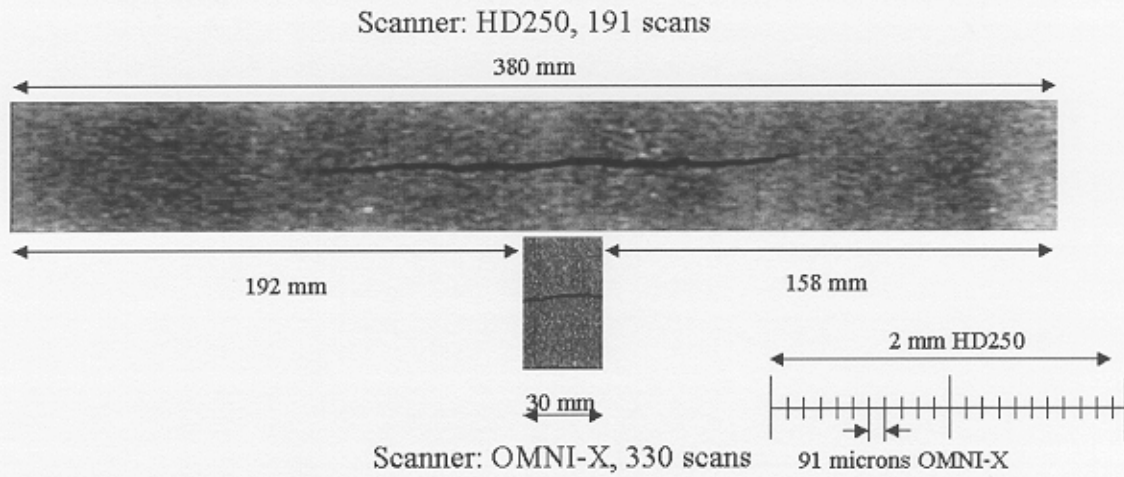
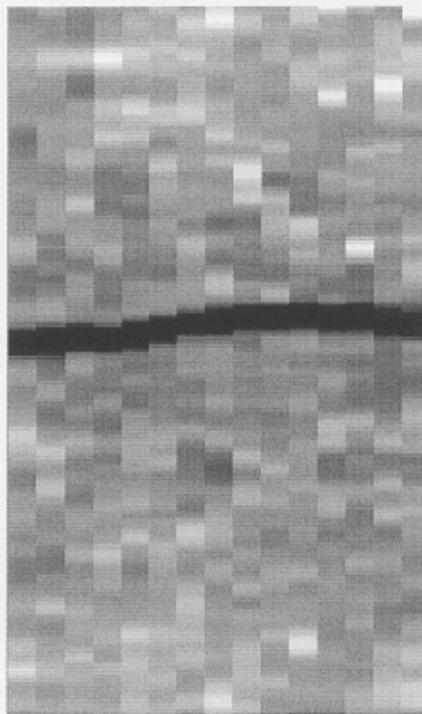
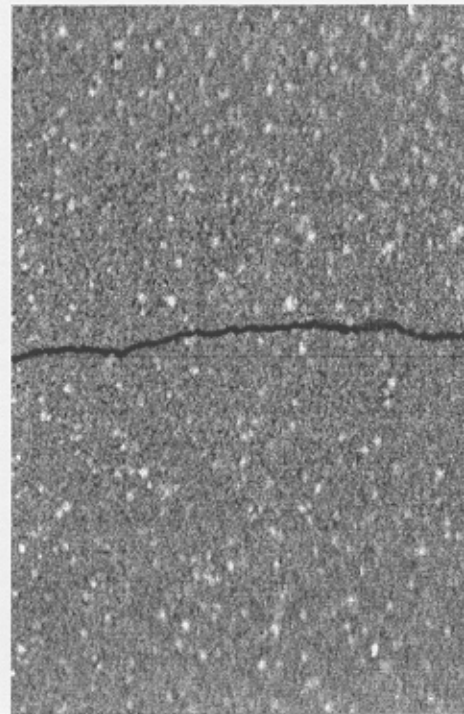


Figure 5-21: Comparison of the section scanned by both scanners.



15 Images. Scanner: HD250



330 images. Scanner: OMNI-X

Figure 5-22: Enlargement of the horizontal section of 30 mm scanned by both scanners.

5.2.1 Medical Scanner HD250

The entire core was scanned three times at the following conditions: dry, saturated with NaI-tagged water, and saturated with distilled water. Each of the three sequences consisted of 191 images that have a thickness of 2 mm. The images were reduced to a matrix size of 200x200 pixels. Even though all 191 images were used to compute the basis for the porosity distribution, the analysis of the HD250 images is focused on the 15 images that match the same location of the 15 averages obtained from the OMNI-X images.

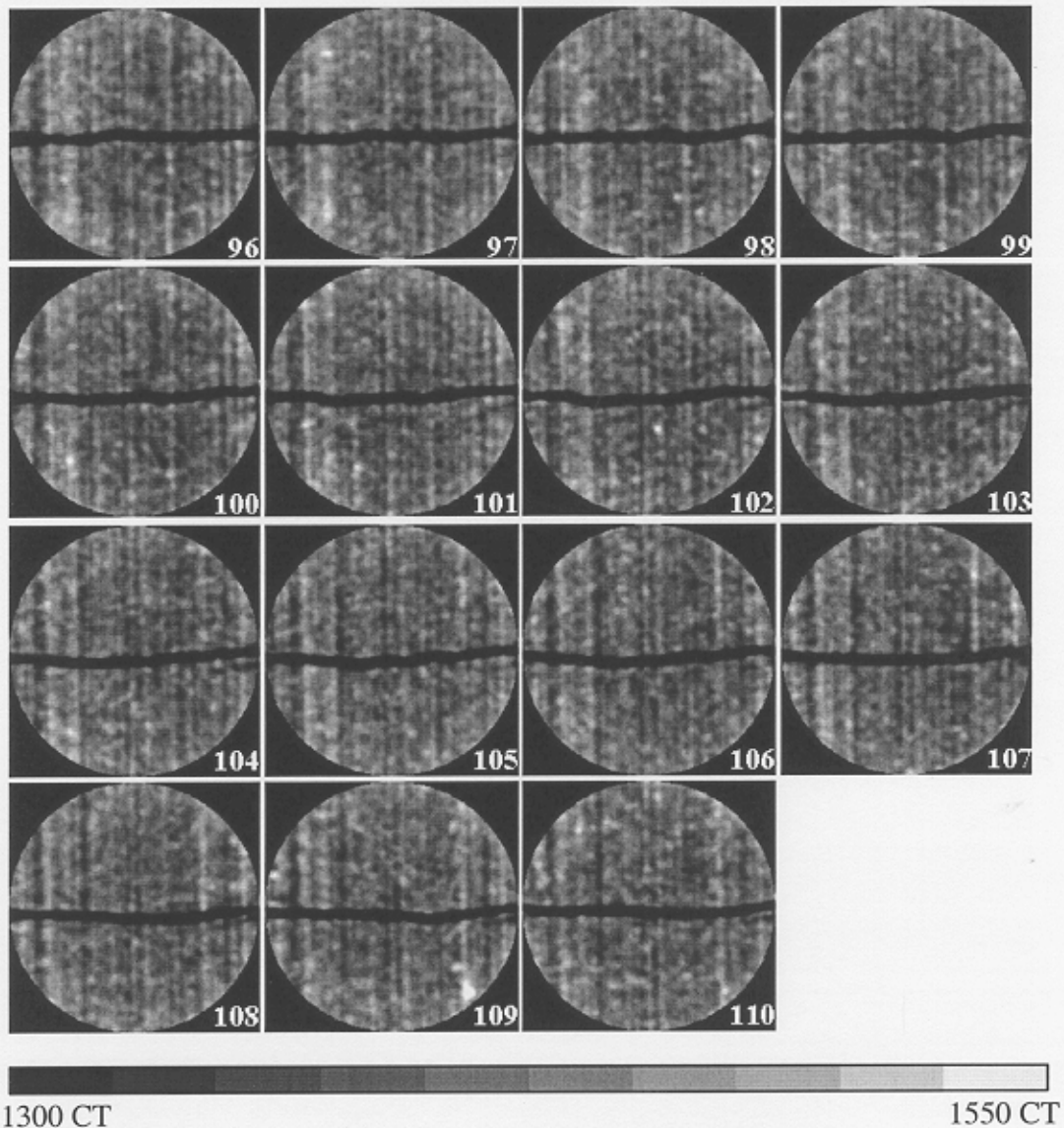
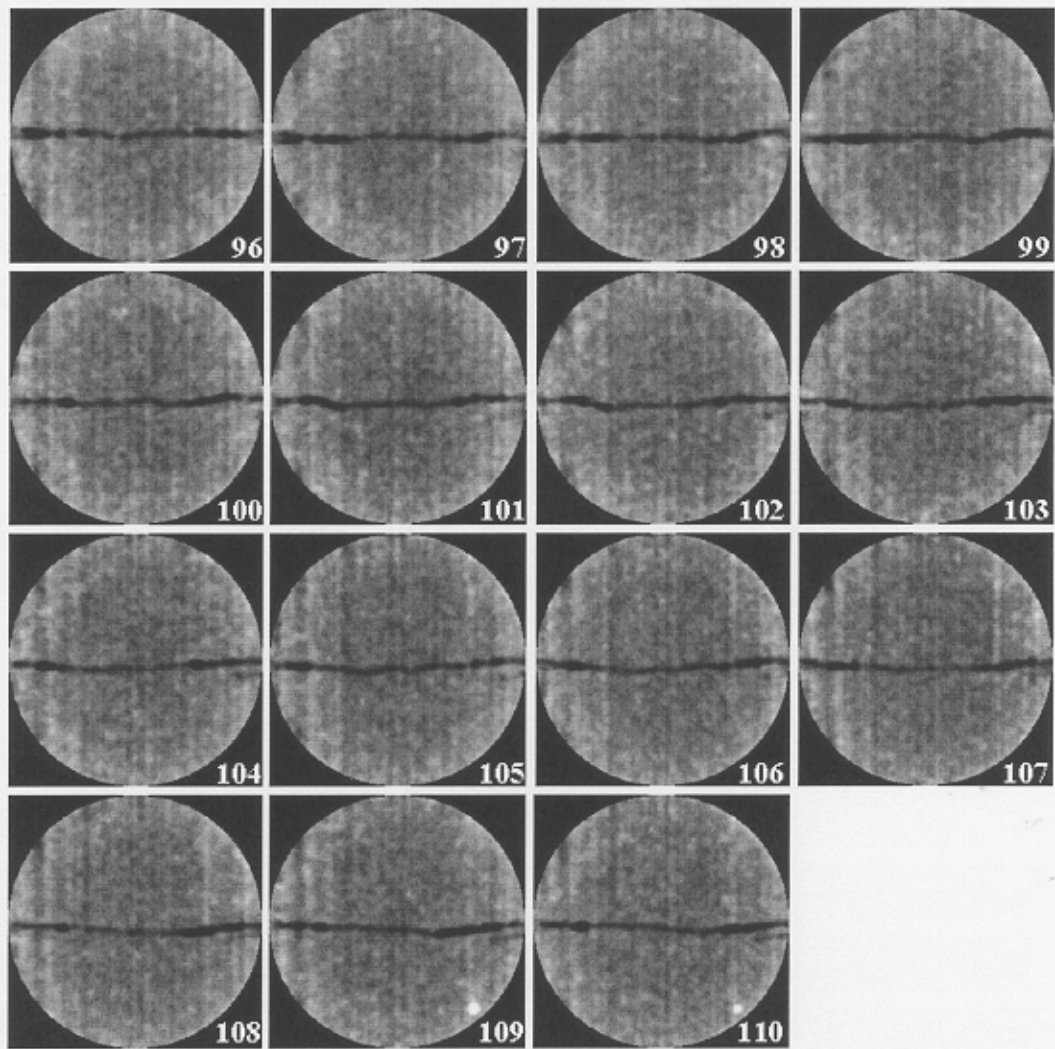


Figure 5-23: Plate of 15 dry images scanned by the HD250 scanner.

Figure 5-23 displays these 15 single dry images, Figure 5-24 displays the 15 single NaI-tagged water images at the same location, and Figure 5-25 shows the same 15 images after the core was flooded with distilled water. Notice that the CT scales are different in all three figures because different material attenuation leads to different CT

number spectra. The layers of the core are better exposed in the dry images while they are a little diffused in the wet images, specifically in the NaI-tagged water ones. The high CT attenuation of the tagged water causes the contrast between the layers to be reduced. The fracture in the tagged water images appears thinner because of the reduced contrast effect. The main reason for tagging the water is to enhance the values resulting from the subtraction of the dry images from the wet ones.



1680 CT 1980 CT
Figure 5-24: Plate of 15 NaI-tagged water images scanned by the HD250 scanner.

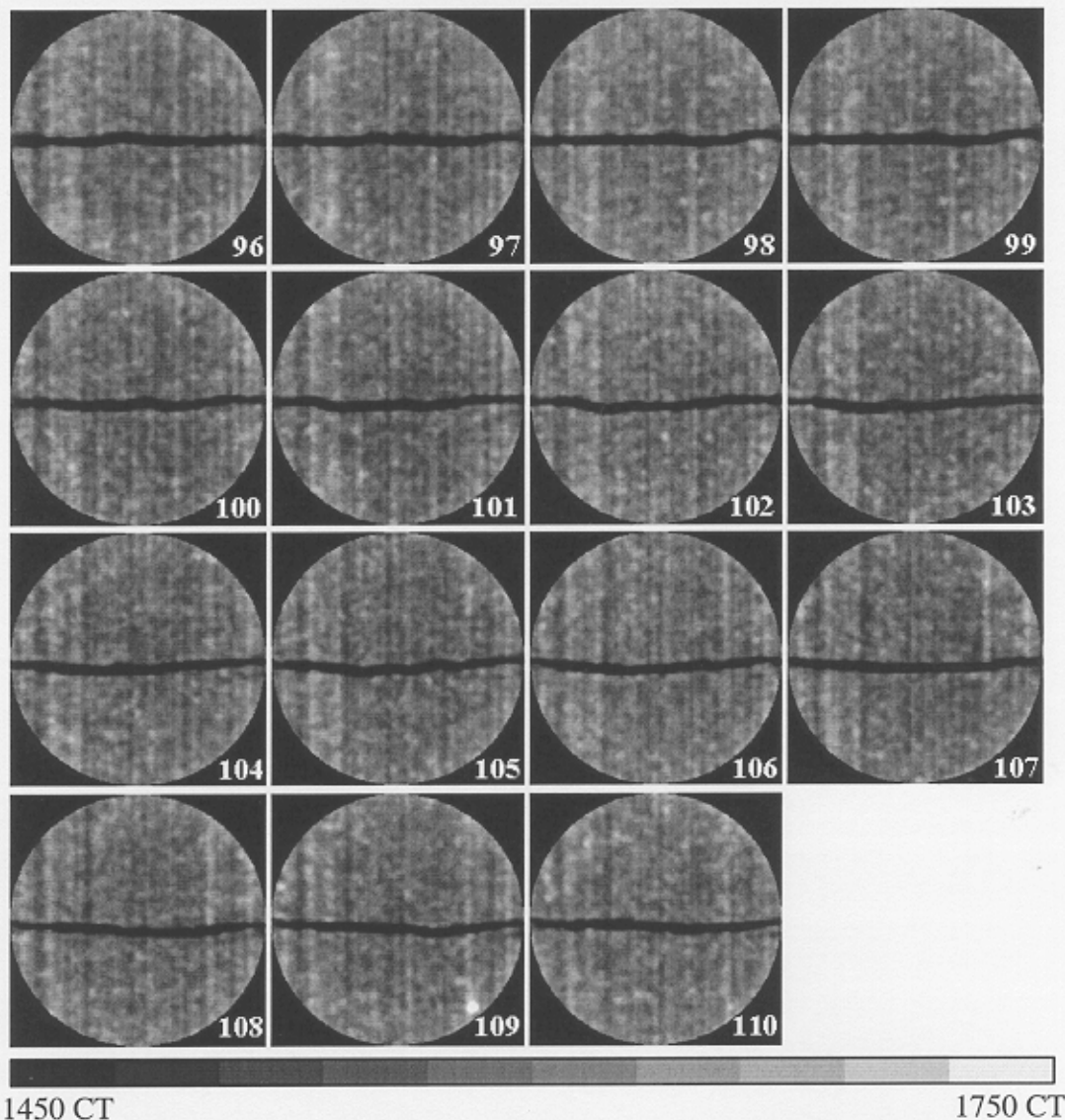


Figure 5-25: Plate of 15 distilled water images scanned by the HD250 scanner.

5.2.1.1 CT Profile Analysis

Various CT profiles in the induced fracture and its surrounding matrix were studied. The fractured region was identified using the dry images since the high attenuation of the NaI water affects the appearance of the fracture in the wet images. The

region of the core affected by the fracture was identified by those pixels whose CT numbers were between 0 and 1200. When the CT numbers are above 1200, they were considered as part of the matrix. An index file was generated to identify what pixels correspond to the matrix and the fractured region in the wet images. Once the fractured region was defined, different profiles through the fracture and the matrix were generated.

Figure 5–26 displays only a section of 60x200 pixels of a sample image that contains the fracture. The fractured area is highlighted by adding a value of 350 CT units to each pixel in the fractured region. Therefore, the CT numbers of the region that represents the fracture are artificially raised so that they can be displayed with the same gray scale as the matrix. The white contour that borders the fracture represents the edge of the fractured region. The CT number profile of the fracture is also presented. The values represent vertical averages with respect to the image shown in Figure 5–26 that form as the fractured region.

A profile of the middle of the fracture, shown in Figure 5–27, was generated in order to avoid any effect in the boundaries between the fracture and the matrix caused by heterogeneities or beam hardening. This profile is generated by a line plot of CT values in the middle (vertical) of the previously identified fractured region. The pixels used to create this profile are highlighted in white in the image. The profile is smooth in comparison to the previous one. However, both profiles exhibit the same trend.

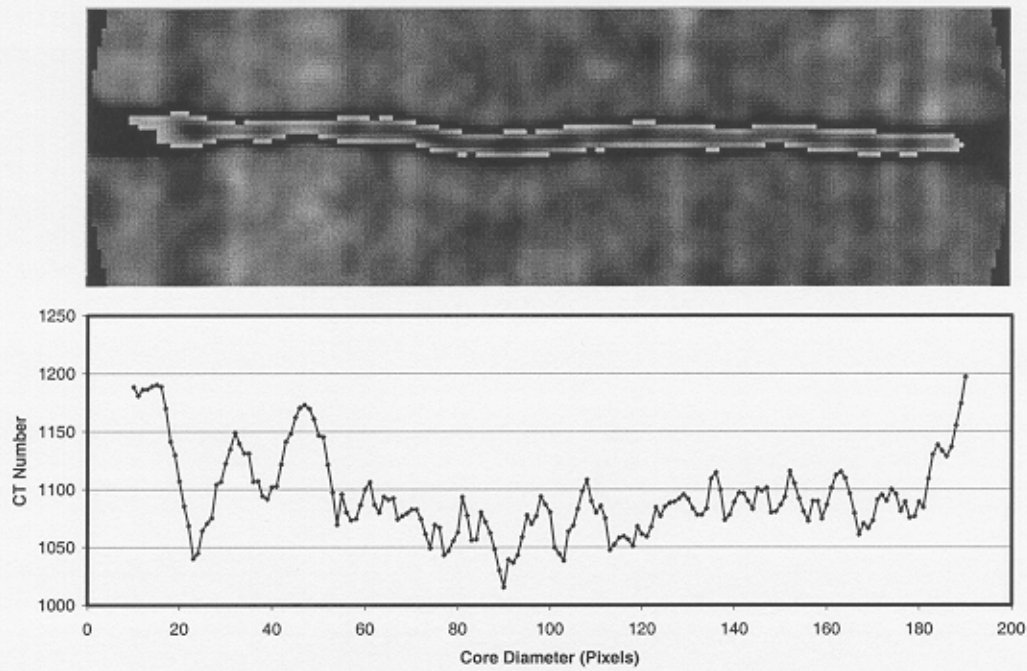


Figure 5-26: Average CT numbers profiled along the fracture in the dry image # 96 acquired by the HD250 scanner.

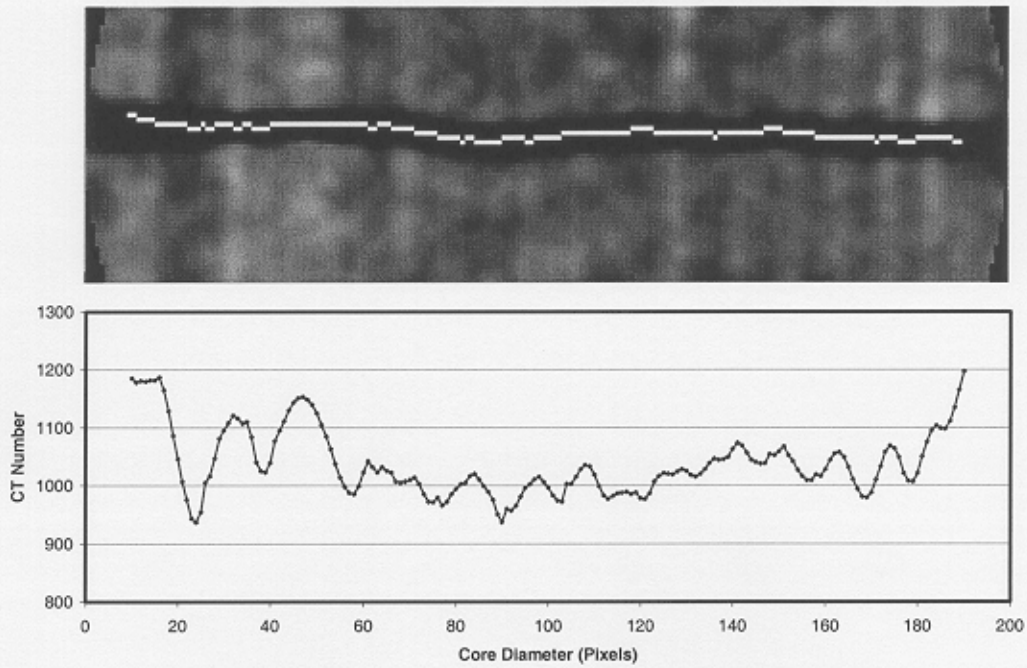


Figure 5-27: CT number profile along the middle of the fracture in the dry image # 96 acquired by the HD250 scanner.

Figure 5–28 exhibits profiles through the matrix located 6 pixels above and below the fracture, as well as their location in the image. Both profiles show similar trends along the diameter of the core. The presence of some heterogeneities and the slightly slanting layers cause mismatches of some peaks. This effect is more notable in the middle of the core where the layers are not clearly delineated. However, most of the layers are continuous on the scale of this portion of the image (the entire height of the image is about 15 mm).

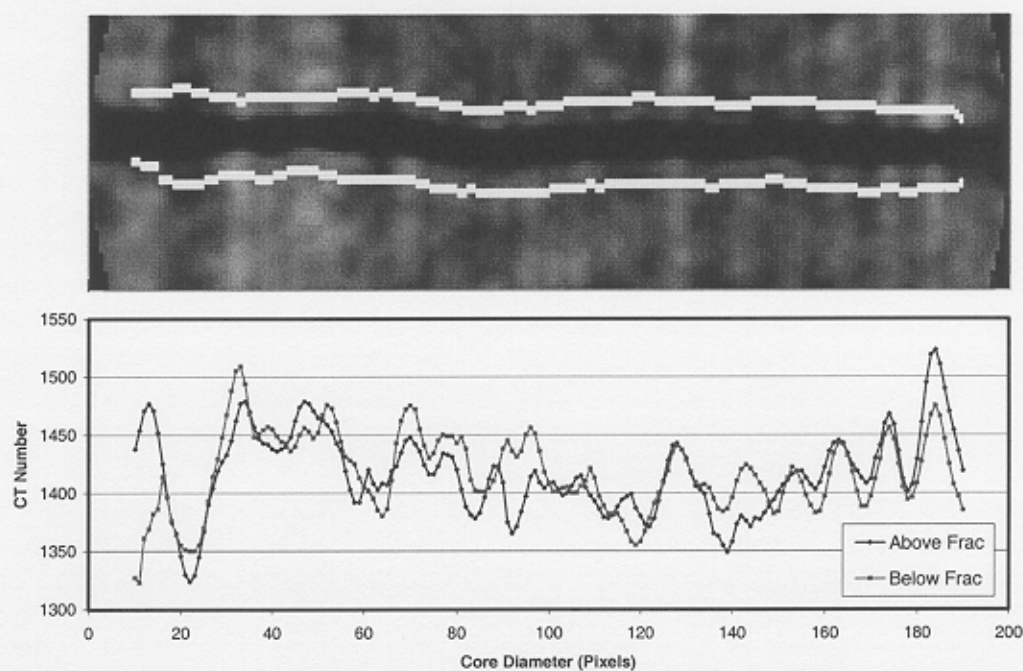


Figure 5–28: CT profiles through the matrix 6 pixels above and below the fractured region in the dry image # 96 acquired by the HD250 scanner.

Since the matrix and the fracture present different material densities, a quantitative comparison of the CT profiles could not be performed. Instead, a qualitative

analysis was done in order to establish if there is a relationship between the CT values of the fracture and the adjacent matrix. Figure 5–29 presents the profiles of the matrix and the fractured region together. Some of the locations where peaks in the matrix and the fracture profiles match are marked by the black vertical lines. There are locations along the profiles where this match is not present. In general, there is a clear relationship between the porosity in the fractured region and the porosity of the adjacent layers. This was referred to by Grader et al. 2000.

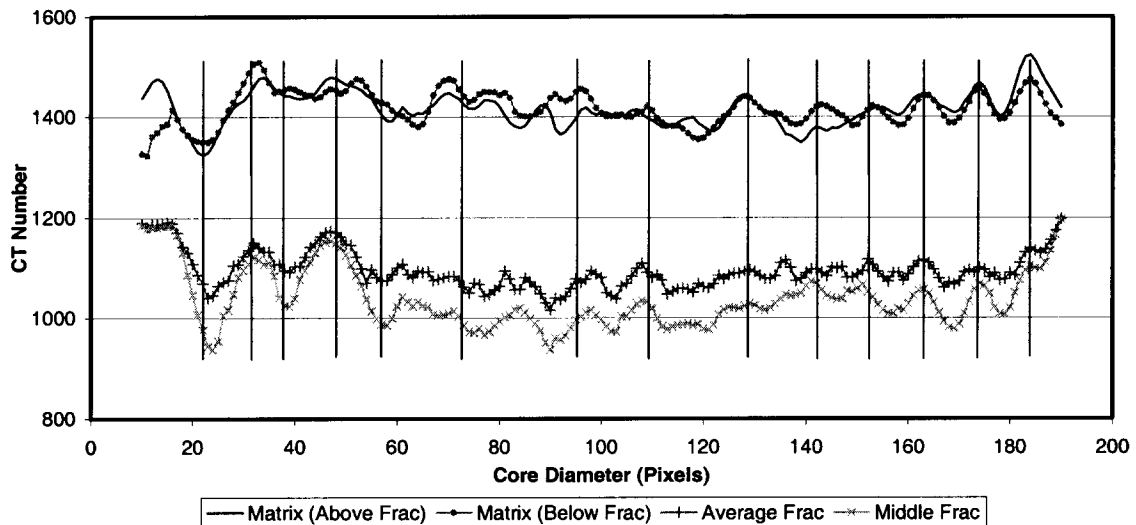


Figure 5–29: Comparison between profiles in the matrix and profiles in the fractured region of the dry image # 96 acquired in the HD250 scanner.

Similar analyses were performed for the NaI-tagged water and distilled water images. Figure 5–30 displays the CT values along the identified fractured region averaged vertically. The trends of the dry and plain water profiles are similar to each other as shown by the vertical markers on the figures. This is also observed in Figure 5–

31, where the profiles of the middle of the fracture are shown. The CT profiles through the fractured region for the dry and distilled water conditions indicate that the morphology of the fracture does not seem to be affected when the core was flooded with water.

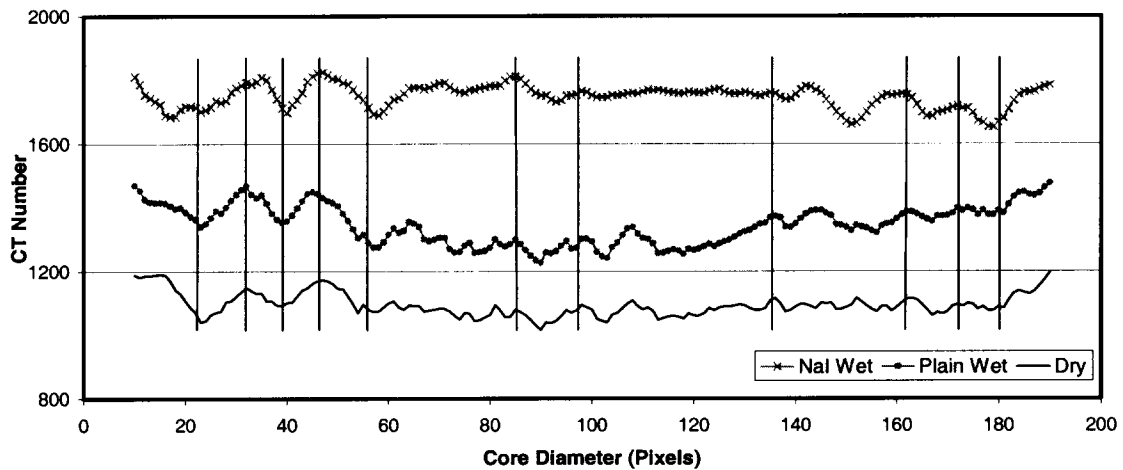


Figure 5–30: Average CT profiles through the fractured region for the following conditions: dry, NaI-tagged water, and distilled water. Scanner: HD250.

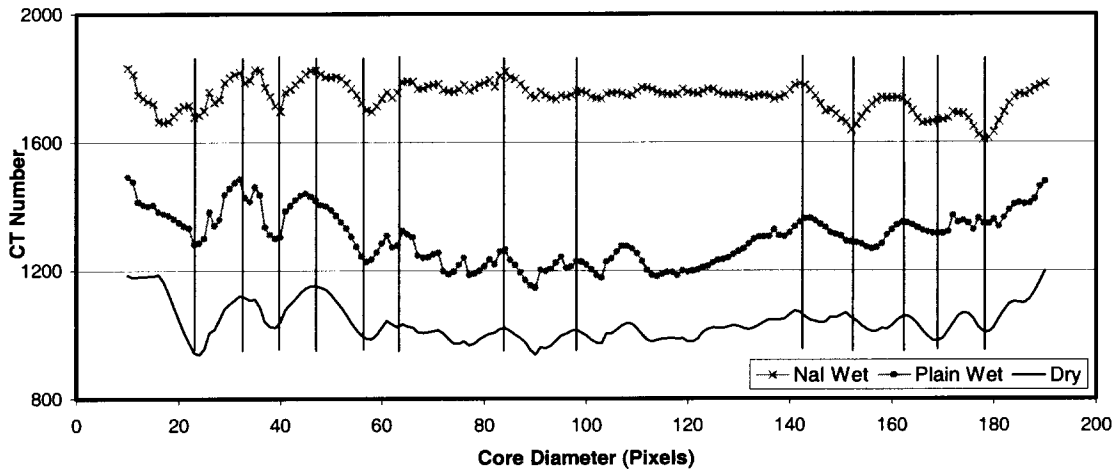


Figure 5–31: CT profiles through the center of the fractured region of the image #96 for the following conditions: dry, NaI-tagged, water, and distilled water. Scanner: HD250.

The CT profiles in the matrix above and below the fracture present the same tendency through the core diameter for all fluid conditions, as shown in Figure 5–32 and Figure 5–33. The high attenuation of the NaI-tagged water does not affect noticeably the matrix, but the fracture, which is a zone of low CT number, is significantly affected. Since the particles in the fractured region are not as compact as in the matrix, more fluid is found in this area.

Figure 5–34 shows the NaI tagged water profiles of the matrix and the fracture. Although the high attenuation of the tagged water is affecting the CT values in the fracture, these profiles show that there is a relationship between the CT values registered in the fractured region and the adjacent layers in the matrix. This relationship is better observed where the vertical layers are mainly homogeneous. The observed relationship needs to be verified by the data obtained with the industrial scanner.

Figure 5–35 displays the distilled water profiles of the matrix and the fracture. Again, a relationship between the CT values of the fracture and the matrix is observed where the vertical layers are mainly homogeneous.

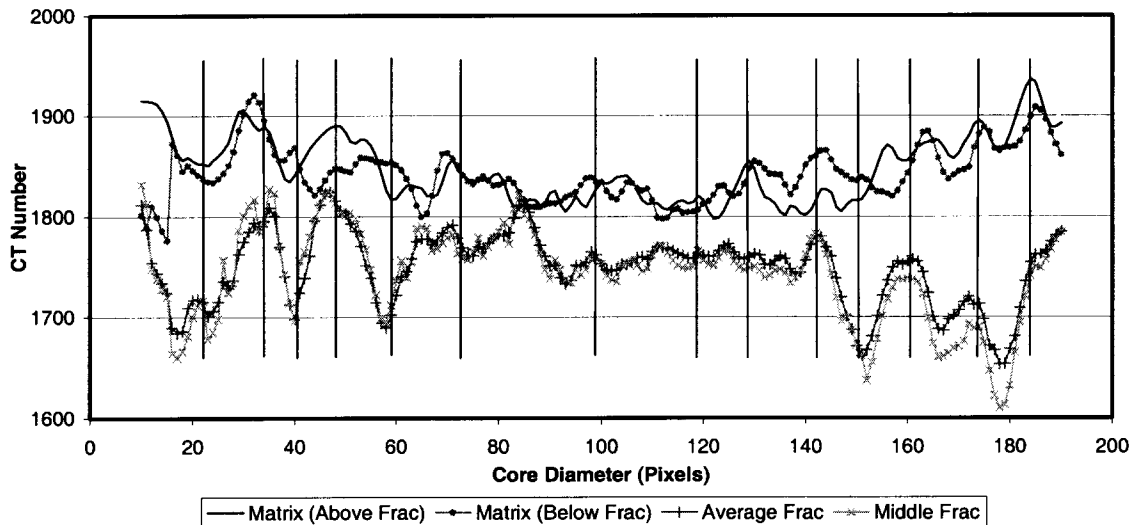


Figure 5–34: Comparison between profiles in the matrix and the fracture of the NaI-tagged water image #96. Scanner: HD250.

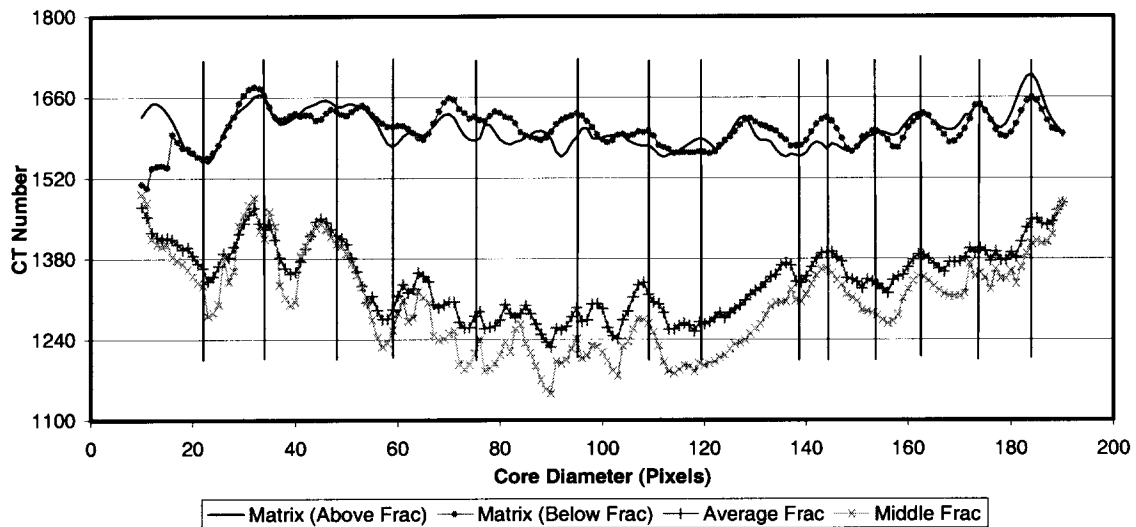


Figure 5–35: Comparison between profiles in the matrix and the fracture of the distilled water image #96. Scanner: HD250.

Similar analyses were performed at other positions in the core to verify that the results are reproducible. Figure 5–36, Figure 5–37, and Figure 5–38 display the profiles in the matrix and in the fracture of image #100 for the dry, NaI-tagged water and distilled water conditions, respectively. The dry and distilled water profiles show a clear relationship between the fractured region and the adjacent layer in the matrix, as indicated by the vertical marks. The profiles of the tagged water also show a relationship, but this correlation is not that clear due to the high attenuation of the NaI water.

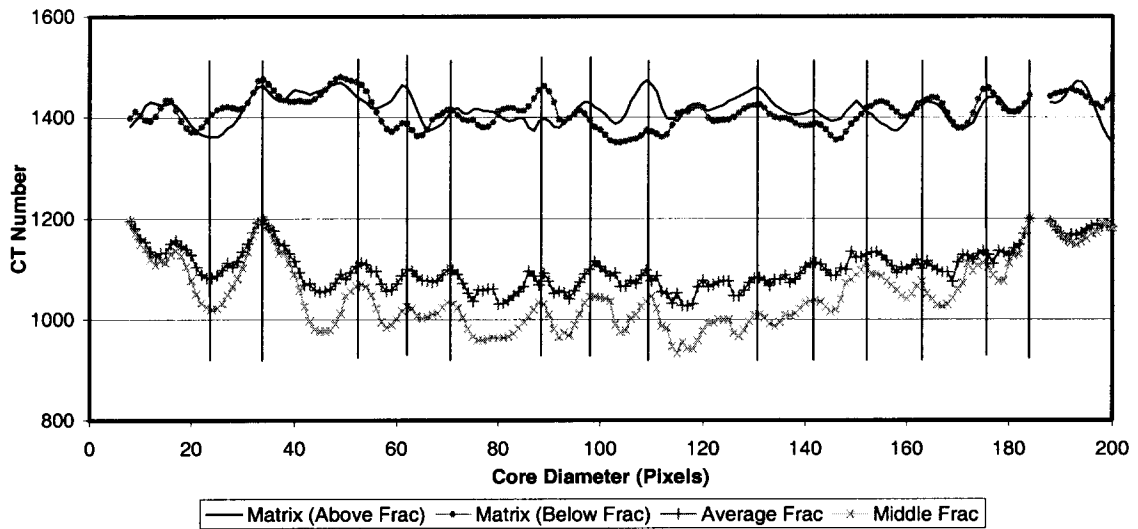


Figure 5-36: Comparison between profiles in the matrix and profiles in the fractured region of the dry image # 100. Scanner: HD250.

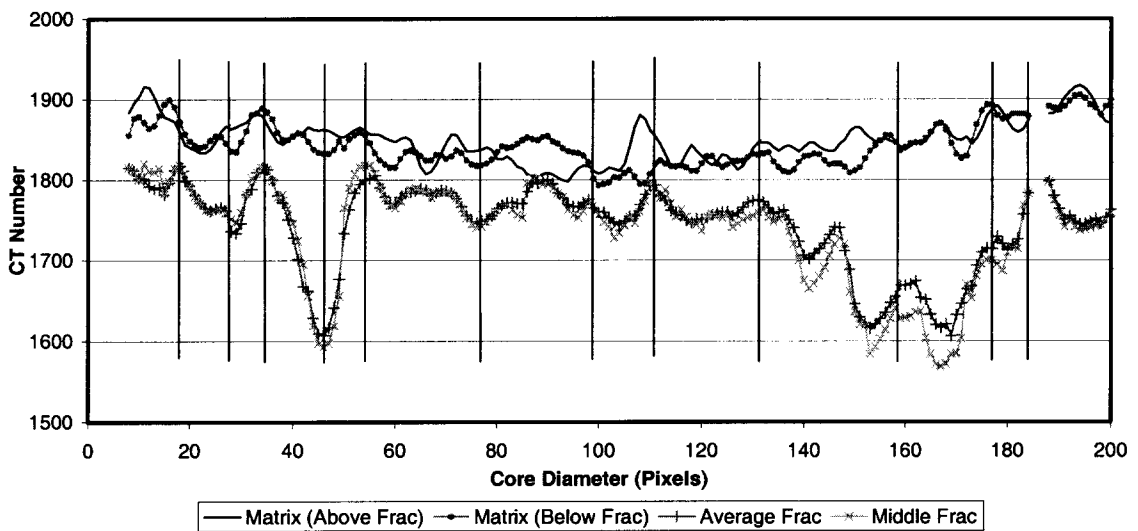


Figure 5-37: Comparison between profiles in the matrix and profiles in the fractured region of the NaI-tagged water image # 100. Scanner: HD250.

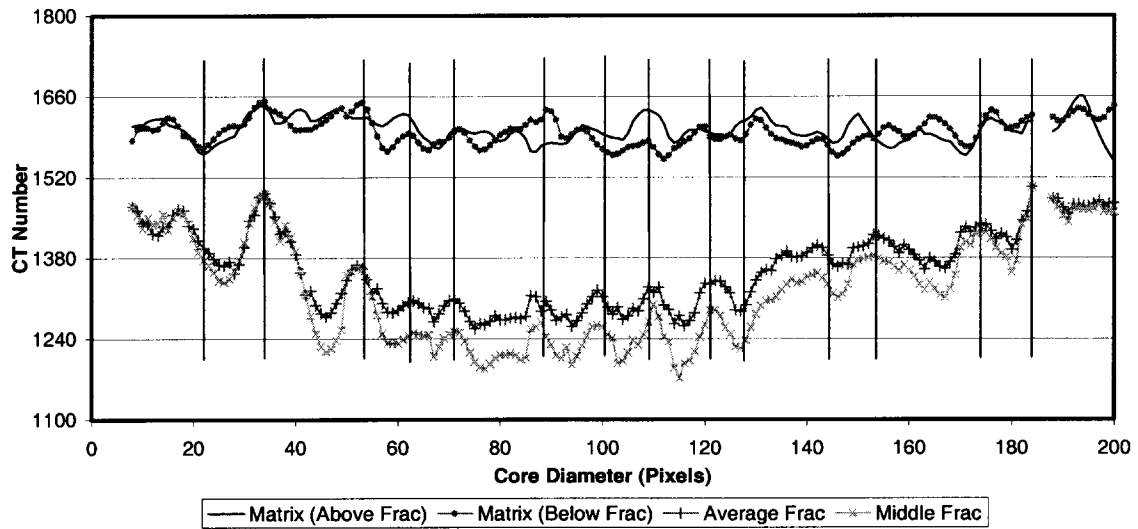


Figure 5–38: Comparison between profiles in the matrix and profiles in the fractured region of the distilled water image #100. Scanner: HD250.

The same analysis was done for image # 105 for all conditions: dry, tagged water and distilled water. The profiles are presented in Figure 5–39, Figure 5–40, and Figure 5–41, respectively. Again, a relationship between the CT values in the fractured region and its surrounding matrix is observed, principally for the dry and distilled water conditions.

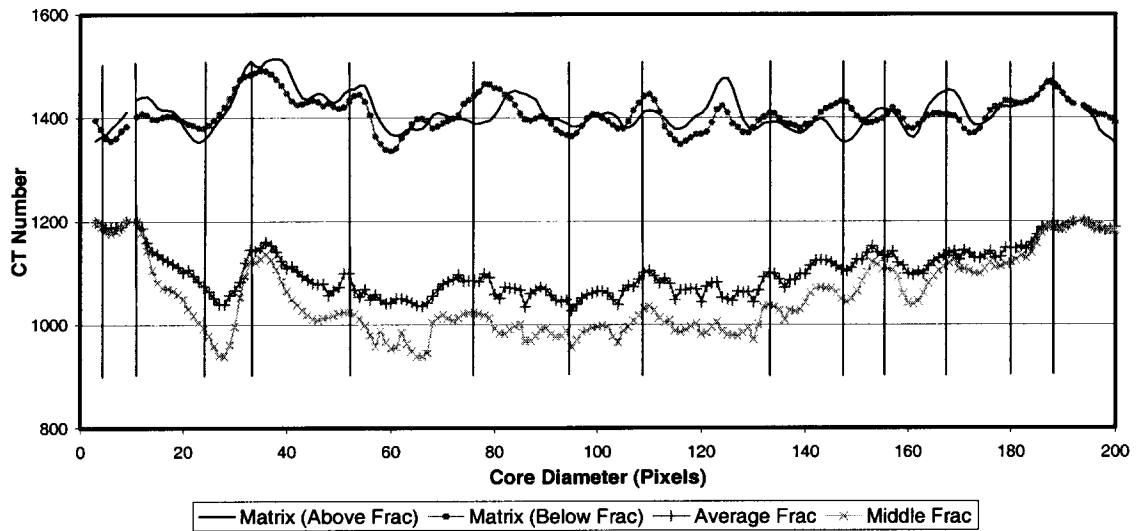


Figure 5-39: Comparison between profiles in the matrix and profiles in the fractured region of the dry image # 105. Scanner: HD250.

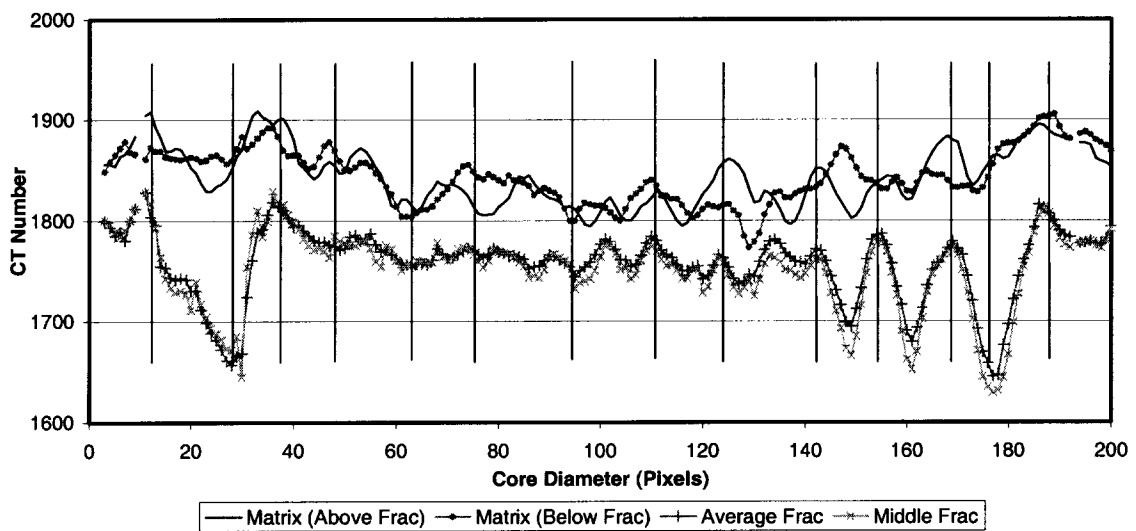


Figure 5-40: Comparison between profiles in the matrix and profiles in the fractured region of the NaI-tagged water image # 105. Scanner: HD250.

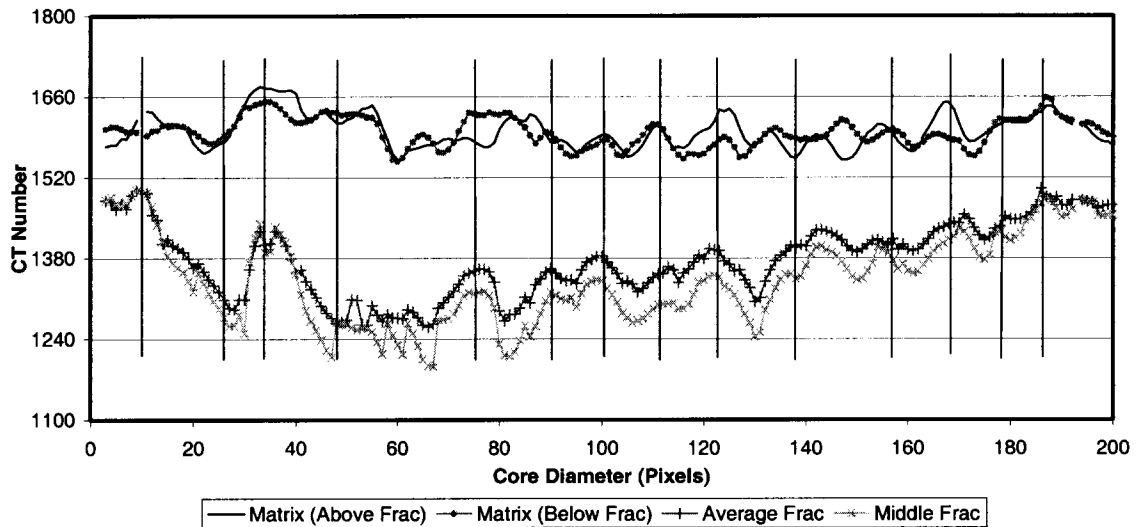


Figure 5-41: Comparison between profiles in the matrix and profiles in the fractured region of the distilled water image # 105. Scanner: HD250.

5.2.1.2 Porosity Distribution

The porosity distribution of the porous media, which is related to the aperture of the fracture, was determined by using the CT images and the average porosity calculated by material balance. Since the rock sample is lithologically homogeneous, the porosity distribution was determined using the following equation:

$$\phi^{\#} = \frac{CT_{Wet}^{\#} - CT_{Dry}^{\#}}{CT_{Ave,Wet} - CT_{Ave,Dry}} \times \phi_{Ave} \quad (5.1)$$

where the “#” symbol denotes a pixel-by-pixel value, and “Ave” denotes average.

All of the 191 dry and wet images were used to compute the basis for the porosity distribution. However, the analysis is focused on the 15 images that match the same location of the 15 averages obtained from the OMNI-X images.

Since two different sets of wet images were acquired with the HD250 medical scanner, two sets of porosity images were calculated. The porosity distribution using the NaI-tagged water is displayed in Figure 5–42 and Figure 5–43 displays the porosity images calculated with the distilled water images. The dark spectrum represents regions of low porosity while the bright spectrum represents regions of high porosity. The near horizontal bright feature represents the induced fracture.

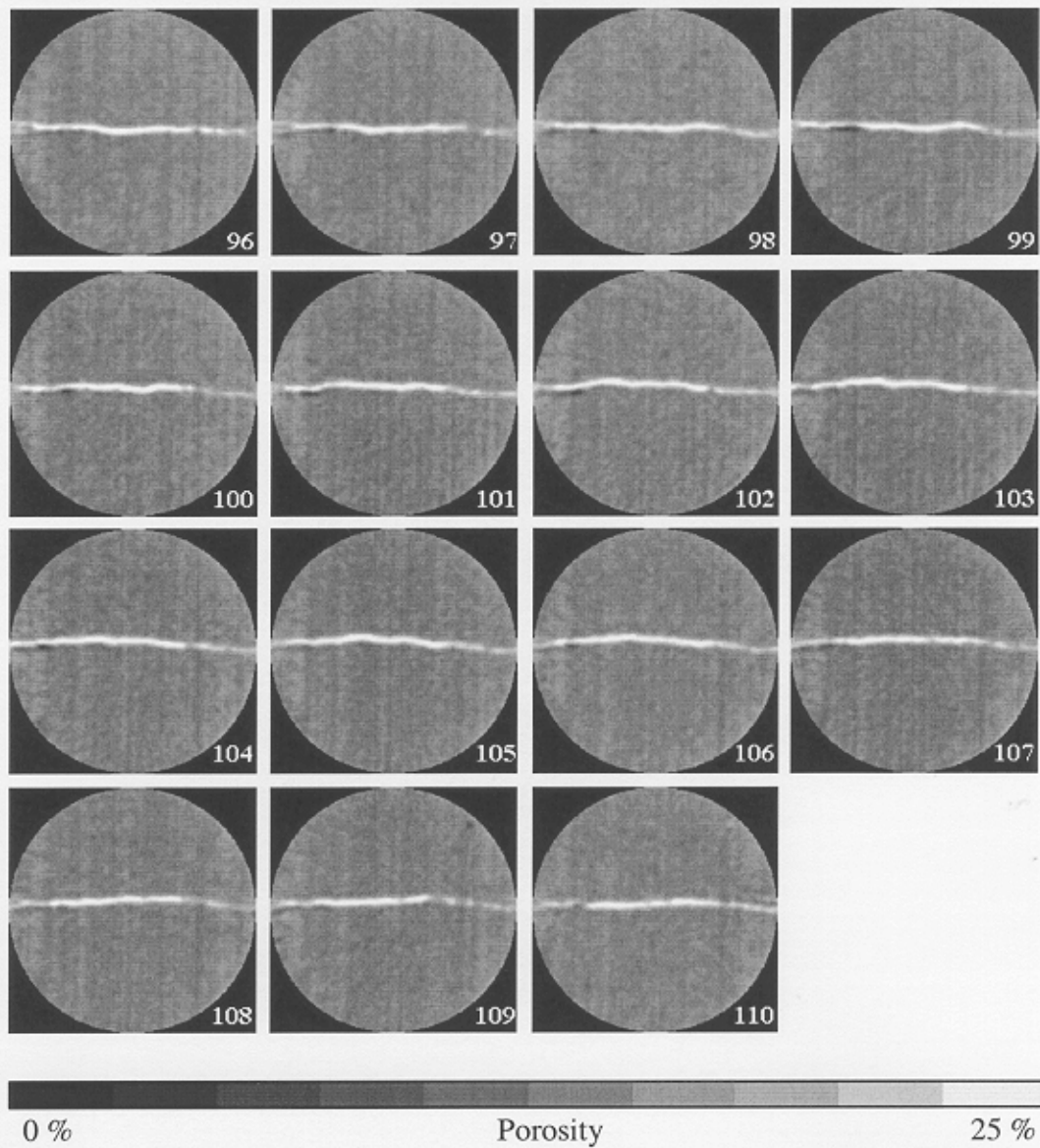


Figure 5-42: Plate of 15 porosity images calculated with the NaI-tagged water images acquired by the HD250 medical scanner.

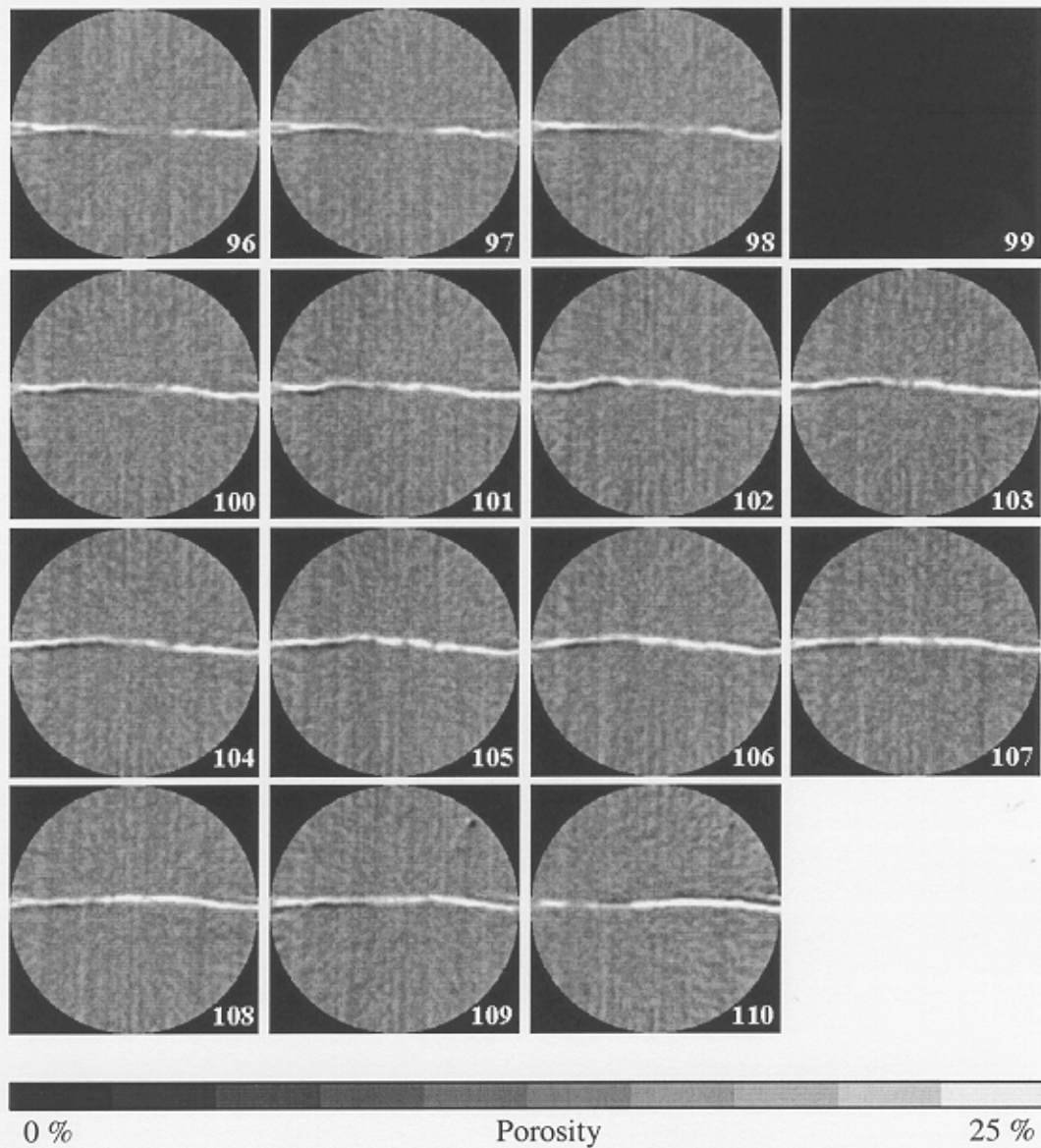


Figure 5-43: Plate of 15 porosity images calculated with the distilled water images acquired by the HD250 medical scanner.

A qualitative comparison of porosity profiles in the fractured region and its adjacent layers was performed. Figure 5-44 displays the profiles for the porosity image #96 calculated using the tagged water images and Figure 5-45 displays similar profiles

using the distilled water image #96. The relationship observed in the profiles of the dry and wet images is also observed in the porosity images.

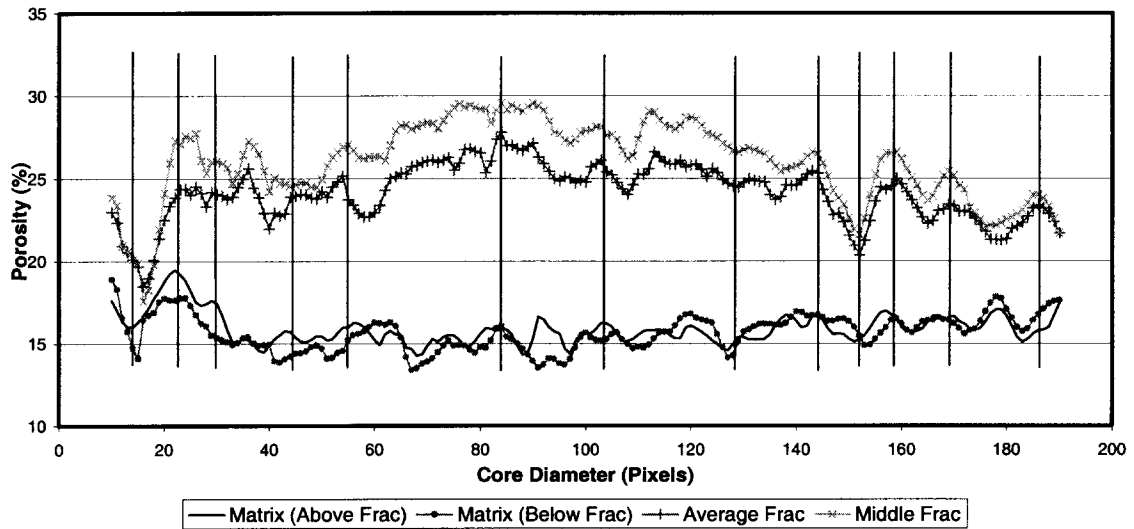


Figure 5-44: Comparison between porosity in the fractured region and the matrix calculated using NaI-tagged water images. Porosity image #96. Scanner: HD250.

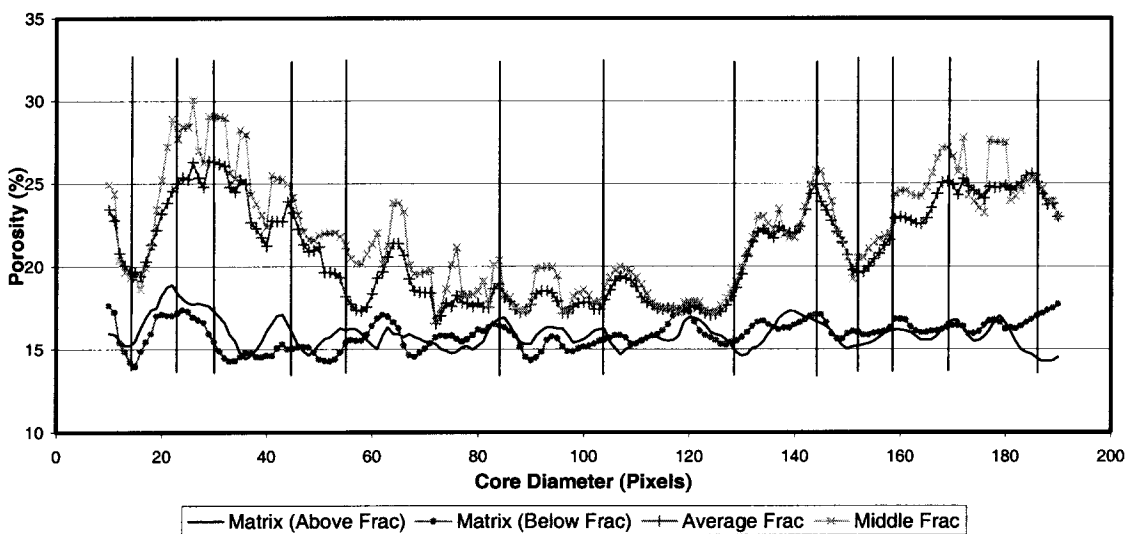


Figure 5-45: Comparison between porosity in the fractured region and the matrix calculated using distilled water images. Porosity image #96. Scanner: HD250.

The porosity profiles in the matrix for both conditions lead to similar values of porosity. However, the profiles in the fractured region do not show the same trend in the middle of the core, where the layers are not clearly delineated and have mainly low rock density, or high porosity. This is clearly observed in Figure 5–46, where the porosity profiles along the fractured region calculated for NaI-tagged water and distilled water conditions are compared. This deviation is mainly because the tagged water was not totally displaced after injecting 8.8 PV of distilled water. The tagged water is displaced rapidly in the fracture, especially in those points adjacent to high porosity layers, while the displacement process is slower in the matrix, resulting in a higher concentration of tagged fluid in the rock matrix far from the fractured region, and a low concentration of NaI water in the fracture. Then, the average CT difference between the wet and dry conditions (denominator of Equation 5.1) is larger than if the core were saturated only with distilled water. This average difference is also fixed. However, the difference between the CT numbers of the pixels for the wet and dry conditions (numerator of Equation 5.1) depends on the concentration of NaI in the pixels. In the fracture, where the concentration of tagged fluid is low, the difference is smaller, decreasing the corresponding calculated porosity.

Figure 5–46 also shows that the porosity calculated for the NaI-tagged and distilled water conditions are similar at the edges of the fracture, where layers of both high and low porosity are present. The presence of layers of high density next to the low density may be slowing down the displacement process in the fracture. Then, the

concentration of NaI-tagged water is higher at those points in the fracture, resulting in a higher porosity.

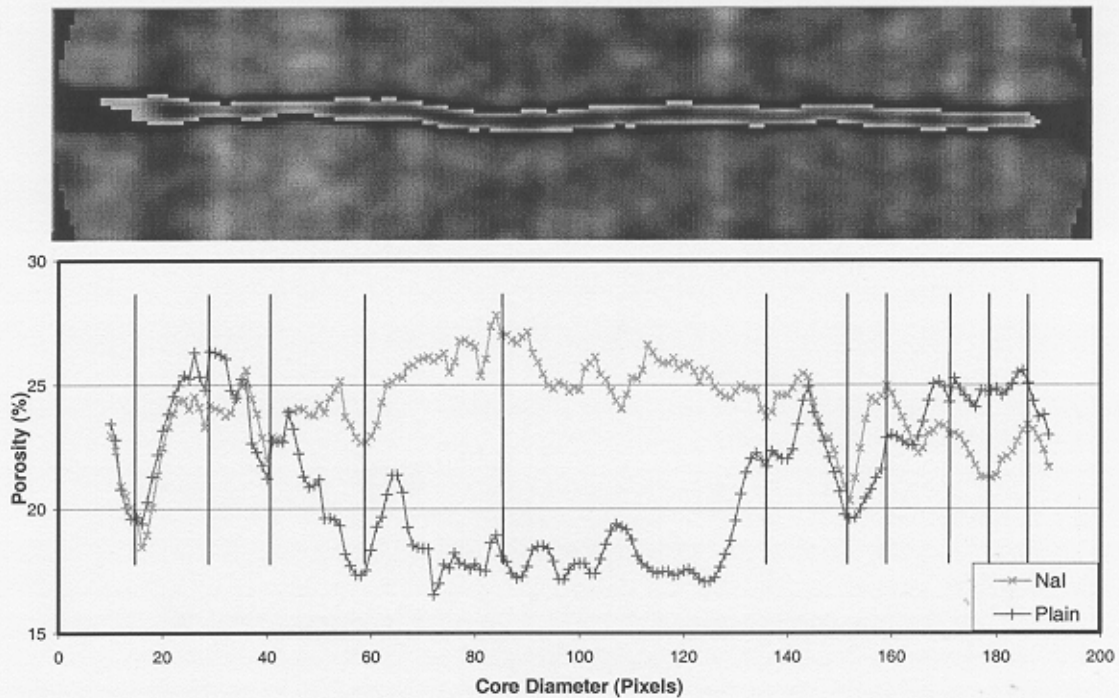


Figure 5-46: Comparison between porosity profiles for image #96. Scanner: HD250.

Figure 5-47 and Figure 5-48 show porosity profiles through the matrix and the fracture for the NaI-tagged and distilled water conditions in image #100, respectively. A relationship exists between the profiles in the fracture and the matrix for both conditions. However, the values of porosity differ from each other as displayed in Figure 5-49. The profile calculated with the distilled water images presents low porosity in the center of the profile, which is consequence of the uncompleted displacement process of the tagged water by the distilled water in the rock.

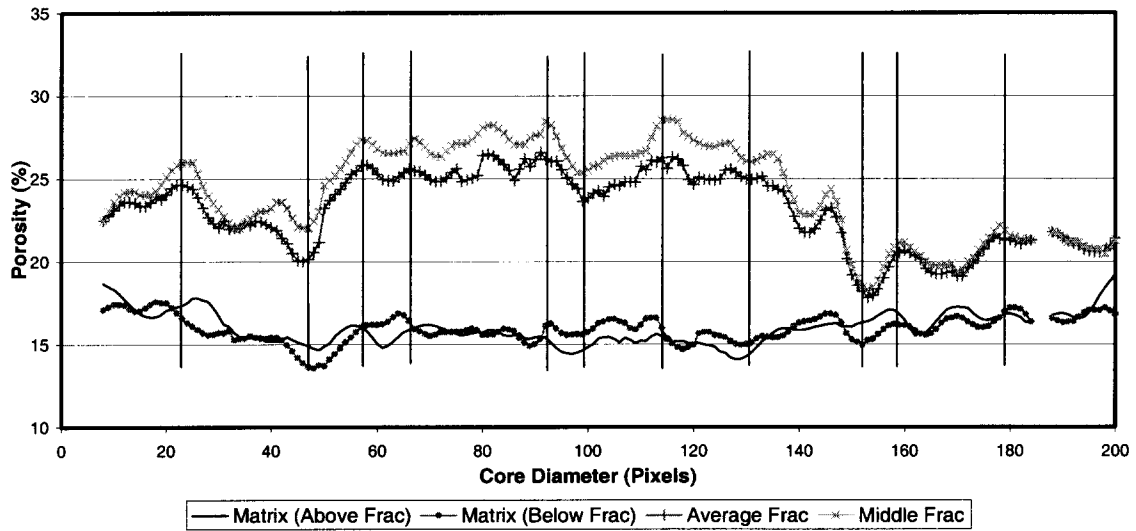


Figure 5-47: Comparison between porosity in the fractured region and the matrix calculated using NaI-tagged water images. Porosity image #100. Scanner: HD250.

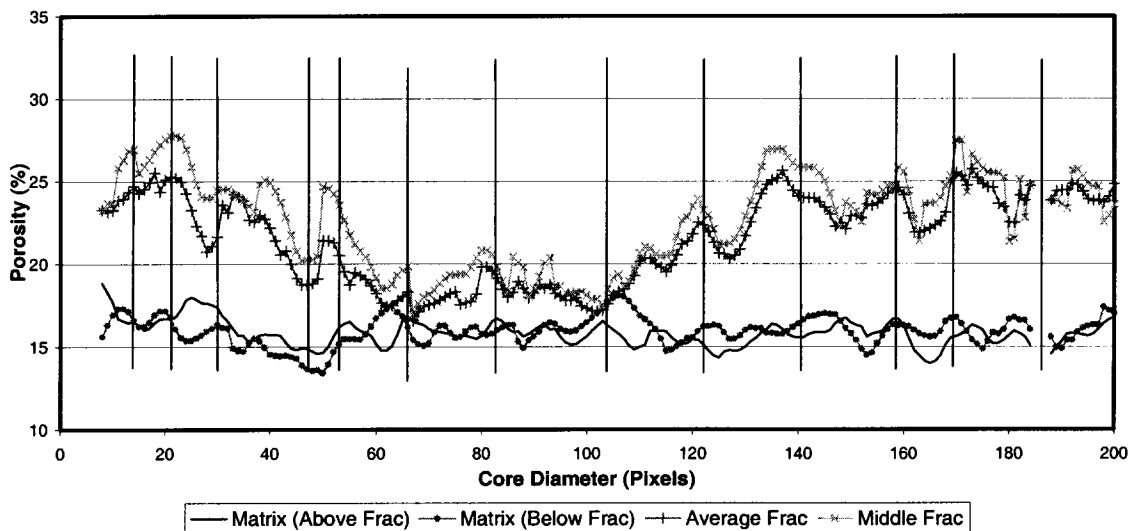


Figure 5-48: Comparison between porosity in the fractured region and the matrix calculated using distilled water images. Porosity image #100. Scanner: HD250.

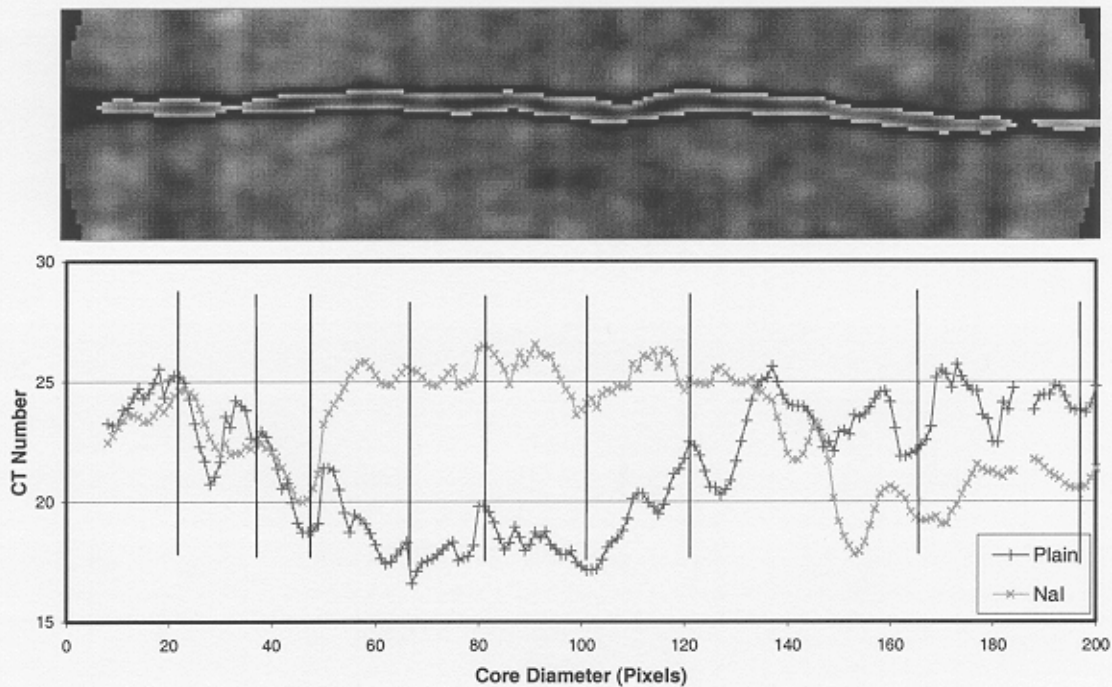


Figure 5-49: Comparison between average porosity profiles in the fracture for image #100. Scanner: HD250.

Figure 5-50 and Figure 5-51 show porosity profiles through the fractured region and the matrix for the NaI-tagged and distilled water conditions in image #105, respectively. The relationship between the porosity distribution in the matrix and the fracture is not clear in these profiles. Figure 5-52 compares the porosity profiles in the fractured region. The calculated porosity, in general, is higher for the NaI-tagged water condition.

In summary, three locations were arbitrarily selected to demonstrate the effect of flooding the sample with distilled water. The resulting responses are not fully conclusive because it was not possible to scan the entire core at all time intervals. The remaining NaI

in the core impacted the calculation of local porosity values. Thus, the flooding experiment is incomplete.

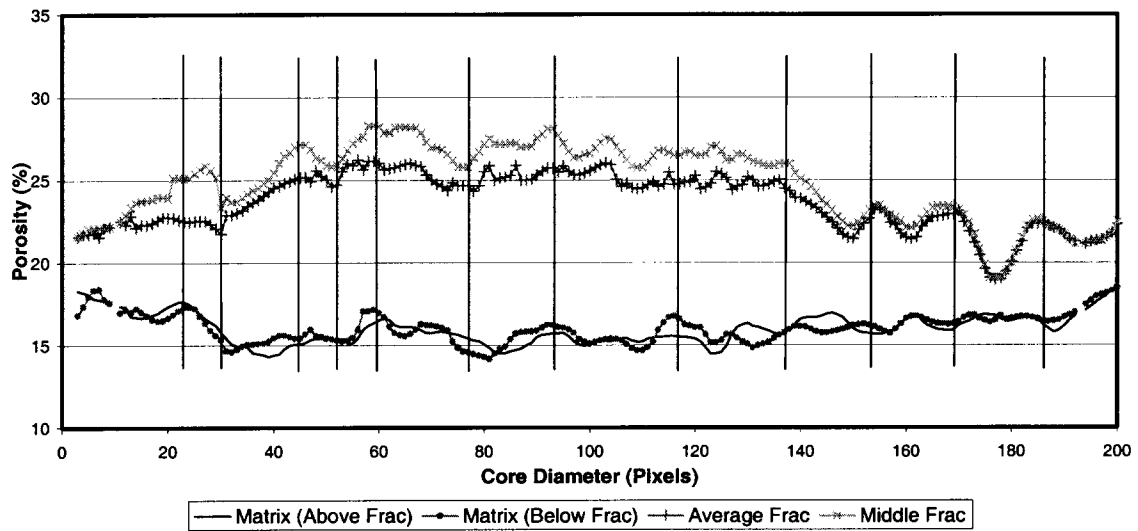


Figure 5–50: Comparison between porosity in the fractured region and the matrix calculated using NaI-tagged water images. Porosity image #105. Scanner: HD250.

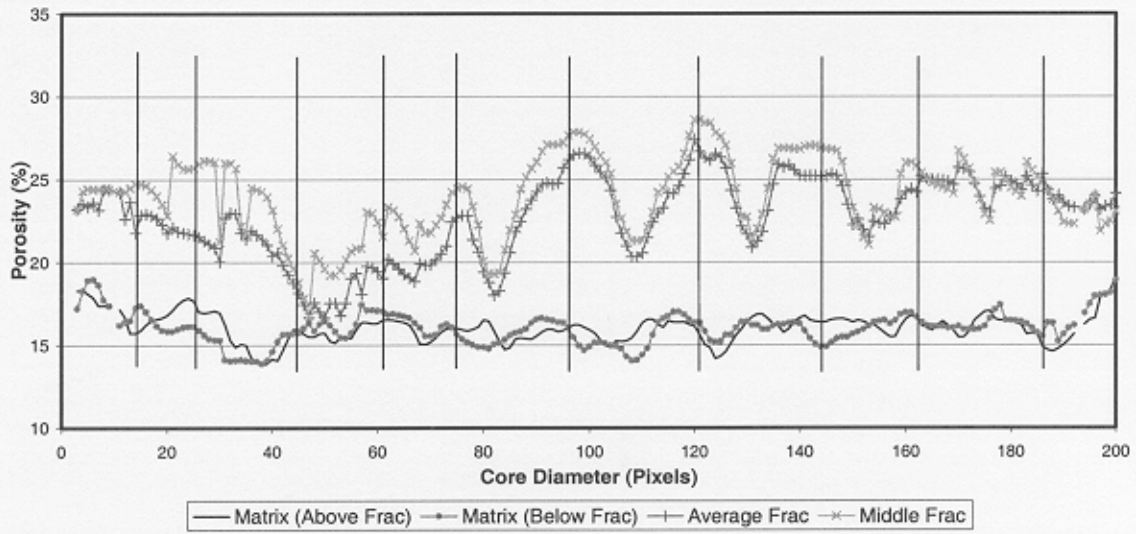


Figure 5-51: Comparison between porosity in the fractured region and the matrix calculated using distilled water images. Porosity image #105. Scanner: HD250.

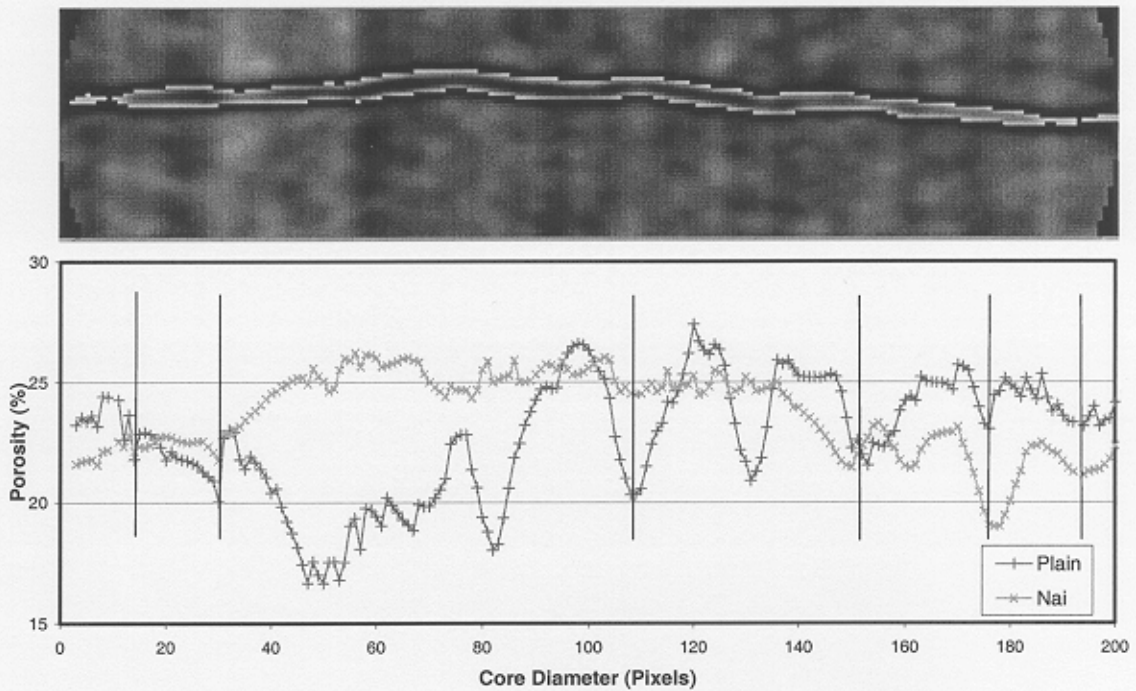


Figure 5-52: Comparison between porosity profiles in the fractured region for image #105. Scanner: HD250.

5.2.2 Industrial Scanner OMNI-X.

A total of 330 images were acquired in single-scan mode by the industrial scanner OMNI-X, with a thickness of 91 mm, covering 30 mm of the core. These images were only reconstructed at one level, 512x512 pixels per image, since it requires less computer storage than the 1024x1024 level of reconstruction, reducing the manipulation time. At the same time this level provides a better resolution than the 256x256 one. In order to compare with the images scanned by the HD250 scanner, the images acquired by the OMNI-X were stacked in groups of 22 to obtain images 2 mm thick, resulting in 15 averages.

Figure 5–53 displays the 15 dry averaged images while Figure 5–54 shows 15 NaI-tagged water averaged images at the same location. The layers and the fractured region are better exposed in the dry images.

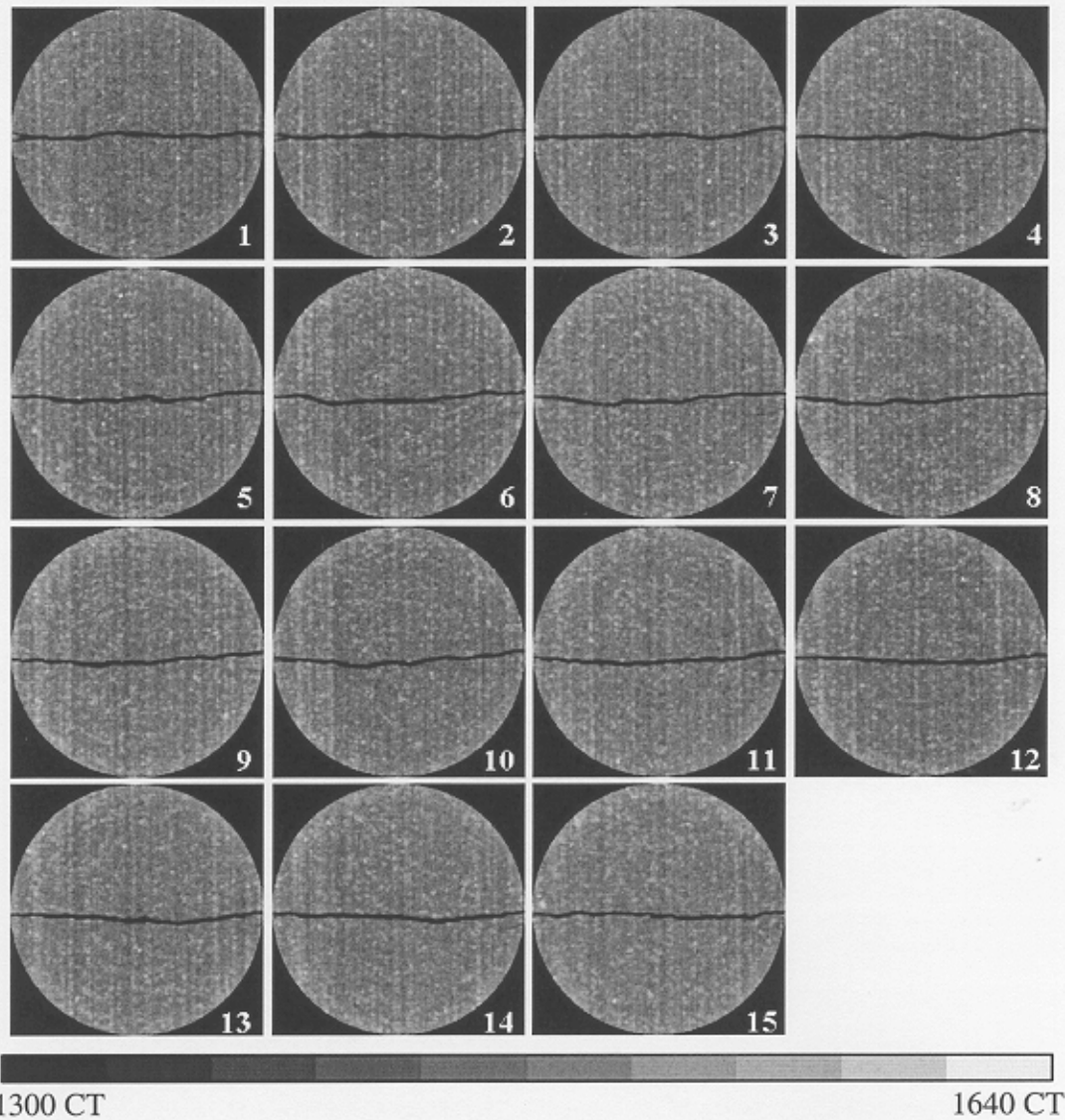
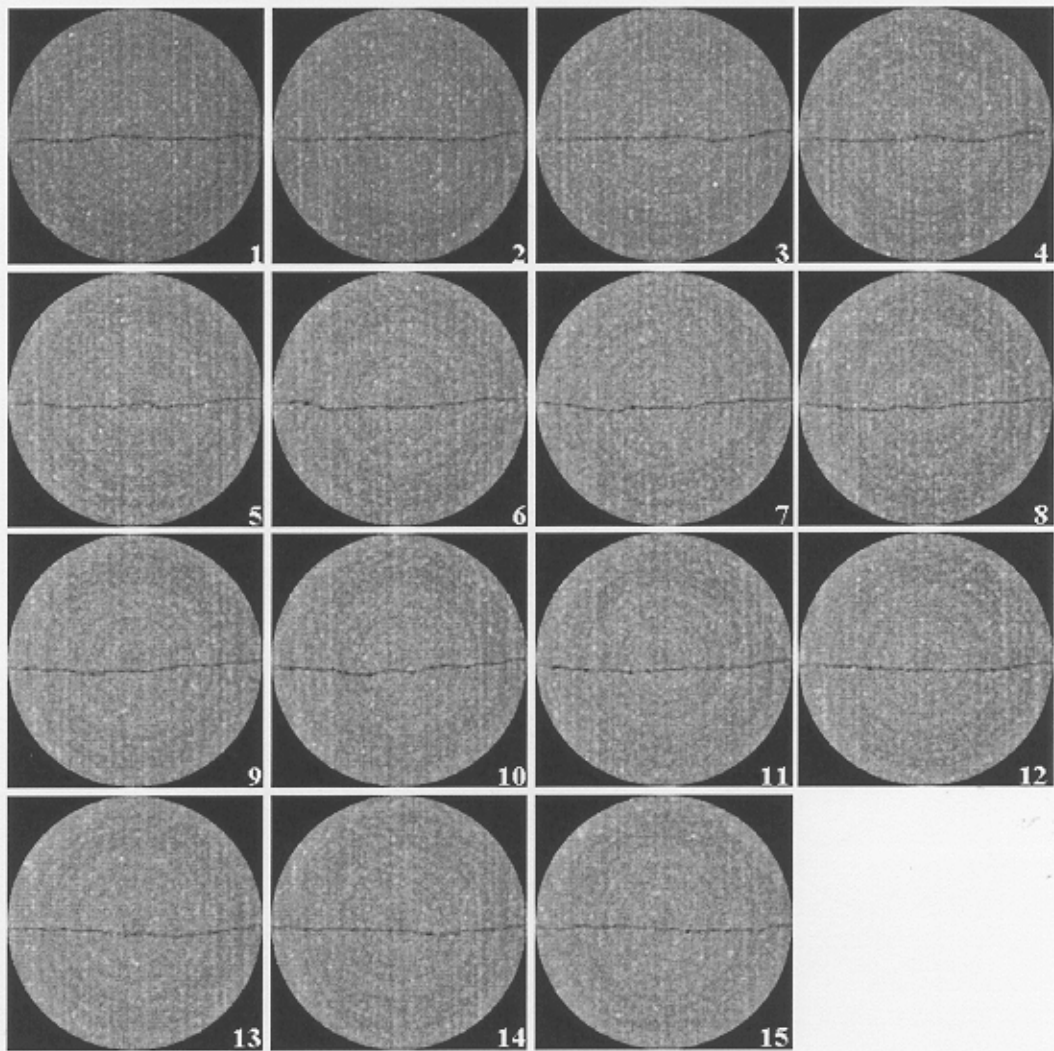


Figure 5-53: Plate of 15 averaged dry images scanned by the OMNI-X scanner.



1450 CT

1700 CT

Figure 5-54: Plate of 15 averaged NaI-tagged water images scanned by the OMNI-X scanner.

5.2.2.1 CT Profile Analysis

The dry images were used to identify the fractured region since the high attenuation of the tagged water affects the appearance of the fracture in the wet images. Because of the difference in resolution that the two scanners provided, and also because of the different calibration, the CT number spectrum of the OMNI-X images is higher than that of the HD250 images. These CT numbers are arbitrary and are not an intensive property of the scanned material. Therefore, the range of CT numbers used to identify the fracture in the OMNI-X images was different than the ones used in the HD250 images. In the OMNI-X images the pixels with CT values between 500 and 1350 were identified as part of the fracture while the pixels with CT values above 1350 were considered as part of the matrix. After detecting the fracture, different profiles in the fracture and in the matrix were performed, similar to those generated for the HD250 images.

Figure 5–55 shows a section of 512x80 of an averaged dry image acquired with the OMNI-X, as well as the CT number profile through the fractured region. The fractured region was highlighted artificially by adding 150 CT units to the CT values of each pixel that belongs to the fractured region.

A profile through the middle of the fractured region, shown in Figure 5–56, was generated in order to minimize the contrast effect between the rock material and the fracture fill. The curve is smooth when compared with the previously averaged profile. However, both graphs exhibit similar tendencies.

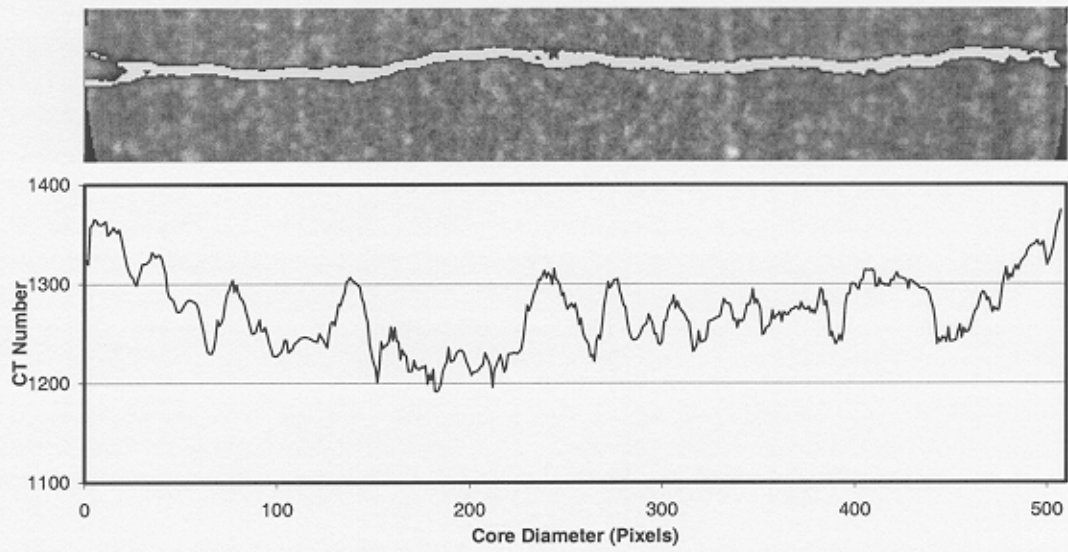


Figure 5-55: Average CT numbers profiled along the fracture in the first averaged dry image. OMNI-X scanner.

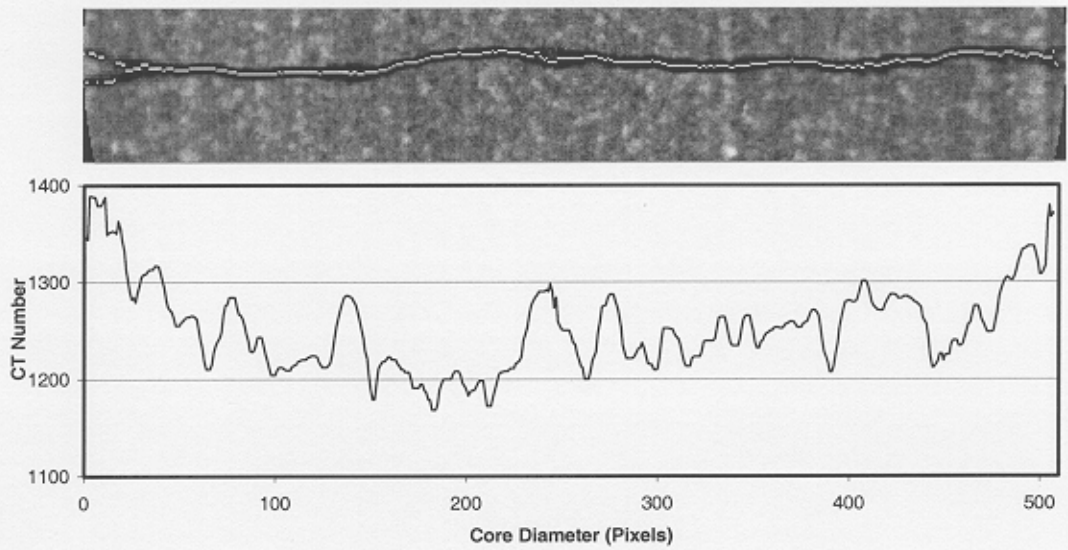


Figure 5-56: CT number profile along the middle of the fracture in the first averaged dry image. OMNI-X scanner.

Figure 5–57 shows average profiles of four vertical pixels, four pixels above and below the fracture, as well as their location in the image. The profiles were determined following the shape of the edges above and along the core diameter because of the heterogeneous nature of the rock at the imaging scale. The high resolution of the industrial scanner allows the detection of the small inclusion even in the averaged images. Then, the comparison between profiles generated with the OMNI-X images is not as easy as with the HD250 images. However, some homogeneous layers in the vertical direction are identified, where both profiles exhibit the same shape.

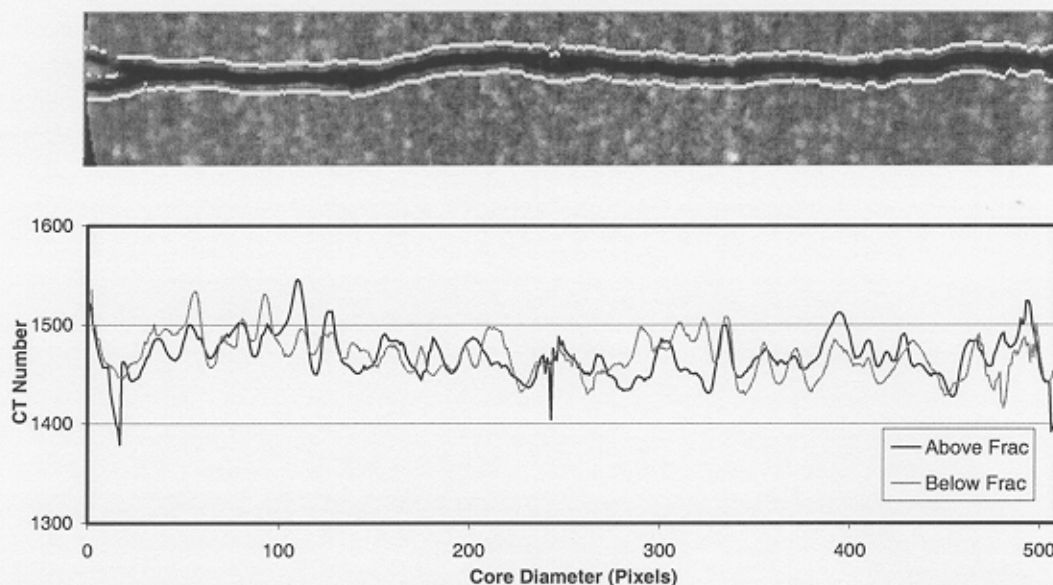


Figure 5–57: CT profiles through the matrix four pixels above and below the fractured region in the first averaged dry image. Scanner: OMNI-X.

Figure 5–58 compares the profiles in the fractured region and its surrounding matrix for the first averaged dry image. Since the industrial scanner provides a very high resolution, the CT profiles are strongly affected by the local heterogeneities of the rock.

Then, the analysis was done where the layers are mainly homogeneous in the vertical direction. However, even if the layer appears to be homogeneous, a heterogeneity in the fracture could be affecting the corresponding profile.

The vertical marks on Figure 5–58 show some of the places in which the matrix above and below the fracture is quite continuous exhibiting a relation to the fracture.

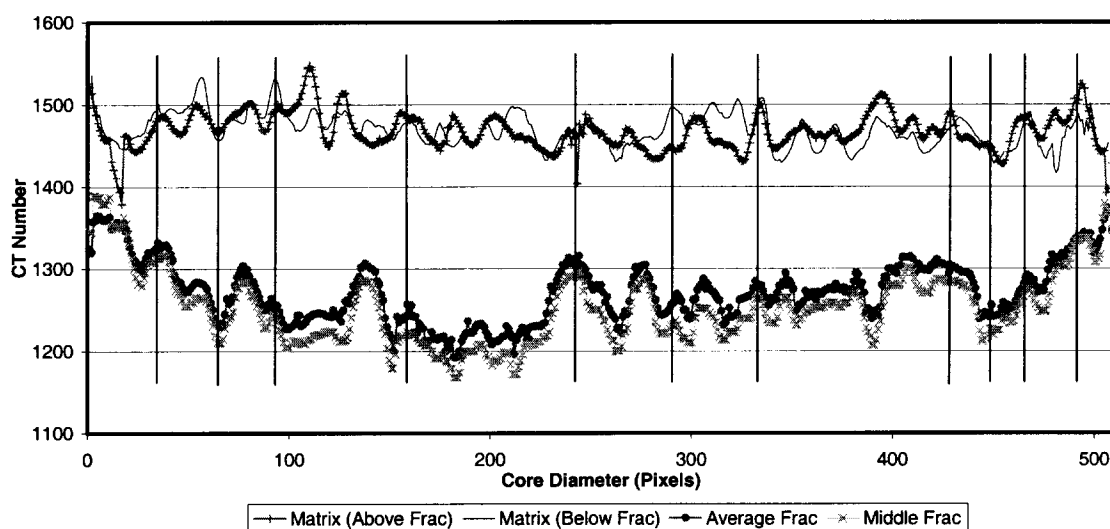


Figure 5–58: Comparison between profiles in the matrix and profiles in the fractured region in the first dry averaged image. Scanner: OMNI-X.

A similar analysis was performed for the wet images. Figure 5–59 compares the CT number of the fractured region under dry and wet conditions. Again, the high attenuation of the tagged fluid affects the shape of the wet profile. Nevertheless, this effect is not observed when the profiles are generated in the matrix, as shown in Figure 5–60 and Figure 5–61. There is a strong correspondence between the CT value in the fracture and the CT values in the adjacent matrix.

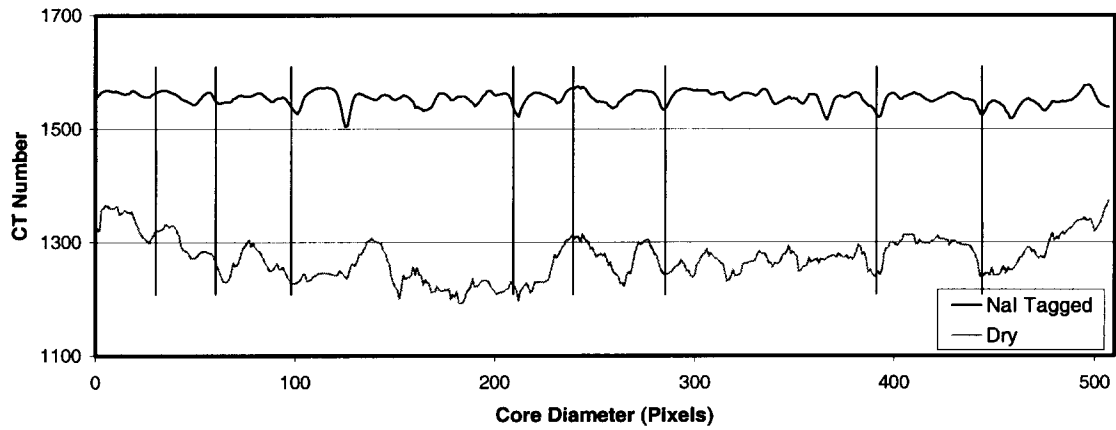


Figure 5-59: Average CT profile through the fractured region for first dry and wet averaged images. Scanner: OMNI-X.

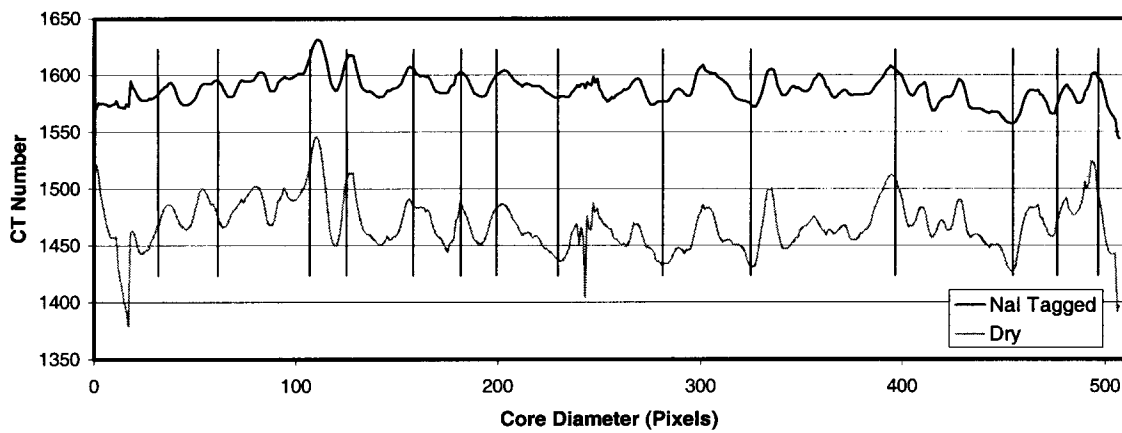


Figure 5-60: Profiles four pixels above the fracture for the first dry and wet averaged images. Scanner: OMNI-X.

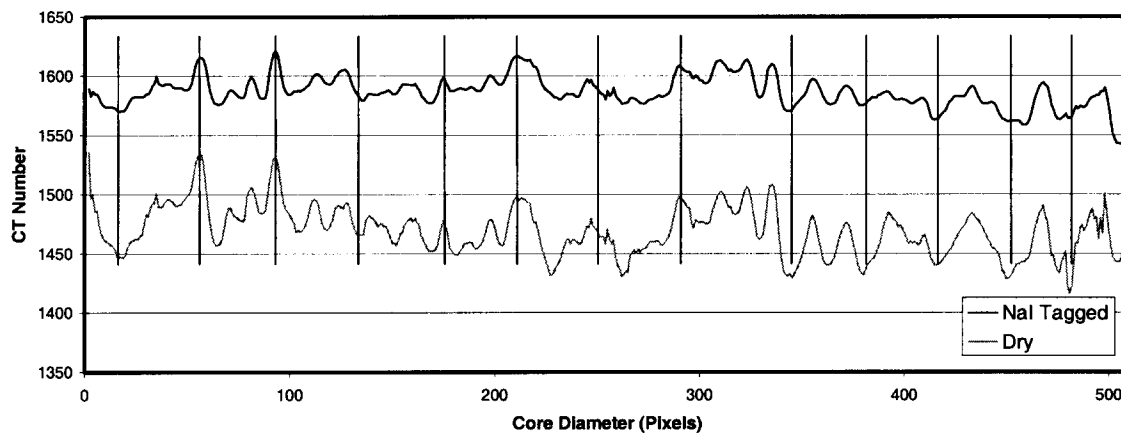


Figure 5–61: Profiles four pixels below the fracture for the first dry and wet averaged images. Scanner: OMNI-X.

Figure 5–62 displays the CT profiles through the fracture and its surrounding matrix for the wet condition. The attenuation of the tagged fluid, in addition to the high resolution of the industrial scanner, complicates the analysis. However, similarly to the analysis for the dry condition, the relationship is found in some points where the layers are in general vertically homogeneous.

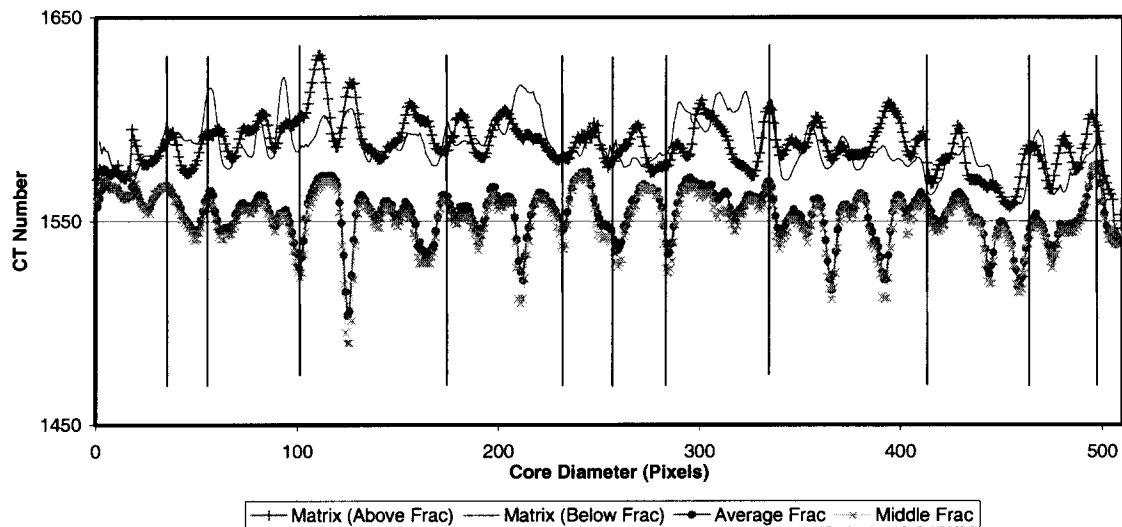


Figure 5–62: Comparison between profiles in the matrix and profiles in the fractured region of the first NaI-tagged averaged image. Scanner: OMNI-X.

Similar analyses were performed for dry and wet averaged images at different locations in the core sample. Figure 5–63 and Figure 5–64 present the profiles of the averaged image #5 for the dry and wet conditions, respectively. Figure 5–65 and Figure 5–66 display similar profiles of the averaged image #10 for the dry and wet conditions, respectively. The vertical marks show some points in which there is a relationship between the fracture and the layers of the rock. The relationship is not as clear as it was demonstrated in the HD250 images due to the difference of resolution of the scanners.

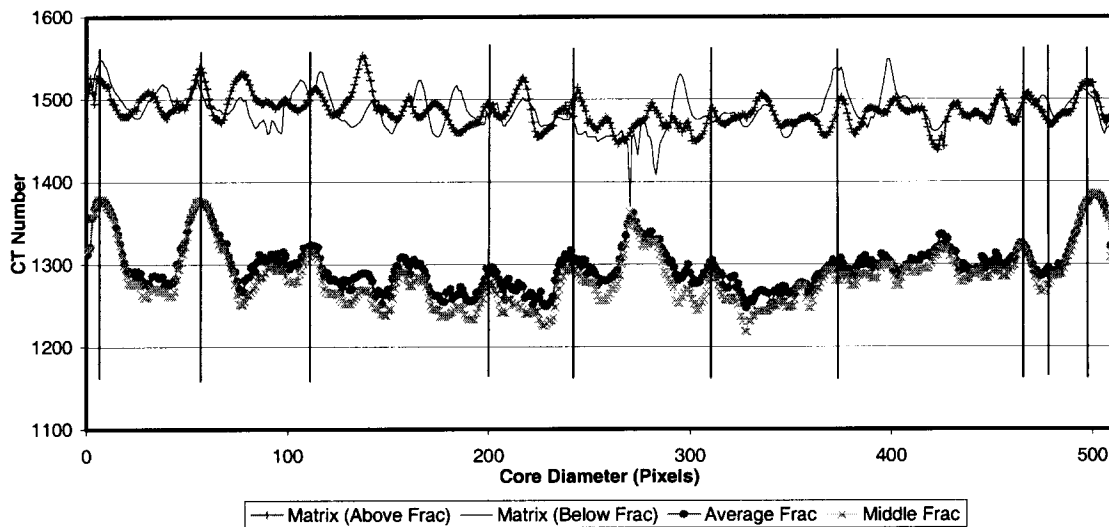


Figure 5-63: Comparison between profiles in the matrix and profiles in the fractured region in the fifth dry averaged image. Scanner: OMNI-X.

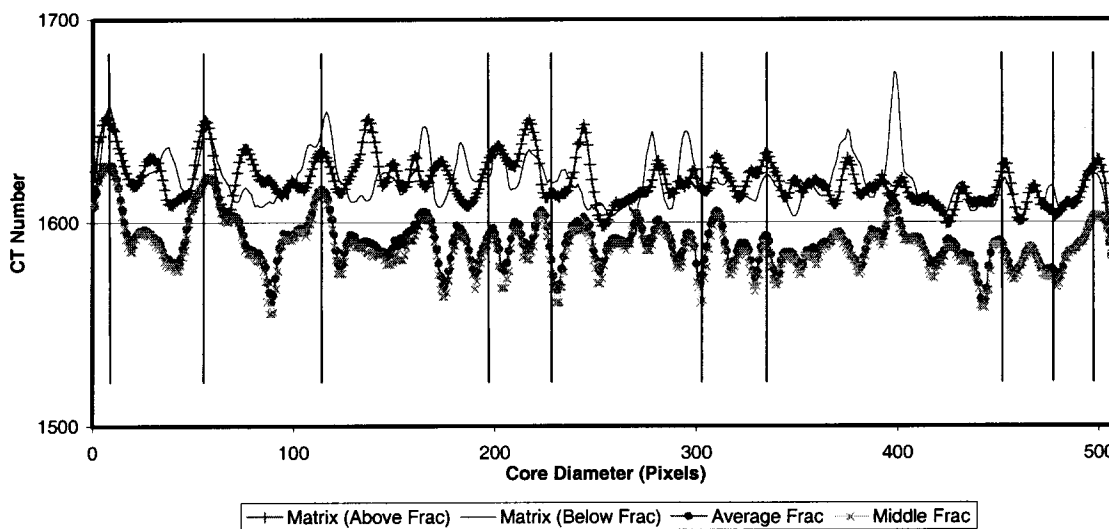


Figure 5-64: Comparison between profiles in the matrix and profiles in the fractured region of the fifth NaI-tagged averaged image. Scanner: OMNI-X.

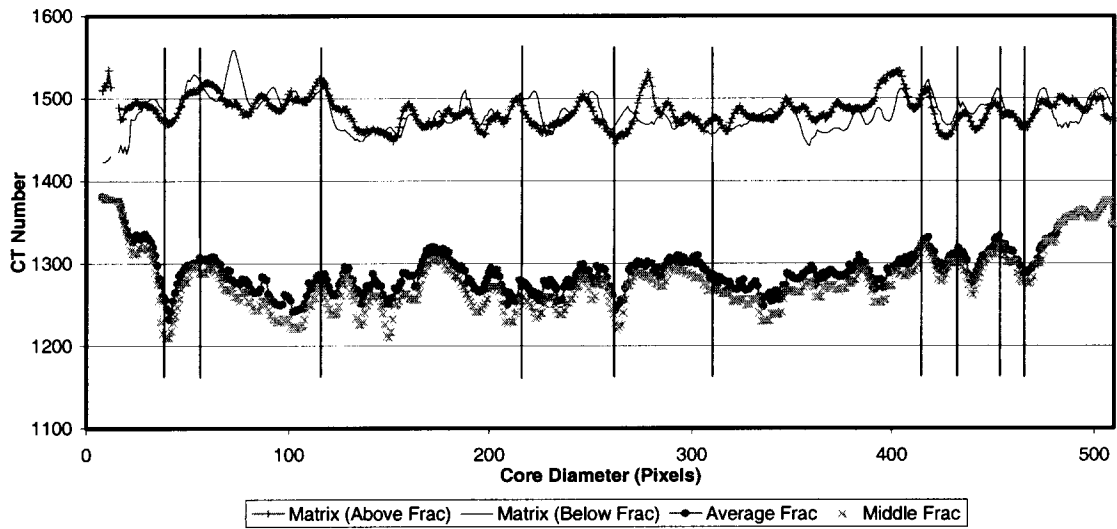


Figure 5-65: Comparison between profiles in the matrix and profiles in the fractured region in the tenth dry averaged image. Scanner: OMNI-X.

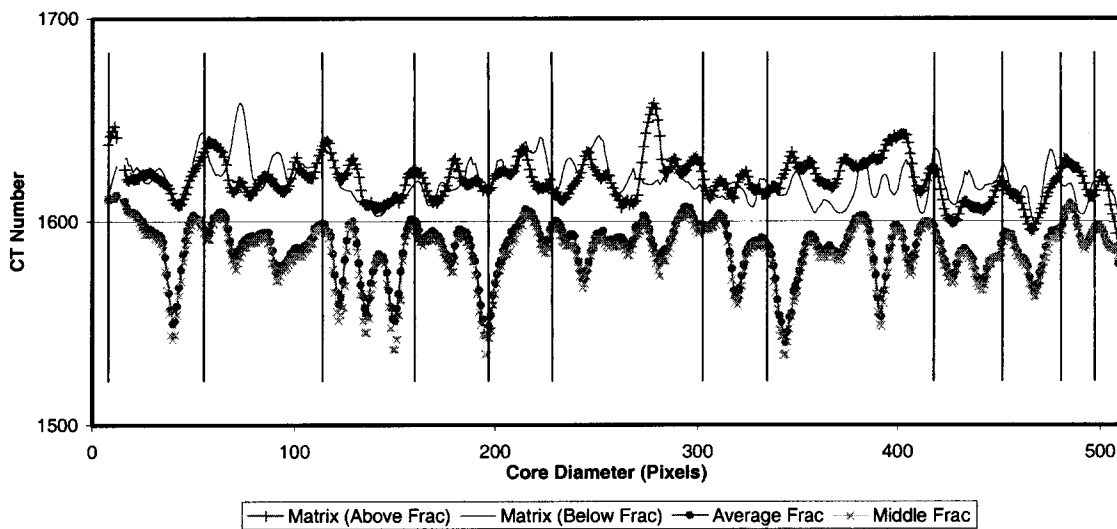


Figure 5-66: Comparison between profiles in the matrix and profiles in the fractured region of the tenth NaI-tagged averaged image. Scanner OMNI-X.

5.2.2.2 Porosity Distribution

Porosity distribution was calculated using the 15 averaged dry and wet images acquired by the industrial scanner, OMNI-X, in the same method that was used to with the images acquired by the HD250 scanner. Figure 5–67 displays a plate of 15 porosity averaged images. The dark spectrum represents regions of low porosity while the bright spectrum represents the regions of high porosity. The layers of the core sample are well exposed as well as the fracture, which is the near horizontal bright feature. Since the porosity images can be considered as net NaI water in the rock, the presence of the layers in these images indicates that more water was absorbed by the layers of high porosity and less water by the layers of high rock density or low porosity.

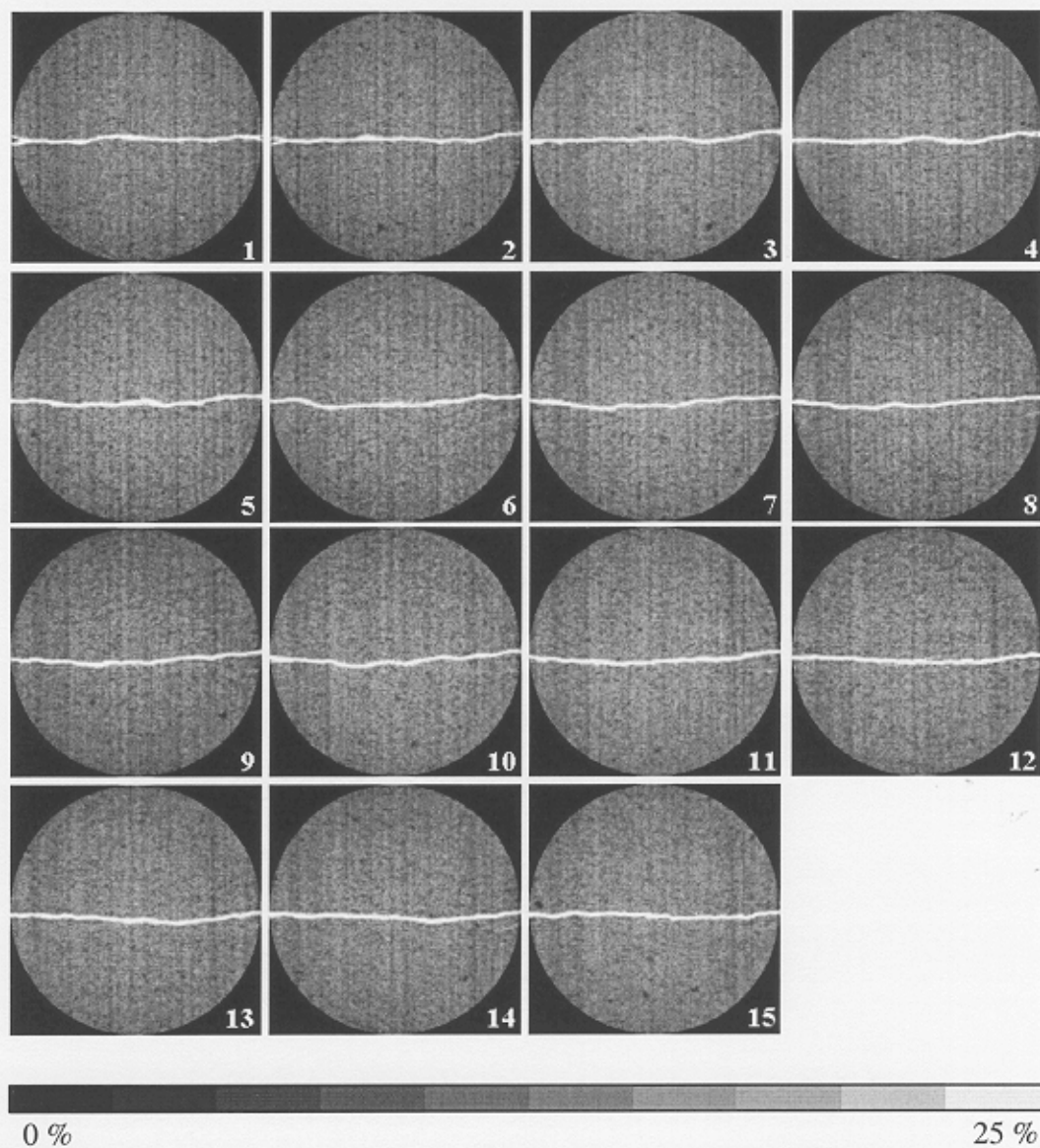


Figure 5-67: Plate of 15 porosity images calculated with the averaged images from the Scanner: OMNI-X.

Profiles through the fracture and the adjacent layers in the matrix were prepared. Figure 5-68 displays these profiles in the averaged porosity image #1. Again, the analysis is limited to those points in which the layers are mainly continuous in the vertical

direction. The relationship is more evident than the one found in the dry and wet images because the subtraction of these images removed the presence of the heterogeneities or inclusion in the rock sample. The profiles in the fractured region exhibit a wider range because of the variation of the fracture fill in comparison to the profiles in the matrix.

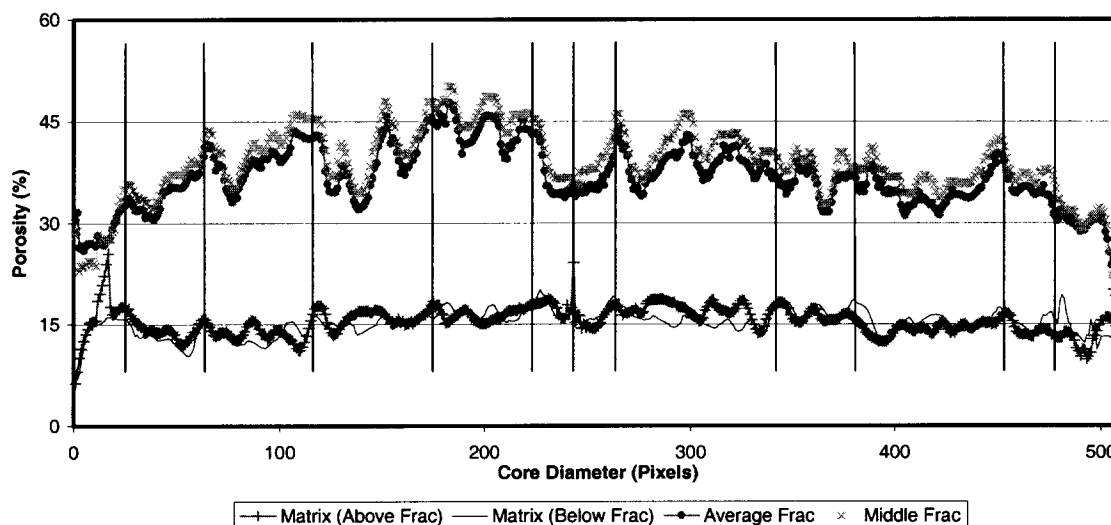


Figure 5–68: Comparison between porosity profiles in the matrix and profiles in the fractured region in the first averaged porosity image. Scanner: OMNI-X.

Figure 5–69 and Figure 5–70 display similar profiles of the average porosity images #5 and #10, respectively. The relationship between the porosity of the fractured region and its adjacent layers is present when the layers are mainly continuous. It is not expected to have a high porosity in the fracture adjacent to all high porosity layers. However, there are indications that there is a strong tendency for this relationship to occur.

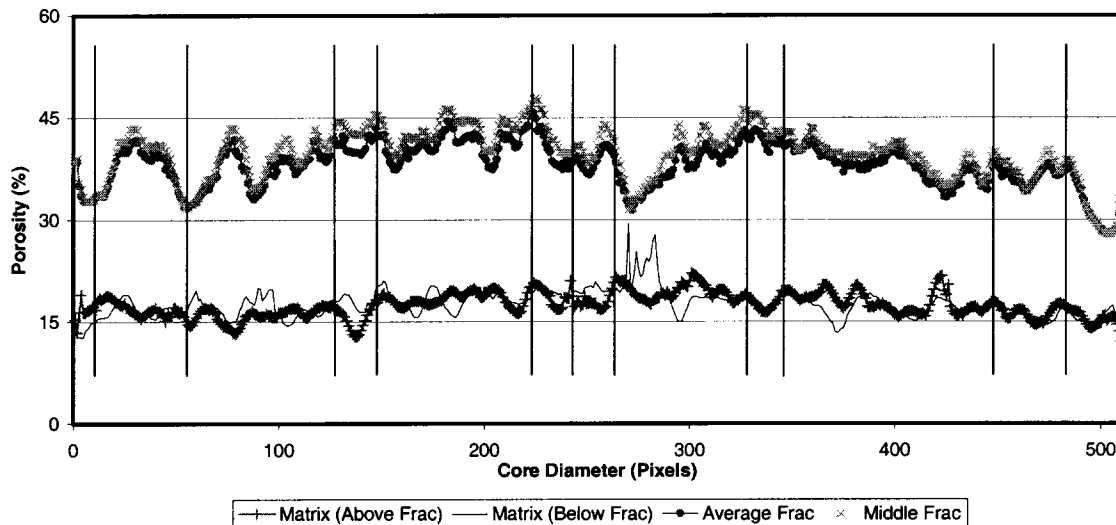


Figure 5-69: Comparison between porosity profiles in the matrix and profiles in the fractured region of the averaged porosity image #5. Scanner: OMNI-X.

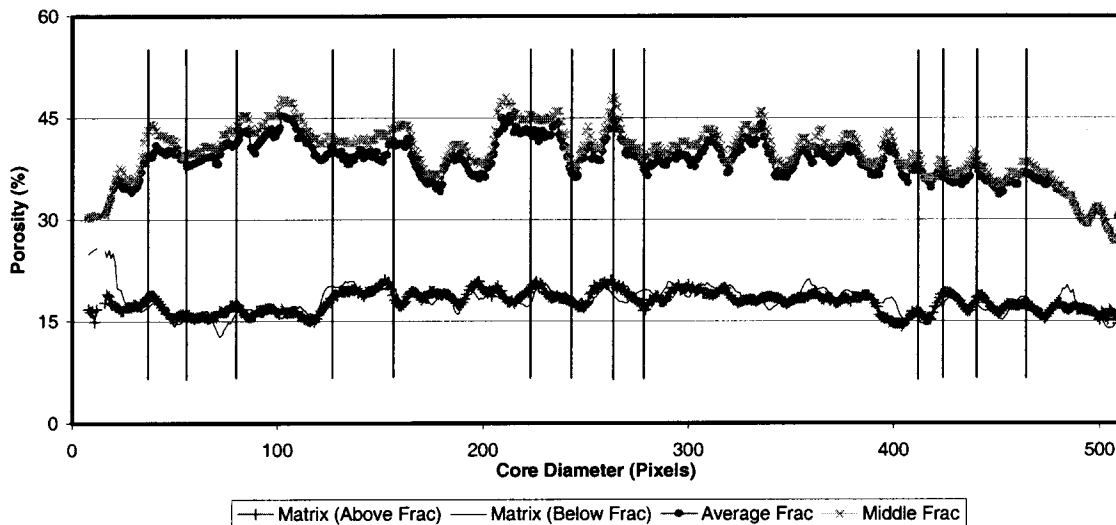


Figure 5-70: Comparison between porosity profiles in the matrix and profiles in the fractured region in the averaged porosity image #10. Scanner: OMNI-X.

5.3 Comparison of Profiles Generated with the Data Acquired by both Scanners

The profiles generated with the data acquired by the OMNI-X were strongly affected by the fact that the small inclusions or heterogeneities in the core were detected even in the averaged images.

Figure 5–71 displays the dry profiles in the fractured region generated with data from both scanners. In general, both profiles show a similar trend. Figure 5–72 displays the profiles in the matrix, above the fracture region, for the same images as in Figure 5–71. The trend of these profiles differs appreciably because the OMNI-X is able to detect the very small homogeneities in the core. This deviation in the profiles is more obvious in the matrix since the particles are more compact. The profiles generated in the fracture include mainly the empty space of the fracture. Additional work is needed to increase the accuracy of the repeatability of the registration of the scans acquired by the two scanners.

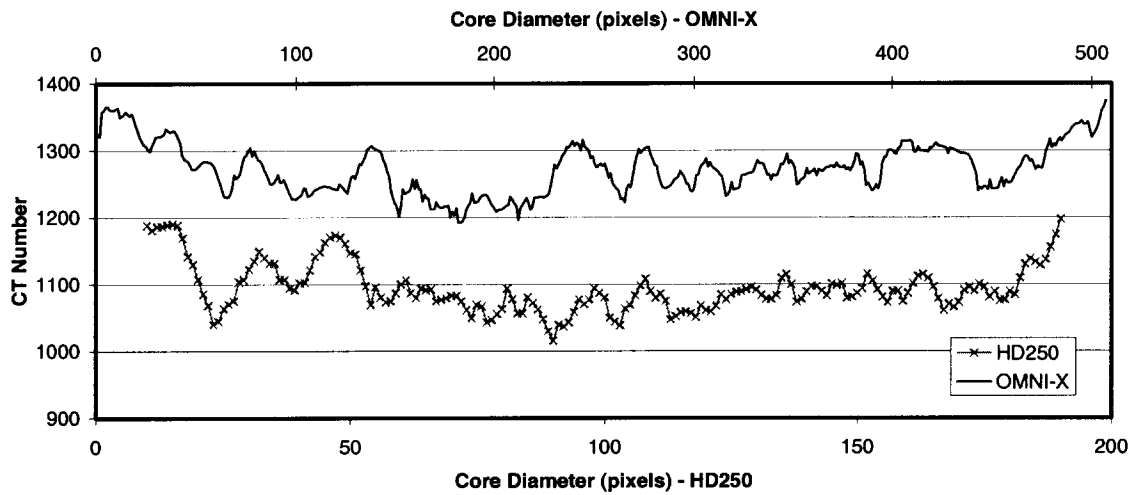


Figure 5-71: Profiles through the fractured region generated with the data acquired by both scanners. HD250 dry image #96 and averaged OMNI-X dry image #1.

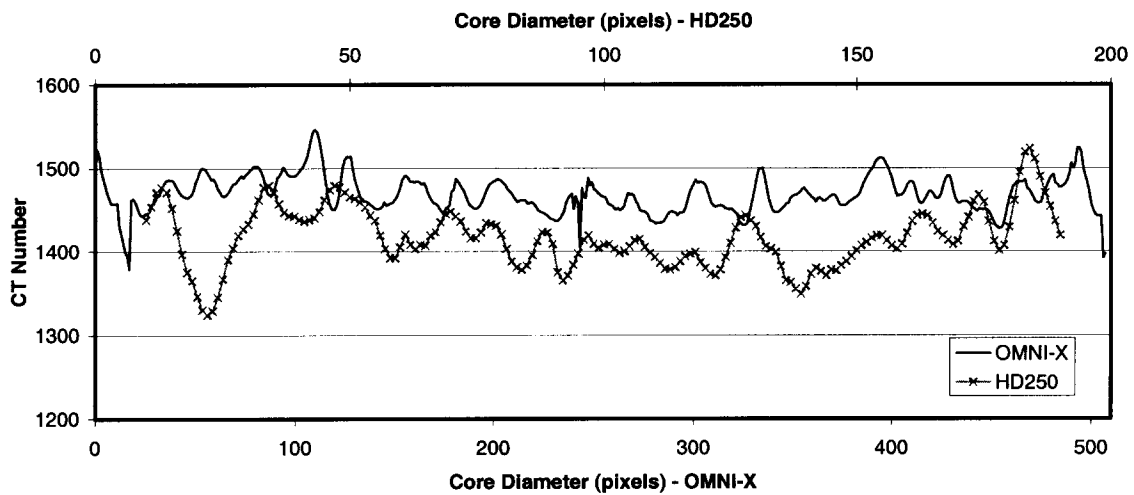


Figure 5-72: Profiles above the fractured region generated with the data acquired by both scanners. HD250 dry image #96 and averaged OMNI-X dry image #1.

Similar comparison of profiles was done with the porosity. Figure 5–73 shows the porosity distribution in the fractured region. The OMNI-X porosity profile exhibits higher porosity values because of the higher resolution that this equipment provides. Since the pixel size is small in the OMNI-X images, the empty space of the fracture dominates the calculations, resulting in a higher porosity. Since the pixel size of the HD250 images is large, the detected fractured region includes not only the fracture but also part of the matrix, decreasing the calculated porosity. This is in agreement with the observation that the fracture width appears to be larger in the HD250 images. Porosity values of 100% indicate that the fracture is totally empty, and the pixels in the fracture region represent the fracture exclusively. This also explains why the real fracture width cannot be estimated from the acquired HD250 data. The resolution of the scanner and also the contrast between the rock material and the fracture fill affect the registration of the fracture width, even in the OMNI-X scanner. However, the fracture width in this specific case can be detected quite well with the OMNI-X scanner.

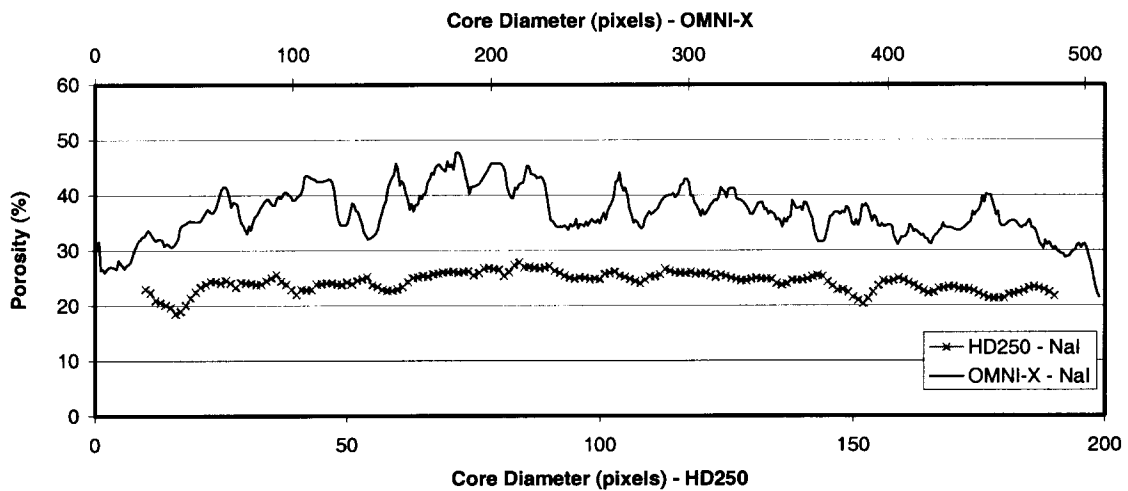


Figure 5–73: Porosity distribution in the fractured region generated with the data acquired by both scanners. HD250 image #96 and averaged OMNI-X image #1.

Figure 5–74 and Figure 5–75 display similar analyses of the dry profiles in the fractured region and the porosity profiles, respectively, for HD250 image #100 and averaged OMNI-X image #5. The dry profiles show a similar trend and the porosity profiles differ from each other. A higher porosity is obtained from the OMNI-X images as expected. The results are reproduced in Figure 5–76 and Figure 5–77 which display the same profiles in the fractured region for the dry condition and the porosity profiles, respectively, for HD image # 105 and averaged OMNI-X image #10.

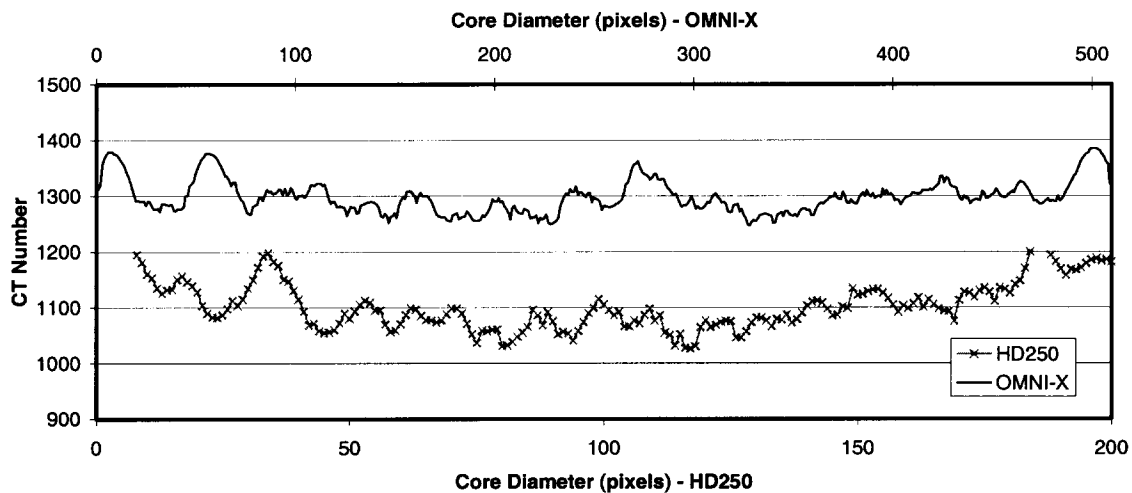


Figure 5-74: Profiles through the fractured region generated with the data acquired by both scanners. HD250 dry image #100 and averaged OMNI-X dry image #5.

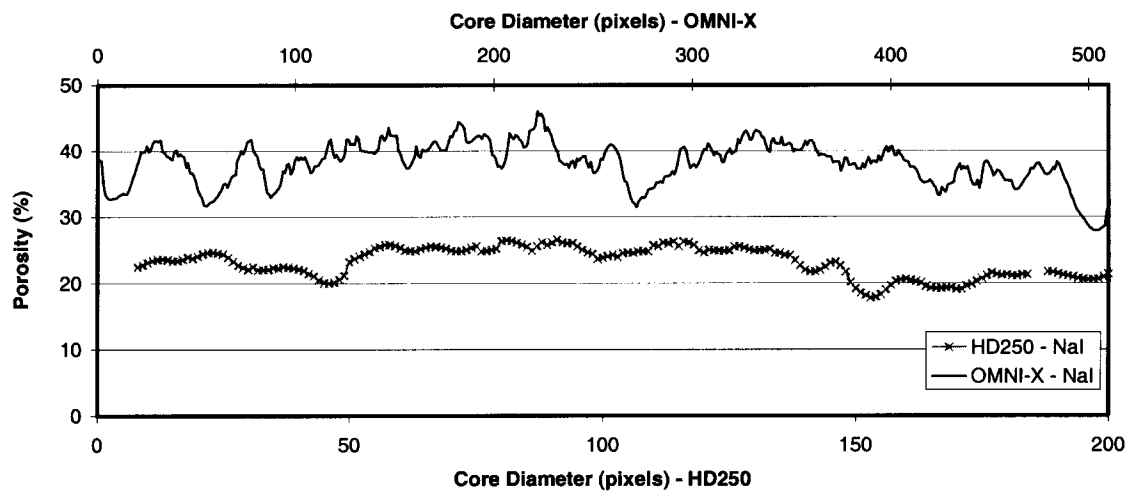


Figure 5-75: Porosity distribution in the fractured region generated with the data acquired by both scanners. HD250 image #100 and averaged OMNI-X image #5.

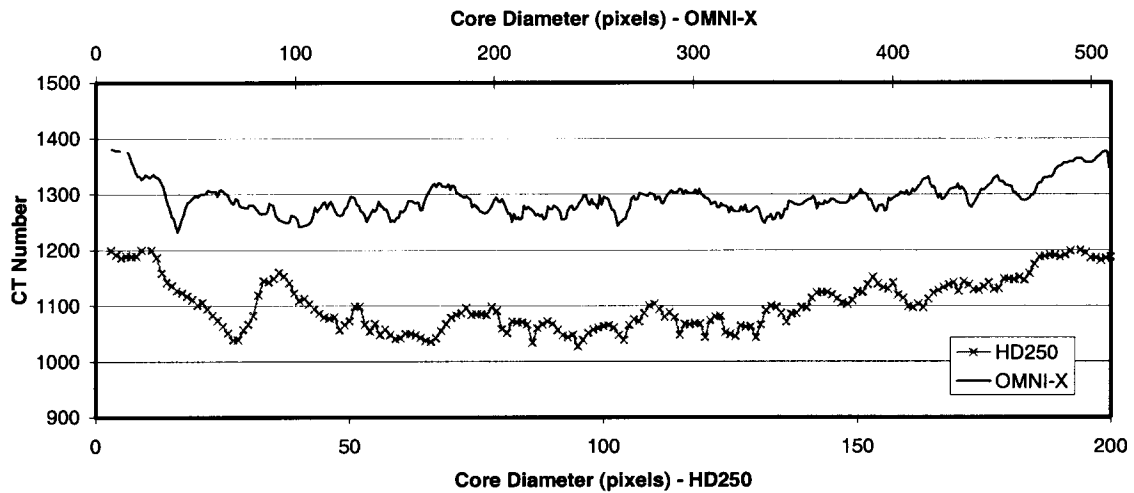


Figure 5-76 Profiles through the fractured region generated with the data acquired by both scanners. HD250 dry image #105 and averaged OMNI-X dry image #10.

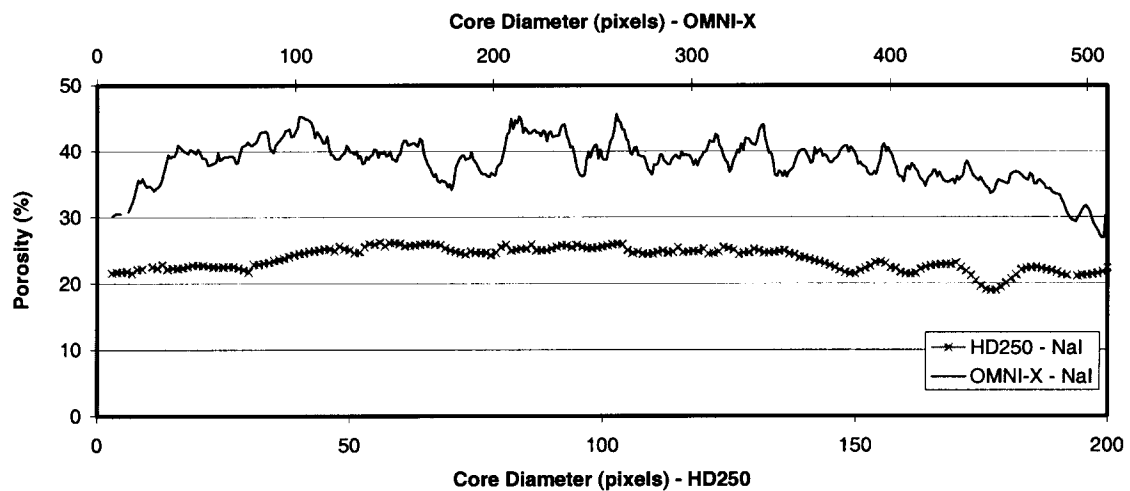


Figure 5-77: Porosity distribution in the fractured region generated with the data acquired by both scanners. HD250 image #105 and averaged OMNI-X image #10.

5.4 Fracture Aperture

An average of 21 OMNI-X images is shown in Figure 5–78. The high porosity layers are distinguished as the dark gray stripes, one of which is highlighted by the white arrow. A small region of interest is marked on the image. Figure 5–79 shows one of the 21 images including the highlighted region of interest. Figure 5–80a is the expanded region of interest of the averaged image shown in Figure 5–78, and Figure 5–80b is the expanded region shown in Figure 5–79. These expanded regions are 200x200 pixels extracted from the 1024x1024 corresponding images. A porosity layer, or low rock density is located between the two white lines in Figure 5–80a, and it is demonstrated that the high porosity layer is aligned with a wide fracture. The same observation is made for the single image shown in Figure 5–80b. Moreover, the left side of the high porosity layer shows a high-density grain protruding into the fracture space, denoted by the arrow. Figure 5–81 is a plate of 20 regions that show that along these images, the fracture aperture is larger in the portion of the fracture that is aligned with the high porosity layer. The general observation made here applies to many parts along the fracture in individual images.

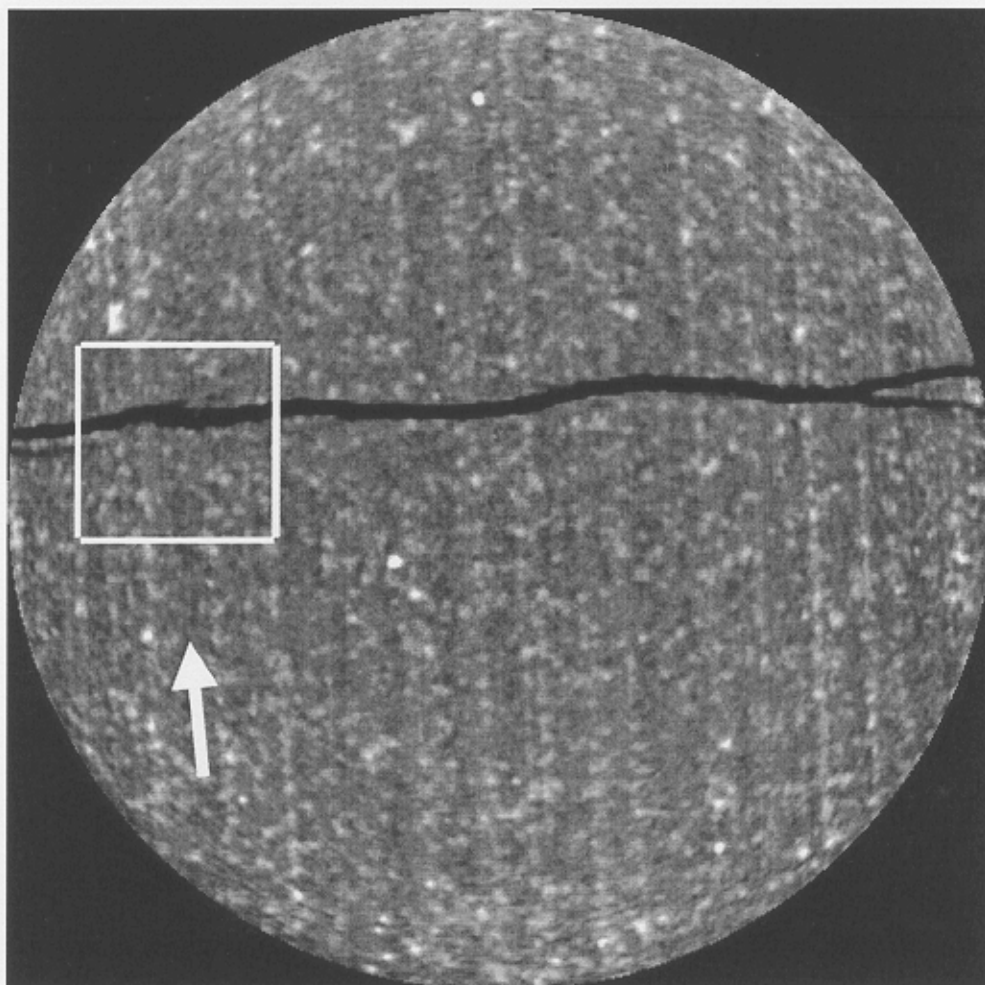


Figure 5-78: Averaged imaged of 21 images acquired by the OMNI-X scanner reconstructed at 1024x1024.

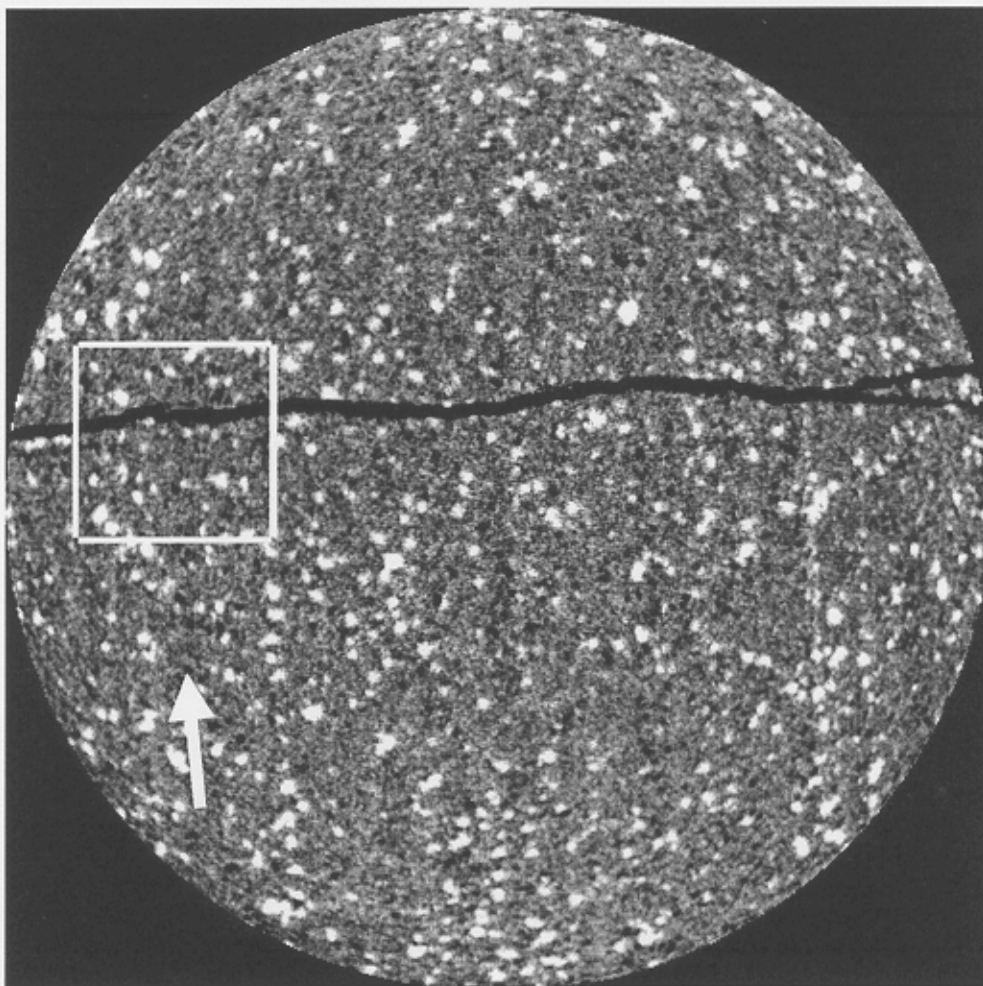
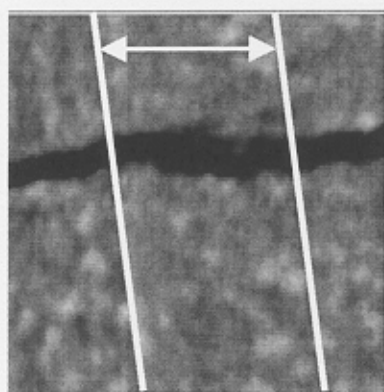
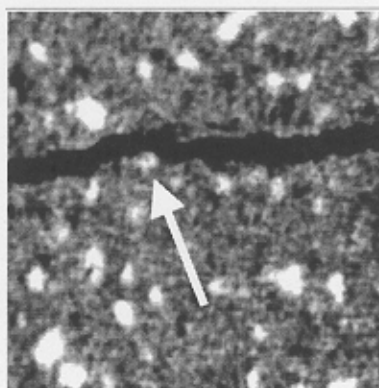


Figure 5-79: Single OMNI-X imaged reconstructed at 1024x1024.



a) Averaged expanded image



b) Single expanded image

Figure 5–80: Expanded sections of 200x200 pixels of an averaged and a single image acquired by the OMNI-X and reconstructed at 1024x1024.

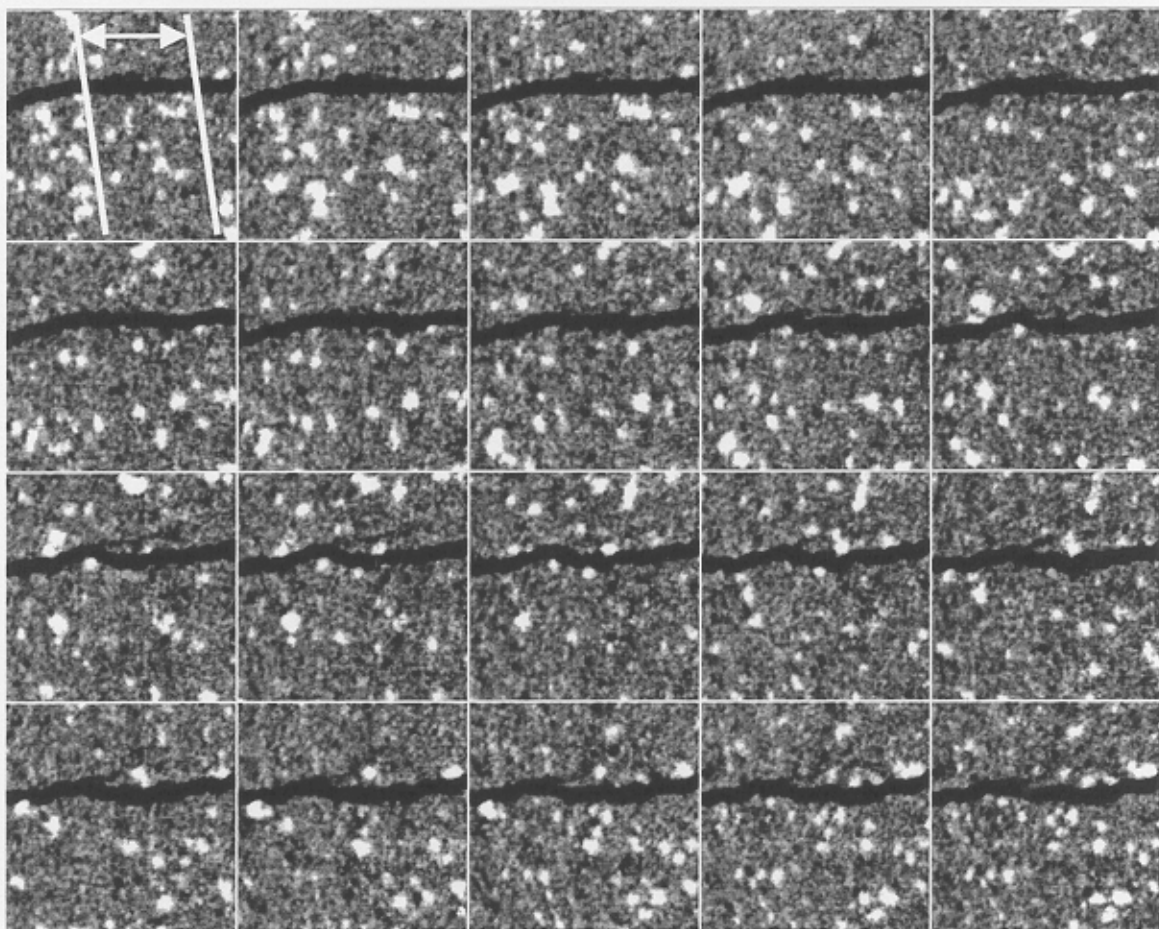


Figure 5-81: Plate of 20 single expanded images acquired by the OMNI-X scanner reconstructed at 1024x1024.

Chapter 6

SUMMARY AND CONCLUSIONS

Summary: Evidence of a relationship between the apparent fracture width distribution in an artificially induced fracture and that in the adjacent layers in a Berea core has been presented. This evidence is in agreement with previous experimental observations.

The correlation between the fracture width adjacent to high porosity layers was determined by analyzing images from the medical and the industrial scanners. The industrial scanner images are very detailed masking the differences between individual layers. Individual high-density inclusions are detectable in the images. Up-scaling high-resolution images does not yield the same images as scanning at low-resolution.

The averaged OMNI-X images are better than the corresponding HD250 images for characterization of the Berea core with an induced fracture.

Conclusions: The present work leads to the following conclusions:

- A correlation between fracture width and porosity of adjacent rock was verified.
- The superiority of the high-resolution images over the corresponding low-resolution medical images was verified.
- A few high-resolution scans improve the interpretation of low-resolution scans.

- Stacking of high-resolution images enhances the detectability of the layers and improves the interpretation of single images acquired by the two scanners.

BIBLIOGRAPHY

- Bergosh, J. L., Marks, T. R., and Mitkus, A. F.: "New Core Analysis Techniques for Naturally Fractured Reservoirs," SPE Paper 13653 proceedings of at the SPE 1985 California Regional Meeting in Bakersfield, California, March 27-29, 1985.
- Fabre, D., Mazerolle, F., and Raynaud, S.: "X-Ray Density Tomography: A Tool to Characterize Pores and Cracks in Rocks," Rock at Great Depth, Proceedings of the International Symposium of Rock Mechanics held in Pau, France, August 28-31, 1989.
- Gilliland, R. E., and Coles, M. E.: "Use of CT Scanning in the Investigation of Damage to Unconsolidated Cores," SCA paper 8902 proceedings of the SCA 1989 Annual Technical Conference in New Orleans, Louisiana, August 2-3, 1989.
- Grader, A. S., Balzarini, M., Radaelli, F., Capasso, G., and Pellegrino, A.: "Fracture-Matrix Flow: Quantification and Visualization Using X-ray Computerized Tomography," AGU Monograph Vol. 122, October 2000.
- Hornarpour, M. M., Cromwell, V., Hatton, D., and Satchwell, R.: "Reservoir Rock Descriptions Using Computed Tomography (CT)," SPE paper 14272 proceedings of the 60th Annual Technical Conference and Exhibition of the SPE in Las Vegas, Nevada, September 22-25, 1985.
- Hornarpour, M. M., McGee, K. R., Crocker, M. E., Maerefat, N. L., and Sharma, B.: "Detailed Core Description of a Dolomite Sample from the Upper Madison Limestone Group," SPE paper 15174 proceedings of the Rocky Mountain Regional Meeting in Billings, Montana, May 19-21, 1986.
- Hubbert, M. K., and Willis, D. G.: "Mechanics of Hydraulic Fracturing". AIME, Vol. 210, 1957, pp153-168.
- Hunt, P. K., Engler, P., and Bajsarowicz, C.: "Computed Tomography as a Core Analysis Tool: Applications, Instrument Evaluation, and Image Improvement Techniques," SPE Formation Evaluation, September, 1988, pp 1203-1210.

- Jasti, J., Jesion, G., and Feldkamp, L.: "Microscopic Imaging of Porous Media Using X-Ray Computer Tomography," SPE paper 20495 proceedings of the 65th Annual Technical Conference and Exhibition of the SPE in New Orleans, Louisiana, September 23-26, 1990.
- Johns, R. A., Steude, J. S., Castenier, L. M., and Roberts, P. V.: "Nondestructive Measurements of Fracture Aperture in Crystalline Rock Cores Using X-Ray Computed Tomography," Journal of Geophysical Research, Vol. 98, February, 1993, pp. 1889-1900.
- Kantzas, A.: "Investigation of Physical Properties of Porous Rocks and Fluid Flow Phenomena in Porous Media Using Computer Assisted Tomography," In Situ, Volume 14, No. 1, 1990, pp. 77-132.
- Moss, R. M., Pepin, G. P., and Davis, L. A.: "Direct Measurement of the Constituent Porosities in a Dual Porosity Matrix," SCA paper 9003 proceedings of the SCA 1990 Annual Technical Conference in Houston, Texas, August 2-3, 1990.
- Narayanan, K., and Deans, H. A.: "A Flow Model Based on the Structure of Heterogeneous Porous Media," SPE paper 18328 proceedings of the 63rd Annual Technical Conference and Exhibition of the SPE in Dallas, Texas, October 2-5, 1988.
- Peters, E. J., and Afzarl, N.: "Characterization of Heterogeneities in Permeable Media with Computed Tomography Imaging," Journal of Petroleum Science and Engineering, Vol. 7, 1992, pp. 283-296.
- Raynaud, S., Fabre, D., Mazerolle, F., Geraud, Y., and Latiere, H. J.: "Analysis of the Internal Structure of Rocks and Characterization of Mechanical Deformation by a Non-Destructive Method: X-Ray Tomodensitometry," Tectonophysics, Vol. 159, 1988, pp. 149-159.
- Sprunt, E. S.: "Arun Core Analysis: Special Procedures for Vuggy Carbonates," The Log Analyst, September – October, 1989, pp. 353-362.

Appendix A
Scanning Sequences Acquired by HD250.

Table A-1, Table A-2, and Table A-3 present the CT data of the scanning sequences taken of the entire core by the medical scanner HD250 used to calculate the porosity distribution in the core.

Table A-1: Dry Scanning Sequence by the CT X-Ray Scanner HD250

# Image	Position (mm)	CT ave DRY	# Image	Position (mm)	CT ave DRY	# Image	Position (mm)	CTave DRY
1	0	1417.64	36	70	1430.26	71	140	1418.12
2	2	1429.99	37	72	1431.95	72	142	1417.87
3	4	1429.84	38	74	1432.21	73	144	1419.49
4	6	1430.20	39	76	1431.15	74	146	1417.23
5	8	1428.28	40	78	1431.45	75	148	1414.33
6	10	1428.16	41	80	1430.87	76	150	1412.21
7	12	1427.77	42	82	1429.91	77	152	1411.89
8	14	1425.93	43	84	1430.28	78	154	1411.85
9	16	1427.39	44	86	1432.10	79	156	1410.87
10	18	1425.35	45	88	1431.51	80	158	1412.56
11	20	1424.42	46	90	1432.28	81	160	1413.14
12	22	1425.72	47	92	1431.50	82	162	1411.89
13	24	1424.75	48	94	1432.88	83	164	1410.26
14	26	1423.31	49	96	1430.97	84	166	1409.65
15	28	1422.31	50	98	1430.92	85	168	1409.23
16	30	1422.76	51	100	1432.26	86	170	1409.58
17	32	1424.81	52	102	1431.96	87	172	1409.58
18	34	1425.90	53	104	1432.23	88	174	1411.13
19	36	1425.11	54	106	1431.10	89	176	1410.27
20	38	1425.47	55	108	1427.91	90	178	1409.80
21	40	1426.22	56	110	1427.64	91	180	1409.87
22	42	1426.07	57	112	1427.18	92	182	1409.60
23	44	1423.60	58	114	1424.92	93	184	1411.49
24	46	1426.34	59	116	1425.75	94	186	1409.73
25	48	1426.60	60	118	1425.30	95	188	1410.16
26	50	1426.73	61	120	1424.69	96	190	1407.65
27	52	1426.17	62	122	1424.14	97	192	1407.01
28	54	1425.33	63	124	1423.34	98	194	1408.15
29	56	1425.88	64	126	1422.20	99	196	1408.36
30	58	1425.37	65	128	1423.93	100	198	1407.35
31	60	1426.76	66	130	1423.80	101	200	1407.79
32	62	1427.79	67	132	1421.92	102	202	1410.72
33	64	1428.65	68	134	1420.37	103	204	1409.99
34	66	1427.00	69	136	1419.01	104	206	1409.26
35	68	1429.15	70	138	1419.84	105	208	1408.78

# Image	Position (mm)	CT ave DRY	# Image	Position (mm)	CT ave DRY	# Image	Position (mm)	CT ave DRY
106	210	1408.24	141	280	1424.32	176	350	1422.00
107	212	1408.53	142	282	1425.66	177	352	1424.67
108	214	1408.11	143	284	1424.29	178	354	1430.97
109	216	1409.16	144	286	1425.42	179	356	1435.35
110	218	1407.32	145	288	1427.84	180	358	1447.78
111	220	1406.82	146	290	1426.64	181	360	1454.83
112	222	1409.12	147	292	1425.70	182	362	1463.75
113	224	1408.96	148	294	1425.48	183	364	1469.27
114	226	1408.11	149	296	1426.89	184	366	1476.58
115	228	1409.23	150	298	1426.48	185	368	1482.00
116	230	1408.29	151	300	1424.95	186	370	1487.93
117	232	1408.69	152	302	1425.44	187	372	1490.10
118	234	1409.18	153	304	1426.32	188	374	1491.53
119	236	1409.79	154	306	1423.98	189	376	1492.96
120	238	1412.97	155	308	1424.72	190	378	1496.41
121	240	1413.45	156	310	1424.48	191	380	1497.06
122	242	1414.72	157	312	1425.17			
123	244	1416.10	158	314	1424.81			
124	246	1416.03	159	316	1425.71			
125	248	1416.60	160	318	1425.96			
126	250	1418.03	161	320	1425.14			
127	252	1417.78	162	322	1424.44			
128	254	1419.57	163	324	1425.51			
129	256	1418.77	164	326	1423.95			
130	258	1420.07	165	328	1423.62			
131	260	1421.08	166	330	1424.00			
132	262	1420.21	167	332	1423.26			
133	264	1418.84	168	334	1421.90			
134	266	1419.21	169	336	1419.60			
135	268	1421.52	170	338	1421.71			
136	270	1424.98	171	340	1422.89			
137	272	1424.00	172	342	1421.73			
138	274	1426.11	173	344	1422.61			
139	276	1425.27	174	346	1421.71			
140	278	1425.79	175	348	1420.76			

Table A-2: Wet Tagged Water Scanning Sequence by the CT X-Ray Scanner HD250

# Image	Position (mm)	CT ave NaI	# Image	Position (mm)	CT ave NaI	# Image	Position (mm)	CT ave NaI
1	0	1849.81	36	70	1852.56	71	140	1859.55
2	2	1858.88	37	72	1853.03	72	142	1858.98
3	4	1858.22	38	74	1853.56	73	144	1860.02
4	6	1857.68	39	76	1854.09	74	146	1859.14
5	8	1855.65	40	78	1853.85	75	148	1856.68
6	10	1854.84	41	80	1854.28	76	150	1856.16
7	12	1853.38	42	82	1853.66	77	152	1856.7
8	14	1850.74	43	84	1854.94	78	154	1855.89
9	16	1849.59	44	86	1856.96	79	156	1854.91
10	18	1847.52	45	88	1858.53	80	158	1857.01
11	20	1845.96	46	90	1858.57	81	160	1858.07
12	22	1846.48	47	92	1857.49	82	162	1857.53
13	24	1844.86	48	94	1859.29	83	164	1856.97
14	26	1843.85	49	96	1859.22	84	166	1856.62
15	28	1842.51	50	98	1859.23	85	168	1855.2
16	30	1843.21	51	100	1859.35	86	170	1855.45
17	32	1844.46	52	102	1861.37	87	172	1855.39
18	34	1844.62	53	104	1861.86	88	174	1855.76
19	36	1845.29	54	106	1861.97	89	176	1856.01
20	38	1845.34	55	108	1859.82	90	178	1855.64
21	40	1845.26	56	110	1860.02	91	180	1854.86
22	42	1845.24	57	112	1861.28	92	182	1854.64
23	44	1843.59	58	114	1860.47	93	184	1855.67
24	46	1845.75	59	116	1860.19	94	186	1853.14
25	48	1845.73	60	118	1860.82	95	188	1852.39
26	50	1847.22	61	120	1860.84	96	190	1851.13
27	52	1847.34	62	122	1861.88	97	192	1849.25
28	54	1846.55	63	124	1860.79	98	194	1850.33
29	56	1847.12	64	126	1860.35	99	196	1849.47
30	58	1847.08	65	128	1861.5	100	198	1849.43
31	60	1847.83	66	130	1861.56	101	200	1848.64
32	62	1848.22	67	132	1860.86	102	202	1849.38
33	64	1848.63	68	134	1859.94	103	204	1848.62
34	66	1847.34	69	136	1859.33	104	206	1847.3
35	68	1850.94	70	138	1859.24	105	208	1846.72

# Image	Position (mm)	CT ave NaI	# Image	Position (mm)	CT ave NaI	# Image	Position (mm)	CT ave NaI
106	210	1845.98	141	280	1842.66	176	350	1753.22
107	212	1845.11	142	282	1843.34	177	352	1751.56
108	214	1844.96	143	284	1840.97	178	354	1749.52
109	216	1844.84	144	286	1839.81	179	356	1743.22
110	218	1843.52	145	288	1838.05	180	358	1737.28
111	220	1841.93	146	290	1834.17	181	360	1722.75
112	222	1842.91	147	292	1828.24	182	362	1706.2
113	224	1842.34	148	294	1824.92	183	364	1683.72
114	226	1839.94	149	296	1824.43	184	366	1668.49
115	228	1840.7	150	298	1823.4	185	368	1657.75
116	230	1838.93	151	300	1820.87	186	370	1651.15
117	232	1837.9	152	302	1820.26	187	372	1648.44
118	234	1837.85	153	304	1819.57	188	374	1649.73
119	236	1837.31	154	306	1815.42	189	376	1648.74
120	238	1837.69	155	308	1813.42	190	378	1645.97
121	240	1837.07	156	310	1809.9	191	380	1640.88
122	242	1836.93	157	312	1806.09			
123	244	1837.22	158	314	1803.42			
124	246	1836.9	159	316	1799.73			
125	248	1835.24	160	318	1796.33			
126	250	1834.04	161	320	1792.48			
127	252	1829.68	162	322	1790.17			
128	254	1828.93	163	324	1788.97			
129	256	1825.96	164	326	1786.07			
130	258	1827.21	165	328	1785.11			
131	260	1830.61	166	330	1782.25			
132	262	1831.31	167	332	1779.39			
133	264	1832.28	168	334	1776.89			
134	266	1834.23	169	336	1771.67			
135	268	1837.78	170	338	1770.46			
136	270	1840.74	171	340	1768.01			
137	272	1840.67	172	342	1764.5			
138	274	1842.2	173	344	1760.93			
139	276	1841.82	174	346	1757.91			
140	278	1842.52	175	348	1753.94			

Table A-3: Wet Plain Water Scanning Sequence by the CT X-Ray Scanner HD250

# Image	Position (mm)	CT ave Plain	# Image	Position (mm)	CT ave Plain	# Image	Position (mm)	CT ave Plain
1	0	1599.42	36	70	1611.78	71	140	1603.29
2	2	1608.33	37	72	1613.01	72	142	1604.36
3	4	1607.98	38	74	1613.27	73	144	1606.16
4	6	1608.35	39	76	1613.45	74	146	1604.23
5	8	1606.64	40	78	1613.64	75	148	1601.66
6	10	1606.85	41	80	1613.43	76	150	1600.18
7	12	1606.87	42	82	1612.45	77	152	1599.62
8	14	1605.52	43	84	1612.80	78	154	1599.19
9	16	1606.72	44	86	1614.82	79	156	1598.35
10	18	1605.35	45	88	1614.43	80	158	1600.39
11	20	1604.78	46	90	1614.08	81	160	1600.72
12	22	1606.31	47	92	1614.15	82	162	1599.40
13	24	1604.93	48	94	1615.47	83	164	1599.32
14	26	1604.12	49	96	1614.17	84	166	1598.71
15	28	1604.51	50	98	1613.90	85	168	1598.26
16	30	1605.12	51	100	1615.05	86	170	1598.71
17	32	1606.87	52	102	1614.88	87	172	1598.72
18	34	1607.89	53	104	1614.91	88	174	1600.00
19	36	1607.34	54	106	1614.11	89	176	1599.29
20	38	1607.93	55	108	1612.42	90	178	1599.85
21	40	1608.18	56	110	1612.18	91	180	1601.10
22	42	1608.13	57	112	1612.21	92	182	1600.93
23	44	1607.13	58	114	1610.66	93	184	1601.67
24	46	1609.30	59	116	1610.45	94	186	1599.57
25	48	1609.85	60	118	1610.13	95	188	1599.94
26	50	1609.72	61	120	1609.56	96	190	1598.23
27	52	1609.78	62	122	1608.88	97	192	1597.45
28	54	1608.17	63	124	1609.19	98	194	1598.09
29	56	1608.62	64	126	1607.97	99	196	1598.09
30	58	1608.05	65	128	1609.45	100	198	1597.65
31	60	1609.79	66	130	1609.48	101	200	1598.27
32	62	1610.88	67	132	1607.84	102	202	1600.93
33	64	1611.27	68	134	1606.43	103	204	1599.83
34	66	1610.23	69	136	1604.78	104	206	1598.54
35	68	1611.42	70	138	1604.87	105	208	1598.66

# Image	Position (mm)	CT ave Plain	# Image	Position (mm)	CT ave Plain	# Image	Position (mm)	CT ave Plain
106	210	1598.64	141	280	1611.88	176	350	1579.61
107	212	1599.87	142	282	1613.18	177	352	1579.35
108	214	1599.81	143	284	1611.44	178	354	1579.02
109	216	1600.35	144	286	1613.27	179	356	1576.47
110	218	1599.02	145	288	1615.06	180	358	1576.84
111	220	1597.78	146	290	1613.92	181	360	1575.69
112	222	1600.41	147	292	1612.89	182	362	1574.46
113	224	1600.33	148	294	1612.58	183	364	1572.99
114	226	1600.21	149	296	1613.39	184	366	1574.16
115	228	1601.52	150	298	1612.88	185	368	1574.61
116	230	1600.49	151	300	1610.65	186	370	1575.99
117	232	1600.66	152	302	1611.41	187	372	1575.27
118	234	1600.99	153	304	1610.89	188	374	1574.13
119	236	1601.17	154	306	1608.16	189	376	1573.76
120	238	1603.57	155	308	1608.12	190	378	1574.61
121	240	1604.58	156	310	1607.22	191	380	1572.92
122	242	1605.70	157	312	1606.73			
123	244	1606.53	158	314	1605.67			
124	246	1606.68	159	316	1605.19			
125	248	1606.99	160	318	1604.74			
126	250	1608.34	161	320	1603.18			
127	252	1607.50	162	322	1601.71			
128	254	1608.68	163	324	1602.33			
129	256	1607.50	164	326	1599.26			
130	258	1608.22	165	328	1597.06			
131	260	1608.75	166	330	1594.36			
132	262	1607.83	167	332	1591.38			
133	264	1608.41	168	334	1588.08			
134	266	1608.69	169	336	1584.02			
135	268	1610.47	170	338	1585.02			
136	270	1613.93	171	340	1584.64			
137	272	1612.43	172	342	1582.44			
138	274	1613.79	173	344	1582.03			
139	276	1612.79	174	346	1580.9			
140	278	1613.06	175	348	1579.45			

Appendix B

Scanning Sequences Acquired by the OMNI-X High Resolution Scanner

Table B-1 and Table B-2 present the CT data obtained by the Industrial Scanner OMNI-X used to calculate the porosity distribution in the core.

Table B-1: Dry Scanning Sequence of 38 mm Length at One Tip of The Fracture

#	CT ave DRY	#	CT ave DRY	#	CT ave DRY	#	CT ave DRY	#	CT ave DRY
1	1447.15	36	1460.38	71	1465.18	106	1474.82	141	1475.27
2	1449.14	37	1462.31	72	1465.22	107	1474.92	142	1475.14
3	1450.17	38	1463.51	73	1468.84	108	1475.63	143	1475.61
4	1450.83	39	1463.77	74	1471.78	109	1474.66	144	1474.56
5	1453.98	40	1462.78	75	1472.84	110	1474.25	145	1473.17
6	1454.44	41	1465.39	76	1474.05	111	1472.74	146	1471.85
7	1456.74	42	1465.56	77	1472.76	112	1471.62	147	1472.37
8	1457.68	43	1465.02	78	1473.61	113	1471.79	148	1473.47
9	1455.87	44	1463.99	79	1474.66	114	1472.75	149	1473.08
10	1458.58	45	1465.93	80	1473.93	115	1472.78	150	1474.15
11	1458.60	46	1464.05	81	1473.92	116	1473.23	151	1475.14
12	1460.33	47	1463.63	82	1473.06	117	1474.61	152	1475.83
13	1461.22	48	1460.98	83	1473.04	118	1475.38	153	1476.48
14	1460.80	49	1463.23	84	1473.22	119	1474.87	154	1476.09
15	1463.96	50	1463.48	85	1473.13	120	1474.11	155	1476.46
16	1464.73	51	1462.90	86	1472.80	121	1474.23	156	1475.60
17	1464.58	52	1463.03	87	1472.97	122	1475.12	157	1474.66
18	1462.51	53	1463.05	88	1472.97	123	1475.84	158	1475.17
19	1463.49	54	1463.08	89	1474.46	124	1476.06	159	1475.02
20	1464.37	55	1464.35	90	1474.52	125	1476.43	160	1475.28
21	1464.64	56	1465.41	91	1474.00	126	1476.35	161	1476.78
22	1465.31	57	1466.66	92	1474.66	127	1477.58	162	1477.19
23	1465.30	58	1471.55	93	1473.81	128	1477.61	163	1476.98
24	1467.97	59	1468.42	94	1471.30	129	1477.96	164	1477.42
25	1467.66	60	1467.35	95	1470.64	130	1478.38	165	1478.09
26	1468.73	61	1464.95	96	1471.20	131	1477.38	166	1478.30
27	1466.33	62	1465.13	97	1472.07	132	1475.16	167	1477.91
28	1462.90	63	1465.37	98	1472.93	133	1474.03	168	1479.72
29	1462.03	64	1465.95	99	1472.05	134	1473.22	169	1480.08
30	1460.40	65	1464.78	100	1472.05	135	1474.40	170	1478.61
31	1462.39	66	1463.58	101	1472.17	136	1473.95	171	1478.87
32	1462.39	67	1462.84	102	1471.83	137	1474.33	172	1477.63
33	1463.60	68	1464.24	103	1473.29	138	1475.02	173	1477.76
34	1463.27	69	1463.15	104	1474.11	139	1474.09	174	1477.36
35	1462.75	70	1464.49	105	1474.11	140	1474.89	175	1477.76

#	CT ave DRY	#	CT ave DRY	#	CT ave DRY	#	CT ave DRY	#	CT ave DRY
176	1478.02	211	1472.76	246	1475.13	281	1480.43	316	1474.44
177	1478.75	212	1472.84	247	1475.36	282	1480.59	317	1474.73
178	1479.90	213	1473.49	248	1475.61	283	1480.90	318	1476.27
179	1480.65	214	1473.14	249	1474.94	284	1480.29	319	1476.79
180	1483.51	215	1472.21	250	1474.76	285	1479.86	320	1477.63
181	1481.98	216	1472.16	251	1474.32	286	1478.96	321	1477.57
182	1481.88	217	1473.03	252	1474.72	287	1477.48	322	1476.95
183	1480.65	218	1473.49	253	1474.90	288	1477.86	323	1477.63
184	1479.36	219	1473.53	254	1475.07	289	1477.25	324	1477.23
185	1479.19	220	1474.29	255	1475.43	290	1478.03	325	1476.73
186	1480.45	221	1475.16	256	1476.48	291	1478.31	326	1475.38
187	1481.91	222	1474.91	257	1477.13	292	1478.17	327	1475.65
188	1481.87	223	1473.66	258	1476.86	293	1478.05	328	1475.29
189	1481.70	224	1472.59	259	1477.10	294	1478.13	329	1475.42
190	1480.76	225	1473.27	260	1476.98	295	1478.08	330	1475.79
191	1481.97	226	1473.71	261	1477.40	296	1478.84		
192	1481.68	227	1473.04	262	1477.48	297	1477.95		
193	1480.28	228	1473.30	263	1477.54	298	1477.20		
194	1479.71	229	1473.75	264	1476.77	299	1476.96		
195	1480.44	230	1473.58	265	1477.47	300	1477.56		
196	1480.74	231	1473.83	266	1477.28	301	1478.49		
197	1480.75	232	1474.29	267	1476.31	302	1478.57		
198	1481.26	233	1474.56	268	1476.10	303	1477.55		
199	1482.28	234	1474.73	269	1474.93	304	1477.58		
200	1480.81	235	1474.43	270	1474.94	305	1477.13		
201	1471.02	236	1473.98	271	1474.92	306	1476.14		
202	1471.97	237	1473.39	272	1473.86	307	1475.60		
203	1472.79	238	1473.24	273	1474.78	308	1475.65		
204	1472.13	239	1473.33	274	1475.36	309	1475.81		
205	1471.40	240	1473.82	275	1475.28	310	1476.66		
206	1471.39	241	1474.31	276	1476.43	311	1477.14		
207	1471.32	242	1474.26	277	1477.72	312	1476.60		
208	1472.87	243	1475.35	278	1478.16	313	1475.96		
209	1471.86	244	1474.46	279	1478.35	314	1474.41		
210	1473.01	245	1474.50	280	1479.29	315	1474.13		

Table B-2: Wet Tagged Water Scanning Sequence of 38 mm Length at One Tip of The Fraction.

#	CT ave WET	#	CT ave WET	#	CT ave WET	#	CT ave WET	#	CT ave WET
1	1533.74	36	1549.00	71	1561.33	106	1570.66	141	1573.43
2	1533.90	37	1548.65	72	1562.88	107	1571.15	142	1573.82
3	1535.28	38	1548.04	73	1565.68	108	1572.23	143	1572.47
4	1538.69	39	1549.90	74	1568.01	109	1574.06	144	1570.23
5	1538.43	40	1550.33	75	1570.45	110	1570.82	145	1569.26
6	1539.13	41	1550.73	76	1563.84	111	1566.73	146	1568.80
7	1541.84	42	1550.72	77	1563.59	112	1564.90	147	1570.26
8	1542.26	43	1550.57	78	1562.29	113	1564.89	148	1570.31
9	1542.78	44	1550.51	79	1563.65	114	1565.07	149	1570.95
10	1544.11	45	1550.86	80	1565.11	115	1565.30	150	1571.27
11	1544.42	46	1551.55	81	1564.7	116	1565.41	151	1570.94
12	1545.76	47	1551.98	82	1564.17	117	1566.44	152	1571.22
13	1545.39	48	1552.70	83	1564.98	118	1567.21	153	1571.70
14	1545.97	49	1553.89	84	1565.44	119	1568.04	154	1572.11
15	1546.48	50	1554.76	85	1565.49	120	1569.13	155	1573.29
16	1546.55	51	1555.72	86	1566.65	121	1571.22	156	1573.25
17	1546.32	52	1555.35	87	1568.35	122	1571.18	157	1572.62
18	1545.98	53	1556.66	88	1569.09	123	1572.21	158	1573.71
19	1546.41	54	1558.5	89	1569.58	124	1572.99	159	1574.92
20	1546.77	55	1559.95	90	1568.07	125	1572.22	160	1575.48
21	1547.48	56	1560.28	91	1568.63	126	1571.18	161	1574.60
22	1546.95	57	1560.17	92	1568.87	127	1571.41	162	1574.12
23	1547.78	58	1560.28	93	1569.50	128	1572.14	163	1574.68
24	1548.30	59	1561.66	94	1569.53	129	1572.35	164	1571.75
25	1548.98	60	1564.29	95	1569.62	130	1572.21	165	1571.31
26	1549.03	61	1567.32	96	1570.31	131	1572.43	166	1570.94
27	1547.91	62	1569.29	97	1568.31	132	1570.25	167	1570.85
28	1548.82	63	1565.66	98	1568.02	133	1570.57	168	1570.48
29	1547.94	64	1560.50	99	1568.48	134	1572.13	169	1571.00
30	1549.47	65	1560.90	100	1568.53	135	1572.70	170	1570.91
31	1549.46	66	1561.89	101	1568.34	136	1571.19	171	1570.90
32	1549.17	67	1560.59	102	1569.10	137	1570.28	172	1570.83
33	1548.78	68	1558.20	103	1568.43	138	1570.81	173	1571.41
34	1548.76	69	1559.43	104	1569.26	139	1572.16	174	1571.39
35	1549.22	70	1560.20	105	1569.98	140	1573.00	175	1572.03

#	CT ave WET	#	CT ave WET	#	CT ave WET	#	CT ave WET	#	CT ave WET
176	1571.59	211	1570.21	246	1573.64	281	1570.28	316	1570.05
177	1571.77	212	1570.36	247	1573.97	282	1569.74	317	1571.27
178	1571.44	213	1570.59	248	1574.58	283	1570.40	318	1571.64
179	1571.66	214	1570.24	249	1574.41	284	1570.91	319	1571.35
180	1572.55	215	1570.33	250	1574.79	285	1570.55	320	1571.78
181	1571.03	216	1570.95	251	1575.38	286	1570.09	321	1572.03
182	1570.46	217	1570.65	252	1575.59	287	1570.12	322	1571.92
183	1569.98	218	1571.18	253	1575.92	288	1569.81	323	1572.11
184	1569.22	219	1571.12	254	1575.92	289	1569.69	324	1571.74
185	1569.01	220	1571.92	255	1574.95	290	1569.35	325	1571.58
186	1567.86	221	1571.92	256	1574.40	291	1569.64	326	1571.17
187	1569.49	222	1571.35	257	1574.72	292	1569.71	327	1571.19
188	1569.69	223	1570.65	258	1573.50	293	1569.73	328	1571.08
189	1570.52	224	1570.88	259	1573.15	294	1570.09	329	1571.73
190	1571.06	225	1570.98	260	1574.32	295	1569.29	330	1572.90
191	1572.58	226	1570.84	261	1574.69	296	1569.22		
192	1573.35	227	1570.64	262	1573.82	297	1569.28		
193	1573.8	228	1571.18	263	1573.74	298	1569.24		
194	1574.22	229	1571.00	264	1572.98	299	1569.48		
195	1572.85	230	1570.66	265	1572.74	300	1570.30		
196	1571.74	231	1570.31	266	1573.57	301	1570.83		
197	1572.19	232	1570.79	267	1574.32	302	1571.01		
198	1572.71	233	1570.56	268	1574.90	303	1571.06		
199	1573.71	234	1570.78	269	1574.87	304	1570.81		
200	1574.85	235	1570.37	270	1574.61	305	1571.31		
201	1567.77	236	1570.08	271	1573.94	306	1570.27		
202	1568.00	237	1570.08	272	1574.33	307	1570.37		
203	1568.33	238	1570.42	273	1574.55	308	1569.87		
204	1568.53	239	1570.91	274	1573.43	309	1570.34		
205	1567.93	240	1571.75	275	1572.06	310	1571.41		
206	1568.20	241	1572.40	276	1570.26	311	1571.36		
207	1568.88	242	1571.73	277	1570.48	312	1571.24		
208	1569.07	243	1571.79	278	1570.10	313	1570.89		
209	1568.99	244	1572.01	279	1570.28	314	1570.12		
210	1569.46	245	1573.17	280	1570.17	315	1570.19		

**XII. “A Real-time State Estimation of the Standpipe of a Circulating
Fluidized Bed using an Extended Kalman Filter”**

**Hoowang Shim (S) and Parviz Famouri (F), West Virginia University
with
Edward Boyle (M), NETL**

A Real-time State Estimation of the Standpipe of a Circulating Fluidized Bed using an Extended Kalman Filter

Hoowang Shim & Parviz Famouri*

Lane Department of Computer Science &
Electrical Engineering
West Virginia University
P. O. Box 6109
Morgantown, WV 26506-6109

Edward J. Boyle

National Energy Technology Laboratory
3610 Collins Ferry Rd.
P.O. Box 880
Morgantown, WV 26507-0880

December 18, 2001

*SHIM@CSEE.WVU.EDU

Contents

1	Introduction	3
2	Mathematical Model	4
3	Experimental	5
4	Conclusion	11

List of Figures

1	Estimated Void-fraction (left) and Measured & Estimated Pressure (right) Profiles after 1 second.	5
2	Estimated Void-fraction (left) and Measured & Estimated Pressure (right) Profiles after 10 second.	6
3	Estimated Void-fraction (left) and Measured & Estimated Pressure (right) Profiles after 20 second.	6
4	Estimated Void-fraction (left) and Measured & Estimated Pressure (right) Profiles after 30 second.	7
5	Estimated Void-fraction (left) and Measured & Estimated Pressure (right) Profiles after 40 second.	7
6	Estimated Void-fraction (left) and Measured & Estimated Pressure (right) Profiles after 50 second.	8
7	Estimated Void-fraction (left) and Measured & Estimated Pressure (right) Profiles after 60 second.	8
8	Estimated Void-fraction (left) and Measured & Estimated Pressure (right) Profiles after 70 second.	9
9	Estimated Void-fraction (left) and Measured & Estimated Pressure (right) Profiles after 80 second.	9
10	Estimated Void-fraction (left) and Measured & Estimated Pressure (right) Profiles after 90 second.	10
11	Estimated Void-fraction (left) and Measured & Estimated Pressure (right) Profiles after 100 second.	10

1 Introduction

An Extended Kalman Filter(EKF) is used to estimate the state of the standpipe for a circulating fluidized bed(CFB). The dynamic model of the flow within the standpipe is based on mass conservation and a modified Richardson-Zaki correlation. The truncated Ergun equation is used to relate the pressure drop measurements to the amount and velocity of solids in the standpipe. One of the most applied solutions for the state estimation problem for nonlinear systems in the presence of process and measurement noise is the *extended Kalman Filter* or EKF, which is a Kalman filter that linearizes about the current mean and covariance. This research applies an EKF as an estimator for the state of the standpipe for a circulating fluidized bed.

2 Mathematical Model

The model is based on conservation of mass as expressed by the one-dimensional continuity equation for both phases. If gas compressibility can be neglected the equations for both phases have the same form.

$$\frac{\partial \varepsilon_p}{\partial t} + \frac{\partial j_p}{\partial z} = 0 ,$$

where $p = g$ for gas or s for granular solid and ε is volume fraction and j is volumetric flux. When the standpipe is divided into cells, a discrete form of the controlling dynamic equation is obtained by integrating the gas phase equation over the i^{th} and replacing the time derivation by a forward difference. The resulting equation is:

$$\varepsilon_{k+1}^i = \varepsilon_k^i + \frac{\Delta t}{\Delta z} \left(j_k^{i-\frac{1}{2}} - j_k^{i+\frac{1}{2}} \right) , \quad (1)$$

where ε_k^i is the void fraction at the center of the i^{th} cell at the time step k and $j_k^{i-\frac{1}{2}}$ is the volumetric gas flux between cell $i - 1$ and cell i at the time step k . The time increment and the length of each cell along the standpipe are Δt and Δz , respectively.

The measurement model that relates the pressure difference between cell i and the topmost cell of the standpipe at the time-step k is the numerically integrated version of the truncated Ergun equation. The pressure difference p_k^i is

$$p_k^i = \frac{1}{2} C_1 V_t \sum_{\ell=i}^{N-1} (z_{\ell+1} - z_\ell) \{ q(\varepsilon_k^\ell) + q(\varepsilon_k^{\ell+1}) \} , \quad (2)$$

where

$$q(\varepsilon) = \frac{(\varepsilon - 1)^2}{\varepsilon^2} \zeta(\varepsilon)$$

$$\zeta(\varepsilon) = \begin{cases} \frac{(\varepsilon_{mf})^{n-1}}{\varepsilon_{mf} - \varepsilon_{pb}} (\varepsilon - \varepsilon_{pb}) & \text{if } \varepsilon < \varepsilon_{mf} \\ \varepsilon^{n-1} & \text{if } \varepsilon \geq \varepsilon_{mf} \end{cases} .$$

where N is the number of cells in the standpipe, C_1 is a constant $\frac{150\mu}{d_{vs}^2}$, μ is the fluid viscosity, and d_{vs} is the effective particle diameter.

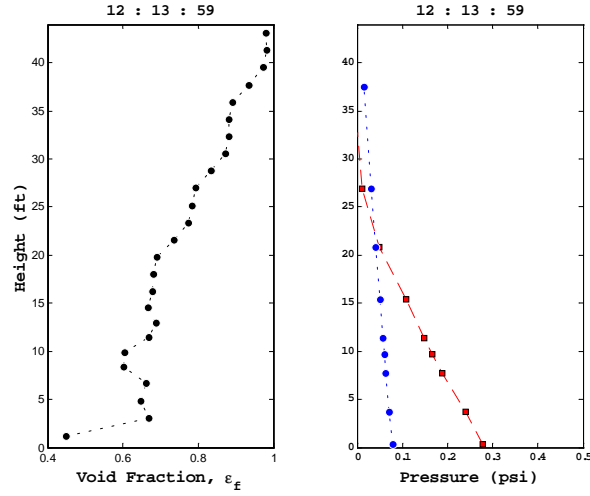


Figure 1: Estimated Void-fraction (left) and Measured & Estimated Pressure (right) Profiles after 1 second.

3 Experimental

In this year we build a program using Matlab[®] that gets data from the standpipe in real-time from a data acquisition system for a circulating fluidized bed.

Figure 1 shows the estimated void-fraction profile in the left and the measured pressure (\square) from the standpipe and the estimated pressure (\bullet) profile from EKF in the right at the very beginning of the simulation. Next figures show that how EKF is working with the pressure measurements from the standpipe and how fast it estimates void-fraction and pressure profiles. We can assume that there is a bed-height between dense and dilute region in void-fraction profile. In the figure 10, the void-fraction profile shows that there is a bed-height around $25ft$ and it is very close to an observed bed-height, $26ft$.

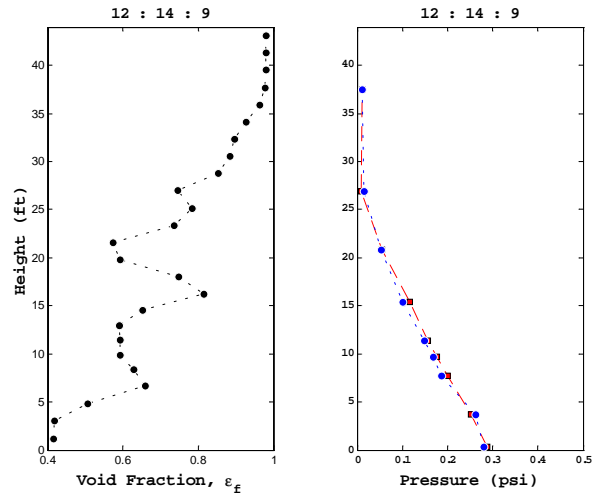


Figure 2: Estimated Void-fraction (left) and Measured & Estimated Pressure (right) Profiles after 10 second.

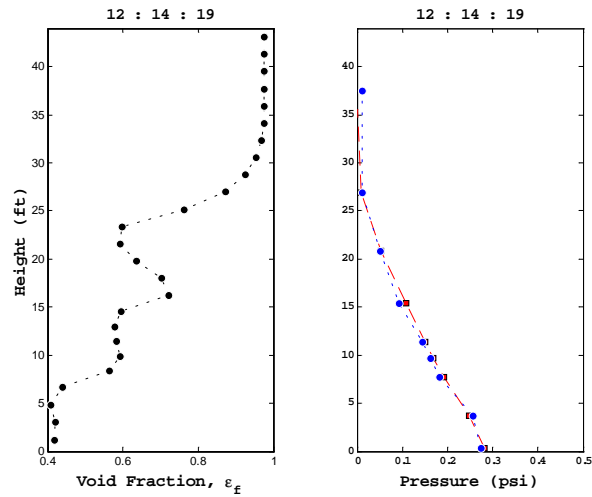


Figure 3: Estimated Void-fraction (left) and Measured & Estimated Pressure (right) Profiles after 20 second.

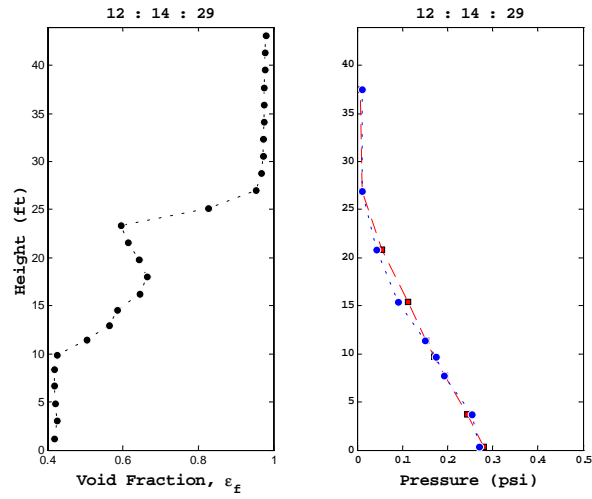


Figure 4: Estimated Void-fraction (left) and Measured & Estimated Pressure (right) Profiles after 30 second.

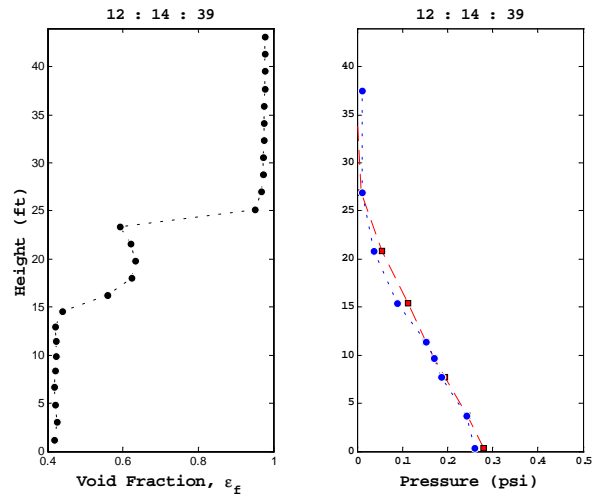


Figure 5: Estimated Void-fraction (left) and Measured & Estimated Pressure (right) Profiles after 40 second.

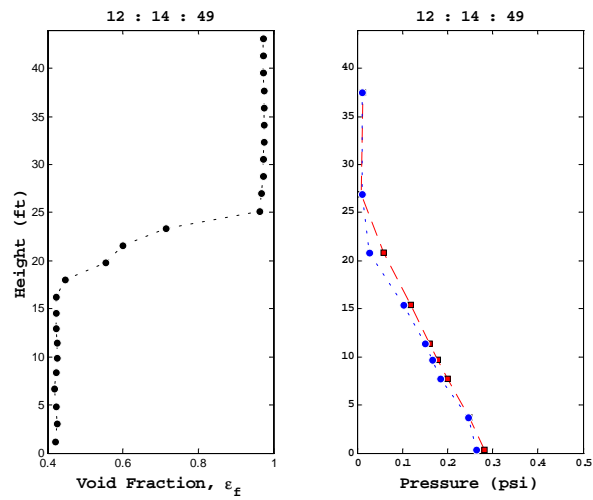


Figure 6: Estimated Void-fraction (left) and Measured & Estimated Pressure (right) Profiles after 50 second.

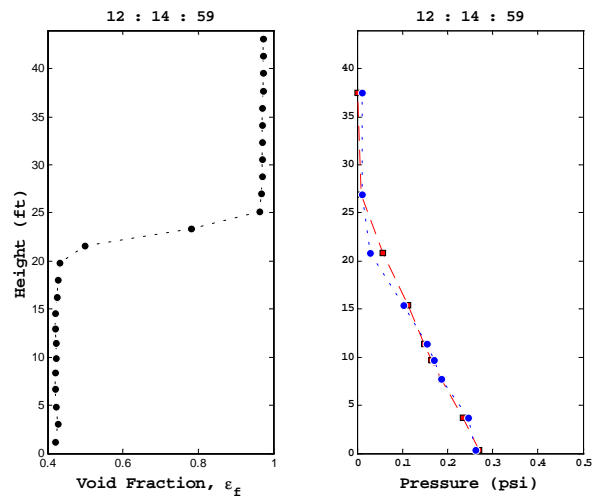


Figure 7: Estimated Void-fraction (left) and Measured & Estimated Pressure (right) Profiles after 60 second.

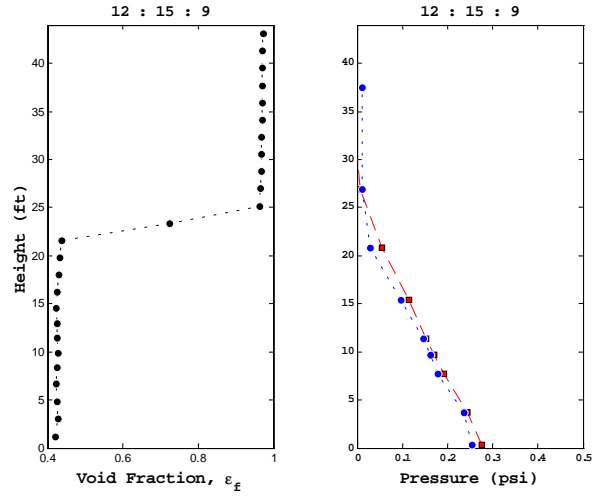


Figure 8: Estimated Void-fraction (left) and Measured & Estimated Pressure (right) Profiles after 70 second.

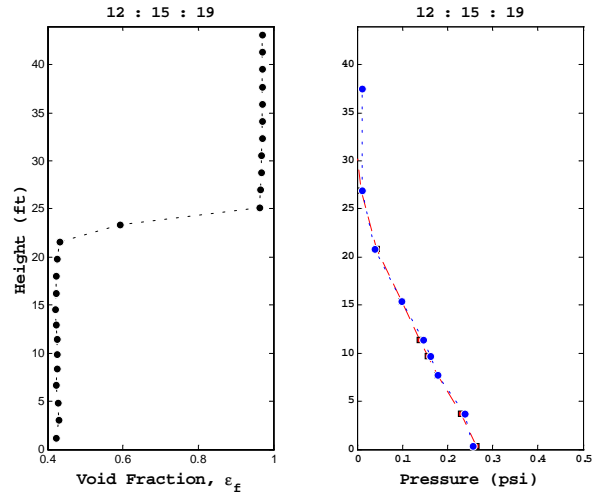


Figure 9: Estimated Void-fraction (left) and Measured & Estimated Pressure (right) Profiles after 80 second.

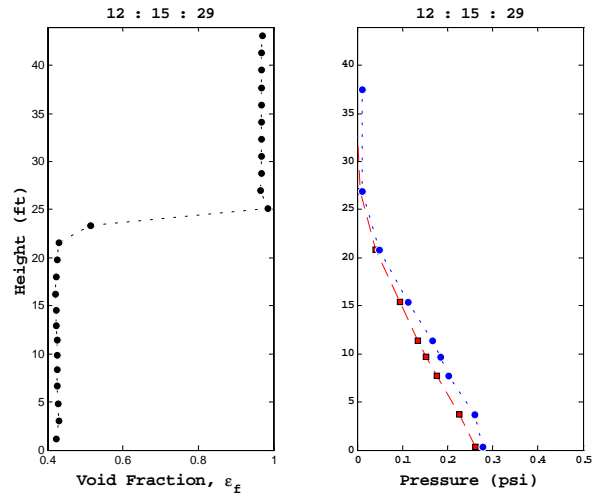


Figure 10: Estimated Void-fraction (left) and Measured & Estimated Pressure (right) Profiles after 90 second.

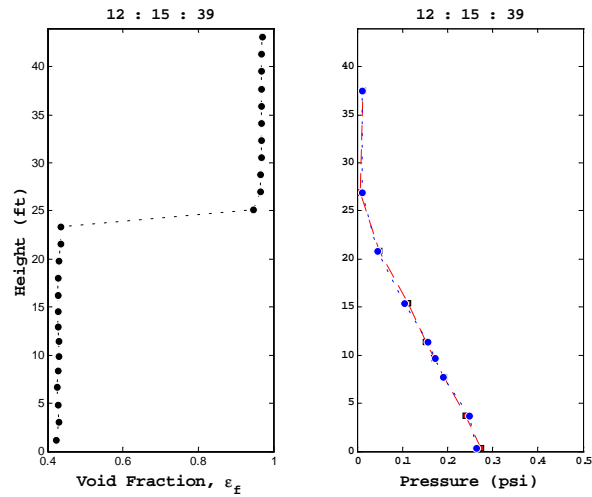


Figure 11: Estimated Void-fraction (left) and Measured & Estimated Pressure (right) Profiles after 100 second.

4 Conclusion

In this report, the extended Kalman filter(EKF) is successfully applied to estimate the void fraction and the pressure profiles in the standpipe for a circulating fluidized bed in real-time. The bed-height from the estimated void-fraction profile is close to the observed bed-height.

References

- [1] H. Shim, P. Famouri, W. Sams, E. Boyle, “ A state estimation of the stand-pipe of a circulating fluidized bed using an extended Kalman filter.”, The 16th International Conference on Fluidized Bed Combustion, Reno, Nevada, 2001
- [2] A. Gelb, Ed. *Applied Optimal Estimation.*, M.I.T. Press, Cambridge, MA, 1974
- [3] M. S. Grewal and A. P. Andrews *Kalman Filtering: Theory and Practice.*, Prentice Hall, Upper Saddle River, NJ, 1993
- [4] P. S. Maybeck, *Stochastic Models, Estimation, and Control, Volume I.*, Academic Press, New York, NY, 1979

**UNIVERSITY/NETL STUDENT PARTNERSHIP PROGRAM
(DE-FC26-98FT40143)**

3rd Year Technical Report

September 1, 2000 – August 31, 2001

Submitted to:

National Energy Technology Laboratory

Submitted by:

**Gerald D. Holder
School of Engineering
University of Pittsburgh
Pittsburgh, PA 15261**

Volume III of VI

**XIII. “Experimental Investigation of Oscillatory Heat Release Mechanisms
and Stability Margin Analysis in Lean-Premixed Combustion”**

**Don Ferguson (S) and Mridul Gautam (F), West Virginia University
with
George Richards (M), NETL**

**Experimental Investigation of Oscillatory Heat
Release Mechanisms and Stability Margin
Analysis in Lean-Premixed Combustion**

by

Don H. Ferguson

2001 Annual Report

University / NETL Student Partnership Program

Dr. George A. Richards – National Energy Technology Laboratory, US DOE

Dr. Mridul Gautam (Chair) – Mechanical and Aerospace Engineering at WVU

**Experimental Investigation of Oscillatory Heat
Release Mechanisms and Stability Margin
Analysis in Lean-Premixed Combustion**

by

Don H. Ferguson

Research proposal submitted for approval to the faculty
of West Virginia University in partial fulfillment of the
requirements for the degree of

Doctor of Philosophy
in
Mechanical Engineering

Graduate Committee

Dr. Mridul Gautam (Chair) – Mechanical and Aerospace Engineering at WVU
Dr. Larry Banta - Mechanical and Aerospace Engineering at WVU
Dr. John Loth - Mechanical and Aerospace Engineering at WVU
Dr. Gary Morris - Mechanical and Aerospace Engineering at WVU
Dr. George A. Richards – National Energy Technology Laboratory, US DOE

1.0 INTRODUCTION AND BACKGROUND.....	1
1.1 INTRODUCTION	1
1.2 LITERATURE REVIEW	3
1.2.1 <i>Historical Overview of the Study of Thermoacoustic Instabilities</i>	<i>4</i>
1.2.2 <i>Mechanisms of Heat Release Resulting in Combustion Instabilities.....</i>	<i>8</i>
1.2.3 <i>Flame Surface Area as the Mechanism of Heat Release</i>	<i>11</i>
1.2.4 <i>Experimental Heat Release and Flame Surface Identification.....</i>	<i>12</i>
1.2.5 <i>Flow Measurement and Visualization in Combustion.....</i>	<i>16</i>
1.2.6 <i>Modeling of Flame Dynamics.....</i>	<i>20</i>
2.0 DESCRIPTION OF PROPOSED PROJECT.....	25
2.1 PROJECT OVERVIEW	25
2.2 SPECIFIC RESEARCH AREAS	26
2.2.1 <i>Evaluation of Heat Release Mechanisms.....</i>	<i>26</i>
2.2.2 <i>Flow Visualization and Measurement</i>	<i>26</i>
2.2.3 <i>Effects of Fuel Composition.....</i>	<i>27</i>
2.2.4 <i>Flame Dynamics Model and Stability Analysis</i>	<i>27</i>
3.0 WORK DONE TO DATE.....	28
3.1 EXPERIMENTAL SETUP.....	28
3.2 EXPERIMENTAL RESULTS AND DISCUSSION.....	34
3.2.1 <i>Experimental Procedure</i>	<i>34</i>
3.2.2 <i>Results and Discussion</i>	<i>34</i>
3.3 PRELIMINARY CONCLUSIONS	39
4.0 PROPOSED WORK.....	40
4.0.1 <i>Flame Surface Area</i>	<i>40</i>
4.0.2 <i>Flowfield Measurement</i>	<i>41</i>
4.0.3 <i>Effects of Fuel Composition.....</i>	<i>41</i>
4.0.4 <i>Flame Dynamics Model and Stability Analysis</i>	<i>42</i>
5.0 CONCLUSION	42
6.0 REFERENCES.....	43

1.0 Introduction and Background

1.1 Introduction

Lean pre-mixed (LPM) combustion has become a recognized means of reducing thermal NO_x production by lowering peak combustion temperatures. However, the presence of combustion instabilities within the desired operating range has complicated the use of this technology in stationary gas turbine applications. Left unchecked, instabilities can lead to degradation in engine and emissions performance and shorten component life. In some instances, large-amplitude pressure oscillations can result in severe structural damage.

The stability of a combustion device can be evaluated by monitoring the instantaneous heat release or pressure. Periodic or sudden changes in either of these parameters may indicate the onset of static or dynamic combustion instability. Static stability addresses the phenomena of flashback and blow-off, and is of particular interest for lean-premixed combustors operating near the lean flammability limit. Of greater concern, and the focus of this study, are dynamic (thermoacoustic) instabilities, which can be defined as the occurrence of combustion oscillations. In some devices, such as pulse combustors, oscillations can actually be utilized to improve the combustion process, however as noted above, instabilities in gas turbine engines can be quite detrimental.

It is well known that thermoacoustic instabilities occur as a result of feedback between the combustion heat release and pressure oscillations associated with the acoustic characteristics of the system. Apart from testing, no certain method exists to determine if a given combustor is dynamically stable. Design phase testing may be limited to single combustor can and nozzle test rigs, and unanticipated interactions occurring when components are integrated may lead to instabilities. Additionally, variations in test and operational fuel properties can initiate undesirable dynamics, and modifications necessary to reduce the effects of or eliminate thermoacoustic instabilities late in the design, production or operational phase can be quite costly. Even when stable combustion is achieved in prototype testing, there is no established method to report the *stability margin*, i.e., the proximity to oscillations when changes occur in fuel type, ambient conditions, or equivalence ratio.

Modeling has helped to improve our understanding of how and when combustion instabilities occur, but models depend on knowledge of the mechanisms responsible for initiating and sustaining oscillations in lean premixed systems, as well as the response of the flame to

various inputs. Investigations of combustion dynamics dating back to the Apollo rocket program have represented the combustion/acoustic behavior as a closed-loop feedback system, linking pressure and heat release fluctuations (Harrje and Reardon, 1971). This approach is a direct application of automatic control theory, where the dynamic response of transfer function sub-models is linked in a closed loop system. The system stability can then be evaluated from the open-loop Bode or Nyquist analysis (Franklin et al., 1994). However, the analytical determination of the system's transfer function can be quite difficult due in part to the nonlinear, limit-cycle behavior of the flame, thus models must be supplemented with experimental results.

The first step in identifying mechanisms responsible for thermoacoustic oscillations is to realize that without proper damping, the fluid in virtually any cavity or duct is susceptible to dynamic instabilities (Blackshear, 1952). Air forced over a cavity or through a duct can excite, to some degree, one or more of the natural modes of vibration resulting in pressure waves. Rayleigh (1945) realized that by adding (withdrawing) thermal energy at the moment of greatest (least) pressure, the excitation could be driven (damped). In LPM gas turbines, unsteady heat released from combustion provides the needed energy for thermoacoustic oscillations to occur. Variations in fuel/air mixing, vortex shedding and periodic changes in the flame structure are a few mechanisms that are believed to be a source of heat release oscillations. However, the inherent complexity due to the interaction of multiple mechanisms makes determining the impact of individual components very difficult. Several published studies (Markstein, 1964; Kaskan, 1952; Putnam and Dennis, 1953; Fliefil et.al., 1996) have considered unsteady heat release resulting from variations in the flame surface area initiated by flow perturbations. Analytical models, simplified by linear assumptions, have been developed that investigate this relationship concentrating on the phase and gain differences between oscillating flow, flame surface area and heat release. However, there appears to have been no effort to experimentally quantify these effects. In part, this may be due to the difficulty in measuring changes in the flame surface area, or in separating surface area effects from other mechanisms.

By studying simplified systems in which a conscious effort is made to reduce the impact of some of the suspected mechanisms, it may be possible to isolate particular phenomena contributing to fluctuations in heat release. This information can then be utilized to build the transfer-function sub-model of the flame in order to predict the phase and gain of the input required for stability as well as the stability proximity of a particular operating condition.

Demonstration of this procedure on a simple burner can identify difficulties and limitations in carrying out the complete procedure in more practical problems.

This was the approach that will be adopted for the proposed study, which focuses on flame structure variations as the mechanisms for heat release fluctuations. The experimental portion attempts to identify changes in the flame structure (in particular, flame surface area) as well as the surrounding flow that may lead to sustained thermoacoustic instabilities. The knowledge gained from this exercise will then supplement the development of a transfer function of the flame dynamics describing the response of the heat release rate to variations in the reaction zone flow and acoustic velocity upstream of the flame. By evaluating the frequency response of the flame to various inputs it would be possible to predict the phase-gain relationship of the entire system, and thus the overall stability boundaries.

This proposal is divided into several sections with the first being an introduction to the overall problem. A detailed review of past research and a general background of concerning issues are provided in Section 2. The next section, Section 3, is an overview of the entire project with a detailed description of the individual areas of investigation. The primary experimental apparatus has been constructed and some preliminary results and conclusions have been collected and are discussed in Section 4 of this report. The proposed work plan is presented in the final section, Section 5, with an accompanying time line for completion

1.2 Literature Review

Combustion instabilities have been observed in many practical energy-producing devices such as furnaces, rocket engines, ramjet engine, afterburners, and gas turbine engine combustors. A considerable amount of research, both experimental and theoretical, has been performed in the area of combustion dynamics on these devices and from these studies, three general classifications of combustion instabilities have been identified (Crocco et al., 1960 and Markstein, 1964). First, low-frequency oscillation due to the geometry of the combustion chamber and propellant feed system (shear mode). Second, a cyclical behavior in the chamber due to the non-isentropic relationship between the density and the pressure of the gas downstream of the gas-phase reaction zone; the density and temperature oscillations are related to the pressure oscillations by conditions that are not isentropic. The consequent spatial and temporal oscillations of entropy are known as “entropy waves” or entropy mode (Williams,

1985), however their impact on the overall combustion stability is negligible in comparison to the other two modes. The third form of instability is the excitation of the acoustic vibrational modes of the combustion chamber (pressure mode). While these modes may act individually or in concert, both Markstein, 1964 and Crocco et al., 1960 noted that for flames enclosed in a duct, the pressure mode exhibits the dominant disturbance and can be the most destructive. Thus the pressure mode is the primary focus of this research study, however consideration is also given to the vorticity mode as a mechanism for variations in the heat release.

1.2.1 Historical Overview of the Study of Thermoacoustic Instabilities

One of the first recorded studies of combustion-driven oscillations was published by Higgins (1777). Higgins (1777) produced what has come to be known as organ-pipe oscillations by enclosing a hydrogen diffusion flame in a large tube open at both ends. For certain positions of the flame in the tube and for certain lengths of the tube, the flame could be made to “sing”, or oscillate. The name “organ-pipe oscillation” stems from the fact that the enclosed instabilities vibrate in the same manner as the gas column in a sounding organ pipe (Putnam and Dennis, 1956). Using a similar apparatus as Higgins (1777), Rijke (1859) found that by inserting a heated wire mesh gauze into the lower half of an open-ended vertical tube, strong oscillations could be obtained with the maximum intensity occurring when the distance of the gauze from the lower end of the tube was approximately one-fourth of its entire length. Rijke (1859) attributed this phenomenon to the rising convection current expanding in the region of the heated wire mesh and compressing downstream from the heater due to the cooling of the pipe walls. While this explanation provided some insight on the occurrence of organ-pipe oscillations it did not provide detail into the heat exchange mechanism causing the instabilities (Feldman, 1968). Although Higgins (1777) had originally demonstrated the use of an open-ended tube for studying combustion oscillations, the occurrence of oscillations in such a device induced by the placement of a heat source within the tube is referred to as the Rijke phenomena.

It was not until 1896 that a qualitative explanation of this phenomenon was offered by Lord Rayleigh (1945). The Rayleigh Criteria, as it has come to be known, states that for a heat-driven oscillation to occur, there must be a varying rate of heat release having a component in phase with the varying component of the pressure (Putnam and Dennis, 1953). It can be expressed mathematically as the following

$$Ra = \oint h'(t)P'(t)dt \quad (1)$$

where Ra is the Rayleigh Index, h' is the varying rate of heat release, P' is the oscillating component of the pressure, and t is the time. When Ra is positive the pressure instability is amplified by the heat release, and when Ra is negative the perturbations are damped. Rayleigh (1945), however, did not provide a detailed explanation of the coupling between the combustion process and the pressure pulsation, or the mechanisms for the varying heat release (Mugridge, 1980).

Many authors have provided a theoretical as well as experimental analysis of the Rayleigh Criteria. One such study was that of Putnam and Dennis (1953) in which a thermodynamic analysis of the phase requirements between the heat addition and pressure was conducted. Although slightly more generalized, Culick (1987) offered a derivation of the Rayleigh Criteria for which the fluctuations of heat release were directly coupled with the normal modes of the acoustics. Nonlinear, limit-cycle behavior could be accounted for through the appropriate definition of the heat release fluctuations.

Organ-pipe oscillations occur in devices such as rocket motors, afterburners, and gas turbine combustors. This type of oscillation is known as a standing wave, and for a tube open at both ends the pressure nodes exist at the inlet and outlet for the fundamental mode and the maximum pressure occurs at the center (Putnam and Dennis, 1953). Conversely, the velocity has a node at the center and antinodes (maximums) at the ends, thus the pressure and velocity are 90° out of phase. This is represented schematically in Figure 1.

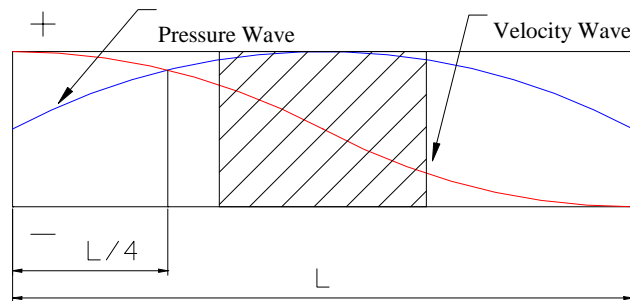


Figure 1: Velocity and pressure waves in an open-ended tube

Putnam and Dennis (1956) amassed a collection of studies on organ-pipe oscillations in combustion systems in which consideration was given to “singing flames” of the Higgins type,

flash tube studies, gauze tubes, rocket-shaped burners (gas and solid fuels), refractory tube combustion and ram-jet type combustors. In their own study, Putnam and Dennis (1953) investigated organ-pipe oscillations in three burner configurations. A general explanation of the oscillations was obtained for all three cases by considering 1) the system acoustics, and 2) the heat release location. They demonstrated that in order to sustain oscillations 1) the phase difference between rate of heat release and the pressure fluctuations had to be less than $\pi/4$, and 2) the point of heat release must be “near” the point of maximum pressure in the combustion tube. In response to the second stipulation, the authors suggested that for maximum effectiveness and to overcome damping effects, the heat should be released in the middle third of the pressure wave. This region is indicated by the hatchmarks in Figure 1. This assumes that the heat can be arbitrarily added to the combustion tube and is not dependent on the velocity wave. If in fact the heat release rate were subject to the acoustic velocity, then one would expect the largest amplitude thermoacoustic oscillation to occur at $L/4$, as in the Rijke experiment. In a subsequent paper, Putnam and Dennis (1952) developed a mathematical expression for the driving criteria which depended on: 1) variation of flame-front position with time, 2) flow of gases relative to the flame front, 3) heat release rate of the burning gases, and 4) relation of the heat release rate to the pressure variation along the tube. The model assumed all of the energy from combustion was released at a single point and in general, was a model of the Rayleigh criteria based on determining the theoretical phase difference between the pressure and heat release. Damping and Lewis number effects were neglected, and no reference was made to the heat release variation mechanisms. However, this study supported the findings that for oscillations to be driven at the peak amplitude, the heat release must occur near the pressure antinode.

Much of our present day understanding of combustion instabilities stems from research initiated in the 1950's and 60's to support the development of advanced rocket motors. Crocco et al. (1960) observed instabilities in a liquid fuelled rocket motor and applied a time lag theory to predict the effect of the combustion chamber length on the stability boundary. However, the authors noted the difficulty in generalizing the theoretical model developed for this study. The same time lag theory was used by Crocco and Mitchell (1969), but the oscillations were considered to be nonlinear and possess a limit cycle behavior. Analysis of the nonlinear

perturbations resulted in a nonlinear ordinary differential equation governing the shape of the nonlinear periodic wave.

As previously noted, modern stationary gas turbines use lean premixed combustion as a means of meeting restrictive emission limits and designers must address thermoacoustic instabilities. Keller (1995) stated that due to the vast differences between conventional diffusion style and low-NO_x combustors, instabilities occurring in the latter are actually similar to those of rocket motors. Therefore, much of the continuing effects have resembled those of previous rocket motor studies, in particular the use of the time lag theory, which primarily states that thermoacoustic oscillations occur when the time scale of the acoustic pressure field, τ_1 , is similar to that of the combustion characteristic time, τ_2 . In premixed combustion, the characteristic time combines mixing, transport and chemical kinetics.

Richards and Janus (1997) investigated combustion instabilities in a rig designed to closely resemble actual gas turbine conditions. A simple time lag model was adopted to experimentally characterize instabilities produced by a premix fuel nozzle. The model suggested that the nozzle velocity played an important role in the stability of the combustor. Tests conducted at conditions between stable and unstable combustion were studied and resulted in intermittent perturbations. Thus, the authors emphasized the need to identify stability boundaries in new combustors.

Studies have also been performed on full-scale gas turbine engines (Konrad et al., 1998; Scholtz and Depietro, 1997; Hobson et al., 2000). However, these investigations are often system specific and stress the need for more accurate models to help predict the occurrence of instabilities and the stability boundaries. Additionally, due to the complex interactions present in full-scale engines it is often difficult to identify the source of the oscillations. Thus information obtained on a particular mechanism through testing on simplified test rigs could aid in the development of complex models of complicated combustion systems.

The Rijke tube provides an elementary example of thermoacoustic oscillation of the organ-pipe type and has been used extensively in both theoretical and experimental studies (Carrier, 1955; Yoon et al., 1998; Friedlander et al., 1964; Maling, 1963; Neuringer and Hudson, 1952). Additionally, Feldman (1968) provided an extensive review of literature on Rijke thermoacoustic oscillations which included many of the papers listed above. The author noted

that although a considerable amount of effort has been directed towards this phenomenon, the detailed heat transfer mechanism causing large amplitude oscillations has yet to be explained.

Using the Rayleigh criteria given in Equation 1, the wave diagram (Figure 1), and assuming the heat release perturbations are proportional to the acoustic velocity, the Rayleigh index can be shown to be positive in the lower half on the tube, and negative in the upper half. Thus sustaining self-excited thermoacoustic oscillations when the heat source is added in the lower half, and damping oscillations when the source is located in the upper half.

1.2.2 Mechanisms of Heat Release Resulting in Combustion Instabilities

Published literature presents evidence of a variety of mechanisms to describe the process that occurs over the characteristic time, τ_2 , that results in a fluctuation of the heat release. Theoretical and experimental studies investigating mechanisms such as: variations in fuel / air mixing and fuel composition, vortex shedding and periodic changes in flame structure have been performed and will be discussed below. However, experimental results are often system specific, and theoretical studies must be simplified due to the complex interactions involved between mechanisms. Thus, a thorough description of the flame transfer function (i.e. how the flame reacts to the acoustic feedback within the system) and the coupling process between the heat release and the system acoustics is often unavailable in even simple flames.

Equivalence ratio fluctuations, ϕ' , were considered to be the primary driving mechanism by Lieuwen et al. (1999). They concluded that a coupling between the combustion chamber and fuel / air premixer acoustics produces small changes in equivalence ratio, and at lean conditions this could have a significant impact on various combustion characteristics (flame speed, flame temperature, chemical time, etc.), thus causing large fluctuations in the heat release rate. Similar findings were reported by several other authors (Mongia and Dibble, 1998; Shih et al., 1996; Oran and Gardner, 1985; Darling et al., 1995) who also considered equivalence ratio variations alone or in combination with flow instabilities as the primary mechanism for fluctuations in the heat release rate.

The presence of large-scale coherent structures in the flow can act to enhance the instability if the shear layer instability frequency matches the acoustic frequency. This was shown in Schadow et al. (1989) by acoustically forcing a ducted jet at its resonant frequency and altering the flow rate to obtain a match with the vortex merging frequency in the shear layer. It

was found that the size of the stabilized vortex is controlled, to some degree, by the acoustic frequency (Schadow et al., 1989). The vortices will be smallest when the acoustic frequency equals the initial vortex shedding frequency and will be largest when the acoustic frequency is near the preferred-mode or vortex merging frequency.

The vortices do not significantly alter the acoustic field in a combustor, however when combustion is present they can feed back and affect the heat release in a variety of ways (Schadow et al., 1992). Large-scale coherent structures have the capability of convecting heat away from the primary reaction zone (Poinsot et al., 1987). In addition, the shedding of vortices due to combustor and nozzle geometries can result in the periodic dilution of the unreacted mixture with hot combustion products leading to a sudden change in the heat release (Schadow et al., 1992). Flow instabilities leading to fluctuations in the reaction rate caused by a similar mixing process were considered by Keller (1995). By combining schlieren photography and natural C_2 chemiluminescence, Poinsot et al. (1987) were able to determine the phase relationship between vortex formation and heat release. They demonstrated that the interaction between several vortices results in a sudden heat release, and when coupled with the system acoustics results in flame instability. A short note presented by Gutmark et al. (1991) supported this result through an experimental study of a step expansion combustor in which the maximum pressure oscillation amplitude was obtained when the acoustic frequencies were within 20% of the vortex merging frequency.

Variations in the flame front, and subsequently the heat release, resulting from interactions with the plane acoustic waves has been considered by a number of authors (Merk, 1956; Mugridge, 1980; Fleifil et al., 1996; Blackshear, 1952). Lee and Lieuwen (2001) presented a numerical model of the acoustic nearfield flow characteristics. By imposing a plane disturbance on the flow upstream of the flame, the authors found the acoustic velocity in the vicinity of the flame, especially at the base of the flame, to be two-dimensional having both a transverse component as well as an axial one. Furthermore, unlike low frequency instabilities in which the flame essentially “sloshed” back and forth in a bulk motion, high frequency oscillations, where $L/\lambda = 0.99$, produced changes in the phase of the velocity oscillations along the flame surface. An analytical model developed by Fleifil et al. (1996) described the reaction of the flame surface to velocity perturbations which showed the perturbations in the heat release to be a function of the variations of the flame surface area. Their model indicated that the flow

Strouhal number, $\omega R/u$, determines the amplitude of the flame surface oscillation while the flame Strouhal number, $\omega R/S_u$, defines its shape. Where ω , R , and S_u are defined as the acoustic mode frequency, the tube radius and the laminar burning velocity, respectively. Peracchio and Proscia (1998) utilized the methodology of Fleifil et al. (1996) to create a model describing the coupling of linear acoustics and nonlinear heat release. The coupling process is said to originate from acoustic pressure perturbations affecting the equivalence ratio of the mixture being delivered to the flame, resulting in a fluctuation in the heat release due to both ϕ variations and flame front oscillations. From experimental results and previous observations, Peracchio and Proscia (1998) believed that the model under-predicts the flame surface area fluctuations. However, by adjusting the flow and flame Strouhal numbers, the under-prediction could be accounted for, resulting in a change in the flame shape from a wrinkled, sinusoidal surface to more of a bulk motion.

Several other authors have considered flame surface area variations as the mechanism controlling the heat release. In an early study presented by Chu (1956), the author presented a physical interpretation of the Rayleigh Criteria through an analogy with a piston driving a mechanical spring-mass system. The physical model was then used as a basis for a purely analytical solution that demonstrated how small amplitude disturbances could be amplified by fluctuations in the rate of heat release from the heat source. Chu (1956) noted that since the rate of heat release from a flame front is controlled, in part by the flame surface area, any change in this variable would result in a change in the heat release rate. Blackshear (1952) presented a model indicating that a wave can pass through the flame zone unaltered provided that the flame area remains constant. However, if the flame area were to change, the flame could drive or damp depending on the phase lag between the gas velocity and flame area perturbations and the magnitude of the area perturbations. Studies presented by Markstein (1964), Kaskan (1952), and Putnam and Dennis (1953) provide a similar argument for explaining that variations in the flame surface area contributed to thermoacoustic instabilities. In their study of the effects of coherent structures on flame instability, Schadow et al. (1992) noted that as vortices are shed they convected downstream causing the flame surface to become distorted. This distortion results in an oscillatory change in the flame surface area and hence results in an oscillatory heat release rate. Unfortunately, none of these studies provide an experimental verification of the effects of flame surface area variations on the heat release

1.2.3 Flame Surface Area as the Mechanism of Heat Release

The flame front can be approximated by a thin sheet provided the characteristic chemical times of the major heat release reactions are much shorter than those of the heat and mass diffusion (Law, 1988). Based on this assumption the total rate of heat release is proportional to the flame surface area by the following

$$Q(t) = \rho S_u A_f \Delta q_r \quad (2)$$

where ρ is the mixture density, S_u is the flame speed, A_f is the flame surface area and Δq_r is the heat of reaction per unit mass of the mixture. Equation (2) shows the dependence of the heat release rate on both the flame surface area and the flame speed, which is a function of the equivalence ratio. While this explains the relationship between the heat release and the flame area it does not explain the mechanism that forces the flame surface to become distorted.

As stated earlier, the flow in virtually any duct is susceptible to dynamic instabilities. Consider a small acoustic perturbation at the nozzle exit. As the upstream (downstream) wave propagates from the point of initiation a reduction (increase) in the velocity of the oncoming (outgoing) flow at the flame surface occurs. If the flame speed is assumed to remain constant, then the change in flow causes a deformation of the surface resulting in a variation in the flame surface area and thus the heat release rate according to Eq. (2). When the acoustic energy gain provided by the heat release variation is sufficiently greater than the acoustic losses in the system, and in phase with the pressure perturbations, $\angle(q'-p') \leq 90^\circ$, the instability is driven, providing a feedback mechanism to sustain the instability. The magnitude of the oscillations is limited by nonlinear mechanisms in the pressure and heat release.

Unfortunately the existence of flame stretch complicates this analysis, especially in the assumption of constant flame speed. Few flames exist without the influence of flame stretch and strain on the surface. Law (1988) classified the influence of strain on the flame surface in two categories: hydrodynamic stretch and flame stretch. Hydrodynamic stretch was considered to occur from an interaction of the normal and tangential velocity gradients at the flame surface. This interaction produces a change of the flame surface and the volumetric burning rate due to a distortion of the flame topography and displacement of the flame surface. Flame stretch occurs when the tangential velocity modifies the heat and mass diffusion and the mass flux of the

reactants. The temperature and concentration profiles in the reaction zone are modified by this action, subsequently altering the burning intensity, reaction temperature and completeness.

Law (1988) also noted that except in highly strained cases, stretch has little influence on the reaction zone. In Bunsen flames, flame stretch may be more prevalent in the highly curved tip of the flame more so than along the sides. However, this study focuses on relatively low-frequency oscillations resulting in flame surface perturbations that are much larger than the flame thickness. In addition, by maintaining a laminar flow into the reaction zone the effect of turbulence with length scales on the order of the flame thickness can be lessened.

1.2.4 Experimental Heat Release and Flame Surface Identification

An experimental evaluation of the impact of flame surface area variation on the rate of heat release requires the measurement of both these parameters. Unfortunately, there is no direct method to quantify either the surface area or heat release rate, and thus they must be inferred from other measurable parameters. This necessary approach assumes an implicit correlation between the particular flame measurables and the rate quantities in question (Najm et al., 1998). A detailed understanding of the reaction mechanisms has provided a means of correlating both chemical (e.g. chemiluminescence and laser-induced fluorescence) and physical (e.g. flow dilatation and temperature) measurements to specific events, such as major heat release reactions, in the flame. A majority of these studies were performed in the fifties and sixties, where overall flame emission was correlated to the reactant flow rates (Samaniego et al., 1995)

Flame surface area provides a unique challenge. The area of a surface can be defined from principles of general calculus for describing the area of surface of revolution (Edwards and Penney, 1986). Therefore, the instantaneous flame surface area can be obtained by integrating the axial displacement of the flame surface, ξ , over the nozzle exit

$$A_f = 2\pi \int_0^R r \sqrt{\left(\frac{\partial \xi}{\partial r}\right)^2 + 1} dr \quad (3)$$

Thus by identifying the flame surface it would be possible to determine the flame surface area. However, the use of Equation (2) depends on a constant flame speed along the flame front (Flieffil et al., 1996). In typical flames the flame speed at the flame front would be altered due to flame stretch, but with the statements made above with regards to stretch, the assumption of a constant flame speed is justified.

If the flame surface is to be identified and measured, it must first be defined. The flame can be divided into two zones (Borghi, 1988; Turns, 1996): the preheat zone and the reaction zone. The reaction zone is the region in which all of the exothermic chemical reactions (heat release) take place. In order to satisfy Equation (1), this zone must be approximated as a thin-sheet. If the reaction zone were considered “thick”, variations in the release of chemical energy within its bounds could occur without altering the flame surface area. Prior to entering the reaction zone, the unburned mixture passes through the preheat zone where it is heated to the ignition temperature by diffusion and convective processes. Gaydon and Wolfhard (1953) define the preheat zone as the region between the point of ignition and where the temperature has risen just 1% with reference to the temperature rise in the zone, $T_i = T_u + 0.01*(T_b - T_u)$. Here T_i is the temperature at the upstream boundary of the preheat zone, T_u is the unburned mixture temperature and T_b is the temperature of the burned gases (for an ideal case, this would be the adiabatic flame temperature). Thus for the thin-sheet approximation to be true the temperature of the mixture must increase rapidly to the point of ignition and the subsequent reaction must progress quickly. This would indicate that the flame thickness would depend on the Lewis Number ($Le = k/\rho c_p D$ – ratio of thermal diffusivity to mass diffusivity) of the mixture components, as well as the chemical reaction rates. Borghi (1988) provides the following empirical relationship for the flame thickness

$$\delta = K'' * \tau_c * u_L \quad (4)$$

where K'' is a Lewis Number defined term, τ_c is the characteristic reaction time for the given species, and u_L is the flame speed. Equation (5) is commonly used to determine the flame or “characteristic” thickness and was first given by Zeldovich (Jarosinski, 1984) and later by Williams (1985) and Lewis and von Elbe (1987).

$$\Delta = k / c_p \rho_u S_L \quad (5)$$

where k , c_p , ρ_u and S_L are the thermal conductivity, specific heat with constant pressure, density of the unburned mixture, and the laminar flame speed, respectively. Turns (1996) provided a similar relationship except the thickness was determined to be twice that given by equation (5), 2Δ . However, unlike the previous authors, Turns (1996) assumed a linear temperature profile across the flame front. Using the definition of the preheat zone given by Gaydon and Wolfhard (1953) and equation (5), the preheat zone thickness was determined to be approximately 4.6Δ .

Jarosinski (1984) derived a simple experimental method for determining the flame thickness on the basis of the energy equation. Given the temperature profile of the flame, the flame thickness can be approximated by the following

$$\delta = 2 \frac{(T_b - T_u)}{(dT/dz)_{\max}} \quad (5)$$

where the $(T_b - T_u)$ and $(dT/dz)_{\max}$ are the measured values of the temperature difference and the maximum temperature gradient, respectively. In general the thin-sheet approximation depends on a short characteristic time lending itself to a steep temperature gradient and a thin reaction zone. As long as the reaction times are short for the major heat producing reactions, the thin-sheet approximation will be valid.

From the above analysis it can be seen that one means of determining the flame surface is to measure the temperature above the burner to locate regions in which there is a steep temperature gradient. While this may mark the start of the reaction zone, convective and radiative effects may falsely indicate a thicker zone than actually exists. As an alternative physical measurement, Mungal et al. (1995), using Particle Image Velocimetry (PIV – to be discussed later), demonstrated the use of flow dilatation ($\nabla \cdot \mathbf{u}$) as a marker for the flame zone, which was expected as it is directly related to a change in density. However, as will be discussed, the measurement of this parameter can be somewhat difficult and it requires the use of costly equipment.

Optical techniques, on the other hand, based on the measurement of flame emittance from combustion products has been utilized as a means to identify the flame surface, as well as the global heat release within hydrocarbon flames by correlating their recorded intensity with fuel flow rates (Najm et al., 1998; Dandy et al., 1992; Haber et al., 2000; Gaydon and Wolfhard, 1953; Samamiego et al., 1995). Chemiluminescence occurs in the natural visible and near-ultraviolet range with the primary emitters from hydrocarbon flames considered to be CO_2^* , OH^* , CH^* and C_2^* , with weaker emissions from HCO^* and CH_2O^* . Meaningful interpretation of chemiluminescence measurements requires knowledge of kinetics leading to the formation of the excited state, the exact identity and spectroscopy of the excited state, and the kinetics of physical quenching reactions, which may compete with spontaneous emission to deactivate the excited state (Najm et al., 1998).

Samamiego et al. (1995) provided a numerical analysis that included the effects of strain on laminar and turbulent premixed flames supporting the use of CO_2^* as an indicator of fuel consumption and heat release rates. The favored mechanism for the formation of CO_2^* is $\text{CO} + \text{O} + \text{M} \rightarrow \text{CO}_2^* + \text{M}$. While marginal correlation was obtained for fuel consumption, a monotonic relationship was observed between the predicted heat release rates and intensity of CO_2^* chemiluminescence for all cases considered. However, CO_2^* chemiluminescence occurs over a very broad range, 340-600 nm (Samamiego et al., 1995), thus a number of narrow band filters would be needed to prevent concurrent measurement of OH^* , CH^* and C_2^* emissions.

Alternatively, OH^* and CH^* chemiluminescence occurs over a very narrow band, 306.4nm (near-ultraviolet) and 431nm (visible), respectively (Gaydon and Wolfhard, 1953). The primary source reaction for OH^* is considered to be $\text{CH} + \text{O}_2 \rightarrow \text{OH}^* + \text{CO}$ (Becker et al., 1977), however Haber et al. (2000) also proposed $\text{HCO} + \text{O} \rightarrow \text{CO} + \text{OH}^*$. This second reaction is somewhat questionable as it is not commonly used and Dandy and Vosen (1992) suggest the reaction produces ground state OH as opposed to the excited state. A comparison study between the total mean reaction rate and OH^* chemiluminescence measurements in an unstable flame conducted by Lee et al. (2000) showed good agreement.

For CH^* , the primary mechanism is considered to be $\text{C}_2\text{H} + \text{O} \rightarrow \text{CH}^* + \text{CO}$ (Najm et al., 1998). Najm et al. (1998) advised caution when studying highly turbulent flames where experimental results for CH^* indicated a breakage in the primary flame surface that was not evident in planar laser induced fluorescence (PLIF) images of HCO. However, HCO PLIF emissions (360 nm) are particularly weak, requiring filtration to reject as much natural flame emission as possible and frame averaging to obtain a usable image, thus the simplicity of OH^* and CH^* measurements make an attractive and useful alternative. Additionally, the flow of carbon into CH^* is negligible for methane flames and thus may not be an appropriate indicator of the total heat release (Najm et al., 1998).

Laser induced fluorescence (LIF) offers an alternative spatially resolvable method to natural chemiluminescence and can potentially reveal more detailed information. Unlike chemiluminescence, LIF measures the concentration of a species in the ground state and in the absence of the quantity being measured the signal is zero (Najm et al., 1998). This technique can easily be extended to a planar geometry (PLIF), thus allowing for the 2-D isolation of specific regions within the flame, which is not possible in chemiluminescence.

Lee et al. (2000), Najm et al. (1998a), Najm et al. (1998b), and Paul et al. (1998), provide excellent studies of PLIF imaging of OH, CH and HCO. OH PLIF was successfully used by Lee et al. (2000) to identify flame structure in stable and unstable methane-air flames. However, it was also noted that unlike OH*, the long-lived, ground state OH exists not only in the flame front but extends into the post-flame region. This may act to "blur" the heat release and the flame structure, especially in highly unstable or wrinkled flames. In stable and moderately unstable flames, the absence of OH in the pre-heat zone helps to identify the leading edge of the flame front.

CH PLIF has often been used to mark the surface of the flame due to its relatively short life span. However, like CH*, CH PLIF results obtained by Paul et al. (1998) and Najm et al. (1998) indicated a breakage in the primary flame surface when a vortex pair was imposed on the flame. This breakage was not evident when the flame was imaged by HCO PLIF. For this reason, these authors suggested the use of HCO PLIF as a flame marker and additionally demonstrated excellent temporal and spatial correlation between HCO and heat release rate. The latter statement was believed to be due to 1) the rapid decomposition of HCO, and 2) HCO production accounts for a substantial fraction of the carbon flow. However, the weak signal strength of HCO PLIF due in part to the rapid decomposition reaction and quenching of the excited species, requires additional filtration and image averaging. This makes the identification of the instantaneous heat release and flame front locations in turbulent or unsteady flames difficult, if not impossible. Both Paul et al. (1998) and Najm et al. (1998) addressed this issue by considering the concentration product of species responsible for the production of HCO.

The reaction $\text{CH}_2\text{O} + \text{OH} \rightarrow \text{H}_2\text{O} + \text{HCO}$ is a major production path for HCO (Paul et al., 1998). Thus by obtaining single pulse images of CH₂O and OH concentrations, which are both much stronger signals than HCO, and a pixel-by-pixel product of these two images, it was possible to derive an image that was closely correlated to the temporal and spatial heat release rate and flame front topography.

1.2.5 Flow Measurement and Visualization in Combustion

As previously noted, the interaction between large-scale coherent structures and acoustic oscillations can significantly influence thermoacoustic instabilities. To describe or model this behavior researchers must not only be able to measure the response of the flame to a given input,

but also be able to quantitatively describe the nature of the input. Measurement of the flame response was discussed in the previous section with regards to flame spectroscopy and pressure perturbations, and although flow measurements in a combusting environment have been performed for some time, obtaining an adequate description of a dynamically unstable combusting flow field can be quite difficult. Measurements must be made in such a way as not to significantly alter the geometry or the natural response of the flame.

Conventional flow measurements that have been used in a combustion research can be divided into qualitative and quantitative methods. Schadow et al. (1992) reviewed a number of experimental papers focusing on the role of large-scale coherent structures in the combustion process that utilized a variety of techniques, including: hot-wire anemometry, Planar Laser Induced Fluorescence (PLIF), Schlieren photography, spark shadowgraphy, and Laser Doppler Velocimeter (LDV).

Qualitative methods provide a means of visualizing the reacting and non-reacting flow fields and may consist of schlieren photography, spark shadowgraphy, laser sheet visualization and high speed photography. Poinso et al. (1987) used spark Schlieren photography to visualize the flow field in a step combustor. The recorded images provided a visual representation of the flame and flow field at specific instances in the oscillating cycle and were correlated with simultaneously measured heat release through C_2^* emissions and pressure to obtain a phase relationship between these parameters. Results indicated that the time lag between the vortex formation and the maximum heat release was about $\frac{1}{2}$ of the period of oscillation, and that between the vortex formation and the pressure oscillation maximum was $\frac{1}{4}$ of the period. An alternative approach was taken by Schadow et al. (1992) in which the fluid dynamic-combustion interaction was visualized by PLIF imaging of in situ OH radicals. Phase-locked average images revealed that the initial reactions occur in the circumference of the vortices and are convected downstream as the reaction reaches the vortex core. While these qualitative techniques may yield estimates of desired parameters and instantaneous images of the flow and flame quality, they fail to provide a detailed quantitative measurement of the flow field that can be compared to other sampled parameters.

Quantitative flow measurements provide the level of detail needed to understand the flow-combustion interactions and build / verify models of this behavior. However the use of conventional techniques is complicated by the existence of a reacting flow field. Hot-wire

anemometry has been used in a number of studies (Gutmark et al., 1991; Blackshear, 1952; Schadow et al., 1989) but is limited to isothermal flows. Thus flow measurement must be performed in the absence of combustion with the assumption that little change occurs in a reacting environment. The effect of frequency matching between the acoustics and vortices can be determined by acoustically forcing the flow field (Schadow et al., 1989).

Techniques do exist that allow for measurement of the fluid dynamics during combustion. Wagner and Ferguson (1985) utilized Laser Doppler Velocimeter (LDV) in an attempt to measure the laminar flame speed in a premixed Bunsen flame. In LDV the flow is seeded with highly refractive material capable of accurately following the flow and a point velocity is obtained by determining the Doppler shift between the scattered laser light and a reference beam. Keller and Saito (1987) investigated the flow-flame interaction through the use of LDV in a pulse combustor. Alumina Oxide (Al_2O_3) powder of approximately $1.0 \mu\text{m}$ in size, capable of a frequency response in excess of 1 kHz, were used to seed the combustor flow operating at a frequency of 50 Hz. Measurement of the velocity variance distinctly resolved the large mean velocity fluctuation in the reacting, pulsing flow.

The measurement of the acoustic velocity for use in the development of transfer functions to describe the relationship between the heat release fluctuations and the velocity variations for a given burner geometry using LDV was performed by Ducruix et al. (2000) Due to the planar nature of the acoustic wave, its velocity was measured at a single point above the burner exit, while global CH^* emissions of the flame were recorded to indicate heat release. The developed transfer function was intended to support the model developed by Fleifil et al. (1996). At moderate and high frequency values the predicted phase difference were significantly smaller than measured.

Methods such as hot-wire anemometry and LDV are point measurements. Thus in order to map an entire flow field a large number of measurements would be needed. This can be quite time consuming and unless the flow is reproducible, only generalized results could be obtained. Additionally, hot-wire anemometry is an intrusive measurement which can influence the fluid dynamics-combustion interaction.

In addition to velocity, the measurement of vorticity, strain rate and dilatation could provide insight into the effect of flame stretch on combustion instabilities. These parameters require the measurement of instantaneous velocity gradients in at least two dimensions, and the

spatial resolution of the velocity measurements must be sufficient to resolve the integral length scales (Reuss et al., 1989). Particle Image Velocimetry (PIV) is a flow measurement technique that allows a large portion of the flow field to be evaluated simultaneously. Like LDV, the fluid motion is made visible by adding small tracer particles. The particles are illuminated by a laser sheet pulsed over a short time interval and the subsequent images are recorded on either film or a CCD array. The displacement of the particles between the light pulses is determined by a correlation analysis of the recorded image(s) (Raffel et al., 1998; Westerweel, 1997; Christensen et al., 2000).

Reuss et al. (1989) utilized PIV to measure the laminar flow field velocity distribution in a Bunsen type burner for reacting and non-reacting flows. For the velocity, vorticity and strain rate results for the non-reacting case correlated quite well with the theoretical profile based on Poiseuille flow. Measurement in the reacting flow was complicated by the poor distribution of seeding particles between the unburned and burned gases. The image of the flame indicated a heavily seeded unburned gas region inside the boundary of the flame, while the burned gas region outside and above the luminous flame zone was very lightly seeded. This light seeding resulted in a failure of the interrogation in the burned gas region. The low seeding density was believed to be a result of two factors: volume expansion due to combustion and a decrease in the scattering cross section of the seeding material, TiO_2 . Utilizing particles that have a constant scattering cross section such as Aluminum Oxide (Al_2O_3) could prevent the second factor.

Unlike Reuss et al. (1989), Mungal et al. (1995) heavily seeded a laminar Bunsen flame and the turbulent tip region in an unstable premixed flame with Alumina powder in hopes of measuring both the non-reacting and reacting flow fields. As with the previous study, in both cases the unburned region within the flame boundaries was much more heavily seeded, thus indicating the strong volume expansion associated with the presence of the flame. The heavier seeding level marks the region of the flow up to the preheat region of the flame, in which a thin region exists before the flame surface (location of maximum reaction rate). The authors noted that the error in the analysis increases in regions that overlap the burned and unburned portions of the flow due to the large particle image density gradient. This gradient leads to a bias in the measured velocity towards the non-reacted (heavier seeded) values. However, fairly good results were obtained with a velocity error of less than 3% of the maximum velocity with a portion of the error due to thermophoresis effects in the vicinity of the flame zone.. It was also shown that

the dilatation ($\nabla \cdot \mathbf{u}$) provided an excellent marker for the flame zone, which was expected as it is directly related to a change in density.

1.2.6 Modeling of Flame Dynamics

Few papers have used *quantitative* measures (or predictions) of transfer function sub-models to actually predict the stability of practical combustors. Instead, most investigations use control theory models to understand trends and predict qualitative behavior. For practical applications, quantitative evaluation of the combustion or acoustic transfer function sub-models is a current research topic, see Pascheriet et al. (1998) for an example. Thus, complete stability analysis of practical systems has seldom been carried out using quantitatively accurate sub-models. The recent paper by Krueger et al. (1995) approaches this goal, but some aspect of the problem is (necessarily) simplified. Therefore, actual prediction of the stability margin, in terms of the phase and gain, is qualitative.

In a two-part report concerning the combustion stability of liquid fuelled rocket motors Crocco⁹ developed an analytical model that addressed the sensitivity of the combustion process to changes in pressure, n , and the time lag, τ , from fuel injection to combustion. The interaction index n , which is essentially the gain factor, was assumed to be constant over the time lag (Harrje and Reardon, 1971). Consideration was given to a uniform, as well as a non-uniform time lag in which spatial variations in the time lag were believed to exist. It was shown that n must exceed a minimum value before the system can become unstable, and that the effect of non-uniformity of the time lag acts to improve the overall stability. The n - τ model, as it has come to be known, is widely used as a means of describing the quantitative behavior of a combustion system (Harrje and Reardon, 1971).

An analytical model resulting in a nonlinear ordinary differential equation was developed to describe periodic oscillations in rocket motors by Crocco and Mitchell (1969). The nonlinearity of the problem accounts for the limit cycle behavior, which ensures finite oscillation amplitude. The combustion process was represented by the sensitive time-lag, or n - τ , model and considered to be well distributed over the length of the combustion chamber. An oscillation was imposed onto a reacting environment with and without a shock with feedback provided by the combustion process. The model did not account for the system geometry, thus damping and driving were controlled entirely by the presence and strength of a shock wave, the magnitude of

the combustion feedback terms (interaction index, n) and the characteristic (or “stretched”) time lag, τ .

Mitchell (1994) discussed the need to include all of the important driving and damping mechanisms in models developed to predict combustion stability in liquid fuelled rockets. Two general approaches to stability modeling were proposed: 1) attempt a direct analytical solution of the partial differential equations (pde’s) that describe the flowfield of the rocket; or 2) numerical analysis or direct numerical integration of the pde’s. The latter of these two was also subdivided into linear and nonlinear analysis. The bulk of the study focused on the small oscillation amplitude linear model that utilized the time-lag (n - τ) model to represent the combustion response, given as the following:

$$Q' = \bar{Q}n(1 - e^{i\omega\tau})p' / \bar{p} \quad (5)$$

Models were additionally provided for the nozzle response and acoustic absorbers to evaluate the impact of axially distributed combustion on stability. Results indicated that if the time lag, τ , were relatively short, distributing the combustion is stabilizing, whereas if τ were relatively long, distributing the combustion is destabilizing. The author notes the need for nonlinear models to predict the occurrence of the finite amplitude waveform, or limit cycle behavior; and to address the phenomena of triggering in which the introduction of disturbances of sufficient amplitude and correct form can initiate an instability in an intrinsically stable engine.

The primary difficulty in modeling combustion driven oscillations is the description of the response of the flame to various inputs. An early attempt at modeling the flame dynamics in a simple laminar conical flame utilizing a linear stability analysis was presented by Merk (1956). In this analysis, the author described the combustion driven oscillations by a flame transfer function, in which the fluctuations in the heat production were shown to be dependent on velocity fluctuations.

Mugridge (1980) applied the previous model to a simple combustion tube system. With Merk’s (1956) assumption of a small pressure change across the flame, Mugridge (1980) suggested that changes in the heat release were associated with fluctuations in the flame volume, which in turn produced an increase in the acoustic velocity between the input (x_1) and output (x_2) planes of the flame. This change in velocity was considered to be a velocity “jump” condition given as

$$u_2 - u_1 = \left(\frac{\gamma - 1}{\rho c^2} \right) q_{(x_2 - x_1)} \quad (6)$$

where q is the fluctuating heat release per unit cross sectional area between planes x_1 and x_2 . In comparison with experimental results it was shown that combustion instabilities are a function of the amplification properties of the flame and the impedance either side of the combustion zone. The theoretical results qualitatively suggested that for a given flame transfer function an instability could be suppressed by altering the supply impedance. However, Merk's (1956) transfer function was found to be inadequate due to the experimental occurrence of resonance in modes that were not predicted by theory. It was suggested that the non-linear effect of observed changes in the flame structure due to intense pressure waves were the cause of this discrepancy.

As a comparison to Equation (6), two aforementioned studies (Chu, 1956; Fleifel et al., 1996) also provided a relationship between the heat release rate and the change in acoustic velocity across the flame.

$$\text{Chu} \quad (u_2)_h - (u_1)_h = \frac{\gamma_2 - 1}{\gamma_2} \left(\frac{q}{p_1} - \frac{\gamma_1 - \gamma_2}{(\gamma_2 - 1)(\gamma_1 - 1)} (u_1 - S_a)_h \right) \quad (7)$$

Where the "h" subscript indicates conditions at the heat source, and S_a is the apparent fluctuating flame speed.

$$\text{Fleifel} \quad n(u_2 - u_1) = \frac{\gamma - 1}{\rho_1 c_1^2} q_{x_2 - x_1} e^{-i\omega\tau} \quad (8)$$

The relationship given by Fleifel et al. (1996) is similar to that given by Mugridge (1980), except for the inclusion of the n - τ model in Equation 8. This is due to the fact that Mugridge (1980) did not include variations in the air / fuel ratio that would have effected the characteristic time and gain of the heat release rate. Equation (7) takes a slightly different approach by considering the ratio of specific heats on either side of the flame. Additionally, variations in characteristic time are accounted for adjusting the apparent flame speed, S_a .

Janus and Richards (1996) developed a simple, nonlinear model of premixed combustion oscillations based on a control volume. The combustion process was simplified by modeling it as a well-stirred reactor with finite kinetics. A set of ordinary differential equations were developed and solved by applying the Euler predictor-corrector algorithm. While not posed as a rigorous model, the intent was to provide a means of quickly examining instability trends

associated with changes in equivalence ratio, mass flow rate, geometry, ambient conditions, and other relevant parameters. The results displayed qualitative agreement with a limited set of experimental results.

Baade (1979) investigated combustion driven oscillation by utilizing stability criteria based on feedback loop analysis. Through the use of feedback loop analysis it is possible to quantitatively account for both magnitude and phase of all the cause-effect relationships associated with the instability. Three linear transfer functions were developed to describe the acoustic impedance of the combustion chamber, the dependence of the flame volumetric expansion on the pressure fluctuations in the combustion chamber, and the flame itself. Using these transfer functions, the author re-stated the Rayleigh Criteria, given in Equation (1), into a form that lead to the same criteria as the feedback loop analysis. This was verified by comparison to a number of other theoretical models, in which relatively good agreement was obtained for both phase and magnitude at low frequencies.

A number of recent studies have considered modeling thermoacoustic oscillations as a network of acoustic elements (Paschereit and Polifke, 1998; Paschereit et al., 1999; and Schuermans et al., 1999). The elements, which are defined by transfer matrices, are frequently referred to as an acoustic “two-port” due to fact that the transfer function describes the relation between the acoustic quantities on either side of the element. Schuermans et al. (1999) developed an adaptation of the classic n - τ model based on this approach for a premix swirl stabilized burner. Due to the complex nature of the flow field in the burner and the uncertainty of the time lag, several parameters were determined empirically by exciting the burner with and without combustion. Acoustic measurements were conducted at various locations in order to determine the Riemann invariants, which can in turn be used to derive the transfer matrices for the burner and the flame.

Richards et al. (2001) developed a simplified model of a variable geometry fuel injection system to evaluate its impact on the dynamic response of the combustion system. Acoustic transfer functions were used to relate acoustic pressure and mass flow at various points along the nozzle, and a dynamic model for the premixer orifice flow was developed from a linearized momentum balance. Although not performed, it was suggested that open-loop Bode or Nyquist analysis could be performed as a means of evaluating the system stability. The authors did verify the assumption of Mugridge (1980), that by changing the acoustic impedance of the fuel

system it was possible to modify the phase of fuel fluctuations and under certain conditions enhance the stability of the combustor. Experimental measurements indicated that with the current configuration, a phase shift of approximately 70° was possible and the results were found to have excellent agreement with the model predictions for the magnitude and phase response of the orifice model.

In two separate studies, Ducruix et al. (2000) and Khanna et al. (2000) experimentally determined the open-loop flame transfer functions for laminar, premixed flames. In both cases an inherently stable flame was excited to evaluate its response to acoustic modulations. Determination of the open-loop flame transfer function is dependent on the measurement of the fluctuating heat release rate and the acoustic velocity upstream of the flame. Global heat release rates were inferred from chemiluminescence measurements of CH^* and OH^* , respectively. Ducruix et al. (2000) utilized laser Doppler velocimetry (LDV) to measure velocity perturbations and Khanna et al. (2000) used a velocity probe based on a two-microphone technique and the 1-D Euler equation. The transfer function in the Khanna et al. (2000) study was found to be fourth-order by determining the best fit of the experimental data, which is quite different than the widely accepted first-order response. However, a flat flame burner was used in which there was a significant interaction between the honeycomb substrate flame anchor and the flame via heat transfer. The authors believe this may have contributed to the higher order model. Two pairs of complex conjugate poles were obtained, with the first resonant response believed to be dictated by a fluctuating flame speed and the second resonant response attributed to the chemical kinetics of the combustion process. Results indicated an increase in damping and bandwidth with an increase in the mean energy content of the mixture.

Although while Ducruix et al. (2000) did not obtain a mathematical description of the flame transfer function, its amplitude and phase were determined from the experimental data and compared to two analytically derived models, including that of Fleifil et al. (1996). Fairly good agreement was obtained between the experimentally determined amplitude and that of the analytical models, however considerable difference was seen in the phase comparison. The experimental phase difference indicated a nearly constant time lag between the velocity perturbations and the heat release fluctuations, which only agreed with the analytical results at relatively low frequencies. This discrepancy was believed to be due to assumptions made in the modeling, such as constant flame speed.

2.0 Description of Proposed Project

2.1 Project Overview

Emissions reduction through lean-premixed combustion necessitates the control of thermoacoustic instabilities. A possible strategy would be to modify engine designs as needed when instabilities are encountered in the testing or operational phases. However, design modifications made late in production can be quite costly, and alterations aimed at eliminating a particular mode of combustion oscillations may in fact excite another mode at a different operating condition. Another possibility is to model this behavior to predict when and where instabilities will occur, as well as their magnitude. However, past research has thus failed to adequately model the complex flame dynamics and interactions in full-scale gas turbines. Simpler systems offer less complexity, but still the nonlinear nature of flame dynamics during instabilities is not fully understood. Thus theoretical model development of even simple combustion systems must be supplemented with experimental results.

Currently there is no general consensus in the research community as to the mechanisms that bring about variations in the heat release rate (flame dynamics) which later couple with the acoustic pressure waves. Experimental studies aimed at understanding this behavior must be capable of isolating or nearly isolating individual mechanisms that contribute to heat release variations. Knowledge of the impact of single components can be used to build more complex models aimed at predicting the behavior of full-scale gas turbine engines.

The intent of this study is to isolate several individual mechanisms by studying a relatively simple combustion system, and evaluating the impact of those mechanisms on the stability of the system over a range of operating conditions and fuel compositions. A Rijke tube combustor is utilized to impart an active acoustic boundary while excluding phenomena such as swirl and complex nozzle and exhaust geometries. The combustor has a well-defined stability boundary and is capable of sustaining both stable and unstable combustion, depending on the operating conditions.

Using the experimental data it will be possible to create sub-models of the individual mechanisms that can be combined to form a closed-loop feedback system that describes the overall behavior of the combustor to changes in operating conditions. This system model can be used to quantitatively predict the stability characteristics of combustion, and a comparison with

experimental data can be performed. With the appropriate understanding of how particular mechanisms contribute to combustion driven instabilities it would be possible to incorporate this information in CFD models to predict the stability margin in full-scale gas turbine engines.

2.2 Specific Research Areas

2.2.1 Evaluation of Heat Release Mechanisms

The Literature Review discusses several mechanisms that may contribute to variations in the heat release rate from combustion operating under lean-premixed conditions. Of these mechanisms, the effects of flame surface area and flow field variations were chosen for this study. In studying flame surface area, the impact of flame stretch on the simple system used in this study as well as in full-scale rigs must be clarified.

In considering the task at hand, the first question that must be addressed is how to isolate the mechanisms that have been chosen for this study. Given a means of independently measuring the flame surface area and the heat release rate, it must be shown that the area actually changes and that this change results in fluctuations of the heat release. Thus phase differences must exist such that the area variation leads the heat release, and the changes must be related proportionality. Under conditions of natural instability several mechanisms may be present, however by artificial excitation of a stable flame it would be possible to determine if the flame surface area actually changes due to an acoustic interruption and how much that change directly affects the heat release rate.

Isolation of the flame surface area mechanism may be possible by excitation of stable flames so as to eliminate the impact of phenomena such as vortex shedding. This neglects the potential for flow entrainment, which may accompany larger amplitude self-excited oscillations. By imposing flow instabilities of various magnitudes and frequencies on a stable flame it would be possible to determine if flow conditions directly effect heat release oscillations, such as through re-entrainment of reacted gases into the fresh mixture, or indirectly by invoking flame surface area variations.

2.2.2 Flow Visualization and Measurement

As previously mentioned, several of the mechanisms thought to contribute to variations in the heat release rates are controlled by the flow into and/or around the reaction zone. For this

study, there are two primary interests regarding the flow. First is the occurrence of vortex shedding or flow disturbances leading to deformation of the flame surface and subsequent variations in the heat release. Second is the re-entrainment of ambient air or reacted gases back into the reaction zone that acts to dilute the incoming fuel-air mixture and results in a variation in the heat release.

Particle Image Velocimetry (PIV) offers a non-intrusive method of measuring not only the velocity field across a planar region in a reacting flow, but also the strain rate, vorticity and dilatation. By studying the impact of these parameters through imposed flow instabilities on stable flames and naturally unstable flames it would be possible to evaluate the extent to which they influence combustion instabilities.

2.2.3 Effects of Fuel Composition

Methane, ethane and propane are the primary components in natural gas, however the quantity of each of these gases may vary geographically or seasonally. As the composition of the fuel changes, so too does many of its properties, such as: energy content (enthalpy), Lewis Number and Damkohler Number. Small changes in these as well as other properties may result in a shift of the stability regions, forcing a previously stable operating state into an unstable one. Fuel composition may additionally impact the steepness of the stability boundary. Tests will be conducted on various combinations of methane, ethane and propane in an attempt to quantify the effect of fuel composition on the phase-gain relationship between heat release, flame surface and pressure.

2.2.4 Flame Dynamics Model and Stability Analysis

The primary focus of this research is to develop a method of quantifying the stability boundary in a simple, pre-mixed, laminar flame. Although the bulk of the study is consumed with experimental analysis, it is merely a tool to gain the necessary knowledge with which to develop predictive models. Previous research (Khanna, 2000) and control theory has shown that it is possible to develop transfer functions describing input-output response from experimental data. Through the measurement of the aforementioned parameters, a dynamic model of the closed-loop feedback system will be developed. Open-loop Bode and Nyquist analysis permits one to evaluate the system stability for a variety of operating conditions. It is intended to keep

these models as general as possible in order to draw conclusions regarding the modeling and control of thermoacoustic instabilities in full-scale gas turbine combustors.

3.0 Work Done to Date

3.1 Experimental Setup

The combustion system utilized for this study is a ring-stabilized premixed laminar methane-air flame inserted in a Rijke tube combustor operating at atmospheric conditions (Figure 2).

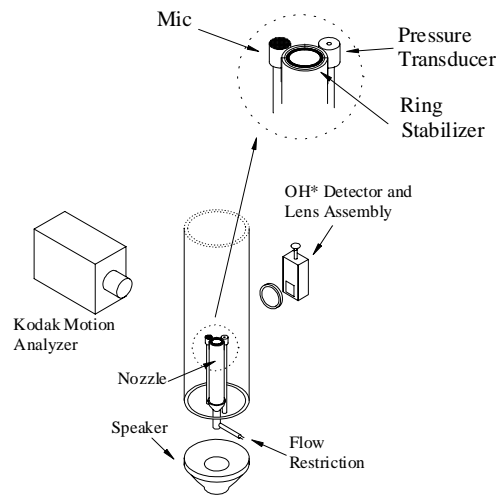


Figure 2: Experimental Setup

The Rijke tube is a long, open-ended tube of uniform cross section and has been used to study thermoacoustic oscillations since its conception by Rijke in 1859 (Rijke, 1859; Putnam and Dennis, 1953; Maling, 1963; Carrier, 1955). By placing an energy source at the appropriate distance from the inlet a strong instability is obtained in the form of a tone approximately at the fundamental frequency of the tube. Thus, the Rijke tube provides the necessary acoustic environment needed to generate combustion oscillations for this study, while at the same time provide a simplified system that nearly allows for the study of the effect of individual mechanisms on the heat release rate.

The main body consists of a vertically mounted, 80 cm long, 8.0 cm diameter quartz tube, allowing optical access and suitable transmittance even in the ultraviolet range (Appendix A). The mixture nozzle, a 2.54 cm o.d. / 2.18 cm i.d. stainless steel tube, extends 20 cm ($\frac{1}{4}L$) into the main body. The flame is anchored on a 2.0 cm o.d. / 1.8 cm i.d. ring stabilizer at the top of the

nozzle (see insert - Fig 2). The ring, mounted flush with the top of the nozzle, acts as a bluff-body that provides static stability under lean and high flow operation (Johnson et.al.²⁹). Johnson et.al.¹⁶ stressed the necessity of a small gap between the outer diameter of the ring and the inner diameter of the nozzle in order to create a stable recirculation zone in the wake of the ring. Without the gap the flame would revert back to a rim stabilized flame with limited static stability. Due to the lack of an acoustic feedback mechanism, the burner utilized by Johnson et.al. (1998) did not experience thermoacoustic instabilities, however it is interesting to note that without the ring stabilizer in place dynamic instabilities within the Rijke tube used in this study could not be attained.

Laboratory grade methane and air (dried to a dew point of -40°C) are mixed well upstream ($L/D = 67$) of the nozzle inlet. Two mass flow controllers providing a combined flow of air slightly over 45 slpm, with an additional mass flow controller regulating fuel flow to a maximum of 5 slpm. As previously stated, perturbations in the fuel / air mixture composition are considered one of the possible mechanisms driving heat release variations in the reaction zone. Acoustic feedback from combustion or flow instabilities could travel into the mixing region and disproportionately alter the air or fuel flow resulting in perturbations in the mixture composition. However, for this study it was imperative that this effect be limited. A small restriction ($d_{\text{res}}/d_{\text{noz}} = 0.1$) was placed at the base of the nozzle, resulting in a 60% pressure drop, to prevent the influence of acoustic feedback on fuel / air mixing. To verify the success of the restriction the pressure signals were monitored, with Kistler model 206 transducers, upstream of the restriction and at the exit plane of the nozzle during operation at the maximum amplitude instability attainable by this system ($P' = 0.68$ psi, $U = 150$ cm/sec, $\phi = 1.0$), Figure 3. The transducers record the AC pressure signal, and the traces have been background corrected for flow without combustion. Figure 4 is the amplitude of the frequency response from the pressure signals. It indicates that the pressure upstream of the nozzle has very little response at the combustion oscillations of 228 Hz, thus indicating that instabilities in the combustor due to thermoacoustic oscillations are not being transmitted into the mixing region.

The effective nozzle exit area was determined to be 2.32 cm^2 ($A_{\text{nozz}} - A_{\text{ring}}$), thus providing a maximum flow velocity of 360 cm/sec and Reynold's number of approximately 4100. However, in order to maintain laminar flow at the nozzle exit, testing was restricted to an exit velocity of less than 150 cm/sec ($Re \approx 1700$).

OH* emissions (308 nm) were used to measure the global heat release from the flame. A single fused silica lens ($f = 50.8$ mm) was used to focus 9.65 cm² of the combustion region, centered 1.25 cm above the nozzle exit, onto UG-11 bandpass filter coupled to a Hamamatsu model R636-10 photomultiplier tube. The 150 nm bandpass filter is centered at 320 nm with

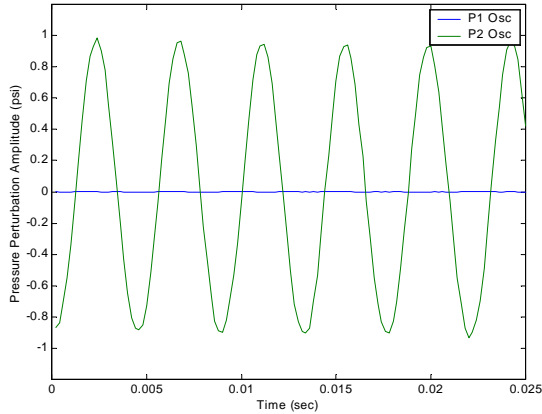


Figure 3: Pressure amplitude trace during peak oscillations ($U=150$ cm/sec, $f=1.0$) upstream and downstream of nozzle

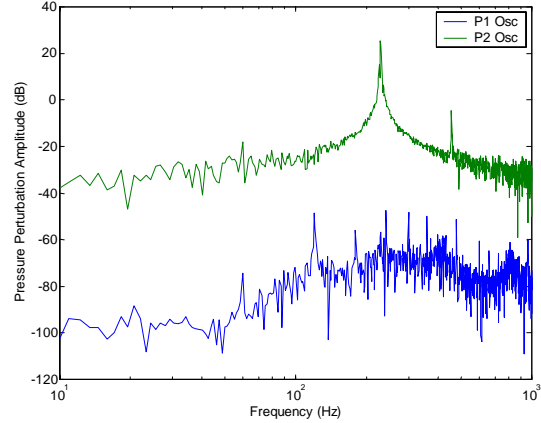


Figure 4: Pressure amplitude frequency response during peak oscillations ($U=150$ cm/sec, $f=1.0$) upstream and downstream of nozzle restriction.

> 85% transmittance at 308 nm, while the photomultiplier tube has a 20-25% quantum efficiency at 300-350 nm and a response time of 10-20 nsec.

A high speed Kodak Motion Analyzer, Model 1000 HRC, capable of recording speeds of 1500 frames per second and a resolution of 512 x 384 pixels, was used to record the visible flame surface which consist primarily of CH* emissions (430 nm). The camera was operated at 1000 frames per second and triggered to allow time alignment with other data. An area of 11.275 cm x 8.448 cm was captured equating to a resolution of 45.4 pixels/cm, which provided sufficient detail of the flame structure.

Assuming the flame surface to be a thin sheet and flame wrinkling to be axisymmetric, an algorithm developed with the MATLAB Image and Signal Processing Toolboxes, and based on intensity differences and Equation 2, identifies points along one edge of the flame surface. For each data set, 682 images are recorded. Images are imported into MATLAB where each image is stored as a two-dimensional array of pixel intensities. Pixel intensity is adjusted to improve the contrast between the flame edge and the background, and the image is cropped to include only the region of interest (ROI). By restricting the ROI the speed of the algorithm is greatly

improved. To identify the flame edge, pixel intensities were interrogated starting at the lower left side of the image working horizontally across the image until a sharp gradient in pixel intensity was obtained. The gradient is a measure of the difference over 5 pixels. When the gradient is larger than a predetermined value then the left most pixel indicates a position on the flame surface. Once the edge pixel has been identified for a row, the algorithm shifts to the first pixel in the next row until the entire ROI is complete, Figure 5. It should be noted that based on the assumption of symmetry either the left or right side of the image can be used.

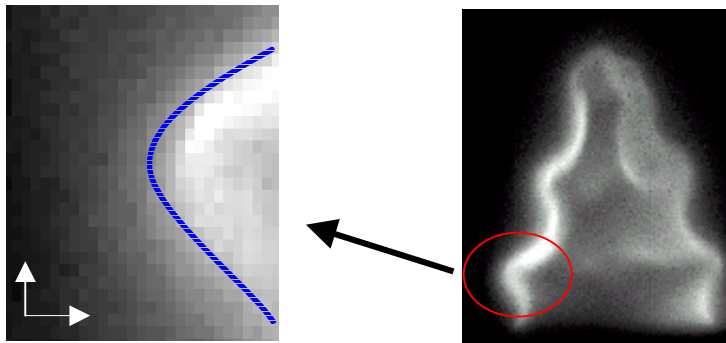


Figure 5: Pressure amplitude trace during peak oscillations ($U=150$ cm/sec, $f=1.0$) upstream and downstream of nozzle restriction.

Figure 6 provides a symbolic representation of the procedure which was used to determine the flame location, calculate the flame surface area and perform correlation studies with heat release rates and pressure oscillations.

Pressure and acoustic signals are recorded at the exit plane of the nozzle by a Kistler Model 206 transducer and a Knowles BL 1994, respectively. These signals along with the heat release data, fuel and air flow rates, and image and data triggering were collected simultaneously

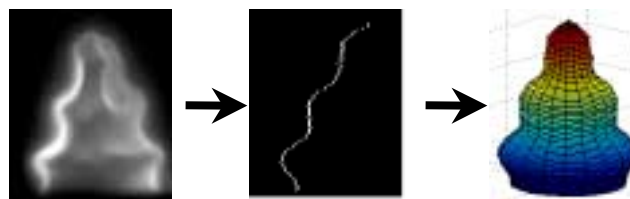


Figure 6: Representation of algorithm to determine the flame surface area from digital image of flame.

at 5000 Hz using a Data Translation DT3001-PGL board (capable of sampling at 330 kHz) and HP Vee Version 5.0 data acquisition software.

Time alignment was critical for the phase analysis portion of the study. A short pulse emitted by the motion analyzer at the start of each frame was aligned with the trigger event, Figure 7. Once the trigger is initiated, data storage begins at the next frame event. This

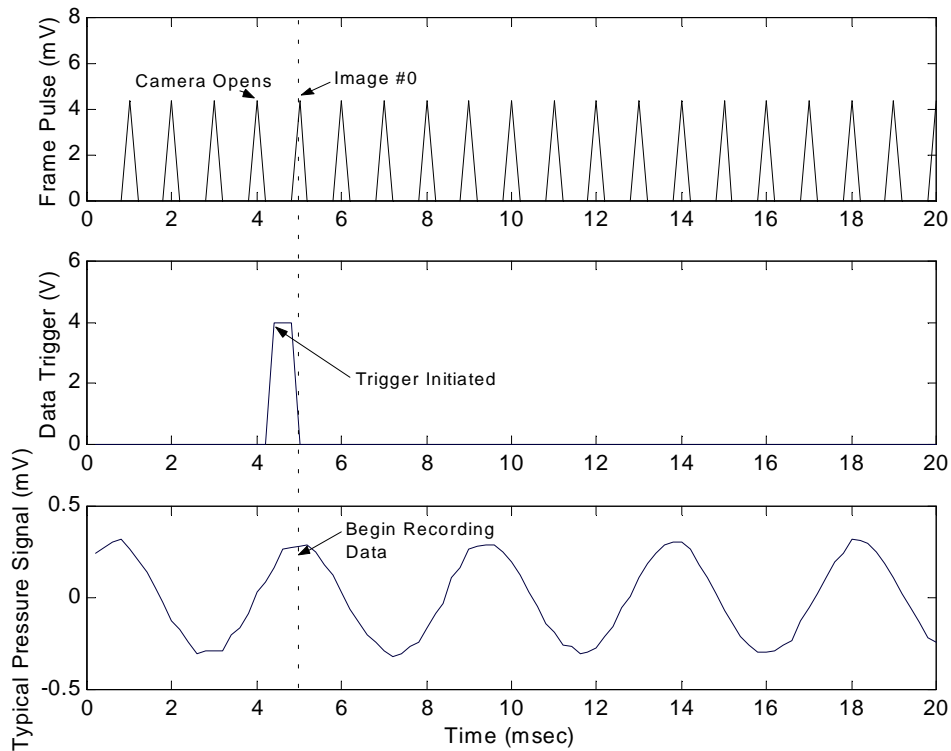


Figure 7: Thermoacoustic feedback loop used in this study and location of data sampling.

ensures the proper alignment of the data. Based on the sampling frequency of the data acquisition system it was determined that for a flame oscillating at 221 Hz, the maximum phase error would be less than $\pm 8^\circ$. It should be noted however, that phase-locking the data acquisition and image collecting could significantly reduce this error.

Since the unstable flame is repeatable from cycle-to-cycle, it is possible to utilize the pressure or heat release signal as a trigger. Data could be ensemble averaged over a number of cycles at a given phase shift from the trigger. By adjusting the phase shift between tests, it should be possible to improve the accuracy to better than 1° . However, this process will greatly increase the test time and the number of tests required.

Excitation of stable flames was also performed in order to evaluate the effect of oscillation amplitude on the phase relationship between flame surface area, pressure and heat release oscillations. A 20 cm, 100 W speaker mounted at the base of the Rijke tube provides a controlled acoustic excitation to the flame and convective flow entering at the base, resulting in small amplitude oscillations of the flame surface. A Stanford Research Model 560 Function Generator, capable of internal or external triggering, provided the speaker signal. Following the ensemble averaging technique described above, the input signal to the speaker could be used to trigger the data collection incorporating the necessary phase shift.

Figure 8 provides a block diagram representation of the feedback loop considered in this study. Unlike typical thermoacoustic closed loop systems (Paschereit et al., 1999) which may consist of addition inputs to the flame, such as turbulence or equivalence ratio fluctuations; the inputs to the flame for this study are limited to pressure and velocity fluctuations. Laminar flow maintained through the nozzle helps to reduce the affects of turbulence, while the restriction placed in the reactant feedline downstream of the mixing chamber prevents equivalence ratio perturbations. It should be noted however, that some degree of mixture dilution might take place in the reaction zone due to entrainment of burned gases or air from the convective flow through the tube. Figure 8 also indicates the locations within the loop that pressure, surface area and OH* perturbations are evaluated.

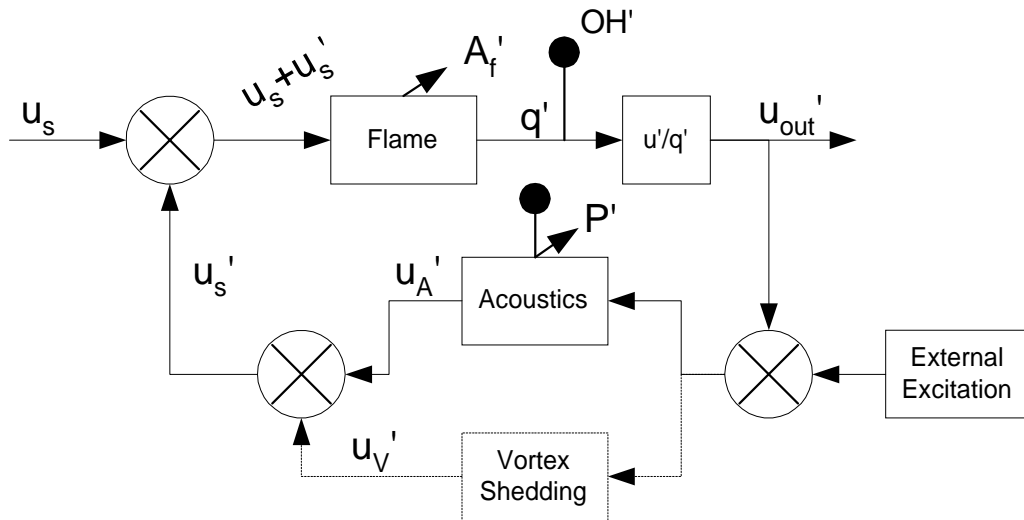


Figure 8: Thermoacoustic feedback loop used in this study and location of data sampling.

3.2 Experimental Results and Discussion

3.2.1 Experimental Procedure

For this study, it was desired to have test conditions that would provide a varying degree of instability, ranging from stable to highly dynamic oscillations. The flame was considered stable if a particular resonating frequency could not be identified above the broadband noise in the time-averaged pressure signal. Test conditions covered a range of nozzle exit flows from 50 – 150 cm/sec ($Re = 570 - 1700$) and equivalence ratios of $\phi = 0.6 - 1.1$. The unstable frequencies at each operating condition along with the normalized pressure perturbations are provided in Table 1. The oscillating frequency is centered at 225 Hz, however a slight increase in frequency can be seen with an increase in nozzle flow rate.

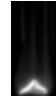
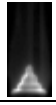
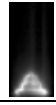


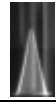



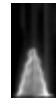
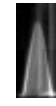




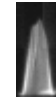


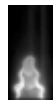
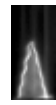
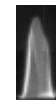




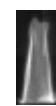
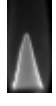
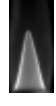

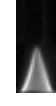
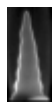
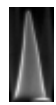
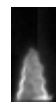
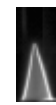
In addition to the naturally occurring instabilities, lean ($\phi=0.68$) and rich ($\phi=1.1$) stable flames operating at 75 and 110 cm/sec were externally excited with the base mounted speaker at 50 W (Table 1). The excitation provides a means of studying the phase-gain coupling of various parameters in the flame while the system is stable. Built-in and user created algorithms in MATLAB provided frequency domain analysis of the data.

3.2.2 Results and Discussion

Figures 9 – 12 are examples images of stable, unstable and excited flames. The coherence between the surface area, OH*, and pressure perturbations at the fundamental frequency was determined to be greater than 0.85 for all of the conditions studied with $\phi > 0.68$ for the naturally unstable cases. The externally excited cases also had excellent coherence except for $u=75$ cm/sec, $\phi=1.1$ where the coherence was only 0.72 between the area-OH* and area-pressure. Data analysis is primarily limited to cases where the coherence is greater than 0.85, however some lower coherence data is included to show general trends.

Figures 13 - 15 show the change in perturbation amplitude for pressure, OH* and surface area, respectively, due to changes in equivalence ratio and nozzle flow rates. The results indicate that the burner becomes generally unstable when operated above $\phi = 0.7$ at any flow rate, with the maximum instability occurring between $\phi=0.8-0.9$, decreasing slightly as a stoichiometric condition is approached. The burner becomes stable again for all cases at $\phi = 1.1$. Comparing Figure 14 and 15 one can see that both the heat release (OH*) and surface area perturbations are directly proportional, thus indicating the influence of surface area fluctuations on heat release

Table 1: Flame Response to Changes in Nozzle Exit Velocity and Equivalence Ratio Conical Flame

Nozzle Exit Velocity (cm/sec)	Equivalence Ratio				
	$\phi=1.0$	$\phi=0.9$	$\phi=0.8$	$\phi=0.7$	$\phi=0.6$
50	P' = 0.69 f = 219 Hz 				
75	P' = 0.48 f = 219 Hz 	P' = 0.53 f = 219 Hz 	P' = 0.57 f = 219 Hz 	P' = 0.35 f = 219 Hz 	P' = 0.14 Stable 
100	P' = 0.68 f = 223 Hz 	P' = 0.57 f = 223 Hz 	P' = 0.68 f = 223 Hz 	P' = 0.67 f = 223 Hz 	P' = 0.14 Stable 
110	P' = 0.54 f = 227 Hz 	P' = 0.63 f = 227 Hz 	P' = 0.64 f = 223 Hz 	P' = 0.51 f = 223 Hz 	P' = 0.15 Stable 
125	P' = 0.60 f = 227 Hz 	P' = 0.67 f = 227 Hz 	P' = 0.56 f = 223 Hz 	P' = 0.51 f = 227 Hz 	P' = 0.18 Stable 
150	P' = 0.68 f = 230 Hz 	P' = 0.69 f = 230 Hz 	P' = 0.64 f = 227 Hz 	P' = 0.34 f = 230 Hz 	P' = 0.15 Stable 
75 Excited	$\phi = 1.1$ P' = 0.6 f = 223 Hz 	$\phi = 1.1$ Stable 		$\phi = 0.68$ P' = 0.6 f = 219 Hz 	$\phi = 0.68$ Stable 
110 Excited	$\phi = 1.1$ P' = 0.54 f = 227 Hz 	$\phi = 1.1$ Stable 		$\phi = 0.68$ P' = 0.68 f = 223 Hz 	$\phi = 0.68$ Stable 

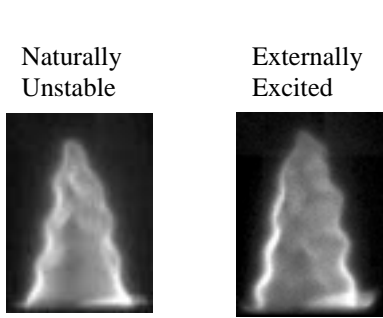


Figure 9: Flame images for $U = 110$ cm/sec. Unstable flame, $\phi = 0.7$; Excited flame, $\phi = 0.68$.

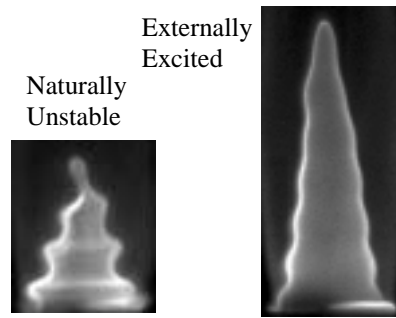


Figure 10: Flame images for $U = 110$ cm/sec. Unstable flame, $\phi = 1.0$; Excited flame, $\phi = 1.1$.

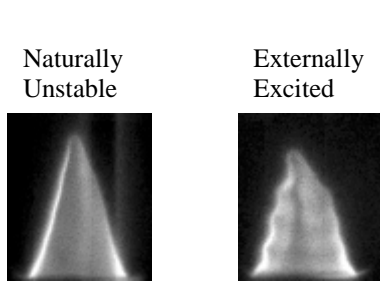


Figure 11: Flame images for $U = 75$ cm/sec. Unstable flame, $\phi = 0.7$; Excited flame, $\phi = 0.68$.

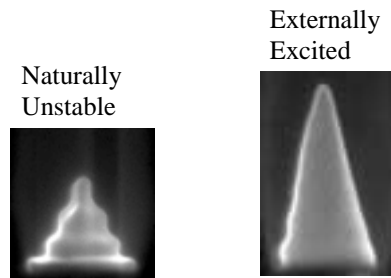


Figure 12: Flame images for $U = 75$ cm/sec. Unstable flame, $\phi = 1.0$; Excited flame, $\phi = 1.1$.

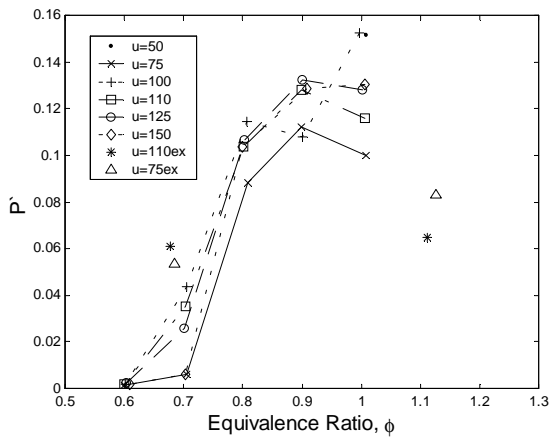


Figure 13: Normalized pressure perturbation as a function of equivalence ratio at various nozzle exit velocities.

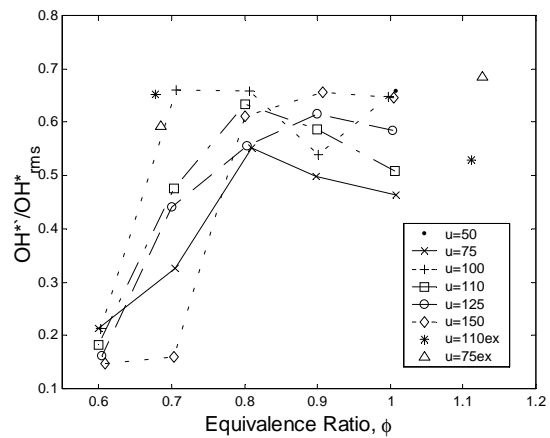


Figure 14: Normalized OH^* perturbations as a function of equivalence ratio at various nozzle exit velocities.

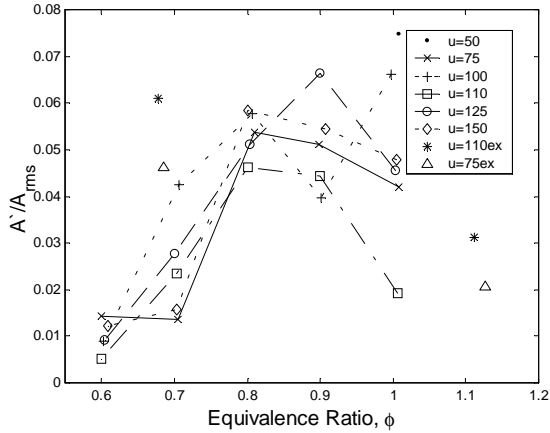


Figure 15: Normalized flame area perturbation as a function of equivalence ratio at various nozzle exit velocities.

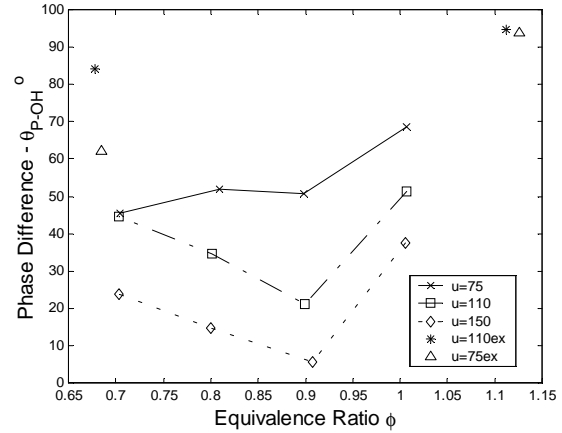


Figure 16: Phase angle between pressure and OH* as a function of pressure perturbation amplitude. Supports Rayleigh criteria.

(OH*) oscillations. At stoichiometric and richer conditions the OH* perturbations no longer follow the same trend even for the externally excited cases. However, higher equivalence ratio cases are beyond the scope of this study due to interactions with the external air supply and will not be considered in depth.

Close examination of Figures 14 and 15 will reveal a small discrepancy in the data that is still under investigation. Although the data clearly indicates a proportional relationship between OH*'/OH and A_f'/A_f , the OH* normalized results are an order of magnitude higher than those of the normalized surface area. This could indicate the influence of another heat release mechanism or may be the result of an error in the reduction algorithms. Explanation of this phenomena will be pursued as part of the proposed work.

Satisfaction of the Rayleigh criteria can be seen in Figure 16, which demonstrates a decrease in the phase angle difference between pressure and heat release (OH*) perturbations at the condition of maximum oscillation. Referring back to Table 1 it can be seen that for the three naturally unstable cases shown, the instability (measured by the amplitude of the pressure perturbation) is greatest at $U = 150$ cm/sec and $\phi=0.9$ which is shown in Figure 16 to have the smallest phase difference.

The phase of the externally excited cases is very different than the naturally unstable conditions. The phase difference displays an acute sensitivity to changes in the equivalence ratio at the stability boundaries. Although the difference in equivalence ratio between the excited case and the adjacent unstable is very small (0.02 on the lean side and 0.1 on the rich side) there is a sizable difference in phase between OH* and pressure and a steeper transition across the boundary as

compared to values within the naturally unstable regime. It is important to note that the oscillation occurring in the externally excited cases is not a result of the Rayleigh phenomena, but rather an imposed excitation and the flame surface is merely responding to the speaker signal.

Figure 17 compares the phase difference between the surface area and OH* perturbations. In the kinematic model developed by Fliefel et.al¹⁸, it was assumed that area perturbations resulted in an immediate change in heat release.

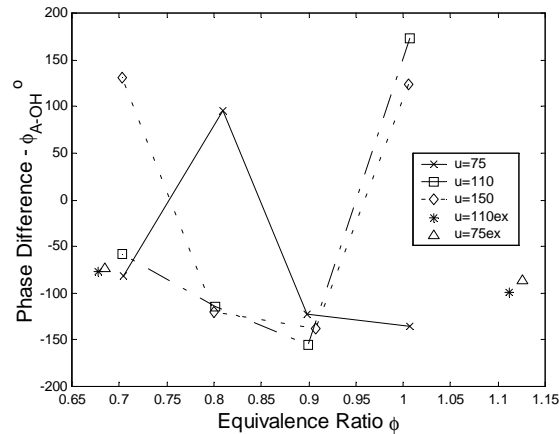


Figure 17: Phase angle between surface area and OH* perturbations as a function of equivalence ratio.

If this were true these two quantities would be in phase. While not zero, the phase difference for the excited and small amplitude cases is nearly constant regardless of flow or equivalence ratio (Figure 17). Recall that these are actually stable cases that were made to oscillate. Thus while the phase angle may not be zero it does fit the kinematic model at these states if a constant delay were added, possible due to reaction kinetics. However, within the instability regime the phase angle varies considerably. The exact reasons for this discrepancy are under investigation but may include the effects of flame stretch or entrainment of air or reacted gases. The practical implication is that the evaluation of the flame response based on flame surface area perturbations alone will not describe the phase necessary for closed loop stability.

3.3 Preliminary Conclusions

This study investigated the phase-gain relationship between flame surface area and heat release perturbations in a dynamically unstable and externally excited flame. Both passive and active control strategies for combustion dynamics will depend on knowledge of the various mechanisms as well as

their individual and compounded impact on flame dynamics. Thus, the study described here provides insight into the complex interactions that must be recognized in order to achieve system stability.

Natural chemiluminescent CH* emissions, used to define the flame surface, was captured by high-speed photography and individual images were evaluated to form a signal representing surface area perturbations. By properly time-aligning this data with pressure and OH* chemiluminescent emissions, heat release indicators, it was possible to investigate the phase relationship between these parameters.

Results indicated that while area perturbations could adequately describe the magnitude of OH* fluctuations, they were not capable of determining the OH* phase necessary for closed loop stability. This suggests that other mechanisms may act to influence the heat release rate. Thus flame models based solely on the kinematics processes will not accurately predict the heat release phase, and control systems utilizing these models may actually increase or induce thermoacoustic instabilities. Therefore, additional mechanisms must be considered and studied under naturally unstable and excited conditions, in order to include their effects in flame models.

4.0 Proposed Work

4.0.1 Flame Surface Area

Thus far in the study, high-speed recording of the visible CH* chemiluminescence has been the primary means of identifying the flame surface. While it is believed that in the case of low-medium frequencies and laminar flames CH* emissions provide an adequate representation of the flame surface, previous research presented in the literature review (Najm et al., 1998a) advised caution in using this measure.

PLIF images of HCO were considered to be the most reliable means of flame surface identification (Najm et al., 1998b), however the limited life cycle of this species makes its detection rather difficult. In contrast, induced fluorescence of OH and CH₂O emissions are much easier to obtain and are precursors to HCO, and a pixel-by-pixel product of these two species can yield an image similar to that of HCO. Because the flame is quite reproducible from cycle to cycle, simultaneous images are not necessary thus allowing for same plane viewing of the flame, the use of a single laser (~283 nm for OH and 338.1 nm for CH₂O), and the use of a single imaging device. Testing will be conducted over a range of flow (75-150 cm/sec nozzle velocity) and fueling ($\phi = 0.6-1.0$) conditions at various degrees of stability (oscillating, stable, along the stability boundary and induced instability).

Surface area data will be cross-correlated with heat release to determine phase difference. From results obtained thus far, there is an apparent need to describe the cause of the discrepancy in the gain relationship between the heat release rate and the flame surface area. While this may merely be an issue in the reduction algorithm, there is also the possibility that an additional mechanism is contributing to variations in the heat release rates.

Apart from identifying flame structure, these emissions are also excellent indicators of heat release, and 2-D PLIF images will provide a spatial distribution of the heat release rates. Comparison between the spatially resolved OH PLIF images and the global heat release rate, as recorded by OH* chemiluminescence, should help to clarify the discrepancy between flame surface area and heat release discussed above.

Some improvement is needed in the algorithm used to actually determine the surface area of the flame. The intensity of the luminescence (chemi or induced) will vary based on operating conditions. The edge detection portion of the algorithm needs to be improved to better account for this change in intensity from one condition to the next.

4.0.2 Flowfield Measurement

It is believed that re-entrainment of reacted gases may act to dilute the fresh mixture in the reaction zone. High-speed digital images display a periodic lift-off of the flame from the burner nozzle that may allow entrained air to enter. Additionally, flow conditions at the nozzle exit are difficult if not impossible to control without changes to the geometry, thus in order to differentiate their impact on heat release variation from flame surface area effects the flow field needs to be realized.

Through particle image velocimetry (PIV), velocity, vorticity, strain rate and dilatation rates ($\nabla \cdot \mathbf{V}$) in the combustion region and surrounding area will be evaluated. It is possible that energy needed to initiate thermoacoustic instabilities originates from instabilities in the flow field. Comparisons will be made at different stages of stability. It is expected that the flow patterns will be somewhat different between induced instabilities and naturally occurring instabilities.

4.0.3 Effects of Fuel Composition

To determine the impact of fuel composition on the stability margin of the Rijke tube combustor, flame and flow visualization studies will include operation on various combinations of methane, ethane and propane. As a preliminary approach the following compositions are proposed:

1. 100% Methane

2. 95% Methane, 3% Ethane and 2% Propane
3. 90% Methane, 7% Ethane and 3% Propane

4.0.4 Flame Dynamics Model and Stability Analysis

Figure 8 is a block diagram representation of the closed-loop feedback model for the Rijke tube combustor. The acoustic component can be theoretically obtained from a one-dimensional acoustic transfer matrix (Munjaj, 1987) or experimentally by acoustic excitation. However, neither of these methods would include the temperature differences brought on by the flame. Alternatively, the reacting flow acoustic velocity within the nozzle can be determined from theoretical analysis by measuring the acoustic pressure at two separate locations in the nozzle. Results from this measurement can be used to supplement the proposed transfer functions to improve the acoustic model.

The dotted-line elements of Figure 8 describe the effects of vorticity and strain rate. This box could have been included in the overall flame response, thus maintaining a reduced order model and greatly simplifying the analysis. However it is believed that the flow characteristics play a significant role in the overall system stability and if a general model of thermoacoustic instabilities is to be obtained a higher-order model separating these effects is necessary. This requires the ability to isolate the effects of vorticity and strain rate, which may prove to be quite difficult.

Using the proposed flow measurements it will be possible to define the characteristics of the flow during periods of instability. This should allow the identification of the frequencies and length-scales of the vortices present in the flowfield. Utilizing this information, it should be possible to generate a similar vortex structure and imposed it upon a stable flame, thus isolating their impact from other mechanisms. As this is a proposal of intended work, there is a need to stress the difficulty in achieving this goal. The alternative is to role-up the flow effects into the flame transfer function, which would still allow the proposed Nyquist or Bode stability analysis however the outcome may not be as general.

5.0 Conclusion

Several novel techniques have been suggested from the identification of the flame surface area, the measurement of the flowfield in an oscillating flame, and the separation of flow characteristics to develop a higher-order feedback loop model.

Through theoretical and experimental analysis, it is the intent of the author to develop an overall systems model from which to evaluate system stability. A number of experimental methods

have been proposed in order to evaluate the impact of suspected mechanisms that lead to fluctuations in the heat release rate in unstable flames. Results from subsequent tests utilizing these methods will aid in the development of a closed-loop feedback model describing the flame behavior. Generalization of the model should help to extend its use to more complex combustion systems.

6.0 References

1. Baade, P.K., "Design Criteria and Models for Preventing combustion Oscillations", *ASHRAE Symposium on Combustion Driven Oscillations*, Atlanta, GA, 1979.
2. Barrere, M., and Williams, F.A., "Comparison of Combustion Instabilities found in Various Types of Combustion Chambers", , pp 169-181, 1968.
3. Becker, K.H., Kley, D., Norstrom, R.J., "OH* Chemiluminescence in Hydrocarbon Atom Flames", *Fourteenth Symposium (International) on Combustion*, pp. 405-411, 1977.
4. Beer, J.M., "Clean Combustion in Gas Turbines: challenges and technical responses – a review", *J. Inst. Energy*, V 68, pp 2-10, March 1995.
5. Blackshear, P.L., "Driving Standing Waves by Heat Addition", *Fourth Symposium (International) on Combustion*, pp 553-566, The Williams and Wilkins Co., Baltimore, 1952.
6. Borghi, R., "Turbulent Combustion Modelling" , *Prog. Energy Combust. Sci.*, 14, pp. 245-292, 1988.
7. Carrier, G.F., "The Mechanics of the Rijke Tube", *Q. Appl. Math*, 12, pp. 383-395, 1955.
8. Christensen, K. T., Soloff, S. M. & Adrian, R. J., "PIV Sleuth -Integrated Particle Image Velocimetry Interrogation/Validation Software", TAM Report No. 943, University of Illinois at Urbana-Champaign, 2000.
9. Chu, B.T., "Stability of Systems Containing a Heat Source – The Rayleigh Criteria", NACA RM 56D27, 1956.
10. Crocco, L., "Aspects of Combustion Stability in Liquid Rocket Motors", *J. Am. Roc. Soc.*, Part 1: V 21, p. 163, Nov-Dec 1951; Part 2: V 22, p. 7, Jan-Feb 1952.
11. Crocco, L., Grey, J., Harrje, D.T., "Theory of Liquid Propellant Rocket Combustion Instability and Its Experimental Verification", *Am. Rocket Soc. J.*, 30, pp 159-168, 1960.
12. Crocco, L. and Mitchell, C.E., "Nonlinear Periodic Oscillations in Rocket Motors with Distributed Combustion", *Combust. Sci. and Tech.*, 1, pp. 147-169, 1969.
13. Culick, F., "A Note on Rayleigh's Criteria", *Comb. Sci. and Tech.*, V 56, pp 159-166, 1987.
14. Dandy, D. and Vosen, S., "Numerical and Experimental Studies of Hydroxyl Radical Chemiluminescence in Methane-Air Flames", *Combust. Sci. and Tech.*, 82, pp. 131-150, 1992.
15. Darling, D., Radhakrishnan, K., Oyediran, A., cowan, E., "Combustion_Acoustic Stability Analysis for Premixed Gas Turbine Combustors", AIAA-95-2470, 1995.
16. Ducruix, S., Durox, D., and Candel, S., "Theoretical and Experimental Determination of the Transfer Function of a Laminar Premixed Flame", *Twenty-Eighth Symposium (International) on Combustion*, pp. 765-773, 2000.
17. Edwards, C.H. and Penney, D., "Calculus and Analytic Geometry", Prentice-Hall, New Jersey, 1986.
18. Feldman, K.T., "Review of the Literature on Rijke Thermoacoustic Phenomena", *J. Sound Vib.*, 7, pp. 83-89, 1968.

19. Fleifil, M., Annaswamy, A.M., Ghoneim, Z.A., and Ghoniem, A.F., "Response of a Laminar Flame to Flow Oscillations: A Kinematic Model and Thermoacoustic Instability Results", *Combustion and Flame*, 106, pp. 487 – 510, 1996
20. Franklin, G.F., Powell, J.D. and Emami-Naeini, A., *Feedback Control on Dynamic Systems*, Addison-Wesley, New York, 1994.
21. Friedlander, M., Smith, T., Powell, A., "Experiments on the Rijke-Tube Phenomena", *J. Acoust. Soc. Am.*, 36, pp. 1737-1738, 1964.
22. Gaydon, A.G., and Wolfhard, H.G., *Flames-Their Structure, Radiation and Temperature*, Chapman and Hall, London, 1953.
23. Gutmark, E., Schadow, K.C., Sivasegaram, S., Whitelaw, J.H., "Interaction Between Fluid-Dynamic and Acoustic Instabilities in Combusting Flows Within Ducts", *Comb. Sci. and Tech.*, V 79, pp 161-166, 1991.
24. Haber, L., Vandsburger, U., Saunders, W.R., Khanna, V., "An Examination of the Relationship Between Chemiluminescent Light Emissions and Heat Release Rate Under Non-Adiabatic Conditions", ASME, 2000-GT-0121, 2000.
25. Harrje, D.T. and Reardon, F.H., *Liquid Propellant Rocket Combustion Instability*, NASA SP-194, 1971.
26. Higgins, B., "On the Sound Produced by a Current of Hydrogen Gas Passing Through a Tube", *J. Natural Philosophy, Chemistry and the Arts*, 1, pp 129-131, 1802.
27. Hobson, D.E., Fackrell, J.E., Hewitt, G., "Combustion Instabilities in Industrial Gas Turbines – Measurements on Operating Plant and Thermoacoustic Modeling", *Trans. ASME*, V 122, 2000.
28. Janus, M.C. and Richards, G.A., "A Model for Premixed Combustion Oscillations", Technical Note DOE/METC-96/1026, 1996.
29. Jarosinski, J., "The Thickness of Laminar Flames", *Combustion and Flame*, 56, pp. 337-342, 1984.
30. Johnson, M.R., Kostiuk, L.W., Cheng, R.K., "A Ring Stabilizer for Lean Premixed Turbulent Flames", *Combustion and Flame*, 114, pp. 594-596, 1998.
31. Kaskan, W.E., "An Investigation of Vibrating Flames", *Fourth Symposium (International) on Combustion*, pp 575-591, The Williams and Wilkins Co., Baltimore, 1952.
32. Keller, J.J., "Thermoacoustic Oscillations in Combustion Chambers of Gas Turbines", *AIAA Journal*, 33, 1995.
33. Keller, J.O. and Saito, K., "Measurements of the Combusting Flow in a Pulse Combustor", *Combust. Sci. and Tech.*, 53, pp. 137-163, 1987.
34. Khanna, V.K., Vandsburger, U., Saunders, W.R., Baumann, W.T., and Hendricks, A.D., "Dynamic Analysis of Burner Stabilized Flames, Part 1: Laminar Premixed Flame", *AFRC International Symposium*, Newport Beach, CA, 2000.
35. Konrad, W., Brehm, N., Kameier, F., Freeman, C., Day, I.J., "Combustion Instability Investigations on the BR710 Jet Engine", *Trans. ASME*, V 120, 1998.
36. Krueger, U., Huren, J., Hoffman, S., Krebs, W., Flohr, P., Bohn, D., "Prediction and Measurement of Thermoacoustic Improvements in Gas Turbines with Annular Combustion Systems", ASME, 2000-GT-0095, 1995.
37. Law, C.K., "Dynamics of Stretched Flames", *Twenty Second Symposium (International) on Combustion*, pp. 1381-1401, 1988.
38. Lee, D.H. and Lieuwen, T.C., "Acoustic Nearfield Characteristics of a Premixed Flame in a Longitudinal Acoustic Field", ASME, 2001-GT-0040, 2001.
39. Lee, S.Y., Seo, S., Broda, J.C., Pal, S. and Santoro, R.J., "an Experimental Estimation of Mean Reaction Rate and Flame Structure During Combustion Instability in a Lean Premixed Gas Turbine Combustor", *Twenty-Eighth Symposium (International) on Combustion*, pp. 775-782, 2000.

40. Lewis, B. and von Elbe, G., *Combustion, Flames and Explosions of Gases*, Academic Press, Inc., Orlando, FL, 3rd Ed., 1987.
41. Lieuwen, T., Torres, H., Johnson, C., Zinn, B.T., “A Mechanism of Combustion Instability in Lean-Premixed Gas Turbine Combustors”, ASME, 99-GT-3, 1999.
42. Maling, G.C., “Simplified Analysis of the Rijke Phenomena”, *J. Acoust. Soc. Am.*, 35, pp. 1058-1060, 1963.
43. Markstein, G.H., *Nonsteady Combustion Propagation*, Pergamon Press, Oxford, England, 1964.
44. Merk, H.J., “An Analysis of Unstable Combustion of Premixed Gases”, *Sixth Symposium (International) on Combustion*, pp. 500-512, 1956.
45. Mitchell, C.E., “Analytical Models for combustion Instability”, *Liquid Rocket Engine Combustion Instability*, V 169, AIAA, 1994.
46. Mongia, R., Dibble, R., Lovett, J., “Measurement of Air-Fuel Ratio Fluctuations Caused by Combustor Driven Oscillations”, ASME, 98-GT-304, 1998.
47. Mugridge, B.D., “Combustion Driven Oscillations”, *J. Sound Vib.*, 70, pp. 437-452, 1980.
48. Mungal, M.G., Lourenco, L.M., and Krothapalli, A., “Instantaneous Velocity Measurements in Laminar and Turbulent Premixed Flames Using On-Line PIV”, *Combust. Sci. and Tech.*, 106, pp. 239-265, 1995.
49. Munjal, M.L., *Acoustics of Ducts and Mufflers*, Wiley-Interscience, New York, 1987.
50. Najm, H., Paul, P., Mueller, C., Wyckoff, P., “On the Adequacy of Certain Experimental Observables as Measurements of Flame Burning Rate”, *Combustion and Flame*, 113, pp. 312-332, 1998.
51. Najm, H., Kino, O.M., Paul, P., Wyckoff, P., “A Study of Flame Observables in Premixed Methane – Air Flames”, *Combust. Sci. and Tech.*, 140, pp. 369-403, 1998.
52. Neuringer, J.L. and Hudson, G.E., “An Investigation of Sound Vibrations in a Tube Containing a Heat Source”, *J. Acoust. Soc. Am.*, 24, pp 667-674, Nov. 1952.
53. Oran, E. and Gardner, J., “Chemical-Acoustic Interactions in Combustion Systems”, *Prog. Energy Combust. Sci.*, 11, pp. 253-276, 1985.
54. Paschereit, C.O. and Polifke, W., “Investigation of the Thermoacoustic Characteristics of a Lean Premixed Gas Turbine Burner”, ASME, 98-GT-582, 1998.
55. Paschereit, C.O., Schuermans, B., Polifke, W., and Mattson, O., “Measurement of Transfer Matrices and Source Terms of Premixed Flames”, ASME, 99-GT-133, 1999.
56. Paul, P.H. and Najm, H.N., “Planar Laser-Induced Fluorescence Imaging of Flame Heat Release Rate”, *Twenty-Seventh Symposium (International) on Combustion*, pp. 43-50, 1998.
57. Peracchio, A.A. and Proscia, W.M., “Nonlinear Heat-Release / Acoustic Model for Thermoacoustic Instability in Lean Premixed Combustors”, ASME, 98-GT-269, 1998.
58. Poinot, T., Troune, A., Veynante, D., Candel, S., Esposito, E., “Vortex-Driven Acoustically Coupled Combustion Instabilities”, *J. Fluid Mech.*, 177, pp. 265-292, 1987.
59. Putnam, A.A., and Dennis, W.R., “A Study of Burner Oscillations of the Organ-Pipe Type”, *Trans. ASME*, 75, pp 15-28, 1953.
60. Putnam, A.A., and Dennis, W.R., “A Survey of Organ-Pipe Oscillations in Combustion Systems”, *J. Acoust. Soc. Am.*, 28, p 246, 1956.
61. Putnam, A.A., and Dennis, W.R., “Organ-Pipe Oscillations in a Flame-Filled Tube”, *Fourth Symposium (International) on Combustion*, pp 566-575, The Williams and Wilkins Co., Baltimore, 1952.
62. Putnam, A. A. *Combustion Driven Oscillations in Industry*, American Elsevier Publishing, New York, NY (1971).
63. Raffel, M., Willert, C., and Kompenhans, J., *Particle Image Velocimetry: A Practical Guide*, pp 3-8, Springer-Verlag, Berlin, 1998.

64. Rayleigh, J.W.S., *The Theory of Sound*, 2, p. 226, Dover, New York, 1945.
65. Reuss, D.L., Adrian, R.J., and Landreth, C.C., "Two-Dimensional Velocity Measurements in Laminar Flame Using Particle Image Velocimetry", *Combust. Sci. and Tech.*, 67, pp. 73-83, 1989.
66. Richards, G.A. and Janus, M.C., "Characterization of Oscillations During Premix Gas Turbine Combustion", ASME International Gas Turbine and Aeroengine Congress and Exhibition, Orlando, FL, June 1997, 97-GT-244.
67. Richards, G.A. and Robey, E.H., "Dynamic Response of Premix Fuel Injector", ASME TurboExpo Land, Sea, Air 2001, New Orleans, LA, June 2001, 2001-GT-XXX.
68. Rijke, P.L., "Notice of a New Method of Causing a Vibration of the Air Contained in a Tube Open at Both Ends", *Phil. Mag.*, 17, pp. 419-422, 1859.
69. Samaniego, J.M., Egolfopoulos, F.N., and Bowman, C.T., "CO₂* Chemiluminescence in Premixed Flames", *Combust. Sci. and Tech.*, 109, pp. 183-203, 1995.
70. Schadow, K.C., Gutmark, E., Parr, T.P., Parr, D.M., Wilson, K.J., and Crump, J.E., "Large-Scale Coherent Structures as Drivers of Combustion Instability", *Combust. Sci. and Tech.*, 64, pp. 167-186, 1989.
71. Schadow, K.C. and Gutmark, E., "Combustion Instability Related to Vortex Shedding in Dump Combustors and Their Passive Control", *Prog. Energy Combust. Sci.*, 18, pp. 117-132, 1992.
72. Scholtz, M.H. and Dipietro, S.M., "Field-Experience on DLN Typhoon Industrial Gas Turbine", ASME, 97-GT-61, 1997.
73. Schuermans, B., Polifke, W., and Paschereit, C.O., "Modeling Transfer Matrices of Premixed Flames and Comparison with Experimental Results", ASME, 99-GT-132, 1999.
74. Shih, W.P., Lee, J., Santavicca, D.A., "Stability and Emissions Characteristics of a Lean Premixed Gas Turbine Combustor", *Twenty-Sixth Symposium (International) on Combustion*, 1996.
75. Turns, S.R., *An Introduction to Combustion*, McGraw-Hill, Inc., New York, 1996.
76. Wagner, T.C. and Ferguson, C.R., "Bunsen Flame Hydrodynamics", *Combustion and Flame*, 59, pp. 267-272, 1985.
77. Westerweel, J., "Fundamentals of Digital Particle Image Velocimetry", *Meas. Sci. Technol.*, 8, pp. 1379-1392, 1997.
78. Williams, F., *Combustion Theory*, Perseus Books, Massachusetts, 2nd Ed., 1985.
79. Yoon, H.G., Peddieson, J. and Purdy, K.R., "Mathematical Modeling of a Generalized Rijke Tube", *Intl. J. Eng. Sci.*, 36, pp 1235-1264, 1998.

**XIV. “Particle-Wall Shear Stress Measurements within the
Standpipe of a Circulating Fluidized Bed”**

**Angela Sarra (S) and Aubrey L. Miller (F), West Virginia University
with
Lawrence Shadle (M), NETL**

**Particle-Wall Shear Stress Measurements within the Standpipe of a
Circulating Fluidized Bed**

Angela M. Sarra

**Thesis submitted to the
College of Engineering and Mineral Resources
at West Virginia University
in partial fulfillment of the requirements
for the degree of**

**Master of Science
in
Chemical Engineering**

**Aubrey L. Miller, Ph.D., Advisor
Eung H. Cho, Ph.D.
Lawrence J. Shadle, Ph.D.**

Department of Chemical Engineering

**Morgantown, West Virginia.
2001**

**Keywords: Circulating Fluidized Beds, Standpipe, Particle Wall Shear Stress,
Mixture Momentum Balance, Gas Solids Flow
Copyright 2001 Angela Sarra**

ABSTRACT

Particle-Wall Shear Stress Measurements within the Standpipe of a Circulating Fluidized Bed

Angela M. Sarra

Although standpipes are essential to the operation of circulating fluidized bed systems (CFB), their hydrodynamics are poorly understood, and are often unpredictable in displaying effects such as hysteresis which could be due to forces such as particle-wall shear stress.

In this research the one-dimensional gas-solids mixture momentum balance is applied to the standpipe. Neglecting acceleration effects, the important forces are the gas and solids phase pressure drop, weight of the bed, and the particle-wall shear stress. Gas pressure drop is measured using differential pressure transducers. The weight of the bed is assumed constant. The wall shear stress is measured utilizing instruments developed by WVU and NETL in Morgantown. The solids phase pressure drop is inferred to be the residual portion of the momentum balance.

Estimations of these forces are included for both coke breeze and cork bed materials. An attempt to model shear stress and solids pressure has been made.

ACKNOWLEDGEMENTS

I would like to thank the administrators of the Swiger Fellowship from which I was financially supported. I would also like to thank my advisor, Aubrey Miller, for his support and encouragement. I would like to thank Larry Shadle for working very closely with me and giving me the opportunity to work with the group of scientists at the Department of Energy National Energy Technology Laboratory in Morgantown WV. It was an exceptional opportunity to work with this dynamic team and also to work with such large-scale equipment. I would like to thank Larry Lawson and Chris Ludlow of the Department of Energy for listening and offering many helpful suggestions. I would also like to thank Randy Carter for the drawing and expertise in designing the wall probe, and Jim Devault for taking time to show me how to use equipment properly.

TABLE OF CONTENTS

ABSTRACT.....	ii
ACKNOWLEDGEMENT.....	iii
TABLE OF CONTENTS.....	iv
LIST OF TABLES.....	vi
LIST OF FIGURES.....	viii
CHAPTER 1 INTRODUCTION AND OBJECTIVES.....	1
1.1 Introduction to Standpipes in Circulating Fluidized Bed Systems.....	1
1.2 Introduction to the Mixture Momentum Balance.....	2
1.3 Objectives.....	4
CHAPTER 2 LITERATURE SURVEY.....	5
2.1 Flow Regimes.....	5
2.1a Non-Fluidized Regime.....	6
2.1b Fluidized Regime.....	6
2.2 Standpipe Modeling.....	8
2.2.a Non-Fluidized Regime.....	8
2.2.b Fluidized Regime.....	10
2.3 Standpipe Experimental Studies of Solids Pressure and Solids Friction.....	11
2.3.a Solids-Wall Shear Stress.....	11
2.3.b Solids Pressure.....	16
CHAPTER 3 EXPERIMENTAL SET-UP.....	19
3.1 Circulating Fluid Bed.....	19
3.2 Bed Materials and Properties.....	21
3.3 Description of Mass Flow Device.....	21
3.4 Shear Vane.....	22
3.4a Shear Vane General Description.....	22
3.4b Shear Vane Calibration and Error.....	23
3.4c Parasitic Drag Characterization.....	24
3.5 Wall Probe.....	27
3.5a Wall Probe General Description.....	27
3.5b Wall Probe Calibration.....	29
3.5c Wall Probe Purge.....	31
3.5d Wall Probe Repeatability.....	34
3.6 Capacitance Solids Volume Fraction Probe.....	37
3.6a Capacitance Solids Volume Fraction Probe General Description.....	37
3.6b Capacitance Solids Volume Fraction Probe Calibration.....	38
3.6c Cork Particle Density Measurement.....	41
3.7 Experimental Methods.....	42
3.7a Steady State versus Transient Data Sampling.....	42
3.7b Steady State versus Transient Aeration Ramps.....	42
3.8 Internal Angle of Friction and Angle of Wall Friction for the Bed Material.....	45
CHAPTER 4 RELATIVE COMPARISON OF FORCES IN A CFB AND THE JANSSEN COEFFICIENT.....	48

4.1	Mass Circulation.....	48
4.2	Momentum Balance Components During an Aeration Ramp.....	49
4.3	Differential Solids Pressure and Solids Wall Shear Stress Estimates..	51
Chapter 5	DEPENDENCE OF SOLIDS WALL SHEAR STRESS AND SOLIDS PRESSURE ON OPERATING CONDITIONS.....	60
5.1	Testing Theoretical Variables.....	62
5.1a	The Effects of Solids Circulation Rate on a Fluidized Regime.....	62
5.1b	The Effect of Solids Circulation Rate and Standpipe Height on a Packed Regime.....	64
5.1c	The Effect of Solids Circulation Rate and Gas Pressure Drop ($-\Delta P_g/L$) on a Packed Regime.....	68
5.2	Qualitative Study.....	74
5.2a	Filling and Draining Tests.....	75
5.2b	Stationary Bed Aeration Ramps, Coke, in the Standpipe.....	77
5.2c	Bubbling Bed Studies, Nylon Beads, in the 10" Test Bed....	82
5.2d	Bubbling Bed Studies, Cork, in the 10" Test Bed.....	85
5.2e	Circulating Bed Aeration Ramp Tests.....	86
5.2f	Circulating Bed Aeration Ramp Tests – Low Flows.....	90
5.3	CFB Operational Variables.....	92
5.3a	The Effect of Solids Circulation Rate and Riser Pressure Drop.....	92
5.3b	Four Factor Test: Standpipe Height, Riser Flow, Loopseal Flow, and Solids Circulation Rate.....	96
5.3c	The effect of Standpipe Aeration Rate, Riser Gas Velocity, and Fines Concentration.....	102
5.3d	The Effect of Location of Standpipe Move Air, Aeration at 20.8 feet, and Direction of Ramp.....	110
CHAPTER 6	CONCLUSIONS.....	116
APPENDIX	119
A.1	Derivation of Mixture Momentum Balance using Shell Balance Technique.....	119
A.1.a	Gas Momentum Balance.....	119
A.1.b	Solids Momentum Balance.....	121
A.1.c	Mixture Momentum Balance.....	122
A.2	Derivation of Equations For Estimating Shear Stress and Solids Pressure.....	123
A.2a	Assuming Constant $\Delta P_g/L$ Along the Standpipe.....	123
A.2b	Integrating the Mixture Momentum Balance from $z = z_1$ to $z = z_2$	125
A.3	Bulk Solids Mechanics.....	129
NOMENCLATURE	133
REFERENCES	136

LIST OF TABLES

Table 1:	Sign Convention for U_{sl}	5
Table 2:	Modeling Solids-Wall Shear Stress for Non-Fluidized Regime.....	10
Table 3:	Modeling Solids-Wall Shear Stress for Fluidized Regimes.....	11
Table 4:	Riser Conditions and Shear Stress (Van Swaij, 1970).....	13
Table 5:	Commercial Data on Solids-Wall Friction (Matsen, 1976).....	14
Table 6:	Independent Variable Levels for the Parasitic Drag Test.....	24
Table 7:	Description and Values of Constants in Equation Describing Deflection of a Cantilever Beam.....	28
Table 8:	Test Matrix to Understand Purge Air Effects, Test Bed, 1000 μm Cork	32
Table 9:	ANOVA of Purge Air Test for Shear Stress, Test Bed, 1000 μm Cork.	33
Table 10:	Test Sequence of Repeatability Test.....	35
Table 11:	Solids Volume Fraction Probe Calibration Constants.....	39
Table 12:	Solids Volume Fraction Probe Calibration Results.....	40
Table 13:	Cork Particle Density Measurements.....	42
Table 14:	Comparison of Relative Magnitude of Forces (% of Total Force) for Cork and Coke Breeze.....	51
Table 15:	Estimated values of the Janssen Coefficient.....	59
Table 16:	Operational Variables Tested.....	61
Table 17:	Solids Circulation and Standpipe Height Test Independent Variables...	65
Table 18:	Solids Circulation and Standpipe Height Results, Cork.....	66
Table 19:	ANOVA Results for the Shear Stress Component of the Solids Circulation and Standpipe Height Test, Cork.....	67
Table 20:	ANOVA Results for the Solids Pressure Component of the Solids Circulation and Standpipe Height Test, Cork.....	67
Table 21:	Solids Circulation and Gas Pressure Drop ($-\Delta P_g/L$) Test Independent Variables.....	68
Table 22:	Solids Circulation and Gas Pressure Drop ($-\Delta P_g/L$) Test Results, Cork.	68
Table 23:	ANOVA Results for the Shear Stress Component of the Solids Circulation and Gas Pressure Drop ($-\Delta P_g/L$) Test, Cork.....	69
Table 24:	ANOVA Results for Solids Pressure Drop ($-\Delta P_s/L$) of the Solids Circulation and Gas Pressure Drop ($-\Delta P_g/L$) Test, Cork.....	70
Table 25:	Solids Circulation and Gas Pressure Drop ($-\Delta P_g/L$) Test, Higher Circulation Rates, Independent Variables.....	71
Table 26:	Solids Circulation and Gas Pressure Drop ($-\Delta P_g/L$) Test, Higher Circulation Rates, Results, Cork.....	71
Table 27:	ANOVA Results for the Shear Stress Component of the Solids Circulation and Gas Pressure Drop ($-\Delta P_g/L$) Test, Higher Circulation Rates, Cork.....	73
Table 28:	ANOVA Results for the Solids Pressure Component of the Solids Circulation and Gas Pressure Drop ($-\Delta P_s/L$) Test, Higher Circulation Rates, Cork.....	73
Table 29:	ANOVA Results for the Solids Volume Fraction of the Solids Circulation and Gas Pressure Drop ($-\Delta P_g/L$), Higher Circulation rates, Cork.....	74

Table 30:	Filling and Draining Test Variables, 230 μm Coke.....	75
Table 31:	Stationary Bed Aeration Ramp Variables, Riser Flow, 10,000 scfh, 230 μm Coke.....	78
Table 32:	Stationary bed Aeration Ramp Variables, Riser Flow 50,000 scfh, 230 μm Coke.....	81
Table 33:	Circulating Bed Aeration Ramp Variables, 230 μm Coke.....	87
Table 34:	Circulating Bed Aeration Ramp Variables, Aeration at the Bottom, 230 μm Coke.....	89
Table 35:	Riser Pressure Drop and Solids Circulation Rate Test Independent Variables, 230 μm Coke.....	92
Table 36:	Riser Pressure Drop and Solids Circulation Rate Test Results, 230 μm Coke.....	93
Table 37:	ANOVA of Riser Pressure Drop and Solids Circulation Test for Shear Stress ($-2\tau_{\text{sw}}/R$), 230 μm Coke.....	94
Table 38:	ANOVA of Riser Pressure Drop and Solids Circulation Test for Gas Pressure Drop ($-\Delta P_g/L$), 230 μm Coke.....	95
Table 39:	ANOVA of Riser Pressure drop and Solids Circulation Test for Solids Pressure Drop ($-\Delta P_s/L$), 230 μm Coke.....	96
Table 40:	Four Factor Test Independent Variables.....	97
Table 41:	Four Factor Test Results, 230 μm Coke.....	98
Table 42:	ANOVA of Four Factor Test for Shear Stress ($-2\tau_{\text{sw}}/R$), 230 μm Coke.	99
Table 43:	ANOVA of Four Factor Test for Gas Pressure Drop ($-\Delta P_g/L$) across the shear vane, 230 μm Coke.....	101
Table 44:	ANOVA of four Factor Test for Solids Pressure Drop ($-\Delta P_s/L$), 230 μm Coke.....	102
Table 45:	Standpipe Aeration Rate, Riser Gas Velocity and Fines Level Test Independent Variables.....	103
Table 46:	Standpipe Aeration Rate, Riser Gas Velocity and Fines Level Test Independent Variable Results, Coke.....	104
Table 47:	Standpipe Aeration Rate, Riser Gas Velocity, and Fines Level Test Dependent Variable Results, Coke.....	104
Table 48:	Standpipe Aeration Rate, Riser Gas Velocity and Fines Level Test Dependent Variable Results-continued, Coke.....	105
Table 49:	ANOVA of Fines Test for Shear Stress Component, Coke.....	106
Table 50:	ANOVA of Fines Test for all Dependent Variables, Coke.....	108
Table 51:	ANOVA of Fines Test for Dependent Variables- Continued, Coke.....	109
Table 52:	Standpipe Aeration Location, Aeration at 20.8', and Ramp Direction Test Matrix.....	110
Table 53:	Standpipe Aeration Location, Aeration at 20.8', and Ramp Direction Dependent Variable Results, 230 μm Coke.....	111
Table 54:	ANOVA Results of the Shear Stress Component of the Hysteresis Test, 230 μm Coke.....	113
Table 55:	ANOVA of Hysteresis Test for Gas Pressure Drop ($-\Delta P_g/L$), Solids Pressure Drop ($-\Delta P_s/L$), Solids Circulation And Standpipe Height, 230 μm Coke.....	115

LIST OF FIGURES

Figure 1:	Standpipe Force Balance.....	2
Figure 2:	Moveable Wall Device for Solids-Wall Shear Stress (Van Swaaij, 1970).....	11
Figure 3:	Shear Stress versus Solids Flux in a Pneumatic Riser (Van Swaaij, 1970).....	12
Figure 4:	Pressure Drop and Mean Densities (Van Swaaij, 1970).....	12
Figure 5:	Solids-Wall Friction Versus Density of the Bed (Matsen, 1976).....	14
Figure 6:	Tube-Pulling Apparatus (Zenz, 1960).....	16
Figure 7:	Tube-Pulling Experimental Results (Zenz, 1960).....	16
Figure 8:	Solids Pressure Probes (Polashenski, 1999).....	17
Figure 9:	Solids Pressure versus Local Solid fraction (Polashenski, 1999).....	18
Figure 10:	NETL Circulating Fluid Bed.....	20
Figure 11:	Spiral, Mass Circulation Measurement.....	22
Figure 12:	Shear Vane Schematic.....	23
Figure 13:	Shear Vane Calibration.....	23
Figure 14:	Parasitic Drag Steady State, 230 μm Coke.....	25
Figure 15:	Total Force Measured for Each Vane Length and Parasitic Drag, 230 μm Coke.....	26
Figure 16:	Ratio of Shear Force/Total Force (Parasitic Drag study), 230 μm Coke.....	27
Figure 17:	Wall Stress Probe Schematic.....	29
Figure 18:	Factory Supplied Calibration of Displacement Probes, Channel 1.....	30
Figure 19:	Factory Supplied Calibration of Displacement Probes, Channel 2.....	30
Figure 20:	Wall Probe Calibration in the Axial Direction.....	30
Figure 21:	Estimated and Measured Movement of the Tube.....	30
Figure 22:	Importance of Probe Level on Calibration.....	31
Figure 23:	Effects of Purge on Wall Probe Measurements, 1000 μm Cork.....	32
Figure 24:	The Effects of Ramp Direction on Wall Shear, 1000 μm Cork.....	32
Figure 25:	Hysteresis Effect of Wall Probe.....	35
Figure 26:	Wall Probe Repeatability Study.....	35
Figure 27:	Wall Probe Measurement Error for Coke Breeze Range.....	35
Figure 28:	Wall Probe Measurement Error for Cork Range.....	35
Figure 29:	Wall Probe Measurement Error for Coke Breeze Range No Nylon.....	36
Figure 30:	Wall Probe Measurement Error for Cork Range No Nylon.....	36
Figure 31:	Solids Volume Fraction Probe (Louge, 1992).....	38
Figure 32:	Calibration Results of the Solids Volume Fraction Probe.....	41
Figure 33:	Transient Aeration Ramp.....	43
Figure 34:	Steady State Aeration Ramp.....	43
Figure 35:	Comparison of Steady State and Transient Ramps for Solids Circulation, 230 μm Coke.....	44
Figure 36:	Comparison of Steady State and Transient Ramps for Gas Phase Pressure Drop, 230 μm Coke.....	44
Figure 37:	Comparison of Steady State and Transient Ramps for Solids-Wall Shear Stress, 230 μm Coke.....	44

Figure 38:	Internal angle of Friction Measurement Apparatus.....	45
Figure 39:	Measurement of Angle of Wall Friction.....	46
Figure 40:	Solids Circulation versus Aeration, 230 μm Coke.....	48
Figure 41:	Momentum Balance Components versus Solids Circulation, 230 μm Coke.....	49
Figure 42:	Momentum Balance Components versus Aeration, Steady States, Cork Bed material.....	50
Figure 43:	Estimated Values of $\Delta P_s/L$ versus Mass Circulation, 230 μm Coke...	54
Figure 44:	Measured and Estimated Values of $-2\tau_{sw}/R$ versus Mass Circulation, 230 μm Coke.....	54
Figure 45:	Measured and Estimated Values of $-4\tau_{sw}/D$ versus Solids Circulation, Coke Breeze.....	55
Figure 46:	Jenike Shear Cell Measurements of Coke Breeze.....	56
Figure 47:	The Variation of the Product of the Coefficient of Friction and the Janssen Coefficient with Normal Stress.....	56
Figure 48:	Estimated Values of $-\Delta P_s/L$ versus Solids Volumetric Flux.....	57
Figure 49:	Measured and Estimated Values of $-2\tau_{sw}/R$ versus Solids Volumetric Flux, Cork.....	58
Figure 50:	Measured and Estimated Values of $-\Delta P_s/L$ versus Solids Volumetric Flux, Cork.....	58
Figure 51:	Shear Stress Measured by the Shear Vane and Wall Probe for a Fluidized Regime, Cork.....	63
Figure 52:	Shear Stress Measured by the Wall Probe for a Fluidized Regime, Cork.....	63
Figure 53:	Momentum Balance Components versus Solids Circulation for a Fluidized Regime, Cork.....	64
Figure 54:	Shear Stress Component Zero, Cork.....	64
Figure 55:	Effect of Solids Circulation and Standpipe Height on the Shear Stress Component for a Packed Regime, Cork.....	66
Figure 56:	The Effect of Solids Circulation and Standpipe Height on the Solids Pressure Component for a Packed Regime, Cork.....	66
Figure 57:	The Effect of Solids Circulation and Gas Pressure Drop ($-\Delta P_g/L$) on the Shear Stress Component for a Packed Regime, Cork.....	69
Figure 58:	The Effect of Solids Circulation and Gas Pressure Drop ($-\Delta P_g/L$) on the Solids Pressure Component for a Packed Regime, Cork.....	69
Figure 59:	The Effect of Solids Circulation and Gas Pressure Drop ($-\Delta P_g/L$) (at Higher Circulation Rates) on the Shear Stress Component.....	72
Figure 60:	The Effect of Solids Circulation and Gas Pressure Drop ($-\Delta P_g/L$) (at Higher Circulation Rates) on the Solids Pressure Component.....	72
Figure 61:	The Effect of Solids Circulation and Gas Pressure Drop ($-\Delta P_g/L$) (at Higher Circulation Rates) on the Solids Volume Fraction.....	72
Figure 62:	Shear Stress Versus Bed Height, Filling and Draining Tests, 230 μm Coke.....	76
Figure 63:	Gas Phase Pressure Drop versus Bed Height, Draining and Filling Tests, 230 μm Coke.....	76

Figure 64:	Shear Stress versus Aeration for a Stationary Bed, 230 μm Coke.....	79
Figure 65:	Momentum Balance Components for a Stationary Bed (Ramp Up), 230 μm Coke.....	79
Figure 66:	Momentum Balance Components for a Stationary Bed (Ramp Down), 230 μm Coke.....	80
Figure 67:	Momentum Balance Components for a Stationary Bed Ramp, High Riser Flow, 230 μm Coke.....	82
Figure 68:	Shear Stress versus Aeration Rate, Stationary Bed, High Riser Flow, 230 μm Coke.....	82
Figure 69:	Bubbling Bed Aeration Ramp for Nylon Bead Bed Material.....	83
Figure 70:	Bubbling Bed Aeration Ramp for Nylon Bead Bed Material, Decreasing Aeration.....	83
Figure 71:	Bubbling Bed Aeration Ramp for Nylon Beads Bed Material, After Compaction.....	84
Figure 72:	Bubbling Bed Aeration Ramp for Nylon Bead Bed Material, After Compaction, Decreasing Aeration.....	84
Figure 73:	Comparison of the Wall Probe Measurement for the Nylon Bead Bubbling Bed Study.....	84
Figure 74:	Comparison of the Shear Vane Measurements for the Nylon Bead Bubbling Bed Study.....	84
Figure 75:	Bubbling Bed Aeration Ramp for Cork Bed Material.....	85
Figure 76:	Bubbling Bed Aeration Ramp for Cork Bed Material, Decreasing Aeration.....	85
Figure 77:	Bubbling Bed Ramp 2, Cork Bed Material, Increasing Aeration.....	86
Figure 78:	Bubbling Bed Ramp 2, Cork Bed Material, Decreasing Aeration....	86
Figure 79:	Momentum Balance Components for a Circulating Bed Aeration Ramp, 230 μm Coke.....	88
Figure 80:	Mass Circulation and Standpipe Bed Height versus Aeration rate, 230 μm Coke.....	88
Figure 81:	Momentum Balance Components for a Circulating Bed Aeration Ramp, Aeration at the Bottom, 230 μm Coke.....	90
Figure 82:	Shear Stress at Lower Aeration Ramps, 230 μm Coke.....	91
Figure 83:	Shear Stress Component and Gas Pressure Drop versus Aeration Rate for Low Flows, 230 μm Coke.....	91
Figure 84:	Momentum Balance Components versus Aeration for Low Flows, 230 μm Coke.....	91
Figure 85:	Shear Stress ($-2\tau_{sw}/R$) Results of 2X2 Factorial, Riser ΔP and Solids Circulation, 230 μm Coke.....	93
Figure 86:	Gas Pressure Drop ($-\Delta P_g/L$) Results of 2X2 Factorial, Riser ΔP and Solids Circulation, 230 μm Coke.....	93
Figure 87:	Solids Pressure Drop ($-\Delta P_s/L$) Results of 2X2 Factorial, Riser ΔP and Solids Circulation Rate, 230 μm Coke.....	94
Figure 88:	Shear Stress ($-2\tau_{sw}/R$) Results of the Four Factor Test, 230 μm Coke	98
Figure 89:	Gas Pressure Drop ($-\Delta P_g/L$) Results of the Four Factor Test, 230 μm Coke.....	98

Figure 90:	Solids Pressure Drop ($-\Delta P_s/L$) of the Four Factor Test, 230 μm Coke	99
Figure 91:	Shear Stress Component Results of 3 Factor Factorial, Riser Gas Velocity, Standpipe Gas Velocity, and Fines Concentration, Coke....	105
Figure 92:	Gas Pressure Drop ($-\Delta P_g/L$) Results of 3 Factor Factorial, Riser Gas Velocity, Standpipe Gas Velocity, and Fines Concentration, Coke....	105
Figure 93:	Solids Pressure Drop ($-\Delta P_s/L$) Results of 3 Factor Factorial, Riser Gas Velocity, Standpipe Gas Velocity, and fines Concentration, Coke.....	106
Figure 94:	Bed Material Property Results of 3 Factor Factorial, Riser Gas Velocity, Standpipe Gas Velocity, and fines Concentration, Coke....	106
Figure 95:	Results of Shear Stress component for the Hysteresis Test, 230 μm Coke.....	112
Figure 96:	Results of Gas Pressure Drop Component for the Hysteresis Test, 230 μm Coke.....	112
Figure 97:	Results of Solids Pressure Drop Component for the Hysteresis Test, 230 μm Coke	112
Figure 98:	Comparison of Hysteresis Test Replicates, 230 μm Coke.....	114
Figure 99:	Example of Five Minute Steady State for Run Two, 230 μm Coke...	114
Figure 100:	Example of Five Minute Steady State for Run Nine, 230 μm Coke...	114
Figure 101:	Standpipe Force Balance Shell Balance.....	119
Figure 102:	Derivation of Solids Pressure Equation Drawing 1.....	124
Figure 103:	Derivation of Solids Pressure Equation Drawing 2.....	126
Figure 104:	Differential Triangular Element.....	129
Figure 105:	Differential Element and Resulting Forces.....	130
Figure 106:	Mohr Stress Circle for Particulate Solids 1.....	131
Figure 107:	Mohr Stress Circle for Particulate Solids Maximum Ratio of τ to P_s ..	132

CHAPTER 1 INTRODUCTION AND OBJECTIVES

1.1 Introduction to Standpipes in Circulating Fluidized Bed Systems

Circulating fluidized beds (CFB) are common in the chemical process industries. They are especially prevalent in the petroleum and electric power industry. Due to the development of highly active catalysts, circulating fluidized beds are replacing bubbling beds in the petroleum industries. Further, circulating fluidized bed combustors are becoming popular because of the potential of burning coal with low SO₂ and NO_x emissions. (Gidaspow, 1994)

The standpipe is an important component of the circulating fluidized bed. In a circulating fluid bed loop, the standpipe transports the recycled solids from a low pressure at the cyclone to a high pressure at the bottom of the standpipe. In industrial units, this pressure drop is necessary to prevent the “backflow” of gas in the riser up the standpipe, which could both severely spoil the efficiency of the cyclone and lead to the mixing of volatile chemicals. The standpipe is critical in ensuring the stable circulation of mass in the CFB, which moderates temperature and stabilizes combustion at this low temperature. This allows the use of emission reducing sorbent since temperature is controlled in the right range. Shadle (1999) reported some examples of unstable solids circulation rates.

As indicated by Shadle (1999) variables such as inventory and aeration within the standpipe has a large impact on the mass circulation and the stability of mass circulation. Minimizing the aeration while maintaining a high stable mass circulation is desirable to minimize the amount of dilution of the feed. The mixture momentum balance on a section of standpipe gives insight into the forces impacting flow within it. Understanding how aeration affects these forces may be a key in obtaining high stable mass circulation with minimum aeration. Further, this understanding is important in predicting solids feed to the riser.

Due to the high interest in circulating fluidized bed technology in industry and due to the difficulties in scaling these systems, a large effort to model these systems is underway.

1.2 Introduction to the Mixture Momentum Balance

To model the hydrodynamics for standpipes the important forces that contribute to both the gas and solids phase and momentum balances must be identified and understood. In this study the wall shear stress and solids pressure gradient are being studied. These are two important forces that have little experimental information available in the literature. Consider the section of standpipe in Figure 1.

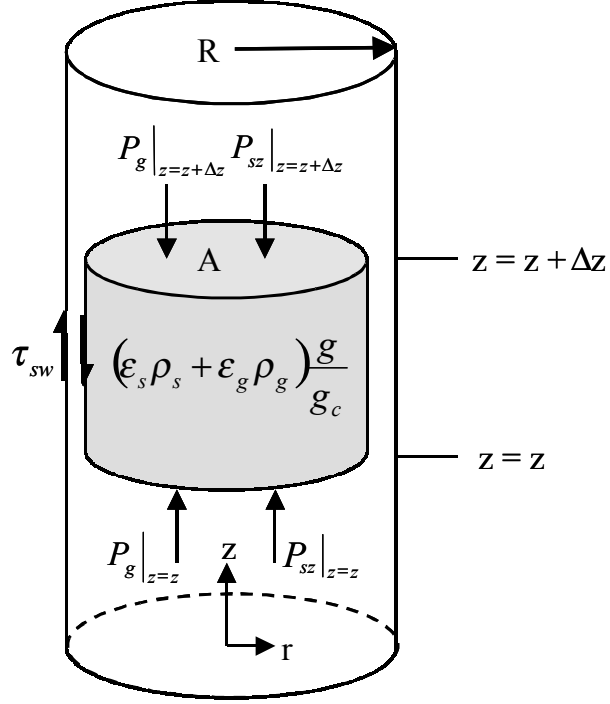


Figure 1: Standpipe Force Balance

The 3-dimensional momentum balance on the total mixture is as follows (Geankoplis, 1993) (Gidaspow, 1994):

$$\frac{\partial}{\partial t} \iiint_{cv} \epsilon_s \rho_s \vec{v}_s dV + \frac{\partial}{\partial t} \iiint_{cv} \epsilon_g \rho_g \vec{v}_g dV + \iint_{cs} \epsilon_s \rho_s \vec{v}_s (\vec{v}_s \cdot \vec{n}) dA + \iint_{cs} \epsilon_g \rho_g \vec{v}_g (\vec{v}_g \cdot \vec{n}) dA = \sum F \quad (1)$$

Writing the 1-dimensional momentum balance in the z -direction, using Cartesian coordinates on the total mixture gives the following:

$$\frac{\partial}{\partial t} \iiint_{cv} \epsilon_s \rho_s v_{sz} dV + \frac{\partial}{\partial t} \iiint_{cv} \epsilon_g \rho_g v_{gz} dV + \iint_{cs} \epsilon_s \rho_s v_{sz} \vec{v}_s \cdot \vec{n} dA + \iint_{cs} \epsilon_g \rho_g v_{gz} \vec{v}_g \cdot \vec{n} dA = \sum F_z \quad (2)$$

The first two terms are the accumulation of momentum for the gas and solids phase, and because the system is assumed to be in steady state, they are assumed to be

zero. The remaining two terms stand for the net outflow of momentum. If we assume plug flow and that bulk density is constant across the cross section, the net outflow of momentum can be expressed by Equation (3).

$$\iint_{cs} \epsilon_s \rho_s v_{sz} \vec{v}_s \cdot \vec{n} dA + \iint_{cs} \epsilon_g \rho_g v_{gz} \vec{v}_g \cdot \vec{n} dA = \dot{m}_g (v_{gz}|_{z=z} - v_{gz}|_{z=z+\Delta z}) + \dot{m}_s (v_{sz}|_{z=z} - v_{sz}|_{z=z+\Delta z}) \quad (3)$$

If there is steady state flow and the solids volume fraction is constant, then the velocity-in equals the velocity-out and the right hand side of Equation (3) is zero.

The right hand side of Equation (2) is the sum of the forces and can be expanded as follows:

$$0 = \pi R^2 (P_g + P_{sz})|_{z=z} - \pi R^2 (P_g + P_{sz})|_{z=z+\Delta z} + \tau_{gw} (2\pi R \Delta z) + \tau_{sw} (2\pi R \Delta z) - (\epsilon_s \rho_s + \epsilon_g \rho_g) \frac{g}{g_c} (\pi R^2 \Delta z) \quad (4)$$

In this equation, the forces acting on the control volume are gas phase pressure, solids phase pressure, gas-wall shear stress, solids-wall shear stress, gas phase weight, and solids phase weight. Dividing by Δz , and taking the limit as Δz goes to zero results in:

$$-\frac{\partial P_{sz}}{\partial z} - \frac{\partial P_g}{\partial z} + \frac{2\tau_{sw}}{R} + \frac{2\tau_{gw}}{R} - \rho_g \epsilon_g \frac{g}{g_c} - \rho_s \epsilon_s \frac{g}{g_c} = 0 \quad (5)$$

The wall shear stress and body force terms are considered small for the gas phase and are ignored (Jones 1985, Picciotti, 1995), leaving Equation (5) in terms of process variables.

$$-\frac{\partial P_{sz}}{\partial z} - \frac{\partial P_g}{\partial z} + \frac{2\tau_{sw}}{R} - \rho_s \epsilon_s \frac{g}{g_c} = 0 \quad (6)$$

Equation (6) is the microscopic form of the mixture momentum balance, and a derivation of it from shell balance techniques has been provided in Appendix A.1.

Experimentally, the gas pressure drop is determined using differential pressure transducers and the weight of the bed is determined by assuming solids volume fraction deviated little from the packed state. Shear stress measurements are obtained using a shear vane and/or the new wall device. The solids pressure is the only term not measured directly. However, it is inferred by difference from the other measurements, Equation (7). Rearranging Equation (4) and neglecting gas phase wall shear stress and gas phase body force results in Equation (7).

$$\frac{\Delta P_{sz}}{\Delta z} = -\rho_s \epsilon_s \frac{g}{g_c} + \frac{4\tau_{sw}}{D} - \frac{\Delta P_g}{\Delta z} \quad (7)$$

1.3 Objectives

The objective of this research project is to experimentally quantify the solids-wall shear stress and to estimate the differential solids pressure. The shear stress is measured under a variety of aeration conditions, and this measured value is used to predict the differential solids phase pressure drop. Further, accepted methods of predicting shear stress and solids pressure in the literature are investigated. Results using predictions from these methods are compared to the experimentally obtained values. The objectives of this research are:

1. Facilitating a literature search to understand if/how shear stress and solids pressure have been measured in the past, and to understand how shear stress and solids pressure are estimated in models.
2. Experimentally measuring solids-wall shear stress as a function of solids circulation rate using the shear vane and wall probe.
3. Using solids-wall shear stress to estimate differential solids pressure by inferring it to be the residual portion of the momentum balance.
4. Independently estimating shear stress and solids pressure for packed and transitionally packed bed regimes by obtaining bed material properties and using them with bulk solids mechanics as suggested by Picciotti 1995; Mountziaris and Jackson 1990, and Jones and Leung 1985. This method is explained in detail in section 2.2a of this proposal.
5. Understanding the effects of operational variables on shear stress. The variables studied are listed in Chapter 5.

Further, the shear stress at the wall and the local solids volume fraction at the wall were simultaneously measured using the new wall device and a capacitance wall probe developed by Michel Louge (1992,1995). Limitations of these devices are described in Chapter 6.

CHAPTER 2 LITERATURE SURVEY

Standpipes have been in use for over 40 years (Knowlton, 1986). As a result, a large volume of material has been published regarding them. This literature survey will focus on papers utilizing the mixture momentum balance and the forces within it. Experimental measurements of these forces are of largest interest.

2.1 Flow Regimes

Many papers have been published that use the mixture momentum balance in their modeling efforts. In most cases the shear stress and axial solids pressure are treated differently depending on the fluidization regime of the bed. Therefore, in order to follow this work it is necessary to discuss the possible flow regimes of the standpipe.

Leung and Jones (1985) outlined two flow regimes of the standpipe, fluidized and non-fluidized regime. They further subdivided these two regimes and discussed the possibility of multiple regimes coexisting in the standpipe at the same time. Knowlton (1986) suggested a third regime, streaming flow, which is characterized by dilute phase flow with a high void fraction. This type of flow is unlikely under the conditions of this work.

Leung and Jones (1985) used slip velocity (U_{sl}) and void fraction (ϵ) to differentiate between the regimes. U_{sl} is defined by the following equation:

$$U_{sl} = \frac{-U_g}{\epsilon} + \frac{U_s}{1-\epsilon} \quad (8)$$

The sign convention is that solid and gas velocities are positive down and U_{sl} is positive up. Solids velocity is always down and positive. See Table 1 for clarification.

Table 1: Sign Convention for U_{sl}

U_{sl}	U_g	U_s	
Negative	Positive	Positive	$U_g > U_s$
Positive	Positive	Positive	$U_g < U_s$
Positive	Negative	Positive	

2.1.a Non-Fluidized Regime

A slip velocity less than minimum fluidization velocity and a void fraction less than minimum fluidization void fraction characterize the non-fluidized regime. See Equation (9) and (10) (Leung, 1985).

$$U_{sl} < (U_{mf}/\epsilon_{mf}) \quad (9)$$

$$\epsilon < \epsilon_{mf} \quad (10)$$

Leung and Jones further subdivided this regime into packed-bed flow and transitional packed bed flow. In both regimes U_{sl} is negative which means that the gas is flowing down with the solids but at a greater rate. Equation (11) and (12) define packed-bed flow.

$$U_{sl} < 0 \quad (11)$$

$$\epsilon = \epsilon_c \quad (12)$$

ϵ_c is the vibrated void fraction. Transition packed-bed flow is defined by Equations (13) through (15)

$$0 > U_{sl} > (U_{mf}/\epsilon_{mf}) \quad (13)$$

$$\epsilon_c < \epsilon < \epsilon_{mf} \quad (14)$$

$$\epsilon = \epsilon(U_{sl}) \quad (15)$$

Equation (15) means that void fraction is a function of the slip velocity for transition packed-bed flow, and it is defined to be constant for packed-bed flow.

2.1.b Fluidized Regime

The fluidized regime is characterized by a slip velocity equal to or greater than the minimum fluidization velocity and a void fraction equal to or greater than the minimum fluidization void fraction (Leung, 1985). See Equation (16) and (17).

$$U_{sl} > (U_{mf}/\epsilon_{mf}) \quad (16)$$

$$\epsilon > \epsilon_{mf} \quad (17)$$

This regime is further subdivided into type I fluidized flow and type II fluidized flow. Type I fluidized flow is defined by Equation (18) and (19), and type II fluidized flow is defined by Equation (20) and (21).

$$\left(\frac{\partial U_g}{\partial e} \right)_{U_s} > 0 \quad (18)$$

$$U_{sl} > \frac{U_{mf}}{e_{mf}} \quad (19)$$

$$\left(\frac{\partial U_g}{\partial e} \right)_{U_s} < 0 \quad (20)$$

$$U_{sl} > \frac{U_{mf}}{e_{mf}} \quad (21)$$

Knowlton (1986) divided the fluidized regime into bubbling fluidized flow and non-bubbling fluidized flow. He further divided bubbling flow into four regimes:

- Type 1. Emulsion gas flow up, bubble flow up, net gas flow up

Both the gas flowing in the interstices and the bubbles are flowing up relative to the standpipe wall. This occurs when the velocity of the solids is less than the minimum fluidization velocity.

- Type 2. Emulsion gas flow down, bubble flow up, net gas flow up

In this classification the velocity of the solids is greater than minimum fluidization velocity. Therefore, the gas flowing in the interstices is flowing down. However, the bubble rise velocity is greater than the solids velocity. Because the volumetric flow rate of the bubbles is greater than the volumetric flow rate of the gas in the interstices, the net flow of gas is up.

- Type 3. Emulsion gas flow down, bubble flow up, net gas flow down

This regime is very similar to type 2 because the solids velocity is greater than the minimum fluidization and less than the bubble velocity. However, because the volumetric flow rate of the bubbles is less than the volumetric flow of the gas in the interstices, the net gas flow is down.

- Type 4. Emulsion gas flow down, bubble flow down, net gas flow down.

In this case the solids velocity is greater than the bubble rise velocity. Therefore, the bubbles are carried down at a velocity of equal to the difference between the solids velocity and the bubble rise velocity.

2.2 Standpipe Modeling

In general, researchers use different relationships depending on the flow regime of the standpipe. This is especially common in the treatment of solids wall shear stress and solids pressure. Most researchers model all components of their system such as hoppers feeding the system and valves discharging solids from the system. They also include boundary conditions for transitions between each component, and for each component there is generally a set of equations used, such as a mass and momentum balance. In this work the standpipe will be the only component under consideration, and the mixture momentum balance will be the emphasis. It is also important to note that only steady flow is considered in this work. The mixture momentum balances for each flow regime will be discussed.

2.2.a Non-Fluidized Regime

Researchers have recognized the importance of solids-wall shear and solids pressure for non-fluidized regimes. Bulk solids mechanics has been introduced to estimate these forces. In general, the form of the mixture momentum balance used is Equation (6), and is rewritten below (Picciotti 1995; Leung and Jones 1985).

$$-\frac{\partial P_{sz}}{\partial z} - \frac{\partial P_g}{\partial z} + \frac{2t_{sw}}{R} - \mathbf{r}_s \cdot \mathbf{e}_s \frac{g}{g_c} = 0 \quad (6)$$

Picciotti (1995) and Leung and Jones (1985) suggest substituting a relationship that relates solids shear stress to axial solids pressure into this equation. This relationship comes from bulk solids mechanics and is summarized by Equation (22) through (24).

$$\tau_{sw} = \mu_w P_{sr} \quad (22)$$

$$\mu_w = \tan \delta_w \quad (23)$$

$$P_{sr} = P_{sz} \frac{1 - \sin \mathbf{d}}{1 + \sin \mathbf{d}} \quad (24)$$

Substituting Equation (23) and (24) into Equation (22) gives Equation (25).

$$t_{sw} = \tan \mathbf{d}_w \frac{1 - \sin \mathbf{d}}{1 + \sin \mathbf{d}} P_{sz} \quad (25)$$

The constants δ_w and δ are the angle of wall friction and the effective internal angle of friction respectively. Note Equation (26), and that $1/K$ is the Janssen coefficient and μ_w

in Equation (23) is the coefficient of friction. (Jones, 1985; Picciotti, 1995; Mountziaris, 1990; and Schulze, 2000).

$$\frac{1}{K} = \frac{1 - \sin d}{1 + \sin d} \quad (26)$$

Substituting Equations (26) and (23) into (25) results in Equation (27).

$$\mathbf{t}_{sw} = \frac{\mathbf{m}_w}{K} P_{sz} \quad (27)$$

The previous expression can be substituted into the mixture momentum balance, if the bed is assumed to be in an active state of stress and packed. An active state of stress implies that the major principal stress is in the z -direction, and the corresponding minor principal stress is in the r -direction. This means that the solids are on the verge of compacting in the axial direction and expanding in the horizontal direction (Mountziaris, 1990).

Picciotti (1995) makes this suggested substitution and derives Equation (28) assuming a constant pressure drop per unit length and a boundary condition of zero solids pressure at the top of the bed. Take note that the coordinate system that Picciotti used in the derivation of Equation (28) is the opposite of that used in this work. He used a positive z -axis pointing down. The complete derivation of Equation (28) can be found in Appendix A.2a.

$$P_{sz} = \frac{RK}{2\mathbf{m}_w} \left[\mathbf{r}_s \mathbf{e}_s \frac{g}{g_c} + \frac{\Delta P_g}{H} \right] \left[1 - e^{-\frac{2\mathbf{m}_w z}{RK}} \right] \quad (28)$$

The total pressure drop across the standpipe (pressure at the top minus pressure at the bottom, which should be a negative value) is ΔP , and the height of the bed in the standpipe is H . The location of the estimation of solids pressure measured down from the top of the bed is z .

Mountziaris and Jackson (1990) use essentially the same theory, except the individual gas phase momentum balance and solids phase momentum balance are modeled rather than the mixture balance. The same relationship between solids shear stress and solids pressure is utilized. A summary of the approaches to modeling solids-wall shear stress for non-fluidized regimes is supplied in Table 2.

Table 2 : Modeling Solids-Wall Shear Stress for Non-Fluidized Regime

Reference	Fluidization Regime	Wall Shear Stress
Leung and Jones, 1985	Packed-Bed Flow	$t_{sw} = \tan d_w \frac{1 - \sin d}{1 + \sin d} P_{s,z}$
Leung and Jones, 1985	Transition Packed-Bed Flow	$t_{sw} = \tan d_w \frac{1 - \sin d}{1 + \sin d} P_{s,z}$
Mountziaris and Jackson, 1990	Moving Bed Flow	$t_{sw} = \tan d_w \frac{1 - \sin d}{1 + \sin d} P_{s,z}$
Picciotti, 1995	Packed-Bed Flow	$t_{sw} = \tan d_w \frac{1 - \sin d}{1 + \sin d} P_{s,z}$

2.2.b Fluidized Regime

Unlike non-fluidized regimes where researchers appear to be in agreement in their consideration of solids shear stress, there are varying opinions regarding solids-wall shear stress for fluidized regimes. Leung and Jones (1985) state that for fluidized flow the solids pressure is zero, and they suggest using a friction factor to express shear stress. Leung and Wiles (1976) list various correlations for the friction factors, but Leung and Jones (1985) suggest that for a dense-phase flow with voidage close to that of minimum fluidization the friction factor is constant and can be approximated by $f = 0.003$. Leung and Wiles (1976) cite Stermerding (1962) for this constant friction factor. Stermerding (1962) studied pneumatic transport and back calculated friction factors from slip factors that are calculated from pressure drop, gas velocity and solids mass velocity. Mountziaris and Jackson (1990) assume solids-wall shear stress and solids pressure to be negligible for suspension flow. A summary of the approaches to modeling solids-wall shear stress for non-fluidized regimes is supplied in Table 3.

Table 3: Modeling Solids-Wall Shear Stress for Fluidized Regimes

Reference	Fluidization Regime	Wall Shear Stress
Leung and Jones, 1985	Type I and Type II Fluidized Flow	$t_w = \frac{1}{2} f e_s r_s u_s^2 *$
Knowlton, 1986	Fluidized flow	negligible
Mountziaris and Jackson, 1990	Suspension Flow	negligible

*"For dense-phase flow with voidage close to ϵ_{mf} , the contribution of wall friction is small and a constant value of $f=0.003$ may be used."

2.3 Standpipe Experimental Studies of Solids Pressure and Solids Friction

The section above discussed modeling solids-wall shear stress and solids pressure. The purpose of this section is to discuss attempts to experimentally measure shear stress and solids pressure.

2.3.a Solids-Wall Shear Stress

Van Swaij (1970) measured the solids-wall shear stress directly of cracking catalyst in a 7-inch riser. The measurements were taken using a moveable section of wall in the riser. The total force on this moveable wall was measured, and the shear stress values were taken from these measurements. See Figure 2 for details.

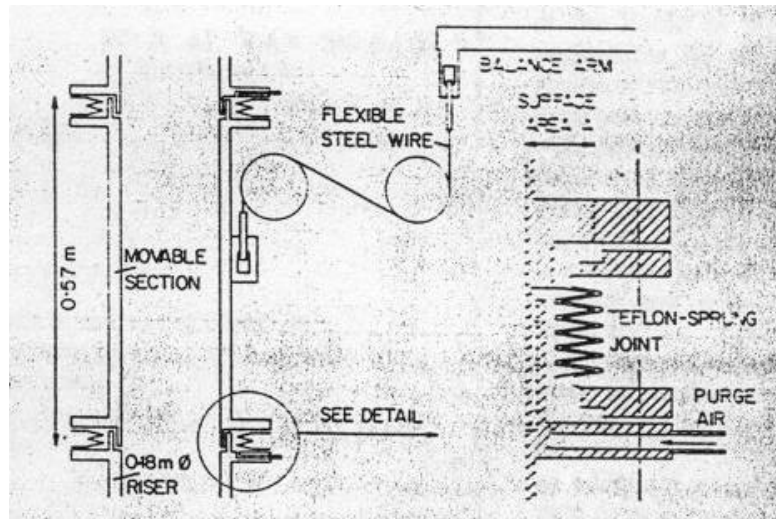


Figure 2: Moveable Wall Device for Solids-Wall Shear Stress (Van Swaij, 1970)

Results are shown in Figure 3. Notice that shear stress increases with solids flux. Notice the sign change in the shear stress values. At higher solids fluxes the shear stress is in the opposite direction of the gas flow due to down flow of solids at the wall.

Van Swaaij (1970) also measured average density of the flow using γ -ray adsorption. He compared density versus the gas pressure drop. See Figure 4 where ρ_s is the particle density and α is the mean solids volume fraction measured. At lower densities the pressure drop was larger than the weight of the bed, and at higher densities the pressure drop was lower than the weight of the bed.

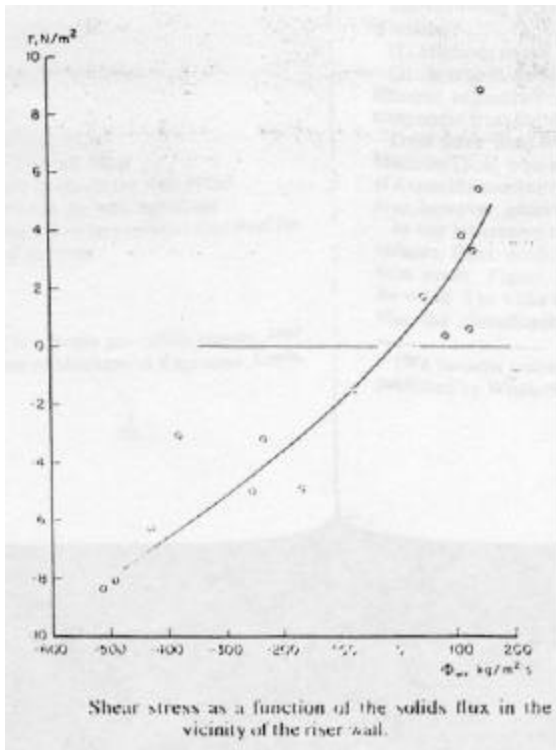


Figure 3: Shear Stress versus Solids Flux in a Pneumatic Riser (Van Swaaij, 1970)

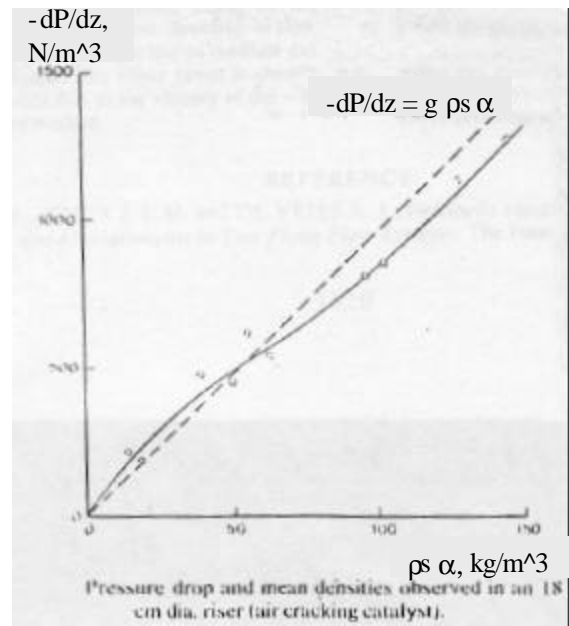


Figure 4: Pressure Drop and Mean Densities (Van Swaaij, 1970)

Table 4 gives the raw data listed by Van Swaaij. The percentage of the total forces cannot be evaluated since density measurements were not given along with shear stress measurements. Φ_w is the solid flux in the vicinity of the wall in units of $\text{kg/m}^2 \text{sec}$.

Table 4: Riser Conditions and Shear Stress (Van Swaij, 1970)

Mean gas Velocity (m/sec)	Mean solids flux (kg/m ² sec)	F_w	F (N)	dp/dz (N/m ³)	t (N/m ²)	Contribution of shear to pressure drop (%)
4.7	133	-430	4.1	844	-6.3	-16
4.3	141	-167	6.3	1090	-4.9	-10
6.0	206	-497	3.3	818	-8.1	-22
5.7	344	-511	6.2	1238	-8.4	-15
8.5	236	-76	3.0	477	-1.5	-7
7.6	385	-255	6.2	1078	-5.0	-10
8.5	432	-384	6.7	1062	-3.1	-6
10.0	152	85	1.7	215	0.4	4
9.4	284	-49	3.0	492	-1.7	-7
12.2	316	126	2.8	355	0.6	4
11.0	514	-236	4.1	705	-3.2	-10
14.9	183	118	2.9	231	3.8	36
15.1	213	132	2.8	229	3.3	31
13.3	419	143	5.4	501	5.4	23
13.06	434	150	7.0	560	8.8	34

Matsen (1976) estimated solids-wall shear stress for large-scale commercial standpipes by the difference between the density of the bed and the gas phase pressure drop per unit length. The density of the bed was measured using the attenuation of gamma radiation. He found that the friction loss due to solids-wall contact increases dramatically as the density of the bed increases, Figure 5. Raw data for large commercial units published by Matsen (1976) is listed in Table 5. Notice that the friction loss increases sharply as the density of the bed increases.

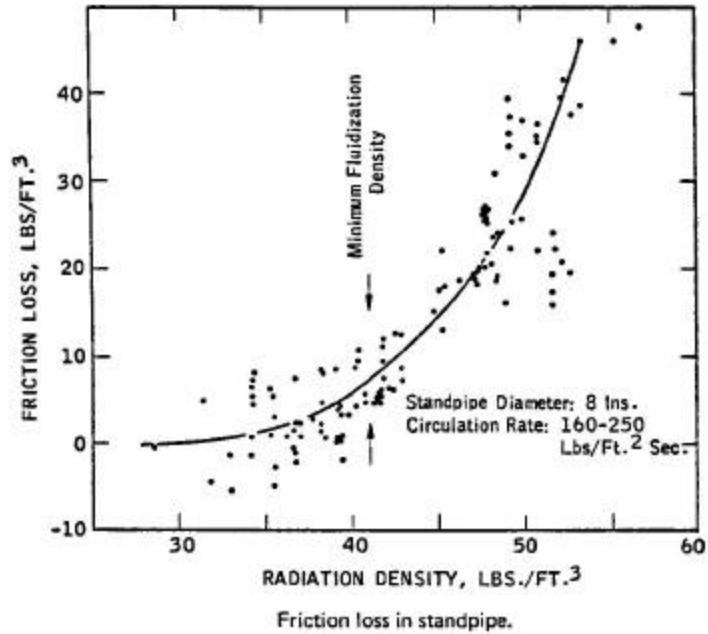


Figure 5: Solids-Wall Friction Versus Density of the Bed (Matsen, 1976)

Table 5: Commercial Data on Solids-Wall Friction (Matsen, 1976)

<u>Diameter</u> <u>Inches</u>	<u>Material</u>	<u>Mass Rate</u> <u>lb/ft²sec</u>	<u>Radiation Density</u> <u>lb/ft³</u>	<u>DP/DL</u> <u>lb/ft³</u>	<u>Friction</u> <u>lb/ft³</u>
23	coke	75	61	31	30
23	coke	75	65	20	45
29	catalyst	145	42	38	4
29	catalyst	145	49	36	13
30	catalyst	160	54	39	15
33	coke	37	60	55	5
42	catalyst	115	47	41	6
42	catalyst	115	53	32	19
42	catalyst	115	55	21	34
50	catalyst	200	39	40.5+/-4.5	-1.5
50			42	40.5+/-4.5	1.5
50			37	40.5+/-4.5	-3.5

Matsen's estimation of solids-wall friction ranged from 2% to as high as 35% of the total forces studied. The forces he included are weight of the bed, gas phase pressure drop per unit length, and shear stress. His estimations of shear stress may be elevated because solids phase pressure drop per unit length has not been included. In this study, shear stress has been estimated over a mass circulation ramp that ranged from 3,000 to 43,000 lb/hr to range from 27% to 6% of the total forces. The forces considered in this

study are the weight of the bed, gas phase pressure drop ($-\Delta P_g/L$), solids phase pressure drop ($-\Delta P_s/L$), and shear stress ($-2\tau_{sw}/R$).

It is difficult to compare the commercial data with data collected in this study, because the commercial data was taken under different conditions. The standpipe diameters are over twice as large as the standpipe used in this work. The data for the commercial units are taken at higher temperatures and pressures than ambient. The unit used in this work is a cold flow unit, which runs at ambient temperatures and close to atmospheric pressure. Further, aeration schemes in Matsen's work are not noted, so operating conditions are not clear. One commonality is one of the bed materials. Coke is used in both studies. The mass fluxes of Matsen's study are larger to those of this study. Matsen's study ranged from 37 to 200 lb/ft²sec and fluxes of this study have ranged from 1.5 to 2.2 lb/ft² sec. Further, due to the large differences in the standpipe diameters the circulation rates of the commercial units are up to four times higher. Another difference was that the commercial data reported in Matsen's study was taken from standpipes that were operating with a poor pressure rise. (Matsen, 1976). The desired pressure drop across the standpipe was not achieved, leading to instabilities in the system.

Zenz (1960) estimated solids wall shear stress for packed and fluidized conditions with the use of a tube-pulling apparatus. See Figure 6 for a schematic of the device. A fixed piston and the tube wall support the bed material. A water-filled balloon is placed at the bottom of the bed material and, the pressure exerted on this balloon is measured. An aeration ring is also placed at bottom of the bed material for fluidized conditions. A hand crank pulls the tube. The tube velocity was measured using the analysis of high-speed motion photography. Zenz (1960) estimated the shear stress to be the difference between the pressure exerted at the bottom of the bed when tube is stationary and when the tube is in motion.

Zenz (1960) found that for fluidized conditions the difference was negligible regardless of the velocity of the tube. However, for packed condition the difference decreased with increasing tube velocity. See Figure 7 for experimental results. Notice that similar results were found for 3 1/2" and 5 1/2" diameter tubes. His results give values ranging from 4 - 3.5 to 4 - 0.5" H₂O which corresponds to 2.6 to 18.2 lb/ft². His upper end of the range is much higher than what has been seen in this study, 1.74 to 7.2 lb/ft².

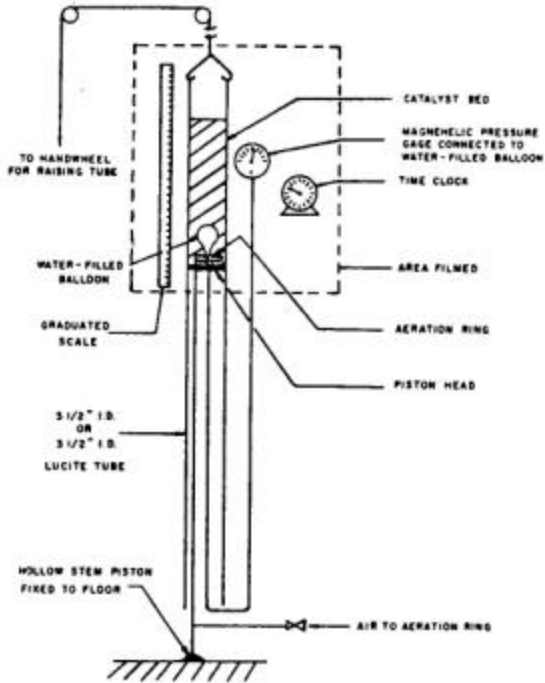


Figure 6: Tube-Pulling Apparatus (Zenz, 1960)

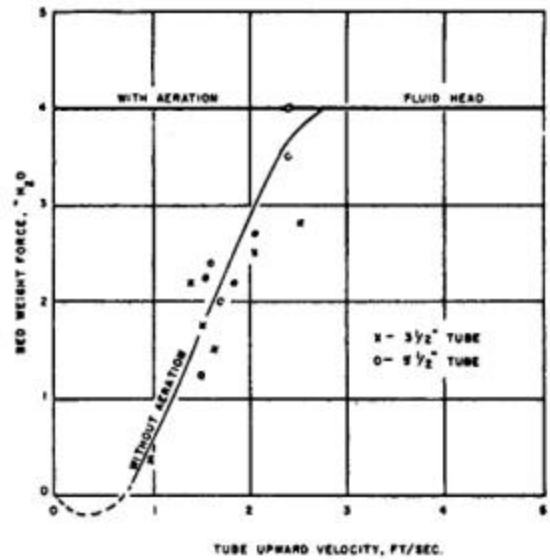


Figure 7: Tube-Pulling Experimental Results (Zenz, 1960)

2.3.b Solids Pressure

Polashenski (1999) measured local time-averaged solids pressure in the riser of a CFB. The measurements were taken internally and at the wall for both dilute and dense beds. Polashenski's device is illustrated in Figure 8. A diaphragm, which is in contact with the solids and gas, is mounted flush with a sensitive transducer. A screened vent tube is connected to the rear of the probe to allow the gas to equalize on both sides of the diaphragm. The net response of the diaphragm is due to solids pressure in the radial direction only. Solids fraction was also measured using a capacitance probe. Two bed materials were studied which were sand (Geldart Group B $d_p = 140 \mu\text{m}$, $\rho_s = 2500 \text{ kg/m}^3$) and FCC (Geldart Group A $d_p = 94 \mu\text{m}$, $\rho_s = 1500 \text{ kg/m}^3$).

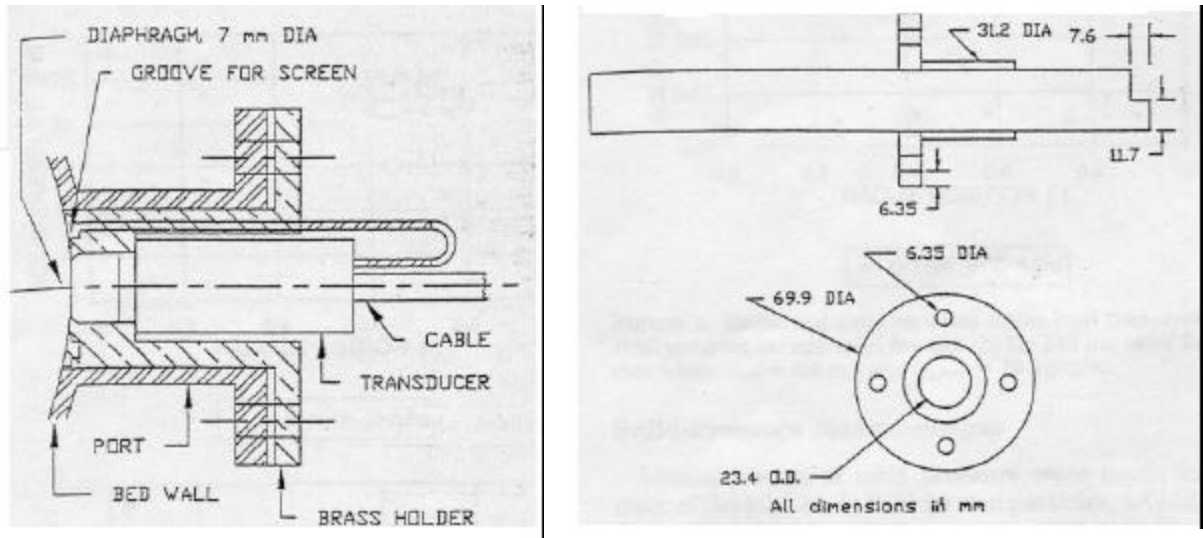


Figure 8: Solids Pressure Probes (Polashenski, 1999)

Polashenski (1999) found that the strongest correlating factor for local time-averaged solids pressure is solids volume fraction. See Figure 9 for experimental data. Solids pressure is essentially constant for low solids fraction. However, after a solids fraction of approximately 0.05 the local time-averaged solids pressure increases with increasing solids fraction. Polashenski (1999) gave a relationship for this correlation, Equation (29).

$$P_{s,r} = \left[(16.5e_s^{0.1})^5 + (518e_s^{1.1})^5 \right]^{0.2} \quad (29)$$

$P_{s,r}$ is in units of Pa.

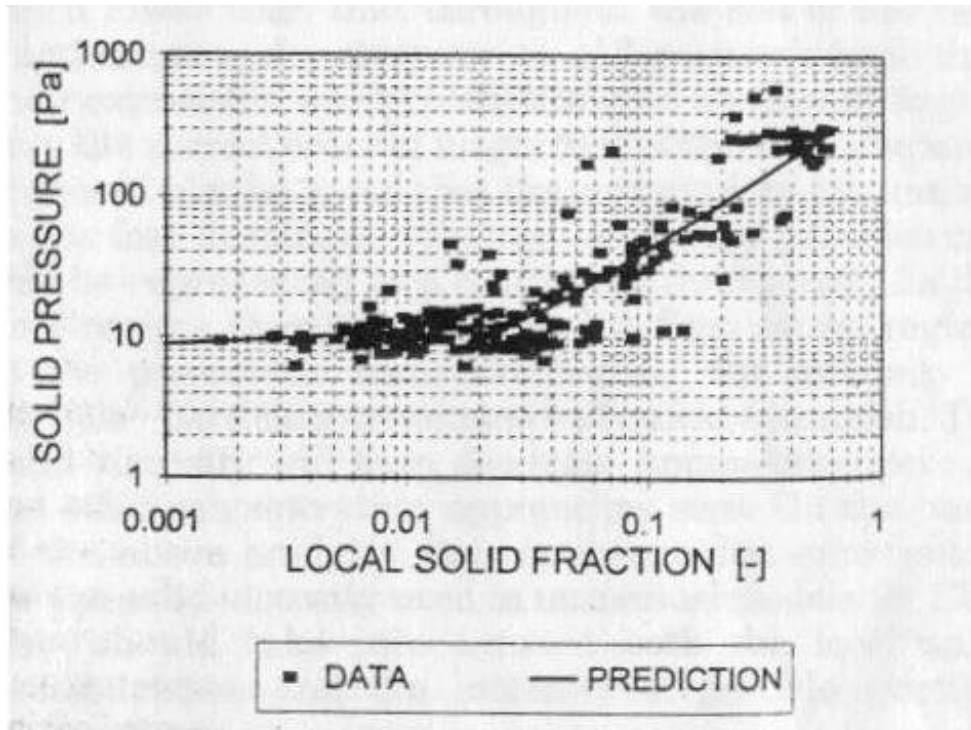


Figure 9: Solids Pressure versus Local Solid fraction (Polashenski, 1999)

Since the solids pressure measurements taken under Polashenski's study are in the radial direction and in the riser of the CFB, they are several orders of magnitude less than our estimated pressures. For example, solids pressure ranged from 10 to 300 Pa, which corresponds to 0.209 to 6.27 lb/ft² for Polashenski's study. In this study, solids pressure was estimated to range from 86 to 143 lb/ft². Also, we are operating in a packed bed state. Polashenski operated in the more dilute CFB riser.

CHAPTER 3 EXPERIMENTAL SET-UP

3.1 Circulating Fluid Bed

The circulating fluidized bed (CFB) under study is located at the National Energy Technology Lab located in Morgantown, WV. The size of the CFB is large for an experimental system. The riser is 12" ID with 50 ft height, and the standpipe is 10" ID. A nominal rate of 40,000-lb/hr circulation of solids (coke breeze) can be attained. The system is rated at 100 psi, but most of the tests for this study were carried out at atmospheric pressure and ambient temperature. The standpipe and riser are equipped with pressure transducers along their length. Mass flow controllers are used to supply aeration. Solids are transported from the standpipe to the riser through a loopseal, which is a nonmechanical valve. The standpipe and loopseal are equipped with pressure transducers and aeration ports. Solids are collected coming out of the riser and returned to the standpipe through a primary cyclone. A schematic of the CFB is in Figure 10. Circles denote location of pressure transducers. Arrows pointing toward the vessel walls indicate aeration ports. One particular aeration port of importance is located at 0.3' on the diagram. This aeration controls solids circulation rate, and is referred to as move air, F_m .

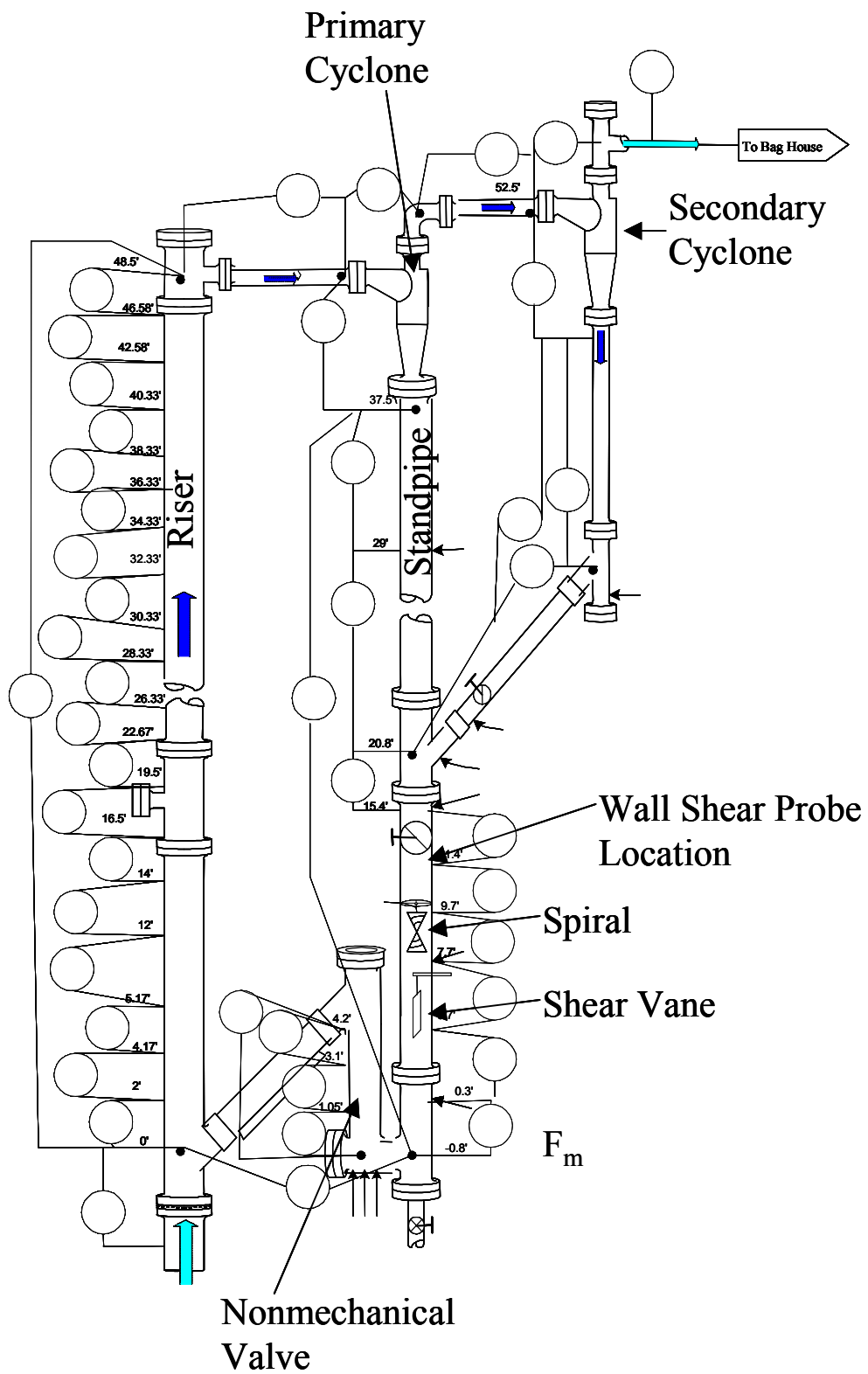


Figure 10: NETL Circulating Fluid Bed

3.2 Bed Materials and Properties

The materials utilized in this study are coke breeze and cork.

Coke breeze is a Geldart group B (Gidaspow, 1994) with an average particle diameter of 230 micron. Its bulk density is 49 to 55 lb/ft³ with a particle density of 110.8 lb/ft³. Particle density is measured using a water displacement technique similar to the discussion in Section 3.6c. Solids volume fractions under vibrated and minimum fluidization conditions were measured as 0.50 and 0.445, respectively. These measurements were obtained by measuring the bulk density under vibrated and minimum fluidization conditions and using the above particle density. The minimum fluidization velocity is 0.072 ft/sec with a sphericity of 0.84. Sphericity was calculated using the Ergun equation. From Jenike shear cell measurements, the internal angle of friction of the new material has been estimated to be 33.57 to 43.87°, and angle of wall friction associated with galvanized sheet metal (shear vane) was estimated to be 18°. The angle of wall friction associated with painted carbon steel (Phenalic Resin) was estimated to be 24°. All carbon steel parts of the NETL CFB are painted with phenalic resin. A full description of the measurement techniques and the full meaning of these angles can be found in A.3.

Cork is a Geldart group B (Gidaspow, 1994) with an average particle diameter of 1,000 micron. Its bulk density is 5.5 to 6.7 lb/ft³ with an intrinsic density of 13 lb/ft³. Solids volume fractions under vibrated and fluffed conditions were measured as 0.515 and 0.423, respectively. The minimum fluidization velocity is 0.555 ft/sec. Utilizing the technique of Zenz (1960), the internal angle of friction of the new material has been estimated to be 74.3°, and angle of wall friction associated with galvanized sheet metal (shear vane) was estimated to be 37.2°.

3.3 Description of Mass Flow Device

A spiral device developed by NETL is placed at approximately 8-9' in the standpipe and is used to measure mass circulation. As the solids pass by this spiral, the solids force it to rotate. The speed of this rotation is measured and gives a volumetric flow rate. This volumetric flow rate is converted to mass circulation using the bulk

density (Ludlow, 2002). Take note that the void fraction is assumed to be constant. A picture of the spiral is shown in Figure 11.

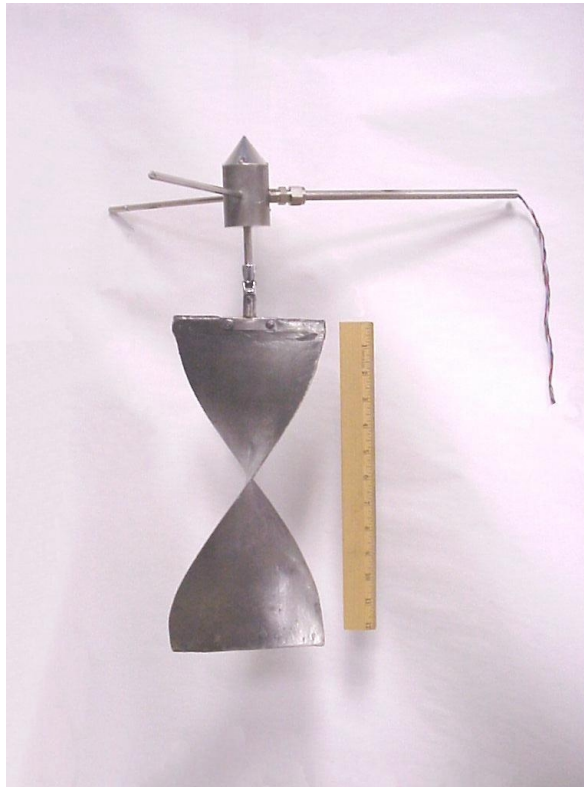


Figure 11: Spiral, Mass Circulation Measurement

3.4 Shear Vane

3.4a Shear Vane General Description

The shear vane is a device used to measure shear stress within the standpipe, developed concurrently by WVU and NETL. It is a thin, flat metal sheet suspended from a 10 lb load cell probe. The load cell measures the weight of the vane plus the forces the bed particles exert on it as they move past it. The vane hangs along the centerline of the standpipe. The top of the vane is located about 7.7 feet from the bottom of the standpipe. The vane is 3 inch in width, 24 inch in length, and 1/32 inch in thickness (Figure 16). The active area of the shear vane is 1/5th the surface area of the same length of 10" pipe. It is assumed that the shear stress measured by the vane along the centerline of the pipe is the same as the shear stress at the wall. This is a reasonable assumption if we assume plug flow in the standpipe or radial variation in shear stress.

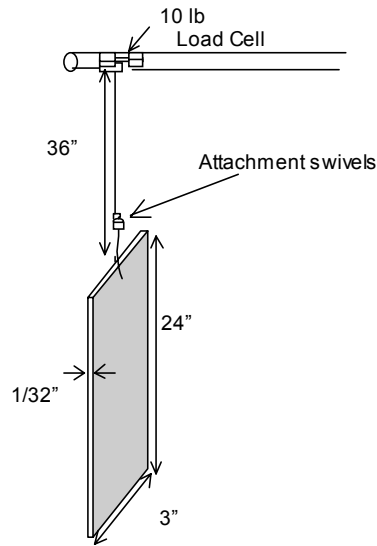


Figure 12: Shear Vane Schematic

3.4b Shear Vane Calibration and Error

To calibrate the shear vane, twelve weights, that span the force expected for coke breeze, were applied first in an increasing manner followed by a decreasing manner. The results are in Figure 13. Based on the variability in Figure 13, the error associated with the shear vane is $\pm 0.14 \text{ lb/ft}^2$ for a $\pm 2s$ limits (Doebelin, 1983). This corresponds to a 2% of scale for coke breeze and a 6% of scale for cork.

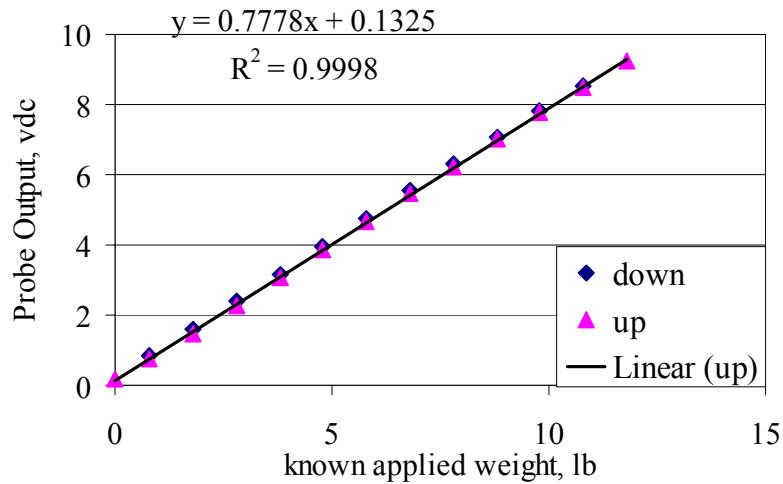


Figure 13: Shear Vane Calibration

3.4c Parasitic Drag Characterization

It was mentioned above that the shear vane measures the weight of the vane and the forces the bed particles exert on it as they move past it. Unfortunately other forces are measured such as the drag associated with the leading edge of the metal vane and drag along the cable. These forces are referred to as parasitic drag. The purpose of this section is to describe the test and results used to characterize the parasitic drag.

In this experiment the vane length and mass circulation was varied, and the response variables were the force measured by the vane and the pressure drop across the interval that contained the vane. The aeration to the riser and loopseal were held constant. The aeration, referred to as move air (F_m in Figure 10) was changed to obtain desired mass circulation rates. The pressure drops across the riser, standpipe, and loopseal were monitored at all times.

Two tests were performed. First, a steady state analyses was made with two different mass circulation rates for three different lengths of otherwise identical metal shear vanes. The levels of vane lengths and mass circulation rates are in Table 6. Under the steady state analyses, the standpipe height was held constant. In the second test the move air was increased from 55 scfh to 405 scfh at a rate of 20 scfh/min for each vane length. Take note that under the second test the standpipe height was not constant.

Table 6: Independent Variable Levels for the Parasitic Drag Test

Index	A	B
No.	Mass Circulation lb/hr	Vane Length ft
1	35000	1
2	45000	1
3	35000	2
4	45000	2
5	35000	3.49
6	45000	3.49

The six steady state conditions are plotted in Figure 14. Each vane was run at two different mass circulation rates, which corresponded to two different aeration rates. Regression lines are also plotted along with corresponding equations and R^2 values.

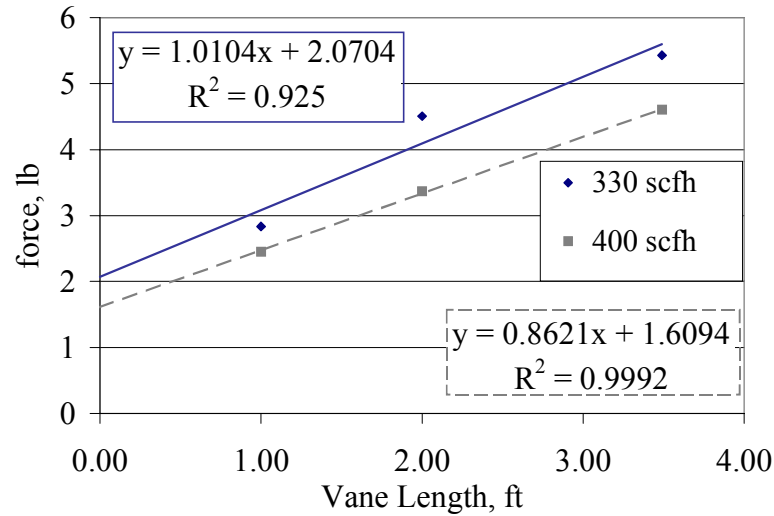


Figure 14: Parasitic Drag Steady Steady State, 230 μ m Coke

When examining Figure 14, it is important to note that there was a problem with several of the steady states. During the study, the two vanes not in use were hanged at the wall lower in the standpipe. Under a few conditions, the 3.49 ft vane partially blocked the standpipe outlet to the loopseal. This increased the aeration required to obtain the circulation rates listed in Table 6.

The objective was to determine how much of the force was due to shear and how much was due to drag along the leading edge and cable. If both of the regression lines are extrapolated to the point where they cross zero, the amount of force due to drag will be the intercept. In other words, as the length of the vane or as the area over which shear occurs goes to zero, the force measured goes to 2.07 lb for a move air of 330 scfh and 1.61 lb for a move air of 400 scfh.

The above analysis has been applied to the ramp data. There are force measurements for each vane for all move air values from 55 to 405 scfh. To determine the y-intercept, which is the point at which the length of the vane goes to zero, a simple linear regression was performed on each increment of move air. Figure 15 gives the total force measured for each vane and the parasitic drag versus aeration rate. Notice that as aeration increases the force measured for all of the vanes decreases. Also, as the vane length increases the overall force measured increases, because the area over which shear occurs increases. The parasitic drag is relatively constant at high aeration rates.

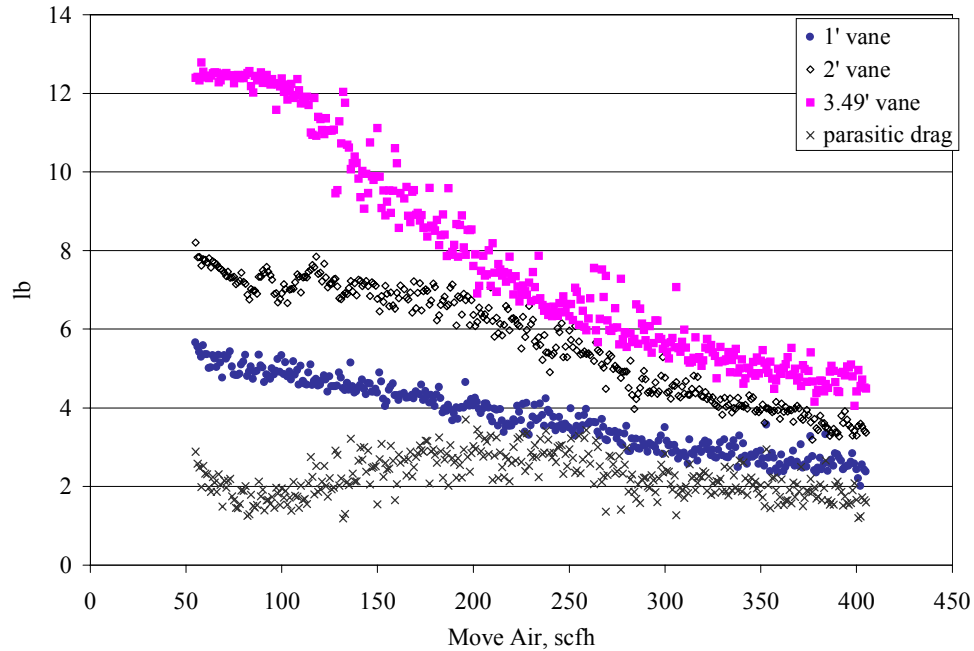


Figure 15: Total Force Measured for Each Vane Length and Parasitic Drag, 230 μm Coke

Because the magnitude of the force increases with increasing vane length and also because the parasitic drag at a given move air is the same for any vane length, and the percentage of the force measured due to parasitic drag increases as the length of the vane decreases. This means that the ratio of actual shear force to force measured increases with increasing vane length. In Figure 16, the ratio of shear force to total force is plotted as a function of the aeration rate. At high flows this ratio is constant for all vane lengths, and at low flows the ratio decreases as the aeration rate increases. At very low flows, the ratio actually increases as the aeration rate increases. This behavior has been captured with a 4th order polynomial regression. Notice that the ratio is as low as 0.25 for a vane of 1' length, which means that $\frac{3}{4}$ of the total force measured is due to parasitic drag. The 2' vane gives much better results with the lowest ratios being roughly one half. There is an improvement in the ratio in going from a 2' to 3.49' length, but this improvement is small. It is desirable to take the measurement over a small length to decrease the size of the control volume, and stay within the assumption that the shear changes little along the length of the control volume. For these reasons the 2' vane length has been selected and used. The 4th order polynomial regression of the ratio of shear Force/Total force for the

2' vane for flows lower than 270 scfh is given in Equation (30). The R^2 value of the regression is 0.664. This R^2 is low due to the high spread in the data

$$\frac{ShearForce}{TotalForce} = -6.193 \cdot 10^{-10} F_m^4 + 5.311 \cdot 10^{-7} F_m^3 - 1.554 \cdot 10^{-4} F_m^2 + 1.673 \cdot 10^{-2} F_m + 0.1646 \quad (30)$$

For flows higher than 270 scfh a linear regression was used, Equation (31). The R^2 value for the linear regression is 0.0012.

$$\frac{ShearForce}{TotalForce} = -5.06 \cdot 10^{-5} F_m + 0.526 \quad (31)$$

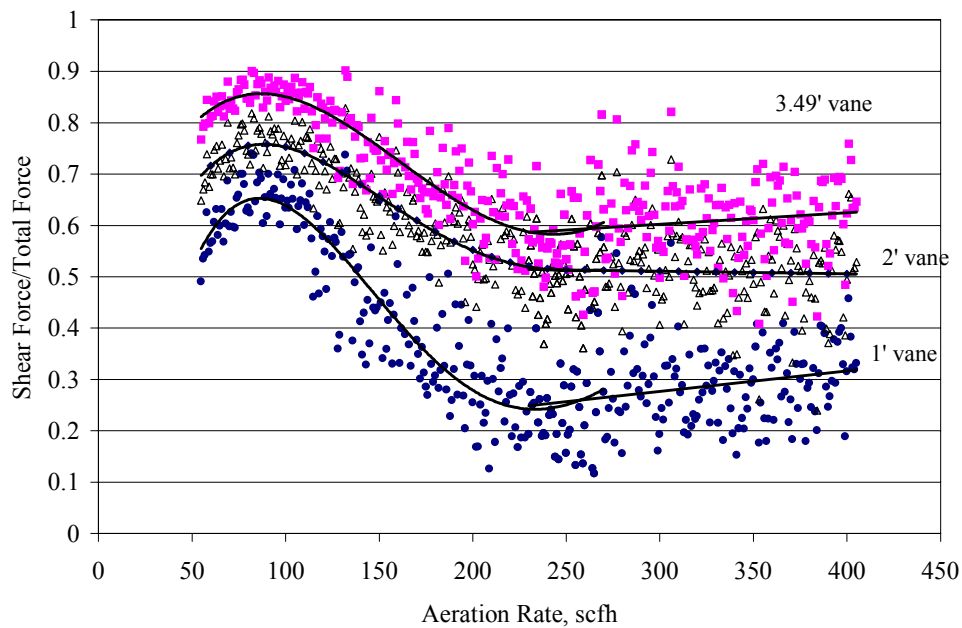


Figure 16: Ratio of Shear Force/Total Force (Parasitic Drag study), 230 μ m Coke

3.5 Wall Probe

3.5a Wall Probe General Description

Although the shear vane is easy to use and gives very good qualitative data for trends and differences, there are necessary assumptions when using it. For example, to complete the force balance in a standpipe section, the assumption that the stress measured at the center of the pipe is the same as the stress at the wall is applied. Another assumption is that the amount of force measured by the vane that is due to the drag along the cable and leading edge is very high, about half of the total force measured.

A new device has been designed to eliminate all of these assumptions. The measurement is taken at the wall. There is no leading edge or cable to create drag. However, there are other issues regarding isolating the probe from particles that will be discussed

A schematic of the wall device is shown in Figure 17. It is based on the deformation of a cantilever beam. The most important aspect of the device is the highly sensitive capacitance displacement sensors. A coupon with a diameter of approximately 5” is attached to a 5/8” OD aluminum tube that is attached to a fixed end. Aluminum was chosen for its lower modulus of elasticity. The load or shear applied to the coupon bends the aluminum beam. The capacitance devices measure this displacement. This displacement is linear with the amount of force placed on the coupon, Equation (32) (Higdon, 1985).

$$d = \frac{-Fx^2}{9EI}(3L - x) \quad (32)$$

Where d is the displacement, and F is the total force on the free end of the tube. The values and description of the constants in equation (32) are listed in Table 7.

Table 7: Description and Values of Constants in Equation Describing Deflection of a Cantilever Beam

Constant	Description	Value
x	Location of desired deflection from the fixed end of the tube	7 in
E	Modulus of elasticity of aluminum 6061-T6	10000 ksi
I	Moment of inertia	$1.366 \cdot 10^{-7} \text{ ft}^4$
L	Length of the cantilever beam (tube)	8 in
r_o	Outer radius of the tube	5/16 in
r_i	Inner radius of the tube	0.278 in

As mentioned, I is the moment of inertia and is defined by the following Equation (33).

$$I = \frac{\pi}{4}(r_o^4 - r_i^4) \quad (33)$$

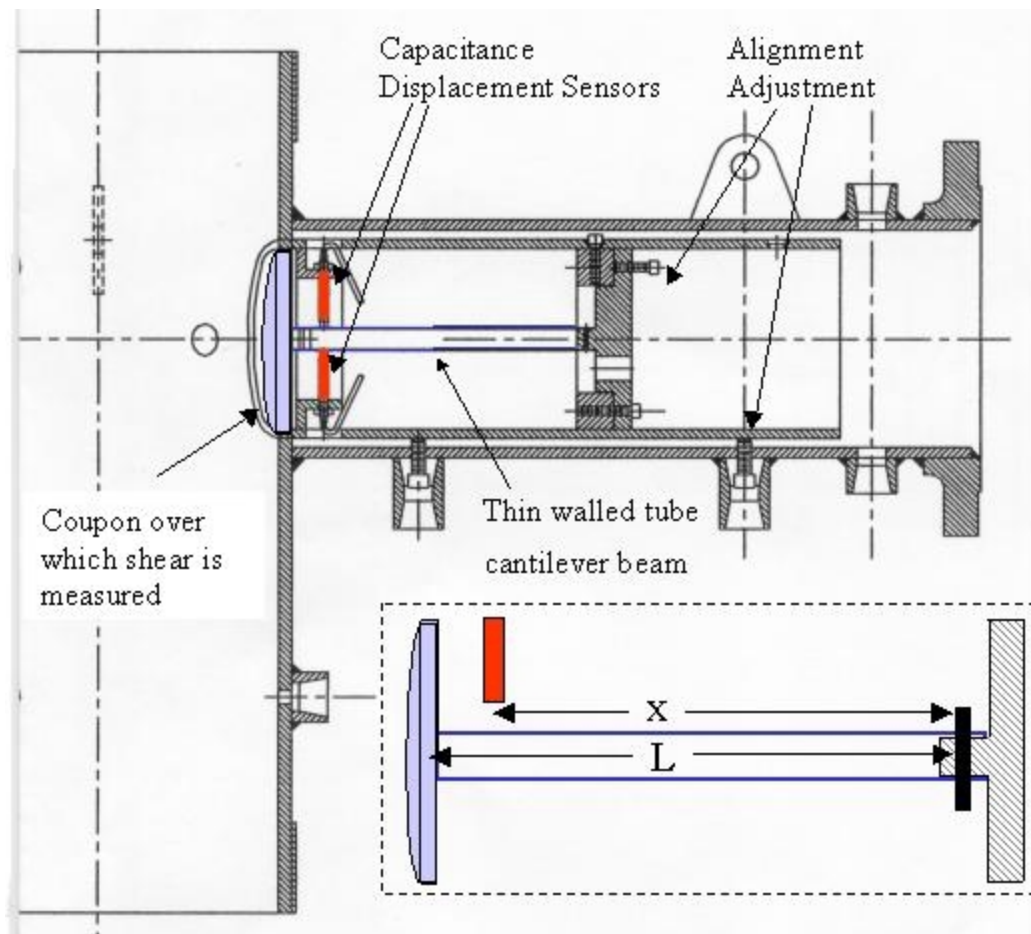


Figure 17: Wall Stress Probe Schematic

3.5b Wall Probe Calibration

As described above the capacitance sensors measure the displacement of the tube with the load placed on the coupon. The sensors are highly sensitive and measure distances between 0.01” and 0.02”. The factory-supplied calibration has been provided in Figure 18 and Figure 19. There are two probes. One measures change in the axial (up-down) direction, and the other measures side-to-side stresses. In the standpipe, mostly axial stresses are expected.

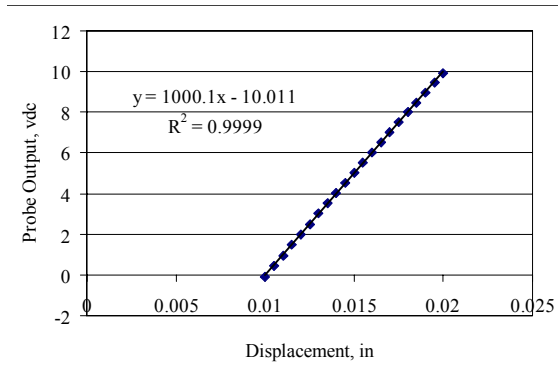


Figure 18: Factory Supplied Calibration of Displacement Probes, Channel 1

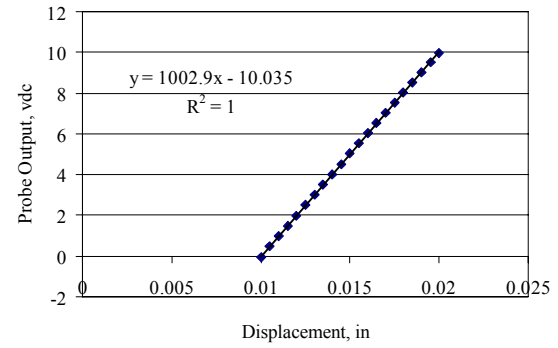


Figure 19: Factory Supplied Calibration of Displacement Probes, Channel 2

Figure 20 shows the calibration for the axial direction probe for stresses pushing downward. It is assumed that stresses pushing up will have the same slope as those pushing down. The probe output is direct current voltage (vdc). Using this calibration, the measured deflection of the beam can be compared with the deflection estimated using Equation (32). See Figure 21.

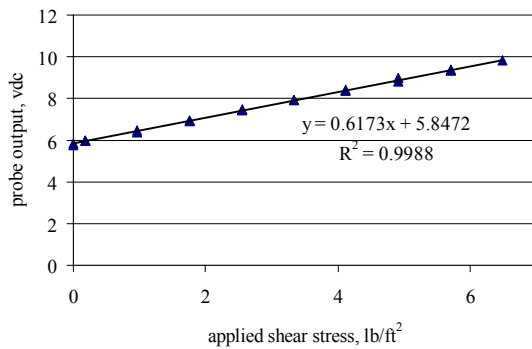


Figure 20: Wall Probe Calibration in the Axial Direction

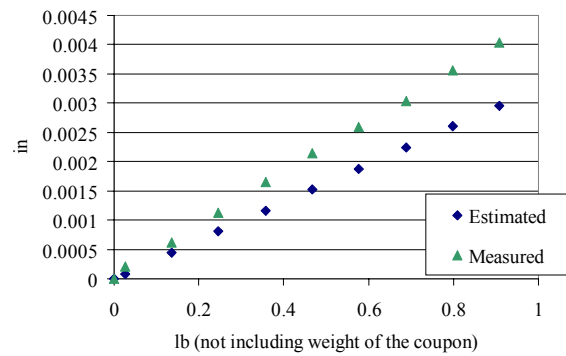


Figure 21: Estimated and Measured Movement of the Tube

The results in Figure 21 suggest that the aluminum tube is bending easier than what the theory would predict. This could be due to error in any of the parameters listed in Table 7. The modulus of elasticity may not be exactly correct. The boundary conditions that define Equation (32) may not be the conditions actually in practice.

Initially the wall probe was used in a stationary bubbling bed. A summary of this work can be found in Chapter 6. During this work, the zero of the probe varied significantly. The level or tilt (not bed height) of the bed was changing due to the nature of the temporary setup. It is believed that the variation in the probe zero was from this

change in bed level. Figure 22 shows the importance of the level of the probe. Although, the probe zero is dependent on levelness, the slope is essentially constant.

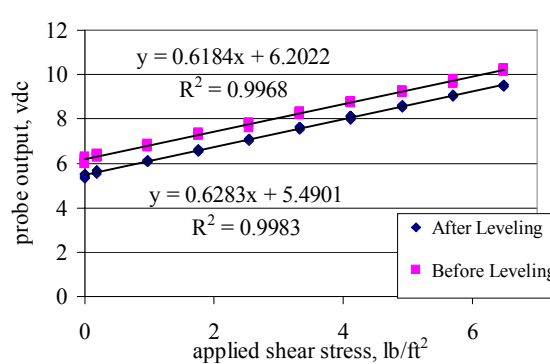


Figure 22: Importance of Probe Level on Calibration

Since the levelness of the standpipe is unlikely to change, the result from Figure 22 has little impact in the operation of the probe. However, when the probe is located in the standpipe, it is very difficult to calibrate the probe in place, but it is relatively easy to check the zero of the probe. Figure 22 suggests that the slope does not change much. As a result, the zero can be adjusted while keeping a constant slope. An average slope of 6.23 vdc/(lb/ft²) is used.

3.5c Wall Probe Purge

As described above the leading edge and drag issues are eliminated, but in their place there are problems with alignment of the probe and particles clogging it. If the probe is misaligned and the edge of the coupon protrudes into the bed, solids pressure in the z-direction, solids impact, and shear will all be measured. In other words the values measured will be inflated. If the probe is not flush with the wall and it is actually depressed in the wall the voidage may increase causing lower measurements. Further, there is 1/16" clearance between the coupon and the outer assembly of the probe. Initially, it has been proposed that this clearance is left open, and aeration can be used to keep the solids out. This will be tricky since too much aeration may increase the void fraction where the measurement is being taken, and too little aeration may allow particles to clog up the probe.

A three variable factorial study was run to understand the effects of purge aeration, bed aeration ramp direction, and bed aeration level on the solids wall shear

stress in a stationary bed. Bed aeration refers to the air coming across the distributor plate. This study was conducted in the 10” bubbling bed with cork bed material. The experimental matrix is listed in Table 8.

Table 8: Test Matrix to Understand Purge Air Effects, Test Bed, 1000 μm Cork

Run Order	Ramp Direction	Bed Aeration	Purge Aeration	Shear Stress by Wall Probe	ϵ_s	ΔP	Bed Height
		scfh	scfh	lb/ft ²		“H ₂ O	in
15	up	100	0	0.637	0.44	0.6	29.4
9	up	100	50	0.525	0.38	0.9	30
6	up	400	0	0.271	0.40	2.4	29.5
13	up	400	50	0.287	0.42	2.6	30
2	down	100	0	0.557	0.43	0.7	29
8	down	100	50	0.51	0.37	0.9	30.3
12	down	400	0	0.43	0.45	2.2	31.7
4	down	400	50	0.398	0.37	2.4	32
7	up	100	0	0.525	0.44	0.6	29.2
3	up	100	50	0.653	0.40	0.9	29
1	up	400	0	0.271	0.39	2.4	29.3
5	up	400	50	0.303	0.42	2.6	30
14	down	100	0	0.653	0.42	0.65	29.6
16	down	100	50	0.35	0.42	2.8	32.5
10	down	400	0	0.446	0.38	2.3	31.5
11	down	400	50	0.382	0.44	2.4	32.5

These results for shear stress have been summarized in Figures 23 and 24.

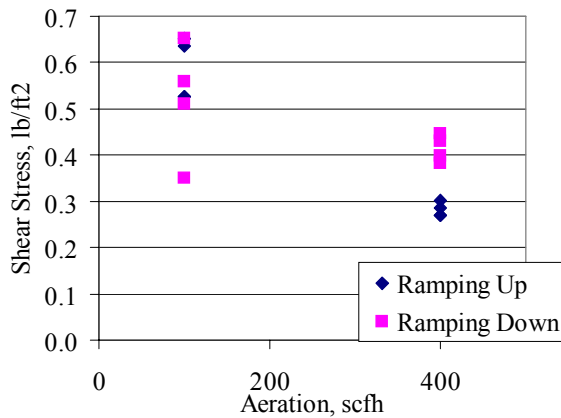


Figure 23: Effects of Purge on Wall Probe Measurements, 1000 μm Cork

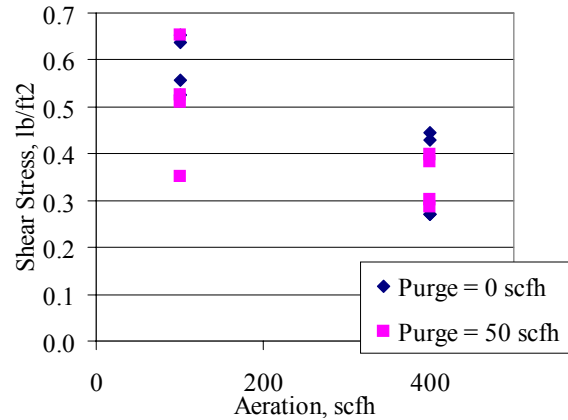


Figure 24: The Effects of Ramp Direction on Wall Shear, 1000 μm Cork

A type I sum of squares analyses was applied to the three independent variables listed in Table 8. Table 9 shows the typical output for a variable. It is specifically for the wall shear stress. Notice that ramp direction, bed aeration, and purge aeration are denoted as RDIR, AERATION, and PAIR respectively.

Table 9: ANOVA of Purge Air Test for Shear Stress, Test Bed, 1000 µm Cork

Tests of Between-Subjects Effects

Dependent Variable: ShearStress by Wall Probe

Source	Type I Sum of Squares	df	Mean Square	F	Sig.	Eta Squared	Noncent. Parameter	Observed Power ^a
Corrected Model	.241 ^b	7	3.449E-02	8.554	.004	.882	59.879	.980
Intercept	3.238	1	3.238	803.125	.000	.990	803.125	1.000
RDIR	4.032E-03	1	4.032E-03	1.000	.347	.111	1.000	.143
AERATION	.164	1	.164	40.781	.000	.836	40.781	1.000
PAIR	9.120E-03	1	9.120E-03	2.262	.171	.220	2.262	.264
RDIR * AERATION	3.940E-02	1	3.940E-02	9.772	.014	.550	9.772	.781
RDIR * PAIR	1.626E-02	1	1.626E-02	4.032	.080	.335	4.032	.424
AERATION * PAIR	5.112E-03	1	5.112E-03	1.268	.293	.137	1.268	.169
RDIR * AERATION * PAIR	3.080E-03	1	3.080E-03	.764	.408	.087	.764	.121
Error	3.226E-02	8	4.032E-03					
Total	3.512	16						
Corrected Total	.274	15						

a. Computed using alpha = 0.05

b. R Squared = .882 (Adjusted R Squared = .779)

The ANOVA table in Table 9 gives insight into which variables have a significant impact and the strength of the model. Any variable that has significance less than 0.05 made a significant impact on the solids wall shear stress, or that there is a 95% confidence that variable had a significant impact. From Table 9, aeration and an interaction between aeration and ramp direction are significant. Further, the interaction between ramp direction and purge air is very close to being significant. Eta-squared is the proportion of total variability of the dependent variable that is described by the variation in the independent variable. It is the ratio between groups sum of square and the total sum of square (SPSS Inc., 1997). Bed aeration had the largest eta-squared, which means changes in it resulted in the largest changes of shear stress. The R-squared measures the proportion of variability of the dependent variable that is explained by the relationship between the independent variable and dependent variables (Schmidt, 1998).

The model explains 78% of the variability of shear stress and 22% of the variation is noise or unexplained variation.

As a result of this test, there is not enough evidence to show that purge air affects the wall shear stress. However, because the significance level of the interaction between ramp direction and purge air is less than 0.1 and due to the lower R-squared value it is difficult to throw this effect out. Staged aeration on the order of 50 scfh is often used to produce desired changes in the standpipe. Because of the two previous concerns and also due to operational concerns, another alternative has been investigated. Nylon mesh has been stretched across the front of the probe. Another coupon sandwiches this mesh between it and the original carbon steel coupon. This coupon is the surface that comes in contact with the particles. Concerns with the mesh is that it provides a rough area over which shear can occur. Further, it does not allow the beam to rebound as easily, and lastly, it is fragile and susceptible to fraying.

3.5d Wall Probe Repeatability

A repeatability study was run to understand the measurement error associated with using the wall probe. Eight weights, which correspond to eight different shear stresses, were selected over the range of shear stress expected for coke breeze. First, the weights were added to the probe in an increasing manner, and then they were removed in a decreasing manner. This was done twice, and the intent was to determine if there was any hysteresis effect of the probe. See Figure 25 for the first set of increasing and decreasing data.

The actual probe output versus applied shear stress in Figure 25 does not show much hysteresis. However, the difference between increasing stress and decreasing stress was plotted on the right y-axis. This difference shows that the hysteresis increases at lower shear stresses. In other words there is more error associated with the hysteresis at lower shear stresses.

The next part of the repeatability test was to randomly apply the eight shear stresses. This was repeated three times. The sequence of this test is shown in Table 10. Figure 26 shows all of the repeatability data taken as well as the hysteresis data.

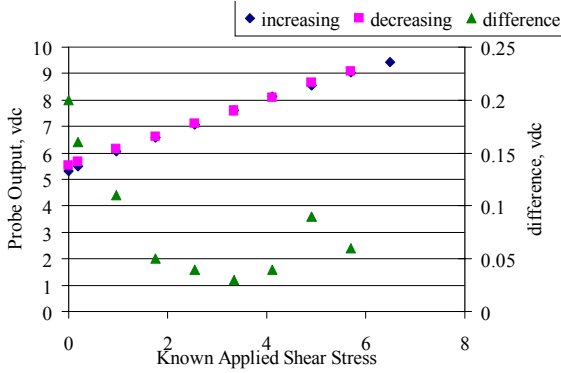


Figure 25: Hysteresis Effect of Wall Probe

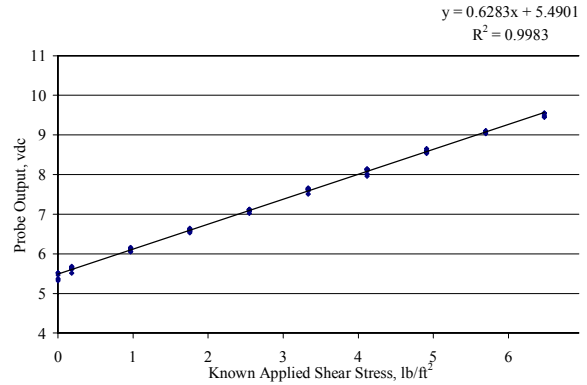


Figure 26: Wall Probe Repeatability Study

Table 10: Test Sequence of Repeatability Test

Test 1 sequence (lb/ft ²)	Test 2	Test 3
0	0	0
0.182	0.182	0.182
4.911	4.118	2.549
6.482	5.698	6.482
3.334	1.756	4.911
0.967	4.911	5.698
2.549	6.482	3.334
5.698	3.334	1.756
4.118	2.549	4.118
1.756	0.967	0.967

Using the regression shown in Figure 26, the amount of error in the measurement can be seen from Figure 27 for coke breeze range and Figure 28 for cork range.

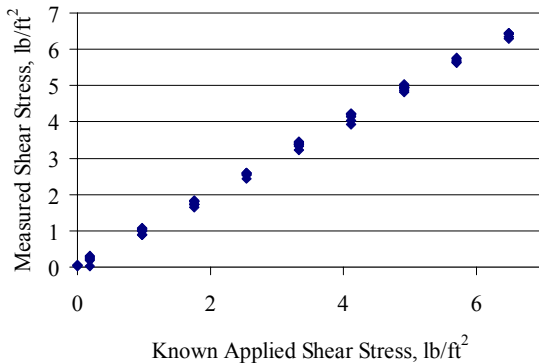


Figure 27: Wall Probe Measurement Error for Coke Breeze Range

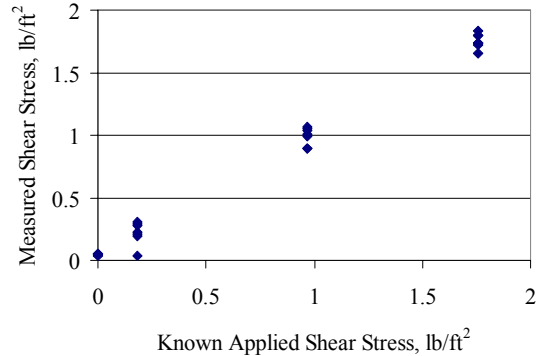


Figure 28: Wall Probe Measurement Error for Cork Range

Based on the variability shown in Figure 27, the error associated with the wall probe is ± 0.18 for a $\pm 2s$ limits (Doebelin, 1983). This corresponds to a 4% of scale for coke breeze and a 14% of scale for cork. The percent of scale for cork is poor. However, keep in mind that the repeatability study was performed with coke breeze in mind. This included ranges that would never be seen with cork. Therefore, including higher ranges in the repeatability study may have inflated the amount of error.

Comparing the error for wall probe in this study to the error reported for the shear vane in Section 3.4b. There is more error in the wall probe measurement than the shear vane measurement. However, in comparing the error it is important to note that the studies were performed differently. The shear vane included simply one ramp up and down in weight. The wall probe included two ramps up and down and three randomized repeatability test. The randomized test is designed to give an unbiased measurement of error. Also, keep in mind that the shear vane measures shear stresses over a two-foot length in the center of the pipe. The wall probe measures shear stress at the wall over an approximately five-inch diameter coupon.

To understand where the error is coming from, the above analysis has been applied to the wall probe when there was no nylon covering the front. The amount of error seen for both the coke breeze range and the cork range is shown below in Figures 29 and 30, respectively.

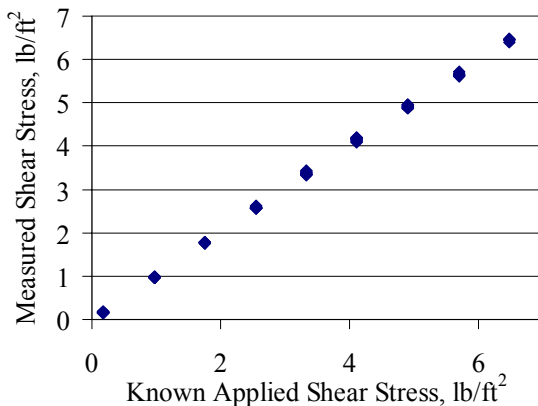


Figure 29: Wall Probe Measurement Error for Coke Breeze Range No Nylon

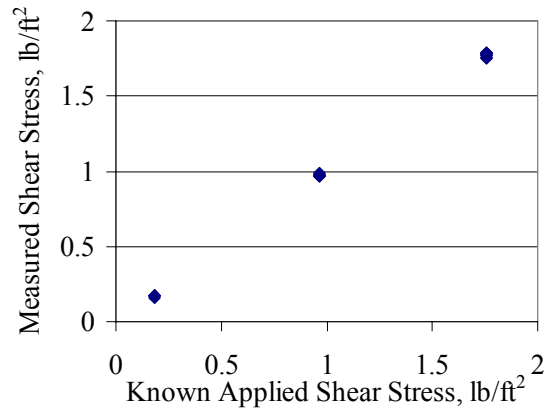


Figure 30: Wall Probe Measurement Error for Cork Range No Nylon

Based on the variability shown in Figures 29 and 30, the error associated with the wall probe without the nylon covering is ± 0.075 for a $\pm 2s$ limits (Doebelin, 1983). This

corresponds to a 2% of scale for coke breeze and a 5% of scale for cork. Since the two studies are carried out identically, this shows that the nylon mesh contributes much to the error. Using the nylon mesh as opposed to using purge air is a trade off. Problems associated with the mesh include the noticeably increase in error and the possibility of over predicting the shear due to the shear of the nylon. A problem associated with the purge is the concern of changing the void fraction where the measurement is being taken. Further, there are operational issues such as maintaining aeration on the wall probe at all times, even when the unit is not in operation.

3.6 Capacitance Solids Volume Fraction Probe

3.6a Capacitance Solids Volume Fraction Probe General Description

A capacitance probe, developed by Michel Louge, Cornell University (1992), has been used to measure solids volume fraction. A schematic of the probe has been provided in Figure 31. The probe is mounted flush with the inside of the wall. The probe itself is electrically isolated from the rest of the spool piece and standpipe. An electric field develops between the sensor in the center of the probe and the ground, which is the outer ring of the probe. The probe gives a voltage output (V), which is proportional to the capacitance of this electric field. The capacitance is a function of the geometry of the field and the properties of the material within it. Since the geometry of the field is not changing, the probe will measure changes in the properties of the material. The property of interest is the solids volume fraction, which is related to the effective dielectric constant of the suspension in the field, K_{eff} . The voltage of the wall section with no solids, just gas, is of importance and is denoted as V_0 . The ratio of V_0/V , where V is the voltage output due to the suspension, is equal to the effective dielectric constant of the suspension, K_{eff} . Louge (1992) suggest using a model by (B tcher, 1945) to relate the effective dielectric constant to the solids volume fraction, Equation (34).

$$\frac{K_{eff} - K_h}{3K_{eff}} = \epsilon_s \frac{K_p - K_h}{K_p + 2K_{eff}} \quad (34)$$

K_h is the same as K_{eff} when the vessel is filled only with gas. Louge (1992) suggests the Equation (35) to estimate the dielectric constant of the bed material with no voids. This equation can be found by solving Equation (34) for K_p .

$$K_p^{est} = K_{eff} \frac{3\epsilon_c K_h + 2K_{eff} - 2K_h}{K_{eff}(3\epsilon_c - 1) + K_h} \quad (35)$$

In this equation K_{eff} is the dielectric constant of the packed material of known solids fraction, ϵ_c . Note that this method of solids volume fraction cannot be applied to conductive bed materials. As a result, measurements cannot be made of coke breeze.

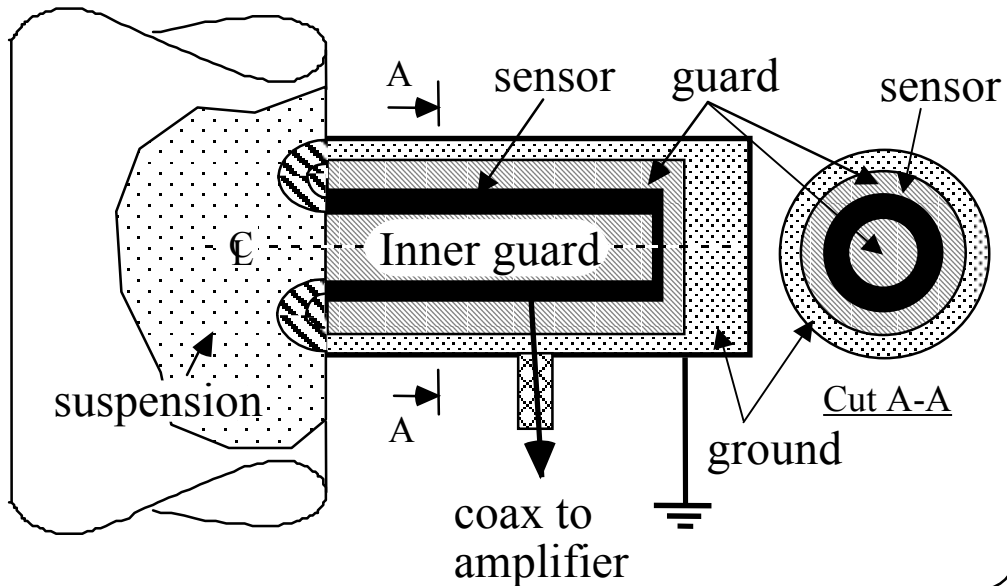


Figure 31: Solids Volume Fraction Probe (Louge, 1992)

The volume over which the solids volume fraction is measured is worth noting. According to Michel Louge (1992), the depth of the measurement is about 16% of the diameter of the probe. The probe diameter is 3/8". Therefore, the measurement reaches as far as 0.06" into the bed. This corresponds to 1.5 cork particles that are 1000 micron in diameter.

3.6b Capacitance Solids Volume Fraction Probe Calibration

The solids volume fraction probe was calibrated in a four-inch I.D. bubbling bed. To calibrate the probe it is necessary to estimate the dielectric constant of cork using Equation (35), since the dielectric constant of cork could not be found in the literature. The closest material to cork listed was balsa wood at 1.4 (Von Hippel, 1954). To use

Equation (35) the solids volume fraction must be known for at least one condition. The bulk density is easily measured using the volume of the bubbling bed and the total weight of the bed material, Equation (36). If the density of the cork particle is known, the solids volume fraction can be found. See Equation (36)

$$\rho_b = \frac{W_{bed}}{V_{bed}} = \epsilon_s \rho_s \quad (36)$$

ρ_b and ρ_s are the bulk and particle densities respectively. V_{bed} is the volume of the bed material measured by the cross sectional area of four-inch pipe and the height of the bed. W_{bed} is the total weight of the bed added, and ϵ_s is the solids volume fraction.

A search of the literature turned up a specific gravity range for cork of 0.12 to 0.2 and it was suggested that 89% of cork tissues consists of gaseous matter (Granorte, 2001). To narrow this range, an attempt to measure the particle density of cork was made. A description of these measurements is in Section 3.6c. The specific gravity for the cork used in this study was approximately 0.214, which is slightly heavier than what was found in the literature. This corresponds to 13.36 lb/ft³.

The calibration sequence included taking readings at a range of packings of cork from no cork to compressed, packed cork. First, to determine the V_0 discussed in Section 3.6a, a reading was taken with no cork introduced to the bed. Next a known weight of cork material was added to the bed. Readings were taken at this packing state. Aeration was introduced to the bed, and readings were taken for a range of aeration. Further, the bed was compressed to get high solids volume fraction readings. The bed height readings for all of the above tests were used to estimate bulk densities and solids volume fraction with the assumption that the bed expands homogeneously. Unfortunately, visually the bed was not expanding homogeneously. Bubbles tended to run up the side of the bed opposite of the probe. Constants used in this study are listed in Table 11.

Table 11: Solids Volume Fraction Probe Calibration Constants

Constant Description	Constant Value
ID (inches)	4
Bed Material Weight (lb)	0.45
Particle Density (lb/ft ³)	13.36
K_h	1
K_p , balsa wood	1.4
V_0	7.02

The results from the calibration test are listed in Table 12.

Table 12: Solids Volume Fraction Probe Calibration Results

Test Num	Bed Height in	Air Scf h	Probe Output vdc	ΔP “H ₂ O	ρ_b lb/ft ³	ϵ_s by ρ_b	K_{eff}	K_p	ϵ_s by probe output	ϵ_s by Balsa K_p
1	11.3	0	3.59		5.47	0.42	1.96	4.15	0.36	2.16
2	10.	0	2.82		6.07	0.46	2.49	5.52	0.49	3.18
3	11.7	0	3.19		5.29	0.40	2.20	5.43	0.42	2.64
4	11.7	10	3.26		5.29	0.40	2.15	5.21	0.41	2.55
5	11.7	20	3.27	0.2	5.29	0.40	2.15	5.18	0.41	2.54
6	11.7	30	3.27	0.35	5.29	0.40	2.15	5.18	0.41	2.54
7	11.7	40	3.27	0.5	5.29	0.40	2.15	5.18	0.41	2.54
8	11.7	50	3.275	0.6	5.29	0.40	2.14	5.16	0.41	2.53
9	11.9	>50	3.308	0.9	5.21	0.40	2.12	5.18	0.40	2.49
10	12.1	>50	3.32	0.95	5.10	0.39	2.11	5.30	0.40	2.47

Variables that were recorded during the study were bed height, aeration, probe output and pressure drop across the bed, which are the first four columns in Table 12. The bulk density was calculated using the bed height, diameter of the bed and total weight of material in the bed using Equation (36). The solids volume fraction (by ρ_b) was calculated using ρ_b , the density of cork, and Equation (36). K_{eff} is simply the voltage output with no bed material, V_0 , divided by the voltage output of the suspension under test conditions. K_p is calculated using Equation (35). The solids volume fraction by probe output was found by using the average K_p found in this study, 5.148, with the K_{eff} in equation (34). Solids volume fraction by Balsa K_p was found by using the balsa wood K_p from the literature in equation (34). The K_p using this calibration technique was considerably higher than the K_p listed for balsa wood in the literature. This may be due to the adjustment of the gain of the probe. The gain of the probe was turned up to give a larger voltage change between the absence of bed material and packed cork. The differences between the K_p estimated for cork and the K_p listed for balsa wood would explain why the balsa K_p gives solids volume fraction values that are obviously incorrect. If the solids volume fraction measurements using the bulk density are compared with the solids volume fraction measurements using the probe, Figure 32 results.

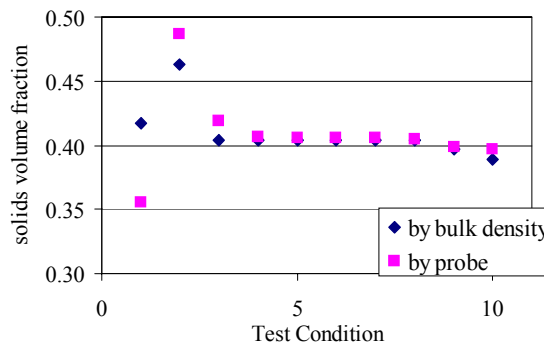


Figure 32: Calibration Results of the Solids Volume Fraction Probe

Differences between measurements made using the probe and measurements made using the bulk density may be due to the assumption made when using the bulk density. When the bulk density is used to measure solids volume fraction, it is assumed that the bed expands homogeneously. As already mentioned, this may not be the case.

3.6c Cork Particle Density Measurement

It is necessary to measure the particle density of cork in order to perform the calibration sequence of the solids volume fraction probe in Section 3.6b. A simple water displacement technique is used. However, special techniques are employed because cork generally floats on top of the water. It is assumed that any water absorbed by the cork and any air bubbles trapped in the cork during this study are negligible. A weighed graduated cylinder is partially filled with cork. The weight of the cork is noted. Water is then poured into the cylinder that contains the cork, and the weight of the water is noted. The volume of the water is found by dividing this weight by the density of water. A water density of 1 gr/cc was used. The cork is then submerged into the cylinder by pushing a screen that is attached to a rod down on it. The total volume of the mixture is measured. The volume of the screen is ignored. The volume of the cork is found by subtracting the volume of the water from the total volume of the mixture. The density of the cork is the weight of the cork divided by the calculated volume of the cork. A summary of our measurements is in Table 13.

Table 13: Cork Particle Density Measurements

Person Making Measurement	Material	Solids Weight gr	Water Weight gr	Total Volume cc	Particle Density gr/cc	Particle density lb/ft³
CL	clean cork	29.92	462.19	605	0.210	13.079
AS	clean cork	15.6	345.43	411	0.238	14.852
AS	coke contam. cork	28.72	260.97	401	0.205	12.804
AS	coke contam. cork	27.71	310.49	445	0.206	12.861
AS	clean cork	29.54	328.27	420	0.322	20.104

3.7 Experimental Methods

3.7a Steady State versus Transient Data Sampling

Throughout this work both steady state and transient data have been utilized. Understanding the difference between each type of data is necessary to understand the limitations in each method.

To record steady state data, the desired process condition was obtained. This condition was held until all variables were relatively constant over time. Once all variables were constant, the condition is held for another five minutes, over which time a five-minute running average of all pertinent variables was recorded. Steady state data was taken when noteworthy conditions were obtained. Further, steady state data was used in the statistical studies, which will be described in Chapter 5.

Transient data sampling was recorded at all times. Transient data sampling is how variables change with time. All process variables were continuously sampled every second except for solids circulation, which was averaged over two seconds.

3.7b Steady State versus Transient Aeration Ramps

Aeration ramps have been used to sweep through a large range of operating conditions in a short period of time. This technique allowed the comparison of the forces in the momentum balance across flow regimes.

Two different methods, which have been discussed in Section 3.7a, were used to perform aeration ramps. An example of each is plotted in Figures 33 and 34 for transient

and steady state ramps, respectively. Note that the x-axis is the time in seconds since an arbitrary start time.

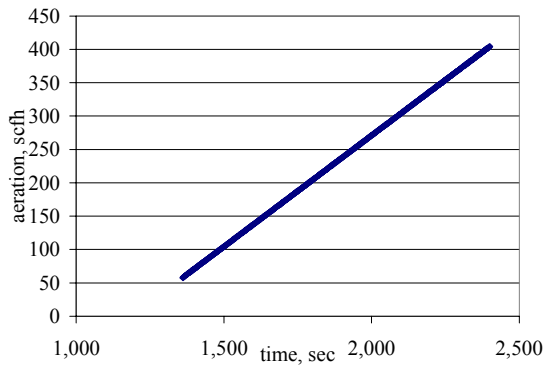


Figure 33: Transient Aeration Ramp

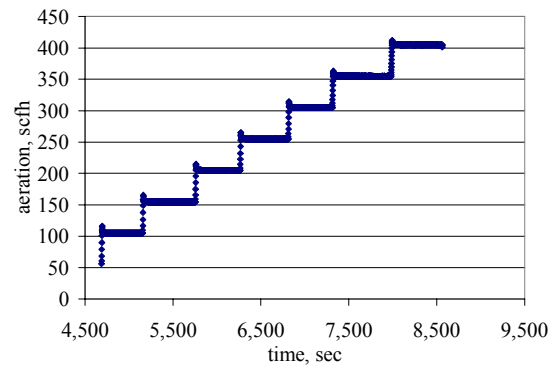


Figure 34: Steady State Aeration Ramp

In the transient ramp the aeration at the bottom of the standpipe was ramped from 50 to 400 scfh at a rate of 20 scfh/min. The steady state ramp was performed by first reaching an aeration of 100 scfh then pausing for five minutes. Next, an aeration of 200 scfh was achieved and again the system was held at this aeration for 5 min. This sequence was continued until 400 scfh was achieved.

To compare results of a transient aeration ramp to results of steady state aeration ramp, both were performed. In general, the response variables in this study were the solids circulation rate, gas phase pressure drop, and solids-wall shear stress. A comparison of transient ramp to aeration ramp values of each of these response variables is plotted in Figures 35-37. The error bars are based on two standard deviations of the 300 data points taken over five minutes for the steady state aeration ramp.

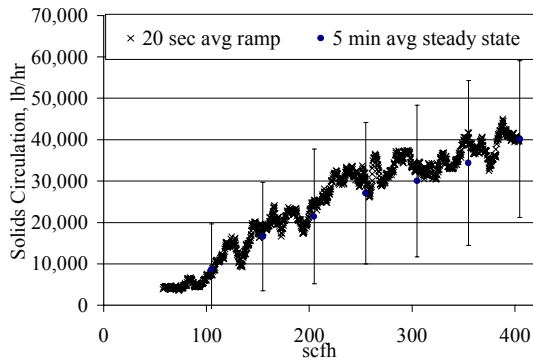


Figure 35: Comparison of Steady State and Transient Ramps for Solids Circulation, 230 μ m Coke

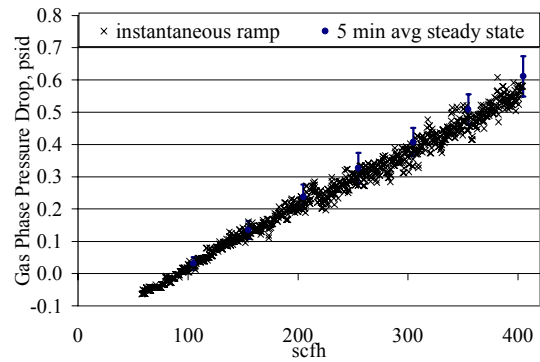


Figure 36: Comparison of Steady State and Transient Ramps for Gas Phase Pressure Drop, 230 μ m Coke

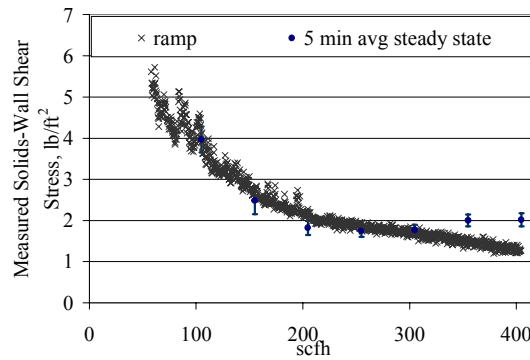


Figure 37: Comparison of Steady State and Transient Ramps for Solids-Wall Shear Stress, 230 μ m Coke

In general, the steady state ramp agreed well with the transient ramp. In Figure 35, the steady state points for solids circulation run slightly lower than the transient values, but the transient values fall within the error bars. The transient values also fall within the error bars for gas pressure drop. Although most of the transient values fall within the error bars for shear stress, at higher flow rates the transient values are slightly lower. Because the error bars are based on one steady state ramp, they may be too small for shear stress. If this analysis was repeated multiple times for the steady states and obtaining the steady state values from multiple directions, the error bars for both methods would probably cross, even for shear stress at higher flows. As a result, transient ramps have been used in this study for convenience. However, steady state ramps have also been used when possible.

3.8 Internal Angle of Friction and Angle of Wall Friction for the Bed Material

A simple visual technique was used to determine the internal angle of friction of the bed materials (Zenz, 1960). This technique is not necessarily accepted by today's standards that are typically using the Jenike shear cell, which is more accurate (Schulze, 2000). This technique was chosen for its ease of implementation. Measurements for coke breeze have been obtained using the Jenike shear cell.

The procedure involves filling a clear tube with a flat bottom with the test material. The flat bottom must have a concentric hole, which is plugged during the filling process. Once the tube is filled, the top is leveled off, and the plug is removed. The top of the material is carefully watched as the material discharges. The top should move as a plug or undisturbed, until a certain height where a dimple forms. The height at which the dimple forms is the measurement of interest. This set-up is illustrated in Figure 38.

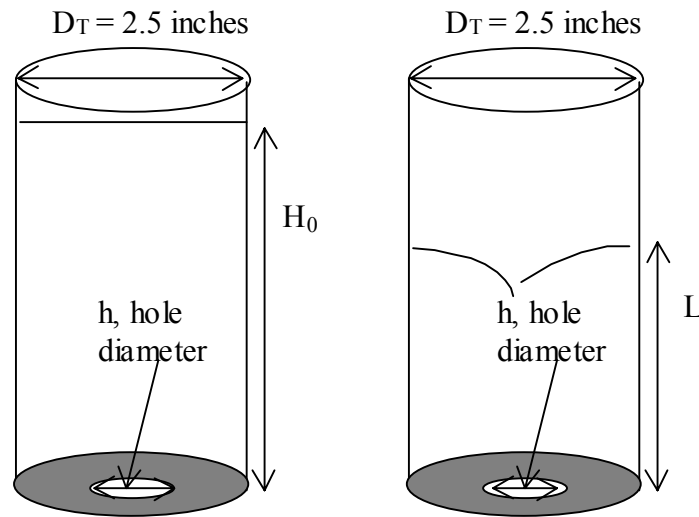


Figure 38: Internal angle of Friction Measurement Apparatus

According to Zenz (1960), the internal angle of friction, δ , is related to the height that the dimple forms by Equation (38).

$$\frac{L}{D_T} = \tan \delta \quad (37)$$

A simple visual technique was used to determine the angle of wall friction of bed materials with galvanized sheet metal, the metal that was used in the fabrication of the shear vane. This procedure was found in Zenz (1960), and it was called angle of slide. This technique is not necessarily accepted by today's standards. Typically the Jenike shear cell is reported to be more accurate (Schulze, 2000). Shear cell measurements have been obtained for coke breeze. However, for most of the materials, the Zenz (1960) technique was chosen for its ease of implementation.

The procedure involved sprinkling test material onto a horizontal flat plate made out of the wall material. The plate was then tilted until the material starts to slide. The angle at which the material started to slide is the angle of slide, and we can use this to approximate the angle of wall friction. This set-up is illustrated in Figure 39.

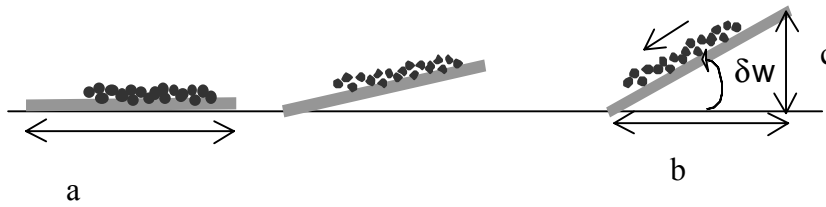


Figure 39: Measurement of Angle of Wall Friction

The length of the plate, a , is known. During these test it ranged from 11 to 10 ³/₄ inch. The angle of wall friction can be estimated using the following simple trigonometric relationships.

$$a^2 = b^2 + c^2 \quad (38)$$

$$\tan \delta_w = \frac{c}{b} \quad (39)$$

The product of the Janssen coefficient and the coefficient of friction, $\frac{\mu_w}{K}$, was calculated using Equation (40).

$$\frac{\mu_w}{K} = \tan \delta_w \frac{1 - \sin \delta}{1 + \sin \delta} \quad (40)$$

Equation (27), rewritten below for convenience, is used in the mixture momentum balance to develop equations for solids pressure.

$$\tau_{sw} = \frac{\mu_w}{K} P_{s,z} \quad (27)$$

CHAPTER 4 RELATIVE COMPARISON OF FORCES IN A CFB AND THE JANSSEN COEFFICIENT

In Section 3.7b two methods, that have been useful in sweeping through a large range of operating conditions in a short period of time, have been presented. These techniques along with the shear vane and wall probe tools were used to compare the relative magnitude of the forces across flow regimes and they were used to compare measured shear stress values to estimated solids wall shear stress values using the Janssen coefficient.

4.1 Mass Circulation

The mass flowrate of solids through the standpipe is primarily a function of the amount of air used in partial fluidization, but also depends on inventory, riser velocity, and system pressure.

Figure 40 is a typical plot showing how the circulation rate varied with changes in aeration. The flowrate of air was ramped from 50 to 405 scfh at a rate of 20 scfh/min. It has been shown in Section 3.7b that at this gradual ramp rate, measured variables obtained from the CFB reflect a near steady state relationship. That is, the time dependent effects can be neglected. Take note that the solids circulation values are 20-second averages. The 20 –second average is necessary because of the high degree of natural variability in the circulation rates over a one second time span (Ludlow, 2002).

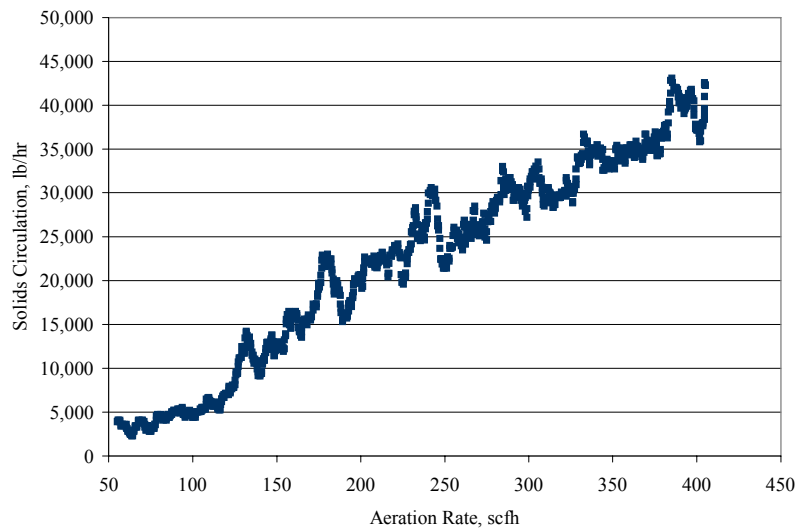


Figure 40: Solids Circulation versus Aeration 230 μ m Coke

4.2 Momentum Balance Components During an Aeration Ramp

Using aeration ramps, the comparison of the forces in the momentum balance across flow regimes was made. As a result, it was seen that percentage of contribution of shear stress was heavily dependent on bed material. For coke breeze, solids phase shear stress and solids phase pressure drop ($-\Delta P_s/L$) were important forces in the momentum balance that could not be ignored. For coke breeze, the solids shear stress component was on the same order of magnitude as the gas phase pressure drop ($-\Delta P_g/L$). However, for cork the shear stress component was always the smallest contribution to the momentum balance. It ranged from 9 to 2% of the total forces. This material dependence could be due from a large number of things such as particle size, sized distribution, shape, and density.

In Figure 41 the gas phase pressure drop ($-\Delta P_g/L$), wall shear stress ($-2\tau_{sw}/R$), and solids phase pressure drop ($-\Delta P_s/L$) are plotted as a function of solids circulation. The weight of the bed is assumed constant on this plot. The relative magnitude of these forces is compared as the aeration rate was ramped from 50 to 405 scfh. During the ramp the gas phase pressure drop ($-\Delta P_g/L$) ranged from 2 to 21 percent of the forces, the solids shear stress ($-2\tau_{sw}/R$) ranged from 28 to 6%, and the solids phase pressure drop ($-\Delta P_s/L$) ranged from about 23 to 30% of the total forces. Because voidage is assumed constant and (Equation (7)), the weight of the bed never changed from 50% of the total force.

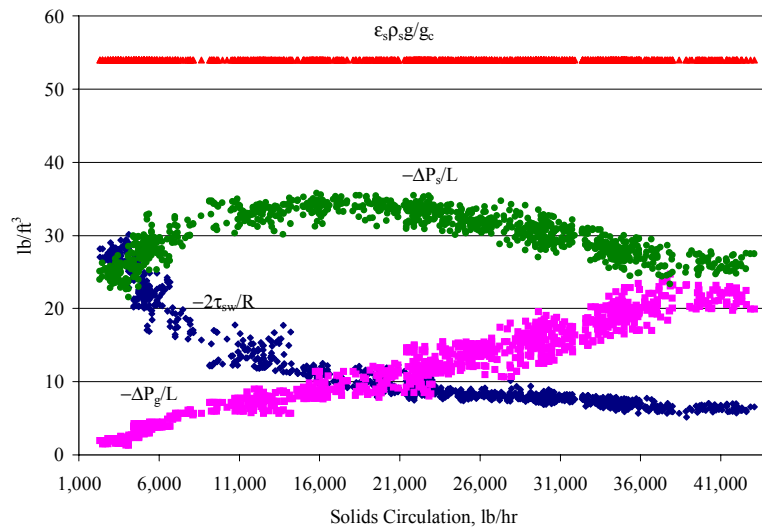


Figure 41: Momentum Balance Components versus Solids Circulation 230 μ m Coke

In Figure 41 all of the forces are significant over some portion of the solids flow ramp. The shear stress ($-2\tau_{sw}/R$) and solids phase pressure drop ($-\Delta P_s/L$) are major components of the mixture momentum balance that must be quantified if we are to have a thorough understanding of standpipe hydrodynamics.

In Figure 42 the gas phase pressure drop ($-\Delta P_g/L$), wall shear stress ($-2\tau_{sw}/R$), and solids phase pressure drop ($-\Delta P_s/L$) are plotted as a function of solids circulation for cork. The weight of the bed is assumed constant on this plot. The relative magnitude of these forces is compared as the aeration rate was ramped in a steady state manner from 450 to 1200 scfh. During the ramp the gas phase pressure drop ($-\Delta P_g/L$) ranged from 11 to 42% of the forces, the wall shear stress ($-2\tau_{sw}/R$) ranged from 9 to 2%, and the solids phase pressure drop ranged from about 33 to 4% of the total forces. Because solids pressure drop ($-\Delta P_s/L$) is estimated by difference (Equation (7)), the weight of the bed never changed from 50% of the total force.

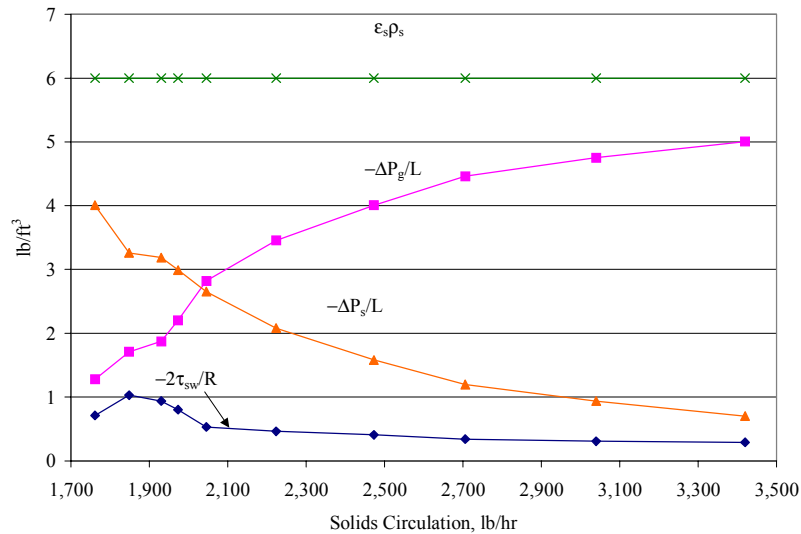


Figure 42: Momentum Balance Components Versus Aeration, Steady States, Cork

In Figure 42, the momentum balance components follow trends similar to Figure 41. Differences between Figure 42 and 41 are that Figure 41 is for coke breeze measured by the shear vane using a transient ramp and that Figure 42 is for cork measured by the wall shear probe using a steady state ramp. Further, in Figure 41 the measurements are located at about 7', and in Figure 42 the measurements are at about 13.5'. Unlike coke

breeze, the shear stress component for cork is low in magnitude compared to gas pressure drop per unit length.

In Table 14 relative magnitude of the forces is compared. An attempt to estimate the flow regime based on gas pressure drop ($-\Delta P_g/L$) and slopes of the shear and solids pressure drop components has been made. For example, in Figure 41 at low flows the shear stress component dropped steeply at which time the solids pressure component increased with increasing solids circulation rate. This was interpreted to be a transitional packed regime at which time the bed was in slip-stick flow. Above circulation rates that corresponded to transitional packed regime, the shear stress was relatively constant. The bed was interpreted to be packed under these conditions. At higher flows, all three components approached a constant state. This state was said to be a fluidized regime. The only conflicting problem was that the gas pressure drop in the fluidized regime was much less than the weight of the bed for coke breeze.

Table 14: Comparison of Relative Magnitude of Forces (% of Total Force) for Cork and Coke Breeze

<u>Material</u>	<u>Flow Regime</u>	<u>$-2\tau_{sw}/R$</u>	<u>$-\Delta P_g/L$</u>	<u>$-\Delta P_s/L$</u>	<u>$\epsilon_s \rho_s g/g_c$</u>
Coke	Transitional Packed	27-10%	1-8%	22-32%	50%
Coke	Packed	10-5%	8-20%	32-25%	50%
Cork	Transitional Packed	6-9%	11-15%	33-26%	50%
Cork	Packed	9-2%	1-43%	2-5%	50%
Cork	Fluidized	2%	43%	5%	50%

4.3 Differential Solids Pressure and Solids Wall Shear Stress Estimates

Aeration ramps were used to compare measured shear stress values with the shear stress predicted using the product of the Janssen coefficient and coefficient of friction. Using this product to predict wall shear stress resulted in values higher than four times the measured values. If the product of the Janssen coefficient and coefficient of friction was adjusted such that the predicted values matched the measured values, a value of 0.003 was found to work well for both cork and coke breeze. This result was startling due to its magnitude and the fact that the same value worked well for both materials.

This suggests that the product of the Janssen coefficient and coefficient of friction, which are measured under non-aerated, incipient flow conditions, may not be the correct parameters to be used in the standpipe of a CFB.

Before discussing the comparison of the predicted shear stress and measured shear stress values, the method of predicting shear stress must be outlined in detail. As discussed in section 2.2a, Picciotti (1995) suggests that the solids pressure is related to the wall shear stress by Equation (27), which is rewritten below for reference.

$$\tau_{sw} = \frac{\mu_w}{K} P_{s,z} \quad (27)$$

Picciotti (1995) substituted Equation (27) into the microscopic form of the mixture momentum balance, Equation (6), which is rewritten below for reference.

$$-\frac{\partial P_{sz}}{\partial z} - \frac{\partial P_g}{\partial z} + \frac{4\tau_{sw}}{D} - \rho_s \epsilon_s \frac{g}{g_c} = 0 \quad (6)$$

He integrated this equation from the top of the bed to any height, z . This resulted in an equation that gave solids pressure as a function of height, Equation (28). Several assumptions were used such as constant solids volume fraction and that the bed is in an active state of stress. Further, it was assumed that the solids pressure at the top of the bed is zero, and the gas pressure drop per unit length is constant. Under the conditions of this study, the gas pressure drop per unit length is not always constant due to inventory heights and staged aeration.

To improve this assumption, Equation (41) has been developed by integrating the mixture momentum balance between two arbitrary heights. A complete derivation of Equation (41) can be found in Appendix A.2b. Unlike in the derivation of Equation (28), Equation (41) was derived with a positive z -coordinate axis pointing up against gravity.

$$P_{sz} \Big|_{z=z_1} = \frac{DK}{4\mu_w} \left(e^{\frac{-4\mu_w}{DK}(z_2-z_1)} \right) \left(\frac{\Delta P_g}{\Delta z} + \frac{4\mu_w}{DK} P_{sz} \Big|_{z=z_2} - \rho_s \epsilon_s \frac{g}{g_c} \right) - \frac{DK}{4\mu_w} \left(\frac{\Delta P_g}{\Delta z} - \rho_s \epsilon_s \frac{g}{g_c} \right) \quad (41)$$

Like Equation (28), assumptions made in the derivation of Equation (41) are constant solids volume fraction, constant gas pressure drop ($-\Delta P_g/L$), and that the bed is in an active state of stress. Because of the assumption of constant gas pressure drop ($-\Delta P_g/L$), this equation is applied over several small sections of the standpipe where measured values of the gas pressure are known and the incremental values of the solids

pressure along the standpipe can therefore be determined. The procedure used to determine the solids pressure is a step wise one, starting at the top of the bed. Assuming a zero solids pressure at the top of the bed, a solids pressure at some interval into the bed is calculated. Using this solids pressure at the bottom of the first interval as the top pressure for the next interval, solids pressures are calculated until the location of interest is reached. Also, equations (41) and (27) can be used together to estimate a solids wall shear stress. For clarity this method of estimating shear stress and solids pressure drop ($-\Delta P_s/L$) will be referred to as Method II.

In addition to the method described above, the solids pressure drop ($-\Delta P_s/L$) can be approximated using measured shear stress values and Equation (7). For clarity this method of estimating solids pressure drop ($-\Delta P_s/L$) will be referred to as Method I.

In summary, two different methods have been presented to estimate solids phase wall shear stress and solids phase pressure drop.

Method I is to experimentally measure gas phase pressure and solids phase shear stress of the control volume, and then to use these measurements to calculate the solids phase pressure drop assuming a constant solids volume fraction and using Equation (7).

$$\frac{\Delta P_{sz}}{\Delta z} = -\rho_s \varepsilon_s \frac{g}{g_c} + \frac{4\tau_{sw}}{D} - \frac{\Delta P_g}{\Delta z} \quad (7)$$

Method II is to measure gas phase pressure drop at increments along the standpipe and measure the height of the bed. Then equation (41) is applied successively down the standpipe until the solids pressure across the control volume of interest is known. These solids pressure values can be used with equation (27) to find shear stress. Take note that the second method is independent of direct shear stress measurements, and is the typical approach of researchers (Leung, 1985; Mountziaris, 1990; Picciotti, 1995). Further, both methods assume a constant solids volume fraction and use experimentally measured gas pressure differential.

In Figure 43 the solids phase pressure drop as determined by both methods is plotted versus circulation rate. The two methods utilize experimentally determined gas pressure drop and assume a constant void fraction. Solids pressures ($-\Delta P_s/L$) calculated using Method II were considerably lower in value than the solids pressure from shear stress measurements, Method I. For lower circulation rates Method I increases with

increasing mass circulation, while the Method II decreases with increasing mass circulation rate.



Figure 43: Estimated Values of $\Delta P_s/L$ versus Mass Circulation for 230 μm coke

In Figure 44 the predicted and measured values of the shear stress as a function of circulation rate are plotted. Here the predicted values over estimate the measured values. Similarly to Figure 43, the results show very different trends at mass circulation rates below 10,000 lb/hr where the measured values drop more steeply with increasing mass circulation.

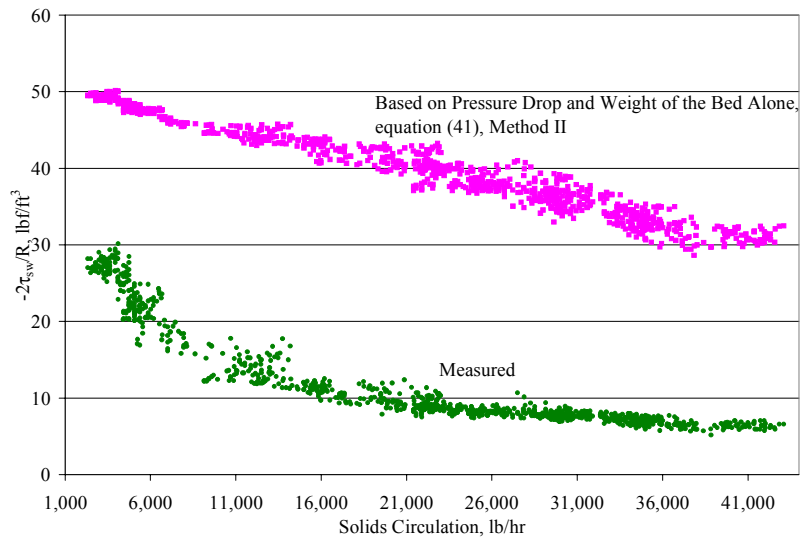


Figure 44: Measured and Estimated Values of $-2\tau_{sw}/R$ versus Mass Circulation 230 μm Coke

An explanation for this difference in trends for the two methods in Figures 43 and 44 may be explained by a regime change. It is the same initial region in the plot. Method II assumes a packed regime and an active state of stress. At the lower circulation rates which correspond to lower aeration rates, it is plausible that the bed is transitionally packed (slip-stick flow) and not in an active state.

In Figure 45 the solids phase shear stress as measured and from Method II is plotted versus solids volumetric flux. The predicted method used experimentally determined gas pressure drop and an assumed a constant solids volume fraction. Direct shear stress measurements are in gray. Shear stresses calculated with Method II using a μ_w/K of 0.059 are in black, and were higher in value then the measured values as in Figure 44. The black filled-in circles and the black line correspond to estimated shear stress such that μ_w/K was changed until the predicted fitted the measured shear stress. The product of the Janssen coefficient and coefficient of friction appeared to change with increasing solids volumetric flux until after a point where it reached a limiting value of 0.003.

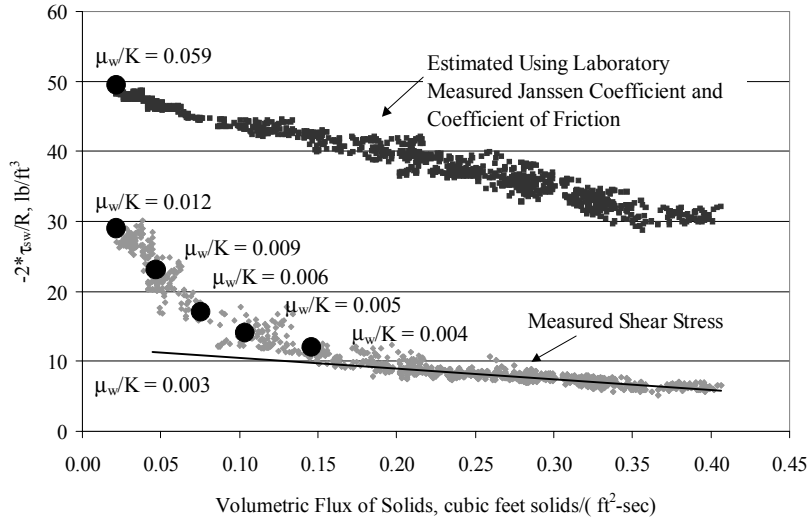


Figure 45: Measured and Estimated Values of $-4\tau_{sw}/D$ versus Solids Circulation, Coke Breeze

The product of the Janssen coefficient and coefficient of friction that fitted the measured shear stresses was much lower then the product measured by a Jenike shear cell, 0.059. The Jenike shear cell measurements are under non-aerated incipient flow

conditions. Most of the conditions in Figure 45 are aerated and high fluxes. Further, it has been reported in the literature that the product of the Janssen coefficient and the coefficient of friction is a function of the solids volume fraction (Abou-Chakr, 1999). At lower solids volumetric fluxes, the bulk density could be changing.

In Figure 46, the Jenike shear cell measurements of the angle of wall friction, internal angle of friction, and bulk density have been plotted versus the normal stress applied to the cell. Due to the consolidation of the solids, the bulk density increased with increasing normal stress. The shear cell measurements showed that the internal angle of friction decreased with increasing normal stress, and that the angle of wall friction decreased steeply and leveled off at a constant value of 15° with increasing normal stress. This suggested that the product of the coefficient of friction and Janssen coefficient varied with normal stress or bulk density, Figure 47.

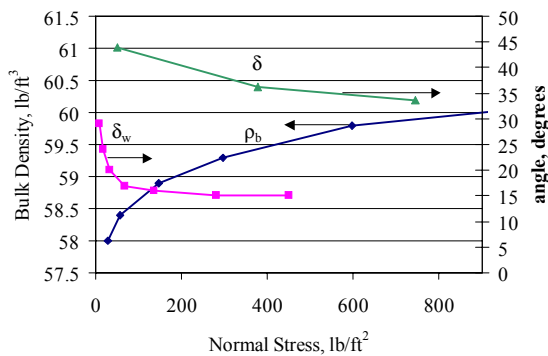


Figure 46: Jenike Shear Cell Measurements of Coke Breeze

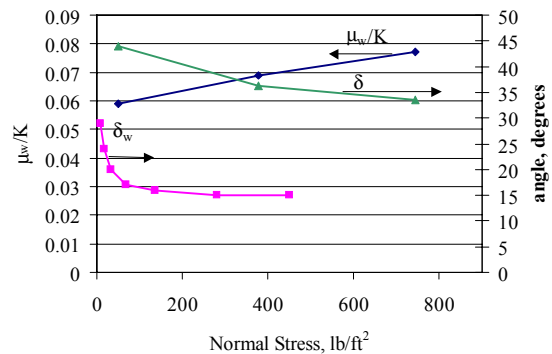


Figure 47: The Variation of the Product of the Coefficient of Friction and the Janssen Coefficient with Normal Stress

In Figure 48 the solids phase pressure drop ($-\Delta P_s/L$) as determined by difference (Method I) and from Equation (41) (Method II) is plotted versus solids volumetric flux. The two methods utilize experimentally determined gas pressure drop and assume a constant void fraction. Solids pressure drop ($-\Delta P_s/L$) from shear stress measurements are in gray. Solids pressure drop ($-\Delta P_s/L$) calculated using Method II using a μ_w/K of 0.059 are in black, and were lower in value than the solids pressure drop ($-\Delta P_s/L$) from shear stress measurements. As with the shear stress, the black filled-in circles correspond to estimated solids pressure drop ($-\Delta P_s/L$) such that μ_w/K was changed until the predicted solids pressure drop ($-\Delta P_s/L$) fitted the method using the experimental shear stress

measurements (Method I). The product of the Janssen coefficient and coefficient of friction appear to change with increasing fluxes and come to a limiting value of 0.003. Since solids pressure calculated by either method is strongly dependent on the shear stress of either method, the same fitted values of μ_w/K that worked for shear stress agree well for solids pressure.

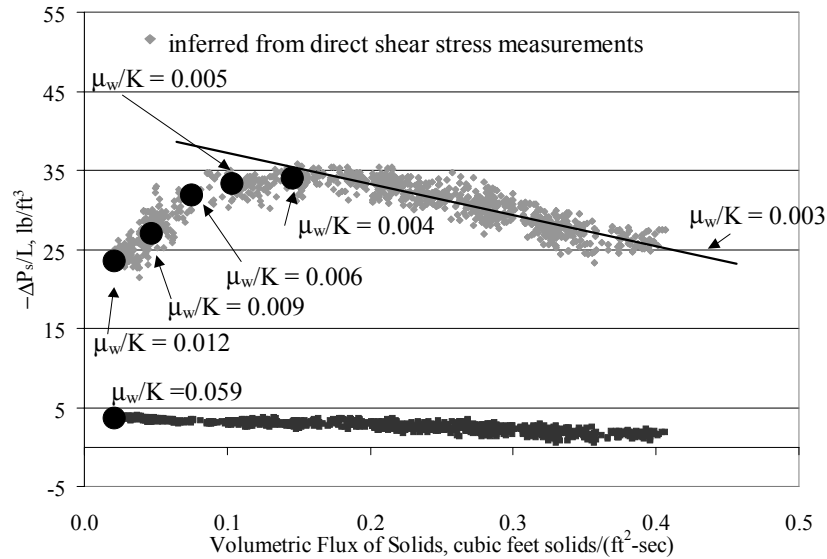


Figure 48: Estimated Values of $-\Delta P_s/L$ versus Solids Volumetric Flux

The estimates using a coefficient value of 0.003 were also good for cork (Figures 49 and 50), except for very low circulation rates where the shear stress decreased. In Figure 49 the μ_w/K for the predicted shear stress was adjusted such that the estimated shear stress fitted the measured. These values are in green triangles and overlay the measured values which are blue diamonds. The corresponding μ_w/K are plotted in black on the right hand y-axis. For cork, the product of the Janssen coefficient and coefficient of friction necessary to fit the data increased with increasing flux. This is the opposite of the trend seen with coke breeze. It is hard to conjecture on the meaning of this trend, because shear cell measurements for this material have not yet been obtained.

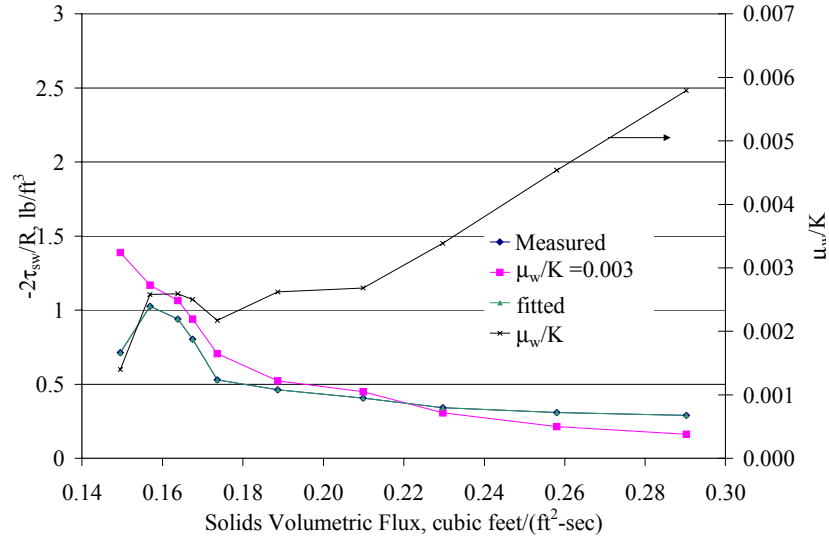


Figure 49: Measured and Estimated Values of $-2\tau_{sw}/R$ versus Solids Volumetric Flux, Cork

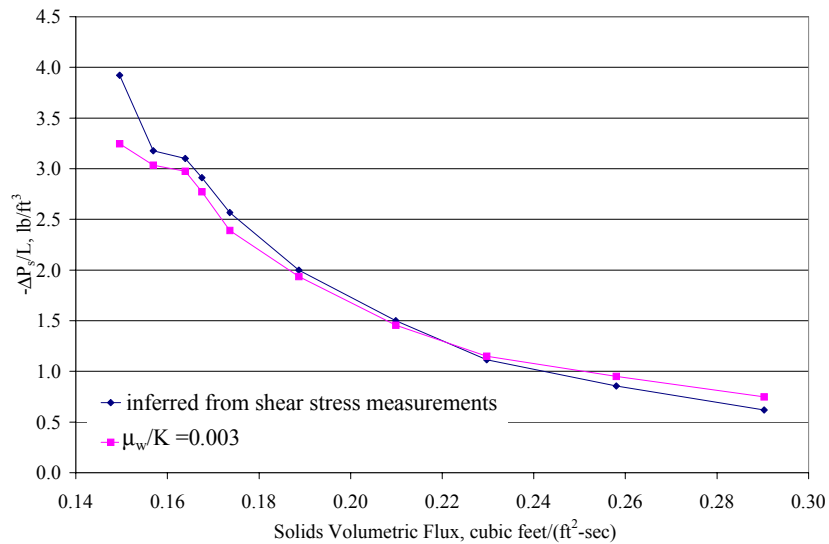


Figure 50: Measured and Estimated Values of $-\Delta P_s/L$ versus Solids Volumetric Flux, Cork

Measurements of μ_w/K are shown in Table 15. Note that the measured values are much higher than those suggested by McCabe (1993), who suggests angles between 15° and 30° for free-flowing granular materials. Further, the measurement using the shear cell is significantly lower than the value obtained using the Zenz (1960) technique. The different values listed for coke breeze shows how the material properties change over

time. Over time, the fines level decreased. Fines were intentionally added to the material referred to as coke-coarse-11/30. The resulting material is listed as Coke-coarse+fines-12/6. The corresponding internal angle of friction increased.

Table 15: Estimated values of the Janssen Coefficient

Material	Angle of Internal Friction , °, δ	Angle of Wall Friction for galvanized sheet metal, °, δ_w	$\frac{\mu_w}{K}$ for galvanized sheet metal, Equation (41)
Coke Breeze-10/31	74.2	34.2	0.013
Coke Breeze-L-20 New	76.4	30.8	0.008
Coke-coarse-11/30	73.1	34.7	0.0153
Coke-coarse+fines-12/6	74.4	34.4	0.0129
Coke-coarse+fines-12/6— Shear Cell	ranged between 33.57-43.87	29-18	0.059-0.077
Sand 70/140	65.1	30.9	0.029
glass beads	56.1	20.5	.035
PVC new	77.5	40.2	.0101
Cork 20-40	74.3	37.2	0.014

The angle of internal friction and the angle of wall friction give insight into when the material is stationary and when it moves. The angle of internal friction described carefully in Appendix A.3. The angle of internal friction is the angle that the yield locus makes with the normal stress axis on the Mohr diagram. If the stress state of the material is such that the Mohr circle touches the yield locus, the material will move (Brown, 1970).

According to Picciotti (1995) these angles can give insight into whether the bed moves at the wall or if there is a stationary film at the wall and the bed moves internally. He states that if the angle of wall friction is greater than the angle of internal friction the solids will be stationary at the wall and the bed will move internally. On the other hand, if the angle of wall friction is less than the angle of internal friction the solids will move along the wall. The measurements in Table 15 indicate that the angle of wall friction is less than the internal angle of friction for all materials studied. Therefore, all materials studied should slide at the wall.

CHAPTER 5 DEPENDENCE OF SOLIDS WALL SHEAR STRESS AND SOLIDS PRESSURE ON OPERATING CONDITIONS

In Chapter 4 the relative magnitude of the forces was studied, and the experimental results were compared to results obtained using the product of the Janssen coefficient and coefficient of friction. In this chapter, the effects of key variables, discussed in Chapter 2 and Chapter 4, were tested. Furthermore, solids wall shear stress has been measured under a large variety of operating conditions. This chapter discusses the effects of different CFB operational variables such as mass circulation, standpipe height, and level of fines on shear stress and solids pressure. A list of variables has been provided in Table 16. A mixture of experimental techniques ranging from aeration ramps to statistical factorial studies has been used in this study. Both cork and coke breeze have been studied. The shear vane and the wall shear probe have been used.

Table 16 organizes all of the work of this study into three sections. Tests that were designed with the purpose in mind to test the theory developed in Chapters 2 and 4 are described in the first section. Transient aeration ramps that gave insight into the effect of gas pressure drop per unit length, bed material, bed compaction, and ramp direction are discussed in the second section. A few CFB operating variable tests are described in the last section.

Table 16: Operational Variables Tested

<u>Purpose of Test</u>	<u>Variables Studied</u>	<u>Experimental Method</u>
Test Theoretical Variables 5.1	Solids Circulation Rate	Factorial Design
	Standpipe Height	
	$\Delta P_g/L$	
Qualitative Study 5.2	Move Air Location	Transient Ramps
	Bed Material	
	Solids Circulation Rate	
	$\Delta P_g/L/\epsilon_s$	
	Bed Compaction	
	Ramp Direction	
CFB Operational Variables 5.3	Riser ΔP	Factorial
	Solids Circulation Rate	
	Standpipe Height	
	Gas Velocity in the Riser	
	Aeration in the Loopseal	
	Gas Velocity into the Standpipe	
	Concentration of Fines in Coke	
	Location of Move Aeration	
	Staged Aeration	
	Ramp Direction	

5.1 Testing Theoretical Variables

As described in Chapter 2, Leung and Jones (1985) suggest using a friction factor to estimate shear stress for a fluidized regime Equation (42). Others suggest that the shear stress for a fluidized regime is negligible (Knowlton, 1986; Mountziaris and Jackson, 1990). As a result, shear stress for a fluidized regime is dependent on solids volume fraction and solids circulation.

$$\tau_w = \frac{1}{2} f \epsilon_s \rho_s u_s^2 \quad (42)$$

As discussed in Chapters 2 and 4, for packed bed states researchers relate the shear stress to the solids pressure by Equation (27) (Leung, 1985; Mountziaris, 1990; Picciotti, 1995). This equation assumes a packed regime and an active state of stress.

$$\tau_{sw} = \frac{\mu_w}{K} P_{sz} \quad (27)$$

Equation (27) is then substituted into the steady state mixture momentum balance, and it is integrated between two different heights to give Equation (41). This development can be found in Chapter 4.

$$P_{sz} \Big|_{z=z_1} = \frac{DK}{4\mu_w} \left(e^{\frac{-4\mu_w}{DK}(z_2-z_1)} \left(\frac{\Delta P_g}{\Delta z} + \frac{4\mu_w}{DK} P_{sz} \Big|_{z=z_2} - \rho_s \epsilon_s \frac{g}{g_c} \right) - \frac{DK}{4\mu_w} \left(\frac{\Delta P_g}{\Delta z} - \rho_s \epsilon_s \frac{g}{g_c} \right) \right) \quad (41)$$

Using Equations (41) and (27) gives a method for estimating shear stress. From Equation (41), shear stress for a packed regime is dependent on axial location in the bed, gas pressure drop per unit length, and solids volume fraction.

Chapter 4 discusses the magnitude and effect of the proportionality constant, μ_w/K , in Equations (41) and (27). This section discusses the effects of the independent variables in Equations (41) and (42). A series of steady state runs were conducted to test the dependencies described above.

All data in this section was taken with cork in the standpipe at a level of 13.5'. In general shear stress measurements were made with the wall shear probe.

5.1a The Effects of Solids Circulation Rate on a Fluidized Regime

This study was designed to test Equation (42), which suggests that for a fluidized regime the shear stress is related to the solids velocity squared. Five different circulation

rates were achieved while holding the gas pressure drop ($-\Delta P_g/L$) constant at 4 lb/ft^3 . This selected gas pressure drop ($-\Delta P_g/L$) of 4 lb/ft^3 was selected because it is approaching the weight of the bed that is approximately $5\text{-}5.5 \text{ lb/ft}^3$. Higher values were not used, because of the concern of slugs forming in the standpipe. In Figure 51 the shear stress as measured by the wall probe at $13.5'$, as measured by a shear vane at $8'$, and as measured by a shear vane at $23'$ in the standpipe is plotted versus circulation rate. In Figure 52 the shear stress as measured by the wall probe is plotted alone versus solids circulation.

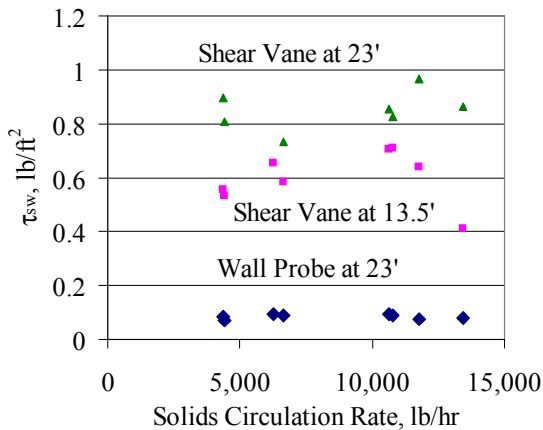


Figure 51: Shear Stress Measured by the Shear Vane and Wall Probe for a Fluidized Regime, Cork

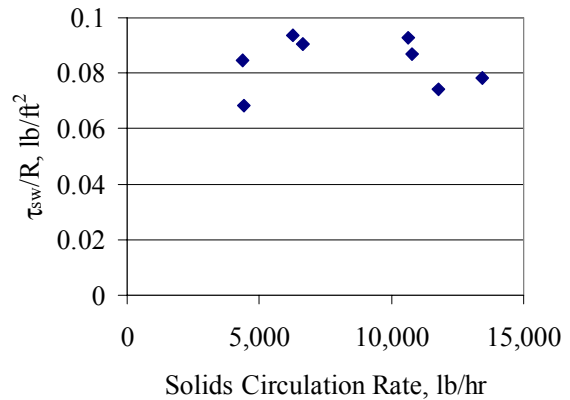


Figure 52: Shear Stress Measured by the Wall Probe for a Fluidized Regime, Cork

In Figure 51, the shear vane measurements are higher than the wall probe measurements. One explanation could be that parasitic drag is not accounted for in the shear vane measurements. However, as discussed in Section 3.4c, parasitic drag only accounted for 50% of the total force measured by the shear vane. Visual observations of the cork in the standpipe indicate that at high circulation rates the cork is stationary at the wall and is moving in the center. The fact that conditions at the wall are much different than in the center of the pipe may be a more plausible explanation for the differences in the shear vane and wall probe measurements in Figure 51. In Figure 52 the shear stress is very low in agreement with Knowlton (1986) and Mountziaris (1990). We cannot measure any significant change with solids circulation.

The momentum balance components are plotted in Figure 53. The shear stress component is the smallest component in the momentum balance for cork in a fluidized regime. The shear stress is measured at $13.5'$ by the wall probe. This is different than

results for coke breeze under packed regimes in Chapters 4 where the shear stress component at lower aeration rates was larger than gas pressure drop per unit length.

From this study, it is apparent that shear stress is small in this regime, and does not vary measurably with circulation rate. The dependence suggested by Equation (41) is either incorrect or the wall probe is not sensitive enough to pick up the dependence.

It has been found that there is very little difference between the shear stress and the probe zero. To illustrate this, when the standpipe was in a fluidized state, the valve above the wall probe in Figure 10 was closed, and the bed level was allowed to drop below the wall probe. This was done to give a direct comparison of the shear of a fluidized state with no shear. In Figure 54 the shear stress component is plotted versus time during the time period of interest.

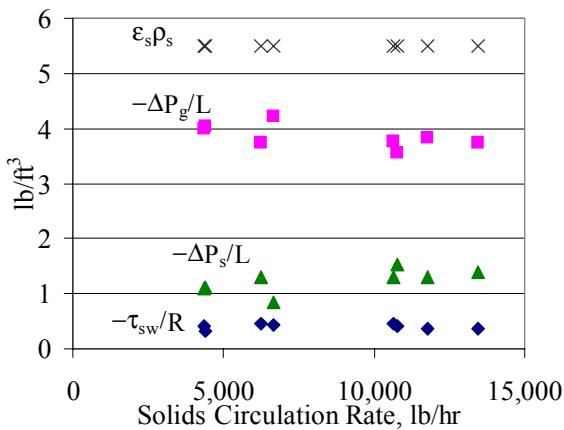


Figure 53: Momentum Balance Components versus Solids Circulation for a Fluidized Regime, Cork

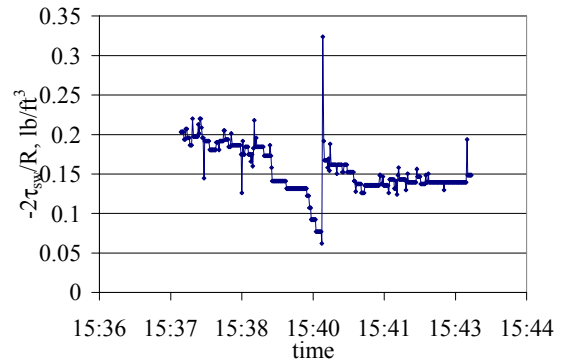


Figure 54: Shear Stress Component Zero, Cork

In Figure 54, the lowest shear stress component measured was approximately 0.062 lb/ft^3 . This corresponds to the point when the bed has been drained below the probe. The highest shear stress component measured was about 0.2 lb/ft^3 . This corresponds to a fluidized state. This shows that there is a measurable though very small difference between no shear and shear due to a fluidized regime.

5.1b The Effect of Solids Circulation Rate and Standpipe Height on a Packed Regime

From Equations (41) and (27) estimated values of shear stress for a packed bed regime are dependent on axial location in the bed, gas pressure drop ($-\Delta P_g/L$), and solids

volume fraction. Further, studies presented in Chapters 4 and 5 suggest that shear stress is dependent on solids circulation. As a result, two different studies were conducted to understand standpipe height, gas pressure drop ($-\Delta P_g/L$) and solids circulation rate. The three independent variables could not be lumped together in one experiment, because we could not vary them independently. As a result, the effects of solids circulation and gas pressure drop ($-\Delta P_g/L$) on shear stress for a packed regime was studied, and it is discussed in the next section. Furthermore, the effects of solids circulation and standpipe height on shear stress in a packed bed regime was studied and is discussed in this section. Standpipe height was selected because the location of the probe is fixed. Therefore, to vary the axial location of the measured shear stress, the height was varied.

In Table 17 the independent variables and settings are listed, and the results are listed in Table 18. The shear stress was measured at 13.5' by the wall shear probe. The test was a 2^2 factorial, randomized, and fully duplicated. In Figure 55 and 56 the duplicates are portrayed as same symbols for each of the two levels of standpipe height. The repeatability is reflected by the spread in the shear for these duplicates.

Table: 17: Solids Circulation and Standpipe Height Test Independent Variables

<u>Run</u>	<u>Standpipe Height</u> <u>ft</u>	<u>Solids Circulation</u> <u>lb/hr</u>	<u>$-\Delta P_g/L$</u> <u>lb/ft³</u>
1	27	2,000	2.8
2	27	4,000	2.8
3	31	2,000	2.8
4	31	4,000	2.8
5	27	2,000	2.8
6	27	4,000	2.8
7	31	2,000	2.8
8	31	4,000	2.8

Table 18: Solids Circulation and Standpipe Height Results, Cork

<u>Run</u>	<u>Standpipe Height ft</u>	<u>Solids Circulation lb/hr</u>	$-\Delta P_g/L$ <u>lb/ft³</u>	$-2\tau_{sw}/R$ <u>lb/ft³</u>	$-\Delta P_s/L$ <u>lb/ft³</u>
1	27	2,051	2.78	0.605	2.111
2	27.5	3,799	2.78	0.666	2.053
3	31	1,873	2.75	0.575	2.179
4	31.4	3,762	2.73	0.531	2.241
5	27.5	1,857	2.75	0.738	2.013
6	27.5	3,703	2.76	0.649	2.092
7	31.4	1,907	2.87	0.711	1.915
8	31.2	3,757	2.71	0.682	2.109

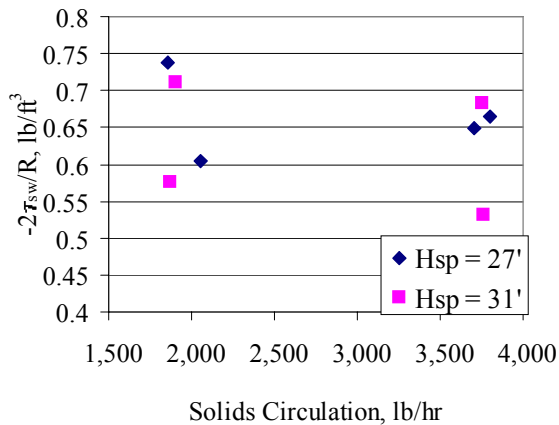


Figure 55: The Effect of Solids Circulation and Standpipe Height on the Shear Stress Component for a Packed Bed Regime, Cork

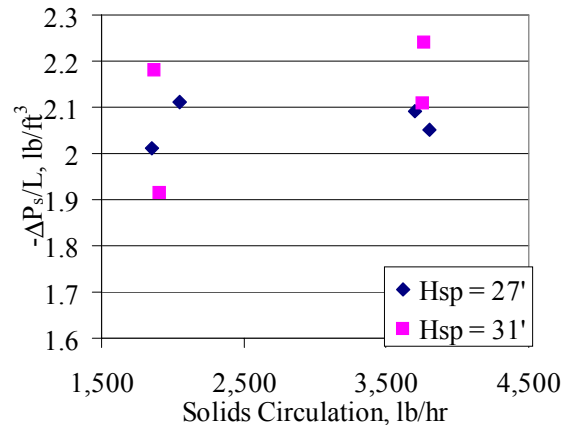


Figure 56: The Effect of Solids Circulation and Standpipe Height on the Solids Pressure Component for a Packed Bed Regime, Cork

Looking at Figures 55 and 56, neither solids circulation or standpipe height had an effect on the shear stress and solids pressure components of the momentum balance, at least within the ranges of the tested circulation rates and standpipe heights. The resulting ANOVA tables (Tables 19 and 20) for the shear stress component and the solids pressure component, which statistically confirm the lack of any significance for these factors. Notice that standpipe height and solids circulation are denoted as HSP and MS, respectively.

Table 19: ANOVA Results for the Shear Stress Component of the Solids Circulation and Standpipe Height Test, Cork

Tests of Between-Subjects Effects

Dependent Variable: Shear Stress Component

Source	Type I Sum of Squares	df	Mean Square	F	Sig.
Corrected Model	4.624E-03 ^a	3	1.541E-03	.209	.886
Intercept	3.323	1	3.323	449.634	.000
HSP	3.096E-03	1	3.096E-03	.419	.553
MS	1.281E-03	1	1.281E-03	.173	.699
HSP * MS	2.470E-04	1	2.470E-04	.033	.864
Error	2.957E-02	4	7.391E-03		
Total	3.358	8			
Corrected Total	3.419E-02	7			

a. R Squared = .135 (Adjusted R Squared = -.513)

Table 20: ANOVA Results for the Solids Pressure Component of the Solids Circulation and Standpipe Height Test, Cork

Tests of Between-Subjects Effects

Dependent Variable: Solids Pressure Drop Per Unit Length

Source	Type I Sum of Squares	df	Mean Square	F	Sig.
Corrected Model	2.036E-02 ^a	3	6.787E-03	.553	.673
Intercept	34.913	1	34.913	2842.483	.000
HSP	3.865E-03	1	3.865E-03	.315	.605
MS	9.597E-03	1	9.597E-03	.781	.427
HSP * MS	6.899E-03	1	6.899E-03	.562	.495
Error	4.913E-02	4	1.228E-02		
Total	34.983	8			
Corrected Total	6.949E-02	7			

a. R Squared = .293 (Adjusted R Squared = -.237)

Section 3.5c discussed the information given in the ANOVA table in detail. From Tables 19 and 20 neither of the independent variables have a significant effect on either of the dependent variables.

5.1c The Effect of Solids Circulation Rate and Gas Pressure Drop ($-\Delta P_g/L$) on a Packed Regime

In this section the test to determine the effect of solids circulation rate and gas pressure drop on the shear stress component is discussed. The experimental matrix listed in Table 21 was a randomized 2^2 factorial test fully duplicated.

Table 21: Solids Circulation and Gas Pressure Drop ($-\Delta P_g/L$) Test Independent Variables

<u>Run</u>	<u>Solids Circulation lb/hr</u>	<u>$-\Delta P_g/L$ lb/ft³</u>	<u>Standpipe Height ft</u>
1	2,000	2.3	29
2	2,000	3.3	29
3	4,000	2.3	29
4	4,000	3.3	29
5	2,000	2.3	29
6	2,000	3.3	29
7	4,000	2.3	29
8	4,000	3.3	29

The results and the response variables are listed in Table 22 and summarized in Figures 57 and 58. The shear stress was measured at 13.5' by the wall shear probe

Table 22: Solids Circulation and Gas Pressure Drop ($-\Delta P_g/L$) Test Results, Cork

<u>Run</u>	<u>Solids Circulation lb/hr</u>	<u>$-\Delta P_g/L$ lb/ft³</u>	<u>Standpipe Height ft</u>	<u>$-2\tau_{sw}/R$ lb/ft³</u>	<u>$-\Delta P_s/L$ lb/ft³</u>
1	1,904	2.349	29.3	0.148	2.919
2	1,944	3.283	28.8	0.066	2.376
3	4,101	2.372	28.7	0.092	3.189
4	4,012	3.259	29.3	0.076	2.378
5	2,040	2.295	29.3	0.100	3.225
6	1,852	3.437	29	0.079	2.162
7	4,193	2.252	29.1	0.121	3.144
8	3,695	3.168	29	0.091	2.374

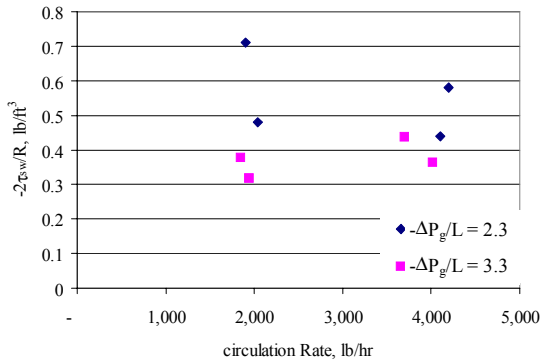


Figure 57: The Effect of Solids Circulation and Gas Pressure Drop ($-\Delta P_g/L$) on the Shear Stress Component for a Packed Regime, Cork

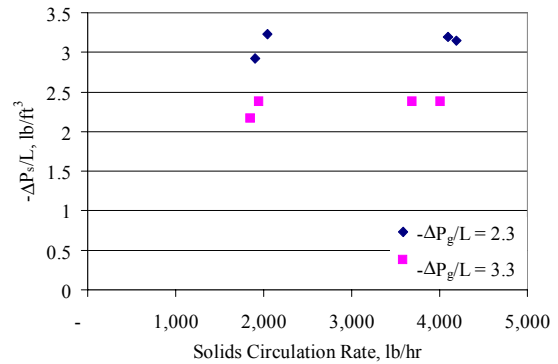


Figure 58: The Effect of Solids Circulation and Gas Pressure Drop ($-\Delta P_g/L$) on the Solids Pressure Component for a Packed Regime, Cork

In Figure 57 the shear stress component appeared to be higher with lower gas pressure drop ($-\Delta P_g/L$). In Figure 58 the solids pressure component appeared to increase with lower gas pressure drop ($-\Delta P_g/L$). In general the shear stress component measured were very small compared with the bulk density of cork, 6.6 lb/ft³.

A type I sum of square analyses was applied to the two independent variables listed in Table 22. Table 23 describes the results for the shear stress component of the momentum balance. Notice that gas pressure drop ($-\Delta P_g/L$) is denoted as DPGDL and solids circulation rate is denoted as MS.

Table 23: ANOVA Results for the Shear Stress Component of the Solids Circulation and Gas Pressure Drop ($-\Delta P_g/L$) Test, Cork

Tests of Between-Subjects Effects

Dependent Variable: Shear Stress Component

Source	Type I Sum of Squares	df	Mean Square	F	Sig.
Corrected Model	3.212E-03 ^a	3	1.071E-03	2.433	.205
Intercept	7.441E-02	1	7.441E-02	169.077	.000
MS	2.476E-05	1	2.476E-05	.056	.824
DPGDL	2.786E-03	1	2.786E-03	6.331	.066
MS *	4.009E-04	1	4.009E-04	.911	.394
Error	1.760E-03	4	4.401E-04		
Total	7.938E-02	8			
Corrected Total	4.972E-03	7			

a. R Squared = .646 (Adjusted R Squared = .380)

Section 3.5c discussed the information given in the ANOVA table in detail. From Table 23, the significance level for gas pressure drop ($-\Delta P_g/L$) on the shear stress component is within 90% confidence of being significant.

Table 24: ANOVA Results for Solids Pressure Drop ($-\Delta P_s/L$) of the Solids Circulation and Gas Pressure Drop ($-\Delta P_g/L$) Test, Cork

Tests of Between-Subjects Effects

Dependent Variable: solids pressure drop per unit length

Source	Type I Sum of Squares	df	Mean Square	F	Sig.
Corrected Model	1.290 ^a	3	.430	24.316	.005
Intercept	59.225	1	59.225	3349.065	.000
MS	2.030E-02	1	2.030E-02	1.148	.344
DPGDL	1.270	1	1.270	71.794	.001
MS * DPGDL	7.813E-05	1	7.813E-05	.004	.950
Error	7.074E-02	4	1.768E-02		
Total	60.586	8			
Corrected Total	1.361	7			

a. R Squared = .948 (Adjusted R Squared = .909)

In Table 24, gas pressure drop ($-\Delta P_g/L$) has a significant effect on solids pressure drop ($-\Delta P_s/L$). This is consistent, since solids pressure drop ($-\Delta P_s/L$) is calculated directly from gas pressure drop ($-\Delta P_g/L$) assuming a constant bulk density and using measured shear stress values, which are very small in comparison to the other three forces.

The experiment outlined in Table 21 was repeated using higher circulation rates and an adjusted gas pressure drop per unit length. Solids volume fraction measurements were obtained for this experiment. The experimental matrix outlined in Table 25 is a randomized 2^2 factorial matrix fully duplicated.

Table 25: Solids Circulation and Gas Pressure Drop ($-\Delta P_g/L$) Test, Higher Circulation Rates, Independent Variables

<u>Run</u>	<u>Solids Circulation lb/hr</u>	<u>$-\Delta P_g/L$ lb/ft³</u>	<u>Standpipe Height ft</u>
1	3,000	2.4	29
2	3,000	3.3	29
3	6,000	2.4	29
4	6,000	3.3	29
5	3,000	2.4	29
6	3,000	3.3	29
7	6,000	2.4	29
8	6,000	3.3	29

The results and the response variables are given in Table 26 and summarized in Figures 59 and 61. The last column, ϵ_s , corresponds to the measured solids volume fraction at the wall, using the probe described in Chapter 3. The shear stress was measured at 13.5' by the wall shear probe.

Table 26: Solids Circulation and Gas Pressure Drop ($-\Delta P_g/L$) Test Results, Higher Circulation Rates, Cork

<u>Run</u>	<u>Solids Circulation lb/hr</u>	<u>$-\Delta P_g/L$ lb/ft³</u>	<u>Standpipe Height ft</u>	<u>$-2\tau_{sw}/R$ lb/ft³</u>	<u>$-\Delta P_s/L$ lb/ft³</u>	<u>ϵ_s</u>
1	3,047	2.374	29.2	0.495	3.131	0.342
2	2,955	3.253	28.7	0.494	2.254	0.347
3	5,862	2.496	29	0.473	3.032	0.344
4	5,918	3.246	28.7	0.402	2.352	0.363
5	3,047	2.400	28.8	0.513	3.087	0.352
6	3,016	3.202	29.3	0.467	2.330	0.333
7	5,920	2.436	28.8	0.586	2.978	0.358
8	5,949	3.289	29	0.398	2.312	0.371

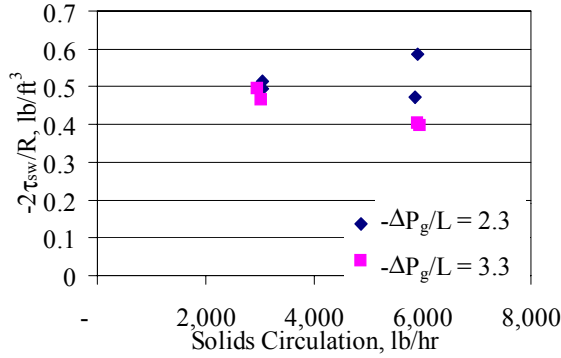


Figure 59: The Effect of Solids Circulation and Gas Pressure Drop ($-\Delta P_{g/L}$) (at Higher Circulation Rates) on the Shear Stress Component

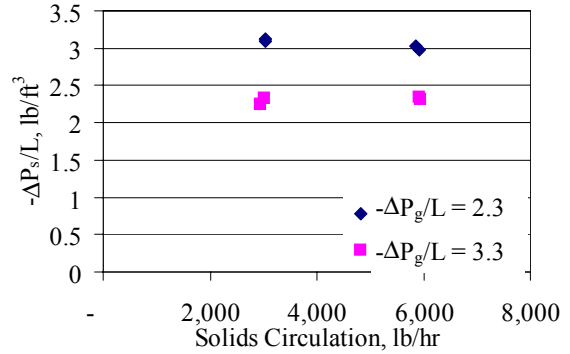


Figure 60: The Effect of Solids Circulation and Gas Pressure Drop ($-\Delta P_{g/L}$) (at Higher Circulation Rates) on the Solids Pressure Component

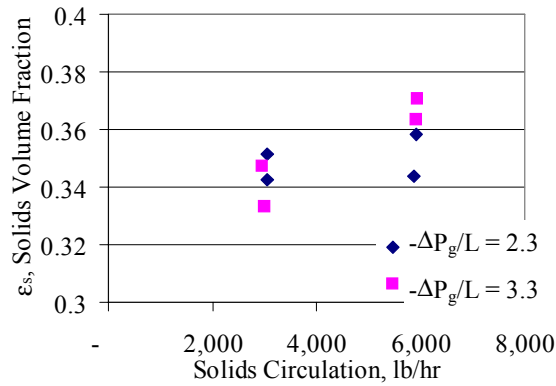


Figure 61: The Effect of Solids Circulation and Gas Pressure Drop ($-\Delta P_{g/L}$) (at Higher Circulation Rates) on the Wall Solids Volume Fraction

In Figure 60, the solids pressure drop ($-\Delta P_s/L$) increased with decreasing gas phase pressure, which is consistent with what was seen in the previous test. However, in Figure 57 the shear stress component appeared to increase with decreasing gas pressure drop ($-\Delta P_{g/L}$) at high circulation rates. Furthermore, the solids volume fraction measurements in Figure 61 appear to increase with increasing gas pressure drop ($-\Delta P_{g/L}$) at higher circulation rates. As will become evident in Section 5.2d, absolute solids volume fraction measurements are not yet fully trusted due to the calibration of the instrument. Relative solids volume fraction measurements were not so much an issue.

A type I sum of square analyses was applied to the three independent variables listed in Table 26. Table 27 describes the results for the shear stress component of the

momentum balance. Notice that gas pressure drop ($-\Delta P_g/L$) is denoted as DPGDL and solids circulation rate is denoted as MS.

Table 27: ANOVA Results for the Shear Stress Component of the Solids Circulation and Gas Pressure Drop ($-\Delta P_g/L$) Test, Higher Circulation Rates, Cork

Tests of Between-Subjects Effects

Dependent Variable: shear stress component

Source	Type I Sum of Squares	df	Mean Square	F	Sig.
Corrected Model	1.870E-02 ^a	3	6.233E-03	3.606	.124
Intercept	1.831	1	1.831	1059.403	.000
MS	1.525E-03	1	1.525E-03	.882	.401
DPGDL	1.167E-02	1	1.167E-02	6.751	.060
MS * DPGDL	5.505E-03	1	5.505E-03	3.185	.149
Error	6.914E-03	4	1.728E-03		
Total	1.857	8			
Corrected Total	2.561E-02	7			

a. R Squared = .730 (Adjusted R Squared = .528)

Section 3.5c discussed the information given in the ANOVA table in detail. From Table 27, the significance level for gas pressure drop ($-\Delta P_g/L$) is within 90% confidence of being significant.

Table 28: ANOVA Results for the Solids Pressure Component of the Solids Circulation and Gas Pressure Drop ($-\Delta P_g/L$) Test, Higher Circulation rates, Cork

Tests of Between-Subjects Effects

Dependent Variable: solids pressure drop per unit length

Source	Type I Sum of Squares	df	Mean Square	F	Sig.
Corrected Model	1.122 ^a	3	.374	243.456	.000
Intercept	57.653	1	57.653	37525.903	.000
MS	2.060E-03	1	2.060E-03	1.341	.311
DPGDL	1.110	1	1.110	722.276	.000
MS * DPGDL	1.037E-02	1	1.037E-02	6.751	.060
Error	6.145E-03	4	1.536E-03		
Total	58.781	8			
Corrected Total	1.128	7			

a. R Squared = .995 (Adjusted R Squared = .990)

Table 29: ANOVA Results for the Solids Volume Fraction of the Solids Circulation and Gas Pressure Drop ($-\Delta P_g/L$) Test, Higher Circulation rates, Cork

Tests of Between-Subjects Effects

Dependent Variable: Solids Volume Fraction

Source	Type I Sum of Squares	df	Mean Square	F	Sig.
Corrected Model	7.815E-04 ^a	3	2.605E-04	3.817	.114
Intercept	.987	1	.987	14463.969	.000
MS	4.777E-04	1	4.777E-04	7.000	.057
DPGDL	4.301E-05	1	4.301E-05	.630	.472
MS * DPGDL	2.608E-04	1	2.608E-04	3.821	.122
Error	2.730E-04	4	6.825E-05		
Total	.988	8			
Corrected Total	1.055E-03	7			

a. R Squared = .741 (Adjusted R Squared = .547)

In Table 28, the significance of gas pressure drop ($-\Delta P_g/L$) on solids pressure drop ($-\Delta P_g/L$) is apparent, which is consistent with previous results. In Table 29, the solids circulation is very close to being significant for solids volume fraction at a 95% level. In Figure 61, the solids volume fraction increased with increasing solids circulation, though this was more evident for the higher level of gas pressure drop ($-\Delta P_g/L$). Variations in solids volume fraction were quite small. Because this is a local measurement of solids volume fraction, this may provide an indication that the solids are beginning to stick to the wall.

5.2 Qualitative Study

The qualitative tests discussed in this section in general are transient ramps. These ramps allowed us to compare material-material differences. Hysteresis and compaction of the bed were apparent in these studies. Several of the ramps were for a stationary condition (bubbling bed). In a stationary bed the fluidization regime was clearly defined. Therefore, fluidization regimes as well as the collective effect of gas pressure drop and solids volume fraction were studied.

5.2a Filling and draining Tests

A series of tests in which the standpipe was filled and drained were run to determine the effects of bed height on shear stress. These tests were conducted under packed/moving, unaerated conditions. Bed heights up to 40” above the shear vane were investigated, as well as heights below the vane. Along the length of the vane, a dependence on height was expected, since shear stress is force per unit area and the area is not constant as the bed either fills or drains past the vane. Further, heights that are below the vane do not register any force at all.

A list of relevant variables and their settings are shown in Table 30. A shear vane at 7’ measured the shear stress in this study.

Table 30: Filling and Draining Test Variables, 230 μm Coke

Independent Variables	Dependent Variables	Controlled Variables
Height of standpipe (37” to 108”)	Shear stress $-2\tau_{sw}/R$ 1.1 to 11.7 lb/ft ³	Standpipe Aeration 0 scfh
Butterfly valve in standpipe Closed Drain/ Opened Fill	$-\Delta P_g$ across SV -0.07 To 0.35 psi	Riser Aeration 80,000 scfh
Loopseal Aeration 2250scfh Drain/ 0 scfh Fill	ϵ (not measured)	Aeration at 15’ 0 scfh
Aeration at 7.5’ 40 scfh Drain/0 scfh fill		The total inventory was approximately 750 lb

The test started with the standpipe filled. To drain the bed past the vane, aeration in the loopseal was set at 2,250 scfh and staged aeration at 7.5’ was set at 40 scfh. This staged aeration is directly above the shear vane. The butterfly valve at a height of 13.5’ in the standpipe was placed in the closed position to keep the bed from circulating back. The aeration allowed the bed to drain into the riser and return above the butterfly valve. Bed height measurements were taken as the bed drained past the vane. Once the bed was drained, all aeration was shut off to prohibit the bed from moving during the fill. To conduct the filling test the butterfly valve was cracked opened and the bed filled around the vane while height measurements were taken.

Shear stress versus height has been plotted in Figure 62. Keep in mind that the area of the vane is 1 ft². Therefore, a plot of force measured in lb versus height would give the exact same trends and magnitudes as a plot of shear stress in lb/ft² versus height.

The 1-ft² area was used for all of the shear stress calculations including the cases when the vane was not completely immersed in the bed.

The two bold, vertical lines indicate the location of the leading and trailing edges of the shear vane. The leading and trailing edges are at 68" and 44" respectively. As expected the shear stress increases as the length of the vane covered by the particles increases. This relationship is almost linear for the filling situation.

At the same heights the drain values are lower in magnitude than the fill values. This could be a result of the aeration that was used at 7.5' and the loopseal aeration. No aeration other than riser flow was used during the fill. The aeration during the drain may have resulted in a higher void fraction and possibly another fluidization state. Unfortunately, void fraction was not measured. Due to the split of aeration at the bottom of the standpipe gas velocities and fluidization states are unknown. To give an idea of the difference made by the aeration, the pressure drop across the section of interest was plotted against the different heights during filling and draining (Figure 63). Notice that the pressure drop in the drain case was larger and in the opposite direction compared to the fill case. This indicates that the gas was moving down relative to the solids for the drain case and up for the fill case. Keep in mind that gas pressure drop ($-\Delta P_g/L$) was the only significant variable for the shear stress component when operating in a packed or transitionally packed regime in Section 5.1c.

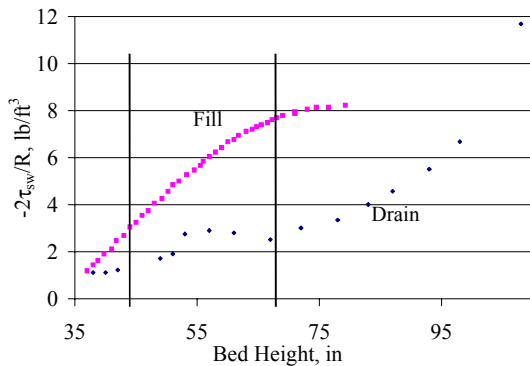


Figure 62: Shear Stress Versus Bed Height, Filling and Draining Tests, 230 μm Coke

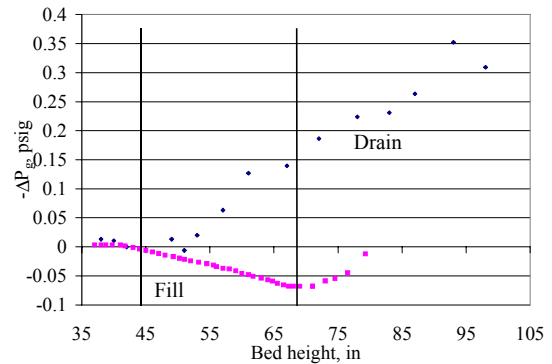


Figure 63: Gas Phase Pressure drop versus Bed Height, Draining and Filling Tests, 230 μm Coke

The draining bed measurements are spaced farther apart, because the speed at which the bed was drained was faster than the speed at which it was filled. This may also

be an explanation for the differences between the two behaviors, because the solids velocities and gas velocities are very different between the two cases.

The shear stress values for the draining bed are constant once the bed height is below the trailing edge of the vane. This is expected since there are no particles acting along the length of the vane. It is also expected that this constant value should be close to zero. Any offset can be attributed to calibration or possibly gas shear.

In contrast to the case for the draining bed, the magnitude of the shear stress values increase linearly as the bed height increases for values of height below the trailing edge of the vane. This is due to particle shear past the vane during filling.

The steady state momentum balance was not applied here because these were not steady conditions. Also, parasitic drag was not considered in this analysis.

Although it was not a significant variable in section 5.1b, height appears to have an effect on shear vane measurements in this study especially along the length of the vane. However, more importantly the pressure drop in the control volume that holds the shear vane had a strong effect on the measurements. This pressure drop indicates changes in gas flow direction, and possible changes in the void fraction and fluidization state. See section 5.1c. Further, this pressure drop may have a larger impact on the shear stress than the variation in bed height.

5.2b Stationary Bed Aeration Ramps, Coke, in the Standpipe

To understand the effect of aeration alone on shear stress measurements, aeration ramps were performed. Due to the split of aeration at the bottom of the standpipe fluidization states can only be presumed using the gas pressure drop ($-\Delta P_g/L$). If the gas pressure drop ($-\Delta P_g/L$) was constant and high (near the weight of the bed), the bed is assumed to be fluidized, otherwise it is packed.

A list of variables and settings used in these ramps is shown in Table 31. A shear vane at 7' measured shear stress in this section.

**Table 31 Stationary Bed Aeration Ramp Variables, Riser Flow 10,000 scfh,
230 μ m Coke**

Independent Variables	Dependent Variables	Controlled Variables
Standpipe Aeration (move air) 0 to 400 scfh	Shear stress $-2*\tau_{sw}/R$ 23 to -1.5 lb/ft^3	Loopseal Aeration 0 scfh
	$\Delta P_g/L$ 19.2 to 54 lb/ft^3	Riser Aeration 10,000 scfh
	ϵ not measured	Aeration at 15' 0 scfh
	$-\Delta P_s/L$ 16 to -5 lb/ft^3	Aeration at 7.5' 0 scfh
	V_g (unknown)	Aeration at the bottom of the standpipe 0 scfh
		Aeration at the dipleg 0 scfh
		Height of standpipe 8 ft

Before the ramp test was conducted, a riser flow of 10,000 scfh was established, and the loopseal aeration was increased to 1,200 scfh to move solids from the standpipe into the riser. This resulted in standpipe and fluidized riser heights of 8' and 7', respectively. Next, the loopseal aeration was cut off to stop circulation. The standpipe aeration was increased at a rate of 20 scfh/min from essentially 0 to 400 scfh. Then the aeration was decreased at a rate of 20 scfh/min from 400 to 0 scfh. No circulation took place during the ramps.

In Figure 64 the shear stress component of the momentum balance ($-2\tau_{sw}/R$) is plotted versus standpipe aeration for both ramping up and ramping down. Take note that parasitic drag was not considered since the bed was stationary. The discontinuities in the up ramp can be explained by the vane slipping through the bed. In other words on the ramp up the vane was under tension. Once the bed had relaxed enough, the shear decreased, and the vane slipped through the bed. There are no discontinuities in the down ramp since the bed is compacting around and pulling the vane down. Notice the sharp shift in shear stress from 10 to -1.2 lb/ft^3 between aeration rates of 270 to 315 scfh. This shift could be due to fluidization of the section in which the vane is immersed. This

aeration rate corresponds to velocities of 1.4 and 1.6 ft/sec, which is considerably higher than the measured minimum fluidization velocity of 0.07 ft/sec. After this point the shear stress actually goes negative. The weight of the vane was lifted due to buoyancy. The maximum positive value measured was 1.59 lb/ft³.

In Figure 65 the components of the momentum balance are plotted against aeration air. The gas pressure drop ($-\Delta P_g/L$) increased with aeration, and on the up ramp it flattened out around 50 lb/ft³ that corresponded to approximately 275 scfh in the aeration. This is a typical minimum fluidization velocity determination, which appeared to have the same result as the shear stress. The gas pressure drop ($-\Delta P_g/L$) flattened at higher flows than the discontinuity in the shear stress, which suggests that shear stress may be a more sensitive measurement of fluidization. The velocity that corresponded to this point was approximately 1.5 ft/sec.

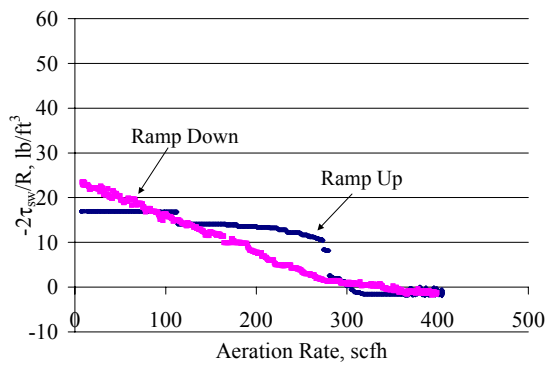


Figure 64 Shear Stress versus Aeration for a Stationary Bed, 230 μm Coke

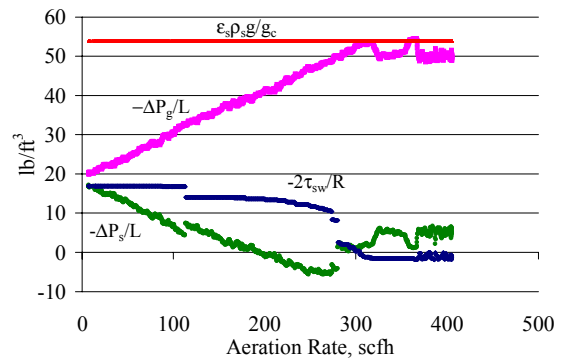


Figure 65: Momentum Balance Components for a Stationary Bed (Ramp Up), 230 μm Coke

The solids pressure drop ($-\Delta P_s/L$) was found by difference using the mixture momentum balance, Equation (7) (Section 1.2). As in Figure 64 the magnitude of the solids pressure drop ($-\Delta P_s/L$) in Figure 65 decreased as the aeration increased. Also, note that if the bed was fluidized above 275 scfh, the method of estimation of solids pressure drop ($-\Delta P_s/L$) was flawed because one of the assumptions is a constant void fraction. Above fluidization, the solids volume fraction decreases with increasing aeration. This may lead to an estimation of larger magnitude of solids pressure drop ($-\Delta P_s/L$) than what

is actually occurring because the actual solids volume fraction is lower than what is used to estimate solids pressure drop ($-\Delta P_s/L$).

Figure 65 illustrates the importance of each term in the mixture momentum balance as the aeration was increased. It is intuitive that the gas pressure drop ($-\Delta P_g/L$) increased with increasing aeration relieving shear stress at the wall and solids pressure drop ($-\Delta P_s/L$). At the point that the bed was assumed to be fluidized, 275 scfh, gas pressure drop ($-\Delta P_g/L$) had the largest magnitude contributing to the momentum balance, while shear stress ($-2\tau_{sw}/R$) and solids pressure drop ($-\Delta P_s/L$) were close to zero. Also note that at a very low aerations shear stress ($-2\tau_{sw}/R$) magnitudes were comparable to the magnitudes of the gas pressure drop ($-\Delta P_g/L$). This is similar to results presented for a moving standpipe in Chapter 4 (for coke breeze). This also supports the accepted method of including shear stress in models for standpipes that are in either packed bed or transitional packed regimes and neglecting shear stress in standpipes that are fluidized.

For completion the components of the momentum balance for the down ramp have been plotted against aeration in Figure 66. All of the trends discussed above apply here. However, the discontinuities seen in shear stress during the up ramps did not occur in the down ramps. In this case the bed was slowly compacting down.

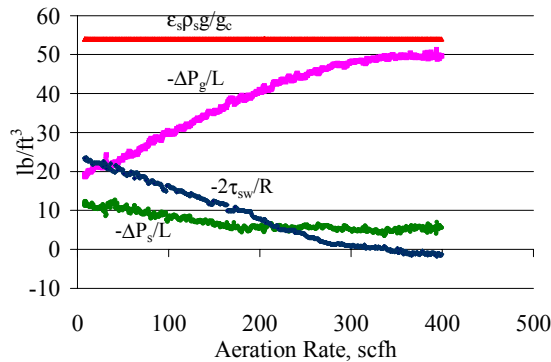


Figure 66: Momentum Balance Components for a Stationary Bed (Ramp Down), 230 μm Coke

Another stationary bed aeration ramp test is worth mentioning, because it resulted in very different results. A list of variables and settings in this test is shown in Table 32. Notice that all settings were similar except the riser flow in the above test was much lower than this test. A shear vane at 7' measured shear stress in this section.

Table 32: Stationary Bed Aeration Ramp Variables, Riser Flow 50,000 scfh, 230 μm Coke

Independent Variables	Dependent Variables	Controlled Variables
Standpipe Aeration 0 to 400 scfh	Shear stress $-2*\tau_{sw}/R$ 23 to 12 lbf/ft ³	Loopseal Aeration 0 scfh
	$\Delta P_{g/L}$ 1.1 to 29 lbf/ft ³	Riser Aeration 50,000 scfh
	ϵ not measured	Aeration at 15' 0 scfh
	ΔP_s 48 to 5 lb/ft ³	Aeration at 7.5' 0 scfh
	v_g (unknown)	Aeration at the bottom of the standpipe 0 scfh
		Aeration at the dipleg 0 scfh

There is one strong difference in this test as compared to the first one discussed. The riser flow is 50,000 scfh, which is 5 times that was used in the low riser flow test. Therefore, any solids that move into the riser were quickly returned to the standpipe. In the earlier test, the low riser flow was used to increase the amount of backpressure in the riser. The resulting difference is the amount of the aeration supplied to the standpipe that goes to the riser and the amount that goes up the standpipe. In the higher riser flow test, more aeration in the standpipe went toward the riser because there was less resistance to flow in the riser rather than the height of packed bed in the standpipe. In the lower riser flow test, more aeration went up the standpipe due to the 7' fluid bed in the riser that resulted from low flow.

The riser flow was set at 50,000 scfh, and there was no aeration in the loopseal or along the standpipe except for the standpipe aeration at the bottom. The aeration was ramped from 20 to 400 scfh at a rate of 20 scfh/min.

Figure 67 is a plot of the components of the momentum balance versus standpipe aeration. There are two aspects that stand out when looking at Figure 67. The shear stress was almost flat with aeration, and the lack of noise in the shear stress signal. The flat profile can be explained by the low amount of aeration actually going up the standpipe due to the high riser flow as compared to the previous test where there was a

significant amount of aeration rising through the standpipe. This low aeration also explains the lack of noise in the signal. There was more noise in the signal for the low riser flow test because of the fluctuations in the higher density bed in the riser. The pressure fluctuations in this bed caused the aeration split to vary more.

If Figure 67 is expanded, there are some interesting trends at higher aerations (Figure 68). It is interesting that the shear stress actually increased in magnitude at aerations of 300 scfh. It increased to a maximum and then started to decrease in magnitude. Further, it went through this maximum before the bed actually circulated at 375 scfh. The bed may in fact be rearranging and compacting while the stress magnitude was increasing.

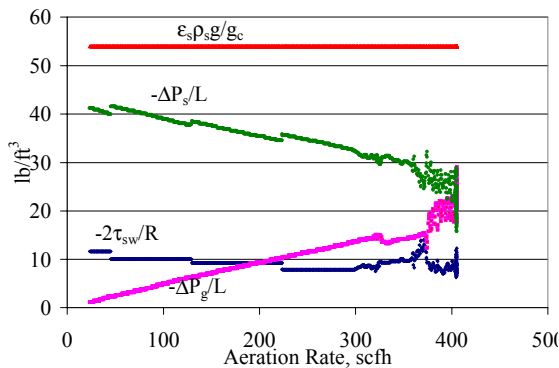


Figure 67: Momentum Balance Components for a Stationary Bed Ramp, High Riser Flow, 230 μm Coke

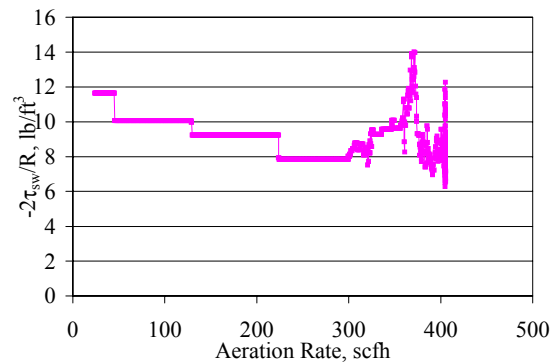


Figure 68: Shear Stress versus Aeration Rate, Stationary Bed, High Riser Flow, 230 μm Coke

5.2c Bubbling Bed Studies, Nylon Beads, in the 10" Test Bed

Nylon beads, 1/8-inch diameter, were used in the bubbling test bed due to their size. This bed material was selected due to the issues regarding purge air discussed in Section 3.5c. The particles were large enough not to get into the gap of the wall probe. In the test bed the aeration was increased from zero to 6,800 scfh. No nylon mesh or purge air was used.

The first aeration ramp is shown in Figure 69. In an increasing aeration ramp, the wall probe measured about half the shear stress measured by the shear vane. Although, the trends were similar for low aeration flows, at high flows the wall probe measurements went through a minimum, which was not exhibited by the shear vane.

In Figure 70, the decreasing aeration trend is plotted. In the down ramp in aeration, the trends for both the wall probe and the shear vane were very similar. Also, the difference between the two was less than what was seen in the increasing aeration test. This suggested that there was either a hysteresis effect or a compaction effect.

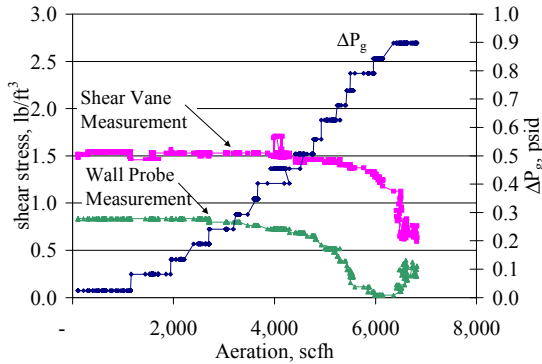


Figure 69: Bubbling Bed Aeration Ramp for Nylon Bead Bed Material

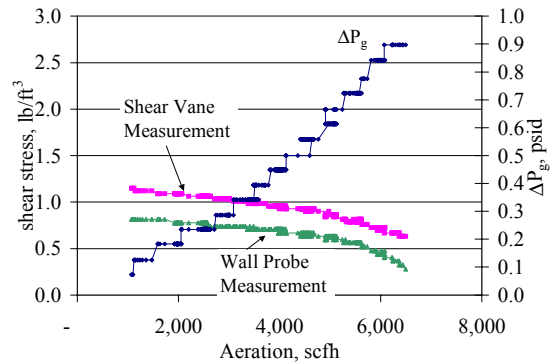


Figure 70: Bubbling Bed Aeration Ramp for Nylon Beads Bed Material, Decreasing Aeration

To see the effects of compaction, the bed was mechanically vibrated first, and then the aeration was increased over time, Figure 71. Comparing Figure 69 and Figure 71, much larger shear stress as measured by the wall probe were seen after the compaction. After the compaction, the wall probe measurements were significantly larger than the measurements by the shear vane for mid to lower flows. At high flows both instruments showed similar values. Like Figure 69, the minimum exhibited by the wall probe measurements at high flows was seen in Figure 71.

Figure 72 resulted when the aeration was decreased after compaction. The wall probe and shear vane had very similar results at high aeration in Figure 72. However, at lower aeration the wall probe measured higher stresses after compaction. It did not reach stress as high as seen in Figure 71, which still suggests a hysteresis effect. All four of the wall probe measurements have been plotted in Figure 73 to compare the difference between increasing aeration and decreasing aeration and to compare before and after compaction. All four of the shear vane measurements have been plotted in Figure 74.

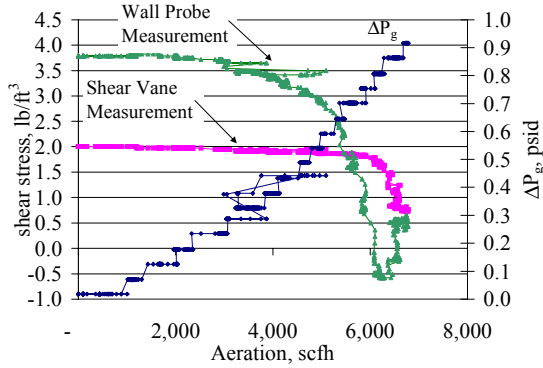


Figure 71: Bubbling Bed Aeration Ramp for Nylon Beads Bed Material, After Compaction

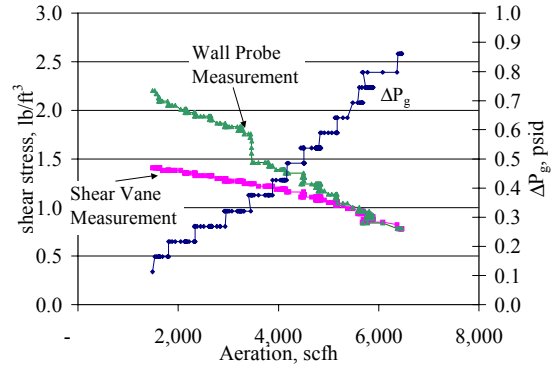


Figure 72: Bubbling Bed Aeration Ramp for Nylon Bead Bed Material, After Compaction, Decreasing Aeration

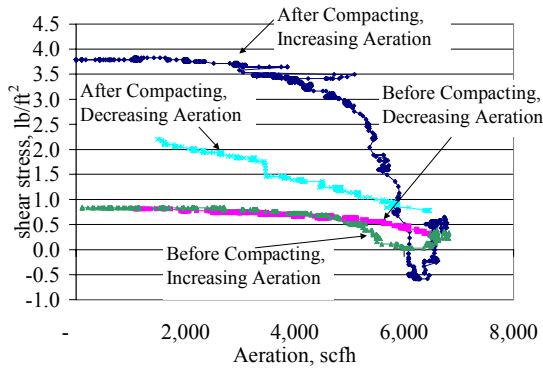


Figure 73: Comparison of the Wall Probe Measurements for the Nylon Bead Bubbling Bed Study

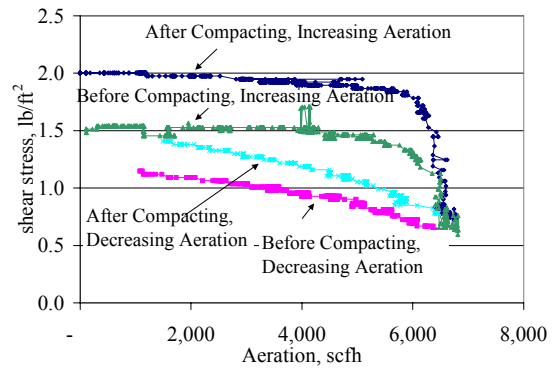


Figure 74: Comparison of the Shear Vane Measurements for the Nylon Bead Bubbling Bed Study

Compaction had a large effect on the wall probe and shear vane measurements (Figures 73 and 74), and at a high compaction the decreasing aeration trend gave a lower shear than the increasing aeration trend. Further, regardless of compaction the wall shear probe measurement exhibited a minimum at high flows for the increasing aeration trends. The impact of compaction gives insight into the importance of the history and stress state of the bed. In general, shear stress measurements from the shear vane do not approximate measurements from the wall probe. This suggests that either the shear stress at the center of the pipe is different than that at the wall, and/or that the measurement equipment are fundamentally different and are measuring different forces.

5.2d Bubbling Bed Studies, Cork, in the 10" Test Bed

In the test bed the aeration was increased from zero to 500 scfh for cork bed material. Nylon mesh was used for the wall probe as opposed to purge aeration. The bed height ranged from 28 to 32 ft.

In Figure 75 an increasing aeration trend is shown. As in the nylon bead study, the shear stress followed a similar trend of decreasing with increasing aeration. Further, the wall probe measured lower values than the shear vane. Also, the local solids volume fraction has been plotted in Figure 75. The probe described in Section 3.6 was used to measure it. This instrument was still in its early stages and is not necessarily trusted at this point obvious problems. However, the values reported in Figure 75 look reasonable and follow an intuitive trend. As aeration increased, solids volume fraction decreased.

Figure 76 is the corresponding decreasing aeration. There is a little more variability in the solids volume fraction measurements, but the values are reasonable. Further, the wall probe measurements do not increase up to the values seen in Figure 75. This is more evidence of a hysteresis effect. However, the shear vane shows measurements larger than that in Figure 75.

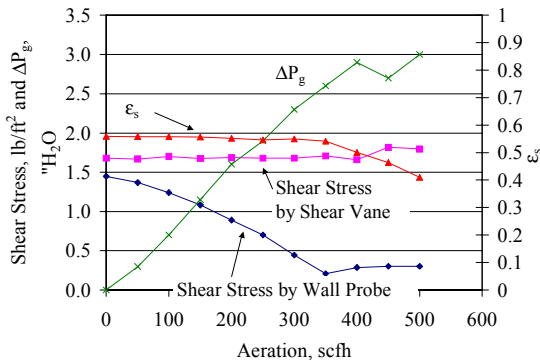


Figure 75: Bubbling Bed Aeration Ramp for Cork Bed Material

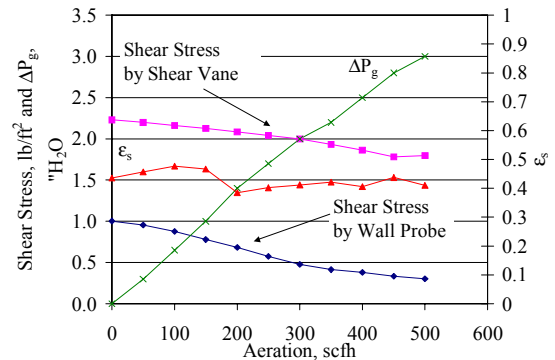


Figure 76: Bubbling Bed Aeration Ramp for Cork Bed Material, Decreasing Aeration

Figures 77 and 78 show another increasing/decreasing aeration ramp sequence. In this case unreasonable measurements of solids volume fraction measurements were seen. The trends in Figure 77 look reasonable except for the highest aeration rate at which

point the solids volume fraction increases. The solids volume fraction measurements seen in Figure 78 are unreasonably high since the vibrated solids volume fraction has been estimated to be approximately 0.58. Solids volume fraction measurements near 0.6 appear to be questionable. Solids volume fraction measurements of 0.88 cannot be correct. There are few speculations as to what caused these erroneous readings. The probe zero may have drifted. The calibration sequence described in Section 3.6b may be poor. A dense piece of cork may be sitting in the measurement volume. Fines residue may be building up on the face of the probe.

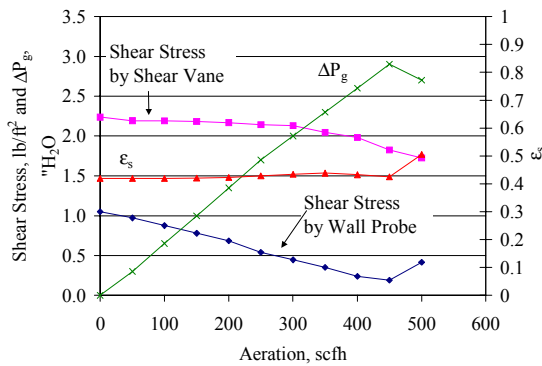


Figure 77: Bubbling Bed Ramp 2, Cork Bed Material, Increasing Aeration

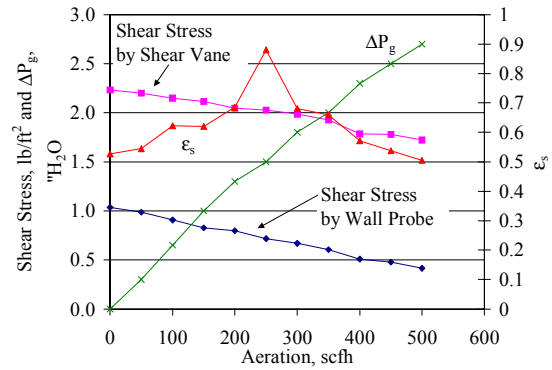


Figure 78: Bubbling Bed Ramp 2, Cork Bed Material, Decreasing Aeration

Further cork studies to understand the effects of purge air have been conducted and were summarized in Section 3.6b. From this study, we still do not have the capability to measure local solids volume fraction measurements. Either the probe readings or the calibration method is capable of giving unrealistic values at high aeration rates. Further, in general the shear vane did not give the same measurements as the wall probe. It is uncertain if this means that the shear at the center of the pipe is different from the shear at the wall, or if there is a fundamental difference between the measurements.

5.2e Circulating Bed Aeration Ramp Tests

Aeration ramps were performed to determine the effect of aeration alone on shear stress measurements in a circulating bed. Bed height in the standpipe was allowed to vary. Due to the split of aeration at the bottom of the standpipe fluidization states can only be presumed using the changes in pressure profile along the length of the standpipe.

A list of variables and settings are shown in Table 33. Shear stress in this test was measured using a shear vane at the 7' level.

Table 33: Circulating Bed Aeration Ramp Variables, 230 μm Coke

Independent Variables	Dependent Variables	Controlled Variables
Standpipe Aeration 0 to 400 scfh	Shear stress $2*\tau_{sw}/R$ 26 to 9 lb/ft ³	Loopseal Aeration 600 scfh
	$\Delta P_g/L$ 0.3 to 26 lb/ft ³	Riser Aeration 90,000 scfh
	ϵ not measured	Aeration at 15' 25 scfh
	$\Delta P_s/L$ 58 to 15 lb/ft ³	Aeration at 7.5' 25 scfh
	V_g (unknown)	Aeration at the bottom of the standpipe 0 scfh
	Height of standpipe 28 to 23 ft	Aeration at the dipleg 80 scfh
	V_s 189 to 2,342.8 lb/hr	Total Inventory 856lbm
	Mass Circulation 3,500 to 69,000 lbm/hr	

A slow circulation of about 3,500 lb/hr was established with standpipe aeration of 50 scfh, riser flow of 90,000 scfh, and loopseal aeration of 600 scfh. The standpipe was then ramped to 400 scfh at a rate of 20 scfh/min. The standpipe bed height was allowed to vary.

Figure 79 is a plot of the change in momentum balance components with aeration rate. The wall shear stress magnitude decreased with increasing aeration. There were changes in slopes similar to what was seen in Chapter 4. The curve appeared to be flat from 50 to just above 100 scfh. Between 100 and 300 scfh it was steep and after 300 it appeared to be flat again. The magnitude of the shear stress component seen in this test was slightly larger than what was seen in the stationary cases. The shear stress components in the stationary cases were from 23 to about zero lb/ft³. The shear stress component in this circulating case was from 28 to 5 lb/ft³, which was very similar to what was seen in Chapter 4. Other differences between this ramp and the stationary ramp were

staged aeration. There was 25 scfh at 15' and 7.5' in this situation. This aeration may have compressed the bed around the shear vane.

Keep that in mind other variables were changing along with the aeration. As aeration in the standpipe increased the bed height in the standpipe decreased and the mass circulation increased (Figure 80).

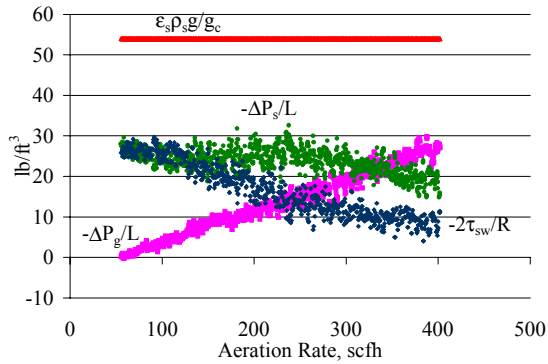


Figure 79: Momentum Balance Components for a Circulating Bed Aeration Ramp, 230 μm Coke

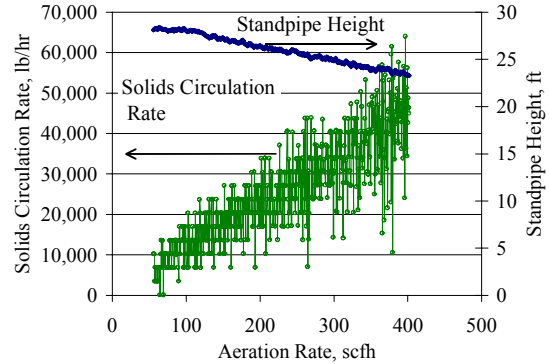


Figure 80: Mass Circulation and Standpipe Bed Height versus Aeration rate, 230 μm Coke

The gas pressure drop ($-\Delta P_g/L$) increased in magnitude almost linearly with aeration (Figure 79). The magnitude increased from almost zero to about 30 lb/ft^3 . Like wall shear stress ($-2\tau_{sw}/R$) the magnitude of the solids pressure drop ($-\Delta P_s/L$) decreased with standpipe aeration. Note that if the standpipe was fluidized during the ramp, the method of estimation of the solids pressure drop ($-\Delta P_s/L$) was flawed because one of the assumptions was a constant void fraction. If the bed was fluidized or in a transitional packed bed state, then according to Leung (1985) the void fraction increased with gas velocity. The solids volume fraction was decreasing. This may have lead to an estimation of larger magnitude of solids pressure drop per unit length than what was actually occurring because the actual solids volume fraction was lower than what was used to estimate the solids pressure drop. Because a portion of the aeration fed to the standpipe splits and goes towards the riser, it is difficult to determine the gas velocity and corresponding fluidization state.

A similar experiment was run with ramping standpipe aeration, but with a different aeration scheme. A list of variables and settings is shown in Table 34.

Table 34: Circulating Bed Aeration Ramp Variables, Aeration at the Bottom, 230 μm Coke

Independent Variables	Dependent Variables	Controlled Variables
Standpipe Aeration 0 to 400 scfh	Shear stress $2*\tau_{sw}/R$ 9 to 3 lb/ft ³	Loopseal Aeration 500 scfh
	$\Delta P_g/L$ 1 to 32 lb/ft ³	Riser Aeration 95,000 scfh
	ϵ not measured	Aeration at 15' 25 scfh
	$\Delta P_s/L$ 43 to 17 lb/ft ³	Aeration at 7.5' 25 scfh
	V_g (unknown)	Aeration at the bottom of the standpipe 100 scfh
	Mass Circulation 10,000 to 74, 000 lb/hr	Aeration at the dipleg 90 scfh
		Total Inventory 1000 lbm

Figure 81 is a plot of the momentum balance components versus aeration rate. Although in Figure 79 there were similar trends to Figure 81, the shear stress values were much lower in Figure 81. One large difference between the two tests was the location of the aeration at the bottom of the standpipe. For the test depicted in Figure 81 100 scfh was always applied to the very bottom of the standpipe. Furthermore, solids circulation rates achieved in this ramp were from 10,000 to 74,000 lb/hr, which was higher than those achieved in Figure 79, which were 3,500 to 69,000 lb/hr.

As a result, aeration located at the bottom of the standpipe had not only a large impact on solids circulation, but also a large impact on measure shear stress values.

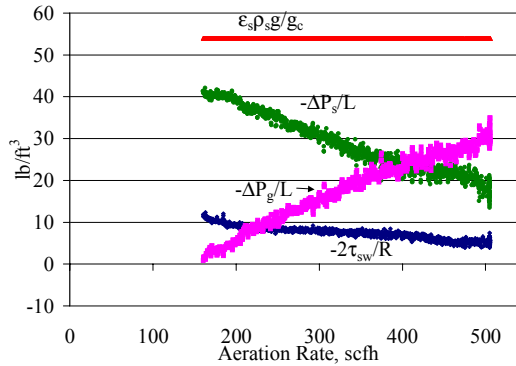


Figure 81: Momentum Balance Components for a Circulating Bed Aeration Ramp, Aeration at the Bottom, 230 μm Coke

5.2f Circulating Bed Aeration Ramp Tests – Low Flows

A few aeration ramps at lower flows gave very different qualitative information regarding shear stress than what was discussed in section 5.2e. All of the aeration ramps presented in Chapter 4 and 5 start with aeration rates of 50 scfh. From this study, the ramps were run from 0 to 150 scfh.

An example of the how lower flows effect shear stress is in Figure 82. A shear vane at 7' was used to measure the shear stress in this section. In Figure 82, initially, the shear stress component increased with increasing aeration rate. It reached a maximum, and then decreased with increasing aeration rate. In Chapter 4 and Section 5.2e, the shear stress always decreased with increasing aeration. However, aeration rates below 50 scfh were not seen in Chapter 4 and Section 5.2e.

In Figure 83, the shear stress component and gas pressure drop are plotted as a function of aeration (move air). As mentioned above, at low flows as aeration rate increased shear stress increased to a maximum after which it started to decrease. From Figure 83, as the aeration increased the gas pressure drop increased. However, at low flows the gas pressure drop was negative, which meant that the gas phase was pushing down, and the gas flow was flowing down. After a certain point, approximately 130 scfh the gas pressure drop became positive, which meant that the gas pressure was pushing up on the bed and the gas was flowing up.

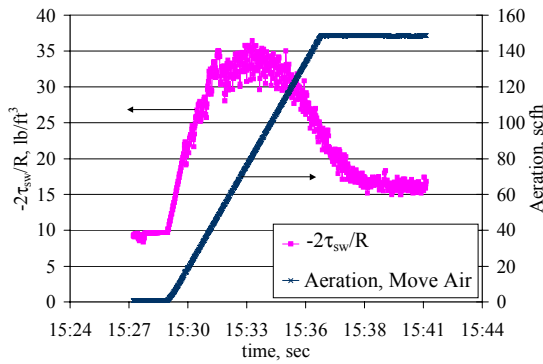


Figure 82: Shear Stress at Lower Aeration Ramps, 230 μm Coke

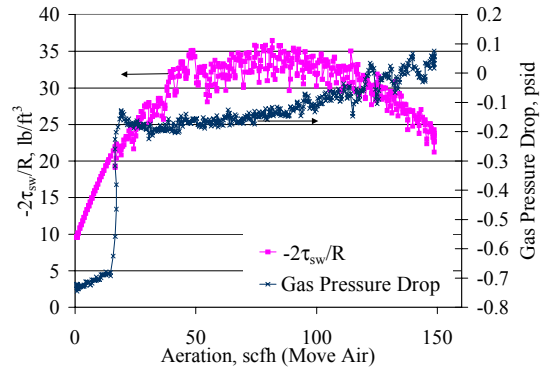


Figure 83: Shear Stress Component and Gas Pressure Drop versus Aeration Rate for Low Flows, 230 μm Coke

All of the momentum balance components are shown in Figure 84. In Figure 84, the shear stress component was the largest force other than the weight of the bed. For most of the aeration ramp, the gas pressure drop component was negative which was added to the force necessary for the shear stress component and solids pressure component to balance.

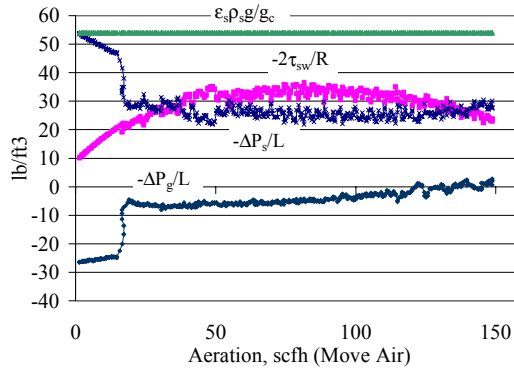


Figure 84: Momentum Balance Components versus Aeration for Low Flows, 230 μm Coke

At low flows for coke breeze, the shear stress was the largest component, and the gas pressure drop ($-\Delta P_g/L$) was working in the direction of the weight of the bed. Furthermore, the shear stress component at low flows increased with aeration and went through a maximum after which point it decreased with increasing aeration.

5.3 CFB Operational Variables

Section 5.1 studied the effects of theoretical variables on shear stress. Section 5.2 was a qualitative study of shear stress using the aeration ramp to study effects such as hysteresis and compaction. In this section statistical, factorial studies were used to understand the effects of CFB operational variables. In Section 5.1, gas pressure drop ($-\Delta P_g/L$) was an independent variable, and it appeared to have an impact on the solids wall shear stress. In this section gas pressure drop ($-\Delta P_g/L$) was a dependent variable, and factors that effect it as well as the shear stress component and solids pressure drop ($-\Delta P_s/L$) were studied.

5.3a The Effect of Solids Circulation Rate and Riser Pressure Drop

A two-factor experiment was run to understand the effect of riser pressure and solids circulation rate on shear stress. An increase in riser pressure resulted in a corresponding increase in the incremental standpipe pressure. This pressure increase changed the aeration split at the bottom of the standpipe. Furthermore, changing solids circulation rate and the pressure drop in the riser changed the relative velocity in the standpipe. Therefore, the balance of the forces in the standpipe changed. Table 35 lists the runs made to understand these variables using a fully duplicated and randomized 2X2 factorial test.

Table 35: Riser Pressure Drop and Solids Circulation Rate Test Independent Variables, 230 μ m Coke

<u>Run</u>	<u>Riser Pressure Drop</u> <u>psi</u>	<u>Solids Circulation Rate</u> <u>lb/hr</u>
1	1.5	10,000
2	1.5	25,000
3	2.0	10,000
4	2.0	25,000
5	1.5	10,000
6	1.5	25,000
7	2.0	10,000
8	2.0	25,000

The results from these runs were summarized in Table 36. Notice that the bed height was relatively constant. A shear vane at 7' was used to measure the shear stress in this experiment.

Table 36: Riser Pressure Drop and Solids Circulation Rate Test Results, 230 μ m Coke

<u>Run</u>	<u>Riser Pressure Drop psi</u>	<u>Solids Circulation Rate lb/hr</u>	<u>Standpipe Height ft</u>	<u>Shear Stress lb/ft²</u>	<u>-2*Shear Stress/R lb/ft³</u>	<u>$-\Delta P_g/L$ lb/ft²</u>	<u>$-\Delta P_s/L$ lb/ft²</u>
1	1.48	11,365	21	3.02	14.51	23.06	16.43
2	1.51	24,653	19	1.10	5.29	31.06	17.65
3	1.97	13,461	19	2.65	12.71	29.18	12.1
4	2.01	24,291	19	1.53	7.32	33.64	13.03
5	1.51	11,339	19	1.18	5.67	26.22	22.11
6	1.51	24,490	19	0.63	3.01	29.23	21.76
7	2.00	12,581	19	1.48	7.11	30.55	16.34
8	1.99	23,583	16.5	1.20	5.78	37.87	10.35

Figures 85 through 87 illustrate these results graphically. Notice that the pressure drop in the riser is denoted as DPr.

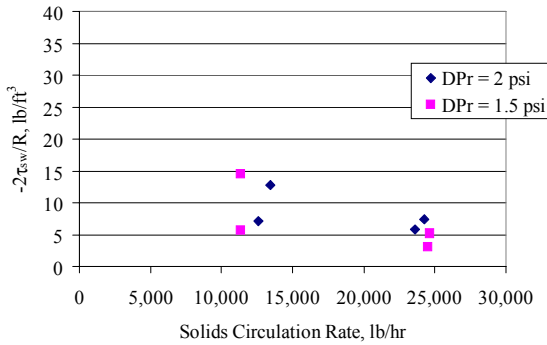


Figure 85: Shear Stress ($-2\tau_{sw}/R$) Results of 2X2 factorial, Riser ΔP and Solids Circulation Rate, 230 μ m Coke

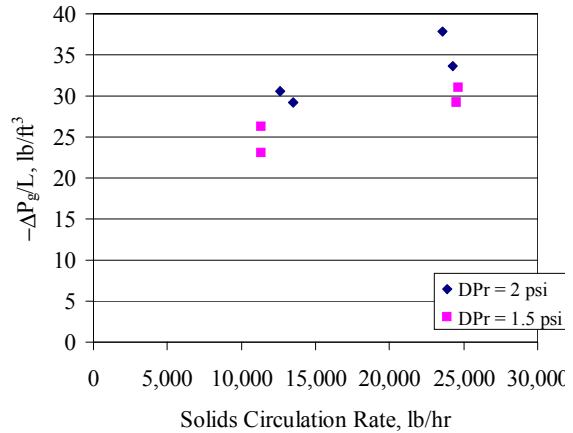


Figure 86: Gas Pressure Drop ($-\Delta P_g/L$) Results of 2X2 factorial, Riser ΔP and Solids Circulation Rate, 230 μ m Coke

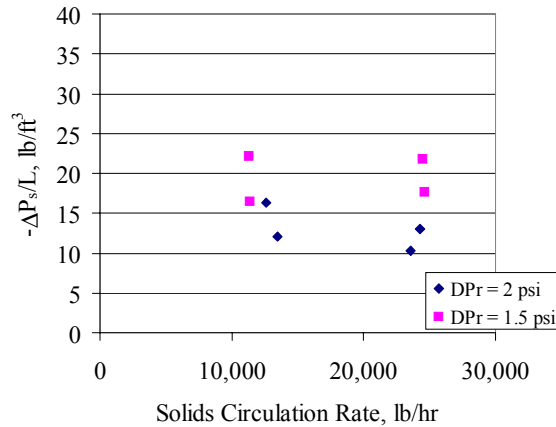


Figure 87: Solids Pressure Drop ($-\Delta P_s/L$) Results of 2X2 factorial, Riser ΔP and Solids Circulation Rate, 230 μm Coke

A type I sum of squares analyses was applied to the three dependent variables listed in Table 36. Table 37 describes the results for the shear stress component of the momentum balance. Notice that pressure drop in the riser is denoted as DPR and solids circulation rate is denoted as MS.

Table 37: ANOVA of Riser Pressure drop and Solids Circulation Test for Shear Stress ($-2\tau_{sw}/R$), 230 μm Coke

Tests of Between-Subjects Effects

Dependent Variable: shear stress

Source	Type I Sum of Squares	df	Mean Square	F	Sig.	Eta Squared	Noncent. Parameter	Observed Power ^a
Corrected Model	49.037 ^b	3	16.346	1.117	.441	.456	3.351	.149
Intercept	471.245	1	471.245	32.201	.005	.890	32.201	.984
DPR	2.464	1	2.464	.168	.703	.040	.168	.062
MS	43.245	1	43.245	2.955	.161	.425	2.955	.264
DPR * MS	3.328	1	3.328	.227	.658	.054	.227	.066
Error	58.538	4	14.634					
Total	578.820	8						
Corrected Total	107.575	7						

a. Computed using alpha = 0.05

b. R Squared = .456 (Adjusted R Squared = .048)

Section 3.5c discussed the information given in the ANOVA table in detail. From Table 37 no variable variables were significant. The model explains only 4.8% of the variability of shear stress. The independent variables were not the right variables to

explain the variability seen in the shear stress. The variability between the replicates was as large as the variability from level to level of the controlled variables.

Due to Section 5.1 it was not surprising that solids circulation rate did not have a significant effect on the shear stress. However, Section 5.1 suggested that gas pressure drop ($-\Delta P_g/L$) affected shear stress. If the riser pressure was significant for gas pressure drop ($-\Delta P_g/L$), then it could have had an effect on the shear stress ($-2\tau_{sw}/R$). The ANOVA results for gas pressure drop ($-\Delta P_g/L$) in the standpipe section around the shear vane are in Table 38.

Table 38: ANOVA of Riser Pressure drop and Solids Circulation Test for Gas Pressure Drop ($-\Delta P_g/L$), 230 μm Coke

Tests of Between-Subjects Effects

Dependent Variable: Pressure Drop per Unit Length across shear vane interval

Source	Type I Sum of Squares	df	Mean Square	F	Sig.	Eta Squared	Noncent. Parameter	Observed Power ^a
Corrected Model	123.809 ^b	3	41.270	9.961	.025	.882	29.882	.795
Intercept	7249.808	1	7249.808	1749.774	.000	.998	1749.774	1.000
DPR	58.750	1	58.750	14.179	.020	.780	14.179	.801
MS	64.988	1	64.988	15.685	.017	.797	15.685	.837
DPR * MS	7.214E-02	1	7.214E-02	.017	.901	.004	.017	.051
Error	16.573	4	4.143					
Total	7390.190	8						
Corrected Total	140.382	7						

a. Computed using alpha = 0.05

b. R Squared = .882 (Adjusted R Squared = .793)

Unlike the shear stress component model, the main effects were significant, and were almost equal in magnitude of importance according to Eta squared. From Figure 86 it was apparent that an increase in solids circulation rate and riser pressure drop both resulted in an increase in gas pressure drop ($-\Delta P_g/L$) in the control volume.

ANOVA results for solids pressure ($-\Delta P_s/L$) as calculated from the force balance in the control volume are in Table 39.

Table 39: ANOVA of Riser Pressure drop and Solids Circulation Test for Solids Pressure Drop ($-\Delta P_s/L$), 230 μm Coke

Tests of Between-Subjects Effects

Dependent Variable: Solids Pressure drop per unit length

Source	Type I Sum of Squares	df	Mean Square	F	Sig.	Eta Squared	Noncent. Parameter	Observed Power ^a
Corrected Model	91.937 ^b	3	30.646	3.299	.140	.712	9.897	.358
Intercept	2105.032	1	2105.032	226.608	.000	.983	226.608	1.000
DPR	85.347	1	85.347	9.188	.039	.697	9.188	.628
MS	2.195	1	2.195	.236	.652	.056	.236	.067
DPR * MS	4.396	1	4.396	.473	.529	.106	.473	.084
Error	37.157	4	9.289					
Total	2234.126	8						
Corrected Total	129.094	7						

a. Computed using alpha = 0.05

b. R Squared = .712 (Adjusted R Squared = .496)

Like in the gas pressure drop across the shear vane ($-\Delta P_g/L$) model, the riser pressure drop was significant for the solids phase pressure drop ($-\Delta P_s/L$). From Figure 87 it can be seen that an increase in riser pressure drop resulted in a decrease in solids pressure drop ($-\Delta P_g/L$) in the control volume.

5.3b Four Factor Test: Standpipe Height, Riser Flow, Loopseal Flow, and Solids Circulation Rate

A four-factor experiment was run to understand the effect of riser flow, solids circulation rate, standpipe height, and loopseal flow on shear stress. It was felt that changes in these variables could change the aeration split and pressure drop across the interval of interest. Changes in these variables could also change the relative velocity and the void fraction in the interval of interest. Therefore, the balance of the forces in the standpipe would change. Table 40 lists the runs made to understand these variables.

Table 40: Four Factor Test Independent Variables

Run	Riser Flow ft/sec	Solids Circulation Rate lb/hr	Standpipe Height ft	Loopseal Flow scfh
1	15.9	12,500	16.5	600
2	15.9	12,500	16.5	1200
3	15.9	12,500	19.0	600
4	15.9	12,500	19.0	1200
5	15.9	25,000	16.5	600
6	15.9	25,000	16.5	1200
7	15.9	25,000	19.0	600
8	15.9	25,000	19.0	1200
9	19.1	12,500	16.5	600
10	19.1	12,500	16.5	1200
11	19.1	12,500	19.0	600
12	19.1	12,500	19.0	1200
13	19.1	25,000	16.5	600
14	19.1	25,000	16.5	1200
15	19.1	25,000	19.0	600
16	19.1	25,000	19.0	1200

The results from these runs are summarized in Table 41. A shear vane at 7' was used to measure the shear stress in this study.

Table 41: Four Factor Test Results, 230 μm Coke

<u>Run</u>	<u>Riser Flow VR ft/sec</u>	<u>Solids Circulation Rate MS lb/hr</u>	<u>Standpipe Height HSP ft</u>	<u>Loopseal Flow FLPSL scfh</u>	<u>-2*Shear Stress/R lb/ft²</u>	<u>-ΔP_g/L lb/ft²</u>	<u>-ΔP_s/L lb/ft²</u>	<u>Comments</u>
1	15.61	12,604	16.5	601.82	5.62	33.48	14.90	
2	15.82	12,460	16.5	1201.29	7.38	27.90	18.73	
3	15.80	12,569	19	597.92	9.18	27.21	17.61	
4	15.95	12,480	19	1202.71	10.68	20.67	22.65	
5	15.77	24,406	16.5	600.47	0.12	46.73	7.14	vane tangled?
6	15.65	25,414	16.5	1200.85	0.87	49.45	3.68	vane tangled?
7	15.94	25,090	19	603.21	6.32	32.71	14.97	7.5' 40 scfh, slugging
8	16.07	24,059	19	1201.05	1.68	39.11	13.21	vane tangled? slugging
9	19.13	12,464	16.5	601.68	9.26	25.51	19.22	
10	19.30	12,529	16.5	1201.34	6.07	23.89	24.04	
11	19.15	12,629	19	599.22	7.70	21.86	24.44	
12	19.38	12,691	19	1200.32	7.30	14.19	32.51	vane tangled?
13	18.84	24,693	16.5	603.02	4.16	37.52	12.32	
14	19.19	24,254	16.5	1203.01	4.02	25.98	24.00	7.5' 40 scfh
15	18.95	25,067	19	594.60	4.29	38.16	11.55	7.5' 40 scfh, SP B 200scfh
16	19.05	25,373	19	1205.44	5.48	30.87	17.65	7.5' 40scfh

Figures 88 through 90 illustrate these results graphically. Notice that the standpipe bed height is represented as Hsp.

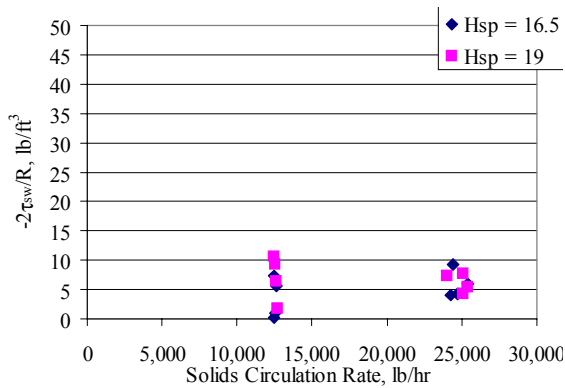


Figure 88: Shear Stress ($-2\tau_{sw}/R$) results of the Four Factor Test, 230 μm Coke

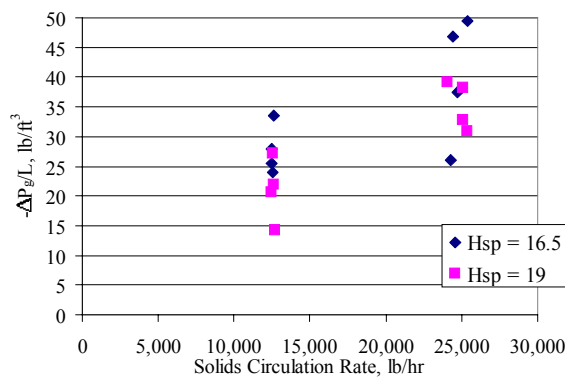


Figure 89: Gas Pressure Drop ($-\Delta P_g/L$) Results of the Four Factor Test, 230 μm Coke

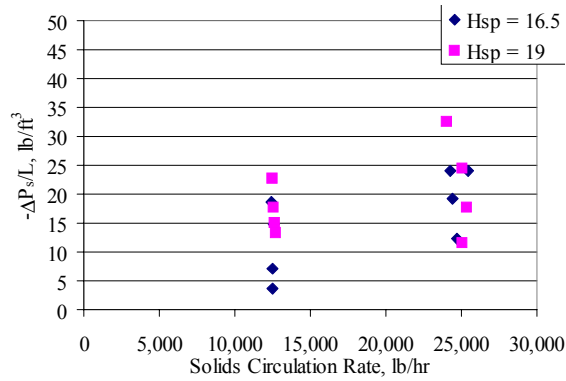


Figure 90: Solids Pressure ($-\Delta P_s/L$) Length Results of the Four Factor Test, 230 μ m Coke

A type I sum of squares analyses was applied to the three dependent variables listed in Table 41. Table 42 describes the results for the shear stress component of the momentum balance.

Table 42: ANOVA of Four Factor Test for Shear Stress ($-2\tau_{sw}/R$), 230 μ m Coke

Tests of Between-Subjects Effects

Dependent Variable: Shear Stress Component

Source	Type I Sum of Squares	df	Mean Square	F	Sig.	Eta Squared	Noncent. Parameter	Observed Power ^a
Corrected Model	118.799 ^b	10	11.880	3.229	.104	.866	32.292	.499
Intercept	507.915	1	507.915	138.063	.000	.965	138.063	1.000
VR	2.578	1	2.578	.701	.441	.123	.701	.106
MS	82.073	1	82.073	22.309	.005	.817	22.309	.961
HSP	14.290	1	14.290	3.884	.106	.437	3.884	.360
FLPSL	.631	1	.631	.172	.696	.033	.172	.063
VR * MS	8.235	1	8.235	2.238	.195	.309	2.238	.231
VR * HSP	9.961	1	9.961	2.708	.161	.351	2.708	.268
VR *								
FLPSL	.229	1	.229	.062	.813	.012	.062	.055
MS * HSP	.269	1	.269	.073	.798	.014	.073	.056
MS *								
FLPSL	.390	1	.390	.106	.758	.021	.106	.058
HSP *								
FLPSL	.143	1	.143	.039	.852	.008	.039	.053
Error	18.394	5	3.679					
Total	645.108	16						
Corrected Total	137.193	15						

a. Computed using alpha = 0.05

b. R Squared = .866 (Adjusted R Squared = .598)

Section 3.5c discussed the information given in the ANOVA table in detail. From Table 42 mass circulation rate was the only significant main effect. The model explains

60% of the variability of shear stress and 40% of the variation is noise or unexplained variation.

These results are surprising, since solids circulation in Section 5.1 was not a significant variable. Keep in mind that in Section 5.1 the gas pressure drop per unit length was a controlled variable. In this experiment it was not controlled, and it may have changed with solids circulation rate, making solids circulation rate significant.

ANOVA results for the gas pressure drop ($-\Delta P_g/L$) in the control volume are in Table 43. As in the shear stress component model the solids circulation rate was significant. However, gas velocity in the riser was also significant, and the standpipe height was almost significant. Using the Eta squared values, the change in solids circulation had the largest impact on the gas pressure drop ($-\Delta P_g/L$) followed by the riser velocity and the standpipe height. None of the interactions were significant, and all of the interactions were almost equal in magnitude of importance according to Eta squared. From Figure 89, an increase in solids circulation rate resulted in an increase in gas pressure drop ($-\Delta P_g/L$) in the control volume.

Table 43: ANOVA of Four Factor Test for Gas Pressure Drop ($-\Delta P_g/L$) across the shear vane, 230 μm Coke

Tests of Between-Subjects Effects

Dependent Variable: Gas Pressure Drop Per Unit Length across the shear vane interval

Source	Type I Sum of Squares	df	Mean Square	F	Sig.	Eta Squared	Noncent. Parameter	Observed Power ^a
Corrected Model	1227.408 ^b	10	122.741	4.659	.052	.903	46.591	.666
Intercept	15328.916	1	15328.916	581.868	.000	.991	581.868	1.000
VR	219.632	1	219.632	8.337	.034	.625	8.337	.640
MS	699.867	1	699.867	26.566	.004	.842	26.566	.981
HSP	130.416	1	130.416	4.950	.077	.498	4.950	.437
FLPSL	60.528	1	60.528	2.298	.190	.315	2.298	.235
VR * MS	8.497	1	8.497	.323	.595	.061	.323	.075
VR * HSP	56.400	1	56.400	2.141	.203	.300	2.141	.223
VR * FLPSL	39.438	1	39.438	1.497	.276	.230	1.497	.170
MS * HSP	4.020	1	4.020	.153	.712	.030	.153	.062
MS * FLPSL	8.556	1	8.556	.325	.593	.061	.325	.076
HSP * FLPSL	5.290E-02	1	5.290E-02	.002	.966	.000	.002	.050
Error	131.722	5	26.344					
Total	16688.046	16						
Corrected Total	1359.130	15						

a. Computed using alpha = 0.05

b. R Squared = .903 (Adjusted R Squared = .709)

ANOVA results for solids pressure drop ($-\Delta P_s/L$) in the control volume are in Table 44. Similarly to the gas pressure drop ($-\Delta P_g/L$) across the shear vane model the riser gas velocity and solids circulation main effects were significant for the solids pressure drop ($-\Delta P_s/L$) model, and were almost equal in magnitude of importance according to Eta squared. From Figure 90, an increase in solids circulation rate resulted in a decrease in solids pressure ($-\Delta P_s/L$) in the control volume.

Table 44: ANOVA of Four Factor Test for Solids Pressure Drop ($-\Delta P_s/L$), 230 μm Coke

Tests of Between-Subjects Effects

Dependent Variable: Solids Pressure Drop Per Unit Length

Source	Type I Sum of Squares	df	Mean Square	F	Sig.	Eta Squared	Noncent. Parameter	Observed Power ^a
Corrected Model	685.488 ^b	10	68.549	3.563	.087	.877	35.629	.542
Intercept	4852.186	1	4852.186	252.194	.000	.981	252.194	1.000
VR	174.533	1	174.533	9.071	.030	.645	9.071	.675
MS	302.685	1	302.685	15.732	.011	.759	15.732	.882
HSP	58.382	1	58.382	3.034	.142	.378	3.034	.294
FLPSL	73.588	1	73.588	3.825	.108	.433	3.825	.355
VR * MS	2.172E-03	1	2.172E-03	.000	.992	.000	.000	.050
VR * HSP	18.961	1	18.961	.985	.366	.165	.985	.129
VR * FLPSL	45.659	1	45.659	2.373	.184	.322	2.373	.242
MS * HSP	6.380	1	6.380	.332	.590	.062	.332	.076
MS * FLPSL	5.278	1	5.278	.274	.623	.052	.274	.072
HSP * FLPSL	2.126E-02	1	2.126E-02	.001	.975	.000	.001	.050
Error	96.199	5	19.240					
Total	5633.873	16						
Corrected Total	781.688	15						

a. Computed using alpha = 0.05

b. R Squared = .877 (Adjusted R Squared = .631)

5.3c The effect of Standpipe Aeration Rate, Riser Gas Velocity, and Fines Concentration

At any time the balance of pressures determines this split in the system, and because the split is unknown, it is very difficult to determine the relative velocities in the standpipe. Because operational variables such as standpipe aeration rate and the riser gas velocity change the balance of pressures, they also have an effect on the relative velocity of solids and gases in the standpipe. The level of fines is also of interest, because fines have an impact on the solids volume fraction, which will also affect relative velocities.

A three-factor experiment was run to understand the effect of standpipe gas velocity, riser gas velocity and level of fines on shear stress. Table 45 lists the runs completed to understand these variables.

Table 45: Standpipe Aeration Rate, Riser Gas Velocity and Fines Level Test Independent Variables

<u>Run</u>	Riser Gas Velocity <u>ft/sec</u>	Standpipe Gas Velocity <u>ft/sec</u>	Fines Level <u>Lb</u>
1	17.5	.099	0
2	17.5	.099	200
3	17.5	.155	0
4	17.5	.155	200
5	22.5	.099	0
6	22.5	.099	200
7	22.5	.155	0
8	22.5	.155	200
9	17.5	.099	0
10	17.5	.099	200
11	17.5	.155	0
12	17.5	.155	200
13	22.5	.099	0
14	22.5	.099	200
15	22.5	.155	0
16	22.5	.155	200

The results from the independent variables are summarized in Table 46. Notice that the high level for fines was always reported as 200 lb. Throughout the test fines were separated out using the secondary cyclone. In an effort to maintain a constant level of fines, they were collected and returned to the system. The total inventory of the system was maintained as constant. This was done with the use of the initial standpipe height when the material was completely stored in the standpipe. When the system was operated with coarse material the mass of the solids was determined using the initial height of the standpipe with no circulation and the known bulk density of coarse material. Once the fines were mixed into the system, the standpipe height with no circulation was adjusted so that the same amount of mass was in the system as in the coarse material cases. The change in bulk density, which varied from 54 to 56 lb/ft³ from coarse to coarse mixed with fines, was considered. Eight dependent variables were considered and the results for the independent and dependent variables are summarized in Tables 46 through 48. A shear vane at 7' was used to measure the shear stress.

Table 46: Standpipe Aeration Rate, Riser Gas Velocity and Fines Level Test Independent Variable Results, Coke

Run	Riser Gas Velocity ft/sec	Standpipe Gas Velocity ft/sec	Fines Level lb
1	17.519	0.098	0
2	17.548	0.100	200
3	17.479	0.153	0
4	17.487	0.154	200
5	22.538	0.099	0
6	22.461	0.099	200
7	22.358	0.157	0
8	22.510	0.155	200
9	17.517	0.099	0
10	17.430	0.099	200
11	17.510	0.153	0
12	17.528	0.154	200
13	22.419	0.099	0
14	22.464	0.099	200
15	22.458	0.157	0
16	22.483	0.154	200

Table 47: Standpipe Aeration Rate, Riser Gas Velocity and Fines Level Test Dependent Variable Results, Coke

Run	$-2\tau_{sw}/R$ lb/ft³	$(-\Delta P_g/L)_{\text{Shear Vane}}$ lb/ft³	$-\Delta P_s/L$ lb/ft³	Solids Circulation lb/hr	Standpipe Height ft	$(-\Delta P_g)_{\text{Riser}}$ psid
1	8.560	11.515	34.949	22,262	27.7	0.875
2	11.392	11.781	34.553	28,405	27.6	1.125
3	5.920	21.222	28.745	30,409	23.5	1.635
4	5.773	28.602	23.441	39,627	23.4	2.007
5	9.373	10.310	36.240	23,939	28.5	0.649
6	11.059	10.158	35.647	28,790	28.4	0.863
7	8.142	17.790	28.195	32,521	25.5	1.102
8	7.735	23.848	24.977	41,636	26.2	1.379
9	8.726	11.612	34.712	22,219	27	0.903
10	9.671	12.260	37.599	28,734	27	1.138
11	7.070	21.499	27.054	29,686	23.8	1.657
12	6.733	28.639	22.061	40,572	23.4	1.999
13	10.640	10.984	33.794	23,198	28.4	0.644
14	10.578	10.308	36.917	29,440	28.2	0.889
15	7.482	17.583	29.731	33,590	25.5	1.089
16	8.772	23.533	24.965	42,982	28.2	1.380

Table 48: Standpipe Aeration Rate, Riser Gas Velocity and Fines Level Test Dependent Variable Results-continued, Coke

<u>Run</u>	Bulk Density ρ_b lb/ft³	Average Particle Diameter d_p μm	Standard deviation of d_p μm
1	55.023	253.08	9.515
2	57.727	197.45	5.469
3	55.887	261.33	9.492
4	57.817	211.88	4.170
5	55.923	241.78	6.096
6	56.863	205.91	18.860
7	54.127	262.31	8.647
8	56.560	211.61	23.363
9	55.050	258.39	4.825
10	59.530	212.56	17.180
11	55.623	257.34	3.222
12	57.433	230.13	7.896
13	55.417	252.67	8.062
14	57.803	221.49	22.704
15	54.797	274.12	3.478
16	57.270	213.52	10.147

Figures 91 through 94 illustrate these results graphically.

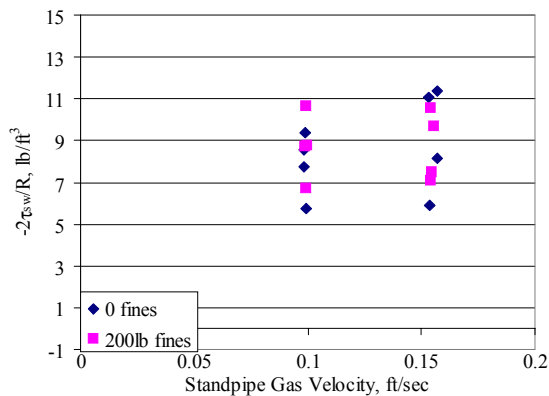


Figure 91: Shear Stress Component Results of 3 Factor Factorial, Riser Gas Velocity, Standpipe Gas Velocity, and Fines Concentration, Coke

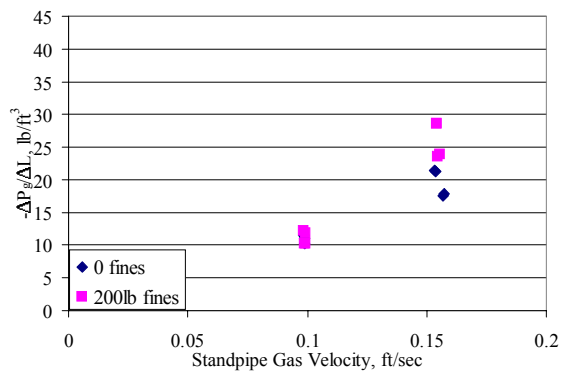


Figure 92: Gas Pressure Drop ($-\Delta P_g/L$) Results of 3 Factor Factorial, Riser Gas Velocity, Standpipe Gas Velocity, and Fines Concentration, Coke

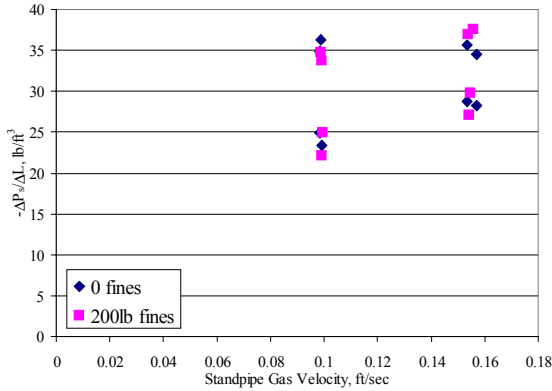


Figure 93: Solids Pressure Drop ($-\Delta P_s/L$) Results of 3 Factor Factorial, Riser Gas Velocity, Standpipe Gas Velocity, and fines Concentration, Coke

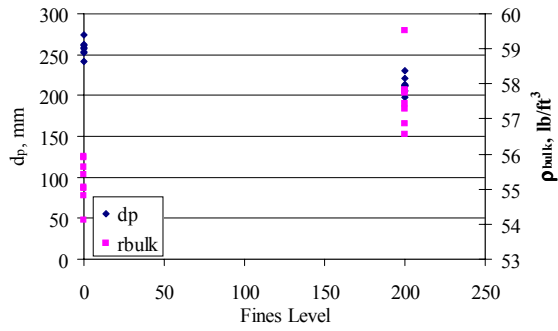


Figure 94: Bed Material Property Results of 3 Factor Factorial, Riser Gas Velocity, Standpipe Gas Velocity, and fines Concentration, Coke

A type I sum of squares analyses was applied to the nine dependent variables listed in Tables 47 and 48. The ANOVA results for the shear stress component are listed in Table 49. Notice that riser gas velocity, standpipe gas velocity, and fines concentration are denoted as VR and FM, and FINES respectively.

Table 49: ANOVA of Fines Test for Shear Stress Component, Coke

Tests of Between-Subjects Effects

Dependent Variable: Shear Stress Component

Source	Type I Sum of Squares	df	Mean Square	F	Sig.	Eta Squared	Noncent. Parameter	Observed Power ^a
Corrected Model	41.810 ^b	5	8.362	16.385	.000	.891	81.926	1.000
Intercept	1183.771	1	1183.771	2319.599	.000	.996	2319.599	1.000
VR	6.171	1	6.171	12.092	.006	.547	12.092	.879
FM	31.277	1	31.277	61.288	.000	.860	61.288	1.000
FINES	2.103	1	2.103	4.121	.070	.292	4.121	.450
VR * FM	.695	1	.695	1.363	.270	.120	1.363	.185
FM * FINES	1.563	1	1.563	3.063	.111	.234	3.063	.353
Error	5.103	10	.510					
Total	1230.684	16						
Corrected Total	46.913	15						

a. Computed using alpha = 0.05

b. R Squared = .891 (Adjusted R Squared = .837)

Section 3.5c discussed the information given in the ANOVA table in detail. From Table 49, riser gas velocity and standpipe gas velocity were significant, and fines concentration was very close to being significant. No interactions between independent

variables were significant. Standpipe gas velocity had the largest eta-squared which meant that changes in standpipe gas velocity resulted in the largest changes of shear stress. The model explained 84% of the variability of shear stress and 16% of the variation was noise or unexplained variation.

ANOVA results for all of the dependent variables are summarized in Table 50 and 51. All of the models for the independent variables were very strong, above 0.89 except for the shear stress model. However, R^2 value of 0.837 for the shear stress component was very high compared to other tests. In all cases standpipe velocity was significant. Level of fines was significant for all variables except for the standpipe height. None of the interaction effects were significant for the shear stress model. However, all of the interaction effects were significant for the gas pressure drop ($-\Delta P_g/L$).

Segregation in the riser may have been an indication of the poor fit for shear stress. Further, shear stress was the last variable to come to steady state. It may have not been at steady state for all of the conditions in the fines test.

Table 50: ANOVA of Fines Test for Dependent Variables, Coke

<u>Statistic</u>	<u>$-2\tau_{sw}/R$ lb/ft³</u>	<u>$-\Delta P_g/L$ shear vane lb/ft³</u>	<u>$-\Delta P_s/L$ lb/ft³</u>	<u>Solids Circulation, lb/hr</u>	<u>Standpipe Height, ft</u>
Mean Square, VR	1.537	31.978	3.379	12,570,217	15.016
Mean Square, FM	7.788	549.762	353.82 5	4.41E+08	33.931
Mean Square, Fines	0.524	44.268	10.986	2.43E+08	0.391
Mean Square, VR*FM	0.173	8.704	2.090	2,796,763.0	3.151
Mean Square, VR*FINES		1.131		624,433.32	0.856
Mean Square, FM*FINES	0.389	43.699	33.944	13,799,578	0.681
F, VR	12.092	571.076	2.662	41.492	38.115
F, FM	61.288	9,817.815	278.66 9	1,456.861	86.127
F, Fines	4.121	790.556	8.652	802.310	0.992
F, VR*FM	1.363	155.447	1.646	9.232	7.997
F, VR*FINES		20.196		2.061	2.172
F, FM*FINES	3.063	780.395	26.734	45.550	1.728
Sig, VR	0.006	0.000	0.134	0.000	0.000
Sig, FM	0.000	0.000	0.000	0.000	0.000
Sig, FINES	0.070	0.000	0.015	0.000	0.345
Sig, VR*FM	0.270	0.000	0.228	0.014	0.020
Sig, VR*FINES		0.002		0.185	0.175
Sig, FM*FINES	0.111	0.000	0.000	0.000	0.221
Eta Squared, VR	0.547	0.984	0.210	0.822	0.809
Eta Squared, FM	0.860	0.999	0.965	0.994	0.905
Eta Squared, FINES	0.292	0.989	0.464	0.989	0.099
Eta Squared, VR*FM	0.120	0.945	0.141	0.506	0.471
Eta Squared, VR*FINES		0.692		0.186	0.194
Eta Squared, FM*FINES	0.234	0.989	0.728	0.835	0.161
Adjusted R squared	0.837	0.999	0.954	0.994	0.897

Table 51: ANOVA of Fines Test for Dependent Variables- Continued, Coke

Statistic	D_p μm	St. Dev d_p μm	ρ_b lb/ft³	(-ΔP_g)_{Riser} psid
Mean Square, VR	0.0995	97.963	1.776	0.699
Mean Square, FM	389.13	31.068	0.914	1.644
Mean Square, Fines	7,942	199.168	22.936	0.310
Mean Square, VR*FM				0.114
Mean Square, VR*FINES		105.723		0.00186
Mean Square, FM*FINES				0.00711
F, VR	0.001	4.664	3.890	3,045
F, FM	5.325	1.479	2.002	7,252
F, Fines	108.68	9.483	50.248	1,349
F, VR*FM				497
F, VR*FINES		5.034		8.09
F, FM*FINES				30.97
Sig, VR	0.971	0.054	0.072	0.000
Sig, FM	0.040	0.249	0.183	0.000
Sig, FINES	0.000	0.010	0.000	0.000
Sig, VR*FM				0.000
Sig, VR*FINES		0.046		0.019
Sig, FM*FINES				0.000
Eta Squared, VR	0.000	0.298	0.245	0.997
Eta Squared, FM	0.307	0.119	0.143	0.999
Eta Squared, FINES	0.901	0.463	0.807	0.993
Eta Squared, VR*FM				0.982
Eta Squared, VR*FINES		0.314		0.473
Eta Squared, FM*FINES				0.775
Adjusted R squared	0.881	0.526	0.780	0.999

Most of the variables in Table 51 are related to intended changes when adding fines to the system. Although the models had lower R squared values, they indicated that the addition of fines was a significant variable for all three dependent variables. This suggested that effect of changing the average particle diameter or fines content in the bed was accomplished.

5.3d The Effect of Location of Standpipe Move Air, Aeration at 20.8 feet, and Direction of Ramp

A study was conducted to understand the effects of the location of the move air on the momentum balance components. In section 5.2, evidence of hysteresis was discussed. Furthermore, a difference between the behavior of the momentum balance components for aeration ramps with and without aeration at the very bottom of the standpipe was suggested. Mountziaris (1990) studied the effects of hysteresis on standpipe circulation. Hysteresis in this context means the effect of a condition may be dependent on the way you come to that condition. As a result, part of this experiment was to study the difference between ramping up to the desired move aeration and ramping down to it. Also, the aeration at 20.8 feet was tested to see if it could compress the bed below it. The experimental matrix is in Table 52.

Table 52: Standpipe Aeration Location, Aeration at 20.8 feet, and Ramp Direction Test Matrix

<u>Standard</u>	<u>Run Order</u>	<u>Location of Move Aeration</u>	<u>Aeration at 20.8 feet, scfh</u>	<u>Ramp Direction</u>
1	12	-0.8'	25	increasing
2	11	-0.8'	25	decreasing
3	4	-0.8'	50	increasing
4	3	-0.8'	50	decreasing
5	2	0.3'	25	increasing
6	1	0.3'	25	decreasing
7	8	0.3'	50	increasing
8	7	0.3'	50	decreasing
9	14	-0.8'	25	increasing
10	13	-0.8'	25	decreasing
11	16	-0.8'	50	increasing
12	15	-0.8'	50	decreasing
13	6	0.3'	25	increasing
14	5	0.3'	25	decreasing
15	10	0.3'	50	increasing
16	9	0.3'	50	decreasing

All of the tests in Table 52 were for a move air of 150 scfh. The way this aeration was achieved was one of the variables studied, ramp direction. The location of the move air was another variable studied. The location of 0.3' corresponded to the typical move air location in Figure 10, and the location of -0.8' corresponded to aeration at the bottom

of the standpipe. For example, the first row in Table 52 corresponded to a condition in which the aeration at the bottom of the standpipe was set at 150 and the aeration at 0.3' was zero. Furthermore, this total aeration of 150 was achieved by ramping the aeration from 0 to 150scfh. In contrast, the next condition was achieved by ramping the same aeration from 300 to 150 scfh. A strict regimen was used in that the steady states were taken holding this condition for exactly six minutes. This was done so the ramps could also be directly compared over the time domain. As a result, variables slow to reach steady state were less likely to provide reproducible results over up and down flow periods. The results for the dependent variables are in Table 53. A shear vane at 7' was used to measure the shear stress in this study.

**Table 53: Standpipe Aeration Location, Aeration at 20.8', and Ramp Direction
Dependent Variable Results, 230 μ m Coke**

<u>Standard</u>	$\frac{-2\tau_{sw}}{R}$ <u>lb/ft³</u>	$\frac{-\Delta P_g/\Delta L}{}$ <u>lb/ft³</u>	$\frac{-\Delta P_g/\Delta L}{}$ <u>lb/ft³</u>	<u>Standpipe Height ft</u>	<u>Solids Circulation lb/hr</u>
1	22.134789	2.77	29.090295	27.2	19,079
2	19.810634	3.12	31.222534	27	19,095
3	15.598503	0.73	37.669617	27.3	19,413
4	15.539647	0.57	37.894037	27.6	19,542
5	12.839003	4.46	36.701641	27.4	20,096
6	18.559469	1.79	33.648955	28.6	18,827
7	14.188862	2.17	37.644838	27	20,510
8	15.778635	2.25	35.971185	27.2	20,395
9	22.439678	2.98	28.581934	27.1	19,282
10	17.521493	1.97	34.505419	27.2	18,615
11	16.900975	1.37	35.724473	26.9	20,295
12	24.531632	0.97	28.498960	26.9	19,895
13	14.603802	4.68	34.718898	27.2	19,839
14	14.667025	4.20	35.136815	27.5	19,698
15	23.933653	2.59	27.476795	27	20,520
16	17.298615	2.19	34.509453	27	20,798

The data in Table 53 is plotted in Figures 95 through 97.

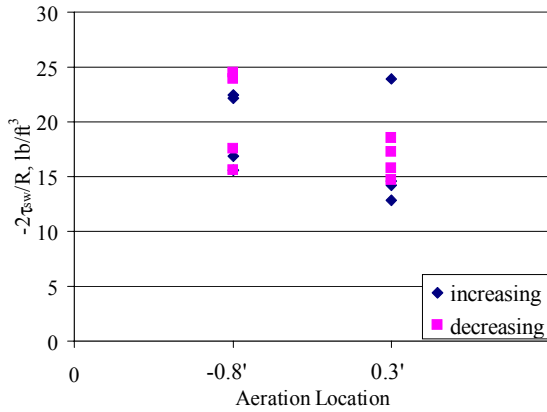


Figure 95: Results of Shear Stress Component for Hysteresis Test, 230 μm Coke

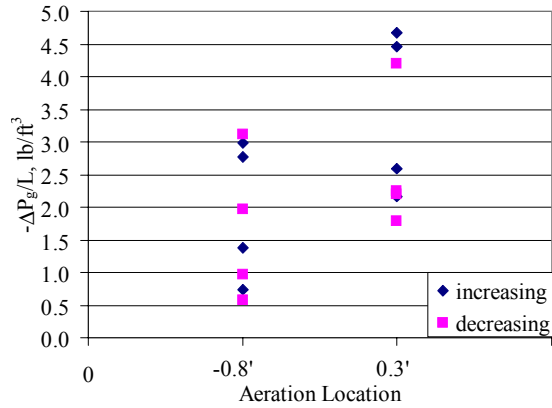


Figure 96: Results of Gas Pressure Drop Component for Hysteresis Test, 230 μm Coke

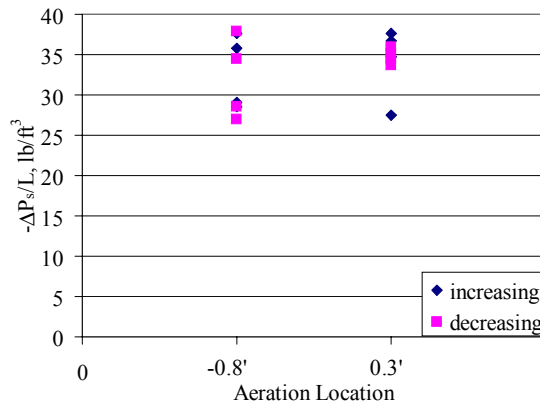


Figure 97: Results of Solids Pressure Drop Component for Hysteresis Test, 230 μm Coke

A type I sum of squares analyses was applied to the five dependent variables listed in Table 53. The ANOVA results for the shear stress component are listed in Table 54. Notice that aeration location, aeration at the dipleg, and ramp direction are denoted as AERATLOC and DPLGAERA, and RAMPDIR respectively.

Table 54: ANOVA Results of the Shear Stress Component of the Hysteresis Test, 230 μm Coke

Tests of Between-Subjects Effects

Dependent Variable: Shear Stress Component

Source	Type I Sum of Squares	df	Mean Square	F	Sig.	Eta Squared	Noncent. Parameter	Observed Power ^a
Corrected Model	98.874 ^b	7	14.125	1.111	.438	.493	7.777	.244
Intercept	5124.642	1	5124.642	403.074	.000	.981	403.074	1.000
AERATLOC	31.946	1	31.946	2.513	.152	.239	2.513	.287
DPLGAERA	8.920E-02	1	8.920E-02	.007	.935	.001	.007	.051
RAMPDIR	7.127E-02	1	7.127E-02	.006	.942	.001	.006	.051
AERATLOC * DPLGAERA	24.667	1	24.667	1.940	.201	.195	1.940	.233
AERATLOC * RAMPDIR	1.045E-02	1	1.045E-02	.001	.978	.000	.001	.050
DPLGAERA * RAMPDIR	.993	1	.993	.078	.787	.010	.078	.057
AERATLOC * DPLGAERA * RAMPDIR	41.098	1	41.098	3.233	.110	.288	3.233	.354
Error	101.711	8	12.714					
Total	5325.227	16						
Corrected Total	200.585	15						

a. Computed using alpha = 0.05

b. R Squared = .493 (Adjusted R Squared = .049)

Section 3.5c discussed the information given in the ANOVA table in detail. From Table 54, there were no significant variables, which was seen in Figure 95. The model explained 5% of the variability of shear stress. The shear stress component was not affected by any of the variables tested. Explanations for the lack of dependence could have been that the shear stress was not quite at steady state when the data was recorded. In Figure 98 the range of the shear stress component can be seen as well as how well the replicates repeated.

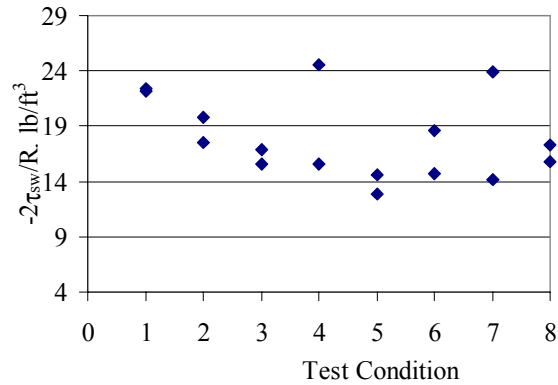


Figure 98: Comparison of Hysteresis Test Replicates, 230 μm Coke

In Figure 98 the test condition corresponds to the eight replicated runs that are outlined in Table 52. For example, test condition number 3 in Figure 98 corresponds to standard number 3 and 11 in Table 52. Both have identical test conditions. From Figure 98 three of the replicates did not repeat well and the overall changes in the test were small compared to the differences in the replicates for conditions four and seven. There were no obvious reasons for the lack of repeatability for conditions four, six, and seven.

Already mentioned was the concern that shear stress was not at steady state for a number of the test conditions. It has been found that for several conditions the shear stress was not steady state. Figures 99 and 100 are examples of this for runs two and nine. These are plots of the shear stress component over time for the five-minute period over which the steady state was averaged.

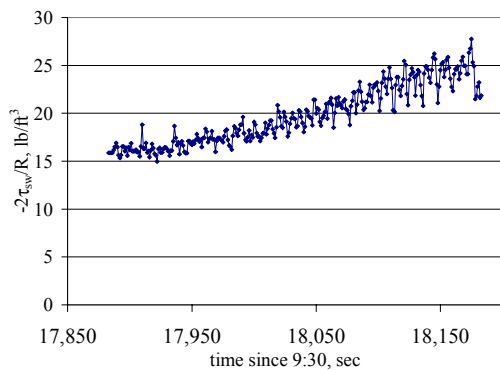


Figure 99: Example of Five Minute Steady State for Run Two, 230 μm Coke

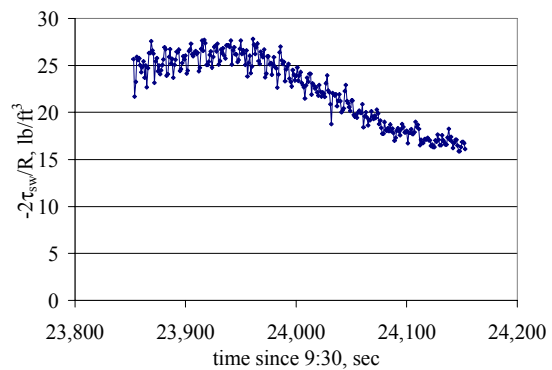


Figure 100: Example of Five Minute Steady State for Run Nine, 230 μm Coke

From Table 55, the models for the hysteresis were relatively poor. Only two that had significant variables were the gas pressure drop ($-\Delta P_g/L$) and the solids circulation,

which had R squared values of 0.72 and 0.71 respectively. The significant variables were aeration location and aeration at the dipleg. Further, ramp direction was close to being significant for the gas pressure drop ($-\Delta P_g/L$).

Table 55: ANOVA of Hysteresis Test for Gas Pressure Drop ($-\Delta P_g/L$), Solids Pressure Drop ($-\Delta P_s/L$), Solids Circulation, and Standpipe Height, 230 μm Coke

<u>Statistic</u>	$-\Delta P_g/\Delta L$ Shear Vane <u>lb/ft³</u>	$-\Delta P_s/\Delta L$ <u>lb/ft³</u>	Solids Circulation <u>lb/hr</u>	Standpipe Height <u>ft</u>
Mean Square, AERATLOC	6.234	9.956	1,808,654	0.181
Mean Square, DPLGAERA	10.526	8.677	2,846,390	0.331
Mean Square, RAMPDIR	1.468	0.892	269,987	0.226
Mean Square, AERATLOC*DPLGAERA		27.539		0.456
Mean Square, AERATLOC*RAMPDIR		0.174		
Mean Square, DPLGAERA*RAMPDIR		3.118		
Mean Square, AERATLOC* DPLGAERA*RAMPDIR		33.208		
F, AERATLOC	14.470	0.742	14.509	1.454
F, DIPLGAERA	24.434	0.646	22.834	2.661
F, RAMPDIR	3.408	0.066	2.166	1.816
F, AERATLOC*DPLGAERA		2.052		3.667
F, AERATLOC*RAMPDIR		0.013		
F, DPLGAERA*RAMPDIR		0.232		
F, AERATLOC*DPLGAERA* RAMPDIR		2.474		
Sig, AERATLOC	0.003	0.414	0.002	0.253
Sig, DPLGAERA	0.000	0.445	0.000	0.131
Sig, RAMPDIR	0.090	0.803	0.167	0.205
Sig, AERATLOC*DPLGAERA		0.190		0.082
Sig, AERATLOC*RAMPDIR		0.912		
Sig, DPLGAERA*RAMPDIR		0.643		
Sig, AERATLOC*DPLGAERA* RAMPDIR		0.154		
Eta Squared, AERATLOC	0.547	0.085	0.547	0.117
Eta Squared, DPLGAERA	0.671	0.075	0.656	0.195
Eta Squared, RAMPDIR	0.221	0.008	0.153	0.142
Eta Squared, AERATLOC*DPLGAERA		0.204		0.250
Eta Squared, AERATLOC*RAMPDIR		0.002		
Eta Squared, DPLGAERA*RAMPDIR		0.028		
Eta Squared, AERATLOC* DPLGAERA*RAMPDIR		0.236		

CHAPTER 6 CONCLUSIONS

Solids phase shear stress has been experimentally measured, and solids phase pressure drop ($-\Delta P_s/L$) has been inferred under a large variety of CFB operating conditions. The purpose of the thesis was to experimentally measure solids phase shear stress to close the force balance in a section of the standpipe.

The relative contribution of the solids phase shear stress was heavily dependent on bed material. For coke breeze, solids phase shear stress and solids phase pressure drop per unit length were important forces in the momentum balance that could not be ignored. For coke breeze, the wall shear stress component was on the same order of magnitude as the gas phase pressure drop per unit length. However, for cork the wall shear stress component was always the smallest contribution to the momentum balance. It ranged from 9 to 2% of the total forces.

Equation (37) was developed from the theory commonly used for handling solids wall shear stress in standpipes that are in a packed regime (Leung, 1985; Mountziaris, 1990; Picciotti, 1995).

$$P_{sz}|_{z=z_1} = \frac{DK}{4\mu_w} \left(e^{\frac{-4\mu_w}{DK}(z_2-z_1)} \left(\frac{\Delta P_g}{\Delta z} + \frac{4\mu_w}{DK} P_{sz}|_{z=z_2} - \rho_s \epsilon_s \frac{g}{g_c} \right) - \frac{DK}{4\mu_w} \left(\frac{\Delta P_g}{\Delta z} - \rho_s \epsilon_s \frac{g}{g_c} \right) \right) \quad (37)$$

The constant μ_w/K , the product of the Janssen coefficient and coefficient of friction, is repeatedly in Equation (37). The values of this constant are dependent on bed material properties. Using this product to predict wall shear stress resulted in values higher than four times the measured values. When the product of the Janssen coefficient and coefficient of friction was adjusted such that the predicted values matched the measured values, a value of 0.003 was found for both cork and coke breeze. This result was startling due to its magnitude and the fact that the same value worked well for both materials. This demonstrates that the Janssen coefficient, which is measured under non-aerated, incipient flow conditions, may not be the correct parameter to be used in the standpipe of a CFB.

Further examination of Equation (37), indicates that for a packed regime, solids phase shear stress and solids phase pressure drop ($-\Delta P_s/L$) are based on the gas pressure drop ($-\Delta P_g/L$), axial location in the bed, and solids volume fraction of the bed material.

For a packed regime, the axial location dependence could not be measured with confidence, and the gas pressure drop ($-\Delta P_g/L$) dependence was detected with a 90% confidence.

For a fluidized regime the solids phase shear stress and pressure drop ($-\Delta P_s/L$) are based on the solids velocity and solids volume fraction. For a fluidized regime, the solids velocity dependence was quite small and differences were below detectable limits.

Stationary bed aeration ramps show that shear stress is a strong indicator of fluidization. These ramps also indicate that effects such as hysteresis and compaction have a large impact on solids wall shear stress.

The completed work on this project is only the start. A list of recommendations for continuing this work is below.

1. Collaborate with CFB modelers, to understand how the solids wall shear stress measurements can enhance their efforts.
2. Build a more sensitive device to measure solids-wall shear stress in the riser.
3. Evaluate the effects of wall surface roughness on wall shear stress and solids pressure. Currently, galvanized sheet metal is under study. However, there is utility in studying acrylic pipe and refractory lined pipe. Most of the CFB at NETL is constructed of acrylic, and standpipes found in energy facilities are generally refractory lined.
4. Improving calibration of probe. Check slope for upward forces. Calibrate for side-to-side stresses.
5. Use the shear vane to measure particle-particle shear, coating the sides of the vane with particles can do this. Studying particle-particle shear can give insight into what is happening away from the wall.
6. Develop a 2-D mixture momentum balance; try to predict location of inner shear layer. An interpretation of the internal angle being larger than the angle of wall friction is that the material does not slide at the wall, but breaks within the bulk. A 2-D momentum balance may be useful in predicting where this occurs.

7. Explore the option of using the shear vane or wall probe to define fluidization. Of course standpipe regimes would have to be expressed in terms of shear stress first.
8. Continue studying different bed materials to see if the Janssen coefficient that fits the operational data varies from 0.003. This should also be done with different surface roughness as discussed in number 1.
9. Continue development of solids volume fraction probe. Suspect problems are changing zeros, too small of a sampling volume, poor equation that relates ϵ_s to K_{eff} , and static discharge.

APPENDIX

A.1 Derivation of Mixture Momentum Balance using Shell Balance Technique

A.1.a Gas Momentum Balance:

Consider the section of standpipe under study in the Figure 101 below.

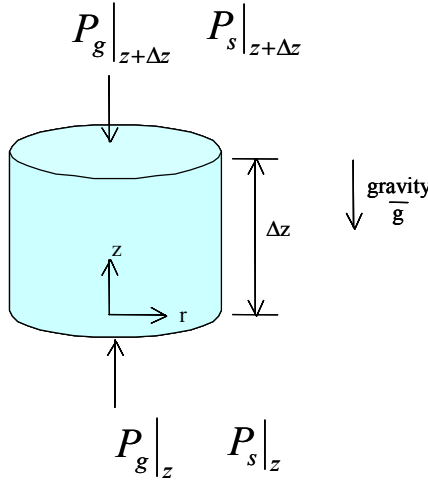


Figure 101: Standpipe Force Balance Shell Balance

The momentum balance is presented by Bird as follows:

{rate of momentum accum.} = {rate of momentum in} - {rate of momentum out} + {sum of forces acting on the system} (Bird, 1960) Each component of the momentum balance in the z-direction will be summarized below:

- {rate of momentum accumulation} = 0. This is due to an assumption of steady state.
- {rate of momentum in} = $(\pi R^2 v_{gz}) (\rho_g \epsilon_g v_{gz})|_{z=z+\Delta z}$
- {rate of momentum out} = $(\pi R^2 v_{gz}) (\rho_g \epsilon_g v_{gz})|_{z=z}$
- {sum of forces action on the system} = {gravity} + {gas-wall shear stress} + {gas-particle drag} + {pressure force acting at $z=z$ } + {pressure force acting at $z=\Delta z$ }

Each force is described as follows:

- {gravity} = $-(\pi R^2 \Delta z) \rho_g \epsilon_g \frac{g}{g_c}$. Note that gravity in the z-direction is negative since the z-axis was defined to be positive up.

- {gas-wall shear stress} = $(2\pi R \Delta z) \tau_{gw}$
- {gas-particle drag} = $-B_A (v_{gz} - v_{sz}) (\pi R^2 \Delta z)$
- {pressure force acting at $z=z$ } = $\pi R^2 P_g \Big|_{z=z}$ Force is acting in the positive z -direction.
- {pressure force acting at $z=z+\Delta z$ } = $-\pi R^2 P_g \Big|_{z=z+\Delta z}$ Force is acting in the negative z -direction.

Placing all the components into the momentum balance gives the following assuming that the gas flows down:

$$0 = (\pi R^2 v_{gz}) (\rho_g \epsilon_g v_{gz}) \Big|_{z=z+\Delta z} - (\pi R^2 v_{gz}) (\rho_g \epsilon_g v_{gz}) \Big|_{z=z} - (\pi R^2 \Delta z) \rho_g \epsilon_g \frac{g}{g_c} + (2\pi R \Delta z) \tau_{gw} +$$

$$- B_A (v_{gz} - v_{sz}) (\pi R^2 \Delta z) + (\pi R^2) P_g \Big|_{z=z} - (\pi R^2) P_g \Big|_{z=z+\Delta z}$$

If ϵ_g is assumed to be constant over Δz , then by the continuity equation and the assumption of steady state, the first two terms cancel out, and the following equation results:

$$0 = -(\pi R^2 \Delta z) \rho_g \epsilon_g \frac{g}{g_c} + (2\pi R \Delta z) \tau_{gw} - B_A (v_{gz} - v_{sz}) (\pi R^2 \Delta z) + (\pi R^2) P_g \Big|_{z=z} - (\pi R^2) P_g \Big|_{z=z+\Delta z}$$

Dividing through by $\pi R^2 \Delta z$ results in the following:

$$0 = -\rho_g \epsilon_g \frac{g}{g_c} + \frac{2\tau_{gw}}{R} - B_A (v_{gz} - v_{sz}) + \frac{P_g \Big|_{z=z} - (\pi R^2) P_g \Big|_{z=z+\Delta z}}{\Delta z}$$

Rearranging and taking the limit as Δz goes to zero gives the following equation.

$$0 = -\rho_g \epsilon_g \frac{g}{g_c} + \frac{2\tau_{gw}}{R} - B_A (v_{gz} - v_{sz}) - \lim_{z \rightarrow 0} \left(\frac{P_g \Big|_{z=z+\Delta z} - P_g \Big|_{z=z}}{\Delta z} \right)$$

$$0 = -\rho_g \epsilon_g \frac{g}{g_c} + \frac{2\tau_{gw}}{R} - B_A (v_{gz} - v_{sz}) - \frac{dP_g}{dz}$$

The first two terms are so small that they can be ignored. As a result, the gas momentum balance is given as follows:

$$0 = -B_A (v_{gz} - v_{sz}) - \frac{dP_g}{dz}$$

A.1.b Solids Momentum Balance:

The derivation of the solids momentum balance follows exactly the derivation of the gas momentum balance.

The momentum balance as presented by Bird is as follows:

{rate of momentum accum.} = {rate of momentum in} - {rate of momentum out} + {sum of forces acting on the system} (Bird, 1960). Each component of the momentum balance in the z-direction will be summarized below.

- {rate of momentum accumulation} = 0. This is due to an assumption of steady state.
- {rate of momentum in} = $(\pi R^2 v_{sz}) (\rho_s \epsilon_s v_{sz}) \Big|_{z=z+\Delta z}$
- {rate of momentum out} = $(\pi R^2 v_{sz}) (\rho_s \epsilon_s v_{sz}) \Big|_{z=z}$
- {sum of forces action on the system} = {gravity} + {solid-wall shear stress} + {particle-gas drag} + {solids pressure force acting at z=z} + {solids pressure force acting at z=Δz}

Each force is described as follows:

- {gravity} = $-(\pi R^2 \Delta z) \rho_s \epsilon_s \frac{g}{g_c}$. Note that gravity in the z-direction is negative since the z-axis was defined to be positive up.
- {solids-wall shear stress} = $(2\pi R \Delta z) \tau_{sw}$
- {particle-gas drag} = $-B_A (v_{sz} - v_{gz}) (\pi R^2 \Delta z)$
- {pressure force acting at z=z} = $\pi R^2 P_s \Big|_{z=z}$ Force is acting in the positive z-direction.
- {pressure force acting at z=z+Δz} = $-\pi R^2 P_s \Big|_{z=z+\Delta z}$ Force is acting in the negative z-direction.

Placing all the components into the momentum balance gives the following:

$$0 = (\pi R^2 v_{sz}) (\rho_s \epsilon_s v_{sz}) \Big|_{z=z+\Delta z} - (\pi R^2 v_{sz}) (\rho_s \epsilon_s v_{sz}) \Big|_{z=z} - (\pi R^2 \Delta z) \rho_s \epsilon_s \frac{g}{g_c} + (2\pi R \Delta z) \tau_{sw} +$$

$$- B_A (v_{sz} - v_{gz}) (\pi R^2 \Delta z) + (\pi R^2) P_s \Big|_{z=z} - (\pi R^2) P_s \Big|_{z=z+\Delta z}$$

If ε_s is assumed to be constant over Δz , then by the continuity equation and the assumption of steady state, the first two terms cancel out, and the following equation results:

$$0 = -(\pi R^2 \Delta z) \rho_s \varepsilon_s \frac{g}{g_c} + (2\pi R \Delta z) \tau_{sw} - B_A (v_{sz} - v_{gz}) (\pi R^2 \Delta z) + (\pi R^2) P_s|_{z=z} - (\pi R^2) P_s|_{z=z+\Delta z}$$

Dividing through by $\pi R^2 \Delta z$ results in the following:

$$0 = -\rho_s \varepsilon_s \frac{g}{g_c} + \frac{2\tau_{sw}}{R} - B_A (v_{sz} - v_{gz}) + \frac{P_s|_{z=z} - (\pi R^2) P_s|_{z=z+\Delta z}}{\Delta z}$$

Rearranging and taking the limit as Δz goes to zero gives the following equation.

$$0 = -\rho_s \varepsilon_s \frac{g}{g_c} + \frac{2\tau_{sw}}{R} - B_A (v_{sz} - v_{gz}) - \lim_{\Delta z \rightarrow 0} \left(\frac{P_s|_{z=z+\Delta z} - P_s|_{z=z}}{\Delta z} \right)$$

$$0 = -\rho_s \varepsilon_s \frac{g}{g_c} + \frac{2\tau_{sw}}{R} - B_A (v_{sz} - v_{gz}) - \frac{dP_s}{dz}$$

Unlike in the gas momentum balance the first term cannot be ignored. The second term is solids-wall shear stress, and is the term under study.

A.1.c Mixture Momentum Balance:

The mixture momentum balance is found simply by adding the gas momentum balance and solids momentum balance. (Gidaspow, 1994)

$$0 + 0 = -B_A (v_{gz} - v_{sz}) - \frac{dP_g}{dz} - \rho_s \varepsilon_s \frac{g}{g_c} + \frac{2\tau_{sw}}{R} - B_A (v_{sz} - v_{gz}) - \frac{dP_s}{dz}$$

Fortunately, the gas-particle drag terms cancel out and the resulting equation is as

$$\text{follows: } 0 = -\frac{dP_g}{dz} - \rho_s \varepsilon_s \frac{g}{g_c} + \frac{2\tau_{sw}}{R} - \frac{dP_s}{dz}$$

A.2 Derivation of Equations For Estimating Shear Stress and Solids Pressure

A.2a Assuming Constant DP_g/L Along the Standpipe

Starting with the microscopic form of the mixture momentum balance below:

$$\frac{\partial P_{sz}}{\partial z} + \frac{\partial P_g}{\partial z} + \frac{2\tau_{sw}}{R} - \rho_s \epsilon_s \frac{g}{g_c} + v_s \epsilon_s \rho_s \frac{dv_s}{dz} = 0$$

Signs are slightly different due to positive z -axis is down in the direction of gravity. See Figure 106.

It is assumed that the solids velocity is not a function of height in the standpipe.

Therefore, the last term is zero.

$$\frac{\partial P_{sz}}{\partial z} + \frac{\partial P_g}{\partial z} + \frac{2\tau_{sw}}{R} - \rho_s \epsilon_s \frac{g}{g_c} = 0$$

From bulk solids mechanics, shear stress is related to the axial solids pressure by the following equation.

$$\tau_{sw} = \frac{\mu_w}{K} P_{sz}$$

Substituting this equation into the into the mixture momentum balance gives

$$\frac{\partial P_{sz}}{\partial z} + \frac{\partial P_g}{\partial z} + \frac{2\mu_w P_{sz}}{RK} - \rho_s \epsilon_s \frac{g}{g_c} = 0$$

Assuming that pressure drop per unit length is constant, the following relationship can be substituted for dP_g/dz . See Figure 102 below.

$$\frac{dP_g}{dz} = \frac{P_1 - P_2}{0 - H} = -\frac{\Delta P_g}{H}$$

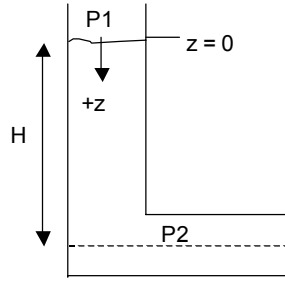


Figure 102: Derivation of Solids Pressure Equation Drawing 1

Substituting this relationship into the mixture momentum balance gives

$$\frac{dP_{sz}}{dz} - \frac{\Delta P_g}{H} + \frac{2\mu_w P_{sz}}{RK} - \rho_s \epsilon_s \frac{g}{g_c} = 0$$

The above equation is integrated from $z = 0$ to $z = z$. Keep in mind that solids pressure is zero at $z = 0$, the top of the bed. This integration is performed using separation of variables below.

Rearranging.

$$\frac{\partial P_{sz}}{\partial z} = \frac{\Delta P_g}{H} - \frac{2\mu_w P_{sz}}{RK} + \rho_s \epsilon_s \frac{g}{g_c}$$

Dividing by dz

$$dP_{sz} = \left(\frac{\Delta P_g}{H} - \frac{2\mu_w}{RK} P_{sz} + \rho_s \epsilon_s \frac{g}{g_c} \right) dz$$

Rearranging

$$\frac{1}{\left(\frac{\Delta P_g}{H} - \frac{2\mu_w}{RK} P_{sz} + \rho_s \epsilon_s \frac{g}{g_c} \right)} dP_{sz} = dz$$

$$\int \frac{1}{\left(\frac{\Delta P_g}{H} - \frac{2\mu_w}{RK} P_{sz} + \rho_s \epsilon_s \frac{g}{g_c} \right)} dP_{sz} = \int dz$$

$$\text{let } u = \frac{\Delta P_g}{H} - \frac{2\mu_w}{RK} P_{sz} + \rho_s \epsilon_s \frac{g}{g_c}$$

$$\frac{du}{dP_{s,z}} = -\frac{2\mu_w}{RK}$$

$$dP_{sz} = -\frac{RK}{2\mu_w} du$$

$$-\frac{RK}{2\mu_w} \int_{u_1}^{u_2} \frac{1}{u} du = \int_0^z dz$$

$$-\frac{RK}{2\mu_w} \ln \frac{u_2}{u_1} = z$$

$$\ln \frac{u_2}{u_1} = -\frac{2\mu_w}{RK} z$$

$$\frac{u_2}{u_1} = e^{-\frac{2\mu_w}{RK} z}$$

$$\frac{u_2}{u_1} = \frac{\frac{\Delta P_g}{H} - \frac{2\mu_w}{RK} P_{sz}|_{z_2} + \rho_s \varepsilon_s \frac{g}{g_c}}{\frac{\Delta P_g}{H} + \rho_s \varepsilon_s \frac{g}{g_c}} = e^{-\frac{2\mu_w}{RK} z}$$

$$\frac{\Delta P_g}{H} - \frac{2\mu_w}{RK} P_{sz}|_{z_2} + \rho_s \varepsilon_s \frac{g}{g_c} = \left(e^{-\frac{2\mu_w}{RK} z} \right) \left(\frac{\Delta P_g}{H} + \rho_s \varepsilon_s \frac{g}{g_c} \right)$$

$$-\frac{2\mu_w}{RK} P_{sz}|_{z_2} = \left(e^{-\frac{2\mu_w}{RK} z} \right) \left(\frac{\Delta P_g}{H} + \rho_s \varepsilon_s \frac{g}{g_c} \right) - \left(\frac{\Delta P_g}{H} + \rho_s \varepsilon_s \frac{g}{g_c} \right)$$

$$P_{sz}|_{z_2} = -\frac{RK}{2\mu_w} \left(e^{-\frac{2\mu_w}{RK} z} \left(\frac{\Delta P_g}{H} + \rho_s \varepsilon_s \frac{g}{g_c} \right) + \frac{RK}{2\mu_w} \left(\frac{\Delta P_g}{H} + \rho_s \varepsilon_s \frac{g}{g_c} \right) \right)$$

$$P_{s,z} = \frac{RK}{2\mu_w} \left[\rho_s \varepsilon_s \frac{g}{g_c} + \frac{\Delta P_g}{H} \right] \left[1 - e^{-\frac{2\mu_w}{RK} z} \right]$$

A.2b Integrating the Mixture Momentum Balance from $z=z_1$ to $z=z_2$

Starting with the microscopic form of the mixture momentum balance below:

$$-\frac{\partial P_{sz}}{\partial z} - \frac{\partial P_g}{\partial z} + \frac{4\tau_{sw}}{D} - \rho_s \varepsilon_s \frac{g}{g_c} + v_s \varepsilon_s \rho_s \frac{dv_s}{dz} = 0$$

It is assumed that the solids velocity is not a function of height in the standpipe. Therefore, the last term is zero.

$$-\frac{\partial P_{sz}}{\partial z} - \frac{\partial P_g}{\partial z} + \frac{4\tau_{sw}}{D} - \rho_s \varepsilon_s \frac{g}{g_c} = 0$$

From bulk solids mechanics, shear stress is related to the axial solids pressure by the following equation.

$$\tau_{sw} = \frac{\mu_w}{K} P_{sz}$$

Substituting this equation into the into the mixture momentum balance gives

$$-\frac{\partial P_{sz}}{\partial z} - \frac{\partial P_g}{\partial z} + \frac{4\mu_w P_{sz}}{DK} - \rho_s \varepsilon_s \frac{g}{g_c} = 0$$

Assuming that pressure drop per unit length is constant, the following relationship can be substituted for dP_g/dz . See Figure 103 below

$$-\frac{dP_g}{dz} = -\frac{P_g|_{z2} - P_g|_{z1}}{z2 - z1} = -\frac{\Delta P_g}{\Delta z}$$

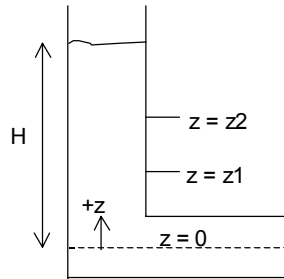


Figure 103: Derivation of Solids Pressure Equation Drawing 2

Substituting this relationship into the mixture momentum balance gives

$$-\frac{dP_{sz}}{dz} - \frac{\Delta P_g}{\Delta z} + \frac{4\mu_w P_{sz}}{DK} - \rho_s \varepsilon_s \frac{g}{g_c} = 0$$

The above equation is integrated from $z = z1$ to $z = z2$. Keep in mind that solids pressure is zero at $z = H$, the top of the bed. This integration is performed using separation of variables below.

Rearranging.

$$\frac{\partial P_{sz}}{\partial z} = -\frac{\Delta P_g}{\Delta z} + \frac{4\mu_w P_{sz}}{DK} - \rho_s \varepsilon_s \frac{g}{g_c}$$

Dividing by dz

$$dP_{sz} = \left(-\frac{\Delta P_g}{\Delta z} + \frac{4\mu_w}{DK} P_{sz} - \rho_s \varepsilon_s \frac{g}{g_c} \right) dz$$

Rearranging

$$\frac{1}{\left(-\frac{\Delta P_g}{\Delta z} + \frac{4\mu_w}{DK} P_{sz} - \rho_s \varepsilon_s \frac{g}{g_c} \right)} dP_{sz} = dz$$

$$\int \frac{1}{\left(-\frac{\Delta P_g}{\Delta z} + \frac{4\mu_w}{DK} P_{sz} - \rho_s \varepsilon_s \frac{g}{g_c} \right)} dP_{sz} = \int dz$$

$$\text{let } u = -\frac{\Delta P_g}{\Delta z} + \frac{4\mu_w}{DK} P_{sz} - \rho_s \varepsilon_s \frac{g}{g_c}$$

$$\frac{du}{dP_{s,z}} = \frac{4\mu_w}{DK}$$

$$dP_{sz} = \frac{DK}{4\mu_w} du$$

$$\frac{DK}{4\mu_w} \int_{u_1}^{u_2} \frac{1}{u} du = \int_{z_1}^{z_2} dz$$

$$\frac{DK}{4\mu_w} \ln \frac{u_2}{u_1} = (z_2 - z_1)$$

$$\ln \frac{u_2}{u_1} = \frac{4\mu_w}{DK} (z_2 - z_1)$$

$$\frac{u_2}{u_1} = e^{\frac{4\mu_w(z_2-z_1)}{DK}}$$

$$\frac{u_2}{u_1} = \frac{-\frac{\Delta P_g}{\Delta z} + \frac{4\mu_w}{DK} P_{sz} \Big|_{z=z_2} - \rho_s \varepsilon_s \frac{g}{g_c}}{-\frac{\Delta P_g}{\Delta z} + \frac{4\mu_w}{DK} P_{sz} \Big|_{z=z_1} - \rho_s \varepsilon_s \frac{g}{g_c}} = e^{\frac{4\mu_w(z_2-z_1)}{DK}}$$

$$-\frac{\Delta P_g}{\Delta z} + \frac{4\mu_w}{DK} P_{sz}|_{z=z_1} - \rho_s \epsilon_s \frac{g}{g_c} = \left(e^{\frac{-4\mu_w}{DK}(z_2-z_1)} \right) \left(-\frac{\Delta P_g}{\Delta z} + \frac{4\mu_w}{DK} P_{sz}|_{z=z_2} - \rho_s \epsilon_s \frac{g}{g_c} \right)$$

$$\frac{4\mu_w}{DK} P_{sz}|_{z=z_1} = \left(e^{\frac{-4\mu_w}{DK}(z_2-z_1)} \right) \left(-\frac{\Delta P_g}{\Delta z} + \frac{4\mu_w}{DK} P_{sz}|_{z=z_2} - \rho_s \epsilon_s \frac{g}{g_c} \right) - \left(-\frac{\Delta P_g}{\Delta z} - \rho_s \epsilon_s \frac{g}{g_c} \right)$$

$$P_{sz}|_{z=z_1} = \frac{DK}{4\mu_w} \left(e^{\frac{-4\mu_w}{DK}(z_2-z_1)} \right) \left(-\frac{\Delta P_g}{\Delta z} + \frac{4\mu_w}{DK} P_{sz}|_{z=z_2} - \rho_s \epsilon_s \frac{g}{g_c} \right) - \frac{DK}{4\mu_w} \left(-\frac{\Delta P_g}{\Delta z} - \rho_s \epsilon_s \frac{g}{g_c} \right)$$

A.3 Bulk Solids Mechanics

This section discusses bulk solids mechanics and the derivation of equations (22) thru (27). McCabe (1993) listed distinctive properties of solids:

1. Solids exert pressure, which is not the same in all directions. The pressure is a minimum at right angles to the direction it is applied.
2. Shear stress applied to the surface of a static mass is transmitted throughout the mass until failure occurs.
3. The density of the mass depends on the packing (solids volume fraction)
4. Before a mass of tightly packed particles can flow, it must expand to permit interlocking particles to move past one another.

McCabe (1993) also discussed the two classes of particulate solids, cohesive and noncohesive. Noncohesive materials readily flow, and cohesive solids are more resistant to flow. Some examples of noncohesive materials are dry sand and grain. An example of cohesive materials is clay.

Number (4) above suggests that the pressure normal to the applied is the minimum pressure. McCabe suggests that the ratio of the applied to normal pressure is a constant K' , and that this constant is a function of material properties such as shape and stickiness. Consider the right-angled triangular differential section of thickness, b , and hypotenuse, dL in Figure 104 below.

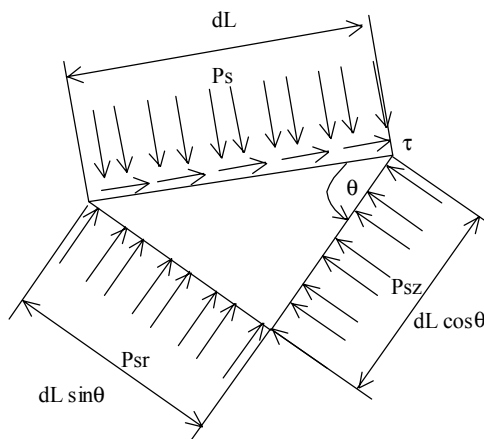


Figure 104: Differential Triangular Element

The applied pressure is P_{sz} and the normal pressure is P_{sr} . P_s is the pressure at any intermediate angle, and τ is the shear stress necessary to keep the element from rotating. The element and the forces resulting from the pressures and stresses are shown in Figure 105.

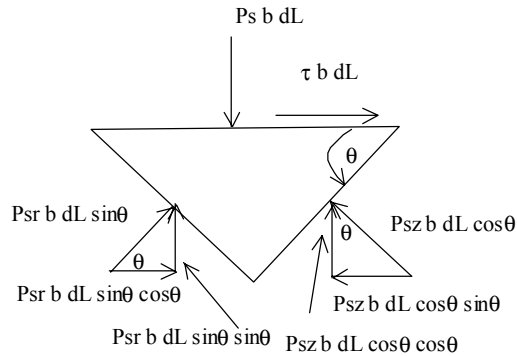


Figure 105: Differential Element and Resulting Forces

Equating the components at right angles to the hypotenuse gives the following:

$$P_s b dL = P_{sr} b dL \sin^2 \theta + P_{sz} b dL \cos^2 \theta$$

Dividing by $b dL$ gives the following

$$P_s = P_{sr} \sin^2 \theta + P_{sz} \cos^2 \theta$$

Note that $\sin^2 \theta = 1 - \cos^2 \theta$

$$P_s = P_{sr} (1 - \cos^2 \theta) + P_{sz} \cos^2 \theta$$

$$P_s = (P_{sz} - P_{sr}) \cos^2 \theta + P_{sr}$$

Equating forces parallel to the hypotenuse gives the following:

$$\tau b dL = P_{sz} b dL \cos \theta \sin \theta - P_{sr} b dL \sin \theta \cos \theta$$

dividing by $b dL$

$$\tau = (P_{sz} - P_{sr}) \sin \theta \cos \theta$$

If all corresponding values of P_s and τ are plotted for all θ , then a Mohr circle results.

This circle has a radius of $(P_{sz} - P_{sr})/2$, and its horizontal center is at $P_s = (P_{sz} + P_{sr})/2$.

See Figure 106 below.

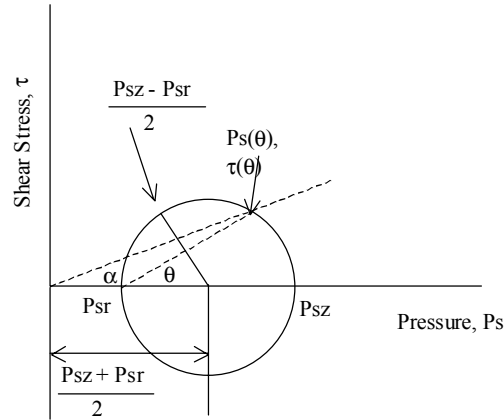


Figure 106: Mohr Stress Circle for Particulate Solids 1

Looking at Figure 106, it is evident that when θ is zero degrees, P_s is P_{sz} and shear stress is zero. Also, when θ is 90 degrees, P_s is P_{sr} and shear stress is zero. For an intermediate value of θ , there is a corresponding P_s and shear stress. The ratio of τ to P_s at any value of θ is the tangent of the angle, α . This angle is formed by a line drawn from the origin to the corresponding point on the Mohr circle with the x-axis. As θ is increased, this ratio increases to a maximum at which point the line through the origin is tangent to the Mohr circle after which point the ratio decreases. Figure 107 shows this maximum point.

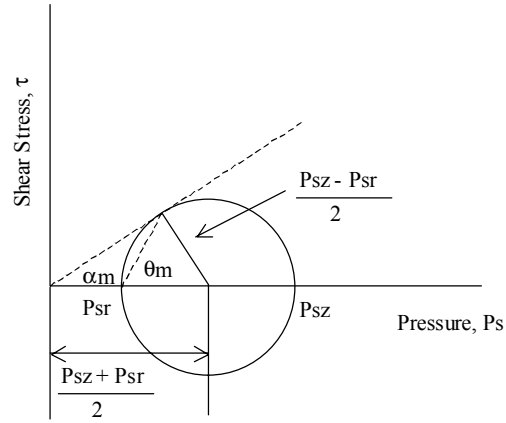


Figure 107: Mohr Stress Circle for Particulate Solids Maximum Ratio of τ to P_s

$$\text{From Figure 107, } \sin \alpha_m = \frac{(P_{sz} - P_{sr})/2}{(P_{sz} + P_{sr})/2} = \frac{P_{sz} - P_{sr}}{P_{sz} + P_{sr}}$$

$$\text{Let } \frac{P_{sr}}{P_{sz}} = K. \text{ Then, } P_{sr} = KP_{sz}$$

$$\sin \alpha_m = \frac{P_{sz} - KP_{sz}}{P_{sz} + KP_{sz}} = \frac{P_{sz}((1 - K))}{P_{sz}((1 + K))} = \frac{1 - K}{1 + K}$$

$$\sin \alpha_m = \frac{1 - K}{1 + K}$$

$$1 - K = (1 + K)\sin \alpha_m = \sin \alpha_m + K \sin \alpha_m$$

$$1 - \sin \alpha_m = K + K \sin \alpha_m = K(1 + \sin \alpha_m)$$

$$K = \frac{1 - \sin \alpha_m}{1 + \sin \alpha_m}$$

The tangent of the internal angle of friction is the coefficient of friction between two layers of particles.

NOMENCLATURE

A	Surface area of the control volume
B_A	Drag
CV	Control Volume
CS	Control Surface
D	Diameter of the standpipe
d	Displacement distance for the bending tube in the wall probe
d_p	Particle diameter
E	Modulus of elasticity
F	Total Force applied to the control volume
F	Total force applied to the free end of the bending tube in the wall probe
F_m	Aeration rate at 0.3' in the standpipe
F_z	Forces in the z-direction
e	Coefficient of restitution for particle-particle collisions
g	Acceleration due to gravity
g_c	Universal gravitational constant
g_o	Radial distribution function
H	Height of the bed in the standpipe
I	Moment of inertia
1/K	Janssen coefficient
K_p	Particle dielectric constant
K_h	Dielectric constant of host material (air)
K_{eff}	Effective Dielectric constant of the suspension
L	Length of the control volume, or the length of the bending tube in the wall probe
\dot{m}_g	Mass flowrate of gas phase
\dot{m}_s	Mass flowrate of solids phase
P_1	Gas phase pressure at the top of the standpipe
P_2	Gas phase pressure at the bottom of the standpipe
P_g	Gas phase pressure
P_s	Solids phase pressure

P_{sz}	Solids phase pressure in the axial direction
P_{sr}	Solids phase pressure in the radial direction
T_s	Granular Temperature
U_g	Gas phase velocity
U_s	Solids phase velocity
U_{sl}	Slip velocity
U_{mf}	Superficial minimum fluidization velocity
V	Volume of control volume
V	Voltage response to suspension
V_{bed}	Volume of the bed
V_0	Voltage response due to air
v_{gz}	Gas phase velocity in the axial direction
\vec{v}_g	Gas phase velocity vector
\vec{v}_s	Solids phase velocity vector
v_{sz}	Solids phase velocity in the axial direction
R	Radius of standpipe
r_o	Outside radius of the bending tube in the wall probe
r_i	Inside radius of the bending tube in the wall probe
x	distance from the fixed end of the tube to the estimation of “d” for the bending tube in the wall probe
z	axial direction
z_1	Top of standpipe section measured down from the top of the bed
z_2	Bottom of standpipe section measured down from the top of the bed
α	Resistance of the material to flow
δ	Effective internal angle of friction
δ_w	External angle of friction
ΔP	Total pressure drop across the standpipe
ϵ_c	Vibrated void fraction
ϵ_g	Void fraction
ϵ	Void fraction
ϵ_{mf}	Void fraction at minimum fluidization

ϵ_s	Volume fraction of the solids phase
ρ_b	Bulk density
ρ_g	Density of gas phase
ρ_s	Density of solids phase
τ_{sw}	Solids wall shear stress
τ_{gw}	Gas wall shear stress
μ_w	Coefficient of friction between solid and wall surface

REFERENCES

- Bird, R.B., W.E. Stewart, and E.N. Lightfoot. *Transport Phenomena*. New York: John Wiley & Sons (1960).
- Brown, R.L., J.C. Richards. *Principles of Powder Mechanics*. Oxford: Pergamon Press (1970).
- Doebelin, Ernest O. *Measurement Systems Application and Design 3rd Edition*. New York: McGraw-Hill Book Company (1983).
- Geankoplis, Christie J. *Transport Process and Unit Operations 3rd Edition*. Englewood Cliffs, NJ: PTR Prentice Hall (1993)
- Gidaspow, Dimitri. *Multiphase Flow and Fluidization Continuum and Kinetic Theory Descriptions*. San Diego, California: Academic Press, Inc (1994).
- GRANORTE - Revestimentos de Cortiça, Lda. "Properties of Cork," <http://www.granorte.pt/properties.htm> (2001).
- Higdon, Archie, Edward Ohlsen, William Stiles, John Weese, William Riley. *Mechanics of Materials Fourth Edition*. New York: John Wiley & Sons (1985).
- Knowlton, T.M. "Standpipes," in D. Geldart. *Gas Fluidization Technology*. Chichester, New York: John Wiley and Sons Ltd. (1986).
- Jones, P.J. and L.S. Leung. "Downflow of Solids through Pipes and Valves," in J.E.Davidson. *Fluidization second Edition*. London: Academic Press (1985).
- Louge, Michel. "Measuring particle concentration with capacitance probes," provided by Capacitech Inc. (1992).
- Louge, Michel, Mark Tuccio, Eduardo Lander, and Patric Connors. "Capacitance measurements of the volume fraction and velocity of dielectric near a grounded wall," *Rev. Sci. Instrum.*, Vol. 67, No.5, May, pp. 1869-1877 (1996).
- Leung, L.S. and Robert J. Wiles. "A Quantitative Design Procedure for Vertical Pneumatic Conveying Systems," *Ind. Eng. Chem., Process Des. Dev.*, Vol. 15, No. 4, pp. 552-557 (1976).
- Ludlow, J. Christopher, Lawrence J. Shadle, and Madhava Syamlal. (2002). "Development of Spiral Device for Measuring Solids Flow," to be presented at the 7th International Conference on Circulating Fluidized beds, (2002).

- Matsen, J.M. “Some Characteristics of Large Solids Circulation Systems,” in D.L. Keairns. *Fluidization Technology Vol II*. Washington, D.C.: Hemisphere Publishing Corporation, pp. 135-149 (1976).
- McCabe, Warren L., Julian C. Smith, and Peter Harriott. *Unit Operations of Chemical Engineering*. New York: McGraw-Hill, Inc. (1993).
- Miller, A. and D. Gidaspow. “Dense, Vertical Gas-Solids Flow in a Pipe,” *AIChE Journal*. 1992, 38, 1801 (199).
- Mountziaris, Triantafillos and Roy Jackson. “The Effects of Aeration on the Gravity Flow of Particles and Gas in Vertical Standpipes,” *Chemical Engineering Science*, Vol. 46, No.2 pp. 381-407 (1990).
- Picciotti, Marcello. “Specify standpipes and feeder valves for packed beds,” *Chem. Eng. Prog.* 91(1),54-63 (1995).
- Polashenski, William Jr., and John C. Chen. “Measurement of Particle Phase Stresses in Fast Fluidized Beds,” *Ind. Eng. Chem. Res.*, 38, 705-713 (1999).
- Shadle, Lawrence J., J. Christopher Ludlow, Larry O. Lawson, and Esmail R. Monazam. “Transport Reactor studies in FETC’s Cold Flow Circulating Fluid Bed,” Transport Reactor Cooperative Research and Development Agreement Report. CRADA NO. 98-F015, December 1999
- SPSS Inc., *Trial Run 1.0 User’s Guide*. (1997).
- Schmidt, Stephen, and Robert Launsby. *Understanding Industrial Designed Experiments*. Colorado Springs, Colorado: Air Academy Press (1998).
- Schulze, Dietmar. “Fundamentals of Bulk Solids Mechanics,” <http://www.dietmar-schulze.de/grdle1.html> (2000).
- Stermerding, S. “The pneumatic transport of cracking catalyst in vertical risers,” *Chemical Engineering Science*, 1962, 17, 599-608 (1962).
- Von Hippel, Arthur. *Dielectric Materials and Applications*. Cambridge, Massachusetts: The MIT Press (1954)
- Zenz, Frederick A. and Donald F. Othmer. *Fluidization and Fluid-Particle Systems*. New York: Reinhold publishing Corporation (1960).

**UNIVERSITY/NETL STUDENT PARTNERSHIP PROGRAM
(DE-FC26-98FT40143)**

3rd Year Technical Report

September 1, 2000 – August 31, 2001

Submitted to:

National Energy Technology Laboratory

Submitted by:

**Gerald D. Holder
School of Engineering
University of Pittsburgh
Pittsburgh, PA 15261**

Volume IV of VI

**XV. “Application Evaluation of a Prototype
Backscatter Imaging LDV system (BILS)”**

**Preetanshu Pandey (S) and Richard Turton (F), West Virginia University
with
Lawrence Shadle (M), NETL**

Application Evaluation of a prototype Backscatter Imaging

LDV system (BILS)

by

Preetanshu Pandey

Annual report

Master of Science
in
Chemical Engineering

WVU Advisor : Dr. Richard Turton
NETL mentor : Dr. Lawrence Shadle
NETL advisor : Dr. Paul Yue

Funding : University/NETL Student Partnership program

Department of Chemical Engineering

Morgantown, West Virginia
2001

Abstract

This study focuses on the application evaluation of a prototype backscatter imaging LDV system (BILS). Its ability to measure velocity and size of particles in a cold flow circulating fluidized bed (CFB) is to be tested. A series of validation tests were conducted for velocity measurements. A set-up involving a wire (acting as a particle) attached to a rotating disc was constructed. The velocity values measured from the instrument were in good agreement with the theoretical values.

Some pre-scaled targets will be used to calibrate the imaging part of the instrument. Terminal velocity and size measurements will be made to characterize different materials used in a CFB. After this, size and velocity data will be recorded for a 50 ft high riser section of a CFB located at NETL, Morgantown. This will be done for various operating conditions and at different axial-locations.

Table of Contents

Section 1: Introduction	1
Section 2: Literature Survey	3
2.1 Previous uses of a Laser Doppler Velocimeter	3
2.2 Use of a Laser Doppler Velocimeter on a Circulating Fluidized Bed	6
Section 3: Experimental Set-up and Procedure	11
3.1 Experimental Set-up	11
3.2 The Components and Operating Principles	12
3.2.1 Main Components of the Instrument	12
3.2.2 Basic Operating Principles of the Instrument	19
3.3 Capabilities and Limitations of the Equipment	21
3.4 Results and Discussion of Work Performed to Date	23
Section 4: Safety Considerations	26
Section 5: References	27
Section 6: List of Acronyms and Abbreviations	29

List of graphical materials

Figures		Page
1	Particle axial velocity at center of the pipe and $Z/H = 0.5$, $U_g = 1\text{m/s}$, Van den Moortel, 1998	8
2	Mean air-velocity distribution in the presence of 1 mm particles, Tsuji et al., 1984	9
3	Radial mean velocity profiles, Arastoopour et al., 1997	10
4	Set-up for instrument's data validation	11
5	The circulating fluidized bed set-up	13
6	Backscatter Imaging LDV System (BILS)	14
7	The BILS instrument set-up at NETL location, Morgantown	18
8	Basic operating principle of LDV part of the instrument	20
9	Velocity data of BILS for 1 mm and 0.5 mm diameter wire	24
10	Velocity data at various positions of wire diameter = 0.5 mm in the measurement volume	24

1. Introduction

The present study will focus on the application and evaluation of a prototype backscatter imaging laser Doppler velocimetry (LDV) system (BILS). This instrument is developed by TSI Inc., MN. The goal of this study is to test its ability to measure the velocity as well as the particle size in a circulating fluidized bed. Before using this instrument on a large-scale bed, a series of validation experiments will be conducted in order to assess the operation of the instrument and the software associated with it. A separate test will be conducted to validate the data obtained from the instrument.

The instrument will be used to study the size and velocities of particles in a small scale circulating fluidized bed (CFB). An important parameter to be studied is the ability of the laser beam to penetrate the bed and to take velocity measurements not only near the wall but also away from it. An analysis showing the laser penetration ability as a function of bed density will be made. This will be achieved by taking velocity measurements in the riser section of the CFB at various radial positions as a function of the bed density.

Measurements of the particle size and terminal velocities of various types of materials will be made. Particles will be allowed to fall freely in the standpipe section of the CFB and velocity measurements will be carried out at different axial locations. Terminal velocity calculations will be used to validate the instrument's readings. A

comparison will be made between the velocity values predicted from theoretical models, for a particular size of particles, and the values obtained from the instrument.

The backscatter imaging LDV system (BILS) incorporates and extends the particle velocity measurement ability of the laser Doppler velocimeter (LDV) with the ability to measure particle size. The combined measurement of particle size and velocity allows the user to construct the particle size-velocity correlation. In this sense, the BILS may appear to function like a phase Doppler particle analyzer (PDPA). However, this is not the case. In fact, BILS and PDPA serve mutually exclusive applications. PDPA requires the particle to be homogeneous and smooth (usually spherical) in order to obtain a meaningful measurement. On the other hand, BILS requires the particles to have rough surfaces in order to obtain non-specular scattering. In addition to obtaining particle size and velocity data, BILS provides particle shape information, such as aspect ratio and circularity, TSI Inc. Manual [2000a]. This is an added advantage over a conventional PDPA.

2. Literature Survey

Gas-solid circulating fluidized beds (CFB's) are used widely in many processes in the petroleum and chemical industries and find major application in fluidized catalytic cracking units (FCC). Due to development of highly active catalysts, circulating fluidized beds replaced bubbling beds in the Petroleum Industry. The presence of the dispersed phase, i.e., solid particles, bubbles and droplets, not only have an effect on the flow patterns of the continuous phase (gas in a CFB), but also on the heat, mass and momentum transfers. Thus characteristics of the dispersed phase, such as size and velocity, as well as the continuous phase, directly affect the performance of the bed, Arastoopour et al. [1997]. A large amount of effort has been extended to model these systems in order to study parameters like the concentration profiles, velocity profiles, and size distribution at the walls and inside the bed. This information is critical to solve the momentum balance. Such measurements have been made using a laser Doppler velocimeter, Thompson and Stevenson [1978].

2.1 Previous Uses of Laser Doppler Velocimeter

The use of laser Doppler velocimetry (LDV) for flow measurement was first demonstrated in 1964, Menon [1982]. Since that time, it has evolved from a laboratory instrument into a practical tool for research and industrial use. The LDV's obvious advantage is its ability to make measurements without perturbing the flow under conditions where other instruments provide questionable results or cannot be used. All the flow field characteristics are retained and hardly any calibration is required. Flow

velocity is measured directly and is not strongly dependent on the temperature, density, or composition of the flow medium. Although the basic principles of LDV are easy to understand, proper interpretation of the data is sometimes difficult.

The LDV made its debut in 1964 with the appearance of the classic paper by Yeh and Cummins, Durst et al. [1981]. They presented the basic theory for a reference-beam LDV and included excellent data obtained for the laminar velocity profile in a circular tube. The instrument capabilities increased and commercial devices became available as more applications for this instrument were realized. In early investigations, it was often a major accomplishment to obtain a reasonably good Doppler signal. Currently, the problem is often what to do with the massive amount of data that can be generated in a short time, Thompson and Stevenson, [1978].

For many years the fundamental concept of a frequency shift in radiation received from a moving body by a stationary detector has been understood, and used in the communication and astronomy industries. The equation relating the measured frequency difference, ν_D , to the instantaneous velocity can be derived from the Doppler-shift of scattered radiation, from fringe considerations, or from wave theory. It is of the form:

$$\mathbf{n}_D = const * V_p \quad (1)$$

and shows a linear relationship between the frequency difference and the instantaneous velocity (V_p). After the first work by Yeh and Cummins [1964], much progress has been made on the subject. The research effort in laser-Doppler anemometry has thus been directed towards applying a familiar principle in a new way to coherent light sources.

Currently, many pre-aligned optical systems are available and they also are adaptable to different flow situations, Durst et al. [1981].

There are three kinds of optical arrangement modes that are used, reference-beam, dual-beam, and the two-scattered beam. The third type is rarely used in commercial device. The earlier LDV's used the reference beam technique where the reference beam is split into an intense scattering beam and a weak reference beam. The frequency of the scattered beam is altered by the Doppler effect, and its combination with the reference beam gives rise to a frequency difference, which is proportional to the particle velocity, Durst et al. [1981]. The dual-beam mode is the most widespread because of its simplicity. The two coherent beams interfere to produce fringes in the intersection region. A small particle crossing the fringe pattern scatters light, producing intensity fluctuations at a frequency corresponding to the rate at which the fringes are crossed. The particle scatters the Doppler-shifted light from each beam into the detector. The two optical frequencies are mixed to give a beat note. The frequency will depend on the fringe spacing and the velocity component, Kaufman [1986].

There are two kinds of scattering currently used. These are the forwardscatter mode and the backscatter mode. Previously, the forwardscatter mode was predominantly used, since the signals from the backscatter mode were very weak. Generally, forward scattering is used when the particles are transparent and the receiving probe is on the other side of the emitting probe. Whereas the backscatter mode has the receiving probe on the same side. This helps in implementing the method when access to the flow is

limited to one side. The basic optical principle involved behind the forwardscatter is refraction and that for the backscatter is reflection.

The introduction of the dual beam mode, Thompson and Stevenson [1978], has increased the use of the backscatter arrangement, so that only one-sided optical access to the flow is needed. Flow measurements in large wind tunnels, rotating machinery and combustion chambers are routinely done in the backscatter mode. BILS is also based on the backscatter mode and is an even more advanced version of the instrument in the sense that the transmitter and the receiver probes, which are two separate entities in a LDV, are combined in a single probe called the transceiver. This requires only one optical port access to the flow region and also gives a very light and compact design.

The potential applications of the technique range from very low velocity measurements, as in blood flow and other biological flows, to measurements in chemical reacting flows, hypersonic flows, and flows within blade rows in rotating machinery, Menon [1982]. Much research has been done to study the aerodynamic properties of aircraft and land vehicles and to design more efficient turbines and internal combustion engines.

2.2 Use of a Laser Doppler Velocimeter on a Circulating Fluidized Bed

The application of interest in this study is the use of LDV measurements with a BILS instrument along with the particle size measurements in a Circulating Fluidized Bed. Some research has been done in the analysis of the gas-particle flow using a phase-

Doppler particle analyzer (PDPA). The differences in PDPA and BILS have already been discussed. The different flow regimes obtained in a CFB depend on the operating parameters, e.g., the superficial velocity, physical properties of both the phases, solid size distribution, shape and size (diameter) of the riser.

In the upper region of the riser section, the solid volume fraction is lower and decreases with height. Rhodes and Geldart (1986) observed an exponential decay of the solid concentration with height. Monceaux et al. (1985) showed that a characteristic flow regime in CFB was a core-annulus configuration in the dilute zone of the riser. The riser bed in the dilute region is described as a rapidly-rising dilute suspension core zone surrounded by a slower falling suspension near the riser walls.

The LDV is able to characterize the velocity profiles in the gas-solid (diphasic) flow system in CFB. Tadrict and Cattiuw [1993] used a phase Doppler particle analyzer (PDPA) in the dilute zone of the CFB riser to determine solid size, velocity profiles, and local mass fluxes. Van den Moortel et al. [1998] used a one dimensional PDPA and measured the hydrodynamic characteristics of the solid phase (size, axial and transversal velocities) at various heights in the riser. Their study showed a segregation phenomenon and typical velocity profiles for the gas-solid flow in a CFB. They used a CFB with a square cross-section in order to ensure a good quality optical signal for their LDV. Their instrument used a transmitter and a receiver as two separate probes and therefore optical alignment was difficult. This problem is eliminated in the BILS to be used in the current work. Their experiments were carried-out in the dilute zone of the gas-particle flow,

where the solid volume fraction does not exceed 1.5%. The riser used was 2 m high with a 0.2 square meter cross-section. A typical velocity profile from their work is shown in Figure 1 where V_{pax} is the particle axial velocity in m/s and N is the number of particles validated during the acquisition period.

Tsuji et al., [1984] used a LDV to make measurements of velocity in a vertical pipe having two-phase flow. They used a dual beam forward scattering mode with a 15mW He-Ne laser and a 100 mm focal length lens. A typical graph for the velocity profile for 1 mm particles, that they generated, is shown in Figure 2, where m is defined as the particle-to-air-mass-flow-rate, u_c is the velocity at the pipe center, D is the diameter of the pipe and r is the radial distance from the center.

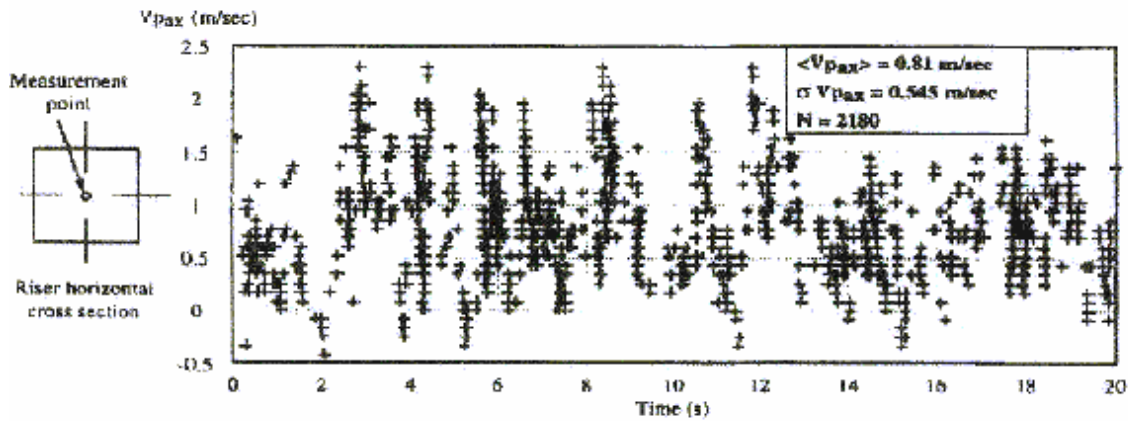


Figure 1. Particle axial velocity at center of the pipe and $Z/H = 0.5$, $U_g = 1\text{m/s}$, Van den Moortel, [1998]

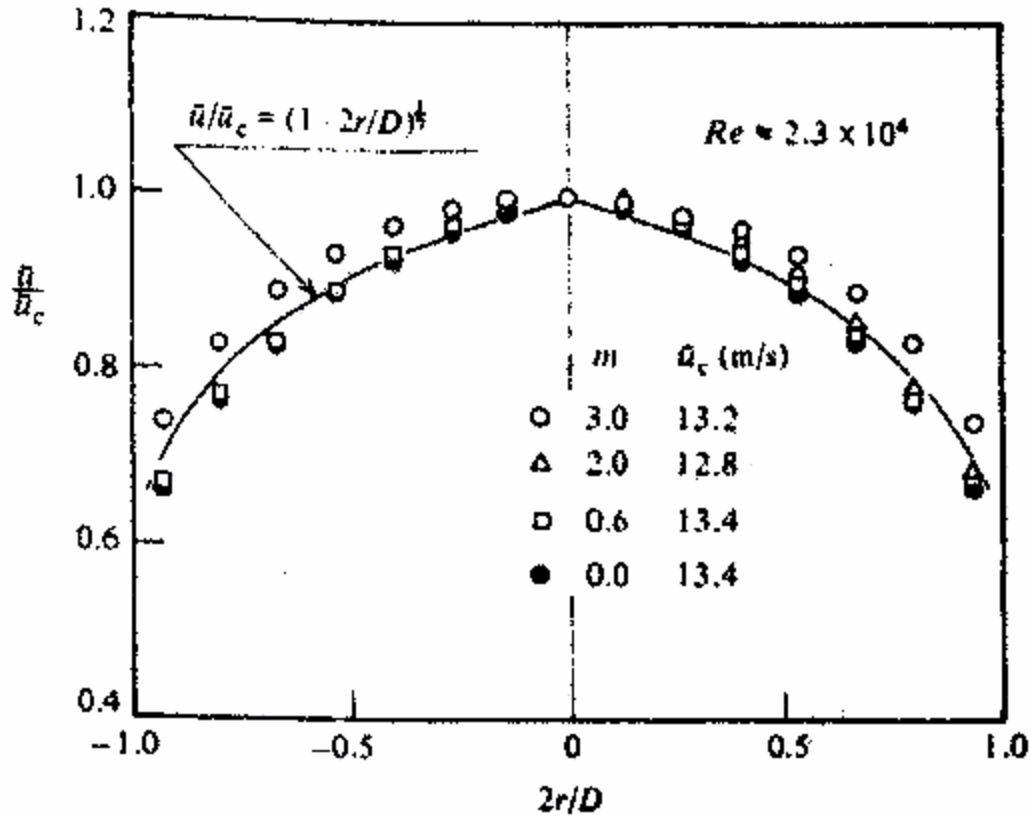


Figure 2. Mean air-velocity distribution in the presence of 1 mm particles [Tsuji et al., 1984]

Arastoopour et al., [1997] used a laser Doppler anemometer (LDA) to obtain velocity profiles in a CFB. The solid volume concentration used was below 3%. The riser was a 9 ft high, PVC pipe with a 5 cm ID. Figure 3 shows the radial mean velocity at different superficial gas velocities, where D_p is the particle diameter. At low gas velocity, the mean particle velocities approached zero between $r/R = 0.85$ and the wall. At the wall boundary an instantaneous reversal of flow was observed. A decrease in the wall boundary region with increase in gas velocity was attributed to an increase in the number of collisions between the particles at the wall region and particles in the core region.

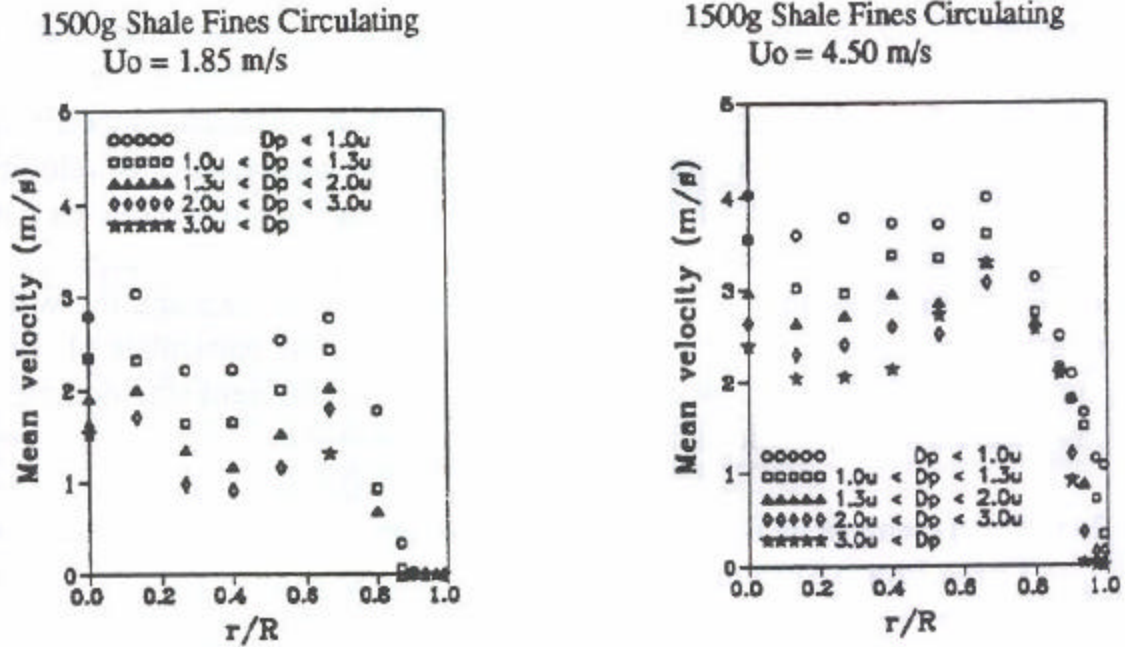


Figure 3. Radial mean velocity profiles [Arastoopour et al., 1997]

The study here will concentrate on establishing velocity profiles in a CFB riser using a two-dimension backscatter imaging LDV system (BILS). A size-velocity correlation will be constructed using the particle sizing capability of BILS.

3. Experimental Set-up and Procedure

3.1 Experimental Set-up

To validate the instrument's method of velocity measurement, the following set-up was implemented. A wire was attached to the rim of a rotating wheel whose rotation speed was known. It was possible to calculate the velocity of the wire, by knowing the radial distance of the wire from the center ($v = r \omega$). The wire is attached perpendicularly to the plane of the rotating wheel (Figure 4). Each time the wire passes through the measurement volume, formed by the intersection of the lasers, the BILS measures and records a velocity datum point. This value can then be compared to the theoretical value to validate the measurement method. The key variables in this set of experiments were the rotation speed, the diameter of wire, and the position of wire in the measurement volume.

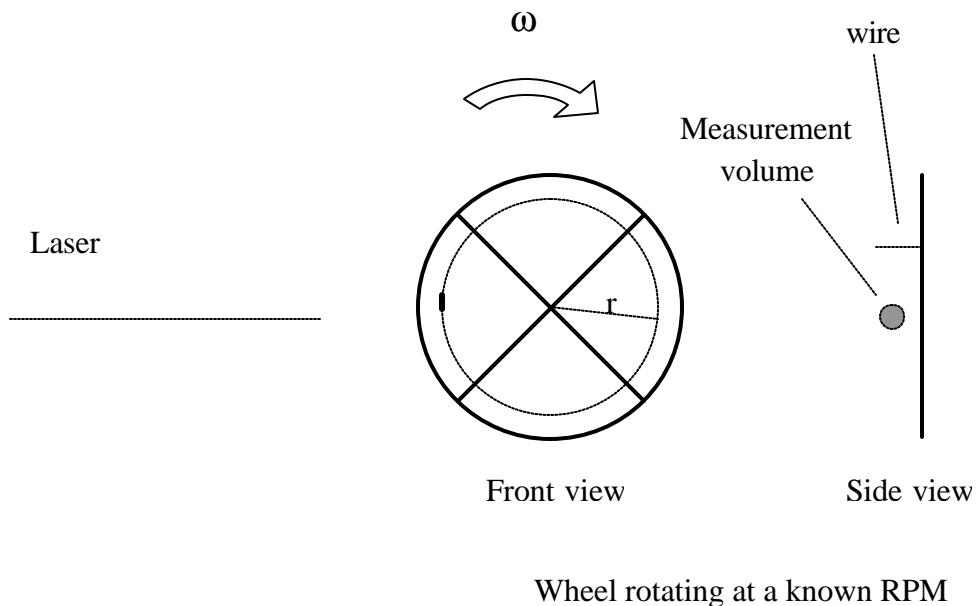


Figure 4. Set-up for instrument's data validation

After validation, the instrument will be used to measure particle velocity and size in a small scale CFB. The basic structure of the fluidization loop used for the present work is shown in Figure 5. This small-scale set-up will be used to understand further the operation of the instrument. It will also be used to evaluate the laser's penetration ability in the fluidized bed. This set-up is much smaller than the full-scale set-up that has a riser section 12 inches in diameter and 50 feet tall. The small-scale set-up has a riser section 5.5 feet tall with a diameter of 2.25 inches. The standpipe section is smaller and is 1.25 inches in diameter. The particles used in the work will be cork that has a particle density of 13.36 lb/ft³ and a diameter of approximately 1000 microns.

3.2 The Components and Operating Principles

3.2.1 Main Components of the Instrument

BILS consists of two main components: the LDV and the imaging system. The LDV used here is different from the conventional LDV in the sense that it has both the probes (transmitter and the receiver) combined into one single probe called the transceiver.

An overview of the various optical and electronic hardware components involved is illustrated in Figure 6. The first component is the argon ion laser that is a source of the beam. The laser used in this work is a Class IV argon ion laser. It is an air-cooled, continuous laser and has a peak power output of 750 mW. Proper safety precautions must be taken to deal with a Class IV laser. The laser beam is directed to a 2-D fiber drive. The fiber drive manipulates the laser beam before directing the beams into single-mode fibers,

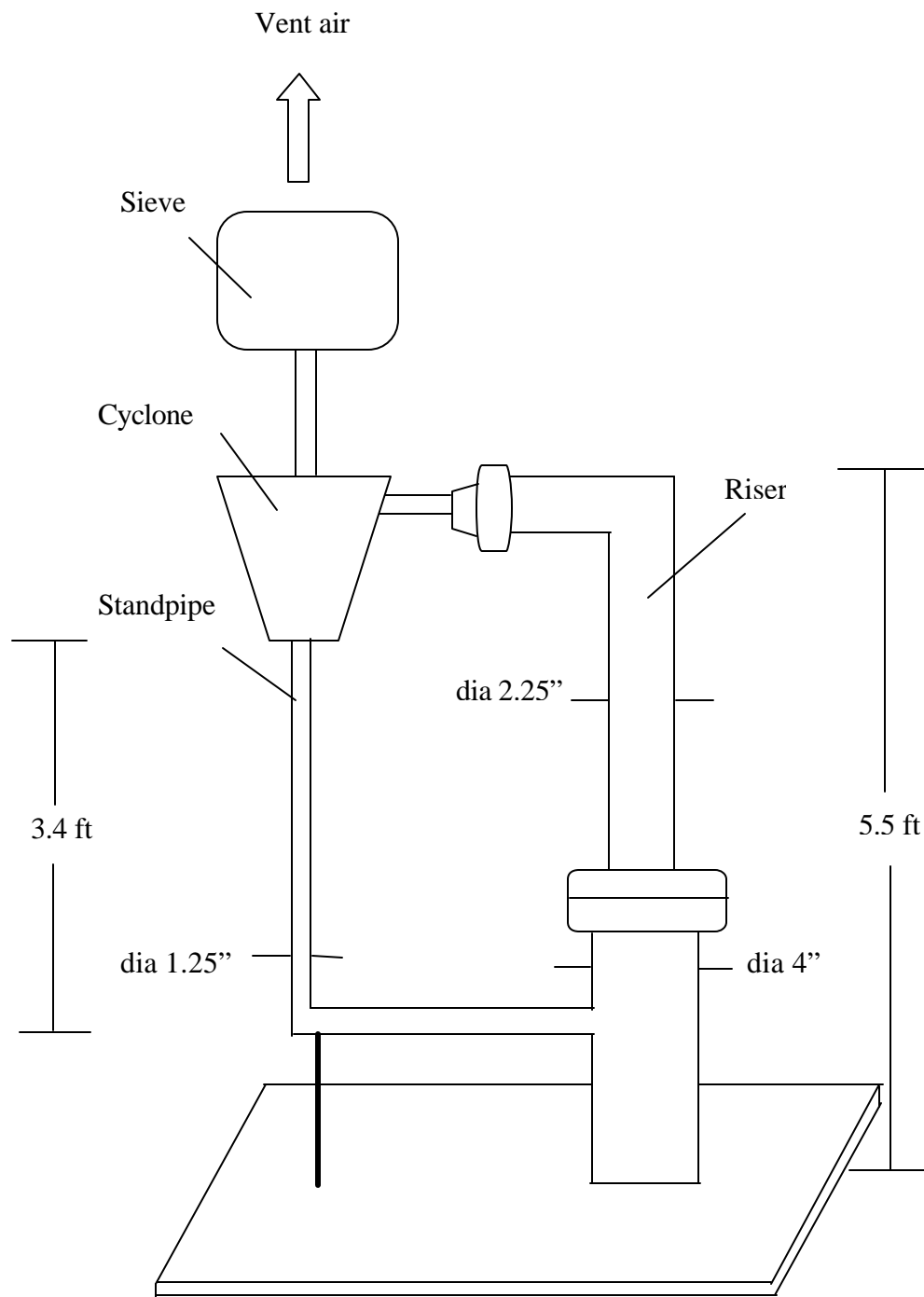


Figure 5. The circulating fluidized bed set-up

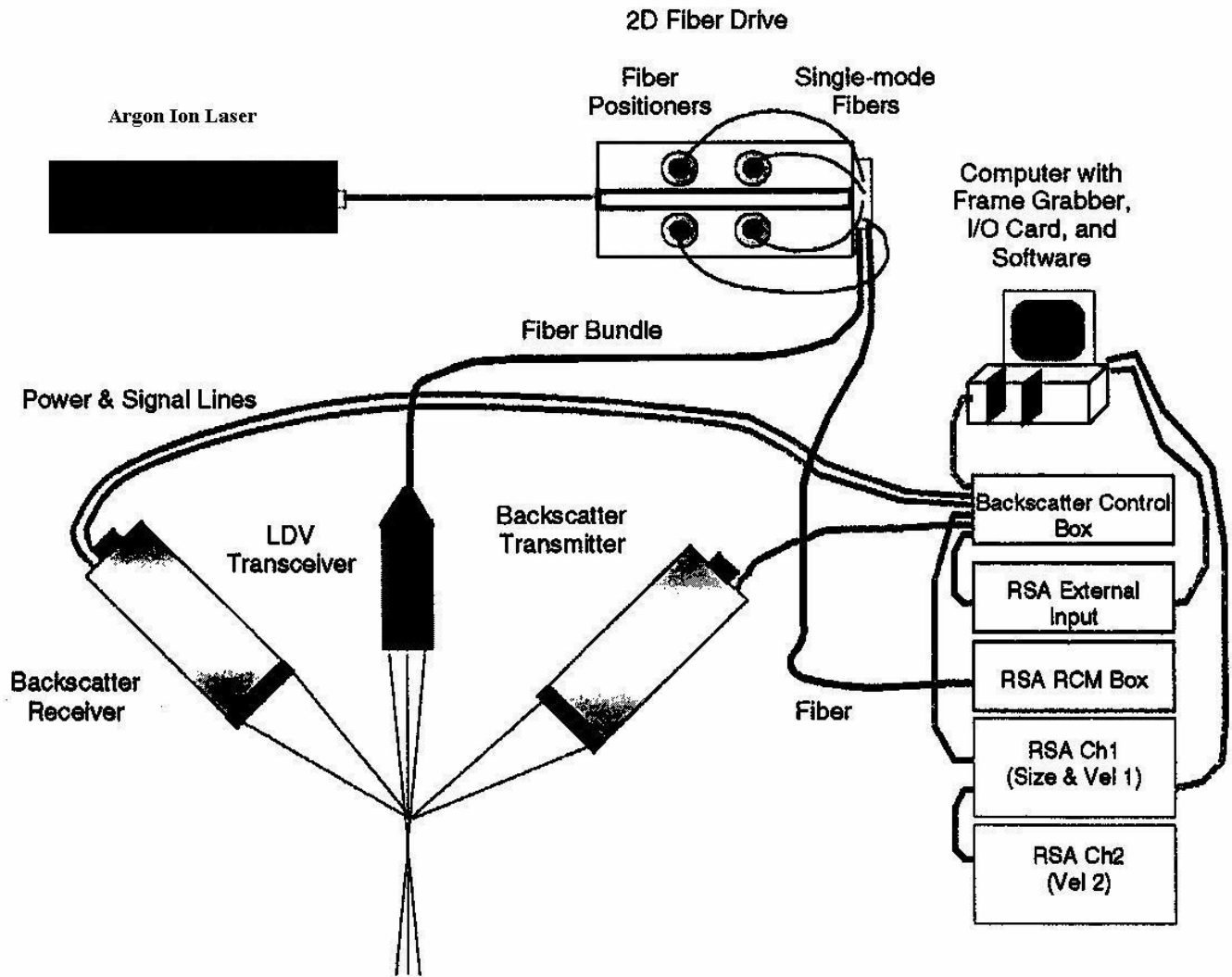


Figure 6 Backscatter Imaging LDV System (BILS)

TSI Inc. Manual [2000b]. The fiber drive thus provides beam splitting, frequency shifting, and color separation. A Bragg cell is used to split the incoming beam into two beams of equal intensity. Two dispersion prisms that separate the beams into individual colors further manipulate these beams. These are then directed into the optical fibers for transmission. The 40 MHz reference frequency, used to modulate the Bragg cell, is received from the signal processor. The beams directed through the fiber optics cables go to the main transceiver.

The transceiver contains all the optics necessary to create the sampling volume for particle velocity measurements. The transceiver is linked to the rest of the system only by optical fibers, thus providing a convenient, compact, and robust LDV probe for a wide range of applications [Figure 7]. Because this is a transceiver, it has all the optics to be able to receive the backscattered signals and it uses a series of optical fibers and lenses to transmit laser light. Beam pairs intersect and create a measurement volume at the focal spot. The receiver fiber directs the light away from the probe head, back through the fiberoptic cable and to the receiver module (RCM) for separation and photodetection, TSI Inc. Manual [2000b]. The function of the RCM is to convert phase-Doppler light signals from the receiver optics into electronic signals. The RCM box contains the photomultiplier tubes (PMTs) and the optomechanical hardware for separating the receiver light (by wavelength) and steering into the PMTs. The PMT high voltage is software controlled. The signals from PMTs are processed in the real-time analyzers (RSAs). There are two RSAs for a two-dimensional velocity system. The BNC terminal labeled RAW is used to monitor the raw signal being sent from the receiver module to the

RSA. The terminal labeled COMPUTER is used for connecting the RSA to the controlling computer. Both the RSAs are also interconnected with each other. The RSA is capable of precise measurements in test situations where the signal-to-noise ratio is beyond the capability of other processors. The RSA External Input accepts up to 16 channels of data that can be tagged to incoming velocity and/or size measurements. Operation of this external input is controlled through the RSA software, DataVIEW. The input to the external input is measured at the end of the Doppler Burst from any of the active RSAs. If a velocity measurement comes from channel 2 and not from channel 1, the external input will measure the input. If both channels give a signal at the same time, the input is also recorded. DataVIEW compares the time for the different RSA channels. If they overlap then the measurements are assumed to be from the same particle and they are linked to the external input measurement at that time. If they don't match then the measurement on the display as well as the external input measurement are removed. The external input is connected directly to the RSA I/O card inside the computer. The DataVIEW-NT Software, included with the system, contributes to the overall ease of use and is very user friendly.

The BILS imaging system consists of three main components: the backscatter imaging receiver, the backscatter imaging transmitter, and the backscatter imaging controller. The RSA processors and RSA external input are shared with the LDV component. The backscatter probe volume, a region well under 1 square mm in size must be aligned both with the backscatter transmitter and receiver as well as the LDV probe volume. The LDV probe volume is of the order 100 μm in size. Essentially all the three

probes are ‘looking’ at the same point in space, through which the measured particles must pass. The transmitter is mounted on the same base plate as the other probes. It contains a diode laser of the wavelength 905 nm and pulse width 15ns and maximum repetition rate of 5 kHz. The focal length of front lens is 750 mm, TSI Inc. Manual [2000a]. This diode laser illuminates the particle for imaging.

The receiver probe images the particle onto a CCD camera using a 750 mm front lens. A long pass filter is used to block the Ar-ion laser beam and other light sources. The maximum speed of the camera is 955 Frames per second. The backscatter controller receives a trigger signal from the processor and then it activates the pixels to ‘expose’ mode. The controller fires the diode laser 50 ns later and 175 ns later the controller stops exposure and begins an image readout sequence by triggering the frame grabber to acquire the image data. The backscatter imaging system has no ‘stand-alone’ operating mode, although the LDV system is able to take the data whether the backscatter controller is connected or not. The backscatter system operates in total synchronization with the RSA processors. The RSA acts as the “master” to the backscatter controller and the controller doesn’t trigger the laser diode unless the particle has been detected and validated by the RSA Fourier transform burst detector. The Backscatter software used is “BackscaPP” and is a Windows NT application. It can analyze single as well as a series of images.

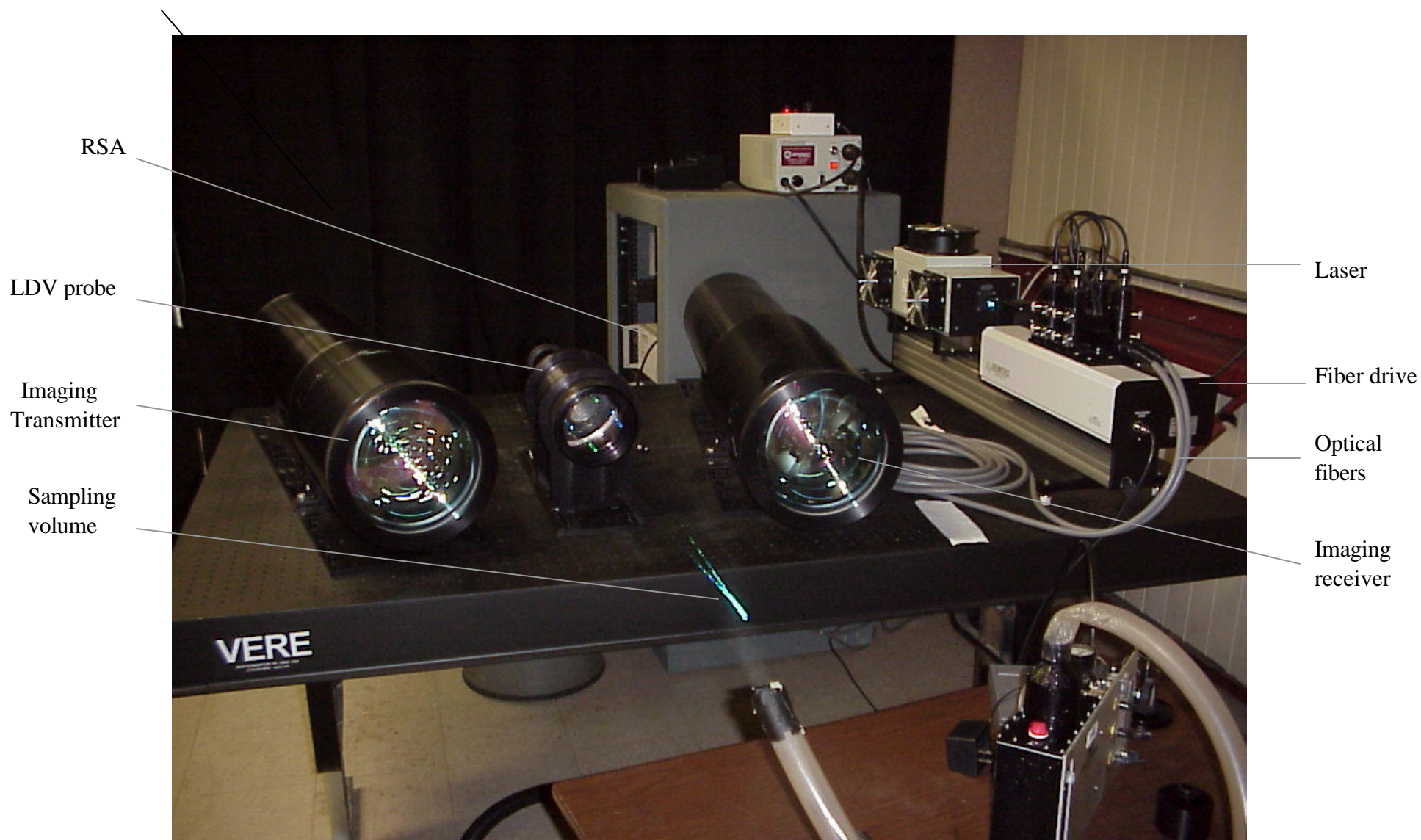


Figure 7. The BILS instrument set-up at NETL location, Morgantown

3.2.2 Basic Operating Principles of the Instrument

An interference pattern is setup in the plane where the two laser beams intersect. The interference pattern is an area of bright and dark fringes. As a particle passes through the bright fringes, it scatters pulses of light [Figure 8]. The frequency of the pulses of scattered radiation is proportional to the speed of the particle in the fluid. Imagine the interference pattern as a picket fence. The bright fringes correspond to the slats, while the dark fringes are the spacing between the slats. If one drags a stick across the slats, a certain frequency of sound is produced. The faster one drags the stick, the higher the frequency, the slower one drags the stick, the lower the frequency. If one imagines the particle in the fluid to be the stick, it is easy to visualize how a faster moving particle would produce a higher frequency signal while a slower moving particle would produce a lower frequency signal. When a particle passes through the fringes, the photomultipliers produce uniform Doppler bursts. These are proportional to the particle velocity component perpendicular to the plane of the fringes. These velocities are calculated using the following equation:

$$V_P = \frac{\lambda_0}{2 \sin(\Gamma/2)} F_D \quad (2)$$

where λ_0 is the wavelength of the laser beam, F_D is the Doppler frequency, V_P is the particle velocity and Γ is the beam-crossing angle. The beam-crossing angle for this instrument is about 8 degrees. The fringe spacing can be obtained by the expression:

$$d = \frac{\lambda_0}{2 \sin(\Gamma/2)} \quad (3)$$

where d is the fringe spacing. The blue color laser has a wavelength of 488 nm and the green one has a wavelength of 514 nm. The fringe spacing for the blue one is 3.6 μm .

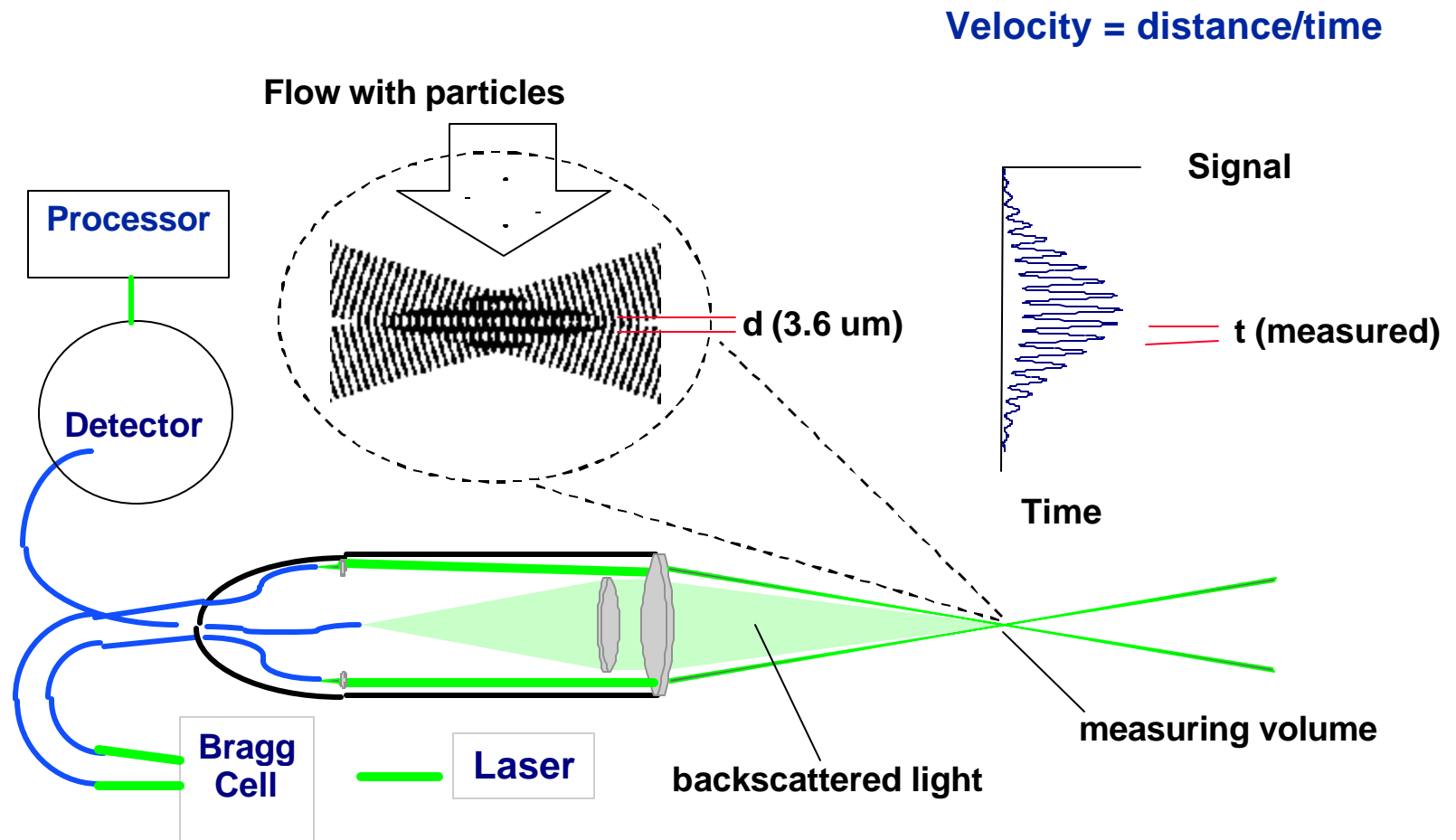


Figure 8. Basic operating principle of LDV part of the instrument

The laser diode emitters help to make the particle visible to the camera. These lenses provide approximately 1:1 imaging. An image of the particle is captured and sent to the computer via an interface board. Timing is controlled by the backscatter imaging controller. Generally, several thousands images are grabbed in a single run and upon completion, both LDV and imaging data are saved on the hard drive. Statistical analysis of this data is done by post-processing software.

3.3 Capabilities and Limitations of the Equipment

BILS has the following capabilities:

- Non-invasive measurement and simultaneous two component velocity measurements
- Imaging capability of nearly 1000 frames per second
- Measurement of particle circularity and aspect ratio
- Needs just one optical window access to the flow
- Provide frozen pictures and simultaneous velocity data, even if particles are moving at several hundred meters per second.

The limitations include:

- Doesn't work well on smooth surfaces as the glare spots spoil the information
- Particle size resolution and accuracy are limited by CCD pixel dimensions
- Particle shape information can be misleading since it is based on 2-D images, especially for particles having rod-like shape.

For the initial part of the experiment, a temporary set-up in the B-17 location in NETL, Department of Energy, Morgantown was used and this is as shown in Figure 7. In an attempt to characterize various particles used in the CFB, the terminal velocities will be measured as a function of the concentration of the particles in the bed. The effect of solid loading or concentration will be considered along with the particle size, shape and density dependencies on terminal velocity. For high solids concentration, terminal velocity will be influenced by hindered settling and an appropriate correlation will be applied to test the accuracy and consistency of the data. With these calculations, information about the how deep the laser beam can penetrate inside the flow field and at what concentrations data can be obtained will be investigated. After this initial set-up and evaluation, the instrument will be moved to the full-scale model of a cold flow CFB for velocity measurements to be taken at the riser section. The velocity profiles will be obtained along with particle size and shape.

3.4 Results and Discussion of Work Performed to Date

The first set of experiments was performed to study the effect of certain parameters on the velocity measured by the instrument. The set-up was shown in Figure 4. The parameters that were investigated are listed below:

- The wire diameter – representative of the particle size
- Position of the wire in the measurement volume
- The rotation speed of the wheel

The experimental and the theoretical values were also compared and a good match was observed [Figure 9,10]. Comparing the two data sets for different sizes of wire, it was observed that the wire diameter does not have any significant influence on the readings [Figure 9]. It was observed that the position of the wire in the measurement volume does not have a significant effect on data obtained by the instrument [Figure 10]. The maximum percentage difference between any two sets of values for the same RPM was found to be 9% and was in most cases below 5%. More tests will be made to ensure that the readings obtained from the instrument are reliable. A random array of experiments of different wire sizes at different speeds will be examined.

Some terminal velocity measurements will also be made. The basic equation to calculate the terminal velocity used will be [Gidaspow, 1994]:

$$v_t = \frac{0.153d_p^{1.14} g^{0.71} (\mathbf{r}_s - \mathbf{r}_g)^{0.71}}{\mathbf{m}^{0.43} \mathbf{r}_g^{0.29}} \quad \text{for } 2 < \text{Re}_p < 1000$$

For the case of $d_p = 1000$ microns and $\rho_s = 13.36 \text{ lb/ft}^3$, $\rho_g = 1.206 \text{ kg/m}^3$, $\mu_g = 2 \cdot 10^{-5} \text{ kg/m-s}$, the terminal velocity for single particle is $v = 1.3 \text{ m/s}$. The next set of

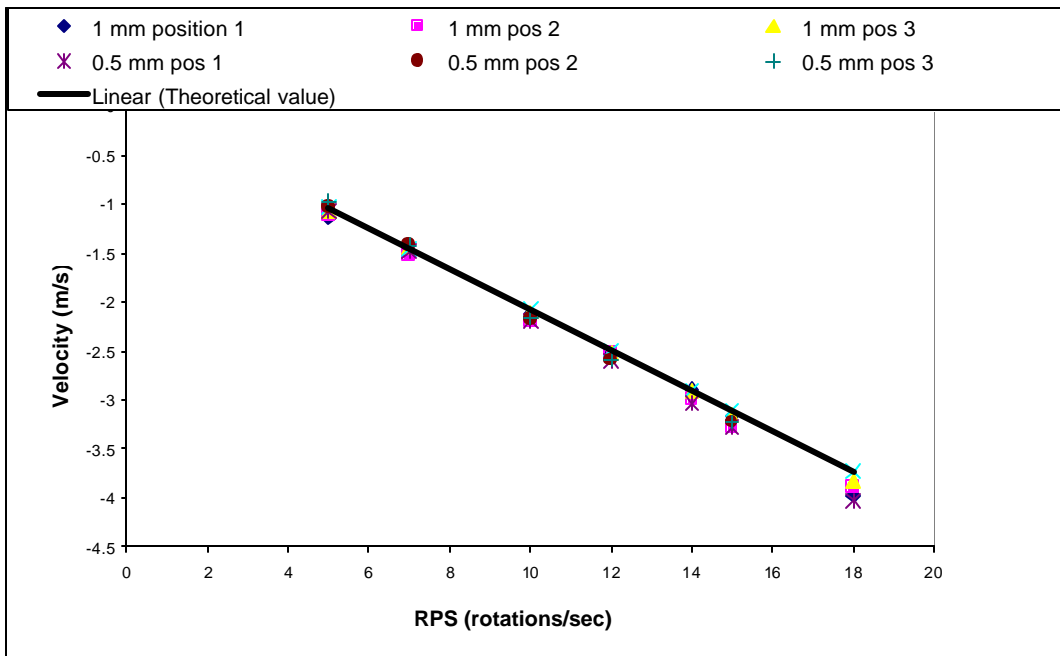


Figure 9. Velocity data of BILS for 1 mm and 0.5 mm diameter wire

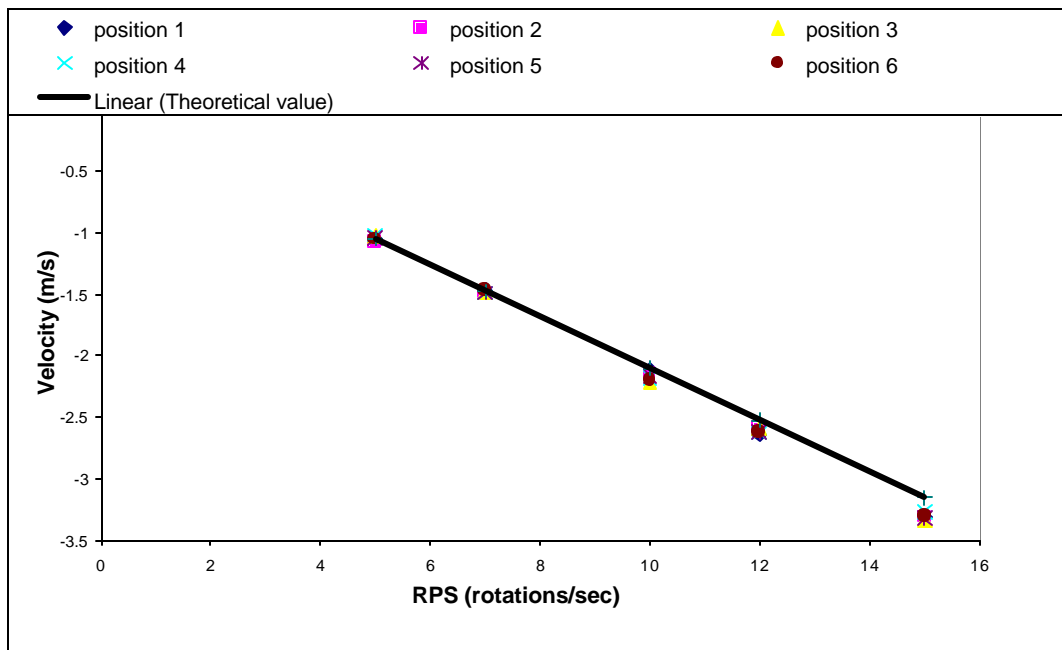


Figure 10. Velocity data at various positions of wire dia = 0.5 mm in the measurement volume

experiments will concentrate on getting data of terminal velocity of particles in the fluidized bed. One of the problems faced here is the possible curvature effect of the wall of the riser section of the CFB and also the fact that the optical window may not be clean. The curvature of the bed may cause the beams to refract causing them to intersect at a different location than expected. This new location can be predicted using the refractive index values of the glass section. Another problem is that the glass curvature can cause the backscattered signal to refract in several directions, rather than coming straight back into the probe. Thereby the signal reaching the probe might get weaker.

4. Safety Considerations

The laser beam used here is a class IV Ar ion laser and has a peak power output of 750 mW. Strict safety measures must be taken when operating because for a class IV laser even the reflections of the beam from secondary surfaces can be harmful to the eyes. Direct exposure of the beam to the eyes can cause permanent blindness even if it is for a very short duration. A safety analysis has been done at NETL, Morgantown where the instrument will be installed. The hazards associated with the operation are identified and proper mitigation steps have been taken. The area where the instrument will be set-up is enclosed by the appropriate safety curtains to avoid any exposure to the beam reflections to those outside the work area. Safety goggles appropriate for this class and type of laser are required for those in the work area.

An interlocking device is installed in such a way so that if any trespasser opens the laser curtain when the instrument is 'ON' then the circuit breaks and a beam shutter comes in front of the laser beam thereby cutting the beam off. To be able to get a beam from the probes and to get any readings, the laser curtains must be closed. The whole set-up for processing using software is placed outside this curtain-enclosed area. A safety light displaying three different modes of operation: 'SAFE', 'CAUTION' and 'DANGER' is placed outside the working area to indicate the hazard associated at every instant. Similar precautions need to be taken when the set-up is moved to the large scale CFB.

5. References

- Arastoopour H., Shao S., “Laser Doppler Anemometry: Applications in multiphase flow systems”, *Non-invasive Monitoring of Multiphase flows*, Elsevier, 1997
- Durst F., Melling A., Whitelaw J., “Principles and practice of laser Doppler Anemometry”, 2nd ed., 1981
- Gidaspow D., “Multiphase Flow and Fluidization”, Academic Press, c1994
- Kaufman L. Stanley, “Fiberoptics in Laser Doppler Velocimetry”, *Lasers and Applications*, 71-73, July 1986
- Menon K. Rajan, “Laser Doppler velocimetry: Performance and Applications”, *American Laboratory*, Feb 1982
- Monceaux, L. Azzi M., Molodtsov, Y. and Large, J.F. (1985) Overall and local characteristics of flow in a circulating fluidized bed. International Conference on Circulating Fluidized Beds, Halifax, Canada , pp 185-191
- Rhodes, M.J. and Geldart, D. (1986) The hydrodynamic of recirculating fluidized beds. In *Circulating Fluidized Bed Technology*, ed. I.P. Basu, pp 193-200, Pergamon Press, Toronto
- Tadrist, L. and Cattiew, P. (1993) Analysis of two-phase flow in a circulating fluidized bed, *Proceedings of the 4th International Conference on Circulating Fluidized Beds*, Pennsylvania, USA, pp 702-707
- Thompson H., Stevenson W., “Laser velocimetry and particle sizing”, International workshop on Laser Velocimetry; 3rd, Purdue University, July 11-13, 1978
- TSI Inc.; “Backscatter Imaging LDV System, Hardware, Software and Analysis: Users Manual”, April 2000a

TSI Inc.; “Phase Doppler Particle Analyzer (PDPA): Operations Manual”, April 2000b

Tsuji Y., Morikawa Y. and Shiomi H, “LDV measurements of an air-solid flow in a vertical pipe”, *J. Fluid Mech* 139, pp. 417-434, 1984

Van den Moortel, T., Santini, R., Tadrict, L. and Pantaloni, J. (1997), “Experimental study of the particles flow in a circulating fluidized bed using a Phase Doppler Particle Analyzer”. *Int. J. Multiphase Flow* 23(6), pp. 1189-1209, 1997

Van den Moortel, T., Azario, E., Santini, R., and Tadrict, L. (1998), “Experimental analysis of the gas-particle flow in a circulating fluidized bed using a phase Doppler particle analyzer”, *Chem. Eng. Sc.* 53(10), pp. 1883-1899, 1998

6. List of Acronyms and Abbreviations

BILS	backscatter imaging laser Doppler velocimeter system
CCD	charged couple device
CFB	circulating fluidized bed
D	diameter of the pipe, m
D_p	particle diameter, m
FCC	fluidized catalytic cracking
LDV	laser Doppler velocimeter
m	particle-to-air-mass-flow-rate
N	number of particles validated during the acquisition period
NETL	national energy technology laboratory
PDPA	phase Doppler particle analyzer
PMT	photo multiplier tube
RCM	receiver module
RPM	rotations per min
RPS	rotations per sec
RSA	real-time system analyzer
r	radial distance from the center, m
u_c	velocity at the pipe center, m/s
V_p	instantaneous velocity, m/s
V_{pax}	particle axial velocity, m/s
v_t	terminal velocity, m/s

ν_D	measured frequency difference, Hz
ω	angular frequency of rotating disc, rad/sec
ρ_s	particle density, kg/m ³
ρ_g	gas density, kg/m ³
μ_g	gas viscosity, kg/m-s

**XVI. “Transient Modeling of a Gas Turbine in a Hybrid System
Including a Fuel Cell”**

**Emre Tatli (S), Daniel DeFede and Ismail Celik (F), West Virginia University
with
Randy Gemmen (M), NETL**

Transient Modeling of a Gas Turbine in a Hybrid System Including a Fuel Cell

Emre Tatli (Current Graduate Student)
Daniel P. DeFede (Former Graduate Student)
Ismail B. Celik (Principle Investigator)

Mechanical and Aerospace Engineering Department
West Virginia University
Morgantown West Virginia 26505

Annual Report No: MAE-IC-01/03

December 2001

Submitted to: U.S. Department of Energy
National Energy Technology Laboratory
Morgantown, WV 26507

As requirement of the NETL/University Partnership Project
No:10002621 Award No: 1000989R

TABLE OF CONTENTS

Title Page.....	1
Table of Contents.....	2
List of Figures.....	4
Nomenclature.....	5
Abstract.....	7
1.0 INTRODUCTION	
1.1 Combined Cycles.....	8
1.2 Indirect Cycles (Molten Carbonate Fuel Cell).....	8
1.3 Direct Cycles (Solid Oxide Fuel Cell).....	9
1.4 Problem Description.....	10
2.0 LITERATURE REVIEW	
2.1 Compressor Models.....	12
2.2 Turbines.....	17
2.3 Radial Turbines.....	17
2.4 Solid Oxide Fuel Cell Models.....	18
2.5 Molten Carbonate Fuel Cell Models.....	18
3.0 COMPRESSOR MODEL	
3.1 Dimensional Equations for Constant Speed Model.....	20
3.2 Nondimensional Equations for Constant Speed Model.....	22
3.3 Dimensional Equations for Variable Speed Model.....	27
3.4 Nondimensional Equations for Variable Speed Model.....	29
3.5 Non-Surging Compressor Model.....	34

3.6 The Compressor Characteristic.....	35
4.0 TURBINE MODEL	
4.1 Fluid Dynamic Processes.....	40
4.2 Turbine Map.....	42
5.0 INTEGRATION OF MODELS INTO PROTRAX	
5.1 Compressor Model.....	48
5.2 Turbine Model.....	48
6.0 APPLICATION AND RESULTS	
6.1 Test Cases for Constant Speed Compressor Model.....	49
6.2 Real Cases for Constant Speed Compressor Model.....	50
6.3 Test Cases for Variable Speed Compressor Model.....	50
6.4 Real Cases for Variable Speed Compressor Model.....	51
6.5 Test Cases for Turbine Model.....	51
6.6 Real Cases for Turbine Model.....	52
7.0 DIMENSIONAL ANALYSIS IN TURBOMACHINES.....	53
8.0 SURGE AND STALL.....	64
9.0 CONCLUSION.....	67
10.0 REFERENCES.....	68

LIST OF FIGURES

Figure 1: A direct pressurized fuel cell system	10
Figure 2: Equivalent Compression System used in Analysis	20
Figure 3.6.1: Fink's Nondimensional compressor characteristics	35
Figure 3.6.2: Nondiscontinuous Created Compressor characteristics	38
Figure 3.6.3: Fink's efficiency versus C_x/U	38
Figure 3.6.4: Created efficiency versus nondimensional mass flow	39
Figure 4.2.1: Known turbine map	43
Figure 4.2.2: Created nondimensional turbine map	45
Figure 4.2.3: Created turbine map	46
Figure 4.2.4: Efficiency versus U/C_s for created map	47
Figure 6: Compressor map with transient response	50-52
Figure 7.1: Nondimensional turbine map	58
Figure 7.2: Cordier diagram	62
Figure 7.3: Efficiency versus Specific Diameter	63

NOMENCLATURE

a = speed of sound at ambient

\bar{m}_c = nondimensional mass flow through the compressor

\bar{m}_t = nondimensional mass flow through the throttle

$\bar{\Delta P}$ = nondimensional plenum pressure rise

\bar{C} = nondimensional compressor pressure rise

\bar{F} = nondimensional throttle characteristic = $(\bar{m}_t)^2 * S$

S = valve parameter = $(A_c/A_t)^2$

\bar{C}_{ss} = nondimensional steady state compressor pressure rise

A_c = flow area of the compressor duct

A_t = flow area of the throttle duct

G = geometric parameter = $(L_t * A_c)/(L_c * A_t)$

B = stability parameter = $U/(2 * \omega_H * L_c)$

$\bar{\tau}$ = nondimensional compressor flow relaxation time = $(\pi * R/L_c) * (N/B)$

τ = compressor flow relaxation time = $(N * 2\pi R)/U$

L_t = effective length of the throttle duct

L_c = effective length of the compressor duct

V_p = plenum volume

R = impeller tip radius

N = time lag in revolutions

U = tip speed of the rotor

ω_H = Helmholtz resonator frequency

ω = angular velocity

N = number of rotor revolutions

TN = the slope of the throttle characteristic = $d(\overline{\Delta P})/d(\overline{m}_t)$

CN = the slope of the compressor characteristic = $d(\overline{C})/d(\overline{m}_c)$

I_p = spool inertia parameter

ψ = isentropic head coefficient

I = polar moment of inertia

M_{t0} = impeller tip Mach index

M_{tp} = impeller tip Mach index calculated with plenum temperature

Π = overall pressure ratio for compressor

Π_m = nondimensional corrected mass flow through turbine

Π_s = nondimensional corrected speed for turbine

Π_{PR} = overall pressure ratio for turbine

W_T = specific power for turbine

J_T = power for turbine

T = temperature

X = scaling factor

Δ = scaling delta

Note: All variables with a bar over it are non-dimensional. When they appear without a bar over it then they are dimensional.

ABSTRACT

Large amount of heat is dissipated from fuel cells. This can be used to increase the efficiency of the fuel cell by introducing a cycle including a gas turbine. But the components of the gas turbine, such as the turbine and the compressor need to provide small amounts of power. Ordinary turbomachines and their maps can't be used for this process because of the large scales. This report deals with scaling of turbomachines so that predictions can be made for small turbines that will be used in a hybrid system including a fuel cell. The transient analysis of such a cycle is the major objective of this study. The scaling procedure will provide the data necessary to perform surge-stall predictions on the system.

1.0 INTRODUCTION

1.1 Combined Cycles

Fuel cells are used to produce electricity from electro-chemical reactions. A solid oxide fuel cell operates at about a temperature of 900 degrees Celsius. Due to this high temperature the fuel cell produces waste heat. For a combined cycle, the waste heat produced by the fuel cell can be used to make the system in which the fuel cell is installed more efficient. This can be done in several ways. One way the waste heat can be used is to heat up anything in the fuel cell system that needs to be heated thus making the system more efficient.

Ultimately, more electricity from the fuel cell system would be desired because use of electricity is more versatile. A gas turbine can be used to extract this additional electricity since the temperature at which a solid oxide fuel cell operates is ideal for a turbine. Since fuel cells usually operate at atmospheric conditions the gases that come out of the fuel cell are not pressurized, and for a gas turbine the gases must be expanded to do work. If the gases from the fuel cell are at atmospheric pressure, then they can not be expanded to get useful work from the turbine. There are two ways to use a gas turbine combined with a fuel cell.

1.2 Indirect Cycles (Molten Carbonate Fuel Cell)

The first is to keep the fuel cell at atmospheric pressure, which is called an indirect cycle. In an indirect cycle the gas turbine combustor is replaced by a heat exchanger. The high temperature gases from the fuel cell are sent through a heat exchanger and used

to heat compressed air from a compressor. The heated compressed air is then expanded through a turbine to provide useful work in the form of electricity.

1.3 Direct Cycle (Solid Oxide Fuel Cell)

The second way is to use a direct pressurized fuel cell system shown in Figure 1. In this system the heat will be used directly off of the fuel cell. For this system to work the fuel cell must be pressurized. It is known from system studies that a solid oxide fuel cell that operates at a higher pressure has a better efficiency; however, tradeoffs occur once the pressure range exceeds 3-6 bars.

compressor and turbine. The transients predicted by the model can then be used to determine when a deep surge event might occur, thus providing time to correct the problem to eliminate the surge event. The objective of this research is to dynamically model the transient response of a compressor used in conjunction with a gas turbine in a hybrid system including a fuel cell.

2.0 LITERATURE REVIEW

2.1 Compressor Models

E. M. Grietzer (1976) wrote a paper on surge and rotating stall in axial flow compressors. A theoretical study of axial compressor surge is investigated. The transient response, due to a perturbation from steady operating conditions, of a compression system is nonlinearly modeled. An important non-dimensional parameter based upon the mean rotor velocity effects this response greatly. At the stall line, if the value of the parameter is above the critical value, then surge is encountered. If the value of the parameter is below the critical value at the stall line, then rotating stall is encountered.

Jan Foeke Kikstra and Adrian H. M. Verkooijen (1999) wrote a paper on the dynamic modeling of a closed cycle gas turbine CHP plant. The energy conversion system of a combined heat and power plant, based on a helium-cooled reactor in combination with a closed cycle gas turbine system, is dynamically modeled. The helium flow and the two-phase water flow through the whole plant are modeled using a one dimensional flow model, using different source terms for different pieces of equipment. The radial compressor and axial turbine are modeled stage-by-stage. Due to changes in reactor power, valve position, etc. an open-loop response for the controlled parameters of shaft speed, temperatures, and pressures have been developed with this model.

S. M. Camporeale, B. Fortunato, and A. Dumas (1998) wrote a paper on the dynamic modeling and control of regenerative gas turbines. The dynamic behavior of single-shaft or multi-shaft regenerative gas turbines is simulated using a nonlinear model. The blade thermal transients for the air-cooled turbine expansion are accounted for using a stage by stage model. From the nonlinear model a linearized model is developed to

help design a multivariable controller for the plant. Describing the gas turbine are transfer functions that relate the fuel rate and variable inlet guide vanes (input variables) to the shaft speed and turbine output temperature (state variables).

J. E. Pinsley, G. R. Guenette, A. H. Epstein, and E. M. Greitzer (1991) wrote a paper on the active stabilization of centrifugal compressor surge. The centrifugal compressor is equipped with a servo-actuated plenum exit throttle controller. The control technique will directly address the dynamic behavior of the compression system to displace the surge line to lower mass flows. A fast acting control valve is used to receive the feed back on the perturbations in plenum pressure rise. The resulting valve motion increases the aerodynamic damping of incipient oscillations thus allowing stable operation past the normal surge line.

F. K. Moore and E. M. Greitzer (1986) wrote a paper on the theory of post-stall transients in axial compression systems. A set of three simultaneous nonlinear third-order partial differential equation for pressure rise and average and disturbed values of flow coefficient as a function of time and angle around the compressor are developed. The angular dependence is averaged using a Galerkin procedure to make the equations first-order in time. These equations can describe the growth and possible decay of a rotating-stall cell during a compressor mass-flow transient. It is also shown that through these equations the rotating-stall-like and surgelike motions are coupled. It should also be noted that during the transient stall process the instantaneous compressor pumping characteristic changes.

D. A. Fink, N. A. Cumpsty, and E. M. Greitzer (1992) wrote a paper on the surge dynamics in a free-spool centrifugal compressor system. Stall initiation phenomena as

well as the behavior of the compressor characteristics when operating in surge are examined using two very different compression systems. The first compression system has a large downstream volume and the second compression system is one that has the smallest possible downstream volume. A key phenomena, determined from measurement, in initiating surge is impeller stall at the inducer tips. In the large volume system (which gave surge) the compressor characteristic is observed to be flatter and to lag that in the stabilized small volume system.

J. S. Simon, L. Valavani, A. H. Epstein, and E. M. Greitzer (1993) wrote a paper on the evaluation of approaches to active compressor surge stabilization. The first systematic definition of the influence of sensor and actuator selection on increasing the range of stabilized compressor performance is presented. The ability to stabilize these systems is primarily affected by the proper choice of sensor and actuator. Also, those actuators most closely coupled to the compressor, as opposed to the plenum or throttle, appear most effective. The unsteady compressor pressure rise or the unsteady combustor heat release, the driving source of the disturbances of the system, has a strong influence on control effectiveness.

D. L. Gysling, J. Dugundji, E. M. Greitzer, and A. H. Epstein (1990) wrote a paper on the dynamic control of centrifugal compressor surge using tailored structures. By using structural feedback, the compression system dynamic behavior will be modified to suppress surge. One wall of a downstream volume is constructed to move in response to small perturbations in pressure. The unsteady energy perturbations produced by the compressor are absorbed due to this structural motion, and thus the stable operating range of the compression system is extended.

K. E. Hansen, P. Jorgensen, and P. S. Larsen (1981) wrote a paper on the experimental and theoretical study of surge in a small centrifugal compressor. For a small single-stage centrifugal compressor the experimental results for deep surge are compared to predictions based on the lumped parameter Greitzer model developed for axial compressors. By using a relaxation time smaller than the one proposed by Greitzer for axial compressors, one can get the predictions to be in fair agreement with the data.

E. A. Liese, R. S. Gemmen, F. Jabbari, and J. Brouwer (1999) wrote a paper on the technical development issues and dynamic modeling of gas turbine and fuel cell hybrid systems. Safety issues important to the operation of a combined fuel cell and gas turbine are described. The paper also describes two models, a steam reformer and a fuel cell, that will be used to investigate the dynamic performance of a hybrid system. The performance of the individual models should be understood before integration into a complete hybrid system model.

G. D. Garrard, M. W. Davis, Jr., and A. A. Hale (1995) wrote a paper on the recent advances in gas turbine engine dynamic models developed through JDAPS. A. K. Owen, A. Daugherty, D. Garrard, H. C. Reynolds, and R. D. Wright (1999) wrote a couple of papers on the parametric starting study of an axial-centrifugal gas turbine engine using a one-dimensional dynamic engine model and comparisons to experimental results: Part 1- Model development and facility description, Part 2- Simulation Calibration and trade-off study. M. Nakhmkin and S. C. Gulen (1995) wrote a paper on the transient analysis of the cascaded humidified advanced turbine. S. A. Ali and R. R. Moritz (1999) wrote a paper on the hybrid cycle: Integration of turbo machinery with a fuel cell. B. G. Vroemen, H. A. van Essen, A. A. van Steenhoven, and J. J. Kok (1998)

wrote a paper on the nonlinear model predictive control of a laboratory gas turbine installation. G. Crosa, G. Ferrari, and A. Trucco (1995) wrote a paper on modelling and recoupling the control loops in a heavy-duty gas turbine plant. B. de Jager (1995) wrote a paper on rotating stall and surge control: a survey. G. Gu, S. Banda, and A. Sparks (1996) wrote a paper on an overview of rotating stall and surge control for axial flow compressors. J. D. Paduano, L. Valavani, A. H. Epstein, E. M. Greitzer, and G. R. Guenette (1994) wrote a paper on the modeling for control of rotating stall. L. N. Hannett and A. Khan (1992) wrote a paper on combustion turbine dynamic model validation from tests. R. V. Monopoli (1980) wrote a paper on the model following control of gas turbine engines. R. N. Gamache and E. M. Greitzer (1990) wrote a paper on reverse flow in multistage axial compressors. K. K. Botros, P. J. Campbell, and D. B. Mah (1991) wrote a paper on the dynamic simulation of compressor station operation including centrifugal compressor and gas turbine. W. M. Jungowski, M. H. Weiss, and G. R. Price (1996) wrote a paper on pressure oscillations occurring in a centrifugal compressor system with and without passive and active surge control. J. L. Dussourd, G. W. Pfannebecker, and S. K. Singhania (1977) wrote a paper on an experimental investigation of the control of surge in radial compressors using close coupled resistances. J. P. Longley, H. W. Shin, R. E. Plumley, P. D. Silkowski, I. J. Day, E. M. Greitzer, C. S. Tan, and D. C. Wisler (1994) wrote a paper on the effects of rotating inlet distortion on multistage compressor stability. A. Layne, S. Samuelsen, M. Williams, and P. Hoffman (1999) wrote a paper on the developmental status of hybrids. J. D. Leeper (1999) wrote a paper on the hybrid cycle: integration of a fuel cell with a gas turbine. G. Crosa, L. Fantini, G. Ferrari, L. Pizzimenti, and A. Trucco (1998) wrote a paper on the

steady-state and dynamic performance prediction of an indirect fired gas turbine plant. A. Leonessa, V. S. Chellaboina, and W. M. Haddad (1997) wrote a paper on the multi-mode control of axial compressors via Lyapunov stability-based switching controllers. W. M. Haddad, A. Leonessa, V. S. Chellaboina, and J. L. Fausz (1997) wrote a paper on the nonlinear robust disturbance rejection controllers for rotating stall and surge in axial flow compressors. A. Leonessa, V. S. Chellaboina, and W. M. Haddad (1998) wrote a paper on the robust stabilization of axial flow compressors with uncertain pressure-flow maps. H. Li, A. Leonessa, and W. M. Haddad (1998) wrote a paper on globally stabilizing controllers for a centrifugal compressor model with spool dynamics.

2.2 Turbines

P. P. Walsh and P. Fletcher wrote a book on gas turbine performance. E. Logan wrote a book on turbomachinery basic theory and applications. L. Fielding wrote a book on turbine design and the effect on axial flow turbine performance of parameter variation.

2.3 Radial Turbines

N.C. Baines wrote a paper on introduction to radial turbine technology. N.C. Baines and H. Chen wrote a paper on performance parameters and assessments. A. Whitfield wrote a paper on the non-dimensional conceptual design of radial inflow turbines. M. Zangeneh wrote a paper on numerical methods for inviscid and viscous flow analysis. S. T. Kitson wrote a paper on the aerodynamic investigation of radial turbines using computational methods. M. Zangeneh wrote a paper on the inverse design method for radial turbomachines. I. H. Skoe wrote a paper on the integration of geometric

modeling into an inverse design method and application of a PC-based inverse design method and comparison with test results. N.C. Baines wrote a paper on partial admission and unsteady flow in radial turbines. N. C. Baines wrote a paper on testing techniques. R. J. Roelke wrote a paper on radial turbine cooling. W. M. Marscher wrote a paper on structural analysis and fatigue life assessment.

2.4 Solid Oxide Fuel Cell Models

S. E. Veyo and W. L. Lundberg (1999) wrote a paper on solid oxide fuel cell power system cycles. S. Ahmed, C. McPheeters, and R. Kumar (1991) wrote a paper on the thermal-hydraulic model of a monolithic solid oxide fuel cell. A. F. Massardo and F. Lubelli (1998) wrote a paper on the internal reforming solid oxide fuel cell-gas turbine combined cycles: Part A- cell model and cycle thermodynamic analysis. E. Achenbach (1994) wrote a paper on the three-dimensional and time-dependent simulation of a planar solid oxide fuel cell stack. J. R. Ferguson, J. M. Fiard, and R. Herbin (1996) wrote a paper on the three-dimensional numerical simulation for various geometries of solid oxide fuel cells. J. Hartvigsen, S. Elangovan, and A. Khandkar (1993) wrote a paper on the modeling, design and performance of solid oxide fuel cells. M. Krumpelt, R. Kumar, and K. M. Myles (1994) wrote a paper on the fundamentals of fuel cell system integration.

2.5 Molten Carbonate Fuel Cell Models

W. He wrote a paper on a simulation model for integrated molten carbonate fuel cell systems. W. He wrote a paper on the dynamic performance of a molten carbonate

fuel cell in power-generation systems. P. J. Kortbeek and J. A. F. de Ruijter wrote a paper on a dynamic simulator for a 250 kW class ER-MCFC system. R. S. Gemmen, E. A. Liese, J. G. Rivera, F. Jabbari, and J. Brouwer wrote a paper on the development of dynamic modeling tools for solid oxide and molten carbonate hybrid fuel cell gas turbine systems.

3.0 COMPRESSOR MODEL

3.1 Dimensional Equations for Constant Speed Model

The compressor model must be able to predict and quantify stall and surge events in order to either prevent or limit large pressure changes that could be damaging to the fuel cell. Greitzer (1976) studied surge and stall in axial compressors and developed a model. Using Greitzer's work, a nonlinear, lumped parameter, model is developed that will be used to predict the transient response of a compression system subsequent to a perturbation from steady state operating conditions. A schematic of the equivalent compression system used in analysis is shown in Figure 2.

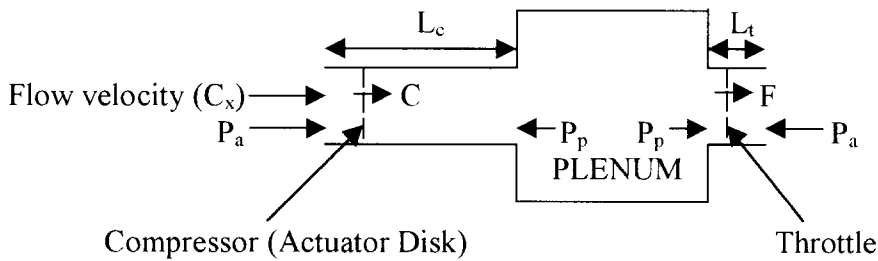


Figure 2. Equivalent Compression System Used in Analysis

The assumptions used in modeling the compression system are the compressor and throttle behave quasi-steady, the pressure in the plenum is uniform, the process in the plenum is polytropic, the one-dimensional flow in the ducts is incompressible, and the throttle has negligible inertance (Greitzer 1976).

The integral form of the one-dimensional momentum equation for the compressor duct is

$$(P_a - P_p + C)A_c = d(\rho A_c L_c C_x)/dt \quad 3.1.1a$$

$$P_a - P_p + C = \rho L_c (dC_x/dt). \quad 3.1.1b$$

Now the plenum pressure rise is defined as $\Delta P = P_p - P_a$. Then equation 3.1.1b becomes

$$C - \Delta P = \rho L_c (dC_x/dt). \quad 3.1.2$$

Equation 3.1.2 needs to be in terms of mass flow. Knowing that $\rho C_x = m_c/A_c$ we get

$$C - \Delta P = L_c/A_c (dm_c/dt). \quad 3.1.3$$

The integral form of the one-dimensional momentum equation for the throttle duct is

$$(P_p - P_a - F)A_t = d(\rho A_t L_t C_x)/dt \quad 3.1.4a$$

$$P_p - P_a - F = \rho L_t (dC_x/dt). \quad 3.1.4b$$

Using the plenum pressure rise definition equation 4 becomes

$$\Delta P - F = \rho L_t (dC_x/dt). \quad 3.1.5$$

Equation 3.1.5 needs to be in terms of mass flow also. Knowing that $\rho C_x = m_t/A_t$ we get

$$\Delta P - F = L_t/A_t (dm_t/dt). \quad 3.1.6$$

The throttle pressure drop (F) can be written explicitly in terms of the velocity at the throttle discharge plane where the static pressure is ambient if the throttle is either a variable area nozzle or a valve and is as follows

$$F = 0.5 \rho C_{xt}^2. \quad 3.1.7$$

substituting in for $C_{xt} = m_t/\rho A_t$ we get

$$F = 0.5 m_t^2 / \rho A_t^2. \quad 3.1.8$$

The compressor and throttle mass flows are linked by mass conservation in the plenum and is as follows

$$m_c - m_t = V_p (d\rho_p/dt). \quad 3.1.9$$

Assuming that the process in the plenum is polytropic, then the density change will be related to the changes in plenum pressure by

$$d\rho_p/dt = (\rho_p/\kappa P_p)(dP_p/dt) \quad 3.1.10$$

where κ is the polytropic exponent. It is an extremely good assumption to take κ equal to the specific heat ratio (γ). The quantity (ρ_p/P_p) is not significantly different from (ρ/P) because the overall temperature and pressure ratios of the compression system are near unity. Therefore the latter can be substituted into the pressure density relationship. The mass conservation equation in the plenum can now be written as

$$m_c - m_t = (\rho V_p/\gamma P) (dP_p/dt). \quad 3.1.11$$

There is a definite time lag between the onset of instability and the establishment of the fully developed rotating stall pattern when the stall limit line is reached and the axisymmetric compressor flow field becomes unstable. The times needed for the stall cell to develop can be long enough that the compressor mass flow can undergo significant changes during this time. Therefore, a quasi-steady approximation will not be appropriate for the modeling here. A first order transient response model will be used to simulate this lag in compressor response. The approximation for the transient compressor response can be written explicitly as

$$\tau(dC/dt) = (C_{ss} - C). \quad 3.1.12$$

3.2 Nondimensional Equations for Constant Speed Model

Equations 3.1.3, 3.1.6, 3.1.8, 3.1.11, and 3.1.12 will be nondimensionalized.

Mass flows will be nondimensionalized with the quantity $\rho A_c U$, pressures will be nondimensionalized with the quantity $0.5\rho U^2$, and time will be nondimensionalized with the Helmholtz resonator frequency ($1/\omega_H$). All parameters with a bar over it are nondimensional. There are seven nondimensional parameters which are listed below.

$$\bar{C} = C/(0.5\rho U^2)$$

$$\bar{\Delta P} = \Delta P / (0.5 \rho U^2)$$

$$\bar{F} = F / (0.5 \rho U^2)$$

$$\bar{m}_c = m_c / (\rho A_c U)$$

$$\bar{m}_t = m_t / (\rho A_c U)$$

$$\bar{t} = t(\omega_H)$$

$$\bar{\tau} = \tau(\omega_H).$$

Nondimensionalizing equation 3.1.3 leads to the following equation

$$\bar{C}(0.5 \rho U^2) - \bar{\Delta P}(0.5 \rho U^2) = (L_c / A_c) [d(\bar{m}_c \rho A_c U) / d(\bar{t} / \omega)]. \quad 3.2.1$$

Dividing by $\rho U L_c \omega$ and simplifying, equation 3.2.1 becomes

$$(U / 2 L_c \omega)(\bar{C} - \bar{\Delta P}) = d\bar{m}_c / d\bar{t}. \quad 3.2.2$$

An important nondimensional parameter must be defined at this point. The stability parameter, B , will determine which kind of instability, stall or surge, will occur once the stall line on the compressor characteristic has been crossed. The stability parameter is

$$B = (U / 2 L_c \omega). \quad 3.2.3$$

Substituting the stability parameter into equation 3.2.2 we get

$$d\bar{m}_c / d\bar{t} = B(\bar{C} - \bar{\Delta P}). \quad 3.2.4$$

Nondimensionalizing equation 3.1.6 leads to the following equation

$$\overline{\Delta P} (0.5\rho U^2) - \overline{F}(0.5\rho U^2) = (L_t/A_t)[d(\overline{m}_t\rho A_c U)/d(t/\omega)]. \quad 3.2.5$$

Dividing by $\rho U L_t \omega A_c / A_t$ and simplifying, equation 3.2.5 becomes

$$(U A_t / 2 L_t A_c \omega)(\overline{\Delta P} - \overline{F}) = d\overline{m}_t / dt. \quad 3.2.6$$

Multiply equation 3.2.6 on top and bottom by L_c to get

$$(U / 2 L_c \omega)(A_t L_c / A_c L_t)(\overline{\Delta P} - \overline{F}) = d\overline{m}_t / dt. \quad 3.2.7$$

Another nondimensional parameter must be defined at this point. The geometric parameter, G , does not play a significant role in the determination of which mode of instability will be encountered when the stall line is crossed. The geometric parameter is

$$G = A_c L_t / A_t L_c. \quad 3.2.8$$

Substituting equations 3.2.3 and 3.2.8 into equation 3.2.7 we get

$$(B/G)(\overline{\Delta P} - \overline{F}) = d\overline{m}_t / dt. \quad 3.2.9$$

Nondimensionalizing equation 3.1.11 leads to the following relationship

$$\overline{m}_c(\rho A_c U) - \overline{m}_t(\rho A_c U) = (\rho V_p / \gamma P)[d\overline{\Delta P}(0.5\rho U^2)/d(t/\omega)]. \quad 3.2.10$$

Dividing by $\rho^2 U^2 \omega V_p / 2\gamma P$ and simplifying, equation 3.2.10 becomes

$$(2A_c \gamma P / \rho U \omega V_p)(\overline{m}_c - \overline{m}_t) = d\overline{\Delta P} / dt. \quad 3.2.11$$

The definition of the speed of sound is

$$a^2 = \gamma P / \rho. \quad 3.2.12$$

Substituting equation 3.2.12 into equation 3.2.11 we get

$$(2A_c / U \omega V_p) (a^2) (\bar{m}_c - \bar{m}_t) = d\bar{\Delta P} / dt. \quad 3.2.13$$

The Helmholtz resonator frequency is defined as

$$\omega = a(A_c / V_p L_c)^{0.5}. \quad 3.2.14$$

Solving for a^2 in equation 3.2.14 we get

$$a^2 = \omega^2 V_p L_c / A_c. \quad 3.2.15$$

Substituting equation 3.2.15 into equation 3.2.13 we get

$$(2A_c / U \omega V_p) (\omega^2 V_p L_c / A_c) (\bar{m}_c - \bar{m}_t) = d\bar{\Delta P} / dt. \quad 3.2.16$$

Simplifying equation 3.2.16 we get

$$(2\omega L_c / U) (\bar{m}_c - \bar{m}_t) = d\bar{\Delta P} / dt. \quad 3.2.17$$

Substituting equation 3.2.3 into equation 3.2.17 we get

$$(1/B) (\bar{m}_c - \bar{m}_t) = d\bar{\Delta P} / dt. \quad 3.2.18$$

Nondimensionalizing equation 3.1.12 leads to the following equation

$$(\bar{\tau} / \omega) [d\bar{C} (0.5 \rho U^2) / d(\bar{t} / \omega)] = (0.5 \rho U^2) (\bar{C}_{ss} - \bar{C}). \quad 3.2.19$$

Dividing by $0.5 \rho U^2$ and simplifying, equation 3.2.19 becomes

$$\overline{dC/dt} = (1/\overline{\tau})(\overline{C_{ss}} - \overline{C}). \quad 3.2.20$$

Finally, nondimensionalizing equation 3.1.8 leads to the following equation

$$\overline{F}(0.5\rho U^2) = (\overline{m_t}\rho A_c U)^2/2\rho A_t^2. \quad 3.2.21$$

Dividing by $0.5\rho U^2$ and simplifying, equation 3.2.21 becomes

$$\overline{F} = (\overline{m_t}A_c/A_t)^2. \quad 3.2.22$$

The relaxation time constant, τ , and the stability parameter, B , can be related.

The relaxation time constant is defined as

$$\tau = N(2\pi R/U) \quad 3.2.23$$

where N is the number of rotor revolutions.

Nondimensionalizing equation 3.2.23 and rearranging terms gives

$$\overline{\tau} = N(2\pi R\omega/U). \quad 3.2.24$$

Multiply equation 3.2.24 on top and bottom by L_c to get

$$\overline{\tau} = N(2\omega L_c/U)(R\pi/L_c). \quad 3.2.25$$

Substituting equation 3.2.3 into equation 3.2.25 we get

$$\overline{\tau} = (N/B)(R\pi/L_c). \quad 3.2.26$$

It can be seen that the relaxation time constant, τ , is proportional to $1/B$ since R , N , and L_c are all constants.

Equations 3.2.4, 3.2.9, 3.2.18, 3.2.20, and 3.2.22 are a set of coupled nonlinear equations to be solved to predict the transient behavior of the compression system (Greitzer 1976).

3.3 Dimensional Equations for Variable Speed Model

D. A. Fink, N. A. Cumptsy, and E. M. Greitzer extended the scope of Greitzer's constant speed analysis by allowing the speed of the system to vary. The major assumptions for this analysis are one-dimensional incompressible flow in the compressor duct, isentropic plenum expansion or compression, choked throttle nozzle where flow is assumed quasi-steady and compressible, variable compressor rotor speed, density discontinuity across the compressor is modeled as an actuator disc, throttle duct length is short and inductance free, negligible velocity in the plenum, and negligible gas angular momentum in the compressor passages compared to the wheel angular momentum. Conservation of momentum in the compressor duct, conservation of mass in the plenum, and angular momentum variations in the turbo-spool are to be described through the use of equations. The integral form of the one-dimensional momentum equation for the compressor duct is

$$(P_a - P_p + C)A_c = d(\rho A_c L_c C_x)/dt \quad 3.3.1a$$

$$P_a - P_p + C = L_c(d\rho C_x/dt). \quad 3.3.1b$$

Now the plenum pressure rise is defined as $\Delta P = P_p - P_a$. Then equation 3.1.1b becomes

$$C - \Delta P = L_c(d\rho C_x/dt). \quad 3.3.2$$

Equation 3.1.2 needs to be in terms of mass flow. Knowing that $\rho C_x = m_c/A_c$ we get

$$C - \Delta P = L_c/A_c(dm_c/dt). \quad 3.3.3$$

The compressor and throttle mass flows are linked by mass conservation in the plenum and is as follows

$$m_c - m_t = (d\rho_p V_p/dt). \quad 3.3.4$$

The density change will be related to the changes in plenum pressure by

$$d\rho_p/dt = (\rho_p/\kappa P_p)(dP_p/dt) \quad 3.3.5$$

where κ is the polytropic exponent. From thermodynamics the relationship below is

given

$$P_p/\rho_p = RT_p \quad 3.3.6$$

The mass conservation equation in the plenum can now be written as

$$m_c - m_t = (V_p/\gamma RT_p) (dP_p/dt). \quad 3.3.7$$

Conservation of angular momentum in the turbocharger spool is written as

$$I(d\omega/dt) = \Gamma_d - \Gamma_c \quad 3.3.8$$

There is a definite time lag between the onset of instability and the establishment of the fully developed rotating stall pattern when the stall limit line is reached and the axisymmetric compressor flow field becomes unstable. The times needed for the stall cell to develop can be long enough that the compressor mass flow can undergo significant changes during this time. Therefore, a quasi-steady approximation will not be appropriate for the modeling here. A first order transient response model will be used to simulate this lag in compressor response. The approximation for the transient compressor response can be written explicitly as

$$\tau(dC/dt) = (C_{ss} - C). \quad 3.3.9$$

3.4 Nondimensional Equations for Variable Speed Model

Equations 3.3.3, 3.3.7, 3.3.8, and 3.3.9 will be nondimensionalized. Mass flows will be nondimensionalized with the quantity $\rho A_c U$, pressures will be nondimensionalized with the quantity $0.5\rho U^2$, time will be nondimensionalized with the Helmholtz resonator frequency ($1/\omega_H$), and torques will be nondimensionalized by the quantity $\rho A_c R_t U^2$. All parameters with a bar over it are nondimensional. There are seven nondimensional parameters which are listed below:

$$\bar{C} = C/(0.5\rho U^2)$$

$$\bar{\Delta P} = \Delta P/(0.5\rho U^2)$$

$$\bar{\Gamma} = \Gamma/\rho A_c R_t U^2$$

$$\bar{m}_c = m_c/(\rho A_c U)$$

$$\bar{m}_t = m_t/(\rho A_c U)$$

$$\bar{t} = t(\omega_H)$$

$$\bar{\tau} = \tau(\omega_H).$$

Nondimensionalizing equation 3.3.3 leads to the following equation

$$\bar{C}(0.5\rho U^2) - \bar{\Delta P}(0.5\rho U^2) = (L_c/A_c)[d(\bar{m}_c \rho A_c U)/d(\bar{t}/\omega)]. \quad 3.4.1$$

Dividing by $0.5\rho U^2$ and simplifying, equation 3.4.1 becomes

$$(\bar{C} - \bar{\Delta P}) = (2L_c/U^2)(d\bar{m}_c U \omega_H / d\bar{t}). \quad 3.4.2$$

Multiply equation 3.4.2 on top and bottom on the right hand side by $2L_c\omega_H^2$ gives

$$(\bar{C} - \bar{\Delta P}) = (4L_c^2\omega_H^2/U^2)[(\bar{dm}_c/dt)(U\omega_H/2\omega_H^2L_c)]. \quad 3.4.3$$

Employing the relationship $B = U/2\omega_H L_c$ equation 3.4.3 becomes

$$1/B^2(\bar{dm}_c B/dt) = (\bar{C} - \bar{\Delta P}). \quad 3.4.4$$

Nondimensionalizing equation 3.3.7 leads to the following relationship

$$\bar{m}_c(\rho A_c U) - \bar{m}_t(\rho A_c U) = (V_p/\gamma RT_p)[d\bar{\Delta P}(0.5\rho U^2)/d(t/\omega_H)]. \quad 3.4.5$$

The Helmholtz frequency is calculated using the speed of sound in the plenum at the starting steady state operating point and is given below as

$$\omega_H = a_{po}*(A_c/V_p L_c)^{0.5} \quad 3.4.6$$

The speed of sound on the plenum can also be written as

$$a_{po} = (\gamma RT_p)^{0.5} \quad 3.4.7$$

Equations 3.4.6 and 3.4.7 can be combined to give

$$\gamma RT_p = \omega_H^2 V_p L_c / A_c. \quad 3.4.8$$

The right hand side of equation 3.4.5 needs to have the quantity of $\omega_H^2 V_p L_c / A_c$. To accomplish this the right hand side of equation 3.4.5 needs to be multiplied on top and bottom by the quantity $L_c \omega_H$, and then equation 3.4.5 needs to be divided by ρA_c to give

$$(\bar{m}_c - \bar{m}_t)U = (\omega_H^2 V_p L_c / A_c)(1/\gamma RT_p)[(d\bar{\Delta P}/dt)(U^2/(2\omega_H L_c))]. \quad 3.4.9$$

Employing the relationship found in equation 3.4.8 into equation 3.4.9 gives

$$(\bar{m}_c - \bar{m}_t)U = (\gamma RT_{p0}/\gamma RT_p)[(d\bar{\Delta P}/dt)(U^2/(2\omega_H L_c))]. \quad 3.4.10$$

Equation 3.4.10 needs to be multiplied by T_p and divided by UT_{p0} to get

$$(\bar{m}_c - \bar{m}_t)(T_p/T_{p0}) = (1/U)[(d\bar{\Delta P}/dt)(U^2/(2\omega_H L_c))]. \quad 3.4.11$$

Knowing that $U = 2B\omega_H L_c$ equation 3.4.11 becomes

$$(\bar{m}_c - \bar{m}_t)(T_p/T_{p0}) = (1/2B\omega_H L_c)[(d\bar{\Delta P}/dt)(U^2/(2\omega_H L_c))]. \quad 3.4.12$$

Take the $2\omega_H L_c$ inside the differential on the right hand side of equation 3.4.12 to obtain

$$(\bar{m}_c - \bar{m}_t)(T_p/T_{p0}) = (1/B)[(d\bar{\Delta P}/dt)(U^2/(4\omega_H^2 L_c^2))]. \quad 3.4.13$$

Knowing that $B^2 = U^2/4\omega_H^2 L_c^2$ equation 3.4.13 becomes

$$(\bar{m}_c - \bar{m}_t)(T_p/T_{p0}) = (1/B)(d\bar{\Delta P}B^2/dt). \quad 3.4.14$$

Nondimensionalizing equation 3.3.8 leads to the following relationship

$$I(d\omega/dt/\omega_H) = (\bar{\Gamma}_d - \bar{\Gamma}_c)\rho A_c R_t U^2. \quad 3.4.15$$

Letting $\bar{\Gamma}_{net} = \bar{\Gamma}_d - \bar{\Gamma}_c$ and knowing that $\omega = U/R_t$ equation 3.4.15 becomes

$$(I/R_t)(dU/dt) = \bar{\Gamma}(\rho A_c R_t U^2/\omega_H). \quad 3.4.16$$

By taking the differential of both sides of $U = 2B\omega_H L_c$ it follows that

$$dU = 2\omega_H L_c dB. \quad 3.4.17$$

Substituting equation 3.4.17 into equation 3.4.16 gives

$$(I/R_t)(2\omega_H L_c)(dB/dt) = \bar{\Gamma}(\rho A_c R_t U^2/\omega_H). \quad 3.4.18$$

The spool inertia parameter must be defined as

$$I_p = 2\rho A_c L_c R_t^2/I. \quad 3.4.19$$

Equation 3.4.18 needs to be multiplied by R_t and divided by $2I\omega_H L_c$ to give

$$(dB/dt) = \bar{\Gamma}(\rho A_c R_t^2/I)(U^2/2\omega_H^2 L_c). \quad 3.4.20$$

Multiply equation 3.4.20 on top and bottom by $2L_c$ to get

$$(dB/dt) = \bar{\Gamma}(2\rho A_c L_c R_t^2/I)(U^2/4\omega_H^2 L_c^2). \quad 3.4.21$$

Employing the relationship found in equation 3.4.19 and knowing that $B^2 = U^2/4\omega_H^2 L_c^2$ equation 3.4.21 becomes

$$dB/dt = \bar{\Gamma} I_p B^2. \quad 3.4.22$$

Using the chain rule on equation 3.4.4 gives

$$1/B^2[\bar{m}_c(dB/dt) + B(d\bar{m}_c/dt)] = (\bar{C} - \bar{\Delta}P). \quad 3.4.23$$

Substituting equation 3.4.22 into equation 3.4.23 gives

$$1/B^2[\bar{m}_c(\bar{\Gamma} I_p B^2) + B(d\bar{m}_c/dt)] = (\bar{C} - \bar{\Delta}P). \quad 3.4.24$$

Rearranging equation 3.4.24 gives

$$\overline{dm_c}/dt = B(\overline{C} - \overline{\Delta P}) - \overline{m_c}\overline{\Gamma} I_p B. \quad 3.4.25$$

Using the chain rule on equation 3.4.14 gives

$$(\overline{m_c} - \overline{m_t})(T_p/T_{po}) = (1/B)[B^2(d\overline{\Delta P}/dt) + \overline{\Delta P}2B(dB/dt)]. \quad 3.4.26$$

Substituting equation 3.4.22 into equation 3.4.26 and then multiply through on the right hand side by 1/B gives

$$(\overline{m_c} - \overline{m_t})(T_p/T_{po}) = B(d\overline{\Delta P}/dt) + 2\overline{\Delta P}\overline{\Gamma} I_p B^2. \quad 3.4.27$$

Rearranging equation 3.4.27 gives

$$d\overline{\Delta P}/dt = (1/B)(T_p/T_{po})(\overline{m_c} - \overline{m_t}) - 2\overline{\Delta P}\overline{\Gamma} I_p B. \quad 3.4.28$$

Nondimensionalizing equation 3.3.9 leads to the following equation

$$(\overline{\tau}/\omega_H)[d\overline{C}(0.5\rho U^2)/d(t/\omega_H)] = (0.5\rho U^2)(\overline{C}_{ss} - \overline{C}). \quad 3.4.29$$

Rearranging equation 3.4.29 gives

$$d\overline{C}/dt = (1/\overline{\tau})(\overline{C}_{ss} - \overline{C}). \quad 3.4.30$$

The throughflow time in equation 3.3.9 is assumed to be given approximately by

$$\tau = |L_t/C_x|. \quad 3.4.31$$

Nondimensionalizing equation 3.4.31 gives

$$\bar{\tau} = \left| L_t / C_x \right| \omega_H. \quad 3.4.32$$

Knowing that $m_c = \rho A_c C_x$ and $\omega_H = U / 2BL_c$ equation 3.4.32 becomes

$$\bar{\tau} = \left| \rho A_c U / m_d \right| (L_t / 2BL_c). \quad 3.4.33$$

Employing nondimensional mass flow through the compressor equation 3.4.33 becomes

$$\bar{\tau} = \left| 1 / \bar{m}_d \right| (L_t / 2BL_c). \quad 3.4.34$$

Equations 3.4.22, 3.4.25, 3.4.28, and 3.4.30 are a set of coupled nonlinear equations to be solved to predict the transient behavior of the variable speed compression system (Fink 1988).

3.5 Non-surging Compressor Model

The non-surging compressor model is a very basic model. This model was developed to make the computer computational time faster for the compressor since a very small time step is required by the compressor model during a surge event to capture all the dynamics of the system. This model has no algorithm to solve the differential equations. Instead the compressor is assumed to be operating on the unstalled part of the compressor characteristic in steady state with the other components of the compression system. The equations derived earlier are still valid for this analysis. If the compressor encounters a situation where a surge event might occur, then the computer program will output a zero for mass flow through the compressor to let the user know that a surge event could occur at this point.

3.6 Compressor Characteristic

The hyper plant requires a compressor that has a mass flow rate of 1.279 kg/s, a pressure ratio of 4:1, a speed of 100 kRPM, and an efficiency of 80% at the design point. The compressor characteristic used in the paper “Surge Dynamics in a Free-Spool Centrifugal Compressor System” has a pressure ratio of 3.58, a corrected mass flow of .522 kg/s, a corrected speed of 69000 RPM, and an efficiency of 74% at the design point and is shown in figure 3.6.1. The compressor characteristic has been nondimensionalized. The x-axis is simply the corrected mass flow rate divided by $\rho U A_c$. The y-axis is defined as

$$\psi = (\Pi^{(\gamma-1)/\gamma} - 1) / ((\gamma-1)M_{to}^2) \quad 3.6.1$$

where Π (pressure ratio) is the pressure in the compressor divided by ambient pressure of 101325 Pa, and M_{to} is the impeller tip Mach index.

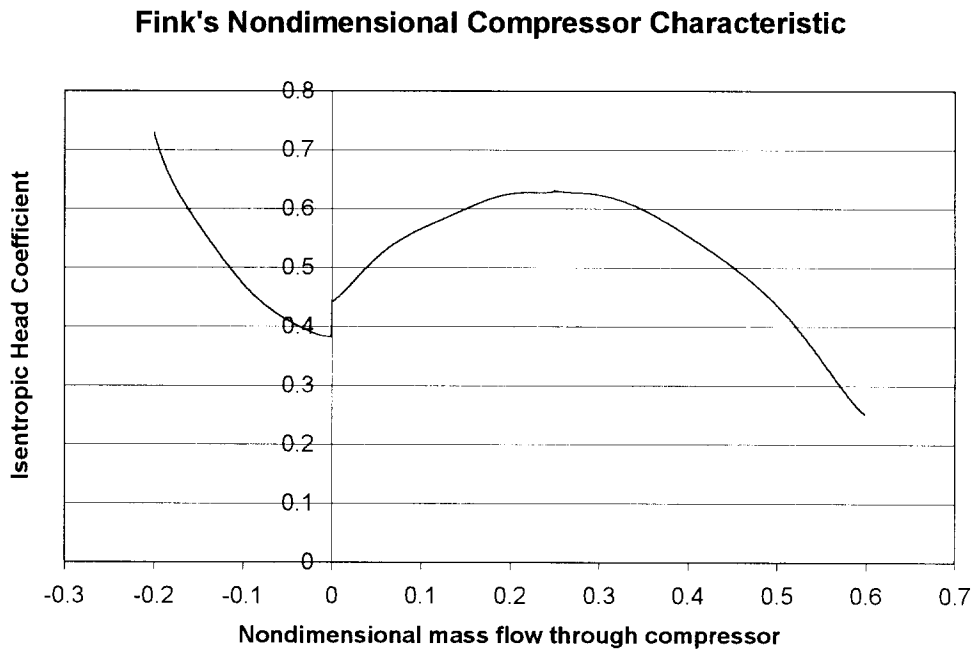


Figure 3.6.1

By applying factors and deltas to the known compressor map, a compressor map with the desired design point can be created. The map scaling procedure is to be used on maps with corrected mass flow, corrected speed, and overall pressure ratio. The design points for the known and wanted compressor characteristics will be used to determine the factors and deltas for the scaling procedure. Once the factors and deltas are determined then they will be applied to the off design conditions of the compressor characteristic as well. Since the compressor map can be scaled in dimensional form, then it must be able to be scaled in nondimensional form also. The known compressor characteristic from Fink is already nondimensionalized. Finks' dimensional compressor characteristic has corrected mass flow, pressure ratio, and corrected speed as parameters. The major parameters that Fink nondimensionalizes for the compressor characteristic are corrected mass flow and overall pressure ratio as noted at the beginning of this section. Therefore, the scaling procedure will work for Finks' nondimensional compressor characteristic.

The scaling procedure equations are shown below

$$W_w = X_1 * W_k + \Delta_1 \quad 3.6.2$$

$$Eff_w = X_2 * Eff_k + \Delta_2 \quad 3.6.3$$

$$PR_w = ((PR_k - 1.0) * X_3 + \Delta_3) + 1.0 \quad 3.6.4$$

$$N_w = X_4 * N_k + \Delta_4 \quad 3.6.5$$

There are four factors and four deltas denoted in the equations by X and Δ respectively. The user has the ability to pick the factors and deltas necessary to align the design points of the machine, then use the factors and deltas on the known off design conditions as well. Equation 3.6.2 is for corrected mass flow denoted by W. Equation 3.6.3 is for Efficiency denote by Eff. It is noted in scaling procedure that factor 2 (X₂) is set to 1.

Equation 3.6.4 is for overall pressure ratio which is denoted by PR. Equation 3.6.5 is for corrected speed which is denoted by N. It is noted in the scaling procedure that delta 4 (Δ_4) is set to zero.

The nondimensional design point data for Fink's nondimensional compressor map were calculated to be:

$$\text{isentropic head coefficient} = \psi_c = .627770048$$

$$\text{nondimensional mass flow} = C_x/U = .270415289$$

The nondimensional design point data for the required compressor for the hyper plant were calculated to be:

$$\text{isentropic head coefficient} = \psi_c = .330398461$$

$$\text{nondimensional mass flow} = C_x/U = .109111906$$

Factor 3 was set to $X_3 = 0.526629706$ and by using equation 3.6.4 and the design data, delta 3 was calculated to be $\Delta_3 = -0.473574189$. Delta 1 was set to $\Delta_3 = 0.0$ and by using equation 3.6.2 and the design data, factor 1 was calculated to be $X_1 = 0.403497548$. For equation 3.6.3 factor 2 is set to $X_2 = 1.0$ and delta 4 is calculated to be $\Delta_3 = 0.06$. These factors and deltas are then applied to the known off design conditions through the use of microsoft excel. The created nondimensional compressor map is shown in figure 3.6.2. It should be noted that the discontinuity that occurs at zero mass flow on Fink's nondimensional compressor map is unwanted on the created nondimensional compressor map. Therefore, the curve was smoothed out in microsoft excel to give a more continuous curve.

Next, an efficiency map for Fink's compressor was developed by using torque data supplied in Fink's paper (Fink 92). The efficiency versus nondimensional mass flow

for Fink's compressor was plotted out and is shown in figure 3.6.3. The map scaling procedure was then applied to Fink's efficiency plot and the results shown in figure 3.6.4.

Nondiscontinuous Created Compressor Characteristic

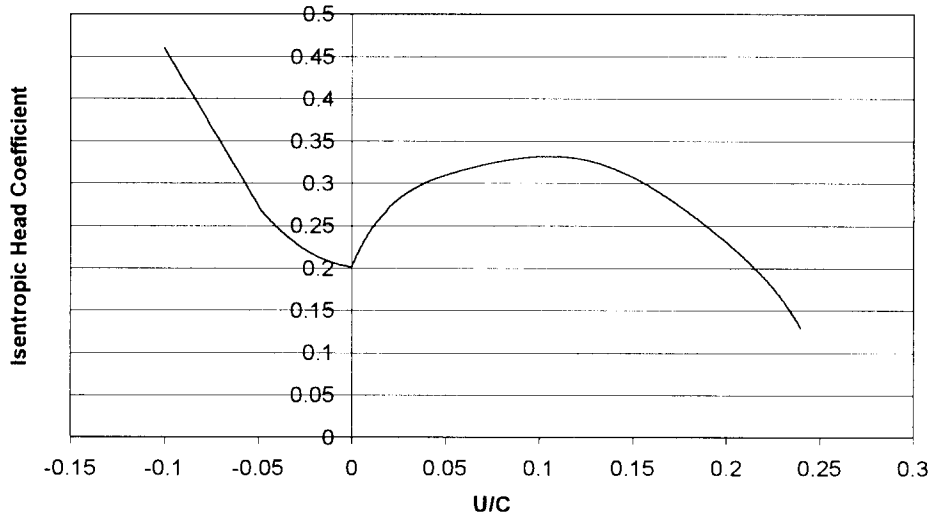


Figure 3.6.2

Fink's Efficiency versus Cx/U

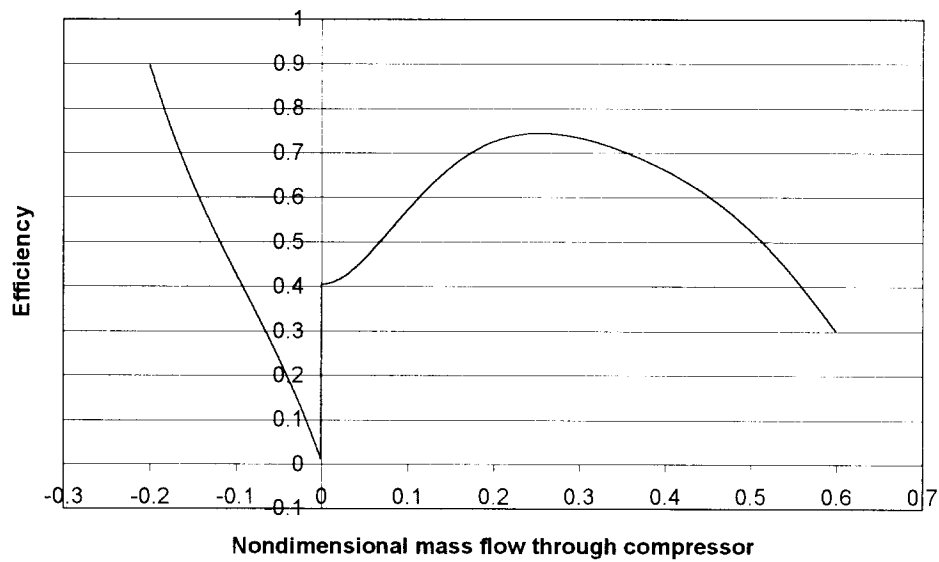


Figure 3.6.3

Created Efficiency Versus Nondimensional Mass Flo Through the Compressor

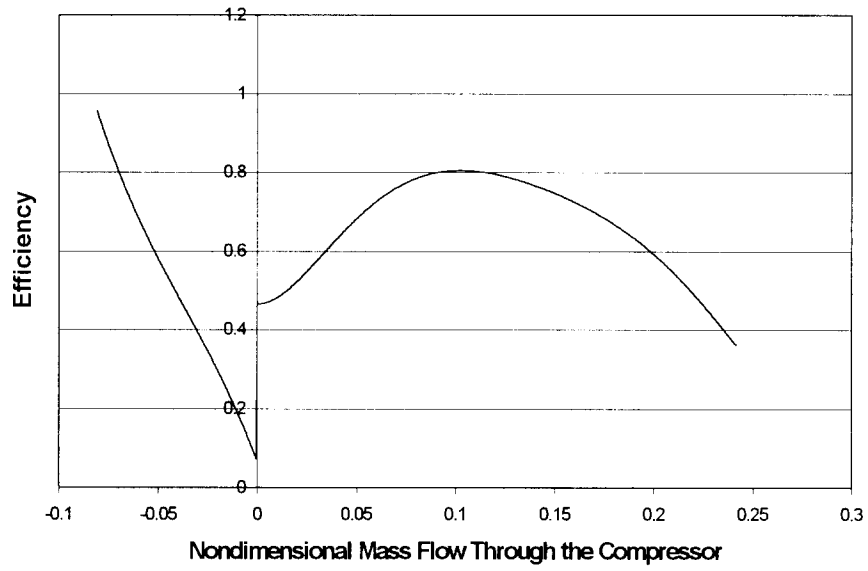


Figure 3.6.4

4.0 TURBINE MODEL

4.1 Fluid Dynamic Processes

The existing compressor model consists of a compressor in a duct followed by plenum and then a throttle in a duct. To tie the turbine model to the compressor model, the turbine will replace the throttle in the compressor model. The compressor will have a given mass flow through the machine. The compressor and turbine, along with a generator, will be on the same shaft; therefore, they will experience the same rotational speed. The inlet pressure and temperature to the turbine, as well as the outlet pressure, will be known. The inlet mass flow to the turbine will be obtained from a turbine map. During steady state conditions, the mass flow through the compressor will be the same as the mass flow through the turbine; however, during a surge event the mass flow through the compressor will not be the same as the mass flow through the turbine. Using the given values, a turbine map can be used to determine the efficiency for the process. From the efficiency the turbine outlet temperature can be calculated.

The turbine map will be based on steady state data. The turbine map will be used on a quasi-steady basis. During a surge event, the turbine will experience a fluctuating mass flow. It is questionable whether this unsteady mass flow can be applied on a quasi-steady basis to the turbine map to get the correct efficiency. In turbomachines the influence of unsteady flows depends on the ratio of the time constant of the unsteadiness to the characteristic time constant of the flow through the blade passage itself. This can be expressed through the Richardson number. The Richardson number is defined as

$$Rn = \omega L / C,$$

in which ω is the angular frequency of the unsteadiness, L is the meridional length of the rotor, and C is the mean relative velocity. If a value on the order of unity is obtained for the Richardson number, then the unsteadiness is important in determining the performance of the machine. If the Richardson number comes out to be greater than unity, then the unsteadiness dominates the flow. However, if a value of less than unity is obtained for the Richardson number, then the flow will behave in a quasi-steady manner. The Richardson number tends to be 0.1 for small, high-speed turbines running with inlet flows pulsating at frequencies typical of turbocharger operation. This helps one to make the assumption that a quasi-steady analysis can be used in this case.

The turbine power and turbine outlet temperature and density will be calculated with the following equations.

First, specific power will be calculated with

$$W_T = \eta_T c_{pT} T_{inlet} (1 - (1/PR)^{((\gamma-1.0)/\gamma)}). \quad 4.1.1$$

Next the outlet temperature will be calculated with

$$T_{outlet} = T_{inlet} - W_T / c_{pT}. \quad 4.1.2$$

The outlet density can then be calculated with

$$\rho_{outlet} = P_{outlet} / RT_{outlet}. \quad 4.1.3$$

Next, the power can be calculated by using the following equation

$$J_T = W_T m_T. \quad 4.1.4$$

4.2 Turbine Map: A turbine map with a pressure ratio of 4:1, mass flow of 1.279 kg/s, speed of 100 kRPM, and an efficiency of 85% at the design point is needed for the turbine model to be complete. The range for the pressure ratio of the turbine map needs to be considered as well. For the current compressor characteristic that was developed by scaling up a nondimensionalized compressor characteristic the B value turns out to be very large. Due to the large B, when the compressor enters into a surge event the pressure in the plenum remains constant as the mass flow through the compressor decreases. The pressure that the turbine will experience comes from the overall system. Therefore, the turbine pressure will not exceed a pressure ratio of 4:1.

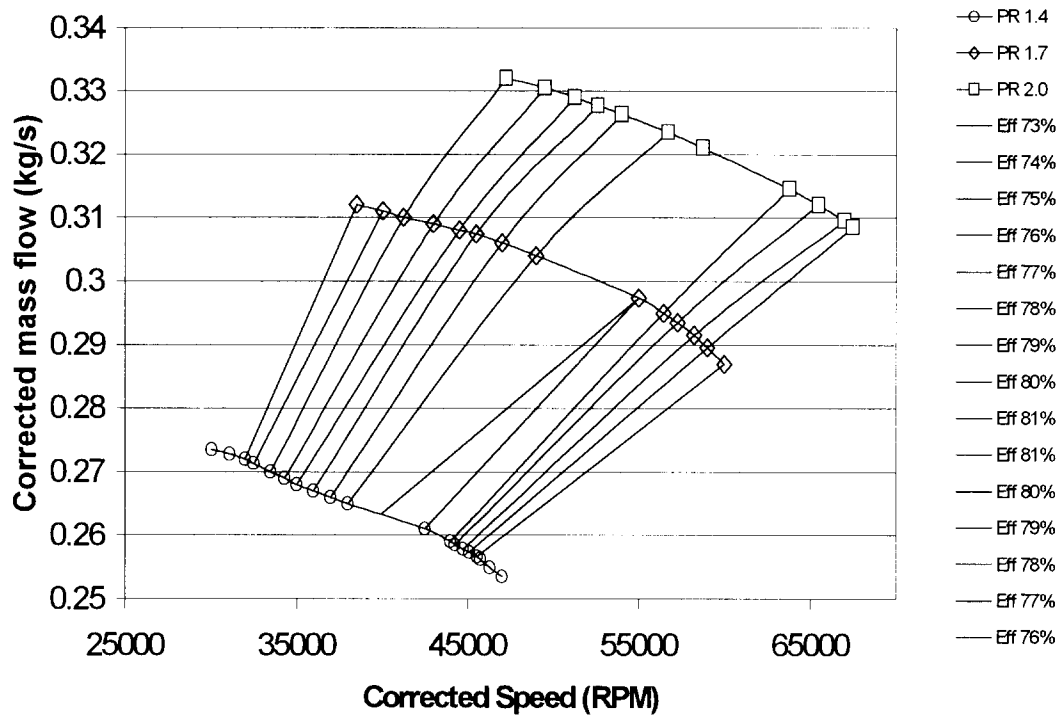
The radius of the impeller can be calculated using a correlation between specific speed, specific diameter, and velocity ratio. When combining these parameters the radius of the impeller can be calculated from the equation below

$$R = ((\text{velocity ratio})/\omega) * (2\Delta h_o/\eta_{ts})^{0.5}.$$

The velocity ratio is just the tip speed divided by the isentropic expansion velocity. The velocity ratio is set to 0.7 which is a maximum for radial inflow turbines. The specific work output is denoted by Δh_o . The radius of the impeller is calculated to be 0.0600m (Baines 2000).

The scaling procedure used for the compressor map can also be used for turbine map. A turbine map with the desired design point could not be found in any of the literature. However, a turbine map that had an overall pressure ratio range of 1.4 to 2.0, a corrected speed range of 30 kRPM to 67 kRPM, and a corrected mass flow range of .25 to .34 was found and is shown in figure 4.2.1 (VKI LS 92). In order to scale the turbine map up to

Known Turbine Map



meet the required design conditions the map must be nondimensionalized. Buckingham Pi theorem was used to determine how to nondimensionalize the corrected mass flow.

The important variables used in Buckingham Pi theorem are P_{inlet} , P_{outlet} , ω , R , m_T , and ρ_{inlet} . The corrected mass flow will be nondimensionalized by the following equation

$$\Pi_m = (\omega * m_T) / (\Delta P * R) \quad 4.2.1$$

where ω is the angular velocity in rad/sec for the current corrected mass flow, m_T is the corrected mass flow, R is the radius of the turbine impeller, and ΔP is the pressure drop across the turbine for the current corrected mass flow and angular velocity. The outlet pressure for the given turbine map is 101305 Pa. Since ΔP is defined as the pressure drop across the turbine

$$\Delta P = P_{inlet} - P_{outlet},$$

and if the pressure ratio is defined as

$$PR = P_{\text{inlet}} / P_{\text{outlet}},$$

Then ΔP can be calculated from the equation

$$\Delta P = P_{\text{outlet}}(PR - 1.0).$$

The corrected speed is nondimensionalized with the following equation

$$\Pi_s = \rho_{\text{inlet}} * (\text{tip speed})^{2.0} / P_{\text{inlet}}. \quad 4.2.2$$

To scale the turbine map up the design points will be the point that is used to do this. The nondimensional corrected mass flow for the turbine map being created is calculated using equation 4.2.1 and a corrected mass flow of 1.279 kg/s, pressure ratio of 4:1, an impeller radius of .0600 m, a speed of 100 kRPM, and an outlet pressure of 107200 Pa and is calculated to be $\Pi_m = 0.815008658$. Next, The nondimensional corrected speed for the map being created is calculated by equation 4.2.2 using an inlet temperature of 1700 °F to give $\Pi_s = 0.831574578$. The nondimensional corrected mass flow and the nondimensional corrected speed for the known map are calculated and shown below respectively.

$$\Pi_m = 0.315788812$$

$$\Pi_s = 0.727287625.$$

Equations 3.6.2-3.6.5 are applicable here. By using equation 3.6.2 and setting

$\Delta_1 = 0.0$, factor 1 is calculated to be $X_1 = 2.580866158$. By using equation 3.6.3

$\Delta_1 = .07$. By using equation 3.6.4 and setting $\Delta_3 = 0.0$, factor 3 is calculated to be $X_3 =$

3.0. By using equation 3.6.5 and setting $\Delta_4 = 0.0$, factor 4 is calculated to be $X_4 =$

1.143391623. Thus once the scaling factors are determined then all the nondimensional

off-design points from the given turbine map must be scaled up as well. This process

was completed and the nondimensional turbine map which was created is plotted in figure 4.2.2.

It can be seen from the nondimensionalized turbine map that each pressure ratio line passes through the origin if they are extended backwards. This is reassuring because if the turbine speed is zero then there should be no mass flow going through the machine. The newly created nondimensional turbine map will need to be dimensionalized in order

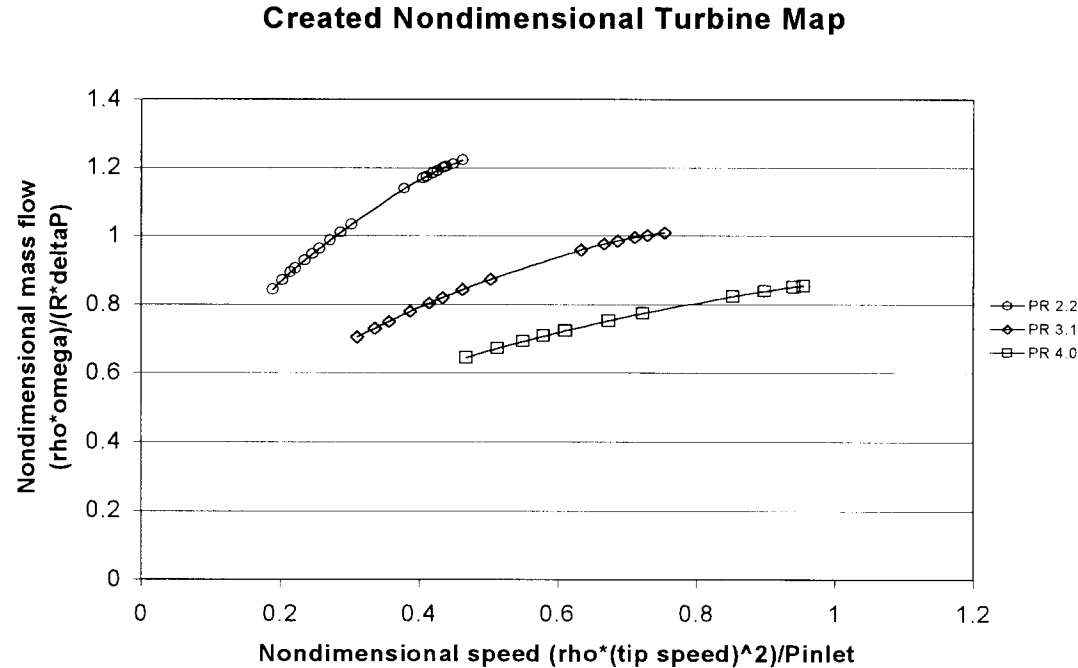


Figure 4.2.2

to be able to determine an efficiency plot for the created turbine map. To do this equations 4.2.1 and 4.2.2 are applied to the created nondimensional turbine map in figure 4.2.2. This process was completed and the turbine map is shown in figure 4.2.3.

The efficiency is plotted against velocity ratio. The velocity ratio is the tip speed of the impeller divided by the isentropic expansion velocity. The isentropic expansion velocity is defined as, $C_s^2 = 2C_p T_{inlet} [1 - (1/PR)^{(\gamma-1.0)/\gamma}]$ (4.2.3).

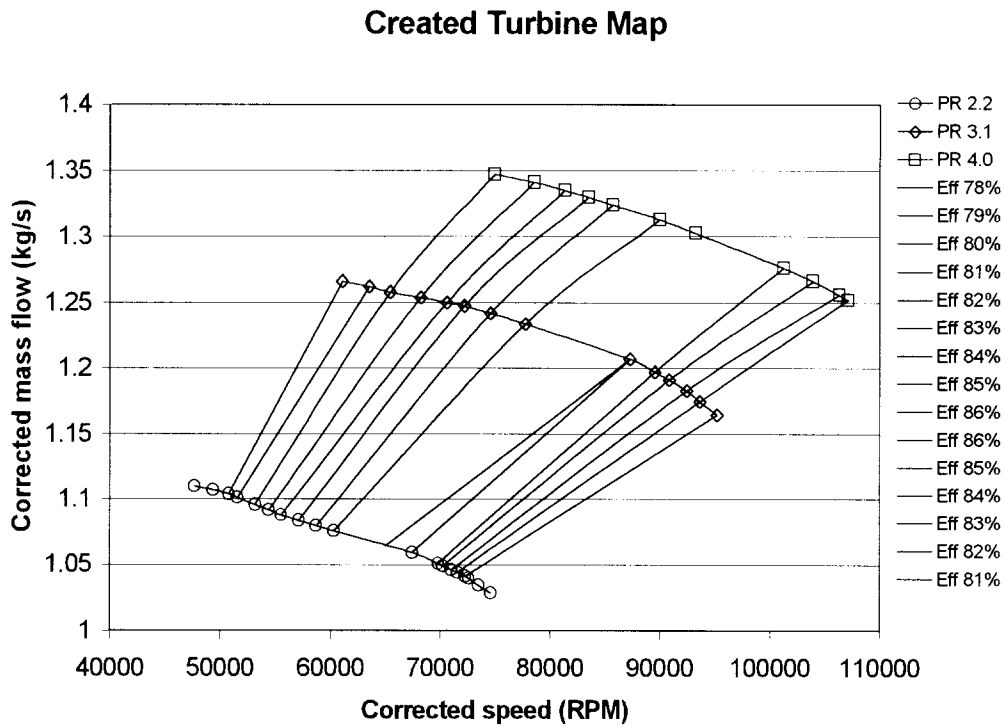


Figure 4.2.3

By using equation 4.2.3, efficiency versus velocity ratio shown in figure 4.2.4 can be plotted from the created turbine map.

Efficiency versus U/Cs For Created Map

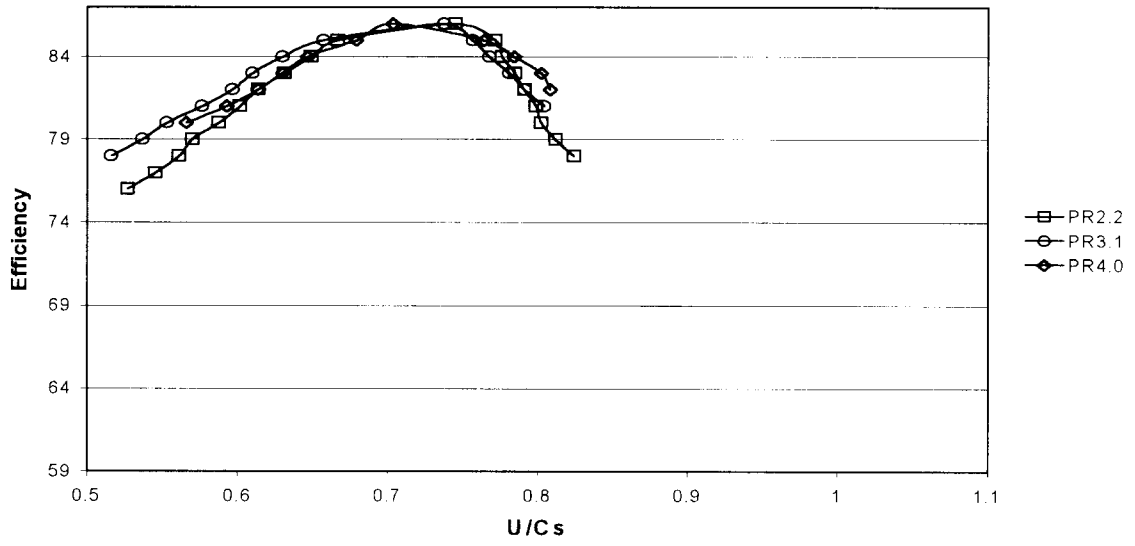


Figure 4.2.4

5.0 INTEGRATION OF MODELS INTO PROTRAX

The compressor/turbine model will be tested by using FORTRAN programming. The model will then be tested in PROTRAX. The results from the two test will be compared to ensure that PROTRAX is running appropriately. When results are in agreement the model will then be used in the overall process of the hyper plant.

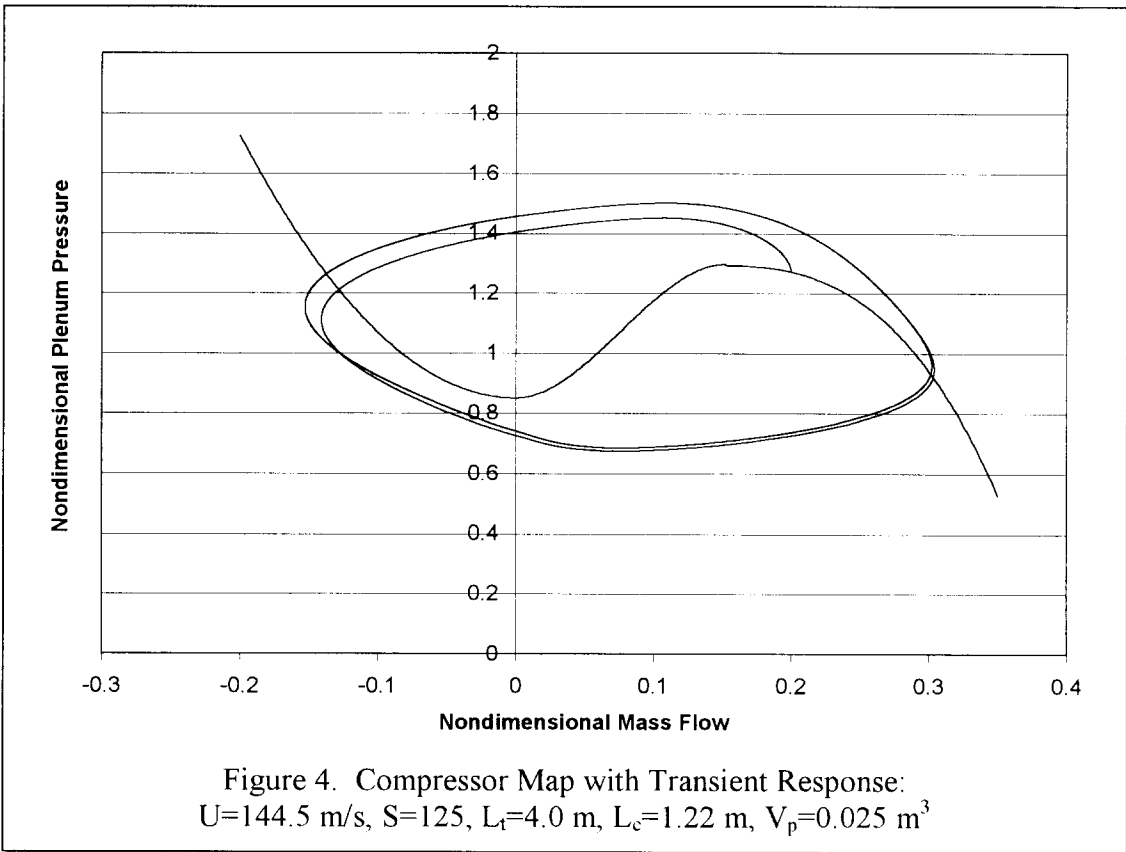
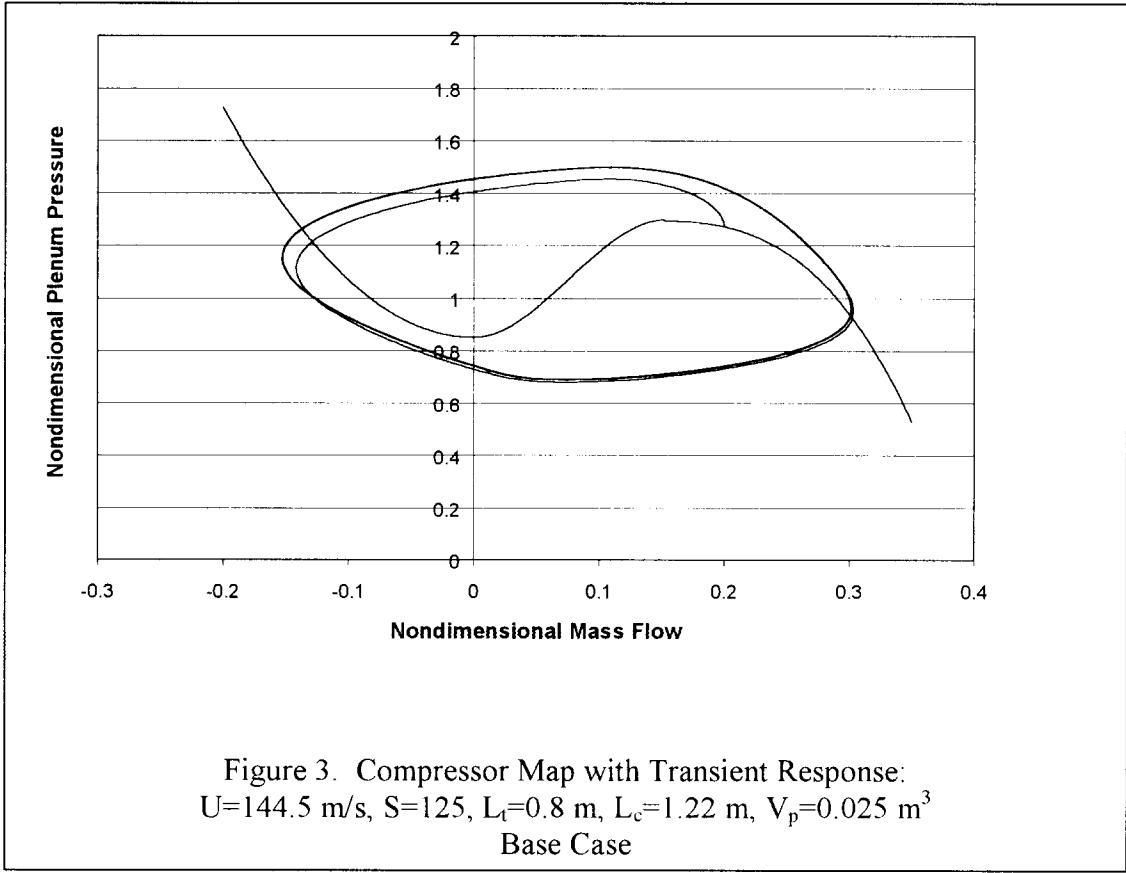
6.0 APPLICATION AND RESULTS

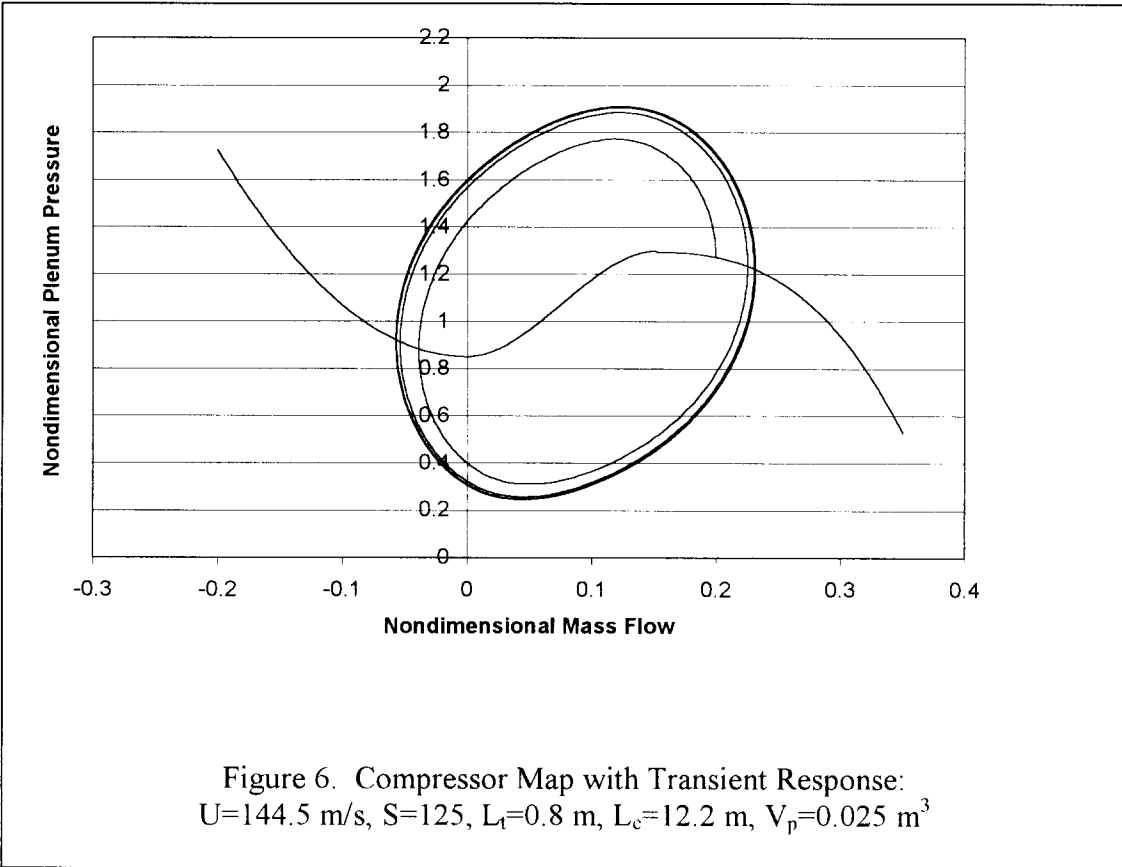
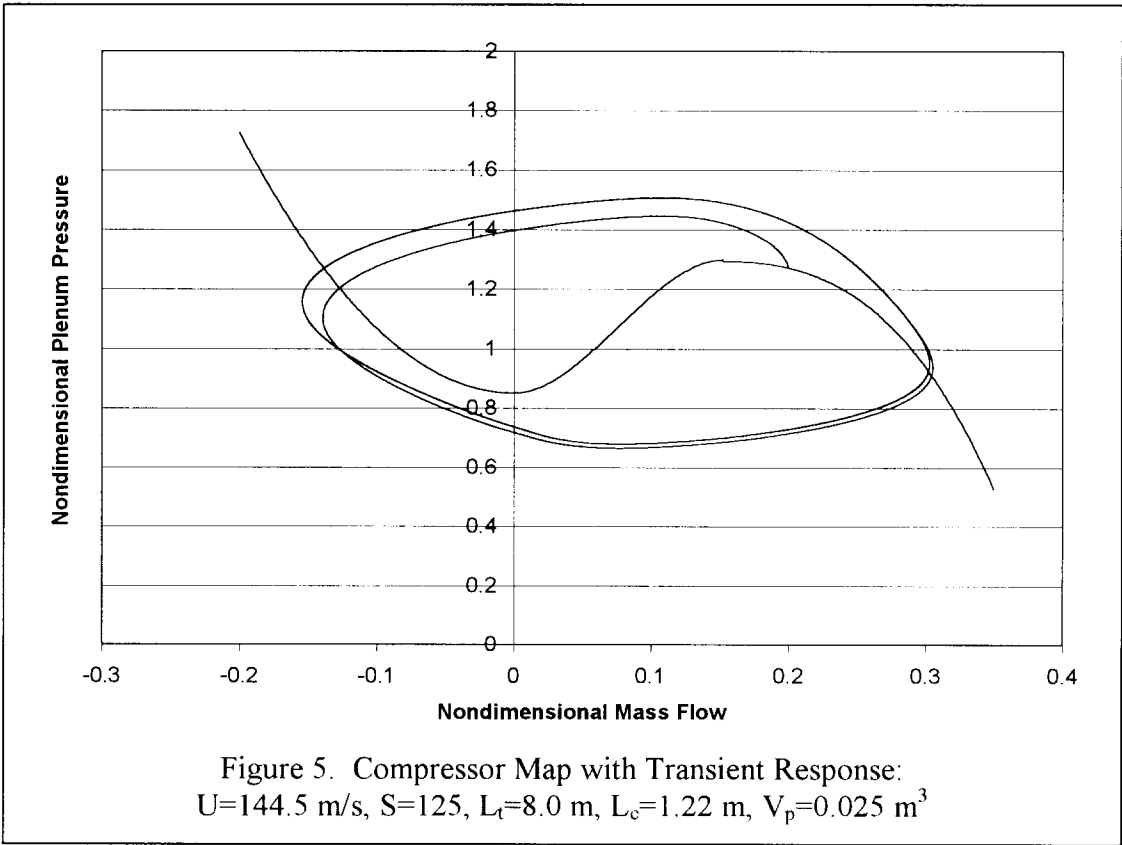
6.1 Test Cases for Constant Speed Compressor Model

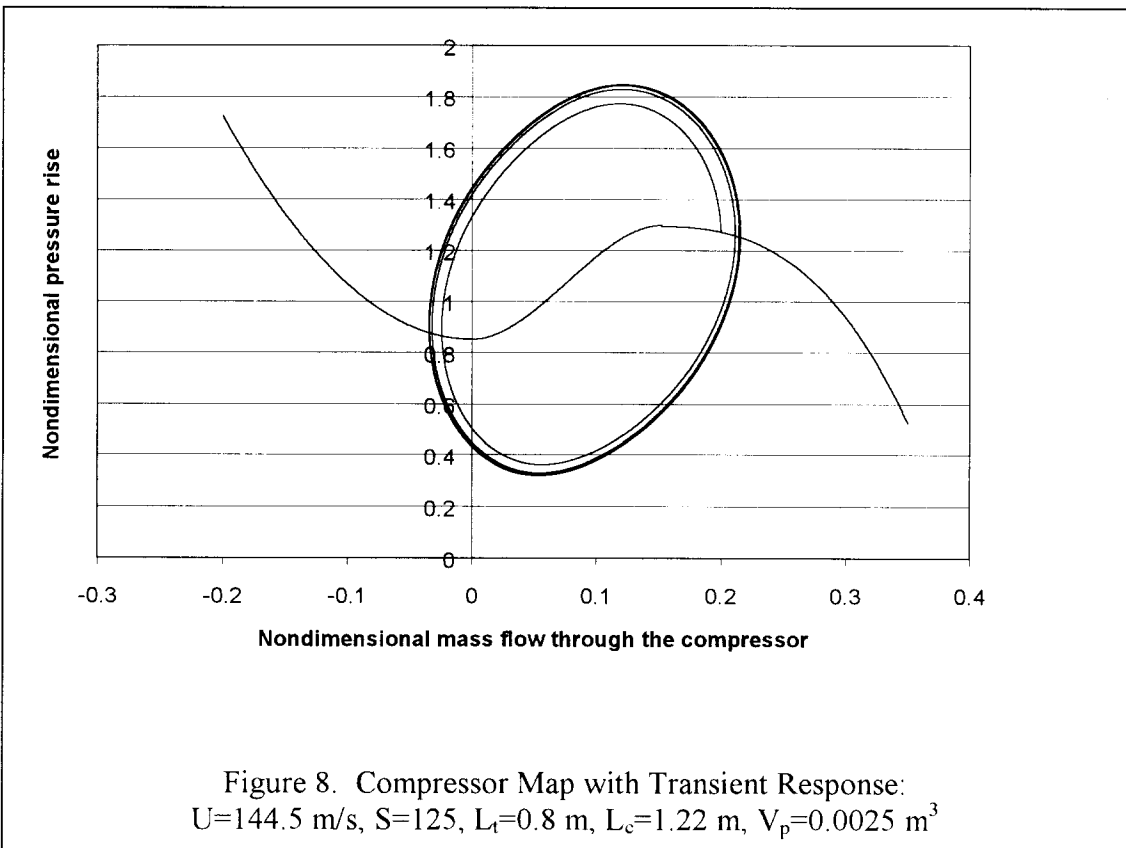
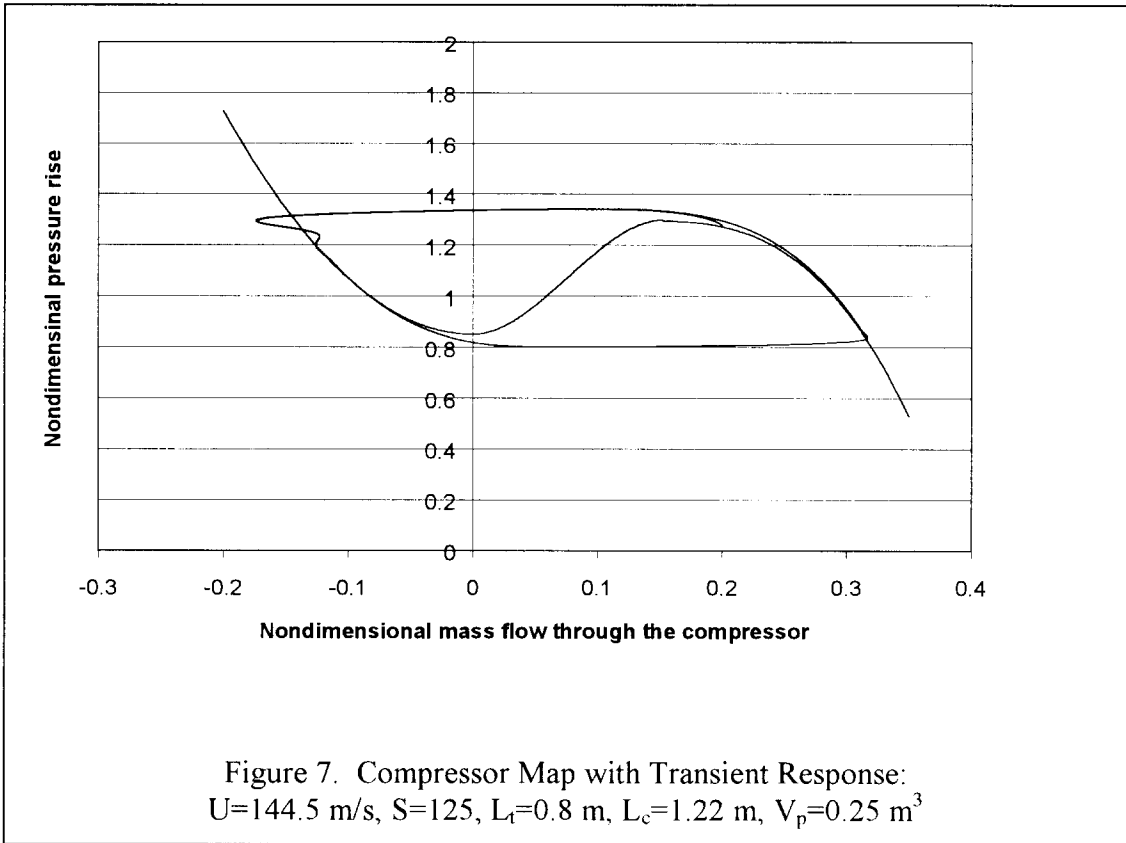
A sensitivity analysis was done on the compressor model testing L_1 , L_c , and V_p . Figure 3 shows the base case. L_1 was increased by a factor of 5 and 10 in Figures 4 and 5 respectively. Comparing Figures 4 and 5 with Figure 3 it can be seen that the overall result of the transient response is hardly effected when L_1 is varied by substantial amounts while keeping other parameters constant. The fact that L_1 does not change the overall results and that it appears only in the G parameter proves that the effect of changes to the G parameter are weak.

Increasing L_c by a factor of ten, as shown in figure 6, we see that the mass flow does not have as big of a range as the base case, and the pressure swings are more violent. When V_p is increased by a factor of ten, as shown in figure 7, the negative mass flow experienced during a surge is larger, and the pressure swings are not as violent.

Comparing the cases where $V_p=0.0025$, as shown in figure 8, and $L_c=12.2$, as shown in figure 6, one can see that the transient response of each case is very similar, which is reasonable because the B parameter value for each of these cases are identical. The slight difference in the transient response between the two cases is because L_c is included in the G parameter but V_p is not. This shows that, irrespect of B being obtained with a smaller volume or a larger compressor duct length, or vice versa, the overall transient response is similar.







7.0 DIMENSIONAL ANALYSIS IN TURBOMACHINES

There are 3 types of similarity, geometric, kinematic and dynamic.

-A model and prototype are *geometrically* similar if all physical or body dimensions in all three axes (for Cartesian coordinates) have the same linear ratio

-The motions of two systems are *kinematically* similar if similar elements lie at similar locations at similar times

-*Dynamic* similarity requires that the additional effects of force-scale or mass-scale be maintained between a model and a prototype, taking length scale and time scale

The goal is to be able to accurately predict the performance or behavior of bodies or machines from another set of conditions or from another situation.

Dimensional analysis is usually performed using product method, (also called Buckingham-Pi Theorem) which states that if one has a set of performance variables based on a number of fundamental dimensions, the object is to group the variables into products that are dimensionless. We have total of three basic dimensions, M, L, T.

The steps in obtaining the number of π terms is as follows:

- 1-List and count the variables (N_v)
- 2-List and count the basic units (N_u)
- 3-Select a number of variables as primary (usually equal to the number in step 2)
- 4-Form π products as many as $(N_v) - (N_u)$

For use in fuel cell cycles, four methods have been introduced in order to scale down existing turbine maps. The reason for scaling down is that the power output of daily usage turbines are much larger than needed. After obtaining all the scaling methods, comparisons will be made with the real values. The best method will be chosen in accordance with the best matching.

Method 1:

The basic non-dimensional parameters are common to all turbomachines and have many different expressions, depending on the working fluid (compressible or incompressible) and the application (compressor, pump, turbine). For turbines operating with compressible flows, one way to write the non-dimensional terms is as follows: [1]

Mass flow rate	$\frac{\dot{m} \sqrt{RT_{01} / \gamma}}{D^2 P_{01}}$	7.1
Pressure ratio	$\frac{P_{01}}{P_2}$	7.2
Speed	$\frac{\pi ND}{\sqrt{\gamma RT_{01}}}$	7.3
Reynolds number	$\frac{\rho_{01} ND^2}{\mu}$	7.4

With the following definitions:

Mass flow rate	:	\dot{m}
Inlet stagnation temperature	:	T_{01}
Inlet stagnation pressure	:	P_{01}
Inlet diameter of the turbine	:	D

Method 2:

For a turbine, the primary objective is to design a machine to deliver a specified power output. The power available from a turbine is a function of: [2]

- The inlet stagnation conditions P_{01} and T_{01}
- The mass flow rate
- The size of the machine
- The shape of the machine
- The angular velocity of the rotor
- The efficiency of the flow process
- The gas viscosity (if the Reynolds number is high, its influence will be small over the normal operating range and can be ignored during design)

The functional relationship then can be written as: (after using the Buckingham-Pi Theorem and non-dimensionalizing the terms)

$$f\left(\frac{W}{P_{01} (RT_{01})^{1/2} D^2}, \frac{m(RT_{01})^{1/2}}{P_{01} D^2}, \frac{ND}{(RT_{01})^{1/2}}, \eta\right) = 0 \quad 7.5$$

where W is the power output different from the previous approach .

For these set of parameters the inlet stagnation speed of sound is used as a reference parameter. Also for this design procedure, the turbines should be geometrically similar, like in all other methods. In scaling turbines from one size to another, or the same turbine from one operating condition to another, it is usually possible to scale all the dimensionless groups except the Reynolds number. This can not be scaled precisely unless the inlet density can be controlled independently. But fortunately, from experiments done on this matter, it has been seen that Reynolds number corrections were very small that they could be neglected. The last step in scaling of turbines is to obtain turbine maps in anyway, digitizing may be a solution, and after validating the new method, apply to our design case.

Method 3:

This dimensional analysis will not result in a unique set of dimensionless variables since there are many ways to choose variables, other variables e.g. $\Delta T, \Delta P$ are dependent on the following parameters, [3]

gH-head variable (velocity scale)

Q –volume flow rate

P – power, Watts

N - speed

D - diameter

ρ - fluid density

μ - fluid viscosity

d/D - dimensionless diameter ratio

L/D - dimensionless duct length

η - efficiency

There are basically three units involved: mass, length and time (M,L,T) So we can reduce the 7 variables to 4. Choosing ρ , N, D as primaries, the π products are formed with the same method before. So:

$$\pi_1 = \frac{Q}{N.D^3} = \phi \quad \text{is called the flow coefficient} \quad 7.6$$

$$\pi_2 = \frac{\mu}{N.D^2.\rho} = \frac{1}{\text{Re}} \quad \text{is the inverse of Reynold's number} \quad 7.7$$

$$\pi_3 = \frac{g.H}{N^2.D^2} = \phi \quad \text{is called the head coefficient} \quad 7.8$$

$$\pi_4 = \frac{P}{\rho \cdot N^3 \cdot D^5} = \xi \quad \text{is called the power coefficient} \quad 7.9$$

Also it can be shown that:

$$\eta = \frac{\phi \cdot \varphi}{\xi} \quad 7.10$$

At the characteristic curves relating P and Δp_T versus Q, we take the known values of ρ, N, D and convert the data tables of P, Δp_T and Q to ϕ, φ, ξ and η . After plotting these, the dimensionless performance plots of the turbomachine is obtained

The advantage is that the $\varphi - \phi, \xi - \phi, \eta - \phi$ curves can be used to generate infinite number of gH-Q, P-Q, η -Q curves by choosing any value of ρ, N, D .

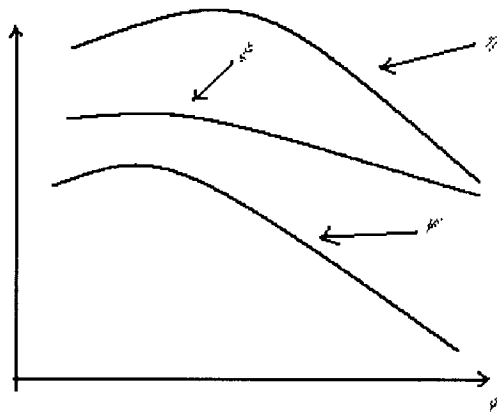


Figure 7.1: Nondimensional Turbine Map

Method 4:

When there are significant changes in density through the turbomachine, the use of volume flow rate and the head rise become inappropriate. We should work with mass flow rate. The head rise must be replaced by the change in stagnation enthalpy Δh_{0s}

, or a related variable. If the flow is adiabatic, Δh_{0s} can be related to the change in stagnation temperature through the turbomachine:

$$\Delta h_{0s} = c_p \cdot \Delta T_0 \quad 7.11$$

In addition, we can consider the relation of the total energy of the fluid with other variables. The aim is to write specific variables in terms of other variables.

$$\Delta h_{0s} = f_1(N, D, m, T_0, \rho_0, \mu, \gamma, \frac{d}{D}) \quad 7.12$$

$$P = f_2(N, D, m, T_0, \rho_0, \mu, \gamma, \frac{d}{D}) \quad 7.13$$

$$\eta = f_3(N, D, m, T_0, \rho_0, \mu, \gamma, \frac{d}{D}) \quad 7.14$$

The new set of parameters needed to be considered in compressible effects are as follows:

R, c_p : gas constant, specific heat

$\Delta h_{0s} = c_p \cdot \Delta T_0$: stagnation enthalpy

m : mass flow rate

$\rho_{01} = p_{01} / RT_{01}$: density

$a_{01} = (\gamma RT_{01})^{1/2}$: stagnation speed of sound

These are to be used with the previous dimensions

μ : viscosity (kg/m.s)

N : rotational speed (radians/s)

D : diameter (m)

The π terms are formed as we did in the previous cases, and they come out to be the followings:

$$\pi_1 = \frac{m}{(\rho_{01}ND^3)} : \text{mass flow coefficient} \quad 7.15$$

$$\pi_2 = \frac{P}{(\rho_{01}N^3D^5)} : \text{power coefficient} \quad 7.16$$

$$\pi_3 = \frac{\Delta h_{0s}}{(N^2D^2)} : \text{work or head coefficient} \quad 7.17$$

$$\pi_4 = \frac{ND}{a_{01}} : \text{Mach number} \quad 7.18$$

$$\pi_5 = \frac{\rho_{01}ND^2}{\mu} : \text{Reynolds number} \quad 7.19$$

Cordier Analysis:

The scaling rules discussed above considered cases which the effects were examined in an isolated fashion. But we need a more systematic way of varying more than one variable at a time in order to change both head and flow performance a specified amount. At this point, we use the specific speed and the specific diameter definitions, which is the Cordier analysis. The specific speed and the specific diameter equations are obtained as follows:

$$\Delta p_T = \rho N^2 D^2 \psi \Rightarrow N = \left(\frac{\Delta p_T}{\rho D^2 \psi} \right)^{1/2} \quad 7.20$$

$$Q = ND^3 \phi \Rightarrow N = \left(\frac{Q}{D^3 \phi} \right) \quad 7.21$$

By equating through N:

$$N = \left(\frac{\Delta p_T}{\rho D^2 \psi} \right) = \left(\frac{Q}{D^3 \phi} \right) \quad 7.22$$

This yields:

$$D^2 = \frac{\left(\frac{Q}{\phi} \right)}{\left(\frac{\Delta p_T}{\rho \psi} \right)^{1/2}} \Rightarrow D = \frac{Q^{1/2}}{\left(\frac{\Delta p_T}{\rho} \right)^{1/4}} \cdot \frac{\psi^{1/4}}{\phi^{1/2}} \quad 7.24$$

Going back to $N = Q / D^3 \phi$:

$$N = \frac{\left(\frac{\Delta p_T}{\rho} \right)^{3/4}}{Q^{1/2}} \cdot \frac{\phi^{1/2}}{\psi^{3/4}} \quad 7.25$$

So the definitions are:

$$D_s = \frac{D \left(\frac{\Delta p_T}{\rho} \right)^{1/4}}{Q^{1/2}} = \frac{\psi^{1/4}}{\phi^{1/2}} \quad 7.26$$

$$N_s = \frac{N Q^{1/2}}{\left(\frac{\Delta p_T}{\rho} \right)^{3/4}} = \frac{\phi^{1/2}}{\psi^{3/4}} \quad 7.27$$

Most importantly these two variables are specified at best efficiency.

The procedure is:

- scale to a performance specification: $\Delta p_T, Q, \rho$
- use N_s and D_s
- arrive at the optimum N and D

This requires geometric similarity.

In the 1950s, Cordier carried out an extensive empirical analysis using experimental data. He attempted to correlate the data in terms of N_s, D_s, η_T using Δp_T . He found that turbomachines which had good to excellent efficiencies tended to group along a definable curve when plotted with their values of N_s, D_s .

He further found out that the efficiencies of these machines grouped into a definable curve as a function of D_s .

The derivation of the Cordier curve is as follows:

$$y = ax^b \Rightarrow \log y = \log a + b \log x \quad (\text{or, } N_s = aD_s^b)$$

Using the graph below, we can derive the values for a and b

$$x = D_s = 1, y = N_s = 9 : a = 9$$

$$x = 8.5, y = 0.1 : b = \frac{(\log(0.1) - \log(9))}{\log(8.5)} = -2.103$$

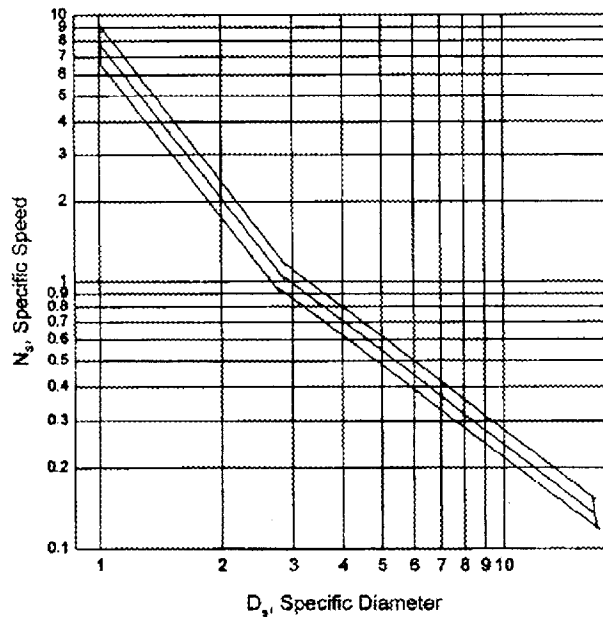


Figure 7.2: Cordier Diagram

So in the upper *box* (Balje's definition)

$$N_s \cong 9D_s^{-2.103} \quad (\text{ for } D_s \leq 2.8) \quad 7.28$$

Similarly for the lower box

$$N_s \cong 3.25D_s^{-1.126} \quad (\text{ for } D_s \geq 2.8) \quad 7.29$$

The efficiency band shown below represents the best total efficiency that can reasonably be expected. This band can be converted into a piecewise set of simple equations as follows:

$$\begin{aligned} \eta_T &= 0.149 + 0.625D_s - 0.125D_s^2 & D_s &\leq 2.5 \\ \eta_T &= 0.864 + 0.0531D_s - 0.01106D_s^2 & \text{for } & 2.5 \leq D_s \leq 5.0 \\ \eta_T &= 1.1285 - 0.0529D_s & & 5.0 \leq D_s \leq 10 \end{aligned}$$

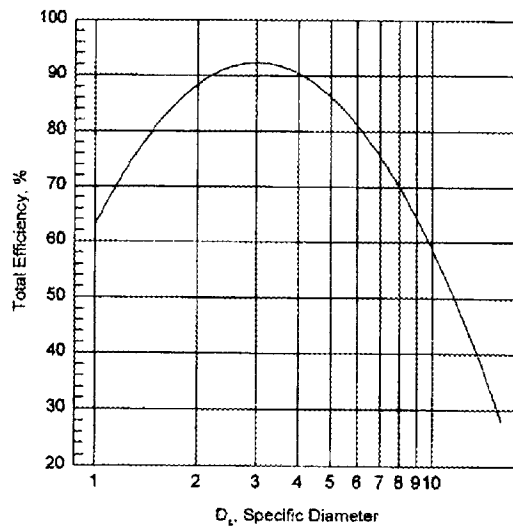


Figure 7.3: Efficiency vs. Specific Diameter

8.0 SURGE AND STALL

An essential part of the design process for a compressor is being able to predict the condition at which instability will occur. In most literature the outcome of the instability will be referred to as stall, but either stall or surge can happen. For example, stall can be used to define fully developed rotating stall. Stall can also refer to the fluid dynamic transient which initiates a surge, or stall can be used to indicate that the flow in a blade row is separated. Compressors can often work quite satisfactorily with regions of separated flow and that the appearance of separation (often called stall) on one blade row is not necessarily an indicator of imminent compressor instability and stall.

Centrifugal compressors can operate fairly satisfactorily with rotating stall present. Centrifugal compressors can also operate with axisymmetric stall near the inducer tips or with stationary non-axisymmetric stall produced by downstream asymmetry, usually the volute. The centrifugal compressors tolerance to the stalled regions is mostly because so much of the pressure rise is produced by centrifugal effects which will occur even in the presence of rotating stall cells or other forms of separated flow. Therefore, surge is usually the mode of low flow behavior which is most important in centrifugal compressors.

If a diffusing flow is found against a surface, then the possibility for the flow to be retarded so severely that it no longer follows the surface exists. The streamlines adjacent to the surface will leave the surface and a region of reverse flow will develop from that point along the surface. Thus, the momentum in the streamlines adjacent to the surface is insufficient to overcome the viscous shear stresses and adverse pressure gradient along the surface. If the adverse pressure gradient and viscous shear stresses are

high enough to reduce the fluid velocity to zero, it is forced to deviate from the surface. Large viscous shear stresses predominate locally and the flow becomes reoriented or separated.

Several elements of a compressor stage can stall without the entire stage stalling. If a stage has a very strong stall in one of its elements, or a number of elements together collectively stall, so that the head versus flow characteristic is no longer stable (negatively sloped), then the stage has entered stage stall. Basically, stage stall is the condition where the basic flow characteristic of the stage alone is no longer stable and the head/flow characteristic becomes positive.

For a compressor operating at a given speed, as the flow is continuously reduced there is usually a condition where the system will no longer operate in a stable manner. Large oscillations in the impeller discharge and inlet conditions will result. The system and stage then interact together in a violent manner giving surge. A phenomenon in which a compressor interacts in an unstable manner with other components to give a strongly coupled, fluctuating flow in the network, with complete flow reversal throughout the stage on cyclic basis is known as surge.

The idea of rotating, or dynamic, stall is far more difficult to report in detail than static stall. Static stall conditions are stationary in nature and can be associated with a fixed location in the machine. Dynamic stall conditions are not fixed and rotate in the machine system at some fraction of the rotational speed of the machine. The blockage caused by the stall cell leads to a reduction in the blade incidence on one side and an increase on the other. The blade with the increased incidence will stall next. The stall tends to run in the direction in which the incidence is increased. For a rotor row it means

that the cell moves backwards relative to the rotor, for a stator it moves in the direction of the rotor. If viewed by a stationary observer, the rotation of the stall cell is always in the same direction as the rotor. Such dynamic conditions can exist in the inducer, in the impeller, or in the diffuser. In centrifugal compressors, the vaneless diffuser is by far the most common part to suffer problems of dynamic instability.

Diffuser rotating stall can be triggered by a local inversion of the radial velocity component in the vaneless diffuser as shown by Jansen (1964) theoretically and experimentally. So, the initiation of vaneless diffuser rotating stall depends on the boundary layer (local return flow and increased blockage), but the dynamic characteristics (number of stall cells and propagation speed) depend on the inviscid part of the flow.

Large amplitude velocity and pressure variations in the vaneless diffuser and upstream of the impeller are characteristics of abrupt impeller rotating stall. It can occur on either the negative or positive slope sides of the performance curve and results in a discontinuity in the pressure rise curve.

9.0 CONCLUSIONS

Since direct pressurized fuel cell system is used, the transients caused by both the turbine and the compressor must be understood. If any of the turbomachines enter a deep surge, serious damage will occur in the fuel cell system caused by the pressure fluctuations and reversal of the mass flow of air through the pipes. In this report, the transient response of a compressor or a turbine is dynamically modelled. The transients predicted by this model then can be used to determine when a deep surge event may occur, thus providing time to correct the problem to eliminate the surge event.

The model is still under testing and needs realistic turbine maps from which various different scenarios can be predicted. This will be accomplished using the powerful tool of dimensional analysis. The ground work for the latter analysis has been layed out in this report.

10.0 REFERENCES

- 1) Walsh, P.P., Fletcher, P., 1998, "Gas Turbine Performance", Blackwell Science, ASME Press
- 2) "Radial Turbines", Lecture Series, 1992-05, VKI
- 3) "Unsteady Flow in Turbomachines", Lecture Series, 1996-05, VKI
- 4) BAINES, N.C., Introduction to radial Turbine Technology, VKI Lecture Series, 1992-07
- 5) BAINES N. C., Performance parameters and assessment, VKI Lecture Series 1992-07
- 6) BALJE O. E., A contribution to the designing of turbomachines, Trans ASME 74:451, 1952
- 7) JAPISKE D., Advanced concepts in turbomachinery design and analysis, Concepts ETI, 1983 PO Box 643, Norwich, Vermont, USA
- 8) SCRIMSHAW K. H. and WILLIAMS T. J., Size effects in small radial turbines ASME paper 84-GT-215
- 9) WHITFIELD, A., Design of radial Turbomachines, Longman Scientific and Technical, 1990
- 10) WISLICENUS G., Fluid mechanics of Turbomachinery, 2nd edition, Dover Publications, 1965
- 11) Fink, D.A., Cumpsty, N.A., Greitzer, E.M., 1992, "Surge Dynamics in a Free-Spool Centrifugal Compressor System", ASME Journal of Turbomachinery, Vol. 114, pp. 321-332

- 12) Greitzer, E.M., 1976, “ Surge and Rotating Stall in Axial Flow Compressors, Part I: Theoretical Compression System Model”, ASME Journal of Engineering for Power, Vol. 98 pp. 190-198
- 13) Greitzer, E.M., 1976, “Surge and Rotating Stall in Axial Flow Compressors, Part II: Experimental Results and Comparison with Theory”, ASME Journal of Engineering of Power, Vol. 98, pp.199-217
- 14) Fink, D.A., Cumpsty, N.A., Greitzer, E.M., 1992, “Surge Dynamics in a Free-Spool Centrifugal Compressor System”, ASME Journal of Turbomachinery, Vol. 114, pp.321-332
- 15) Kurzke, J., Riegler, C., 2000, “A New Compressor Map Scaling Procedure For Preliminary Conceptual Design of Gas Turbines”, Proceedings of ASME IGTI Turbo Expo 2000, 8-11 May , Munich
- 16) Hansen, K.E., Jorgensen, P., Larsen, P.S., 1981, “Experimental and Theoretical Study of Surge in a Small Centrifugal Compressor”, ASME Journal of Fluids Engineering, Vol. 103, pp. 391-395

**XVII. “Synthesis of Methane Gas Hydrate in Porous Sediments and Its
Dissociation by Depressurizing”**

**Feng Song (S), Sridhar Narasimhan (S), and H.O. Kono (F), West Virginia University
with
Duane Smith (M), NETL**

Synthesis of Methane Gas Hydrate in Porous Sediments and Its Dissociation by Depressurizing

Hisashi O. Kono [#], Sridhar Narasimhan, Feng Song

Department of Chemical Engineering
West Virginia University
Morgantown, WV 26505
USA

Duane H. Smith

US-Dept. of Energy
National Energy Technology Laboratory
Morgantown, WV 26507-0880
USA

To whom the correspondence is to be addressed

ABSTRACT

The clathrate compounds of methane gas hydrate (MGH) was synthesized in laboratory at a temperature of 273.5 K and at a pressure of 6.8 ~ 13.6 MPa, consisting of solid phase MGH dispersed within various custom designed porous sediments. This synthesized MGH looks like almost the MGH made by Mother Nature in the strata in the natural gas hydrate (NGH) field. Using these synthesized MGH, the dissociation rate was measured by depressurizing method. From the experimental results, the kinetic dissociation rate equation and the order of the reaction were derived. It was found through experiments that the dissociation rate could be adjusted by the control of the sediment properties. With respect to the MGH formation reaction, the reaction rate equation and its reaction order were also derived.

INTRODUCTION

Methane Gas Hydrates are solid phase crystalline inclusion compounds (also called clathrates) that consists of a host water lattice with cavities in which methane gas is caged as a guest gas. They are frequently referred to as solid solutions and are bonded by van der Waals forces under the condition of low temperature e. g. 273.5 K and high pressure e. g. 6.8 ~ 13.6 MPa. The guest molecule is necessary to support the cavities in the water lattice. The host water molecules on account of hydrogen bonding form a three-dimensional lattice into whose voids the guest gas molecules penetrate.

In general, Natural Gas Hydrate (NGH) consists of a family of clathrate compounds such as methane-, ethane- and propane gas hydrates. However, this paper is limited only to the kinetics of Methane Gas Hydrate (MGH) formation and decomposition. Methane gas hydrate ($\text{CH}_4 \cdot n\text{H}_2\text{O}$), where $n = 5.66$, has a crystalline structure of the category sI.

In the past, several investigators have studied the thermodynamics and crystal structures of natural gas hydrates including methane gas hydrates and the corresponding compounds were well understood. However, the reaction engineering kinetic data of formation and dissociation of MGH together with heat and mass transfer considerations have not yet been clearly accomplished experimentally and only scattered qualitative kinetic data obtained under limited conditions were published. Therefore, a systematic study of the reaction engineering kinetics of formation and dissociation of MGH has been accomplished in this work.

The study of reaction engineering overall reaction rates of formation and decomposition of MGH within several well-defined synthetic sediments was accomplished by using our custom built high-pressure batch and semi-continuous

reactors (patent application in process). These synthetic sediments are very well defined in terms of their powder packing structures and chemical surface characteristics. The formation of gas hydrates is an exothermic reaction that is carried out at high pressure (6.8 – 13.6 MPa) and low temperature (273.5 K). The decomposition of hydrates is an endothermic reaction that is carried out at pressures below the equilibrium pressure on the three-phase diagram. Decomposition of hydrate was accomplished through a controlled depressurization technique starting at a pressure of 2.7 MPa, maintaining the temperature constant at 273.5 K.

The entire reactor assembly consisted of methane gas feeding system, various custom designed sediments, methane hydrate formation rate measuring system and decomposition rate measuring system.

Overall kinetic rate constants both for the formation and decomposition reactions were determined from experiments including the overall order of the reaction for several different sediments. Based on the experimental results, we obtained a reaction engineering rate equation of the quasi-first order type of chemical reaction for the formation reaction where the rate constant k_f is practically a function of the pressure, temperature, sediment type and their corresponding catalytic reactivity. During decomposition, two types of rate behavior were observed depending on the type of sediment used. In some cases, the decomposition followed a zero-order reaction rate while in others a first order reaction rate was observed.

In view of the production of natural gas from the underground strata either in the tundra land or in offshore fields, it becomes practically important to understand and control the decomposition rates of natural gas hydrate samples by the depressurizing technique. In the past, decomposition rates were studied by several investigators (Bishnoi

(1983), Englezos (1987) and Kim et al (1987)), in which the hydrate samples were actually suspended in a bulk volume of water. The decomposition was accomplished by increasing the temperature at a certain pressure. In the studies of the above investigators, the reaction system consisted of either $[\text{CH}_4(\text{g}) - \text{H}_2\text{O}(\text{l}) - \text{MGH}(\text{s})]$ or $[\text{CH}_4(\text{g}) - \text{H}_2\text{O}(\text{l}) - \text{H}_2\text{O}(\text{s}) - \text{MGH}(\text{s})]$ in contrast to our reacting system, which is $[\text{CH}_4(\text{g}) - \text{H}_2\text{O}(\text{l}) - \text{Sediment} - \text{MGH}(\text{s})]$

From the practical viewpoint of the natural gas industry, gas production from hydrates was found to be more economical through the use of the depressurization technique in comparison to thermal heating. Hence it becomes important to produce natural gas from hydrates through the depressurization technique.

Yousif (1994) investigated the kinetics of hydrate formation in bulk water and reported induction times for the onset of hydrate formation based on the first nucleation of the hydrate crystals. It was concluded that the formation of nuclei seeds is essential for the complete growth of the hydrate crystals. However, through our experimental results it was found that the formation of nuclei seeds is not always essential for the complete growth of hydrate crystals.

Sloan (1991) reported some experimental data on the formation and dissociation of methane hydrates within Berea sandstone cores, however the well-defined distribution of water within the cores is not clearly studied. Circone et al (1998) reported the decomposition rates of methane hydrates formed using solid ice at temperatures as low as 272.5 K. However neither of these studies reported reaction engineering data and the studies did not suggest any kinetic equation or the overall order for the reactions.

The importance of studying the kinetic behavior of hydrates formed within sediments stems from the fact that hydrates exist in Mother Nature either in permafrost or

in deep sea sediments and not just in free water. In most of the studies carried out so far, hydrates have been formed in a bulk volume of water and consequently the formation and decomposition studies performed on these samples do not exactly represent the actual kinetic behavior of the hydrate samples existing in nature. Therefore we propose to study the kinetics of methane hydrate formation and decomposition within consolidated sediments.

Finally it is emphasized that the formation and decomposition of hydrates within sediments is important and significant since these synthetic samples could almost exactly reproduce the actual hydrates existing in Mother Nature either in permafrost or in deep sea sediments.

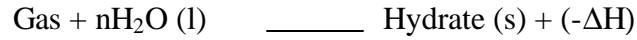
Gas hydrates are crystalline inclusion-compounds (clathrates) and are characterized by uniquely different structures for different gases. The hydrate unit cell for methane has a structure named SI. Structure I is cubic and the unit cell consists of 46 water molecules, which form 2 small (dodecahedra) and 6 large (tetradecahedra) cages. In other words, 2 small cages and 6 large cages are combined to give a unit cell of structure I hydrate. The small cages of structure I hold gas molecules with a molecular diameter less than 5.2 \AA while the large cages hold gas molecules with a molecular diameter less than 5.9 \AA . The molecular diameter of methane is between 4 \AA and 5 \AA and hence it forms structure I.

In addition to structural differences, there are several properties that are unique to gas hydrates through which it is possible to distinguish between a hydrate and ice. One such property is the increase in specific volume of water during the hydrate formation process. The specific volume of water increases by about 26-32% during the hydrate formation process whereas during the formation of ice the increase is only about 9% (Makogon

1997). Further detailed analysis of the hydrate structure could be obtained from several literatures of Sloan (1991) and Makogon (1997).

THEORETICAL BACKGROUND

The formation of gas hydrates is a non-stoichiometric, exothermic reaction between a gas and water and can be represented by the following equation,



Where n is called the hydration number (number of water molecules per mole of gas) and ΔH is the associated enthalpy change which is negative by sign convention.

Figure 1 shows the pressure temperature diagram for methane indicating clearly the zones of hydrate formation and decomposition. In this figure the co-ordinate (T_e, P_e) indicates the equilibrium temperature and pressure for hydrate formation whereas the co-ordinates (T_f, P_f) indicate the operating conditions of our experiments.

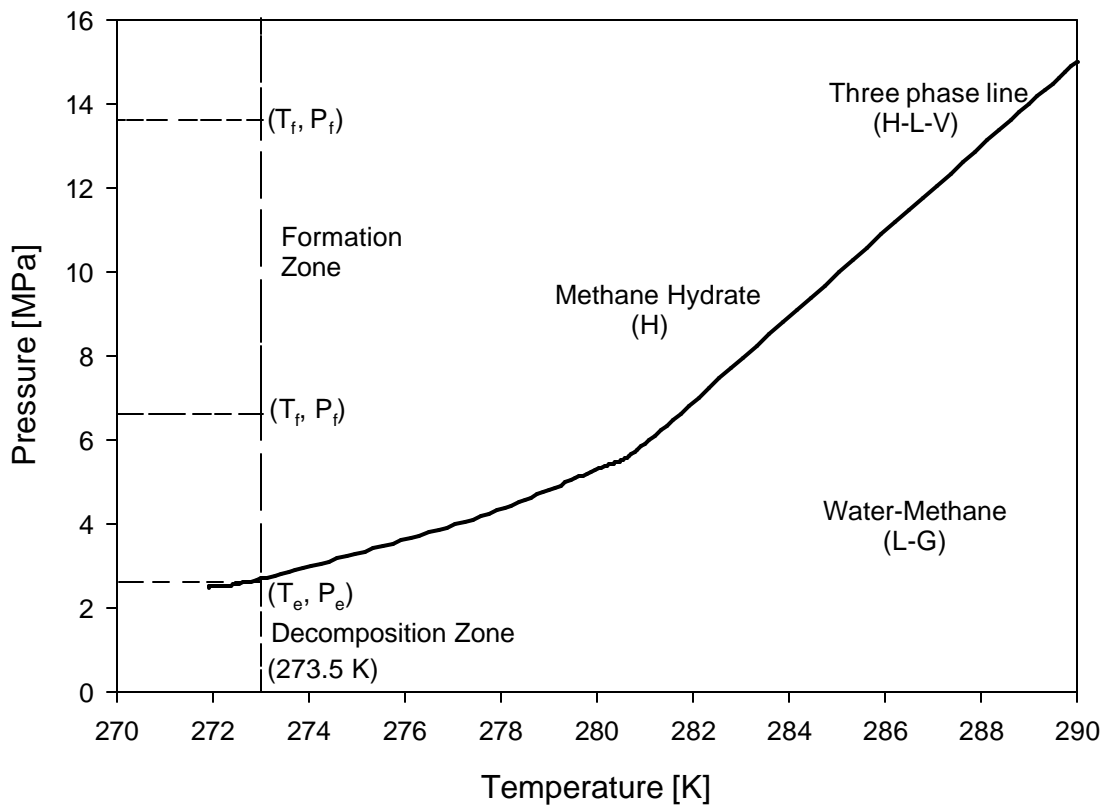


Figure 1 Three-phase equilibrium curve for hydrate-liquid water-methane gas system.

As could be seen from the following published papers, some data are existing for the kinetics of methane hydrate formation and decomposition under a limited condition such as CH_4 (g) - water (l) - MGH (s). However, there have been only a few data corresponding to the formation and decomposition of methane hydrates within porous sediments. In the nature, hydrates exist not only in bulk water but also within porous rocky sediments.

Vysniauskas and Bishnoi (1983) investigated the kinetics of methane hydrate formation using a semibatch stirred tank reactor. The experiments were carried out in bulk water under the operating conditions of 274-284 K and 3-10 MPa. It was concluded through their experiments that the formation kinetics were dependent on the interfacial area, pressure, temperature and degree of supercooling. The formation rate of the hydrates was correlated with the stirring speed. Also, a semi-empirical model was formulated to correlate the experimental data.

Yousif and Sloan (1991) investigated the formation and decomposition of methane hydrate in Berea sandstone cores using a flow reactor system. The operating conditions of the experiments were 273.7 K and 7-8 MPa and a 1.5% NaCl solution was used as the source of water. The onset of hydrate formation was determined by the drop in the reactor pressure and by the change in electric resistance along three cores of different permeabilities. Both linear and non-linear decomposition rates were reported depending on the percentage of water saturation in the core.

EXPERIMENTAL

In this work, the experiments were carried out in the batch reactor made of stainless steel with a total volume of 188 cm³. Figure 2 shows the sketch of the experimental apparatus used for methane hydrate formation and decomposition kinetic studies.

The experimental apparatus consists of a nearly cylindrical packed bed reactor within which known amounts of different sediments and distilled water were added to a certain constant level before the start of reaction as shown in Figure 2. The reactor was equipped with a thermocouple at the center to measure the temperature of the packed bed. The pressure of the reactor was measured at two different points as indicated by P₁ and P₂. The experimental set up was also equipped with a stainless steel pressure relief valve to ensure safety of the high-pressure reacting system. All flow pipelines were made of stainless steel SS 304. For the formation reaction, high purity methane gas (99.90%) and distilled water were used. The methane gas enters the bottom of the reactor through a high-pressure regulator and a needle valve connected in series. The decomposition set up consists of two needle valves connected in series along with a gas flow stabilizer and a water tank with an inverted graduated cylinder that was used as a gas receiver (capacity: 20 liters).

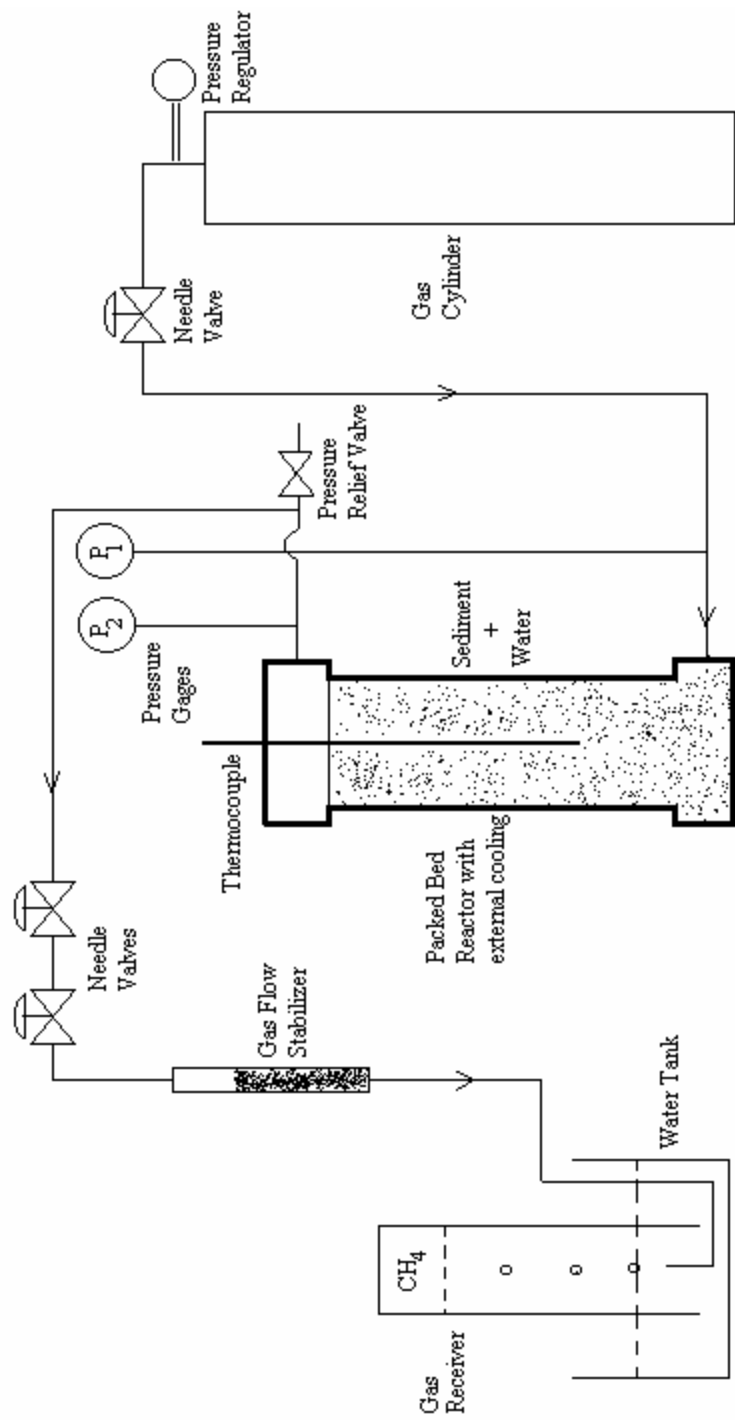


Figure 2 Experimental equipment for the synthesis and decomposition of methane gas hydrate with and without sediments.

As a first step in the experimental procedure, known amounts of sediments and distilled water were mixed in a separate container and fed into the reactor. The amounts of sediment and water added into the reactor were dependent upon material balance design calculations dictated by the total volume of the reactor and by the water saturation coefficient of the granules in the packed bed and relevant chemical reaction stoichiometry. Then the reactor was cooled completely to attain thermal equilibrium at 273.5 K using ice and water. The coolant water and ice were contained in a well-insulated plastic container. The volume of the coolant ice and water was several times larger than the volume of the reactor so that the heat evolved during the exothermic hydrate formation reaction did not really affect the progress of the reaction.

After thermal equilibrium was reached, high purity methane gas was fed into the bottom of the reactor as shown in Figure 2. The operating pressure for the formation of methane hydrate was varied in the range of 6.8 - 13.6 MPa and the temperature was kept constant at 273.5 K. Continuous monitoring of the temperature of the reactor was done using a Fe - CuNi Type J thermocouple (Model: Omega HH-26J) to confirm isothermal reacting conditions.

Since the reaction was carried out at $T > 273.2$ K, the reaction system clearly consists of only three phases at any time. Methane forms the gas phase, water forms the liquid phase and the product gas hydrate forms the solid phase. The progress of the reaction was monitored by recording two different pressures at regular intervals of time, one at the bottom and the other at the top of the reactor indicated respectively as P_1 and P_2 .

RESULT AND DISCUSSION

(1) Methane Gas Hydrate Formation

Table 1 shows the summary of the operating conditions and the amount of gas converted to hydrate for the formation of methane hydrate for various sediments tested. Figure 3 shows the behavior of the reactor pressure and the number of moles of methane consumed as a function of time for methane hydrate formation within a mixture of two different sediments, namely glass beads (100 μ) and synthetic ceramic.

Figure 4 shows the behavior of the reactor pressure and the number of moles of methane consumed as a function of time for methane hydrate formation within two different sediments, namely glass beads (100 μ) and glass beads (5000 μ) in cylindrical sample.

Figure 5 shows the behavior of the reactor pressure and the number of moles as a function of time for methane hydrate formation within the sediment glass beads with a mean diameter of 100 μ .

Figure 6 shows the behavior of the reactor pressure and the number of moles as a function of time for methane hydrate formation using a mixture of sediments containing glass beads (100 μ) and glass beads (5000 μ).

Run	Sediment	Capillary Water Saturation [%]	Reactor Pressure at t = 0 [MPa]	Reactor Pressure at t = t _{end} [MPa]	Reactor Temperature [K]	Reaction Time [hrs.]	Methane converted to Hydrate [%]
1	Glass Beads (100μ) & Synthetic Ceramic	53	13.60	5.50	273.5	330	66
2	Glass Beads (100μ) & Glass Beads (5000μ) in cylindrical sample	29	6.80	4.10	273.5	44	46
3	Glass Beads (100μ)	28	13.30	10.10	273.5	127	19
4	Glass Beads (100μ) & Glass Beads (5000μ)	18	10.20	2.90	273.5	137	78

$$\text{Capillary Water Saturation [\%]} = \frac{\text{Volume of Water}}{\text{Volume of Voids}} \times 100$$

$$\text{Methane Converted to Hydrate [\%]} = \frac{\text{moles of methane consumed}}{\text{moles of methane fed}} \times 100$$

Table 1 Summary of operating conditions for methane hydrate formation using various sediments.

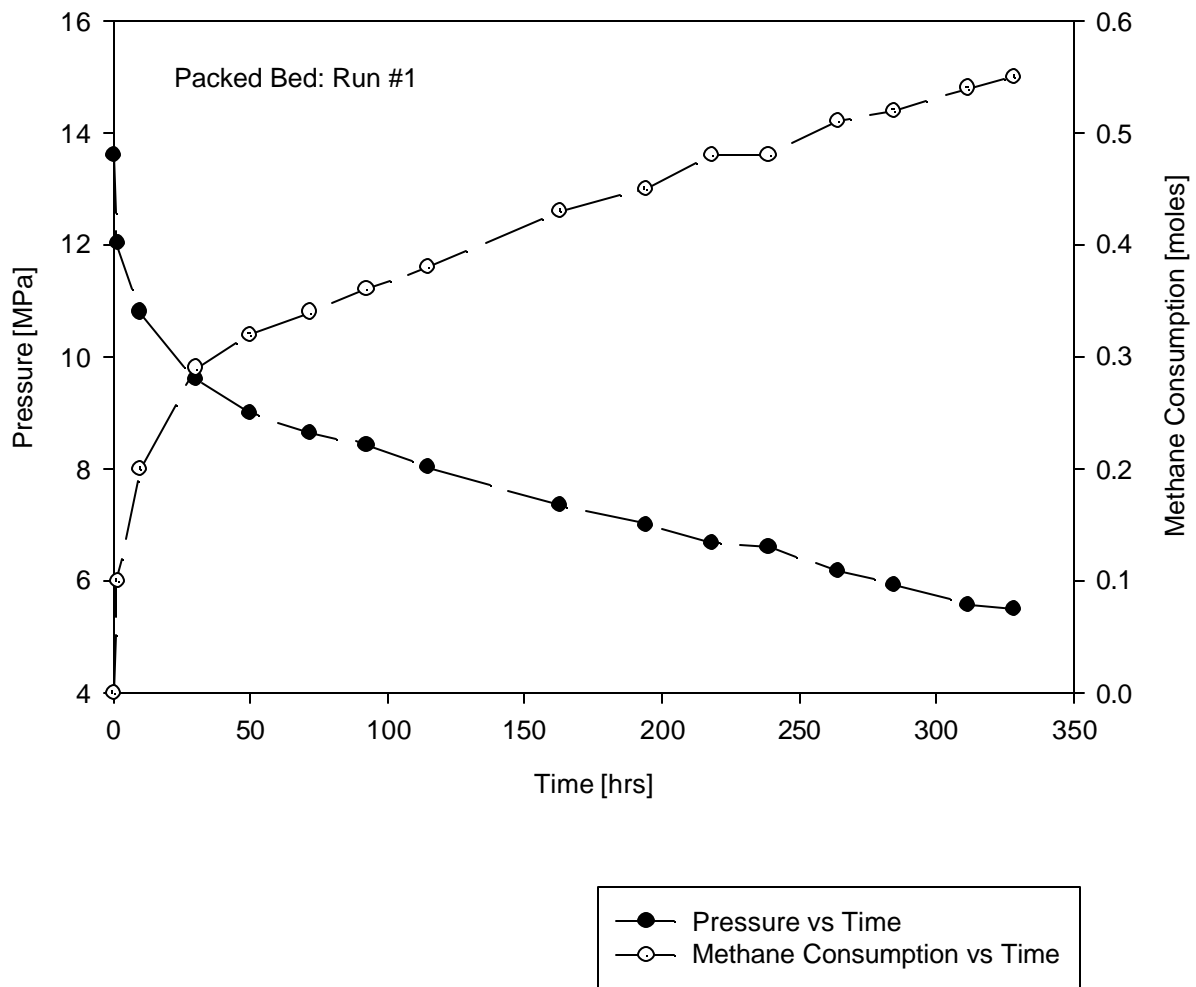


Figure 3 Kinetics of methane hydrate formation using the sediment mixture: glass beads (100 μ) & synthetic ceramic.

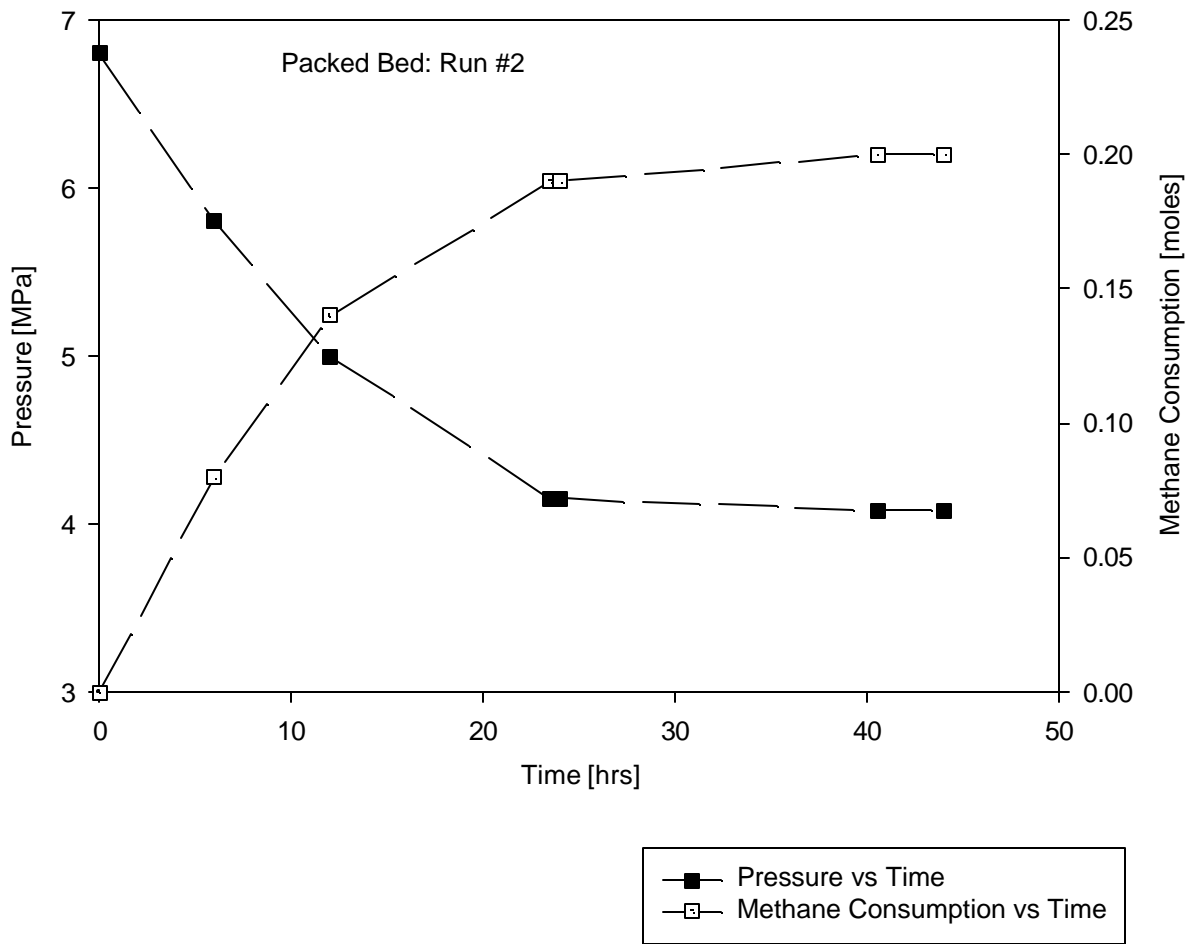


Figure 4 Kinetics of methane hydrate formation using the sediment mixture: glass beads (100 μ) & glass beads (5000 μ) in cylindrical sample.

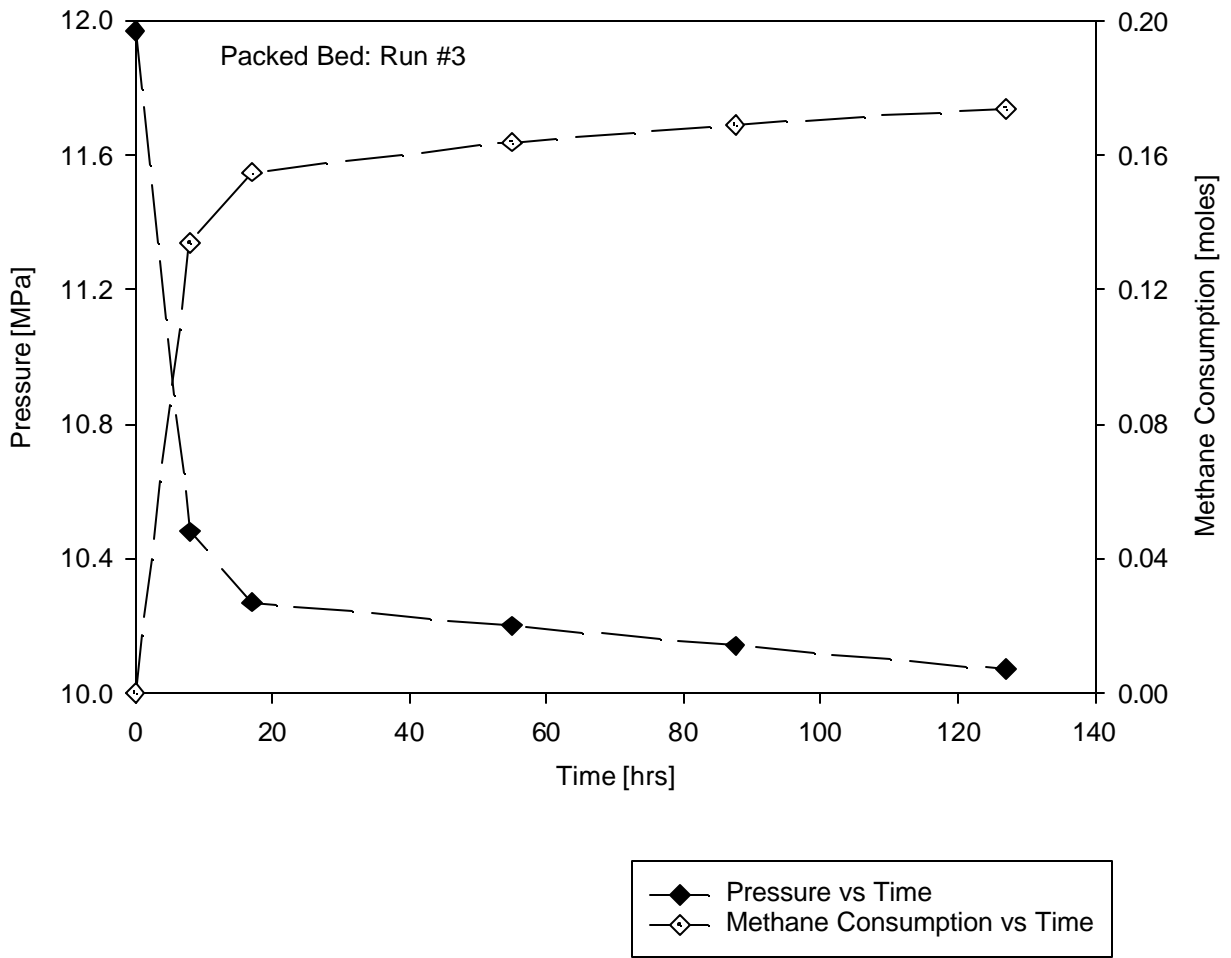


Figure 5 Kinetics of methane hydrate formation using the sediment: glass beads (100μ).

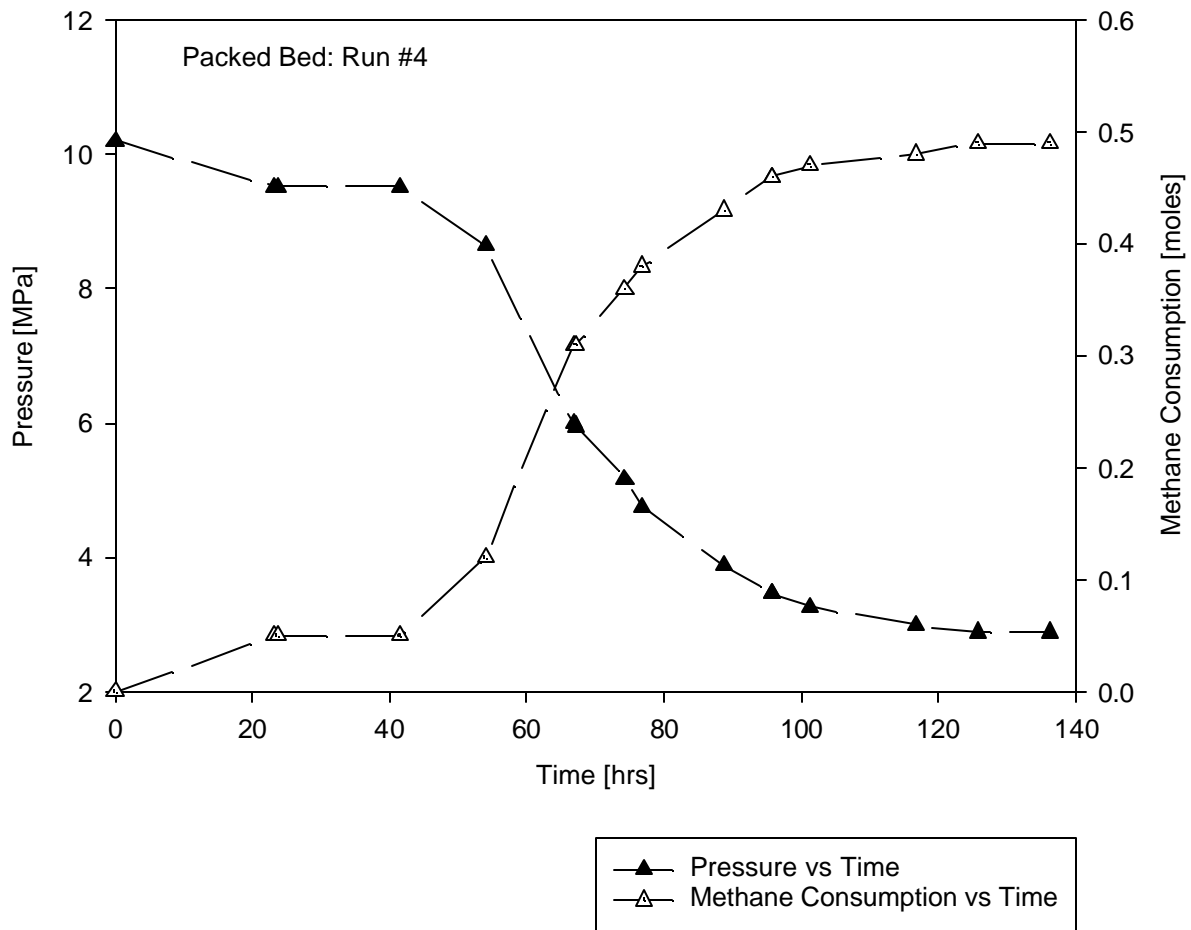


Figure 6 Kinetics of methane hydrate formation using the sediment mixture: glass beads (100 μ) & glass beads (5000 μ).

The variables controlling the rate constant are the starting pressure of reaction P_f , temperature T_f , capillary water saturation coefficient W_s and the surface to volume ratio of packed bed S/V . It was inferred from the experimental data that the formation reaction was first order with respect to the concentration of methane. This overall formation rate constant could be expressed by the following equation

$$-\frac{dn_{CH_4}}{dt} = k_f n_{CH_4}^{n^*}$$

where n^* is the overall order of the hydrate formation process which was found to be unity through our experiments.

Table 2 shows typical values for the overall formation reaction rate constant for the sediments tested. It should be very clearly understood that this formation reaction rate constant is not the same as the intrinsic rate constant of a chemical reaction. On the other hand this is the overall rate constant including the effects of heat transfer, mass transfer and reaction.

Run	Sediment	Rate Constant, k_f [min] ⁻¹	Regression Equation
1	Glass Beads (100 μ) & Synthetic Ceramic	2.07×10^{-4}	$n = n_o(1 - e^{-k_f t})$
2	Glass Beads (100 μ) & Glass Beads (5000 μ) in cylindrical sample	14.42×10^{-4}	$n = n_o(1 - e^{-k_f t})$
3	Glass Beads (100 μ)	25.47×10^{-4}	$n = n_o(1 - e^{-k_f t})$
4	Glass Beads (100 μ) & Glass Beads (5000 μ)	21.20×10^{-2}	$n = \frac{n_o}{1 + e^{\frac{(t-t_o)}{k_f}}}$

Table 2 Formation rate constants of methane hydrate as a function of several different sediments.

(2) Methane Gas Hydrate Decomposition

Hydrate decomposition was accomplished by controlled depressurization starting at a pressure of 2.72 MPa when the temperature was maintained at 273.5 K. The decomposition rates were found to be both zero order and first order based on the concentration of methane depending on the type of sediment. Figures 7 through 10 show the decomposition behavior in terms of the number of moles of methane generated. Material balance of methane was found to be within 10% for all the decomposition experiments. Hydrate decomposition is an endothermic reaction and the variables that control the overall rate constant (k_d) for the decomposition reaction could be expressed as

$$k_{decomposition} = F(P_d, T_d, \epsilon_{bed})$$

The controlling variables are the starting pressure of decomposition P_d , temperature T_d and the voidage of the packed bed ϵ_{bed} . The overall decomposition rate was found to be both zero order and first order depending on the type of sediment and other variables. This overall decomposition rate could be expressed by the following equation

$$\frac{dn_{CH_4}}{dt} = k_d n_{hydrate}^{n^*}$$

where n^* is the overall order of the decomposition reaction which was found to be either 0 or 1 based on our experiments. It should be very clearly understood that this rate constant k_d is not the same as the rate constant of an intrinsic chemical reaction. On the other hand this rate constant simply represents the overall rate including heat transfer and mass transfer effects. Table 3 shows typical values for the overall decomposition rate constant several different sediments.

Run	Sediment	Rate Constant, k_d	Regression Equation
1	Glass Beads (100 μ) & Synthetic Ceramic	$15.1 \times 10^{-2} \text{ (min)}^{-1}$	$n = n_0(1 - e^{-k_d t})$
2	Glass Beads (100 μ) & Glass Beads (5000 μ) in cylindrical sample	2.96×10^{-2} moles/min	$n = k_d t$
3	Glass Beads (100 μ)	0.25×10^{-2} moles/min	$n = k_d t$
4	Glass Beads (100 μ) & Glass Beads (5000 μ)	3.71×10^{-2} moles/min	$n = k_d t$

Table 3 Decomposition rate constants of methane hydrate as a function of several different sediments.

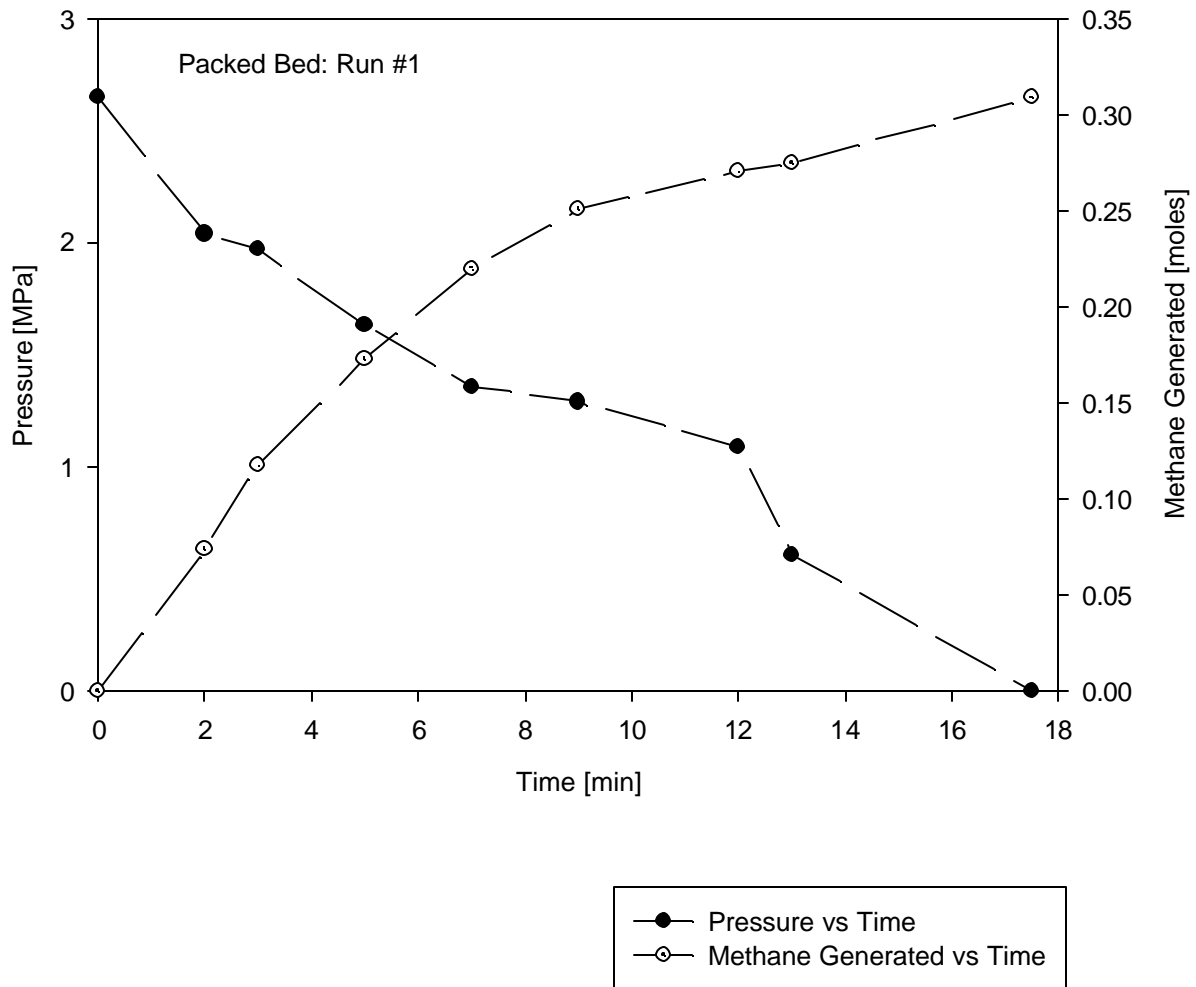


Figure 7 Kinetics of methane hydrate decomposition using the sediment mixture: glass beads (100 μ) & synthetic ceramic.

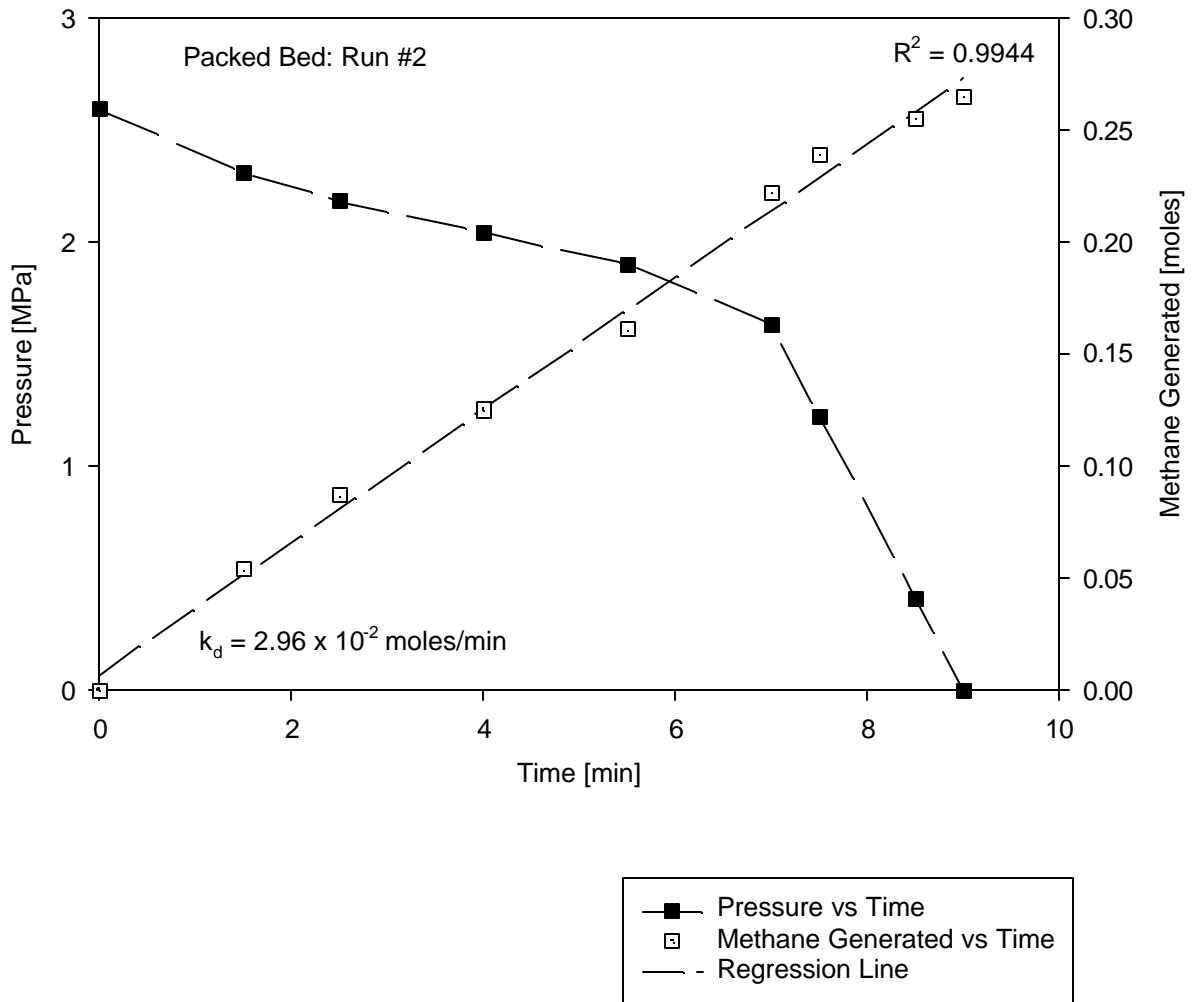


Figure 8 Kinetics of methane hydrate decomposition using the sediment mixture: glass beads (100 μ) & glass beads (5000 μ) in cylindrical sample

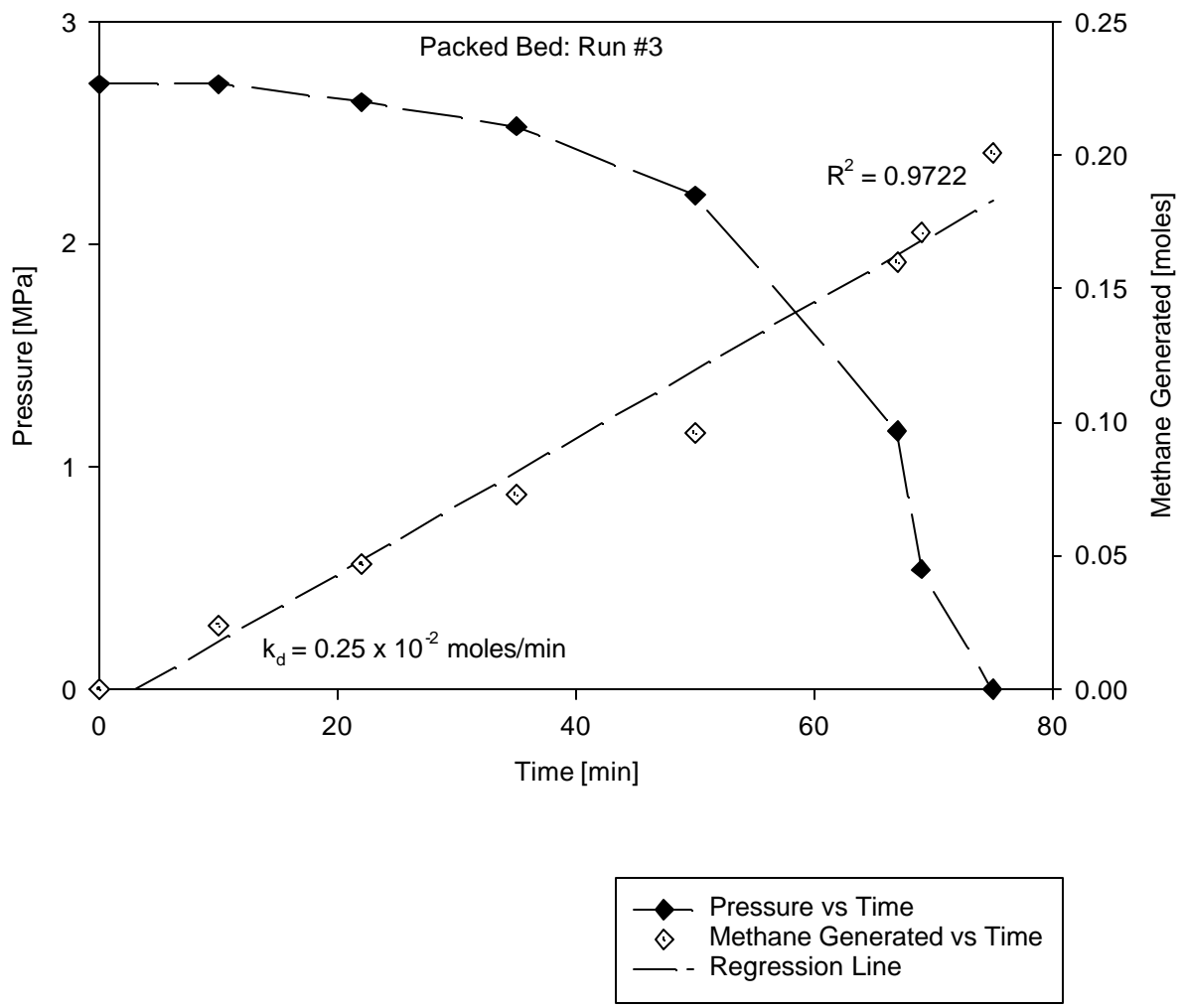


Figure 9 Kinetics of methane hydrate decomposition using the sediment: glass beads (100 μ).

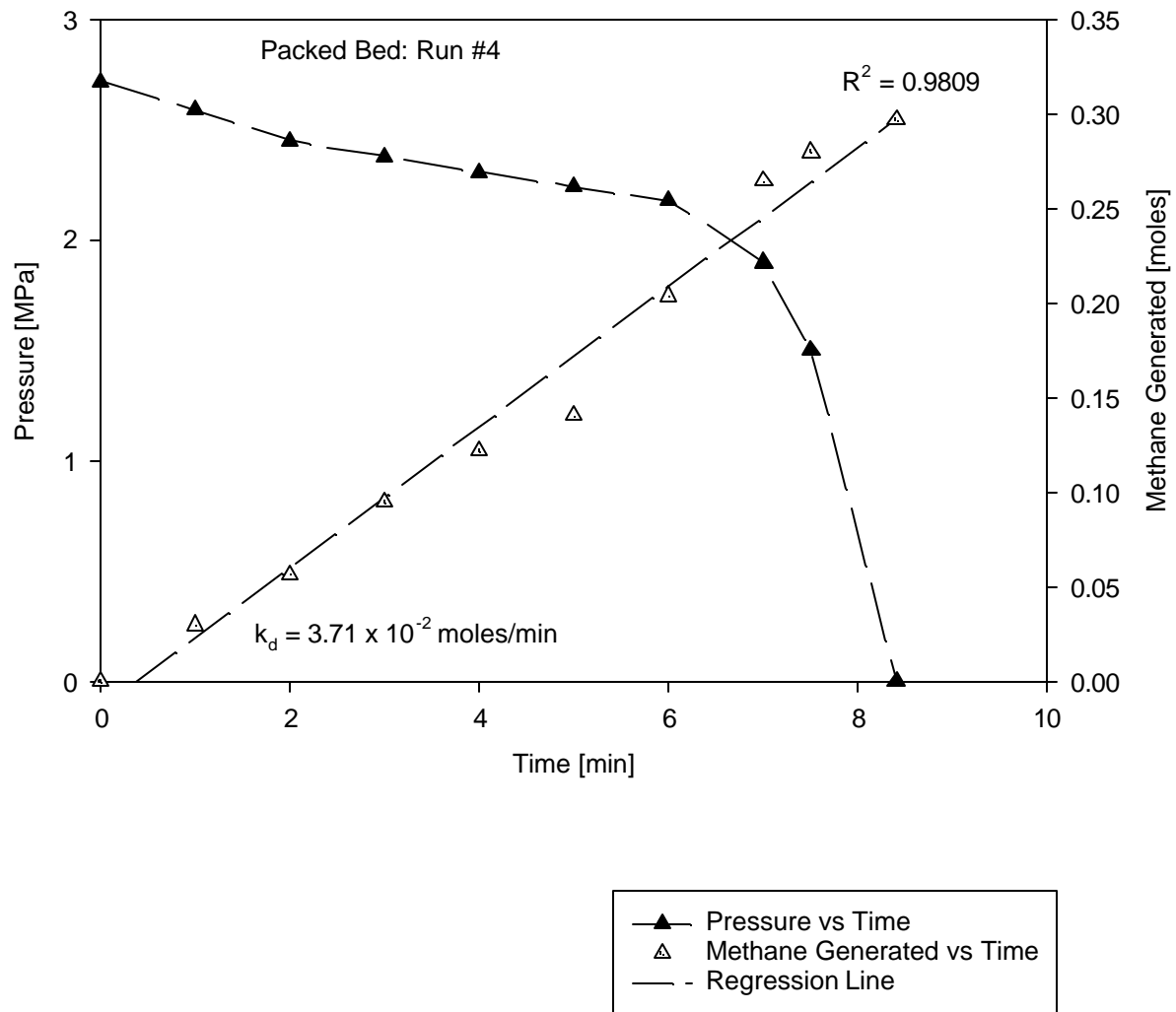


Figure 10 Kinetics of methane hydrate decomposition using the sediment mixture: glass beads (100 μ) & glass beads (5000 μ).

CONCLUSION

1. Using the custom designed structured granules of sediments of several materials, homogeneously reacting solid-state packed bed reactors were designed and operated in batch mode and / or continuous mode.
2. For the formation reaction of clathrate compounds of MGH, the reaction rate equation was developed in terms of reaction engineering from experimental data and the order of the chemical reaction was found to be unity. The reaction rate constants were obtained which could be controlled by the selection of the sediment property and operating condition.
3. For the dissociation (decomposition) reaction of MGH, the reaction engineering rate equation was developed from experiments. The order of the reaction could be controlled by appropriately adjusting the granule property.
4. As the effect of the property and amount of sediments on MGH dissociation rates could reproducibly be investigated in laboratory by the proposed method in this paper, the assessment of NGH resources in the strata in the gas field would efficiently be accomplished.

NOMENCLATURE

H: hydrate

k: overall reaction rate constant [min^{-1}]

L: liquid

n: number of moles of methane gas [moles]

n_0 : total amount of methane gas [moles]

n^* : overall order of reaction [-]

P: pressure [MPa]

T: temperature [K]

V: volume [m^3]

Subscript

f: at formation

d: at decomposition

e: at equilibrium

gs: gas space

ACKNOWLEDGEMENT

This research was partially supported by US-DOE Agreement DE-FC26-98FT40143

PROJECT NO. 001060

REFERENCES

1. Bishnoi, P. R. and Natarajan, V. "Formation and Decomposition of Gas Hydrates", *Fluid Phase Equilibria*, 117, 168-177, 1996.
2. Circone, S., et al, "Methane Hydrate Dissociation Rates at 0.1 MPa and Temperatures above 272 K", *Annals of the New York Academy of Sciences*, vol 912, 544-555, 2000.
3. Englezos, P., et al, "Kinetics of Formation of Methane and Ethane Gas Hydrates", *Chemical Engineering Science*, Vol. 42, No.11, 2647-2658, 1983.
4. Katz, D.L., et al, "Handbook of Natural Gas Engineering", McGraw-Hill Book Company, New York, 1959.
5. Kim, H. C., et al, "Kinetics of Methane Hydrate Decomposition", *Chemical Engineering Science*, Vol. 42, No. 7, 1645-1653, 1987.
6. Makogon, Y. F. "Hydrates of Hydrocarbons", PennWell Books, Tulsa, Oklahoma, 1997.
7. Selim, M. S. and Sloan, E. D. "Hydrate Decomposition in Sediment", *SPE Reservoir Engineering*, 245-251, May 1990.
8. Sloan, E. D. "Clathrate Hydrates of Natural Gases", Marcel Dekker Inc., New York, 1991.
9. Uchida, T., et al, "Decomposition Condition Measurements of Methane Hydrate in Confined Small Pores of Porous Glass", *Journal of Physical Chemistry*, 103, 3659-3662, 1999.
10. Uchida, T., et al, "Summary of physicochemical properties of natural gas hydrate and associated gas-hydrate-bearing sediments", *JAPEX Report*, 205-215, 1998.
11. Ullerich, J. W., et al, "Theory and Measurement of Hydrate Decomposition",

AICHE Journal, Vol. 33, No. 5, 747-752, May 1987.

12. Vysniauskas, A. and Bishnoi, P.R. "A Kinetic Study of Methane Hydrate Formation", Chemical Engineering Science, Vol. 38, No. 7, 1061-1072, 1983.
13. Yousif, M. F. "The Kinetics of Hydrate Formation", SPE 28479, 169-177.

XVIII. “Mapping Acid Mine Drainage with Remotely Sensed Data”

**Jennifer Shogren (S) and Thomas Wilson (F), West Virginia University
with
Terry Ackman (M), NETL**

University Partnership Program – Student Report by Jennifer Shogren

Jennifer was selected for an internship by Tom Wilson (Prof, WVU Department of Geology and Geography) to work with Terry Ackman, Clean Water Team Leader in NETL Pittsburgh's Environmental Science and Technology Division. Tom Wilson is the WVU principal investigator on the University Partnership arrangements with NETL. Jennifer was selected for this internship because of her training and interest in the environmental applications of geophysics.

The U. S. Department of Energy National Energy Technology Lab's (NETL) Clean Water Team has utilized an airborne platform with four different technologies that includes a multi-spectral scanner (MSS) equipped with dual infrared sensors and three geophysical technologies: terrain conductivity, very low frequency, and magnetometry (e.g. Ackman et al., 2000). The airborne approach identifies potential problem areas over whole watershed areas in a short period of time as well as possible relationships between polluted areas that might otherwise be missed by typical surface investigations. Acid mine drainage has had a significant impact on water quality in mining region for decades and will continue to adversely affect these areas unless effective and comprehensive remedial actions can be designed and applied. The DOE has acquired airborne data for several affected areas in the Appalachian region and California.

Working with the US Department of Energy, National Energy and Technology Laboratory, Clean Water Team, Jennifer Shogren has been involved in several projects including, but not limited to, Sulphur Bank Mercury Mine in Clearlake, CA, Yellow Creek Remediation Site in Hammondsville, Ohio, Kempton Mine Complex in Garrett County, MD, and the T and T Mine Complex in Albright, WV.

Sulphur Bank Mercury Mine

- Airborne geophysical data interpretation
- Map-making using GIS programs
- Co-author on reports which are being presented at SAGEEP in February 2002 and ASMR(see attached abstracts)

Yellow Creek Remediation Site

- Conducting EM-31 and EM-34 surveys and collecting GPS data
- Interpreting data
- Generating maps and figures using GIS programs
- Co-author and presenter on a report which is being presented at the AMD Task Force in April 2002 (see attached abstract, work-in-progress)

Kempton Mine Complex

- Attended meeting with the Maryland Bureau of Mines in order to establish a relationship with the DOE such that a partnership between the two organizations could be developed

- Reconnaissance of T and T Complex in order to identify and verify anomalies present in the airborne data
- Data manipulation using GIS programs and tools to enhance airborne geophysical data

T and T Mine Complex

- Collecting down-hole geophysical data
- Performing EM-34 and TDEM soundings in areas of interest
- Interpretation of airborne geophysical data, as well as comparison of airborne data with down-hole geophysical data
- Reconnaissance of T and T Complex in order to identify and verify anomalies present in the airborne data

Additional Work

Nanticoke, PA

- Mapping mine entrances
- Conducting EM-31 and EM-34 surveys
- Interpreting data

Van, WV

- Conducting EM-31 and EM-34 surveys in a stream in order to determine fracture zones within the stream
- Data interpretation

**THE USE OF AIRBORNE EM CONDUCTIVITY TO LOCATE CONTAMINANT
FLOW PATHS AT THE SULPHUR BANK MERCURY MINE SUPERFUND
SITE**

Richard Hammack and Jennifer Shogren
U.S. Department of Energy
National Energy Technology Laboratory
P.O. Box 10940
Pittsburgh, PA 15236-0940
hammack@netl.doe.gov
(412) 386-6585
FAX (412) 386-4579

Abstract- In 1986, the State of California posted an advisory against the consumption of fish from Clearlake, a large, freshwater lake located about 80 miles north of San Francisco, California because of mercury contamination. The inactive Sulphur Bank Mercury Mine on the shore of Clearlake is the suspected source of the mercury. Hermann Impoundment, the now flooded open pit of the Sulphur Bank Mercury Mine is separated from Clearlake by a dam composed of waste rock removed from the open pit. Hydrological and geochemical studies have shown that water is flowing from the open pit through the waste rock dam and into Clearlake. However, an accurate map of flow pathways through the waste rock dam is needed for planning groundwater flow intervention. An airborne EM conductivity survey flown over the mine site and adjacent areas clearly delineated the flow path taken by the highly conductive Hermann Impoundment water through the waste rock dam. The airborne data were then used to focus a ground EM conductivity survey with a Geonics EM34-3XL instrument. The results of the airborne and ground EM conductivity surveys show a distinct flow path for contaminant flow through the waste rock dam. These results will allow flow intervention efforts to be concentrated in smaller areas.

THE USE OF AIRBORNE MAGNETICS AND EM CONDUCTIVITY SURVEYS TO LOCATE GROUNDWATER FLOW PATHS AT THE SULPHUR BANK MERCURY MINE SUPERFUND SITE

Richard W. Hammack, Garret A. Veloski, James I. Sams III, and Jennifer S. Shogren
U.S. DOE, National Energy Technology Laboratory, Pittsburgh, PA

Abstract

Airborne magnetic and electromagnetic (EM) conductivity surveys were conducted at the Sulphur Bank Mercury Mine Superfund Site near Clearlake, California to identify potential pathways for groundwater flow. The total field magnetic survey identified four fault zones that are potential conduits for mercury-contaminated, groundwater flow out of the flooded pit of the abandoned Sulphur Bank Mercury Mine. The location of the four fault zones was corroborated by the EM conductivity survey, which also provided evidence that the fault zones contained highly conductive water, either from a deep, geothermal origin or from meteoric water made acidic by weathering sulfide minerals. This information was used to locate drill holes for a hydrologic investigation and to provide assurance that all possible avenues for groundwater leaving the site were addressed.

AIRBORNE AND GROUND-BASED INVESTIGATIONS OF THE NORTH FORK OF YELLOW CREEK, JEFFERSON COUNTY, OHIO

*Jennifer S. Shogren, Department of Geology and Geography
West Virginia University, Morgantown, WV
Richard W. Hammack and Garret A. Veloski
U.S. Department of Energy, Pittsburgh, PA*

Introduction

On May 17 1991, a sudden blowout of acid mine drainage (AMD) resulted in a major fish kill in the North Fork of Yellow Creek near Hammondsville in Jefferson County, Ohio (1). The source of the blowout was visually evident in the streambed (AMD-1, Fig. 1). Initially, the AMD was thought to be artesian flow from a flooded mine in a coal/clay bed, which occurs about 20 ft beneath the stream (Fig. 2). Based on this assumption, the Ohio Division of Natural Resources constructed a cement seal in the streambed at AMD-1 that was intended to prevent or curtail the flow of AMD into the stream. The seal, completed in June 1993, has been largely successful because there have been no reoccurrence of large, fish-killing discharges. However, AMD has continued to seep into the streambed at the location of the seal (1).

This paper describes the use of airborne thermal infrared imaging (TIR) and ground-based electromagnetic (EM) methods to evaluate the effectiveness of the cement seal and to determine the source(s) of AMD entering the stream in the vicinity of the blowout. The U.S. Department of Energy, National Energy Technology Laboratory (NETL) performed the investigation with funding provided by the U.S. Army Corp. of Engineers.

However, mining records showed no mining in the Middle Kittanning Coalbed at this location. Another potential source for the AMD is a drift mine in the Upper Freeport Coalbed (AMD-2, Fig. 1) located about _ m east of AMD-

1. Severely contaminated AMD flowing from this mine has pooled within a cut-off meander and flows slowly southward through a series of shallow pools until it enters the North Fork of Yellow Creek (confluence, Fig.1) about ___ ft downstream from AMD-1.

XIX. “Modeling and Control of Circulating Fluidized Bed using Neural Networks”

**Amol Patankar (S), Praveen Koduru (S) and Asad Davari (F),
West Virginia University Institute of Technology
with
Lawrence Shadle (M) and Larry Lawson (M), NETL**

Modeling and Control of Circulating Fluidized Bed using Neural Networks

Electrical Engineering Department
WVU Tech

Advisor:
Dr. Asad Davari

Graduate Students:
Amol Patankar
Praveen Koduru

NETL Mentors:
Dr. Lawrence Shadle
Larry Lawson

Annual Project Report
University/NETL Partnership Program

(Subcontract agreement No. 001060-2
under prime DOE agreement No. DE-FC-26-98FT40143)

November 2001

TABLE OF CONTENTS

1. INTRODUCTION	
1.1 CIRCULATING FLUIDIZED BEDS	1
1.2 NEURAL NETWORKS	2
1.2.1. Backpropagation Algorithm	3
1.2.2. Backpropagation Algorithm: The Levenberg-Marquardt (LM) Method	5
1.3. BLACK-BOX MODELING APPROACH	6
2. MODELING THE CFB	9
3. RESULTS AND DISCUSSION	
3.1. MODELING	12
3.1.1 Multi Input Single Output (MISO) Neural Network Model	13
3.1.2. Multi Input Multi Output (MIMO) Neural Network model	18
3.2. DEVELOPMENT OF CONTROLLER	
3.2.1. Inverse Model Control	26
3.2.2. Controller implementation	31
4. CONCLUSIONS	32
5. REFERENCES	33

LIST OF GRAPHICAL MATERIAL

Figure 1. Schematic of CFB	1
Figure 2. Representation of a Feed forward Neural Network	2
Figure 3. Backpropagation Algorithm	5
Figure 4. Schematic of Black Box modeling	7
Figure 5. Black Box Modeling of CFB	7
Figure 6. Sample set of scaled data points	8
Figure 7. P & I diagram of the CFB	11
Figure 8. MISO Neural Network	12
Figure 9. Mean Squared Error (MSE) plot during training of Mass Flow rate (Ms) for MISO model	16
Figure 10. Plot showing prediction of Ms by the trained Neural Network MISO Model	17
Figure 11. Neural network Extrapolation of Mass Flow rate (Ms)	18
Figure 12. MIMO Neural Network	18
Figure 13. Plot showing prediction of Ms by the trained Neural Network MIMO Model	19
Figure 14. Plot showing prediction of PDT 841 by the trained Neural Network MIMO Model	20
Figure 15. Plot showing prediction of PDT 842 by the trained Neural Network MIMO Model	21
Figure 16. Plot showing prediction of PDT 811A by the trained Neural Network MIMO Model	22
Figure 17. Plot showing prediction of PDT 801 by the trained Neural Network MIMO Model	23
Figure 18. Plot showing prediction of PDT 853 by the trained Neural Network MIMO Model	24
Figure 19. Plot showing prediction of PDT 864 by the trained Neural Network MIMO Model	25
Figure 20. Control of Process P to achieve the desired response	26

Figure 21. MISO Neural Network for Controller	27
Figure 22. Mean Squared Error (MSE) plot during training of Controller	29
Figure 23. Plot showing prediction of FY 171 by the trained Neural Network Controller	30
Figure 24. Schematic of Implementation of NN controller on the CFB	31
Figure 25. Controller Simulation	31
<i>Table 1. Training and Testing data of Mass Flow Rate (M_d)</i>	<i>13</i>
<i>Table 2. Training and Testing data of Aeration (F_y)</i>	<i>14</i>

1. INTRODUCTION

1.1 CIRCULATING FLUIDIZED BEDS

Circulating Fluidized beds are a relatively new method of forcing chemical reactions to occur in chemical and petroleum industries. A circulating Fluidized bed is a closed system used to mix a solid with a gas in order to force a chemical reaction. Typically in an industrial setting, CFBs implement combustion as part of the process to speed up the rate of reaction. The CFB under consideration is a “cold” circulating fluidized bed, meaning there is no combustion component in its process. The reason for eliminating combustion from this unit is to isolate and study the effects of the internal pressure of the system, independent of temperature effects.

A schematic of the CFB is shown in figure 1. One of the major problems in the study and

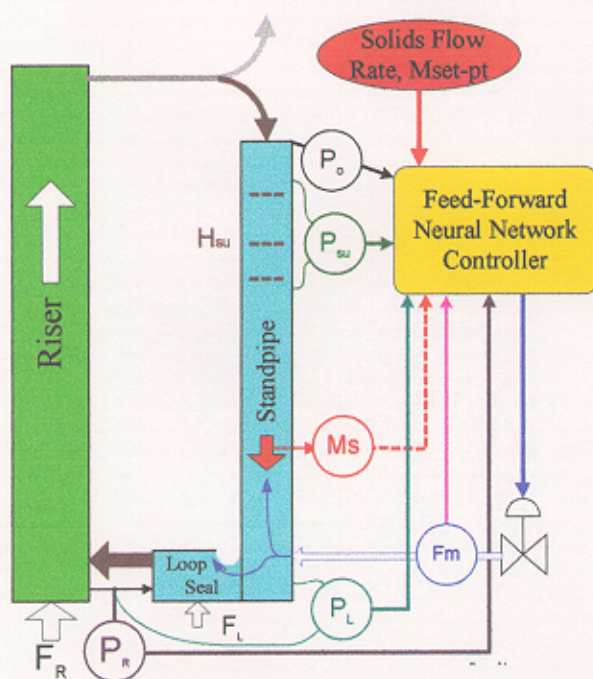


Figure 1. Schematic of CFB

design of these large complex systems is the modeling and prediction of their characteristic behavior. Currently there is no way to construct a reliable model of such a complex system using traditional methods. Three major obstacles in characterizing the system are:

- Chaotic nature of the system
- Non-linearity of the system
- Number of immeasurable unknowns

Artificial Neural Networks (ANNs) have the ability to characterize the system, and can overcome all three of these obstacles. Neural Networks provide a simple way to construct both of these tools. Neural Networks have the greatest promise in the realm of nonlinear control problems. This stems from their theoretical ability to approximate arbitrary nonlinear mappings.

1.2 NEURAL NETWORKS

Neural networks generally consist of a number of interconnected processing elements or neurons. How the inter-neuron connections are arranged and the nature of the connections determines the structure of the network. Its learning algorithm governs how the strength of the connections are adjusted or trained to achieve a desired overall behavior of the network. A simple feed forward neural network is shown in Figure 2.

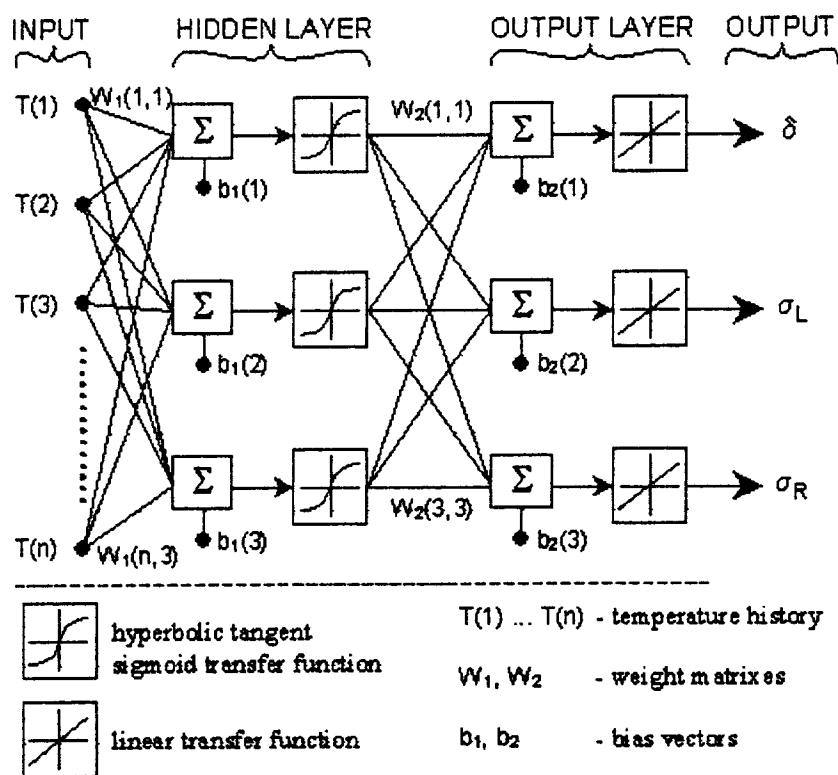


Figure 2. Representation of a Feed forward Neural Network

In feed forward network, the neurons are generally grouped into layers. Signals flow from the input layer through to the output layer via unidirectional connections, the neurons are being connected from one layer to the next, but not within the same layer. Between the input layer and the output layer, we have the hidden layers. As the complexity of the problem being solved increases, the size and number of the hidden layer increases. A supervised learning algorithm adjusts the strengths or weights of the inter-neuron connections according to the difference between the desired and actual network outputs corresponding to a given input. Thus, supervised learning requires a “teacher” or “supervisor” to provide desired or target output signals.

1.2.1. Backpropagation Algorithm

An example of such supervised learning algorithm is Backpropagation (BP) algorithm.

Multi-Layer Perceptrons (MLP) are perhaps the best-known type of feed forward networks. MLP has generally three layers: an input layer, an output layer and an intermediate or hidden layer. Neurons in the input layer only act as buffers for distributing the input signal x_i to neurons in the hidden layer. Each neuron j in the hidden layer sums up its input signals x_i after weighting them with the strengths of the respective connections w_{ji} from the input layer and computes its outputs y_j as a function f of the sum, viz.

$$y_j = f(\sum w_{ji} x_i) \quad (1)$$

f can be a simple threshold function or a sigmoid, hyperbolic tangent or radial basis function.

The output of neurons in the output layer is computed similarly. The BP algorithm, a gradient descent algorithm, is the most commonly adopted MLP training algorithm. It gives the change Δw_{ji} in the weight of a connection between neurons j and i as follows:

$$\Delta w_{ji} = \eta \delta_j x_i \quad (2)$$

Where η is a parameter called the learning rate and δ_j is a factor depending on whether neuron j is an output neuron or a hidden neuron. For output neurons,

$$\delta_j = \left(\frac{\partial f}{\partial net_j} \right) (y_j^{(t)} - y_j) \quad (3)$$

and for hidden neurons,

$$\delta_j = \left(\frac{\partial f}{\partial net_j} \right) \sum_q w_{jq} \delta_q \quad (4)$$

In equation (3), net_j is the total weighted sum of input signals to neuron j and $y_j^{(t)}$ is the target output of neuron j .

As there are no target outputs for hidden neurons, in equation (4), the difference between the target and actual output of a hidden neuron j is replaced by the weighted sum of the δ_q terms already obtained for neurons q connected to the output of j . Thus, iteratively, beginning with the output layer, the δ term is computed for neurons in all layers and weight updates determined for all connections. The steps have been clearly illustrated in Figure 3.

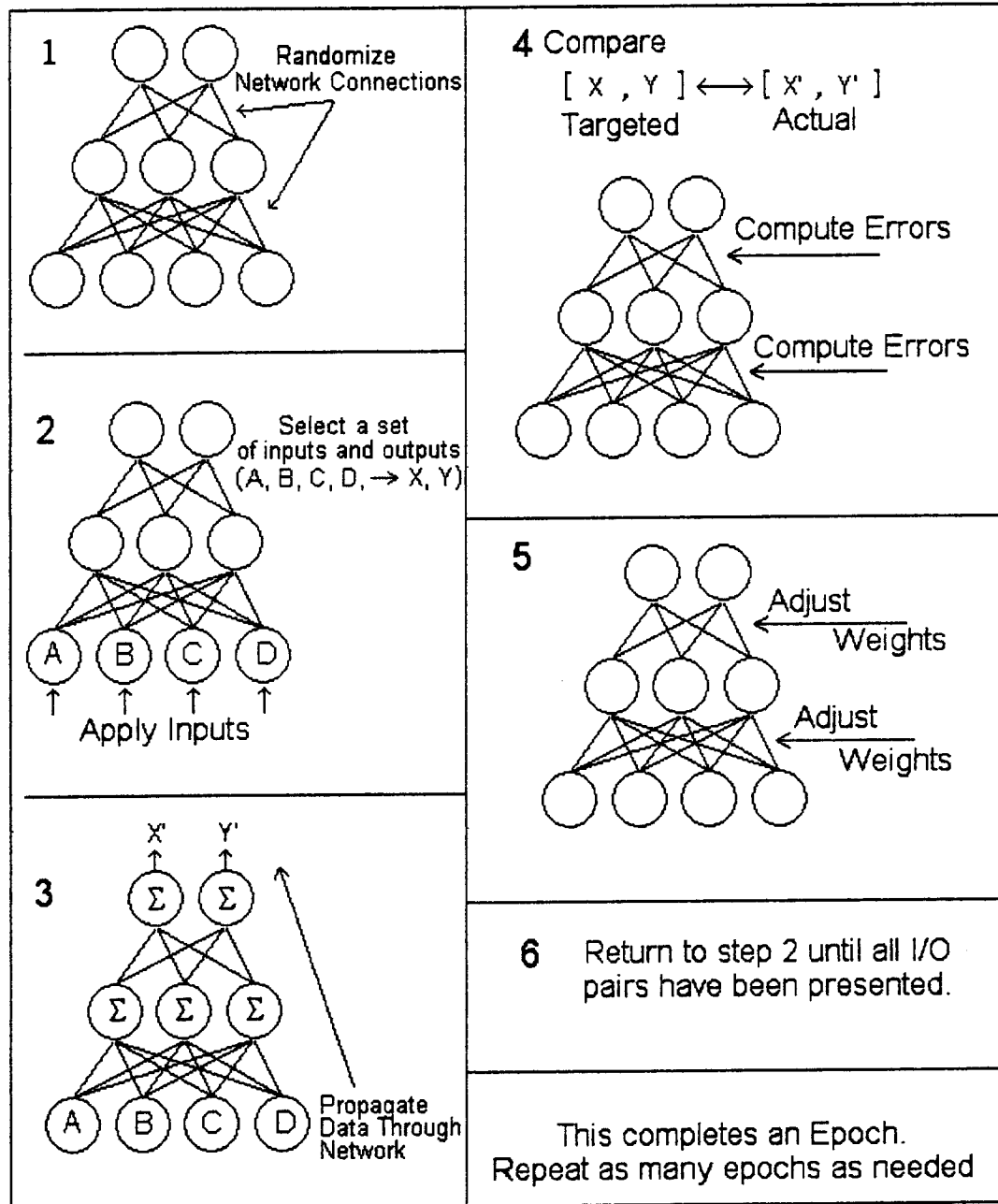


Figure 3. Backpropagation Algorithm

1.2.2. Backpropagation Algorithm: The Levenberg-Marquardt (LM) Method

The LM method, a second order optimization method, was used to determine the weights in the NN. Network training aims at minimizing the sum of squares of errors, the errors measured as the difference between the calculated output and the desired output. Minimizing the quadratic error is not always the best way of training a NN, but for this

application, it suffices. Most algorithms for least-square optimization problems use either steepest descent or Taylor-series models. The Levenberg-Marquardt method uses an interpolation between the approaches based on the maximum neighborhood (a “trust region”) in which the truncated Taylor series gives an adequate representation of the nonlinear model. The method has been found to be advantageous compared to other methods, which use only one of the two approaches. This makes LM training much faster than gradient descent. For networks that are not explicitly recurrent LM training is very good method.

The equations for changing the weights during training are given as follows:

$$e_k = O(t_k) - \tilde{O}(t_k) \quad \text{where } \tilde{O}(t_k) \text{ is the neural network output.}$$

$$J_{kl} = \left. \frac{\partial O}{\partial W_l} \right|_{t_k}$$

$$O \cong \vec{e} + \frac{\partial \vec{e}}{\partial \vec{W}} \Delta \vec{W} = \vec{e} - J \Delta \vec{W}$$

$$\Delta \vec{W} = (J^T J)^{-1} J^T \vec{e}$$

$$\text{Modifying} \Rightarrow \Delta \vec{W} = (J^T J + \mu I)^{-1} J^T \vec{e} \quad (5)$$

1.3. BLACK-BOX MODELING APPROACH

These is the most common form of supervised learning, giving the NN, off-line data of the plant, and mapping the correlation between the inputs and outputs, forming a black-box model of the plant as shown in Fig 4. In the system under consideration, we have tried to model the mass flow rate as a function of the differential pressures in the standpipe section and the flow rate of the aeration. The ultimate aim of the work is to

develop a neural network controller to manipulate the mass flow rate by varying the aeration.

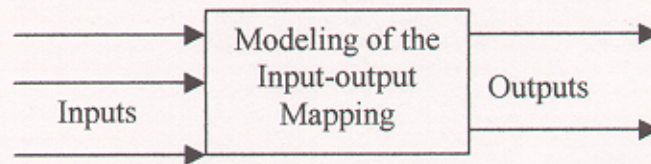


Figure 4. Schematic of Black Box modeling

Figure 5 shows the schematic of Black Box modeling approach as implemented on the present CFB.

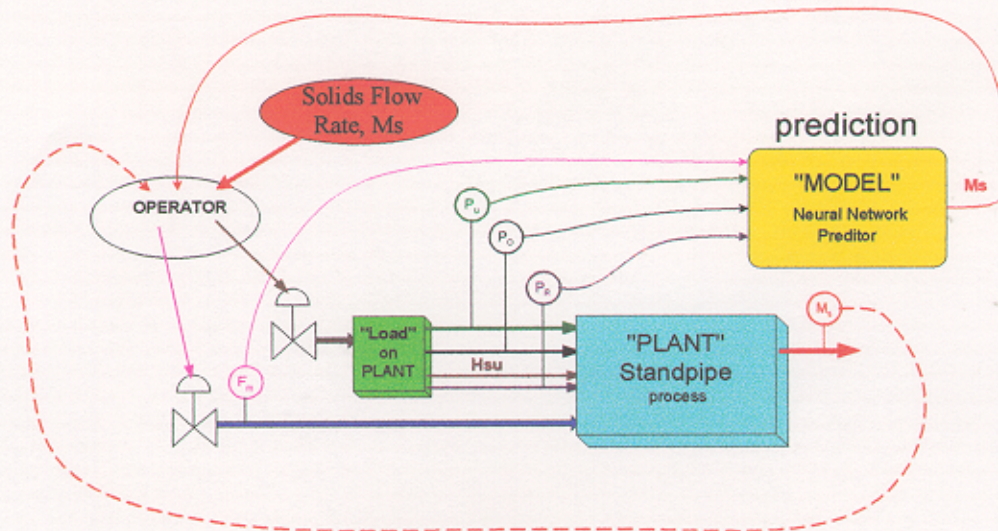


Figure 5. Black Box Modeling of CFB

The tricky part in modeling the system was the collection of data to span over the entire operating range. The data points had to be chosen in such a way that all the system dynamics were captured. Figure 6 shows a sample set of data variables collected, showing the variation of each variable over that period. Note that all variables have been scaled between 0 and 1 to fit on same graph.

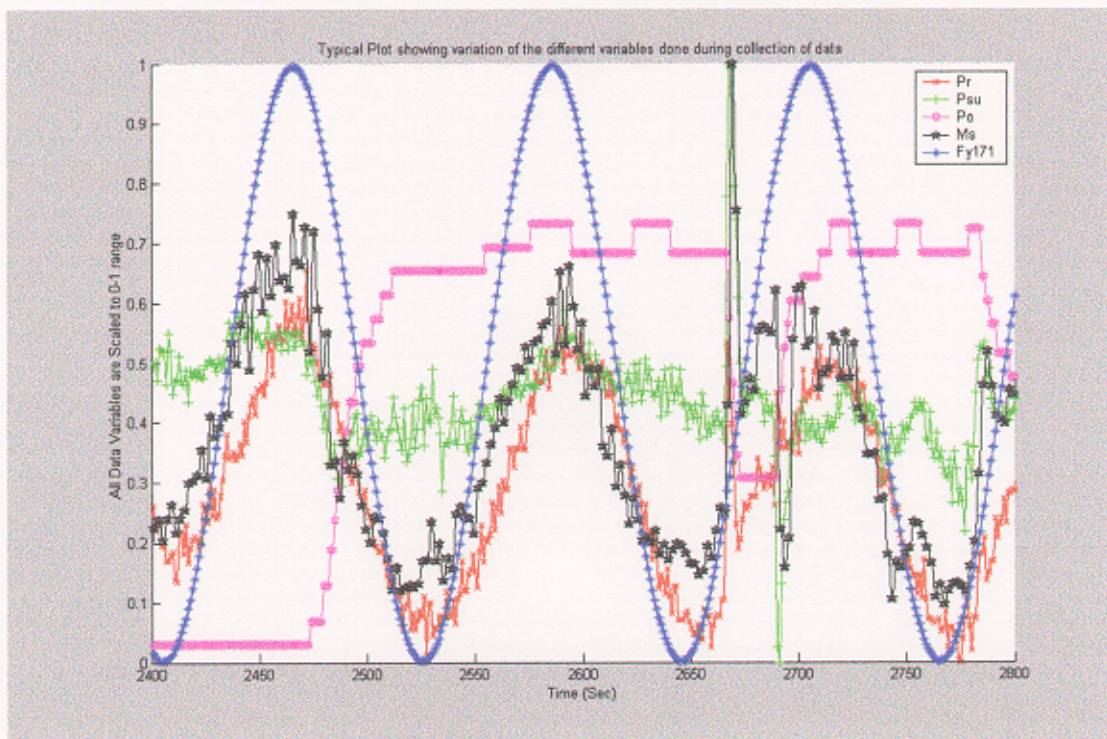


Figure 6. Sample set of scaled data points

Out of the 3600 data points collected, 1800 points were used for modeling and the remaining points were used for extrapolation of the results over unseen data points for validation of the obtained model.

Determining the size of the layers is an important issue. One of the most used approaches is the constructive method. Constructive methods determine the topology of the network during the training phase as an integral part of the learning algorithm. The common strategy of the constructive methods is to start with a small network, train the network until the performance criterion has been reached, add a new node and continue until a 'global' performance in terms of error criterion has reached an acceptable level.

The expected benefits using such algorithms are:

- Trial-and-Error: The usual trial and error process for finding the 'best' topology is avoided.

- Speed: Because of fewer free parameters the network is expected to converge faster.

The main objective of this work is to train the neural network model to provide a suitable off-line model that simulates CFB operation. If the neural network plant model is capable of approximating with sufficient accuracy the highly complex process in the CFB, it may be used within a model based control strategy.

2. MODELING THE CFB

In the system under consideration, we have modeled the mass flow rate as a function of the differential pressures in the standpipe section and the flow rate of the aeration. The ultimate aim is to develop a neural network controller to manipulate the mass flow rate by varying the aeration. A P & I diagram of the CFB is shown in Figure 7.

The major variables used for modeling and their range are as follows:

PDT 841	}	Riser Pressure (P_r)	Range 0.3 – 0.7 psid
PDT 842			
PDT 811A			
PDT 801			
PDT 853	}	Upper Stand pipe pressure (P_{su})	Range 0 – 0.4 psid
PDT 864			
PIC 941		Back pressure (P_o)	Range 0 – 2.6 psig
F874		Mass flow rate (M_s)	Range 600 – 6000 lb/hr
FY 171		Aeration rate (F_m)	Range 300 – 700 scfh

We have also incorporated the time-delayed signals as FY171 (t-1) and FY 171 (t-2) to enable capturing the delayed effects of respective variables as FY 171 on the system.

Here all the PDTs and PIC represent the differential pressures in the standpipe, F874 represents the mass flow rate and FY 171 represents the aeration.

To model the system we have used multi layered neural network with neurons in the input layer, hidden layer and the output layer. We have used the Levenberg Marquardt (LM) algorithm for training the neural network. The training was done using the Neural Network toolbox in Matlab. The tricky part in modeling the system was the collection of data to span over the entire operating range. Data was collected by varying move air (aeration) in a sinusoidal manner over its whole range. All other variables were also being manipulated manually over their respective range. The data points had to be chosen in such a way that all the system dynamics were captured. Out of the 3600 data points collected, 1800 points were used for modeling and the remaining points were used for extrapolation of the results over unseen data points for validation of the obtained model. The blue signal in the plots is the plant response and the red signal is the neural network output. The first 1800 points represent the data points used for training while the remaining points were used for validation of the model.

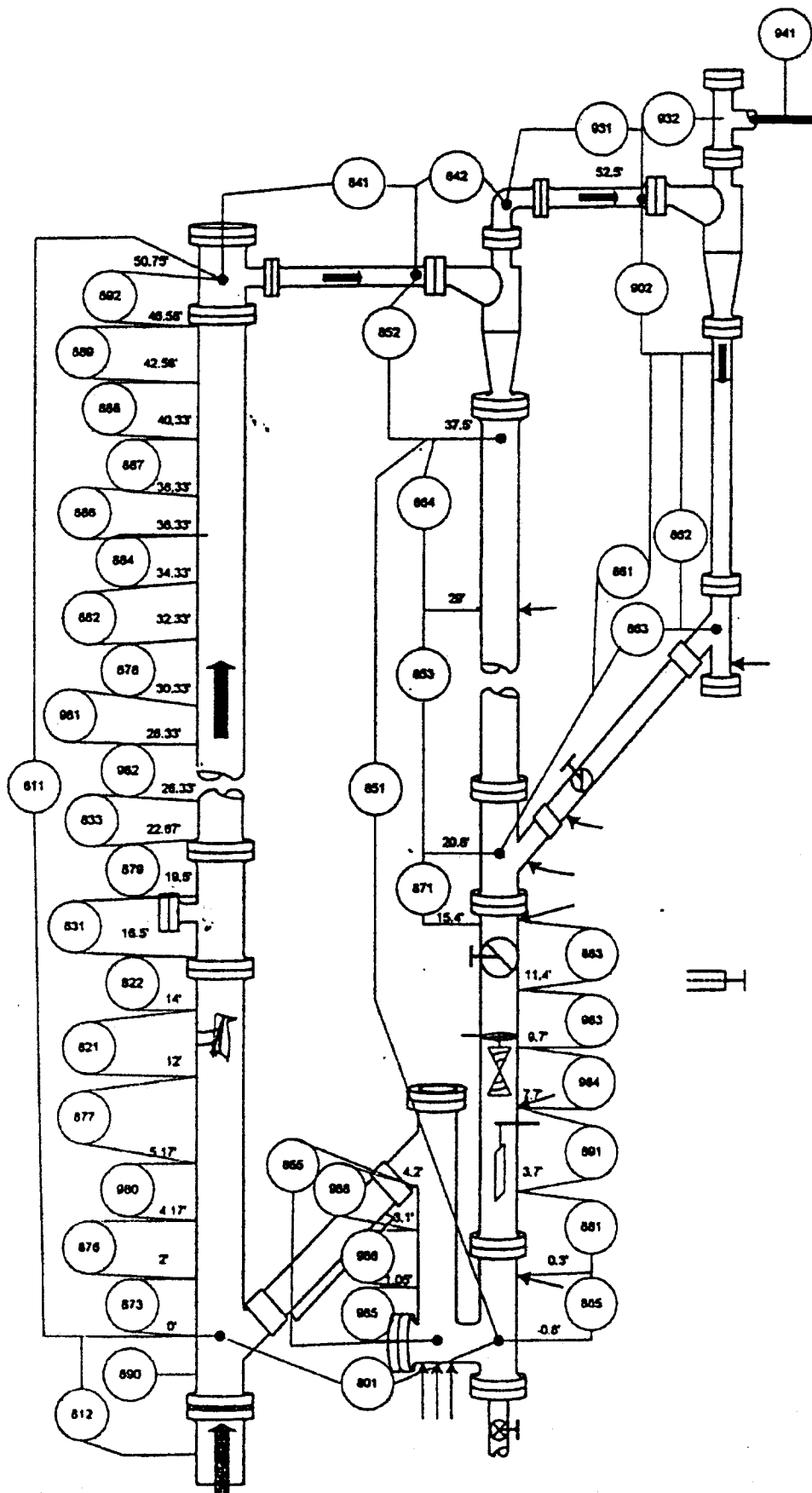


Figure 7. P & I diagram of the CFB.

3. RESULTS AND DISCUSSION

3.1. MODELING

Two related problems that must be addressed in training a NN are: how to determine the architecture (how many neurons and layers) and how to avoid over fitting. Since NN is highly redundant and over-parameterized, it is easy to fit the noise in the data as well as signal. To avoid this problem, the standard NN modeling practice is to separate the data into a “training set”, which is used to train the model, and a “testing set”, which is used to determine when to stop training. Only the training set is used to adjust the network weights. During training, the model is evaluated periodically using the training set. A decrease in testing performance signals that over fitting is setting in. In addition, a “validation set” may be set aside for evaluating the model on data that was not involved in the training process. We have also incorporated the time-delayed signals of the

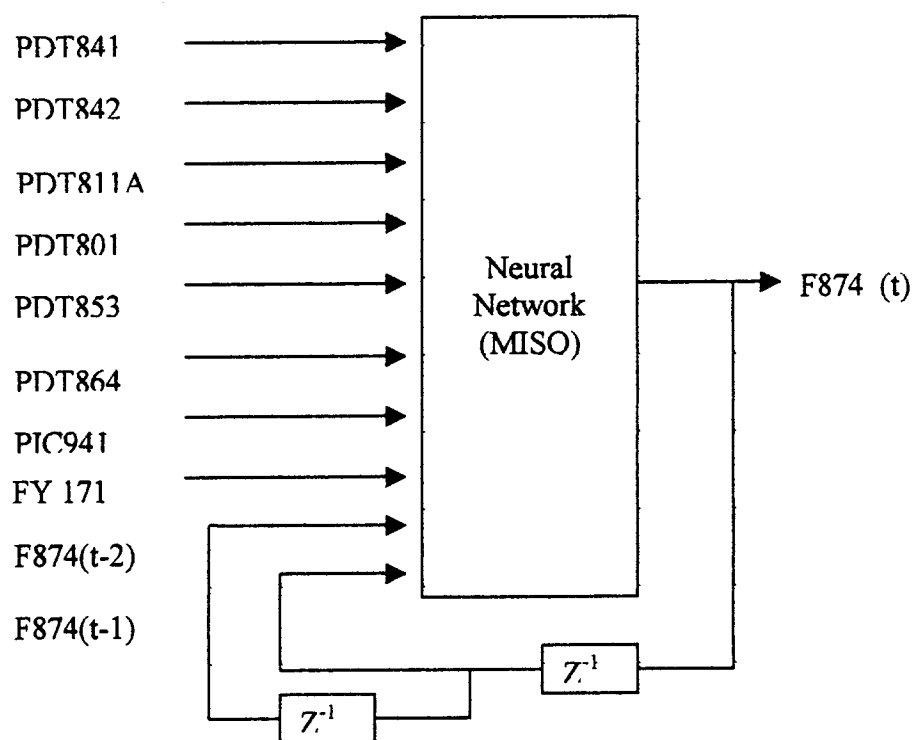


Figure 8. MISO Neural Network

predicted variable to enable capturing the delayed effects of that variable on the system. Also normalizing the variable within the range of [0,1], has given better results with a smaller network and better approximation.

3.1.1 Multi Input Single Output (MISO) Neural Network Model

A schematic of the MISO neural network model for the prediction of the Mass flow rate (M_s) is shown in Figure 12.

The training and the extrapolation data for the two most dominating variables of the CFB, the Mass flow rate and the Aeration are being presented in Tables 1 and 2. The value of Mean Squared Error (MSE) for both the training set and the Test set indicate the optimal network for the process variable and also help in reducing the chances of over-fitting the data. The Network Size represents the number of hidden layers and the number of neurons in the hidden layer.

Table 1. Training and Testing data of Mass Flow Rate (M_s).

Network Size	Training Algorithm	Activation Function	Training Time (min)	No. of Iterations	MSE Error <i>Training</i>	MSE Error <i>Test</i>
5	LM	Tansig	0.3160	25	0.0021	0.0034
10	“	Tansig	0.3538	“	0.0019	0.0034
“	“	“	0.4271	50	0.0018	0.0033
“	“	Logsig	0.3544	25	0.0021	0.0036
15	“	Tansig	0.3710	“	0.0021	0.0032
”	“	“	0.4822	50	0.0019	0.0034
25	“	“	0.4428	25	0.0020	0.0034
25	GD	Tansig	0.3266	“	0.0291	0.0321

Table 2. Training and Testing data of Aeration (Fy).

Network Size	Training Algorithm	Activation Function	Training Time (min)	No. of Iterations	MSE Error <i>Training</i>	MSE Error <i>Test</i>
5	LM	Tansig	0.3392	25	9.86e-6	2.55e-5
10	“	Tansig	0.3744	“	2.12e-5	6.50e-5
“	“	“	0.5403	50	8.94e-6	1.63e-5
“	“	Logsig	0.5011	25	0.0267	0.0275
15	“	Tansig	0.4698	“	9.39e-6	1.49e-5
“	“	“	0.6903	50	9.19e-6	1.33e-5
25	”	“	0.6913	25	3.46e-5	1.12e-4
25	GD	“	0.3435	“	0.1224	0.1226

It is clearly evident from Table 1 and Table 2, the optimal NN for the modeling of the Mass flow rate and Aeration Rate is a single hidden layer of 15 neurons and “Tansig” as the activation function which is represented in bold. Aeration rate needed more number of iterations for better prediction, so as to minimize the error in the Test data. Note from the Tables, the “logsig” activation function was not able to do a good job here. And also we see that the LM training algorithm is superior to the Gradient Descent (GD) training algorithm previously used in modeling. In Figure 11, a magnified view of the extrapolation is shown wherein the variables have been varied over the short range by manipulating the back pressure P_o thereby affecting riser pressure, which in turn affects the mass flow rate. The network extrapolates the mass flow rate correctly even in this interacting condition proving that it has correctly learnt this intricate relationship between

variables. The plots of the training and the extrapolation of Mass Flow Rate, M_s (F874) are presented in the Figures 9 & 10. The plots clearly show that the Neural Network model has not only learnt the system dynamics but was also able to extrapolate over unseen data, which was an acid test for the validity of the model. Only the data from 1-1800 sec was given for the training, and the rest of the data was unseen by the Neural Network during training. It was only in the testing phase that data was being used to test the Trained Network.

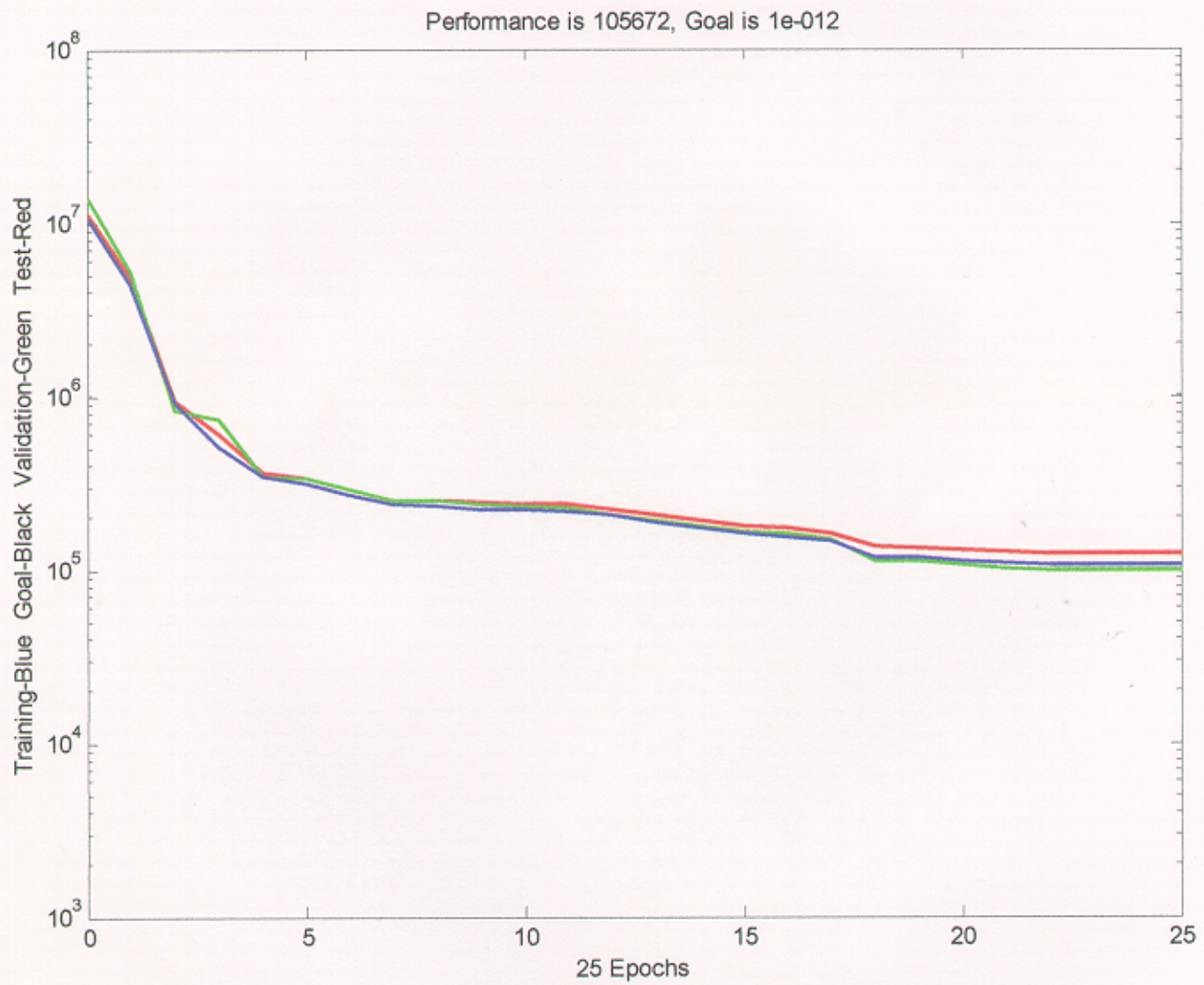


Figure 9. Mean Squared Error (MSE) plot during training of Mass Flow rate (Ms) for MISO model

Mass Flow Rate F874 (Ms) Training is done on 1:1800 Points, Validation is done on points from 1800:2400 and Testing is done on points from 1800:3600

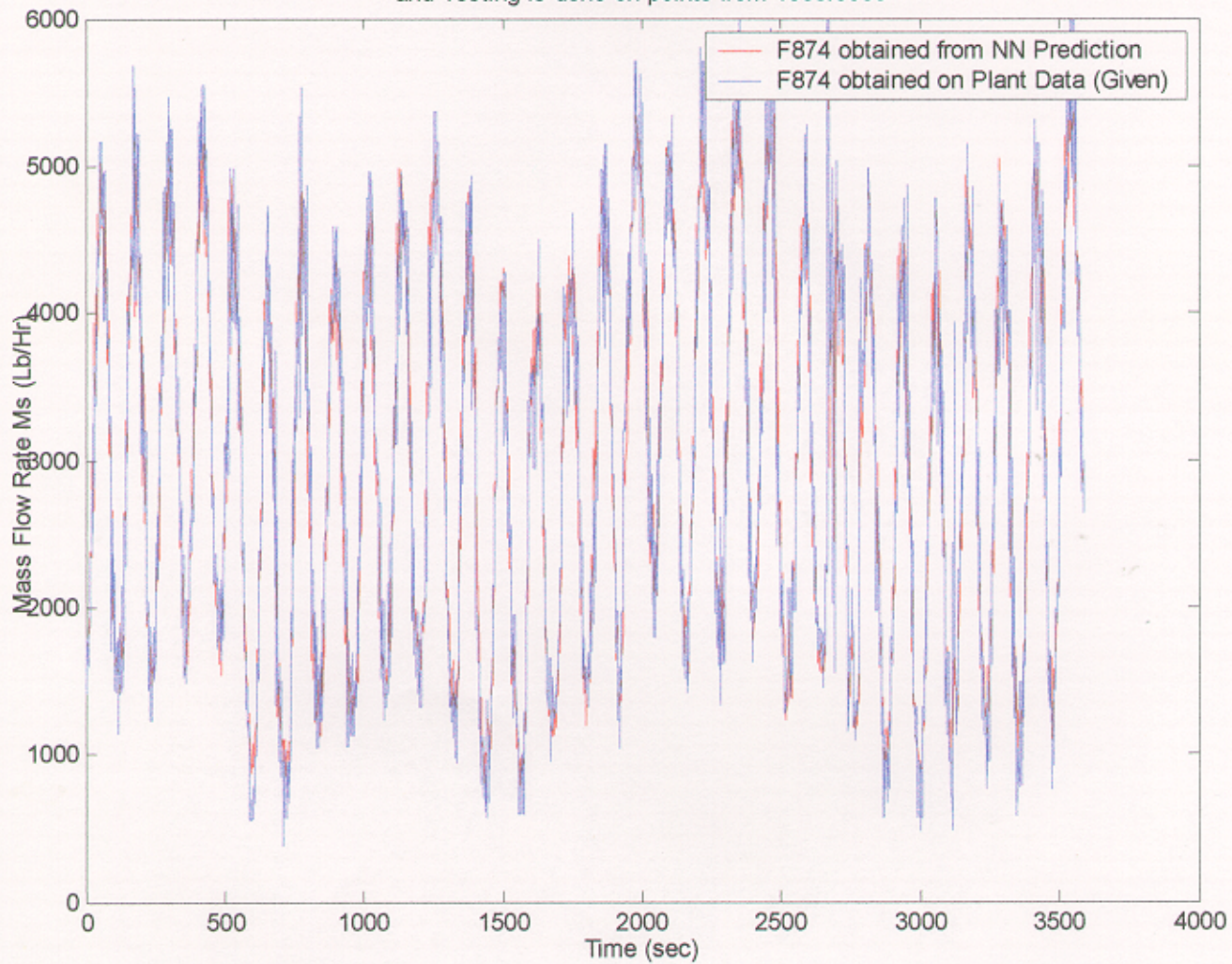


Figure 10. Plot showing prediction of Ms by the trained Neural Network MISO Model

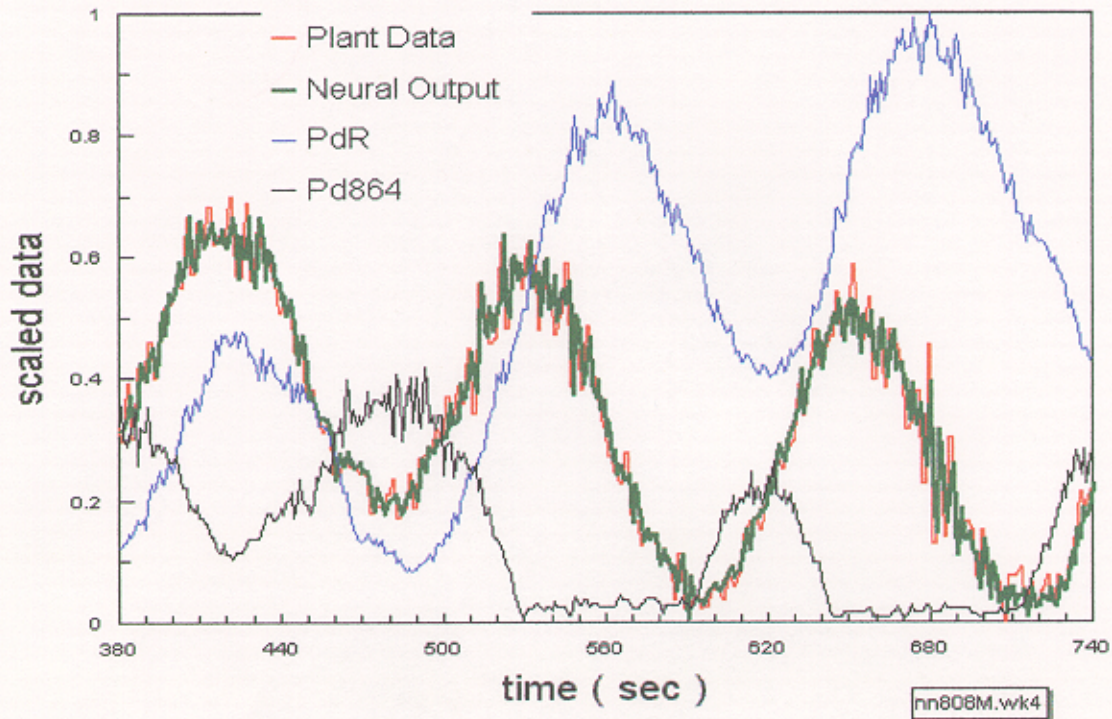


Figure 11. Neural network Extrapolation of Mass Flow rate (Ms)

3.1.2. Multi Input Multi Output (MIMO) Neural Network model

A schematic of the Multi Input Multi Output Neural Network model is shown in Figure

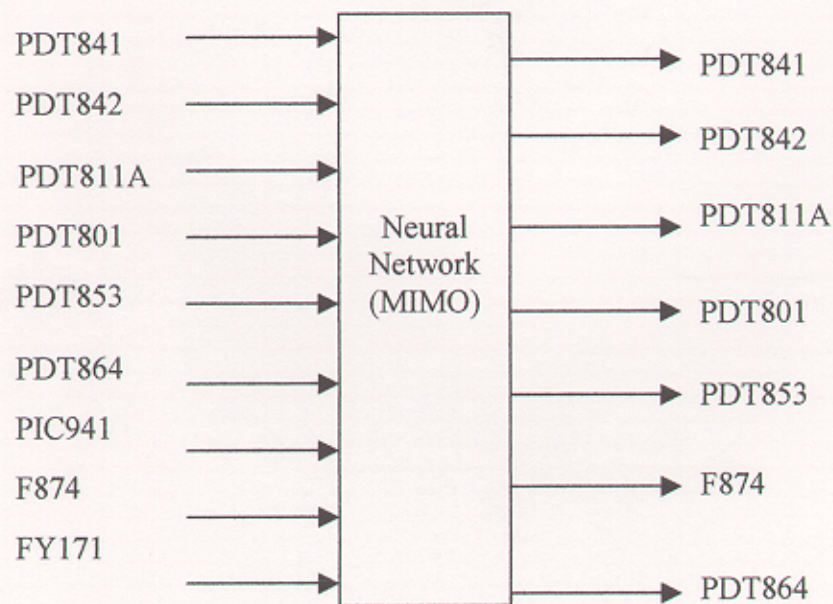


Figure 12. MIMO Neural Network

12. The inputs are at time 't' and the NN predicts outputs for time 't+1'. The plots showing the extrapolation by the MIMO Neural Network model are shown in the Figures 13 through 19.

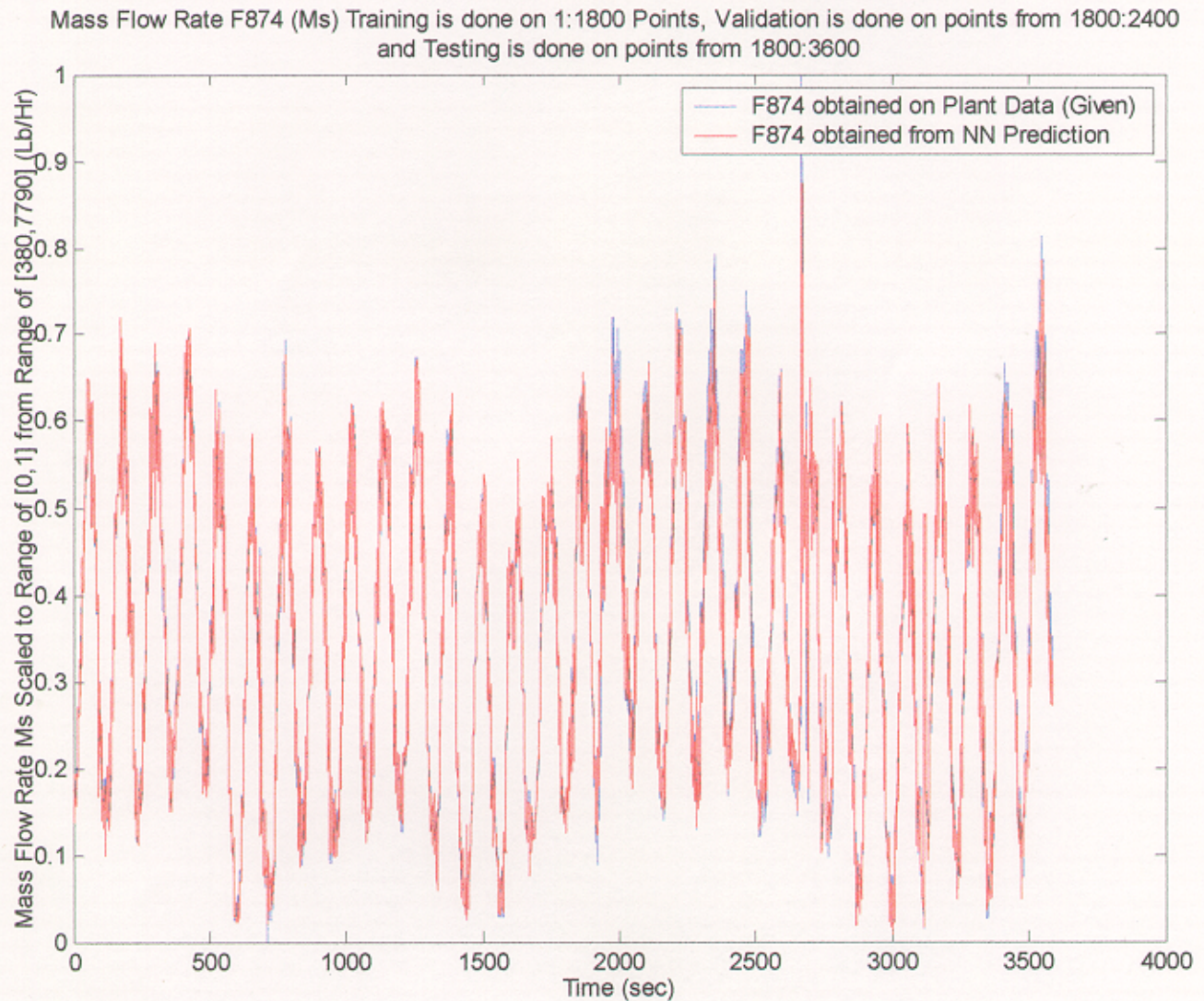


Figure 13. Plot showing prediction of Ms by the trained Neural Network MIMO Model

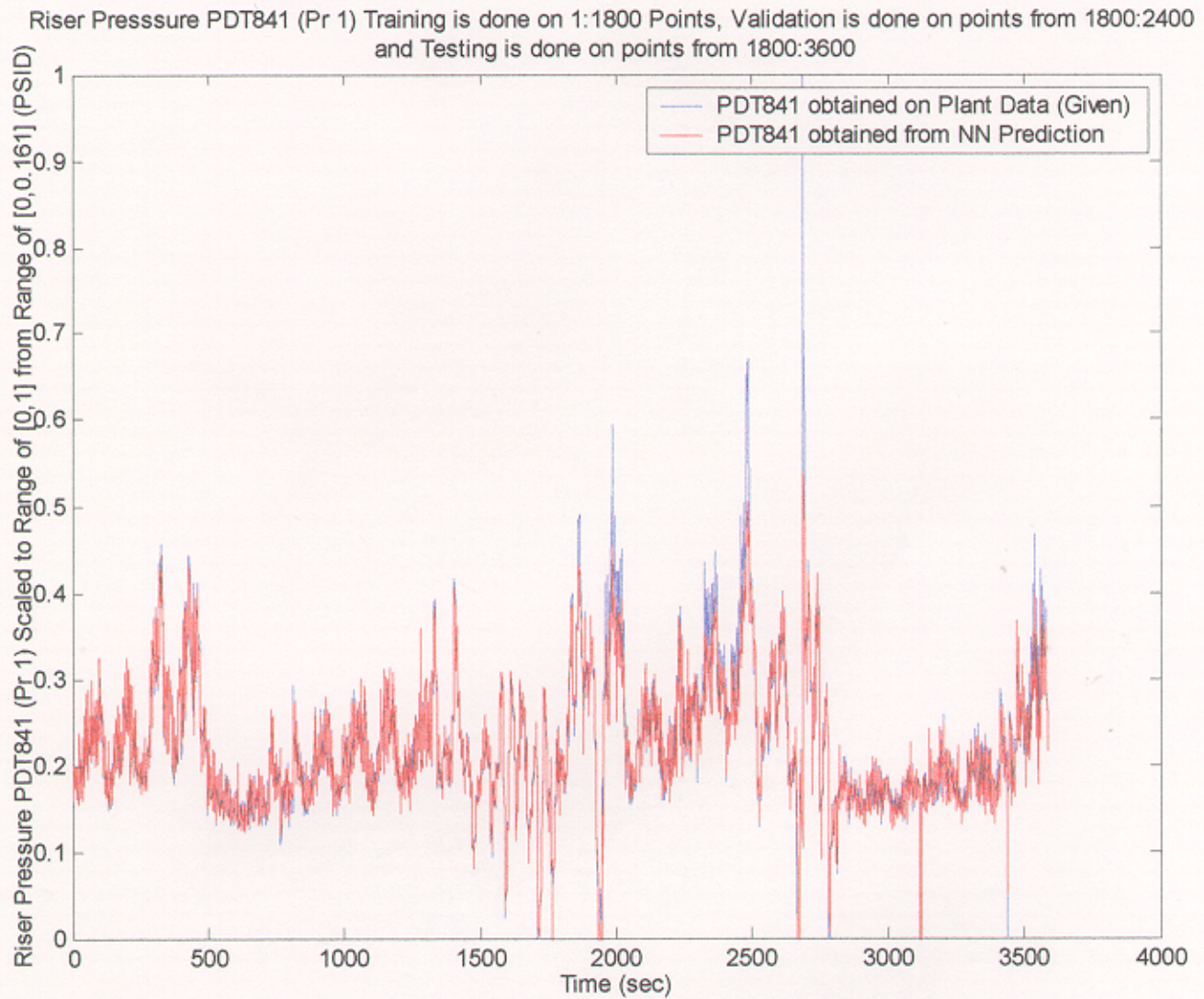


Figure 14. Plot showing prediction of PDT 841 by the trained Neural Network MIMO Model

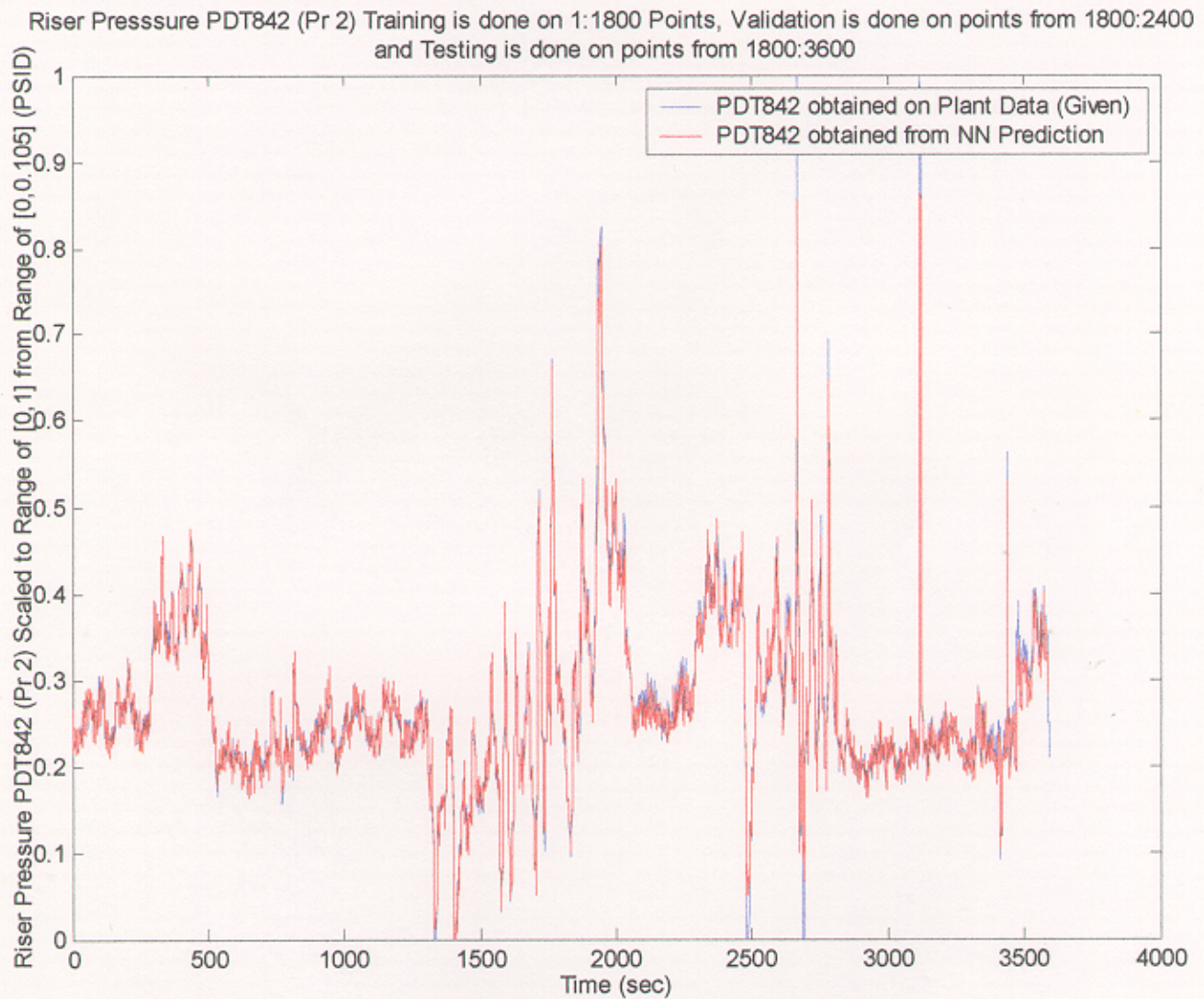


Figure 15. Plot showing prediction of PDT 842 by the trained Neural Network MIMO Model

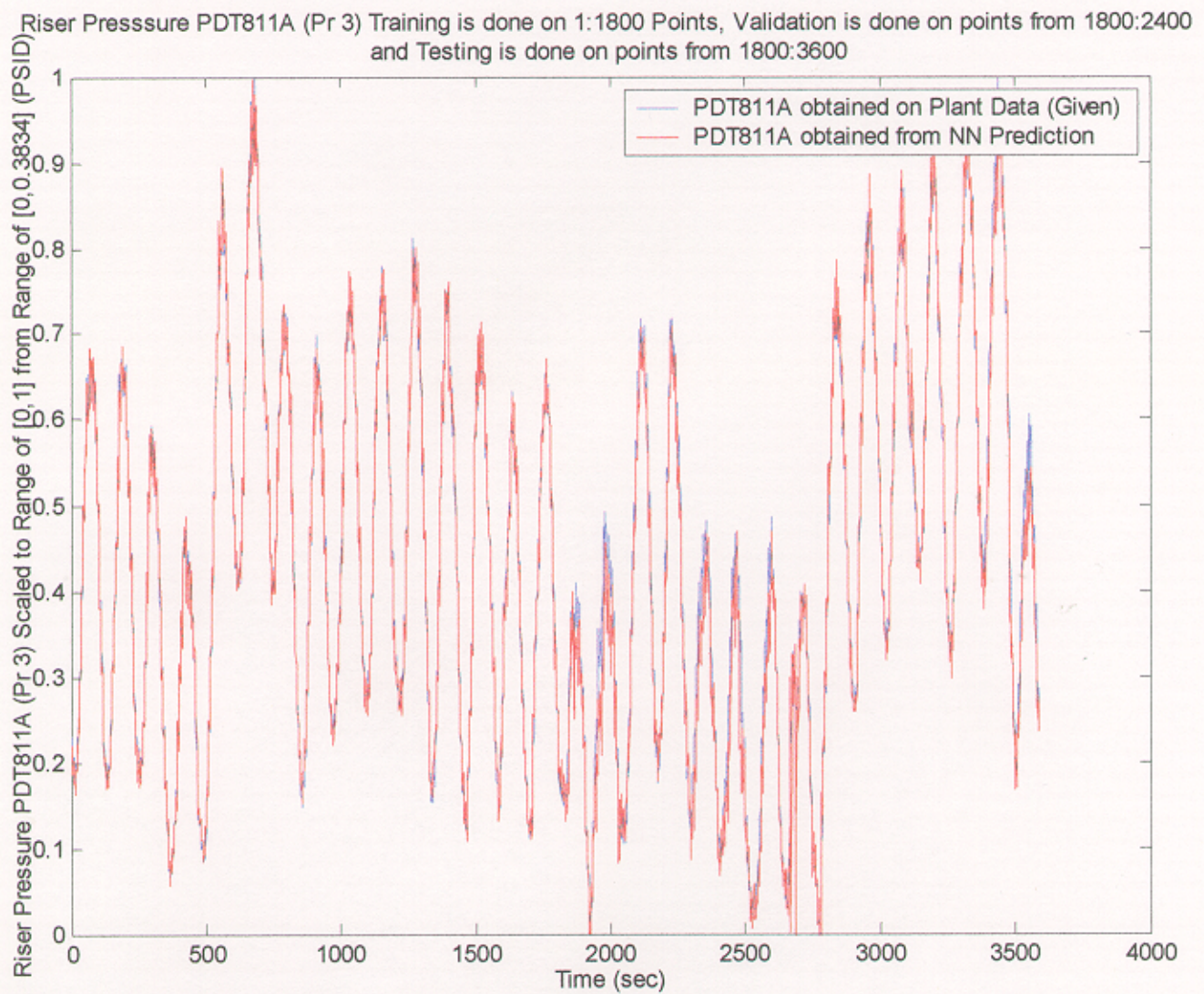


Figure 16. Plot showing prediction of PDT 811A by the trained Neural Network MIMO Model

Riser Pressure PDT801 (Pr 4) Training is done on 1:1800 Points, Validation is done on points from 1800:2400 and Testing is done on points from 2400:3600

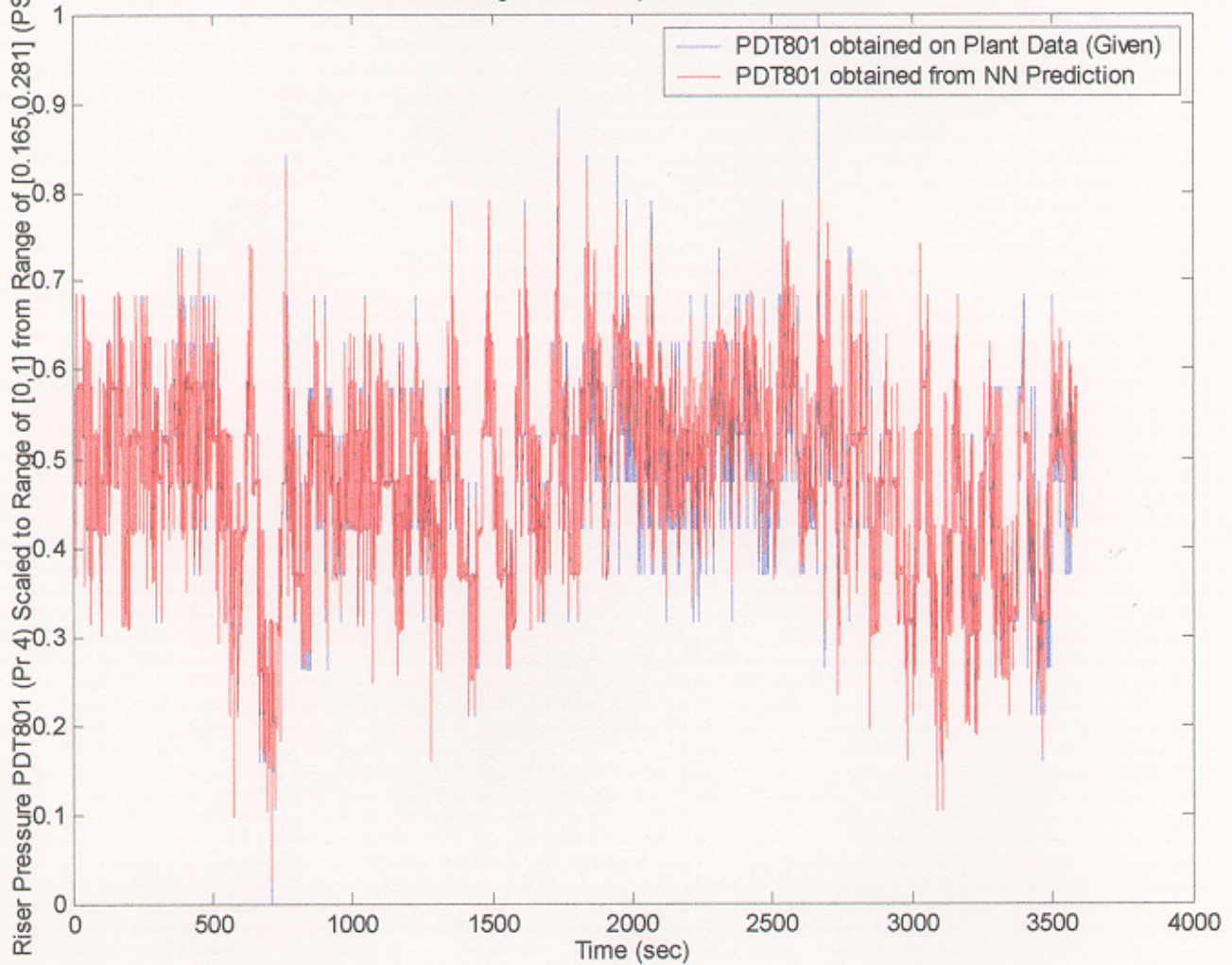


Figure 17. Plot showing prediction of PDT 801 by the trained Neural Network MIMO Model

Upper Standpipe Presssure PDT853 (Psu 1) Training is done on 1:1800 Points, Validation is done on points from 1800:2400 and Testing is done on points from 1800:3600

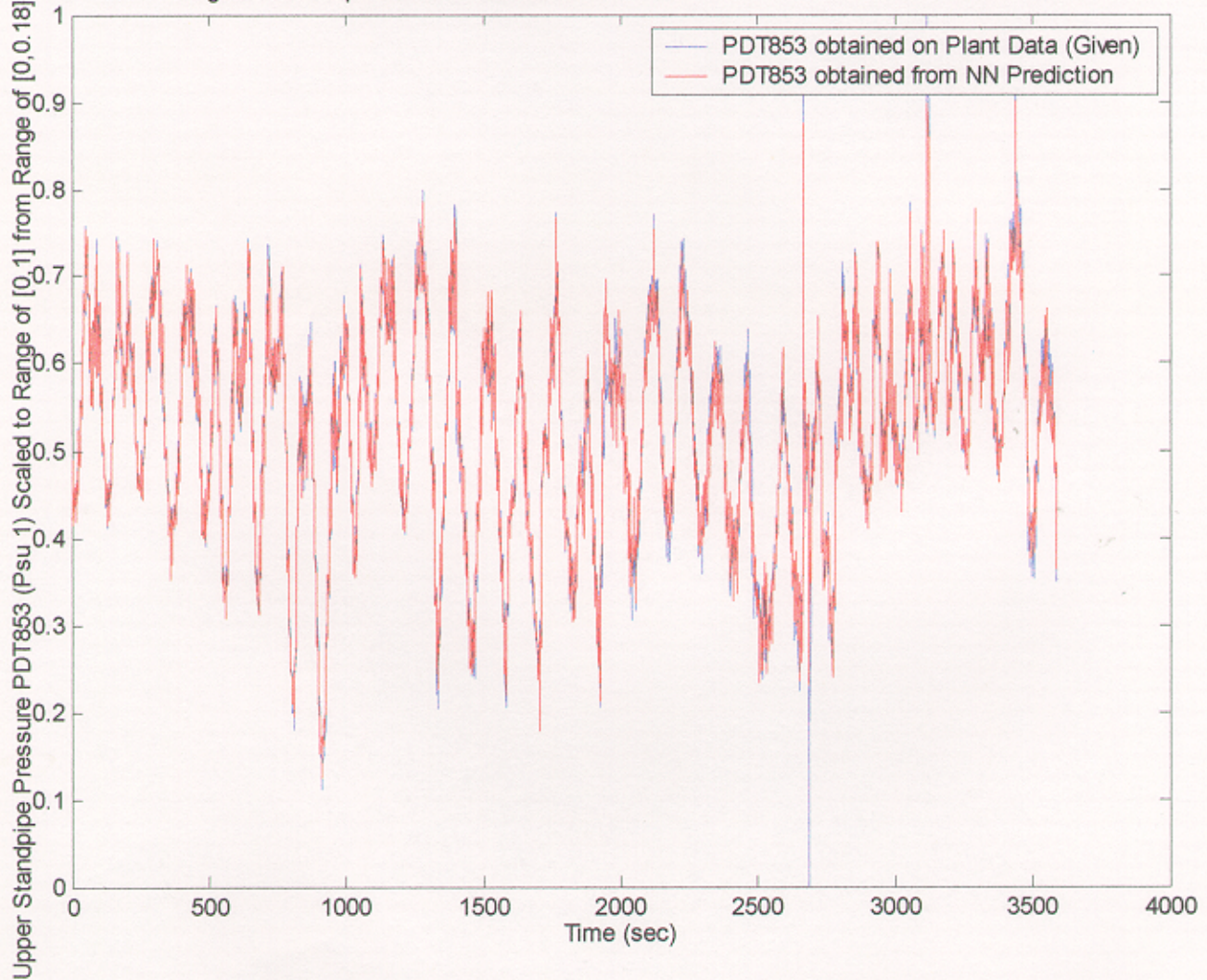


Figure 18. Plot showing prediction of PDT 853 by the trained Neural Network MIMO Model

Upper Standpipe Pressure PDT864 (Psu 2) Training is done on 1:1800 Points, Validation is done on points from 1800:2400 and Testing is done on points from 1800:3600

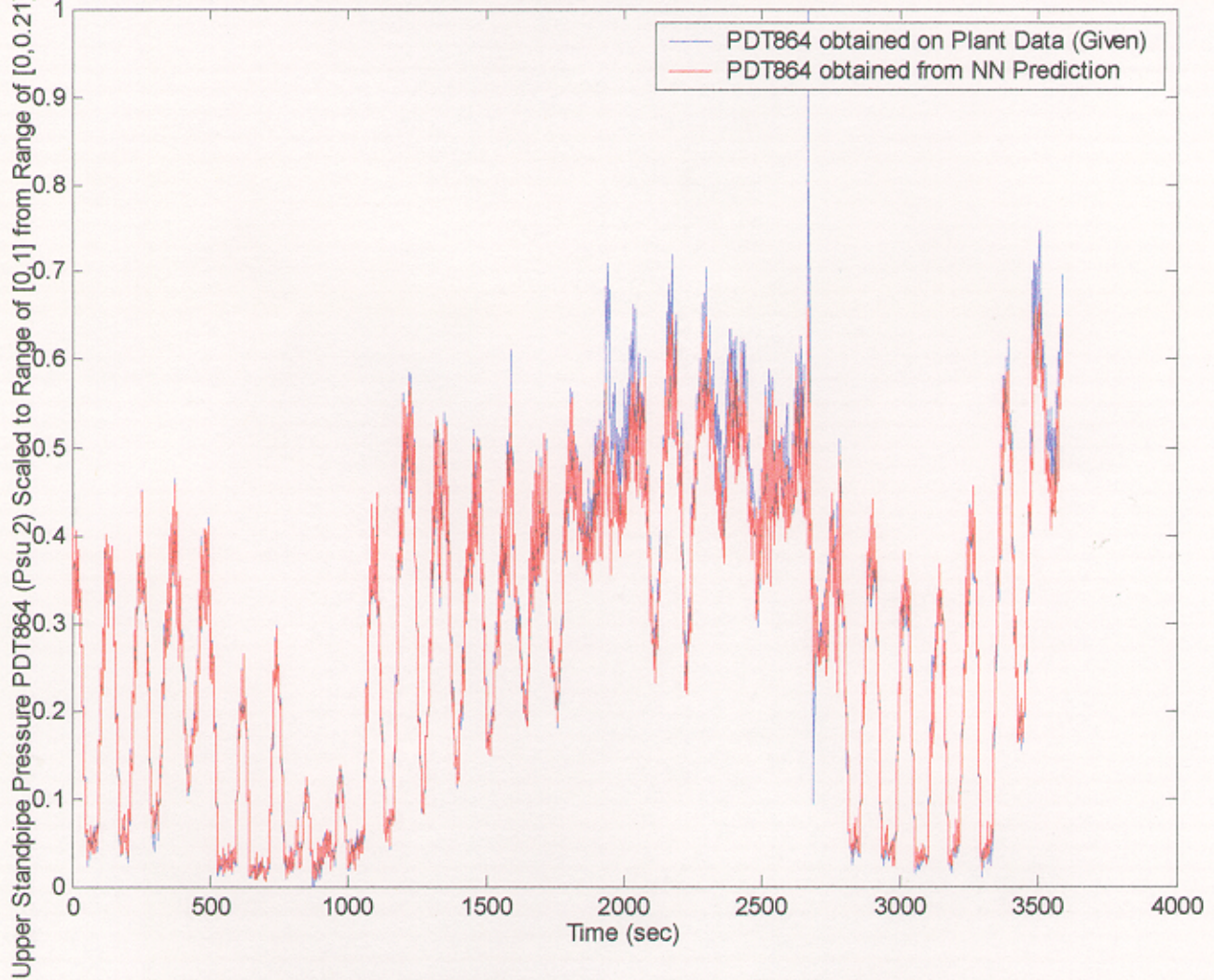


Figure 19. Plot showing prediction of PDT 864 by the trained Neural Network MIMO Model

3.2. DEVELOPMENT OF CONTROLLER

3.2.1. Inverse Model Control

Consider a system transfer function $\frac{Y(s)}{X(s)}$ where $Y(s)$ is the system output and $X(s)$ is the

input to the system. The significance of the transfer characteristics in system and control theory is based on the fact that response of a static system to an arbitrary excitation can be computed as a product of its transfer characteristics and of the excitation. Similarly, the transform of the response of a dynamical system can be expressed as a product of the transfer function and transform of the excitation.

For a plant that is completely known, any desired relationship between input and

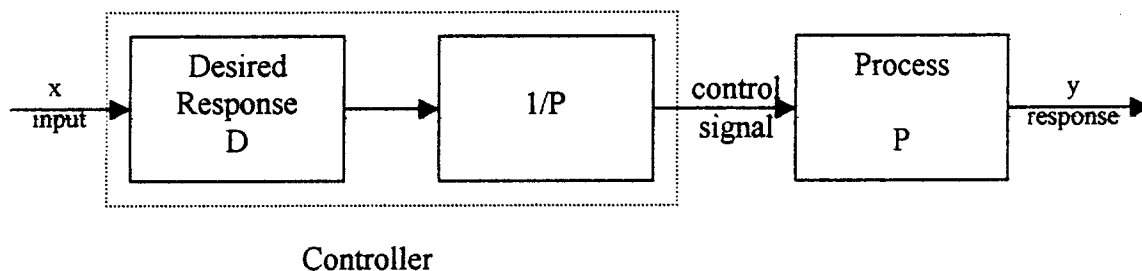


Figure 20. Control of Process P to achieve the desired response.

response can be realized by a simple open loop control configuration as shown in Figure 20. The feed forward controller consists of two parts connected in cascade. The second one cancels the process transfer function because its own transfer function has been chosen as the inverse of the known process transfer function. In addition, the front part of the controller introduces the desired overall transfer function of the controller and the plant equal to D . Thus the controller's transfer function should be equal to D/P . This approach is known as inverse control since the most essential part of the controller should provide the inverse of the plants transfer function. The transfer function of the inverse

feed forward control system from the figure computed between its input and output becomes $D(s) = \frac{Y(s)}{X(s)}$. In this approach involving the cascade connection of the controller driving the plant and involving no feedback, the neural controller that acts as the plant inverse needs to be designed.

For the system under consideration, the inverse model was derived from a neural network that predicted the value of the aeration required to produce a desired mass flow rate. This predicted value of aeration was used to control the mass flow rate to a desired set-point value.

To model the system we have used a 3-layered neural network with 10 neurons in the input layer, 15 neurons in the hidden layer and 1 neuron in the output layer. We have used the Levenberg Marquardt (LM) algorithm for training purposes. The data points had

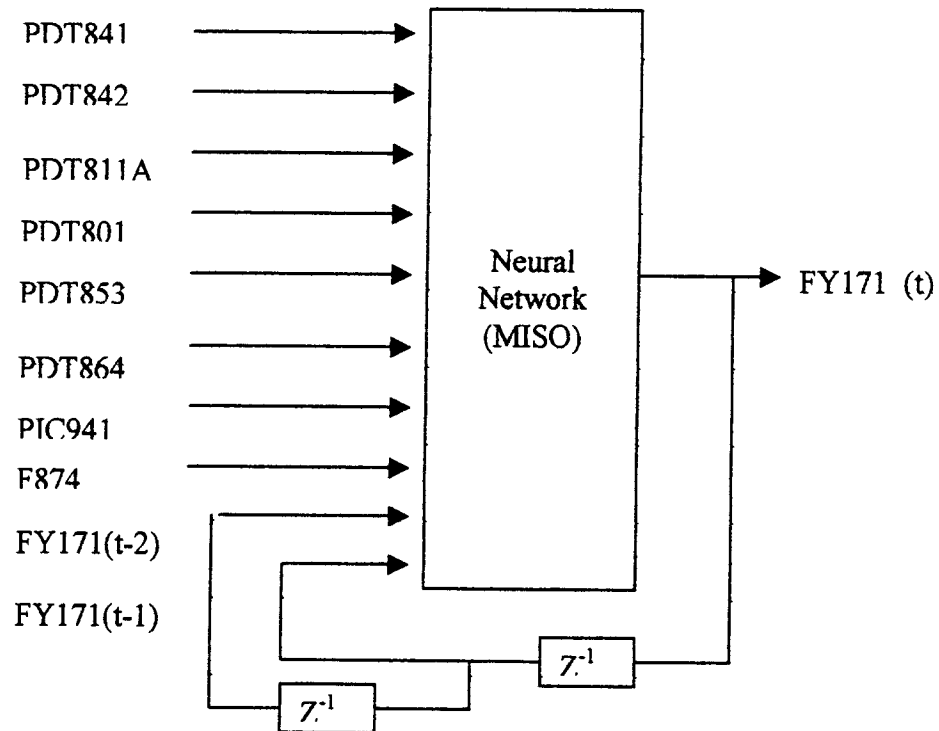


Figure 21. MISO Neural Network for Controller

to be chosen in such a way that all the system dynamics were captured. Out of the 3600 data points collected, 1800 points were used for modeling and the remaining points were used for extrapolation of the results over unseen data points for validation of the obtained model. The trained controller is implemented as an Inverse model of the plant which is explained later. Detailed plots showing the training of the Neural Network controller over the data set being provided and its extrapolation are being shown in Figures 22 & 23.

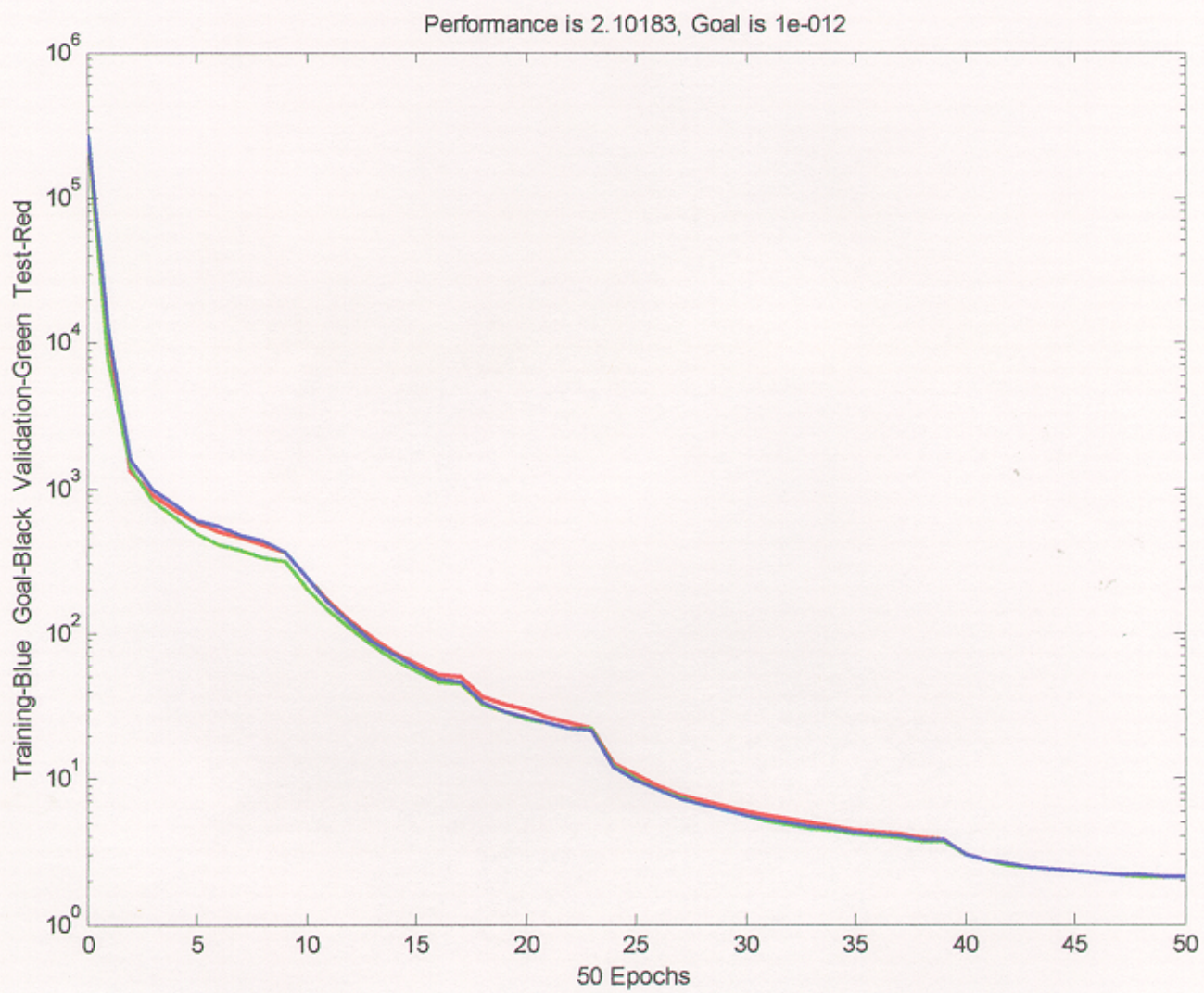


Figure 22. Mean Squared Error (MSE) plot during training of Controller

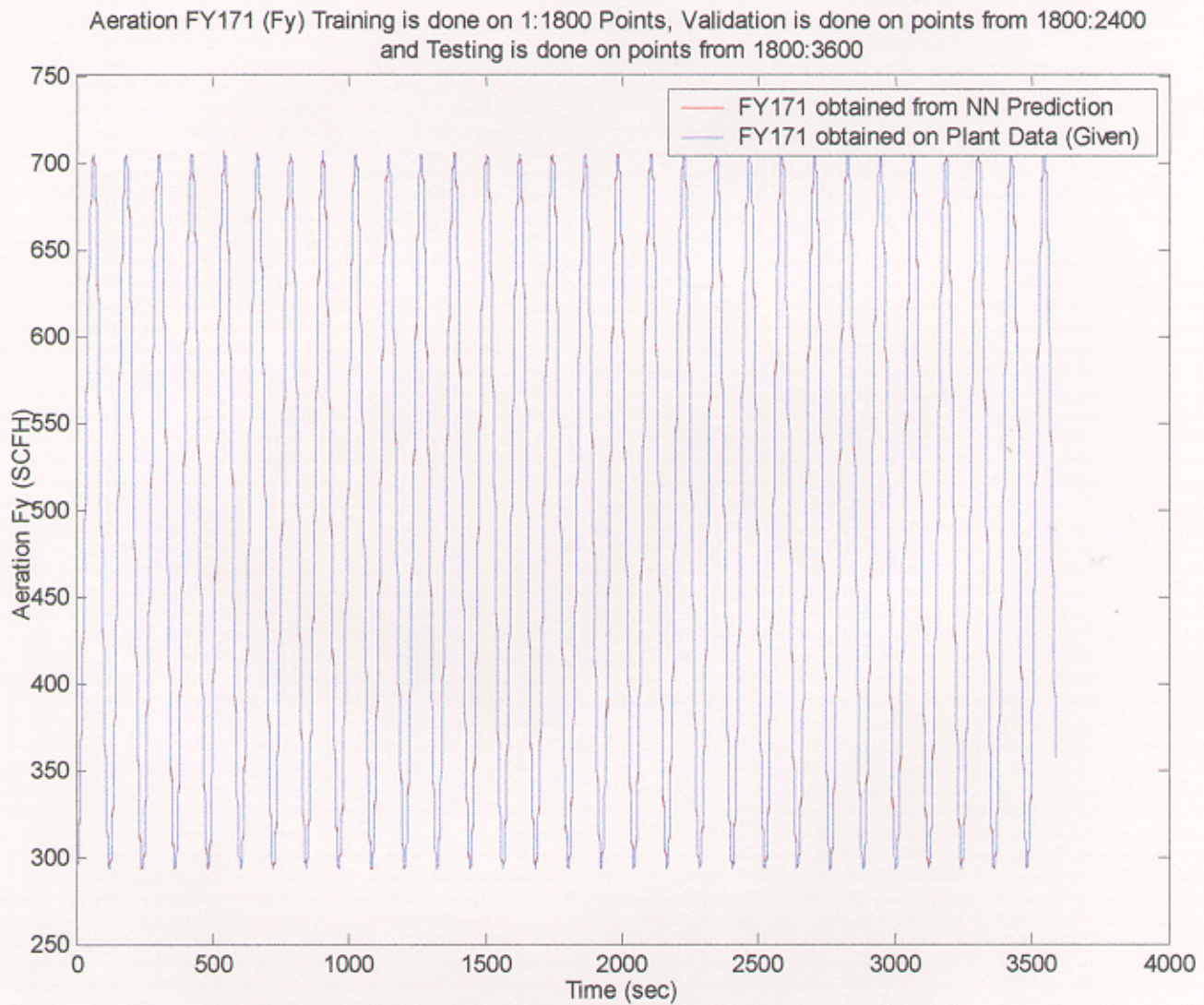


Figure 23. Plot showing prediction of FY 171 by the trained Neural Network Controller

3.2.2. Controller implementation

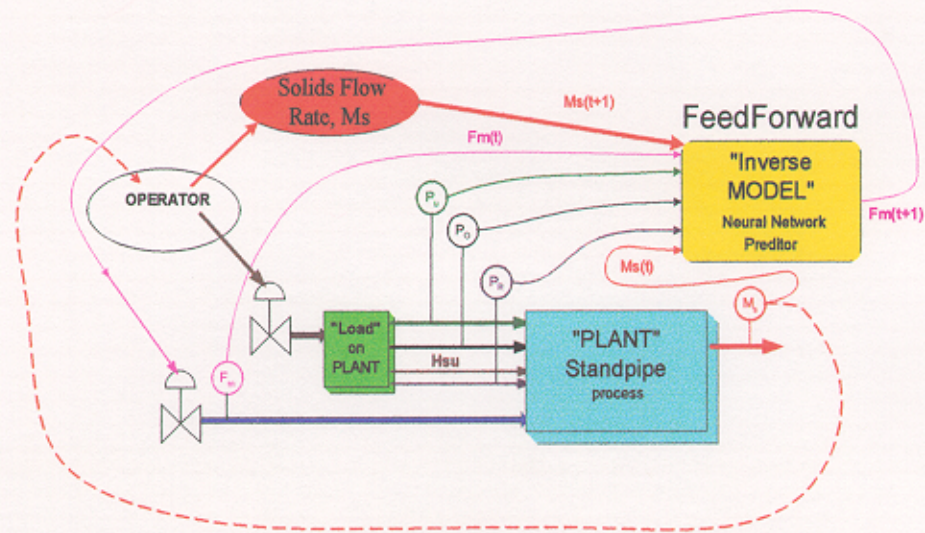


Figure 24. Schematic of Implementation of NN controller on the CFB

We have implemented a feed forward inverse controller where the neural network predicts the values of the aeration rate (FY 171) to achieve a desired value of the mass flow rate as shown in Figure 24. We tested the controller and found it to have a stabilizing effect on the plant. A simulation of this controller is shown in Figure 25.

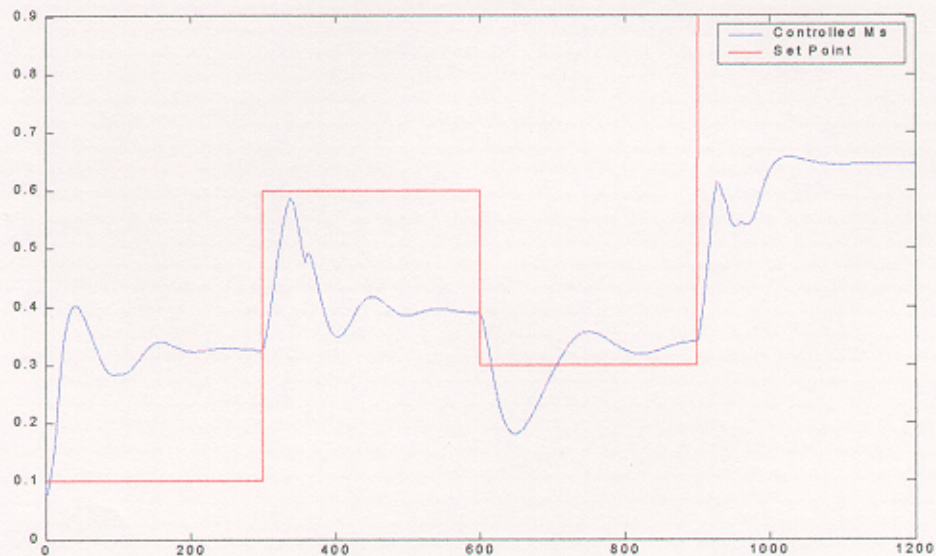


Figure 25. Controller Simulation

4. CONCLUSIONS

With the use of efficient back propagation training algorithm, we were able to make an efficient and accurate model of the CFB. Previous attempts were restricted to the data set and failed on extrapolating the results over unseen data, where we have succeeded. Equipped with an accurate model, the next step is to design and implement an appropriate controller for the CFB.

We are now working on various techniques of implementing the controller, like Internal model control that incorporates feedback signal and relays information about the amount of correction necessary for the control signal to achieve more accurate control. Also, efforts are underway to make the model adaptive to any changes in the plant dynamics.

* * *

4. REFERENCES

1. Daniel Vandel, Asad Davari and Parviz Famouri, " Modeling of Fluidized bed with Neural Networks", Proceedings of 32nd IEEE SSST, March 2000, FAMU-FSU Tallahassee, Florida.
2. Asad Davari, Sridhar Macha and Rammohan Sankar, "Neural Network predictor of a circulating fluidized bed", Proceedings of 33rd IEEE SSST, March 2000, Ohio Univ, Athens, Ohio.
3. Asad Davari, Sridhar Macha and Rammohan Sankar, "Improved Neural Networks modeling and predicting of circulating Fluidized Beds", Proceedings of the IASTED Intl. Conf., May 2001, Pittsburgh, Pennsylvania.
4. A. Davari, and D. Vandel, " Modeling and Predicting the Output of a Circulating Fluidized Bed with Neural Network," Technical Report, DOE/NETL October 1999.
5. A. Davari, and R. Sankar, "Neural Network Predictor of the Output of a Circulating Fluidized Bed," Technical Report, DOE/NETL November 2000.
6. A. Davari, and S. Macha, " Improved Model of Circulating Fluidizes Bed with Neural Networks," Technical Report, DOE/NETL November 2000
7. Levenberg, K., " A method for the solution of certain nonlinear problems in least squares", Quart. Appl. Math., n 2, pp164-168, 1944.
8. Marquardt, D.W., " An algorithm for least-squares estimation of nonlinear parameters", J. Soc. Indust. Appl. Math., n 11, pp 431-441, 1963.

9. Narendra, K.S. and Parthasarathy, K., "Identification and Control of Dynamical systems using NN", IEEE Transactions on NN, v 1, n 1, pp 4-27, 1990.
10. Hornik, K., and Stinchcombe, "Multilayer feed forward networks are universal approximators, Neural Networks", n 2, pp 359-366, 1989.
11. James R. Muir, Clive Brereton, John R. Grace and C. Jim Lim, "Dynamic Modeling for Simulation and Control of a Circulating Fluidized Bed Combustor", AIChE, v 43, n 5, pp 1141-1152.
12. Bhat, N., Minderman, P., and Jr. Thomas McAvoy, "Modeling chemical process systems via neural computation", IEEE Control Systems Magazine, v 10, pp 24-25, 1990.
13. Hunt, K.J., and Sbarbaro, D., "Neural networks for non-linear internal model control", IEEE Proceedings-D, v 138, n 5, pp 431-438, 1991.
14. Rao Vemuri, Artificial neural networks : concepts and control applications, Los Alamitos, Calif. : IEEE Computer Society Press, 1992
15. Handbook of intelligent control : neural, fuzzy, and adaptive approaches edited by David A. White, Donald A. Sofge, New York : Van Nostrand Reinhold, c1992.
16. Neuro-control systems : theory and applications, edited by Madan M. Gupta, Dandina H. Rao, New York : IEEE Press, c1994
17. Thomas E. Quantrille and Y.A. Liu., Artificial intelligence in chemical engineering, San Diego : Academic Press, c1991

**UNIVERSITY/NETL STUDENT PARTNERSHIP PROGRAM
(DE-FC26-98FT40143)**

3rd Year Technical Report

September 1, 2000 – August 31, 2001

Submitted to:

National Energy Technology Laboratory

Submitted by:

**Gerald D. Holder
School of Engineering
University of Pittsburgh
Pittsburgh, PA 15261**

Volume V of VI

XX. “Formation of Carbon Dioxide Hydrates from Single-Phase Aqueous Solutions”

**Lakshmi Mokka (S) and Gerald Holder (F), University of Pittsburgh
with
Robert Warzinski (M), NETL**

ACKNOWLEDGEMENTS

The author would like to express her appreciation to Dr. Gerald D. Holder and Robert P. Warzinski for their support, patience and invaluable guidance during this investigation. A special thanks is also given to Ronnie Lynn who programmed the computer to read and acquire data and technicians Jay Levander, Jerry Foster and Ted Jordan who built the equipment used in the experiments.

Most importantly, a sincere thanks is given to my Parents Rao and Bharathi Mokka and my sister Preeti, for without their support a Master's Degree would not have been possible.

ABSTRACT

Signature _____
Gerald D. Holder

FORMATION OF CARBON DIOXIDE HYDRATES FROM SINGLE-PHASE AQUEOUS SOLUTIONS

Lakshmi P.Mokka, M.S.

University of Pittsburgh

Experimental and theoretical studies demonstrate that CO₂ hydrates can form from a single-phase solution consisting of water with dissolved CO₂.

A theoretical analysis of hydrate formation was used to predict hydrate dissociation points for solutions containing various mole fractions of CO₂ dissolved in water. In order to validate the theoretical model, several experimental hydrate equilibrium points were obtained in which CO₂ hydrates were formed from single-phase solutions. Hydrate dissociation points were obtained at mole fractions of 0.016 and

0.018. The average absolute deviation of the hydrate dissociation points obtained was for temperature 1.61% and for pressure of 12.65%.

DESCRIPTORS

Hydrate

Ocean sequestration

Single-phase

Solubility

Thermodynamics

TABLE OF CONTENTS

	Page
ACKNOWLEDGEMENTS	iii
ABSTRACT	iv
LIST OF FIGURES	viii
LIST OF TABLES	x
NOMENCLATURE	xi
1.0 INTRODUCTION	1
2.0 LITERATURE REVIEW AND BACKGROUND	4
2.1 CO ₂ and the Greenhouse Effect.....	4
2.2 The Ocean Sequestration of CO ₂	6
2.3 The Nature of Hydrates.....	8
2.4 Formation of CO ₂ Hydrate From a 2-Phase System.....	11
2.5 Formation of Hydrate From a Single-Phase System.....	11
2.6 Thermodynamic Basis of Hydrate Formation.....	12
3.0 DESCRIPTION OF EQUIPMENT	32
4.0 EXPERIMENTAL PROCEDURES	38
4.1 Assembly of Cell.....	38
4.2 Pressure Testing of Cell.....	38
4.3 Injection of CO ₂ and Water into the Cell.....	39
4.4 Formation of Hydrate.....	40
5.0 TWO-PHASE EXPERIMENTAL RESULTS AND DISCUSSION	41

5.1	Experiment T10-007.....	41
5.2	Experiment T10-009.....	45
5.3	Experiment T10-008.....	47
6.0	SINGLE-PHASE EXPERIMENTAL RESULTS AND DISCUSSION.....	50
6.1	Single-Phase Experiments.....	50
6.2	Analysis of Single-Phase Experiments.....	50
6.3	Experiment T10-006.....	53
6.4	Experiment T10-011.....	57
6.5	Experiment T10-012.....	60
6.6	Experiment T10-013.....	60
7.0	RESULTS AND DISCUSSION.....	66
7.1	Summary of Results.....	66
7.2	Discussion of Results.....	66
8.0	CONCLUSIONS.....	69
9.0	FUTURE WORK.....	70
	APPENDIX: FORTRAN CODE.....	71
	BIBLIOGRAPHY.....	123

LIST OF FIGURES

Figure #	Page
1	CO ₂ Phase Diagram.....2
2	The Global Carbon Cycle: Reservoirs (GtC) and fluxes (GtC/yr).....5
3	Structure I (below) and Structure II (above) Hydrates.....9
4	The Fugacity of CO ₂ as a Function of Pressure for Different Compositions T = 275 K.....18
5	Chemical Potential Difference of Water in the Hydrate Phase at Different Compositions at T = 275 K.....20
6	Chemical Potential Difference of Water in the Hydrate and Aqueous Phases at T = 275 K.....21
7	Hydrate Dissociation Pressures as a Function of Mole Fraction at T = 275 K.....23
8	Solubility Charts.....29
9	Hydrate Dissociation Pressures as a Function of Temperature at Several Different Compositions.....30
10	Overall Laboratory Setup, Chamber Closed.....33
11	Overall Laboratory Setup, Chamber Open.....34
12	Schematic of Equipment.....35
13	View Cell.....36
14	Experiment T10-007 – Raw Data, Pressure as a Function of Temperature and Literature Data.....42
15	Experiment T10-007 – Corrected Pressure and Temperature.....44
16	Experiment T10-009 – Pressure vs. Temperature and VLH Equilibria Data.....46

17	Experiment T10-008 – Pressure vs. Temperature.....	48
18	Slopes vs. Temperature Data at $X = 0.016$ with and without Hydrate Present.....	51
19	Experiment T10-006 – Cycle #3 Pressure vs. Temperature Curve.....	54
20	Experiment T10-011 – Formation of Hydrate from a Single-Phase System.....	58
21	Experiment T10-013 – Slopes vs. Temperature – Cycles 1,2 & 3.....	63
22	Experiment T10-013 – Results from Cycle #7.....	64
23	Summary of Experimental Results from Single-Phase Experiments.....	67
24	Experiment T10-013 – Various Partial Molar Volumes.....	68

LIST OF TABLES

Table #		Page
1	Theoretical Prediction of Hydrate Formation form Single-Phase Aqueous Solutions Containing Various Dissolved Gases at $T = 275$ K.....	27
2	Experiment T10-006 Hydrate Dissociation Points.....	56
3	Experiment T10-011 Hydrate Dissociation Points.....	59
4	Experiment T10-012 Hydrate Dissociation Points.....	61
5	Experiment T10-013 Hydrate Dissociation Points.....	65

NOMENCLATURE

$f_{i,L}$	fugacity of hydrate-forming species i in liquid phase, MPa
$f_{i,H}$	fugacity of hydrate-forming species i in hydrate phase, MPa
f_i	fugacity of hydrate-forming species i , MPa
P^{sat}	bubble-point pressure, MPa
f_i^{sat}	fugacity of hydrate-forming species i at P^{sat} , MPa
GtC	gigatons Carbon
P	pressure, MPa
R	gas constant
T	temperature, K
\bar{V}_i	partial molar volume of species i in water phase, cc/mol
T_o	reference temperature, K
T	temperature, K
Δh	enthalpy difference between empty hydrate and pure liquid water
Δv	volumetric difference between empty hydrate and pure liquid water
X_w	mole fraction of water in the water-rich liquid phase
X_i	mole fraction of gas species in liquid phase
C_{ji}	Langmuir constant for species i in cavity j
μ_L	chemical potential of water in liquid phase, KJ/mol
μ_H	chemical potential of water in hydrate phase, KJ/mol
μ^β	chemical potential of hypothetical empty hydrate lattice, KJ/mol

- v_j ratio of j-type cavities present to number of water molecules present in the hydrate phase
- θ_{ji} fraction of j-type cavities occupied by i-type gas molecules
- $\Delta\mu^\circ$ reference chemical potential of hydrate former, KJ/mol
- $\Delta\mu_H$ chemical potential difference of water in hydrate phase, KJ/mol
- $\Delta\mu_L$ chemical potential difference of water in liquid phase, KJ/mol

1.0 INTRODUCTION

The purpose of this project is to form CO₂ hydrates from a single-phase aqueous solution consisting of dissolved CO₂ and liquid water. The amount of data in the literature addressing the formation of hydrates from a single-phase aqueous solution is limited (Holder et. al., 1988)*. Most data in the literature reporting the formation of hydrates addresses the formation of hydrates from two phases of either gaseous hydrate former and liquid water or liquid hydrate former and liquid water. Obtaining experimental data focusing on the formation of CO₂ hydrate from a single-phase aqueous solution is important because of its potential application to the real world problem of global warming.

The current trend of global warming has been attributed to the rising levels of CO₂ in the atmosphere (Ravkin, 1992). The ocean sequestration of CO₂ is a method that has been proposed to attenuate the increasing levels of CO₂ in the atmosphere. The ocean sequestration of CO₂ involves the disposal of CO₂ from stack gases into the ocean as opposed to its release into the atmosphere. The shallowest depth at which hydrates have been reported to form is 510 m (Brooks et. al, 1991). This point corresponds to a pressure of 4.9 MPa as seen at point A in Figure 1. In Figure 1, hydrate dissociation pressures for seawater were estimated from Sloan, 1998. In Figure 1, hydrate dissociation pressures for pure water were estimated from Larson, S.D, 1955.

* Parenthetical References refer to Bibliography

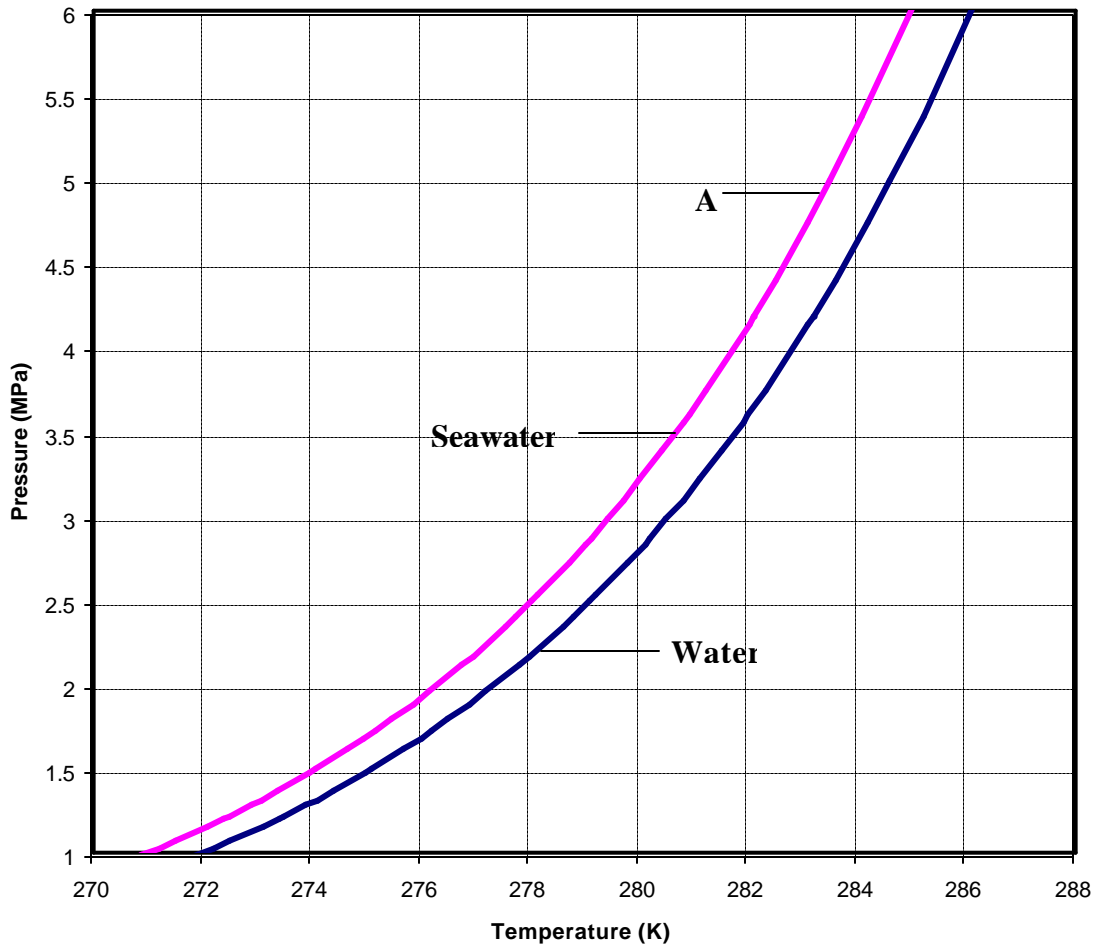


Figure 1 Formation of CO₂ hydrate from Seawater and Pure Water

Once CO₂ is released at a depth of 510 m or below, the CO₂ released may form hydrates with the water in the ocean and sink. Literature data shows that hydrate formed from a single-phase system of CO₂ dissolved in water sinks (Warzinski et. al 1995, Warzinski et. al, 2000). However, when hydrate is formed from a two-phase system, where the CO₂ gas is not completely dissolved in the water phase, experimental data (Unruh et. al, 1949, Masutani et. al, 1993, Warzinski et. al 1995, Warzinski, et. al, 2000) shows the hydrate that is formed is less dense than water possibly due to occluded gas bubbles. This aspect implies CO₂ hydrates formed in the ocean from a two-phase system float, diminishing the ocean sequestration of CO₂. Since published data reports hydrate formed from a single-phase system of dissolved CO₂ and water sinks, enhancing the ocean sequestration of CO₂, this work has a likely relevance to the practical problem of global warming.

In this work, a theoretical model was derived (Holder, et. al., 1988), that describes the formation of hydrate from a single-phase solution. Based on this model, a Fortran code was modified so that for a given temperature and saturation pressure of CO₂, the hydrate dissociation pressure of the aqueous solution can be obtained. After running this program, several theoretical hydrate dissociation points were obtained for various mole fractions of CO₂ dissolved in water. Several laboratory experiments were performed at mole fractions of 0.016 and 0.018 in order to test the accuracy of the theoretical model. In this work, results from experiments where hydrates are formed from CO₂ and water are presented along with theoretical predictions of hydrate dissociation conditions.

2.0 LITERATURE REVIEW

2.1 CO₂ and the Greenhouse Effect

At present rates of emissions, it is predicted that without actions to reduce emissions of anthropogenic CO₂, the concentration of this greenhouse gas in the atmosphere would increase from the present level of 360 ppm to 1500 ppm by the end of the 21st century, which would induce global warming of 2 °C (low estimate) to 5 °C (high estimate) (Ravkin, 1992).

In pre-industrial times, there was no significant release of CO₂ into the atmosphere from fossil fuels and global carbon reservoirs were in equilibrium. However, since the industrial revolution, fossil fuels have become the major source of energy in the world and an amount of 6 GtC/year is being discharged into the atmosphere (International Energy Agency (IEA), 1999) and the carbon reservoirs are no longer in equilibrium as seen in Figure 2.

Several methods of utilizing natural carbon reservoirs to decrease the effects of CO₂ emissions on the atmosphere have been proposed. The reservoirs of carbon that may be used include the earth and the ocean. The ocean sequestration of CO₂ is one of the methods that have been proposed to decrease the rising levels of CO₂ in the atmosphere.

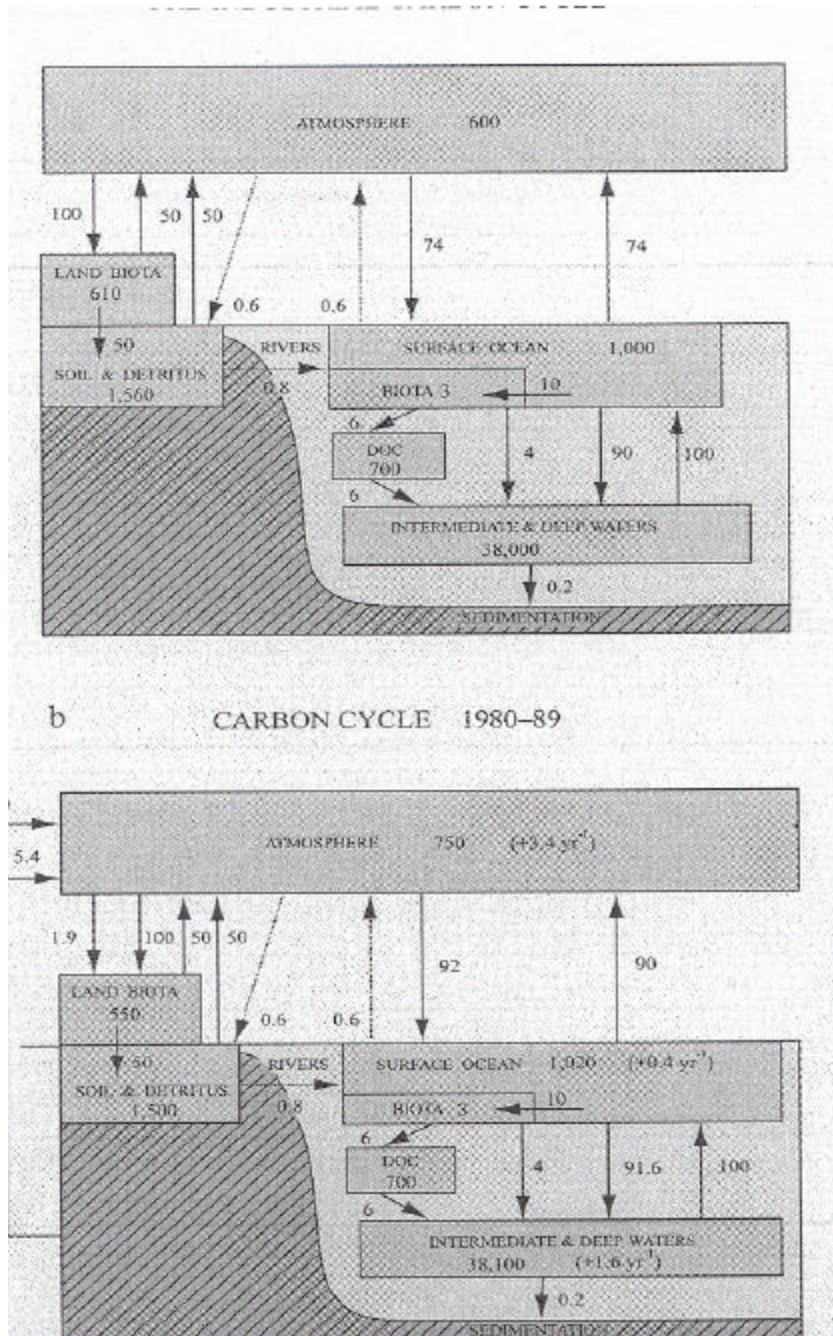


Figure 2 The Global Carbon Cycle: Reservoirs (GtC) and Fluxes (GtC/yr)

2.2 Ocean Sequestration of CO₂

Most CO₂ that man produces is dumped into the atmosphere. A larger reservoir than the atmosphere, the ocean will hold 80-85% of all our emissions on a larger time-scale (hundreds of years) (Herzog, 1998). The disposal of CO₂ into the ocean in order to attenuate the rising levels of CO₂ in the atmosphere was first proposed by Marchetti (1977). On average, the ocean is about 4000 m deep and already contains 40,000 GtC (Intergovernmental Panel on Climate Change (IPCC), 1996). The amount of carbon that would cause a doubling of the atmospheric concentration would change the deep ocean concentration by less than 2% (Carbon Sequestration Research and Development (CSRD), 1999). Due to the high pressures prevailing in the deep ocean, an extremely large quantity of CO₂ (exceeding the estimated available fossil fuel resources of 5000 to 10,000 GtC) may be dissolved in deep ocean waters (CSRD, 1999). Due to the present amount of carbon in the ocean and if CO₂ were released into the ocean, its almost undetectable effects on the increase of concentration of carbon in the ocean and the large capacity of the ocean to sequester carbon, the ocean sequestration of CO₂ is considered a safe and viable alternative to the disposal of CO₂ into the atmosphere. The environmental effects of CO₂ sequestration on marine organisms are currently being tested but are estimated to be minimal.

There are a couple of methods through which one can enhance the sequestration of carbon into the ocean. These methods include the direct injection of a stream of CO₂

into the ocean obtained from an industrial process and the enhancement of the natural uptake of CO₂ by the ocean through the fertilization of the ocean with nutrients.

Although the ocean's biomass represents about 0.05% of the terrestrial ecosystem, it converts about as much inorganic carbon to organic matter (about 50 GtC/year) as do processes on land (CSRD, 1999). Ocean organisms absorb inorganic carbon in the form of CO₂ and then convert it to organic carbon; this is a process through which CO₂ is naturally sequestered into the deep ocean. One can enhance this natural process by fertilizing the ocean with nutrients such as iron, which enhances the growth of phytoplankton. The increased amount of phytoplankton in the ocean will cause an increase in the amount of CO₂ that is drawn down into the ocean. Initial short-term studies of iron fertilization in high-nutrient, low-chlorophyll waters have demonstrated that in-situ fertilization of surface waters with iron to promote growth of phytoplankton is feasible at scales of tens of square kilometers (Coale et al. 1996, Frost 1996, Boyd 2000, Markels, 2001). One can also sequester CO₂ by injecting a stream of CO₂ into the ocean.

Several direct ocean disposal scenarios have been reported to date. One can inject CO₂ at moderate depths (500-2000 m). When CO₂ is released at these depths, its density is less than that of seawater. In this option, in order for CO₂ droplets to be captured in the ocean, the size of the CO₂ droplets released in the ocean and the disposal depth must be appropriately selected (Golomb et al., 1989). One can also release CO₂ at higher depths (>3000 m) where liquid CO₂ becomes denser than water and theoretically sinks to the bottom of the ocean floor.

The first successful field experiment where CO₂ hydrate was formed was conducted by Brewer et. al, 1999. In this experiment, liquid CO₂ and seawater rapidly reacted in order to form a massive hydrate within only a few hours. This experiment indicates that hydrate formation from CO₂ in the deep sea can occur on very short time scales, yielding a dense mass and assisting sequestration time scale from the atmosphere. Injection of CO₂ into the ocean will have some environmental impacts. The most significant impact is expected to be associated with lowered pH as a result of the reaction of CO₂ with seawater (CSRD, 1999). Depending on the depth, CO₂ may be sequestered into the ocean either through its dissolution or through its formation of CO₂ hydrates that are solid, ice-like compounds.

2.3 Nature of Hydrates

A hydrate is a non-stoichiometric, crystalline compound formed from gas and water at low temperatures and high pressures. There are a large number of gases that have the ability to form a hydrate in combination with water. These gases include methane, ethane, propane, iso-butane, carbon dioxide, nitrogen and hydrogen sulfide. It is also possible to form hydrate with mixtures of the mentioned gases in combination with water. Hydrate can also be formed from a mixture of methane and another large molecule such as isopentane. All common natural gas hydrates form one of three crystal structures including cubic structure I (sI), cubic structure II (sII), or hexagonal structure H (sH). Figure 3 was obtained from Sloan, 1998 and depicts structure I and structure II

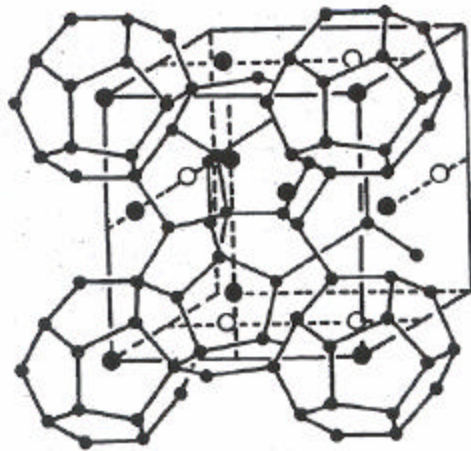
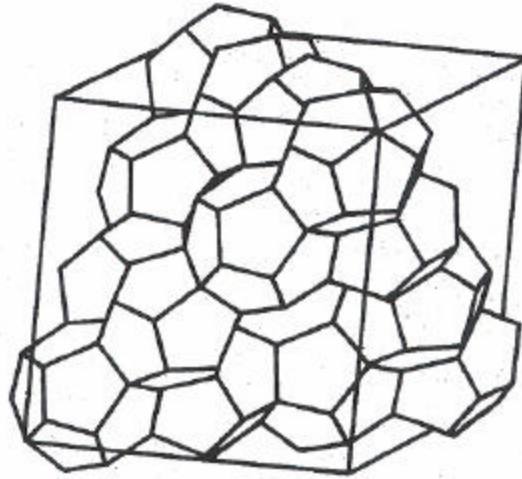


Figure 3 Structure I (below) and Structure II (above) Hydrates.

hydrates. Structure I hydrate is formed from most molecules smaller than 6 \AA , such as methane, ethane, carbon dioxide and hydrogen sulfide. Structure II hydrate is mostly formed from somewhat larger molecules ($6 \text{ \AA} < d < 7 \text{ \AA}$) such as propane or iso-butane or very small molecules such as nitrogen and argon. Still larger molecules such as isopentane or neohexane can form structure H when accompanied by smaller molecules such as methane, hydrogen sulfide or nitrogen. Hydrate is non-stoichiometric because only a fraction of the hydrate cavities need to be occupied.

A CO₂ hydrate is CO₂ trapped in a crystalline cage of water molecules. Pure CO₂ and H₂O can form structure I hydrates under conditions of high pressure and low temperature. In a crystalline cage, a framework is formed by a linkage of 46 water molecules through hydrogen bonding with two pentagonal-dodecahedral cavities (small) and six tetrakaidecahedral cavities (large). Each cavity can at most hold one CO₂ molecule. According to literature data compiled in Sloan, 1998 by Miller, S.L., Smythe, W.D. in 1970 and Takenouchi and Kennedy in 1965 CO₂ hydrates can form in the laboratory at a range of temperatures from 151.5 K to 292.7 K and from pressures as low as 5.35 kPa or 5.35×10^{-4} MPa to pressures as high as 186.20 kPa or 1.86×10^{-1} MPa. CO₂ hydrate, when formed from ice and CO₂ vapor can be formed at temperatures as low as 151.5 K and pressures as low as 5.35×10^{-4} MPa. CO₂ hydrate, when formed from liquid CO₂ and water, can form at temperatures as high as 292.7 K and pressures as high as 1.86×10^{-1} MPa. A considerable amount of experimental work has been reported in the literature on the formation of CO₂ hydrate from a two- phase system where CO₂ is in a separate phase from liquid water present.

2.4 Formation of CO₂ Hydrate From a 2-Phase System

Various equilibrium hydrate pressures and temperatures have been published for the formation of CO₂ hydrate from a 2-phase system of CO₂ and water and has been compiled in the book by Sloan, 1998. This literature data includes von Stackelberg and Muller (1951), Unruh and Katz (1949), Takenouchi and Kennedy (1964), Robinson and Mehta (1971), Berez and Balla-Achs (1983) and Ng and Robinson (1985). Several experimental accounts (Unruh et. al, 1949, Masutani et. al, 1993, Warzinski et. al 1995, Warzinski et. al 2000) indicate that when CO₂ hydrate is formed from a two-phase system, the hydrates formed are less dense than water and float, diminishing the effects of ocean sequestration of CO₂. Pure CO₂ hydrate is denser than water and should sink if it forms upon injection of CO₂. Trapped, unconverted CO₂ may have caused the bulk density of initially formed hydrates to be less than that of water. These accounts led to the conception of experiments where hydrate is formed from a single-phase system of dissolved gas and water.

2.5 Formation of Hydrate from a Single-Phase System

Data in the literature on the formation of hydrate from gases dissolved in water previous to forming hydrate is limited. Formation of hydrate from a single-phase aqueous system using the hydrate former dissolved in the aqueous phase was previously demonstrated at the National Energy Technology Center (NETL) (Warzinski et. al, 2000, Warzinski et. al 1995). Work done by Buffett and Zatsepina in 2000 reports on a

set of experiments in which the hydrate is formed from dissolved gas in natural porous media. Their experiments demonstrate that hydrate crystals can nucleate in the absence of free gas in the presence of dissolved gas. In addition, previous work demonstrating the equilibrium between a gaseous phase and hydrates indicates that hydrates could form from a single gaseous phase containing sufficient gaseous water (Song et. al, 1982; Sloan et. al., 1976). The thermodynamic model and experiments described in this work, demonstrates that it is indeed possible for hydrates to form from dissolved gas and water.

2.6 Thermodynamic Basis of Hydrate Equilibrium

This model is based on classical statistical thermodynamics and is used to predict the thermodynamic conditions under which hydrates dissociate from dissolved gas. van der Waals and Platteeuw presented the earliest model that used classical statistical thermodynamics to predict thermodynamic conditions of hydrate dissociation in 1959. Using this model, Saito et. al. in 1964 developed a method that was later generalized by Parrish and Prausnitz in 1972 in order to predict hydrate equilibria conditions. This method was subsequently simplified by Holder, Corbin and Papadoupoulos in 1980 and has been found to give good predictions of hydrate equilibria. The flaws in this method are only some of the assumptions involved in the original model presented by van der Waals and Platteeuw. Several modifications were made to this model by illuminating some of the weaknesses (John and Holder, 1981, 1982, 1985, John et. al. 1985). The completely modified model used to calculate hydrate dissociation conditions from a two-phase system was presented in its full form in a review paper by Holder et. al in 1988.

This model, used to predict hydrate dissociation conditions from a two-phase system was modified in order to enable the prediction of hydrate dissociation conditions from hydrate formed from dissolved gas and water. This model was recently accepted as a paper in the journal of Chemical engineering science (Holder, Mokka and Warzinski, accepted) and was presented in American Chemical Society (ACS) National Meeting in California (CA) in April of 2001 (Holder, Mokka and Warzinski, 2001). This model is presented as part of this work.

In order enable the calculation of temperature and pressure at which hydrate dissociates, the conditions under which the hydrate phase is in equilibrium with the water-rich phase (the water rich phase consists mostly of water, it is known as water-rich because there is an insignificant amount of hydrate former dissolved in the water). At these conditions, the fugacities and chemical potentials of the species in the various phases must be equal although either equality of fugacity or chemical potential for each species is sufficient to fix the state. We specify the equality for the hydrate forming species, i , using fugacities:

$$f_{i,L} = f_{i,H} = f_i \quad (2-1)$$

and for water using chemical potentials:

$$\mu_H = \mu_L \quad (2-2)$$

If these two conditions are met, hydrate formation can occur from a single water-rich liquid phase (no gas or liquid rich in hydrate former). Equation 2-2 is modified by convention (Holder et. al, 1988)

$$\mu^\beta - \mu_H = \mu^\beta - \mu_L \quad (2-3)$$

or

$$\Delta\mu_H = \Delta\mu_L \quad (2-4)$$

Here, μ^β is the hypothetical chemical potential of the empty hydrate lattice. For the hydrate forming species, the fugacity calculated is dependent on the phase it is in before it forms a hydrate. The calculation of the fugacity of a dissolved gas is slightly more complicated and is calculated using the traditional thermodynamic methods discussed below.

The independent (given) variables are temperature and water-rich liquid composition; i.e., the water phase contains a given mole fraction, X_i , of dissolved hydrate former. It is assumed that the solubility of the hydrate-forming species in water is known as a function of pressure from experimental data or from a model.

The pressure required to obtain a given solubility, X_i , is designated P^{sat} . At pressures lower than P^{sat} the hydrate former will come out of solution as a gas bubble or

possibly as a liquid drop. Due to this behavior, P^{sat} is commonly known as bubble-point pressure.

At P^{sat} , the fugacity of the hydrate former can easily be calculated from a convenient equation of state that is applicable to a phase rich in the hydrate-forming species. For present purposes, this phase is assumed to be a gas and the Peng-Robinson equation of state is used (Peng & Robinson, 1976). Modifications needed to apply this to a liquid hydrate former are straightforward and would be necessary if the specified mole fraction can only be obtained at pressures above which the hydrate forming species is a liquid. At higher pressures the fugacity is corrected by a Poynting-type correction (Prausnitz, Lichtenthaler & Gomes de Azevedo, 1986).

$$f_i = f_i^{sat} \exp \left[\int_{P^{sat}}^P \frac{\bar{V}_i dP}{RT} \right] \quad (2-5)$$

where \bar{V}_i is the partial molar volume of a species i in the water phase. A common assumption is that \bar{V}_i is nearly constant, thus simplifying Equation 2-5:

$$f_i = f_i^{sat} \exp \left[\frac{\bar{V}_i (P - P^{sat})}{RT} \right] \quad (2-6)$$

To satisfy Equation 2-1, the fugacity of hydrate forming species i in the hydrate phase is set equal to \hat{f}_i .

For the water species in the hydrate phase, the value of $\Delta\mu_H$ (the chemical potential of water in the hydrate phase) is calculated from the following equation (Holder, et al., 1988):

$$\Delta m_H = -RT \sum_{j, \text{cavities}} n_j \ln \left(1 - \sum_i q_{ji} \right) \quad (2-7)$$

where v_j is the ratio of j-type cavities present to the number of water molecules present in the hydrate phase and

$$q_{ji} = \frac{C_{ji} f_i}{1 + \sum_i C_{ji} f_i} \quad (2-8)$$

where C_{ji} is the Langmuir constant for species i in cavity j and θ_{ji} is the fraction of j-type cavities, which are occupied by i-type gas molecules. The summation over species i is necessary if multiple hydrate-forming species (i.e. CH_4 and CO_2) are present.

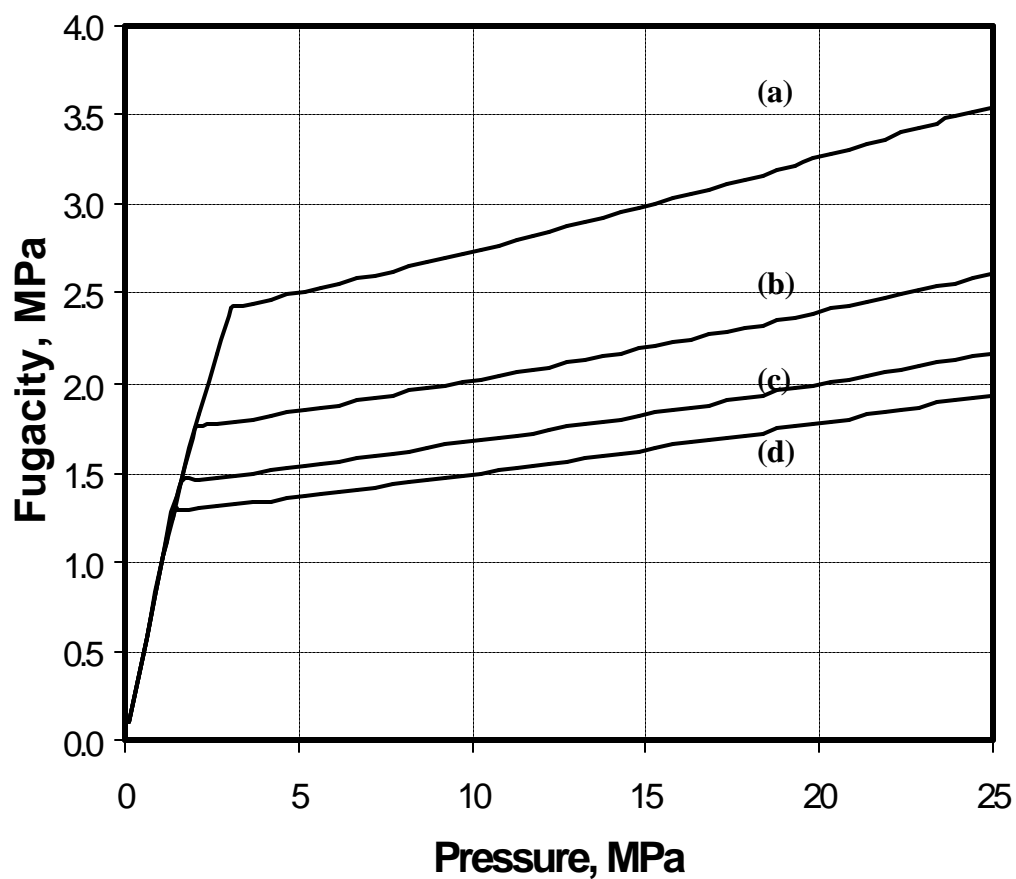
The value of $\Delta\mu_L$ (the chemical potential difference of water in the water-rich phase) is obtained from the following equation (Holder, Corbin & Papadopoulos, 1980):

$$\frac{\Delta m_L}{RT} = \frac{\Delta m^0}{RT_o} - \int_{T_o}^{T_F} \frac{\Delta h}{RT^2} dT + \int_0^P \frac{\Delta v}{RT} dP - \ln X_w \quad (2-9)$$

where $\Delta\mu^0$ is a reference chemical potential treated as a constant whose value can change according to the gas species present. Here, Δh and Δv , are the enthalpy and the volumetric difference between empty hydrate and pure liquid water, respectively. The last term accounts for the effect of dissolved gas using the mole fraction of water in the liquid phase X_w . In our analysis, the activity coefficient of water is unity. While each gas species must reduce the chemical potential of the water in the liquid phase (μ_L) by an equal amount in order to form hydrate, each gas species has a different Langmuir constant, C_{ij} , and consequently the equilibrium pressure required to form hydrates is different for each gas species.

If $\Delta\mu_H$ from Equation 2-7 equals $\Delta\mu_L$ from Equation 2-9, Equation 2-2 is satisfied and hydrates can form a single-phase water-rich liquid system.

Physically, this discussion is unnecessary if hydrates will form from a gas phase at pressures less than P^{sat} at a specific temperature. If this were possible, hydrates would form at some pressure $P < P^{\text{sat}}$ where a gas would still be present and VLH equilibria would pertain. In the experimental section, we report the results of experiments where hydrates are formed from subsaturated systems, where X_i (the mole fraction of hydrate former in the water-rich liquid phase) is less than X_i at the three-phase equilibrium pressure $P^{\text{sat}}_{\text{VLH}}$. To form hydrates at equilibrium conditions from a single water-rich liquid phase (L₁H equilibria), P must be greater than $P^{\text{sat}}_{\text{VLH}}$ and the fugacity of the hydrate former must be greater than $f^{\text{sat}}_{i,\text{VLH}}$. Thermodynamically, pressure increases have a small effect on the fugacity of liquid phase species as illustrated in Figure 4.



(a) $P^{\text{sat}} = 3.0 \text{ MPa}$ $X_i = 0.025$

(b) $P^{\text{sat}} = 2.0 \text{ MPa}$ $X_i = 0.020$

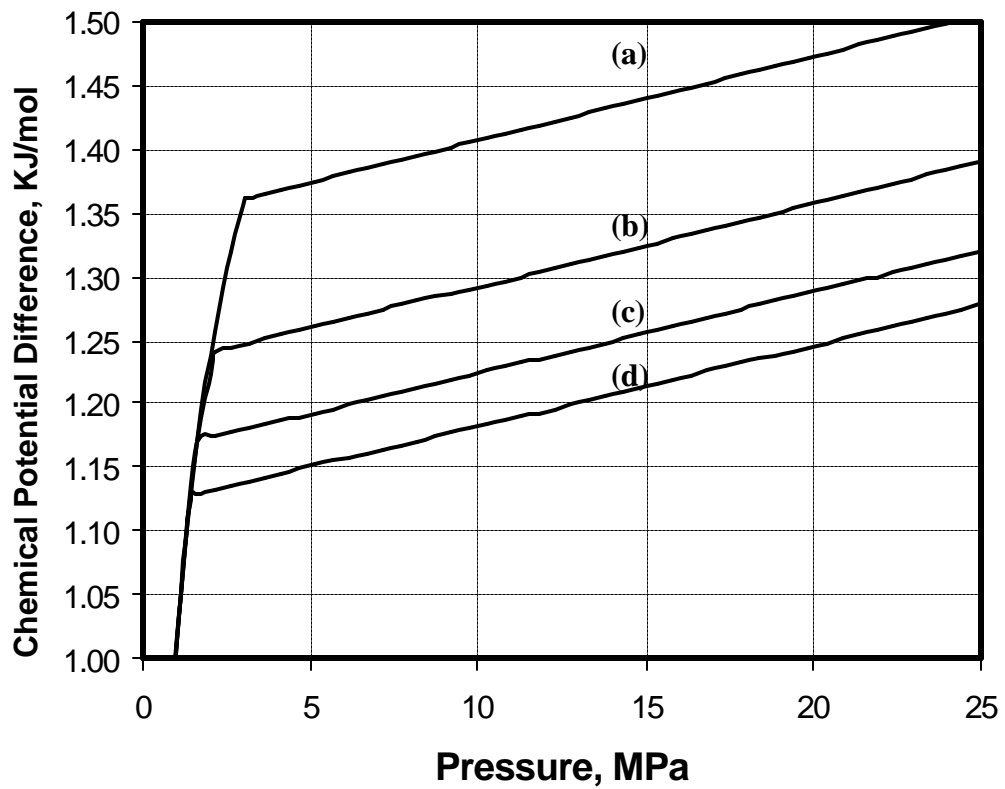
(c) $P^{\text{sat}} = 1.6 \text{ MPa}$ $X_i = 0.017$

(d) $P^{\text{sat}} = 1.4 \text{ MPa}$ $X_i = 0.015$

Figure 4 The Fugacity of CO_2 as a Function of Pressure for Different Compositions at $T = 275 \text{ K}$.

Figure 4 shows the fugacity of CO₂ as a function of pressure for a fixed temperature (275 K). For the purposes of this illustration only, an estimated value for \bar{V}_i for CO₂ of 40 cc/mole is used (Teng et. al, 1997). In this Figure, X_i represents the overall mole fraction of CO₂ in the CO₂/water system. At pressures above P^{sat} there is only one phase present and X_i represents the mole fraction in the water-rich liquid. Note that the increase of fugacity with pressure is much greater when a gas phase exists ($P \leq P^{\text{sat}}$) and the increase in fugacity with pressure is relatively modest when $P \geq P^{\text{sat}}$. As shown in Figure 4, the fugacity of CO₂ is the same regardless of ultimate liquid phase composition until the CO₂ completely dissolves at P^{sat} , which is different for different levels of CO₂ saturation. This is because the gas phase contains pure CO₂ up to the corresponding $P_{x_i}^{\text{sat}}$. The compositions used to construct Figure 4 were chosen to represent values of X_i that were greater and less than those at the VLH point ($X_i = 0.0167$). Using the fugacities from Figure 4 above as the basis we can calculate the chemical potentials from Equation 2-7 as shown in Figure 5. Figure 5 describes the chemical potential difference of water in the hydrate phase from equation 2-7. Note that this chemical potential difference increases when the chemical potential of water decreases. The hydrate phase may or may not be meta-stable.

If we then overlay Equation 9 onto Figure 5, Figure 6 is obtained. In this Figure, the mole fraction of water, X_w , used for Equation 9 is held constant at 0.985 (= 1 – 0.015). Point A very closely approximates the pressure (1.59 MPa) at which hydrates would form if excess CO₂ were present. This represents VLH equilibria. Point B represents the pressure (21.8 MPa) at which hydrates would form from a water-rich liquid



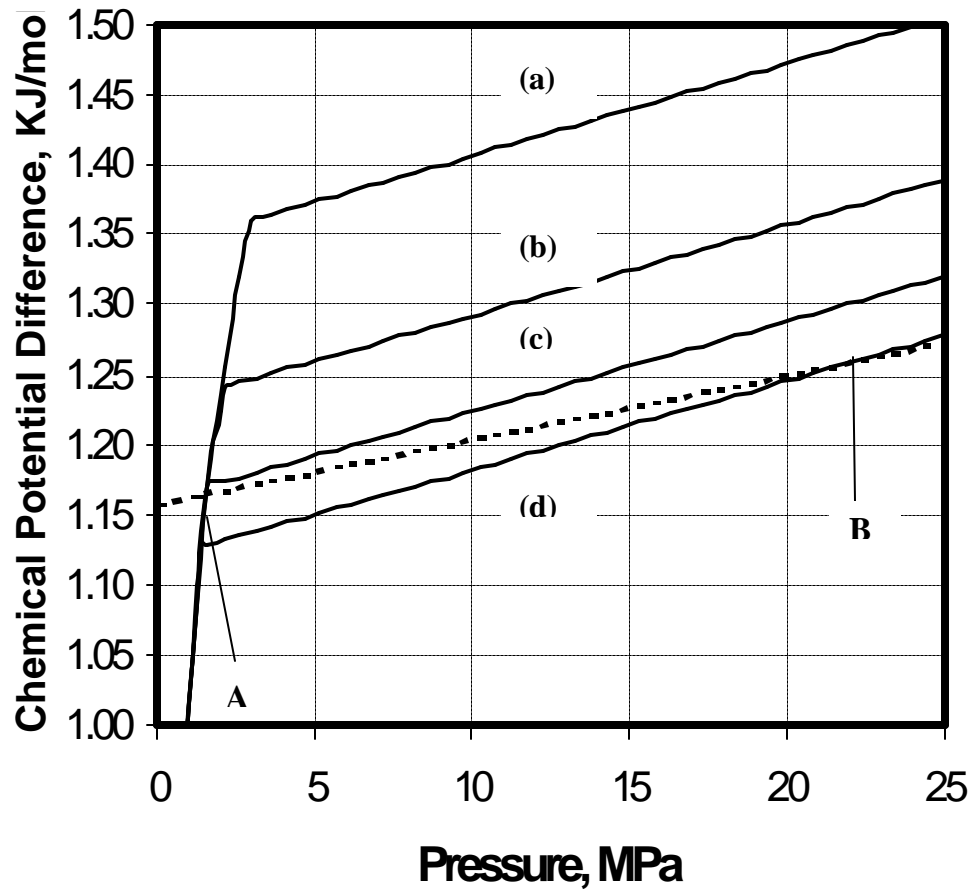
(a) $P^{\text{sat}} = 3.0 \text{ MPa}$ $X_i = 0.025$

(b) $P^{\text{sat}} = 2.0 \text{ MPa}$ $X_i = 0.020$

(c) $P^{\text{sat}} = 1.6 \text{ MPa}$ $X_i = 0.017$

(d) $P^{\text{sat}} = 1.4 \text{ MPa}$ $X_i = 0.015$

Figure 5 Chemical Potential Difference of Water in the Hydrate Phase at Different Compositions at 275 K.



(a) $P^{\text{sat}} = 3.0 \text{ MPa}$ $X_i = 0.025$

(b) $P^{\text{sat}} = 2.0 \text{ MPa}$ $X_i = 0.020$

(c) $P^{\text{sat}} = 1.6 \text{ MPa}$ $X_i = 0.017$

(d) $P^{\text{sat}} = 1.4 \text{ MPa}$ $X_i = 0.015$

Figure 6 Chemical Potential Difference of water in the Hydrate and Aqueous Phases at

$T = 275 \text{ K}$.

containing 0.015 mole fraction CO₂. At the VLH point, the water-rich liquid would contain slightly more CO₂ ($X_i \cong 0.0167$). At all compositions less than that at the VLH point ($X_i < 0.0167$), hydrates could form from a water-rich liquid if the pressure was sufficiently high. This is shown in Figure 7 that depicts the pressure required to form hydrates for various amounts of dissolved CO₂ at 275 K. As the mole fraction of CO₂ decreases, the pressure required to form hydrates will increase. For mole fractions greater than 0.0167, the amount of dissolved gas is greater than that which would exist at the VLH point and hydrates will form at all pressures where this level of solubility can be obtained. However, this level of solubility cannot be obtained at pressures below the VLH pressure.

From Figure 6, it is clear that the formation of hydrates from a subsaturated water-rich liquid requires the slope of the chemical potential of liquid water vs. pressure from Equation 2-9 be less than the slope of the chemical potential of hydrate water vs. pressure from Equation 2-7.

Mathematically this requirement can be expressed as:

$$\frac{\partial \left(\frac{\Delta m_H}{RT} \right)}{\partial P} > \frac{\partial \left(\frac{\Delta m_L}{RT} \right)}{\partial P} \quad (2-10)$$

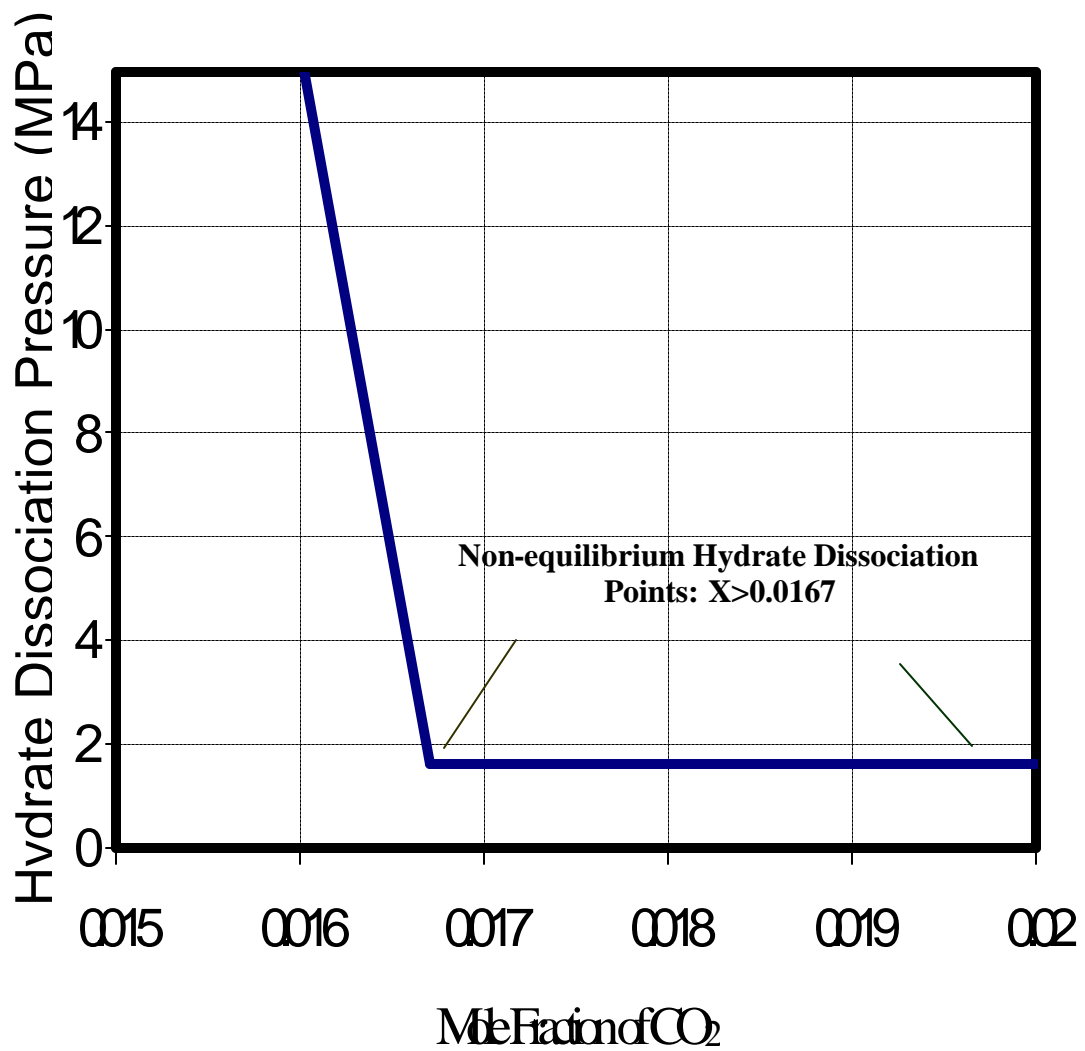


Figure 7 Hydrate Dissociation Pressures as a function of Mole Fraction at T=275 K.

These derivatives can be calculated as follows:

$$\frac{\partial\left(\frac{\Delta m_H}{RT}\right)}{\partial P} = \sum_{j, \text{cavities}} \left[\frac{\mathbf{n}_j \sum_i \left[C_{ji} f_i \left(\frac{V_i}{RT} \right) \right]}{1 + \sum_i C_{ji} f_i} \right] \quad (2-11)$$

For a single hydrate forming gas:

$$\frac{\partial\left(\frac{\Delta m_H}{RT}\right)}{\partial P} = \frac{\mathbf{n}_1 \left[C_{11} f_1 \frac{\bar{V}_1}{RT} \right]}{1 + C_{11} f_1} + \frac{\mathbf{n}_2 \left[C_{21} f_1 \frac{\bar{V}_1}{RT} \right]}{1 + C_{21} f_1} \quad (2-12)$$

For $C_{ji} \gg 1$ and with both cavities filled, the equation simplifies

(in most instances $\theta_{ji} > 0.9$ and $C_{ji} > 9$)

$$\frac{\partial\left(\frac{\Delta m_H}{RT}\right)}{\partial P} = (\mathbf{n}_1 + \mathbf{n}_2) \frac{\bar{V}_i}{RT} \quad \text{if } C_{ji} \gg 1 \quad (2-13a)$$

If only the large cavity is occupied

$$\frac{\partial\left(\frac{\Delta m_H}{RT}\right)}{\partial P} = \mathbf{n}_2 \frac{\bar{V}_i}{RT} \quad (2-13b)$$

For structure I, $v_1 = 1/23$, $v_2 = 3/23$, for structure II, $v_1 = 2/17$, $v_2 = 1/17$ (Holder, et al., 1988). The partial molar volumes of gases dissolved in water are 30 – 80 cc/mole (Toplak, 1989). At 273 K the derivative's value will fall in a relatively narrow range.

$$\frac{\partial\left(\frac{\Delta m_H}{RT}\right)}{\partial P} \approx 0.001 - 0.005 \text{ MPa}^{-1} \quad (2-14)$$

(Note: If only one cavity is filled, as for propane hydrate, the derivatives will be smaller, on the order of $0.001 - 0.002 \text{ MPa}^{-1}$)

For the liquid-phase, estimates of the value of the derivatives can also be made:

$$\frac{\partial\left(\frac{\Delta m_L}{RT}\right)}{\partial P} = \frac{\Delta n}{RT} - \frac{1}{X_w} \frac{\partial X_w}{\partial P} \quad (2-15a)$$

But $X_i + X_w = 1$. Therefore,

$$\frac{\partial X_w}{\partial P} = -\frac{\partial X_i}{\partial P} \quad (2-15b)$$

since $X_w \approx 1.0$

$$\frac{\partial\left(\frac{\Delta m_L}{RT}\right)}{\partial P} = \frac{\Delta n}{RT} + \frac{1}{X_w} \frac{\partial X_i}{\partial P} \approx \frac{\Delta n}{RT} + \frac{\partial(X_i)}{\partial P} \quad (2-15c)$$

where (Holder, et al., 1988)

$$\frac{\Delta n}{RT} \approx 0.002 MPa^{-1} \quad (2-16)$$

Since we are considering fixed composition liquid systems:

$$\frac{\partial X_i}{\partial P} \approx 0 \quad (2-17)$$

Thus,

$$\frac{\partial \left(\frac{\Delta m_H}{RT} \right)}{\partial P} > \frac{\partial \left(\frac{\Delta m_L}{RT} \right)}{\partial P} \quad (2-18)$$

will usually be true as required by Equation 2-10 and hydrates can form from some sub-saturated aqueous systems. Table 1 gives examples based on the type of estimation described above for several hydrate-forming species. As can be seen, this simple method of estimation suggests that hydrates can often form from an aqueous liquid which has less dissolved gas than at the VLH point at the same temperature. However, absolute certainty requires a rigorous calculation as is illustrated in Figure 6.

The above analysis required an accurate description of mole fraction as a function of temperature and saturation pressure. In order to calculate an accurate mole fraction,

Table 1 Theoretical Prediction of Hydrate Formation From Single-Phase Aqueous Systems Containing Various Dissolved Gases at 275 K.

Gas	Hydrate Structure	\bar{V}_i (cc/mole)	T_i (K) for \bar{V}_i	$\frac{\partial\left(\frac{\Delta m_H}{RT}\right)}{\partial P}$ (1/MPa)	$\frac{\partial\left(\frac{\Delta m_L}{RT}\right)}{\partial P}$ (1/MPa)	Hydrates form from liquid water
CH ₄	I	35	301	0.00266	0.00204	Yes
C ₂ H ₆	I	53	301	0.00302	0.00204	Yes
C ₃ H ₈	II	71	298	0.00183	0.00221	No
CO ₂	I	40	275	0.00304	0.00204	Yes
N ₂	II	36	291	0.00278	0.00221	Yes

Partial molar volumes and gas solubilities were obtained from the following literature sources: Wiebe, R., & Gaddy, V.L. (1940); Katz, Cornell, Kobayashi, Poettmann, Vary, Elenbaas & Weinaug, (1959); Munjal, P., & Stewart, P.B. (1970); Prausnitz, Lichtenthaler & Gomes de Azevedo, (1986); Enick, R.M., & Klara, S.M. (1990).

the charts listed in Figure 8 were utilized. Figure 8 is an accumulation of solubility data from Enick & Klara, 1990, Munjal & Stewart, 1970, Wiebe & Gaddy, 1940.

In Figure 8, a mole fraction was obtained based on a specific temperature and saturation pressure. Note the mole fractions listed in the figures above are slightly different from the mole fractions listed in a previously published paper from our group (Holder, Mokka & Warzinski, submitted) due to slight uncertainties associated with the calculation of the mole fraction based on the saturation pressure. The saturation pressure along with the temperature was inserted into a Fortran program in order to calculate a hydrate dissociation pressure. Figure 9 describes the hydrate dissociation pressure for several different mole fractions as obtained from the Fortran program listed in Appendix A.

The above thermodynamic model demonstrates that hydrates can indeed form from dissolved gas, in contrast to the common misconception that hydrate can form only in the presence of free gas. Miller, in 1974 showed the presence of free gas is not necessary for hydrate formation or stability. In order to prove that it is possible for methane hydrate to form from dissolved gas, a similar thermodynamic model was proposed by Handa in 1990. His model was similar to the model discussed in this work however, there were several significant differences. Handa's work utilized a model in which the chemical potential of water in the liquid phase was directly from the original thermodynamic model proposed by van der Waals and Platteauw in 1959. Also, the end result of the model proved that hydrates could indeed theoretically form from dissolved gas, however, it did not empirically define the conditions under which hydrates can form

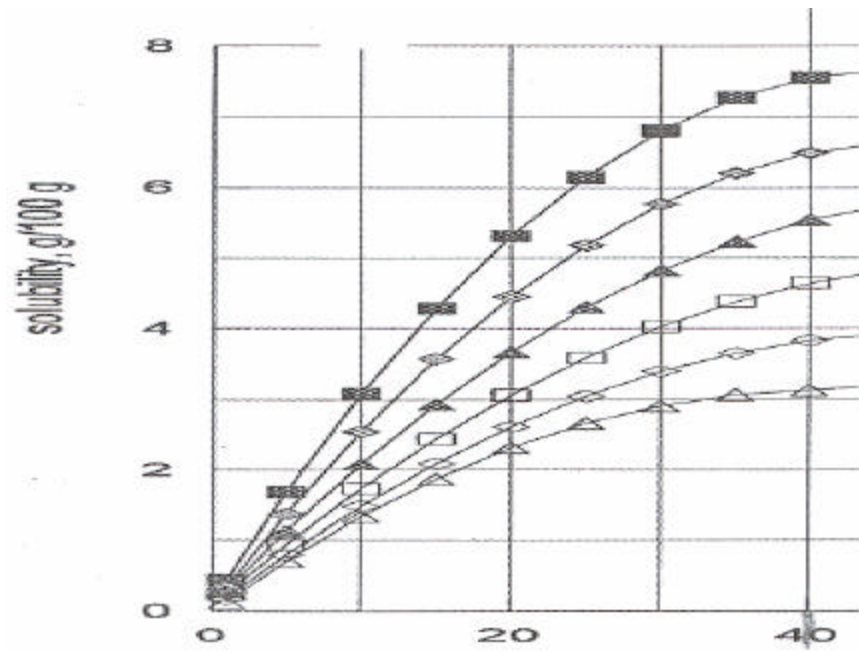


Figure 8 Solubility Charts

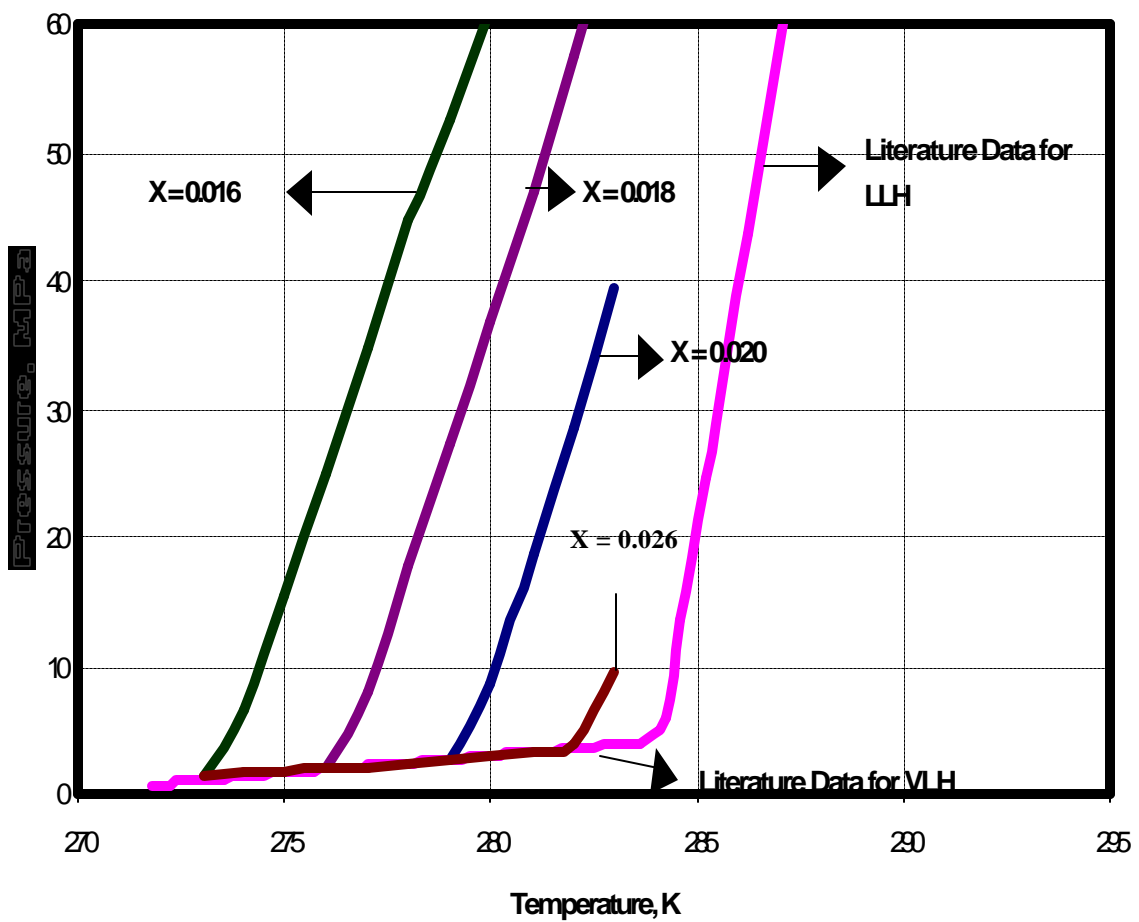


Figure 9 Hydrate Dissociation Pressures as a function of Temperature at Several Different Compositions.

from a dissolved gas. Another phase equilibria model was proposed by Buffett and Zatsepina in 1997 in order to form hydrate from a single-phase aqueous solution. In their work, they utilized a simulated minimum of the Gibbs free energy function rather than utilizing the equality of chemical potentials of either phase. However, this model did not empirically define the conditions under which hydrate could form from a single-phase system either.

This concludes the theoretical section of this work. Now the equipment utilized to perform experiments in order to confirm hydrate can form from a single-phase system in a laboratory will be described, followed by the experimental results and description.

3.0 DESCRIPTION OF EQUIPMENT

Several figures describe the equipment utilized to form hydrate from a single-phase system. Figures 10 and 11 depict the overall laboratory setup. Figure 12 is a schematic of the equipment used in the cell. The following are some of the pieces of equipment utilized to perform experiments to form hydrates.

CO₂ cylinder – Used to pump CO₂ into the system.

Helium cylinder – Utilized in the lab in order to pressure test the system.

Nitrogen – Used in the cell to prevent H₂O from condensing on the transducer – if H₂O condensed on the transducer, it would produce erroneous pressure readings.

Syringe Pumps - ISCO D series syringe pumps. The pumps can be pressurized to pressurize the cell from pressures of 0.170 MPa to 69.05 MPa.

Syringe Pump A – Used to pressurize CO₂ to high pressures before injecting it into the cell. It is attached to a refrigerated bath in order to control the temperature of the CO₂

Syringe Pump B – Used to pressurize the cell by controlling the piston located at the back of the cell.

Chamber – Tenney Environmental test chamber, model T10S containing a programmable Watlow temperature controller.

High pressure cell – Figure 13 is a schematic of the cell used in the experiments. The cell body has an outer diameter of 7 cm and an inner diameter of 1.59 cm. It is fit with a Sapphire Window enabling one to observe the contents of the cell with the boreoscope attached to it. The sapphire window is rated at 427.5 MPa. The boreoscope is attached to a light source that is attached to a video camera, television and VCR to record the picture



Figure 10 Overall Laboratory Setup, Chamber Closed.

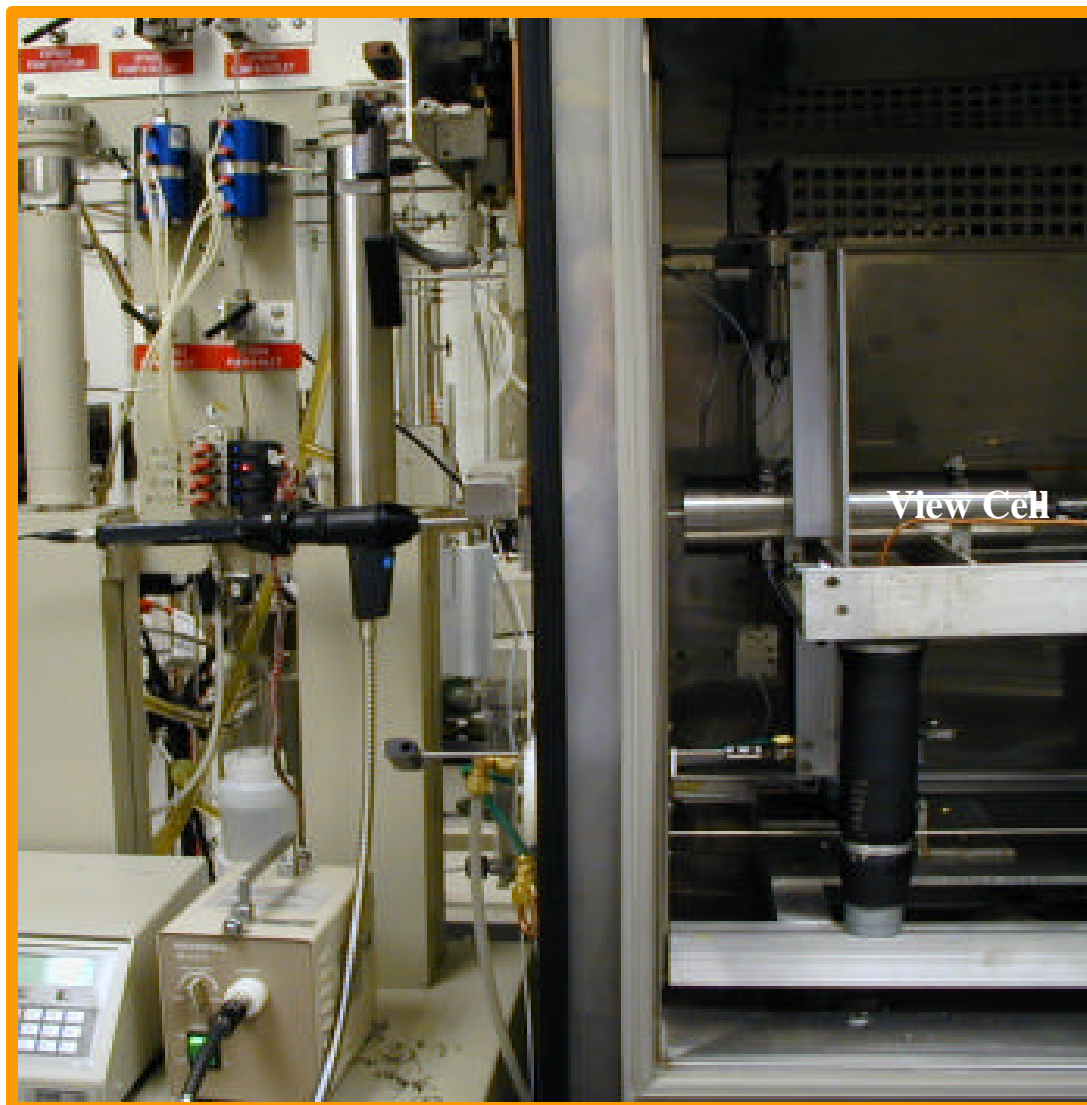


Figure 11 Laboratory Overall Setup, Chamber open

83-307Layout

RPW 11/16/99

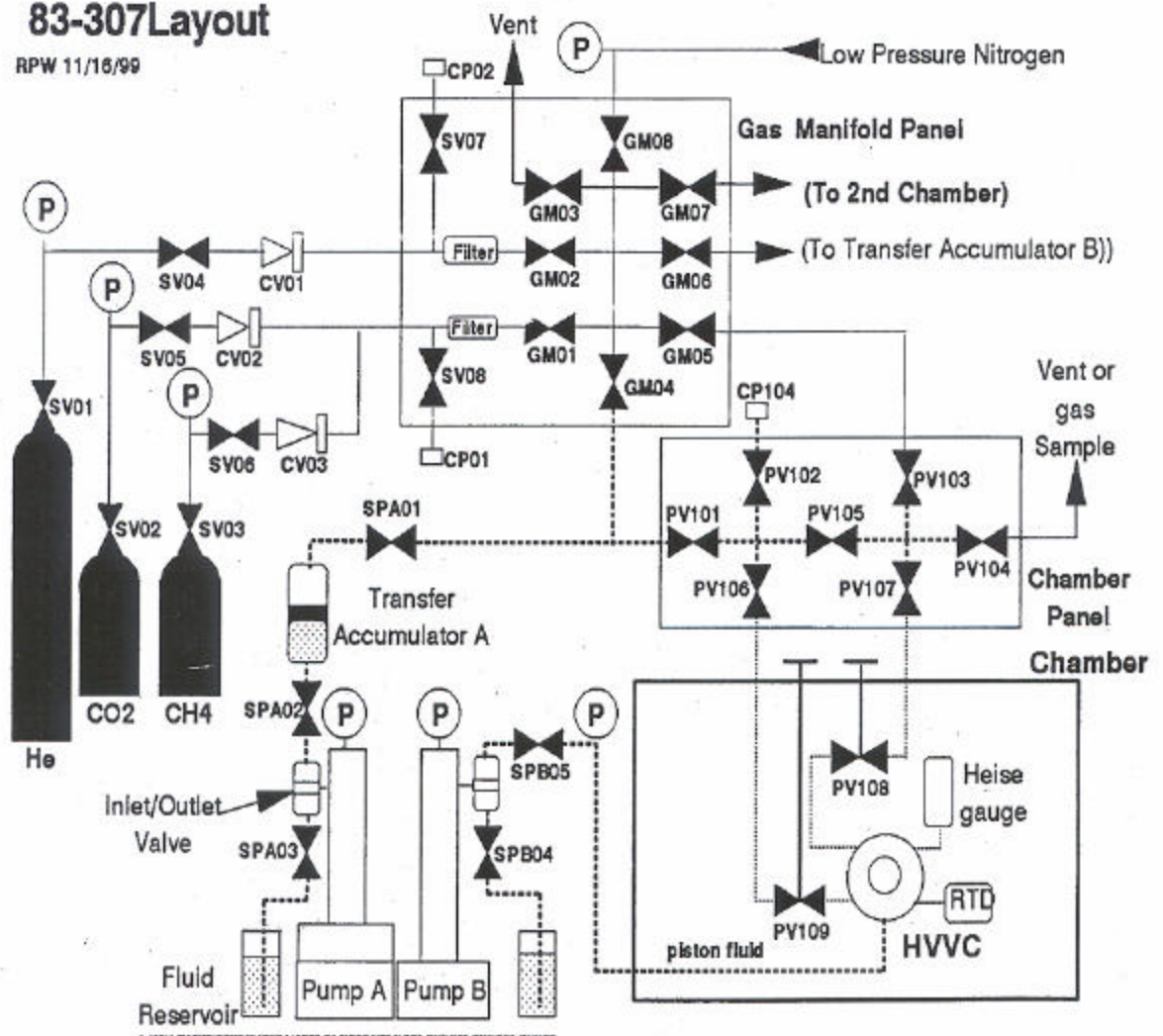


Figure 12 Schematic of Equipment

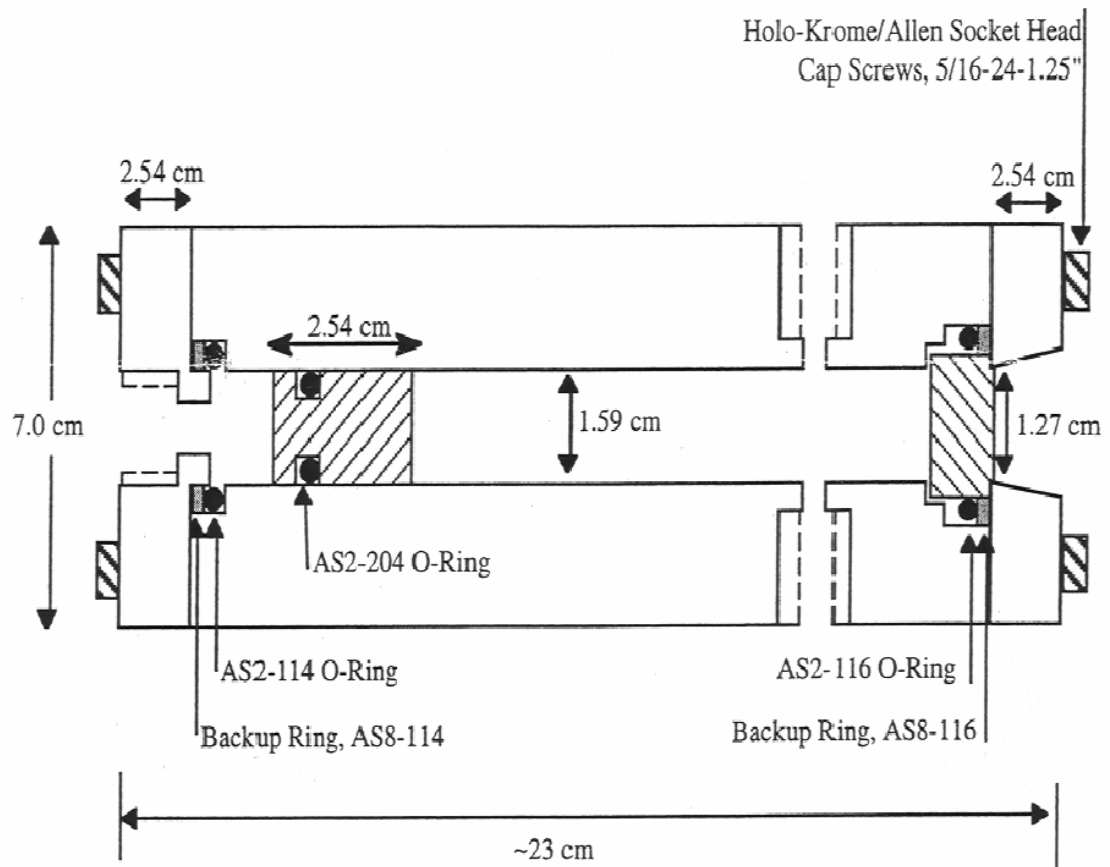


Figure 13 View Cell

in the cell. The cell is constructed of 316 stainless steel. The cell itself has a rating of 154.5 MPa.

Pressure Transducer – The Pressure Transducer used is an ATS2000 Heise Digital Pressure Transducer and has an accuracy of $\pm 0.02\%$

Resistance Temperature Detector – The accuracy of the temperature read is dependent on the LabView program used to collect the data from the experiment. The accuracy of the temperature read is $\pm 0.4078\%$

4.0 EXPERIMENTAL PROCEDURES

4.1 Assembly of Cell

In order to assemble the cell, an o-ring is first placed at the back of the cell. Then, a back-up ring is placed on top of the o-ring. The back end cap is then screwed onto the back of the cell using a torque wrench. The cell is then flipped over and a stir-bar is placed in the cell, through the front of the cell. An o-ring is placed around the sapphire window. The window is then pushed through, into the cell. A back-up ring is then placed around the window and using a spatula is squeezed onto the o-ring. The front-end cap is then placed on top of the cell and is bolted into the cell. The cell is then placed in the environmental chamber and is tightened to its respective lines. The cell is now ready for pressure testing.

4.2 Pressure Testing of Cell

In order to test the ability of the cell to hold pressure, the cell was first placed under bottle pressure of Helium of approximately 13.8 MPa. If no leaks were detected, Helium originally under bottle pressure was pressurized up to approximately 62 MPa utilizing an accumulator. This pressurized Helium was then injected into the cell in order to pressure test the cell at the higher pressure.

4.3 Injection of CO₂ and Water into the Cell.

If no leaks were detected in the cell at the higher pressure, degassed, deionized water was injected into the cell at a pressure of 0.21 MPa utilizing a syringe pump. As soon as the cell reached a pressure of 0.21 MPa the water injection into the cell was stopped. At this pressure, the cell was full of water. The amount of water injected into the cell was determined by measuring the volume of the pump filled with water before and after the cell was filled with water and accounting for the leak rate of the pump during the time it took to fill the cell with water. After water was injected into the cell, the pressure of syringe pump A was increased to 65.5 MPa at a temperature of 292 K. At this temperature and pressure, the density of CO₂ is 1.08715 g/ml according to Angus et. al., 1976. Based on the density of CO₂ and the volume of water injected into the cell, the volume of CO₂ required to obtain a certain mole fraction of CO₂ in the cell was calculated. In order to obtain this volume, the valve attached to the cell was opened in order for the CO₂ to enter the cell. However, the cell's pressure usually reached 65.5 MPa before the required volume was injected to obtain the required mole fraction. Therefore, after the cell's pressure reached 65.5 MPa, the valve leading to the syringe pump was shut off and the CO₂ was allowed to dissolve for several hours in the cell at a temperature of 287 K. After several hours, the CO₂ had dissolved into the water and the pressure of cell would drop from 65.5 MPa to a lower pressure. Once the pressure of the cell had dropped, the rest of the volume required to obtain a certain mole fraction was injected into the cell at 65.5 MPa. The CO₂ was then allowed to dissolve overnight at a temperature of 287 K.

4.4 Formation of Hydrate

If the pressure of the CO₂ in the cell had stopped dropping overnight and remained constant for a few hours at a constant temperature of 287 K, it was determined that the CO₂ had completely dissolved into the water. Once the CO₂ had completely dissolved into the water, the temperature of the cell was rapidly dropped to 271 K. The cell was allowed to stay at 271 K until a pressure-temperature trace revealed that hydrates had formed. After hydrates had formed, the temperature was increased to 287 K at the rate of 0.3 K/hr. The rate of 0.3 K/hr has been used in previous literature where CO₂ hydrate was formed (Ohgaki et. al, 1993). Several experiments were performed in order to form hydrates. Some experiments were performed to form hydrate from a two-phase system in order to ensure data obtained from our experiments confirmed to literature data. After it was verified the experimental results obtained through the formation of hydrate from a two-phase system confirmed to literature data, several experiments were conducted to form hydrate from a single-phase system.

5.0 TWO-PHASE EXPERIMENTAL RESULTS AND DISCUSSION

5.1 Experiment T10-007

This was the first experiment where hydrates were formed from a two-phase system. Even though, this experiment was not chronologically performed first, it will be described first because results from this experiment served to elucidate single-phase experiments conducted before it. In this experiment, the piston was located at the back of the cell and hydrate was formed from a two-phase system of CO₂ and water. The temperature of the chamber was programmed to cycle decrease from 287 K to 275 K and then back up to 287 K at the rate of 0.3 K/hr. The results from this experiment are seen in Figure 14.

The literature data from Figure 14 was obtained from the following sources (Vlahakis et. al, 1972, Deaton and Frost, 1946, Unruh and Katz 1949, Robinson and Mehta, 1971 and Larson, 1955). In Figure 14, hydrate formation is indicated by the rapid pressure drop from A to B. Dissociation is indicated by the rapid pressure rise from C to D. As one can see, the temperatures and pressures at which hydrate is dissociating does not fall on the line of the pressures and the temperatures of the published literature data. Once the cell was pulled apart to remove the glass stir-bar from inside the cell of the experiment, one could see that the stir-bar had leaked metal particles into the cell during the experiment. In order to rectify this problem, a new teflon stir-bar was used in the next set of experiments.

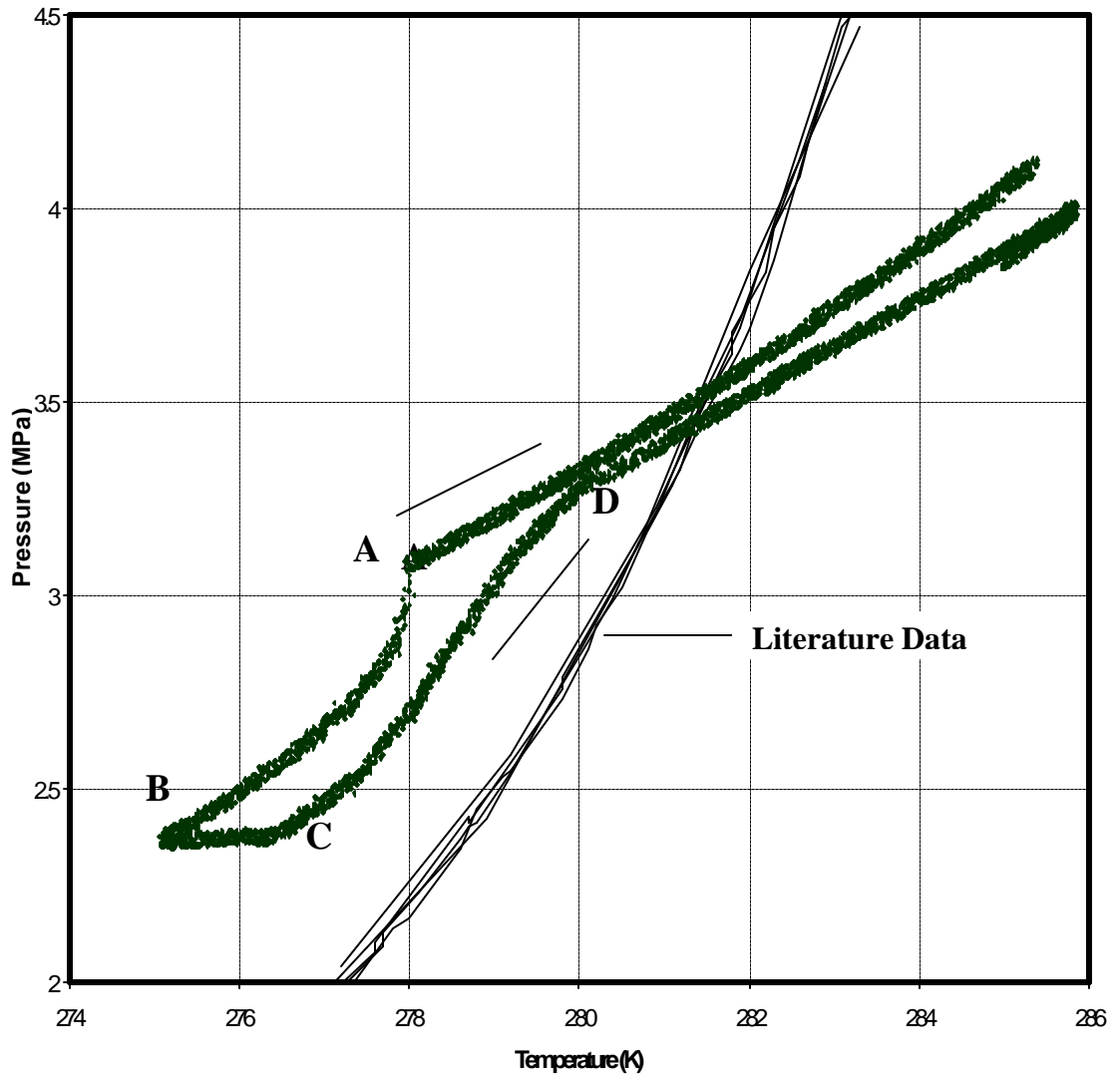


Figure 14 Experiment T10-007 – Raw Data, Pressure as a Function of Temperature and Literature Data.

Since the results above indicated a malfunction of the system, a careful analysis was made of the entire system. The CO₂ was first tested for purity utilizing a gas chromatograph analysis and was found to be 99.9% pure. The thermocouple was calibrated utilizing a calibrated platinum resistance thermocouple; the calibrated thermocouple is traceable to NIST standards. It was found that the thermocouple had a correction factor of $1.088 * T_{reading} (°C) - 0.1686$. The pressure transducer was then calibrated utilizing a dead weight. Based on the results obtained from this calibration, the transducer was programmed to read the pressure properly. Also, due to the errors seen in the data, it was decided that Nitrogen would be run through the cell while the experiment was running in order to prevent H₂O in the cell from condensing on the pressure transducer – causing an erroneous reading. The error in pressure was attributed to the possible condensing of H₂O on the pressure transducer in combination with the erroneous reading of the transducer. Thus, in order to correct the data, the pressure was corrected based on the published experimental data, not based on the correction factor obtained from the calibration of the pressure transducer itself. A pressure correction factor of 0.43 MPa was subtracted from the pressure data recorded in order to obtain an accurate pressure reading. The trace obtained after correcting the temperature based on calibration of the thermocouple and subtracting a pressure of 0.43 MPa from the recorded pressure is depicted in Figure 15. This correction of pressure is only utilized for experiment T10-007.

As one can see from Figure 15, the pressure and temperature correction factors obtained were adequate to bring the experimental data to confirm to literature data. The

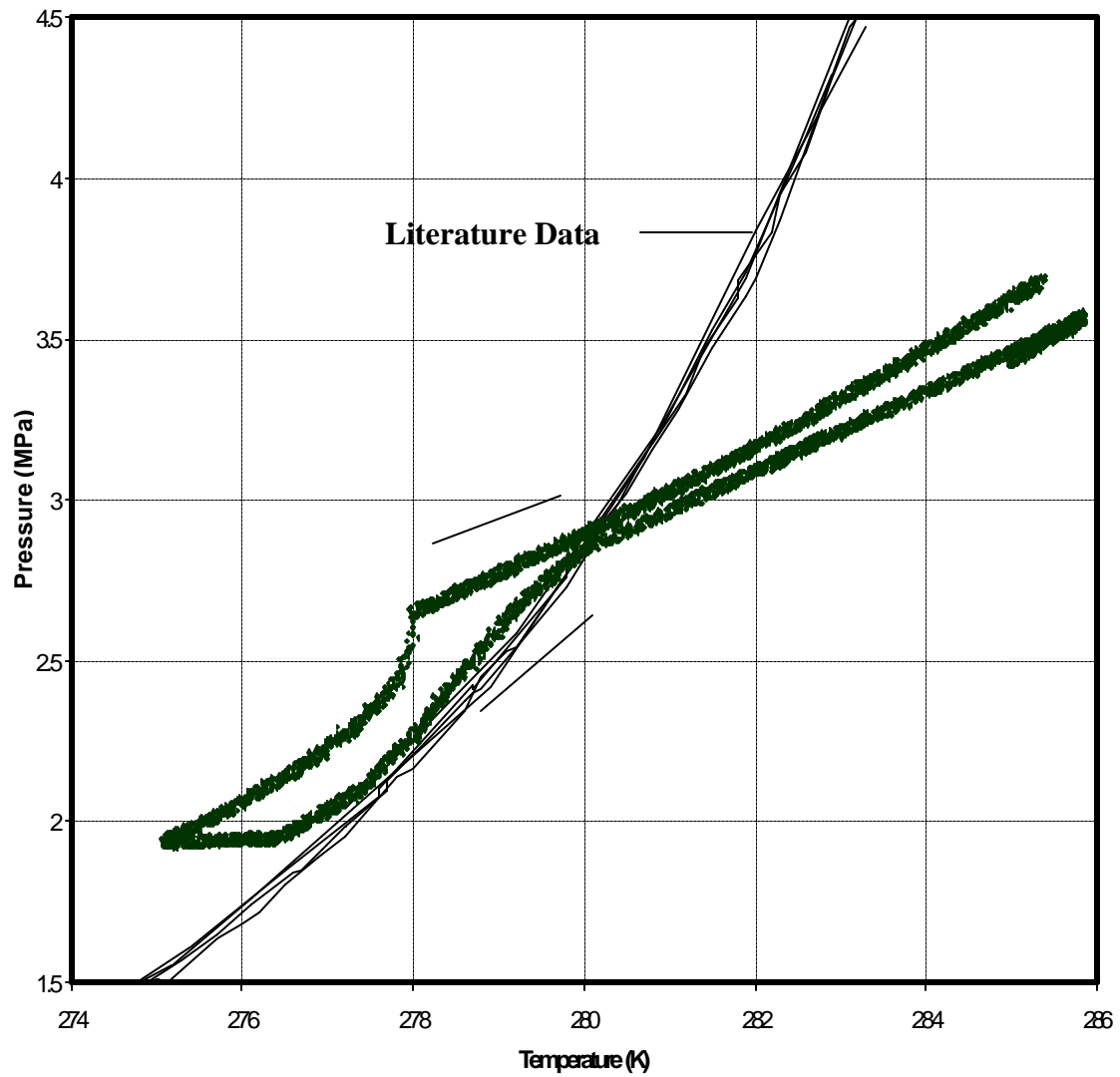


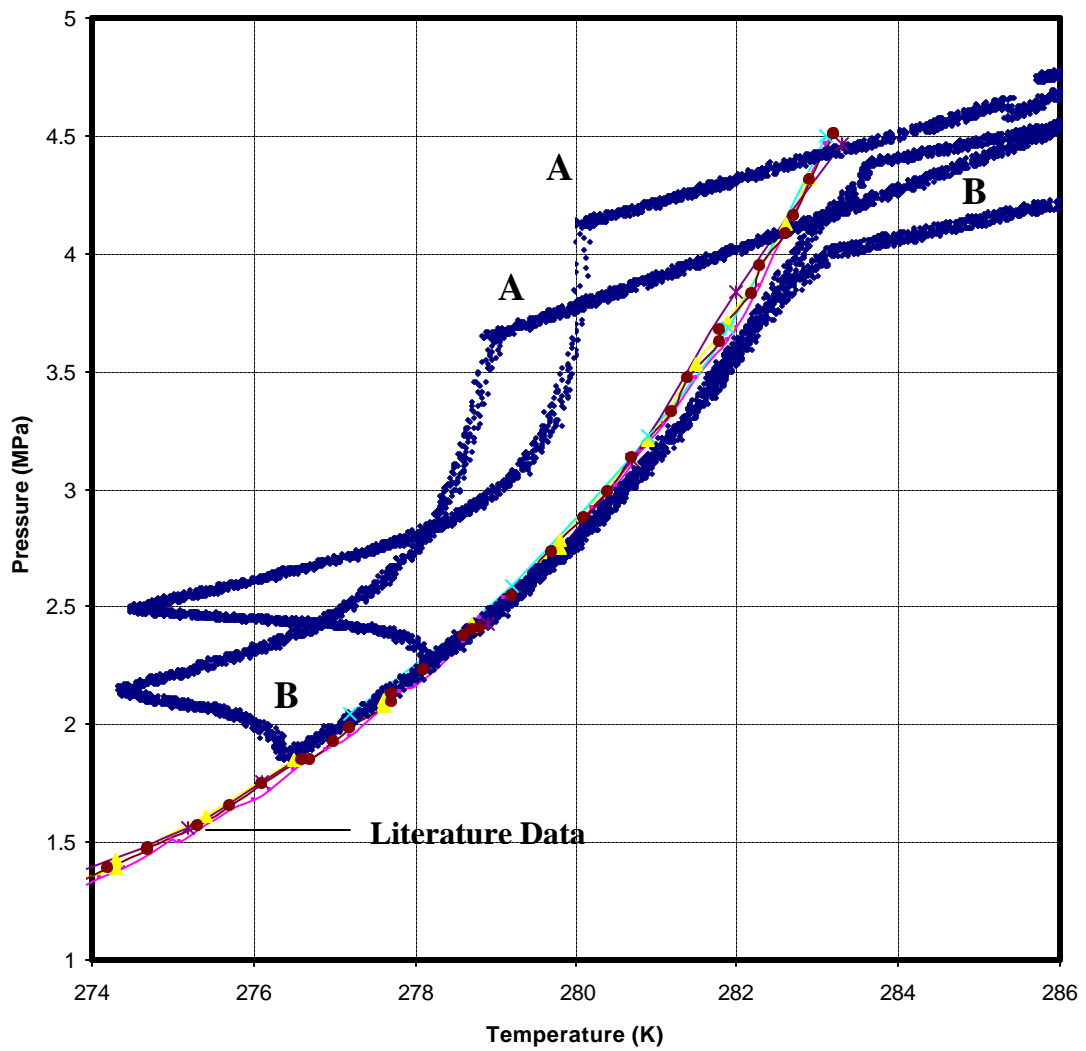
Figure 15 Experiment T10-007 -- Corrected Pressure and Temperature.

pressure correction factor was utilized to correct data obtained from single-phase experiment T10-006. In the next experiment described, experiment T10-009, Nitrogen was kept running through the cell in order to prevent condensation of water on the pressure transducer. The newly programmed transducer was placed in the cell along with the calibrated thermocouple. From now on, the graphs that are seen in all of the following experiments will have a thermocouple correction factor directly built in while the pressure listed is the actual transducer reading.

5.2 Experiment T10-009

In this experiment, hydrate was formed from a two-phase system of gaseous CO₂ and water. In this experiment, the temperature of the chamber water cycled between 287 K and 275 K twice at the rate of 0.3 K/hr. Nitrogen was run through the cell to prevent the condensation of H₂O on the surface of the transducer. The results from this experiment are described in Figure 16.

As one can see from Figure 16, the pressure-temperature trace where the hydrate is dissociating confirms closely to the literature data. However, once the hydrates have completely dissociated, one can see that there is a significant pressure loss at temperatures of 283 K or higher. This pressure loss could be due to the adsorption of CO₂ by the teflon of the stir-bar. However, literature data for the adsorption of CO₂ by teflon was minimal and since the stir-bar contained a gram or less of teflon, this effect was considered negligible. The loss in pressure could have also been due to the leakage of pressure through the o-rings or bore located behind the piston.



A = Cooling Profile
 B = Heating Profile

Figure 16 Experiment T10-009, Pressure vs. Temperature and VLH Equilibria Data

A leakage of metal particles from the teflon-stir bar was seen when the cell was taken apart. In order to prevent this problem in future experiments, another teflon stir-bar was observed carefully under a magnifying glass in order to ensure the stir-bar was intact before putting it into the view cell.

Thus the decision was made to conduct experiments with the removal of the piston from the back of the cell and a carefully examined intact stir-bar. Experiment T10-008 was conducted where hydrates were formed from gaseous CO₂ and water with the piston removed from the back of the cell and the end of the cell capped. Experiment T10-008 is described as follows.

5.3 Experiment T10-008

This experiment utilized the same procedure as listed in the introductory section. In this experiment, the temperature of the chamber was cycled between temperatures of 287 K and 275 K at the rate of 0.3 K/hr. As mentioned above, in this experiment, the piston was removed from the back of the cell in order to prevent a pressure loss. After this experiment, when the cell was taken apart, metal particles were seen inside indicating a leak of metal particles from the teflon stir-bar. The results from this experiment are depicted in Figure 17.

As one can see in Figure 17, the hydrate dissociation points on the curve correlate extremely well with literature data. Based on these results, it was determined that the metal particles seen in the water after the experiment was completed did not affect

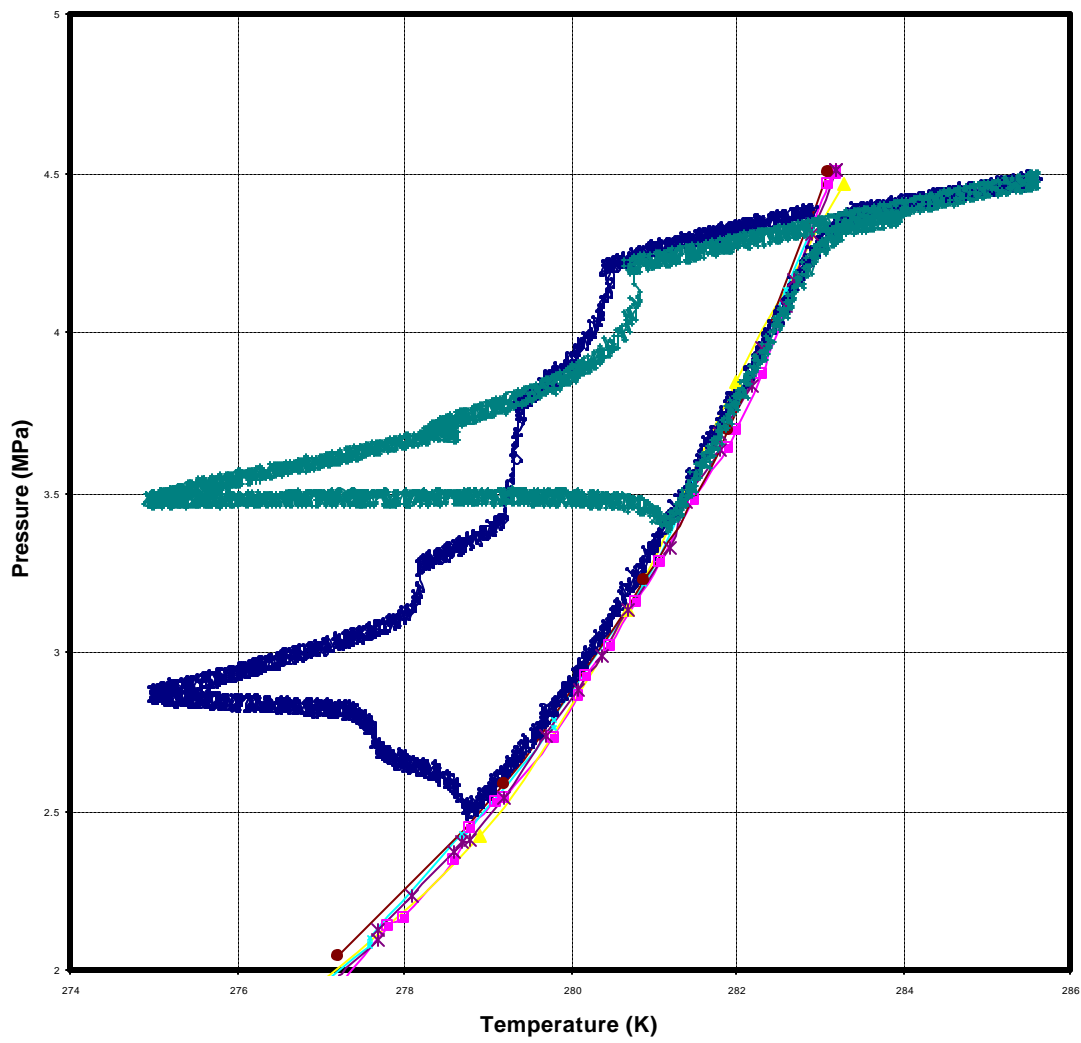


Figure 17 Experiment T10-008 Pressure vs. Temperature

hydrate dissociation values of temperature and pressure. In addition, almost no pressure loss is seen at temperatures past 283 K. This lack of loss of pressure is attributed to the replacement of the piston in the back of the cell with a fitting. Based on the results of this experiment and previous two-phase experiments, the decision was made to perform single-phase experiments without a piston located at the back of the cell, to infuse Nitrogen into the chamber while running experiments in order to prevent H₂O from condensing on the pressure transducer and to use a hardy carefully examined teflon stir-bar. Experiments performed in order to form hydrates from a single-phase system of dissolved CO₂ and water will now be described.

6.0 SINGLE-PHASE EXPERIMENTAL RESULTS AND DISCUSSION

6.1 Single Phase Experiments

Several experiments were conducted in which hydrate was formed from a single-phase system. These experiments included T10-006, T10-010, T10-011, T10-012 and T10-013. In all of these experiments, hydrate was formed from a single-phase system.

6.2 Analysis of Single Phase Experiments

In the experiments in which hydrate was formed from a single-phase system, only one hydrate dissociation pressure and temperature is possible. An elaborate procedure is required in order to analyze the data to obtain the hydrate dissociation point. In a single phase system, with CO₂ dissolved in water, with no hydrate present, as temperature increases, the pressure of the system increases due to the decrease in solubility of the CO₂ dissolved in the solution and due to the expansion of the liquid phase. However, when hydrate forms from a single-phase system, the graph of P-T slopes with respect to temperature does change with respect to temperature as seen in Figure 18.

As one can see from the Figure 18, at lower temperatures the slope of the P-T curve is very low and remains relatively constant temperature when hydrate is

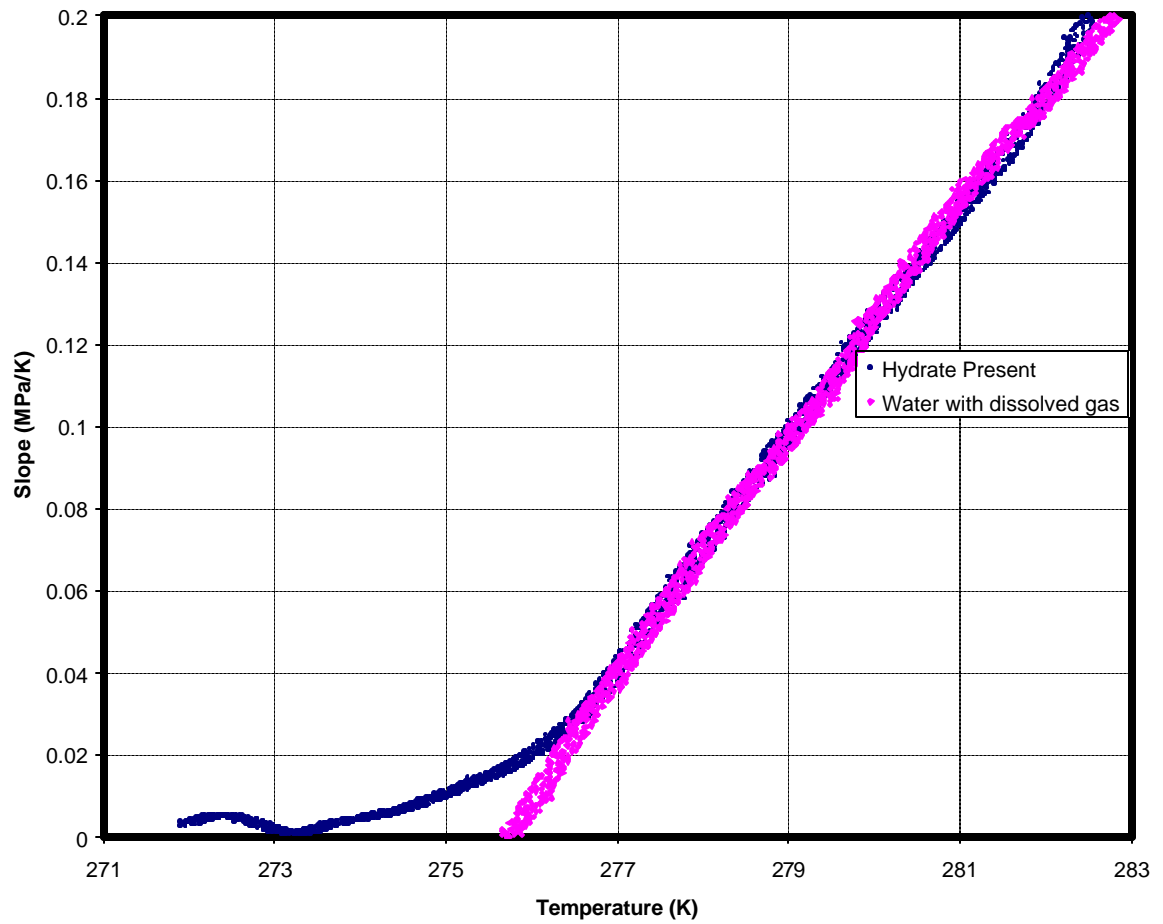


Figure 18 Slopes vs. Temperature Data at $X = 0.016$ with and without Hydrate Present.

present in the system. However, a sharp increase in slope is seen at a certain point, indicating that hydrates have dissociated. The point of exact temperature and pressure at which this rapid change in slope occurred was taken to be the hydrate dissociation point. Similar points in change of slope were seen for different experimental cycles of hydrate formation and dissociation. The temperature and pressure at which this rapid change of slope occurred were obtained as the hydrate dissociation points for different mole fractions. Experimental accounts indicate that the solubility of the hydrate former decreases with decreasing temperature in the presence of the hydrate phase (Buffett and Zatsepina, 2000, Zatsepina and Buffett, 1997, Aya et. al., 1997) as opposed to an increase in the solubility with decreasing temperature in the absence of a hydrate phase. The above finding could account for the low slope of Figure 18 at lower temperatures when hydrate is present and the increase in slope when the hydrate is not present in the solution.

As hydrates dissociate, more CO₂ goes into solution. The effect of temperature $\left(\frac{dP}{dT}\right)_{x_i}$ on solubility increases as the mole fraction of CO₂ increases. Thus the slope increases as the mole fraction of CO₂ increases due to hydrate dissociation. When the hydrates are all dissolved, the slope stops accelerating and the rate of change of slope remains approximately constant although at higher

levels. The single-phase experiments along with the results obtained from them will now be described.

6.3 Experiment T10-006

This experiment was conducted before experiment T10-007 was conducted. Thus, in this experiment, the piston remained in the back of the cell. Also, no Nitrogen was run through the chamber in order to prevent H₂O from condensing on the pressure transducer. A volume of 21.17 ml of H₂O was injected into the cell utilizing a syringe. CO₂ was injected into the cell at a pressure of 20 MPa and 292 K at a density of 0.93168 g/ml (Angus, et. al, 1990). Therefore a mole fraction of 0.018 was injected into the cell. The starting temperature and pressure of the cell was 285.7 K and 23.9 MPa (3461.9 Psig) at a set point of the chamber at 287 K. The chamber was programmed to decrease in temperature from 287 K to 275 K at the rate of 0.3 K/hr. The temperature of the cell during this experiment was cycled 6 times or so in order to produce hydrates several times to ensure the experimental data was reproducible. Figure 19 illustrates the formation of hydrate for cycle #3 of the experiment. The drop in pressure at approximately 275.5 K is due to the formation of hydrate. Theoretically, the hydrate should have dissociated at approximately 278 K as seen in Figure 19. In Figure 19, a pressure correction factor of 62.2 Psia or 0.43 MPa from two-phase experiment T10-007 was subtracted from the original data in order to obtain the curve.

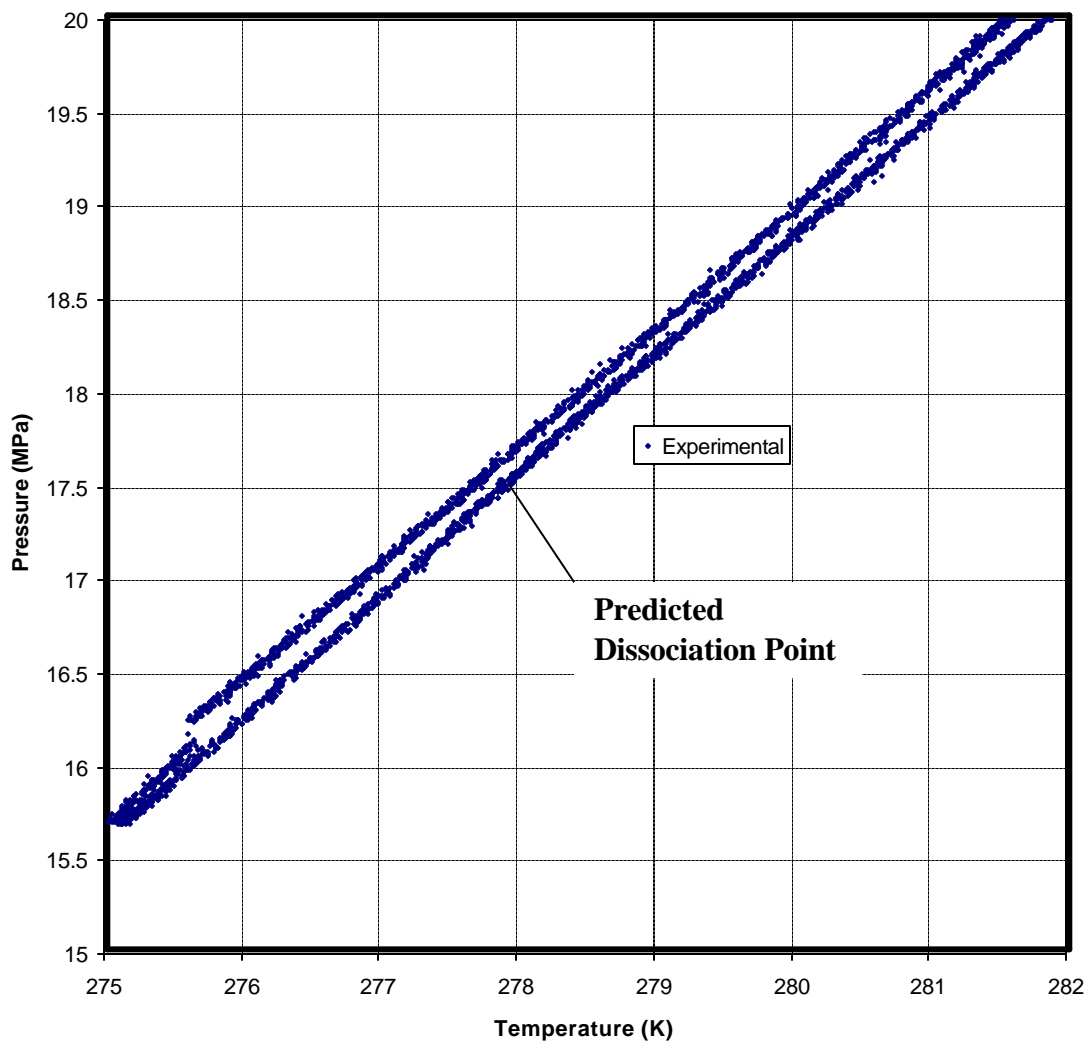


Figure 19 Experiment T10-006 – Cycle #3 P-T Curve. X= 0.018

Six different hydrate dissociation points were obtained from the experiment for the six different cycles performed. Table 2 illustrates the hydrate dissociation points and their relation to the theoretical hydrate dissociation points for experiment T10-006. As seen in Table 2 the hydrate dissociation pressure and temperature decreases as the cycle number increases. This phenomenon indicates a loss of pressure with respect to time causing a decrease in hydrate dissociation pressure with respect to time. This pressure loss can be attributed to the presence of the piston in the back of the cell. Table 2 illustrates the hydrate dissociation points and their error values computed relative to the predicted hydrate dissociation point for a mole fraction of 0.018, for experiment T10-006.

As one can see from Table 2, the error for the pressure for this experiment is much larger than the error for the temperature. This is expected because the method used in the program to calculate the hydrate dissociation pressure was assumed to be less accurate than the temperature prediction. After this experiment, another experiment, (T10-007) was conducted where hydrate was formed from a single-phase system. In this experiment, hydrate was formed from a mole fraction of 0.02568 of CO₂ in the cell. However, the model does not predict the hydrate dissociation pressure and temperature for hydrate formed from a single-phase system of dissolved liquid CO₂ and water. The model only has the ability to predict hydrate dissociation conditions for gaseous CO₂ dissolved in water. Thus, the results from this experiment were discarded.

Table 2 Experiment T10-006 Hydrate Dissociation Points

T (K)	T _{predicted} (K) @ Constant Experimental	T, error %	Pressure (MPa)	P, predicted (MPa) @ Constant Experimental	Temperature	P, error (%)
280.2	278	0.78	19.12	38.60	50.47	Cycle #1
279.5	278	0.53	18.69	32.00	41.60	Cycle #2
279.2	278	0.42	18.19	28.70	36.63	Cycle #3
278.9	278	0.31	17.87	26.00	31.26	Cycle #4
278.5	278	0.18	17.58	22.60	22.21	Cycle #5
278.6	278	0.22	17.54	23.50	25.35	Cycle #6
279.1	278	0.41	18.17	28.57	34.58	Average

6.4 Experiment T10-011

This was the first successful single-phase experiment conducted after the piston was removed from the back of the cell and the end capped. In this experiment, a mole fraction of 0.018 of CO₂ was prepared in the cell. The CO₂ was allowed to dissolve overnight. Starting point of this experiment was a temperature of T=278.15 K and a pressure of 56.8 MPa or 8204.8 Psia. The P-T trace for this experiment is seen in Figure 20. The theoretical and predicted hydrate dissociation values are outlined in Table 3.

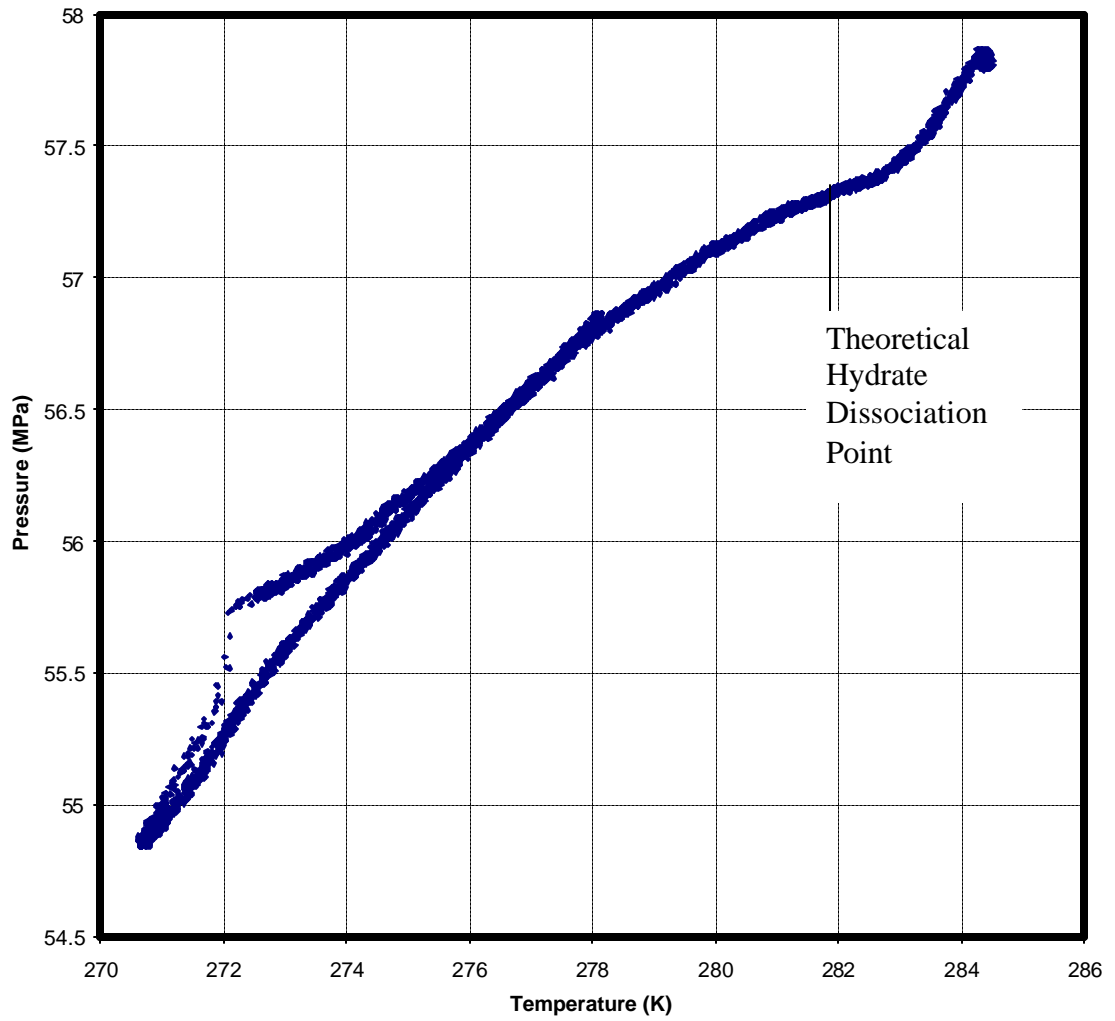


Figure 20 Experiment T10-011 Formation of Hydrate from a Single-Phase System

Table 3 Experiment T10-011 Hydrate Dissociation Points

T (K)	T _{predicted} (K) @ Constant Experimental Pressure	T _{error} %	Pressure (MPa)	P _{predicted} (MPa) @ Constant Experimental Temperature	P _{error} (%)
281.90	281.80	0.04	56.45	56.50	0.09

6.5 Experiment T10-012

In this experiment, a mole fraction of 0.016 was prepared in the cell in order to form hydrate from a single-phase system. In this experiment, the stir bar constantly got stuck and would not become dislodged. Since the stir-bar was working when the CO₂ was trying to dissolve, hydrates were formed from a single phase system. The results from Cycle #1 are listed in Table 4.

6.6 Experiment T10-013

This experiment was conducted using a mole fraction of 0.016. It was a repeat of experiment T10-012 utilizing a home-made stir-bar that would not either leak metal or since it was not very large, would not get stuck in the cell. In this experiment, the temperature was initially cycled between 287 K and 271 K at the rate of 0.3 K/hr at a starting pressure of 53.33 MPa. After Cycle #1 was conducted, a new experimental technique was utilized where the temperature was dropped as fast as possible to 271 K in order to form hydrates. This rapid drop was possible since the determination of an equilibrium hydrate dissociation point was required as opposed to a hydrate formation point. Cycle #1 was repeated in order to ensure the data obtained from both techniques confirmed to one another. Cycle #2 was reproduced again in order to ensure the new experimental technique produced reproducible data. The trends of the P-T (Pressure-Temperature) slopes vs. temperature data for all the three cycles are reproducible as seen in Figure 21. In order

Table 4 Experiment T10-012 Hydrate Dissociation Points.

T (K)	T _{predicted} (K) @ Constant Experimental Pressure	T _{error} %	Pressure (MPa)	P, predicted (MPa) @ Constant Experimental Temperature	P, error (%)
278.94	279.50	0.20	55.60	52.00	6.92

to obtain another experimental point at a lower pressure with the same mole fraction, the pressure in the cell was reduced through opening a valve in the back of the cell and releasing some water from the back of the cell into a small section of 1/16 inch tubing sealed at the other end with a valve. It was assumed that the CO₂ was uniformly dissolved in the cell, thus enabling the reduction of pressure by opening a valve in the back without losing any of the dissolved CO₂. For these experiments, the temperature was cycled at a starting pressure of 33.78 MPa that was much lower than the starting pressure of 53.33 MPa that was utilized in Cycles #1, #2 and #3. Cycle #4 was repeated to obtain Cycle #5. After these two cycles were completed, the pressure was dropped to a pressure of 18.16 MPa. At this pressure, the temperature was rapidly dropped to a temperature of 271 K and increased to a temperature of 287 K, then repeated again to obtain Cycles #6 and #7. The P-T slopes vs. temperature plot was repeatable in Cycles #4 and #5 and in Cycles #6 and #7 as well. The results obtained from one of the cycles of experiment T10-013 are listed in Figure 22 and the results obtained from the experiment are listed in Table 5.

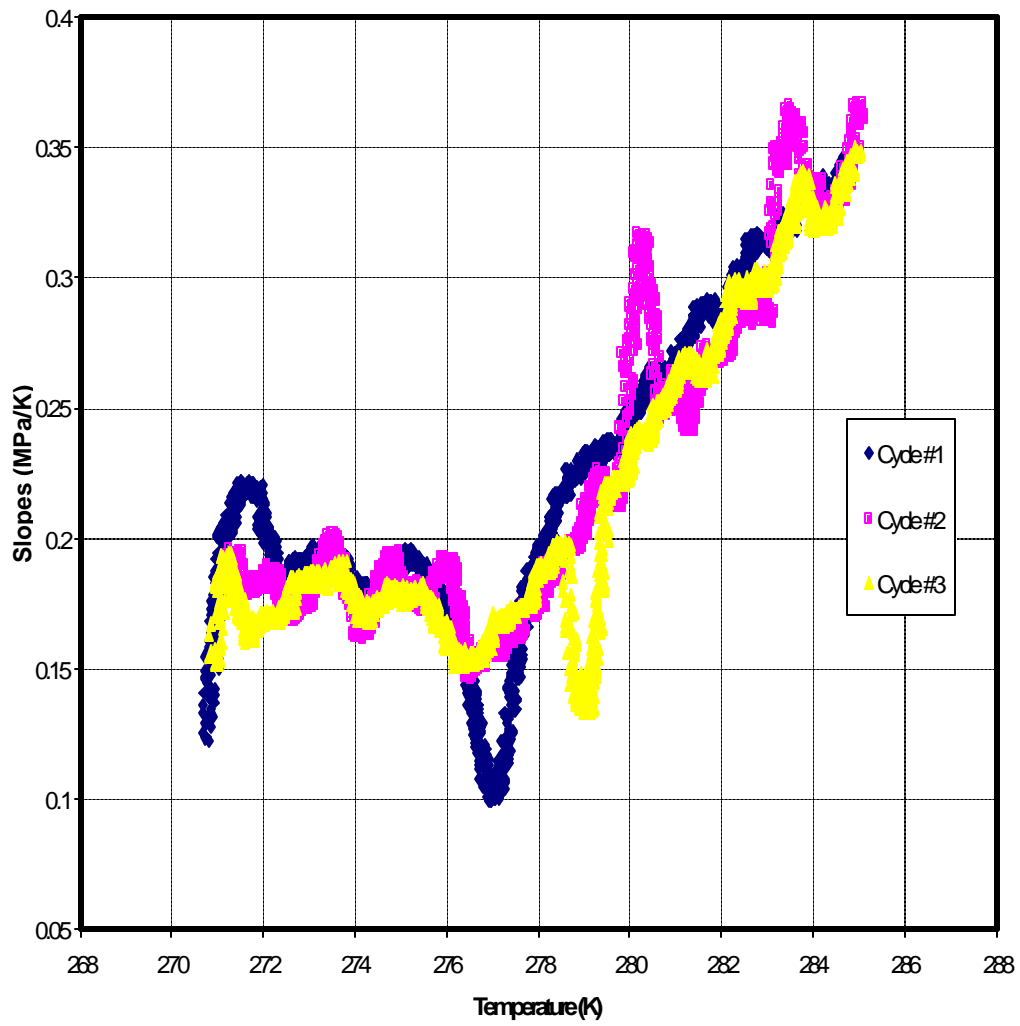


Figure 21 Experiment T10-013 Slopes vs. Temperature – Cycles 1,2 & 3

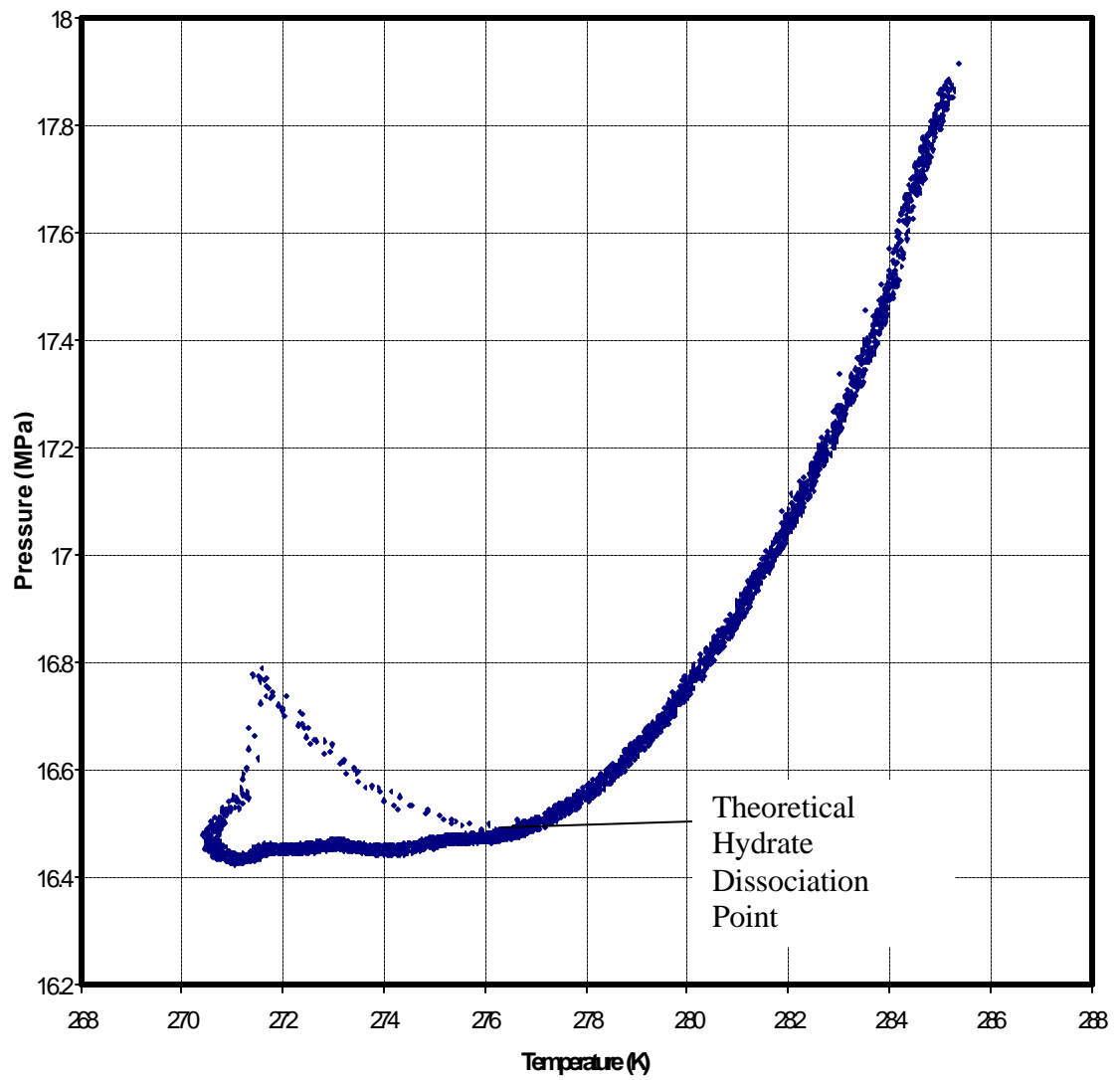


Figure 22 Experiment T10-013 Results from Cycle #7.

Table 5 Experiment T10-013 Hydrate Dissociation Points

T (K)	T _{predicted} (K) @ Constant Experimental Pressure	T _{error} %	Pressure (MPa)	P _{predicted} (MPa) @ Constant Experimental Temperature	P _{error} (%)	
276.79	279.50	0.97	50.01	52.00	3.82	Average of Cycles #1, #2 & #3
275.57	278.75	1.14	31.14	33.00	5.63	Average of Cycle #4 & #5
274.05	276.50	0.89	16.47	20.00	17.64	Average of Cycles #6 & #7
275.47	278.25	1.00	32.54	35.00	9.03	Average

7.0 DISCUSSION AND SUMMARY OF RESULTS

7.1 Summary of Results

The results from the single-phase experiments are summarized in Figure 23. The average absolute deviation obtained for the hydrate dissociation temperatures of the single-phase experiments 1.61 % and a pressure deviation of 12.65 %.

7.2 Discussion of Results

Figure 24 shows theoretical curves using partial molar volumes of 35 cc/mol, 40 cc/mol and 45 cc/mol. In experiment T10-013, the data best reproduces a theoretical curve utilizing a partial molar volume of 35 cc/mol.

With a small absolute average deviation, the theoretical model seems to fit the experimental data relatively well. This method could be used to estimate partial molar volumes but the accuracy of the data and model are probably not sufficient to allow good values of the partial molar volume to be estimated. In order to improve the theoretical model, a correlation for partial molar volume of CO₂ in water could be inserted into the program.

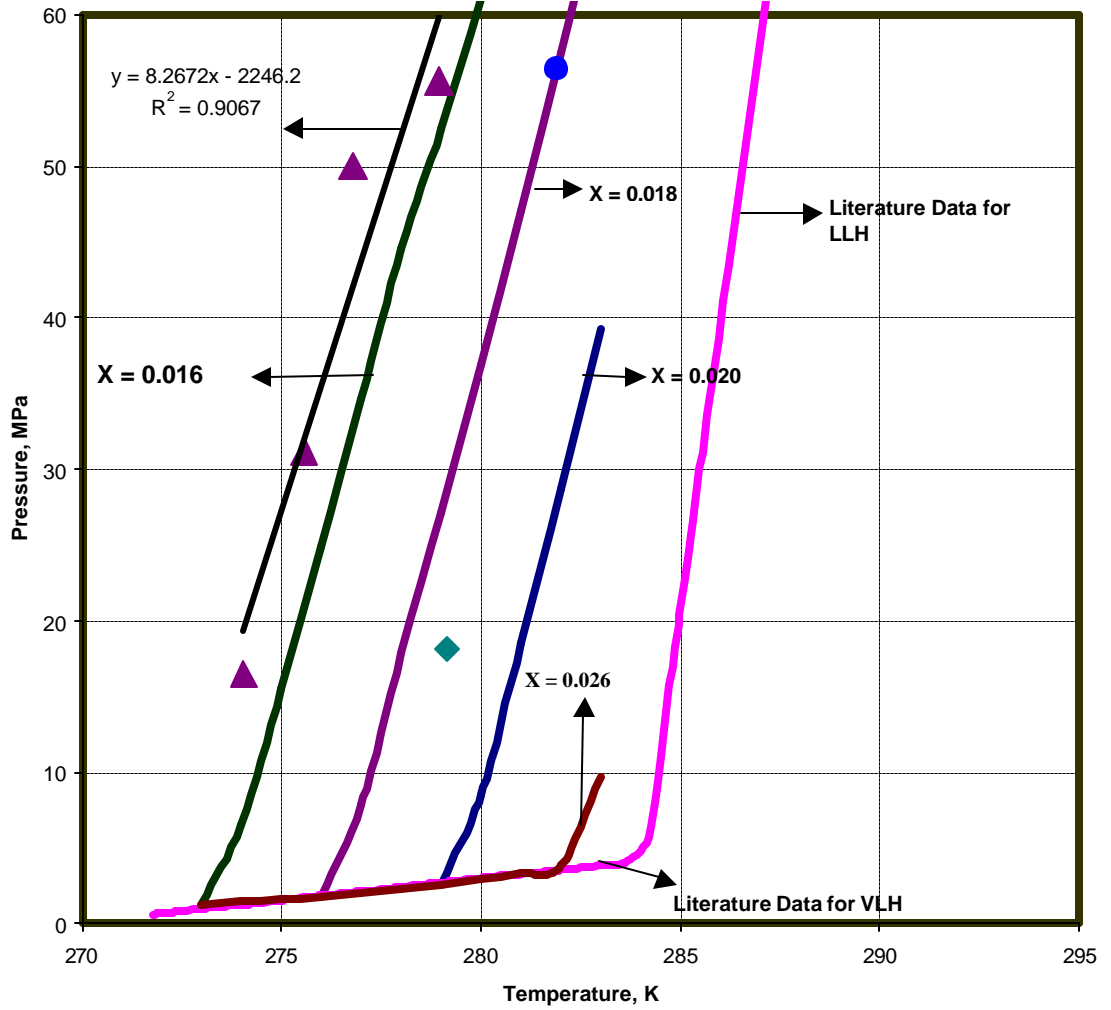


Figure 23 Summary of Experimental Results from Single-Phase Experiments.

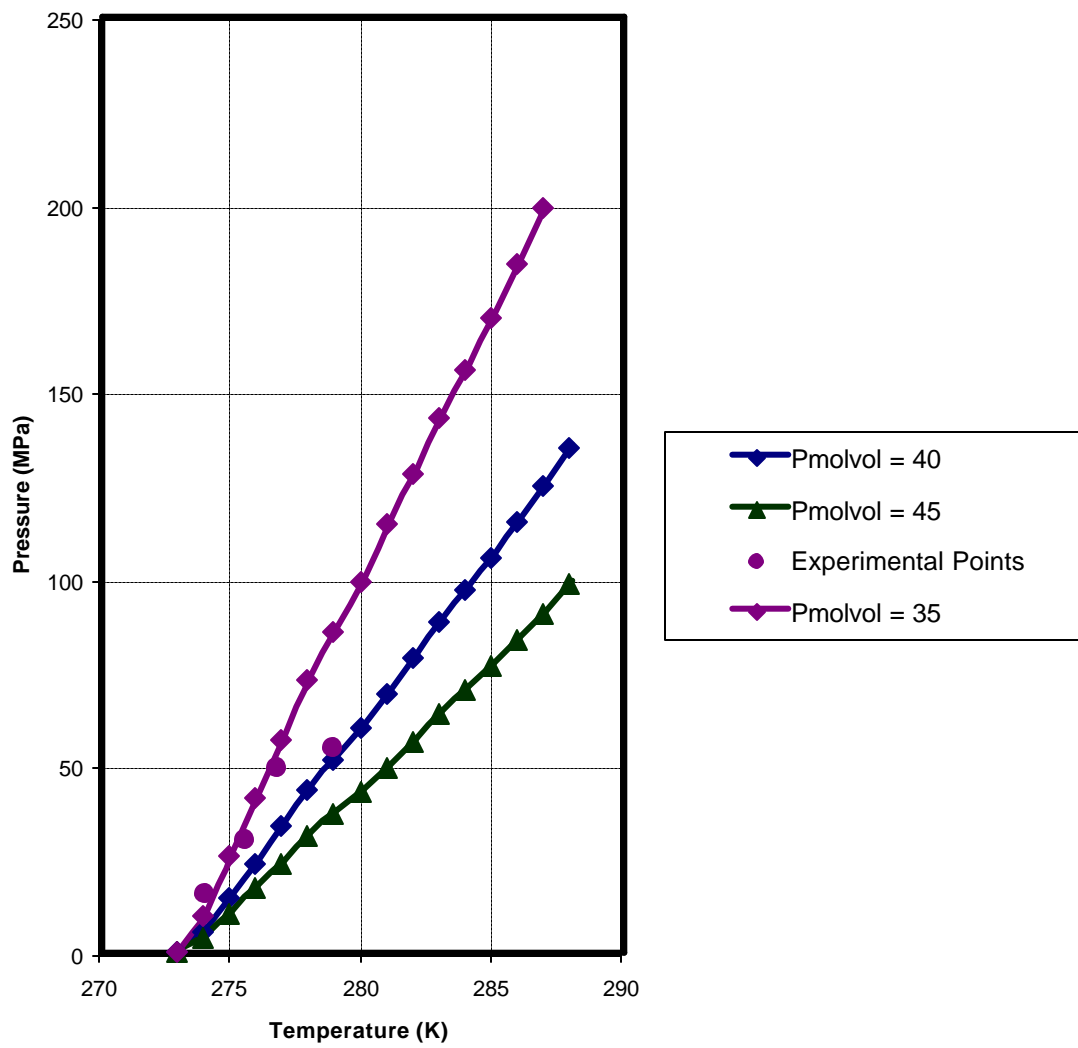


Figure 24 Experiment T10-013, Various Partial Molar Volumes.

8.0 CONCLUSIONS

Hydrate was formed from a single-phase system of dissolved CO₂ and water at mole fractions of 0.016 and 0.018 demonstrating that hydrates can form in such a system. The results obtained from these experiments reasonably correlated with a theoretical model based upon the original van der Waals and Platteaw theory.

9.0 FUTURE WORK

Further experimental studies must be performed on the formation of hydrate from a single-phase system. Further studies where the hydrate is formed and then the pressure is dropped and hydrate is formed again as seen in experiments T10-013 and T10-014 should be performed on the formation of hydrate from a single phase system.

The model must be modified to be able to theoretically predict the formation of hydrate from a single-phase system from CO₂ dissolved in salt water. Also, other single-phase experiments must be conducted where the hydrate is formed from CO₂ dissolved in salt water.

Further experimental studies must be performed to determine the solubility of CO₂ in teflon. The view cell must be modified so that the bore in the back of the cell is snug enough to hold a piston and not allow for any pressure loss. This must be done because it is much easier to conduct experiments when one can vary the piston in the back of the cell. One must not use a glass stir bar because of problems with it breaking and metal leaking out of the cell.

There appears to be a large amount of data in the literature that reports equilibrium hydrate dissociation points however, not much data in the literature that reports experiments on kinetic data – the conditions under which hydrate forms and tends to increase the rate of hydrate formation in the system. More experimental work needs to be done in order to elucidate the above problem. Finally, more data needs to be obtained where hydrates are formed from a single-phase of dissolved CO₂ and water in order to validate the theoretical model.

APPENDIX

```
C *****
C
C CALCULATION OF HYDRATE PHASE EQUILIBRIA.
C *****
C THIS PROGRAM CALCULATES PCALC WHEN TENURED PEXP.
C LANGMUIR COEFFICIENTS ARE CALCULATED BY USING
C Q* CORRELATION METHOD.
C
C
C 25 GASES ARE INCORPORATED INTO THE PROGRAM.
C MIXTURES OF UP TO 10 COMPONENTS CAN BE STUDIED.
C
C *****      COMMON STATEMENTS      *****
C
PROGRAM HYD
IMPLICIT DOUBLE PRECISION (A-H,O-Z)
IMPLICIT INTEGER (I-N)
CHARACTER*5 YCOMP, YNAME, YNAMEL, YNAMEIM
CHARACTER*4 AQ
DIMENSION YNAME(25)
DIMENSION YCOMP(10)
DIMENSION ICASE(30), ILEN(31)
DIMENSION A(10), SIGMA(10), EPS(10), AMW(10), TC(10), VC(10), PC(10)
DIMENSION ZAA(1,25), AK(25,25)
DIMENSION IISCO(25), PPEXP(100)
DIMENSION KYP(20), NCODE(25)
DIMENSION OMEGA(10), ESTAR(10), C1RKV(10), C2RKV(10), C1RKL(10)
DIMENSION C3FREF(10), C4FREF(10), C1FREF(10), C2RKL(10)
DIMENSION C2FREF(10), C0FREF(10)
DIMENSION XX(13), KK(25), ZA(20), ICODE(10)
DIMENSION YNAMEIM(10)
DIMENSION YNAMEL(10)
COMMON/BKSB/NPT, NSETS, IFLAG
COMMON/BLOCK/ISOLVE
COMMON/AZ/KK, N, MK
COMMON/NC/NCODE, NCOMP
COMMON/DV/PVAP(100), AA(3), AB(3), PSAT(3,100), XY(100)
COMMON /AMOL/MA, ICODE(10)
COMMON/TEXPT/PEXP(100), X(15,100), IS(100), T(100), YEXP(100)
COMMON/SERDAT/T1(100), DT(100), T2(100)
COMMON/FUND/SIGMA, EPS, A
COMMON/XXX/XX, DH
COMMON/COR/EP SH, DDU, DDH, BETA1, GAMMA
COMMON/VDO/SIGH1, SIGH2
COMMON/BKSA/AK
COMMON/BKSC/IWATER, IPOS, ISTR, IDH
COMMON/PHAS/NVLLH
COMMON/STRUC/NSTRUC
COMMON/IMP/IMPURE, IMCODE, XIMP(100), YCO2(100)
```

```
COMMON/SOLUT/XSOLU,ACTIV,YYYCO2
COMMON/SEQ/ISEQ,TMIN,DELT,TMAX,TQL
COMMON/LIQUID/LIQ
```

```
*****
```

```
**** READ IN EACH COMPONENT ****
```

```
DATA YNAME/'CH4','C2H6','C2H4','C3H8','C-C3',
*'N-C4','I-C4','C-C4','C5H12','I-C5','NE-C5','C-C5',
*'H2O','H2','CO2','O2','N2','H2S','XE','AR','KR',
*'SF6','CIC4','TRC4','NONE'/
DATA YCOMP / 'Y-1','Y-2','Y-3','Y-4','Y-5','Y-6','Y-7',
*'Y-8','Y-9','Y-10'/
DATA YNAMEL/'XL1','XL2','XL3','XL4','XL5','XL6','XL7',
*'XL8','XL9','X10'/
DATA YNAMEIM / 'MEOH','ETOH','PROH','NACL','CAACL2','KCL'
* , 'NH3','ETGLY','DEGLY','TRGLY' /
```

```
COMPONENT IDENTIFIERS,WHERE FOLLOWING CODE APPLIES.
```

- **** 1= METHANE
- **** 2= ETHANE
- **** 3= ETHYLENE
- **** 4= PROPANE
- **** 5=CYCLO-PROPANE
- **** 6= N-BUTANE
- **** 7= ISO-BUTANE
- **** 8= CYCLO-BUTANE
- **** 9= PENTANE
- **** 10= ISO-PENTANE
- **** 11= NEO-PENTANE
- **** 12= CYCLO-PENTANE
- **** 13= WATER
- **** 14= HYDROGEN
- **** 15= CARBON-DI-OXIDE
- **** 16= OXYGEN
- **** 17= NITROGEN
- **** 18= HYDROGEN SULFIDE
- **** 19= XENON
- **** 20= ARGON
- **** 21= KRYPTON
- **** 22= SULFUR HEXAFLOURIDE
- **** 23= CIS-2-BUTENE
- **** 24= TRANS-2-BUTENE
- **** 25= NO COMPONENT PRESENT


```

C           =1 HEAT OF DISSOCIATION IS CALCULATED
C
C       14>MA=NUMBER OF COMPONENTS
C       15>KK(I)=CODE OF EACH COMPONENT
C       16>N=NUMBER OF DATA POINTS
C       17>EXPERIMENTAL HYDRATE CONDITIONS SUCH AS
C       P/PSIA,T/DEG.R,Y(I),I=1,MA
C
C
C       * * READ IN OPTION SWITCHES * *
C
OPEN(12,FILE='TAPE12.DAT',STATUS='OLD')
OPEN(06,FILE='HYDOUT.DAT',STATUS='UNKNOWN')
READ(12,104)AQ
READ(12,200)ISOLVE,ISTR,ILANG,IN
GO TO(90,91),IN
90  CONTINUE
    WRITE(06,301)
91  CONTINUE
C
C       * * READ IN NUM OF ON LINE SETS TO RUN AND WATER SWITCH * *
C
READ(12,104)AQ
READ(12,302)NSETS,IWATER,NVLLH,NSTRUC,IMPURE,ISEQ,LIQ,IDH
IF(NVLLH.EQ.1.AND.NSTRUC.EQ.0)GO TO 1002
IF(IWATER.NE.0.AND.NVLLH.EQ.1)GO TO 1003
IF(ISEQ.EQ.2.AND.NVLLH.EQ.0)GO TO 1004
IF(LIQ.EQ.1.AND.ISEQ.EQ.1.AND.NVLLH.EQ.1)GO TO 1005
IF(LIQ.EQ.1.AND.ISEQ.EQ.2)GO TO 1006
IFLAG=1
C
C       * * SET CONDITIONS FOR USER'S EXPT OR GUESSED DATA * *
C
IF(NSETS.NE.0)GO TO 56
ILEN(1)=0
ICASE(1)=1
IFLAG=0
C
NSETS=1
GO TO 57
C
56  READ(12,104)AQ
C
C       * * READ IN CODES FOR ON LINE DATA SETS TO BE RUN * *
C
DO 51 I=1,NSETS
READ(12,202)ICASE(I)
51  CONTINUE
    READ(12,104)AQ
C
ILEN(1)=0
C
C       * * READ IN TOTAL NUMBER OF ON LINE DATA SETS * *
C       * * PRESENT IN FOR12.DAT

```

```

C
    READ(12,202)NTSETS
    READ(12,104)AQ
    NTSETS=NTSETS+1
C
C
C    * * READ IN LENGTH OF EACH DATA ON LINE DATA SET * *
C
    DO 50 I=2,NTSETS
    READ(12,202)ILEN(I)
50    CONTINUE
    READ(12,104)AQ
C
C
C    * * CONVERT ILEN VALUES TO CUMULATIVE VALUES * *
C
    DO 55 I=2,NTSETS
    ILEN(I)=ILEN(I)+ILEN(I-1)
55    CONTINUE
C
C
C    57    IMOVE=ILEN(ICASE(1))
C
C
C    * * MOVE THROUGH FOR12.DAT AND GET DESIRED DATA * *
C
    DO 983 IJK=1,NSETS
    IF(IMOVE.EQ.0)GO TO 54
    IF(IJK.EQ.1)GO TO 65
    IMOVE=ILEN(ICASE(IJK))-ILEN(ICASE(IJK-1)+1)
    IF(IMOVE.EQ.0)GO TO 54
C
    65    DO 53 I=1,IMOVE
    READ(12,104)AQ
104    FORMAT(A4)
    53    CONTINUE
    54    IMOVE=1000
C
C
    READ(12,202) MA
C
C
C    ** CHECK WHETHER IMPURITY CALCULATION IS REQUIRED **
    IF(IMPURE.EQ.1)GO TO 185
    READ(12,308) (KK(I),I=1,MA)
    GO TO 186
185    READ(12,309)(KK(I),I=1,MA),IMCODE
C
C
C    ** CHECK FOR PRESENCE OF CO2 WITH INHIBITOR **
C
    DO 1060 JJ=1,MA
    IF(KK(JJ).EQ.15)JJ1=JJ
1060    CONTINUE
C
C
C    ***** READ IN NUMBER OF DATA POINTS *****
C
    186    READ(12,305) N
    NPT=N
C

```



```

C      CHECK FOR HEAT OF DISSOCIATION CALCULATIONS
C
      IF(IDH.EQ.0) GO TO 327
      IF(ISEQ.EQ.1) GO TO 378
      IF(IMPURE.EQ.1) GO TO 326
      DO 328 I=1,N
      READ(12,329) PEXP(I),T(I),IS(I),(X(J,I),J=1,MA)
328    CONTINUE
      GO TO 12
      378    CONTINUE
      IF(IMPURE.EQ.0) GO TO 675
      DO 468 I=1,N
      READ(12,969) PEXP(I),T1(I),DT(I),T2(I),IS(I),(X(J,I),J=1,MA),
1     XIMP(I)
468    CONTINUE
      GO TO 12
      675    CONTINUE
      DO 8132 I=1,N
      READ(12,968) PEXP(I),T1(I),DT(I),T2(I),IS(I),(X(J,I),J=1,MA)
8132   CONTINUE
      GO TO 12
      326    CONTINUE
      DO 341 I=1,N
      READ(12,330) PEXP(I),T(I),IS(I),(X(J,I),J=1,MA),XIMP(I)
341    CONTINUE
      GO TO 12
      327    CONTINUE
C      CHECK FOR WATER CALCULATION
      IF(IWATER.EQ.0.OR.IWATER.EQ.1)GO TO 67
C
C      *****      READ IN N DATA POINTS      *****
      DO 123 I=1,N
      READ(12,100) PEXP(I),T(I),IS(I),(X(J,I),J=1,MA),YEXP(I)
123    CONTINUE
      GO TO 12
      67     IF(IMPURE.EQ.0)GO TO 567
C      **CHECK WHETHER SEQUENTIAL CALCULATION WITH IMPURITIES IS
REQUIRED
C
C
      IF(IMPURE.EQ.1.AND.ISEQ.EQ.0)GO TO 569
      DO 221 I=1,N
      READ(12,181) PEXP(I),T1(I),DT(I),T2(I),IS(I),(X(J,I),J=1,MA)
1,XIMP(I)
C
C      ** CHECK FOR PRESENCE OF CO2 WITH IMPURITY **
C
      YCO2(I)=X(JJ1,I)
221    CONTINUE
      GO TO 12
      569    DO 222 I=1,N
      READ(12,111) PEXP(I),T(I),IS(I),(X(J,I),J=1,MA),XIMP(I)
      YCO2(I)=X(JJ1,I)
222    CONTINUE

```

```

      GO TO 12
C   ** CHECK WHETHER SEQUENTIAL CALCULATION IS REQUIRED **
567   IF(ISEQ.EQ.0)GO TO 568
      DO 240 I=1,N
      READ(12,180) PEXP(I),T1(I),DT(I),T2(I),IS(I),(X(J,I),J=1,MA)
240   CONTINUE
      GO TO 12
568   DO 122 I=1,N
      READ(12,100) PEXP(I),T(I),IS(I),(X(J,I),J=1,MA)
122   CONTINUE
C
C
12   CONTINUE
C
C
C   ***** WRITE OUT ALL INPUT DATA *****
C   DO 978 I=1,MA
C
      WRITE(06,310) I,YNAME(KK(I))
978   CONTINUE
      IF(IMPURE.EQ.1)WRITE(6,344)YNAMEIM(IMCODE)
      IF(IFLAG.NE.0)GO TO 58
      WRITE(06,105)(YCOMP(I),I=1,MA)
      GO TO 59
58   IF(LIQ.EQ.0)WRITE(06,101)(YCOMP(I),I=1,MA)
      IF(LIQ.EQ.1)WRITE(06,101)(YNAMEL(I),I=1,MA)
59   WRITE(06,103)
      IF(IMPURE.EQ.0)GO TO 182
      DO 95 I=1,N
      IF(ISEQ.EQ.1.OR.ISEQ.EQ.2)T(I)=T1(I)
      WRITE(6,112) PEXP(I),T(I),IS(I),(X(J,I),J=1,MA),XIMP(I)
95   CONTINUE
      GO TO 97
182  DO 94 I=1,N
      IF(ISEQ.EQ.1.OR.ISEQ.EQ.2)T(I)=T1(I)
      WRITE(6,102) PEXP(I),T(I),IS(I),(X(J,I),J=1,MA)
94   CONTINUE
97   WRITE(6,315)
C
C   CALL FUN TO EVALUATE PCALC AS A FUNCTION
C   OF TEMPERATURE AND MOLE FRACTION.
C
C
      CALL FUN(NN,XX,FF)
      XX(1)=SIGH1
      XX(2)=SIGH2
      XX(3)=EPSH
      XX(4)=DDU
      XX(5)=DDH
      XX(6)=BETTA1
      XX(7)=GAMMA
      IF(ILANG.NE.1)GO TO 983
      WRITE(06,812) XX(1),XX(3),XX(4),XX(5),XX(6),XX(7),XX(2)
C

```

```

C
983   CONTINUE
C
C
C
C
C
C
C
C
*****   THE FOLLOWING ARE FORMAT STATEMENTS ONLY   *****
309   FORMAT(1(/),11(I2,1X))
968   FORMAT(4(F5.0,1X),I1,1X,9(F5.0,1X))
969   FORMAT(4(F5.0,1X),I1,1X,9(F5.0,1X))
344   FORMAT(' IMPURITY',A15,' PRESENT IN WATER')
112   FORMAT(3X,2(F10.3,4X),4X,I1,6X,11(F6.4,2X))
853   FORMAT(' ERROR IN INPUT DATA ISEQ=2 AND LIQ=1')
843   FORMAT(' ERROR IN INPUT DATA LIQ=1 ISEQ=1 NVLLH=1')
833   FORMAT(' ERROR IN INPUT DATA ISEQ=2 NVLLH=0')
823   FORMAT(' ERROR IN INPUT DATA NVLLH=1 AND WATER CALCULATION')
803   FORMAT(' ERROR IN INPUT DATA NVLLH=1 AND NSTRUC=0')
100   FORMAT(2(F5.0,1X),I1,1X,10(F5.0,1X))
111   FORMAT(2(F5.0,1X),I1,1X,11(F5.0,1X))
180   FORMAT(4(F5.0,1X),I1,1X, 9(F5.0,1X))
181   FORMAT(4(F5.0,1X),I1,1X, 9(F5.0,1X))
101   FORMAT(100('-'),/,30X,'EXPERIMENTAL HYDRATE DATA',
*/,100('-'),/,4X,'PRESSURE',3X,'TEMPERATURE',
*2X,'STRUCTURE',4X,10(A5,3X))
102   FORMAT(3X,2(F10.3,4X),4X,I1,4X,10(F7.4,1X))
103   FORMAT(4X,'PSIA',7X,'DEG.R',/,100('-'),/)
105   FORMAT(100('-'),/,6X,'INPUT HYDRATE DATA
A WITH INITIAL PRESSURE GUESSED',
B/,100('-'),/, 'PRESSURE',3X,'TEMPERATURE',
C2X,'STRUCTURE',10(8X,A5))
200   FORMAT(5(I1,1X))
202   FORMAT(I2)
301   FORMAT(20X,5('*'), 1X,'1 = METHANE'/,20X,5('*'),1X,'2 = ETHANE'
*   ,/,20X,5('*'),1X,'3 = ETHYLENE',/,20X,5('*'),1X,'4 = PROPANE
*   ',/,20X,5('*'),1X,'5 = CYCLO-PROPANE',/,20X,5('*'),1X,
*   '6 = N-BUTANE
*   ',/,20X,5('*'),1X,'7 = ISO-BUTANE',/,20X,5('*'),1X,
*   '8 = CYCLO-BUTANE
*   ',/,20X,5('*'),1X,'9 = PENTANE',/,20X,5('*'),1X,'10 = ISO-
PENTANE
*   ',/,20X,5('*'),1X,'11 = NEO-PENTANE',/,20X,5('*'),1X,'12 =
*   CYCLO-PENTANE
*   ',/,20X,5('*'),1X,'13 = WATER',/, 20X,5('*'),1X,
*   '14 = HYDROGEN',/,20X,5('*'),1X,
*   '15 = CARBON-DI-OXIDE',/,20X,5('*'),
*   1X,'16 = OXYGEN',/,20X,5('*'),1X,'17 = NITROGEN',/,20X,5('*'),
*   1X,'18 = HYDROGEN SULFIDE',/,20X,5('*'),1X,'19 = XENON',/,20X,
*   5('*'),1X,'20 = ARGON',/,20X,5('*'),1X,'21 = KRYPTON',/,
*   20X,5('*'),1X,'22 = SULFUR HEXAFLOURIDE',/,20X,5('*'),1X,'
*23 = CIS-2-BUTENE',/,20X,5('*'),1X,'24 = TRANS-2-BUTENE',/,20X
*   ,5('*'),1X,'25 = NO COMPONENT',/)
302   FORMAT(8(I1,1X))

```

```

330  FORMAT(2(F5.0,1X),I1,1X,11(F5.0,1X))
329  FORMAT(2(F5.0,1X),I1,10(F5.0,1X))
305  FORMAT(I2)
306  FORMAT(10X,5(2X,E12.5),/,10X,5(2X,E12.5),/,10X,5(2X,E12.5),/
1    ,10X,5(2X,E12.5))
307  FORMAT(10X,6(2X,E12.5),/,10X,6(2X,E12.5),/,10X,6(2X,E12.5),/,
1    10X,6(2X,E12.5),/,12X,E12.5)
308  FORMAT(1(/),10(I2,1X))
310  FORMAT(10X,'COMPONENT',I2,'=',A5)
315  FORMAT(100('-',/))
812  FORMAT(///,25('*'),///,5X,' VALUES USED TO CALCULATE PRESSURES',
15X,25('*'),///,' SIGMA,H2O SC.....',F10.5,/,
2' EPSILON,H2O .....',F10.5,/,
3' DELTA U .....',F10.5,/,
4' DELTA H .....',F10.5,/,
5' BETA .....',F10.5,/,
6' GAMMA .....',F10.5,/,
7' SIGMA H2O LC .....',F10.5,///)
GO TO 1000
1002 WRITE(6,803)
GO TO 1000
1003 WRITE(6,823)
GO TO 1000
1004 WRITE(6,833)
GO TO 1000
1005 WRITE(6,843)
GO TO 1000
1006 WRITE(6,853)
*1000 END
1000 stop
end

C
C
C
C
C
C *****
C          SUBROUTINE FUN(NN,XX,FF)
C *****
C
C          THIS PROGRAM CALCULATES THE DIFFERENCES BETWEEN
C          EXPERIMENTAL AND THEORETICAL HYDRATE FORMING
C          CONDITIONS. THE CALCULATED HYDRATE FORMING CONDITIONS
C          DEPEND UPON THE CHOICE OF KIHARA PARAMETERS
C          , SIGMA AND EPSILON, FOR THE VARIOUS COMPONENTS IN
C          THE GAS PHASE.
C
C
C
C          HYDRATE PHYSICAL PROPERTIES ARE ASSIGNED. SUBROUTINE DATA
C          IS CALLED TO READ GAS PROPERTIES. SUBROUTINE HYDRAT IS
C          CALLED TO CALCULATE HYDRATE FORMING CONDITIONS OR SUB-
C          ROUTINE QUAD IS CALLED FOR QUADRUPLE POINT CALCULATIONS
C          OR FOR SEQUENTIAL CALCULATIONS.
C
C
C

```

```

C      ***** COMMON STATEMENTS *****
      IMPLICIT DOUBLE PRECISION (A-H,O-Z)
      DIMENSION ICODE(10)
      DIMENSION KK(10),XA(11)
      DIMENSION XX(13),PCALC(100),SS(100),AXC(10,2),Y(10)
      DIMENSION ERROR(100)
      DIMENSION A(10),SIGMA(10),EPS(10)
      DIMENSION Y3(100)
      DIMENSION ERR(100),SW(100)
      DIMENSION XL(10)
      DIMENSION NCODE(10)
      DIMENSION GAMMA1(2)
      DIMENSION ZZV(100)
      COMMON/BKSB/NPT,NSETS,IFLAG
      COMMON/STAT/SS
      COMMON/NC/NCODE,NCOMP
      COMMON/AMOL/MA,ISCODE(10)
      COMMON/FUND/SIGMA,EPS,A
      COMMON/TEXPT/PEXP(100),X(15,100),IS(100),T(100),YEXP(100)
      COMMON/SERDAT/T1(100),DT(100),T2(100)
      COMMON/DHDATA/DU(2),DH(2)
      COMMON/AZ/KK,N,MK
      COMMON/JK/JCHK
      COMMON/BEGA/BETA1,GAMMA1
      COMMON/COR/EP SH,DDU,DDH,BETA,GAMMA
      COMMON/VDO/SIGH1,SIGH2
      COMMON/BKSC/IWATER,IPOS,ISTR,IDH
      COMMON/HO/YH3
      COMMON/X/XL
      COMMON/PHAS/NVLLH
      COMMON/STRUC/NSTRUC
      COMMON/IMP/IMPURE,IMCODE,XIMP(100),YCO2(100)
      COMMON/SOLUT/XSOLU,ACTIV,YYYCO2
      COMMON/TBLOC/ITAG
      COMMON/SEQ/ISEQ,TMIN,DELT,TMAX,TQL
      COMMON/LIQUID/LIQ
      COMMON/ZV/ZV
      COMMON/HEAT/DDELH(100),DELH
C      *****
      IF(IWATER.EQ.0)GO TO 105
      IF(IWATER.EQ.1)GO TO 102
      WRITE(6,104)
      GO TO 105
102  WRITE(6,103)
105  CONTINUE
      N=NPT
      SUM=0.0
      WSUM=0.0
      IF(ISEQ.EQ.1.OR.ISEQ.EQ.2)GO TO 80
      IF(NVLLH.EQ.0)GO TO 80
      IF(NSTRUC.EQ.2)GO TO 845
      IF(LIQ.EQ.0)WRITE(6,201)
      IF(LIQ.EQ.1)WRITE(6,2011)
      GO TO 80

```

```

845 WRITE(6,202)
80 CONTINUE
DO 9 K=1,N
C REFERENCE PARAMETERS FOR STRUCTURE I AND II
SIGH1=3.56438
SIGH2=SIGH1
EPSH=102.13357
DU(2)=222.371
DDU=DU(2)
DH(2)=300.984
DDH=DH(2)
BETA1=0.0
BETA=BETA1
GAMMA1(2)=-0.00045
GAMMA=GAMMA1(2)
4 CONTINUE
SIGH1=3.56438
SIGH2=SIGH1
EPSH=102.13357
DU(1)=267.74141
DDU=DU(1)
DH(1)=301.32093
DDH=DH(1)
BETA1=0.0
BETA=BETA1
GAMMA1(1)=-0.00145
GAMMA=GAMMA1(1)
3 CONTINUE
DO 10 KI=1,MA
Y(KI)=0.0
10 CONTINUE
DO 101 I=1,MA
Y(I)=X(I,K)
101 CONTINUE
XSOLU=XIMP(K)
YYYCO2=YCO2(K)
CALL DATA(Y,XA,T(K))
DO 901 I=1,MA
708 Y(I)=XA(I)
EPS(I)=(EPS(I)*EPSH)**0.5
SIGMA(I)=0.5*(SIGMA(I)+SIGH1)
901 CONTINUE
PCALC(K)=PEXP(K)
IF(NVLLH.EQ.0.AND.ISEQ.EQ.0)GO TO 79
IF(ISEQ.EQ.0)GO TO 846
T(K)=T1(K)
TMIN=T1(K)
DELT=DT(K)
TMAX=T2(K)
846 CALL QUAD(T(K),PCALC(K),Y,IS)
GO TO 9
79 ITAG=0
IF(LIQ.EQ.1)ITAG=2
CALL HYDRAT( T(K), PCALC(K), Y, AXC, IS(K))

```

```

Y3(K)=YH3
DDELH(K)=DELH
ZZV(K)=ZV
PCALC(K)=PCALC(K)*6.8948
PEXP(K)=PEXP(K)*6.8948
T(K)=T(K)/1.8
IF(IWATER.EQ.1)GO TO 9
IF(IWATER.EQ.2)GO TO 905
ERROR(K)=ABS(PCALC(K)-PEXP(K))*100.0/PEXP(K)
SS(K)=(1.0-PCALC(K)/PEXP(K))**2
SUM=SUM+SS(K)
GO TO 9
905 ERR(K)=ABS(Y(IPOS)-YEXP(K))*100.0/YEXP(K)
SW(K)=(1.0-Y(IPOS)/YEXP(K))**2
WSUM=WSUM+SW(K)
WRITE(6,909)T(K),PEXP(K),Y(IPOS),YEXP(K),ERR(K),PCALC(K),Y3(K)
9 CONTINUE
IF(NVLLH.NE.0)GO TO 960
IF(ISEQ.NE.0)GO TO 960
IF(IWATER.EQ.2)GO TO 906
IF(IWATER.EQ.1)GO TO 960
FF=SUM/N
FF=(FF**0.5)*100.0
IF(IFLAG.EQ.0)GO TO 950
IF(IDH.EQ.0) GO TO 435
IF(IDH.EQ.1) WRITE(6,778)
DO 434 K=1,N
WRITE(6,779) T(K),PCALC(K),DDELH(K),ZZV(K),(X(J,K),J=1,MA)
434 CONTINUE
435 CONTINUE
IF(IDH.EQ.1) GO TO 962
WRITE(06,902)
DO 913 K=1,N
WRITE(06,900)T(K),PEXP(K),PCALC(K),ERROR(K),IS(K)
913 CONTINUE
WRITE(6,206)FF
GO TO 960
906 YFF=WSUM/N
YFF=(YFF**0.5)*100.0
WRITE(6,908)YFF
GO TO 960
950 WRITE(6,951)
DO 952 K=1,N
WRITE(6,953)T(K),PCALC(K)
952 CONTINUE
962 CONTINUE
C
C * * FORMAT STATEMENTS * *
C
778 FORMAT(///20X,'CALCULATED RESULTS'//1X,'TEMPERATURE',3X,
1 'PRESSURE',4X,'DELTA H',13X,'Y-1',5X,'Y-2',5X,'Y-3'
2 /5X,'(K)',8X,'(KPA)',5X,'(KJ/MOLE)',5X,'Z',/80(' - '))
779 FORMAT(2X,F6.2,5X,F8.2,6X,F6.2,4X,F6.4,2X,10(F6.4,2X))
909 FORMAT(5X,F7.3,2X,F9.3,1X,F15.9,1X,F15.9,3X,F6.1,4X,':',2X,

```

```

AF9.3,1X,F15.9)
206   FORMAT(/,3X,'AVERAGE ERROR IS',3X,F6.2,'%')
201   FORMAT(///20X,'CALCULATED RESULTS'//18X,'V L1 L2 H   QUADRUPLE
1 POINTS'/70('-')/5X,'TEMP',7X,'PRESS',5X,'STRUC',5X,'LIQUID COMP
POSITION'/6X,'(K)',7X,'(KPA)',16X,'WATER FREE'/70('-')/)
2011  FORMAT(///20X,'CALCULATED RESULTS'//18X,'V L1 L2 H   QUADRUPLE
1 POINTS'/70('-')/5X,'TEMP',7X,'PRESS',5X,'STRUC',5X,'VAPOR COMP
POSITION'/6X,'(K)',7X,'(KPA)',16X,10X/70('-')/)
202   FORMAT(///,20X,'CALCULATED RESULTS',//,3X,'V H1 H2 L1
QUADRUPLE
1 POINTS',3X,':',3X,'V L1 L2 H   QUADRUPLE POINTS',/,3X,28('-'),3X
2,':',3X,28('-
'),/,2X,'STRUCT',3X,'TEMP',8X,'PRESS',6X,':',6X,'TEMP
3',8X,'PRESS',7X,'LIQUID COMPOSITION',/,2X,'BELOW',5X,'(K)',8X,
'(K
4PA)',6X,':',7X,'(K)',8X,'(KPA)',8X,'X1',7X,'X2',/,1X,'QUAD PT',
526X,':',30X,'WATER FREE',/,3X,28('-'),3X,':',3X,28('-'),//)
900   FORMAT(1X,4(F10.3,2X),8X,I1)
902   FORMAT(///,20X,'CALCULATED RESULTS',/,20X,10('-'),
*1X,7('-'),//,6X,'TEMP',8X,'PEXP',7X,'PCALC',7X,
*'ERROR',7X,'STRUCTURE',/,6X,'(K)',9X,'(KPA)',6X,
*'(KPA)',/,80('-'),//)
951   FORMAT(///,20X,'CALCULATED RESULTS',/,20X,
A 10('-'),1X,7('-'),//,21X,'TEMP',7X,
B 'PCALC',/,21X,'(K)',8X,'(KPA)',/,18X,21('-'),
C //)
953   FORMAT(19X,F10.3,2X,F10.3)
908   FORMAT(' AVERAGE ERROR IN YH2O CALCULATION',F8.2)
103   FORMAT(///20X,'CALCULATED RESULTS'/20X,18('-')//10X,'2-PHASE',
A45X,'3-PHASE'/4X,36('-'),14X,22('-')/5X,'TEMP',6X,'PRESS',
A10X,'Y-2PHASE',10X,':',9X,'PRESS',5X,'Y-3PHASE'/5X,'(K)',
A9X,'(KPA)',9X,'H2O',14X,':',6X,'(KPA)',10X,'H2O'//)
104   FORMAT(///20X,'CALCULATED RESULTS'/20X,18('-')//20X,'2-PHASE',
A50X,'3-PHASE'/5X,60('-'),7X,25('-')/6X,'TEMP',7X,'PRESS',8X,
A'YCALC',12X,'YEXP',8X,'ERROR',4X,':',4X,'PRESS',10X,'Y-3PHASE'
A/7X,'(K)',7X,'(KPA)',9X,'H2O',15X,'H2O',16X,':',5X,'(KPA)',
A11X,'H2O'//)
960   RETURN
      END

C
C
C *****
C SUBROUTINE QUAD(T,P,Y,IS)
C *****
C
C THIS SUBROUTINE CALCULATES QUADRUPLE POINTS BY FINDING THE
C POINT OF INTERSECTION OF 'V L1 H' AND DEW POINT CURVES TO
C GET THE 'V L1 L2 H' POINT ; OR INTERSECTION OF 'L1 L2 H'
C AND BUBBLE POINT CURVE TO GET 'V L1 L2 H' ;
C AND 'V L1 H1' AND 'V L1 H2'
C CURVES TO GET THE 'V L1 H1 H2' POINT.
C
C THIS SUBROUTINE IS ALSO CALLED FOR SEQUENTIAL CALCULATIONS
C AT SPECIFIC INTERVALS.

```



```

C
C   IST0=STRUCTURE AT STARTING TEMP T0
C   IST2=STRUCTURE BEYOND THE QUAD POINT
C   ID=VARIABLE INDICATING WHETHER VLH1H2 QUAD POINT HAS BEEN
C   CALCULATED. 0--NOT CALCULATED; 1--CALCULATED.
C   ITAG=VARIABLE INDICATING WHICH FUGACITY COEFFICIENTS ARE
C   REQUIRED FROM SUBROUTINE PHIMIX. 0--ONLY VAPOR
C   1--VAPOR AND LIQ; 2--LIQUID ONLY.
C
      IMPLICIT DOUBLE PRECISION (A-H,O-Z)
      DIMENSION Y(15),XL(10)
      DIMENSION PH(2),PRESS(2),ISCHEC(2),PBD(2),TQ(60),PQ(60)
      DIMENSION PLP2(60)
      DIMENSION PLP1(60)
      DIMENSION NCODE(10)
      COMMON/STRUC/NSTRUC
      COMMON/PHAS/NVLLH
      COMMON/X/XL
      COMMON/NC/NCODE,NCOMP
      COMMON/TBLOC/ITAG
      COMMON/SEQ/ISEQ,TMIN,DELT,TMAX,TQL
      COMMON/LIQUID/LIQ
      COMMON/CRITCL/NCRIT,TCRIT
      COMMON/HEAT/DDELH(100),DELH
      COMMON/BKSC/IWATER,IPOS,ISTR,IDH
      COMMON/ZV/ZV
      COMMON/HELP/IST0,IST2,ISLOW,N0,NQ
      DOUBLE PRECISION YNEW(100)
C
C
      T0=T
      ITER=0
      DTQ=1.0
      DTH=1.0
      N0=1
      AXC=0
      NQ=N0
      ID=0
      IDEW=0
      M=1
      IF(NVLLH.NE.0)GO TO 107
C
C   IF NVLLH IS ZERO THEN NO QUAD POINTS ARE REQUIRED BUT THIS
C   SUBROUTINE HAS BEEN CALLED FOR SEQUENTIAL CALCULATIONS.
C
      THH=TMAX+2.*DELT
      TQL=TMAX+2.*DELT
      IF(LIQ.EQ.1)TQL=TMIN-2*DELT
      GO TO 10
107  DO 105 K=1,2
17   IF(NSTRUC.EQ.2.AND.ID.EQ.0)GO TO 101
      PRESS(K)=P
      ITAG=0
      IF(LIQ.EQ.1)ITAG=2

```

```

        CALL HYDRAT(T,PRESS(K),Y,AXC,IS)
        IF(NCRIT.EQ.1)GO TO 801
        GO TO 103
101     DO 102 IQ=1,2
        IS=IQ
        PH(IS)=P
        ITAG=0
        CALL HYDRAT(T,PH(IS),Y,AXC,IS)
        IF(NCRIT.EQ.1)GO TO 801
102     CONTINUE
C
C   ** CHECK WHICH STRUCTURE IS FORMED AT TEMP T **
        IF(PH(2).LT.PH(1))IS=2
        IF(PH(1).LT.PH(2))IS=1
        IF(PH(1).EQ.PH(2))GO TO 130
        ISCHEC(K)=IS
16      PRESS(K)=PH(IS)
C
C   ** IST0 IS THE STRUCTURE FORMED AT THE STARTING TEMP (GIVEN TEMP) **
        IF(NQ.EQ.N0)IST0=IS
        NQ=NQ+1
103     CONTINUE
        CALL BUBDEW(T,PBD(K),Y)
        IF(LIQ.EQ.1)GO TO 140
        IF(PBD(K).GE.PRESS(K))GO TO 150
        IDEW=IDEW+1
        IF(IDEW.GT.5)T=T-1.0
        IF(IDEW.LT.5)T=T-0.4
        IF(IDEW.GT.20)GO TO 152
        GO TO 107
140     IF(PBD(K).LT.PRESS(K))GO TO 150
        IDEW=IDEW+1
        IF(IDEW.LE.2)T=T+0.2
        IF(IDEW.GT.2)GO TO 110
        GO TO 107
150     TCOMP=T
        IF((NSTRUC.EQ.1.OR.ID.EQ.1).AND.ABS(TQL-T).LT.5.0)GO TO 45
        IF(LIQ.EQ.0)T=T+1.0
        IF(LIQ.EQ.1)T=T-1.0
        IF(LIQ.EQ.0)DTQ=1.0
        IF(LIQ.EQ.1)DTQ=-1.0
        GO TO 105
45      IF(LIQ.EQ.0)T=T+0.05
        IF(LIQ.EQ.1)T=T-0.1
        IF(LIQ.EQ.0)DTQ=0.05
        IF(LIQ.EQ.1)DTQ=-0.1
105     CONTINUE
        IF(NSTRUC.EQ.1)GO TO 106
        IF(ID.EQ.1)GO TO 106
        IF(ISCHEC(1).EQ.ISCHEC(2))GO TO 106
        T=T-3
        GO TO 107
106     AMH=(DLOG(PRESS(2))-DLOG(PRESS(1)))/DTQ
        CH=DLOG(PRESS(2))-AMH*(T-DTQ)

```

```

AML=(DLOG(PBD(2))-DLOG(PBD(1)))/DTQ
CL=DLOG(PBD(2))-AML*(T-DTQ)
TQL=(CH-CL)/(AML-AMH)
PQL=EXP(AMH*TQL+CH)
IF(NSTRUC.EQ.1)GO TO 109
IF(ID.EQ.1)GO TO 182
IF(T.EQ.(T0+1))PQLOW=PQL
IF(PQL.GT.PQLOW)GO TO 113
PQLOW=PQL
ISLOW=IS
113 TQ(M)=TQL
PQ(M)=PQL
PLP1(M)=PRESS(1)
PLP2(M)=PRESS(2)
IF(IS.NE.IST0)GO TO 111
IF(T.GT.TQL)GO TO 120
M=M+1
IF(M.EQ.50)GO TO 112
GO TO 107
C **IF IST0=ISLOW NO VLHH PRESENT **
111 IF(IST0.EQ.ISLOW)GO TO 114
IST2=IS
AM1=(DLOG(PLP2(M-1))-DLOG(PLP1(M-1)))/DTH
AM2=(DLOG(PLP2(M))-DLOG(PLP1(M)))/DTH
C1=DLOG(PLP2(M-1))-AM1*(T-3)
C2=DLOG(PLP2(M))-AM2*(T-1)
THH=(C1-C2)/(AM2-AM1)
PHH=EXP(AM2*THH+C2)
182 ID=1
IF(ABS(TQL-TCOMP).LE.0.1)GO TO 181
ITER=ITER+1
IF(ITER.GT.500)GO TO 151
T=(TQL+TCOMP)/2.0
GO TO 107
181 CONTINUE
IF(ISEQ.EQ.1.OR.ISEQ.EQ.2)GO TO 10
THH=THH/1.8
TQL=TQL/1.8
PHH=PHH*6.8948
PQL=PQL*6.8948
WRITE(6,203)IST0,THH,PHH,TQL,PQL,(XL(I),I=1,NCOMP)
GO TO 120
114 WRITE(6,117)
TQ(1)=TQ(1)/1.8
PQ(1)=PQ(1)*6.8948
WRITE(6,118)IST0,TQ(1),PQ(1),(XL(I),I=1,NCOMP)
GO TO 120
109 IF(ABS(TQL-TCOMP).LE.0.1)GO TO 110
455 ITER=ITER+1
IF(ITER.GT.500)GO TO 151
T=(TQL+TCOMP)/2.0
IF(LIQ.EQ.1)T=TCOMP
GO TO 107
110 IF(ISEQ.EQ.0)GO TO 104

```

```

10      T=TMIN-DELT
        DO 257 J = 1, NCOMP
        YNEW(J) = Y(J)
257      CONTINUE
        IF(NSTRUC.EQ.2)IS=IST0
C
C      ** CHECK FOR HEAT OF DISSOCIATION CALCULATIONS **
C
        IF(LIQ.EQ.0.AND.IDH.EQ.0)WRITE(6,250)
        IF(LIQ.EQ.1)WRITE(6,2501)
        IF(IDH.EQ.1)WRITE(6,886)
        ITAG=0
        IF(T.GT.TQL)ITAG=2
        IF(ISEQ.EQ.2)TMAX=TQL
        IF(ISEQ.EQ.2.AND.LIQ.EQ.1)GO TO 853
        DO 91 I=1,100
        T=T+DELT
        IF(T.GT.TMAX)GO TO 120
        CALL HYDRAT(T,P,YNEW,AXC,IS)
        TT=T/1.8
        PP=P*6.8948
        IF(IDH.EQ.0) GO TO 14
        WRITE(6,885) TT,PP,DELH,ZV,(YNEW(N),N=1,NCOMP)
        GO TO 8567
14      CONTINUE
        IF(T.LT.TQL)WRITE(6,904)TT,PP,IS,(YNEW(N),N=1,NCOMP)
        IF(T.GT.TQL)WRITE(6,904)TT,PP,IS,(XL(N),N=1,NCOMP)
8567     CONTINUE
        TTHH=THH/1.8
        PPHH=PHH*6.8948
        IF(NSTRUC.EQ.2.AND.(T+DELT).GT.THH)IS=IST2
        IF(NSTRUC.EQ.2.AND.T.LT.THH.AND.(T+DELT).GT.THH)WRITE(6,153)
1TTHH,PPHH
        IF((T+DELT).GE.TQL)GO TO 191
        GO TO 91
191     PPQL=PQL*6.8948
        TTQL=TQL/1.8
        IF(T.LT.TQL.AND.(T+DELT).GE.TQL.AND.ISEQ.NE.2)WRITE(6,71)TTQL
1,PPQL
        IF(T.LT.TQL.AND.(T+DELT).GE.TQL.AND.ISEQ.EQ.2)WRITE(6,72)TTQL
1,PPQL
        ITAG=2
        IF(LIQ.NE.0)GO TO 91
        DO 53 J=1,NCOMP
        Y(J)=XL(J)
53      CONTINUE
91      CONTINUE
        WRITE(6,123)
        GO TO 120
104     TQL=TQL/1.8
        PQL=PQL*6.8948
        WRITE(6,444)(XL(I),I=1,NCOMP)
        WRITE(6,444)(Y(J),J=1,NCOMP)
444     FORMAT(' XL=',10(4X,F6.3))

```

```

C
      WRITE(6,119)TQL,PQL,IS,(XL(I),I=1,NCOMP)
      GO TO 120
112   WRITE(6,121)
      GO TO 114
130   WRITE(6,108)PH(1)
120   T=T0
      GO TO 800
151   WRITE(6,100)
      GO TO 800
152   TQL=TQL/1.8
      PQL=PQL*6.8948
      WRITE(6,154)TQL,PQL
      GO TO 800
853   WRITE(6,823)
      DO 258 I=1,NCOMP
      Y(I)=YNEW(I)
258   CONTINUE
C -----FORMATS-----
885   FORMAT(1X,F6.2,3X,F8.2,4X,F7.3,5X,F6.4,4X,10(F6.4,2X))
886   FORMAT(///25X,'CALCULATED RESULTS',///3X,'TEMP',4X,'PRESSURE'
2     ,3X,'DELTA H',8X,'Z',10X,'GAS COMPOSITION',/4X,'(K)',6X,'(KPA)'
3     ,4X,'(KJ/MOLE)',15X,'Y-1',5X,'Y-2',5X,'Y-3'/80('-'))
121   FORMAT(' NOT CONVERGED IN QUAD, PROBABLY NO V L H1 H2
EXISTS')
100   FORMAT(' QUADRUPLE POINT CALCULATIONS NOT CONVERGED IN QUAD
1. INITIAL TEMP MAY NOT BE IN RANGE.')
119   FORMAT(4X,F6.2,5X,F9.2,4X,I1,5X,10(F6.4,5X))
C901  FORMAT(2F,I,'FOR901')
118   FORMAT(4X,I1,35X,F6.2,5X,F8.2,5X,10(F6.4,5X))
203   FORMAT(4X,I1,5X,F6.2,5X,F8.2,5X,':',5X,F6.2,5X,F8.2,5X,10(F6.4
1,5X))
123   FORMAT(1X,40('-'))
250   FORMAT(///20X,'CALCULATED RESULTS'/20X,10('-'),1X,7('-')/10X,
1'TEMP',10X,'PRESS',4X,'STRUCTURE',8X,'GAS COMPOSITION',/11X,
1'(K)',10X,'(KPA)',16X,'Y 1',4X,'Y 2',4X,'Y 3'/5X,60('-'))
2501  FORMAT(///20X,'CALCULATED RESULTS'/20X,10('-'),1X,7('-')/10X,
1'TEMP',10X,'PRESS',7X,'STRUCTURE',5X,'LIQ COMPOSITION',/11X,
1'(K)',10X,'(KPA)',16X,'XL1',5X,'XL2',5X,'XL3'/5X,60('-'))
904   FORMAT(9X,F6.2,8X,F8.2,6X,I3,3X,10(F6.4,2X))
108   FORMAT(' QUAD PT AT PRESS=',F10.2)
117   FORMAT(' V L H1 H2 EQUILIBRIUM NOT PRESENT')
153   FORMAT(9X,F6.2,8X,F8.2,2X,'QUADRUPLE POINT V L H1 H2')
71    FORMAT(9X,F6.2,8X,F8.2,2X,'QUADRUPLE POINT V L1 L2 H'//53X,
1'LIQUID COMPOSITION'/48X,'X 1',6X,'X 2',6X,'X 3'//)
72    FORMAT(9X,F6.2,8X,F8.2,2X,'QUADRUPLE POINT V L1 L2 H'//)
154   FORMAT('/' NOT CONVERGED DUE TO TEMP CROSSING QUAD POINT'/'
TQL='
1,F6.2,2X,'PQL=',F8.2)
823   FORMAT(' ERROR IN INPUT DATA ISEQ=2 AND LIQ=1')
843   FORMAT(' QUAD POINT NOT CALCULATED'/' VAPOR IS
1 CLOSE TO CRITICAL'/' CRITICAL TEMP OF MIX=',F6.2,'K'//)
C -----
      GO TO 800

```

```

801   TCRIT=TCRIT/1.8
      WRITE(6,843)TCRIT
800   RETURN
      END
C     *****
C
C
C
C
C     *****
C     SUBROUTINE HYDRAT(T,P,XU,VY,IS)
C     *****
C     PROGRAM FOR CALCULATION OF THE DISSOCIATION PRESSURES
C     OF GAS HYDRATES FROM METHANE, ETHANE, AND PROPANE
C     BY JERRY HOLDER, CHEMICAL ENGINEERING U. MICH.
C
C     THE DISSOCIATION PRESSURE IS THAT PRESSURE AT WHICH
C     THE CHEMICAL POTENTIAL OF WATER IN THE HYDRATE IS
C     EXACTLY EQUAL TO THE CHEMICAL POTENTIAL OF THE WATER
C     IN THE WATER PHASE.  THE CHEMICAL POTENTIAL OF THE
C     HYDRATED WATER IS CALCULATED USING THE THEORY DEVELOPED
C     BY VAN DER WAALS WHICH ASSUMES 1) THERE IS ONE MOLECULE
C     OF GAS PER HYDRATE CAVITY, 2) ONLY THE TRANSLATIONAL
C     PARTITION FUNCTION IS AFFECTED IN THE ENCAGED STATE
C     3) ONLY FIRST NEIGHBOR INTERACTIONS ARE IMPORTANT.
C     THE KIHARA POTENTIAL MODEL IS USED.
C
C     THE UPDATED Q* VERSION INCLUDES 2ND AND 3RD SHELL
C     CONTRIBUTIONS AND SHELL ASPHERICITY.
C
C     THIS SUBROUTINE ALSO CALCULATES WATER CONTENT AND
C     HEAT OF DISSOCIATION.
C
C     *** LIST OF VARIABLES ***
C
C     AR, BR, CR - CONSTANTS FOR CALCULATING THE DISSOCIATION
C                 PRESSURE OF THE REFERENCE HYDRATE. THESE ARE
C                 FROM FITTED DATA.
C     C          - THE SO CALLED LANGMUIR ADSORPTION CONSTANTS
C                 WHICH SPECIFY THE RELATIVE AMOUNT OF GAS IN
C                 A GIVEN TYPE OF CAVITY. SUBSCRIPTS I,J REFER
C
C     DH          - DIFFERENCE IN ENTHALPY BETWEEN THE OCCUPIED AND
C                 UNOCCUPIED HYDRATE.
C     DU          - DIFFERENCE IN CHEM. POTENTIAL (AS DH)
C     DV          - DIFFERENCE IN MOLAR VOLUME
C     P0          - DISSOCIATION PRESSURE OF REFERENCE HYDRATE
C                 AT 273 DEG K
C     PR          - DISSOCIATION PRESSURE OF REF. HYD. AT T
C     T           -TEMPERATURE( DEG K)
C                 (NOTE THAT T IS CHANGED FROM R TO K )
C     VM          - NUMBER OF MOLECULES OF WATER PER CAVITY
C     VY(I,J)     - FRACTION OF CAVITIES I OCCUPIED BY MOLECULE J
C     XU(I)       - MOLE FRACTION OF GAS I IN THE GAS PHASE

```

```

C      ZMU,ZMOLD, ETC. - CHEMICAL POTENTIAL DIFFERENCES.
C
C
C      *****      COMMON STATEMENTS      *****
C
C      IMPLICIT DOUBLE PRECISION (A-H,O-Z)
C      external psat
C      DIMENSION KK(10)
C      DIMENSION XX(13)
C      DIMENSION XL(10),PHIL(10)
C      DIMENSION XU(10),PHI(10),XS(10),VY(10,2),VM(2),
2 C(10,2),NCODE(10),SCC(2)
C      DIMENSION XXMAX(10),XXMIN(10),B2(10)
C      DIMENSION XW(10)
C      DIMENSION GAMMA1(2)
C      DIMENSION XHYD(10)
C      DIMENSION VVY(2)
C      COMMON /PVDATA/ DV,AR,BR,CR
C      COMMON/AZ/KK,N,MK
C      COMMON/AMOL/MA,ISCODE(10)
C      COMMON/NC/NCODE,NCOMP
C      COMMON/MAMI/XXMAX,XXMIN
C      COMMON /HYD/ IHYD
C      COMMON/FUND/SIGMA(10),EPS(10),A(10)
C      COMMON/DHDATA/HDU(2),HDH(2)
C      COMMON/JK/JCHK
C      COMMON/VDO/SIGH1,SIGH2
C      COMMON/BEGA/BETA1,GAMMA1
C      COMMON/BKSC/IWATER,IPOS,ISTR,IDH
C      COMMON/TBLOC/ITAG
C      COMMON/HO/YH3
C      COMMON/SOLUT/XSOLU,ACTIV,YYYCO2
C      COMMON/IMP/IMPURE,IMCODE,XIMP(100),YCO2(100)
C      COMMON/TFREEZ/TT0
C      COMMON/ZV/ZV
C      COMMON/X/XL
C      COMMON/PH/PHIL
C      COMMON/WATER/NW
C      COMMON/STOR/XUSTOR(10)
C      COMMON/CRITCL/NCRIT,TCRIT
C      COMMON/HEAT/DDELH(100),DELH
C      COMMON/HELP/IST0,IST2,ISLOW,NQ,N0
C
C      *****
C
C      * * CHECK IF STRUCTURE DATA IS TO BE PRINTED * *
C
C      JACKQ=0
C      Saturation pressure is in atmospheres.  Partial molar volume is in
C
C      ml/mole.  Saturation pressure is the pressure at which a given
C      mole fraction of gas is dissolved in the liquid.
C      PSATD=30.30

```

```

        PMOLVOL=35.

17      CONTINUE
        IF(ITAG.NE.2)GO TO 40
        DO 43 I=1,NCOMP
        XL(I)=XU(I)
43      CONTINUE
40      IF(ISTR.NE.1)GO TO 260
        WRITE(06,351)
        DO 258 I=1,MA
        WRITE(06,352)KK(I),A(I),SIGMA(I),EPS(I)
258     CONTINUE
C
260    DO 5 I=1,NCOMP
        DO 5 J=1,2
5      VY(I,J)=0.0
        T=T/1.8
        PSAVE=P
        P=P/14.696
        IF( IS.EQ.1) GO TO 11
C
C      *** DATA FOR STRUCTURE II
C
        VM(1)=0.11765
        VM(2)=0.058823
        DV=4.99644
        IF(T.LE.(273.15-TT0)) DV=DV-1.6
        DU=HDU(2)
        DH=HDH(2)
        GAMMA=GAMMA1(2)
        GO TO 12
C
C      *** DATA FOR STRUCTURE I ***
C
11     VM(1)=2./46.
        VM(2)=6./46.
        DU=HDU(1)
        DH=HDH(1)
        DV=4.5959
        GAMMA=GAMMA1(1)
        IF(T.LE.(273.15-TT0)) DV=DV-1.6
C
C      *** LANGMUIR CONSTANTS
C
12    DO 15 K=1,NCOMP
        DO 15 J=1,2
        J5=J
        K5=K
        K1=K
777   CONTINUE
        C(K,J)=CC(T,IS,J5,K5,K1)
15    CONTINUE
C
C

```



```

C           AT ZERO DEGREES CENTIGRADE
C
C           ZMUTPR=DU/273.15
C           ZMOLD=ZMUTPR
C           AH=2616.398+DH
C           TO=273.15
C
C           *** ENTHALPIC CHANGE OF CHEMICAL POTENTIAL WITH
C           TEMPERATURE (WATER PHASE)
C
C           ***** ALPHA, BETA, AND GAMMA ARE PARAMETERS *****
C           ***** IN THE ENTHALPIC INTEGRAL *****
C           IF(T.GT.273.1.AND.T.LT.273.2) GO TO 8999
C           ALPHA=DH
C           BETA=BETA1
C           IF(T.LT.(273.15-TT0)) GO TO 8998
C           ALPHA=ALPHA-1436.0+9.054*273.15+0.021163*(273.15**2)
C           BETA=BETA+9.054+0.042326*273.15
C           GAMMA=GAMMA-0.021163
8998      CONTINUE
C           HINT=ALPHA*(1./T-1./273.15)+BETA*DLOG(T/273.15)
C           * +GAMMA*(T-273.15)
C           GO TO 9988
8999      HINT=0.0
9988      CONTINUE
C
C
C           *** VOLUMETRIC CHANGE OF CHEMICAL POTENTIAL WITH
C           TEMPERATURE (DP=DP/DT*DT)
C           GAUSSIAN INTEGRATION IS USED.
C           ZM=HINT+ZMOLD
C           ZMUTPR=T*ZM
C
C           We know that ZMUTPR is the liquid phase chemical potential
C           Instead of having the program calculate the pressure point where
C           the liquid phase chemical potential and the hydrate phase
C           chemical
C           potentials intersect, we need to calculate the plain hydrate and
C           liquid potential. We also need to print out ZMUPTR since it is
C           the liquid phase potential.
C           ***** NEWTONS METHOD IS USED TO FIND THE PRESSURE AT
C           WHICH THE CHEMICAL POTENTIAL OF THE HYDRATED
C           AND LIQUID WATER ARE THE SAME (FOR THE SPECIFIED
C           TEMPERATURE).
C
C
C           P1=1
C           P2=2
C           DO 30 JJ=1,2000
C           DMU1=0.0
C           DMU2=0.0
C           DO 28 JJJ=1,2
C           P=P1
C           P3=P
C           IF (P.GT.PSATD) P3=PSATD

```

```

C      IF(JJJ.EQ.2) P=P2
C      *** GET THE FUGACITY COEFFICIENTS( PHI IS RETURNED)
C
C
C      CALL PHIMIX(XU,14.696*P3,1.8*T,PHI)
C      IF(NCRIT.EQ.1)GO TO 821
C      IF(ITAG.NE.2)GO TO 481
C      DO 44 LI=1,NCOMP
C      PHI(LI)=PHIL(LI)
44      CONTINUE
C      X1=0.0
C      GO TO 56
481     X1=0.0
C      IF(T.LT.(273.15-TT0)) GO TO 56
C      DO 55 J7=1,NCOMP
C      KJ=NCODE(J7)
C      Y7=XU(J7)
C      PHI7=PHI(J7)
C      CALL SOL7(KJ,Y7,PHI7,P3,T,X6)
C      X1=X1+X6
55      CONTINUE
56      CONTINUE
C      IF(ABS(P).LT. .1) P=P+.1
C      ZMUA=ZMUTPR+DV/41.2929*(P)
C      ZMUA=ZMUA-1.987*T*DLOG(1-X1)
C      WRITE(6,8890)ZMUA
C      ZMU=0.0
C      DO 27 I=1,2
C      CCC=0.0
C      DELTAP=0
C      IF(P.GT.PSATD)DELTAP=P-PSATD
C      DO 26 II=1,NCOMP
C      FUGAC=PHI(II)*P3*DEXP(PMOLVOL*DELTAP/(82.1*T))
C      CCC=CCC+ C(II,I)*XU(II)*FUGAC
C      WRITE(6,5000)FUGAC
C      WRITE(6,5001)PSATD
5000    FORMAT(5X,'FUGACITY=',F10.5)
5001    FORMAT(5X,'PSAT=',F10.5)
C      Need to obtain exact value of R with more precision than 82
26      CONTINUE
C      SCC(I)=CCC
C
C      *** POTENTIAL DIFFERENCE OF HYDRATE WATER
C
C      IF(CCC.GT.-0.9) GO TO 461
C      WRITE(6,457) CCC,C(1,1),XU(1),PHI(1),P
457     FORMAT(5F10.2)
461     CONTINUE
C      ZMUTP=1.987*T*DLOG(1.+CCC)*VM(I)
C      WRITE(6,8891)ZMUPT
27      ZMU=ZMUTP+ZMU
C      DMU=ZMUA-ZMU
C      IF(IMPURE.EQ.0.OR.T.LT.(273.15-TT0).OR.XSOLU.EQ.0.0)GO TO 148
C      DMU=DMU-1.987*T*DLOG(ACTIV*(1.0-XSOLU-X1))

```

```

C          GO TO 147
C 148      DMU=DMU-1.987*T*DLOG(1.0-X1)
C          ZMUA1=ZMUA-1.987*T*DLOG(1.0-X1)
C 147      DMU1=DMU2
C          DMU2=DMU
C
C          *** CHECK TO SEE IF CHEMICAL POTENTIALS ARE EQUAL
C          IF NOT, EXTRAPOLATE(OR INTERPOLATE) TO A NEW PRESSURE
C
C          IF(ABS(P2/P1-1.)<.001.AND.ABS(DMU)<1.) GO TO 35
C          IF(ABS(DMU)<.0005) GO TO 35
C 28 CONTINUE
C          IF(ABS((P1-P2)/P2)<1.E-5) P2= P2+1.0
C          IF(ABS(DMU2-DMU1)<.001) GO TO 29
C          P3=P1-(P2-P1)/(DMU2-DMU1)*DMU1
C          IF(P3<=0.0) P3=0.01
C          IF(P3>2.E4) P3=2.E4
C          P1=P3
C 29 P3=P1+3
C 29 P2=P1+2
C          Pold=P1
C          P1=P1+1
C          P=P1
C          WRITE(6,8880)T
C          WRITE(6,8881)Pold
C          WRITE(6,8882)X1
C          WRITE(6,8883)XSOLU
C          WRITE(6,8884)TTO
C          WRITE(6,8885)ACTIV
C          WRITE(6,8886)ZMU
C          WRITE(6,8887)ZMUA
C 30 CONTINUE
C          GO TO 45
C          IHYD=IS
C          P=P1
C          WRITE(6,505) DMU, IS,XU(1),T
C 505 FORMAT(' FAILED TO CONVERGE IN HYDRATE',/,6X,
C          2 'DIFFERENCE IN CHEMICAL POTENTIAL OF WATER',/,
C          3 'IN THE HYDRATE AND WATER PHASES IS',2X,
C          4 E9.2/, ' STRUCTURE IS',I4,2F10.5)
C 35 CONTINUE
C 8880      FORMAT(5X,'T=',F10.5)
C 8881      FORMAT(5X,'P=',F10.5)
C 8882      FORMAT(5X,'X1=',F10.5)
C 8883      FORMAT(5X,'XSOLU=',F10.5)
C 8884      FORMAT(5X,'TTO=',F10.5)
C 8885      FORMAT(5X,'ACTIV=',F10.5)
C 8886      FORMAT(5X,'ZMU=',F10.5)
C 8887      FORMAT(5X,'ZMUA=',F10.5)
C 8888      FORMAT(5X,'XU(1)=',F10.5)
C 8889      FORMAT(5X,'XU(2)=',F10.5)
C 8890      FORMAT(5X,'Chemical potential of liquid phase =',F10.5)
C 8891      FORMAT(5X,'Chemical potential of the hydrate phase =',F10.5)
C          *** CALCULATE FRACTIONAL OCCUPANCY OF THE CAVITY

```

```

C
  DO 45 I=1,2
  DO 45 J=1,NCOMP
  IF(ABS(1+SCC(I)).LT.1.E-4) WRITE(6,9876) SCC(I)
9876 FORMAT(' ERROR IN LANGMUIR CALCULATION',F10.7)
  VY(NCODE(J),I) = C(J,I)*XU(J)*PHI(J)*P/(1+SCC(I))
 45 CONTINUE
    IF(IDH.EQ.0) GO TO 46
C
C   ** HEAT OF DISSOCIATION CALCULATIONS **
C
  JACKQ=JACKQ+1
  IF(JACKQ.EQ.2) GO TO 412
  PH1=P
  TH1=T
  T=T+0.01
  T=T*1.8
  P=P*14.696
  GO TO 17
412  CONTINUE
  JACKQ=0
  VVY(1)=0.0
  VVY(2)=0.0
  DO 7 J=1,NCOMP
  DO 7 I=1,2
  VVY(I)=VVY(I)+VY(NCODE(J),I)
 7   CONTINUE
  IF(IS.EQ.1) GO TO 717
  HN=136./(VVY(1)*16.+VVY(2)*8.)
  DV1=DV
  GO TO 718
717  HN=46./(VVY(1)*2.+VVY(2)*6.)
718  CONTINUE
C   WRITE(6,7777) ZV
C   WRITE(6,7778) T
C   WRITE(6,7779) TH1
C   WRITE(6,7780) P
C   WRITE(6,7781) PH1
C   WRITE(6,7782) VVY(1)
C   WRITE(6,7783) VVY(2)
C   WRITE(6,7784) HN
C   WRITE(6,7785) DV1
7777  FORMAT(' ZV=',F10.5)
7778  FORMAT(' T=',F10.5)
7779  FORMAT(' TH1=',F10.5)
7780  FORMAT(' P=',F10.5)
7781  FORMAT(' PH1=',F10.5)
7782  FORMAT(' VY(1)=',F10.5)
7783  FORMAT(' VY(2)=',F10.5)
7784  FORMAT(' HN=',F10.5)
7785  FORMAT(' DV=',F10.5)
  DELHH=ZV*82.05*T**2*((DLOG(P/PH1))/(T-TH1))
  DELH2=HN*DV*T*((P-PH1)/(T-TH1))
  DELH=DELHH-DELH2

```

```

      DELH=DELH/9869.2
      DELHH=DELHH/9869.2
      DELH2=DELH2/9869.2
C      WRITE(6,7786) DELHH
C      WRITE(6,7787) DELH2
C      WRITE(6,7788) DELH
7786  FORMAT(' DELH1=',F10.3)
7787  FORMAT(' DELH2=',F10.3)
7788  FORMAT(' DELH=',F10.3)
      T=TH1
      P=PH1
46    CONTINUE
      COMSUM=0.0
      DO 143 J=1,NCOMP
      COMSUM=COMSUM+VY(NCODE(J),1)*VM(1)+VY(NCODE(J),2)*VM(2)
143   CONTINUE
      DO 144 J=1,NCOMP
      XHYD(J)=(VY(NCODE(J),1)*VM(1)+VY(NCODE(J),2)*VM(2))/COMSUM
144   CONTINUE
C      WRITE(7,1020)T,(VY(NCODE(J),1),VY(NCODE(J),2),J=1,MA)
1020  FORMAT(' T (K)',4X,'HYDRATE COMPOSITION'/9X,'XH1   XH2'/
      1F6.2,4X,10(F6.4))
700  T=T*1.8
      P=P*14.696
13    CONTINUE
C      WRITE(06,1005)
1005  FORMAT(/,14X,'PHI(I)',20X,'LANGMUIR COEFFICIENTS'
      *  ,/,14X,5('-'),20X,21('-'))
      DO 158 I=1,NCOMP
C      WRITE(06,1008)PHI(I),(C(I,J),J=1,2)
C1008  FORMAT(5X,1F,10X,2F)
158   CONTINUE
C
C      * * CALCULATIONS TO DETERMINE THE WATER CONTENT OF A GAS * *
C      * * IN EQUILIBRIUM WITH THE HYDRATE * *
C      * * TEMP(R) AND PRESSURE(PSIA) * *
C      * * IWATER = 0 : DONT PERFORM CALCULATIONS * *
C      * * IWATER = 1 : CALCULATE YH2O * *
C      * * IWATER = 2 : CALCULATE YH2O AND COMPARE WITH EXPMTL DATA *
      *
C      * *
C
      IF(IWATER.EQ.0)GO TO 821
C
C      * * PH=3-PHASE PRESSURE * *
C      * * P =2-PHASE PRESSURE * *
C
C
      PH=P
      P=PSAVE
      PSW=PSAT(T)
      IF(IS.EQ.1)VHYD=22.6
      IF(IS.EQ.2)VHYD=22.9
      IF(T.LT.491.67)VH2O=19.6

```

```

IF(T.GE.491.67)VH2O=18.0
FWSAT=PSW*(1-X1)*EXP(0.0014926491/T*VH2O*(PH-PSW))
FWSATP=FWSAT*EXP(0.0014926491/T*VHYD*(P-PH))
CALL PHIMIX(XU,P,T,PHI)
T=T/1.8
P=P/14.696
ZWAT=0.0
DO 127 I=1,2
CCC=0.0
DO 126 II=1,NCOMP
CCC=CCC+C(II,I)*XU(II)*PHI(II)*P
126 CONTINUE
ZW=VM(I)*DLOG(1+CCC)
127 ZWAT=ZWAT+ZW
C
DO 23 I=1,NCOMP
XUSTOR(I)=XU(I)
23 CONTINUE
ICOUN=1
COUNT=1
MA=MA+1
NCOMP=NCOMP+1
IPOS=MA
NW=1
PHI(IPOS)=1.0
PHIX=1.0
C**
IF(14.696*P.GT.PH)GO TO 618
GO TO 835
C
C ** 2-PHASE WATER CONTENT CALCULATION **
618 ZMUP=0.0
GO TO 85
85 FWP=FWSATP*DEXP(ZMU/(1.987*T)-ZWAT)
C
C * * CALCULATE A TEST VALUE OF YH20 * *
T=1.8*T
P=14.696*P
C
815 YH20N=FWP/(PHI(IPOS)*P)
IF(YH20.GT.0.05.OR.YH20.LT.0.0)GO TO 800
GO TO 801
800 WRITE(6,803)ICOUN,YH20
YH20=0.05
C
C
C
801 XU(IPOS)=YH20N
CALL NORMW(NCOMP,IPOS,XU)
YH20=YH20N
807 CALL PHIMIX(XU,P,T,PHI)
YH20N=FWP/(PHI(IPOS)*P)
ICOUN=ICOUN+1
IF(ABS((YH20N-YH20)/YH20N).GT.1.E-3.AND.ICOUN.LT.30)GO TO 801

```

```

      XU(IPOS)=YH20N
C
C  ** 3-PHASE WATER CONTENT CALCULATION **
835  DO 825 I=1,MA
      XW(I)=XU(I)
825  CONTINUE
809  YH3=FWSAT/(PHIX*PH)
      IF(ABS(YH3-XW(IPOS)).LT.1.E-7)GO TO 819
      XW(IPOS)=YH3
      CALL NORMW(NCOMP,IPOS,XW)
      CALL PHIMIX(XW,PH,T,PHI)
      COUNT=COUNT+1
      IF(COUNT.GT.30)GO TO 818
      PHIX=PHI(IPOS)
      GO TO 809
818  WRITE(6,828)
819  P2P=P*6.8948
      PH3P=PH*6.8948
      TK=T/1.8
      IF(ICOUN.GE.30)WRITE(6,810)
      IF(P.GT.PH)GO TO 845
      WRITE(6,823)
      GO TO 812
845  IF(IWATER.EQ.2)GO TO 812
      WRITE( 6,811)TK,P2P,XU(IPOS),PH3P,YH3
C
812  P=PH
      NCOMP=NCOMP-1
      MA=MA-1
      NW=0
821  RETURN
C  * * FORMAT STATEMENTS * *
C
828  FORMAT(' 3 PHASE WATER CALCULATIONS NOT CONVERGED')
803  FORMAT('0',T20,'* * YH20 DEFAULTS TO A VALUE OF 0.05 ON'
A  , ' ITERATION# ',I2, / ,1X,T20,'* * FROM A PREVIOUS'
B  , ' VALUE OF YH20 = ',E10.3)
810  FORMAT('0',T20,'* * WATER CONTENT EQUILIBRIUM
C  CALCULATIONS HAVE NOT CONVERGED * * ')
811  FORMAT(5X,F7.3,2X,F9.3,2X,F15.9,8X,':',3X,F9.3,2X,F15.9)
351  FORMAT(/,18X,'CODE #',5X,'A(I)',8X,'SIGMA(I)',8X,'EPS(I)',/)
352  FORMAT(5X,I5,3F10.3)
823  FORMAT(5X,' PRESSURE IS NOT IN 2 PHASE REGION')
C
      END
C
C
C
C
*****
SUBROUTINE NORMW(NCOMP,IPOS,XU)
*****
* * THIS SUBROUTINE NORMALIZES THE VECTOR XU * *
* * WITHOUT CHANGING THE VALUE OF XU(IPOS) * *
C

```

```

      IMPLICIT DOUBLE PRECISION (A-H,O-Z)
      DIMENSION XU(10)
      COMMON/STOR/XUSTOR(10)
C
      SUM=1.0-XU(IPOS)
      DO 1 I=1,NCOMP
      IF(I.EQ.IPOS)GO TO 1
      XU(I)=XUSTOR(I)*SUM
1  CONTINUE
C
      RETURN
      END
C
C *****
      DOUBLE PRECISION FUNCTION PSAT(TR)
C *****
C * * FUNCTION TO CALCULATE THE SATURATION PRESSURE OF * *
C * * WATER USING THE CORRELATION DEVELOPED BY KEENAN * *
C * * KEYES AND MOORE P(PSIA), T(R) * *
C * * A CORRELATION TO CALCULATE THE VAPOR PRESSURE * *
C * * FOR ICE WAS ALSO USED BASED ON THE DATA FROM * *
C * * PERRY'S 5'TH ED. 3-205 * *
C *****
C
      IMPLICIT DOUBLE PRECISION (A-H,O-Z)
      DIMENSION F(8),A1(7),B1(7),TREF(8)
C
      DATA F/-741.9242,-29.721,-11.55286,-0.8685635,
A0.1094098,0.439993,0.2520658,0.05218684/
C
      DATA A1/1.110788E-11,4.813026E-12,1.053791E-12,
A6.92593447E-14,2.289828E-15,4.697288E-18,4.261011E-22/
C
      DATA B1/0.046341356,0.048066983,0.0512724161,
A0.0572912243,0.06528872,0.08110062,0.108179821/
C
      DATA TREF/492.0,484.0,475.0,451.0,426.0,394.0,
A344.0,300/
C
C * * CRITICAL PROPERTIES FOR WATER * *
C
      T1=374.136
      P1=220.88
C
      C=TR/1.8-273.15
      AK1=1800.0/TR
C
C * * CHECK IF LIQ. WATER OR ICE IS PRESENT * *
C
      IF(TR.LT.492.0)GO TO 2
      P=0
      DO 1 J=1,8
1  P=P+F(J)*(0.65-0.01*C)**(J-1)

```



```

P=P1*DEXP(AK1*1.E-5*(T1-C)*P)/10.0
PSAT=P*145.03894
GO TO 40

C
C   * * CORRELATION FOR VAPOR PRESS. OF ICE           * *
C
  2 DO 10 I=1,7
    IF(TR.LE.TREF(I).AND.TR.GT.TREF(I+1))GO TO 20
10  CONTINUE
    WRITE(6,30)TR
20  PSAT=A1(I)*DEXP(B1(I)*TR)

C
30  FORMAT(1X,T20,'* * TEMP BELOW TABLE FOR FUNCT. PSAT
A: T(R)= ',E12.5)

C
C
40  RETURN
    END

C
C
C   *****
C   DOUBLE PRECISION FUNCTION CC(T,IS,IC,I,J)
C   *****
C
C
C   THIS FUNCTION CALCULATES LANGMUIR CONSTANTS FOR HYDRATE
C   FORMATION FROM C1,C2,OR C3 USING THE SPHERICALLY SYMETRIC
C   KIHARA POTENTIAL FUNCTION. THIS PROGRAM CALLS ON THE
C   FUNCTION OMEGA WHICH GIVES THE POTENTIAL AS A FUNCTION OF
C   POSITION. GAUSSIAN INTEGRATION (C&W PAGE 100) IS USED
C   TO INTEGRATE OMEGA OVER THE CELL VOLUME.
C   OMEGA IS A FUNCTION THAT CALCULATES THE
C   SMOOTHED CELL POTENTIAL AS A SUM OF
C   CONTRIBUTIONS OF THE FIRST,SECOND AND
C   THIRD SHELLS.
C   THE VARIABLES ARE
C   IS- CODE FOR WHICH HYDRATE STRUCTURE(I OR II) IS FORMED
C   IC= CODE FOR WHICH CAVITY IS UNDER CONSIDERATION
C   A= CORE RADIUS FOR THE MOLECULE,C1...C3
C   T=TEMPERATURE
C   EPS= EPSILON, DEPTH OF INTERMOLECULAR POTENTIAL WELL, ERG
C   R= RADIAL POSITION OF THE ENCLOSED MOLECULE
C   RR =FIRST SHELL RADIUS.
C   RR2=SECOND SHELL RADIUS
C   RR3=THIRD SHELL RADIUS.
C   Z=FIRST SHELL COORDINATION NUMBER
C   Z2=SECOND SHELL COORDINATION NUMBER.
C   Z3=THIRD SHELL COORDINATION NUMBER.
C
C   REF: PARRISH AND PRAUSNITZ,I&EC PROC. DES & DEV,
11(1),P26(1972)
C

```

```

C
C
      IMPLICIT DOUBLE PRECISION (A-H,O-Z)
      EXTERNAL OMEGA
      COMMON /SIG/ SIGMA, EPS, RR, Z, A, TT, RR2, Z2, RR3, Z3
      COMMON /AMOL/ MA, ISCODE(10)
      COMMON /RRR/ R
      COMMON /FUND/ SSIG(10), EEPS(10), AA(10)
      COMMON /AFAC/ OM(10)
      COMMON /ID/ II, JJ, ISS
      CC=0.0
      II=I
      JJ=IC
      ISS=IS
C      WRITE(06,51) II, JJ, ISS, CC
51      FORMAT(4X,3I2,5X,E15.5)
      PI=3.14159
      QSTAR=1.0
      IF( IS.EQ.1.AND.ISCODE(J).EQ.3)RETURN
      IF( IC.EQ.1.AND.ISCODE(J).EQ.2)RETURN
      IF( IC.EQ.1.AND.ISCODE(J).EQ.3)RETURN
      IF( ISCODE(J).EQ.4)RETURN
      TT=T
      A=AA(I)
      SIGMA=SSIG(I)-A
      EPS=EEPS(I)
C      WRITE(06,1031) SIGMA, EPS, A
1031     FORMAT(5X,3E15.5)
C      ***CHECK FOR WHICH STRUCTURE IS FORMED***
      IF( IS.EQ.2) GO TO 6
C      ***CHECK FOR WHICH CAVITY IS OCCUPIED***
      IF( IC.EQ.2) GO TO 5
      RR=3.875
      Z=20.
      RR2=6.593
      Z2=20.0
      RR3=8.056
      Z3=50.0
      GO TO 8
C      ***STRUCTURE I CAVITY II
5      RR=4.152
      Z=21.
      RR2=7.078
      Z2=24.0
      RR3=8.285
      Z3=50.0
      GO TO 8
6      CONTINUE
C      ***CHECK FOR CAVITY, STRUCTURE II***
      IF( IC.EQ.2) GO TO 7
C      ***STRUCTURE II, CAVITY I***
      RR=3.87
      Z=20.
      RR2=6.667

```

```

      Z2=20.0
      RR3=8.079
      Z3=50.0
      GO TO 8
C    ***STRUCTURE II, CAVITY II***
7    RR=4.703
      Z=28.
      RR2=7.464
      Z2=28.0
      RR3=8.782
      Z3=50.0
8    CONTINUE
C
C    EVALUATE THE INTEGRAL AND RETURN THE VALUE OF C
      CALL YLIMIT(B)
      C=GAUSS(0.,B,10,OMEGA)
      PI=3.14159
      CC=C*4.*PI/T/1.38/9.869/10.
C    QSTAR CORRELATIONS.
      FORM=(SIGMA*OM(I)/(RR-A))*(EPS/273.15)
      IF(IS.EQ.1.AND.IC.EQ.1)QSTAR=DEXP(-35.3446*(FORM**0.973))
      IF(IS.EQ.1.AND.IC.EQ.2)QSTAR=DEXP(-14.1161*(FORM**0.8266))
      IF(IS.EQ.2.AND.IC.EQ.1)QSTAR=DEXP(-35.3446*(FORM**0.973))
      IF(IS.EQ.2.AND.IC.EQ.2)QSTAR=DEXP(-782.8469*(FORM**2.3129))
      CC=CC*QSTAR
C    WRITE(6,552)(FORM,QSTAR)
C552  FORMAT(1X,1F,2X,1F)
      RETURN
      END
C
C
C
C    *****
      SUBROUTINE CUBEQN(A,Z,MTYPE)
C    *****
C
C    THIS SUBROUTINE FINDS THE THREE ROOTS OF THE CUBIC
C    EQUATION GENERATED BY THE EQUATION OF STATE.
C
C
C    IMPLICIT DOUBLE PRECISION (A-H,O-Z)
      DIMENSION A(4),Z(3),B(3)
      B(1)=A(2)/A(1)
      B10V3=B(1)/3.0
      B(2)=A(3)/A(1)
      B(3)=A(4)/A(1)
      ALF=B(2)-B(1)*B10V3
      BET=2.*B10V3**3-B(2)*B10V3+B(3)
      BETOV2=BET/2.
      ALFOV3=ALF/3.
      CUAOV3=ALFOV3**3
      SQBOV2=BETOV2**2
      DEL=SQBOV2+CUAOV3
      IF(DEL) 40,20,30

```

```

20  MTYPE=0
    GAM=DSQRT(-ALFOV3)
    IF(BET) 22,22,21
21  Z(1)=-2.*GAM-B10V3
    Z(2)=GAM-B10V3
    Z(3)=Z(2)
    GO TO 50
22  Z(1)=2.*GAM-B10V3
    Z(2)=-GAM-B10V3
    Z(3)=Z(2)
    GO TO 50
30  MTYPE=1
    EPS=DSQRT(DEL)
    TAU=-BETOV2
    RCU=TAU+EPS
    SCU=TAU-EPS
    SIR=1.
    SIS=1.
    IF(RCU) 31,32,32
31  SIR=-1.
32  IF(SCU) 33,34,34
33  SIS=-1.
34  R=SIR*(SIR*RCU)**.333333
    S=SIS*(SIS*SCU)**.333333
    Z(1)=R+S-B10V3
    Z(2)=- (R+S)/2.-B10V3
    Z(3)=0.866025*(R-S)
    GO TO 50
40  MTYPE=-1
    QUOT=SQBOV2/CUAOV3
    ROOT=DSQRT(-QUOT)
    IF(BET) 42,41,41
41  PEI=(1.570796+DATAN(ROOT/DSQRT(1.-ROOT**2)))/3.
    GO TO 43
42  PEI=DATAN(DSQRT(1.-ROOT**2)/ROOT)/3.
43  FACT=2.*DSQRT(-ALFOV3)
    Z(1)= FACT*DCOS(PEI)-B10V3
    Z(2)= FACT*DCOS(PEI+2.094395)-B10V3
    Z(3)=FACT*DCOS(PEI+4.188790)-B10V3
50  RETURN
    END

```

C
C
C
C
C
C
C
C
C
C

```

*****
SUBROUTINE DATA(Y,XA,T)
*****

```

THIS SUBROUTINE READS THERMODYNAMIC DATA FOR THE GASES,
CALCULATES MIXTURE CRITICAL PROPERTIES, FREEZING POINT
DEPRESSIONS, AND ACTIVITY COEFFICIENTS FOR WATER IN
THE PRESENCE OF INHIBITORS.

IMPLICIT DOUBLE PRECISION (A-H,O-Z)

```

DIMENSION A(10),SIGMA(10),EPS(10)
DIMENSION NCODE(10),KK(10)
DIMENSION ZAA(1,25),AA(10,25)
DIMENSION IISCO(25)
DIMENSION Y(25),XA(25),ZA(20)
DIMENSION X(11),TCIJ(10,10),ZC(10,10),PCIJ(10,10),VCIJ(10,10),
2 PC(10),TC(10),VC(10),OMEGA(10),ESTAR(10),C1RKV(10),C2RKV(10),
3 C1RKL(10),C2RKL(10),AMW(10),C0FREF(10),C1FREF(10),
4 C2FREF(10),C3FREF(10),C4FREF(10),TS(10,10),
5 AK(25,25),DVR(25,25),DTR(25,25)
COMMON /PVTIJ/ OMEGA, PCIJ, TCIJ
COMMON /AMOL/MA,ISCODE(10)
COMMON /AZ/KK,N,MK
COMMON /COEFF/ C0FREF, C1FREF, C2FREF, C3FREF, C4FREF,
2 C0HNRV, C1HNRV, C2HNRV, C3HNRV, C4HNRV, C5HNRV,
3 C0ALFS, C1ALFS, C2ALFS, C3ALFS, C4ALFS, C5ALFS
COMMON /PVT/ RT, TC, PC, VC, NSOLV
COMMON/NC/NCODE,NCOMP
COMMON /ACTVTY/ TS, ESTAR
COMMON /VOL/ DVR, DTR, C1RKL, C2RKL
COMMON /PHMX/ C1RKV, C2RKV
COMMON/AFAC/OM(10)
COMMON/FUND/SIGMA, EPS, A
COMMON/BKSA/AK
COMMON/BKSC/IWATER, IPOS, ISTR
COMMON/IMP/IMPURE, IMCODE, XIMP(100), YCO2(100)
COMMON/SOLUT/XSOLU, ACTIV, YYYCO2
COMMON/TFREEZ/TT0
COMMON/AWAT/ANN(25,25)
IF(IWATER.EQ.0)GO TO 508
MA=MA+1
KK(MA)=13
508 CONTINUE
DATA X1OLD/1./
OPEN(10,FILE='TAPE10.DAT',STATUS='OLD')
I=1
DO 96 I2=1,25
IF(IWATER.EQ.0)GO TO 51
IF(I2.NE.13)GO TO 51
READ(10,306)A(MA),SIGMA(MA),EPS(MA),AMW(MA),TC(MA)
READ(10,306)VC(MA),PC(MA),OMEGA(MA),ESTAR(MA),C1RKV(MA)
READ(10,306)C2RKV(MA),C1RKL(MA)
,C2RKL(MA),C0FREF(MA),C1FREF(MA)
READ(10,306)C2FREF(MA),C3FREF(MA),C4FREF(MA)
READ(10,307)(AK(MA,J),J= 1, 6)
READ(10,307)(AK(MA,J),J= 7,12)
READ(10,307)(AK(MA,J),J=13,18)
READ(10,307)(AK(MA,J),J=19,24)
READ(10,307)(AK(MA,J),J=25,25)
OM(MA)=OMEGA(MA)
READ(10,308)ISCODE(MA)
GO TO 96
51 IF(I2.EQ.KK(I)) GO TO 95
READ(10,306)(ZA(J), J= 1, 5)

```

```

READ(10,306)(ZA(J), J= 6,10)
READ(10,306)(ZA(J), J=11,15)
READ(10,306)(ZA(J), J=16,20)
READ(10,307)(ZAA(1,J),J= 1, 6)
READ(10,307)(ZAA(1,J),J= 7,12)
READ(10,307)(ZAA(1,J),J=13,18)
READ(10,307)(ZAA(1,J),J=19,24)
READ(10,307)(ZAA(1,J),J=25,25)
READ(10,308) IISCO(I)
GO TO 96
95 READ(10,306) A(I),SIGMA(I),EPS(I),AMW(I), TC(I)
READ(10,306) VC(I),PC(I),OMEGA(I),ESTAR(I),C1RKV(I)
READ(10,306) C2RKV(I),C1RKL(I),C2RKL(I),C0FREF(I),C1FREF(I)
READ(10,306) C2FREF(I),C3FREF(I),C4FREF(I)
READ(10,307)(AK(I,J),J= 1, 6)
READ(10,307)(AK(I,J),J= 7,12)
READ(10,307)(AK(I,J),J=13,18)
READ(10,307)(AK(I,J),J=19,24)
READ(10,307)(AK(I,J),J=25,25)
OM(I)=OMEGA(I)
READ(10,308) ISCODE(I)
I=I+1
96 CONTINUE
REWIND(UNIT=10)
CLOSE(UNIT=10)
C 306 FORMAT(10X,5(2X,E12.5),/,10X,5(2X,E12.5),/,10X,5(2X,E12.5),/
C 1 ,10X,5(2X,E12.5))
C 307 FORMAT(10X,6(2X,E12.5),/,10X,6(2X,E12.5),/,10X,6(2X,E12.5),/,
C 1 10X,6(2X,E12.5),/,12X,E12.5)
306 FORMAT(5(E12.5,1X))
307 FORMAT(6(E12.5,1X))
308 FORMAT(I2)
K=1
DO 106 I=1,MA
DO 107 J=1,25
IF(J.NE.KK(K+1)) GO TO 107
AA(I,K+1)=AK(I,J)
K=K+1
107 CONTINUE
K=I+1
106 CONTINUE
DO 108 I=1,MA
DO 109 J=1,MA
AK(I,J)=0.0
AK(I,J)=AA(I,J)
109 CONTINUE
108 CONTINUE
DO 6 I=1,MA
DO 6 J=1,MA
AK(J,I)=AK(I,J)
DVR(I,J)=DVR(J,I)
DTR(I,J)=DTR(J,I)
TS(I,J)=TS(J,I)
6 CONTINUE

```

```

RT=10.73*T
J=0
  JJ=1
DO 10 I=1,MA
  IF(IWATER.NE.0)GO TO 826
  IF(Y(I).LT.1.E-5) GO TO 10
826  J=J+1
     JJ=JJ+1
     NCODE(J)=I
     XA(J)=Y(I)
     NCOMP=J
10  CONTINUE
    DO 20 I=1,NCOMP
      EPS(I)=EPS(NCODE(I))
      SIGMA(I)=SIGMA(NCODE(I))
      A(I)=A(NCODE(I))
      ISCODE(I)=ISCODE(NCODE(I))
      OM(I)=OM(NCODE(I))
      PC(I)=PC(NCODE(I))
      TC(I)=TC(NCODE(I))
      VC(I)=VC(NCODE(I))
      OMEGA(I)=OMEGA(NCODE(I))
      ESTAR(I)=ESTAR(NCODE(I))
      C1RKV(I)=C1RKV(NCODE(I))
      C2RKV(I)=C2RKV(NCODE(I))
      C1RKL(I)=C1RKL(NCODE(I))
      C2RKL(I)=C2RKL(NCODE(I))
      C0FREF(I)=C0FREF(NCODE(I))
      C1FREF(I)=C1FREF(NCODE(I))
      C2FREF(I)=C2FREF(NCODE(I))
      C3FREF(I)=C3FREF(NCODE(I))
      C4FREF(I)=C4FREF(NCODE(I))
      TCIJ(I,I) = TC(NCODE(I))
      AMW(I)=AMW(NCODE(I))
20  CONTINUE
    IF(NCOMP.EQ.1) GO TO 22
C    IF(IWATER.NE.0.AND.(NCOMP-1).EQ.1)GO TO 22
     NCOMP1=NCOMP-1
     DO 21 I=1,NCOMP1
       I1=I+1
       DO 21 J=I1,NCOMP
         TS(I,J)=TS(NCODE(I),NCODE(J))
         TS(J,I)=TS(I,J)
         DVR(I,J)=DVR(NCODE(I),NCODE(J))
         DVR(J,I)=DVR(I,J)
         DTR(I,J)=DTR(NCODE(I),NCODE(J))
         DTR(J,I)=DTR(I,J)
         AK(I,J) = AK(NCODE(I),NCODE(J))
         ZC(I,J)=.291-.04*(OMEGA(I)+OMEGA(J))
         ZC(J,I)=ZC(I,J)
         TCIJ(I,J)=(TC(I)*TC(J))**.5*(1.-AK(I,J))
         TCIJ(J,I)=TCIJ(I,J)
         VCIJ(I,J)=(.5*(VC(I)**.3333333+VC(J)**.3333333))**3
         VCIJ(J,I)=VCIJ(I,J)

```

```

      PCIJ(I,J)=ZC(I,J)*10.73*TCIJ(I,J)/VCIJ(I,J)
      PCIJ(J,I)=PCIJ(I,J)
21  CONTINUE
22  CONTINUE
      DO 31 I3=1,NCOMP
      DO 31 I4=1,NCOMP
      ANN(I3,I4)=AK(I3,I4)
31  CONTINUE
      IF(IWATER.EQ.0)GO TO 507
      MA=MA-1
      NCOMP=NCOMP-1
      ACTIV=1.0
      TT0=0.0
507  IF(IMPURE.EQ.0.OR.XSOLU.EQ.0.0)GO TO 509
      T=T/1.8
C
C  ** ACTIVITY COEFFICIENT OF WATER **
C
      IF(IMCODE.EQ.1)ACTIV=DEXP(-0.90634*XSOLU**2+1.95522*XSOLU**3)
      IF(IMCODE.EQ.2)ACTIV=DEXP(5.77435*XSOLU**2)
      IF(IMCODE.EQ.3)ACTIV=DEXP(-0.90634*XSOLU**2+1.95522*XSOLU**3)
      IF(IMCODE.EQ.4)ACTIV=DEXP(-0.29965*XSOLU**2-172.56293*XSOLU**3)
      IF(IMCODE.EQ.5)ACTIV=DEXP(-199.63879*XSOLU**2+3869.86893*XSOLU
1      **3)
      IF(IMCODE.EQ.6)ACTIV=DEXP(-239.55098*XSOLU**2+9683.44617*XSOLU
1      **3)
      IF(IMCODE.EQ.7)ACTIV=DEXP(((10.44*T-3535.34)*XSOLU**2.+
1      (-32.19*T+10888.7)*XSOLU**3.)/(0.082*T))
      IF(IMCODE.EQ.8)ACTIV=DEXP(-1.84825*XSOLU**2+4.26904*XSOLU**3)
      IF(IMCODE.EQ.9.OR.IMCODE.EQ.10)ACTIV=DEXP((-64.2019)
1*XSOLU**2.+(183.219)*XSOLU**3.)/(0.082*T))
C
C  ** CORRECTION FACTOR FOR SYSTEMS CONTAINING CO2 **
C
      ACTIV=(1-0.30*YYYCO2*XSOLU)*ACTIV
C
C  ** FREEZING POINT DEPRESSIONS **
C
      IF(IMCODE.EQ.1)TT0=-0.13171+105.59*XSOLU+161.82*XSOLU**2
1  -70.233*XSOLU**3
      IF(IMCODE.EQ.2)TT0=-0.33398+109.91*XSOLU+308.25*XSOLU**2
1  -745.82*XSOLU**3
      IF(IMCODE.EQ.3)TT0=-1.1132+161.707*XSOLU-101.0468*XSOLU**2.
      IF(IMCODE.EQ.4)TT0=-0.083176+197.62*XSOLU-175.14*XSOLU**2
1  +8884.6*XSOLU**3
      IF(IMCODE.EQ.5)TT0=0.12618+207.67*XSOLU+6510.4*XSOLU**2
1  +4113.4*XSOLU**3
      IF(IMCODE.EQ.6)TT0=0.0085870+185.53*XSOLU-65.062*XSOLU**2
1  +494.73*XSOLU**3
      IF(IMCODE.EQ.7)TT0=0.0460878+163.998*XSOLU+941.4078*XSOLU**2.
      IF(IMCODE.EQ.8)TT0=-0.019306+104.71*XSOLU+64.867*XSOLU**2
1  +1857.6*XSOLU**3
      IF(IMCODE.EQ.9.OR.IMCODE.EQ.10)TT0=-0.11843+110.2595*XSOLU+
1126.4329*XSOLU**2.

```



```

T=T*1.8
509  RETURN
END
C
C
C *****
C DOUBLE PRECISION FUNCTION DEL(N)
C *****
C
C THE DEL FUNCTIONS EVALUATE DEL OF THE KIHARA FUNCTION FOR
C THE 1ST, 2ND AND 3RD SHELLS OF WATER.
C
C IMPLICIT DOUBLE PRECISION (A-H,O-Z)
COMMON /SIG/ SIGMA, EPS, RR, Z, A, T, RR2, Z2, RR3, Z3
COMMON /RRR/ R
D=(1.-R/RR-A/RR)
DD=(1.+R/RR-A/RR)
D=1.0/D**N - 1.0/DD**N
DEL= D/N
2000 FORMAT(' DEL; ', 1G10.5)
RETURN
END
C
C
C *****
C DOUBLE PRECISION FUNCTION DEL2(N)
C *****
C IMPLICIT DOUBLE PRECISION (A-H,O-Z)
COMMON/SIG/SIGMA, EPS, RR, Z, A, T, RR2, Z2, RR3, Z3
COMMON/RRR/R
D=(1.0-R/RR2-A/RR2)
DD=(1.0+R/RR2-A/RR2)
D=1.0/D**N-1.0/DD**N
DEL2=D/N
RETURN
END
C
C
C *****
C DOUBLE PRECISION FUNCTION DEL3(N)
C *****
C IMPLICIT DOUBLE PRECISION (A-H,O-Z)
COMMON/SIG/SIGMA, EPS, RR, Z, A, T, RR2, Z2, RR3, Z3
COMMON/RRR/R
D=(1.0-R/RR3-A/RR3)
DD=(1.0+R/RR3-A/RR3)
D=1.0/D**N-1/DD**N
DEL3=D/N
RETURN
END
C
C

```

```

C
C      *****
C      DOUBLE PRECISION FUNCTION GAUSS(A,B,M,FUNCTN)
C      *****
C      ***REF: CARNAHAN,LUTHER AND WILKES:APP. NUMERICAL METH'S.
C      ***WILEY & SONS,INC.(1969).
C
C      FORMULA TO COMPUTE THE INTEGRAL OF FUNCTN(X) BETWEEN THE
C      INTEGRATION LIMITS A AND B.
C      IMPLICIT DOUBLE PRECISION (A-H,O-Z)
C      DIMENSION NPOINT(7), KEY(8),Z(24),WEIGHT(24)
C      EXTERNAL FUNCTN
C
C      **PRESET NPOINT,KEY,Z,AND WEIGHT ARRAYS
C      DATA NPOINT /2,3,4,5,6,10,15/
C      DATA KEY / 1,2,4,6,9,12,17,25 /
C      WEIGHT(1)= 1.0
C      WEIGHT(2)= 0.888888889
C      WEIGHT(3)= 0.555555556
C      WEIGHT(4)=0.652145155
C      WEIGHT(5)=0.347854845
C      WEIGHT(6)=0.568888889
C      WEIGHT(7)= 0.478628671
C      WEIGHT(8)= 0.236926885
C      WEIGHT(9)= 0.467913935
C      WEIGHT(10)= 0.360761573
C      WEIGHT(11)= 0.171324493
C      WEIGHT(12)= 0.295524225
C      WEIGHT(13)= 0.269266719
C      WEIGHT(14)= 0.219086363
C      WEIGHT(15)= 0.149451349
C      WEIGHT(16)= 0.066671344
C      WEIGHT(17)= 0.202578242
C      WEIGHT(18)= 0.198431485
C      WEIGHT(19)= 0.186160000
C      WEIGHT(20)= 0.166269206
C      WEIGHT(21)= 0.139570678
C      WEIGHT(22)= 0.107159221
C      WEIGHT(23)= 0.070366047
C      WEIGHT(24)= 0.030753242
C      Z(1)=0.577350269
C      Z(2)=0.0
C      Z(3)=0.774596669
C      Z(4)=0.339981044
C      Z(5)=0.861136312
C      Z(6)=0.0
C      Z(7)=0.538469310
C      Z(8)=0.906179846
C      Z(9)=0.238619186
C      Z(10)=0.661209387
C      Z(11)=0.932469514
C      Z(12)=0.148874339
C      Z(13)=0.433395394
C      Z(14)=0.679409568

```

```

Z(15)=0.865063367
Z(16)= 0.973906529
Z(17)= 0.0
  Z(18)=0.2011941
  Z(19)=0.3941513
  Z(20)=0.5709722
  Z(21)=0.7244177
Z(22)= 0.848206583
Z(23)= 0.937273392
Z(24)=0.987992518
C   *** FIND SUBSCRIPT OF FIRST Z AND WEIGHT VALUE ***
DO 1 I=1,7
  IF(M.EQ.NPOINT(I)) GO TO 2
1 CONTINUE
C   *** INVALID M USED ***
  GAUSS=0.
  RETURN
C
C   *** SET UP INITIAL PARAMETERS ***
2 JFIRST=KEY(I)
  JLAST=KEY(I+1)-1
  C=(B-A)/2.
  D=(B+A)/2.
C
C   *** ACCUMULATE THE SUM IN THE MPOINT FORMULA
  SUM=0.
  DO 5 J=JFIRST,JLAST
    IF( Z(J).EQ.0.0 ) SUM=SUM+WEIGHT(J)*FUNCTN(D)
5 IF( Z(J).NE.0.0 ) SUM=SUM+WEIGHT(J)*(FUNCTN(Z(J)*C+D)
  2 + FUNCTN( -Z(J)*C +D))
C
C   *** MAKE INTERVAL CORRECTION AND RETURN ****
  GAUSS=C*SUM
2100 FORMAT('  GAUSS;      ',1G10.5)
  RETURN
  END
C
C
C
C   *****
  DOUBLE PRECISION FUNCTION OMEGA(R)
  *****
C
C   THIS FUNCTION EVALUATES THE CELL POTENTIAL( SPHERICALLY
C   SYMETRIC KIHARA) WITH THE RADIAL POSITION, R, OF THE
C   MOLECULE IN THE CAVITY AS THE INDEPENDENT VARIABLE.
C
C   IMPLICIT DOUBLE PRECISION (A-H,O-Z)
COMMON /SIG/ SIGMA, EPS, RR, Z, A, T, RR2, Z2, RR3, Z3
COMMON /RRR/ ZZ
ZZ=R
OMEGA=2.*Z*EPS*(SIGMA**12/RR**11/R*(DEL(10)+A/RR*DEL(11))
1 - SIGMA**6/RR**5/R*(DEL(4)+A/RR*DEL(5)))

```

```

OMEGA2=2.0*Z2*EPS*(SIGMA**12/RR2**11/R*(DEL2(10)+A/RR2*DEL2(11))
1  -SIGMA**6/RR2**5/R*(DEL2(4)+A/RR2*DEL2(5)))

```

```

OMEGA3=2.0*Z3*EPS*(SIGMA**12/RR3**11/R*(DEL3(10)+A/RR3*DEL3(11))
1  -SIGMA**6/RR3**5/R*(DEL3(4)+A/RR3*DEL3(5)))

```

```

OMEGA=OMEGA+OMEGA2+OMEGA3

```

```

OMEGA=-OMEGA/T

```

```

IF(ABS(OMEGA).GT. 170.) OMEGA=ABS(OMEGA)/OMEGA*170.

```

```

IF (OMEGA.LE.-60.) OMEGA=-60.

```

```

OMEGA=DEXP(OMEGA)*R*R

```

```

2300 FORMAT(' OMEGA; ', 1G10.5)

```

```

RETURN

```

```

END

```

```

C

```

```

C

```

```

C

```

```

*****

```

```

SUBROUTINE VAPRES(PVAP,T)

```

```

C

```

```

*****

```

```

C

```

```

C THIS SUBROUTINE IS CALLED BY BUBDEW. IT CALCULATES THE VAPOR
PRESSURE

```

```

C

```

```

OF EACH COMPONENT USING RIEDEL'S CORRELATION.

```

```

C

```

```

IMPLICIT DOUBLE PRECISION (A-H,O-Z)

```

```

DIMENSION PVAP(10)

```

```

DIMENSION

```

```

TCIJ(10,10),PCIJ(10,10),PC(10),TC(10),VC(10),OMEGA(10)

```

```

DIMENSION NCODE(10)

```

```

COMMON/PVTIJ/OMEGA,PCIJ,TCIJ

```

```

COMMON/NC/NCODE,NCOMP

```

```

COMMON/PVT/RT,TC,PC,VC,NSOLV

```

```

DO 401 I=1,NCOMP

```

```

TR=T/TC(I)

```

```

IF(TR.GT.1.0)GO TO 400

```

```

B=36./TR-35.-TR**6.0+42.*DLOG(TR)

```

```

ALFAC=5.808+4.93*OMEGA(I)

```

```

RES=0.118*B-7*DLOG10(TR)+(ALFAC-7.)*(0.036*B-DLOG10(TR))

```

```

PVAP(I)=PC(I)/10.**(RES)

```

```

GO TO 401

```

```

400 PVAP(I)=PC(I)

```

```

401 CONTINUE

```

```

RETURN

```

```

END

```

```

C

```

```

C

```

```

*****

```

```

SUBROUTINE BUBDEW(T,P,Y)

```

```

C

```

```

*****

```

```

C

```

```

C

```

```

C THIS SUBROUTINE CALCULATES THE DEW POINT PRESSURE IF LIQ=0 AND

```

```

C

```

```

BUBBLE POINT PRESSURE IF LIQ=1

```

```

C

```

```

IMPLICIT DOUBLE PRECISION (A-H,O-Z)

```

```

DIMENSION XL(10),Y(10),V(10),PHIL(10)

```

```

        DIMENSION PHI(10),PVAP(10)
        DIMENSION NCODE(10)
        DIMENSION ZK(10),ZCN(10)
        COMMON/X/XL
        COMMON/PH/PHIL
        COMMON/NC/NCODE, NCOMP
        COMMON/TBLOC/ITAG
        COMMON/LIQUID/LIQ
        COMMON/HELP/IST0,IST2,ISLOW

C
C
        ITAG=1
        ITER=0
        CALL VAPRES(PVAP,T)
        SFRAC=0
        IF(LIQ.EQ.1)GO TO 8000
C ** DEW POINT CALCULATIONS **
        DO 280 I=1,NCOMP
        FRAC=Y(I)/PVAP(I)
        SFRAC=SFRAC+FRAC
280      CONTINUE
C      MAKE AN INITIAL ESTIMATE OF PRESSURE
        P=1/SFRAC
288      S=0
        DO 201 I=1,NCOMP
        XL(I)=Y(I)*P/PVAP(I)
        S=S+XL(I)
201      CONTINUE
        DO 222 I=1,NCOMP
        XL(I)=XL(I)/S
222      CONTINUE
206      CALL PHIMIX(Y,P,T,PHI)
        SUM=0.0
        DO 202 I=1,NCOMP
        ZK(I)=PHIL(I)/PHI(I)
        ZCN(I)=Y(I)/ZK(I)
        SUM=SUM+ZCN(I)
202      CONTINUE
        DO 203 I=1,NCOMP
        XL(I)=ZCN(I)/SUM
203      CONTINUE
        PNEW=P/SUM
        IF(ABS(SUM-1.0).LT.0.0001)GO TO 205
        P=PNEW
        ITER=ITER+1
        IF(ITER.GT.100)GO TO 207
        GO TO 206
207      WRITE(6,208)
208      FORMAT(' FAILED TO CONVERGE IN BUBDEW')
        GO TO 205
C ** BUBBLE POINT CALCULATIONS **
C      HERE XL IS SET EQUAL TO Y BECAUSE THE VALUES OF Y COMING IN
C      ARE LIQUID COMPOSITION
2000      DO 101 I=1,NCOMP

```

```

      XL(I)=Y(I)
101  CONTINUE
      DO 102 I=1,NCOMP
      FRAC=XL(I)*PVAP(I)
      SFRAC=SFRAC+FRAC
102  CONTINUE
C    MAKE AN INITIAL ESTIMATE OF PRESSURE
      P=SFRAC
      S=0
      DO 103 I=1,NCOMP
      Y(I)=XL(I)*PVAP(I)/P
      S=S+Y(I)
103  CONTINUE
      DO 104 I=1,NCOMP
      Y(I)=Y(I)/S
104  CONTINUE
105  CALL PHIMIX(Y,P,T,PHI)
      SUM=0.0
      DO 106 I=1,NCOMP
      ZK(I)=PHIL(I)/PHI(I)
      ZCN(I)=ZK(I)*XL(I)
      SUM=SUM+ZCN(I)
106  CONTINUE
      DO 107 I=1,NCOMP
      Y(I)=ZCN(I)/SUM
107  CONTINUE
      PNEW=P*SUM
      IF(ABS(SUM-1.0).LT.0.0001)GO TO 225
      P=PNEW
      ITER=ITER+1
      IF(ITER.GT.100)GO TO 207
      GO TO 105
C    INTERCHANGE XL AND Y VALUES AGAIN BY STORING Y VALUES IN V
225  DO 23 I=1,NCOMP
      V(I)=Y(I)
      Y(I)=XL(I)
      XL(I)=V(I)
23   CONTINUE
205  RETURN
      END

C
C
C    *****
      SUBROUTINE PHIMIX(Y,P,T,PHI)
C    *****
C
C
C    ** THIS SUBROUTINE IS TAKEN DIRECTLY FROM PRAUSNITZ
C       AND CHUEH'S BOOK "COMPUTER CALCULATIONS FOR MULTI
C       COMPONENT VAPOR LIQUID EQUILIBRIA"(1968) PRENTICE HALL
C
C    THIS SUBROUTINE CALCULATES THE FUGACITY COEFFICIENTS FOR
C    EACH COMPONENT FROM THE EQUATION OF STATE.
C

```

```

      IMPLICIT DOUBLE PRECISION (A-H,O-Z)
      DIMENSION NCODE(10)
      DIMENSION X(11),TCIJ(10,10),ZC(10,10),PCIJ(10,10),VCIJ(10,10),
2  PC(10),TC(10),VC(10),OMEGA(10),ESTAR(10),C1RKV(10),C2RKV(10),
3  C1RKL(10),C2RKL(10),AMW(10),C0FREF(10),C1FREF(10),
4  C2FREF(10),C3FREF(10),C4FREF(10),TS(10,10),
5  AK(25,25),DVR(25,25),DTR(25,25)
      DIMENSION PHIL(10)
      DIMENSION XL(10)
      COMMON/BLOCK/ISOLVE
      COMMON /PHMX/ C1RKV, C2RKV
      COMMON /PVTIJ/ OMEGA, PCIJ, TCIJ
      COMMON /PVT/ RT, TC, PC, VC, NSOLV
      COMMON/NC/NCODE,NCOMP
      COMMON/AFACT/OM(10)
      COMMON/BKSA/AK
      COMMON/X/XL
      COMMON/PHAS/NVLLH
      COMMON/PH/PHIL
      COMMON/TBLOC/ITAG
      COMMON/ZV/ZV
      COMMON/WATER/NW
      COMMON/AWAT/ANN(25,25)
      COMMON/CRITCL/NCRIT,TCRIT
      COMMON/LIQUID/LIQ
      DIMENSION Y(10),PHI(10),Z(3),ARKV(10,10),
2BRKV(10),AIRKV(10),A(4),AMWT(10,10)
      DIMENSION AA(25),BTC(25),AY(25,25)
      IF(ISOLVE.EQ.1)GO TO 200
      DO 100 I=1,NCOMP
      ARKV(I,I)=C1RKV(I)*10.73**2*TC(I)**2.5/PC(I)
      BRKV(I)=C2RKV(I)*10.73*TC(I)/PC(I)
      IF(I.EQ.NCOMP) GO TO 110
      I1=I+1
      DO 100 J=I1,NCOMP
      ARKV(I,J)=(C1RKV(I)+C1RKV(J))*0.5*10.73**2*TCIJ(I,J)
1**2.5/PCIJ(I,J)
      ARKV(J,I)=ARKV(I,J)
100  CONTINUE
110  CONTINUE
      AMRKV=0.
      BMRKV=0.
      DO 120 I=1,NCOMP
      AIRKV(I)=0.
      BMRKV=BMRKV+Y(I)*BRKV(I)
      DO 120 J=1,NCOMP
      AIRKV(I)=AIRKV(I)+Y(J)*ARKV(I,J)
120  AMRKV=AMRKV+Y(I)*Y(J)*ARKV(I,J)
C
C      CALCULATE VAPOR MOLAR VOLUME FOR MIXTURE
C
      A(1)=1.
      A(2)=-1.
      PBRT=P*BMRKV/RT

```

```

ABRT=AMRKV/(BMRKV*10.72999*T**1.5)
A(3)=PBRT*(ABRT-1.-PBRT)
A(4)=-ABRT*(PBRT**2)
CALL CUBEQN(A,Z,MTYPE)
IF(MTYPE)130,140,140
130 AMAX1=Z(1)
IF(AMAX1.LT.Z(2)) AMAX1=Z(2)
IF(AMAX1.LT.Z(3)) AMAX1=Z(3)
ZV=AMAX1
GO TO 150
140 ZV=Z(1)
150 VV=ZV*RT/P
C
C          CALCULATE FUGACITY COEFFICIENTS WITH THE
C          MODIFIED REDLICH-KWONG EQUATION OF STATE
C
QVVB=DLOG(VV/(VV-BMRKV))
Q1VB=1./(VV-BMRKV)
Q2RTB=2./(10.73*T**1.5*BMRKV)
QVBV=DLOG((VV+BMRKV)/VV)
QARTB=AMRKV/(10.73*T**1.5*BMRKV**2)
QVBV=BMRKV/(VV+BMRKV)
DO 160 I=1,NCOMP
PHI(I)=QVVB+BRKV(I)*Q1VB-AIRKV(I)*Q2RTB*QVBV+
2 BRKV(I)*QARTB*(QVBV-QVBV)-DLOG(ZV)
IF(PHI(I).LT.170.0) GO TO 27
WRITE(6,28) QVVB, BRKV(I), Q1VB, AIRKV(I), Q2RTB, QVBV,
2 QARTB, QVBV, ZV
28   FORMAT(9F10.5)
27   CONTINUE
PHI(I)=DEXP(PHI(I))
160  CONTINUE
RETURN
C
C          ***** CALCULATE FUGACITY COEFFICIENTS USING PENG *****
C          ***** ROBINSON EQUATION OF STATE *****
C
200 BC=0.0
BCX=0.0
DO 201 I=1,NCOMP
AKK=0.37464+1.54226*OMEGA(I)-0.26992*OMEGA(I)**2
ATC=52.643367*TC(I)**2/PC(I)
IF(NW.EQ.0)GO TO 211
DO 81 I1=1,NCOMP
AK(I1,NCOMP)=ANN(I1,NCOMP)*(0.4605*P/T-0.2237)
AK(NCOMP,I1)=AK(I1,NCOMP)
81  CONTINUE
IF(I.LT.NCOMP)GO TO 211
IF((T/TC(I)).LT.0.85)ALPHA=(1.0085677+0.82154*(1.-DSQRT(T/TC(I)
1)))**0.5
IF((T/TC(I)).GE.0.85)GO TO 211
GO TO 212
211 ALPHA=(1.0+AKK*(1.0-DSQRT(T/TC(I))))**2
212 AA(I)=ATC*ALPHA

```



```

BTC(I)=0.834794*TC(I)/PC(I)
BC=BC+Y(I)*BTC(I)
  BCX=BCX+XL(I)*BTC(I)
201 CONTINUE
AC=0.0
  ACX=0.0
DO 202 I=1, NCOMP
DO 203 J=1, NCOMP
AY(I,J)=(1.0-AK(I,J))*DSQRT(AA(I)*AA(J))
AC=AC+Y(I)*Y(J)*AY(I,J)
  ACX=ACX+XL(I)*XL(J)*AY(I,J)
203 CONTINUE
202 CONTINUE
  NCRIT=0
  IF(LIQ.EQ.1)GO TO 809
  IF(NVLLH.EQ.0)GO TO 809
  TCRIT=(AC/BC)/63.061506
  IF((T/TCRIT).GT.0.97)GO TO 808
  GO TO 809
808 NCRIT=1
  GO TO 810
809 CONTINUE
  IF(ITAG.EQ.2)GO TO 288
AP=AC*P/(10.73*T)**2
B=BC*P/(10.73*T)
A(1)=1
A(2)=B-1
A(3)=AP-3.0*B**2-2.0*B
A(4)=B**3+B**2-AP*B
CALL CUBEQN(A,Z,MTYPE)
IF(MTYPE)204,205,205
204 AMAX1=Z(1)
  IF(AMAX1.LT.Z(2))AMAX1=Z(2)
  IF(AMAX1.LT.Z(3))AMAX1=Z(3)
  ZV=AMAX1
  GO TO 206
205 ZV=Z(1)
206 DO 207 I=1, NCOMP
  F1=BTC(I)/BC*(ZV-1.0)
  F2=-DLOG(ZV-B)
  F3=0.0
  DO 208 K=1, NCOMP
  F3=F3+Y(K)*AY(K,I)
208 CONTINUE
  F3=-AP/(2.828427*B)*(2.0*F3/AC-BTC(I)/BC)
  F3=F3*DLOG((ZV+2.414*B)/(ZV-0.414*B))
  PHI(I)=DEXP(F1+F2+F3)
207 CONTINUE
  IF(NVLLH.EQ.0.OR.ITAG.EQ.0)GO TO 810
288 APX=ACX*P/(10.73*T)**2.
  BX=BCX*P/(10.73*T)
  A(1)=1
  A(2)=BX-1
  A(3)=APX-3.0*BX**2.-2.*BX

```

```

      A(4)=BX**3.+BX**2.-APX*BX
      CALL CUBEQN(A,Z,MTYPE)
      IF(MTYPE)214,215,216
214   AMINI=Z(1)
      IF(AMINI.GT.Z(2).AND.Z(2).GT.0)AMINI=Z(2)
      IF(AMINI.GT.Z(3).AND.Z(3).GT.0)AMINI=Z(3)
      ZL=AMINI
      GO TO 217
215   ZL=Z(2)
      GO TO 217
216   ZL=Z(1)
217   DO 218 I=1,NCOMP
      F1=BTC(I)/BCX*(ZL-1.0)
      F2=-DLOG(ZL-BX)
      F3=0.0
      DO 219 K=1,NCOMP
      F3=F3+XL(K)*AY(K,I)
219   CONTINUE
      F3=-APX/(2.828427*BX)*(2.0*F3/ACX-BTC(I)/BCX)
      F3=F3*DLOG((ZL+2.414*BX)/(ZL-0.414*BX))
      PHIL(I)=DEXP(F1+F2+F3)
218   CONTINUE
810   RETURN
C
      END
C
C
C
C *****
C SUBROUTINE YLIMIT(RLIMIT)
C *****
C
C ..... COPIED FROM W. R. PARRISH'S THESIS(BERKLEY)
C
C THIS SUBROUTINE CALCULATES THE UPPER LIMIT OF
C INTEGRATION IN THE SMOOTH CELL LANGMUIR CONSTANT
C EXPRESSION.
C
C
C      IMPLICIT DOUBLE PRECISION (A-H,O-Z)
      COMMON /SIG/ SIGMA,EPS,RR,Z,A,T,RR2,Z2,RR3,Z3
      CA=A/RR
      CHECK=0.0
      RCA=SIGMA/RR*1.122462
      S=1-0.98*(SIGMA/(2*(RR-A)))
      IF(S.LT.0.4) S=0.4
      RCA6=RCA**6
      RCA12=RCA**12
      DO 2 N=1,20
      IF( S.GT.1..OR.S.LE.0.) GO TO 6
      UM=1./(1.-S-CA)
      UP=1./(1.+S-CA)
      UM5=UM**5
      UP5=UP**5
      DA4=UM5+UP5

```

```

DA5=UM5*UM+UP5*UP
DB6=DA4+CA*DA5
UM11=UM**11
UP11=UP**11
DA10=UM11+UP11
DA11=UM11*UM+UP11*UP
DB12=DA10+CA*DA11
DB=RCA12*DB12-2.*RCA6*DB6
A10=UM11/UM-UP11/UP
A11=UM11-UP11
B12=A10/10. + CA*A11/11
A4=UM5/UM-UP5/UP
A5=UM5-UP5
B6=A4/4.+CA*A5/5.
B=RCA12*B12-2.*RCA6*B6
W=Z*EPS/(2.*S*T)*B
DWY=-W/S+Z*EPS*DB/(2.*S*T)
DS=S-(W-10.)/DWY
IF(ABS((DS-S)/DS).LT..01) GO TO 3
IF(DS.LE.0) CHECK=CHECK+1
IF(DS.LE.0) DS=S*1.05
IF(CHECK.GT.5) GO TO 6
2 S=DS
3 RLIMIT=S*RR
RETURN
6 CONTINUE
100 WRITE(6,100)SIGMA,EPS,A,RR,Z,T,S
    FORMAT(' ','BLOW UP ON Y-LIMIT',7F10.5)
RETURN
END

C
C
C *****
C REVISED SOLUBILITY SUBROUTINE
C
C SUBROUTINE SOL7(JK,Y7,PHI7,P,T,X6)
C *****
C
C THIS SUBROUTINE CALCULATES THE SOLUBILITIES OF
C THE GASES IN WATER USING KRICHEVSKY-KASARNOVSKY
C EXPRESSIONS FOR EACH GAS.
C
C IMPLICIT DOUBLE PRECISION (A-H,O-Z)
C DIMENSION A(25),B(25),C(25),D(25)
C DIMENSION VBAR(25),NCODE(25)
C COMMON/NC/NCODE,NCOMP
C
C P IS IN ATM. AND T IS IN K
C
C DATA A/-15.826227,-18.400368,-18.057885,-20.958631,
A -67.557,-22.150557,-20.108263,0.0,0.0,0.0
A , -868.764,0.0,0.0,-357.802,-14.283146,
C -17.160634,-17.934347,-15.103508,-17.979226,
D -336.76,-270.967,-877.845,-20.108263,

```

```

E      -20.108263,0.0/
C
  DATA B/1559.0631,2410.4807,2627.6108,3109.3918,
A      9177.534,3407.2181,2739.7313,0.0,0.0,0.0
B      ,43323.6,0.0,0.0,13897.5,2050.3269,1915.144,
C      1933.381,2603.9795,2530.0405,16170.1,
D      15992.9,42051.0,2739.7313,2739.7313,0.0/
C
  DATA C/0.0,0.0,0.0,0.0,0.072775,
A      0.0,0.0,0.0,0.0,0.0,
B      122.986,0.0,0.0,52.2871,0.0,
C      0.0,0.0,0.0,0.0,46.2117,
D      33.2892,125.018,0.0,0.0,0.0/
C
  DATA D/1.0,1.0,1.0,1.0,760.0,
A      1.0,1.0,1.0,1.0,1.0,
B      0.0,1.0,0.0,-0.029836,1.0,
C      1.0,1.0,1.0,1.0,-0.00608793,
D      0.0260485,0.0,1.0,1.0,1.0/
C
  DATA VBAR/32.0,32.0,60.0,13*32.0,
A      32.8,8*32.0/
C
C
  IF(JK.EQ.20.OR.JK.EQ.21.OR.JK.EQ.14.OR.JK.EQ.11.
AOR.JK.EQ.22)GO TO 10
  IF(JK.EQ.8.OR.JK.EQ.9.OR.JK.EQ.10.OR.JK.EQ.12.
AOR.JK.EQ.6.OR.JK.EQ.7)GO TO 20
  XO=D(JK)*DEXP(A(JK)+B(JK)/T+C(JK)*T)
  GO TO 30
10  XO=DEXP((A(JK)+B(JK)/T+C(JK)*DLOG(T)+
AD(JK)*T)/1.987)
30  F=P*Y7*PHI7
  X6=F*XO*DEXP(-1.0*VBAR(JK)*(P-1.0)/(82.06*T))
  IF(X6.GT.0.05)GO TO 40
  GO TO 50
40  CONTINUE
C  WRITE(6,200)JK,X6
  X6=0.05
  GO TO 50
C 20 WRITE(6,100)JK
 20  X6=0.0
 50  RETURN
100  FORMAT(1X,T20,' * * COMPONENT# ',I3,' NOT YET
A AVAILABLE IN SOL7 * * ')
200  FORMAT(1X,T20,' * * COMPONENT# ',I3,' HAS DEFAULTED
A TO X6 = 0.05 FROM X6 = ',E15.5,' * * ')
C
  END

```

BIBLIOGRAPHY

Angus, S., Armstrong B., & K.M. de Reuck, Eds., Carbon Dioxide, International Thermodynamic Tables of the Fluid State Vol. 3 (IUPAC Project Centre, Imperial College, London: Pergamon Press, 1976.)

Aya, I., Yamane, K. and Nariai, H. "Solubility of CO₂ and density of CO₂ hydrate at 30 MPa" Energy, Vol. 22, No. 2/3 (1997).

Bach, W. et. al (Eds.), Interactions of Energy and Climate, "The Collection, Disposal and Storage of Carbon Dioxide by Baes, C.F., Beall, S.E., Lee, D.W. and Marland, G." (Dordrecht: Reidel Publishing Company, 1980), pp. 495-519

Berecz, E. and M. Balla-Achs, Studies in Inorganic Chemistry "Gas Hydrates", (Amsterdam: Elsevier Publishing Company, 1983), Chapter 4

Boyd, Phillip W. et. al, "A Mesoscale Phytoplankton Bloom in the Polar Southern Ocean Stimulated by Iron Fertilization", Nature Vol. 407 (October 2000) pp. 695-702.

Brewer, P.G. "Gas Hydrates and Global Climate Change", Annals of the New York Academy of Sciences Vol. 912, (2000), pp. 195-199

Brewer, P.G., G. Friedrich, E.T. Peltzer & F.M. Orr, Jr. "Direct Experiments on the Ocean Disposal of Fossil Fuel CO₂". Science Vol. 284 (1999), pp. 943-945

Brooks, J.M., M.E. Field & M.C. Kennicutt II. "Observations of gas hydrates in marine sediments, offshore Northern California" Marine Geology Vol. 96 (1991), pp.103-109

Buffett, B.A., & Zatsepina, O.Y. "Formation of Gas Hydrate from Dissolved Gas in Natural Porous Media" Marine Geology Vol. 164 (2000), pp. 69-77

Coale, K.H., et. al. "A Massive Phytoplankton Bloom Induced by an Ecosystem-scale Iron Fertilization Experiment in the Equatorial Pacific Ocean," Nature Vol. 383 (October 1996), pp. 495-501.

Deaton, W.M. & Frost, E.M., Jr., Gas Hydrates and Their Relation to the Operation of Natural Gas Pipe Lines. (U.S. Bureau of Mines monograph 8, 1946) pp. 101

Enick, R.M., & Klara, S.M. "CO₂ Solubility in Water and Brine under Reservoir Conditions" Chemical Engineering Communications Vol. 90, 1990 pp. 23-33.

Frost, B.F., "Phytoplankton bloom on iron rations" Nature (Oct 1996) pp. 475-476.

Golomb, D.S., Herzog, H., Tester, J., White, D. and Zemba, S.G. Feasibility, Modeling and Economics of Sequestering Power Plant Emissions in the Deep Ocean, (Boston: Massachusetts: MIT Energy Laboratory Report, MIT-EL 89-003, 1989)

Handa, Y.P., "Effect of hydrostatic pressure and salinity on the stability of gas hydrates" Journal of Physical Chemistry Vol. 94 (1990) pp. 2652-2657

Herzog, H. The Fourth International Conference on Greenhouse Gas Control Technologies, Interlaken, Switzerland, August 30 – September 2, 1998. "Ocean Sequestration of CO₂: An Overview"

Holder G.D, Mokka, L.P & Warzinski, R.P., "Hydrate Formation from Single-Phase Aqueous Solutions" (To be published Journal of Chemical Engineering Science)

Holder, G.D., Corbin, G., & Papadopoulos, K.D. "Thermodynamic and Molecular Properties of Gas Hydrates from Mixtures containing Methane, Argon and Krypton." Industrial and Engineering Chemistry Fundamentals, Vol. 19, (1980) pp. 282-286.

Holder, G.D., Mokka, L.P & Warzinski, R.P., "Hydrate Formation from Single-Phase Aqueous Solutions" Proceedings of the Fuel Chemistry Division, American Chemical Society Vol. 46, No. 1 (March 2001) pp. 49-50.

Holder, G.D., Zele, S., Enick R.M and LeBlond, C., "Modeling Thermodynamics and Kinetics of Hydrate Formation." Annals of the New York Academy of Sciences Vol. 715, (April, 1994) pp. 344 – 354.

Holder, G.D., Zetts, S.P. & Pradhan, N. (1988). "Phase Behavior in Systems containing Clathrate Hydrates, a Review" Reviews in Chemical Engineering, Vol. 5(1-4), (1988) pp. 1 – 70.

Houghton, J.T., et. al., eds.. Climate Change 1995: The Science of Climate Change (Intergovernmental Panel on Climate Change, Cambridge University Press, Cambridge, UK, 1996)

John, V.T and Holder, G.D., Journal of Physical Chemistry, Vol. 89, (1985) pp. 3279-3285

John, V.T. and Holder, G.D., Journal of Physical Chemistry, Vol. 85, No. 13 (1981), pp.1811-1814

John, V.T. and Holder, G.D., Journal of Physical Chemistry, Vol. 86, No. 4 (1982a), pp. 455-459

John, V.T., Papadopoulos, K.D. and Holder, G.D., AICHE Journal, Vol. 31 No. 2 (1985), pp. 252-259

Kaplan, I.R., ed., Natural Gas in Marine Sediments, “The Nature and Occurrence of Clathrate Hydrates, by S.L. Miller” (New York: Plenum Press, 1974), pp. 151-177.

Larson, S.D., Phase Studies of the Two-Component Carbon Dioxide-Water System, Involving the Carbon Dioxide Hydrate, University of Illinois, (1955)

Marchetti, C. “On Geoengineering and the CO₂ Problems”, Climate Change Vol.1 (1977) pp. 59-68

Markels, Micheal, Jr. and Barber, Richard T., “Sequestration of Carbon Dioxide by Ocean Fertilization” Proceedings of the Fuel Chemistry Division, American Chemical Society Vol. 46, No. 1 (March 2001) pp. 45 – 48.

Masutani, S.M.; Kinoshita, C.M.; Nihous, G.C.; Ho, T.; Vega, L.A., “An Experiment to Simulate Ocean Disposal of Carbon-Dioxide” Energy Conversion Management, Vol. 34 (1993) pp. 865-872

Miller, S.L., Smythe, W.D., Science, Vol. 170, (1970)

Munjal, P., & Stewart, P.B. “Solubility of Carbon dioxide in Pure Water, Synthetic Sea Water and Synthetic Sea Water Concentrates at –5°C to 25°C and 10 to 45 atm. Pressure” Journal of Chemical and Engineering Data Vol.15 No.1 (1970), pp. 67-71.

Ng, H. –J. and D.B. Robinson Fluid Phase Equilibria, Vol. 21, (1985) pp. 145-155

Ohgaki, K., Makihara, Y. and Takano, K. “Formation of CO₂ Hydrate in Pure and Sea Waters” Journal of Chemical Engineering of Japan Vol. 26, (October, 1993) pp. 558 -564

Ormerod, W.G. et. al. Ocean Storage of CO₂, (International Energy Agency Greenhouse Gas R&D Programme, February 1999)

Pajaras, J.A. & Tascon, J. M. D. eds., Coal Science “Observations of CO₂ Clathrate Hydrate Formation and Dissolution under Deep-Ocean Disposal Conditions” by

Warzinski, R. P., Cugini, A.C., & Holder, G.D. (New York: Elsevier Publishing Company, 1995), pp. 1931-1934.

Parrish, W.R. and Prausnitz, J.M., Industrial Engineering Chemistry Process Design and Development, Vol. 11, No. 1, (1972) (No. 1) pp. 26-34.

Peng, D.Y., & Robinson, D.B. “A New Two-Constant Equation of State” Industrial and Engineering Chemistry Fundamentals, Vol. 15, No. 1, (1976) pp. 59-64 .

Prausnitz, J., Lichtenthaler, R.N., & Gomes de Azevedo, E. Molecular Thermodynamics of Fluid-Phase Equilibria (2nd edition, Englewood Cliffs, NJ: Prentice-Hall, 1986)

Ravkin, A. Global Warming: Understanding the Forecast, (New York: Abbeville Press, 1992)

Reichle, D., et. al, Eds., Carbon Sequestration Research and Development, (Office of Science, Office of Fossil Energy, U.S. Department of Energy, December 1999).

Robinson, D.B., and Mehta, B.R. Journal of Canadian Petroleum Technology Vol. 10, (1971) pp. 33-35

Saito, S., Marshall, D.R. and Kobayashi, R. AIChE Journal, Vol. 10, No. 5, (1964) pp. 734-740

Sloan, E.D. Jr., Clathrate Hydrates of Natural Gases, (2nd edition; New York : Marcel Dekker Inc., 1998)

Sloan, E.D. Jr. “Clathrate Hydrates: The Other Common Solid Water Phase,” Industrial and Engineering Chemistry Research Vol. 39(9) (September 2000) pp. 3123 - 3129

Sloan, Jr., E.D., Khoury, F.M., & Kobayashi, R “Water content of Methane Gas in Equilibrium with Hydrates.” Industrial and Engineering Chemistry Fundamentals, Vol. 15, No. 4, (1976) pp. 318-323

Song, K.Y., & Kobayashi, R. “Measurement and Interpretation of the Water Content of a Methane-Propane Mixture in the Gaseous State in Equilibrium with Hydrate.” Industrial and Engineering Chemistry Fundamentals, Vol. 21 (1982), pp. 391-395

Takenouchi, S. and G.C. Kennedy Geology. (Notes no. 293, Inst. Of Geophys., Univ. of California, 383-390. 1964)

Takenouchi, S., Kennedy, G.C., Journal of Geology, Vol. 73, 1965

Teng, H., Yamasaki, A. and Shindo, Y. “Stability of the Hydrate Layer Formed on the Surface of a CO₂ Droplet in High-Pressure, Low Temperature Water”, Chemical Engineering Science Vol. 51, 1996, pp. 4979-4986

Teng, H., Yamasaki, A. and Shindo, Y. “The Fate of CO₂ Hydrate Released in the Ocean” International Journal of Energy Research Vol. 23 (4) (March 1999) pp.295 - 302

Teng, H., Yamasaki, A., Chun, M.K.-, & Lee, H “Solubility of Liquid CO₂ in Water at Temperatures from 278 K to 293 K and Pressures from 6.44 MPa to 29.49 MPa and

Densities of the Corresponding Aqueous Solutions” Journal of Chemical Thermodynamics Vol. 29, (1997) pp. 1301-1310.

Toplak, G.J. “Solubilities of Hydrocarbon Gas Mixtures in Distilled Water near Hydrate Forming Conditions” (unpublished M.S. Thesis, Department of Chemical and Petroleum Engineering, University of Pittsburgh, 1989).

Unruh, C.H., Katz, D.L. Petroleum Transactions; AIME: New York, April 1949; p. 83.

Van der Waals, J.H. and Platteeuw, J.C., Advances in Chemical Physics, Vol. 2, pp.1-57 (1959)

Vlahakis, J.G., Chen. H.-S., Suwandi, M.S. Barduhn, A.J., The Growth Rate of Ice Crystals: Properties of Carbon Dioxide. Hydrate, A Review of Properties of 51 Gas Hydrates (Syracuse U. Research and Development Report 830, prepared for US Department of Interior, November 1972)

Von Stackelberg, M.W. and H.R. Muller: Journal of Chemical Physics, No. 19, (1951) pp.1319-1320

Warzinski, R.P., Lee, C.-H., & Holder, G.D. “Supercritical-Fluid Solubilization of Catalyst Precursors: The Solubility and Phase Behavior of Molybdenum Hexacarbonyl in Supercritical Carbon Dioxide and Application to the Direct Liquefaction of Coal” Journal of Supercritical Fluids Vol 5 (1992), pp. 60-71.

Warzinski, R.P., Lynn, Ronald J., Holder, Gerald D. “The Impact of CO₂ Clathrate Hydrate on Deep Ocean Sequestration of CO₂: Experimental Observations and Modeling Results” Annals of the New York Academy of Sciences Vol. 912 (2000), pp. 226-234.

Wiebe, R., & Gaddy, V.L. "The Solubility of Carbon Dioxide in Water at Various Temperatures from 12°C to 40°C and at Pressures to 500 Atmospheres. Critical Phenomena" Journal of the American Chemical Society Vol. 60 (1940), pp. 815-817.

Zatsepina, O.Y and Buffett B.A. "Phase Equilibrium of Gas Hydrate: Implications for the Formation of Hydrate in the Deep Sea Floor" Geophysical Research Letters Vol. 24, No. 13 (July, 1997), pp. 1567-1570.

Zatsepina, O.Y. and Buffett B.A., "Thermodynamic conditions for the Stability of Gas Hydrate in the seafloor" Journal of Geophysical Research Vol. 103, No. B10 (October, 1998), pp.127-139.

**XXI. “A Geophysical Investigation and Stream Grouting Trial at Streamflow
Loss Zones in Headwater Reach of Nanticoke Creek, Luzerne County,
Pennsylvania”**

**Robert Dilmore (S), Ronald Neufeld (F), and Kathi Beratan (F), University of
Pittsburgh
with
Terry Ackman (M), NETL**

TITLE

**A geophysical investigation and Stream Grouting
Trial at Streamflow Loss Zones in Headwater
Reach of Nanticoke Creek, Luzerne County,
Pennsylvania**

**Robert Dilmore, Graduate Student Researcher
Terry Ackman, Clean Water Team Leader
United States Department of Energy National Energy Technology
Laboratory**

**2001 University Partnership Program Annual Activity Report
December 10th, 2001**

TABLE OF CONTENTS

TITLE.....	1
TABLE OF CONTENTS	2
LIST OF FIGURES.....	3
ABSTRACT.....	4
SITE DESCRIPTION	5
EXPERIMENTAL APPARATUS AND PROCEDURES	7
Data Collection.....	7
Stream Flow Data.....	7
GEOPHYSICAL DATA.....	8
Electromagnetic Conductivity.....	8
Near Surface Ground EM Condcutivity (EM-31)	8
Mid-Depth Ground EM Conductivity (EM-34).....	9
Very Low Frequency (VLF) Conductivity	10
Geographic Data.....	11
Site Characterization and GIS development	11
Grouting Efforts at the Nanticoke Creek Study Area	11
RESULTS AND DISCUSSION.....	14
Proposed Modified Grouting Technique.....	17
CONCLUSIONS	20
List of Acronyms and Abbreviations	20
SELECTED REFERENCES.....	20

LIST OF FIGURES

- Figure 1. Map of stream segment under consideration, with coal outcrops, stream location flags, and mining related surface features labeled**
- Figure 2. Representation of geologic cross section, showing coal seams and some mine workings near the Nanticoke Creek Study Area.**
- Figure 3. Location of EM-34 survey lines adjacent to Nanticoke Creek**
- Figure 4. Phase I grouting locations and unexpanded polyurethane grout volumes injected**
- Figure 5. Phase II grouting locations and unexpanded polyurethane grout volumes injected**
- Figure 6. Illustration of grout rod and injection to seal mine subsidence related overburden fractures**
- Figure 7. EM-31 vertical dipole electromagnetic conductivity response measurements along Nanticoke Creek Stream Channel before grouting, after grouting Phase I, and after Grouting Phase II**
- Figure 8. EM-34 Survey Line 1 adjacent to Nanticoke Creek study area – vertical and horizontal dipole response.**
- Figure 9. Fractured coal barrier below Nanticoke Creek responsible for stream loss to underlying mine. With time this fractured pillar and the adjacent overburden begin to subside.**
- Figure 10. Collapse of fractured coal barrier and adjacent areas of shallow overburden result in increased stream loss over a larger stream segment.**
- Figure 11. Proposed modification to grouting technique involves shallow injection of grout at multiple locations to produce a waterproof “blanket” in the sub-stream alluvium.**

ABSTRACT

Geophysical techniques were used to delineate both areas of stream flow loss through fractured bedrock to underlying mine workings and unsaturated mine voids near the surface. EM-31, EM-34 and VLF electromagnetic techniques were used to target in-stream polyurethane grout injection in attempt to seal fractures associated with subsidence and resulting in stream flow loss. Through USGS stream flow monitoring and post-grouting geophysical survey, it was found that grouting efforts were largely unsuccessful in sealing the stream and preventing stream loss. Further analysis of geologic conditions and mining techniques used revealed that subsidence features are diffuse and extended across as much as 150 feet for each coal seam under consideration. Because of this, a modified grouting technique based on shallow injection using several injection points has been developed. Trails have been proposed for this modified grouting technique.

SITE DESCRIPTION

Under consideration is a 1000 reach of Nanticoke Creek in Luzerne County, Pennsylvania, near Wilkes-Barre Pennsylvania. This region of Pennsylvania suffers from severe environmental strain as a result of extensive mining of multiple seams of anthracite coal by deep as well as surface mining techniques. The Nanticoke Creek Basin - a small 7.6 mi² sub-watershed of the large Susquehanna River Watershed - is littered extensively with spoil and refuse piles from more than 100 years of un-reclaimed mining operations. Abandoned underground workings, many of which have openings that are not yet sealed, have flooded and in many locations collapsed. These subsurface collapses express themselves as surface subsidence features. A significant portion of runoff and surface water that passes over these collapsed and subsided areas infiltrates into the mine workings. In the mine, this infiltrated water, representing 40 percent of the total annual precipitation according to one study (Skelly & Loy, Inc., 1975), contacts pyritic material and becomes contaminated with acidity, iron, and sulfate. This contaminated water resurfaces at some point down-gradient (not necessarily in the same sub-watershed) as acid mine drainage (AMD). (Babula and Cravotta, 2001)

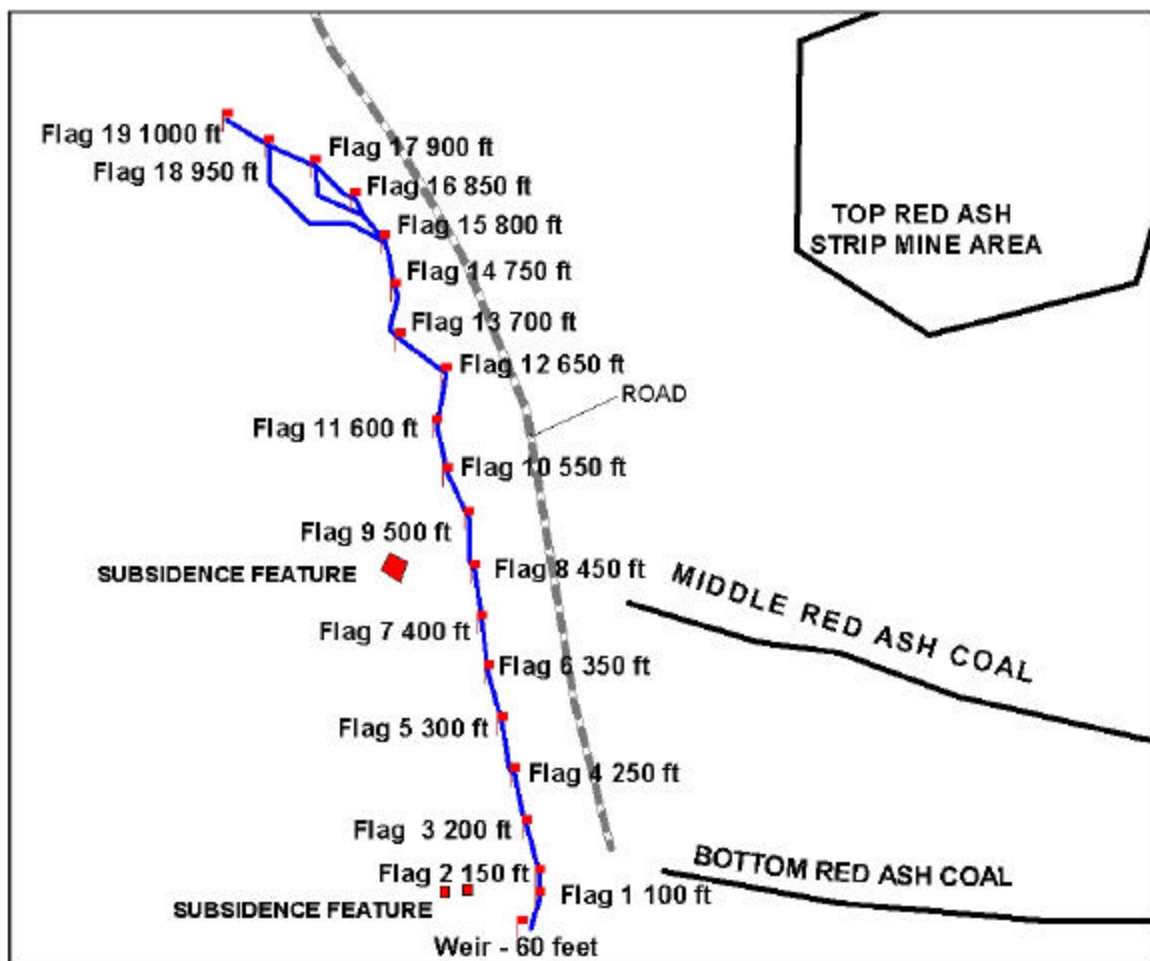


Figure 1. Map of stream segment under consideration, with coal outcrops, stream location flags, and mining related surface features labeled

To date, a number of remediation techniques have been considered, including treatment of AMD at the point of discharge, and preventative techniques such as stream channel lining, re

The 1000-foot stream reach under consideration traverses at least three and possibly four coal seam outcrops. In the sedimentary bituminous coal fields of West Virginia and southwestern Pennsylvania, coal seams run – in general – parallel to the surface of the ground with convex and concave anticline and syncline features. In the metamorphic anthracite fields of northeastern Pennsylvania, coal seams often thrust upwards at angles of 35 to 45 degrees or more (from the earth's surface). A cross-sectional sketch representative of the geologic structure near the Nanticoke Creek study area was drawn at the time of active mining in the site. This illustration (see Figure #1) shows both the angle at which the coal seams dip, as well as the approximate slope of the stream segment in question.

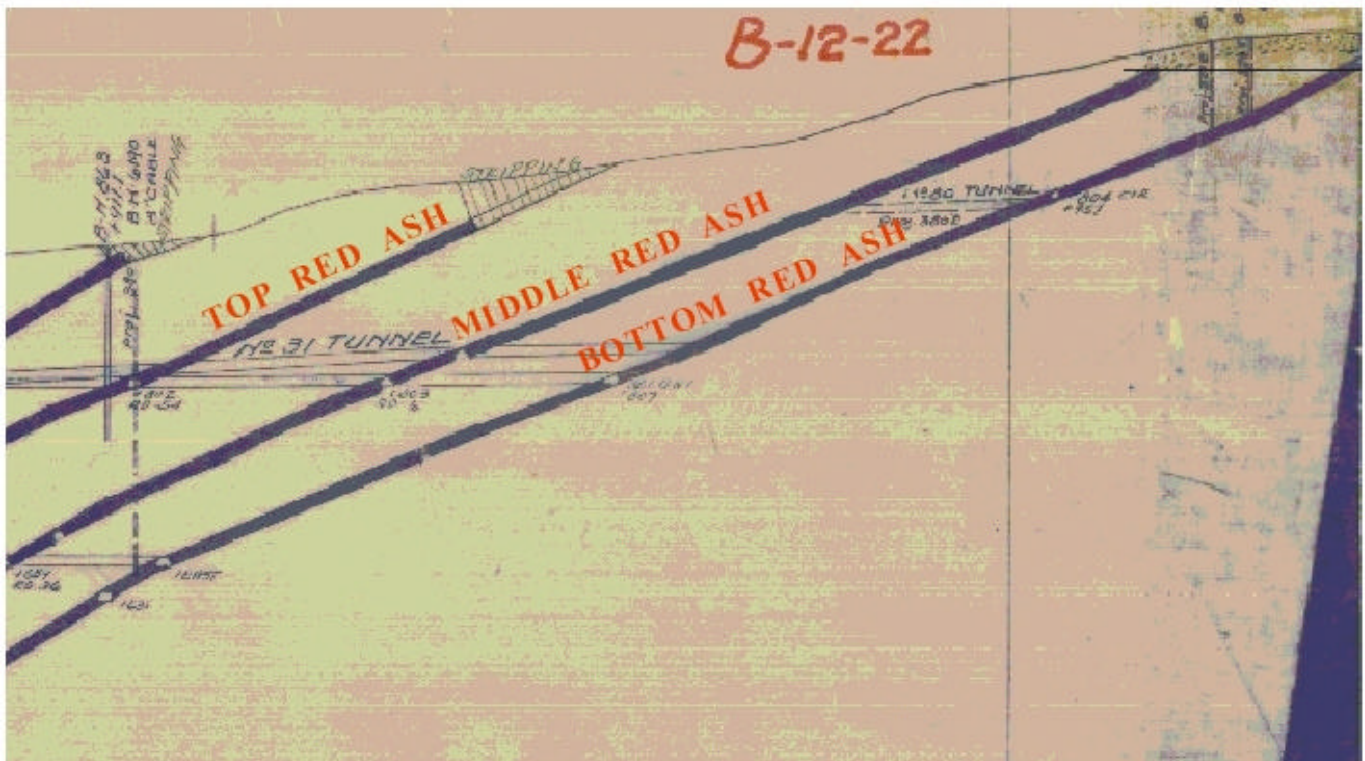


Figure 2. Representation of geologic cross section, showing coal seams and some mine workings near the Nanticoke Creek Study Area.

The upper portion of the 1000-foot stream section slopes steeply with the stream bed comprised of large boulders and steeply dipping bedrock outcrops. Water flowed through this portion of the creek in a step/pool fashion. The lower portion of the stream has a more gradual slope, with the stream bed comprised of cobbles, gravel bed material, and aggregated chunks of mine spoil – appearing to have been fused together

as a result of heating from a refuse pile fire. Along much of the stream reach, banks are steep with significant erosion and uprooted trees. At approximately 450 feet from the upstream start of the study area, there is a large smooth rock face that comprises approximately 30 feet of the creek bed. This rock face is situated at an angle of approximately 45 degrees, and serves as a good indicator of the angle at which the bedrock dips through this section of the stream. At the bottom of this rock face, there is a large pool of water.

Preliminary observation and stream flow monitoring indicated that the stream was decreasing in flow across the 1000-foot section in question. During periods of low flow, total loss of stream flow to mining related infiltration could be observed at points 750 feet downstream from the top of the 1000 foot study area. (Babula and Cravotta, 2001) As an alternative to more costly stream channel lining construction, stream sealing through targeted, sub-surface grouting by injection of polyurethane was investigated along this stretch of Nanticoke Creek. The grouting effort was divided into three distinct tasks, including: geophysical survey of the stream and surrounding area, stream flow gauging, and grouting.

In cooperation with the United States Department of Energy National Energy Technology Laboratory geophysical investigation / grout injection trials, the United States Geological Survey conducted extensive stream flow monitoring of the Nanticoke Creek Headwaters before, during and after grout injection episodes, both above and below targeted stream-loss zones. These data were used to evaluate the effectiveness of selective grouting efforts to decrease infiltration and restore streamflow. (Babula and Cravotta, 2001)

EXPERIMENTAL APPARATUS AND PROCEDURES

Data Collection

Base-line data collected for the Nanticoke Creek site includes stream flow, geophysical and geographic data. These techniques were used to target and evaluate the success of polyurethane grout stream sealing in the Nanticoke Creek.

Stream Flow Data

The United States Geologic Survey (USGS) regularly collects stream flow data at several gauging stations across the area of interest on Nanticoke Creek. This data is collected so that areas of stream-loss can be identified along the study area stream length. If stream flow at a gauging station downstream is significantly lower than stream flow of an adjacent upstream gauging station, the stream length between the two gauging stations is targeted as an area of stream flow loss to the underlying mine through subsidence related or natural fracture systems. It has also been used to determine the effectiveness of stream grouting efforts carried out at the study area by the Clean Water Team.

Flow measurements were conducted with a pygmy (vertical axis) current meter, and carried out at least once a week through the duration of the study. This is the appropriate method for measuring flow of small streams such as Nanticoke Creek. The pygmy meter can accurately measure flow in streams with water depths from 0.3 to 1.5 feet and velocities from 0.2 to 2.5 feet/second (Buchanan and Somers, 1969). At each station,

USGS hydro-geologists established a cross section, and depth and velocity measurements were conducted at a minimum of ten points across the stream. These flow measurements were supplemented with timed volumetric measurements for cascading reaches with small discharges.

GEOPHYSICAL DATA

DOE NETL Clean Water Team members have collected three types of ground based geophysical data at the Nanticoke Creek site: shallow electromagnetics (EM), mid-depth EM, and very low frequency (VLF).

Electromagnetic Conductivity

Electromagnetic (EM) conductivity techniques have demonstrated utility for groundwater studies including: (1) groundwater exploration, (2) mapping industrial groundwater contamination, (3) mapping general groundwater quality (i.e., salinity) and saline intrusion, and (4) mapping soil salinity for agricultural purposes⁶. We have found that EM conductivity techniques can also be used to delimit fracture systems and mine voids that contain water.

EM conductivity techniques use a transmitter coil to generate an electromagnetic field (primary field) with a frequency between 100 Hz and 100K Hz. This primary field propagates through the surrounding area until it encounters a conductive body in which it induces a flow of alternating current. This ground current, in turn, induces a second electromagnetic field (secondary field) which has a field strength that is proportional to the conductivity of the geoelectric structure. The secondary field also propagates through the surrounding area, and with the primary field, make up the complete electromagnetic field that is detected at the receiver coils of the EM conductivity instrument.

EM conductivity instruments measure apparent conductivity, which is expressed in millisiemens per meter (mS/m). The apparent conductivity is calculated as follows:

$$s_a = (4/2\pi f F_0 s^2) (H_s/H_p)$$

where s_a is the apparent ground conductivity, H_p is the primary electromagnetic field, H_s is the secondary electromagnetic field, f is current frequency, s is the distance between the transmitting and receiving coils, and F_0 is the permeability of free space¹⁰. The typical practice is to compare the H_s with a value H_p , the intensity of the primary field. Since the coil positions and the current in the transmitter coil are known, the value of H_p can be calculated. The apparent conductivity is a composite of true conductivities for each geo-electric layer that comprises the semi-infinite half-space below the ground surface.

Near Surface Ground EM Conductivity (EM-31)

Using an EM-31 apparent conductivity device manufactured by Geonics, shallow EM data was collected along the length of the stream. By collecting data in the stream bed, it is possible to detect areas of relatively high conductivity associated with vertical water filled fractures and water filled subsidence related voids within the first 6 meters below surface (about 18 feet). EM-31 data are used to pinpoint areas of focus for grouting efforts to areas as small as one square meter.

Mid-Depth Ground EM Conductivity (EM-34)

A Geonics EM-34 conductivity instrument was used with a 20-m inter-coil separation for the ground survey of the Nanticoke Creek site. The depth of penetration for this instrument is a function of the inter-coil separation, orientation of the transmitter and receiver coils, and conductivity of the geologic strata. The EM-34 can be operated with transmitter and receiver coils in either a coplanar or a coaxial geometry. The coplanar mode is more effective at detecting flat-lying conductive bodies whereas the coaxial mode is better for detecting vertical conductive features. Each mode gives a significantly different response (sensitivity) with depth. The effective exploration depths for the two modes are approximately 0.75 (coaxial) and 1.5 (coplanar) times the inter-coil spacing in a layered earth geometry. Therefore, the effective depth for the EM-34 with a 40-m inter-coil separation is about 15 m (about 50 ft.) for the coaxial mode and 30 m (about 100 ft.) for the coplanar mode.

EM-34 data collected adjacent to Nanticoke Creek show areas of low conductivity that correlate with mine openings and mapped coal outcrops to the surface. Because air is significantly less conductive than soil, rock or water, large air pockets in the subsurface present as a result of mining appear as regions of low apparent conductivity in mid-depth geophysical data.

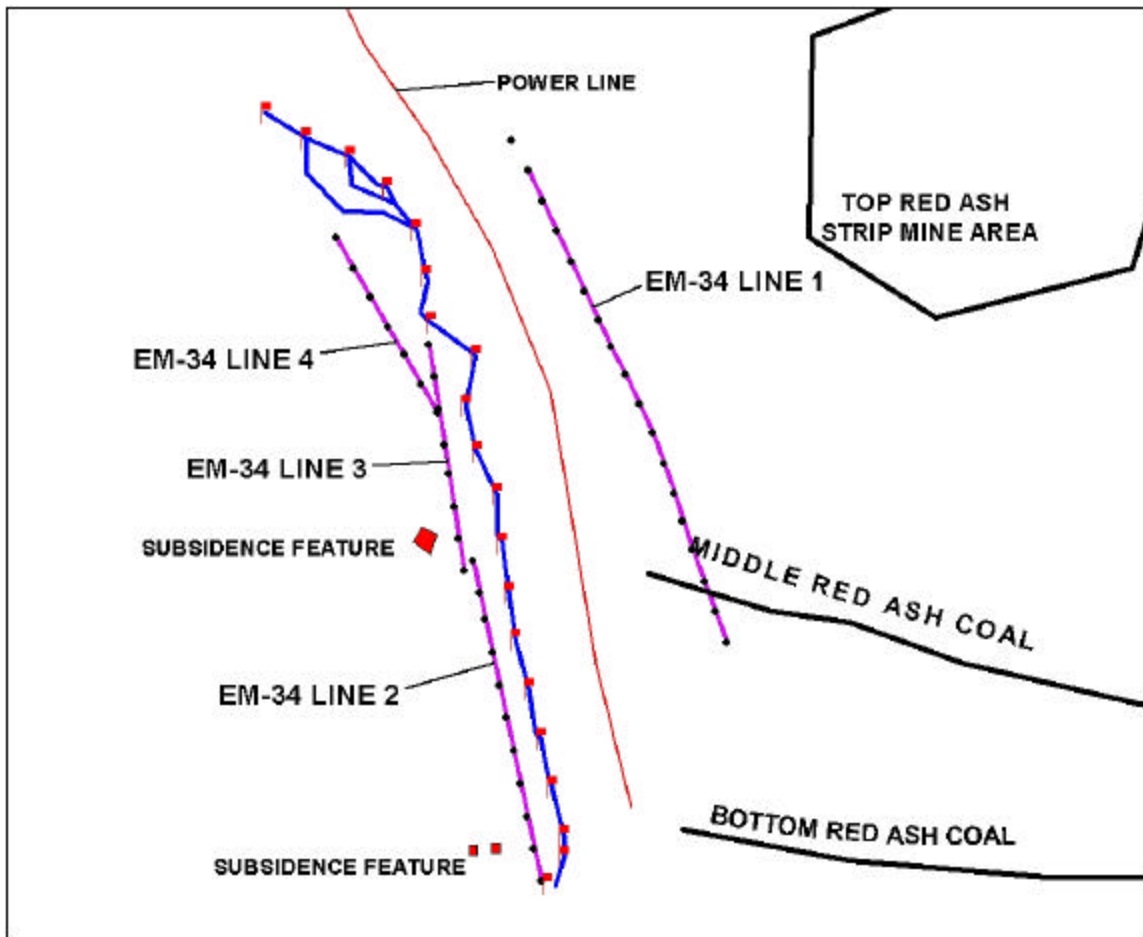


Figure 3. Location of EM-34 Survey Lines Adjacent to Nanticoke Creek

Very Low Frequency (VLF) Conductivity

Very low frequency conductivity is a variant of EM conductivity that uses military transmitters instead of a transmitter coil to generate the primary field. VLF transmitters are in operation at a number of sites throughout the world, including North America, and typically operate at a frequency between 15 and 30 kilohertz (kHz). A VLF transmitter consists of a vertical cable several hundred meters long that emits a very powerful (300-1000 kilowatt) transmission signal. The primary electromagnetic field emitted by the antenna is horizontal, and its magnetic lines are comprised of concentric rings that ripple out from the transmitter. Otherwise, VLF conductivity is similar to coaxial EM conductivity in theory and data interpretation. VLF conductivity instruments are generally lighter, less cumbersome, and less expensive than the corresponding EM conductivity instruments.

The information obtained from VLF conductivity surveys is similar to that obtained from EM conductivity except that VLF is more sensitive to vertical conductors (usually water-filled fractures, conductive ore bodies, or man-made features) that are oriented in the direction of the transmitter. Two U.S. Navy transmitters were used for this survey. A transmitter at Cutler, Maine (24 kHz) was ideally located for the detection of vertical, water-filled fracture zones oriented normal to the major east/west structural trend in the surveyed areas. A second transmitter at Seattle, Washington (24.8K Hz) was appropriately located for the detection of water-filled fractures with trends parallel to the

major east-west structural trend. Although VLF conductivity is not as sensitive as EM conductivity for the detection of water tables and mine pools, it is better suited for the detection of vertical, water-filled fractures that may represent zones of groundwater recharge.

In the Nanticoke Creek study, VLF data was collected along the stream-bed from these two transmitting stations. Preliminary results suggest that anomalous VLF response correlates with location of known coal outcrops, areas of stream flow loss, and other geophysical anomalies.

Geographic Data

Survey data was collected for the Nanticoke Creek study area in order to ensure spatial accuracy of collected data and observed relationships. In addition to a high accuracy land survey conducted by NETL employees, differential GPS data was collected to verify location of various points in X,Y, and Z real world coordinate space. Finally, previously acquired data from an aerial survey provided two foot contour data that was used to develop a high resolution digital elevation model for three dimensional visualization and evaluation of data

Site Characterization and GIS development

In order to investigate spatial relationships between data of various sources, data were collected and integrated in a geographic information system (GIS). Development of a GIS allows incorporation of aerial photography, mine maps, high accuracy GPS survey data, high resolution digital elevation model, stream flow, geophysical, and other data into a spatially related database. This allows spatially explicit evaluation of complicated systems and surface/subsurface interactions in three dimensions.

Grouting Efforts at the Nanticoke Creek Study Area

Previous investigation and experimentation by the NETL Clean Water Team have successfully employed a novel stream grouting technique to prevent flow loss from streams to underlying mines in areas of bituminous coal mining. The Nanticoke Creek study is the first attempt to apply this technique to remediate streams impacted by anthracite coal mining. In the established grouting process, holes are drilled using a pneumatic drill to a depth of four to six feet. Hollow rods are then inserted into the drilled holes. A single component polyurethane grout is then pumped into the drilled holes under compression (up to 3000 psi) via the hollow rods. The polyurethane grout expands through the existing fracture or void to a volume as much as twenty times it's initial volume. Over a period of approximately five hours, the grout solidifies -effectively sealing the fractures and voids that it occupies. Solidified grout has the following physical properties:

- Compressive strength - 25 pounds per square inch (psi)
- Shear strength - 17.1 psi
- Tensile strength - 29.3 psi
- Elongation capacity – 300 %

Finally, the grout has been deemed environmentally safe and is approved for use by the U.S.D.A., NSF 61-198, and U.L.

Two grouting sessions were carried out at the Nanticoke Creek study area. Before grouting, baseline flow and geophysical data were collected to establish existing conditions and pinpoint areas of interest for grouting. Again after stream grouting flow

measurements and geophysical data were collected along the stream to determine changes in subsurface hydrologic conditions resulting from grouting efforts. Based on evaluation of these new data, a second session of drilling and stream grouting was carried out to augment stream sealing from the first session. After this second grouting session, flow and geophysical data were again collected to determine success of grouting efforts. To date, grouting efforts at the Nanticoke Creek study area have met with little success. Effective site characterization and increased understanding of site hydrologic conditions and mining history have led to the development of a new strategy for stream grouting at the Nanticoke Creek study area. Maps of the locations of Phase I and II grout injection along the 1000-foot study area are shown in Figures 4 and 5, respectively

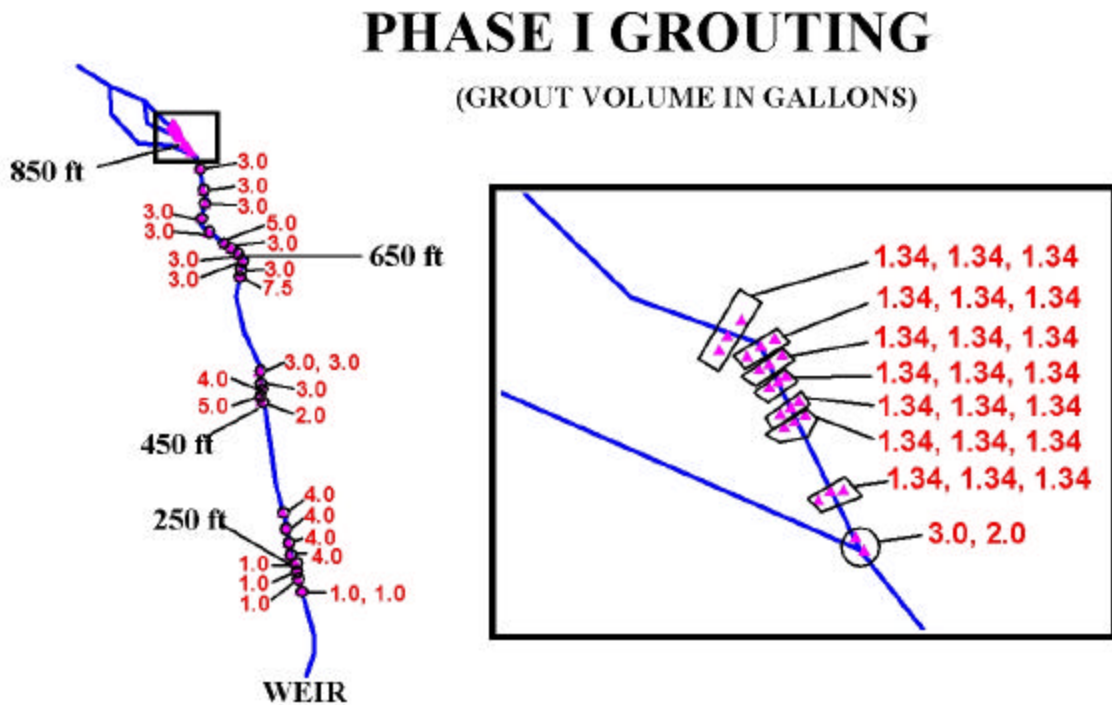


Figure 4. Phase I Grouting Locations and Unexpanded Polyurethane Grout Volumes Injected

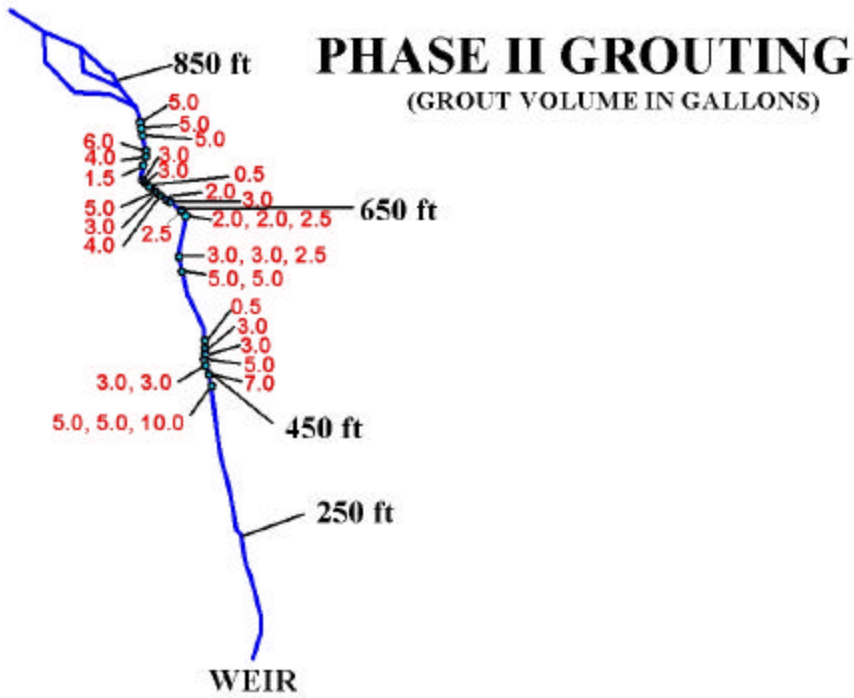


Figure 5. Phase II Grouting Locations and Unexpanded Polyurethane Grout Volumes Injected

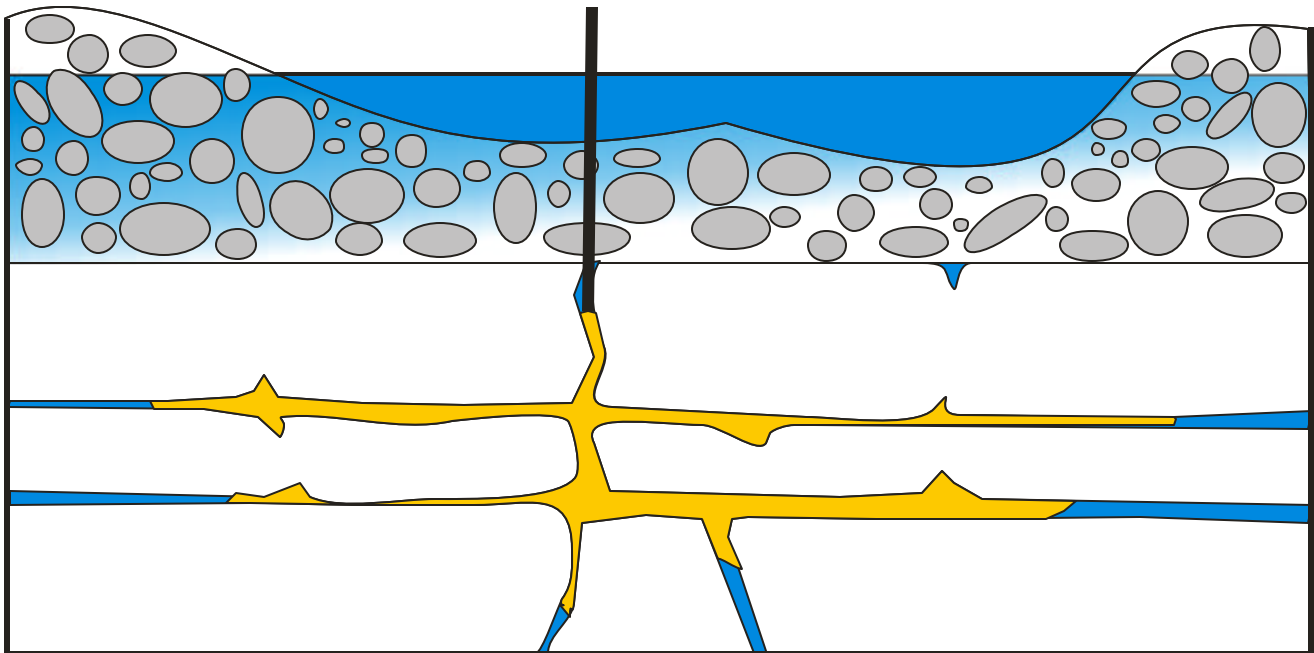


Figure 6. Illustration of grout rod and injection to seal mine subsidence relate overburden fractures

RESULTS AND DISCUSSION

In an attempt to more clearly delineate the location of the coal outcrop, the Nanticoke Creek study area was extensively categorized using a number of methods. First, the site was surveyed for subsidence, mine openings, and other evidence of outcrop location in and around Nanticoke Creek. Locations of these features were logged using a high-resolution global positioning system apparatus. Secondly, historic mine maps were geographically registered and rectified so that they could be integrated into the existing GIS database. These maps show locations of coal outcrops, much of which is not now detectible from observation with the naked eye. Finally, geophysical tools were used to identify anomalous electromagnetic conductivity responses in and adjacent to the creek. EM-31 data were collected along the stream channel. High EM-31 responses both in the horizontal and vertical dipole configuration corresponded well with adjacent subsidence features, mine openings, and with coal outcrop locations from historical maps. Elevated responses also correlated with stream reaches identified as stream loss zones. In-stream EM-31 data were collected before and after each grouting phase in an attempt observe changes in subsurface water flow resulting from grouting efforts. Results shown in Figures 7 and 8 suggest that grouting between 700 and 760 feet carried out during the second grouting session were successful in decreasing subsurface flow. In addition, it should be noted that decreased response in the horizontal dipole on the first data collection (5/9/01) near 900 feet result from lack of flow in the stream at this point. EM-34 data were collected beside the stream in an attempt to find mine workings (mine voids) adjacent to the stream. It was found that the air voids associated with mined out areas have low conductive response (air is a poor conductor). Particularly in the deeper looking vertical dipole (effective depth of 30 m) these voids decrease conductive response to near zero (see Figure 9). Also, it should be noted that as elevation above the stream increases (from left to right on the plot), the EM-34 response in the vertical dipole decreases. This inverse relationship between elevation above conductive material and vertical dipole response is worth noting and could play a role in application where more subtle conductivity is being targeted. Finally, VLF data were collected along the stream reach under study. Results of this VLF survey have as yet not been fully interpreted, but preliminary evaluation suggests good correlation with in-stream EM-31 data.

EM 31 Horizontal Comparison

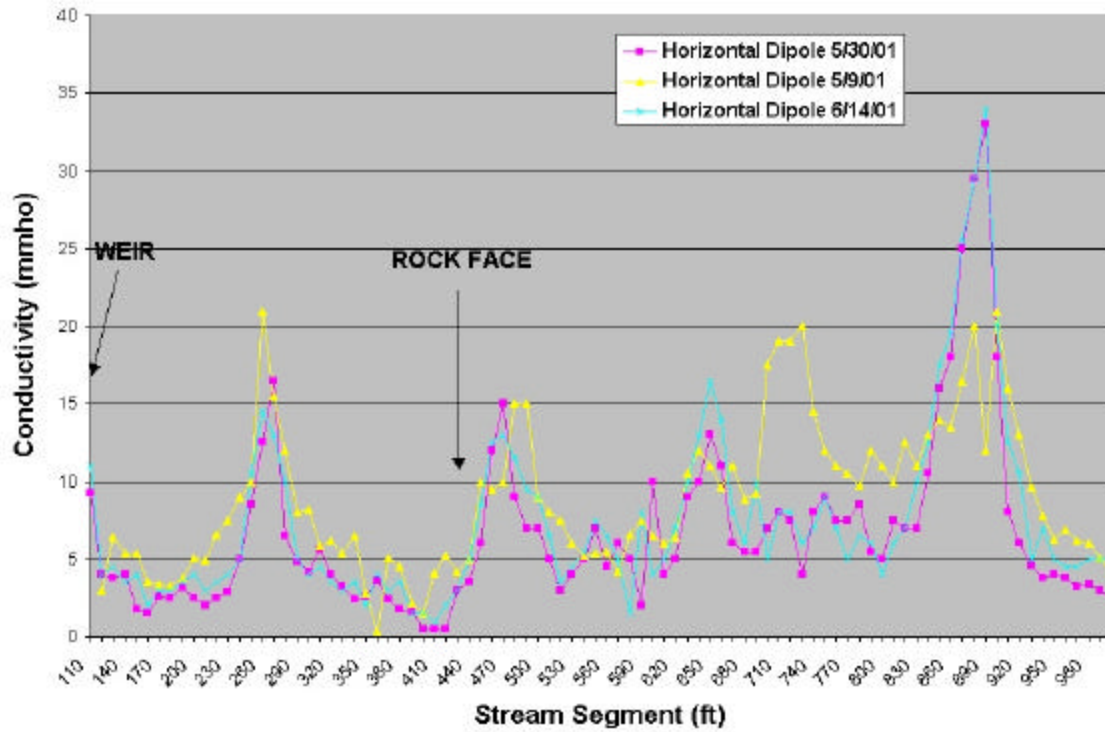


Figure 7. EM-31 horizontal dipole electromagnetic conductivity response measurements along Nanticoke Creek Stream Channel before grouting, after grouting Phase I, and after Grouting Phase II

In Stream EM 31 Vertical Dipole Data

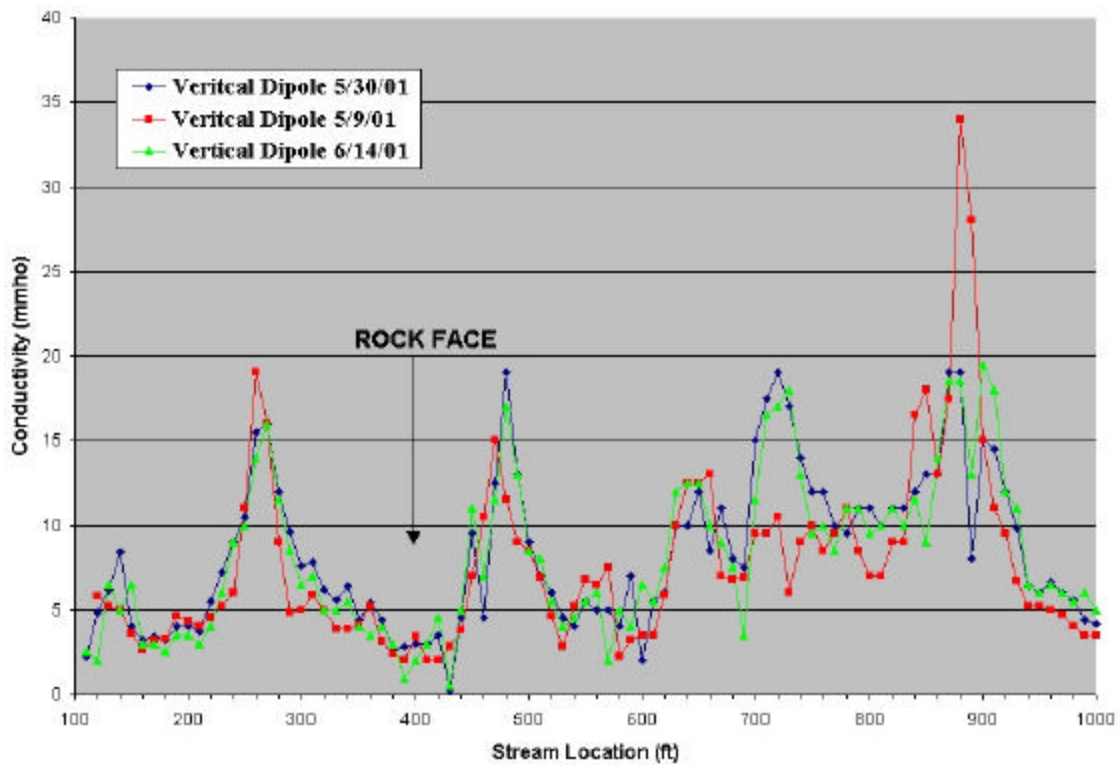


Figure 7. EM-31 vertical dipole electromagnetic conductivity response measurements along Nanticoke Creek Stream Channel before grouting, after grouting Phase I, and after Grouting Phase II

EM-34 Survey (20 m spacing) Nanticoke,PA

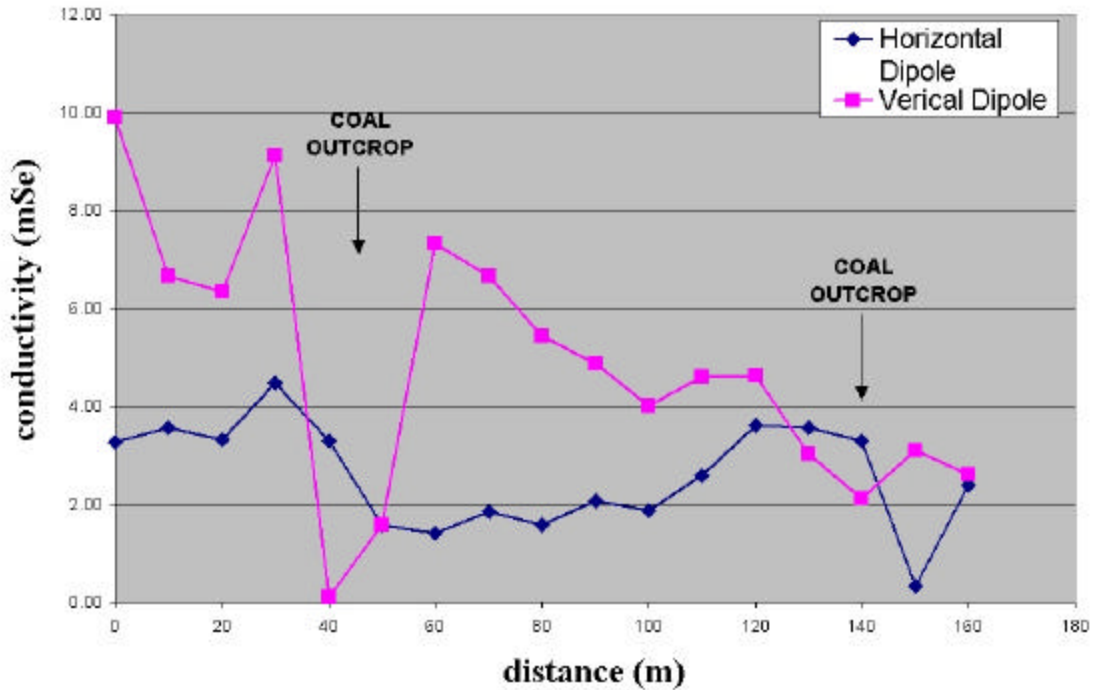


Figure 8. EM-34 Survey Line 1 adjacent to Nanticoke Creek study area – vertical and horizontal dipole response.

Proposed Modified Grouting Technique

Based on NETL Clean Water Team experience to date at the Nanticoke Creek study area, and new knowledge of specific mining techniques, application of a modified grouting method is being proposed. Previous grouting efforts were aimed at drilling into fractures in the existing bedrock at specific sites and filling those fractures that served as conduits for flow from the stream to the mine. These holes were usually four to six feet deep and designed to plug specific fractures that caused most of the stream loss. It has been determined that, as a result of mining techniques specific to the mining anthracite in this region, that stream loss is occurring not at specific fracture locations, but over a stretch of several meters. Anthracite was often mined to within 50 feet of the surface in areas with overlying streams. Over time, this shallow coal barrier, as well as adjacent areas of shallow overburden, begin to collapse into the mine below (see Figure 9). This results in the collapse of large and small material into the subsiding area. This area of unconsolidated material of various size has significant void space, and loses significant amounts of water to the mine void below (see Figure 10). The stream loss occurs not at specific locations, but over a span of as much as 150 feet. Therefore, the proposed modified grouting technique involves injection of grout into a large matrix or grid of shallow (approximately 2 feet) drill holes over the length of subsidence and unconsolidated stream base. This will effectively create an impervious liner below the stream that will allow water to pass over the subsided area (see Figure 11). This grout

lining system will also be flexible such that it can maintain its integrity through shifting and settling of underlying unconsolidated material.

In support of evaluation of this modified stream grouting technique, further data collection will need to be carried out, including continued flow monitoring (to be performed by the USGS) and geophysical data collection. These data will help to quantify the success of this new technique.

Consideration is also being given to development of a program in cooperation with the US Army Corps of Engineers to compare the technical and cost effectiveness of this stream grouting technique with other conventional stream lining techniques, such as clay lining and flume construction. Because the Nanticoke Creek study area has three areas where stream loss is occurring as a result of mining, it would provide a unique opportunity to compare these methods side by side.

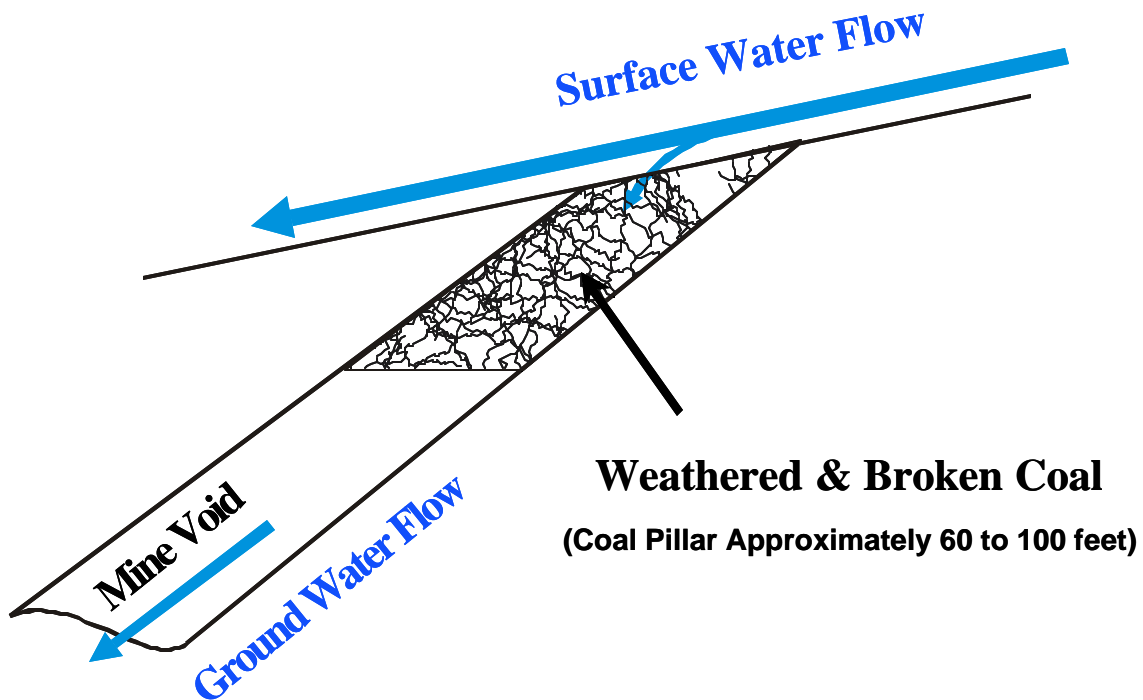


Figure 9. Fractured coal barrier below Nanticoke Creek responsible for stream loss to underlying mine. With time this fractured pillar and the adjacent overburden begin to subside.

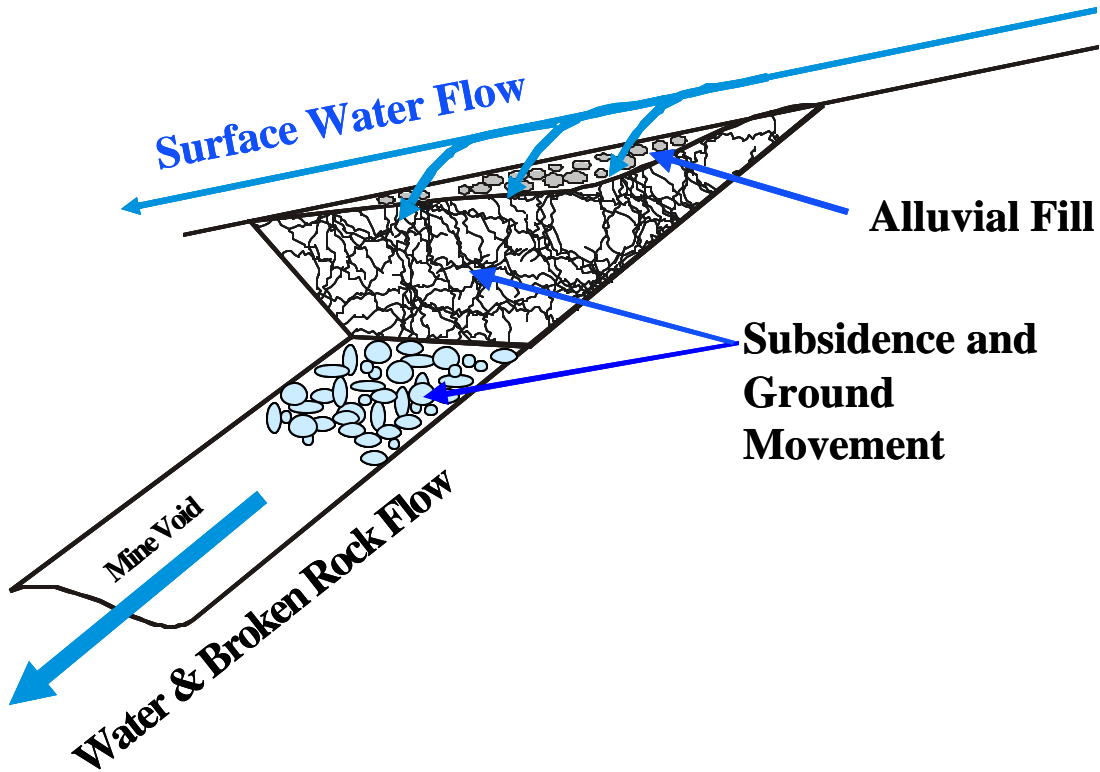


Figure 10. Collapse of fractured coal barrier and adjacent areas of shallow overburden result in increased stream loss over a larger stream segment.

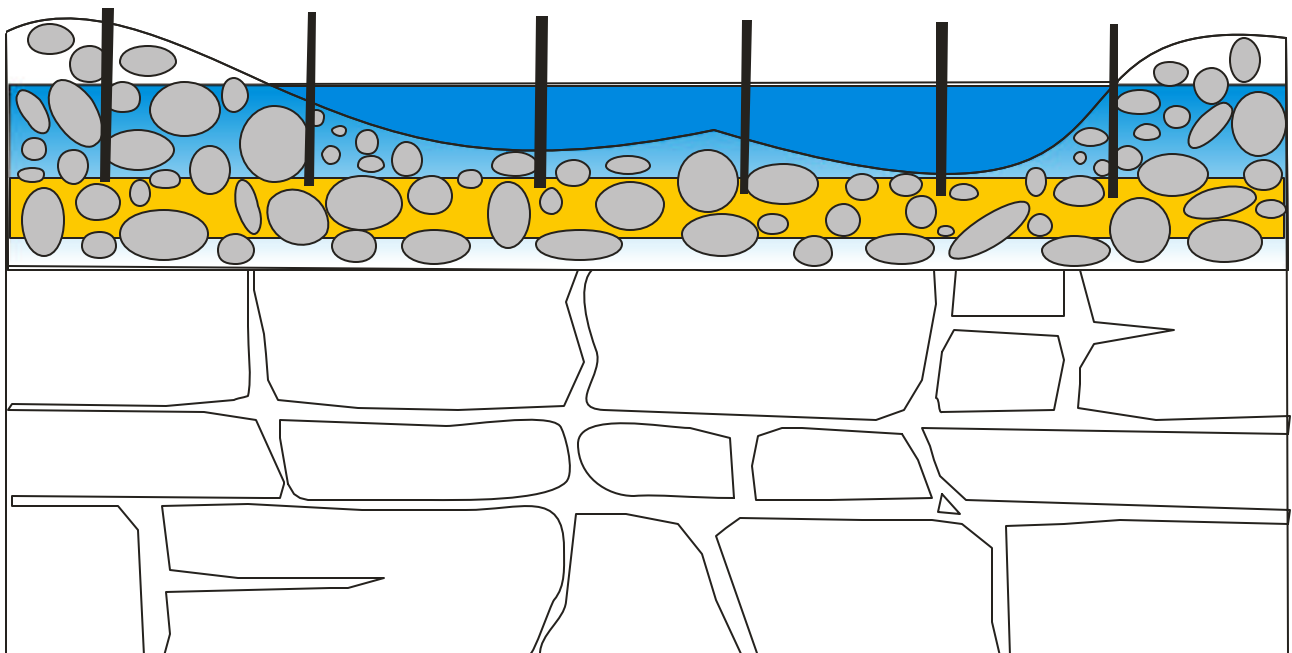


Figure 11. Proposed modification to grouting technique involves shallow injection of grout at multiple locations to produce a waterproof "blanket" in the sub-stream alluvium.

CONCLUSIONS

Geophysical techniques have proven useful in delineating both areas of stream flow loss through fractured bedrock to underlying mine workings, as well as identifying unsaturated mine voids near the surface. These techniques were used to target in-stream polyurethane grout injection in attempt to seal fractures associated with subsidence and resulting in stream flow loss. Through USGS stream flow monitoring and post-grouting geophysical survey, it was found that grouting efforts were largely unsuccessful in sealing the stream and preventing stream loss. Further analysis of geologic conditions and mining techniques used revealed that subsidence features are diffuse and extended across as much as 150 feet for each coal seam under consideration. Because of this, a modified grouting technique based on shallow injection using several injection points has been developed. Trails have been proposed for this modified grouting technique.

List of Acronyms and Abbreviations

EM – Electromagnetic
VLF - Very low frequency
GIS – Geographic information systems
GPS – Global positioning system

SELECTED REFERENCES

Gupta, Ravi P., Remote Sensing Geology. © 1991, Springer-Verlag Berlin Heidelberg. pp. 23 – 33, 279.

Ackman, T. E. and J. R. Jones. A Method to Reduce Surface Water Infiltration Into Underground Mines. Proceedings of the National Symposium on Surface Mining, Hydrology, Sedimentology and Reclamation, December 5-9, Reno, NV, 1988, pp. 79-84.

Babula, Suzanne W, Charles A. Cravotta III, U.S. Geological Survey, 215 Limekiln Rd., New Cumberland, PA 17070, **Effect of Grout Injection on Streamflow Losses in Headwaters Reach of Nanticoke Creek, Luzerne County, Pennsylvania**, 01/08/16
\\Pc40dpahrb\projects\pol\earth_con\report\NanticokeDOE.txt.fm

Skelly & Loy, Inc., 1975, Mine drainage abatement study, Newport Creek, Newport Township and the City of Nanticoke, Luzerne County, Pennsylvania: Harrisburg, Pa., Operation Scarlift project SL 181-2, 102 p.

Chaplin, J.J., and Cravotta, C.A., III, 2000, Abatement of abandoned mine drainage requires characterization of interaction between surface water and underground mine water (abs.), in 2000 Spring Meeting of the American Geophysical Union, Washington, D.C.: EOS Transactions, American Geophysical Union, vol. 81, abs. H6670.

Ash, S.H., Whaite, T.H., 1953, Surface water seepage into anthracite mines in the Wyoming valley basin northern field, anthracite region of Pennsylvania: U.S. Bureau of Mines Bulletin 534, 30 p.

GEO-Technical Services, Inc., 1975, Mine drainage abatement study, Nanticoke, Warrior & Soloman Creeks, Hanover & Wilkes-Barre Townships, Luzerne County, Pennsylvania:
Harrisburg, Pa., Operation Scarlift project SL 181-3, 90 p.

Hedin, R.S., Nairn, R.W., and Kleinmann, R.L.P., 1994, Passive treatment of coal mine drainage: U.S. Bureau of Mines Information Circular 9389, 35 p.
Itter, H.A., 1954, The geomorphology of the Wyoming-Lackawanna region: Topographical and Geologic Survey Bulletin G9, 82 p.

Ladwig, K.J., Erickson, P.M., Kleinmann, R.L.P., and Poslulzszny, E.T., 1984, Stratification in water quality in inundated anthracite mines, eastern Pennsylvania: U.S. Bureau of Mines Report of Investigations 88/37, 35 p.

**UNIVERSITY/NETL STUDENT PARTNERSHIP PROGRAM
(DE-FC26-98FT40143)**

3rd Year Technical Report

September 1, 2000 – August 31, 2001

Submitted to:

National Energy Technology Laboratory

Submitted by:

**Gerald D. Holder
School of Engineering
University of Pittsburgh
Pittsburgh, PA 15261**

Volume VI of VI

**XXII. “Passive Treatment of Coal Mine Drainage and Characterization of
Iron-Rich Precipitates Associated with Coal Mine Drainage”**

**Candace Kairies (S) and Rosemary Capo (F), University of Pittsburgh
with
George Watzlaf (M), NETL**

**Passive Treatment of Coal Mine Drainage and Characterization of Iron-Rich Precipitates
Associated with Coal Mine Drainage**

NETL/DOE Partnership Program

Technical Report

Year Three Progress (Second year in program)

**Candace L. Kairies, Ph.D. candidate, University of Pittsburgh, Dept. of Geology &
Planetary Science**

NETL Mentor: George Watzlaf

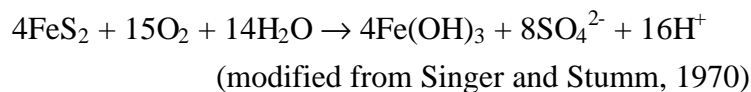
University of Pittsburgh Supervisor: Rosemary C. Capo

Abstract: Drainage from abandoned mined lands (AML) remains a widespread problem in the Appalachian coal fields, with over 2400 miles of streams affected by coal mine drainage (CMD) in Pennsylvania alone (PA Department of Environmental Protection, 1998). Coal mine drainage can contain high concentrations of acidity, sulfates and metals, including iron, aluminum and manganese, as well as lower amounts of arsenic, nickel, zinc and other metals. Over 200,000,000 pounds of iron are discharged from coal mines each year in the United States (Hedin, 1996). The oxidation and hydrolysis of pyrite produces iron hydroxide precipitates, such as goethite, schwertmannite and ferrihydrite, which can coat the bottoms of streams, smothering aquatic life. Iron oxides and hydroxides are known to be excellent scavengers of trace metals, and therefore play an important role in the fate and transport of such elements in the environment (Benjamin and Leckie, 1980; Goldberg, 1954; McCarty et al., 1998). Many studies have thoroughly examined and characterized both acidic and net-alkaline mine waters, but less work has been done on the associated precipitates. The focus of my dissertation project involves the characterization of iron hydroxide precipitates and their relationship to overburden geology, trace elemental composition of the coal, mine water chemistry and trace element removal (possibly through sorption onto the iron hydroxides or co-precipitation). This integrated approach will generate a predictive model for precipitate formation, with implications for resource recovery and the development of more cost effective remediation.

I. Background

Coal mine drainage

Drainage from abandoned mined lands (AML) remains a widespread problem in the Appalachian coal fields. Over 2400 miles of streams are affected by coal mine drainage (CMD) in Pennsylvania alone (PA Department of Environmental Protection, 1998). Coal mine drainage can contain high concentrations of sulfates and metals, including iron, manganese and aluminum (Kleinmann, 1989; Rose and Cravotta, 1998). Mining exposes pyrite (an iron sulfide mineral) to air and water, causing the following reaction to occur:



This reaction produces iron hydroxide precipitates, such as goethite, schwertmanite and ferrihydrite. One goal of mine drainage treatment is to remove metals, especially iron, from the water before it is discharged into streams.

Two general classifications of treatment methods, active and passive, are available for the remediation of mine drainage. Active treatment involves the addition of alkaline chemicals to raise the pH to acceptable levels and to decrease the solubility of dissolved metals so that they will precipitate. Active treatment methods tend to be costly and, in many cases, require considerable time and energy.

Passive treatment of mine drainage

Passive treatment methods allow naturally occurring chemical and biological reactions to occur in the controlled environment of the treatment system, and not the receiving water body. Currently, four types of passive unit operations are commonly used, including (1) aerobic wetlands, (2) compost (anaerobic) wetlands, (3) anoxic limestone drains (ALD) and (4) down flow reducing and alkalinity producing systems (RAPS), also referred to as vertical flow systems (VFW) and successive alkalinity producing systems (SAPS).

It should be noted that selection of a passive treatment system depends on raw water quality as well as the amount of land available for construction of the system. Net alkaline discharges simply require oxygen and time for metals to oxidize and precipitate, as well as a pond to collect the precipitates (Watzlaf et al., 2000). Aerobic wetlands are used for treating net alkaline mine drainage. These wetlands usually consist of an aeration device such as a waterfall, followed by a deep, unvegetated pond and a shallow wetland, which is usually planted with cattails (Watzlaf et al., 2000). The deeper pond is designed to collect the majority of precipitated iron hydroxides, while the shallow wetland slows the flow of water, allowing more time for the remaining iron to precipitate (Watzlaf et al., 2000).

Net-acidic waters require the addition of alkalinity prior to precipitation of metals (Watzlaf et al., 2000). Anoxic limestone drains (ALD) are used for the sole purpose of adding alkalinity to net-acidic water. An ALD is simply a buried bed of limestone designed to intercept water while it is in an anoxic state (Turner and McCoy, 1990). Calcium carbonate in the limestone adds bicarbonate alkalinity through its dissolution. In order to prevent clogging of the ALD, metals removal must take place elsewhere (Watzlaf et al 2000). Waters high in aluminum are not

appropriately treated using an ALD because aluminum becomes insoluble at pH between 4.5 and 8.5, in turn clogging the ALD. Additionally, the water must be kept anoxic to prevent oxidation of soluble ferrous iron to the insoluble ferric form (Watzlaf et al., 2000). Iron precipitated in an ALD will armor the limestone, interfering with its ability to generate alkalinity.

RAPS and compost wetlands are useful for treating net acidic water containing metals. In general these systems consist of a layer of limestone overlain by organic matter (spent mushroom compost is commonly used in western Pennsylvania). In RAPS, a network of perforated pipes is placed in the limestone, causing mine water to flow vertically through the compost and limestone, while water in compost wetlands flow horizontally. Additionally, the compost wetland may be planted with cattails. Both systems promote alkalinity generation as well as anaerobic bacterial activity resulting in sulfate reduction and the precipitation of metals as sulfides (Kepler and McCleary, 1994).

Resource recovery

One problem facing passive treatment systems is the accumulation of iron precipitated in ponds and wetlands. Currently, over 200,000,000 pounds of iron are discharged from coal mines each year in the United States (Hedin, 1996). Over time, accumulation of iron hydroxide precipitates decreases the volume of ponds and wetlands, in turn decreasing their ability to treat the contaminated water. Many passive systems are built to hold 10 to 30 years of the precipitated sludge, but this sludge must eventually be removed or disposed of properly to maintain treatment effectiveness, but removal and disposal can prove to be costly. The potential for use of the iron hydroxide sludge as a renewable resource exists. The iron oxide market in the United States is about 350,000,000 pounds per year, some of which is imported (Hedin, 1996). Iron oxides are used as pigments, colorants, propellants, and are added to magnetic toners for use in copiers and printers. If it can be determined that iron oxides precipitated in passive treatment systems have properties and chemical compositions comparable to those used by industry, then it could be recovered and sold to offset treatment costs and potentially turn a profit.

The four types of passive treatment operations discussed above are not stand-alone units, but are components of a total remediation system (Watzlaf et al., 2000). For example, an ALD may be followed by a series of ponds and wetlands to oxidize and precipitate metals. Long term data on the performance of full scale passive treatment systems is needed. Some of the ALDs and wetlands are only approaching 1/3 of their design life. Performance and limitations of each method of passive treatment must be understood in order to appropriately design and construct an optimal remediation system, given the chemical characteristics of the water to be treated.

II. Statement of work

Many studies have thoroughly examined and characterized both acidic and net-alkaline mine drainage, but much less work has been done on the associated mine drainage precipitates. In order to assess both the potential for a recoverable resource as well as the long term behavior of passive treatment systems, an integrated approach to characterizing mine drainage precipitates and determining the relationship between the precipitates and associated discharge chemistry (and ultimately coal seam and overburden) is necessary.

The focus of my dissertation project involves the characterization of iron hydroxide precipitates and their relationship to discharge chemistry, trace element removal (possibly through sorption onto the iron hydroxides or co-precipitation), and resource recovery. My research can be divided into three main areas: (1) Characterization of iron hydroxide precipitates in passive treatment

systems; (2) Development and evaluation of sequential extraction procedures to determine trace element associations of coal mine drainage precipitates, and (3) Resource recovery of iron oxides. The related ongoing project at NETL (under the direction of George Watzlaf) is the Passive Treatment project. A description of objectives, work to date and future plans follows.

A. Characterization of Iron Hydroxide Precipitates in Passive Treatment Systems.

Objectives

My research for this area focuses on five sites with distinctive discharge characteristics and trace metal associations: Scrubgrass (discharge originates from Pittsburgh coal), Howe Bridge (discharge from Clarion coal), Elklick (discharge from Brookville and Kittanning coals), Morrison II (Discharge from Clarion Coal), and PennAllegh (discharge from Freeport coal). The objective is to examine how the iron hydroxide precipitates change (mineralogy, morphology, trace element associations) throughout passive treatment systems. Additionally, it is believed that discharge chemistry, depositional environment of the coal and overburden characteristics can be linked to precipitate characteristics, including trace element association. The results of this investigation will enhance already available selection and design criteria for passive treatment systems used to remove and collect iron rich precipitates.

Approach

Fieldwork involved collection of iron hydroxide precipitate (sludge) samples and related waters from the previously listed sites. Sludge characterization includes major and trace element determination (ICP-AES and INAA) particle morphology and size (SEM and other particle size analyzers), mineralogy (XRD), and determinations to quantify organic and volatile material (LOI). Associated water samples will be analyzed by ICP-AES. Sequential extraction procedures will be used to determine trace element associations.

Work to Date

All iron hydroxide precipitates to be examined have been collected. Trace and elemental analyses on untreated (not rinsed or leached) samples are complete. Most samples have undergone XRD and preliminary SEM analyses.

Preliminary results indicate that the precipitates from the five systems have distinctive trace element characteristics. Sludge samples from the Scrubgrass sites have up to 0.30% arsenic; Elklick up to 3.6% manganese and Morrison II up to 0.24% zinc and 0.12% manganese. Samples from PennAllegh and Howe Bridge show lower concentrations of these (up to 0.001% arsenic, 0.04% zinc, and 0.23% manganese for Howe Bridge, and up to 0.033% arsenic, 0.016% zinc, and 0.12% manganese for PennAllegh) and other trace metals.

Trace element determinations of samples from three seasons for the Howe Bridge, Elklick and Scrubgrass sites (Fall 1999, Spring 2000 and Summer 2000) indicate that these associations are not a function of seasonality. Only one sludge-sampling event was conducted at PennAllegh and Morrison II. Elemental analysis of the waters associated with the precipitates indicate that the trace metals are enriched relative to the discharges, but it is not yet understood how the metals are associated with the precipitates.

An abstract titled "Characterization of Iron Rich Mine Drainage Precipitates Associated with Monongahela and Allegheny Group Coals" (Kairies et al, 2000) was presented at the national meeting of the Geological Society of America held in Reno, NV in November, 2000.

Goals for the coming year

To determine how the trace metals are enriched in the sludge, two separate sequential extraction procedures will be conducted (discussed in the next section) on selected samples from Elklick, Howe Bridge, Scrubgrass and Morrison II. Remaining mineralogical, morphological and particle size analyses will be completed.

B. Development and Evaluation of Sequential Extraction Procedures to Determine Trace Element Associations of Coal Mine Drainage Precipitates

Objectives

Numerous sequential extraction procedures are currently used for the analysis of contaminated soils. However, no such methods exist for the analysis of precipitates associated with coal mine drainage. It is necessary to develop sequential extraction procedures in order to determine how potentially toxic trace elements are sorbed or bound to the iron hydroxide precipitates.

Approach

Prior sequential extraction work from numerous authors was evaluated, and two separate sequential extraction methods were developed for use specifically with coal mine drainage precipitates. Procedures for these methods are outlined in the Appendix. Please also refer to the flowchart and the explanation of reagents used, found in the appendix. Samples from Elklick, Howe Bridge, Morrison II and Scrubgrass were selected for these procedures based on their trace element associations. Each method will be run twice for five samples. In addition, one sample will be run two additional times for each method (for a total of four runs in each method) for statistical purposes.

Work to Date

Each method has been carried out one time. Leachates still need to be analyzed.

Goals for the Coming Year

Each method needs to be run one more time for all five samples. Two additional runs of each method will be conducted for one sample (giving a total of four runs for each method). All leachate solutions will be analyzed using ICP-AES. Any residue remaining after these procedures will be analyzed using XRD.

C. Resource Recovery of Iron Oxides: Lower Site

Objectives

The focus of this project involves the characterization of precipitates that have accumulated naturally in a single pond, both across the surface and at depth. This characterization will determine the suitability of these precipitates for use as a resource or, alternatively, to determine

if these precipitates may be disposed of in a landfill, based on association of potentially toxic trace elements.

Approach

The Lowber site was selected for an in-depth analysis of the resource recovery potential of precipitates that have accumulated in a single pond over the course of time (10+ years). It is estimated that the pond contains about 172,350 cubic feet of sludge. Sludge characterization includes major and trace element determination (ICP-AES and INAA) particle morphology and size (SEM), mineralogy (XRD), and determinations to quantify organic and volatile material (LOI).

Work to Date

Samples were collected with the assistance of Robert S. Hedin and Theodore Weaver across the pond and at depth. Trace and elemental analyses on untreated (not rinsed or leached) samples are complete. An abstract entitled "Characterization and Resource Recovery Potential of Precipitates Associated with Abandoned Coal Mine Drainage" (Kairies et al, 2001) was presented at the annual meeting of the American Society for Surface Mining and Reclamation, held in Albuquerque, New Mexico this past June.

Goals for the coming year

Remaining mineralogical, morphological and particle size analyses will be completed. In addition, several industry methods will be selected to determine applicability of these precipitates for use as pigments. Sequential extraction experiments (as described earlier) will be carried out on selected samples to determine trace elemental associations.

III. Other related work

In addition to the work described above, I have and will continue to contribute to other aspects of NETL's *Passive Treatment* projects. This work focuses on two areas: Monitoring and Evaluation of Full-scale Passive Treatment Systems; and Ferrous Iron Oxidation Rates in Passive and Semi-Passive Systems. This work has resulted in a presentation at the 18th Annual Meeting of the American Society for Surface Mining and Reclamation in Albuquerque, NM (Watzlaf et al., 2001).

Monitoring and Evaluation of Full-scale Passive Treatment Systems

Objectives

Limitations of each of the previously mentioned passive treatment unit operations need to be understood so that passive treatment systems can be designed and constructed in an appropriate manner, given the chemical characteristics of the mine drainage to be treated. Major objectives include determining the long-term effectiveness of passive treatment unit operations, assessing the effectiveness of flushing aluminum precipitates from RAPS, and to publish a comprehensive, up-to-date manual on the selection and sizing criteria for passive treatment systems.

Approach

Continued long-term monitoring of selected full-scale passive treatment sites. Monitoring at each site consists of measuring flow, conducting field analyses (pH, water temperature, conductivity and alkalinity) and collecting water samples for complete laboratory analysis at

several key locations to determine the performance of the various passive treatment unit operations.

Work to Date

As planned, 35 unit operations were monitored at least twice in 2001, including 7 RAPS, 10 ALDs and 18 ponds/wetlands. In addition, 22 new unit operations have been added to the monitoring program, including 5 RAPS, 13 ponds/wetlands, 2 limestone beds, and 2 low pressure aerators.

In order to quantify metals removed in a RAPS, the DeSale II RAPS was flushed this past summer. Each of 8 discharge pipes were flushed for 9 minutes with samples collected every 15 seconds for the first minute, every 30 seconds from 1-5 minutes and every minute from 5-9 minutes. Flow was determined using three methods: 1) timed volumetric measurements, 2) measurement of the horizontal distance the water fell four vertical inches, and 3) measurement of the elevation drop in the RAPS pond. Dissolved oxygen and pH were continuously monitored and recorded at each sampling interval. Preliminary analysis indicates that only a very small percentage of iron and aluminum precipitates were flushed during this event.

Future work

Sampling of field sites will be continued to build upon the database already compiled to document and evaluate the longevity and performance of various types of passive treatment systems. Changes in water quality and physical changes (e.g. changes in the permeability of ALDs or RAPS) will be documented and quantified. Acidity, iron and manganese removal rates for each unit operation will be calculated. The performance of each system will be examined for seasonal and long-term trends. In addition, these passive systems will be monitored for changes in metals other than iron and manganese that are not traditionally measured (i.e., Al, As, B, Ba, Cd, Co, Cu, Cr, Hg, Ni, Pb, Se, and Zn). The removal efficiency for each of these metals will be determined. Monitoring will continue on a twice a year basis. Four new sites (containing 12 new unit operations) will be monitored at least twice in the coming year.

In 1994, the U. S. Government publication "Passive Treatment of Coal Mine Drainage" was released. This manual has been, and continues to be, widely used for the design of passive treatment systems throughout the world. The 1994 publication mentions ALDs for the treatment of net acidic water, but it does not provide specific guidelines as to water quality limitations, alkalinity generation and sizing. ALDs were only a 3-4 year old technology in 1994. We know significantly more today after 7 additional years of data collection and are now in a position to make very specific recommendations for ALDs. Likewise, RAPS are only alluded to as a potential technology to be used in the 1994 publication. We are now able to make specific recommendations for the sizing and design of these systems (although much is still not known concerning the longevity of these systems). The 1994 publication presents iron removal rates in grams of iron removed per day per square meter of wetland that can be used for sizing. We will be able to split iron removal into ferrous iron oxidation rates and iron oxide settling rates. This will enable the sizing of oxidation ponds and subsequent wetlands. Most of the data needed for publication of this manual has already been collected in the long-term monitoring database. Some additional field data may need to be collected for the iron oxidation and settling guidelines. This manual is targeted for a June 2002 publication date to precede a passive treatment workshop planned for the American Society for Surface Mining and Reclamation meeting in Lexington, KY (June 9-13, 2002).

Data will continue to be collected to quantify the initial permeability of passive systems actively removing aluminum and/or iron. The effect of system design, frequency of flushing (load accumulated between flushing) and duration and intensity of flushing will be assessed at sites where apparently successful flushing has occurred. Total metal precipitates accumulated and flushed will be accurately quantified. The effect on permeability will be determined.

Ferrous Iron Oxidation Rates in Passive and Semi-Passive Systems

Objectives

Iron oxidation rates in aerobic wetlands are relatively slow. Many of the large volume underground mine discharges are net alkaline and only require aerobic wetlands for the oxidation, precipitation and settling of iron. These discharges are typically 500 to 5000 gallons per minute and contain 40 to 100 mg/L of ferrous iron. Using current technology, large areas (up to 30 acres) would be required to treat these discharges. Iron oxidation rates are dependent on the concentration of dissolved iron and oxygen, and the pH (which is strongly affected by dissolved carbon dioxide concentrations in the bicarbonate buffered water from passive treatment systems). The individual and combined effects of these parameters on iron oxidation and removal rates need to be determined to develop more effective and efficient wetland systems.

Approach

Analysis of the water quality data will enable the assessment of various aeration techniques as well as develop models of iron oxidation rates at the point of aeration and downstream in ditches, ponds and wetlands. Analysis of associated precipitate samples will examine changes in the characteristics (analysis will be conducted as previously outlined) of the sludge as they relate to iron oxidation and removal.

Work to Date

In the passive treatment system at the Morrison II site, iron oxidation rates were modeled using pH, temperature, dissolved oxygen and iron concentrations. The system consists of a 224 m ditch receiving the effluent from an ALD, which treats drainage from a reclaimed surface mine in Clarion County, PA. A kinetic model for the loss of ferrous iron from solution was compared to the traditional sizing criteria for iron removal of 10-20 $\text{gd}^{-1}\text{m}^{-2}$. All significant changes occurred soon after aeration, indicating that net alkaline water should be aerated immediately in order to optimize iron removal. A paper (Watzlaf et al, 2001) detailing this work was presented at the 18th Annual meeting of the American Society for Surface Mining and Reclamation, held June 3-7, 2001 in Albuquerque, NM.

Goals for the coming year

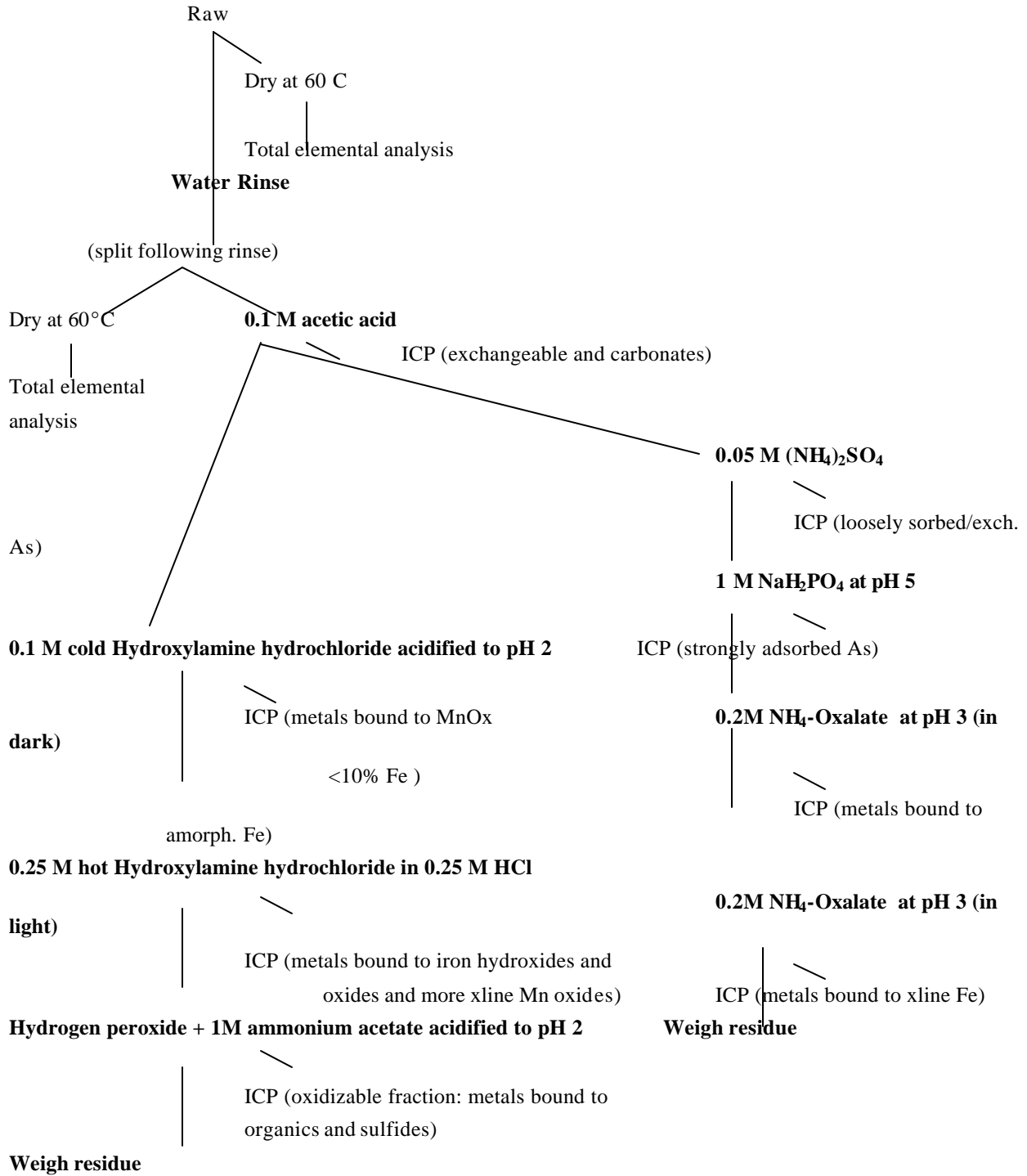
Another round of sampling will be completed at Morrison II (water only). Several locations (including Scrubgrass) with semi-passive types of aeration will be selected and monitored. Analysis of water quality data will enable the assessment of various aeration techniques as well as develop models of iron oxidation rates at the point of aeration and downstream in ditches, ponds and wetlands. Precipitates associated with water samples already collected at Morrison II will be characterized and related to iron loading, oxidation and removal rates.

IV. Appendix

Leaching Procedure for Mine Drainage Precipitates

(Based on the BCR/SMT sequential extraction technique (Ure et al., 1993;

Davidson et al., 1998) ; and sequential extraction work by Wenzel et al, 2001 and Keon et al, 2001).



Multi-Leach Dissolution Procedures for Iron Oxide-Rich AMD Sludge

Modified from Ure et al, 1993, Ure, 1996, McCarty et al, 1998,
Keon et al, 2001; and Wenzel et al 2001.

Objectives of Method 1: to solubilize exchangeable cations, iron and manganese oxyhydroxides, and organic matter and sulfides to determine trace elemental associations with these phases.

Objective of Method 2: to solubilize and extract loosely and strongly sorbed arsenic using an anion exchange method, as well as exchangeable cations. Additionally, this method will use two alternative extractants for differentiating between metals bound to amorphous and crystalline Fe oxides

Materials

Acid-cleaned 50 ml PPE or PTFE centrifuge tubes
Acid-cleaned 50, 125, 500, 1000 ml polyethylene bottles
Acid-cleaned disposable plastic pipettes
Polypropylene gloves
Shaker
Combination shaker/water bath
Centrifuge
Watch glasses
Acid-cleaned borosilicate glass beakers, 250 ml and 1000 ml
Aluminum foil
Teflon tape

Reagents

0.1 M acetic acid (CH_3COOH ; HOAc)
0.1 M hydroxylamine hydrochloride ($\text{NH}_2\text{OH}\cdot\text{HCl}$) acidified to pH 2 with HNO_3
0.25 M hydroxylamine hydrochloride ($\text{NH}_2\text{OH}\cdot\text{HCl}$) in 0.25 HCl
8.8 M hydrogen peroxide (H_2O_2) acid stabilized to pH 2-3 with HNO_3
1 M ammonium acetate (NH_4OAc) acidified to pH 2 with HNO_3
Purified (Milli-Q 18 M-?) water (MQW)
0.05 M ammonium sulfate ($(\text{NH}_4)_2\text{SO}_4$)
1 M sodium dihydrogen phosphate NaH_2PO_4 at pH 5
0.2 M ammonium oxalate $\text{NH}_4\text{-Ox}$ at pH 3.25

IMPORTANT:

- Wear safety glasses at all times
- When working in the Sample Prep Lab, keep sample vials, bottles, and centrifuge bottles open for only the minimum time necessary to avoid contamination.
- Do NOT perform these leaches if any dry sample preparation is going on in the lab (e.g., crushing, splitting, ball milling)!
- Before starting, clean up area you'll be working in, and damp wipe surfaces you'll be in contact with to remove dust and dirt. Put clean Crew wipes down where necessary.
- If you have to leave, cover your tubes with a Kimwipe to prevent dust from settling. Don't leave your stuff in there any longer than necessary – if you do, put name and DATE/TIME.

Preparation

1. Label 50 ml centrifuge tubes, one for each sample. Use Teflon tape as necessary to prevent tubes from leaking. Place in holder.
2. Label 150 ml bottles.

Water Rinse:

1. Weigh each centrifuge tube; record weight. Wear polypropylene gloves for weighing.
2. Carefully empty ~1 g of raw sample into centrifuge tube; replace cap on tube.
3. Reweigh centrifuge tube; record weight of sample placed into bottle.
4. To each centrifuge tube, add 40 ml MQW per 1 g sample.
5. Be sure the caps are placed on tightly; shake the tubes and check for leaks.
6. Place the centrifuge tubes in the sample shaker; they should be placed horizontally, so that the samples don't just sit at the bottom.
7. Agitate the tubes for 10 minutes.
8. Place tubes in the centrifuge; be sure tubes are balanced (add water as needed to equalize weight of opposite bottle); centrifuge for 20-30 minutes.
9. If not sufficiently settled, continue centrifuging until completely settled.
10. Pipette (label one pipette for each sample with sharpie) rinse into a labeled bottle and retain for analysis. *Be careful not to pipette any sediment out; leave 1 cm leachate above the sediment level.*
11. Repeat steps 4 through 10, using 20 ml MQW, saving the second rinse in the same bottle.
12. Cap and store the centrifuge tubes with the solid residue, or proceed to Method 1, or Method 2.

Method 1

A. Acetic Acid Leach (exchangeable cations and carbonates):

1. To each centrifuge tube, add 40 ml 0.1 M HOAc.
2. Be sure the caps are placed on tightly; shake the tubes and check for leaks.
3. Place centrifuge tubes into sample shaker, making sure they are secure; they should be placed horizontally, so that the samples don't just sit at the bottom.
4. Shake the tubes for 16 hours (overnight).
5. Place tubes in the centrifuge; be sure tubes are balanced; centrifuge for 20-30 minutes.
6. If not sufficiently settled, continue centrifuging until completely settled.
7. Pipette (label one pipette for each sample with sharpie) leachate into a clean, labeled poly bottle and retain for analysis. *Be careful not to pipette any sediment out; leave 1 cm leachate above the sediment level.*
8. Add 20 ml 0.1 M HOAc to each centrifuge tube, and agitate (in sample shaker) for 10 min.
9. Centrifuge for 20-30 minutes, continue to centrifuge until settled.
10. Carefully pipette washings and add to the bottle containing the leachate.
11. Store leachate at 4°C until analysis.
12. Cap and store the centrifuge tubes with the solid residue at 4°C, or proceed to the next step.

B. Cold Hydroxylamine Hydrochloride Leach (selective for amorphous Mn hydroxides, <10% Fe oxides/hydroxides):

1. To each centrifuge tube, add 40 ml 0.1 M NH₂OH.HCl (acidified to pH 2).
2. Be sure the caps are placed on tightly; shake the tubes and check for leaks.
3. Place centrifuge tubes into sample shaker, making sure they are secure; they should be placed horizontally, so that the samples don't just sit at the bottom.
4. Shake the tubes for 16 hours (overnight).
5. Place tubes in the centrifuge; be sure tubes are balanced; centrifuge for 20-30 minutes.
6. If not sufficiently settled, continue centrifuging until settled.
7. Pipette (label one pipette for each sample with sharpie) leachate into a clean, labeled poly bottle and retain for analysis. *Be careful not to pipette any sediment out; leave 1 cm leachate above the sediment level.*
8. Add 20 ml 0.1 M NH₂OH.HCl to each centrifuge tube, and agitate (in sample shaker) for 10 min.
9. Centrifuge for 20-30 minutes, continue to centrifuge until settled.
10. Carefully pipette washings and add to the bottle containing the leachate.
11. Store leachate at 4°C until analysis.
12. Cap and store the centrifuge tubes with the solid residue at 4°C, or proceed to the next step.

C. Hot Hydroxylamine Hydrochloride Leach (iron hydroxides):

1. To each centrifuge tube, add 40 ml 0.25 M $\text{NH}_2\text{OH}\cdot\text{HCl}$ (in 0.25 M HCl).
2. Be sure the caps are placed on tightly; shake the tubes and check for leaks. Cover caps with parafilm to protect against leakage while in the water bath.
3. Place the centrifuge tubes in sample shaker with the water bath underneath and bring the bath to 85-90°C.
4. Shake and heat in water bath a total of 16 hours (overnight).
5. Place tubes in the centrifuge; be sure tubes are balanced; centrifuge for 20-30 minutes.
6. If not sufficiently settled, continue centrifuging until settled.
7. Pipette (label one pipette for each sample with sharpie) leachate into a clean, labeled poly bottle and retain for analysis. *Be careful not to pipette any sediment out; leave 1 cm leachate above the sediment level.*
8. Add 20 ml 0.25 M $\text{NH}_2\text{OH}\cdot\text{HCl}$ to each centrifuge tube, and agitate (in sample shaker) for 10 min.
9. Centrifuge for 20-30 minutes, continue to centrifuge until settled.
10. Carefully pipette washings and add to the bottle containing the leachate.
11. Store leachate at 4°C until analysis.
12. Cap and store the centrifuge tubes with the solid residue at 4°C, or proceed to the next step.

D. Hydrogen Peroxide/Ammonium Acetate Leach (oxidizable -organic matter and sulfides)

1. To each centrifuge tube, **Carefully** add 10 ml of H_2O_2 in small aliquots (the reaction can be violent)
2. Cover tube with watch glass and digest for 1 hr at room temperature with occasional manual shaking.
3. Continue digestion by heating in a water bath (85°C) for 1 hr
4. Remove watch glass and evaporate to a small volume
5. Repeat steps 1 through 4.
6. Allow sample to cool
7. To each centrifuge tube, add 50 ml of 1 M ammonium acetate (NH_4OAc) to the cool moist residue, cap and shake.
8. Place centrifuge tubes into sample shaker, making sure they are secure; they should be placed horizontally, so that the samples don't just sit at the bottom.
9. Shake tubes for 16 hours (overnight).
10. Place tubes in the centrifuge; be sure tubes are balanced; centrifuge for 20-30 minutes.
11. If not sufficiently settled, continue centrifuging until settled.
12. Pipette (label one pipette for each sample with sharpie) leachate into a clean, labeled poly bottle and retain for analysis. *Be careful not to pipette any sediment out; leave 1 cm leachate above the sediment level.*
13. Add 25 ml NH_4OAc to each centrifuge tube, and agitate (in sample shaker) for 10 min.

C. L. Kairies: Year Three Technical Report

14. Centrifuge for 20-30 minutes, continue to centrifuge until settled.
15. Carefully pipette washings and add to the bottle containing the leachate.
16. Store leachate at 4°C until analysis.
17. Retain remaining solid residue for further analysis (store at 4°C).

Method 2

Follow the water rinse and acetic acid leach as outlined in Method 1, and then proceed to Step A below.

A. $(\text{NH}_4)_2\text{SO}_4$ leach (to solubilize loosely sorbed arsenate):

1. To each centrifuge tube, add 25 ml 0.05 M $(\text{NH}_4)_2\text{SO}_4$.
2. Be sure the caps are placed on tightly; shake the tubes and check for leaks.
3. Place the centrifuge tubes in the sample shaker, making sure they are secure; they should be placed horizontally, so that the samples don't just sit at the bottom.
4. Shake the tubes for 4 hours.
5. Place tubes in the centrifuge; be sure tubes are balanced; centrifuge for 20-30 minutes.
6. If not sufficiently settled, centrifuge until settled.
7. Pipette (label one pipette for each sample with sharpie) leachate into a clean, labeled poly bottle and retain for analysis. *Be careful not to pipette any sediment out; leave 1 cm leachate above the sediment level.*
8. Add 12.5 ml $(\text{NH}_4)_2\text{SO}_4$ to each centrifuge tube, and agitate (in sample shaker) for 10 min.
9. Centrifuge for 20-30 minutes, continue to centrifuge until settled.
10. Carefully pipette washings and add to the bottle containing the leachate.
11. Store leachate at 4°C until analysis.
12. Cap and store the centrifuge tubes with the solid residue at 4°C, or proceed to the next step.

B. 1 M NaH_2PO_4 at pH 5 (to solubilize strongly sorbed As):

1. To each centrifuge tube add 40 ml 1 M NaH_2PO_4 .
2. Be sure the caps are placed on tightly; shake the tubes and check for leaks.
3. Place centrifuge tubes into sample shaker, making sure they are secure; they should be placed horizontally, so that the samples don't just sit at the bottom.
4. Shake the tubes for 16 hours (overnight).
5. Place tubes in the large centrifuge; be sure tubes are balanced; centrifuge for 20-30 minutes.
6. If not sufficiently settled, continue centrifuging until settled.
7. Pipette (label one pipette for each sample with sharpie) leachate into a clean, labeled poly bottle and retain for analysis. *Be careful not to pipette any sediment out; leave 1 cm leachate above the sediment level.*
8. Add 20 ml MQW to each centrifuge tube, and agitate (in sample shaker) for 10 min.
9. Centrifuge for 20-30 minutes, continue to centrifuge until settled.
10. Carefully pipette washings and add to the bottle containing the leachate.
11. Store leachate at 4°C until analysis.
12. Cap and store the centrifuge bottles with the solid residue at 4°C, or proceed to the next step.

C. 0.2 M ammonium oxalate at pH 3.25, in the dark (to solubilize amorphous Fe):

1. To each centrifuge tube, add 40 ml 0.2 M NH₄-Oxalate.
2. Be sure the caps are placed on tightly; shake the tubes and check for leaks.
3. Completely wrap each tube in aluminum foil so that the extraction can occur in the dark.
4. Place centrifuge tubes into sample shaker, making sure they are secure; they should be placed horizontally, so that the samples don't just sit at the bottom.
5. Shake the tubes for 2 hours.
6. Place tubes in the centrifuge; be sure tubes are balanced; centrifuge for 20-30 minutes.
7. If not sufficiently settled, continue centrifuging until settled.
8. Pipette (label one pipette for each sample with sharpie) leachate into a clean, labeled poly bottle and retain for analysis. *Be careful not to pipette any sediment out; leave 1 cm leachate above the sediment level.*
9. Add 20 ml 0.2 M NH₄-Ox to each centrifuge tube, and agitate (in sample shaker) for 10 min.
10. Centrifuge for 20-30 minutes, continue to centrifuge until settled.
11. Carefully pipette washings and add to the bottle containing the leachate.
12. Store leachate at 4°C until analysis.
13. Cap and store the centrifuge tubes with the solid residue at 4°C, or proceed to the next step.

D. 0.2 M ammonium oxalate at pH 3.25, in the light (to solubilize crystalline Fe):

1. To each centrifuge tube, add 40 ml of 0.2 M NH₄-Oxalate.
2. Be sure the caps are placed on tightly; shake the tubes and check for leaks.
3. Place centrifuge tubes into sample shaker, making sure they are secure; they should be placed horizontally, so that the samples don't just sit at the bottom.
4. Shake the tubes for 2 hours
5. Place tubes in the centrifuge; be sure tubes are balanced; centrifuge for 20-30 minutes.
6. If not sufficiently settled, continue centrifuging until settled.
7. Pipette (label one pipette for each sample with sharpie) leachate into a clean, labeled poly bottle and retain for analysis. *Be careful not to pipette any sediment out; leave 1 cm leachate above the sediment level.*
8. Add 20 ml 0.2 M NH₄-Ox to each centrifuge tube, and agitate (in sample shaker) for 10 min.
9. Centrifuge for 20-30 minutes, continue to centrifuge until settled.
10. Carefully pipette washings and add to the bottle containing the leachate.
11. Store leachate at 4°C until analysis.
12. Cap and store the centrifuge tubes with the solid residue at 4°C.

Explanation of reagents and target phases

Water Leach: soluble fraction (OH^- , Cl^- , SO_4^{2-} , CO_3^{2-} , NH_4^+ , K^+ , and Na^+). Iron oxides will not be free of adsorbed species after the water leach, especially anions that have a high affinity for the oxide surface (Schwertmann and Cornell, 1991).

Acetic Acid Leach: carbonate fraction, exchangeable cations (tightly and loosely bound) (Ure et al, 1993; Ure, 1996, Davidson et al, 1998).

0.1 M Cold Hydroxylamine Hydrochloride (adjusted to pH 2 with HNO_3) Leach: selective for manganese oxides (will release bound metals upon dissolution of the manganese oxides). Does not dissolve crystalline iron oxides, but may dissolve very small amounts of amorphous iron hydroxide (Ure, 1996; Davidson et al, 1998; McCarty et al, 1998).

0.25 M Hot Hydroxylamine Hydrochloride (in 0.25 M HCl) Leach: selective for amorphous iron hydroxides (will release bound metals upon dissolution of the amorphous iron hydroxide), should leave more crystalline iron oxides intact (Tessier et al, 1979).

Hydrogen Peroxide/Ammonium Acetate Leach: organically complexed metals. The hydrogen peroxide will oxidize organic matter present in the sample. Ammonium acetate prevents the adsorption of the metals released by the H_2O_2 leach (Tessier et al, 1979; Ure et al, 1993, Davidson et al, 1998).

0.05 M $(\text{NH}_4)_2\text{SO}_4$ Leach: desorption of loosely sorbed As through anion exchange (Wenzel et al, 2001).

1 M NaH_2PO_4 at pH 5 Leach: desorption of strongly bound As through anion exchange (Keon et al, 2001).

0.2 M Ammonium Oxalate at pH 3.25 in the dark: selective for amorphous iron hydroxides (will release bound metals upon dissolution (Keon et al, 2001; Wenzel et al, 2001; Schwertmann and Cornell, 1991; Ure, 1996)).

0.2 M Ammonium Oxalate at pH 3.25 + oxalic acid in the light at 96°C: selective for crystalline iron hydroxides/oxides (Wenzel et al, 2001; Schwertmann and Cornell, 1991; Ure, 1996).

V. References cited

- Benjamin M. M. and Leckie J. O. (1980) Multiple site adsorption of Cd, Cu, Zn, and Pb on an amorphous iron oxyhydroxide. *J. Colloid Interface Sci.* **79**(209).
- Davidson, C. M., Duncan, A. L., Littlejohn, D., Ure, A. M., and L. M. Garden (1998) A critical evaluation of the three-stage BCR sequential extraction procedure to assess the potential mobility and toxicity of heavy metals in industrially contaminated land. *Anal. Chim. Acta*, v. 363, p. 45-55.
- Goldberg E. (1954) Marine Geochemistry I: Chemical scavengers of the sea. *J. Geol.* **62**, 249 - 265.
- Hedin, R. S. (1996) Recovery of iron oxides from polluted coal mine drainage. Technical Proposal. USDA Small Business Innovative Research Project. pp.32.
- Hedin, R. S., R. W. Nairn and R. L. P. Kleinmann (1994) Passive treatment of coal mine drainage. U.S. Bureau of Mines IC 9389, pp. 35.
- Hedin, R. S., and G. R. Watzlaf (1994) The effects of anoxic drains on mine water chemistry. In: Proceedings of the International Land Reclamation and Mine Drainage Conference and the Third International Conference of the Abatement of Acidic Drainage, Volume 1 (Pittsburgh, PA, April 24-29, 1994). U.S. Bureau of Mines Special Publication SP06B-94.
- Kairies, C. L., R. C. Capo, R. S. Hedin and G. R. Watzlaf (2000) Characterization of iron rich mine drainage precipitates associated with Monongahela and Allegheny group coals. *Geol. Soc. Amer.* Abstracts with programs, vol. 32, p. A-477.
- Kairies, C. L., G. R. Watzlaf, R. S. Hedin and R. C. Capo (2001) Characterization and resource recovery potential of precipitates associated with abandoned coal mine drainage, p. 278-279. In: Proceedings of the 2000 National Meeting of the American Society for Surface Mining and Reclamation (Albuquerque, NM, June 3-7).
- Kepler, D. A. and E. C. McCleary (1994) Successive alkalinity producing systems (SAPS) for the treatment of acid mine drainage, p. 195-204. In: Proceedings of the International Land Reclamation and Mine Drainage Conference and the Third International Conference of the Abatement of Acidic Drainage, Volume 1 (Pittsburgh, PA, April 24-29, 1994). U.S. Bureau of Mines Special Publication SP06B-94.
- Keon, N. E., Swartz, C. H., Brabander, D. J., Harvey, C., and H. F. Hemond (2001) Validation of an arsenic sequential extraction method for evaluating mobility in sediments. *Env. Sci. Tech.* V. 35, p. 2778-2784.
- Kleinmann, R. L. P. (1989) Acid mine drainage. *Eng. Min.* **190**, 16I-16N.
- McCarty, D. K., Moore, J. N., and W. A. Marcus (1998) Mineralogy and trace element association in an acid mine drainage iron oxide precipitate; comparison of selective extractions. *Appl. Geochem.* v.13, p. 165-176.
- PA Department of Environmental Protection (1998) *Healing the land and water: Pennsylvania's Abandoned Mine Reclamation Program.*

- Schwertmann, U. and R. M. Cornell (1991) Iron Oxides in the Laboratory. Weinheim: VCH, 137 pp.
- Singer, P. C. and W. Stumm (1970) Acid mine drainage. *Science* **167**, 1121-1123.
- Tessier, A., Campbell, P. G. C., and M. Bisson (1979) Sequential extraction procedure for the speciation of particulate trace metals. *Anal. Chem.* v. 51(7), p. 844-851.
- Turner, D. and D. McCoy (1990) Anoxic alkaline treatment system, a low cost acid mine drainage treatment alternative, p. 73-75. In: Proceedings of the National Symposium on Mining (Lexington, KY, May 14-18, 1990). University of Kentucky, Lexington, KY.
- Ure, A. M. (1996) Single extraction schemes for soil analysis and related applications. *Sci. Tot. Environ.* v.178, p. 3-10.
- Ure, A. M., P. H. Quevauviller, H. Muntau and B. Griepink (1993) Speciation of heavy metals in soils and sediments: An account of the improvement and harmonization of extraction techniques undertaken under the auspices of the BCR of the Commission of the European Communities. *J. Environ. Anal. Chem.* **51**, 135-151.
- Ure, A. M. (1996) Single extraction schemes for soil analysis and related applications. *Sci. Tot. Environ.* v.178, p. 3-10.
- Watzlaf, G. R., K. T. Schroeder and C. L. Kairies (2001) Modeling of iron oxidation in a passive treatment system, p. 262-274. In: Proceedings of the 2000 National Meeting of the American Society for Surface Mining and Reclamation (Albuquerque, NM, June 3-7).
- Watzlaf, G. R., K. T. Schroeder and C. Kairies (2000a) Long-term performance of alkalinity-producing systems for the treatment of mine drainage, p 262-274. In: Proceedings of the 2000 National Meeting of the American Society for Surface Mining and Reclamation (Tampa, FL, June 11-15, 2000).
- Watzlaf, G. R., K. T. Schroeder and C. L. Kairies (2000b) Long-term performance of anoxic limestone drains for the treatment of coal mine drainage. *Mine Water and the Environment* (accepted for publication).
- Wenzel, W. W., Kirchbaumer, N., Prohaska, T., Stingeder, G., Lombi, E., D. C. Adriano (2001) Arsenic fractionation in soils using an improved sequential extraction procedure. *Anal. Chim. Acta.* V. 436, p. 309-323.

XXIII. "Preliminary Results on the Kinetic Study of the Homogeneous Non-Catalytic High-Temperature, High-Pressure Water Gas Shift Reaction"

**Filipe Bustamante (S) and Robert Enick (F), University of Pittsburgh
with
Kurt Rothenberger (M), NETL**

**PRELIMINAR RESULTS ON THE KINETIC STUDY OF THE
HOMOGENEOUS NON-CATALYTIC HIGH-TEMPERATURE, HIGH-
PRESSURE WATER GAS SHIFT REACTION**

Annual Report for the DOE – University Partnership Program
Period 08/00 to 08/01

Felipe Bustamante
Chemical and Petroleum Engineering Department
University of Pittsburgh
Pittsburgh, PA

**National Energy Technology Laboratory
Department of Energy
December 2001**

ABSTRACT

The first experimental study on the kinetics of the high-pressure (up to 16 atm), high-temperature (up to 900°C) homogeneous non-catalytic water gas shift reaction was conducted. The experiments were carried out in a flow mode using a CSTR reactor. The effect of the walls of the reactor vessel was studied by using Inconel and Quartz reactors. This report shows the preliminary results on the kinetics of the *reverse* water gas shift reaction.

A strong catalytic effect was observed when using a reactor made out of Inconel. A two-orders of magnitude increase in the reaction rate was attained. This effect may be attributable to the enrichment of chromium on the surface due to the depletion of nickel, probably by the formation of carbon structures by reaction with carbon monoxide. The change in surface concentration was evaluated by XPS.

As to end of the period covered in this report the study of the form of the kinetic expression was commenced. During the period 09/01-08/02 this study will be conducted as well as the temperature-dependence study of the rate constant. Besides giving valuable information on the energy of activation this information will allow to study the if there is any change of reaction mechanism with temperature as has been previously suggested.

Finally, although not directly related to my experimental work at NETL, I attach a report I prepared for NETL on hydrogen production and separation technologies. This is intended to be an important background of the research on hydrogen selective membranes.

TABLE OF CONTENTS.

Introduction

Experimental

Results and discussion

References

Appendix: Overview on Hydrogen Production and Separation Technologies.

LIST OF GRAPHICAL MATERIALS.

Figure 1. Block diagram for the HMT unit.

Figure 2. Inconel reactor used in the kinetic studies.

Figure 3. Quartz reactor.

Figure 4. WGS Reverse Reaction Test Data 900°C, 101.3 kPa, Equimolar H₂ and CO₂ feed.

Figure 5. WGS Reverse Reaction Test Data - Quartz reactor 900°C, 101.3 kPa, Equimolar H₂ and CO₂ feed.

Introduction

The Water Gas Shift Reaction (WGSR), an important reaction in industry for production of chemicals and/or hydrogen, is considered to play a key role in the integration of gasification technologies with a H₂ production/recovery unit. The stream of the gasifier, mainly H₂, CO and CO₂ at high pressure (up to 30 atm) and temperature (up to 1000°C), will be directed to the water gas shift reaction where the reaction (1) will take place, increasing the yield of hydrogen.



The WGSR is an exothermic, equilibrium-limited reaction with non-favorable conversions at high temperatures (>600°C). A number of reviews (for instance [1]) on the low-temperature, catalytic WGSR are available on the open literature. The first generation of catalysts was in the market by the 1930s. Since then a good deal of research has been conducted to find highly active and resistant catalysts that operate in the low temperature regime imposed by the thermodynamic equilibrium limit. The catalyst is required because of the lower reaction rate observed at low temperature.

Several papers have been devoted to the high-temperature, non-catalytic water gas shift reaction showing high reaction rates at high temperature. The first study [2] addressed the *forward* (CO + H₂) and *reverse* (CO₂ + H₂O) water gas shift reaction in the temperature range 875-1100°C, finding that the reaction occurs in the homogeneous phase without any catalytic effect due to the walls of the reactor (made out of quartz). They concluded that the reaction follows a chain-reaction mechanism with very good agreement between the predicted and the observed form for the rate expression. However, some of their results on the *reverse* WGSR were confronted by two later papers. Tingey [3] and Kochubei and Moin [4] found a lower value for the rate constant suggesting experimental error in the work by Graven and Long due to the presence of traces of oxygen in the gas phase. The chain-reaction mechanism, expressed as the Bradford mechanism for gas phase reactions, was confirmed for the high-temperature regime. Nevertheless, a

discrepancy in a possible shift of reaction mechanism at low temperatures ($<800^{\circ}\text{C}$) is evident in those papers. Moreover, Graven and Long as well as Tingey and Kochubei and Moin performed the experiments in a high-diluted system at ambient pressure, without suggesting about the influence of the pressure on the reaction rate.

A theoretical study by Karim and Mohindra [5] applied a computer model for gas phase homogeneous to the *reverse* WGSR. By using reported values for the rates of the involved elementary reactions in WGSR they were able to calculate de rate constant. Their result for the rate constant of the *reverse* WGSR is in good agreement with the value reported by Tingey and Kochubei and Moin. However, the value of the activation energy is very different in the computer model.

The possibility of the high-temperature, non-catalytic WGSR is backed, then, by these previous results showing high reaction rates. This report will address the kinetics of the *reverse* WGSR under circumstances not studied previously, namely high-concentration streams, i.e. non-diluted streams, and high-pressures. These conditions are more appropriate to draw conclusions on the application of the WGSR directly to a gasification stream.

Experimental

The high reaction rates expected demand a flow system for the kinetic studies. The Hydrogen Membrane Testing unit (HMT-1) at NETL was slightly modified for this purpose. The unit was initially designed for conducting high-pressure (up to 30 atm), high-temperature (up to 900°C) hydrogen permeation experiments. Basically, the unit has the capability of feeding a gas mixture to a high-pressure, high-temperature chamber. For the permeability experiments the chamber houses a hydrogen selective membrane. For the kinetic study the chamber is made entirely out of inconel; the choice of inconel is dictated by the harsh conditions present. A general overview of the unit is given in Figure 1.

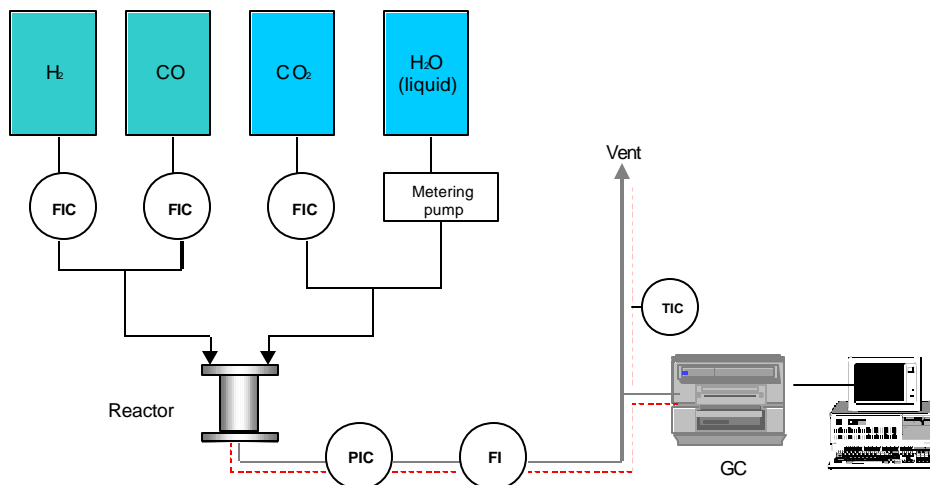


Figure 1. Block diagram for the HMT unit.

Hydrogen and carbon dioxide were fed using electronic mass flow controllers. The tubing downstream the reactor is heat-taped and insulated to avoid condensation of the water. The reactor was put inside a cylindrical oven; the temperature was sensed and controlled with a thermocouple placed directly on the top of the reactor. Pressure was controlled with the pressure controller downstream the reactor. For the initial studies the inconel reactor was used.

A schematic draw of the inconel reactor is presented in Figure 2. The reactants are fed (CO₂ and H₂, for the reverse water gas) in the bottom of the reactor through different lines; the mixing is accomplished by centrifugal force. The reactants and product mixture leaves the reactor through the small tubing at the center. The diameter of this tubing is very small in order to achieve high linear velocities, minimizing the residence time of the reactant-product mixture (CO₂, H₂, CO and H₂O) in a zone of high gradient of temperature.

Two modifications were included in the design of the quartz reactor (see Figure 3). Firstly, an equalization chamber allowing the work at high pressures with a fragile material like quartz was added. The pressure outside the reactor was kept equal to the

reactor pressure by flowing a gas at the same pressure than the reaction mixture. Secondly, reactants were fed to reactor premixed. The residence time of the reaction mixture in the annular space is minimized due to the high linear velocity of the gas (the opening is about 0.1 mm).

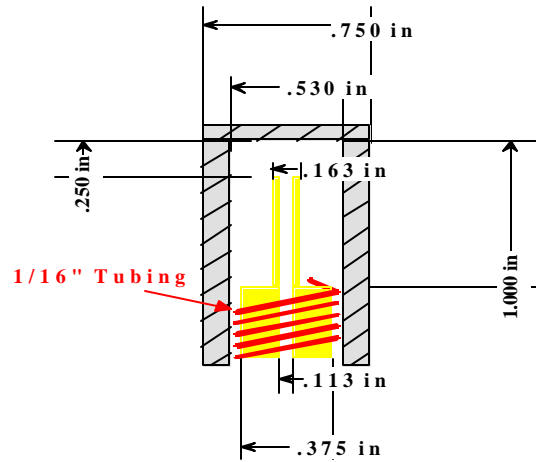


Figure 1. WGS Reactor

Figure 2. Inconel reactor used in the kinetic studies.

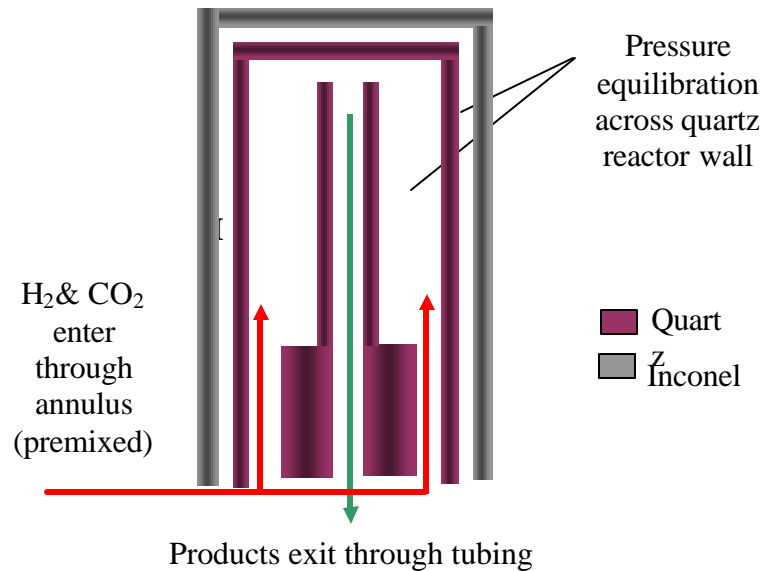


Figure 3. Quartz reactor.

The effluent of the reactor was analyzed with a gas chromatograph equipped with a TCD detector. As carrier gas was used Argon. The column used allowed the quantification of H₂, CO, CO₂ and H₂O in the range of concentrations of interest. In all cases, high-purity gases were used.

The residence time of the reactants in the reactor was chosen to assure low conversions (less than 2 %) thus avoiding any important effect of the opposing reaction; residence time was always lower than 2 s.

Conversions were calculated from the concentrations at the exit of the reactor (GC data). For instance, CO₂ conversion as evaluated as:

$$x_{CO_2} = \frac{C_{CO_2}}{C_{CO_2} + C_{CO}} \times 100$$

Preliminary kinetic studies were conducted for equimolar feed mixtures under different residence time. For determining the rate expression experiments where the concentration of one reactant was held constant while the concentration of the other is varied will be conducted.

The attempt of feeding constant flowrates of water with a metering pump was not successful. This problem remains to be solved for the study of the *forward* WGSR in the upcoming year.

Results and Discussion

In order to test the capabilities of the unit for the kinetic studies, the case of the high-temperature, low-pressure reverse WGSR was first studied. As it has already been mentioned, there is a relatively good agreement between the results for the rate expression and the value of the rate constant. These results would serve as a reference point for the results of the NETL HTM-1.

For the shakedown, equimolar mixtures were fed to the inonel reactor. Reaction conditions were at 900°C and 1 atm, with residence times lower than 0.5 s, in all cases. Under these conditions the expected conversions, modeled with an Excel-Visual Basic script using the kinetic data available in the literature, were less than 1% (typically 0.5%). Figure 4 summarizes the results of the tests with the inonel reactor.

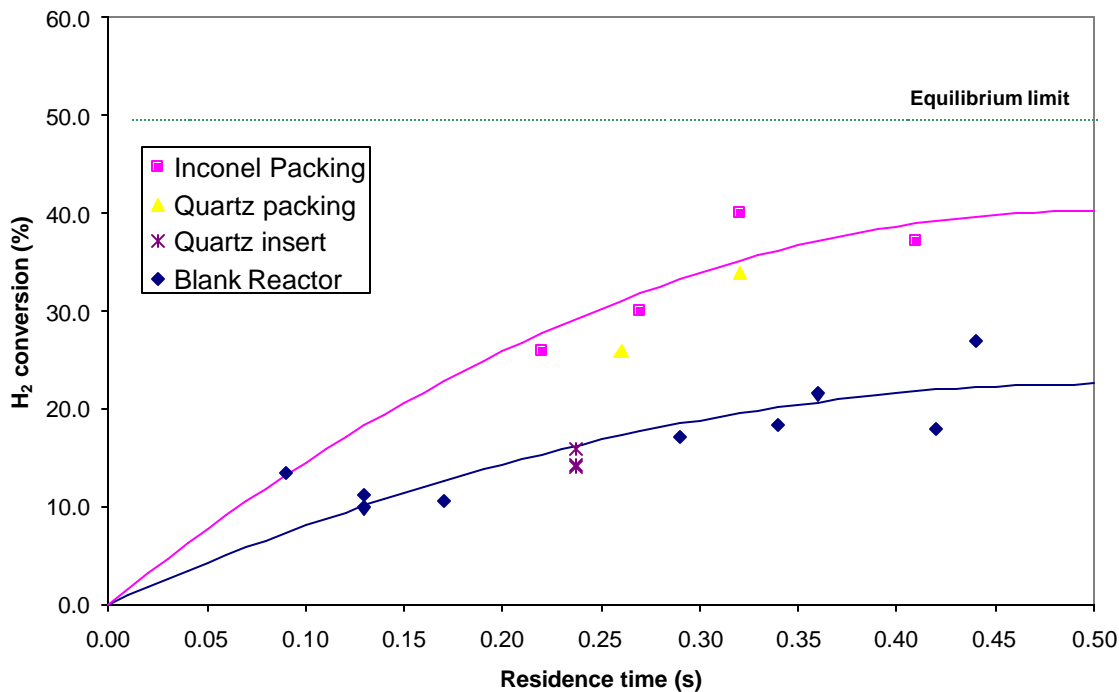


Figure 4. WGS Reverse Reaction Test Data 900°C, 101.3 kPa, Equimolar H₂ and CO₂ feed.

For very small residence times, conversions are very high. Moreover, an almost two order of magnitude increase in H₂ conversion was observed for the empty reactor (reactor without packing), with respect to the expected conversions. This poses the question of a catalytic effect by the walls of the reactor. An increase in the surface area for a given residence time would answer this question. When packed with inonel rings, the observed conversions are twice those observed with the empty reactor. However, the possibility of an increase in reaction rate due to the better mixing, induced with the presence of packing, must be also studied. The replacement of inonel packing with the same surface

area of quartz packing (quartz being inert at the temperature range studied [2]) also induced an increase in the reaction rate. Nevertheless the conversion was lower than for the inconel packing (34% for quartz and 41% for inconel). Being quartz inert for this reaction, its effect may not be attributed to a catalytic surface effect. It is known that the presence of packing increases the turbulence (reducing the boundary layer on the reactor walls), and improves the mixing.

Inconel packing was examined after reaction by XPS. Results showed an increase in the concentration of Chromium, as well as a depletion of Nickel on the surface (Inconel is an alloy made of 72% Ni, 17% Cr, 10% Fe). The surface analysis also revealed considerable amount of carbon. It has been reported [6] the formation of carbon structures on Ni-Fe in gas phase reactions involving CO. As Chromium based materials are used as catalyst for the “high-temperature” (400°C) WGSR [1] this process would transform the surface into an active surface.

The definitive way to rule out the catalytic effect is to avoid any contact of the reaction mixture with inconel. A quartz insert designed to cover the walls was placed inside the reactor. There was no conclusive evidence from this test (see Figure 4); conversions were similar to those of the empty reactor. The mechanical integrity of the insert could not be guaranteed and it was found to be broken when the reactor was dismantled.

The reaction was carried out in the quartz reactor under the same conditions (900°C, 1atm). Preliminary results as to the date of this report are presented in Figure 5. There, NETL results are compared with the previous literature models of the *reverse* WGSR. A good agreement between the expected and experimental conversions is observed. The results predicted by Graven and Long [2] are higher than the rest possible due to a contamination with traces of oxygen [3]; we have taken all precautions to avoid the presence of traces of oxygen in our system. This data supports the conclusion on the catalytic effect of the inconel. Future kinetic experiments will be conducted in the quartz reactor.

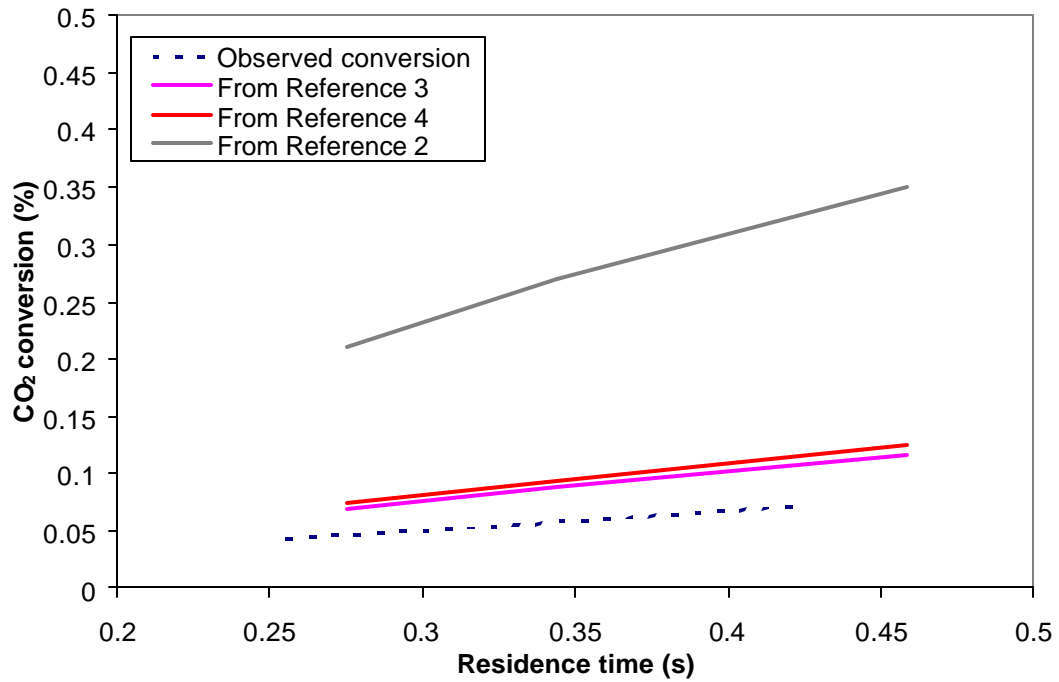


Figure 5. WGS Reverse Reaction Test Data - Quartz reactor 900°C, 101.3 kPa, Equimolar H₂ and CO₂ feed.

Conclusions.

- A shakedown of NETL/HMT-1 unit was successfully conducted in order to study the kinetics of the high-temperature, high-pressure, homogeneous water gas shift reaction. A new reactor was designed and built.
- Preliminary kinetic studies on the reverse water gas shift reaction lead to conclude that the inconel is a strong catalyst for the reaction under the conditions studied. Inertness of quartz was demonstrated for the same temperature and pressure range.

References.

1. Newsome, D. *Catal. Rev. Sci. Eng.* 21 (1980) 275.
2. Graven, W. and Long, J. *J. Amer. Chem. Soc.* 76 (1954) 2602, 6421
3. Tingey, G. *J. Phys. Chem.* 70 (1966) 1406.
4. Kochubei, V. and moin, F. *Kinetika i Kataliz* 10 (1969) 1203
5. Karim, G. and Mohindra, D. *J. Inst. Fuel.* (1974) 219
6. Tan, C. and Baker, T. *Cat. Today* 63 (2000) 3.

**APPENDIX. REPORT ON PRODUCTION AND PURIFICATION OF
HYDROGEN PREPARED FOR NETL**

**HYDROGEN: AN OVERVIEW
SOURCES, USES AND PURIFICATION**

Prepared by:
Felipe Bustamante
University of Pittsburgh
Under the NETL-University Partnership Program

Prepared for:
Hydrogen Separation Team
Ultraclean Fuels Focus Area
Office of Science and Technology
National Energy Technology Laboratory
Pittsburgh, Pa

February 2001

1. Hydrogen: General Characteristics.

Pure hydrogen is found in nature as a diatomic colorless-odorless gas (H_2). Hydrogen is the lightest of all gases, with an extremely low boiling point (20.4 K). The concentration of hydrogen in the atmosphere is extremely low (0.1 ppm), and hydrogen is found mainly forming chemical compounds with almost every other element.

Hydrogen gas is extensively used as raw material in the chemical/petroleum industry, e.g. in the synthesis of ammonia, methanol, urea, in the hydrogenation of oils, and in the processing of metals. By-product hydrogen is used as cryogenic liquid or fuel [1].

Recently hydrogen has received much attention as an energy carrier. Several reasons point in this direction. First, hydrogen is a clean fuel with ultra-low emissions. Second, it can be produced from renewable sources, e.g. water, biomass. Finally, the energy density of hydrogen is higher than that of any other fuel. For instance, the lower heating value of hydrogen (120,000 KJ/kg) is more than double than those of methane (50,000 KJ/kg) or propane (46,000 KJ/kg), both being widely used fuels [2].

2. Current Uses and Demand for Hydrogen.

As recently as the 1980s, the main producer of hydrogen was the petroleum refinery industry. However, as a consequence of more stringent regulations for vehicular emissions, refineries were forced to reduce the amount of aromatics and nitrogen/sulfur in the fuels, and in the process became a net H_2 consumer. (The production of aromatics was accomplished with a high production of H_2 as by-product, whereas the reduction of nitrogen/sulfur demands a higher consumption of hydrogen). [3]

The projected demand of hydrogen in the United States for the year 2000 is 563 billion SCF, with refineries accounting for the 70% of this figure (394 billion SCF). The remaining market consists of: chemical processing (128 billion SCF), electronic industry

(15 billion SCF), food processing (5 billion SCF), metal manufacturing (4 billion SCF), and miscellaneous uses (e.g. rocket launching) [4]. In the chemical industry hydrogen is used mainly in ammonia synthesis (60% of worldwide non-refinery H₂ production) and methanol synthesis [5].

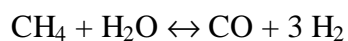
With greater interest in fuel-cell vehicles, the demand of hydrogen is expected to increase dramatically in the next years. According to a study by the Center for Energy and Environmental Studies at the University of Princeton, meeting the demand for hydrogen in the Los Angeles area (if 100% of the cars change to fuel-cells by 2010) will require supplying 355 billion SCF H₂/year [6].

3. Sources of Hydrogen.

There are three established technologies for the production of hydrogen [1,4]: Steam reforming of hydrocarbons, partial oxidation of hydrocarbons or coal, and electrolysis. Research for developing new technologies based on biomass gasification, or production of hydrogen from water with technologies other than electrolysis has not been successful. This paper will address the main characteristics of each of the commercial technologies. Brief descriptions of the new technologies will also be presented. The report “Hydrogen Production: Review of Available Technologies” [7] is an excellent source to complement the information provided here.

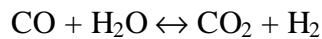
3.1. Steam Methane Reforming (SMR).

In 1988, 48% of the worldwide H₂ was produced from natural gas [4], the main component of which is methane. Steam methane reforming is the reaction of methane and water vapor to produce carbon monoxide and hydrogen:



The SMR [1,2,4] is an endothermic reaction favored at high temperature (1100 K) and moderate pressure (< 20 bar), which occurs over a nickel-based catalyst. It is customary to use an excess of water vapor to reduce the formation of coke by side reactions ($2.5 - 3 \text{ H}_2\text{O} / \text{CH}_4$), thereby inhibiting catalyst deactivation.

The SMR reactor produces a mixture of 70–72% H_2 , 6–8% CH_4 , 8–10% CO and 10–14% CO_2 on a dry basis [8]. The mixture of CO and H_2 is known as “synthesis gas” and is used to produce a great variety of petrochemical products (methanol, gasoline through Fisher-Tropsch synthesis, acetates) [5]. When SMR is utilized to produce hydrogen, the yield can be increased using the water gas shift reaction (WGSR),



The reaction is carried out in a reactor downstream of the steam reforming reactor, at moderate temperature (550 – 650 K) and pressure, over an iron-based catalyst. The product of the WGSR consists of 71–75% H_2 , 15–35% CO_2 , 1–4% CO and 4–7% CH_4 on a dry basis [8]. Pressure Swing Adsorption, or another suitable separation technique, further purifies the hydrogen. Figure 1 shows a block diagram of the SMR process integrated with WGSR to produce H_2 . The system involves a complete design to recover the heat as steam.

Sulfur-containing compounds, such as H_2S , are typically removed from the feed of the reformer to prolong the life of the catalyst. Although it is possible to reform heavy hydrocarbons with steam, coke formation associated with this feed deactivates the catalyst. One important advantage of this process is the lower co-production of CO_2 , in the order of 0.25 mole CO_2 / mole H_2 [4].

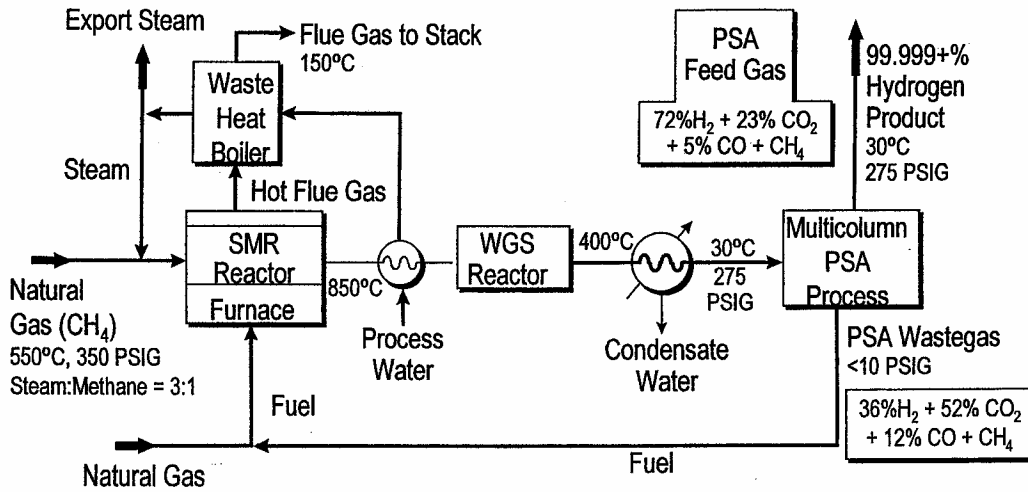


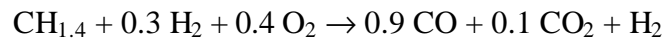
Figure 1. Block diagram of conventional route for production of pure hydrogen [8]

The investment for a SMR plant (production capacity 30 billion SCF H₂/year) is US \$90 million, and the cost of the hydrogen product is around US \$2.4/1000 SCF. The industrial scale production of H₂ by SMR is on the order of 4 Million SCF/h [2].

3.2. Partial Oxidation of Hydrocarbons.

This process consists of the high-pressure, non-catalytic burning of hydrocarbons in an oxygen-deficient atmosphere in presence of steam. The operation temperature and pressure are 1300°C and 30 – 100 atm, respectively. The oxygen stream is supplied as pure oxygen (90–95%) [1,2,4].

The process can be represented as [2]:



Where CH_{1.4} is representative of hydrocarbon feeds such as a heavy hydrocarbon, heavy oil or asphalt.

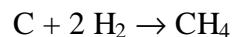
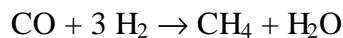
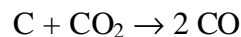
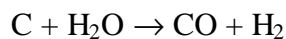
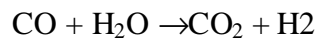
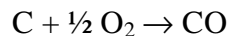
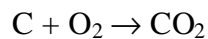
The product gas stream in the partial oxidation of heavy oil typically consists of 46% H₂, 46% CO, 6% CO₂, 1% CH₄, 1% N₂ [1] The hydrogen yield may be increased with the WGS and the stream is finally purified with a PSA unit or other suitable separation technology.

The investment for a Partial Oxidation plant (capacity 30 billion SCF H₂/year) is in the range of US \$135-156 million, and the cost of produced hydrogen is around US \$3.0/1000 SCF [2].

3.3. Partial Oxidation of Coal (Coal Gasification).

The fundamentals of this process are similar than those of the partial oxidation of hydrocarbon, involving the burning of carbonaceous material at high pressure and temperature in the presence of steam. The process normally operates at 1500°C and 28 atm. Although not economically competitive with the steam methane reforming or the partial oxidation of hydrocarbons, this process has been applied successfully in regions where coal is much more abundant than natural gas [1].

The chemistry of the process is more complicated, involving several steps [9]:



The mixture from a Texaco gasification process, for instance, consists of 34% H₂, 48% CO, 17% CO₂, 1% N₂ [1]. Before entering the WGS reactor the gaseous mixture is desulfurized. Finally, the hydrogen is separated by Pressure Swing Adsorption.

The investment for a Partial Oxidation plant (capacity 30 billions SCF H₂/year) is in the range of US \$202-224 millions, and the cost of produced hydrogen is around US \$3.6/1000 SCF [2].

Table 1 summarizes a comparison of steam methane reforming, partial oxidation and coal gasification from the point of view of the production cost, capital cost and by-product CO₂ generated. It is worth noting that the production cost is an approximation and it is influenced by labor cost, energy cost and raw material cost.

Table 1. Comparison of SMR, Partial Oxidation and Coal Gasification in the production of hydrogen (hydrogen capacity of 30 billion SCF/year) [2,4].

	Capital cost (Mill US \$)	Production cost (US \$/1000 scf)	CO ₂ co-production (mol CO ₂ / mol H ₂)
Steam Methane Reforming	90	2.4	0.25
Partial Oxidation	135 – 156	3.0	0.59
Coal gasification	202 – 224	3.6	1.00

3.4. Electrolysis of Water.

This process consists of the splitting of water into oxygen and hydrogen through an electric current. Electrolysis of water has important advantages over the other methods of production of hydrogen. First, electrolysis is the only clean process. It produces high purity hydrogen (99.8%). Finally, the process can be carried out at moderate temperature. The drawback of this process is its high demand of electricity, and because of that it is confined to the regions of high hydroelectric capacity. In 1988, electrolysis accounted for about 4% of the worldwide hydrogen production [1].

The process requires the utilization of membranes to avoid the mixing of hydrogen and oxygen. With the current available technology electrolysis can produce hydrogen at 2 – 5 atm, but through special choice of material and optimization high-pressure hydrogen (50 atm) can be obtained [2].

3.5. Developing Technologies.

3.5.1. Biomass Gasification [1,2].

The term biomass comprises all non-fossil, renewable carbon sources, e.g. vegetation, organic wastes (including municipal waste), etc. Because of the chemical composition of the material ($C_xH_yO_z$), biomass can be used as a source to produce hydrogen and carbon oxides (and energy). One potential advantage of this technology is the CO_2 released to the atmosphere is the same fixed by the organic material from the atmosphere and therefore there is not a net addition of CO_2 in the short run. In 1990, biomass gasification accounted for the generation of 6% of the global energy consumption. In the United States there is an increasing tendency to use biomass gasification as source of energy: in 2000 biomass is predicted to contribute 4.8% of the primary energy consumption, while in 1990 it was just 3.3% [10].

Biomass gasification is a two-step process. First, the organic feed is transformed into coke, methanol and primary gases by pyrolysis, i.e. the application of heat. Then, the material is converted in hydrogen by gasification or steam reforming. The amount of hydrogen in the gases depends on the process conditions. Typically the product gas stream of the biomass gasifier consists of 20% H_2 , 20% CO , 10% CO_2 , 5% CH_4 , 45% N_2 [2].

3.5.2. Other Processes.

The current research on the splitting of water using solar energy and biological or chemical means has not shown promising results. The efficiencies are too low and the chemicals employed are highly toxic and/or corrosive.

The thermolysis of water, i.e. the splitting of water in one-step process at elevated temperature ($2500^\circ C$) presents significant economic and technical challenges in order to be feasible in the near future.

A complete spectrum of developing technologies can be found in the report of the Burns and Roe Corporation [7].

4. Hydrogen Separation/Purification Technologies.

Most of the current available commercial technological processes for hydrogen production generate hydrogen in a mixture with other gases. Therefore all incorporate one or more hydrogen separation technologies. There are three major technologies to achieve hydrogen purification: cryogenic separation, Pressure Swing Adsorption (PSA), and membranes. Research aimed to employ hydrates and hydrides as hydrogen storage materials -and as indirect hydrogen separation systems- is currently under development.

4.1. Cryogenic Separation.

Cryogenic separation is based on the difference of the relative volatility of gases present in a mixture at low temperatures [11]. It takes advantage of the very low boiling point of hydrogen, relative to the other gases. The cryogenic temperature is achieved through a series of heat exchangers, which make use of the Joule-Thompson effect. All compounds with a boiling point higher than hydrogen will condense in the liquid phase, whereas the vapor phase will be rich in hydrogen. The main impurity in the vapor phase is helium, whose boiling point is much lower than that of hydrogen (see Table 2).

Cryogenic separation is the oldest technology for hydrogen recovery, and it is a well-proven and established process. It is suitable in the context of large-scale hydrogen production (more than 300,000 SCF/h), and if tolerance to impurities is permitted [11]. The main applications of cryogenic separation are found in the recovery of hydrogen from petrochemical and refinery off-gases, and in the hydrogen recovery from ammonia purge gas. The process normally operates at high pressure (70 bar) and it can yield hydrogen of relative high purity (90–99%). The purity of the hydrogen is dependent on the composition of the inlet gas. For instance, the purity of the hydrogen from an

ammonia purge gas is 89–92%, whereas the purity of hydrogen from a catalytic reformer off-gas is 97.5%. The hydrogen recovery is 90–95 % [12].

Table 2 shows the composition of the purge ammonia gas along with the boiling point of the components.

Table 2. Composition of the purge gas of an Ammonia Plant [11].

Component	Concentration (mol %)	Boiling Temp. (K)
Helium	2.1	4.25
Hydrogen	58.8	20.3
Nitrogen	19.9	77.4
Argon	5.7	87.3
Methane	10.9	111.6
Ammonia	2.5	239.8
Water	0.1	373.2

4.2. Pressure Swing Adsorption (PSA).

The Pressure Swing Adsorption (PSA) for hydrogen purification is based on the selective adsorption of several components of a stream on the surface of a porous material. Under specific conditions (pressure, adsorbent) all other components in a hydrogen-containing mixture can be retained in the adsorbent, yielding a high purity hydrogen stream. When the adsorbent is saturated it can be regenerated by decreasing the pressure [13].

This technology is the state-of-the-art for hydrogen separation in petrochemical plants. The most common gas streams are the SMR + WGS off-gas (70–80% H₂, 15–25% CO₂, 3–6% CH₄, 1–3 % CO, 8–28 atm), and the refinery off-gas (65–90% H₂, 3–20% CH₄, 4–8 % C₂H₆, 1–3 % C₃H₈, 8–28 atm). The stream after the PSA process is a dry hydrogen-rich gas with high purity (98–99.999%), with a hydrogen recovery of 70–90 % [13].

PSA requires several beds to operate in a continuous mode. According to Sircar et al [13], “typical PSA cycles for H₂ purification consist of various combinations of steps like (a) adsorption at gas pressure, (b) co-current despressurization to intermediate pressure,

(c) counter-current depressurization to atmospheric or sub-atmospheric pressure, (d) counter-current purge with H₂-enriched gas or product at ambient or sub-ambient temperature, (e) co- and counter-current pressure equalization, (f) co-current pressurization with feed gas, (g) counter-current pressurization with H₂-enriched gas or product gas". The stream from step (a) is essentially pure hydrogen, while the effluent of step (b) can be either pure hydrogen (mixed with product) or high purity hydrogen (used in step (d)); this hydrogen is not adsorbed but retained in the void fraction of the adsorbent. The remaining components in the adsorbent are desorbed in step (c). The rest of the cycle accounts for the restoring of the operating pressure.

The drawback of PSA is its low recovery. Hydrogen recovery depends on the feed gas composition. For hydrogen concentration in the range of 60–90% the recovery is 70–90%, whereas with low hydrogen concentrations of 30–50%, the recovery is very low, 30–50% [8].

The most common adsorbents in PSA are zeolites (zeolite 5A) and activated carbons [11], or a mixed bed of zeolite and activated carbon. In the SMR off-gas activated carbons are preferred to adsorb CO₂ and CH₄ and zeolites to adsorb CO, CH₄ and N₂ [13]. The process can be optimized by the selection of the physical characteristics of the activated carbon (pore size, source, surface polarity) or the type of zeolite (framework structure, cations, levels of ion exchange). Sometimes a bed of silica gel is used to adsorb the water from the gas mixture.

Figure 2 shows the adsorption behavior of several gases. The slope of the curves varies with the adsorbent used but the affinity of each compound is the same both for activated carbon and molecular sieves. It can be noted that for operating pressure greater than 20 – 30 bar there is little gain in adsorption.

Table 3 compares the behavior of PSA and cryogenic separation in the hydrogen recovery from catalytic reformer off-gas in a refinery. Depending on the scale of production, cryogenic separation can become a more economic alternative.

Table 3. Comparison of PSA vs cryogenics in the recovery of hydrogen from a catalytic reformer off-gas [12].

Process	Purity (%)	Recovery (%)	Relative Capital Cost	Relative Operating Cost	Relative Product Cost
Cryogenic	97.5	96	1.03	1.22	1.06
PSA	99.9	86.0	1.00	1.00	1.00

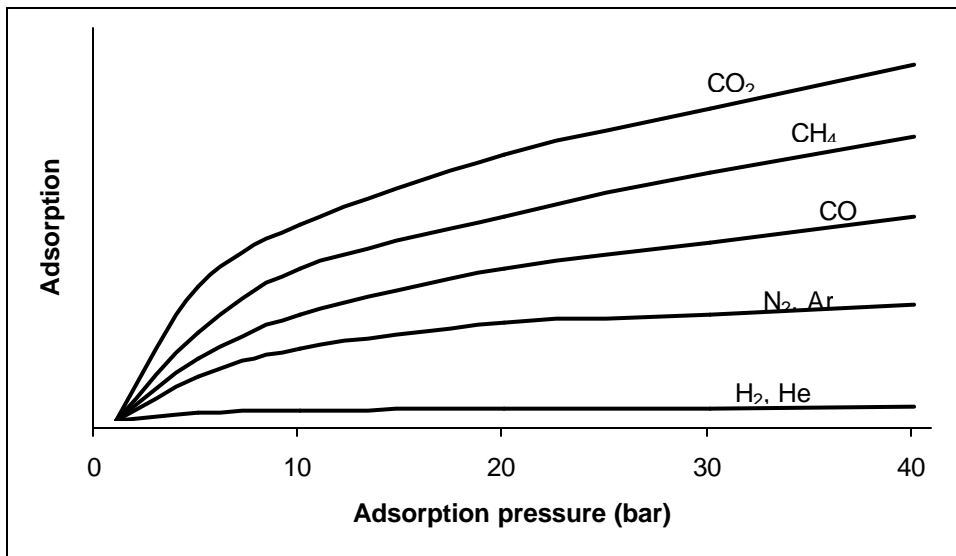


Figure 2. Typical adsorption behavior of several gases on molecular sieves [11].

4.3. Separation by Membranes.

A membrane can be defined as a thin barrier that allows preferential passage of component(s) in a mixture [14,15]. The selectivity of membrane separation is due to the more favored transport of one component through the membrane because of its physical/chemical interactions with the barrier. The type of interactions between the component and the membrane is defined by the nature of the compound and the barrier. The driving force for the permeation of the component is a difference in concentration (partial pressure if the mixture is gaseous) across the membrane.

The membranes can be classified according to their materials as polymeric, ceramic (porous, dense), and metallic. The transport mechanism and the selectivity are different in

each case. Polymer membranes have been employed in industry since 1979 with the Monsanto introduction of the hollow fiber gas membrane concept. Ceramic and metallic membranes are still under development.

4.3.1. Polymeric Membranes.

Polymers used in polymeric membranes include: cellulose derivatives, polysulfone, polyamides, and polyimides. The transport mechanism is based on the differences in diffusion velocity of the components of the mixture. Therefore polymeric membranes are permeable to most gases at some extent and for this reason the selectivity is low. Polymeric membranes have two important practical drawbacks: the operation is limited to low temperatures (normally less than 100°C), and a large pressure drop is required to obtain high permeation flux. Also, polymeric membranes experience limited chemical tolerance [14].

Polymeric membranes have been used in the recovery of hydrogen from the ammonia purge gas. In this case a stream of 86 % H₂, 6% N₂, 8% inerts, at 390 psig is obtained from the purge stream of 61% H₂, 20 % N₂, 19% inerts, at 1990 psig. The purity is lower than those obtained with cryogenic separation under similar conditions [8].

4.3.2. Ceramic Membranes.

4.3.2.1. Porous Membranes.

The behavior of porous membranes depends on the pore size. If the pore diameter is lower than 0.5 nm a molecular sieve effect is observed, with high selectivity (see Fig. 3). For higher pore diameters (0.5 nm < d < 20 nm) the transport mechanism is by Knudsen diffusion. This mechanism is based on the mean path of a gaseous molecule inside the pore channel; the greater the molecular weight/size of the molecule, the higher the number of collisions with the pore walls and the lower the permeation rate. One example

of porous membranes is the $\text{SiO}_2/\text{Al}_2\text{O}_3$, with a pore diameter of 4 nm. Membranes with pore diameters higher than 20 nm cannot achieve selective separation [15].

Porous membranes show high permeation rate and are suitable for high-temperature applications. Their limitation is the low selectivity: A high purity stream can be obtained only from a feed with large difference in the molecular weight of the components. For instance, the selectivity in the separation of H_2 in a mixture H_2/CO_2 is very low for pore diameter higher than 2 nm [15].

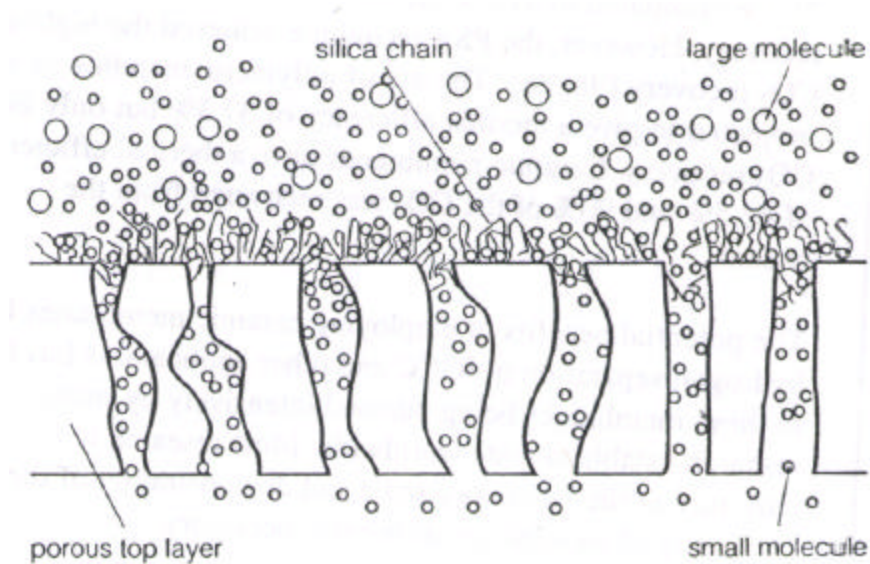


Figure 3. Transport of hydrogen through a porous membrane by the micropore diffusion mechanism [15].

4.3.2.2. Dense Membranes.

In dense membranes hydrogen is transported in the solid phase and not in the vapor phase, which is observed in porous membranes. The transport mechanism in dense membranes is due to the “solution–ionic diffusion” mechanism, observed also in the metallic membranes. Figure 4 depicts this mechanism.

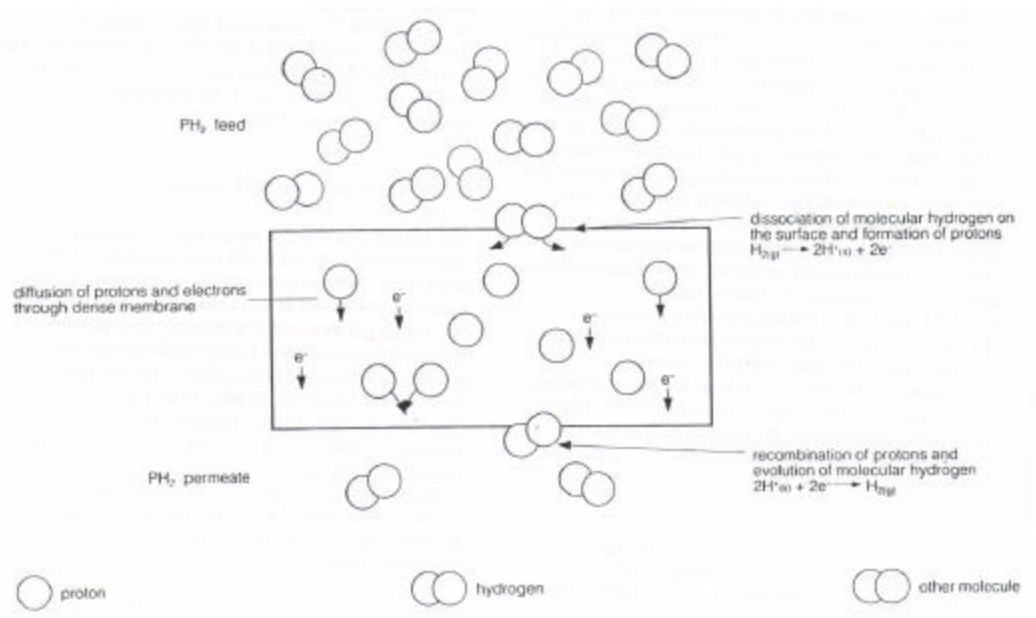


Figure 4. Transport of hydrogen ions through a dense membrane by an ionic diffusion mechanism [15].

The selectivity in dense membranes is extremely high, but with the cost of a permeation flux at least 10 times lower than in porous membranes [14]. Dense ceramic membranes are also suitable for high-temperature applications.

One example of a dense ceramic membrane is the ANL membrane developed at Argonne National Laboratory, which is Yttrium-doped barium cerate ($\text{BaCe}_{0.8}\text{Y}_{0.2}\text{O}_{3-\delta}$).

4.3.2.3. Metallic Membranes.

The transport mechanism in metallic membranes is the same as those in dense ceramic membranes. Metallic membranes also suffer a low permeation rate relative to porous membranes. In some cases the selectivity of metallic membranes is extremely high, or even infinity. For this reason palladium membranes have been subjected to intense research for the separation of hydrogen. One of the drawbacks of metallic membranes is

the compromise between mechanical resistance and thickness; the higher the thickness of the membrane, the lower the permeation flux, and the higher the cost of the membrane. Several researchers have proposed the utilization of composite membranes where a thin layer of palladium is deposited on a porous support [14]; in this case palladium accounts for a high selectivity and the porous support for a high permeation rate. Metallic membranes are a good choice for moderate high-temperature operation (600°C).

Palladium membranes exposed to a hydrogen atmosphere at low temperature (less than 300°C) have been found to experience embrittlement, a problem solved using several metallic alloys (e.g. Pd-Ag) [16]. Nevertheless, other metals have a higher permeation of hydrogen than palladium, and also higher resistance and thermal-mechanical strength (Ta, V, Nb). However, the solubility of hydrogen in the metallic surface is much lower than in palladium. As a consequence the research interest has been focused in “sandwich type” membranes: a thin layer of palladium is deposited on both sides of a thick layer of another high-permeation metal [16].

4.4. Separation by Hydrides.

This technology is based on the selective adsorption of hydrogen by metal hydride precursors. The hydrogen is then recovered by pressure swing or thermal swing cycles. Thermal swing is preferred for the separation of hydrogen from dilute streams. The rate of desorption (hydrogen is chemisorbed, heat of adsorption typically in the range 5-15 kcal/mol H₂) is controlled by the heat transfer to the medium, which can be facilitated using an adiabatic fixed bed. In this case the pressure is reduced and the heat accumulated in the bed helps the desorption process. The adsorbent is used in form of composite pellets, where the composite material accounts for the heat retaining [17].

Literature reports the results of the testing of metal hydrides in the recovery of hydrogen from ammonia purge gas, in pilot plant scale. A 60 % H₂ stream can yield hydrogen of 98.9% purity with a recovery of 90–93% [17].

Metal hydrides are easily poisoned by other gases present in the stream (O₂, N₂, CO, S), reducing the rate of hydrogen adsorption or the total adsorption capacity [16].

REFERENCES

1. Kirk - Othmer. "Hydrogen" *Encyclopedia of Chemical Technology*, 5th edition, 13, 838
2. <http://www.hydrogen.org>
3. Courty, P., Chauvel, A. "Catalysis, the turntable for a clean future" *Cat. Today* 29 (1996), 3 –15.
4. Armor, J. "The multiple roles for catalysis in the production of H₂" *Appl. Cat. A* (1999), 159 – 176.
5. Wender, I "Reactions of synthesis gas" *Fuel Processing Technol.* 48 (1996) 189 – 297.
6. Ogden, J. "Hydrogen Energy Systems Studies" Center for Energy and Environmental studies, Princeton University, 1999.
7. Srivastava, R., McIlvried, H. "Hydrogen production review of available technologies" Burns and Roe Services Corporation, August 1996.
8. Sricart, S., Waldron, W., Rao, M., Anand, M. "Hydrogen production by hybrid SMR-PSA-SSF membrane system" *Sep. Purif. Technol.* 17 (1999) 11 – 20.
9. Kirk - Othmer. "Gasification" *Encyclopedia of Chemical Technology*, 5th edition, 6, 541
10. Kirk - Othmer. "Fuels from Biomass" *Encyclopedia of Chemical Technology*, 5th edition, 12, 17
11. Meindersma, G. "Comparison of several hydrogen separation processes" *Gas. Sep. Technol.* 623 – 630.
12. Spillman, R. "Economics of gas separation membranes" *Chem. Eng. Prog.* (Jan. 1989) 41 – 62
13. Sircar, S., Golden, T. "Purification of hydrogen by pressure swing adsorption" *Sep. Sci. Technol.* 35, 5 (2000) 667 – 687.

14. Tauhidul, M. "Palladium-coated high-flux tubular membranes for hydrogen separation at high temperatures and differential pressures" Master's thesis, The University of Calgary, 1997.
15. Benson, S. "Ceramic hydrogen separation membranes" *In: Ceramics for advanced power generation* (2000) 40 - 64
16. Grashoff, G., Pilkington, C., Corti, C. "The purification of hydrogen" Johnson Matthey Group Research Centre.
17. Sheridan, J., Eisenberg, F., Greskovich, E. "Hydrogen separation from mixed gas streams using reversible metal hydrides" *J. Less-Common Met.* 89 (1983) 447 – 455.

**XXIV. “Phase Transitions of Adsorbed Fluids Computed for
Multiple Histogram Reweighting”**

**Wei Shi (S) and Karl Johnson (F), University of Pittsburgh
with
Brad Bockrath (M), NETL**

Phase Transitions of Adsorbed Fluids Computed from Multiple Histogram Reweighting

Wei Shi^{1,2}, Xiongce Zhao¹, J. Karl Johnson^{1,2*}

¹ *Department of Chemical and Petroleum Engineering, University of Pittsburgh,
Pittsburgh, PA 15261, USA*

² *National Energy Technology Laboratory,
Pittsburgh, PA, 15236 USA*

*To whom correspondence should be addressed. E-mail: karlj@pitt.edu

Abstract

We demonstrate the effectiveness of using multiple histogram reweighting (MHR) to study phase transitions in confined fluids by examining capillary condensation, prewetting, and layering transitions for different systems. Comparison is made with previously published simulations where available to establish the accuracy of MHR as applied to inhomogeneous systems. Overlap between adjacent state points is assessed through single histogram reweighting. Capillary condensation for methane adsorption in slit-like graphite pores exhibits 2-D behavior. Crossover of the effective exponent for the width of the coexistence curve from 2-D Ising-like ($1/8$) farther away from the critical point to mean-field ($1/2$) near the critical point is observed. The reduced critical temperature, density, and the effective value of the exponent for the model system are 0.77, 0.482, and 0.119, respectively, based on a fit to the simulation data. Prewetting transitions are observed for adsorption of Ar on solid CO_2 using model potentials. The wetting temperature is estimated based on the intersection of the prewetting and bulk vapor-liquid lines and also by extrapolation to zero of the difference between the saturation and prewetting chemical potentials. The reduced wetting temperature is estimated to be around 0.69. The reduced prewetting critical temperature, calculated from the disappearance of the two peaks in the density probability distribution, is estimated to be 0.92. The monolayer to bilayer (1-2) transition for propane on graphite is computed over a range of temperatures. Results for the 1-2 layering transition computed from MHR from a small system are in good agreement with grand canonical Monte Carlo simulations for a much larger system.

Contents

I	Introduction	4
II	Theory and Methods	5
III	Capillary Condensation	6
IV	Prewetting	9
V	Layering Transitions	14
VI	Conclusions	16

List of Figures

1	Isotherms for $T^* = 0.7$ (solid line) and 0.6 (dashed line) from multiple histogram reweighting for methane adsorption in a graphitic slit pore of width 5σ . Data from individual GCMC simulations that were (\circ) and were not (\square) included in the MHR calculations are shown.	7
2	The $T^*-\rho^*$ phase diagram for capillary condensation of methane in a graphitic slit pore. The filled circles are the coexistence data calculated from the equal area criterion. The filled diamond is the critical point estimated from fitting the coexistence data to the rectilinear and scaling laws, Eqns. (10)-(11). The solid line is the fit to the data. The squares are the rectilinear diameters. The dashed line is shown as a guide to the eye.	8
3	Scaled width of the coexistence data versus reduced temperatures for the capillary condensation of methane in a graphitic slit pore. The 2-D Ising exponent of $\beta_c = 1/8$ is shown as \bullet and \circ denotes the mean-field value of $\beta_c = 1/2$	9
4	Isotherms for $T^* = 0.83$ (solid line), 0.88 (dashed line), and 1.0 (long dashed line) from multiple histogram reweighting for Ar adsorption on solid CO_2 . Data from individual GCMC simulations that were (\circ) and were not (\square) included in the MHR calculations are shown.	10
5	Density probability distribution for the same system as Fig. 4 at $T^* = 0.83$ and $\mu^* = -3.801$	10
6	Local density profiles obtained from GCMC simulations for the same system as Fig. 4. Profiles are for $\mu^* = -3.9$ (solid line), -3.81 (dotted line), -3.8 (dashed line), -3.78 (long dashed), and -3.77 (dot-dashed) at $T^* = 0.83$	11
7	Local density profiles obtained from GCMC simulations for the same system as Fig. 4. Profiles are for $\mu^* = -3.85$ (solid line), -3.8 (dotted line), -3.76 (dashed line), -3.75 (long dashed), and -3.73 (dot-dashed) at $T^* = 0.88$	11
8	A plot of $\Delta\mu^* = \mu_{sat}^* - \mu_{pw}^*$ as a function of temperature for the same system as in Fig. 4. Filled circles are computed from MHR. Also shown are the fits to the data to the power law form (solid line), and linear form (long dashed).	12
9	The temperature–density phase diagram for the same system as in Fig. 4. The circles are the densities of the bulk gas in equilibrium with the adsorbed fluid at the prewetting transition points calculated from MHR. The squares are the vapor side of the bulk vapor-liquid phase diagram computed from MHR of the bulk fluid. The solid line and the dashed line are polynomial fits to the data. The two lines intersect at $T^* = 0.69$	12
10	The ratio of the prewetting transition pressure to the saturation pressure for the same system as in Fig. 4.	13
11	(a) The density probability distributions for the same system as in Fig. 4 at $T^* = 0.92$. Distributions are for chemical potentials of $\mu^* = -3.72$ (solid line), -3.71 (dotted line), -3.7 (dashed line), -3.67 (long dashed) and -3.65 (dot-dashed). (b) The isotherm computed from MHR at $T^* = 0.92$	14
12	The $T = 100$ K isotherm (solid line) for propane adsorption on graphite predicted from MHR for a small system size (volume = $1000\sigma^3$) compared with GCMC simulations for a larger system volume of $4250\sigma^3$ (circles).	15

13	The $T = 110$ K isotherm (solid line) for propane adsorption on graphite predicted from MHR for a small system size (volume = $1000\sigma^3$) compared with GCMC simulations for a larger system volume of $4250\sigma^3$ (circles).	15
----	---	----

List of Tables

I	Ratios of the grand canonical partition function computed from single histogram reweighting (SHR) and multiple histogram reweighting (MHR). The calculation is for methane adsorption in graphitic slit pore.	19
II	Reduced wetting temperature (T_w^*) and reduced prewetting critical temperature (T_{pwc}^*) for Ar on CO ₂ and Ne on Mg.	20

I. INTRODUCTION

Confined fluids are known to exhibit a rich variety of phase transitions that are absent in bulk fluids [1–3]. Perhaps three of the most interesting phenomena are capillary condensation, prewetting transitions, and layering transitions. Each of these transitions have previously been studied in some detail through the use of a variety of computer simulation techniques. Different simulation methods are often required to characterize these different phenomena; for example grand potential or Gibbs ensemble calculations are needed to locate capillary condensation [4–6]. Prewetting transitions are often located by plotting the isotherms and density profiles from grand canonical Monte Carlo or isothermal-isobaric Monte Carlo simulations [7,8]. Layering transitions have been observed from grand canonical Monte Carlo simulations coupled with grand potential calculations. [5].

In this paper we demonstrate that multiple histogram reweighting (MHR) [9–11] can be an accurate and efficient tool for studying phase transitions in confined fluids. The MHR method has been shown to be useful for studying the phase behavior of bulk fluids [12–15], but has not been widely used for studying the properties of confined fluids.

Gelb and Gubbins have applied the histogram reweighting technique to study the phase diagram of a simple binary liquid mixture in the semi-grand canonical ensemble [16]. They used single histogram reweighting to estimate the biasing potential needed for barrier crossing. Escobedo and de Pablo have studied the secondary transition for a 12-6 Lennard-Jones fluid in a composite large-sphere matrix with histogram reweighting analysis [17]. Recently, Potoff and Siepmann have calculated the effect of branching on the fluid phase behavior of alkane monolayers using histogram reweighting with the finite-size scaling technique [18].

Capillary condensation occurs when a fluid is strongly adsorbed in a micropore below the capillary condensation critical temperature. The transition is characterized by a gas condensing to a liquid-like state that entirely fills the pore space at a bulk pressure less than the saturation value [19,20]. Grand canonical Monte Carlo (GCMC) simulations are typically used to construct the adsorption isotherms for the prediction of capillary condensation. Peterson and Gubbins [4] calculated the grand potential through integration of isotherms and paths of constant chemical potential in order to compute the equilibrium chemical potential for capillary condensation. In a completely different approach, Heffelfinger *et al.* [21] used quenched molecular dynamics to study capillary condensation in cylindrical pores. The chemical potentials of the gas-like and liquid-like regions were computed from the potential distribution theorem for inhomogeneous fluids. Some prior knowledge of the phase behavior is required to implement this approach, because the overall density must be chosen such that the system is in the unstable region when quenched. Panagiotopoulos extended the Gibbs ensemble Monte Carlo method for the prediction of adsorption and capillary condensation [6]. The coexistence densities of gas-like and liquid-like phases in equilibrium inside a pore can be obtained through a single pore-pore calculation. However, a series of pore-fluid calculations are then needed to construct the isotherm.

The existence of wetting transitions was first predicted in 1977 independently by Cahn [22] and Ebner and Saam [23]. It was predicted that a gas that weakly adsorbs onto a solid surface will exhibit nonwetting behavior at low temperature and may undergo a first order transition to wetting behavior at a higher temperature T_w . By nonwetting we mean that the thickness of a film adsorbed on a surface remains finite at all pressures below the saturation vapor pressure; by wetting we mean that the film thickness diverges as the saturation pressure is approached. Prewetting occurs when there is a first order transition from a thin-film to a thick-film adsorbed on the surface. The prewetting transition terminates at the critical prewetting temperature [24,25]. Finn and Monson were the first to observe the existence of a prewetting transition through molecular simulation. [8] They used isothermal-isobaric Monte Carlo to identify the prewetting transition by observing the jump in adsorption on an isotherm associated with the thin- to thick-film transition [8]. Large fluctuations in the coverage typically accompany prewetting transitions, making precise

location of the transition a difficult task. For this reason, later work by Fan and Monson [26] utilized calculation of the surface tensions in the thin- and thick-films in order to locate the prewetting transition more precisely. Experiments and simulations by Mistura *et al.* [27] recently demonstrated that Ar on solid CO₂ actually exhibits triple-point wetting rather than prewetting as predicted by Monson and coworkers. The reason for this discrepancy is that the potential models used in the simulations [8,26] do not accurately represent the potential surface of the real Ar-CO₂ system. More realistic solid-fluid potential models [27] are more strongly attractive than the potential used by Monson *et al.* We note that grand canonical Monte Carlo simulations have been used to study prewetting transitions for a variety of other systems [28,29].

Thick films adsorbing on a substrate can either grow continuously or in a stepwise fashion. If the growth is stepwise, then each layer grows by a succession of first-order layering transitions at pressures lower than the bulk saturation pressure [30]. Layering transitions of simple fluids and lower alkanes on graphite have been studied extensively through experimental techniques [31]. Iwamatsu has shown that layering transitions can be expected to occur for systems that exhibit both incomplete and complete wetting [32]. For wetting growth the thickness of the film increases to infinity as the bulk saturation pressure is approached. If the wetting is incomplete then a transition from incomplete wetting to wetting will occur as the temperature is increased. Layering transitions will persist to T_w if $T_w < T_R$ where T_R is the bulk roughening transition [33]. If $T_w > T_R$ then a thin-film to thick-film prewetting transition precedes divergence of the film thickness. Each of the layers terminates at a layer critical point temperature, $T_c(m)$, where m is the number of layers in the film. It has been found that $T_c(m)$ can approach the triple point either from above [33] or below [34] with increasing m .

In this paper we demonstrate that MHR can be applied accurately and efficiently to compute capillary condensation, prewetting transitions, and layering transitions. Histograms for a given system can be combined in order to compute isotherms at any of the conditions spanned by the simulations. The location of phase transitions can be accurately computed through the equal area criterion [35] without resorting to computation of the grand potential [4,5]. The precision of MHR allows us to observe crossover in the critical exponents for capillary condensation. This is difficult to accomplish through a series of isolated simulations. In this paper, we use MHR to construct estimates for the capillary condensation, wetting temperature and prewetting critical temperatures, and to find layering transition pressures for propane on graphite.

II. THEORY AND METHODS

The basic idea of MHR is that histograms collected from a number of independent simulations may be combined to construct an estimate for the partition function [9–11]. The multiple histogram reweighting technique can be used to accurately calculate phase diagrams of bulk fluids [12–15,35]. This method allows the calculation of equilibrium properties over a range of conditions from a relatively small number of state points. The phase diagrams from histogram reweighting can be very accurate [13]. The coexistence densities and saturation chemical potential can be calculated through the use of the equal area criterion and Hill’s method [35].

Sufficient overlap between histograms of adjacent state points is necessary in order to implement the MHR technique. We here describe one method for checking for the extent of overlap between pairs of state points. The grand canonical partition function can be written as

$$\begin{aligned}\Xi(\mu, V, T) &= \sum_N \sum_{U_N} \exp[N\beta\mu - \beta U_N] \Omega(N, V, U_N) \\ &= \sum_N \sum_{U_N} CH(U_N, N),\end{aligned}\tag{1}$$

where $\beta = 1/kT$, k is the Boltzmann constant, T is the absolute temperature, $\Omega(N, V, U_N)$ is the microcanonical partition function, C is a simulation-specific constant, and $H(U_N, N)$ is the two dimensional histogram of configurational energy, U_N , and number of molecules, N , collected during the simulation. The configurational chemical potential, μ , is defined by

$$\mu = \mu^f - kT \ln \Lambda^3 + kT \ln(q_{\text{int}}),\tag{2}$$

where μ^f is the full chemical potential, Λ is the thermal de Broglie wavelength, and q_{int} is the intramolecular partition function, accounting for density independent terms such as rotational and vibrational Hamiltonians. The grand canonical partition function for a different state point with configurational chemical potential μ' , and temperature T' can be estimated by single histogram reweighting

$$\begin{aligned}\Xi(\mu', V, T') &= \sum_N \sum_{U_N} \exp[N\beta'\mu' - \beta'U_N] \Omega(N, V, U_N) \\ &= \sum_N \sum_{U_N} \exp[N(\beta'\mu' - \beta\mu) - (\beta' - \beta)U_N] H_{\mu, V, T}(U_N, N) C,\end{aligned}\quad (3)$$

where $H_{\mu, V, T}(U_N, N)$ is the histogram collected at (μ, V, T) . The ratio of the grand canonical partition functions between these two state points based on the histogram collected at (μ, V, T) is computed through

$$\frac{\Xi(\mu', V, T')}{\Xi(\mu, V, T)} = \frac{\sum_N \sum_{U_N} \exp[N(\beta'\mu' - \beta\mu) - (\beta' - \beta)U_N] H_{\mu, V, T}(N, U_N)}{\sum_N \sum_{U_N} H_{\mu, V, T}(U_N, N)}.\quad (4)$$

Likewise, one may collect histogram data at the state point defined by (μ', V, T') and extrapolate to (μ, V, T) . The ratio of these two partition functions can be expressed by interchanging μ with μ' and T with T' in Eq. (4). In the thermodynamic limit the following equation must be satisfied,

$$\frac{\Xi(\mu', V, T')}{\Xi(\mu, V, T)} \times \frac{\Xi(\mu, V, T)}{\Xi(\mu', V, T')} = 1.\quad (5)$$

We use Eq. (5) to check the extent of overlap between histograms by performing relatively short GCMC simulations at each state point. Not all of the fluctuations in energy and particle number accessible to the state points in the thermodynamic limit can be observed in a finite simulation. Consequently, Eq. (5) will not be exactly satisfied for state points extrapolated from histogram reweighting, but should be approximately satisfied within some tolerance

$$\left. \frac{\Xi(\mu', V, T')}{\Xi(\mu, V, T)} \right|_{\text{HR}} \times \left. \frac{\Xi(\mu, V, T)}{\Xi(\mu', V, T')} \right|_{\text{HR}} = 1 \pm \delta,\quad (6)$$

where the subscript HR indicates that the partition function in the numerator has been extrapolated from histogram reweighting. We have found that $\delta = 0.65$, that is, values of the left hand side of Eq. (6) between 0.35 and 1.65, indicate sufficient overlap of the two state points. We have used this method to select the state points to simulate in longer production runs. We denote this procedure to check the overlap as the single histogram reweighting method (SHR). Note that Eq. (6) is not symmetric with respect to inversion because we stipulate that the extrapolated partition functions are always in the numerator.

Details of our implementation of the multiple histogram reweighting technique are described elsewhere [35]. The ratios of the Ξ s for several state points were obtained from multiple histogram reweighting and compared with the values calculated from Eq. (4) in order to verify that the degree of overlap between adjacent state points was sufficient. Single histogram reweighting from Eq. (6) and MHR were used to analyze the histograms. The results are presented in Table I. The values computed from MHR are based on a combination of 30 histograms. The values of the ratios Ξ_2/Ξ_1 between 10 pairs of state points as calculated from SHR and MHR are tabulated in Table I. The good agreement between the two methods indicates that a value of $\delta \leq 0.65$ in Eq. (6) is indicative of histograms with sufficient overlap.

III. CAPILLARY CONDENSATION

In this section we present results of MHR for capillary condensation. The potential model used to investigate capillary condensation is the same as that used by Jiang *et al.* [5], namely, methane adsorbing in a graphite slit-like pore of width $H = 5\sigma$, where σ is the Lennard-Jones (LJ) diameter of a methane molecule. The fluid particles in the slit pore interact with each other via the truncated and shifted (TS) LJ potential

$$\phi_{\text{TS}}(r) = \begin{cases} \phi(r) - \phi(r_c) & r \leq r_c \\ 0 & r > r_c \end{cases},\quad (7)$$

where $\phi(r)$ is the full LJ potential given by

$$\phi(r) = 4\epsilon \left[\left(\frac{\sigma}{r} \right)^{12} - \left(\frac{\sigma}{r} \right)^6 \right],\quad (8)$$

where ϵ is the well depth and σ is the molecular diameter. The value of the cutoff was 2.5σ as used in ref. [5]. The solid-fluid interactions are represented by the 10-4-3 solid-fluid potential [36,37]

$$\phi_{\text{sf}}(z) = 2\pi\rho_s\epsilon_{\text{sf}}\sigma_{\text{sf}}^2\Delta \left[\frac{2}{5} \left(\frac{\sigma_{\text{sf}}}{z} \right)^{10} - \left(\frac{\sigma_{\text{sf}}}{z} \right)^4 - \left(\frac{\sigma_{\text{sf}}^4}{3\Delta(0.61\Delta+z)^3} \right) \right], \quad (9)$$

where z is the distance between a fluid particle and a solid surface, Δ is the separation between the individual graphene planes, and ρ_s is the solid density. The cross-parameters σ_{sf} and ϵ_{sf} were calculated from the Lorentz-Berthelot combining rules. The parameters were taken from refs. [36,37]. They are $\sigma_{\text{ff}} = 0.381$ nm, $\epsilon_{\text{ff}}/k = 148.1$ K, $\sigma_{\text{ss}} = 0.340$ nm, $\epsilon_{\text{ss}}/k = 28.0$ K, $\Delta = 0.335$ nm, and $\rho_s = 114$ nm⁻³. For a given slit pore of width H , the external potential experienced by a fluid molecule at z is given by $\phi_{\text{ext}}(z) = \phi_{\text{sf}}(z) + \phi_{\text{sf}}(H - z)$.

The volume of the unit cell was fixed at $900\sigma^3$ with a separation of 5σ between the two opposite adsorbent surfaces. The lateral dimensions of the box were equal in the x and y directions. Periodic boundary conditions in the x and y directions were employed. We used 7×10^7 trials to achieve equilibrium and 7×10^7 moves for data collection. Histograms were collected every 14 moves. Standard reduced units were used with the reduced temperature given by $T^* = kT/\epsilon$ and the reduced density $\rho^* = \rho\sigma^3$. The reduced chemical potential is $\mu^* = \mu/\epsilon$.

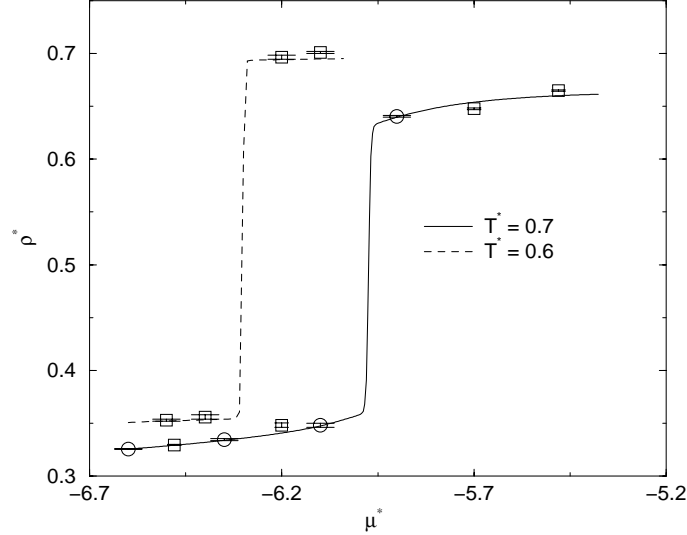


FIG. 1. Isotherms for $T^* = 0.7$ (solid line) and 0.6 (dashed line) from multiple histogram reweighting for methane adsorption in a graphitic slit pore of width 5σ . Data from individual GCMC simulations that were (○) and were not (□) included in the MHR calculations are shown.

We combined 30 histograms in the reduced temperature region from 0.6 to 0.9. Two representative isotherms are plotted in Fig. 1. As a general test of the accuracy of the MHR isotherms we have also plotted state points calculated directly from GCMC simulations in Fig. 1. We show data from simulations that were included in generating MHR isotherms and also data from state points that were not used to construct the histograms in the MHR. The differences between densities obtained from multiple histogram reweighting and those from GCMC simulations are small. The average densities obtained from 19 GCMC simulations not included in multiple histogram reweighting, were compared with densities from multiple histogram reweighting. The isotherms examined were $T^* = 0.9, 0.85, 0.825, 0.8, 0.7,$ and 0.6 . The average absolute error in the densities between GCMC and MHR is 3×10^{-3} . The maximum and minimum absolute errors are 7×10^{-3} and 2×10^{-4} , respectively. Many of the values from MHR agree with those from the simulations within the uncertainty of the simulations.

For $T^* = 0.7$, the values of the coexistence densities computed from MHR are 0.358 and 0.631 for the vapor-like and liquid-like branches, respectively, and the capillary condensation coexistence chemical potential μ_{cc}^* is -5.978 . These data are in excellent agreement with the values from Jiang *et al.* [5], who reported densities of 0.36 and 0.627 for the vapor-like and liquid-like branches, respectively, and $\mu_{cc}^* = -5.93$. Jiang *et al.* located the coexistence points by calculating the grand potentials in each branch. The equilibrium transition occurs when the grand potentials in each phase are equal [4], whereas adsorption and desorption isotherms are plagued by metastability-induced hysteresis.

The lowest temperatures where histograms were collected were 0.6 and 0.65 for the vapor-like and liquid-like sides, respectively. The $T^* = 0.6$ isotherm was generated by extrapolating the histograms at higher temperatures and lower densities in order to generate the liquid-like branch of the isotherms. This is possible because fluctuations recorded at higher temperatures and lower densities sample some of the microstates important at lower temperatures and higher densities, giving a physically realistic extrapolation. The reliability of the extrapolation is confirmed by the agreement

between the MHR isotherm and the two simulation points (not included in the histograms) on the liquid-like branch shown in Fig. 1. The values of coexistence densities from MHR are 0.360 and 0.692 for the vapor-like and liquid-like branches, respectively. These values are very close to those of 0.36 and 0.68 from Jiang *et al.* [5]. The MHR isotherm gives $\mu_{cc}^* = -6.309$, which is in good agreement with the value computed from grand potential calculations of -6.32 [5].

The coexistence densities in the reduced temperature region from 0.68 to 0.76 were fitted to the scaling law and rectilinear law [38].

$$\frac{\rho_l^* + \rho_v^*}{2} = \rho_c^* + A(T^* - T_c^*) \quad (10)$$

$$\rho_l^* - \rho_v^* = B(T_c^* - T^*)^{\beta_c} \quad (11)$$

where ρ_l^* and ρ_v^* are the reduced coexistence densities for the liquid-like and vapor-like branches, respectively, T_c^* and ρ_c^* are the reduced critical temperature and density, β_c is the critical exponent, A and B are fitting parameters. Regression of the MHR equilibrium data to Eqns. (10) and (11) gave $T_c^* = 0.77$, $\rho_c^* = 0.482$, and $\beta_c = 0.119$. The fitted value of β_c is reasonably close to the value of 0.125 (1/8) for the 2-D Ising universality class [39]. The data calculated from MHR and the fitting are shown in Fig. 2.

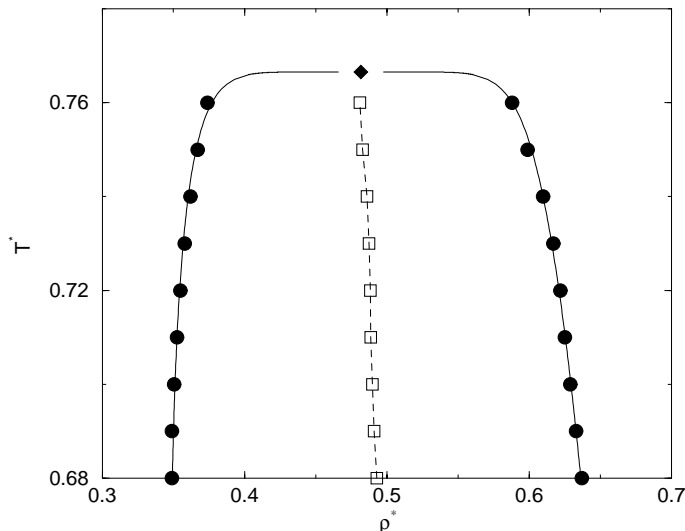


FIG. 2. The $T^*-\rho^*$ phase diagram for capillary condensation of methane in a graphitic slit pore. The filled circles are the coexistence data calculated from the equal area criterion. The filled diamond is the critical point estimated from fitting the coexistence data to the rectilinear and scaling laws, Eqns. (10)-(11). The solid line is the fit to the data. The squares are the rectilinear diameters. The dashed line is shown as a guide to the eye.

The crossover of the effective exponent from 2-D Ising-like (1/8) away from the critical point to the mean-field value (1/2) in the immediate vicinity of the critical point can be observed clearly in Fig. 3. These results reveal the 2-D behavior of capillary condensation. As Mon and Binder have pointed out [40], one expects the observed exponents to correspond to the correct universality class when the correlation length is much less than the simulation box length. This is indeed the case for low temperatures, corresponding to $T^* < 0.74$ for the system represented in Fig. 3. At temperatures near the capillary condensation critical point the correlation length becomes large compared with the box length and the fluid then conforms to mean field behavior due to the suppression of critical fluctuations. Figure 3 is, to the best of our knowledge, the first observation of crossover for capillary condensation.

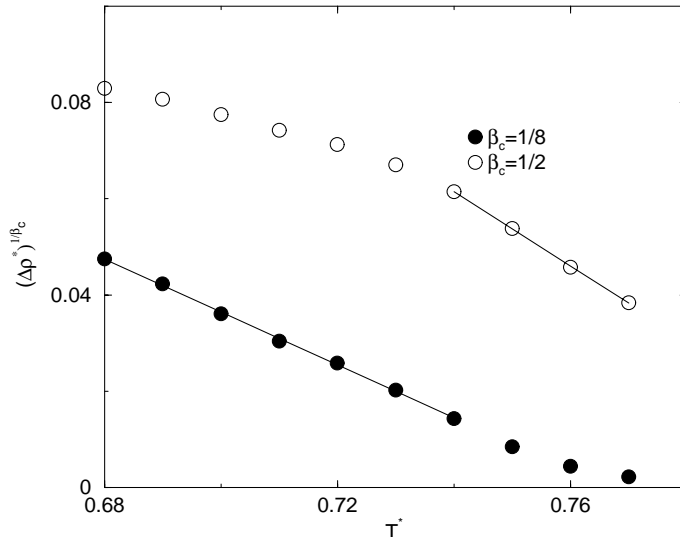


FIG. 3. Scaled width of the coexistence data versus reduced temperatures for the capillary condensation of methane in a graphitic slit pore. The 2-D Ising exponent of $\beta_c = 1/8$ is shown as \bullet and \circ denotes the mean-field value of $\beta_c = 1/2$.

IV. PREWETTING

In this section we present details and results of our MHR calculations for a system that exhibits a prewetting transition. We have investigated the same system studied by Monson and coworkers, namely, Ar adsorbing on a solid CO_2 surface [8,26,41]. Their simulations were performed for a fluid interacting through the truncated LJ potential,

$$\phi_{\text{TR}}(r) = \begin{cases} \phi(r) & r \leq r_c \\ 0 & r > r_c \end{cases}, \quad (12)$$

where $\phi(r)$ is the full LJ potential given by Eq. (8) and r_c is 2.5σ . The fluid-solid interaction at the adsorbing wall is given by the LJ 9-3 potential,

$$\phi_w(z) = \frac{2\pi}{3} \rho_w \sigma_w^3 \epsilon_w \left[\frac{2}{15} \left(\frac{\sigma_w}{z} \right)^9 - \left(\frac{\sigma_w}{z} \right)^3 \right], \quad (13)$$

with $\sigma_w = 0.3727$ nm, $\epsilon_w/k = 153$ K, $\rho_w \sigma_w^3 = 0.988$, and z is the distance between the fluid and the adsorbing wall. The opposite wall was chosen to be reflecting. The parameters for the fluid-fluid interactions are $\epsilon/k = 119.8$ K, and $\sigma = 0.340$ nm.

Monson and coworkers [8,26,41] reported isotherms between $T^* = 0.83$ and 1.0 for pressures up to saturation. Their estimate for the reduced wetting temperature is $T_w^* = 0.84 \pm 0.01$ and the reduced prewetting critical temperature estimate is $T_{pw}^* = 0.94 \pm 0.02$. They observed a prewetting transition at $T^* = 0.88$ from their simulations, but no prewetting transitions at $T^* = 0.83$ and $T^* = 0.80$.

In this work we have chosen the volume of the unit cell for the Ar/ CO_2 model system to be $1620\sigma^3$ with $H = 20\sigma$. Periodic boundary conditions were applied in the x and y directions. We used 10^7 steps for equilibration followed by an additional 10^8 steps for data collection. Histograms were collected at every step. We collected and combined 30 histograms in the temperature region from 0.8 to 1.05. We compute the total, not excess adsorption in this work. Note that the equal area criterion can be used with the total adsorption to find prewetting transitions. The bulk density term adds a constant to both the thin and thick films at a fixed T^* and μ^* . This constant cancels out when computing the difference between the areas of the probability density distributions. The ability to use total instead of excess adsorption isotherms is an advantage because the procedure for computing excess adsorption in a simulation is somewhat ambiguous [42–44].

Several isotherms computed from MHR are shown in Fig. 4, along with results from GCMC simulations. The differences between densities obtained from GCMC simulations and MHR are typically smaller than the errors in the simulations. Prewetting is associated with the first S-shaped rise in coverage in Fig. 4 for $T^* = 0.83$ and 0.88. The second rise and plateau are associated with box filling close to the bulk saturation point. The prewetting transition exhibits considerable rounding due to finite-size effects [45]; hence it is difficult to tell if there is a first order transition

from the shape of the isotherm. The coexistence densities and chemical potentials were computed from the equal area criterion as for capillary condensation. Hill's method was used to get an initial estimate for the value of the coexistence chemical potential [35]. The existence of two distinct peaks with equal areas in the density probability is sufficient to identify the transition as first order. The density probability distribution at $T^* = 0.83$ and $\mu^* = -3.801$ is shown in Fig. 5. We also obtained a two peak equal area density distribution for $T^* = 0.80$. This is significant because Monson and coworkers did not observe prewetting transitions at these temperatures. At these low temperatures, the prewetting transition pressure is closer to the saturation pressure than at higher temperatures, making identification of the prewetting transition especially difficult from standard simulations. However, MHR allows relatively easy identification of prewetting transitions, even very near the saturation pressure.

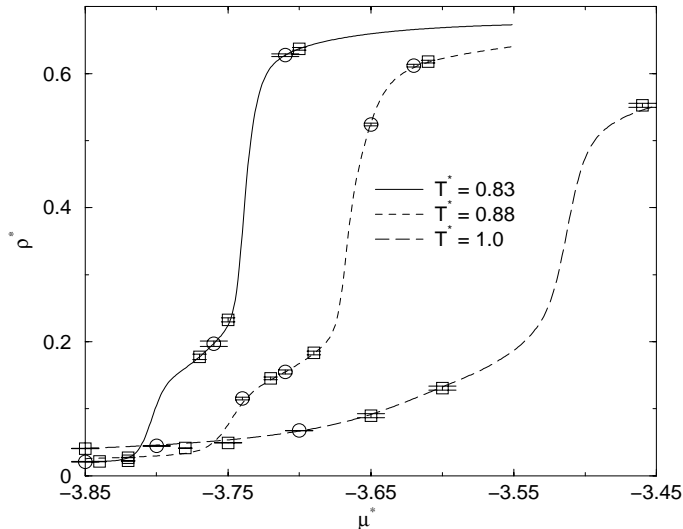


FIG. 4. Isotherms for $T^* = 0.83$ (solid line), 0.88 (dashed line), and 1.0 (long dashed line) from multiple histogram reweighting for Ar adsorption on solid CO_2 . Data from individual GCMC simulations that were (o) and were not (square) included in the MHR calculations are shown.

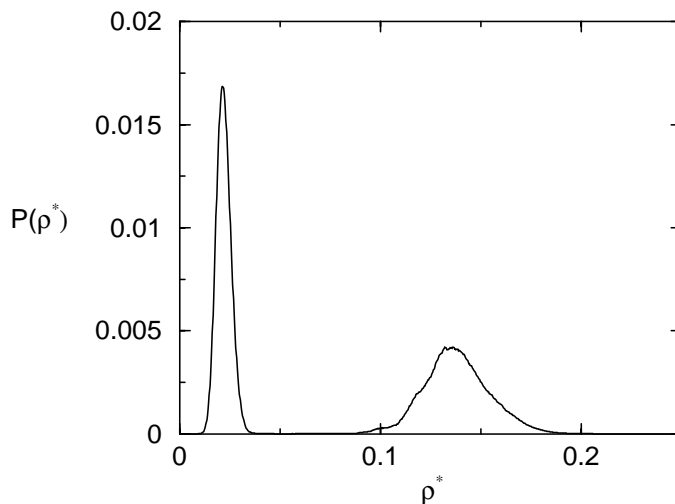


FIG. 5. Density probability distribution for the same system as Fig. 4 at $T^* = 0.83$ and $\mu^* = -3.801$.

The prewetting transitions seen on the $T^* = 0.83$ and 0.88 isotherms can also be characterized by the local density profiles, shown in Figs. 6 and 7. We note that density profiles cannot be computed from MHR because we have not collected histograms of $\rho(z)$ as a function of U_N, N . Referring to Fig. 6, we observe that adsorption is limited to a thin layer on the surface for $\mu^* < -3.8$. For $\mu^* \geq -3.8$ the adsorption abruptly changes to multiple layers that appear to grow continuously as the chemical potential is increased. This behavior is indicative of a prewetting transition occurring. The coexistence chemical potential at this temperature calculated from the equal area criterion is -3.801 ,

in agreement with the local density profiles in Fig. 6. Similar behavior can be seen in Fig. 7, where the thin- to thick-film transition occurs between $\mu^* = -3.76$ and -3.75 . The coexistence chemical potential calculated from MHR is about -3.75 , in agreement with the local density profiles.

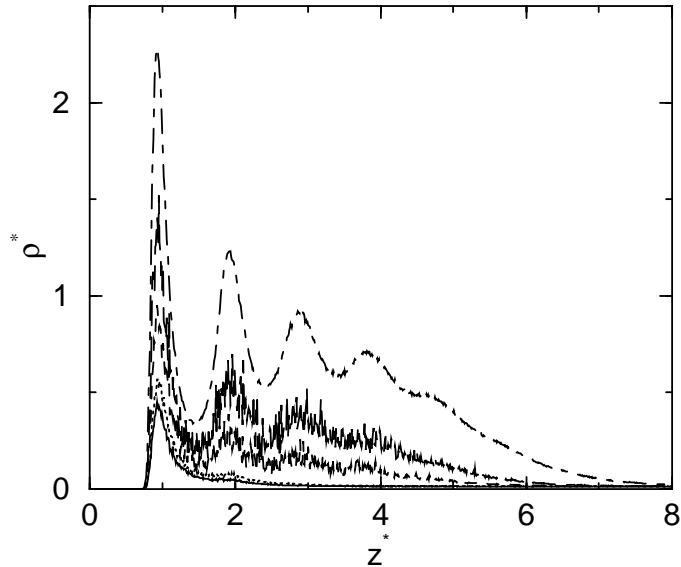


FIG. 6. Local density profiles obtained from GCMC simulations for the same system as Fig. 4. Profiles are for $\mu^* = -3.9$ (solid line), -3.81 (dotted line), -3.8 (dashed line), -3.78 (long dashed), and -3.77 (dot-dashed) at $T^* = 0.83$.

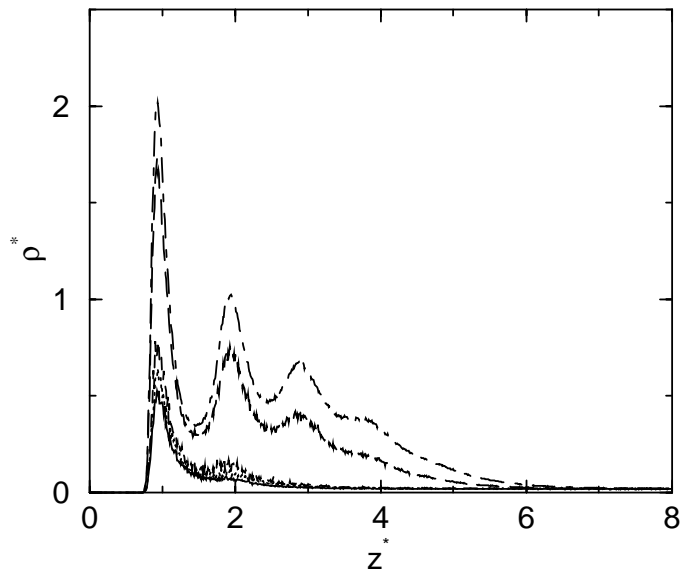


FIG. 7. Local density profiles obtained from GCMC simulations for the same system as Fig. 4. Profiles are for $\mu^* = -3.85$ (solid line), -3.8 (dotted line), -3.76 (dashed line), -3.75 (long dashed), and -3.73 (dot-dashed) at $T^* = 0.88$.

We have computed the saturation chemical potential (μ_{sat}^*) for the bulk phase vapor-liquid transition from $T^* = 0.8$ up to the apparent critical point from MHR of the bulk fluid [35]. The values of the prewetting transition chemical potentials (μ_{pw}^*) were computed over $0.8 \leq T^* \leq 0.88$ from which $\Delta\mu^* = \mu_{sat}^* - \mu_{pw}^*$ was computed. The plot of $\Delta\mu^*$ vs. T^* is shown in Fig. 8. Theoretical predictions indicate that $\Delta\mu^* \propto (T^* - T_w^*)^{3/2}$ [46]. Hence, a plot of $\Delta\mu^*$ vs. T^* can be used to identify the wetting temperature by extrapolating the curve to $\Delta\mu^* = 0$ [47]. The solid line in Fig. 8 is the result of a power law fit to the data using an exponent of $3/2$. However, inspection of simulation data reveals that they lie on a straight line with a correlation coefficient of 0.9994. The estimates of T_w^* from the power law and linear fits are 0.53 and 0.623, respectively.

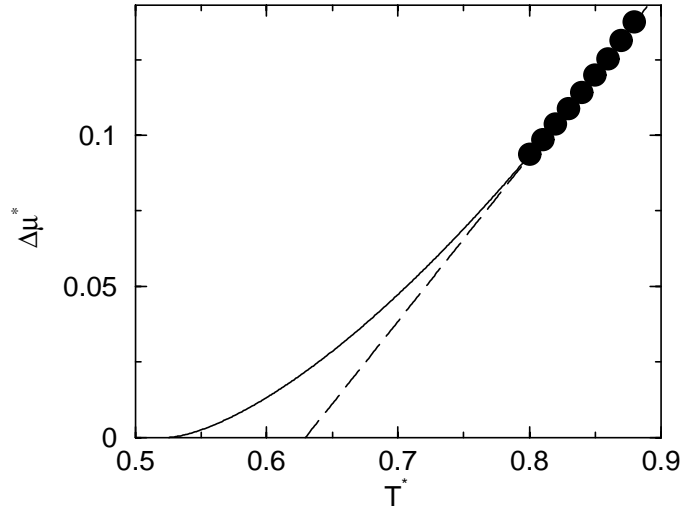


FIG. 8. A plot of $\Delta\mu^* = \mu_{sat}^* - \mu_{pw}^*$ as a function of temperature for the same system as in Fig. 4. Filled circles are computed from MHR. Also shown are the fits to the data to the power law form (solid line), and linear form (long dashed).

The prewetting line for this system was computed [48,49] in order to compare with data from ref. [8]. The density of the gas in equilibrium with the adsorbed phase at the prewetting point was computed by

$$\rho_{pw}^* = \rho_{sat}^* \exp\left(\frac{\mu_{pw}^* - \mu_{sat}^*}{T^*}\right), \quad (14)$$

where ρ_{pw}^* and ρ_{sat}^* are the reduced bulk densities for gas at the prewetting transition and vapor-liquid saturation, respectively. This assumes that the bulk gas is ideal in the calculation. The results are shown in Fig. 9. The prewetting transition densities at $T^* = 0.85, 0.87$ and 0.88 are $0.0146, 0.0170$ and 0.0183 , respectively. These results agree well with values reported by Finn and Monson [8]. We fitted the prewetting line and the saturated vapor line to two separate polynomials. The solid and long dashed lines are the results from the fitting. The value of T_w^* was estimated by extrapolating the two lines to where they intersect. This gave $T_w^* = 0.69$. We note that it has been predicted from theory that the prewetting and bulk saturation lines should meet tangentially [8,48–50]. Therefore, extrapolation of the two polynomials is not only unreliable, but also theoretically not justified. Nevertheless, the estimate of $T_w^* = 0.69$ is in reasonable agreement with $T_w^* = 0.62$ obtained from linear extrapolation of $\Delta\mu^*$ vs. T^* .

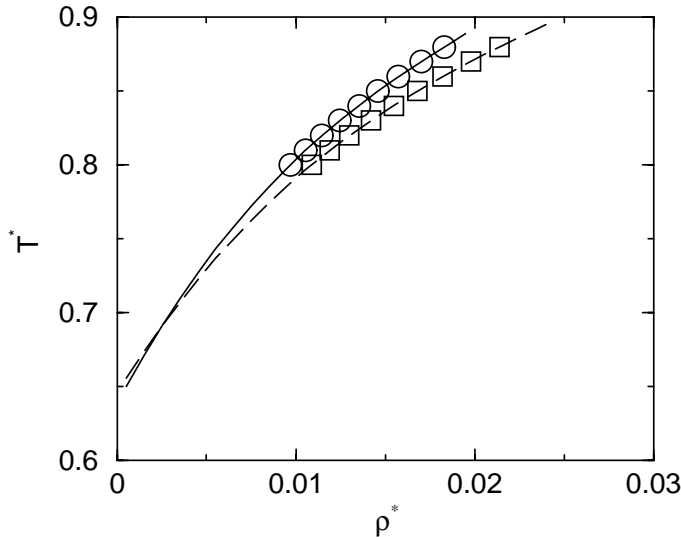


FIG. 9. The temperature–density phase diagram for the same system as in Fig. 4. The circles are the densities of the bulk gas in equilibrium with the adsorbed fluid at the prewetting transition points calculated from MHR. The squares are the vapor side of the bulk vapor-liquid phase diagram computed from MHR of the bulk fluid. The solid line and the dashed line are polynomial fits to the data. The two lines intersect at $T^* = 0.69$.

The reduced wetting and critical prewetting temperatures estimated for the Ar/CO₂ system or similar systems are given in Table II. Note that many of the calculations employed density functional theory, which is not expected to give results identical to simulations given the approximations of the theory. From comparison with the previous estimates of T_w^* we conclude that the power law extrapolation of the $\Delta\mu^*-T^*$ curve is not accurate. We believe that T_w^* for this system is probably close to our estimates from linear $\Delta\mu^*-T^*$ extrapolation and extrapolation of the prewetting line, $T_w^* \sim 0.69$. The estimate of Finn and Monson of $T_w^* = 0.84$ is undoubtedly too high given that we definitely observe a prewetting transition at $T^* = 0.8$.

The relative ratios, P_{wet}/P_{sat} , are plotted in Fig. 10. The ratio was computed from $P_{wet}/P_{sat} = \exp(\frac{\mu_{pw}^* - \mu_{sat}^*}{T^*})$, where P_{wet} and P_{sat} are the pressures at the prewetting transition and saturation, μ_{pw}^* and μ_{sat}^* are the reduced chemical potentials calculated from MHR with the equal area criterion. Ideal gas behavior was assumed in the calculation. As expected, the ratio decreases with temperature. The value at $T = 0.88$ is 85.5%, close to 87.9% calculated by Finn and Monson [8].

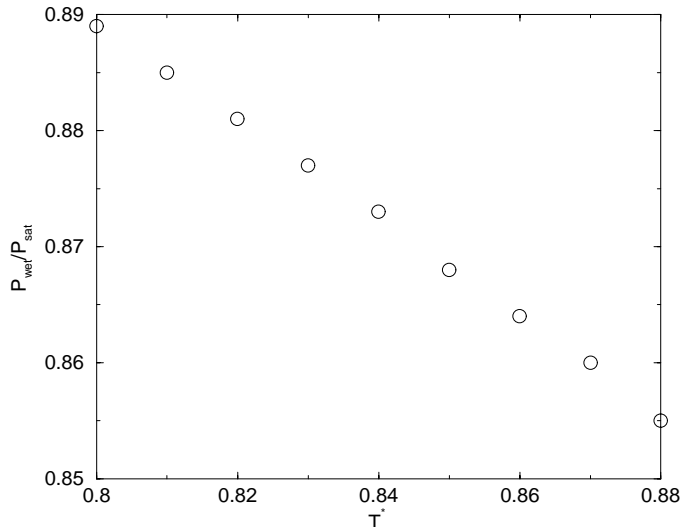


FIG. 10. The ratio of the prewetting transition pressure to the saturation pressure for the same system as in Fig. 4.

The density probability distributions at $T^* = 0.92$ for $-3.72 \leq \mu^* \leq -3.66$ are shown in Fig. 11(a). The isotherm is shown in Fig. 11(b). It is difficult to tell from the isotherm whether or not there is a prewetting transition at this temperature (Fig. 11(b)). However, the density probability distributions are definitive proof that $T^* = 0.92$ is above the prewetting critical point because the equal area criterion can not be satisfied for any choice of μ^* (Fig. 11 (a)). Probability distributions at $T^* = 0.91$ and 0.9 are somewhat ambiguous. They show two peaks that are in the process of merging. From these observations we estimate that T_{pwc}^* is close to 0.92 . This value is in reasonable agreement with other estimates (see Table II). We note that an accurate estimate of T_{pwc}^* would require a finite-size scaling analysis, which is beyond the scope of this work.

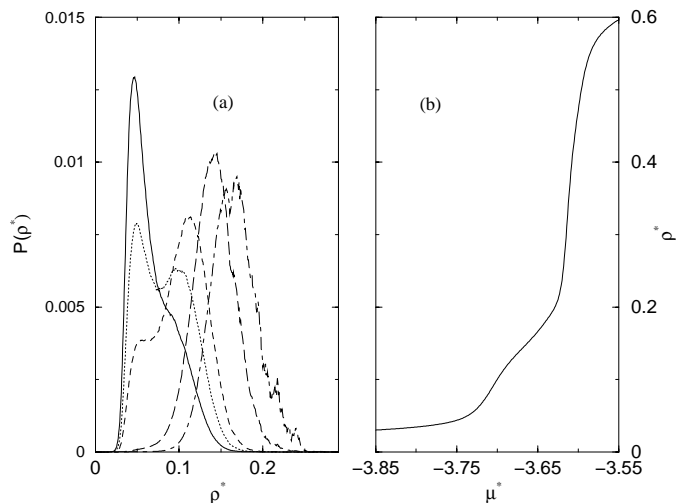


FIG. 11. (a) The density probability distributions for the same system as in Fig. 4 at $T^* = 0.92$. Distributions are for chemical potentials of $\mu^* = -3.72$ (solid line), -3.71 (dotted line), -3.7 (dashed line), -3.67 (long dashed) and -3.65 (dot-dashed). (b) The isotherm computed from MHR at $T^* = 0.92$.

V. LAYERING TRANSITIONS

In this section we present our MHR predictions for the 1-2 layering transition of propane on the basal plane of graphite. Propane was modeled as a three site united atom molecule using the potential of Lustig and Steele [51]. The potential parameters for this model are the LJ parameters ϵ and σ , the bond lengths of the isosceles triangular framework δ , and the bond angle θ . The values of the potential parameters are $\epsilon/k = 119.57$ K, $\sigma = 3.527$ Å, $\delta = 2.16$ Å, and $\theta = 90^\circ$. We note that there are several united atom propane models available in the literature [52–55]. We adopted this model because of its accuracy in predicting the PVT properties and internal energies of pure propane and the good agreement between experimental and simulated adsorption isotherms for propane on graphite [56]. The graphite surface was modeled as a smooth basal plane using the 10-4-3 potential given by Eq. (9).

The volume of the simulation box for histogram collection calculations was set to $1000\sigma^3$. Periodic boundary conditions and minimum image conventions were applied in the x and y directions of the simulation box. The lateral dimensions of the simulation box were equal in x and y directions. One wall of the simulation box was chosen as the adsorbing surface and the opposite wall was chosen to be purely repulsive to keep the molecules in the box. The separation between the two walls was fixed at $H = 10\sigma$ so that the influence of the repulsive wall on the adsorption properties was negligible. The site-site interaction cutoff distance was 3.5σ and no long range corrections were applied. Each simulation was equilibrated for 5×10^7 moves, after which histogram data were collected for another 5×10^7 moves. We collected histograms spanning coverages ranging from a monolayer ($5.9 \mu\text{mol m}^{-2}$) to a complete bilayer ($14.2 \mu\text{mol m}^{-2}$) at a temperature of 130 K. We chose this temperature because it appears to be above the critical layering transition temperature, which allowed sampling of all coverages spanning the 1-2 layering transition. Additional histograms were collected at temperatures down to 100 K, but only sampling a few state points in the monolayer or bilayer regime. A total of 53 histograms from different state points were collected.

An independent series of GCMC simulations were performed (without collecting histograms) for a larger system size with a volume of $4250\sigma^3$ and $H = 20\sigma$ [56]. The isotherms predicted from MHR for the smaller volume are compared with GCMC simulations in Figs. 12 and 13. We observe that the MHR calculations on the small system size give a very reasonable representation of the behavior of the larger system size. The layering transitions occur at close to the same pressures, although there is some difference in the coverages, which may be due to finite size effects. The 1-2 layering transition observed from the GCMC simulations does not appear to be very sharp. In contrast to simple fluids like methane on graphite [57] that show very sharp layering transitions, the propane/graphite system is complicated by orientational changes of the propane in the first layer. The orientational changes allow an increase in coverage in the first layer after the monolayer is apparently “full” and also promotes adsorption in the second layer [56]. Density distributions from MHR at 100 K show two regions that are not well separated. This may be indicative of system size effects. We have previously observed that vapor-liquid density distributions for bulk fluids start to merge for subcritical temperatures, when the system size is small.

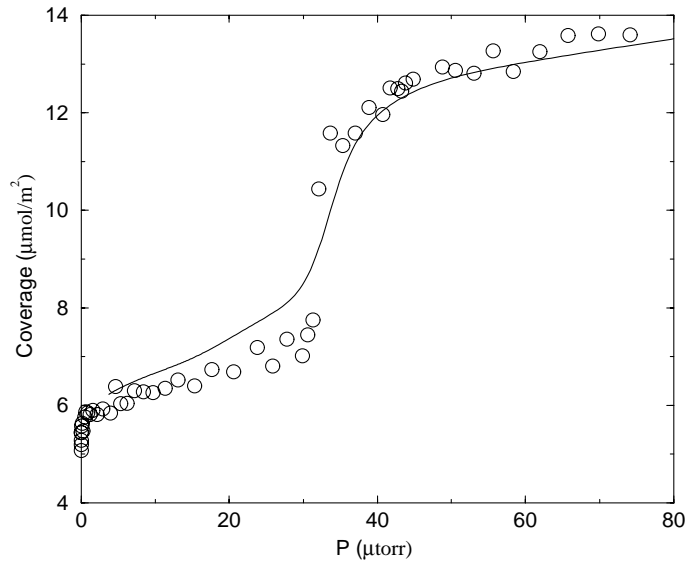


FIG. 12. The $T = 100$ K isotherm (solid line) for propane adsorption on graphite predicted from MHR for a small system size (volume = $1000\sigma^3$) compared with GCMC simulations for a larger system volume of $4250\sigma^3$ (circles).

The value of the critical layering transition temperature is often of interest [31]. In principle, one can estimate the location of the critical layering transition temperature by the disappearance of two distinct peaks in the density distribution. However, the lack of distinct peaks is not a necessary condition for supercriticality, since two peaks in the density probability distribution may be observed for temperatures slightly greater than the apparent critical temperature [58]. A rigorous estimate of the critical layering transition temperature would require finite-size scaling analysis. An additional problem for this system is that the density distributions at subcritical temperatures are not well separated to begin with. Nevertheless, we have estimated $T_c(2)$ to be around 120 K for the propane/graphite system. This value is very close to the experimental result for ethane on graphite of $T_c(2) = 120.8 \pm 0.3$ K [59]. It is somewhat surprising that $T_c(2)$ is so similar for ethane and propane. This may be due to inaccuracies in the potential models used in these simulations or perhaps due to the orientational transitions in the propane monolayer. Additional simulations for ethane adsorption would be useful for understanding the similarities and differences in these systems.

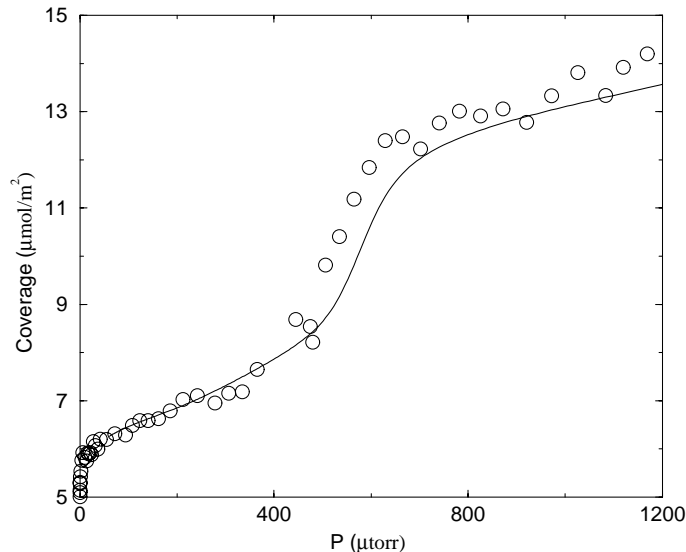


FIG. 13. The $T = 110$ K isotherm (solid line) for propane adsorption on graphite predicted from MHR for a small system size (volume = $1000\sigma^3$) compared with GCMC simulations for a larger system volume of $4250\sigma^3$ (circles).

VI. CONCLUSIONS

The multiple histogram reweighting technique has been used to study capillary condensation, prewetting transitions, and layering transitions. The critical capillary condensation temperature and density are estimated to be $T_c^* = 0.77$ and $\rho_c^* = 0.482$ for methane adsorption in a graphitic slit pore of width $H = 5\sigma$. Crossover of the effective exponent value from 2-D Ising-like to mean-field occurs for capillary condensation. To our knowledge, crossover for capillary condensation has not previously been observed. The precision and abundance of the coexistence data generated from MHR were crucial factors in the successful observation of crossover. Adsorption of Ar on solid CO₂ using the potential models of Finn and Monson shows prewetting transitions at temperatures lower than previously observed. The reduced wetting temperature is estimated to be around 0.69 from the extrapolation of the prewetting transition line and the saturated vapor line. The reduced critical prewetting temperature is about 0.92 as estimated from the disappearance of two distinct peaks in the density probability distribution. Layering transitions were computed from MHR for propane adsorbing on graphite. The transition pressures are in good agreement with previous simulations for larger system sizes, indicating that MHR calculations for small system sizes can be useful for predicting the behavior of larger systems. We estimate $T_c(2) \sim 120$ K based on the merging of the density probability distributions.

We have demonstrated that MHR can be a useful tool for computing the properties of adsorbed fluids, especially when one is interested in investigating phase transitions. There are, however, drawbacks to MHR that we should mention. Efficiency in collecting histograms decreases dramatically with decreasing temperature and increasing volume. It is advisable to use the smallest simulation box size that is possible when performing MHR. The reasons for this are two fold: (1) The overlap between neighboring states becomes smaller as the system size increases, necessitating a larger number of simulations to span the same temperature range. (2) Longer simulations are required to capture the increased number of microstates available in larger systems. We have used standard Metropolis Monte Carlo in our work. Efficiency gains could be made by implementing biasing methods that would increase the width of the density and energy distributions sampled in a single simulation. However, it is clear that MHR is not a very efficient method if large system sizes are needed. Another drawback of the MHR method is that there is no clear way to estimate the precise critical temperature for a transition without resorting to finite-size scaling methods. The disappearance of two peaks in the density distribution is a sufficient but not necessary condition for a system being in the supercritical region. The double peaked distribution is known to persist to temperatures that are slightly supercritical [58], so that absence of the two peaks can only serve as an upper bound measure of the critical point.

ACKNOWLEDGMENTS

We thank Jeffrey Potoff for helpful discussions. This work was supported by the National Energy Technology center and the National Science Foundation through CAREER grant #CTS-9702239. Calculations were performed at the University of Pittsburgh Center for Molecular and Materials Simulations and the National Energy Technology Laboratory.

-
- [1] *Liquids at interfaces*, edited by J. Charvolin, J. F. Joanny, and J. Zinn Justin (North Holland, Amsterdam, 1988).
- [2] *Phase transitions in Surface Films 2*, edited by H. Taub, G. Torzo, H. J. Lauter, and S. C. Fain, Jr. (Plenum Press, New York, 1991).
- [3] L. D. Gelb and K. E. Gubbins, Rep. Prog. Phys. **62**, 1573 (1999).
- [4] B. K. Peterson and K. E. Gubbins, Mol. Phys. **62**, 215 (1987).
- [5] S. Y. Jiang, C. L. Rhykerd, and K. E. Gubbins, Mol. Phys. **79**, 373 (1993).
- [6] A. Z. Panagiotopoulos, Mol. Phys. **62**, 701 (1987).
- [7] S. Curtarolo, G. Stan, M. W. Cole, M. J. Bojan, and W. A. Steele, Phys. Rev. E **59**, 4402 (1999).
- [8] J. E. Finn and P. A. Monson, Phys. Rev. A **39**, 6402 (1989).
- [9] A. M. Ferrenberg and R. H. Swendsen, Phys. Rev. Lett. **61**, 2635 (1988).
- [10] A. M. Ferrenberg and R. H. Swendsen, Phys. Rev. Lett. **63**, 1195 (1989).
- [11] A. M. Ferrenberg and R. H. Swendsen, Comput. Phys. **Sep/Oct**, 101 (1989).
- [12] J. J. de Pablo, Q. L. Yan, and F. A. Escobedo, Annu. Rev. Phys. Chem. **50**, 377 (1999).
- [13] A. Z. Panagiotopoulos, J. Phys.: Condens. Matter. **12**, R25 (2000).
- [14] F. A. Escobedo, J. Chem. Phys. **113**, 8444 (2000).
- [15] J. J. Potoff and J. I. Siepmann, AIChE J. **47**, 1676 (2001).
- [16] L. D. Gelb and K. E. Gubbins, Physica A **244**, 112 (1997).
- [17] F. A. Escobedo and J. J. de Pablo, Phys. Rep. **318**, 85 (1999).
- [18] J. J. Potoff and J. I. Siepmann, Phys. Rev. Lett. **85**, 3460 (2000).
- [19] C. Lastoski and K. E. Gubbins, Langmuir **9**, 2693 (1993).
- [20] L. D. Gelb and K. E. Gubbins, Phys. Rev. Lett. **62**, 1573 (1999).
- [21] G. S. Heffelfinger, F. van Swol, and K. E. Gubbins, Mol. Phys. **61**, 1381 (1987).
- [22] J. W. Cahn, J. Chem. Phys. **66**, 3667 (1977).
- [23] C. Ebner and W. F. Saam, Phys. Rev. Lett. **38**, 1486 (1977).
- [24] D. Bonn and D. Ross, Rep. Prog. Phys. **64**, 1085 (2001).
- [25] M. Schick, in *Liquids at interfaces*, edited by J. Charvolin, J. F. Joanny, and J. Zinn Justin (North Holland, Amsterdam, 1988), pp. 415–498.
- [26] Y. Fan and P. A. Monson, J. Chem. Phys. **99**, 6897 (1993).
- [27] G. Mistura, F. Ancilotto, L. Bruschi, and F. Toigo, Phys. Rev. Lett. **82**, 795 (1999).
- [28] M. W. Cole, J. Low Temp. Phys. **101**, 25 (1995), and references therein.
- [29] M. W. Cole, Fluid Phase Equilibria **151**, 559 (1998), and references therein.
- [30] H. S. Youn, X. F. Meng, and G. B. Hess, Phys. Rev. B **48**, 14556 (1993).
- [31] G. B. Hess, in *Phase transitions in Surface Films 2*, edited by H. Taub, G. Torzo, H. J. Lauter, and S. C. Fain, Jr. (Plenum Press, New York, 1991), pp. 357–389.
- [32] M. Iwamatsu, J. Colloid Interface Sci. **199**, 177 (1998).
- [33] Q. M. Zhang, Y. P. Feng, H. K. Kim, and M. H. W. Chan, Phys. Rev. Lett. **57**, 1456 (1986).
- [34] S. Ramesh, Q. Zhang, G. Torzo, and J. D. Maynard, Phys. Rev. Lett. **52**, 2375 (1984).
- [35] W. Shi and J. K. Johnson, Fluid Phase Equilibria **187-188**, 171 (2001).
- [36] W. A. Steele, Surf. Sci. **36**, 317 (1973).
- [37] W. A. Steele, *The Interaction of Gases with Solid Surfaces* (Pergamon Press, Oxford, 1974).
- [38] B. Smit, J. Chem. Phys. **96**, 8639 (1992).
- [39] O. Dillmann, W. Janke, M. Müller, and K. Binder, J. Chem. Phys. **114**, 5853 (2001).
- [40] K. K. Mon and K. Binder, J. Chem. Phys. **96**, 6989 (1992).
- [41] J. E. Finn and P. A. Monson, Phys. Rev. A **42**, 2458 (1990).
- [42] A. V. Neimark and P. I. Ravikovitch, Langmuir **13**, 5148 (1997).
- [43] O. Talu and A. L. Myers, AIChE J. **47**, 1160 (2001).
- [44] S. Sircar, AIChE J. **47**, 1169 (2001).
- [45] T. L. Hill, *Thermodynamics of Small Systems, Part I* (Benjamin, New York, 1963).
- [46] F. Ancilotto and F. Toigo, Phys. Rev. B **60**, 9019 (1999).
- [47] G. Mistura, H. C. Lee, and M. H. W. Chan, J. Low Temp. Phys. **96**, 221 (1994).
- [48] G. F. Teletzke, L. E. Scriven, and H. T. Davis, J. Colloid Interface Sci. **87**, 550 (1982).
- [49] P. Tarazona and R. Evans, Mol. Phys. **48**, 799 (1983).
- [50] E. H. Hauge and M. Schick, Phys. Rev. B **27**, 4288 (1983).
- [51] R. Lustig and W. A. Steele, Mol. Phys. **65**, 475 (1988).
- [52] W. L. Jorgensen, J. D. Madura, and C. J. Swenson, J. Am. Chem. Soc. **106**, 813 (1984).
- [53] M. G. Martin and J. I. Siepmann, J. Phys. Chem. B **102**, 2569 (1998).

- [54] S. K. Nath, F. A. Escobedo, and J. J. de Pablo, *J. Chem. Phys.* **108**, 9905 (1998).
- [55] J. I. Siepmann, S. Karaborni, and B. Smit, *Nature* **365**, 330 (1993).
- [56] X. Zhao, J. K. Johnson, S. Kwon, R. D. Vidic, and E. Borguet, submitted (2001).
- [57] S. Y. Jiang, J. A. Zollweg, and K. E. Gubbins, *Mol. Phys.* **83**, 103 (1993).
- [58] J. J. Potoff, (private communication).
- [59] H. S. Nham and G. B. Hess, *Phys. Rev. B* **38**, 5166 (1988).
- [60] P. Tarazona and R. Evans, *Phys. Rev. A* **28**, 1864 (1983).
- [61] T. F. Meister and D. M. Kroll, *Phys. Rev. A* **31**, 4055 (1985).
- [62] S. Sokolowski and J. Fischer, *Phys. Rev. A* **41**, 6866 (1990).
- [63] M. J. Bojan, G. Stan, S. Curtarolo, W. A. Steele, and M. W. Cole, *Phys. Rev. E* **59**, 864 (1999).

TABLE I. Ratios of the grand canonical partition function computed from single histogram reweighting (SHR) and multiple histogram reweighting (MHR). The calculation is for methane adsorption in graphitic slit pore.

T_1^*	μ_1^*	T_2^*	μ_2^*	SHR			MHR
				$\frac{\Xi_1}{\Xi_2}$	$\frac{\Xi_2}{\Xi_1}$	$\frac{\Xi_1}{\Xi_2} \times \frac{\Xi_2}{\Xi_1}$	$\frac{\Xi_2}{\Xi_1}$
0.9	-5.57	0.9	-5.50	7.5374×10^{-14}	1.5222×10^{13}	1.1473	1.4971×10^{13}
0.9	-5.50	0.9	-5.45	3.7830×10^{-11}	2.9184×10^{10}	1.1040	2.7088×10^{10}
0.9	-5.45	0.9	-5.40	6.9859×10^{-12}	1.352×10^{11}	0.9444	1.3634×10^{11}
0.85	-5.65	0.9	-5.57	7.5537×10^{27}	1.3189×10^{-28}	0.9962	1.2211×10^{-28}
0.75	-5.90	0.7	-6.10	2.5573×10^{-26}	1.6060×10^{25}	0.4107	3.3113×10^{25}
0.7	-6.6	0.7	-7.0	3.7151×10^{71}	2.7838×10^{-72}	1.0342	2.7188×10^{-72}
0.65	-7.2	0.6	-7.6	2.4925×10^{17}	4.0865×10^{-18}	1.0185	4.4315×10^{-18}
0.9	-5.0	0.85	-5.0	1.1024×10^{-65}	1.4597×10^{65}	1.6091	1.1898×10^{65}
0.725	-5.90	0.725	-5.8	1.8069×10^{-34}	8.9568×10^{33}	1.6184	6.8511×10^{33}
0.7	-5.9	0.685	-6.02	1.8520×10^{14}	4.9617×10^{-15}	0.9189	4.5241×10^{-15}

TABLE II. Reduced wetting temperature (T_w^*) and reduced prewetting critical temperature (T_{pwc}^*) for Ar on CO₂ and Ne on Mg.

Source	T_w^*	T_{pwc}^*
Ebner and Saam [23]	0.77	0.92
Tarazona and Evans [60]	0.957	0.988
Meister and Kroll [61]	0.90	...
Finn and Monson [8]	0.84 ± 0.01	0.94 ± 0.02
Sokolowski and Fischer [62]	0.975 ± 0.025	...
Bojan <i>et al.</i> [63]	0.65	0.88 ± 0.03
This work	0.69	0.92

XXV. “Strontium Isotopic Tracers as Indicators of AMD Provenance and Abatement Efficiency”

**Barbara Homison (S) and Brian Stewart (F), University of Pittsburgh
with
Ann Kim (M), NETL**

STRONTIUM ISOTOPIC TRACERS AS INDICATORS OF AMD PROVENANCE AND ABATEMENT EFFICIENCY

University of Pittsburgh

University/NETL Student Partnership Program

2001 Annual Project Report

Student: B. L. Hamel *Department of Geology and Planetary Science*

University Advisor: Brian Stewart

NETL Mentor: Ann Kim

ABSTRACT

Strontium (Sr) isotope ratios for acid mine drainage (AMD) from the Omega Mine near Morgantown West Virginia show variations that indicate their usefulness for the determination of the provenance of continuing discharge after a grouting operation that was intended to eliminate it.

The isotopic tracers will be used to attempt to determine if the remaining discharge is the result of surface or shallow subsurface flow, water seeping out from areas of the mine that are ungrouted, grouted but porous, or if the grouting operation was ineffective. The isotopic ratio of dissolved Sr in water is generated by leaching reactions of the water with solid materials in its flow path and creates a unique "fingerprint". Because of this fact, the ratios can be used to characterize the flow regime.

There are eight repeatable sampling sites located around the downdip perimeter of the mine. Results so far show strontium concentrations of 1400 µg/L in the grouted portion of the mine versus <700 µg/L in the ungrouted part. Waters discharging from the grouted segment have a ⁸⁷Sr/⁸⁶Sr ratio of ~ 0.7140 (typical 2 σ uncertainty ~ 0.00002) and those discharging from the ungrouted portion have a range of 0.7152-0.7159. The method shows promise for tracking solid-water interactions in abandoned mine systems.

TABLE OF CONTENTS

ABSTRACT.....2

LIST OF GRAPHICAL MATERIALS.....4

INTRODUCTION.....5

SITE DESCRIPTION.....6

SAMPLING AND ANALYTICAL METHODS.....6

RESULTS AND DISCUSSION.....8

ACKNOWLEDGEMENTS.....9

REFERENCES CITED.....10

LIST OF ACRONYMS AND ABBREVIATIONS.....11
APPENDIX.....12

LIST OF GRAPHICAL MATERIAL

Figure 1. Omega Mine Complex - Existing Site Conditions. GAI Consultants.....12
Figure 2. Omega Mine Complex - Injection Plan. GAI Consultants.....13
Figure 3. Omega Mine site, Morgantown, West Virginia. DOE.....14
Figure 4. Strontium Concentrations. Robert Thompson, DOE.....15
Table 1. Isotopic Ratios from the Omega Mine. B. L. Hamel.....16

INTRODUCTION

The Omega Coal Mine, located approximately six miles south of Morgantown, was closed in the early 1990's. At that time AMD had already been seeping into the watershed west of US Route 119 from earlier mining operations. With the final closure of the mine, acid mine drainage (AMD) seepage began to increase to the west. In addition, AMD began to discharge into the watershed to the east of Route 119 initiating an unacceptable impact on the local urban water supply (Gray et.al., 1997).

The West Virginia Department of Environmental Protection (WVDEP) assumed the responsibility for AMD abatement at the site when a joint venture to reduce it with a mine grouting project was proposed. The grouting mixture of fly ash, fluidized bed combustion byproducts, and cement was to be injected into the northern lobe of the mine from which the AMD was emanating. A grout slurry was to be injected into boreholes spaced close enough to facilitate complete closure of that segment of the mine. The pre-existing AMD collection and treatment system was to be upgraded and maintained until abatement was complete (Gray et.al., 1997).

The grouting project was completed in 1998. Prior sampling locations continued to be monitored and AMD was still being discharged in 2000. In an effort to determine the source of

the continuing AMD, a new project using strontium isotope ratios as tracers was proposed (Kim, 1999).

SITE DESCRIPTION

The Omega Mine is located approximately six miles south of Morgantown, West Virginia. The Northern Lobe, which releases the AMD, is under a hilltop with an elevation range of 1550-1750 feet. The mine is in a segment of the Upper Freeport Coal which is approximately 4.5 feet thick. The dip of the coal seam is to the northwest at a grade of 11%. (Gray et. al., 1997) (Figure 1).

The borehole spacing varied across the location based on video reconnaissance that appraised the volume of grout needed to fill the void, the degree of slope, and the amount of rubble on the mine floor. (Gray et. al., 1997) (Figure 2).

The AMD collection and treatment system included all known AMD discharge points located around the perimeter of the northern lobe. Sampling points remained accessible for continued monitoring. Some sites collected seeping water from punch mines, some collected the AMD still emanating from the grouted lobe, and one collection point was discharging water from the central mine pool that is located in the ungrouted portion of the mine (Figure 3).

SAMPLING AND ANALYTICAL METHODS

Samples were collected at roughly monthly intervals. Three samples were taken at each location. One was collected for pH, conductivity, sulfate, and chloride. A second, acidified sample was collected for metals analysis by inductively coupled plasma-atomic emission spectroscopy (ICP-AES) The final sample was collected in acid cleaned polyethylene bottles for strontium isotope analysis. These samples were filtered through 0.45 μ m SFCA-membrane

filters (from Cole-Parmer) using 60 cc syringes (from Becton Dickinson & Co.) and then acidified to 2% with ultrapure HCL.

The total amount of Sr in the sample was calculated using the ICP-AES data. Then, an aliquot of the filtered sample that contained approximately 3000 nanograms (ng) of Sr was put into an acid cleaned teflon beaker and dehydrated on a hot plate kept at 195° C. A 0.15 mL aliquot of 3 N ultrapure nitric acid (HNO₃) was added to dissolve the Sr. The resulting solution was centrifuged in order to remove any remaining solids and then dripped through columns containing Sr-SPEC® resin. Here, a series of rinses flushed out everything except the Sr. The final rinse of 18.2 MΩ MilliQ® water (highly purified) released the Sr from the resin.

The Sr collected in the rinse water was dried down completely again at 195°C in acid-washed Teflon. To prepare it for isotope ratio analysis, the Sr residue was dissolved in 1 microliter (μL) of ultrapure 3 N HNO₃ (which resulted in approximately 400 ng of Sr). This 1 μL was placed onto a filament that was loaded with a carrier agent prior to the sample. The sample was then dried and cured and inserted into a carousel that holds up to twelve samples at a time in the Finnigan MAT 262 thermal ionization mass spectrometer (TIMS).

Each ratio was measured approximately 100 times during the analyses. The final ratio was then calculated from those interim measurements. In addition to the samples, an NBS 987 strontium standard was also analyzed.

RESULTS AND DISCUSSION

Twenty-two metal concentrations were determined for each acidified sample. The completed Sr results that are available are shown in Figure 4. Each sampling date is associated

with a different color. The isotope ratios are shown in Table 1. Many more samples have been collected for future analyses.

The preliminary results indicate that the highest Sr concentration is found in the grouted portion of the mine. The lowest values are from the ungrouted Central Pool area (except for the anomalous Punch Mine 24B). The other values are intermediary to these end points.

The high values found in the Marshall House (grouted) samples may reflect leaching from the grout itself or they may reflect the accelerated weathering of host rock material by the highly acidified mine waters. Until all of the data has been collected, complete appraisal of the situation cannot be made.

The isotope ratios show a reverse trend from that shown by Sr concentration. In this case the highest values are found in the Central Pool samples and the lowest values are found in the grouted Marshall House sample. Once again, all other values fall within these endpoints. These preliminary results indicate that the proposed isotopic ratio method is viable. There are differences in the isotopic fingerprints from the different sampling points that may reflect varying mixtures of source waters and interaction with in situ solids.

The data that remain to be compiled includes pH, determination of Sr isotopic ratios for the overburden, the coal, and the grout, and completion of the analyses of all remaining collected samples. Additional sample collection in the spring would validate the stability of the system if the ratio values remain constant.

After the data collection is complete, mixing equations will be used to determine the hydrological regime within the mine. Once the hydrological system has been assessed, recommendations can be proposed for the enhancement of abatement efforts.

ACKNOWLEDGEMENTS

This study has been funded by the US Department of Energy (DOE) under a University Partnership grant. I am grateful for the mentoring, analytical assistance and technical direction provided by Ann G. Kim, Brian W. Stewart, and Brian K. Games.

REFERENCES CITED

- Faure, G, 1977. Principles of Isotope Geology: John Wiley & Sons, p. 117-153, p. 183-199.
- Gray, T. A., Moran, T. C., Broschart, D. W., and Smith, G. A., 1997. Plan for injection of coal combustion byproducts into the Omega Mine for the reduction of acid mine drainage: American Society of Surface Mining and Reclamation 1997 National Meeting, May 10-16, Austin, Texas, 8 p.
- Johnsan, T., 2000. Groundwater "fast paths" in the Eastern Snake River Plain aquifer: radiogenic isotope ratios as natural groundwater tracers: *Geology*, v. 28, n. 10, p. 871-874.
- Kim, A. G., 1999. The use of strontium isotope ratios to determine the source of mine drainage: US Department of Energy Proposal.
- Land, M., Ingri, J., Andersson, P. S., Ohlander, B., 2000. Ba/Sr, Ca/Sr and $^{87}\text{Sr}/^{86}\text{Sr}$ ratios in soil water and groundwater: implications for relative contributions to stream water discharge: *Applied Geochemistry*, v. 15, p. 311-325.
- Worrall, F., Pearson, D. G., 2000. The development of acidic groundwaters in coal-bearing strata: Part I. Rare earth element fingerprinting: *Applied Geochemistry*, v. 16, p. 1465-1480.

LIST OF ACRONYMS AND ABBREVIATIONS

AMD - Acid Mine Discharge or Drainage

DOE - Department of Energy

HCL - Hydrochloric Acid

ICP-AES - Inductively Coupled Plasma Atomic Emission Spectrometer

TIMS - Thermal Ionization Mass Spectrometer

WVDEP - West Virginia Department of Environmental Protection

APPENDIX

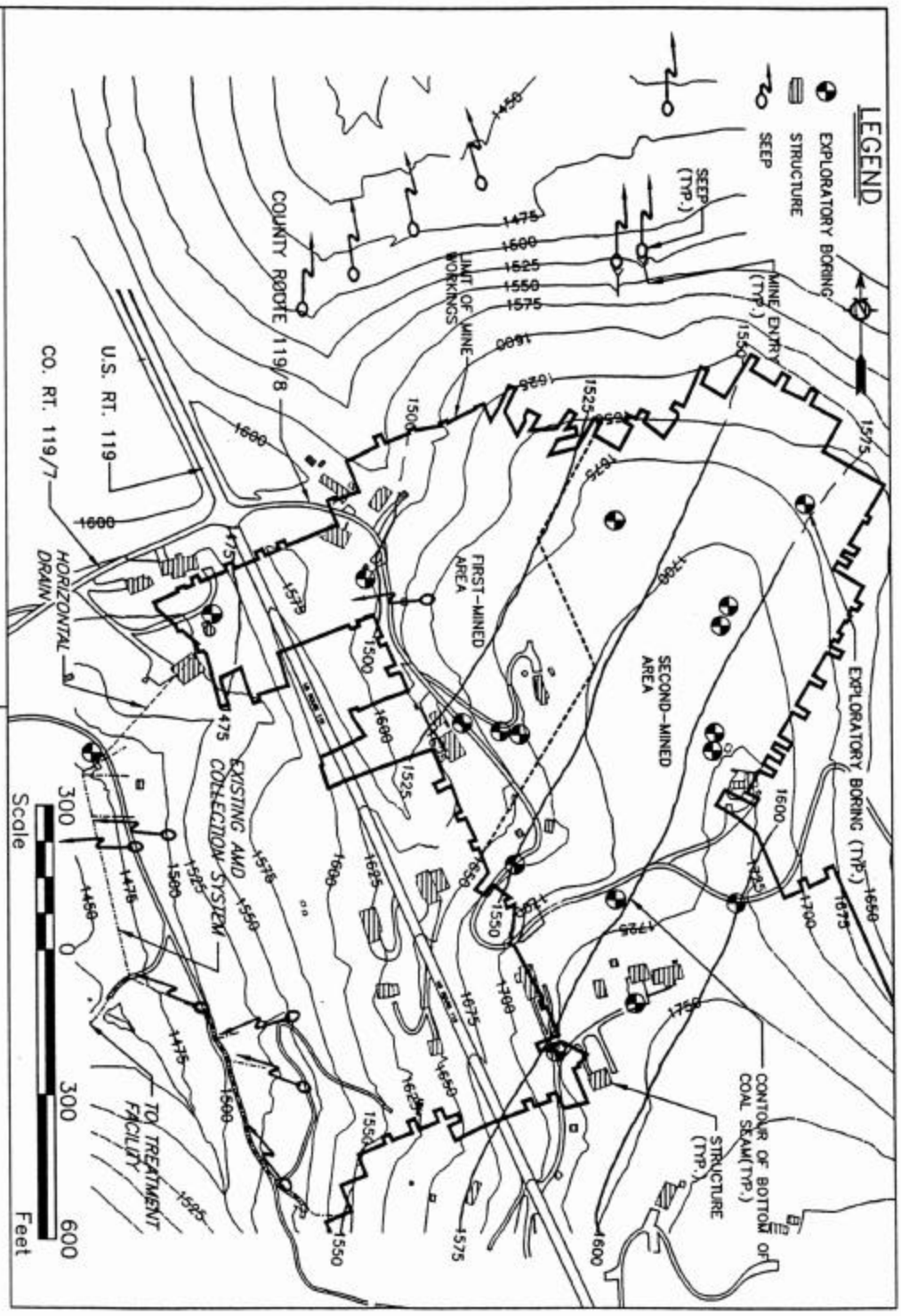


Figure 1. Omega Mine Complex – Existing Site Conditions

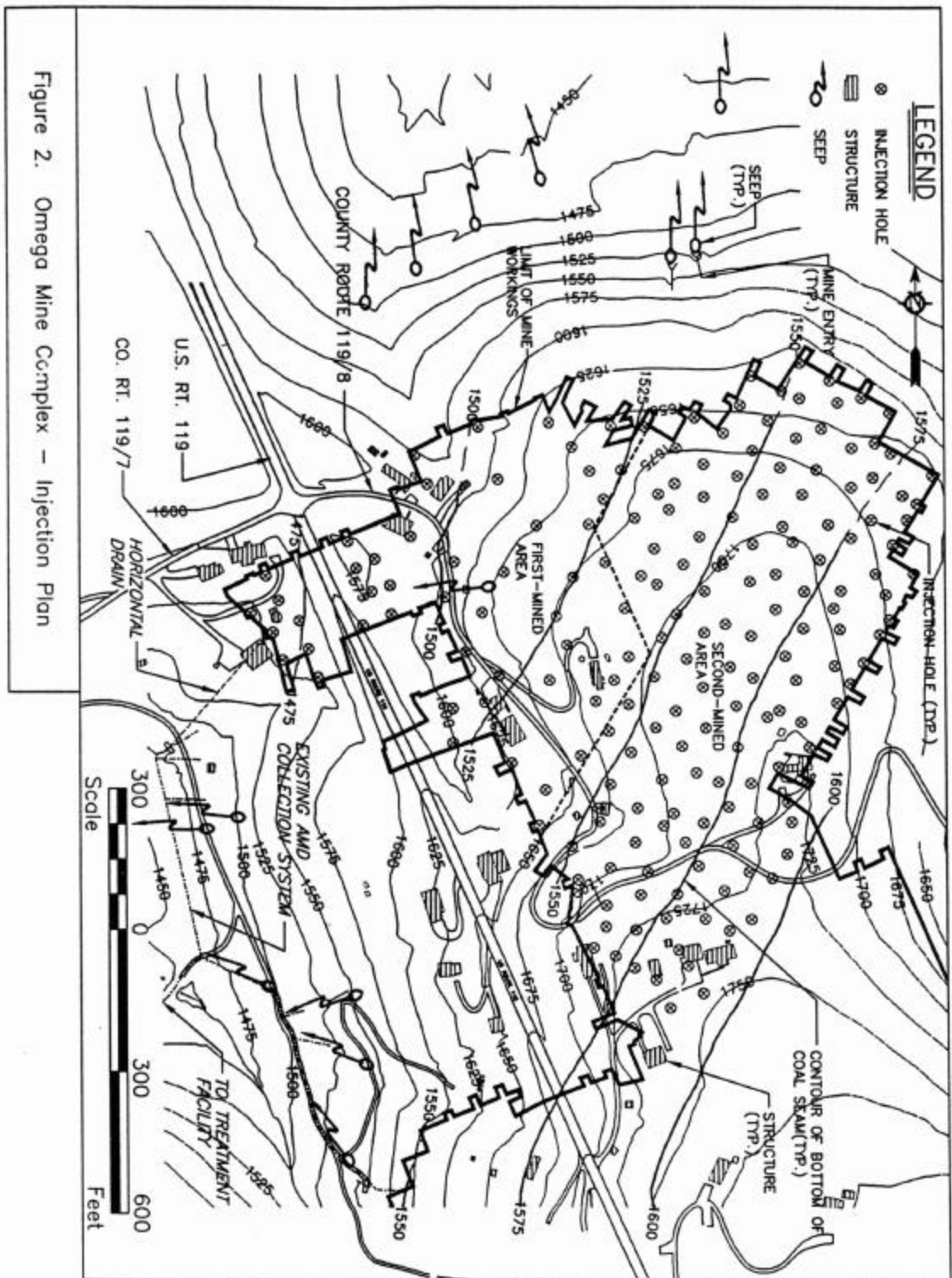


Figure 2. Omega Mine Complex – Injection Plan

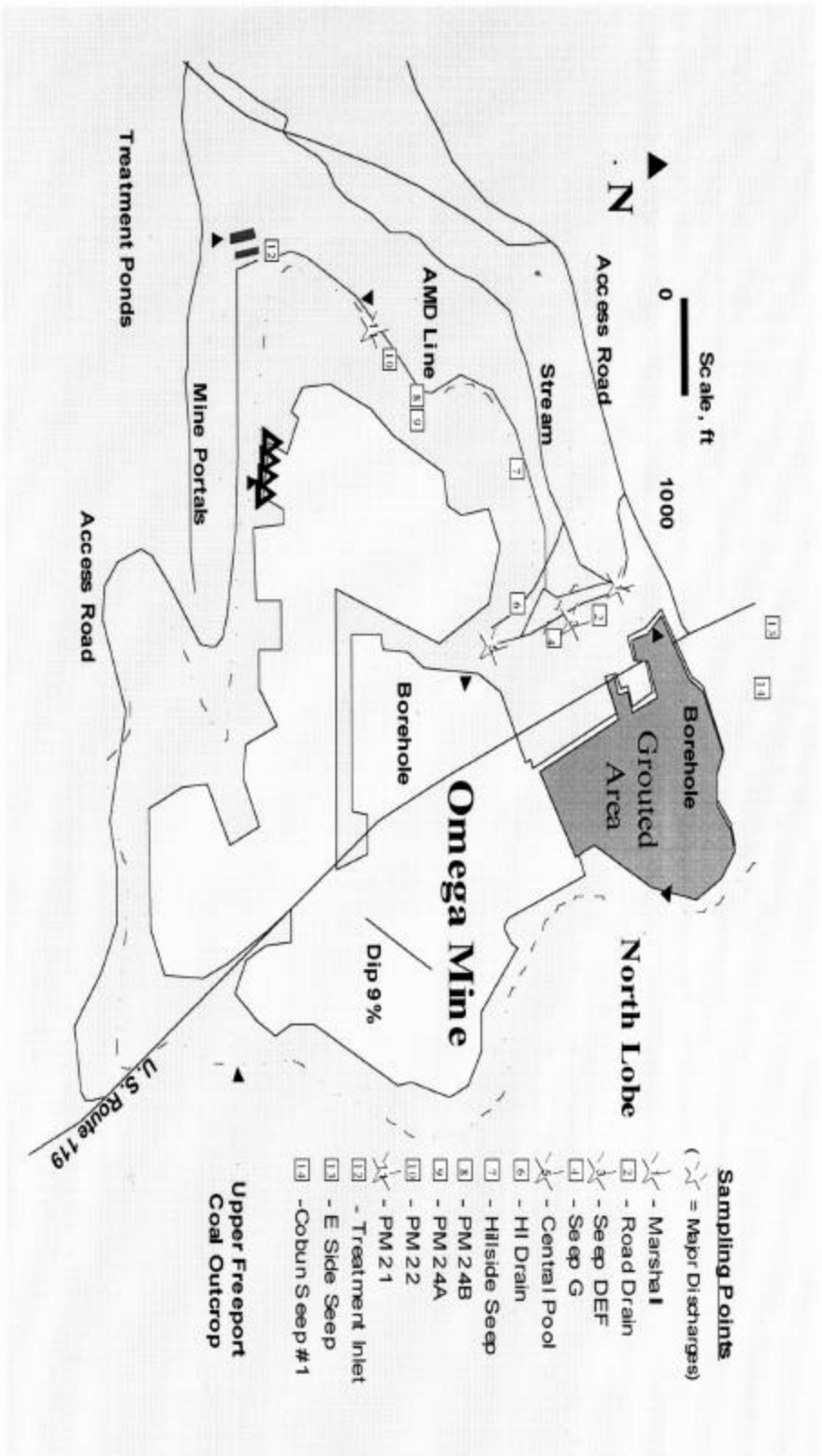
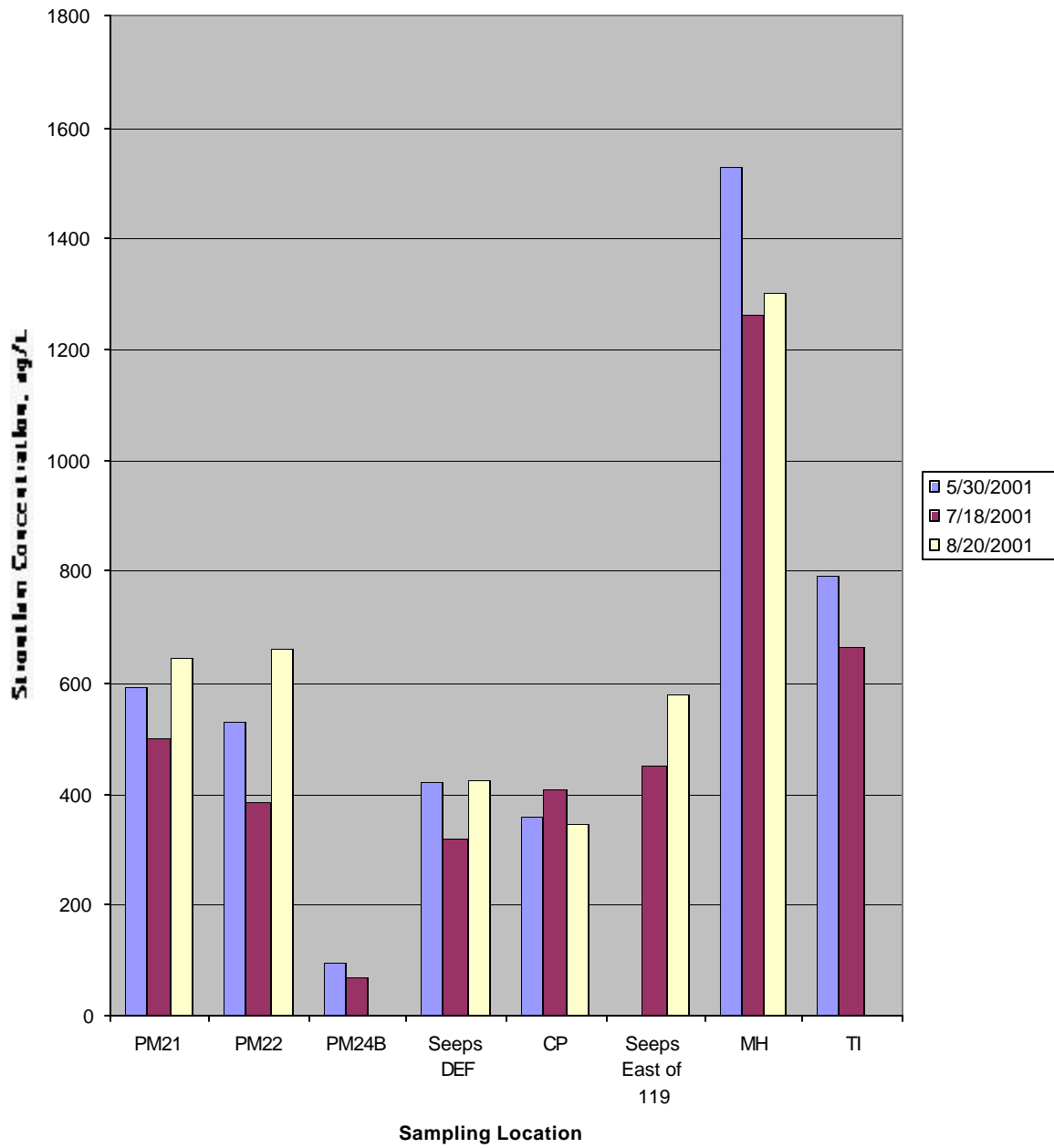


Figure 3. Omega Mine site, Morgantown, West Virginia.





Omega Mine	Isotopic Ratios, ⁸⁷ Sr/ ⁸⁶ Sr	
Sample Location	Date: 5/30/01	Date: 7/18/01
TI (Treatment Inlet)	0.714700 ±10	0.714793±01
PM21 (Punch Mine)	0.715883±09	0.715884±09
PM22 (Punch Mine)	0.715241±11	
PM24B (Punch Mine)		
MH (Marshall House)	0.714034±10	
Seeps DEF	0.715869±11	0.715719±09
CP (Central Pool)	0.715918±09	0.715898±09
Seeps East Side of Rt 119		0.714311±13

Uncertainty shown is 2 σ in-run uncertainty. Estimated external reproducibility is ± 3 SRM987 was analyzed with each run to establish precision

Table 1. Isotopic Ratios from the Omega Mine. B. L. Hamel

XXVI. “Chemistry of Coal Seam Sequestration of Carbon Dioxide”

**Ekrem Ozdemir (S) and Badie Morsi (F), University of Pittsburgh
with
Karl Schroeder (M), NETL**

SEQUESTRATION OF CARBON DIOXIDE (CO₂)
IN
COAL SEAMS

Report # 1
December, 2001

Submitted to:

University Partnership Program
Department of Energy (DOE)-National Energy Technology Laboratory (NETL)
P.O.Box 10940, Pittsburgh, PA 15236

by

Ekrem Ozdemir
Advisor: Prof. Badie I. Morsi
Mentor: Karl Schroeder

Chemical and Petroleum Engineering Department
University of Pittsburgh
1249 Benedum Hall, Pittsburgh, PA 15261

SUMMARY

Increasing concentration of anthropogenic carbon dioxide (CO_2) in the atmosphere has been threatening the world's climate system. Coal seam sequestration is one of the geologic options to mitigate atmospheric CO_2 , which requires an extensive knowledge on coal- CO_2 interaction such as the maximum amount of CO_2 to be injected, the stability of the adsorbed CO_2 after the sequestration is completed, and the injection rate as well as the distribution of CO_2 through the coal seam.

Up to date, the adsorption and desorption isotherms of carbon dioxide (CO_2) on a selection of the Argonne Premium coal samples, Pocahontas No.3, Upper Freeport, Illinois No.6, Wyodak, and Beulah-Zap, were measured at temperatures of 22, 30, 40, and 55°C and up to pressures of 5 MPa. The shape and extent of adsorption isotherms were found to be rectilinear at high pressures and could not be fitted to traditional adsorption equations. The rectilinear form of adsorption isotherms was related to the swelling of coal, which occurs when it is contacted with CO_2 and other adsorbing gases and organic vapors. To model the behavior of the CO_2 -coal system, an equation was derived accounting for the change in accessible pore volume of the coal during the adsorption measurement. The derived equation appeared to fit the experimental data very well.

The adsorption capacity and characteristic heat of adsorption were estimated by applying newly derived equation accounting the volume change of coals due to swelling and shrinkage effect. The adsorption capacities and characteristic heat of adsorption of

Argonne Premium coals were found to be ‘U’ shaped with respect to coal rank. The adsorption capacities and characteristic heat of adsorption were estimated to be between 0.9-1.7 mmole/g-coal and 26-30 kJ/mole, dry-ash-free basis, respectively, regardless of rank. The change in accessible pore volume for various ranks of coals was 7%-70%, and was higher for low-rank coals.

The effect of moisture on the shape of adsorption isotherms was estimated. Coals with high moisture content show a linear-like isotherm whereas coals with less moisture content show more Langmuir-like isotherm. Although moisture content did not affect the adsorption capacity of the coals studied, it affected equilibrium constant between the gas phase and the coal.

The surface areas of coals were compared with the literature values and found little deviation for high-rank coal where as a large deviation for low-rank coals due to the high-swelling nature of low-rank coals.

TABLE OF CONTENTS

SUMMARY	II
LIST OF FIGURES	VI
LIST OF TABLES	VIII
NOMENCLATURE	IX
1. INTRODUCTION	1
2. OBJECTIVES	8
3. EXPERIMENTAL METHOD	9
3.1. Materials and Chemicals	9
3.2. Gas adsorption apparatus	10
3.3. Adsorption/Desorption Isotherms	11
3.4. Physical Data for He and CO₂	12
4. RESULTS AND DISCUSSION	13
4.1. Adsorption Isotherm of CO₂	13
4.1.1. Typical Calculation Methodology	15
4.1.2. Mathematical Model of the Adsorption Isotherm of CO ₂ which Accounts for Swelling	18
4.1.3. Conventional Evaluation of Adsorption Isotherm Data at Low Pressures (0<P/P ₀ <0.12).....	22

4.1.4. Evaluation of Adsorption Isotherm Data for the Entire Range of Adsorption Isotherm ($0 < P/P_o < 0.61$)	24
4.1.5. Accounting for Swelling in the Evaluation of the Entire Adsorption Isotherm Data ($0 < P/P_o < 0.61$).....	27
4.2. Evaluation of the Surface Area of Coals	31
4.3. Effect of Temperature on the Adsorption Isotherm of CO₂ on Coal	33
4.4. Sorption Capacity and Heat of Adsorption of Selected Argonne Premium Coals	38
4.5. Effect of Moisture on the Adsorption Isotherms of CO₂ on Coals	40
CONCLUDING REMARKS	43
REFERENCES	45

LIST OF FIGURES

Figure 1. Coal Seam Sequestration of CO ₂	3
Figure 2. Manometric Gas Adsorption Apparatus: R: Reference Cell, S: Sample Cell, P: Pressure Transducer, I: ISCO Syringe Pump, V: Vacuum Pump T: Thermocouples B: Constant Temperature Bath.....	11
Figure 3. Adsorption-desorption isotherms of CO ₂ on selected Argonne Premium coals at 22 °C. Open symbols: Adsorption; solid symbols: Desorption	14
Figure 4. Schematic Representation of Change in Volume in Sample Chamber due to Sorption of Gases.....	19
Figure 5. Adsorbed Amount of CO ₂ on selected Argonne Premium Coals (a) Langmuir Equation (b) D-R Equation.....	26
Figure 6. Adsorbed amount of CO ₂ on selected Argonne Premium coals modified Langmuir equation (Eq.12).....	28
Figure 7. Adsorption isotherms of selected Argonne Premium coals in the presence of accessible pore volume change. Lines are derived using the following models: (a) Pocahontas No.3 - modified Langmuir Eq. (Eq.12) (b) Beulah-Zap - modified D-A Eq. (Eq.15)	30
Figure 8. Comparison of the CO ₂ - surface area of coals obtained in this work with the some literature values.....	32
Figure 9. Adsorption/desorption isotherms of CO ₂ on Argonne Premium coals at temperatures of 22, 30, 40, and 55 °C.....	34
Figure 9. Cont.	35

Figure 9. Cont.	36
Figure 10. Adsorption capacity and heat of adsorption for different coal ranks	39
Figure 11. Effect of Moisture on the CO ₂ adsorption isotherms of the Argonne Premium Wyodak Coal.....	42

LIST OF TABLES

Table 1. Proximate and Ultimate Analyses of Argonne Premium Coal Samples (Vorres, 1993)	10
Table 2. Pressure and amount of gas at each adsorption/desorption steps in reservoir and sample chambers.....	16
Table 3. The general form of the adsorption equation resulting from the substitution of several adsorption models for n_{ads} term in Eq.10.....	21
Table 4. Monolayer/Micropore Adsorption Capacity of Carbon Dioxide on Selected Argonne Premium Coals at Pressures $0 < P/P_o < 0.12$	23
Table 5. Monolayer/Micropore Adsorption Capacity of CO ₂ on Selected Argonne Premium Coals for Entire range of Isotherms ($0 < P/P_o < 0.61$).....	24
Table 6. Monolayer/Micropore Adsorption capacity of CO ₂ on Selected Argonne Premium Coals: Account of Swelling ($0 < P/P_o < 0.61$)	27
Table 7. Modified-Langmuir, Dubinin-Radushkevich, and Dubinin-Astakhov Curve Fit Parameters	37
Table 8. Adsorption capacities and heats of adsorption of the selected Argonne Premium coals	39
Table 9. Effect of moisture content on the Adsorption capacity, Langmuir constant, and increase in pore volume of Argonne Premium coals at various ranks ^a :	42

NOMENCLATURE

n_{exp} : experimentally calculated total amount of adsorbed gas when the void volume of the sample chamber (V_o) is presumed constant and is estimated by the He-expansion method;

n_{ads} : amount of gas actually adsorbed;

DV/w : change in accessible pore volume per g of sample;

DV/V : ratio of the change in accessible pore volume of sample;

ρ : helium density of the sample;

R : the universal gas constant;

T : temperature;

P : equilibrium pressure;

z : compressibility factor;

n_o : monolayer/micropore capacity of coals (mmole/g-coal, daf);

b : Langmuir constant (MPa^{-1});

j : the structural heterogeneity parameter;

β : affinity coefficient;

E : heat of adsorption obtained from the D-R or D-A equation (kJ/mole);

$\Delta V\%$: percent change in accessible pore volume;

P_0 : saturation pressure;

P/P_0 : relative pressure;

C : constant related to the net heat of adsorption;

v : molar volume;

1. INTRODUCTION

Atmospheric concentrations of greenhouse gases (GHGs) such as carbon dioxide (CO₂), methane (CH₄), and nitrous oxide (N₂O) are increasing due to human-induced (anthropogenic) activities (Hansen et al., 1997 [¹]). Among these, CO₂, which is mainly produced by the burning of fossil fuels, is the most abundant greenhouse gas. The atmospheric concentration of CO₂ increased from 280 ppm during the preindustrial era to 365 ppm in 1998 at a rate of approximately 1.5 ppmv per year (Halman and Steinberg, 1999 [²]). Future predictions show that emission of CO₂ will continue to increase over the next decades as fossil fuels continue to be the major source of energy (IPCC, 1996 [³]). CO₂ is responsible for about 64% of the anthropogenic greenhouse effect and is the most important (Bachu, S., 2000 [⁴]). Due to the large contribution of CO₂ to the climate change, a huge reduction of CO₂ emission became unavoidable to stabilize CO₂ in the atmosphere.

The CO₂ concentration in the atmosphere can be controlled either by reducing its production and release into the atmosphere, or by capturing and disposing of the produced CO₂ in a safe way. Any strategy needs to be safe, predictable, reliable, measurable, and verifiable (U.S.DOE, 1999 [⁵]). In the last few decades, various CO₂ sequestration options have been proposed including placement in the deep oceans; placement in geologic formations such as deep saline aquifers, abandoned oil and gas reservoirs, enhance oil recovery processes, and unmineable, deep coal seams; and consumption via advanced chemical and biological processes. Presently, these options are

still under investigation in order to determine their feasibility in terms of their storage capacity and safety.

Coal seam sequestration of CO₂ is particularly attractive in those cases where the coal contains large amounts of methane. In these cases not only the CO₂ gas is stored in the coal seams in an adsorbed state but the coalbed methane can also be produced to generate a profit to offset sequestration expense. Thus, long-term sequestration of CO₂ in coal seam might be more cost-effective. However, a better understanding is needed in order to determine which, if any, coal seams might be good disposal sites and under what environmental conditions the adsorbed CO₂ would remain stable.

A representation of the coal seam sequestration of CO₂ is shown in Figure 1. Carbon dioxide and the other flue gases including water vapor, nitrogen, excess oxygen, SO_x and NO_x are mainly produced by burning of the fossil fuels. Because coal has high affinity to CO₂ and the other combustion gases, the flue gas may be injected directly into a coal seam in order to reduce the sequestration costs. However, current information for flue gas injection is limited and needs to be investigated further for the effect of each component on the adsorption capacity and stability of the post-sequestration species. Therefore, the current study focuses on the CO₂-coal interaction for better understanding the CO₂ sequestration in coal seams.

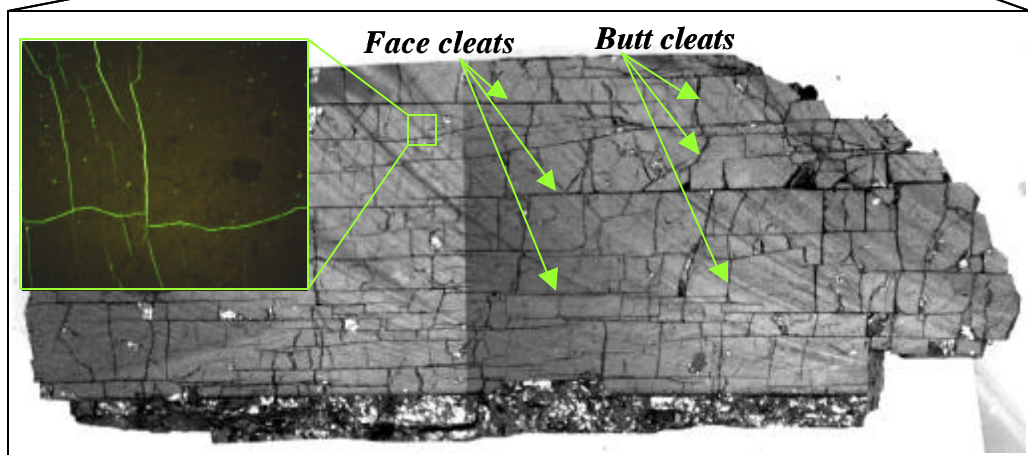
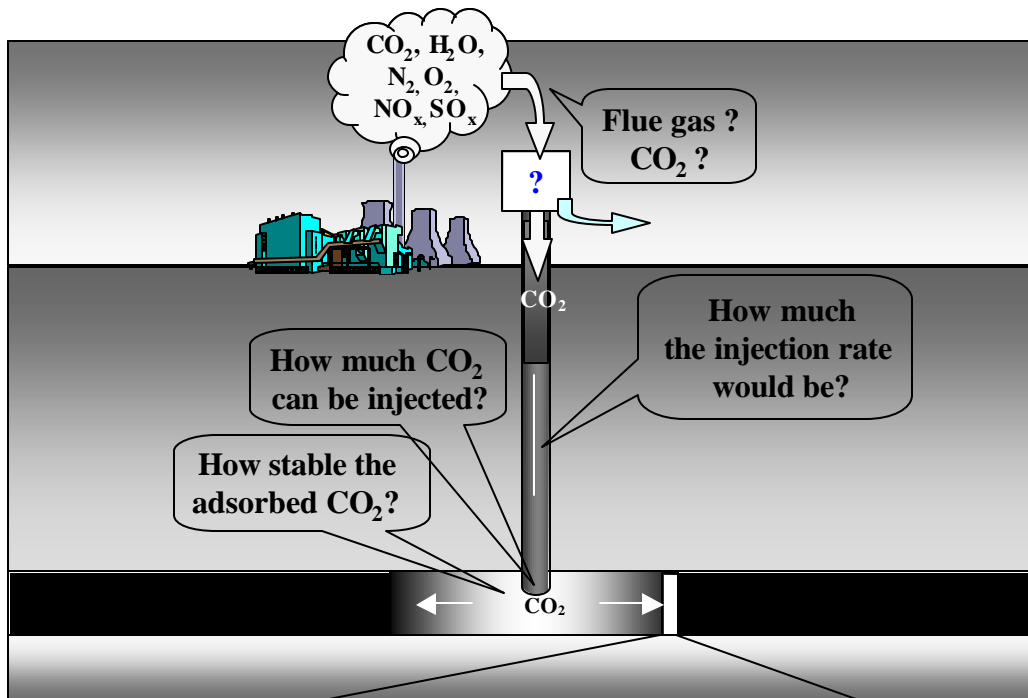


Figure 1. Coal Seam Sequestration of CO₂

When CO₂ is injected into a coal seam, several phenomena are expected to occur: (1) the adsorption of the injected CO₂ within the micropores of the coal matrix, (2) transport of gasses through the cleat system of the coal seam, (3) swelling of coal, and (4) a sudden decrease in pH because of the presence of water in coal seam. Coal contains a wide variety of organic and mineral phases in a complex, porous, three-dimensional network, which varies from one coal deposit to another and from one location to another within the same seam. The organic portion of the coal is thought to capture CO₂ via surface adsorption, pore filling, and solid solution (Larsen et al. 1995 [6]). Less recognized is the possibility that the mineral phases present in the coal may assist via mineral carbonate formation. Thus, the nature of the coal seam itself is an important variable to be considered.

In the absence of external influences, underground temperatures tend to be constant over time but increase with depth. The adsorption of CO₂ is exothermic (Starzewski and Grillet, 1989 [7]) and will provide a heat source, at least during the active pumping phase of sequestration. Also, some sequestration scenarios would provide additional heating mechanisms such as by the dissolution of co-sequestered acidic gases (SO_x, NO_x) or by reaction with residual oxygen in the combustion gas. Thus, it is important to know how temperature will affect the CO₂ adsorption onto the coal and whether the magnitude of this effect is universal for all coals or is rank or maceral dependent.

Even if initially dry, the seam will certainly become wet as a result of drilling operations, fracturing of the coal bed and over-lying strata, and the deposition of a

combustion gas which may contain residual water of combustion. Thus, an aqueous phase will be present and will vary in composition according to its source and the nature of the coal bed and the surrounding minerals with which it is in contact.

In natural systems, pH is often an important parameter (Stumm and Morgan, 1996 [8]) and it will change during sequestration. Because of the formation of carbonic acid, the pH within the sequestration media will drop to around 2-3 at high CO₂ pressures, favoring the dissolution of some minerals. This may be beneficial if mineral dissolution provides better access to the organic matrix, but would be detrimental if dissolution of cap-rock caused containment failure. The effect of the sequestration on pH would be more dramatic for those scenarios in which the SO_x and NO_x were not removed by prior separation and are sequestered along with the CO₂. Little is known about the potential effect of such a pH change on the ability of the organic matrix to adsorb CO₂. It is well recognized that adsorption of CO₂ on solid surfaces is affected by the pH of the surrounding media (Stumm and Morgan, 1996 []). Solids in contact with solutions with a pH above their isoelectric point acquire a net negative surface charge; those in contact with solutions with a pH below their isoelectric point acquire a net positive surface charge. The extent to which pH changes will affect the CO₂ adsorption capacity of coals has not been investigated.

Depending on the capture technology, the CO₂ stream may be nearly pure CO₂, raw combustion gas, or something in between. In addition, gases such as hydrogen, methane, ethane, and higher hydrocarbons may be present in the coal seam (Kim and Kissell, 1986

[⁹]) and act to inhibit or enhance the CO₂ sequestration. In the case of a gassy coal seam, it may be advantageous to displace and capture the methane as a profit-making part of the operation. This displacement may be enhanced by secondary combustion gases in the CO₂ such as SO_x and NO_x. The composition of the post sequestration gas and liquid phases may change with time. Even slow reactions can become important over geologic-sequestration time scales. Also, microbes have an uncanny ability to adapt to many environments and are known to populate even deep geologic strata, at least to 9000 feet below the surface (Amy and Haldeman, 1997 [¹⁰]). Under oxic conditions, gases such as SO_x, NO_x, and CO may be produced either chemically or biologically. Under anoxic conditions, methane and H₂S may be produced by anaerobic microbes. These gases may displace CO₂ and thus limit the durability of the sequestration.

Coal swelling upon adsorption of gases or liquid solvents is a well-known phenomenon (Reucroft and Petel, 1986 [], Reucroft and Sethuraman, 1987 [], Walker et al., 1988 []). However, the adsorption capacities of coals are usually obtained by fitting the experimental data to one of the adsorption equations such as the Langmuir, Brunauer, Emmett and Teller (BET), Dubinin-Radushkevich (D-R), and Dubinin-Astakhov (D-A), none of which account for coal swelling. In order to extract valuable information contained in the adsorption isotherm data, it is necessary to understand the effect of coal swelling on the shape of adsorption isotherm.

Although the adsorption of CO₂ on coals has been studied since 1914 (Ettinger et. al., 1965 [¹¹]), many of these studies have been performed at low pressures and often low

temperatures in order to estimate the surface area of coals (Anderson et. al., 1965 [¹²]; Walker and Kini, 1965 [¹³]). These low pressure data may not be useful for coal sequestration projects. In order to evaluate the long-term storage capacity of candidate seams, knowledge of the extent to which coals can adsorb CO₂ under a variety of conditions is needed. The nature of the coal will determine its maximum adsorption capacity, but the dynamic nature of the sequestration environment will determine the extent to which that capacity can be realized. In order to evaluate the long-term storage capacity of a coal seam, possible changes in the sequestration environment need to be anticipated and their effect understood.

The following questions are addressed in the present study for a safe, cost-effective sequestration of large volumes of CO₂ in coal seams:

1. How much CO₂ can be injected into a candidate coal seam?
2. How stable is the adsorbed CO₂ during the post injection periods?
3. How would the injected CO₂ distribute along the coal seam and what would the injection rate be?

2. OBJECTIVES

The ultimate goal of this research is to obtain data in order to understand and quantify the extremely complex coal-CO₂ interaction. Quantitative determination of fundamental properties such as adsorption capacities, equilibrium constant, and heats of adsorption can then be used in mathematical models to simulate the complex processes, which occur during the sequestration of CO₂ in coal seams.

The objectives are

1. Estimate the adsorption isotherms and sorption capacity of CO₂ on various ranks of coals at seam conditions including pressures up to 2250 psia and temperatures up to 55 °C for gas and supercritical CO₂.
2. Estimate the effect of pH on adsorption isotherms and sorption capacity of CO₂ on coal.
3. Estimate the effect of moisture content on adsorption isotherms and sorption capacity of CO₂ on coal
4. Develop a model/method to assess the effect of swelling of the coal on the adsorption/desorption isotherms of CO₂
5. Apply the information gathered to the mathematical modeling of the CO₂ sequestration process in coal seam

3. EXPERIMENTAL METHOD

3.1. Materials and Chemicals

The interaction of Argonne Premium coals samples with CO₂ was studied under a variety of conditions. Argonne samples, which include a representative sample of most ranks, are among the most widely studied coals in the world. Because of this, there exists a vast database of measurements and studies, which can aid in the interpretation of the results (Vorres, 1993).

The proximate and ultimate analyses for both coals are shown in Table 1 (Vorres, 1993 []). Minus 100 mesh samples were used in all experiments. Because coals rapidly and irreversibly adsorb atmospheric oxygen (Schmidt, 1945 []), efforts were devoted maintaining an oxygen-free environment. Vials of the Argonne Premium coal were opened in accordance with the provided mixing instructions. The sample handling was performed in an inert gas (nitrogen) flushed glove bag under a positive pressure of nitrogen gas. Coal samples were removed from the glove bag only after they had been placed in the sample cell and capped.

Table 1. Proximate and Ultimate Analyses of Argonne Premium Coal Samples (Vorres, 1993)

<u>Coal Sample</u>			<u>Proximate Analysis (wt%)</u>			<u>Ultimate Analysis (wt%, daf)</u>				
Seam	State	Rank	Moisture	Ash^a	VM^a	C	H	O	S	N
Pocahontas No. 3	VA	Low Vol. Bit.	0.65	4.74	18.48	91.0	4.40	2.0	0.70	1.27
Upper Freeport	PA	Med. Vol. Bit.	1.13	13.20	27.45	85.5	4.70	7.5	0.74	1.55
Illinois No. 6	IL	High Vol. Bit.	7.97	15.50	40.05	77.7	5.00	13.5	2.38	1.37
Wyodak-Anderson	WY	Subbit.	28.09	6.31	32.17	75.0	5.40	18.0	0.60	1.20
Beulah-Zap	ND	Lignite	32.24	6.59	30.45	73.0	4.8	20.0	0.8	1.04

^a dry basis

3.2. Gas adsorption apparatus

Gaseous carbon dioxide adsorption isotherms were obtained using the manometric gas adsorption apparatus as shown schematically in Figure 2. The manometric apparatus consists of a reservoir cell of approximately 13 ml and a sample cell of about 6 ml; both contained within a temperature-controlled bath (± 0.1 °C). Advantages of the small apparatus include reaching equilibrium faster and using less of the Argonne samples. The cell volumes were estimated by the He-expansion method. The pressure within each of the cells was monitored using a pressure transducer (Omega PX300-5KGV), accurate to $\pm 0.25\%$ full scale. A syringe pump (ISCO 260D) was used to pressurize CO₂.

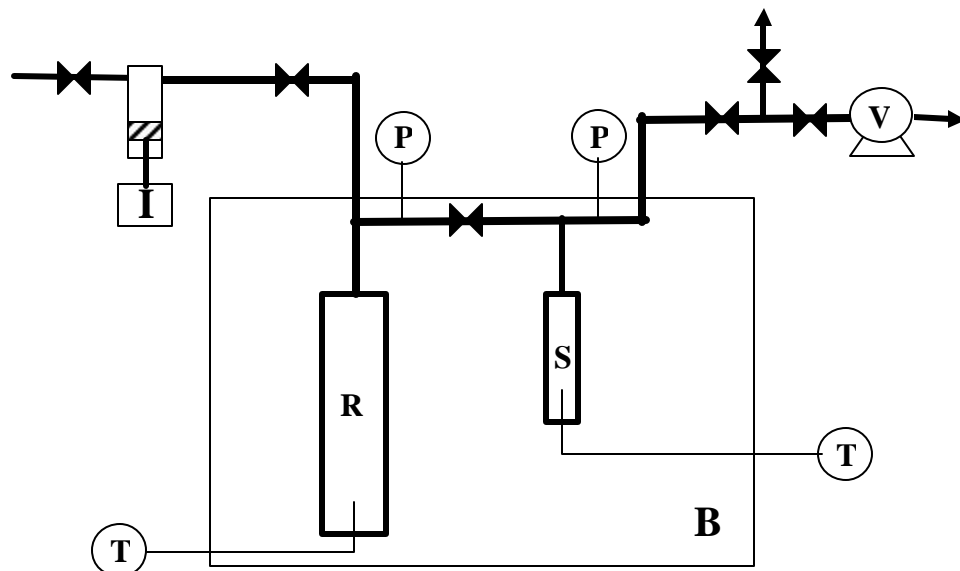


Figure 2. Manometric Gas Adsorption Apparatus: R: Reference Cell, S: Sample Cell, P: Pressure Transducer, I: ISCO Syringe Pump, V: Vacuum Pump T: Thermocouples B: Constant Temperature Bath

3.3. Adsorption/Desorption Isotherms

The manometric method for collecting the adsorption and desorption isotherm data is reviewed in detail in Section 4.1.1. The reference cell was pressurized to the desired level as indicated on a pressure transducer. Thermocouples within the cells showed that thermal equilibrium was established within 3 min. A portion of the gas was then transferred from the reference cell to the sample cell. It was found that 20-30 min was sufficient for the adsorption to reach equilibrium as evidenced by stable temperature and pressure readings. From the known volumes of the reference and sample cells, and the constant temperature, the amount of gas that was transferred from the reference cell to

the sample cell was calculated using the real gas law, which accounts for the gas compressibility. The difference between the moles transferred from the reservoir cell and the mole in the gas phase in the sample cell was accounted to the adsorption of CO₂ on the coal. The pressure in the reference cell was then increased and the process was repeated. Adsorption isotherms were plotted as the total amount of adsorbed gas at each equilibrium pressure.

3.4. Physical Data for He and CO₂

The compressibility factor for He and CO₂ were calculated using the equations of state by Angus et al. (Angus et al., 1977) and Span and Wagner (Span and Wagner, 1996), respectively. The value used for β in the D-R and the D-A equations for CO₂ was 0.35 (Goetz and Guillot, 2001 [¹⁴]). The saturation pressure of CO₂ (P_o) was calculated as 5.98 MPa at 22 °C from an equation given by Kamiuto et al. (Kamiuto et al., 2001).

4. RESULTS AND DISCUSSION

4.1. Adsorption Isotherm of CO₂

The adsorption and desorption isotherms for CO₂ on Argonne Premium coals of various ranks, including Pocahontas No.3, Upper Freeport Illinois No.6, Wyodak, and Beulah-Zap, were measured at 22 °C and up to 4 MPa as shown in Figure 3. Although microporous solids generally show a type I isotherm in the Brunauer, Deming, Deming and Teller (BDDT) classification, the shapes of the isotherms differ from the Langmuir type for every rank of coal examined. The isotherms of the high-rank (Pocahontas No.3 and Upper Freeport) coals appear to be more Langmuir-like whereas those of the low-rank (Illinois No.6, Wyodak, and Beulah-Zap) coals show a rectilinear type of isotherm. Unfortunately, conventional isotherm equations do not fit the experimental adsorption/desorption data probably due to the noticeable volumetric expansion or shrinkage of coal (0.36% to 4.18 % as reported by Reucroft and Petel, 1986[]; Reucroft and Sethuraman, 1987 []; Walker et al., 1988a).

The manometric adsorption isotherm data reported so far in the literature have not considered the noticeable volumetric expansion and shrinkage of coal during adsorption or desorption of gases, respectively. The effect of the volume change on the isotherm shape is significant, especially in low rank coals. Any information obtained from a simple fitting of empirical isotherm data to one of the model equations such as Langmuir,

Brunauer, Emmett and Teller (BET), Dubinin-Radushkevich (D-R), and Dubinin-Astakhov (D-A) equations has poor physical meaning (Duda and Duda, 1997 [15]). Thus, development of a more rigorous mathematical model is needed based on an analysis of the physical phenomena occurring in coal-sorbate systems. This will provide more information about the mechanism of the coal-CO₂ interaction.

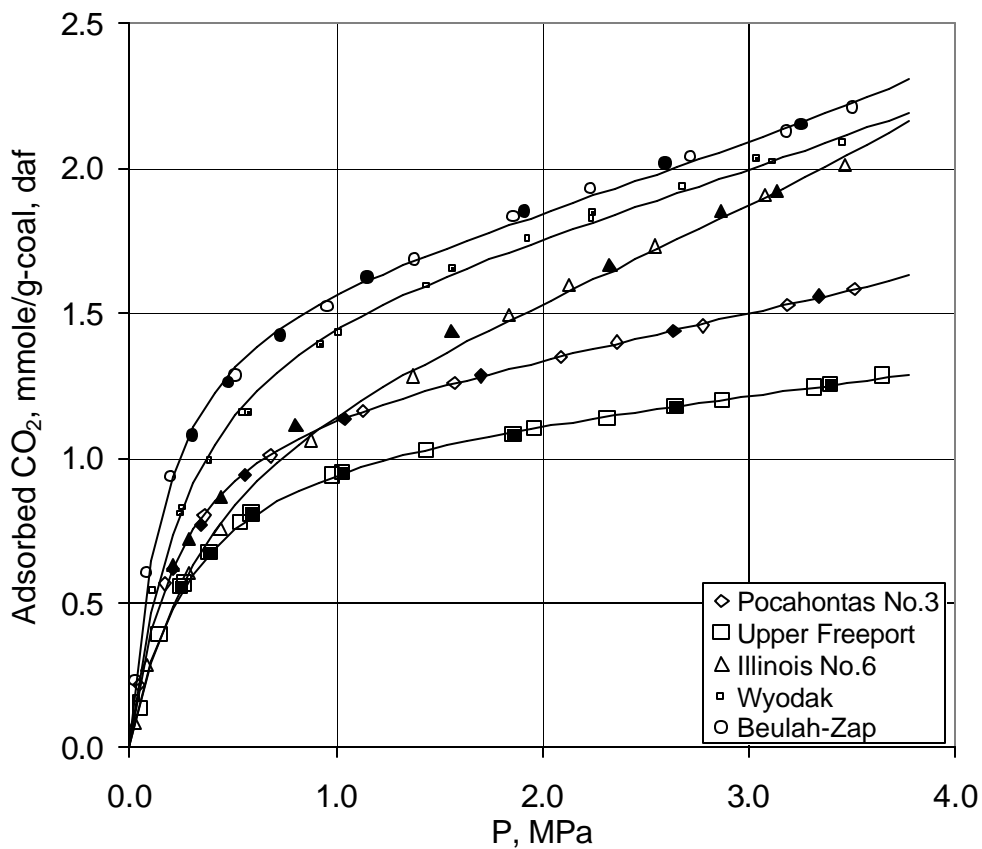


Figure 3. Adsorption-desorption isotherms of CO₂ on selected Argonne Premium coals at 22 °C.
 Open symbols: Adsorption; solid symbols: Desorption

4.1.1. Typical Calculation Methodology

A typical manometric adsorption apparatus consists of a reservoir chamber, a sample chamber, and pressure transducers attached to each chamber as shown in Figure 8. Each chamber is isolated from each other as well as from the inlet and outlet by valves. Both chambers and additional tubing are placed within a constant temperature water bath for temperature control. Volumes of each chamber are estimated by the He expansion method.

Because the volume of each chamber is known, the temperature of the system is constant, and the pressure within each chamber is measured, the number of gas-phase moles of any adsorbate in each chamber can be calculated from Eq.1

$$n = \frac{PV}{zRT} \quad (1)$$

The compressibility factor for adsorbates, for instance, for He and CO₂, can be calculated from the analytic equation of state (Angus et al., 1977 [¹⁶]; Span and Wagner, 1996 [¹⁷]).

In order to estimate the amount of gas adsorbed at each incrementally increasing pressure, a portion of the gas is transferred from reservoir chamber into sample chamber and the pressure in both chambers is allowed to stabilize. Pressures in reservoir and sample chambers are recorded before and after the gas transfer. A summary of the procedure is shown in Table 2.

Table 2. Pressure and amount of gas at each adsorption/desorption steps in reservoir and sample chambers

Adsorption / Desorption Step	Definition	Reservoir Chamber		Sample Chamber	
		mole	P	mole	P
1	1. Initially	n_{R1}	P_{R1}	n_{S1}	P_{S1}
	2. Pressurize reservoir chamber with fresh gas	$n_{R1}+n$	P_{R2}	-	-
	3. Transfer gas from Res. to sample chamber	$n_{R1}+n-? n_1$	P_{R3}	$n_{S1}+? n_1$	P_{S3}
2	4. Pressurize reservoir chamber with fresh gas	$n_{R3}+n$	P_{R4}	-	-
	5. Transfer gas from Res. to sample chamber	$n_{R3}+n-? n_2$	P_{R5}	$n_{S3}+? n_2$	P_{S5}
3	6. Pressurize reservoir chamber with fresh gas	$n_{R5}+n$	P_{R6}	-	-
	7. Transfer gas from Res. to sample chamber	$n_{R5}+n-? n_3$	P_{R7}	$n_{S5}+? n_3$	P_{S7}
.
.
i	2i. Pressurize reservoir chamber with fresh gas	$n_{R5}+n$	P_{R2i}	-	-
	2i+1 Transfer gas from Res. to sample chamber	$n_{R5}+n-? n_i$	P_{R2i+1}	$n_{S5}+? n_i$	P_{S2i+1}

The amount of adsorbed gas can be calculated from the mass balance as

$$\Delta n_{ads} = \frac{1}{w} \left\{ [(n_{R1} + n) - (n_{R1} + n - \Delta n_1)]_R - [(n_{S1} + \Delta n_1) - (n_{S1})]_S \right\} \quad (2)$$

or

$$\Delta n_{ads} = [\Delta n_1]_R - [\Delta n_1]_S \quad (3)$$

where w is the weight of the coal sample, $[\Delta n_1]_R$ is the amount of gas transferred from reservoir chamber and $[\Delta n_1]_S$ is the increase in the amount of the gas in gas phase present in sample chamber after equilibrium is achieved during the first step. From the mass balance, the missing gas is considered to be adsorbed on the solid.

Eq.2 can be expressed in the form of measurable quantities to give

$$\Delta n_{ads} = \frac{1}{w} \left[\left(\frac{P_{R_2}}{z_{R_2}} - \frac{P_{R_3}}{z_{R_3}} \right) \frac{V_R}{RT} - \left(\frac{P_{S_3}}{z_{S_3}} - \frac{P_{S_1}}{z_{S_1}} \right) \frac{V_0}{RT} \right] \quad (4)$$

where V_0 is the void volume of sample chamber, which is not occupied by adsorbent (coal).

Note that Eq.4 is valid only when the void volume in the sample chamber (V_0) is constant. In the literature, the adsorption experiments assumed that the void volume of sample chamber was constant ^[Sircar]. However, no publication has considered volume changes, which may occur due to the shrinkage or swelling of the sample as a result of compression or sorption, respectively. For example, it is well known that coal swells considerably upon the sorption of gases such as carbon dioxide^[Walker, 1988], methane^[George and Barakat], and alcohol vapors (Shimizu et al., 1998 ^[18]; Takanohashi et al., 2000 ^[19]). Also, coals have been reported to shrink under higher pressures of helium, a non-adsorbing gas ^[George and Barakat]. For this reason, the model equations (Langmuir, BET, D-R and D-A) fit the adsorption isotherms of coal only poorly (Duda et al., 2000 ^[20]). Thus, changes in the void volume occurring in the sample chamber should be taken into consideration. The model we developed in the next section accounts for such volume changes during collection of adsorption isotherm data of CO₂ on coal.

4.1.2. Mathematical Model of the Adsorption Isotherm of CO₂ which Accounts for Swelling

Coals can be described as highly cross-linked and entangled networks of macromolecular chains of irregular structure (Walker and Mahajan, 1993 [21]). It is generally accepted that coals contain an interconnected pore network of high surface area with a slit-shaped pores having constricted opening of molecular dimensions (Mahajan, 1991 [22]). Toda (Toda, 1972 [1]) reported that while some of the pores are closed to helium, they can be accessed by CO₂. Thus, one can visualize that during the measurement of the adsorption isotherm of any sorbed gases or vapors, the void volume measured by helium would not be the same as the void volume when these gases and vapors are introduced into the sample cell. In other words, it is expected that helium cannot access restricted pores during the estimation of the volume of coal and the void volume of sample chamber. However, such pores may be accessible to gases or vapors during the measurement of the gas adsorption isotherms, thereby, creating extra accessible volume within the sample chamber. The nascent void volume of the sample chamber invalidates the assumption of a constant void volume and affects the calculation of the adsorbed amount of gas. The ability of a gas or vapor to access this restricted volume is related to its ability to swell the coal. Thus, major deviations from 'normal' isotherm behavior would be expected for good coal swelling agents. This is indeed the phenomenon observed in the literature although alternate explanations have been formulated. A schematic representation of the mechanism of the sorbate-induced swelling is shown in Figure 4.

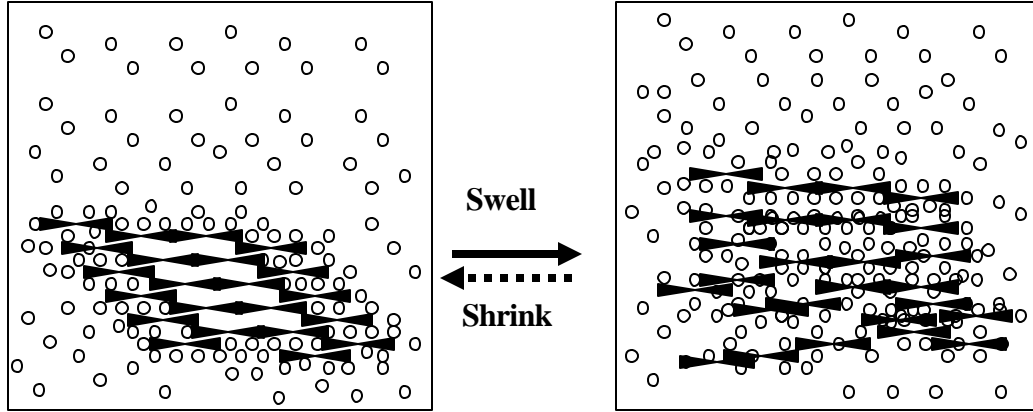


Figure 4. Schematic Representation of Change in Volume in Sample Chamber due to Sorption of Gases

In the presence of volume change, Eq.4 can be written as

$$\Delta n_{ads} = \left(\frac{P_{R_2}}{z_{R_2}} - \frac{P_{R_3}}{z_{R_3}} \right) \frac{V_R}{wRT} - \left(\frac{P_{S_3}}{z_{S_3}} \frac{V_1}{wRT} - \frac{P_{S_1}}{z_{S_1}} \frac{V_0}{wRT} \right) \quad (5)$$

where V_1 is the void volume of sample chamber after adsorption and V_0 is the initial void volume of sample chamber, measured initially by the He expansion method.

Let the change in the accessible pore volume be α defined as

$$\alpha_i = \frac{V_i - V_{i-1}}{V_{i-1}} \quad (6)$$

where α_i is the pore opening coefficient, which is dependent on the change in volume at each step (shown as indices i) of adsorption/desorption.

From Eq.6, the new volume, V_1 , due to the expansion of the coal can be written as

$$V_1 = (1 + \mathbf{x}_1)V_0 \quad (7)$$

and thus, the adsorbed amount can be calculated from Eq.5 as

$$\Delta n_{ads} = \left(\frac{P_{R_2}}{z_{R_2}} - \frac{P_{R_3}}{z_{R_3}} \right) \frac{V_R}{wRT} - \left(\frac{P_{S_3}}{z_{S_3}} \frac{(1 + \mathbf{x}_1)V_0}{wRT} - \frac{P_{S_1}}{z_{S_1}} \frac{V_0}{wRT} \right) \quad (8)$$

or

$$\Delta n_{ads} = \underbrace{\left(\frac{P_{R_2}}{z_{R_2}} - \frac{P_{R_3}}{z_{R_3}} \right) \frac{V_R}{wRT} - \left(\frac{P_{S_3}}{z_{S_3}} - \frac{P_{S_1}}{z_{S_1}} \right) \frac{V_0}{wRT}}_{PART I} - \underbrace{\frac{P_{S_3}}{z_{S_3}} \frac{\mathbf{x}_1 V_0}{wRT}}_{PART II} \quad (9)$$

As shown in Eq.9, the adsorbed amount has two parts. The first part is the experimentally determined amount of adsorbed gas, in which there is no change in the volume in sample chamber and it remains constant at the value estimated by the He expansion. The second part is the amount of gas occupied by the nascent cell volume, which was created as a result of the change in the accessible pore volume that occurred when the adsorbent became swollen or shrank upon gas adsorption or desorption, respectively.

The calculation of the amount of gas adsorbed during subsequent pressure increases can be formulated as shown in Table 2. After close evaluation, a '**general form of the adsorption equation**' is derived as

$$n_{exp} = n_{ads} + k \left(\frac{P}{z} \right) \quad (10)$$

where

$$k = \frac{(\Delta V/w)}{RT} = \frac{(\Delta V/V_0)}{r_0 RT} \quad (11)$$

In Eq.11, the only unknowns are the n_{ads} and k . Several model equations can be used for the gas adsorption term, n_{ads} , in Eq.11. The Langmuir monolayer model equation, Brunauer, Emmett and Teller (BET) multilayer model equation, and Dubinin-Radushkevich (D-R) or Dubinin-Astakhov (D-A) volume filling model equations are listed in Table 3 along with the swelling term. When a particular adsorption equation is used to fit the experimental adsorption isotherm data, its constants (such as the monolayer adsorption capacity, the micropore volume, the equilibrium (Langmuir) constant, and the heat of adsorption) can be estimated along with the change in the accessible pore volume in coal.

Table 3. The general form of the adsorption equation resulting from the substitution of several adsorption models for n_{ads} term in Eq.10

Model	Adsorption term (n_{ads})	General Form (n_{exp})	Equation
Langmuir	$\frac{n_0 b P}{1 + b P}$	$\frac{n_0 b P}{1 + b P} + k \left(\frac{P}{z} \right)$	Eq.12
BET	$\frac{n_0 C P}{(P_0 - P)[P_0 + (C - 1)P]}$	$\frac{n_0 C P}{(P_0 - P)[P_0 + (C - 1)P]} + k \left(\frac{P}{z} \right)$	Eq.13
D-R	$n_0 \exp \left\{ - \left[\frac{RT}{bE} \ln \left(\frac{P_0}{P} \right) \right]^2 \right\}$	$n_0 \exp \left\{ - \left[\frac{RT}{bE} \ln \left(\frac{P_0}{P} \right) \right]^2 \right\} + k \left(\frac{P}{z} \right)$	Eq.14
D-A	$n_0 \exp \left\{ - \left[\frac{RT}{bE} \ln \left(\frac{P_0}{P} \right) \right]^j \right\}$	$n_0 \exp \left\{ - \left[\frac{RT}{bE} \ln \left(\frac{P_0}{P} \right) \right]^j \right\} + k \left(\frac{P}{z} \right)$	Eq.15

4.1.3. Conventional Evaluation of Adsorption Isotherm Data at Low Pressures

($0 < P/P_0 < 0.12$)

The monolayer and micropore capacities of coals were estimated from the linear forms of the Langmuir, BET, and R-A adsorption equations at low pressures ($0 < P/P_0 < 0.12$). This corresponds to the first 4 points of the adsorption isotherm data (Figure 3) where the pressures were less than 0.72 MPa.

The estimated monolayer/micropore capacities (n_o), Langmuir (b) and BET (C) constants, and heat of adsorption values (E) calculated from Dubinin-Radushkevich equation, of the selected Argonne coals obtained by an evaluation of the low-pressure region of their adsorption isotherms are given in Table 4. While n_o represents the monolayer adsorption capacity for both Langmuir and BET equations, it represents micropore volume for Dubinin-Radushkevitch equation. As shown in Table 4, the Langmuir monolayer adsorption capacities of coals are 0.25 ± 0.01 mmoles/g-coal (dry, ash free basis) higher than that of BET, regardless of the rank of coals examined. The deviation between monolayer adsorption capacity of coals estimated using Langmuir equation and BET equation is about 20%. On the other hand, the micropore volume obtained by the D-R equation is 0.3 ± 0.1 mmoles/g-coal higher than BET monolayer adsorption capacity of the coals. The micropore volume estimated by D-R equation is always higher than the monolayer adsorption capacity of coals estimated by Langmuir and BET equations at this low-pressure range. The Langmuir and BET constants are also estimated. As shown in the table, both constants for each rank of coals change in the

same directions; first decreases as the rank decreases then increases as the rank further decreases like a “U” shape. Indeed, the Langmuir and BET constants are related to the heat of adsorption (Gregg and Sing, 1982) such as

$$b = m' e^{RT / q_1} \quad (16)$$

$$C = m'' e^{RT / (q_1 - q_L)} \quad (17)$$

where m' and m'' are constants with values range from 0.02 to 20, q_1 is the isosteric heat of adsorption of the first layer, q_L is the heat of condensation of multiplayer. On the other hand, heat of adsorption can be calculated from the Dubinin Radushkevich equation. As shown in the table, the calculated heat of adsorption is in the same trend as the Langmuir and BET constant with the rank of coals. The heat of adsorption for different ranks of coals also shows a “U” shape. However, the difference is not larger than 4 ± 0.2 kJ/mole.

Table 4. Monolayer/Micropore Adsorption Capacity of Carbon Dioxide on Selected Argonne Premium Coals at Pressures $0 < P/P_o < 0.12$

	Langmuir		D-R		BET	
	n_o	b	n_o	E	n_o	C
POC#3	1.37	4.03	1.53	24.46	1.12	31.59
UF	1.24	3.13	1.28	23.90	0.98	25.55
IL#6	1.56	2.40	1.32	24.31	1.02	27.13
WY	1.63	4.27	1.74	25.78	1.36	32.92
BZ	1.65	6.70	1.87	28.21	1.42	50.75

4.1.4. Evaluation of Adsorption Isotherm Data for the Entire Range of Adsorption Isotherm ($0 < P/P_o < 0.61$)

The adsorption of CO₂ on the Argonne Premium coals was estimated from the linear form of the Langmuir and D-R adsorption equations over the entire range of adsorption data. The monolayer/micropore capacity of coals obtained from these equations is shown in Table 5. The BET equation, on the other hand, failed to provide a reasonable fit to the entire data and was dropped from further consideration.

Table 5. Monolayer/Micropore Adsorption Capacity of CO₂ on Selected Argonne Premium Coals for Entire range of Isotherms ($0 < P/P_o < 0.61$)

	Langmuir		D-R	
	n _o	b	n _o	E
POC#3	1.73	2.07	1.51	24.81
UF	1.40	2.21	1.25	24.16
IL#6	2.42	1.07	1.77	21.58
WY	2.33	1.86	1.99	24.01
BZ	2.37	2.39	2.07	26.62

As shown in Table 5, the monolayer adsorption capacity of the coals increased considerably compared to the evaluation of the data at low-pressure range (Table 4). Additionally, the micropore volume did not change for high rank coals but it changed significantly for the low-rank coals compared to the evaluation of the data at low-pressure range. On the other hand, while the heat of adsorption estimated by the D-R equation is almost the same, the Langmuir constant decreased to almost half of its values compared to the low-pressure evaluation.

Furthermore, the amount of gas adsorbed calculated using the Langmuir and D-R equations deviated significantly from the experimental values as shown in Figure 5. In the case of Langmuir equation, the deviations reflect an underestimation in the lower pressure region and an overestimation in the higher-pressure region of the isotherms. In the case of the D-R equation, better agreement is obtained between the calculated and experimental values in the low-pressure region but much larger deviations occur in the high-pressure region. It seems that, in both cases, the experimental data do not fit the adsorption equations due to the rectilinear form of the adsorption isotherms at high pressures.

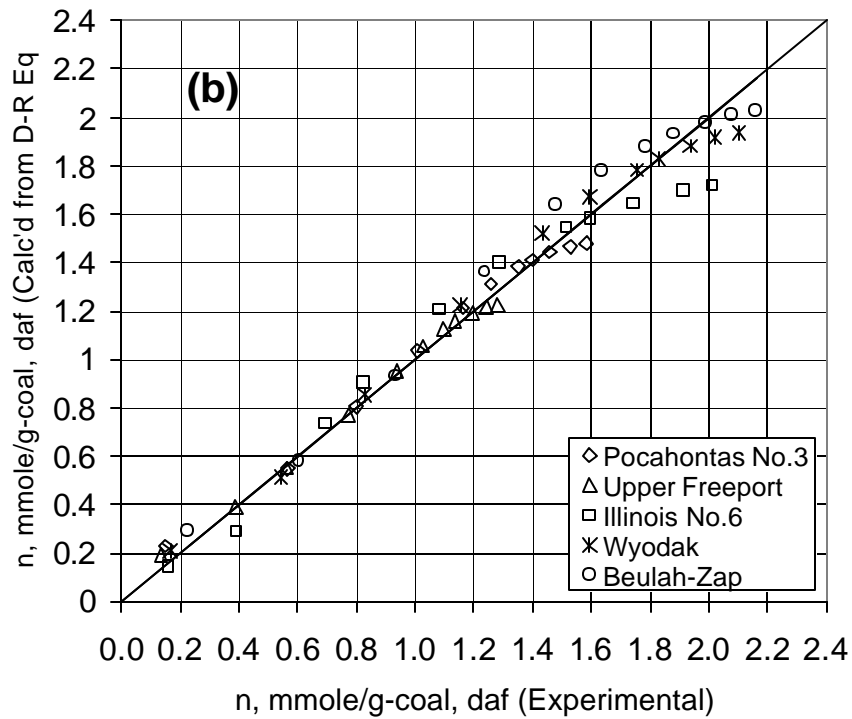
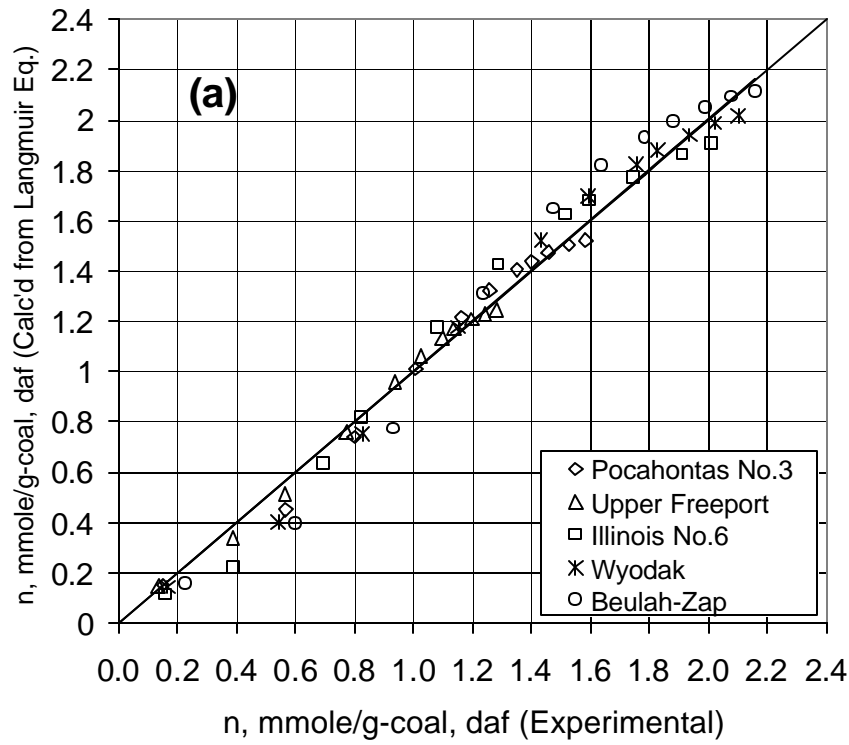


Figure 5. Adsorbed Amount of CO₂ on selected Argonne Premium Coals (a) Langmuir Equation (b) D-R Equation

4.1.5. Accounting for Swelling in the Evaluation of the Entire Adsorption Isotherm

Data ($0 < P/P_o < 0.61$)

The adsorption of CO₂ on the Argonne Premium coals was estimated by fitting the entire range of adsorption data to the modified Langmuir (Eq.12), modified D-R (Eq.14), and modified D-A (Eq.15) equations. The calculated monolayer/micropore capacities along with the percent change in accessible pore volume of the coals obtained from these equations are shown in Table 6. The monolayer/micropore capacities of the coals determined by the un-modified equations (Table 5) are higher than those determined by the present methods (Table 6). As can be seen in both tables, the effect of the coal swelling on the estimation of the adsorption parameters is significant. The experimental adsorption data fit the derived equations very well as shown in Figure 6. It is apparent that the deviations observed for the Langmuir equation (Figure 5a) and the D-R equation (Figure 5b) are not present for the modified equations considered in this study (Figure 6).

Table 6. Monolayer/Micropore Adsorption capacity of CO₂ on Selected Argonne Premium Coals: Account of Swelling ($0 < P/P_o < 0.61$)

	Modified Langmuir Eq. (Eq.36)			Modified D-R Eq. (Eq.38)			Modified D-A Eq. (Eq.39)			
	n _o	b	?V%	n _o	E	?V%	n _o	E	j	?V%
Pocahontas No.3	1.27	4.41	29.4	1.32	26.4	20.0	1.16	27.8	2.58	31.6
Upper Freeport	1.17	3.25	14.3	1.18	24.5	7.5	0.98	26.3	2.92	22.2
Illinois No.6	1.28	2.61	71.1	1.23	23.8	66.8	1.33	22.8	1.82	59.9
Wyodak	1.66	3.65	44.4	1.71	25.1	32.7	1.57	26.1	2.29	42.8
Beulah-Zap	1.63	6.16	52.8	1.77	28.1	36.0	1.56	29.7	2.59	52.4

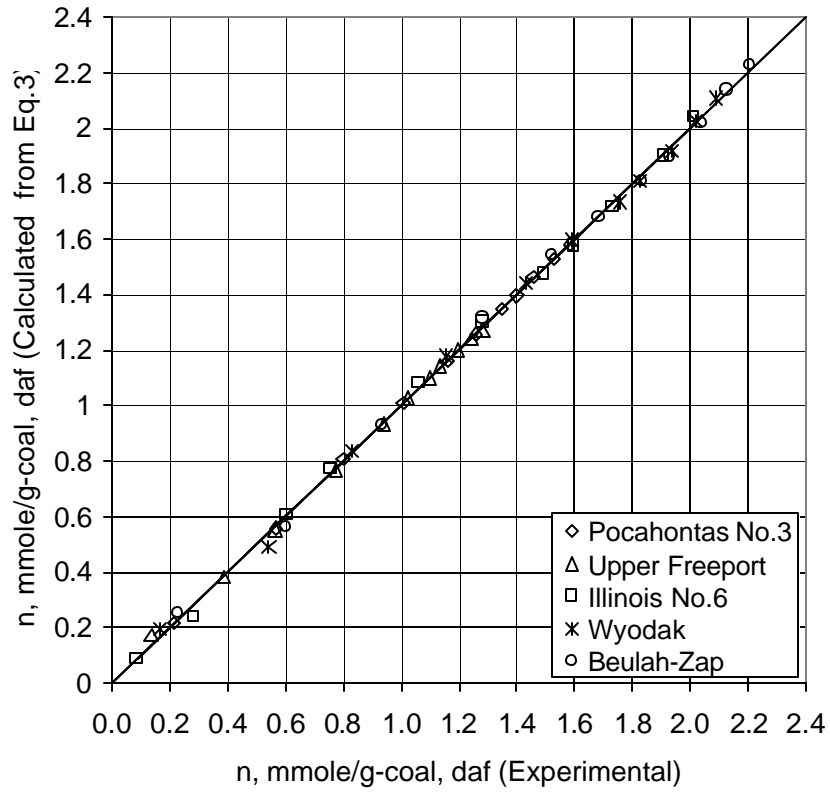


Figure 6. Adsorbed amount of CO₂ on selected Argonne Premium coals modified Langmuir equation (Eq.12)

The measured adsorption isotherms can be divided into two contributing parts. One is the actual, physical adsorption of CO₂, and the other is the effect of the change in accessible pore volume. Due to CO₂-induced swelling of the coal during adsorption, the accessible pore volume changes so that more volume becomes accessible by the CO₂ than the initial volume estimated by helium. At low-pressure, the effect of swelling on the adsorption isotherm is small when compared with the amount actually adsorbed. At high pressure, however, the amount of gas in the additional void volume is considerably higher due to the compressibility of CO₂. The additional volume accessible by CO₂ is listed as $\Delta V\%$ in Table 8. Values range from 7% (Upper Freeport) to 71% (Illinois No.6) and are sensitive to the adsorption model used. The rectilinear increase in the adsorption isotherm affected by $\Delta V\%$ can be clearly seen in Figure 7.

Although Eq.12, Eq.14 and Eq.15 in Table 3 all fit the experimental data well, the Eq.15 gives more information about the pore structure of the coal and the energies of the CO₂-coal interaction. From the values of j and E , the size and distribution of micropore structure of the coal can be estimated (Bradley and Rand, 1995 []).

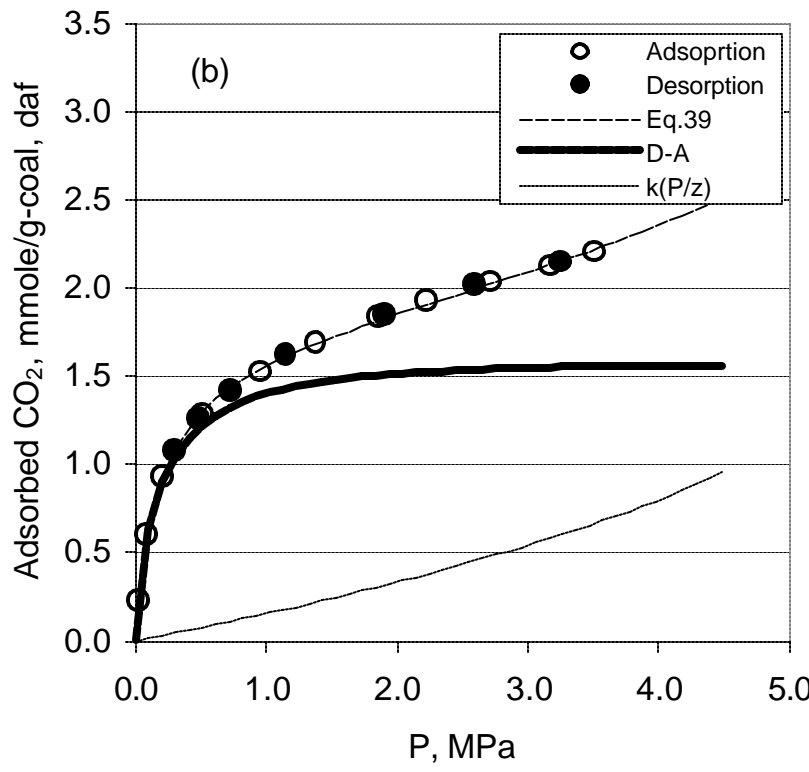
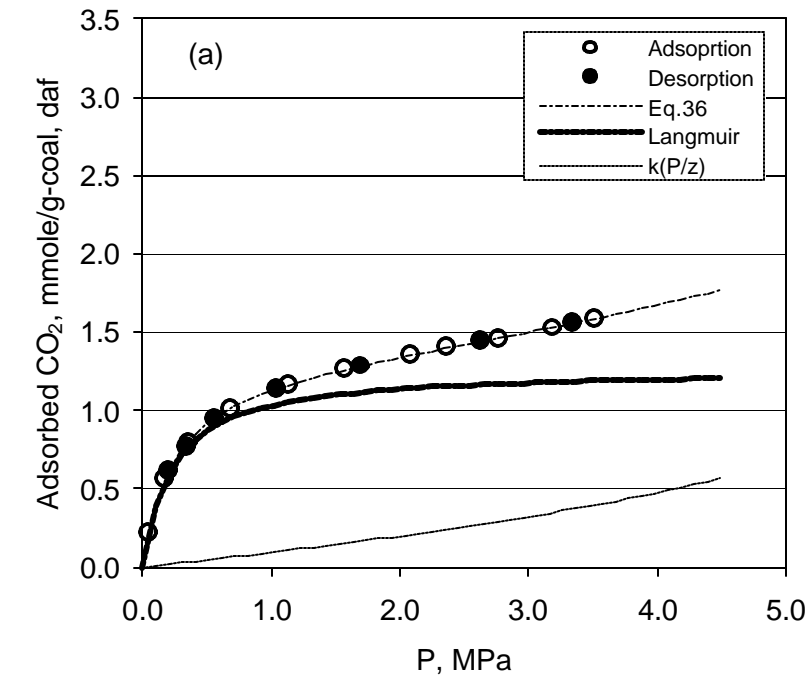


Figure 7. Adsorption isotherms of selected Argonne Premium coals in the presence of accessible pore volume change. Lines are derived using the following models: (a) Pocahontas No.3 - modified Langmuir Eq. (Eq.12) (b) Beulah-Zap - modified D-A Eq. (Eq.15)

4.2. Evaluation of the Surface Area of Coals

Figure 8 shows the surface areas of selected coals and compares them with literature values (Gan et al., 1972 [²³]; Walker et al., 1988b [²⁴]). The literature values do not take into account the effect of coal swelling. However, because they are obtained near atmospheric pressure where the effect of swelling is small, they are reasonably accurate. At low pressures the adsorbed amount is much larger than the change in the accessible volume, so the error is not significant. The surface areas calculated by the modified equations are slightly smaller than the literature surface areas, which were calculated without taking swelling into account. Of particular interest are the data from Larsen et al. who used some of the same Argonne coals. For high rank coals (daf carbon > 85%) the agreement between Larsen results and ours is very good. For lower rank coals, the agreement is poorer. Because we have already shown that the moisture content has a large effect on the CO₂ adsorption, especially for low-rank coals, and difference in the two drying methods may account for the poorer agreement. However, there is currently no good statistical study of the interlab precision for the generalization of these isotherms and other explanations are possible.

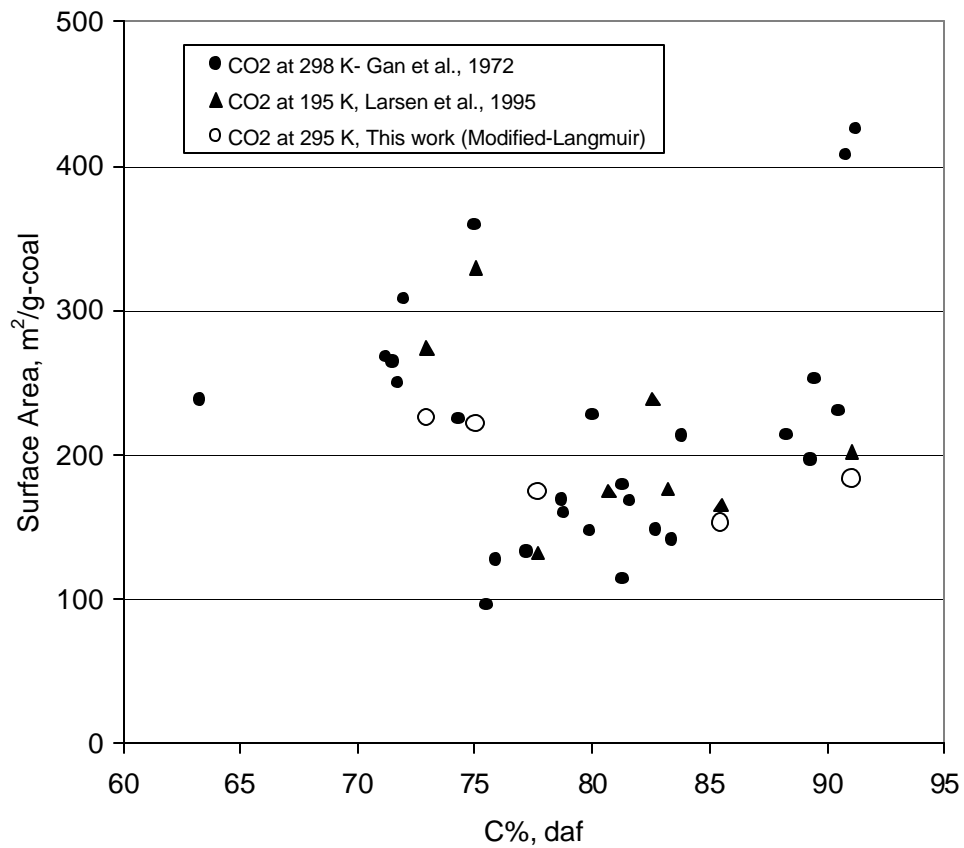


Figure 8. Comparison of the CO₂ - surface area of coals obtained in this work with the some literature values

4.3. Effect of Temperature on the Adsorption Isotherm of CO₂ on Coal

Adsorption isotherms of CO₂ on the selected Argonne Premium coal samples, Pocahontas No.3, Upper Freeport, Illinois No.6, Wyodak, and Beulah-Zap, were measured at temperatures of 22, 30, 40, and 55°C and up to pressures of 5 MPa as shown in Figure 9. As seen in the figure, the amount of adsorbed CO₂ decreases as the temperature increases. However, the adsorption capacities of the coals remain nearly constant, as shown in Table 7, because the numbers of active adsorption sites on the coal surface do not change at these moderate temperatures. Application of the modified adsorption equation (one of equations 12 through 15), accounts for the effect of coal swelling and enables one to calculate the adsorption capacity of the coal, the heat of adsorption, the change in accessible pore volume, and the average pore size (when Dubinin-Astakhov equation is used) directly. These values are listed in Table 7 for the various ranks of Argonne coals.

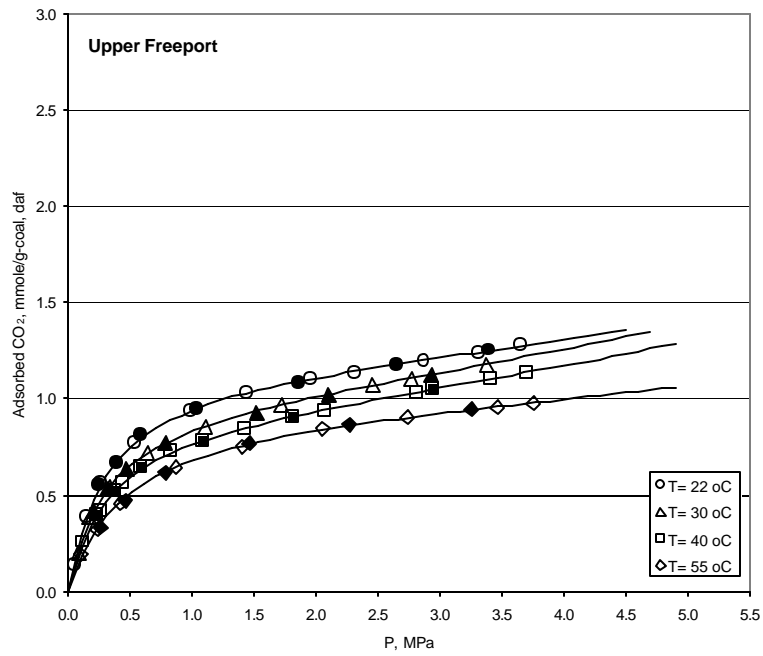
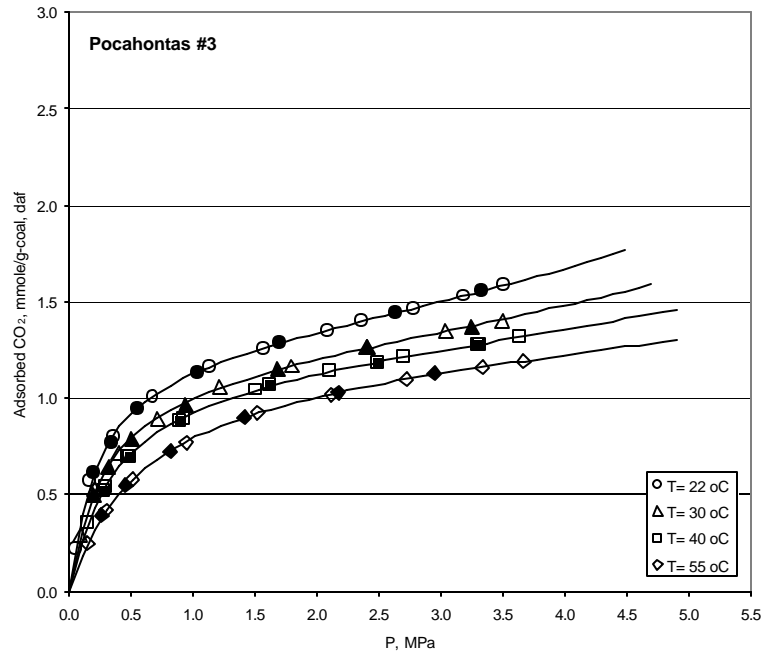


Figure 9. Adsorption/desorption isotherms of CO₂ on Argonne Premium coals at temperatures of 22, 30, 40, and 55 °C.

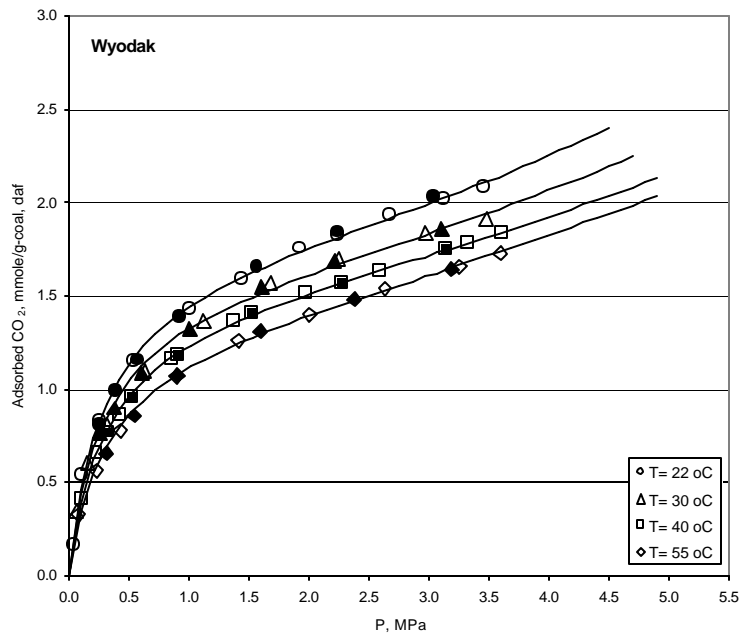
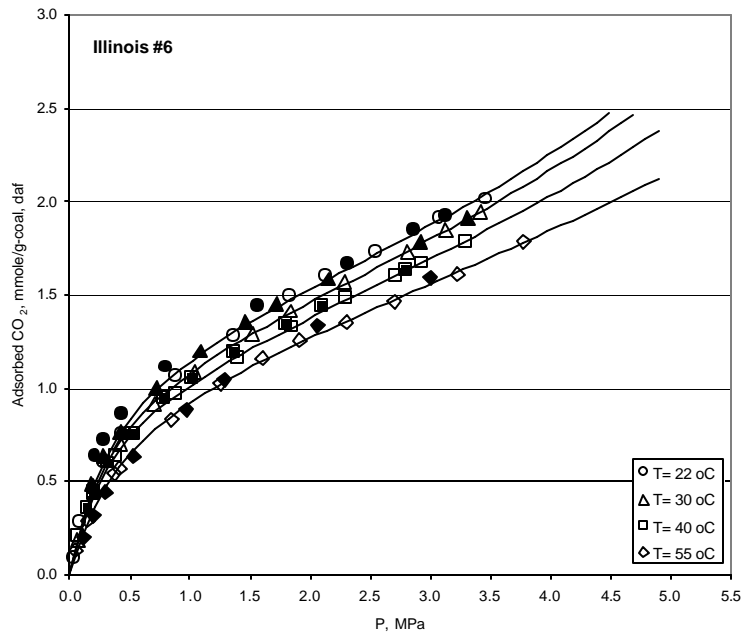


Figure 9. Cont.

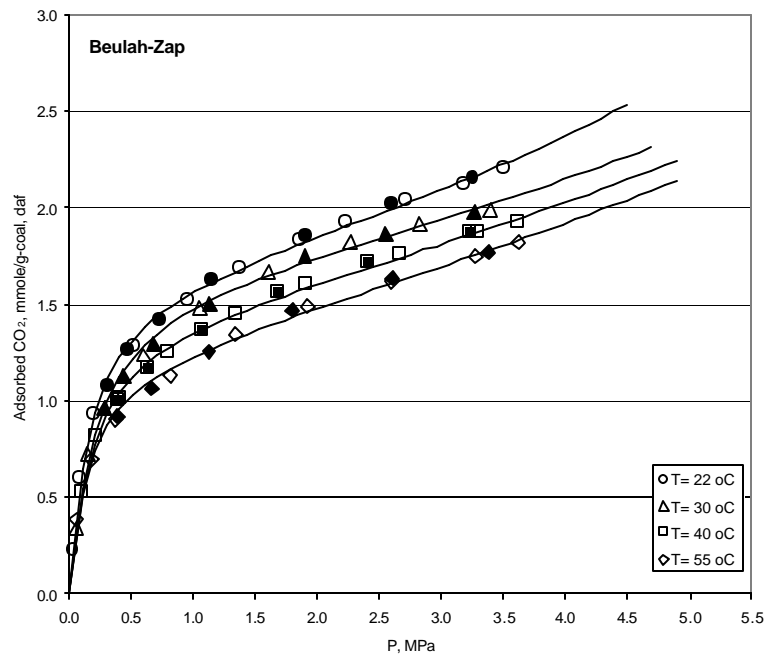


Figure 9. Cont.

Table 7. Modified-Langmuir, Dubinin-Radushkevich, and Dubinin-Astakhov Curve Fit Parameters

Temp. °C	Modified-Langmuir			Modified-D-R			Modified-D-A				
	POC#3	n _o	b	?V%	n _o	E	?V%	n _o	E	j	?V%
22		1.27	4.41	29.4	1.32	26.4	20.0	1.16	27.8	2.58	31.6
30		1.18	3.51	24.8	1.27	26.5	13.5	1.09	28.1	2.57	25.2
40		1.19	2.70	19.1	1.24	26.6	9.3	1.11	27.8	2.42	17.6
55		1.18	1.73	14.6	1.19	25.5	6.0	1.05	26.9	2.35	14.3
UF											
22		1.17	3.25	14.3	1.18	24.5	7.5	0.98	26.3	2.92	22.2
30		1.00	3.22	22.3	1.08	25.8	11.5	0.88	27.9	2.77	26.0
40		0.92	3.09	23.8	0.98	27.3	14.3	0.81	29.0	2.91	25.9
55		0.93	2.25	13.1	0.97	27.1	4.8	0.98	26.9	1.97	4.1
IL#6											
22		1.28	2.61	71.1	1.23	23.8	66.8	1.33	22.8	1.82	59.9
30		1.17	2.72	77.4	1.22	24.9	65.0	1.11	26.0	2.29	72.8
40		1.07	2.84	78.7	1.18	26.4	61.6	1.18	26.4	1.98	61.1
55		1.06	2.14	73.5	1.16	26.4	54.9	1.15	26.4	2.01	55.1
WY											
22		1.66	3.65	44.4	1.71	25.1	32.7	1.57	26.1	2.29	42.8
30		1.50	3.78	44.4	1.62	27.1	29.3	2.00	24.1	1.56	7.2
40		1.42	3.49	43.8	1.54	28.1	27.7	1.54	28.0	2.00	27.6
55		1.24	3.54	53.1	1.40	29.9	33.3	1.60	27.9	1.70	22.1
BZ											
22		1.63	6.16	52.8	1.77	28.1	36.0	1.56	29.7	2.59	52.4
30		1.64	4.67	41.5	1.83	28.1	19.7	1.68	29.1	2.29	30.7
40		1.43	5.39	49.4	1.61	31.2	30.0	1.49	32.0	2.31	37.6
55		1.22	6.68	60.7	1.45	34.2	35.8	1.36	35.1	2.25	41.8

4.4. Sorption Capacity and Heat of Adsorption of Selected Argonne Premium Coals

The adsorption capacities and heats of adsorption of the selected Argonne Premium coals were calculated from the adsorption isotherms using the modified-Langmuir equation as shown in Figure 10 and in Table 8. It can be seen in Figure 10 that the adsorption capacity and heat of adsorption are functions of coal rank. Both decrease with maturation of the coal up to 80-86% C, then increase with increasing maturation. This data is consistent with the literature data. The 'U' shaped dependence is typical of surface areas, densities, and porosities of different ranks of coal. However, the overall range of values is not large. The minimum and maximum adsorption capacity and heat of adsorption are 0.9-1.7 mmole/g-coal, daf basis and 26-30 kJ/mole, regardless of coal rank.

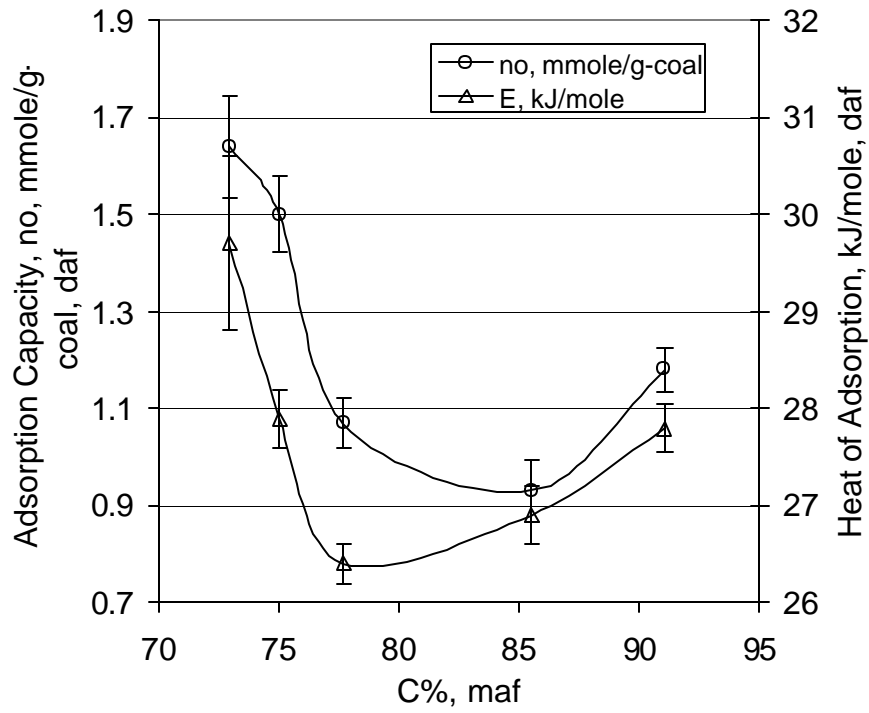


Figure 10. Adsorption capacity and heat of adsorption for different coal ranks

Table 8. Adsorption capacities and heats of adsorption of the selected Argonne Premium coals

Coals	Adsorption Capacity (mmole/g-coal)	Heat of Adsorption (kJ/mole)
Pocahontas No.3	1.18 ± 0.09	27.8 ± 0.5
Upper Freeport	0.93 ± 0.13	26.9 ± 0.6
Illinois No.6	1.07 ± 0.10	26.4 ± 0.4
Wyodak	1.50 ± 0.16	27.9 ± 0.6
Beulah-Zap	1.64 ± 0.21	29.7 ± 1.8

4.5. Effect of Moisture on the Adsorption Isotherms of CO₂ on Coals

The question of the effect of the moisture content of the coal on its CO₂ adsorption isotherm is a challenging one. A linear decrease in the adsorption capacity of methane with moisture content up to a critical coal moisture content has long been known (Joubert et al., 1973 [²⁵]; Joubert et al., 1974 [²⁶]). However, the interaction of methane with coal and water is expected to be different from the interaction of CO₂ with coal and water. CO₂ dissolves in water forming carbonic acid at high pressures whereas methane does not react with water. Our preliminary data show that the moisture content of the coal affects the shape of the CO₂ adsorption isotherm as shown in Figure 11. The effect is very significant especially for lower-rank coals because they contain more moisture than higher-rank coals. The parameters obtained from the best fit of the adsorption isotherm data to the modified-Langmuir equation are given in Table 9. As can be seen, the adsorption capacities of the coals are unchanged by drying whereas the Langmuir constant (or equilibrium constant) and the accessible pore volume are altered. A number of conclusions can be drawn from these preliminary data. (1) The number of adsorption sites is remained unchanged. (2) The Langmuir constants for lower-rank coals change significantly. Possibly CO₂ binds in both the presence and absence of pore water but as a different species. For example, it may bind as CO₂ in the absence of moisture but as carbonic acid in its presence. As a result, the adsorption capacity does not change. Alternatively, the attachment site of the CO₂ may change from CO₂-coal to CO₂-water-coal without the actual formation of H₂CO₃. This will be investigated in future work. (3) The change in accessible pore volume increases for higher-rank coals whereas it

decreases for lower-rank coals. A possible explanation for this is that for higher-rank coals, the moisture may block the entrance to the pores so that the access of He is prohibited during the void volume estimation. During the subsequent experiments, however, the pore may become accessible to CO₂ due to the swelling of the coal. On the other hand, lower-rank coals shrink when they are dried and their pore size becomes smaller. This would provide less change in accessible pore volume. These issues will be studied further in the future.

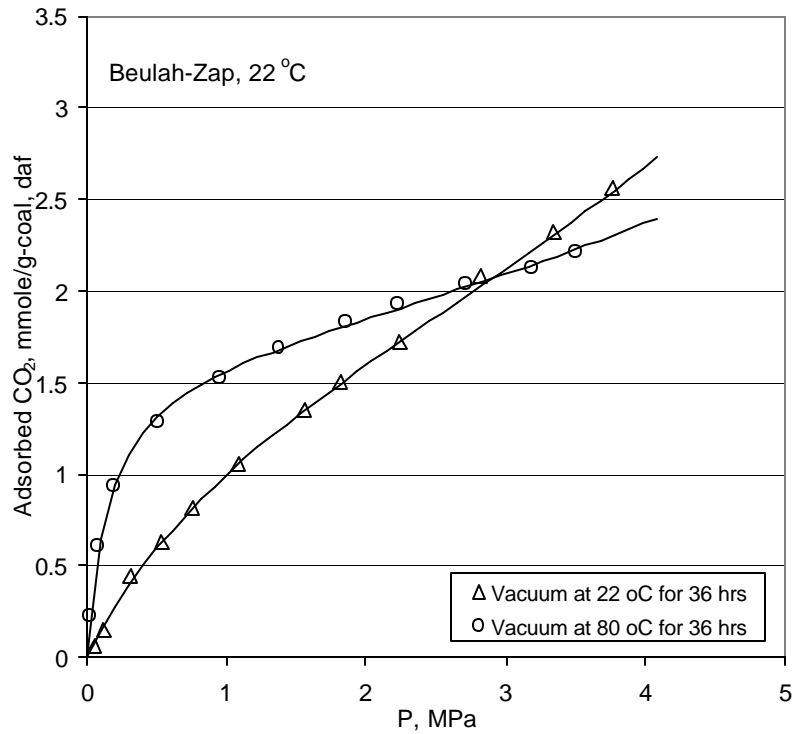


Figure 11. Effect of Moisture on the CO₂ adsorption isotherms of the Argonne Premium Wyodak Coal

Table 9. Effect of moisture content on the Adsorption capacity, Langmuir constant, and increase in pore volume of Argonne Premium coals at various ranks^a:

Coal Sample	Adsorption Capacity (n ₀) (mmole/g-coal, 22 °C)		Langmuir Constant (b) (MPa ⁻¹)		Change in total pore volume (%V/V) %	
	22 °C	80 °C	22 °C	80 °C	22 °C	80 °C
Pocahontas No. 3	1.27	1.27	3.46	4.41	25	29
Upper Freeport	1.07	1.17	2.79	3.25	10	14
Illinois No. 6	1.21	1.28	3.50	2.61	73	71
Wyodak-Anderson	1.61	1.66	0.99	3.65	65	44
Beulah-Zap	1.62	1.63	0.78	6.16	93	53

^a daf basis

CONCLUDING REMARKS

The influence of coal swelling on the adsorption isotherms of CO₂ has been evaluated. The equation derived has been shown to be capable of estimation of the parameters for coal-CO₂ interactions such as adsorption capacity, heat of adsorption, surface heterogeneity as well as pore size distribution (from Dubinin-Astakhov equation).

The adsorption capacity and the characteristic heat of adsorption for various ranks of dry, ash free Argonne Premium coals have been estimated. The effect of swelling on the estimation of surface areas of coals has been compared with the literature data. The preliminary data for the effect of the moisture content on the adsorption isotherm and adsorption capacity of CO₂ on various ranks of coals were also estimated.

FUTURE WORK

1. pH-effect on the adsorption capacity of coals will be investigated in order to relate the data for the stability of the adsorbed CO₂ on coals.
2. Model the sequestration process

REFERENCES

-
- ¹ Hansen, J., Sato, M., Ruedy, R., Lacis, A., and Oinas, V., "Global Warming in the Twenty-First Century: An Alternative Scenario", Proc. Natl. Acad. Sci., 9875-9880, 1997
- ² Halmann, M., M., and Steinberg, M., Greenhouse Gas Carbon Dioxide Mitigation Science and Technology, Lewis Publishers, New York, 1999
- ³ Intergovernmental Panel on Climate Change (IPCC), 1996. Climate Change 1995: The Science of Climate Change, Cambridge University Press, Cambridge, UK
- ⁴ Bachu, S., "Sequestration of CO₂ in Geological Media: Criteria and Approach for Site Selection in Response to Climate Change", Energy Conv.& Mangm., 41, 953-970, 2000
- ⁵ Carbon Sequestration: Research and Development, U.S. Department of Energy (DOE) Report, Dec. 1999
- ⁶ Larsen J.W., Hall P., Wernett P.C., "Pore structure of the Argonne premium coals", *Energy & Fuels*, 9, 324-330, 1995
- ⁷ Starzewski P. and Grillet Y., "Thermochemical studies of adsorption of He and CO₂ on coals at ambient temperature", *Fuel* **68**, 375-379, 1989
- ⁸ Stumm W. and Morgan J.J., 1996, Aquatic Chemistry: Chemical Equilibria and Their Rates in Natural Waters, John Wiley & Sons, New York.
- ⁹ Kim A.G. and Kissell F.N., "Methane formation and migration in coalbeds", In: *Methane control research: summary of results, 1964-80. U.S. Dept. of the Interior, Bureau of Mines Bulletin/1988, Bulletin 687*, Deul M. and Kim A.G (eds.) Chapter 3, pp. 18-25, 1986

-
- ¹⁰ Amy P. and Haldeman D.L., 1997, *The Microbiology of the Terrestrial Deep Subsurface*. CRC Press, New York.
- ¹¹ Ettinger, I., Chaplinsky, A., Lamba, E., and Adamov, V., “Natural Factors Influencing Coal Sorption Properties III-Comparative Sorption of Carbon Dioxide and Methane on Coals”, *Fuel*, 351-356, 1965
- ¹² Anderson, R., B., Bayer, J., and Hofer, L., J., E., “Determination Surface Areas from CO₂ Isotherms”, *Fuel*, 1965
- ¹³ Walker, P., L., and Kini, K., A., “Measurement of the Ultrafine Surface Area of Coals”, *Fuel*, 1965
- ¹⁴ Goetz, V., and Guillot, A., “An Open Activated Carbon/CO₂ Sorption Cooling System”, *Ind. Eng. Chem. Res.*, 40, 2904-2913, 2001
- ¹⁵ Duda, J., M., Duda, J., “Hard Coal Surface Heterogeneity in the Sorption Process”, *Langmuir*, 13, 1286-1296, 1997
- ¹⁶ Angus, S., Reuck, K., M., and McCarty, R. D., *Helium International Thermodynamic Tables of the Fluid State –4*, Pergamon Press, New York, 1977
- ¹⁷ Span, R. and Wagner, W., "A New Equation of State for Carbon Dioxide Covering the Fluid Region from the Triple-Point Temperature to 1100 K at Pressures up to 800 MPa", *J. Phys. Chem. Ref. Data*, 25(6), 1509-1596, 1996
- ¹⁸ Shimizu, K., Takanohashi, T., and Iino, M., “Sorption Behaviors of Various Organic Vapors to Argonne Premium Coal Samples”, *Energy & Fuels*, 12, 891-896, 1998
- ¹⁹ Takanohashi, T., Terao, Y., Yoshida, T., and Iino, M., “Adsorption and Diffusion of Alcohol Vapors by Argonne Premium Coals”, *Energy & Fuels*, 14, 915-919, 2000

-
- ²⁰ Duda, J., M., Duda, J., Nodzinski, A., and Lakatos, J., “Absorption and Adsorption of Methane and Carbon Dioxide in Hard Coal and Active Carbon”, *Langmuir*, 16, 5458-5466, 2000
- ²¹ Walker, P., L. and Mahajan, O., P., “Pore Structure in Coals”, *Energy & Fuels*, 7, 559-560, 1993
- ²² Mahajan, O., P., “CO₂ surface area of coals: The 25-year paradox”, *Carbon*, 29, 735, 1991
- ²³ Gan, H., Nandi, S., P., and Walker, P., L., “Nature of the Porosity in American Coals”, *Fuel*, 51, 272-277
- ²⁴ Walker, P. L., Verma, S., K., Utrilla, J., R., and Davis, A., “Densities, Porosities and Surface Areas of Coal Macerals as Measured by Their Interaction with Gases, Vapors and Liquids”, *Fuel*, 67, 1615-1623, 1988
- ²⁵ Joubert, J., I., Grein, C., T., and Bienstock, D., “Sorption of Methane in Moist Coal”, *Fuel*, 52, 181-185, 1973
- ²⁶ Joubert, J., I., Grein, C., T., and Bienstock, D., “Effect of Moisture on the Methane Capacity of American Coals”, *Fuel*, 53, 186-191, 1974

PUBLICATIONS

1. Ozdemir, E., Schroeder, K., and Morsi, B., I., “Effect of Volume Change on Adsorption Isotherms of CO₂ on Coals”, to be submitted.
2. Ozdemir, E., Schroeder, K., and Morsi, B., I., “Adsorption Capacity of CO₂ on Argonne Premium Coals”, in preparation.
3. Ozdemir, E., Schroeder, K., and Morsi, B., I., “Sequestration of Carbon Dioxide (CO₂) in Coal Seams-A Review”, in preparation.
4. Ozdemir, E., Schroeder, K., and Morsi, B., I., “Adsorption Capacity of CO₂ on Argonne Premium Coals”, **ACS National Meeting-Fuel Chemistry Division Preprints**, April 7-11, 2002, Orlando, Florida (accepted).
5. Ozdemir, E., Schroeder, K., and Morsi, B., I., “Evaluation of Adsorption Isotherms of CO₂ on Coals in the Presence of Swelling”, **ACS National Meeting-Fuel Chemistry Division Preprints**, April 7-11, 2002, Orlando, Florida (accepted).
6. Ozdemir, E., Schroeder, K., and Morsi, B., I., “Global Warming: Carbon Dioxide Sequestration in Coal Seams”, **ACS National Meeting-Environmental Chemistry Division**, April 7-11, 2002, Orlando, Florida (accepted).
7. Ozdemir, E., Schroeder, K., and Morsi, B., I., “Adsorption-Desorption Isotherms of Carbon Dioxide (CO₂) on Argonne Premium Coals”, **AIChE-Separations Technologies Proceedings**, Nov.4-9, 2001, Reno, Nevada.
8. Ozdemir, E., Morsi, B., I., and Schroeder, K., “Effect of Ranks on the Sorption of Carbon Dioxide on Argonne Premium Coals at High Pressures”, **International**

Conference on Coal Science (ICCS), 30 Sept.-5 Oct. 2001, San Francisco, California.

9. Schroeder, K., Ozdemir, E., and Morsi, B., I., “Sequestration of carbon Dioxide in Coal Seams”, **First National Conference on Carbon Sequestration**, May 14-17, 2001, Washington D.C.

PRESENTATIONS

1. Ozdemir, E. “Effect of Swelling on Adsorption Isotherms of CO₂ on Coals”, **ACS National Meeting-Fuel Chemistry Division Preprints**, April 7-11, 2002, Orlando, Florida (accepted).
2. Schroeder, K., Ozdemir, E., and Morsi, B., I., “Adsorption Capacity of CO₂ on Argonne Premium Coals”, **ACS National Meeting-Fuel Chemistry Division Preprints**, April 7-11, 2002, Orlando, Florida (accepted).
3. Ozdemir, E. “Adsorption-Desorption Isotherms of CO₂ on Argonne Premium Coals”, **AIChE Annual Meeting**, Nov.4-9, 2001, Reno, Nevada.
4. Schroeder, K., Ozdemir, E., and Morsi, B., I., “Sequestration of carbon Dioxide in Coal Seams”, **First National Conference on Carbon Sequestration**, May 14-17, 2001, Washington D.C.

POSTERS

1. Ozdemir, E., Schroeder, K., and Morsi, B., I., "Evaluation of Adsorption Isotherms of CO₂ on Coals in the Presence of Swelling", **Sci-Mix at the ACS National Meeting-Fuel Chemistry Division**, April 7-11, 2002, Orlando, Florida (accepted).
2. Ozdemir, E., Schroeder, K., and Morsi, B., I., "Global Warming: Carbon Dioxide Sequestration in Coal Seams", **ACS National Meeting-Environmental Chemistry Division**, April 7-11, 2002, Orlando, Florida (accepted).
3. Ozdemir, E., Schroeder, K., and Morsi, B., I., "Carbon Dioxide Sequestration in Coal Seams", **AIChE Annual Meeting**, Nov.4-9, 2001, Reno, Nevada.
4. Ozdemir, E., Schroeder, K., and Morsi, B., I., "Global Warming: Carbon Dioxide Sequestration in Coal Seams", **Science2001**, Sept.12-14, 2001, Pittsburgh, PA.

XXVII. “CFD Simulation of Slurry Bubble Column”

**Jonghwun Jung (S) and Dimitri Gidaspow (F), Illinois Institute of Technology
with
Isaac Gamwo(M), NETL**

CFD SIMULATION OF SLURRY BUBBLE COLUMN REACTORS

**Jonghwun Jung, Ph.D Candidate
Dimitri Gidaspow* Distinguished Professor**

**Department of Chemical and Environmental Engineering
Illinois Institute of Technology
Chicago, IL 60616**

Isaac K. Gamwo**

**National Energy Technology Laboratory
US Department of Energy
Pittsburgh, PA 15236**

December 2001

* Tel. : 312-567-3045, Fax : 312-567-8874, E-mail : gidaspow@iit.edu

** Tel. : 412-386-6537, Fax : 412-386-5936, E-mail : Isaac.Gamwo@netl.doe.gov

ABSTRACT

The objective of this study is to develop a reliable well-validated computational fluid dynamic (CFD) model for gas-liquid-solid flow and the second objective is to optimize the Slurry Bubble Column Reactors (SBCR). A two dimensional transient computer code for the coupled Navier-Stokes equations for each phase was developed. The principal input into the model was a measured viscosity of the slurry phase (Matonis, 2000).

The computed time averaged particle concentrations agree with experimental measurements obtained using a combination of γ - ray and X-ray densitometers in a slurry bubble column reactor. Both the experiment and the simulation show several flow patterns as a function of time and nearly uniform particle concentration in a slurry bubble column reactor.

A search was made to determine the optimum catalyst size. Computations were made over a range of particle size. The granular temperature was the highest for 60 μ m particles. The computed turbulent intensity was 0.5, in agreement with kinetic theory of granular flow.

Table 1. Governing Equations applied to gas-liquid-solid flow

Continuity Equation for Each Phase, k=g,l,s

$$\frac{\partial(\mathbf{r}_k \mathbf{e}_k)}{\partial t} + \nabla \cdot (\mathbf{r}_k \mathbf{e}_k \bar{\mathbf{v}}_k) = 0$$

Momentum Balance for Each Phase

Continuous Phase (Liquid)

$$\frac{\partial(\mathbf{r}_l \mathbf{e}_l \bar{\mathbf{v}}_l)}{\partial t} + \nabla \cdot (\mathbf{r}_l \mathbf{e}_l \dot{\mathbf{v}}_l \dot{\mathbf{v}}_l) = -\nabla P \bar{\mathbf{I}} + \nabla \cdot \bar{\bar{\mathbf{t}}}_l - \sum_{m=g,s} \mathbf{b}_{lm} (\dot{\mathbf{v}}_m - \dot{\mathbf{v}}_l) + \mathbf{r}_l \dot{\mathbf{g}}$$

Dispersed Phase (Gas or Solid)

$$\begin{aligned} \frac{\partial(\mathbf{r}_k \mathbf{e}_k \dot{\mathbf{v}}_k)}{\partial t} + \nabla \cdot (\mathbf{r}_k \mathbf{e}_k \bar{\mathbf{v}}_k \bar{\mathbf{v}}_k) = & -\nabla P_k \bar{\mathbf{I}} + \nabla \cdot \bar{\bar{\mathbf{t}}}_k + \sum_{\substack{m=l,g,s \\ m \neq k}} \mathbf{b}_{km} (\bar{\mathbf{v}}_m - \bar{\mathbf{v}}_k) \\ & + \frac{\mathbf{e}_k}{\mathbf{e}_l} (\mathbf{r}_k - \sum_{m=l,g,s} \mathbf{e}_m \mathbf{r}_m) \bar{\mathbf{g}} \end{aligned}$$

Constitutive Equations

(1) Definitions

$$\sum_{k=l,g,s} \mathbf{e}_k = 1$$

(2) Equation of State

$$\mathbf{r}_l = 1, \quad \mathbf{r}_g, \mathbf{r}_s = \text{constant}$$

(3) Viscous Stress Tensor

$$\bar{\bar{\mathbf{t}}}_k = 2 \mathbf{m}_k \bar{\bar{D}}_k - \frac{2}{3} \mathbf{m}_k \text{tr}(\bar{\bar{D}}_k) \bar{\mathbf{I}}$$

$$\bar{\bar{D}}_k = \frac{1}{2} \left[\nabla \bar{\mathbf{v}}_k + (\nabla \bar{\mathbf{v}}_k)^T \right]$$

where $\mathbf{m}_k = \mathbf{e}_k \mathbf{m}_k$ for each Phase

(4) Solid Stress Modulus

$$\nabla P_k = G(\mathbf{e}_k) \nabla \mathbf{e}_k$$

$$G(\mathbf{e}_k) = 10^{-8.686 \mathbf{e}_k + 6.385}$$

(5) Inter-Phase Drag Coefficient

For $e_l \leq 0.8$

$$\mathbf{b}_{lk} = \mathbf{b}_{kl} = 150 \frac{(1 - e_l) \mathbf{e}_k \mathbf{m}_l}{(\mathbf{e}_l d_k \mathbf{j}_k)^2} + 1.75 \frac{\mathbf{r}_l \mathbf{e}_k |v_l - v_k|}{\mathbf{e}_l d_k \mathbf{j}_k}$$

For $e_l > 0.8$

$$\mathbf{b}_{lk} = \mathbf{b}_{kl} = \frac{3}{4} C_d \frac{\mathbf{r}_l \mathbf{e}_k |v_l - v_k|}{d_k \mathbf{j}_k} \mathbf{e}_l^{-2.65}$$

where

$$C_d = \frac{24}{\text{Re}_k} \left[1 + 0.15 \text{Re}_k^{0.687} \right] \quad \text{for } \text{Re}_k < 1000$$

$$C_d = 0.44 \quad \text{for } \text{Re}_k > 1000$$

$$\text{Re}_k = \frac{\mathbf{e}_l \mathbf{r}_l d_l |v_l - v_k|}{\mathbf{m}_l}$$

$$\mathbf{b}_{kl} = \frac{\mathbf{a}(1 + e) \mathbf{e}_k \mathbf{r}_k \mathbf{e}_l \mathbf{r}_l (d_k + d_l)^2 \left[1 + 3 \left(\frac{\mathbf{V}_{kl}}{\mathbf{e}_k + \mathbf{e}_l} \right)^{\frac{1}{3}} \right]}{2 \mathbf{e}_f (\mathbf{r}_k d_k^3 + \mathbf{r}_l d_l^3) \left[3 \left(\frac{\mathbf{V}_{kl}}{\mathbf{e}_k + \mathbf{e}_l} \right)^{\frac{1}{3}} - 1 \right]} |\vec{v}_k - \vec{v}_l|$$

$$\mathbf{V}_{kl} = \begin{cases} \left[(\mathbf{f}_k - \mathbf{f}_l) + (1 - \mathbf{a})(1 - \mathbf{f}_k) \mathbf{f}_l \right] \left[\mathbf{f}_k + (1 - \mathbf{f}_l) \mathbf{f}_k \right] \frac{\mathbf{c}_k}{\mathbf{f}_k} + \mathbf{f}_l & \text{for } \mathbf{c}_k \leq \frac{\mathbf{f}_k}{[\mathbf{f}_k + (1 - \mathbf{f}_k) \mathbf{f}_l]} \\ (1 - \mathbf{a}) \left[\mathbf{f}_k + (1 - \mathbf{f}_k) \mathbf{f}_l \right] (1 - \mathbf{c}_k) + \mathbf{f}_k & \text{for } \mathbf{c}_k > \frac{\mathbf{f}_k}{[\mathbf{f}_k + (1 - \mathbf{f}_k) \mathbf{f}_l]} \end{cases}$$

$$\mathbf{a} = \sqrt{\frac{d_l}{d_k}} \quad d_k \geq d_l$$

$$\mathbf{c}_k = \frac{\mathbf{e}_k}{\mathbf{e}_k + \mathbf{e}_f}$$

Table 2. Equations for stress calculations.

$$\langle v'v' \rangle = \left[\frac{1}{N(t)} \sum v(x,y,z,t)v(x,y,z,t) \right] - (\langle v(x,y,z) \rangle)^2$$

$$\langle u'v' \rangle = \langle v'u' \rangle = \frac{1}{N(t)} \sum \left[\{u(x,y,z,t) - \langle u(x,y,z) \rangle\} \{v(x,y,z,t) - \langle v(x,y,z) \rangle\} \right]$$

$$\langle u'u' \rangle = \left[\frac{1}{N(t)} \sum u(x,y,z,t)u(x,y,z,t) \right] - (\langle u(x,y,z) \rangle)^2$$

with N(t) being the number of vectors in the time-average

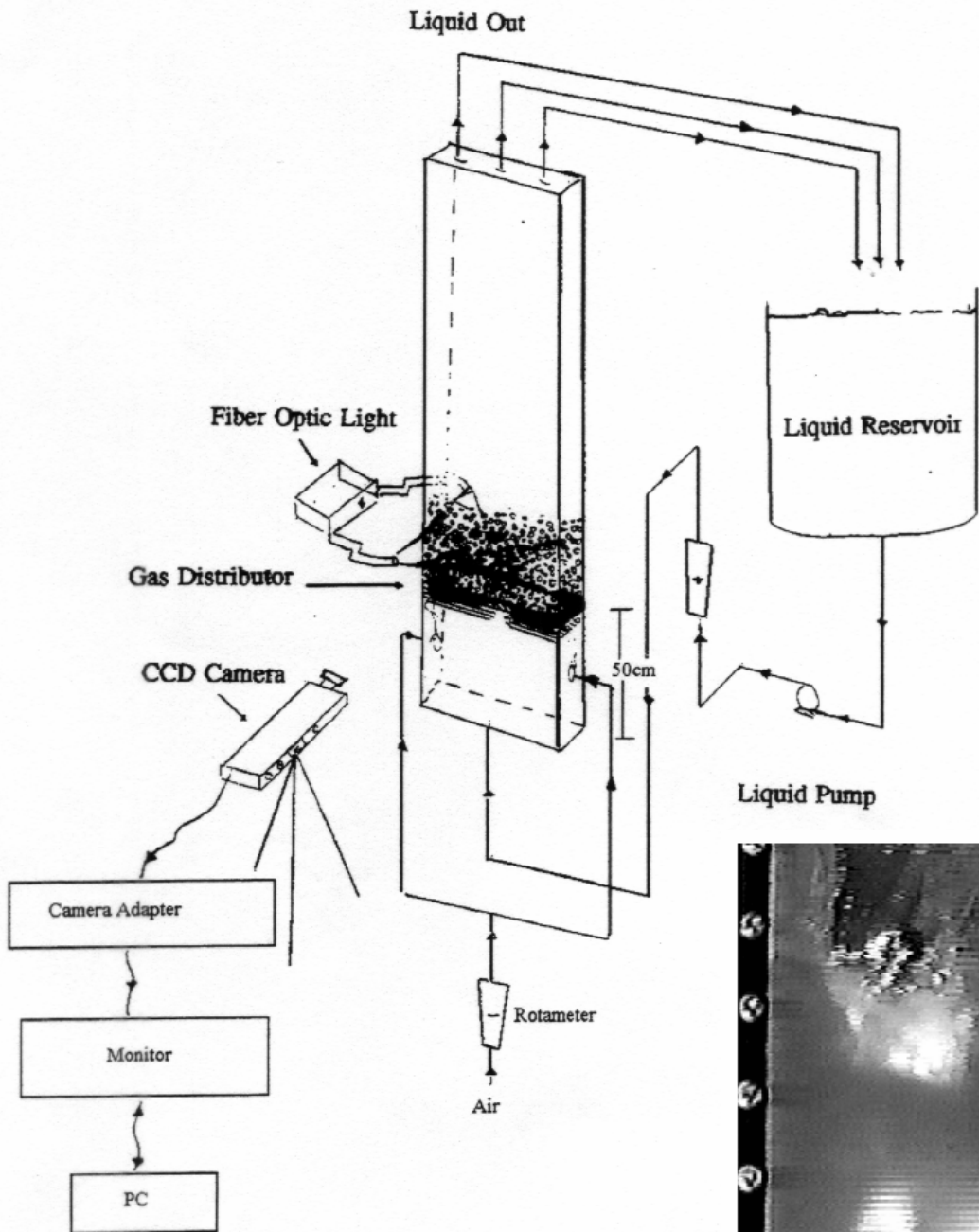


Figure 1. Experimental Schematic Diagram for the IIT Slurry Bubble Column.



Figure 2. Typical Bubble Photograph in IIT Slurry Bubble Column with $V_G = 3.37\text{cm/sec}$ and $V_L = 2.02\text{cm/sec}$.

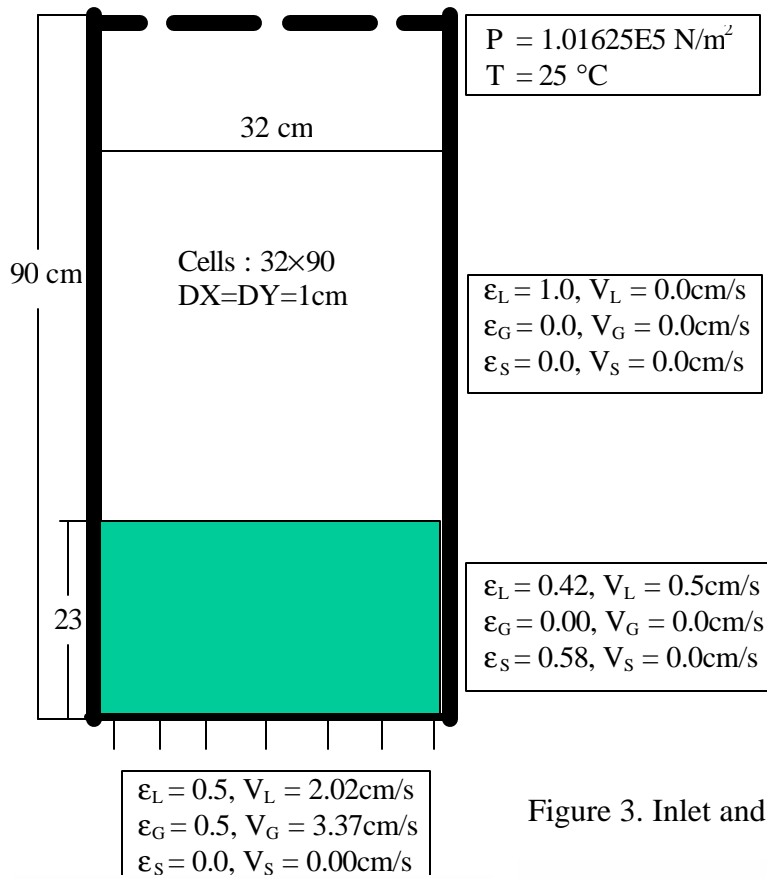


Figure 3. Inlet and Initial Conditions for Simulation

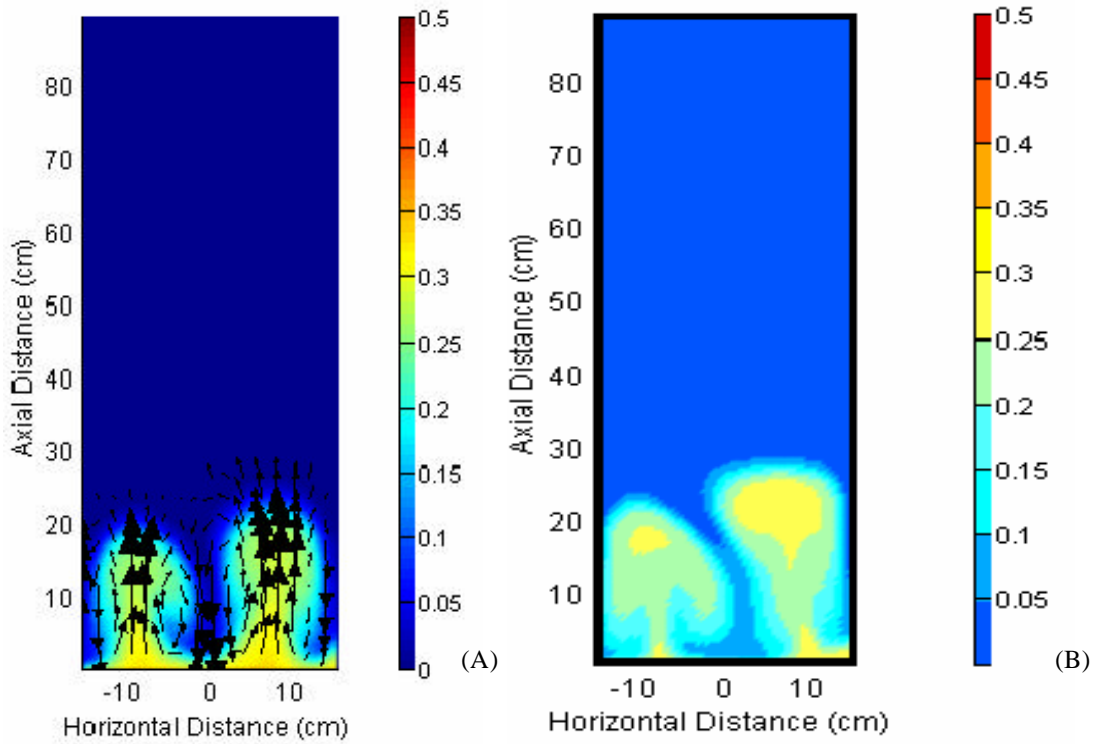


Figure 4. Gas Volume Fraction and Velocity Vector Plots at 0.5cm Grid Size for 800 μm Particles. A) 2.3sec and B) 2.7sec

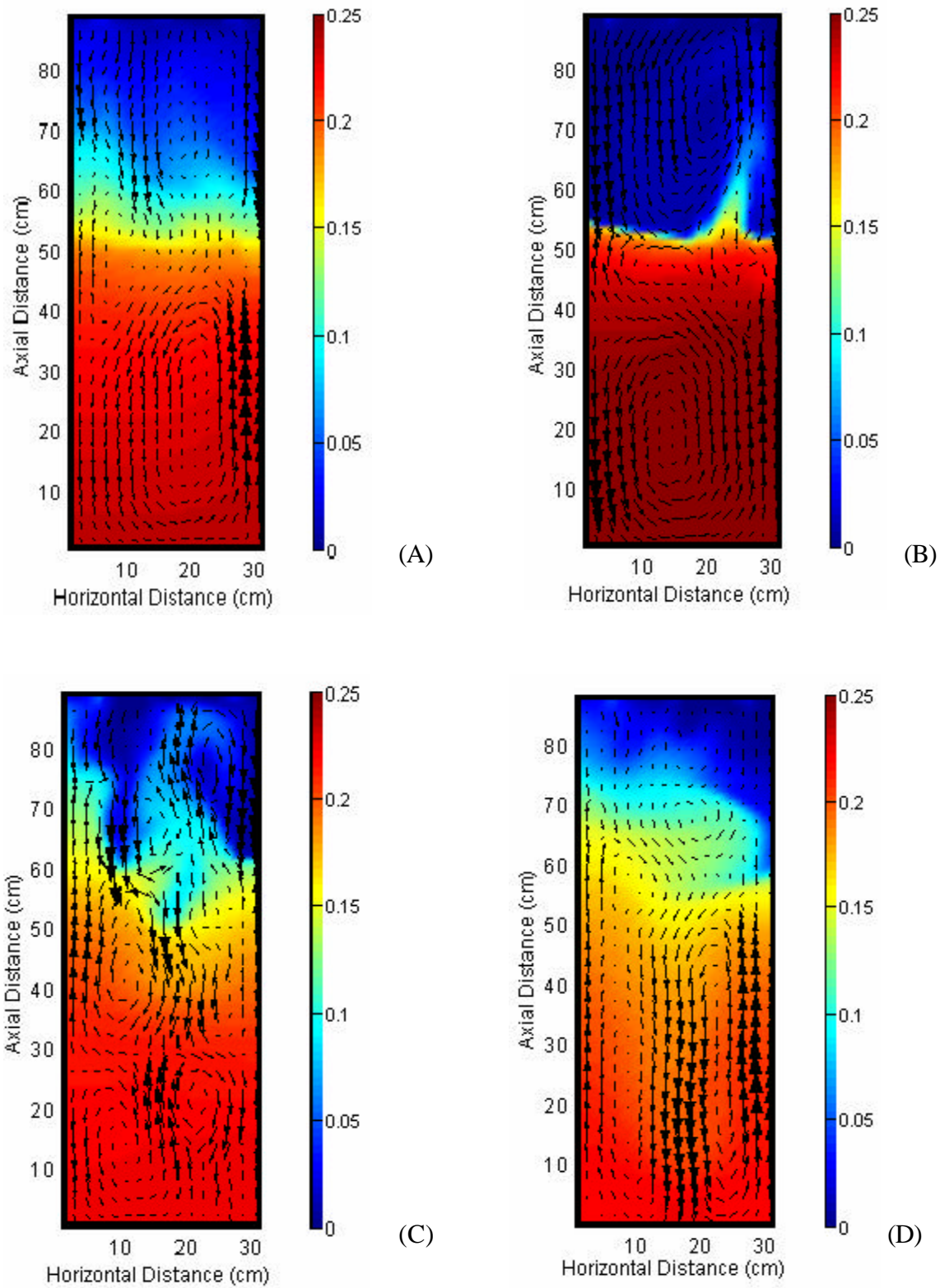
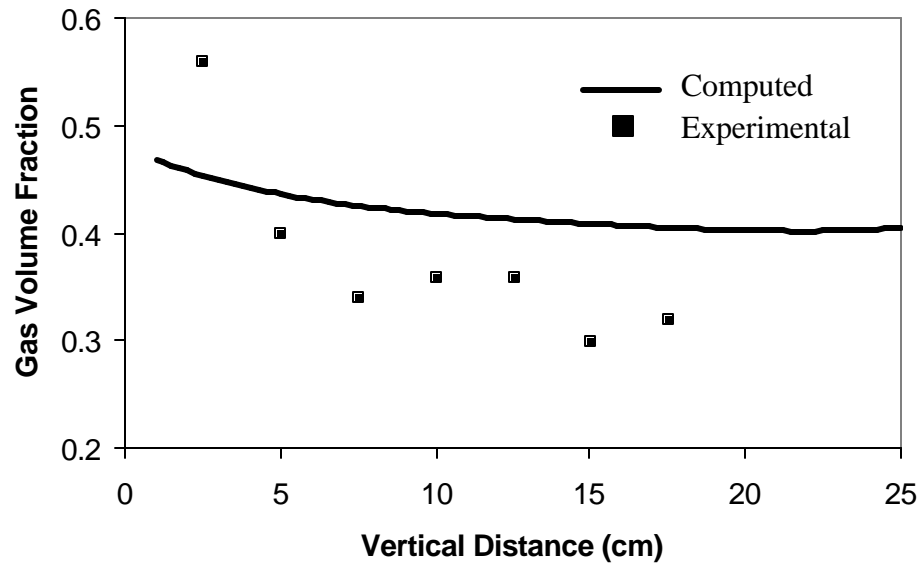
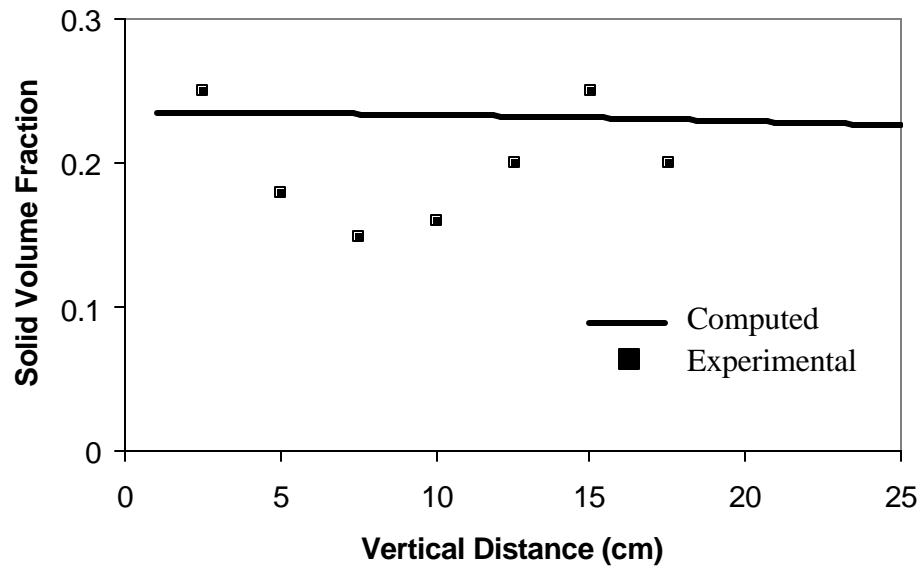


Figure 5. Volume Fraction and Velocity Vector Plots of Solid for 800µm Particles. A) Averaged from 15 to 36 sec, Instantaneous Time B)17sec, C) 28sec and D) 32sec.



(A)



(B)

Figure 6 (A),(B). Comparison of Measured and Computed Phase Hold-up in Bubbly Coalesced Regime for $V_L=2.02$ cm/s and $V_G=3.37$ cm/s at 4 cm from Horizontal Center of Bed.

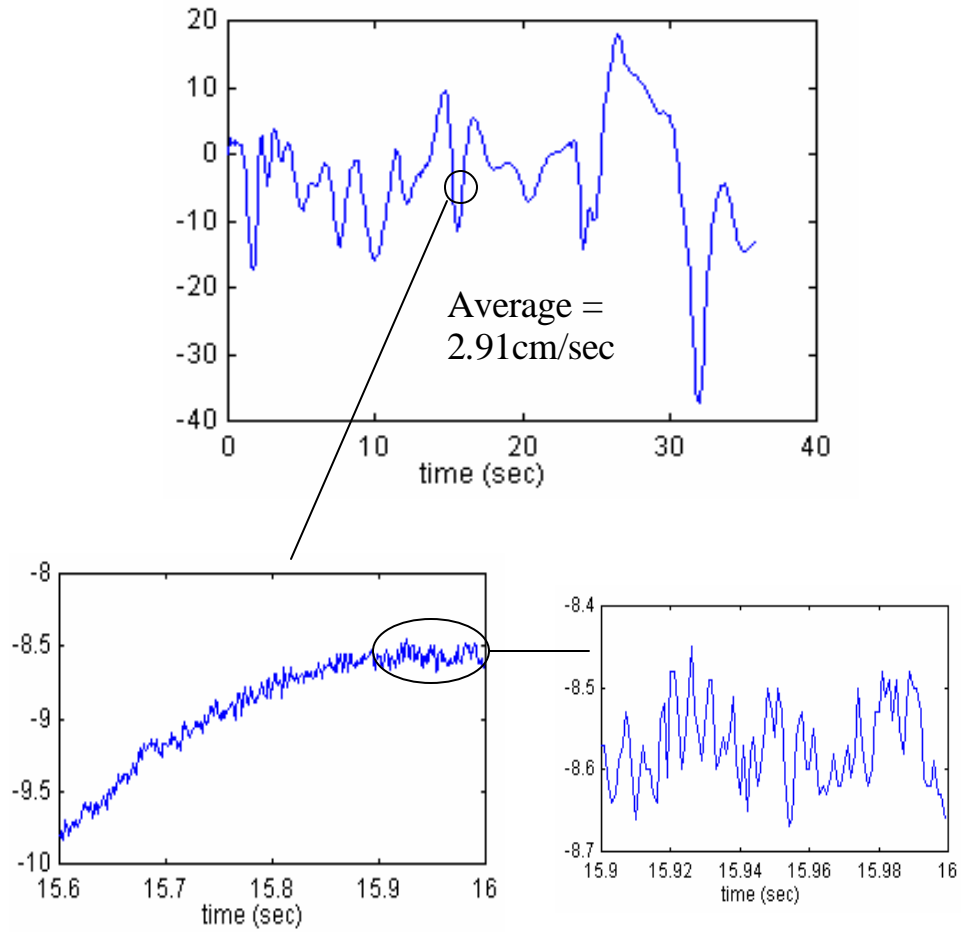


Figure .7 Large and Small Scales Oscillations for Axial Velocity of Solid As a Function of Time at x=15.5cm, y=11.5cm.

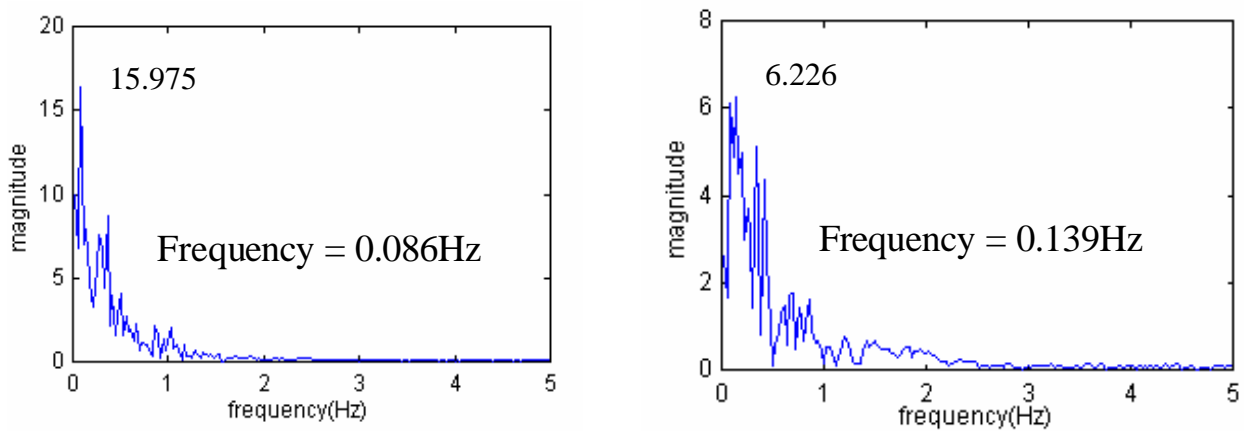


Figure .8 Effect of Gravity on Dominant Frequency. A) 980cm/sec^2 and B) $2,940\text{cm/sec}^2$

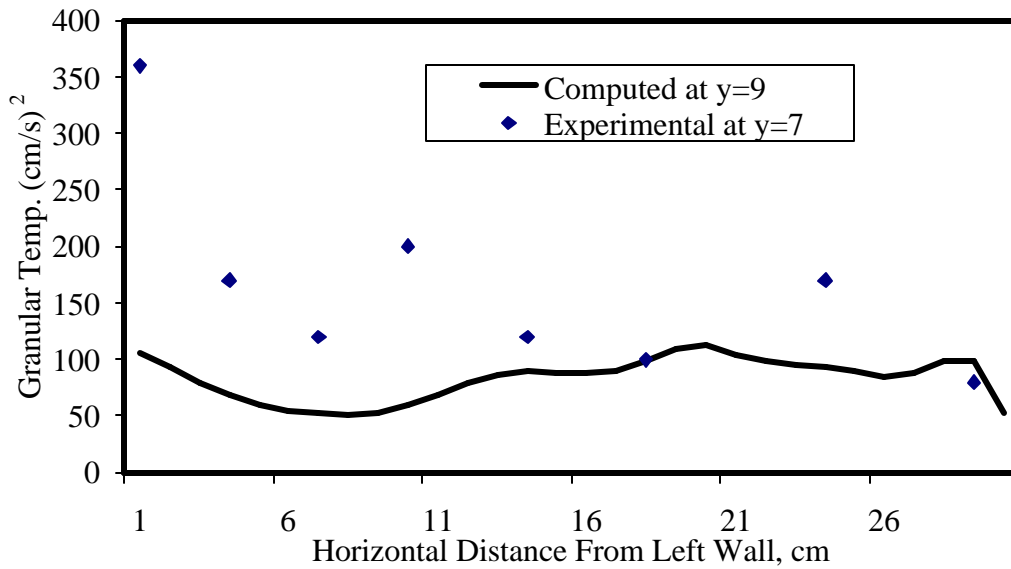


Figure 9. Comparison of Computed and Experimental Granular Temperatures for 800µm particles at a Bed Height of 9 cm with $V_G = 3.37$ cm/sec and $V_L = 4.04$ cm/sec.

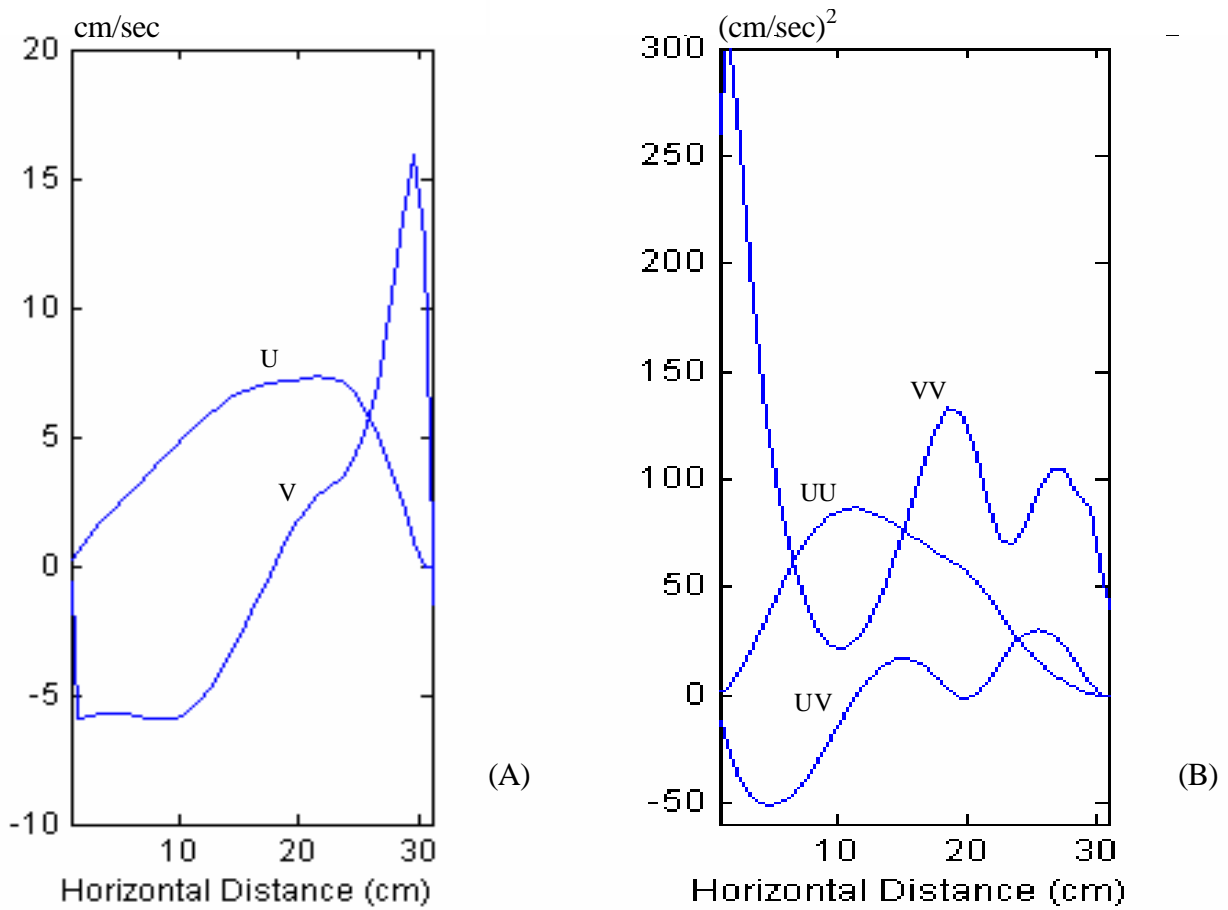


Figure 10. Axial(V) Velocity, Radial(U) Velocity and Variance(VV, UU, UV) for 800µm Particles at a Bed Height of 9cm.

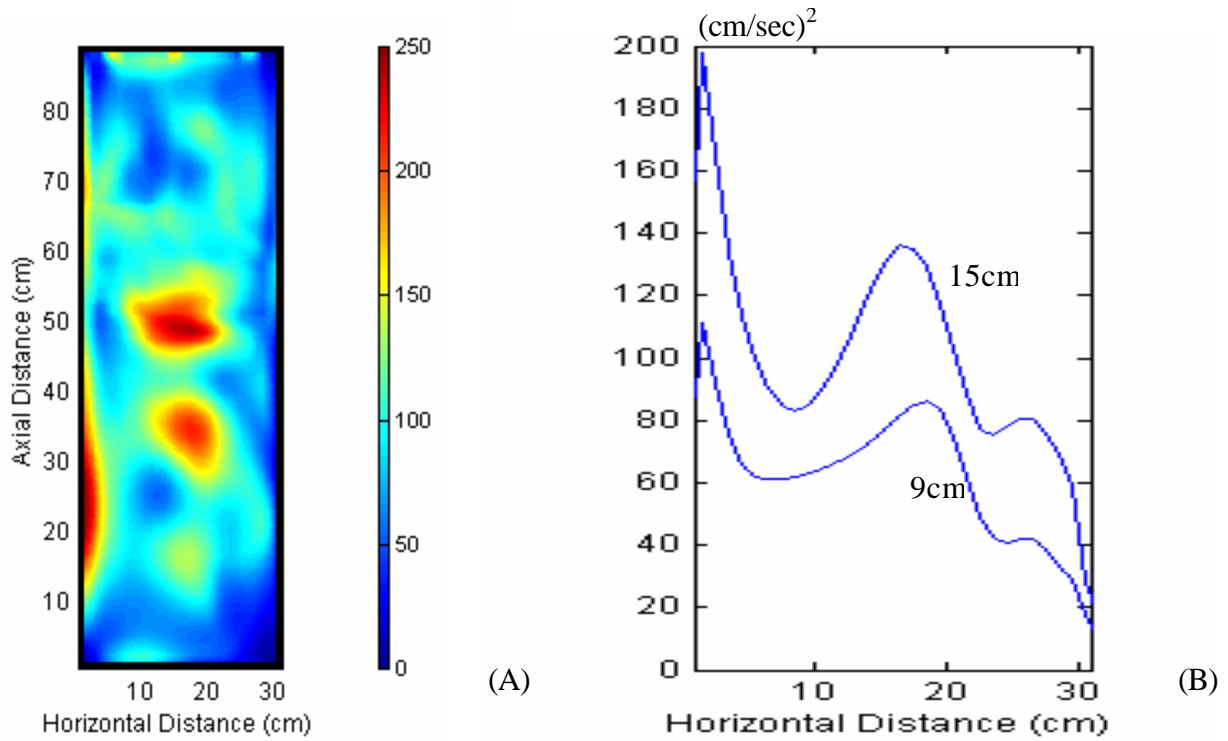


Figure .11 Granular Temperature Calculated from Standard Deviation (A) at the Whole Bed and (B) at a Bed Height of 9 cm and 15 cm.

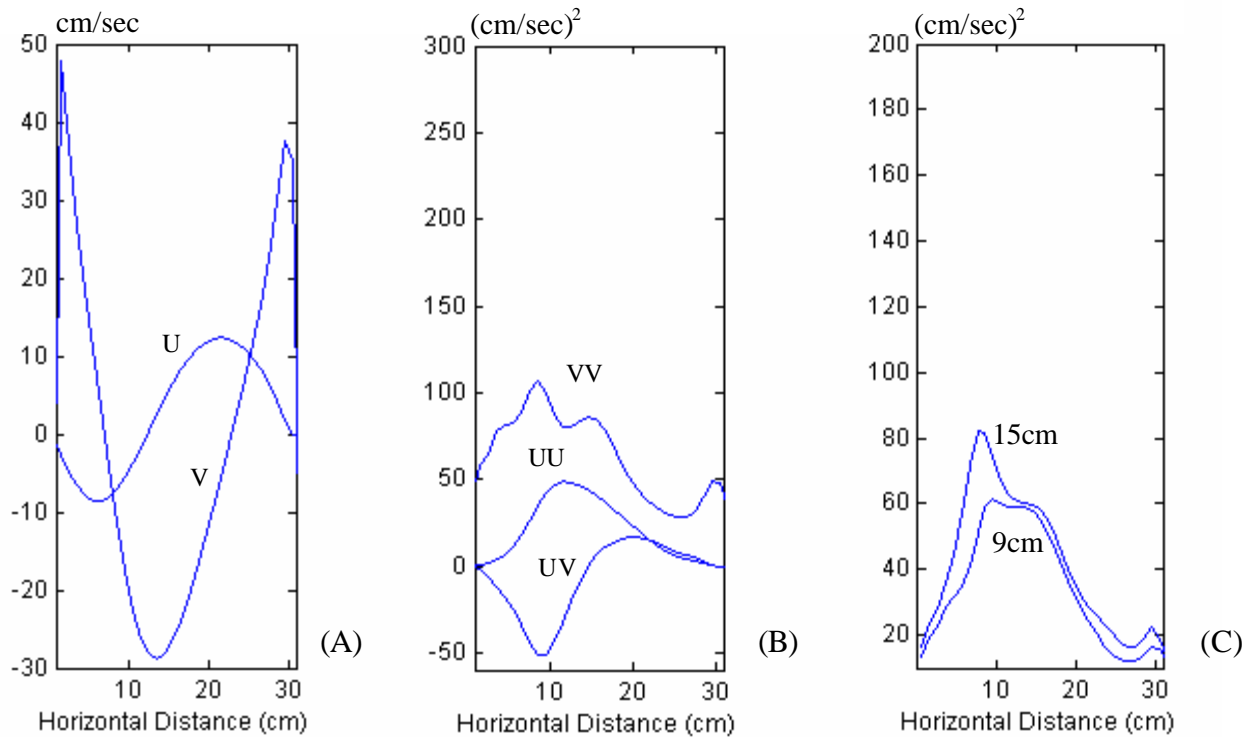


Figure 12. (A) Axial(V) Velocity, Radial(U) Velocity, (B) Variance(VV, UU, UV) at a Bed Height of 9cm and (C) Granular Temperature Calculated from Standard Deviation at a Bed Height of 9 cm and 15 cm for 500 μm Particles.

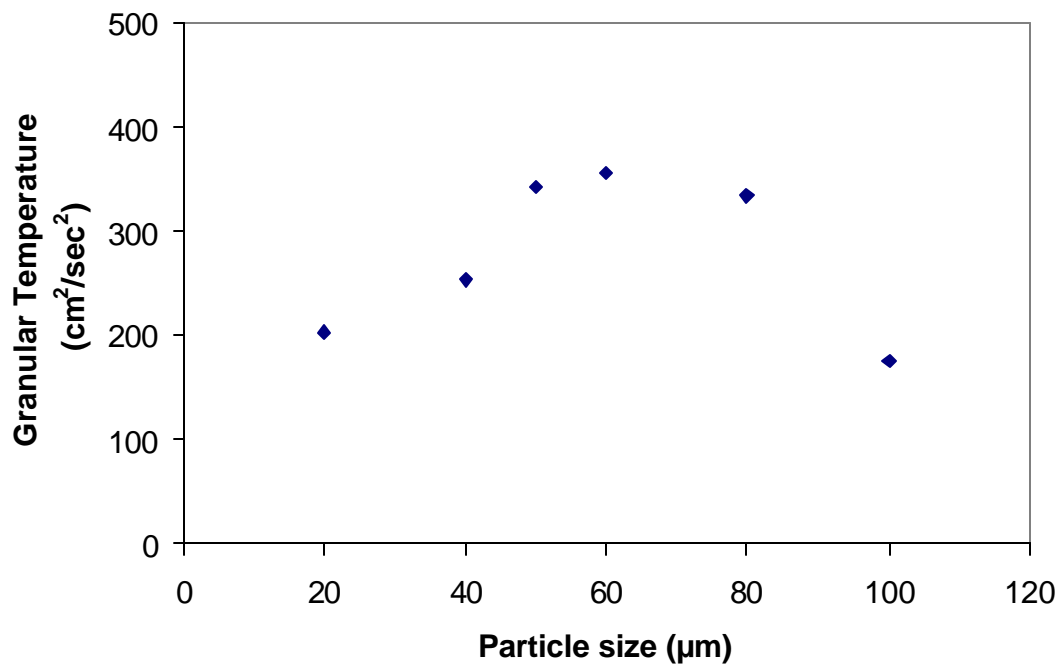


Figure 13. Optimum Particle Size for Mixing (Maximum Granular Temperature) in the IIT Slurry Bubble Column..

INTRODUCTION

Slurry bubble column reactors have recently (Parkinson, 1997) become competitive with traditional fixed bed reactors for converting synthesis gas into liquid fuels. The gas refinery based on Fischer-Tropsch and methanol-to-gasoline technology (Katzner, Ramage and Sapre, 2000) is driven by the availability of large quantities of remote natural gas and the abundant coal resources. For conversion of synthesis gas into methanol or hydrocarbon liquid fuels, a slurry bubble column reactor has several advantages over a fixed bed reactor (Bechtel Group, 1990; Viking Systems International, 1994). It has better heat and mass transfer due to constant agitation of catalyst, the ability to introduce and remove the catalyst into the reactor and lower operating and capital costs. The design of these reactors require, among others, precise knowledge of the kinetics, hydrodynamics, and heat as well as mass transfer characteristics. To date, there is no adequate mathematical model available which can predict the performance of slurry bubble column reactors with reasonable accuracy.

Several types of CFD models are being used in the literature to model multiphase flow for bubble column reactors. The viscosity input model is a method similar to the DNS (Direct Numerical Simulation) of the Navier-Stokes equations in single phase turbulent flow. With particular empirical viscosities, a system of coupled Navier-Stokes equations is solved producing instantaneous fluctuating velocities. Averaging of these velocities produces the normal and the shear Reynolds stresses for the various phases. Such computations were recently done by Matonis, Gidaspow and Bahary (2001) for gas-liquid-solid flow and by Pan, Dudukovic and Chung (1999, 2000) for gas-liquid flow. Matonis, Gidaspow and Bahary (2001) treated the gas phase as a dispersed phase with a constant bubble size. This model is used in this study. Pan, Dudukovic and Chung (1999, 2000) compared the Particle Image Velocity (PIV) data of Mudde, et al (1997) to the computed results using the Los Alamos CFDLIB code. Pfleger, et al (1999) and Krishna, et al (1999) applied the commercial CFX code to bubble columns in the churn-turbulent regime using the k-epsilon model, where three phases which consisted of liquid, small bubbles (1-6mm) and large bubbles (20-80mm). Wu and Gidaspow (2000) developed the model based on the kinetic theory of granular flow (Savage, 1983; Sinclair and Jackson, 1989; Gidaspow, 1994). This model treated the catalyst phase as another fluid with its own temperature, called the granular temperature, its own pressure due to particle collision and its own viscosity. Wu and Gidaspow (2000) modeled the production of methanol from synthesis gas in an Air Products/DOE LaPorte slurry bubble column reactor. Gamwo, et al (2001) applied the kinetic model for predicting the maximum production of methanol in an Air Products/DOE LaPorte reactor.

This report presents a similar computation as that of Matonis, Gidaspow and Bahary (2001) for three phases, using Bahary's (1994) experimental data. The computed time average particle gas and solids hold-ups generally agree with the measurements in a slurry bubble column.

EXECUTIVE SUMMARY

The objective of this study is to develop a reliable well-validated computational fluid dynamic (CFD) model for gas-liquid-solid flow and the second objective is to optimize the Slurry Bubble Column Reactors (SBCR). A two dimensional transient computer code for the coupled Navier-Stokes equations for each phase was developed. The principal input into the model was a measured viscosity of the slurry phase.

The computed time averaged particle concentrations agree with experimental measurements obtained using a combination of γ - ray and X-ray densitometers in a slurry bubble column reactor. Both the experiment and the simulation show several flow patterns as a function of time and nearly uniform particle concentration in a slurry bubble column reactor.

A search was made to determine the optimum catalyst size. Computations were made over a range of particle size. The granular temperature was the highest for 60 μ m particles. The computed turbulent intensity was 0.5, in agreement with kinetic theory of granular flow.

A review of the literature, suggests that there exists an optimum catalyst size in the slurry bubble column reactor. A new algorithm was developed to find the optimum size. The numerical simulation has shown that this size is 60 μ m.

EXPERIMENTAL

A. Experimental Setup for Slurry Bubble Column Reactors. The experimental setup used for the slurry bubble column reactor simulation is shown schematically in figure 1. A rectangular bed was constructed from transparent acrylic (Plexiglas) sheets to facilitate visual observation and video recording of the bed operations such as gas bubbling and coalescence, and the mixing and segregation of solids. The bed height was 213.36 cm and cross-section was 30.48 cm by 5.08 cm. A centrifugal pump was connected to the bottom of the bed by a 1.0-inch (2.54 cm) diameter stainless steel pipe. Gas injection nozzles from an air compressor were connected to the sides of the bed. Liquid was stored in and recycled back to a fifty-five gallon storage tank. The liquid and gas distributors were located at the bottom of the bed. Two perforated Plexiglas plates with many 0.28 cm diameter holes distributed the liquid. They were placed at 35.6 cm and 50.8 cm above the bottom of the bed, with 0.25 cm size glass bead particles filled inside. The gas distributor consisted of six staggered porous tubes of 15.24 cm length and 0.28 cm diameter. The fine pores of porous tubes had a mean diameter of 42 μm . The porous tubes were placed at the bottom of the bed just below the top liquid distributor plate. Both gas and liquid from the top of the bed were directed through three openings of 1.0-inch (2.54 cm) diameter back to the storage tank, where the gas was separated from the liquid.

Air and water were used as the gas and liquid, respectively, in this experiment. Ballotini (leaded glass beads) with an average diameter of 0.08 cm and a density of 2.94 g/cm^3 were used as the solids. The minimum fluidization velocity was 0.76 cm/sec . The initial bed height for experiment was from 22 cm to 24 cm. Figure 2 shows a picture of the experiment for $U_g = 3.37 \text{ cm}/\text{s}$ and $U_l = 2.02 \text{ cm}/\text{s}$. Two distinct bubbles are seen in the middle of the bed.

B. Volume Fraction Determination. X-ray and γ -ray densitometers have been used previously to measure porosities of fluidized beds (Seo and Gidaspow, 1987; Miller and Gidaspow, 1992; Gidaspow, et al, 1995) and solids concentrations in nonaqueous suspensions (Jayaswal, 1991). These techniques are based on the fact that the liquid, gas and solid phases under consideration have different absorptivities for X-ray and γ -rays. The intensity of the transmitted X-rays or γ -rays can be described as a linear function of the volume fractions of liquid, gas and the solid phases. The X-ray and γ -ray densitometer were calibrated and performed in order to calculate the volume fractions of each phase using same methods described earlier by Gidaspow et al (Seo and Gidaspow, 1987; Bahary, 1994). The same concept was adopted to measure concentration profiles inside our three phase fluidization systems. Two densitometers were used alternatively for measuring the time-averaged volume fractions of three phases at a designated location by means of the X-ray and γ -ray adsorption techniques. The X-ray and γ ray densitometer assemblies are that described in Gidaspow's book(1994). They consist of a source, a detector and a positioning table, respectively.

(1) Radioactive Source. The source is a 200-mCi Cu-244 source having 17.8-year half-life. It emitted X-rays with photon energy between 12 and 23 keV. The source was contained in ceramic enamel, recessed into a stainless steel support with a tungsten alloy

packing, and sealed in welded Monel Capsule. The device had brazed Beryllium window. For the γ -ray densitometer, a 20-mCi Cs-137 source having a single γ -ray of 667 keV and a half-life of 30 years was used. The source was sealed in a welded, stainless steel capsule. The source holder was welded, filled with lead, and provided with a shutter to turn off the source. This is the same unit used previously by Seo and Gidaspow (1987).

(2) Detecting and Recording Devices. The intensity of the X-ray beam was measured by using a NaI crystal scintillation detector (Teledyne, ST-82-I/B). It consisted of a 2-mm thick, 5.08 cm diameter tube with 0.13-mm thick Beryllium window. For γ -ray densitometer, the intensity of the γ -ray beam was detected by another NaI crystal detector (Teledyne, S-44-I/2). The dimensions of the crystal were as follows: 5.08 cm thick and 5.08 cm in diameter. The two detectors could be switched for use with different sources. The photomultiplier of the detector was connected sequentially to a preamplifier, an amplifier and a single-channel analyzer, a rate meter, and a compatible personal computer. The rate meter has a selector and a 0-100-mV scale range.

(3) Positioning Table. Both the source holder and detector were affixed to either side of the bed on a movable frame and could be moved anywhere up-or-down or to-and-fro by means of an electric motor.

C. Velocity Measurements and Granular Temperature. The particle velocity and granular temperature was measured by means of the color video camera used a charge-coupled device (CCD) shown in figures 1. In this technique, the particle velocity is measured by means of a length of a streak divided by the elapsed time. It was first used by Bahary (1994) and Gidaspow et al. (1995) for measurements in a three-phase fluidized bed and described by Gidaspow and Huilin (1996, 1998) in great detail. In order to get a good visualization of microscopic movement of particles, a fiber-optic light was reflected on the field of view being 5 x 20 mm area in most experiments. As the particles were fluidized inside the bed, the camera with a zoom lens, 18-108 mm, and close up focus transferred its field of view to the monitor with streak lines. These streak lines represented the space traveled by the particles in a given time interval specified on the camera. The images were then captured and digitized by a micro-imaging board and analyzed using Image-Pro Plus software. Radial and axial velocity measurements were conducted at different locations inside the bed. The velocity vector was calculated as,

$$v_x = \frac{\Delta L}{\Delta t} \cos a$$

$$v_y = \frac{\Delta L}{\Delta t} \sin a \quad (1)$$

where, ΔL is the distance traveled, a is the angle from horizontal, Δt is the inverse of shutter speed, and v_x and v_y are the vertical and horizontal velocity components, respectively.

The granular temperature, which is 2/3 of the random particle kinetic energy, is obtained from the standard deviation of the measured instantaneous particle velocities. The variances (square of standard deviation) of particle velocities in statistics are represented by the following relation.

$$\mathbf{s}_i^2 = \frac{1}{N} \sum_{i=1}^N (v_i - v_m)^2 \quad (2)$$

It is reasonable to use the assumption that the y direction variance equals the x direction variance, described earlier by Gidaspow and Huilin (1998), since the velocity components in x- and y-direction are small compared to z-direction, the vertical direction. Hence the granular temperature is related to the variances by means of the following relation.

$$\mathbf{q} = \frac{1}{3} [\mathbf{s}_x^2 + \mathbf{s}_y^2 + \mathbf{s}_z^2] = \frac{1}{3} [2\mathbf{s}_x^2 + \mathbf{s}_z^2] \quad (3)$$

SIMULATION

A. Hydrodynamic Model. A transient, isothermal, multiphase flow model for describing the hydrodynamics developed earlier (Gidaspow, 1994) was used. The present model was modified by Matonis (2000). The hydrodynamic model uses the principle of mass conservation and momentum balance for each phase. The governing equations applied to multiphase flow are shown table 1. This approach is similar to that of Soo(1967) for multiphase flow and of Jackson (1985, 2002) for fluidization. In this model the total pressure, P, is only in the continuous (liquid) phase momentum balance. The drag and the stress relations were altered to satisfy Archimedes' buoyancy principle and Darcy's Law, as illustrated by Jayaswal (1991). No volume fraction is put into the liquid gravity term, while in the gas/solid momentum balance contains the buoyancy term. This is a generalization of hydrodynamic model B for gas-solid systems as discussed by Gidaspow(1994) in section 2.4.

For the simulation of the three-phase flow, we use the constitutive equations shown in table 1. We use the input viscosity model, in which the solid viscosity has the value of 10poises times the particle concentration obtained by fitting the experimental viscosity values for given superficial liquid and gas velocities (Bahary, 1994). The solids' pressure as a function of a particular phase is calculated by the solids stress modulus obtained from well-defined hopper experiments (Gidaspow, 1994). It was used for 75 μ m FCC particles (Sun and Gidaspow, 1999) in the riser.

As a particle moves through a viscous liquid there exists a resistance of the liquid to the motion of the particle, hence the interphase drag has to be defined. For $e_L < 0.8$, the interphase drag coefficients model applied in slurry bubble column reactors is based on Ergun equation obtained experimentally from pressure drop measurements at packed-bed. For $e_L = 0.8$, it is based on the empirical correlation obtained from settling experiments. Arastoopour, Lin and Gidaspow (1980) observed that solid-solid momentum transfer is necessary to correctly predict the segregation among particles of different sizes in a pneumatic conveyor. Particle-particle drag equations to describe such interactions have been derived by several researchers: Soo (1967), Nakamura and Capes(1976) and Syamlal (1985). In the present work the particle-bubble drag coefficient is based on kinetic theory (Syamlal, 1985). Here the gas phase is treated as a particulate phase with a

bubble diameter of 100 μm , since it consists primarily of small bubbles. The value of an α in the particle-bubble drag coefficient was 0.75 for particle diameter lower than 200 μm and 0.5 for particle diameter larger than 200 μm .

From the parameter estimation, there are nine nonlinear-coupled partial differential equations for nine dependent variables in two-dimensional transient three-phase flow. The variables to be computed are the volume fractions, $\epsilon_{\text{phases-1}}$, the liquid phase pressure P , and the phase horizontal velocity, x-direction, and vertical velocity, z-direction components, u_{phase} and v_{phase} . This leads to an unconditionally well-posed problem, as discussed in detail by Gidaspow(1994) and Lyczkowski, et al. (1978).

To obtain the numerical solution of nonlinear-coupled partial differential equations, a uniform computational mesh (1 by 1cm or 0.5 by 0.5cm) is used in finite-differencing the equations based on the ICE (Implicit Continuous Eulerian, Rivard, 1977; Jayaswal, 1991) method with appropriate initial and boundary conditions. Stewart and Wedroff (1984) have critically reviewed the ICE algorithm and related staggered mesh conservative schemes. The scalar variables are located at the cell center and the vector variables at the cell boundaries. The momentum equation is solved using a staggered mesh, while the continuity equation is solved using a donor cell method.

B. Coordinate system and numerical considerations. The definition of appropriate initial and boundary conditions is critical for the carrying out of a realistic simulation for adequate comparison to experiment. All the simulations are carried out in a two-dimensional Cartesian coordinates with a total of 32×90 computational meshes and a total of 64×180 computational meshes for fine grid size. The computation for fine grid size was performed on J90 supercomputer with double precision at Pittsburgh Supercomputing Center. No slip velocity boundary conditions are employed for three phases at the left and right walls. Neumann boundary conditions are applied to the three-phase flow with the constant pressure of $1.01625 \times 10^5 \text{ N/m}^2$ at the top wall. Dirichlet boundary conditions are applied with a constant liquid and gas velocity and zero solid velocity at the bottom wall. The initial conditions and the configuration for the simulation are shown in figure 3. The convergence criterion for the simulation was 10^{-5} with a time interval of 5×10^{-6} sec. The simulation was run for 40 seconds with different particle sizes and then averaged from 15sec to 36sec.

RESULTS AND DISCUSSION

A. Flow patterns and velocity profiles. The flow patterns in slurry bubble column reactors are obtained from the simulation, in which the particle and bubble diameter are 800 μm and 100 μm , respectively, as described previously by Matonis (2000). Figure 4 shows the gas volume fraction and velocity vector plots at initial time for the fine grid size of 0.5cm. Figure 5A shows the two-dimensional time-averaged, 16 to 42 seconds, solid volume fraction contour plots, along with the time-averaged velocity vectors. Figures 5B-D illustrates the instantaneous solid contour plot with corresponding velocity vectors as a function of time. Figure 6 shows the comparison of measured and computed phase hold-up in the bubbly coalesced regime at 4 cm from horizontal center of bed.

The experimental value obtained from the calibration curves of the x-ray and γ -ray densitometers was presented by Bahary (1994) for the same bubble coalesced regime.

The computational bubble obtained from the fine-grid size shows two distinct bubbles in the middle of the bed and the higher velocity vectors of the gas phase in the spots of bubble formation. There is agreement with experimental bubble shown in figure 2. The gas volume fraction of the computational bubble agrees with experimental value of about 0.3 shown in figure 6. The computational result of averaged gas volume fraction was about 20% higher than experimental value. The computational averaged solid flow patterns show uniformity in solids concentration distribution. They agree well with experimental results shown in figure 6. The flow patterns as a function of time agree with the literatures (Chen et al, 1989; Gidaspow, 1994; Wu and Gidaspow, 2000). Figure 5C shows upward flow in the center region and downward flow near the wall of lower part of the bed. There is also downward flow in the center region and upward flow near the wall of middle part of the bed. Figure 5D shows the gulf -stream effect consisting of two vortex cells with downward flow in the center region and upward flow near the wall. The solid velocity fluctuates upward and downward in the center region as visually confirmed in the experiment. This fluctuating particle velocity and the flow structure of multiple vortex cells cause the particle concentration to be uniform throughout the bed. Hence it gives good mixing in the slurry bubble column reactors. That is in contrast to the case of Wu and Gidaspow (2000) for the methanol synthesis with no liquid inlet flow, where there is a vertical density gradient. It was described previously by Matonis, Gidaspow and Bahary (2001). They predicted the difference in the bed expansion.

B. Turbulence of particles. Figure 7 shows the large- and small-scale oscillations for axial velocity of solids as function of time at 15.5cm from left wall and at a vertical height of 11.5cm from bottom of bed. The dominant frequency due to gravity is presented in figure 8. The averaged mean velocity for the large-scale oscillation is -2.91cm/sec in the computed range and the fluctuation velocity, the instantaneous velocity minus mean velocity, is about $\pm 8\text{cm/sec}$. The fluctuation velocity for the small-scale oscillation is less than $\pm 0.1\text{cm/sec}$. The turbulent kinetic energy of the large-scale oscillation calculated from square of the fluctuation velocity is significantly higher than that of the small-scale oscillation. Hence the energy from the large-scale oscillation is dominant in the slurry bubble column reactors. It agrees well with the theory that small-scale energy is small compared to the large-scale energy. Therefore, most of the energy is associated with large-scale motions (Tennekes and Lumley, 1972).

The dominant frequency is 0.086 Hz with the maximum power spectral magnitude of 15.975 and the second frequency is about 0.3 Hz with the maximum power spectral magnitude of 7. It is calculated from the fast Fourier transform (FFT) method. Bahary (1994) has measured similar low frequencies and Muddle, et al., (1997) had found a similar low frequency in the bubble columns with no solids. Gidaspow, et al (2001) show that the basic frequency is that caused by gravity, $(g/X_o)^{1/2}$ and that the frequency becomes very small as the volume fraction of particles becomes small. Figure 8B predicts this very well. The dominant frequency is 0.139 Hz.

C. Granular temperature and turbulent intensity. The granular temperature, $2/3$ turbulence kinetic energy, can be introduced as a function of the fluctuation velocity for a large-scale oscillation. Figure 9 shows the comparison of computed and experimental granular temperatures at a bed height of 9 cm with inlet air velocity of 3.37 cm/sec and

inlet liquid velocity of 4.04 cm/sec for 800 μm particles. The experimental results were obtained from particle velocity measurements using a CCD camera technique as a function of radial distance at a bed height of 7cm by Bahary (1994). The computed results were presented from the two-dimensional numerical simulation by Matonis, Gidaspow and Bahary (2001). The granular temperature is about $100(\text{cm/s})^2$, except near the left side in the experiments, where there is a higher granular temperature.

Figure 10 illustrates averaged axial velocity, radial velocity and variance (Reynolds stress) from 15sec to 36sec at a bed height of 9cm for 800 μm particles in our simulation. The computed granular temperature is shown figure 11. Figure 12 shows the profiles for 500 μm particles. The vertical velocity for 800 μm particles shows the asymmetrical structure with a higher at right side and lower at left side due to the flow patterns in shown figure 5. The vertical velocity for 500 μm particles shows the symmetrical profile with a minimum value at the center regime. Both radial velocities are parabolic, with a maximum value in near the center regime. The velocity profiles depend on the selected range for time-averaging in our computed rectangular coordinates system. The stresses are calculated from the velocity vectors directly using equations presented in Table 2. The profiles of figures 10 and 12 and all cases studied show that the vertical and radial Reynolds stress peak generally in near the center regime. Degaleesan, Dudukovic and Pan (2001) show that the vertical and radial Reynolds stresses give higher values in center. The solid volume fraction (0.18 : dilute regime) for 500 μm particles in the slurry bubble column is less than that (0.23 : dense regime) of 800 μm particles with same inlet conditions. Hence the computed results for 500 μm particles show better profiles, with a maximum value in near the center regime.

The granular temperature plot for the whole bed gives higher values in the center region shown in Figure 11(A). The computed granular temperature profile at a bed height of 9cm shown in figure 11(B) has a similar trend to that of the measured profile with a peak at a bed height of about 10cm. Figure 12(C) shows a parabolic granular temperature, with a maximum value in the center region for 500 μm particles. The granular temperature distribution obtained from the fluctuation velocity of solids is generally a parabola of the fourth degree. It is reasonable because the normal stress has a maximum value in the center region, shown in figures 10(B) and 12(B). The computed granular temperature profiles agree well with the maximum granular temperature theory in the developed riser regime for solids-gas flow, described by Gidaspow and Mostofi (2001).

We follow the theory of Sinclair and Jackson (1989) for the granular temperature. In developed flow in a channel with flat walls with flow of elastic particles, the granular temperature balance (Gidaspow, 1994; Jackson, 2000) involves a balance between conduction and generation. In rectangular coordinates it is as follows for a constant conductivity, κ and particle viscosity, μ_s .

$$k \frac{d^2 \mathbf{q}}{dx^2} = -\mathbf{m}_s \left(\frac{\partial v_s}{\partial x} \right)^2 \quad (4)$$

As a limit we had assumed that all dissipation occurs at the wall. We prescribe the wall granular temperature at wall surface; $x = X_0$

$$\mathbf{q}(X_o) = \mathbf{q}_w \quad (5)$$

Assuming, again, the usual Poiseuille flow in a channel with flat walls, integration of equation (4) then gives a fourth-power dependence of granular temperature on radius, like the thermal temperature rise in Poiseuille flow (Schlichting, 1960). In terms of the mean velocity v_s , the relation between the maximum granular temperature, θ_{\max} and v_s then is the same as the relation between the thermal temperature and the mean velocity.

$$\mathbf{q}_{\max} - \mathbf{q}_w = \frac{3}{4} \left(\frac{\mathbf{n}_s}{k} \right) \overline{v_s} \quad (6)$$

Equation (6) shows that the granular temperature is of the order of the solid velocity squared. In the dilute limit the ratio of viscosity to conductivity is 4/15 (Gidaspow, 1994). In dense regime this ratio is near one, which was illustrated with the plots of solids viscosity and granular conductivity as a function of volume fraction for various theories (van Wachem, et al, 2001). Cody, et al (1996) empirically found a similar relation in the bubbling regime for gas-solids flow. Gidaspow and Mostofi (2001) defined turbulent intensity as the granular temperature scaled with the averaged solids velocity (θ_{\max}/v_s), where the wall granular temperature at wall is negligible. They show that the turbulent intensity in the riser flow regime (2% to 20% solid volume fraction) is roughly 50%, or five times higher than that of single phase flow in a pipe.

In this study, the turbulent intensity is estimated as the granular temperature scaled with the absolute value of averaged solids velocity. The turbulent intensity at a bed height of 9cm is about 1.0 for 800 μm particles and 0.45 for 500 μm particles. Degaleesan, Dudukovic and Pan (2001) measured averaged liquid velocity and Reynolds stress in the 14cm bubble column with superficial gas velocity of 9.6 cm/sec and 12 cm/sec, which represents the churn turbulent flow regime. Turbulent intensity scaled with the averaged liquid velocity is about 0.96 and 0.76 for the gas hold-up of 0.2, respectively. The computed values are close to the kinetic theory prediction. Hence it is very important to understand the granular temperature behavior for scale-up and optimum design in the slurry bubble column reactors.

D. Optimum particle size for slurry bubble column reactors. Wu and Gidaspow (2000) used the catalyst size of 50 μm for the methanol synthesis in an Air products/DOE LaPorte slurry bubble column reactor. Krishna, et al. (1997, 1999) used the porous silica particles with a mean diameter of 38 μm in the slurry bubble column reactor. The size of catalyst is typically in the range of 20 μm to 100 μm .

The granular temperature as a function of particle size was computed for the optimum condition in the slurry bubble column reactors. Figure 11 depicts it for particles in the range of 20 μm to 200 μm . The computed granular temperature is about 202 (cm/sec)² for 20 μm . It rises to 356 (cm/sec)² for 60 μm and then decreases to 138 (cm/sec)² for 200 μm . The maximum granular temperature is at 60 μm , with a solid loading of about 10%. It agrees well with the experimental results of Buyevich and Cody (1998) for gas-solid bubbling bed. They showed that Geldart A glass spheres exhibit an order magnitude

higher granular temperature than neighboring Geldart B glass spheres based on the experiments in a gas-solid bubbling bed. The maximum granular temperature at a ratio of fluid velocity to the velocity of minimum fluidization of two is about 35 (cm/sec)^2 for $88\mu\text{m}$ monodispersed glass beads, where the gas was Argon. This difference exists due to the use higher superficial velocity in our computation. The decrease of the granular temperature with the solids volume fraction can be explained due to the decrease of the mean free path of the particles. The rise of granular temperature with the solids volume fraction under dilute conditions is analogous to compression of a gas, where the gas gets hot upon compression (Gidaspow and Mostofi, 2001).

CONCLUSIONS

A review of the literature, suggests that there exists an optimum catalyst size in the slurry bubble column reactor. A new algorithm was developed to find the optimum size. The numerical simulation has shown that this size is $60\mu\text{m}$.

REFERENCES

- Arastoopour, H., D. Lin and D. Gidaspow, "Hydrodynamic Analysis of Pneumatic Transport of a Mixture of Two Particle Sizes," in "Multiphase Transport," ed. T.N. Veziroglu, Hemisphere Pub. Corp., 4, 1853-1871(1980).
- Bahary, M., "Experimental and Computational Studies of Hydrodynamics in Three-Phase and Two-Phase Fluidized Beds," PhD Thesis, Illinois Institute of Technology, Chicago (1994).
- Bechtel Group, "Slurry Reactor Design Studies. Slurry vs. Fixed Bed Reactors For Fischer-Tropsch and Methanol: Final Report, No. DE91005752, Jun. 1990.
- Buyevich, Y. A. and G. D. Cody, "Particle Fluctuations in Homogeneous Fluidized Beds," Prep. for Brighton Word Congress on Particle Tech., 3, Brighton, UK, Paper 207(1998)
- Chen, J. J. J., M. Jamialahmadi and S. M. Li, "Effect of Liquid Depth on Circulation in Bubble Columns: A Visual Study," Chem. Eng. Des., 67, 203-207(1989)
- Cody, G. D., D. J. Goldfarb, G. V. Storch, Jr and A. N. Norris., "Particle Granular Temperature in Gas Fluidized Beds," Powder Technology, 87, 211-232(1996)
- Degaleesan, S., M. Dudukovic and Y. Pan, "Experimental Study of Gas-Induced Liquid-Flow Structures in Bubble Columns," AIChE Journal, 47, 1913-1931(2001).
- Gamwo, I. K., J. S. Halow, D. Gidaspow, R. Mostofi and D. Matonis, "CFD Models for Slurry Bubble Column Reactors," 6th World Congress of Chemical Engineering, Melbourne, September (2001)
- Gidaspow, D., "Multiphase Flow and Fluidization: Continuum and Kinetic Theory Descriptions," Academic Press, New York, NY., (1994).
- Gidaspow, D. M. Bahary and Y. Wu, "Hydrodynamic Models for Slurry Bubble Column Reactors," Proceedings of Coal Liquefaction and Gas Conversion Contractors Review Conference, PP. 397-401, DOE/PETC, Aug. 1995.
- Gidaspow, D., and L. Huilin, "Collisional Viscosity of FCC Particles in a CFB," A.I.Ch.E. Journal, 42, 2503-2510(1996).
- Gidaspow, D., and L. Huilin, "Equation of State and Radial Distribution Functions of FCC Particles in a CFB," A.I.Ch.E. Journal, 44, 279-293(1998).
- Gidaspow, D., L. Huilin and R. Mostofi, "Large Scale Oscillations or Gravity Waves in Risers and Bubbling beds," Proceedings of the Tenth Engineering Foundation Conference on Fluidization, Kwauk M., Li J. and Yang W. -C. editors, New York, 317-324(2001)
- Gidaspow, D. and R. Mostofi, "Maximum Carrying Capacity and Granular Temperature of A, B and C Particles," submitted for publication,(2001)
- Jackson, R., "Hydrodynamic Stability of Fluid-Particle Systems," in Fluidization, edited by J.F.Davidson, R. Cliff and D. Harrison, Academic Press, New York, 47-72(1985).
- Jackson, R., "The Dynamics of Fluidized Particles," Cambridge University Press(2000).
- Jayaswal, U.K., "Hydrodynamics of Multiphase Flows: Separation, Dissemination and Fluidization," Ph.D. Thesis, Illinois Institute of Technology, Chicago (1991).
- Katzer R. J., M. P. Ramage and A. V. Sapre, "Petroleum Refining: Poised for Profound Changes," Chem. Eng. Progress, July, 41-51(2000).

- Krishna, R., J. W. A. de Swart, J. Ellenberger, G. B. Martina and C. Maretto, "Gas Holdup in Slurry Bubble Columns: Effect of Column Diameter and Slurry Concentrations," *AICH Journal*, 43, 311-316(1997).
- Krishna, R., M.I. Urseanu, J.M. Van Baten and J. Ellenberger, "Influence of Scale on the Hydrodynamics of Bubble Columns Operating in the Churn-Turbulent Regime: Experiments vs. Eulerian Simulations," *Chem. Eng. Sci.*, 54, 4903-4911(1999).
- Lyczkowski, R.W., D. Gidaspow, C.w.Solbrig and E.C. Hughes, "Characteristics and Stability Analysis of Transient One-dimensional Two-Phase Flow Equations and their Finite Difference Approximations," *Nuclear Science and Eng.*, 66, 378-396(1978).
- Matonis, D., "Hydrodynamic Simulation of Gas-Liquid-Solid Fluidized Bed," PhD Thesis, Illinois Institute of Technology, Chicago (2000).
- Matonis, D., D. Gidaspow and M. Bahary, "CFD Simulation of Flow and Turbulence in a Slurry Bubble Column," submitted for publication(2001)
- Miller, A. and D. Gidaspow, "Dense, Vertical Gas-Solid Flow in a Pipe," *A.I.Ch.E. Journal*, 38, 1801-1815 (1992).
- Mostofi, R., PhD Thesis in progress, (2000).
- Muddle, R.F., D.J. Lee, J. Resse and L.-S. Fan, "Role of Coherent Structures on Reynolds Stresses in a 2-D Bubble Column," *A.I.Ch.E. Journal*, 43, 913-926(1997).
- Nakamura, K. and C.E. Capes, "Vertical Pneumatic Conveying of Binary Particle Mixtures," *Fluidization Technology*, Vol. II, New York, 1976.
- Pan, Y., M.P. Dudukovic, M. Chang, "Dynamic Simulation of Bubbly Flow in Bubble Columns," *Chem. Eng. Sci.*, 54, 2481-2489(1999).
- Pan, Y., M.P. Dudukovic, M. Chang, "Numerical Investigation of Gas-Driven Flow in 2-D Bubble Columns," *AICHE J.*, 46, 434-448(2000).
- Parkinson, G., "Fischer-Tropsch Comes Back," *Chem. Eng.*, 104, 39-41(1997).
- Pfleger, D., S. Gomes, N. Gilbert, h.-G. Wagner, "Hydrodynamic Simulations of Laboratory Scale Bubble Columns Fundamental Studies of Eulerian-Eulerian Modeling Approach," *Chem. Eng. Sci.*, 54, 5091-5099(1999).
- Rivard, W.C., and M.D. Torrey, "K-FIX: A Computer Program for Transient Two-dimensional, Two-Fluid Flow," LA-NUREG-6623, Los Alamos (1977).
- Savage, S. B., "Granular Flows at High Shear Rates," In R. E. Meyer, *Theory of Dispersed Multiphase Flow*, New York, Academic Press, 339-358(1983)
- Schlichting H., "Boundary Layer Theory," McGraw Hill, New York,(1960)
- Seo, Y. and D. Gidaspow, "An X-ray-gamma-ray of Measurement of Binary Solids Concentrations and Void in Fluidized Beds," *Ind. Eng. Chem. Res.*, 26, 1622-1628 (1987).
- Soo, S.L., "Fluid Dynamics of Multiphase Systems," Blaisdell Publ. Co., Waltham, Ma., (1967).
- Sinclair, J.L. and R. Jackson, "Gas-Particle Flow in a Vertical Pipe with Particle-Particle Interactions," *AICHE J.*, 35, 1473(1989).
- Stewart, H.B. and B. Wendroff, "Two-Phase Flow: Models and Methods," *J. Comput. Phys.*, 56, 363-409 (1984).
- Sun, B. and D. Gidaspow, "Computation of Circulating Fluidized-Bed Riser Flow for the Fluidization VIII Benchmark Test," *Ind. Eng. Chem. Res.*, 38, 787-792 (1999).

- Symal, M. "Multiphase Hydrodynamics of Gas-Solid Flow," Ph.D. Thesis, Illinois Institute of Technology, Chicago, Il., (1985).
- Tennekes H., and J. L. Lumley, "A First Course in Turbulence," The MIT Press, Cambridge, Massachusetts(1972)
- Van Wachem, B. G. M., J. C. Schouten, C. M. van den Bleek, R. Krishna and J. L. Sinclair, "Comparative Analysis of CFD Models of Dense Gas-solid Systems, AIChE Journal, 47, 1035-1051(2001)
- Vikings System International, "Design of Slurry Reactor for Indirect Liquefaction Applications," Report to DOE/PETC by A. Prakash and P.B. Bendale, DE-AC22-89PC89870.
- Wu, Y. and D. Gidaspow, "Hydrodynamic Simulation of Methanol Synthesis in Gas-Liquid Slurry Bubble Column Reactors," Chem. Eng. Sci., 55, 573-587(2000).

ABBREVIATIONS

Abbreviation	Term
C_D	drag coefficient
d_k	characteristic particulate phase diameter
e	coefficient of restitution
g	gravity
G	solid compressive stress modulus
g_o	radial distribution function at contact
k	conductivity
P	continuous phase pressure
P_k	dispersed(particulate) phase pressure
Re_k	Reynolds number for phase k
t	time
u	horizontal velocity, x-direction
v	vertical velocity, z-direction
w	depth velocity, y-direction
v_s	solid velocity of vertical direction
Greek Letters	
β_{km}	interphase momentum transfer coefficient between k and m
e_k	volume fraction of phase k
θ	granular temperature
μ	viscosity
ρ	density
τ_k	stress
f_k	solids' volume fraction at maximum packing
ϕ	particle sphericity
σ^2	variances